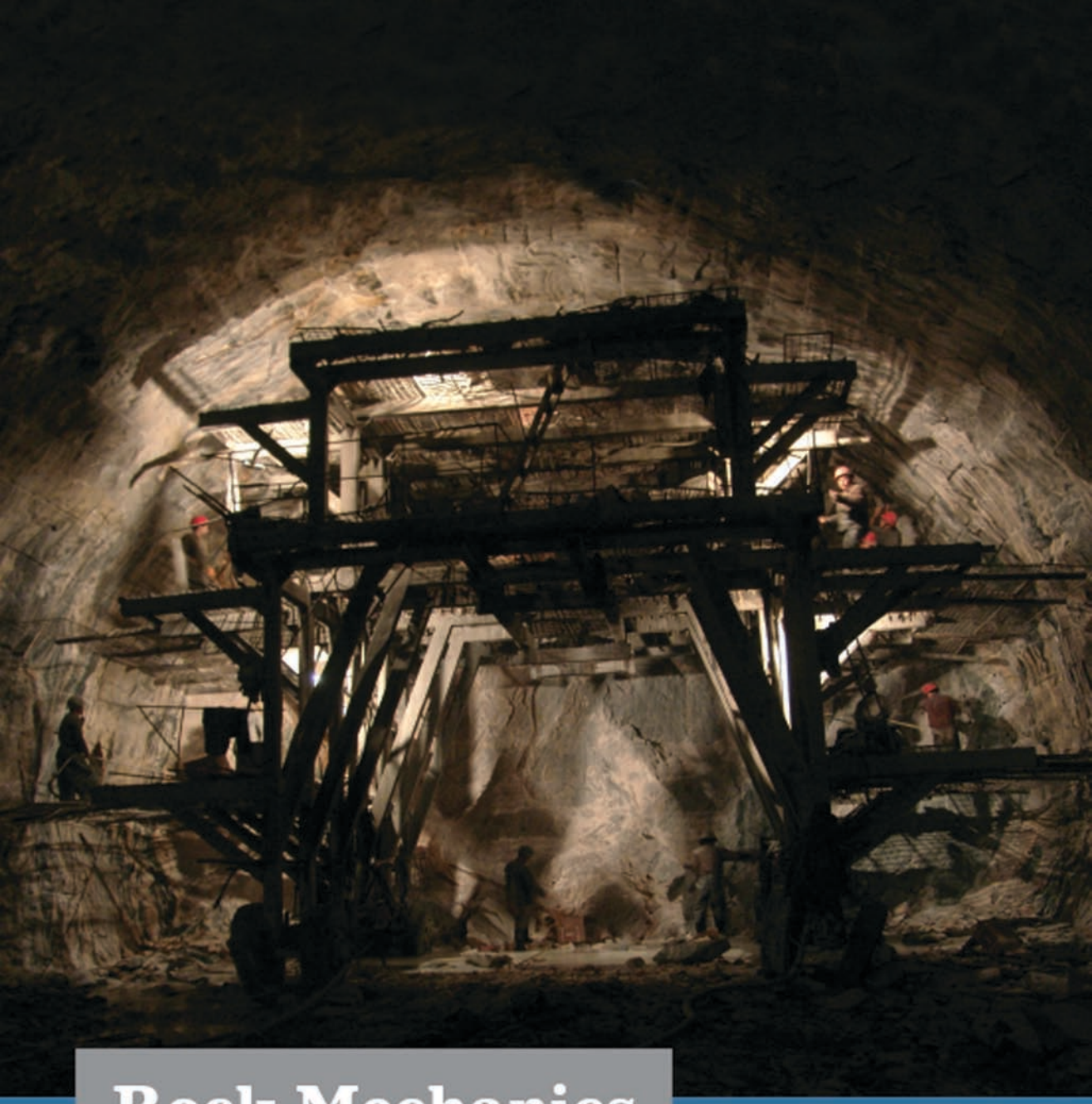


Rock Mechanics and Engineering

Editor: Xia-Ting Feng

Volume 4: Excavation, Support and Monitoring

CRC Press
Taylor & Francis Group
A BALKEMA BOOK

Rock Mechanics and Engineering



Taylor & Francis
Taylor & Francis Group
http://taylorandfrancis.com

Rock Mechanics and Engineering

Volume 4: Excavation, Support and Monitoring

Editor

Xia-Ting Feng

Institute of Rock and Soil Mechanics, Chinese Academy of Sciences, State Key Laboratory of Geomechanics and Geotechnical Engineering, Wuhan, China



CRC Press
Taylor & Francis Group
Boca Raton London New York Leiden

CRC Press is an imprint of the
Taylor & Francis Group, an **informa** business

A BALKEMA BOOK

CRC Press/Balkema is an imprint of the Taylor & Francis Group, an informa business

© 2017 Taylor & Francis Group, London, UK

Typeset by Integra Software Services Private Ltd

Printed and bound in Great Britain by Antony Rowe (A CPI-group Company), Chippenham, Wiltshire

All rights reserved. No part of this publication or the information contained herein may be reproduced, stored in a retrieval system, or transmitted in any form or by any means, electronic, mechanical, by photocopying, recording or otherwise, without written prior permission from the publisher.

Although all care is taken to ensure integrity and the quality of this publication and the information herein, no responsibility is assumed by the publishers nor the author for any damage to the property or persons as a result of operation or use of this publication and/or the information contained herein.

Library of Congress Cataloging-in-Publication Data
Names: Feng, Xia-Ting, editor.
Title: Rock mechanics and engineering / editor, Xia-Ting Feng, Institute of Rock and Soil Mechanics, Chinese Academy of Sciences, State Key Laboratory of Geomechanics and Geotechnical Engineering, Wuhan, China.
Description: Leiden, The Netherlands ; Boca Raton : CRC Press/Balkema, [2017]– | Includes bibliographical references and index. Contents: volume 1. Principles
Identifiers: LCCN 2016053708 (print) | LCCN 2017004736 (ebook) | ISBN 9781138027596 (hardcover : v. 1) | ISBN 9781315364261 (ebook : v. 1)
Subjects: LCSH: Rock mechanics.
Classification: LCC TA706 .R532 2017 (print) | LCC TA706 (ebook) | DDC 624.1/5132–dc23
LC record available at https://lccn.loc.gov/2016053708

Published by: CRC Press/Balkema
P.O. Box 11320, 2301 EH Leiden, The Netherlands
e-mail: Pub.NL@taylorandfrancis.com
www.crcpress.com – www.taylorandfrancis.com

ISBN: 978-1-138-02762-6 (Hardback)
ISBN: 978-1-315-36423-0 (eBook)

Contents

Foreword *ix*
Introduction *xi*

Excavation Methods **1**

1 Excavation 3
R. GALLER

2 Mechanics of directional drilling 51
E. DETOURNAY, J. MARCK & L. PERNEDER

3 Challenges and issues for CO_2 storage in deep coal seams 87
A.S. RANATHUNGA, P.G. RANJITH & M.S.A. PERERA

Support Technology **121**

4 Drift reinforcement design based on Discrete Fracture Network (DFN) modeling 123
J. HADJIGEORGIOU & M. GRENON

5 The needs and technologies for measuring the in situ performance of rock bolts 147
A.J.S. SPEARING, T.R. KOSTECKI & K.V. JESSU

6 Non-deformable support system in swelling and squeezing rocks 179
C.O. AKSOY & G. GULSEV UYAR

7 On-site visualization for advanced safety management in rock engineering 205
S. AKUTAGAWA

8 Longer-term performance of grouted bolts in different lithologies in Illinois mines 237
Y.P. CHUGH, H. GURLEY & W. BELL

9 Tunnel support in South African mines 257
L. J. GARDNER

10 Design of rockburst support systems for deep hard rock mines 279
B.P. SIMSER

11 Energy-absorbing rockbolts 311
C.C. LI

Monitoring Technology 337

12 Microseismic monitoring technologies for deep mining 339
R.J. DURRHEIM

13 Large landslides with seismicity 365
E. BRÜCKL

14 Seismic monitoring of geological CO_2 storage 421
S. LÜTH & A. LIEBSCHER

15 Observation-based design of geo-engineering projects with emphasis on optimization of tunnel support systems and excavation sequences 449
M. SHARIFZADEH, M. GHORBANI & S. YASROBI

16 Moment tensor evaluation of acoustic emission sources in rock 487
G. MANTHEI

17 Fiber-optic monitoring in underground rock engineering 529
H.F. WANG & J.R. GAGE

18 A 3D laser scanning technique and its application to rock mechanics and rock engineering 561
Q. FENG, G. WANG & K. RÖSHOFF

19 Review of GPS displacement monitoring in rock engineering 593
N. SHIMIZU & S. NAKASHIMA

Integrated Engineering Monitoring and Analysis 627

20 Multidisciplinary monitoring of progressive failure processes in brittle rock slopes 629
S. LOEW, V. GISCHIG, F. GLUEER, R. SEIFERT & J. MOORE

21 Particle velocities for rockbursts recorded at seismic stations distributed throughout the Karviná coal mining district 663
K. HOLUB, J. RUŠAJOVÁ & J. HOLEČKO

22 Rockburst induced ground motion 687
Z. ZEMBATY

23 Settlements induced by TBM excavation 701
S. AVERSA, E. BILOTTA, A.M. FERRERO & M. MIGLIAZZA

Series page 725



Taylor & Francis
Taylor & Francis Group
http://taylorandfrancis.com

Foreword

Although engineering activities involving rock have been underway for millennia, we can mark the beginning of the modern era from the year 1962 when the International Society for Rock Mechanics (ISRM) was formally established in Salzburg, Austria. Since that time, both rock engineering itself and the associated rock mechanics research have increased in activity by leaps and bounds, so much so that it is difficult for an engineer or researcher to be aware of all the emerging developments, especially since the information is widely spread in reports, magazines, journals, books and the internet. It is appropriate, if not essential, therefore that periodically an easily accessible structured survey should be made of the currently available knowledge. Thus, we are most grateful to Professor Xia-Ting Feng and his team, and to the Taylor & Francis Group, for preparing this extensive 2017 "Rock Mechanics and Engineering" compendium outlining the state of the art—and which is a publication fitting well within the Taylor & Francis portfolio of ground engineering related titles.

There has previously only been one similar such survey, "Comprehensive Rock Engineering", which was also published as a five-volume set but by Pergamon Press in 1993. Given the exponential increase in rock engineering related activities and research since that year, we must also congratulate Professor Feng and the publisher on the production of this current five-volume survey. Volumes 1 and 2 are concerned with principles plus laboratory and field testing, *i.e.*, understanding the subject and obtaining the key rock property information. Volume 3 covers analysis, modelling and design, *i.e.*, the procedures by which one can predict the rock behaviour in engineering practice. Then, Volume 4 describes engineering procedures and Volume 5 presents a variety of case examples, both these volumes illustrating 'how things are done'. Hence, the volumes with their constituent chapters run through essentially the complete spectrum of rock mechanics and rock engineering knowledge and associated activities.

In looking through the contents of this compendium, I am particularly pleased that Professor Feng has placed emphasis on the strength of rock, modelling rock failure, field testing and Underground Research Laboratories (URLs), numerical modelling methods—which have revolutionised the approach to rock engineering design—and the progression of excavation, support and monitoring, together with supporting case histories. These subjects, enhanced by the other contributions, are the essence of our subject of rock mechanics and rock engineering. To read through the chapters is not only to understand the subject but also to comprehend the state of current knowledge.

I have worked with Professor Feng on a variety of rock mechanics and rock engineering projects and am delighted to say that his efforts in initiating, developing and seeing

through the preparation of this encyclopaedic contribution once again demonstrate his flair for providing significant assistance to the rock mechanics and engineering subject and community. Each of the authors of the contributory chapters is also thanked: they are the virtuosos who have taken time out to write up their expertise within the structured framework of the "Rock Mechanics and Engineering" volumes. There is no doubt that this compendium not only will be of great assistance to all those working in the subject area, whether in research or practice, but it also marks just how far the subject has developed in the 50+ years since 1962 and especially in the 20+ years since the last such survey.

John A. Hudson, Emeritus Professor, Imperial College London, UK
President of the International Society for Rock Mechanics (ISRM) 2007–2011

Introduction

The five-volume book "Comprehensive Rock Engineering" (Editor-in-Chief, Professor John A. Hudson) which was published in 1993 had an important influence on the development of rock mechanics and rock engineering. Indeed the significant and extensive achievements in rock mechanics and engineering during the last 20 years now justify a second compilation. Thus, we are happy to publish 'ROCK MECHANICS AND ENGINEERING', a highly prestigious, multi-volume work, with the editorial advice of Professor John A. Hudson. This new compilation offers an extremely wide-ranging and comprehensive overview of the state-of-the-art in rock mechanics and rock engineering. Intended for an audience of geological, civil, mining and structural engineers, it is composed of reviewed, dedicated contributions by key authors worldwide. The aim has been to make this a leading publication in the field, one which will deserve a place in the library of every engineer involved with rock mechanics and engineering.

We have sought the best contributions from experts in the field to make these five volumes a success, and I really appreciate their hard work and contributions to this project. Also I am extremely grateful to staff at CRC Press / Balkema, Taylor and Francis Group, in particular Mr. Alistair Bright, for his excellent work and kind help. I would like to thank Prof. John A. Hudson for his great help in initiating this publication. I would also thank Dr. Yan Guo for her tireless work on this project.

Editor
Xia-Ting Feng
President of the International Society for Rock Mechanics (ISRM) 2011–2015
July 4, 2016



Taylor & Francis
Taylor & Francis Group
http://taylorandfrancis.com

Excavation Methods



Taylor & Francis
Taylor & Francis Group
http://taylorandfrancis.com

Chapter 1

Excavation

Robert Galler
Chair of Subsurface Engineering, Montanuniversität Leoben, Leoben, Austria

1 INTRODUCTION

In the past excavation technologies were mainly driven by the expected ground conditions and the state of the art technologies available in different parts of the world. In principle this situation has not changed a lot, but nowadays many other influencing factors like environmental issues, vibrations, noise, etc. for choosing the best excavation technology have to be considered. The chapter "excavation" deals with the most common excavation technologies, namely NATM and TBM, where a lot of progress was made in the last few years due to intensive research. Furthermore some failure mechanisms which were often observed at different underground construction sites are summarized. As on many tunnel construction sites the excavated materials are still treated as a waste, the outcome of the European research project DRAGON – which was created for developing resource efficient tunneling – shows. The main goal of this related research was to produce high quality raw materials out of the excavated materials, which is of high interest in regions where depositing areas are not available and primary resources for the construction site as well as for the mineral resources consuming industry are rare.

2 EXCAVATION BY NATM

The development of tunneling methods and construction practices within a particular nation is influenced by many geographical, political, social and cultural factors. Such factors include the geographical situation, topography, existing infrastructure and buildings, environment, natural resources, geological and hydrogeological conditions, the demand for underground works, the political, social and economic situation, technical standards, the legal status and competence of owners, the availability of qualified workforce, mining tradition and contractual views.

Situated in central Europe, Austria is and has always been a vital corridor for the transportation of both people and goods. The country is mainly mountainous and partly hilly; large plains and wide valleys are rare.

In terms of tunneling, the geological conditions in Austria are generally difficult and tend to change rapidly along a tunnel route. Tunneling in the Alps is characterized by high overburden and, in some cases, heavily squeezing rock. However large scale underground construction projects are also common in urban areas where the protection of both the population and the natural environment is paramount.

In the 1950s tunnels in the Alps were primarily constructed in conjunction with hydroelectric projects. Since 1970 an increasing number of tunnels for infrastructure have been built. During this period, owners experienced in tunnel design and construction together with specialized contractors developed an on-site decision making procedure, which became common practice in Austrian tunneling.

At this time Austria had a number of brilliant engineers like Rabcewicz, Müller, Pacher, Lauffer, Seeber, and others who greatly influenced and promoted the development of tunneling in Austria with innovative ideas. Their most important contribution was the development of NATM (New Austrian Tunneling Method), which included the observational approach.

Since 1950 new materials, namely shotcrete and rock anchors, replaced the old timber support and a permanent, in-situ concrete lining was provided in lieu of the traditional masonry lining. In addition, the standardized use of synthetic membranes and fabrics significantly improved the quality of tunnels in terms of water tightness. The technological development along with improved engineering practices paved the way for new theoretical explanations to substantiate an economically beneficial design approach.

The Austrian methodology of tunneling is based on a procedure which requires both construction partners to make immediate, joint decisions with regard to ground conditions. The flexibility to make such decisions is incorporated into the contractual framework to ensure an immediate and effective response to changes in ground conditions. The successful application of the NATM is made possible through the collaboration of qualified and experienced owners, designers, contractors and site engineers working with a knowledgeable, experienced workforce within the framework of a suitable contractual model.

Within the Austrian tunneling community emphasis is placed on good cooperation between all parties involved. Technical questions regarding safe, fast and economical tunneling take priority over contractual considerations. This approach is of general benefit to all parties. It is based on a profound technical expertise and a willingness to cooperate. As a general rule, tunneling projects in Austria are executed on the basis of a unit price contract.

2.1 Principles of conventional tunneling

NATM is based on the concept that the ground around the tunnel not only acts as a load, but also as a load-bearing element. Typically, the excavation and support activities are continuously adjusted to suit the ground conditions, always considering the technical/design requirements. The ground reaction, in the form of lining displacements is measured in order to check the stability of the opening and to optimize excavation and support process.

Depending on the project conditions (*e.g.* shallow soft ground tunnel, deep rock tunnel) and the results of the geotechnical measurements, the requirements for a specific support are determined. Contractual arrangements must be flexible to ensure that the most economical type and amount of support is used.

The typical support elements in NATM are shotcrete and rock dowels. Steel ribs or lattice girders provide limited early support before the shotcrete hardens and ensure correct profile geometry. If ground conditions require support at or ahead of the

excavation face, face dowels, shotcrete, spiles or pipe canopies are installed as required.

The excavation cross-section is subdivided into top heading, bench and invert depending on both ground conditions and logistical requirements (*i.e.* to facilitate the use of standard plant and machinery). Side drift galleries are provided to limit the size of large excavation faces and surface settlements.

2.1.1 Hard rock conditions

The basis for the design of tunnels in rock depends on both the ground conditions and the use of the tunnel (water, road, railway tunnel, etc.). Tunnels excavated in sound rock are generally horse-shoe shaped, whereas tunnels excavated in poor rock generally require an invert arch to ensure stability. The tunnel is typically advanced by drill and blast following a sequential excavation method (top heading, bench, invert). However if favorable rock conditions are anticipated, full-face excavation can be used. The bench is excavated simultaneously to the top heading, up to a few hundred meters behind the excavation face, providing a ramp for access to the heading. Some distance behind the bench, the invert is excavated. If ground conditions are unfavorable, an invert arch is provided to close the lining, forming a complete ring.

2.1.2 Squeezing rock conditions

Tunnels excavated in weak rock and high overburden exhibit fracturing and large deformations due to high stresses around the opening which exceed the ground



Figure 1 Pilot tunnel in hard rock conditions [Photo: Site Supervision Exploration Tunnel Paierdorf, Koralm Tunnel, ÖBB].



Figure 2 Yielding elements installed in longitudinal slots in the top heading [Photo: PORR Tunnelbau GmbH, Tauerntunnel, ASFINAG].

strength. In order to effectively manage these large deformations, a number of important design parameters must be established. These include definition of the over-excavation required to provide the deformation allowance, as well as the determination of support measures. A support system which allows controlled deformation is chosen to limit the required support resistance and to achieve stability. To increase the shear strength of the rock mass, the key support element is the use of rock dowels. The shotcrete lining thickness is typically 0.2 m to 0.3 m. In case of large displacements longitudinal slots in the shotcrete lining and yielding support elements are placed to allow deformation without damage to the lining. Once the rock pressure is significantly reduced and stabilization of the opening is confirmed by monitoring, the slots in the lining are closed with shotcrete. Yielding elements are integrated into the shotcrete lining. These yielding elements act to limit the normal forces in the shotcrete lining, thus preventing overstressing and preserving the support capacity. Figure 2 shows the use of the deformable support system.

2.1.3 Soft ground conditions

Shallow tunnels in soft ground require the use of both a rigid support and a predetermined sequence of advance. In conventional soft ground tunneling, the emphasis is on a rigid shotcrete lining, a short advance length and a rapid invert closure. If required, the cross section is divided into side and center drifts. Auxiliary measures like dewatering wells, compressed air, jet grouting or even ground freezing are also applied where necessary. In addition to the geological, hydrogeological and geotechnical conditions, the design of tunnels in soft ground must also consider the use of the tunnel, environmental factors and minimizing surface settlements.

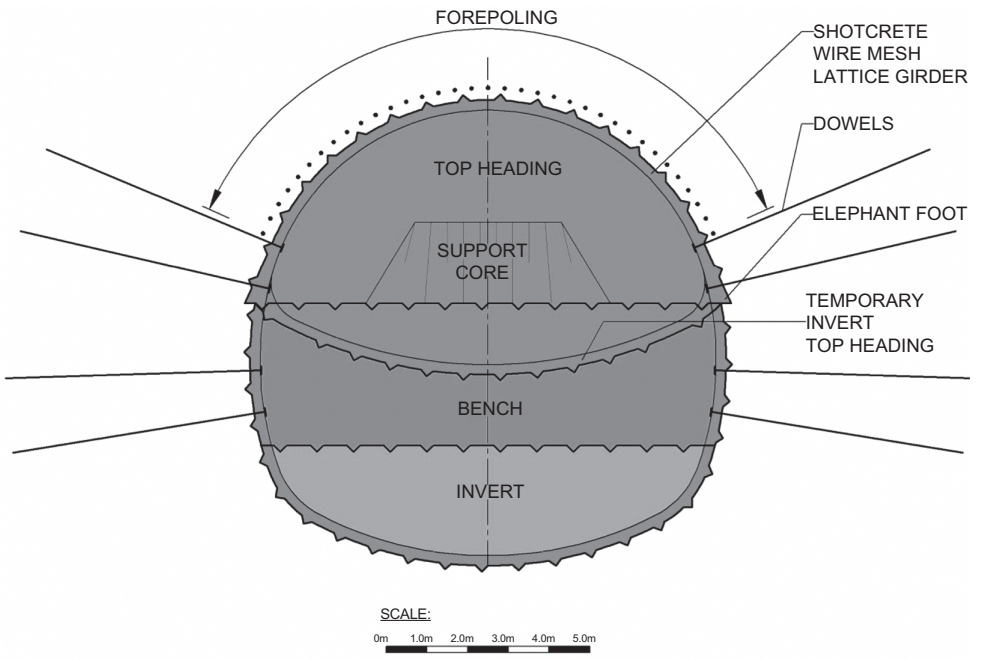


Figure 3 Typical excavation and support in soft ground conditions [NATM – the Austrian way of conventional tunneling; ISBN 978-3-200-01989-8].

The excavation sequence is typically split into top heading – bench – invert. Face support (supporting core), elephant feet, a temporary invert in the top heading and the arrangement of a pipe canopy can be employed.

The length of the excavation rounds for this example is limited to a maximum of 1.0 m in the top heading, 2.0 m in the bench and 4.0 m in the invert. The closure of the temporary invert follows 5.0 m to 7.0 m behind the face of the top heading. The closure of the invert follows 2.0 m to 6.0 m behind the face of the bench. The advance rate is related to the quality of the young shotcrete. Typically it is restricted to 5.0 m in 24 hours in the top heading and 8.0 m in 24 hours in the bench and invert to limit stresses in the primary lining.

The excavation of tunnels with large cross sections in shallow overburden requires that the size of the excavation face be reduced to limit surface settlement. This can be achieved by using an excavation sequence consisting of two sidewall drifts and a center core.

In this example the side wall drifts serve as both a pilot tunnel and a foundation for the crown support. The side wall drifts are advanced individually employing an excavation sequence with a short top heading followed by early invert closure as shown in Figure 4.

Particular attention is given to facilitate the connection of side wall drift linings with the crown support and invert of the core. After breakthrough, or at a substantial distance behind the side wall drifts, Core 1 is advanced as an essentially independent operation, using 1.0 m long rounds and a top heading and bench sequence (see Figure 4). Core 2

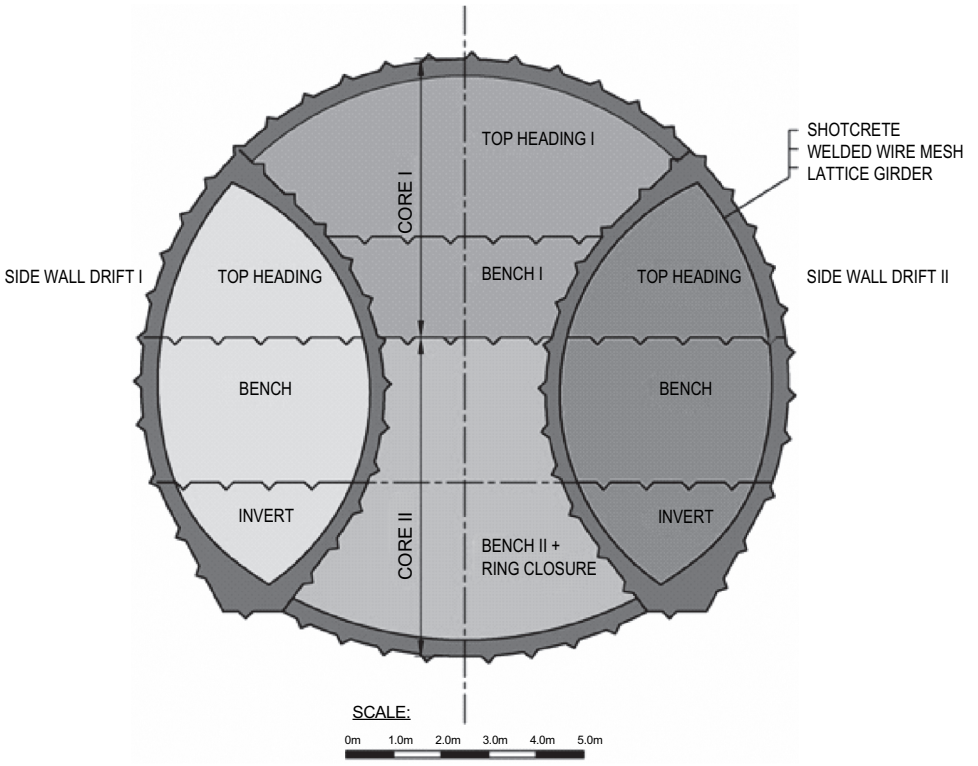


Figure 4 Typical excavation and support for side wall drift method [NATM – the Austrian way of conventional tunnelling; ISBN 978-3-200-01989-8].



Figure 5 Double track railway tunnel in urban environment [Design Team Lainzer Tunnel LT31, ÖBB].

excavation follows at a distance which is dependent on the arrangement of plant employed by the contractor. Just before ring closure of the complete cross section (in typically 2.0 m long advance rounds) the temporary side walls are removed at this location.

2.2 Design stages

In general, tunnel design can be carried out by the client's own engineering team, by the design engineer appointed by the client or by the construction contractor's design team. In Austria, a client would typically appoint a design engineer to be responsible for the design in all stages of a conventional tunnel project. However, on rare occasions, multiple design consultants are appointed, each being responsible for a different stage of the project.

The design of a tunnel project is subdivided into four principal stages which are the conceptual design including feasibility study, the Preliminary design, the Tender design and the Final design. The purpose of the conceptual design is to select or finalize the tunnel alignment and to provide a cost estimate. In the preliminary design stage, the conceptual design of the project is refined based on the selected alignment and an Environmental Impact Study is carried out. In this stage the main focus is on environmental matters, particularly on the legal aspects of water resources, forestry and nature protection. However, the common target in the preliminary design is to receive the approval for construction of the project by the authorities. The scope of the tender design is to detail the works to the extent that the exact pricing of each work item can be determined. At this stage, the contractual documents are compiled. The scope of the final design is to detail the work described in the tender stage for construction purposes.

2.3 Overview of ground investigations

The geological investigations are the client's responsibility. Geological, hydrogeological and geotechnical investigations shall be planned and supervised by experienced geologists in close cooperation with the design engineer and the client. All investigated data (geological, hydrogeological, geotechnical) are summarized in a report. Full disclosure of all data is provided for geotechnical design.

The extent of the site investigation program carried out is always project-specific. The investigations are executed in steps which correspond to the design stages and the complexity of the geological conditions. In zones of predicted hazards such as faults, high in-situ stresses, mass movements, cavities, in portal areas and in zones with shallow overburden the ground must be investigated in greater detail. During construction, further site investigations especially probing ahead of the face may be required depending on the remaining degree of uncertainty, the type of hazards predicted, the sensitivity of excavation method to changes in ground conditions and the actual conditions encountered.

2.3.1 Geological conditions

A complete understanding of the geological structure of the area forms the basis for the description of the geological conditions. This includes the regional geological environment, the lithological sequences and the tectonic setting. A description of the geological

conditions shall be provided for each geological unit, which is defined by comparable lithology and structure. The qualitative description shall be accompanied by quantitative information. In the description of soils, geological units are normally grouped according to the origin of the geological formations (*e.g.* moraines, river gravels, colluvium, and clay deposits). Soils are described according to their geotechnical properties and are classified into standard groups. These properties include grain sizes, shape, degree of roundness, degree of weathering, strength, swelling capacity, soil structure like layering and anisotropy, plasticity, compaction as well as special features like the presence of blocks or organic constituents or sensitivity when exposed to water. The intact rock description shall include elements like mineral content, structure and texture and petrographic identification, while the description of rock mass shall include elements like the geological composition (*e.g.* stratification, foliation), discontinuities, degree of weathering, karst formations and hydrothermal alterations. Fault zones are treated as individual homogeneous zones when they are of special significance to the project.

2.3.2 Hydrogeological conditions

A description of hydrogeological conditions must include both local and regional characteristics. In particular, aquifers, their possible interaction, confined / unconfined aquifers and water barriers as well as the flow conditions and the connection to water at the surface are summarized. In particular items like Groundwater levels, permeability, type of circulation, type of aquifer, direction of water flow, velocity of water flow, hydraulic conductivity, water chemistry, carbonate reaction, carbonate equilibrium, pore pressure, location of springs and wells with registration of field parameters, storage capacity of rocks and soils are required.

2.3.3 Geotechnical investigations and tests

Geotechnical parameters which are relevant for design and construction are determined in laboratory and field tests. Parameters like primary stresses, geophysical properties, strength properties (*e.g.* UCS, cohesion, angle of friction), Young's modulus, deformation modulus, swelling potential, conductivity, transmissivity and abrasivity shall be measured.

When defining the testing program, the number of tests, size of specimen, internal structure of specimens in relation to testing direction, type of failure mode and the range of values shall be indicated. Comparative values, empirical values and estimates shall be denoted as such. The sources of testing shall be given. If available, standard procedures for testing such as provided by the ISRM may be adopted. For rock, it is necessary to clearly distinguish between the geotechnical data for the intact rock and the rock mass including discontinuities (*i.e.* rock boundaries, fracture surfaces, weathering) and their properties. Additional information relevant for the specific project like gas occurrence (type of gas, potential gas source, gas reservoir with migration paths), creep movements and landslides, neotectonic occurrences, temperature (ground, ground water), seismic activity, substances generating health hazards (quartz, asbestos etc.), radioactivity, residual waste or contaminated ground as well as ground water contamination shall be studied.

2.4 Geotechnical design and geotechnical safety management

A sound and economically viable tunnel design depends on a realistic geological model, an accurate ground characterization and the assessment of key contributing factors such as primary stresses, groundwater and kinematics. Despite this requirement, a tunnel design based primarily on experience and basic empirical calculations. In addition, modifications to excavation and support designs made on site are often based on site specific analysis. To improve transparency of the design and construction process a *Guideline for the Geotechnical Design of Underground Structures with Conventional Excavation* was developed and published by the Austrian Society for Geomechanics.

In the design of underground structures, the geotechnical conditions, the static system and the load bearing capacity of the ground and support can be quite variable. As such, the design of underground structures cannot be compared to the structural design of buildings, where the loads and the material properties are well known. To minimize these risks, a safety management system shall be implemented. The safety management system must cover design requirements for excavation and support, criteria for the assessment of stability during construction, a monitoring plan including all technical and organizational measures to allow continuous comparison between the expected and actual conditions as well as a management plan to deal with deviations from the predicted System Behavior.

The main task of the geotechnical design is the economic optimization of the construction considering the ground conditions as well as safety, long term stability, and environmental requirements. The variability of the geological composition including the local ground structure, ground parameters, stress and ground water conditions require a consistent and specific procedure be used during the design process. In spite of all uncertainties in the description of the ground conditions, underground engineering needs a strategy, allowing a consistent and coherent design procedure that is traceable throughout the entire project, and an optimal adjustment of the support measures to the actual ground conditions encountered on site. Geotechnical design is typically accomplished in two main phases, namely the design phase and the construction phase.

Phase 1: Design

This phase involves the determination of expected ground properties, the classification into Ground Types (GT), the assessment of the Ground Behaviors, its categorization into Behavior Types (BT), as well as the determination of support measures derived from the ground behavior under consideration of the project specific boundary conditions. On this basis the expected System Behavior is predicted. Excavation classes are then determined according to the rules stipulated in ONORM B 2203-1. The results of all phases of the geotechnical design are summarized in a geotechnical report. The geotechnical report must clearly state the ground conditions, boundary conditions, and other assumptions on which the design is based. The framework plan is part of the geotechnical report. This plan has to contain clear application criteria, and shall indicate which measures shall not be modified during construction without consent of the designer, as well as the criteria for possible modifications and adjustments during construction.

Phase 2: Construction
During construction, all ground parameters relevant to the geotechnical design have to be collected, recorded and evaluated to determine the ground type. Excavation and support measures have to be chosen based on the criteria laid out in the framework plan and the safety management plan. The geotechnical design and the framework plan have to be continuously updated based on the findings on site. The improved quality of the geotechnical model allows an optimization of the construction while observing all safety and environmental requirements.

The relevant data and assumptions made for all decisions during design and construction have to be recorded. Relevant information in connection with the ground properties and system behavior has to be documented, evaluated and analyzed in both phases. All concepts, considerations and decisions shall be recorded in a way that a review of the decision making process is possible. The basic procedure for geotechnical design begins with the determination of the Ground Types and ends with the definition of the excavation classes.

2.5 Monitoring and data evaluation

Systematic and frequent monitoring, observation and interpretation are important components of the NATM. The program for monitoring, observation and interpretation is designed to capture the range of expected system behaviors. The main function of the program is to determine whether the observed system behavior lies within expected limits and to validate the appropriateness of the excavation and support measures. Another aspect is the prediction of the system behavior and the update of the geological/geotechnical model. Typically 3D displacement measurement in the tunnel and on the surface (if required), extensometers, sliding micrometers, inclinometers, load cells for dowels, strain gauges, pressure cells and piezometers are used to observe the system behavior. To enable a quick visualization, reliable evaluation and interpretation of the monitoring results, special software is used.

Measurements are done by using a total station and targets. Precise prism-targets as well as bireflex-targets are used to obtain their spatial position. Geotechnical conditions govern the intervals and layout of the monitoring sections.

Typically 3 to 7 targets are installed in a monitoring cross section. The distance between measurement cross sections is typically 5.0 m to 25.0 m, depending on the ground behavior and the sensitivity of the project environment. The targets are mounted on special bolts with an adapter (see Figure 8). Targets are installed close to the face and zero readings done immediately after installation. Readings are typically taken daily; the frequency is reduced with distance to the face and decreasing rates of displacements. Extensometers and sliding micrometers are used to determine the shortening or elongation between two points in the ground. Inclinometers provide information on the deflection along a line in the ground. They are usually installed from the surface to monitor displacements of the ground caused by the tunnel advance. Extensometers and in some cases longitudinal inclinometers are also installed in the tunnel. Strain gauges are installed to measure the strain in the lining. The pressure between lining and ground as well as the stresses in the lining are obtained by pressure cells. Occasionally load cells are installed to measure the force in dowels. Piezometers are used to measure the ground water pressure.

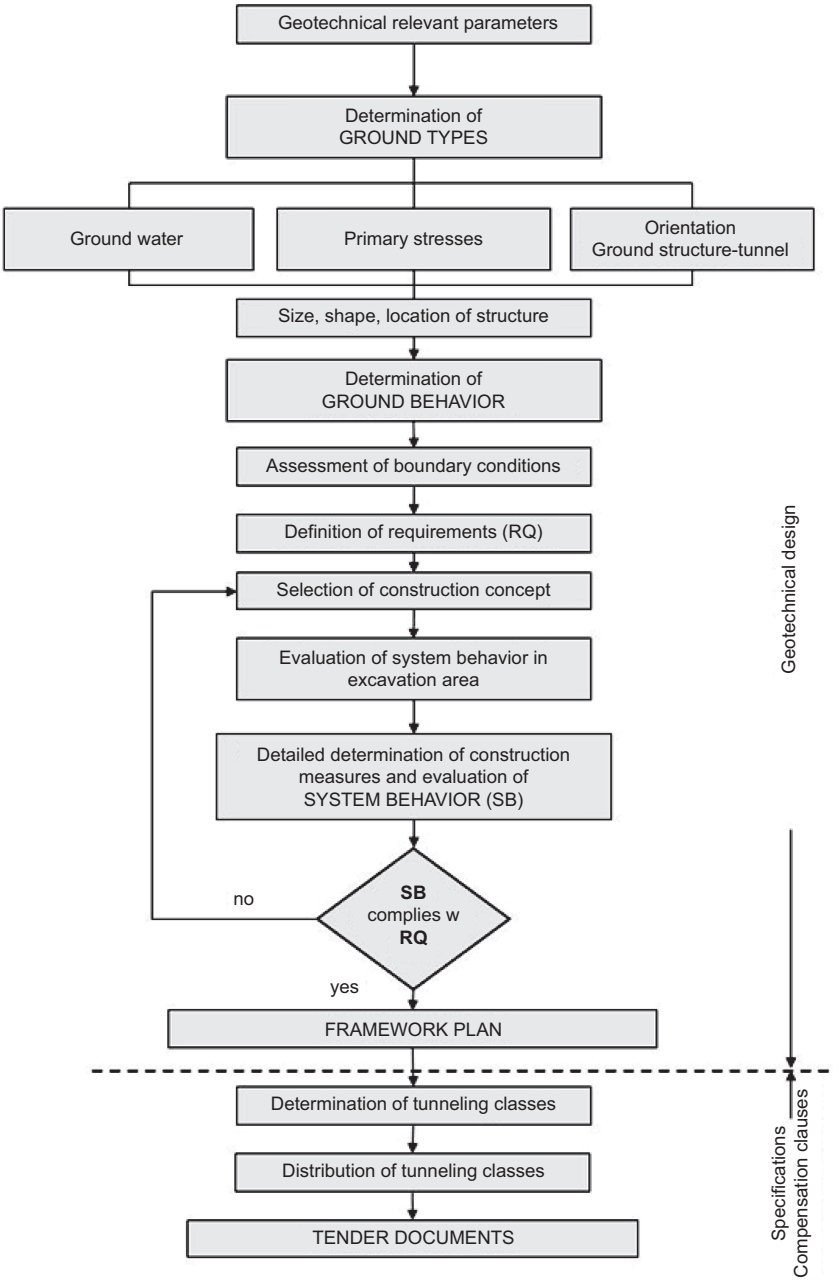


Figure 6 Flow chart showing the geotechnical design process [ÖGG – Guideline for the Geotechnical Design of Underground Structures with Conventional Excavation].

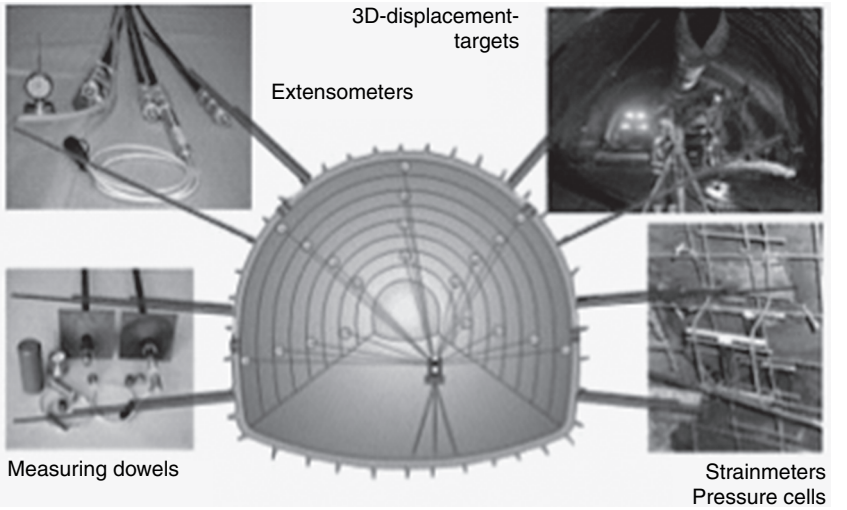


Figure 7 Example of monitoring section – optical 3D displacement measurements, extensometers, piezometers, measuring dowels, strain gauges and pressure cells [GEODATA, Leoben, Austria].

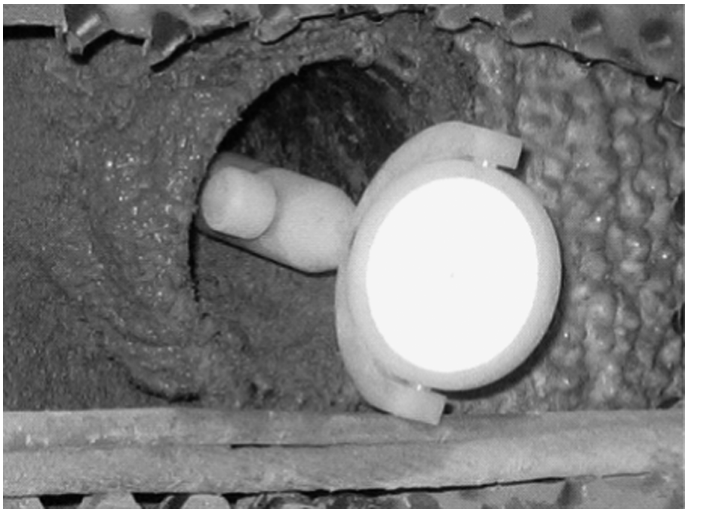


Figure 8 Example of monitoring target with protection pipe to avoid damage of the bolt [NATM – the Austrian way of conventional tunnelling; ISBN 978-3-200-01989-8].

2.5.1 Presentation of monitoring data

Monitoring data are usually presented in time-displacement diagrams, distance-displacement diagrams, deflection curve diagram with trend lines, displacement vector diagrams, contour plots of the level of loading in the lining and contour plot of surface settlements.

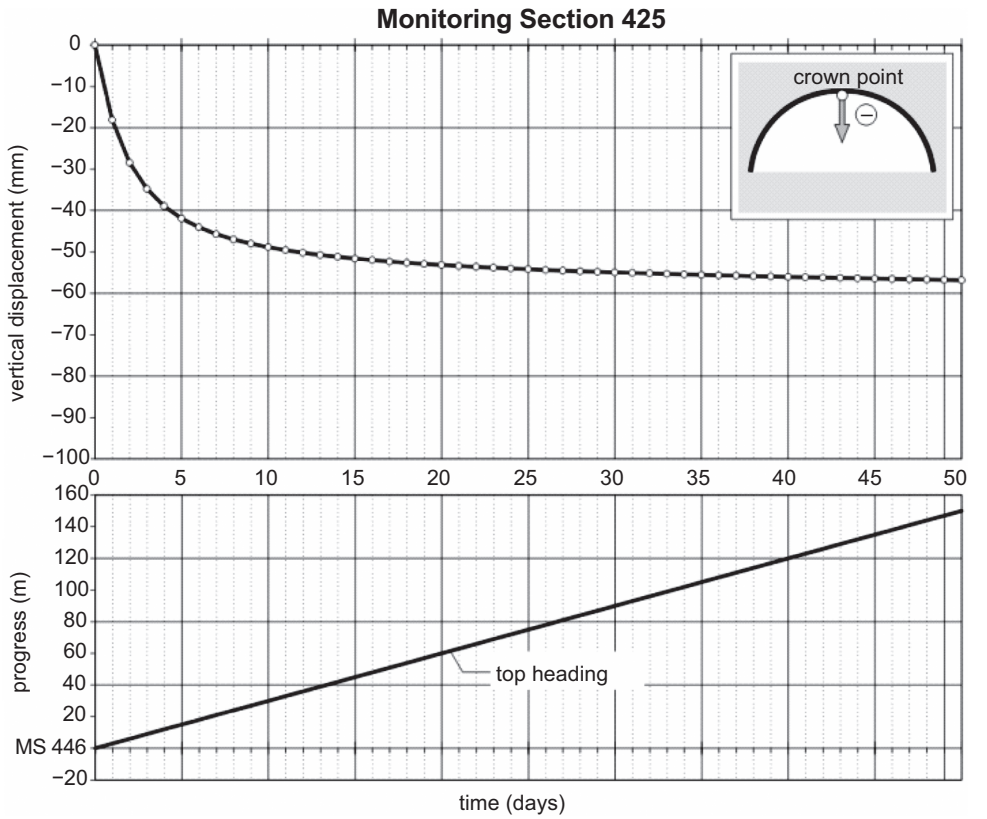


Figure 9 Typical time-displacement plot for constant excavation rate [ÖGG – Handbook for Geotechnical Monitoring in Conventional Tunnelling].

Time – displacement diagram

Time-displacement diagrams are used to present vertical, horizontal and longitudinal displacement components versus time. Typically, the results of the displacement measurements of all targets in one monitoring cross section are plotted in one diagram. Construction phases are also presented on the same plot, allowing correlation between construction activities and displacements. The displacement history is used to assess the stabilization process. Figure 9 shows an example of a characteristic time-displacement plot.

Displacement – distance diagram

In Figure 10 the vertical displacements are plotted versus the distance to the tunnel face. Time dependent displacements during the stop of the excavation are shown in the vertical offset 6.0 m behind the face.

Deflection curve diagram with trend line

A deflection curve represents the status of displacements of one position in cross section along the tunnel (*e.g.* crown points) at a particular time. Deflection curves of

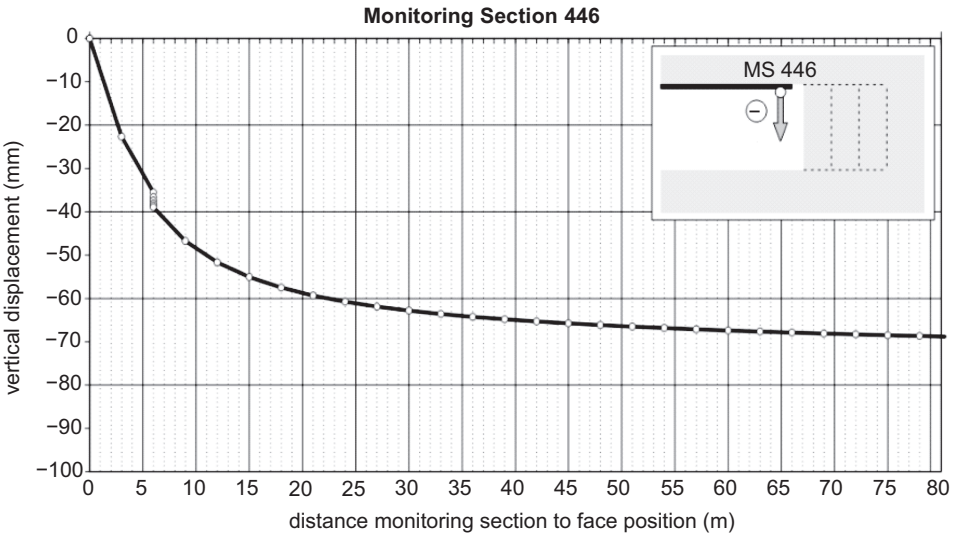


Figure 10 Distance-displacement plot for discontinuous excavation [ÖGG – Handbook for Geotechnical Monitoring in Conventional Tunnelling].

consecutive readings are plotted on one diagram for each component of the displacement vector (x, y, z-coordinate). Figure 11 shows the influence of each excavation step on previously excavated and supported tunnel sections.

The "pre-displacement" is the displacement occurring between the face and the zero reading of the first target. This cannot be measured. Therefore it has to be determined by extrapolation and added to compare the measurements. Deflection curves are

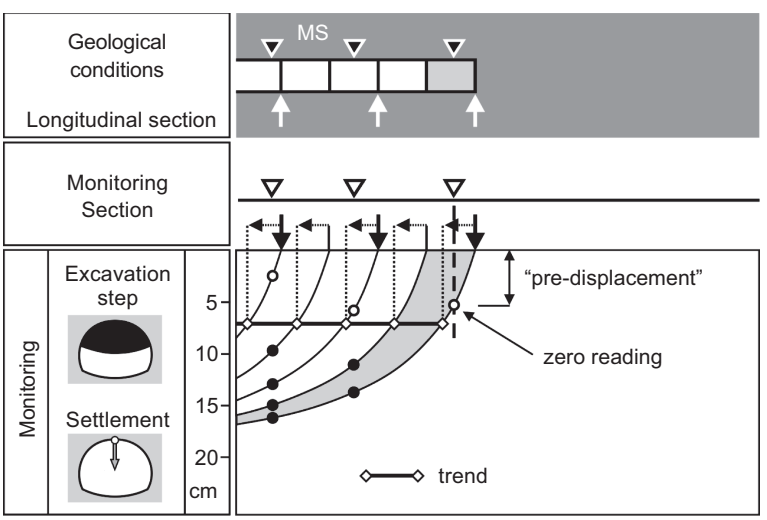


Figure 11 Deflection curve diagram for crown position showing the estimation of "pre-displacements" and construction of trend line [ÖGG – Handbook for Geotechnical Monitoring in Conventional Tunnelling].

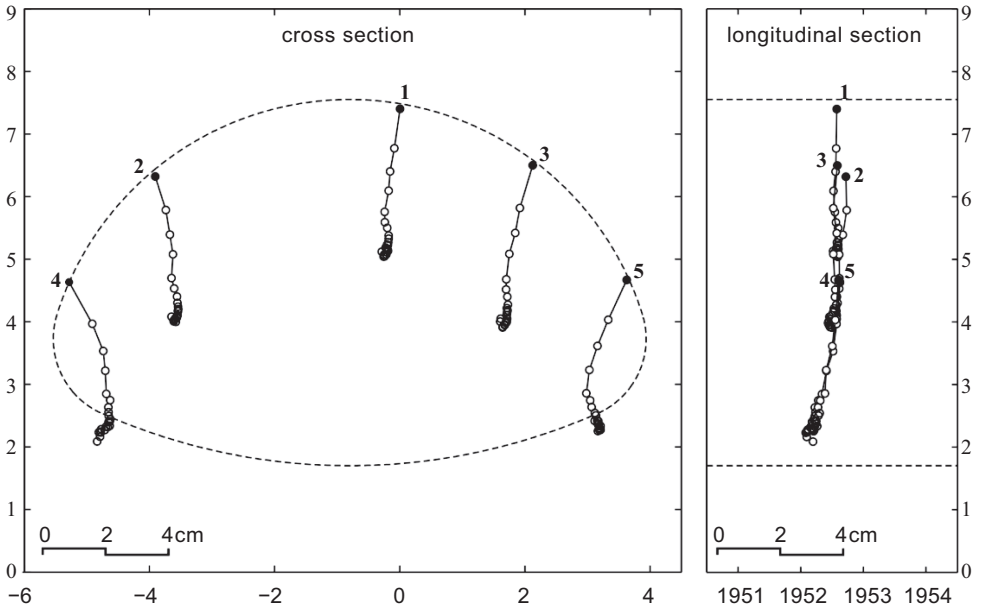


Figure 12 Deflection curve diagram for crown position showing the estimation of "pre-displacements" and construction of trend line [ÖGG – Handbook for Geotechnical Monitoring in Conventional Tunnelling].

usually combined with a trend line. Trend lines are created by connecting values from the deflection curves at a constant distance behind the face.

Displacement vector diagram

The displacement vector diagram assists in interpreting the influence of the ground structure (*e.g.* the orientation of discontinuities) on the behavior.

Vector plots evaluated for a monitoring cross section are used to show the orientation of displacements as well as the development of displacements with time.

Level of loading in the shotcrete lining

The displacements measured can also be used to evaluate the strains in the lining.

The time dependent development of the shotcrete properties is considered in the calculation of the lining stresses. The level of loading is defined as the ratio between the stress and the ultimate strength of shotcrete. It is usually shown as contour plot. The example shown in Figure 13 is from a tunnel with shallow overburden in an urban environment, excavated with side galleries followed by core excavation. The contour plot provides a quick overview of the utilization of the shotcrete lining.

2.5.2 Interpretation

Plotting the displacement vectors allows the detection of deviations from the normal behavior caused by features outside the excavated cross section. Figure 14 shows an example of the influence of a steeply dipping fault, striking sub-parallel to the

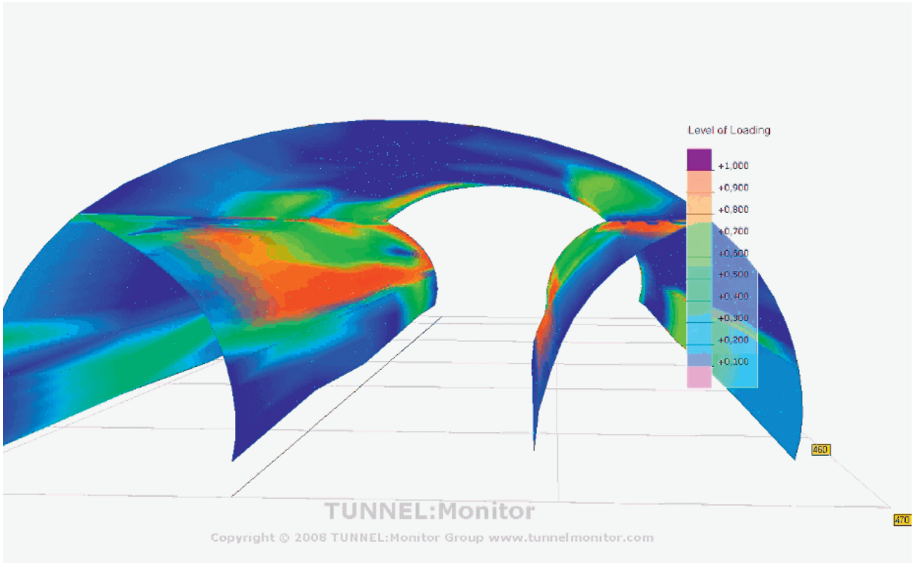


Figure 13 Example of the distribution of the level of loading in the shotcrete lining at a certain time; Tunnel driven with side wall galleries and core excavation (Note: Red color indicates very high load level; Blue color indicates a low load level [ÖGG –Handbook for Geotechnical Monitoring in Conventional Tunnelling].

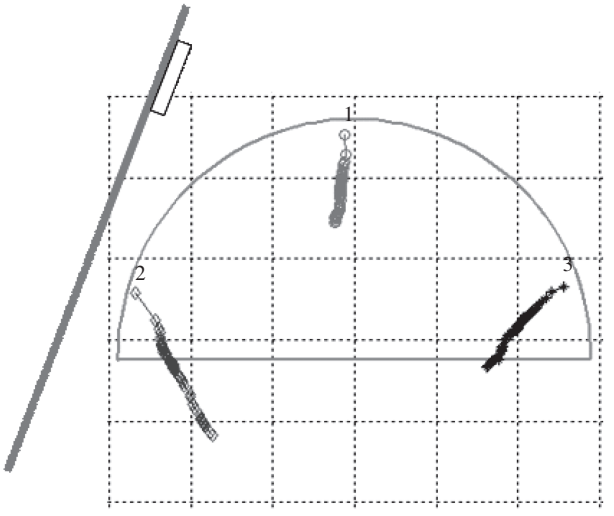


Figure 14 Displacement vector plot – influence of a fault outside the excavated cross section [ÖGG – Handbook for Geotechnical Monitoring in Conventional Tunnelling].

tunnel axis. The stress concentration between sidewall and fault causes increased displacements.

2.6 Construction site organization

The organization of the project execution according to the NATM contract model is outlined in the following figure.

The client is finally responsible for the measures implemented to solve technical problems, any variations in cost or schedule and acceptance of remedial measures to correct defects. The project management is carried out by the client's experienced personnel or by an appointed consultant. During construction the design engineer prepares the detailed design in accordance with the contractor's means and methods. Therefore he is to be involved in site decisions which require changes to the design. Upon completion of the work, the design engineer and the site supervision jointly commission the works. The client usually appoints a consulting engineer to act as the site supervising engineer, responsible for the overall supervision of the construction work. The site supervision safeguards the interests of the client by ensuring that the work is completed in accordance with the contract conditions. The resident engineer (site supervising engineer) reviews the encountered geological conditions with the contractor's representative (site manager) and determines the details of the excavation method – *e.g.* round length, partial opening of the face, amount and type of support measures etc. in mutual agreement. This requires daily meetings with the

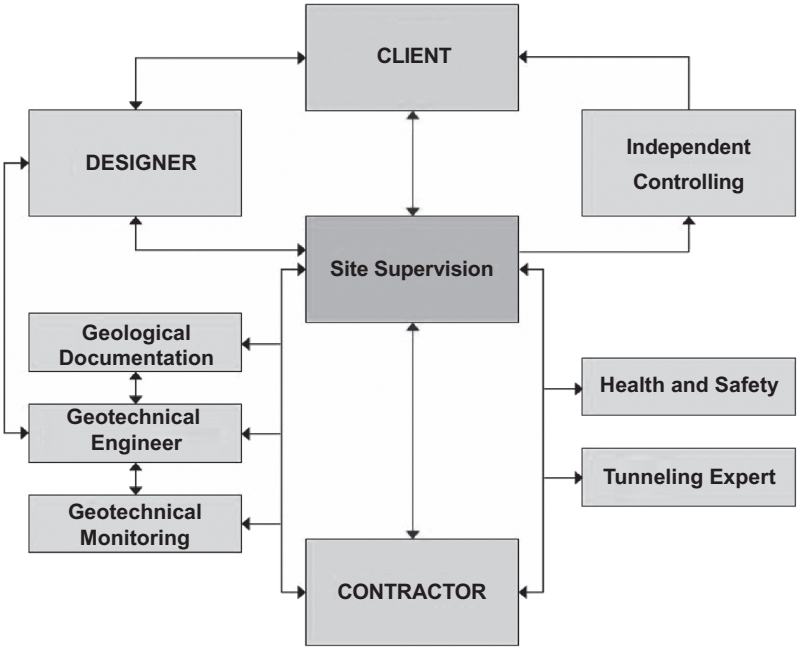


Figure 15 Organisation chart [NATM – the Austrian way of conventional tunnelling; ISBN 978-3-200-01989-8].

contractor at the face of the excavation. Regarding quality and costs of the construction works the supervision engineer has to check the proper use and handling of construction material, establish measurement schedules and review the contractor's invoices. Finally he supervises the remediation of any defects. The contractor carries out the work according to the contract conditions. Means and methods are the contractor's responsibility. He is also responsible for the safety of works and the health of workers. The contractor's site manager participates in daily meetings with the client's site supervising engineer, where details of the excavation method and adjustments of the support measures are mutually agreed.

Apart from organization and execution of the work, the site manager of the contractor must ensure quality requirements are met and completed on schedule. The client appoints geologists which independently record geological conditions at the face and eventually advise on additional probing ahead. It is their task to produce short term predictions for the next round length. It is general practice in Austria to appoint a monitoring team independently from other surveying works. This team carries out all geotechnical measurements day by day and is responsible for evaluation and distribution of monitoring results. The client usually appoints a geotechnical engineer who supports the site manager and the site supervision in the interpretation of the geotechnical monitoring results and in the determination of the support measures taking into account the geological documentation and short term predictions. The preferred solution is to appoint the design engineer to take over this position.

Rather than retaining an independent dispute resolution board, the Austrian standard stipulates that for technical disputes an independent expert is selected by the client in agreement with the contractor during the tender process. The commitment of a dispute review board is a recommended alternative. The implementation of health and safety measures is controlled by an independent ordinance. In addition to the design engineer, in complex projects additional specialists and consultants are called in, such as environmentalists etc.

The mutual decisions of the site supervisor and the contractor's representative are made in daily meetings regarding face observations and geotechnical interpretation of the ground behavior and documented in "Required Support Sheets", which are signed by the client's and contractor's representative.

3 EXCAVATION BY TBM – SOME DIFFERENCES TO EXCAVATION BY NATM

3.1 Geotechnical design

Compared to NATM the use of TBMs requires some process-related design-aspects, which are considered in the Austrian Guideline for Underground works using TBMs. Due to the fact that parameters evaluated from any exploration step have limited accuracy and past projects showed that TBMs have almost no flexibility, excavation by a TBM needs much more exploration for the design *e.g.* to be able to pass fault zones. It is very clear that there is almost no chance to change the construction concept after having started the TBM drive. Depending on the type of TBM there is a fixed spatial distance for installing the support. Forepoling support can only be done with

very high efforts. The system behavior design has to be determined by considering both the excavation and the type of TBM. 3D-displacement monitoring is almost impossible but some machine monitoring parameters are available. Related to the safety management based on the Eurocode 7 a clear strategy for the verification of the assumptions, evaluation of safety, proofing the allowed impacts on the environment and steering the required construction and mechanical measures have to guaranteed. A monitoring and management concept including all technical and organizational requirements, which allows an online comparison between the expected and the in-situ conditions, has to be installed. Regarding the design both RVS09.01.42 and the guideline for segmental lining design should be acknowledged.

3.2 Rock failure and crack propagation beneath disk cutters

In parallel with mini cutter tests using scaled disks in the laboratory, the cutting process should also be numerically modeled. The objective of the numerical simulation is on the one hand to obtain approximately similar rolling forces as in a real cutting test, and on the other hand to realistically portray the rock-specific crack patterns, which should be used as basic information for the selection and the geometrical configuration of the disks on the cutter head.

3.3 Penetration tests for TBMs and their practical application

Characterizing performance of tunnel boring machines is important for numerous contractual and technical reasons. A common tool to determine machine performance in the field is the penetration test. The purpose of the penetration test is to operate the TBM for a defined period of time under normalized conditions that allow for interpretation and comparison between tests. The result of a penetration test is a thrust-penetration curve that reflects the excavatability of the rock mass. Prediction models use thrust-penetration curves to calculate the expected performance of a TBM in specific ground conditions. A very generic approach to show the excavatability is to use a thrust-penetration curve as shown in Figure 16. Thrust per disk cutter is shown on the y-axis and the corresponding penetration rate is shown on the x-axis.

At low penetration rates, the thrust increases significantly until a penetration rate of about 1 to 2 mm is exceeded where the relationship between penetration rate and thrust becomes almost linear. At very low penetration rates, only crushing occurs, but no tensile cracks form. In addition, a stress field is induced into the rock mass which leads to tensile cracks perpendicular to the trajectories of compressive stress. Once the cracks intersect, rock chips form and are expelled from the rock, corresponding to the linear portion of the curve.

The main purpose of penetration tests is to record the performance of a TBM in a given geology. Hence, geological mapping is an integral part of this penetration test. The procedure calls for at least four different thrust levels ranging from 70 to 100 % of the thrust used prior to the beginning of the test. An additional 105 % thrust level is recommended if this is permissible. A minimum of 30 revolutions of the cutterhead must be made for each thrust level. Cutterhead torque, net penetration rate, and RPM are recorded during the test. In addition, operating data before

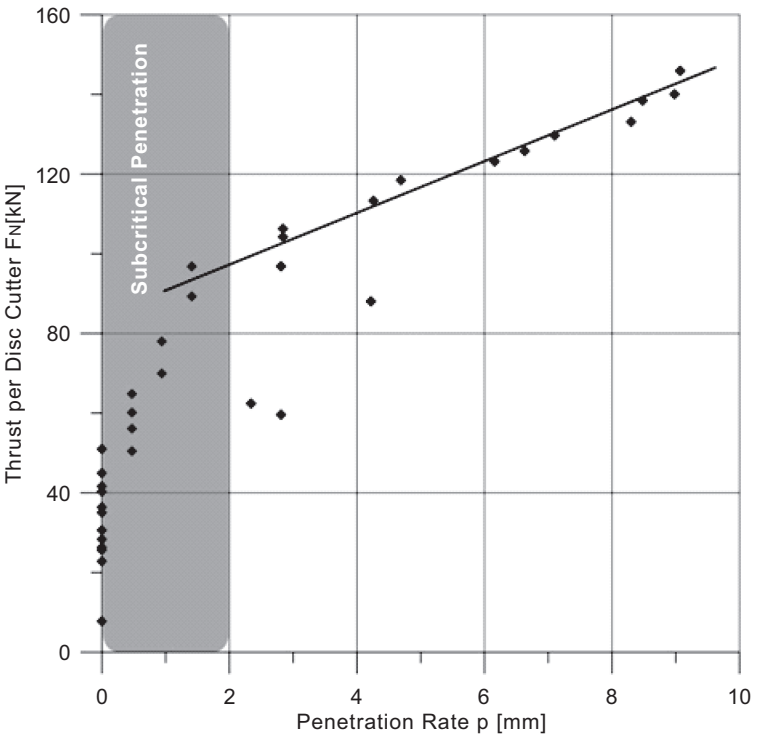


Figure 16 Example of a thrust-penetration curve in gneiss, data from Frenzel *et al.* (2012): Penetration tests for TBMs and their practical application, Geomechanics and Tunneling 5 (2012), No. 5.

and after the test is recorded along with the position of the TBM during the stroke, cutter wear measurements, vibration, and collection of chip samples. The test procedure assumes that the data acquisition system of the TBM records instantaneous values every 10 s of date, time, penetration rate, advance speed, cutterhead speed, cutterhead torque and total thrust. As pre-requisite for comparable results disk cutters should be in good condition, which is typically the case after cutter changes. If the tip width of the disk cutters has been changed between penetration tests in the same tunnel comparing the results will be more difficult. Geological mapping should be performed, which includes mapping of the tunnel face and/or side walls and extraction of core samples for laboratory testing. Laboratory tests that should be conducted include uniaxial compressive strength, Brazilian tensile strength, and Cerchar Abrasivity Index. In anisotropic rock, the cores should be taken perpendicular to the structures to obtain comparable results between rock masses. Ideally, the impact of anisotropy on rock strength and chipping should be determined through laboratory testing. A detailed description of the penetration test procedure is given in Figure 16. Penetration rates below 2 mm/rev are considered to be subcritical which means crushing occurs, but not chipping. The suggestion is to use a linear relationship between penetration rate and thrust once the critical thrust is exceeded. This penetration function is similar to existing performance prediction

models, but somewhat simpler from a mathematical point of view. The intent of this proposed procedure is to provide a quick and repeatable methodology for assessing excavatability that can be compared between different projects.

3.4 Newest developments

While image-based face documentation is well established in NATM, this technical aid was not available in mechanized tunneling. Thus an imaging device was developed, which is mounted in the cutterhead of a TBM and takes pictures during the maintenance shift that can be used for a photogrammetric reconstruction of the face. First test images were undertaken on a tunnel boring machine on the ÖBB project Koralm Tunnel KAT2.

Beside the optical imaging of the face, the determination of the load acting on disk cutters was another focus of the research Figure 16. The Disk Cutter Load Monitoring (DCLM) system together with the face monitoring can be used to provide detailed information about the face and its properties affecting excavation with disks, and further forecasts about penetration and tool wear can be made. The development of a modern disk cutter load monitoring system is part of the DRAGON project, which was supported by the European Commission under the FP7 Programme.

3.4.1 TBM performance prediction with scaled rock cutting tests

For the design of a mechanized tunnel, reliable forecasting is one of the most important matters right from very early stage. Performance forecasting models have therefore been developed, typically based on standard geotechnical tests. These models, which make use of the unconfined compressive strength and the tension strength as their input parameters, cannot reproduce the actual cutting forces with sufficient accuracy. In addition to the standard forecasting models the best forecast of performance is gained from cutting tests, for which several test rigs are available all over the world. Full-scale cutting tests do indeed deliver reliable results but are time-consuming and expensive. The large samples required for such tests are almost impossible to obtain. This was the motivation for the development of a new scaled rock cutting test. The test apparatus is designed so that it can be installed in a conventional rock testing device and thus is simpler and more practical than the test rigs available until now. The cutting tool is a 1:8 model of a standard 17 inch disk with a diameter of 56mm. With this disk geometry, a maximum penetration of 7.5 cm is reached.

The penetration for each cut is between 1 and 3 mm. The spacing can be varied between 0 and maximum 30 mm. The test samples used for the test are half cylinders with a diameter of 100 mm and a height of 90 mm, which are already available at an early stage of a project. The samples are glued to the sample holder with a two-part epoxy resin. After hardening, the sample holder is bolted in the clamping plates.

The tests are performed with a servo-hydraulic rock testing press. Each cutting test is carried out with two cutting tracks and five cuts per cutting track. The penetration of each cut is 1.5 mm, giving a maximum penetration of 7.5 mm

for each sample. For each of the ten cuts, the rolling force is calculated as a function of the cylinder stroke.

3.4.2 Cutter force measurement on tunnel boring machines

Scientific investigations have been performed to determine loads on disk cutters since the 1970s. The measurement system of the Mobydic project is based on measurement disks with applied strain gauges. The disadvantage of this system is the effect of abrasive wear on the disk, which has been specially adapted at great cost. Further possibilities of determining loads can be found in the area of the disk axle bearing. Herrenknecht AG has developed a system based on piezo-resistive sensor plates. In the MUL Entacher system, which uses measurement bolts with applied strain gauges, the load measurement technology is positioned right next to the disk axle. Comparative laboratory tests on the DCLM Systems were undertaken at the University of Leoben using a servo-hydraulic testing machine MTS Model 315. The maximum applied force of 500 kN is twice the normal load on a standard 17-inch disk. The intention of the laboratory tests is to evaluate the measured signal under the defined test loading set. For the evaluation of the measured signal, the linearity, amplification factor and hysteresis behavior are used as properties of the measured signal.

Current developments in the field of disk cutter load measurement are being undertaken within the framework of the DRAGON project of the FP7 Programme of the European Union. In addition to the measurement technology required for a monitoring system, the work is concentrating on operating strength and functionality under the adverse conditions in which the cutterhead is excavating and to ensure rapid and uncomplicated tool changing.

The sensors of the DCLM are based on strain gauge technology with a temperature-compensated full bridge sensor and are located at the bearing of the disk axle. The sensor data is transmitted digitally through a signal amplifier to the control stand of the tunnel boring machine, where it is evaluated, displayed and archived. The development of the DCLM Disk Cutter Load Monitoring System offers the potential of precise prediction of tool wear and penetration of a tunnel boring machine.

3.4.3 Development of a face monitoring system

Face mapping is a fixed part of the geological documentation of conventional and mechanized tunnel drives. The tasks include the most comprehensive possible recording of the sequence and formation of strata, bedding conditions, spatial location of interfaces such as joints, cleavage planes and fault zones. The requirements also include the recognition of lithologies, zones of tectonic overstressing and other factors, which could reduce the strength of the rock mass. The classic recording of interfaces using a compass, with errors due to steel in the vicinity, is increasingly supported by photogrammetry. This combines the visual impression, which is important in geological mapping, with the recording of the spatial geometry. Further advantages of the method are continued processing in CAD programs and the good suitability for integration into tunnel documentation and export in various formats.

Face documentation on a mechanized drive is normally performed by recording the face through access and bucket openings in the cutterhead. This means that only small areas of the face are visible. For this reason, an image stitching method has been developed. The images are extracted from a video frame and assembled frame by frame until a closed ring is created. The video is recorded while the cutterhead is rotated during the maintenance shift. This method greatly enlarges the area visible through the cutterhead. In addition, it is possible to generate orthophotos of the face. Since no scale can be determined from the images alone, this 3D reconstruction has to be transferred into an overall coordinate system using fitting points.

4 NATM VERSUS TBM – HOW TO CHOOSE THE RIGHT METHOD

The main goal from the owner's perspective is the functionality of the project within the commonly agreed level of quality, the realization of the project within given time limits and within a given budget. Other conditions which have to be taken into consideration are geometrical restrictions, accessibility and logistics, occupational health and safety, environmental and economic aspects, technological developments, public acceptance and stakeholder interests, market conditions, experiences from comparable projects as well as costs and financing.

Thus the selection of the tunneling method depends on the fulfillment of many requirements. The owner should leave this decision to the forces of the market, as long as he has no compelling reasons to prefer one or the other method. In principle there are two options:

a) The owner tenders both methods on the same level
b) The owner tenders only his preferred method but allows contractor's alternatives for the second method.

Regarding the advantages of tunnel boring machines, they provide a smooth circular cross-section with a maximum stability and a minimum of overbreaks. Considering planning aspects TBM tunneling does not permit major alterations during construction. TBMs reach highest efficiency in homogeneous geological conditions with low to moderate water ingress. If everything works well the long manufacturing phase is compensated by the much faster boring rates. In NATM tunneling, the time between the contract award and the start of tunneling is considerably shorter, as machines are normally used for a number of tunnels and do not have to be specially built for each project.

Regarding the excavated material the TBM material is characterized by an increased amount of very fine grained material and plate- or stalk-shaped grains. This hinders the use of the excavated material as aggregate for concrete as they worsen the workability of the concrete and increase the required amount of cement. To some extent this can be counteracted by optimized processing and mixing recipes.

Due to the circular tunnel profile, TBM tunneling will produce a larger quantity of material and at the same time needs a larger quantity of concrete compared to NATM – tunneling, where in most cases a horse-shoe-shaped tunnel profile is used.

Every TBM-tunnel drive demands some weeks of training and a start-up period. A long familiarization phase of up to six months can be expected depending on the complexity of the TBM. However, high investment costs for the TBM and backup are balanced against relatively low total wage costs.

The design and construction of a TBM has to be carefully matched to the prognosis of the rock mass behavior along the alignment. A deviation of the geological-geotechnical conditions from the prognosis represents a change of tunneling conditions for the TBM, usually resulting in a significant slowing down of the penetration rate.

Due to high capital and start-up costs for TBMs, NATM tunnel excavation is in many cases more economical – especially for short tunnels. Introduction of hydraulic drills, computer-controlled jumbos and better explosives has dramatically increased the speed of NATM, which works in a cyclic operation. Used in a professional way NATM will not get stuck even in low-quality rock masses, which might cause severe problems by using TBMs.

The main advantages and thus selection criteria of NATM can be summarized by facts like lower capital cost for equipment, high flexibility, meaning that variations in the size of the tunnel can easily be accommodated as well as the ability to change the support to cope with rapid changes in ground conditions. The possibility of dividing the cross-section of the face according to the geological conditions is a clear advantage compared to TBM-tunneling. Another advantage, particularly for utility tunnels, is the possibility of driving any curves and gradients. Good organization of construction works along the tunnel can make a considerable contribution to the performance. However, NATM is labor intensive; a well-trained crew with experience of excavation and support is required.

Regarding Working safety ventilation becomes more difficult with increasing length in NATM tunneling; in TBM tunneling, the air quality is considerably better. Actual frequency and extent of accidents are approximately similar for both methods.

Due to its flexibility NATM is relatively simple to regulate contractually in case of geological challenges. In contrast, TBMs are very limited in their flexibility, hence difficult to define contractually.

5 EXEMPLARY FAILURE MECHANISMS WHICH WERE OFTEN OBSERVED IN THE PAST

Failure mechanisms can be classified in many different ways. Some of these rough differentiating factors are stated in this chapter. Most failure mechanisms occur suddenly and therefore present a tremendous danger for the staff in the hazard area (Schneider, 2002). Nevertheless in many cases there are certain signs of an impending failure:

- Material crumbling down
- Bang like or cracking rock sounds
- Gradually widening of joints
- Turbid mountain water inflow
- Trickling joint fillings

5.1 Dome-like failure mechanisms

As a result of the settlement in the top respectively the "deflection" of the top, a relaxation in horizontal direction occurs. The "natural rock-vault" is thus pushed

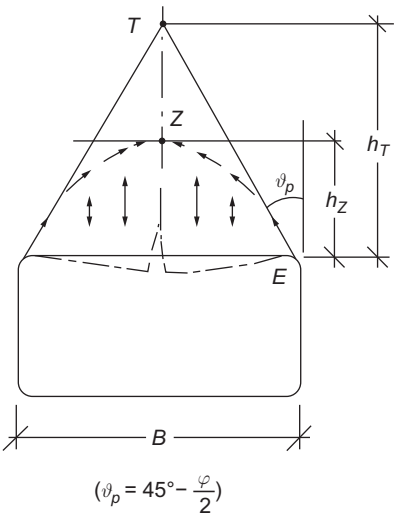


Figure 17 Dome-like cave-in principle (Vavrovsky, 1987).

into higher areas (secondary-vault). This "natural rock-vault" is limited by the breaking angle of the passive limit state ϑ_P, as shown in Figure 17, but mostly in a more flat angle (Feder, 1978).

5.2 Failure of jointed rock mass

Most often this kind of failure mechanisms occurs, when unstable blocks detach along the surface of the underground structure. The gravity fixes the direction of the movement

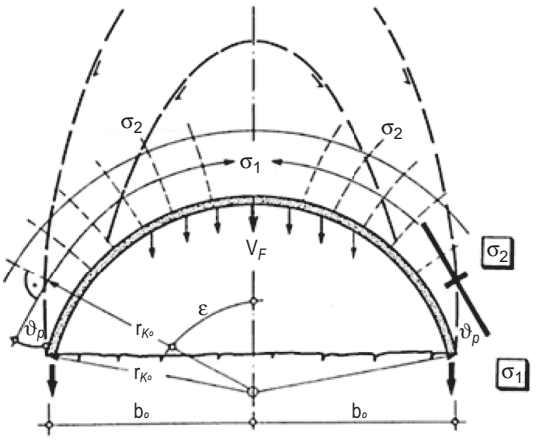


Figure 18 Shear zone development over the arched crown (Vavrovsky, 1987).

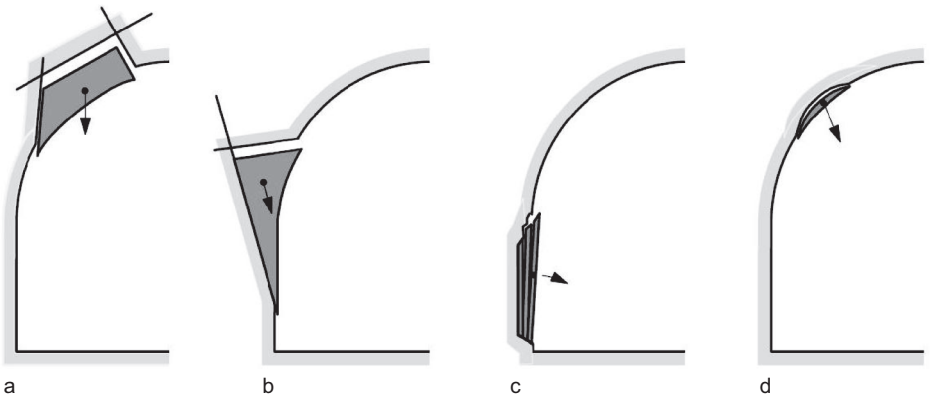


Figure 19 Kinematics of detachment: a. detaching - b. sliding - c. dumping - d. spalling (Schneider, 2002).

of the blocks. In many cases the sliding of a block follows one or two steep standing sliding faces. The movement of the block is given by the sliding plane (Schneider, 2002). The dumping of blocks finally is often observed in layered rocks, where unstable blocks dump in by steep stratification (Schneider, 2002).

5.3 Instability of the face

Soft ground conditions tend to respond to small deformations with loosening its bearing capacity. In such conditions a rigid support of the face is required. If the support is not strong enough to avoid movements in the ground shear zones in front of the face might occur.

As a consequence, the related settlement-rates at the face might result in stability problems, which are called chimney-like failure. One possibility to avoid the failure is a reduction of the excavation area in order to stiffen the face.

5.4 Failure mechanism of the spatial protection-arch

In tunnels with an overburden of about 1.5 to 2.0 diameters it was often observed that high pressure phenomena occur in an area about one to two diameters behind the face (Vavrovsky, 1987). This pressure often overloads the bolts in the sidewall and radial cracks in the area of the crown were often observed. Above the crown a chimney shaped rock mass is build up. An overload of the spatial rock-vault can almost always be detected in sufficient time, if there is an appropriate geotechnical measurement program and interpretation installed (Ruse, 2004; Vavrovsky, 1987).

5.5 Failure-mechanism in the foundation area of the top heading

A top heading drive without temporary ring closure causes high pressure in the foundation area of the shotcrete shell. If, however, the deformation-rate during

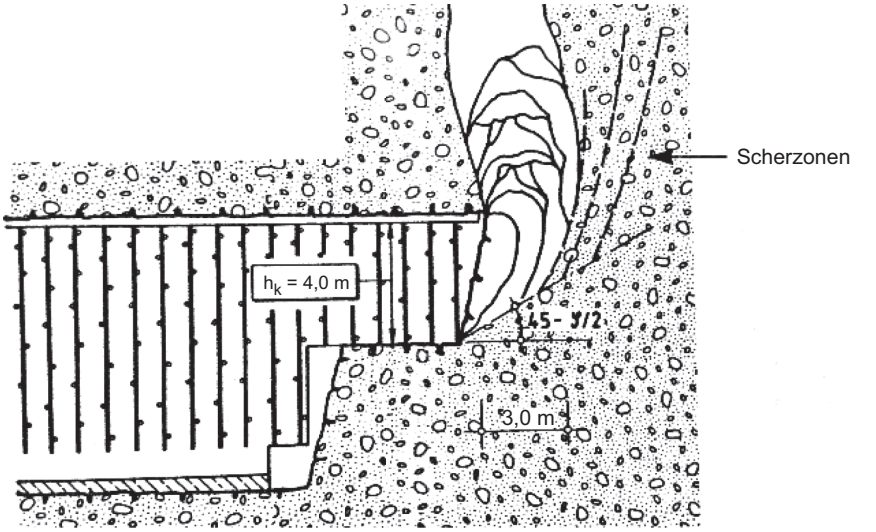


Figure 20 Progressive chimney-like cave-in mechanism above the heading-face (Vavrovsky, 1987).

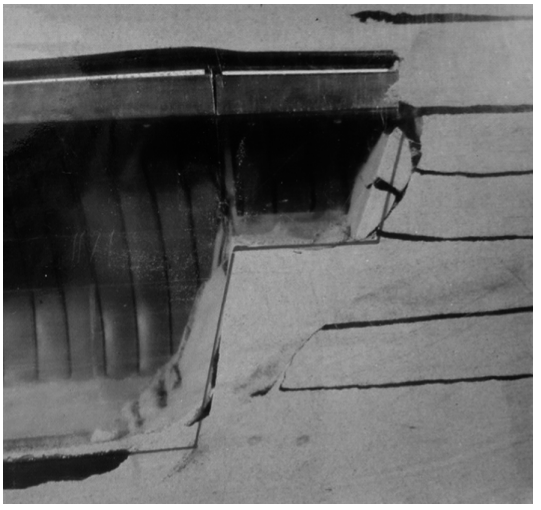


Figure 21 Fracture of the heading-face (Vavrovsky, 1987).

installation of the support in the top heading area is too high, the shotcrete shell may slowly be pressed into the foundation area which might cause a ground failure mechanism.

To avoid a ground failure mechanism support measurements like extending the shotcrete shell to a so called elephant foot in the area of the foundation or installing

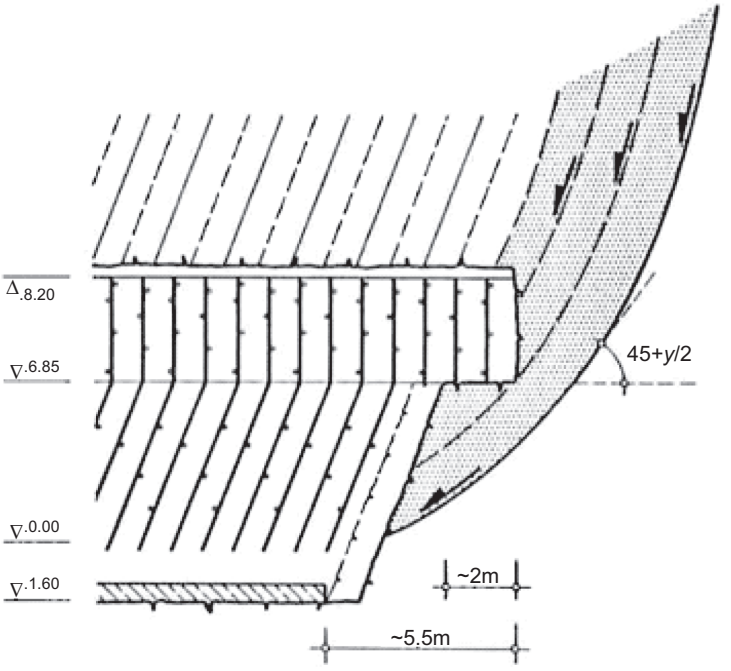


Figure 22 Form of the leading shear zone by short top heading and low friction stability of the rock mass (Vavrovsky, 1987).



Figure 23 Failure of the bench – east-facing advance Ganzsteintunnels (Dr. W. Gobiet) – cracks on the left side (Vavrovsky, 1987).

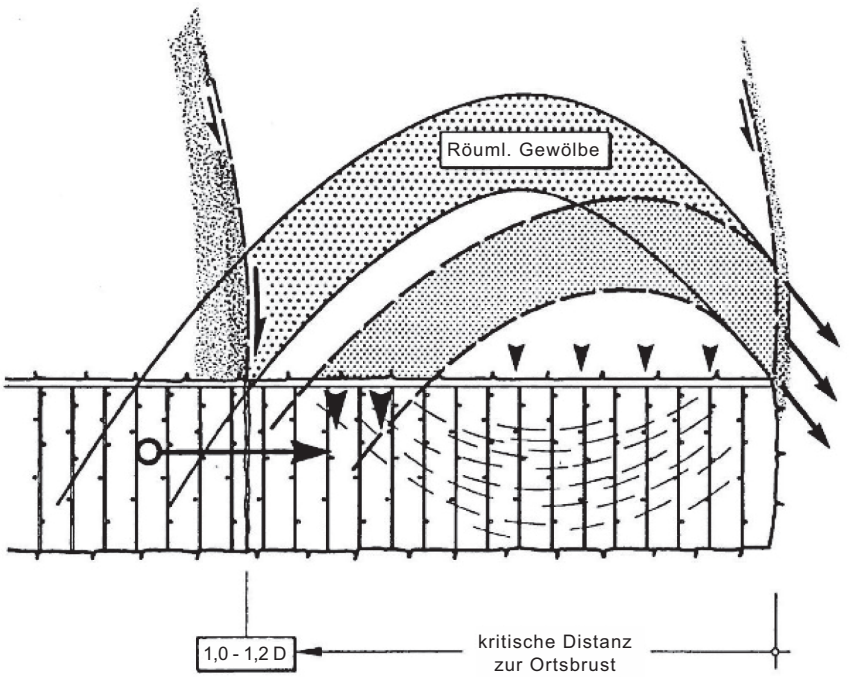


Figure 24 Schematic illustration of a spatial protection vault, which is "sliding off" an existing shear zone (Vavrovsky, 1987).

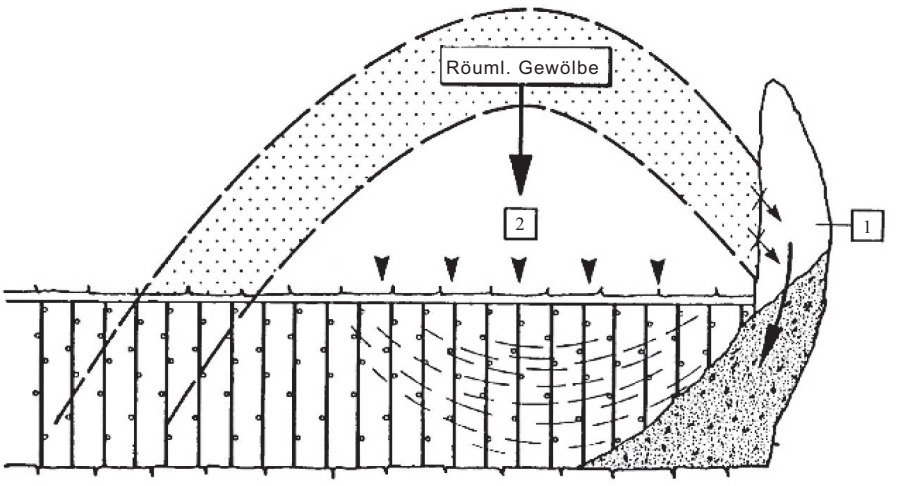


Figure 25 Loss of the spatial bracing-vault due to a delayed eruption at the face (Vavrovsky, 1987).

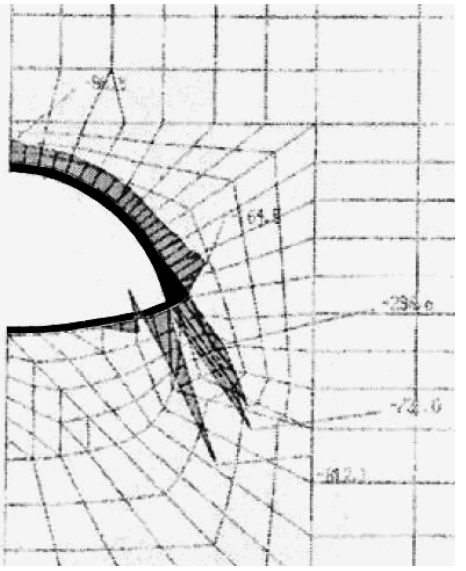


Figure 26 Support-resistance and foundation pressure after excavation of top heading (Fries, 2000).

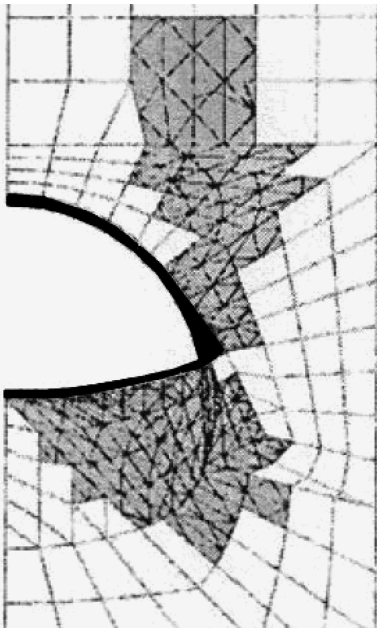


Figure 27 Plastic zones after excavation of top heading (Fries, 2000).

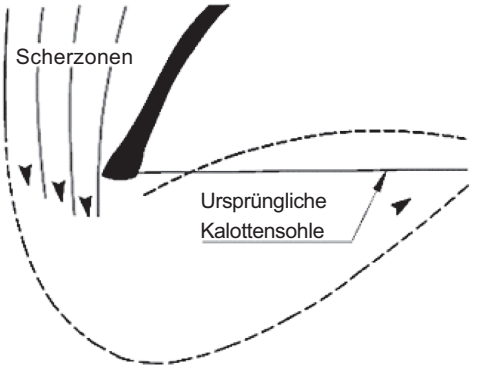


Figure 28 Support-measurements to avoid ground failure (Klobetanz, 2014).

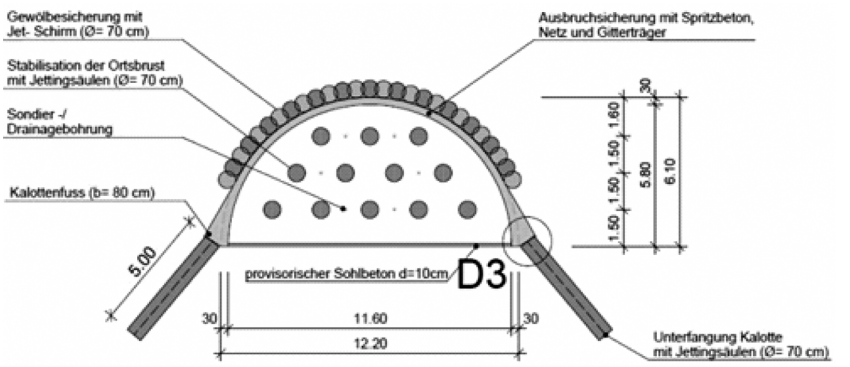


Figure 29 Widening of the loading-effective tunnel-width due to a ground failure mechanism (Vavrovsky, 1987).

of foot piles or installing a temporary invert can be done (Entacher, 2012; Entacher & Galler, 2013; Vavrovsky, 1987).

5.6 Sagging of the top-heading in the portal area

These failure-mechanisms occur mainly near the tunnel portal or at areas with overburden between 12 – 18 m. The material of the overburden is characterized through cohesionless properties and missing horizontal pressure. Due to a missing abutment on the portal-side a spatial vault cannot be formed. As a consequence the loading on the support is relatively high.

The shotcrete-structure increases according to the resulting loads of the overburden, so it mostly depends on the bearing capacity of the foundation area. Lack of resistance in the foundation area results in a sagging of the more or less intact heading-structure.

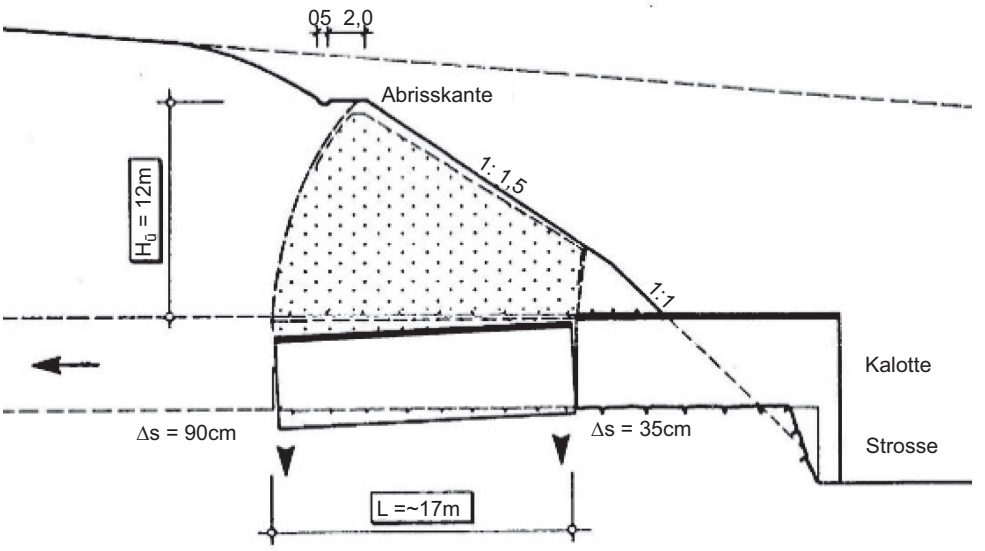


Figure 30 Sagged heading during advance in cohesionless loose material (Quaternary deposits, gravel, sand, silt). (Vavrovsky, 1987).



Figure 31 Sagged heading-vault at tunnel portal; surface-side situation. (Vavrovsky, 1987).

6 DEVELOPMENT OF RESOURCE-EFFICIENT UNDERGROUND TECHNOLOGIES - NEW TECHNOLOGIES ON THE WAY FROM WASTE TO RAW MATERIAL

6.1 Europe's strategies

Europe 2020 is the European Union's ten-year growth strategy and is about delivering growth that is smart, through more effective investments in education, research and innovation and sustainable, thanks to a decisive move toward a low-carbon economy. Of relevance to the DRAGON project were the targets related to climate change and energy sustainability. The ambitious targets that were set by the EU have been adopted into the *Europe 2020* strategy which are a reduction in EU greenhouse gas emissions of at least 20% below 1990 levels, 20% of EU energy consumption to come from renewable resources and a 20% reduction in primary energy use compared with projected levels, to be achieved by improving energy efficiency. Collectively these are known as the 20-20-20 targets. *A resource-efficient Europe* is one of seven flagship initiatives of the *Europe 2020 Strategy* and aims to support the shift toward a resource-*efficient*, low-carbon economy to achieve sustainable growth. This recognizes that natural resources underpin our economy and our quality of life and that continuing our current patterns of resource use is not an option. Increasing resource efficiency is the key to secure growth and jobs for Europe and will potentially bring major economic opportunities, improve productivity, drive down costs and boost competitiveness. This flagship initiative has moved the extraction and use of natural resources into the center of the political agenda of the European Commission. The strategy establishes resource efficiency as the guiding principle for EU policies on energy, transport, climate change, industry, commodities, agriculture, fisheries, biodiversity and regional development. The flagship initiative connects policies related to resources such as the *Roadmap for a resource efficient Europe* (EC, 2011b) and the *Raw Materials Initiative* (EC, 2009c).

The DRAGON project – Development of Resource-efficient and Advanced Underground Technologies – intends to improve resource efficiency in tunneling and other underground construction processes by providing the excavated material as a raw material for the construction site as well as for other industrial sectors which are using primary mineral resources. Within DRAGON a system of automated chemical, physical

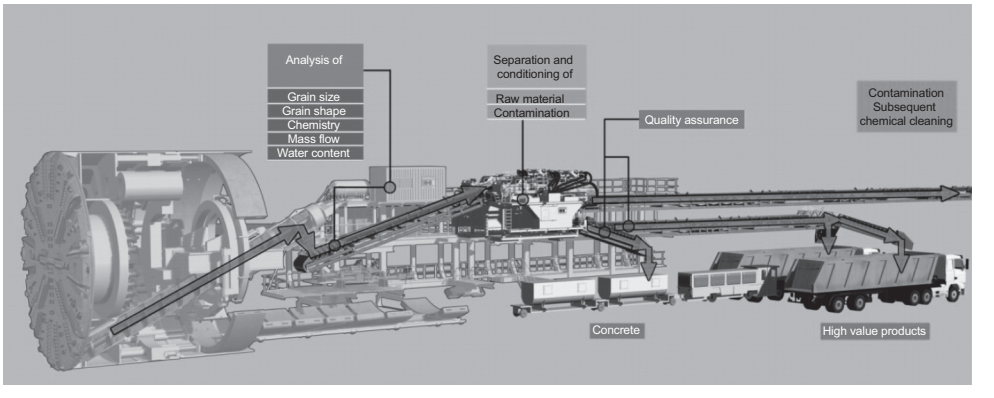


Figure 32 The concept of the DRAGON consortium [EU-research project - grant agreement No 308389].

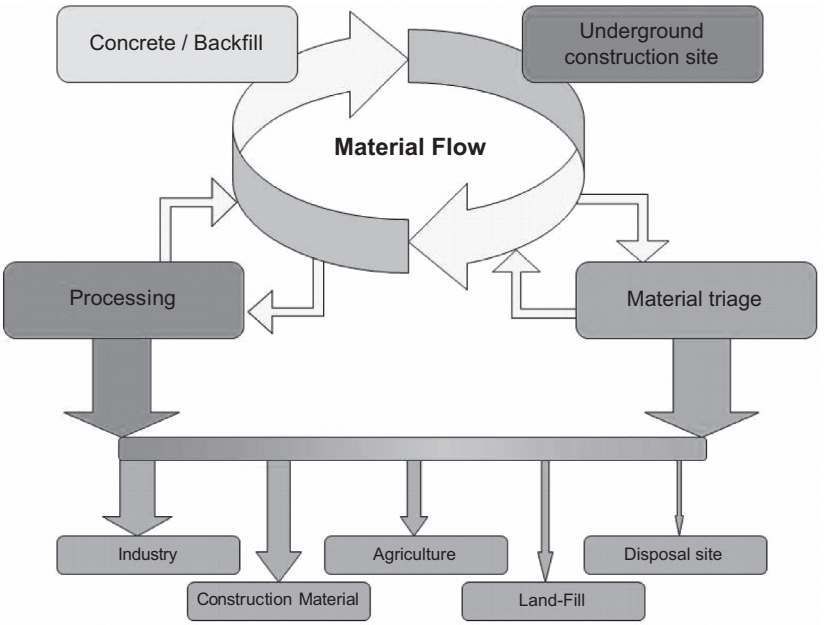


Figure 33 Material flow using new analyzing, separating and recycling techniques to reach zero waste.

and mineralogical online-analysis techniques all mounted on a bypass conveyor belt are developed. These analyzing techniques are followed by a separation plant using recycling units like crushers, sieves, etc. (Figure 32). The excavation material can directly be reused either on site or by being transported to the particular industry sector. One aim of the project is to place the whole process, starting from the characterization of the excavated material to its classification and processing, completely underground.

The results of the project will help to reduce or even eliminate any material deposits, thus aiming the production of zero waste originated from underground construction sites; furthermore environmental impacts like production of noise and dust will significantly be reduced. The DRAGON project applies the methodology of Life Cycle Assessment (LCA) according to ISO 14040/14044[1] in order to include life cycle thinking into the project. Additionally the mass flows are analyzed by the Mass Flow Analysis[2] according to Baccini and Brunner (1991). The reason for applying these methods is to compare different scenarios of re-use or disposal of excavation material. This allows observation of the whole system in order to avoid any problem shifting into other parts of the environmental system. Substitution effects caused by replacement of primary material with excavation materials are identified and quantified. Considering these aspects, underground constructions in the future will much more contribute to resource efficiency and the reduction of CO_2- emissions compared to today's state of the art.

1 ISO 14040: Environmental management - Life cycle assessment - Principles and framework / ISO 14044: Environmental management - Life cycle assessment - Requirements and guidelines

2 Brunner, P.H.; Rechberger, H. (2004) "Practical Handbook of Material Flow Analysis", CRC Press LLC, Boca Raton, Florida.

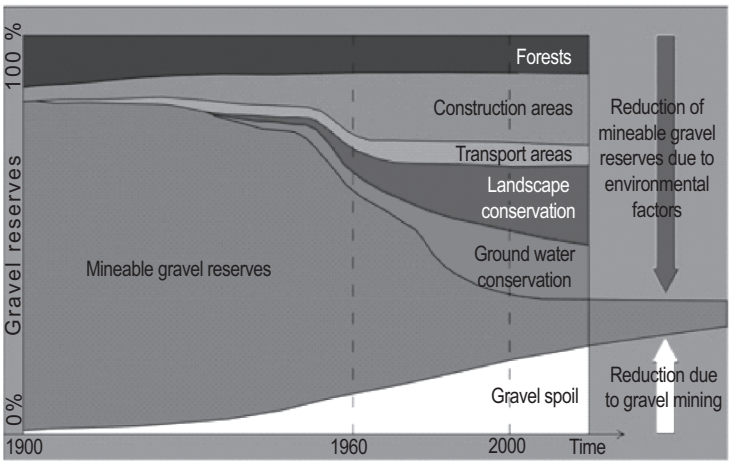


Figure 34 The conflicting utilization claims of the resource gravel (according to Kündig *et al.*, 1997; Jäckli & Schindler, 1986, modified).

6.2 Overall strategy and general description

The current legal framework for the utilization of excavation material is not yet completely satisfying and requires a change of rules where geochemical, geotechnical, mineralogical parameters are clearly specified for being allowed to reuse the excavated material as mineral product. The declared goal is to reach zero waste from underground construction sites.

A legally binding rule that material extracted in tunneling is preferred for use as long as its suitability can be demonstrated would not only create new raw materials potential but also enable companies in the mineral raw materials industry to obtain already crushed material at favorable rates, save their existing quarries and thus extend the lifetime of their companies. Following the results of the studies of Kündig *et al.* (Kündig, 1997) such a legally binding rule will get significantly important at least for European countries as mineable resources get dramatically less in future (Figure 34).

The fear that insufficiently stringent statutory guidelines could lead to the propagation of hazardous substances is unfounded with regard to tunnel spoil as long as thresholds and tests are specified for the material, corresponding to the products of the mineral raw materials industry. A clear differentiation must be made between geogenous and anthropogenous contamination. In order to gain legal certainty, a product status is still lacking for tunnel spoil, which is allowed to be reused as quality-assured recycling material. To go a step ahead Austrian engineers together with the Federal Ministry of Agriculture, Forestry, Environment and Water Management wrote a first guideline called *Verwendung von Tunnelausbruch* published by the ÖBV – Österreichische Bautechnik Vereinigung (2015).

6.3 Impact on society, economical and environmental impacts

The DRAGON prototype could also be of interest for mining companies which focus on resources of critical raw materials like gold, platinum, rare earths and others. Extracting the minerals containing such elements in a selective manner could facilitate

the separation from dead rock and could allow the exploitation of minerals deposits which are currently not attractive enough due to their relatively low concentration of valuable elements. One of the main objectives of the DRAGON project is to contribute to the natural resource conservation within the European Union. The reduction of solid waste volume in a range of about 300 million m^3 going to the landfill is a desired impact of the project. Depending on the geological composition of the material it is possible to recycle up to 100% of the excavated material. The reduction of transport ways, the diminution of pollutants as well as the reuse of the excavation material possess a large environmental protection potential. The main expected outcome of the LCA (life cycle analysis) is to provide scientific evidence that the reuse of excavated tunneling material will result in more resource-efficient and more closed-loop related systems (even in the industry-related economy) in Europe.

The DRAGON consortium aims to establish a close relationship to the external surroundings (national environmental authorities; standardization bodies etc.) of the project in order to implement and integrate the project results and findings quite smoothly within the specific regional, national and/or international environment. Main target of the DRAGON project is to act as Best Practice case how underground excavation material can be reused as valuable material in diverse industrial processes and sectors. By finalizing the research project the DRAGON Consortium will get in close contact with diverse national & European stakeholders and will try to influence the European and national directives in order to guarantee the reuse of underground extraction material as new valuable input material for other industrial processes and industries.

6.4 Topics to be considered

The dependencies of the individual fields of interest which have to be considered in order to reuse excavation material from underground construction sites are shown in Figure 35. The intention to continuously analyze the tunnel excavation material will result in an objective geological documentation of a previously unknown extent,

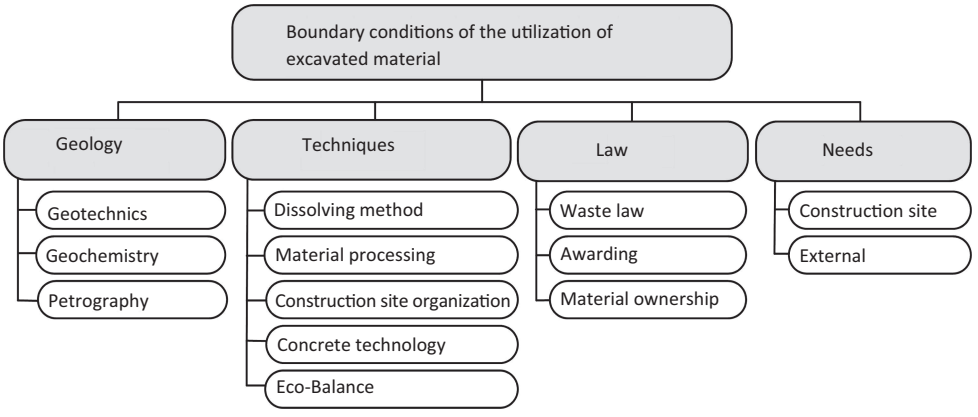


Figure 35 Topics to be considered for utilization of excavation materials from underground construction sites.

which offers the potential to avoid disputes about the actually encountered conditions.

6.4.1 Economic considerations

When tunnel spoil is recycled as a construction raw material, this has extensive economic effects in addition to the ecological effects. The economic benefit comes from the earnings that can be made by selling a certain material quality and also from savings, first from the substitution of purchased aggregates for the internal needs of the site with tunnel spoil, and second through reduced landfill costs. As soon as the sum of earnings and savings exceeds the cost of additional materials handling, the reuse and recycling of tunnel spoil can be considered profitable.

6.4.2 Possible reuses

The recovery and marketing of excavated material can only be achieved when the material meets the requirements of the consumer companies and there is also a market for it. If the material meets the requirements for concrete aggregates, it should be reused directly on the site during the construction phase of the project. If the production of high-quality and problem-free aggregates is greater than the internal demand, then the second recycling route market to local producers and processors of raw materials should be tried. If lithology is encountered, whose analysis has indicated suitability for recycling as industrial minerals during the site investigation, then the aim is to reuse this rock in mineral-processing companies. Excavated material, which cannot be used for more high-quality applications can be used for landscaping inside and outside the site, as long as its suitability can be demonstrated. Rock, which cannot be used due to possible background contamination or insufficient technical suitability, has to be tipped. The intention of reuse is not to set up as a competitor to local raw materials companies but to make the material available at a reasonable price in order to save raw material deposits.

6.5 Tunneling data base

DRAGON is providing a prototype of a tunneling database. Within this database, inputs from the geological forecast are compared with data coming online from the face of the tunnel works. Furthermore, potential clients of mineral products are connected to the database. Thus the database represents a link between the actual developments on site which are compared to the prognosis and forms the basis for the material management, which enables interactive trading and exchange of material among an extended circle of interested parties.

6.5.1 Excavated material database

One of the key aims in order to achieve higher rates of recycling is the efficient digital processing of the online recorded data regarding the tunnel spoil with simultaneous access to selected information for a wide circle of interested parties,

including mineral processing industries outside the construction site. The interested circle can include not only construction material producers and companies in the mineral raw material processing industry but also waste processors, landfill operators and authorities. Each interested group should have online access to the information that is relevant for them and the files including their requirements in the customer database. All information from the current project is saved in a design database, which is published by the client in the phase before the start of construction and should be regularly updated. The database system also contains, in addition to this project-specific information, a product database, which displays a defined list of preconditions for economic and profit-making processing of mineral raw materials. This can make clear, even at an early stage of a project, which tunnel section offers the greatest potential for recycling and can thus save costs and resources, and reduce landfill quantities.

6.5.2 Provided data

The data in the tunnel database is provided during the construction works by the continuous information flow from the material analysis unit on the TBM. If a deviation from the forecast geology and thus from the forecast quantities and time of production of a certain class of material is detected, the potential consumer automatically receives a notification about a possible delivery delay or bottleneck.

6.6 A short insight into some of the technical developments within the project

The main technological developments within the DRAGON project include fully automatic processes for:

1) fast detection of usable materials,
2) Recycling the materials immediately on the tunnel boring machine.

Conveyor belts offer great opportunities to automate analyses, classification and processing of the excavation material to ensure proper reuse and resource recycling. Newly developed measuring gear for online-measurements need to be installed directly onto the hauling installations (Müller *et al*., 1991). The main parameters of the material concerning its suitability as a resource are Chemistry and impurities, grain size distribution, water content, grain shape and mass flow.

6.6.1 DCLM – Disk Cutter Load Monitoring

The physical characterization of excavated material can be best detected by measuring the disk force. Entacher (2013) has shown that geological conditions in front of the cutterhead can be described with the disk cutter force characteristics. These

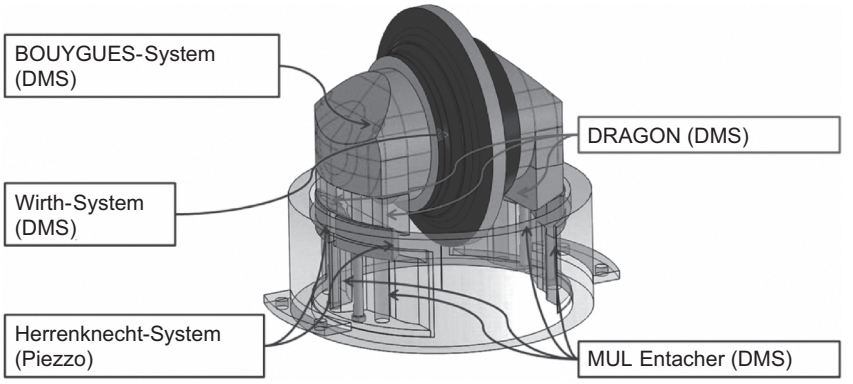


Figure 36 Overview of the available disk cutter measurement systems, example: wedge lock system of HERRENKNECHT.

developments should lead to a better understanding of the relationship between pure rock parameters, rock mass strength, geology, cutting forces cutter wear. For this purpose, Herrenknecht AG and the Montanuniversität Leoben developed various methodologies for measuring the cutter force on disks while the machine is boring (Entacher, 2013).

6.6.2 Automated sampling from the conveyor belt

The sampling has to be done very close to the tunnel face. With automated sampling procedures new standards are set in underground constructions.[3] The sampling system has to be available throughout the whole construction time with only short breaks for cleaning and maintenance during TBM standstill times. One possibility could be a so called hammer sample as shown in Figure 36.

6.6.3 Automated measuring of grain size and grain shape

For various reuses the grain size distribution is an important input data. Therefore DRAGON uses a technology which determines the particle size distribution of the material fully automated. The excavated material is analyzed photo-optical and the resulting image is evaluated digitally[4,5]. This measurement method is able to analyze grain sizes and shapes of dry, non-agglomerating particles in the range from 10 µm to 400 mm. The main advantages of photo-optical particle analysis to be used

3 Lecture 3; FLSmidth; Sheets 4 and 7 from 24; not translated literally
4 Ursula Stark: Korngröße und Kornform von Recyclingbaustoffen – schnelle und effektive Methode zur Beurteilung, 2011.
5 http://www.uni-weimar.de/Bauing/aufber/Professur/RC03/Vortrag%20Stark%20RC03.pdf, Stand: 7.10.2011.

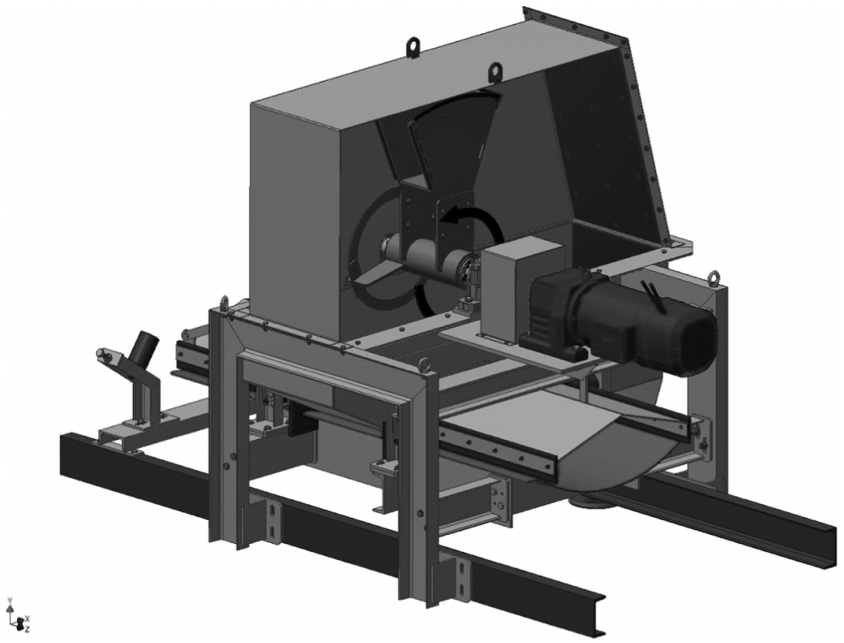


Figure 37 Working principle of a hammer sampler [SICON Probenahmetechnik].

underground are the rapid detection of particle size, particle shape and particle number, the time savings in the measurements compared to a sieve analysis and the high level of automation.[6]

6.6.4 Material analysis techniques by X-ray fluorescence analysis

The X-ray fluorescence spectroscopy is one of several possible methods to find out the exact elementary composition qualitatively and quantitatively. The results are converted to the oxides of the single elements and give an overview of the percentage of each component in the sample. This analyzing technology is installed immediately behind the particle size analyzer.

6.7 Materials management

One of the key points for the successful use and recycling of tunnel excavation material is the management of materials. This includes the aspects of material classification, material separation, material transport, material intermediate storage, material

6 Abstract 15; Haver & Boecker; Page 1 of 1; not translated literally.

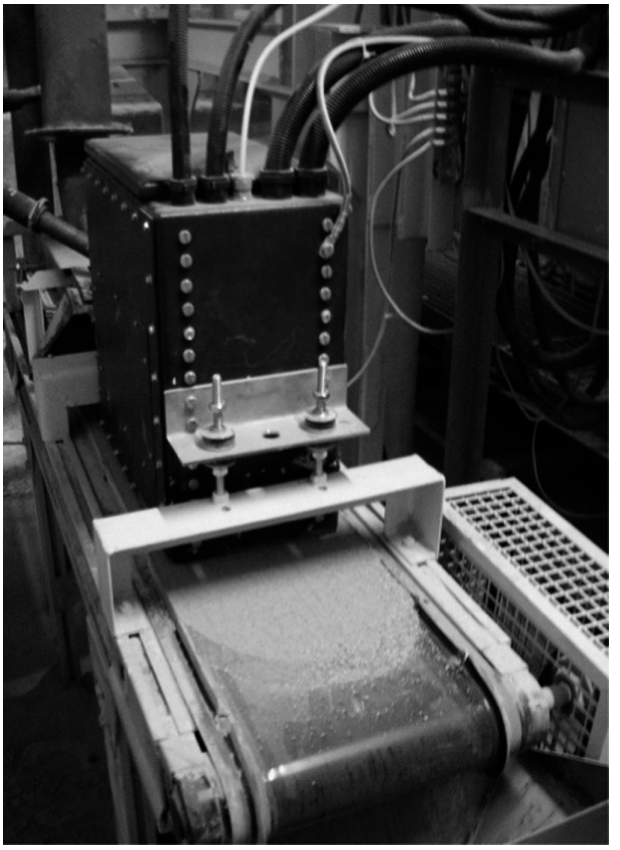


Figure 38 Online x-ray chemical element analyser OXEA (by INDUTECH).

processing and material storage. Each of these points is decisive for the success of reuse, since only correct classification and separation enables the quantity of material that is finally tipped to landfill to be minimized.

6.7.1 Material processing

In addition to the material demand on site, the suitability of the lithology encountered as a construction material is the most decisive factor. If there is no internal demand on the site, then preparation on site is inappropriate. If, however, the excavated material is suitable for reuse in the construction works, the normal practice has to install a stationary processing plant on the site facilities area. However, the disadvantage here is that if the excavated material is to be used for support measures for tunnel construction, then the material has to leave the tunnel first in order to be processed above ground and then transported back into the tunnel as concrete. In case of long tunnels this causes increased electrical power

consumption, complicated logistics, noise and dust nuisance as well as an increased need for space in front of the portal. DRAGON therefore pushes techniques for performing all required analyzing and processing tasks underground directly behind the tunnel face.

6.7.2 *Material storage*

Material storage, whether intermediate or final, is a critical point on tunnel projects due to the large quantities of excavated material preceded in tunneling. However, it is necessary to think about any future use of the material under changed economic conditions or raw materials policy. The material should be stored separately according to type, so that the exact tipping sequence is known, which means to create a secondary mineral deposit. This will be assisted by the detailed and complete recording of the entire material flow in the excavated material database. Thus it is ensured that raw materials are correctly sorted and can be extracted economically by future generations.

6.8 User scenarios

As partners of DRAGON are involved in three huge upcoming underground projects in Europe, where the prognoses show very different geological conditions, it was decided to take these projects as use-cases.

6.8.1 *Railroad projects in Germany*

PORR is involved in major projects in southern Germany, where 26 km of tunnels, producing 4.5 million tons of excavation materials, shall be built within the next years. A large amount of these materials will have a high content of gypsum, salt and clay. Other layers are mainly formed of sandstone. The goal is to clearly separate materials which can be used for dams, noise protection walls, concrete production and diaphragm walls from such which can only be used for landfilling. Some of the materials also have the potential to be used in the ceramic industries for bricks and other coarse ceramic products. The sandstones could mainly be used in the construction sector. It can be clearly stated that the addressed industries are only willing to accept the materials if the quality is near or equivalent to the raw materials they are used to procure. In any case an early detection of the chemical and morphological characteristics would help to increase the amount of usable materials and would be a precondition for utilization in some industries. On the other hand the detection and separation of some expected metals like Nickel, Chromium, Cadmium could either lead to an industrial utilization or at least to a reduction of disposal areas required for hazardous waste. In both cases it is mandatory not to mix up excavation materials containing these metals in a relatively high content with others because that would lead to a dilution and so to an unfavorable increase of the masses which have to be processed or disposed.

6.8.2 Tunnel Lyon – Turin connecting France and Italy

The new railway line from Lyon to Torino is part of the West-East European corridor linking Barcelona to Kiev. Some 250 km of tunnels will be built on the section including the French and the Italian parts. The key part of this new route is the Maurienne-Ambin Base tunnel, about 57 km long, crossing various and difficult geological formations. The valorization of the excavated material is a major issue for this project which will produce some 35 million tons of rocks, of which an aggregate for a total quantity of about 12 million tons could be produced for the 6 million m^3 of concrete for the project. On the central section, sulfated materials are expected, and they must be identified on the transportation system, into the tunnel, before the stockpiling and before the transformation into aggregates.

6.8.3 Les Farettes – Romande energie hydropower project in Switzerland

This case study is of major interest for the DRAGON project because it is showing that it is possible to process excavation material with a light dry process and to produce concrete on a simple way, inside the tunnel, if the diameter of the tunnel is big enough to implement the required processing equipment.

6.8.4 Nant de Drance hydropower project in Switzerland

This case study is representing the most beautiful case for the *on the job site* excavation material monitoring and processing organization. The Owner is supported by a dedicated staff managing the excavation material classification, handling, storing and the aggregates production. The aggregates processing plant is fitted with the latest technology equipment. It is possible to feed a large range of concrete types with TBM and NATM excavation materials. Furthermore the quality of the aggregates is completely in accordance with the special requirements for crushed aggregates and high quality concrete for underground works.

The analysis of the 9 Reference Projects is showing that the objectives of the DRAGON Project are definitely on the right track in order to develop online excavation materials analysis methods for both chemical and physical characterization and to settle concrete production equipment on the TBM Back-up for "in situ" shotcrete production. First applications can be already mentioned for the Bossler Tunnel using the DCLM for siltstone/sandstone characterization and the Maurienne-Ambin Tunnel, where chemical analysis for SO_3 detection in the Modane section, the DCLM for sandstone detection within the Saint Martin la Porte section, and in situ shotcrete production on the long TBM drive from Modane to France/Italy border with a length of 14.000 m within the homogeneous Ambin Micashale section is foreseen.

6.9 Conclusion

Using the analyses techniques developed in DRAGON allows an immediate analyses and recognition of valuable materials close to the tunnel face and thus forces the direct utilization of the excavated material. The DRAGON Consortium

provides sufficient experience and scientific excellence in order to guarantee the successful implementation of the DRAGON project on a European level. The new developed technologies in order to reuse the excavation material will have a strategic impact on sustainable management of limited mineral resources, higher resource efficiency through a recovery process and related decrease of EU dependency on resource imports, lower environmental impact, more competitiveness of all underground construction related companies and organizations and new resource-efficient environmental technologies. The rate of utilization of excavated materials from tunneling will be significantly increased. The goal of DRAGON is to achieve valuable minerals which could be used for construction materials, steel production, ceramics, electronics, pigments and others. Regarding the scientific impact DRAGON aims, in a multidisciplinary way, the optimization of the research outcome and commercial exploitation of its results by mobilizing the critical mass of scientific knowledge as well as eco-environmental application skills. Most of this expertise is already based on previous funded national projects and initiatives, in which some of the partners have been involved dealing with the reuse of tunneling excavation material and the development of an innovative separation technology for bentonite. The new and innovative technologies within DRAGON are the control of a tunnel boring machine by the fragmentation of the excavated rock which leads to an optimization of the machine operation. Such a concept has never been realized before. However, previous fundamental research work at the Montanuniversität Leoben has shown that such a concept is feasible. Scientific challenges in the DRAGON approach are the combination of optical particle size measurements on a continuous sample and its evaluation with respect to the natural breakage characteristics. In addition the combination with a Laser based spectrometer has never been tested and realized before. Therefore the connected scientific impact embraces technologies which allow online-analyses considering grain size, grain shape, etc. under outstanding underground conditions as well as which allow separation processes and which facilitate recycling technologies of underground excavation materials under very limited space conditions. The exploitation of minerals is usually affected by conflicts between the economic interests of the extractive industries or the construction sector and environmental protection concerns, but also declining sizes of natural stocks have an influence. To overcome such problems new ways of making minerals available on a regional and local level through tunnel excavation projects is a possible solution. The excavation close to the users is very important as it will help to reduce the consumption of fossil fuels for production, processing and transport.

ACKNOWLEDGMENT

This project has received funding from the European Union's Seventh Programme for research, technological development and demonstration under grant agreement No 308389.



REFERENCES

Baccini, P., Brunner, P.H. (1991) Metabolism of the Anthrosphere, Springer, Berlin, Heidelberg, New York, p. 157.

Bergmair, Michael Dr. – Huber, Günter Ing. „Das natürliche Gebirgsgewölbe“ – Bestimmung der räumlichen Entwicklung auf Grundlage geotechnischer Messungen.

Brunner, P.H., Rechberger, H. (2004) Practical Handbook of Material Flow Analysis, CRC Press LLC, Boca Raton, Florida.

Burg, Jean-Pierre, Prof. Dr. – ETH Zürich – Department of Earth Sciences – Geological Institute – Skriptum „Spröde Bruchbildung“.

Entacher, M., Lassnig, K. (2012) Erkenntnisse aus Diskenschneidversuchen an alpinen Lithologien, Geomechanics and Tunnelling 5, No. 5, S. 547–556.

Entacher, M., Resch, D., Reichel, P., Galler, R. (2011) Wiederverwertung von Tunnelausbruchmaterial – Abfallrecht im Berg- und Tunnelbau, Geomechanics and Tunnelling 4, No. 6, S. 692–701.

Entacher, M., *et al.* (2012) Cutter force measurement on tunnel boring machines – System design, Tunnelling and Underground Space Technology 31, S. 97–106.

Entacher, M. (2013) Measurement and interpretation of disc cutting forces in mechanized tunnelling, Dissertation, Lehrstuhl für Subsurface Engineering, Montanuniversität, Leoben.

Entacher, M., Galler, R. (2013) Development of a disc cutter force and face monitoring system for mechanized tunnelling, Geomechanics and Tunnelling 6, No. 6, S. 725–731.

Entacher, M., Lorenz, S., Schuller, E., Galler, R. (2013) TBM Leistungsprognose mit Modellschneidversuchen, BHM, 158 (12), Springer, Wien, S. 501–506.

Entacher, M., Winter, G., Galler, R. (2013) Cutter force measurement on tunnel boring machines – Implementation at Koralm tunnel, Tunnelling and Underground Space Technology 38, 487–496.

Entacher, M., Schuller, E., Galler, R. (2014) Rock Failure and Crack Propagation Beneath Disc Cutters, Rock Mechanics and Rock Engineering, Springer, Wien, Published online.

Entacher, M., Lorenz, S., Galler, R. (2014) Tunnel boring machine performance prediction with scaled rock cutting tests, International Journal of Rock Mechanics & Mining Sciences 70, Elsevier Ltd, Oxford, S. 450–459.

Erben, H., Galler, R. (2014) Tunnel spoil – New technologies on the way from waste to raw material, Geomechanics and Tunnelling 7, No. 5, 402–410.

Feder, Georgo, Prof. Dr.techn.Dipl.-Ing., Montanuniversität Leoben –„Firstniederbrüche im Tunnelbau“, In: Forschung und Praxis, Bd. 27 (1978).

FFG – Forschungsförderungsgesellschaft: Recycling von Tunnelausbruch, FFG – Projekt Nummer 834231.

Fries, Thomas „Ausfahrtstunnel Ristet – Erfahrungen aus dem Lockergesteinsvortrieb“ – Mitteilungen der Schweizerischen Gesellschaft für Boden- und Felsmechanik – Frühjahrstagung, 27. April 2000, Zürich.

Galler, R., Krispel, S. (2012) ÖBV–Forschungsprojekt – Verwertung von Tunnelausbruch; Vortrag in der Sektion Forschung im Rahmen des Österreichischen Betontages am 19.04.2012.

Galler, R. (2014) Development of immediate re-use of the underground excavated material as mineral resource, Tunnels and underground space risks and opportunities, Congress International Lyon, 13th–15th Octobre, C052–B2.

Galler, R., Voit, K. (2014) Tunnelausbruch – wertvoller mineralischer Rohstoff, Betonkalender, 103, Jahrgang, Verlag Ernst & Sohn, S. 423–468.

ISO 14040: Environmental management – Life cycle assessment – Principles and framework / ISO 14044: Environmental management – Life cycle assessment – Requirements and guidelines.

Klobetanz, Denis „Umfahrung Untertägi“ – Bachelorarbeit 2014 – Architektur, Gestaltung und Bauwesen.

Kühne, Manfred Dipl.Geol., Dissertation- 2003 – „Untersuchung von Einflussfaktoren zur Ortsbruststabilität und Vortriebsgeschwindigkeit beim Tunnelbau im Rheinischen Schiefergebirge“ – Johannes-Gutenberg-Universität Mainz – Fachbereich Geowissenschaften.

Kündig, R. (1997) Die mineralischen Rohstoffe der Schweiz, S. 100, Zürich, Schweizerische Geotechnische Kommission.

Lassnig, K. (2012) Verwendung von Tunnelausbruchmaterial – Geologische und Geotechnische Aspekte; Dissertation, Lehrstuhl für Geologie, Montanuniversität, Leoben, unveröffentlicht.

Mair, R.J., Taylor, R.N. – Burland, J.B. „Prediction of ground movements and assessment of risk of building damage due to bored tunneling“ – Geotechnical Aspects of Underground Construction in Soft Ground. Mair & Taylor (eds) – 1996 Balkema. Rotterdam. ISBN 9054108568.

Müller, S. B., Zwicky, C. N., Blahous, L. (2011) Kalibrierung eines NIR-Online-Analysators mittels Bohrmehlproben zur Optimierung des Zement- Rohmaterials, Berg- und Hüttenmännische Monatshefte, 156. Jg. 2011, Heft 6, S. 225–226.

ÖBV (2015) Verwendung von Tunnelausbruch, Richtlinie published by Österreichische Bautechnik Vereinigung, May.

Okrusch, M., Matthes, S. (2009): Mineralogie: Eine Einführung in die spezielle Mineralogie, Petrologie und Lagerstättenkunde, 8. Auflage, Spinger Verlag, Berlin.

Resch, D., Lassnig, K., Galler, R., Ebner, F. (2009) Tunnel excavation material – high value raw material, Geomechanics and Tunnelling 2, No. 5, 612–618.

Resch, D. (2012) Verwendung von Tunnelausbruchmaterial – Entscheidungsgrundlagen. Dissertation, Lehrstuhl für Subsurface Engineering, Montanuniversität, Leoben.

Ruse, Nico Michael, Dissertation – 2004 – „Räumliche Betrachtung der Standsicherheit der Ortsbrust beim Tunnelvortrieb“ – Universität Stuttgart – Fakultät für Bau- und Umweltingenieurswissenschaften – Institut Geotechnik.

Schneider, Alexander H. Dipl. Bauing. ETHZ – Dissertation ETH Nr.14556 – „Sicherheit gegen Niederbruch im Untertagebau“ – Eidgenössische Technische Hochschule Zürich – 2002.

Schubert, Wulf, O. Univ. Prof. D.I. Dr. – Technische Universität Graz – Institut für Felsmechanik und Tunnelbau – Skriptum „Grundlagen der New Austrian Tunneling Method“.

Schumann, W. (1997) Der neue BLV Steine- und Mineralienführer, BLV Verlagsgesellschaft, München.

Seidenfuß, Timo Dipl.-Ing. (FH) – Master Thesis – No.870003 – 2006 – „Collapses in Tunnelling“ – Fachhochschule Stuttgart – Foundation Engineering and Tunneling.

Stallmann, Miriam Diplomarbeit – „Verbrüche im Tunnelbau, Ursachen und Sanierung“ – Fachhochschule Stuttgart – Studiengang Bauingenieurwesen.

Thalmann, C. (1999) Ergänzende Prüfungen zu den bestehenden Beton-Normen für gebrochene Zuschlagstoffe – Erfahrungen beim AlpTransit Gotthard. Zeitschrift Schweizer Ingenieure und Architekten, Nr. 24, Zürich.

Vavrovsky, G.M. Dissertation – 1987 – „Entspannung, Belastungsentwicklung und Versagensmechanismen bei Tunnelvortrieben mit Geringer Überlagerung“ – Montanuniversität Leoben – (vormals) Institut für Konstruktiven Tiefbau.

Yeates, John Bsc, CEng, MICE, „The Response of buried pipelines to ground Movements caused by tunnelling in Soil“ – Northumbrian Water Authority Newcastle upon Tyne, England.

Zbinden, P., Hitz, A. (2002) Materialbewirtschaftung des Gotthard- Basistunnels, Felsbau, Nr. 5, S. 83, Essen, Verlag Glückauf.



Taylor & Francis
Taylor & Francis Group
http://taylorandfrancis.com

Chapter 2

Mechanics of directional drilling

Emmanuel Detournay, Julien Marck & Luc Perneder
Department of Civil, Environmental and Geo-Engineering, College of Science & Engineering, University of Minnesota, Minneapolis, MN, USA

1 INTRODUCTION

Drilling deep boreholes that weave complex trajectories in the subsurface has been made possible with the development of directional drilling. The need for complicated well paths arises, within the context of oil-and-gas exploration and production, from a variety of reasons. These include accessing a hydrocarbon reservoir capped by a salt dome, complying with constraints on the location of the rig relative to the target, drilling multiple wells from one location to reduce cost or limit environmental impacts, and rescuing a distressed well. A key factor in the ability to complete complex wells has been the emergence of the *rotary steerable systems* (RSS) in the late 1990s. These servo-controlled downhole robots steer the bit by either applying a force on the borehole wall or by tilting the bit.

Figure 1 sketches a typical rotary drilling structure used in the oil and gas industry. This structure comprises a rig, from which is suspended the *drillstring*, a hollow slender tube that can be several kilometers long. The rotary speed and the axial force (*hookload*) are imposed at the rig. The lower part of the drillstring is the *bottomhole assembly* (BHA), which is usually about one hundred meters long. It consists of heavier pipes and short elements of larger diameter, called *stabilizers*, which center the BHA in the borehole (Inglis, 1987). The bit is at the lower extremity of the BHA. While the main part of the drillstring is in tension under its own weight, the BHA or part of it is in compression in order to induce a sufficient *weight on bit*, the axial force transmitted to the bit.

The RSS is located close to the bit. Such a semi-automated device works in association with sensors and downhole control units in order to steer the borehole (Downton *et al.*, 2000). Considerations are restricted here to *push-the-bit* RSS, which apply a lateral force at a designated location on the BHA using a set of extensible pads that directly push on the borehole wall.

Once stripped of all its mechanical components, a drilling structure is in its simplest abstraction an extremely slender elastic body constrained to deform inside the borehole. It is subject to gravity, hydraulic forces associated to the flow of drilling mud, imposed forces at the rig and at the RSS, a force and a moment at the bit, and reaction forces at its contacts with the borehole. The directional propagation of the borehole depends on the force and moment at the bit; they are affected not only by the action of the RSS but also by the deformed configuration of the BHA, which is constrained by the

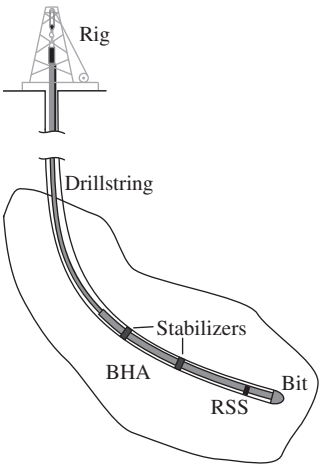


Figure 1 Sketch of a typical directional drilling apparatus equipped with a push-the-bit RSS. The number of stabilizers is usually greater than 2.

stabilizers to espouse the existing borehole. The propagation of the borehole is thus governed by the interaction between a geometrical object, the wellbore, and a mechanical object, the drilling structure.

The evolving borehole is described at the scale of the BHA as a propagating 3D curve. When viewed at the scale of the bit it is also characterized by its varying cross section. The overgauge of the borehole with respect to the bit diameter is caused in part by the tilt of the bit on the borehole. Hence, the borehole can conveniently be described by four functions of a curvilinear coordinate running along its axis: the axis inclination and azimuth describe the geometry of the borehole viewed as a curve and two tilt angles characterize the borehole geometry at the scale of the bit.

Study of this dynamical system is motivated by engineering issues, which include defining criteria for bit selection, designing the BHA to either increase, maintain, or decrease the borehole inclination with or without the presence of a RSS, preventing borehole spiraling — an expression of self-excited oscillations triggered by a directional instability of the drilling system, or devising an appropriate controller for the RSS with the objective of tracking a predefined well path (Lubinski & Woods, 1953; Murphey & Cheatham, 1966; Bradley, 1975; Callas, 1981; Millheim, 1982; Brett *et al.*, 1986; Birades & Fenoul, 1988; Ho, 1987; O'Bryan and Huston, 1990; Neubert & Heisig, 1996; Genevois *et al.*, 2003; Pastusek *et al.*, 2005; Downton, 2007; Studer *et al.*, 2007; Kremers *et al.*, 2015; Marck & Detournay, 2016b).

The starting point of this study is to formulate a mathematical model for a propagating borehole, *i.e.*, to derive the equations governing the spatial evolution of the inclination and azimuth of the borehole and of the tilt angles. These equations must embed a description of the mechanical system that creates the borehole. However, notwithstanding our contributions (Detournay & Perneder, 2011; Perneder & Detournay, 2012; Perneder & Detournay, 2013; Marck & Detournay, 2016b), only a handful of papers dealing with the formulation of such a mathematical model can

be found (Neubert & Heisig, 1996; Downton, 2007; Downton & Ignova, 2011). On the other hand, many numerical solutions without any explicit description of the underlying mathematical model have been proposed (Callas, 1981; Millheim, 1982; Brett *et al*., 1986; Rafie, 1988; Maouche, 1999; Studer *et al*., 2007). Related efforts include those aimed at understanding the mechanics of the BHA constrained to deform within the borehole (Murphey & Cheatham, 1966; Fischer, 1974; Bradley, 1975; Millheim *et al*., 1978; Ho, 1986; Rafie *et al*., 1986; Birades & Fenoul, 1988; Jogi *et al*., 1988; Dogay *et al*., 2009) and at deriving the interface laws that govern the interaction of the bit with the rock formation (Cheatham & Ho, 1981; Ho, 1987; Ho, 1995; Menand *et al*., 2002; Detournay *et al*., 2008; Franca, 2010; Perneder *et al*., 2012).

The formulation of a directional drilling model hinges on the recognition that propagation of a borehole is predominantly affected by the positions along the BHA of the stabilizers closest to the bit, all other parameters being fixed. Indeed, the first n stabilizers mainly control the steering of the bit in the sense that altering the composition of the BHA by removing or repositioning the $n + 1^{th}$ stabilizer, while keeping the first n unchanged, hardly affects the directional response of the system. (For most practical purposes, $n = 3$ is sufficient.) The weakening influence of an additional stabilizer derives from the nature of the equations governing the deformation of the BHA. This implies that it is appropriate to "cut" the BHA above the n^{th} stabilizer and replace the rest of the drillstring by forces and moments, which themselves are supposed to be unaffected by the steering of the bit.

Three length scales can naturally be identified in this problem. One corresponds to the dimensions of the bit, typically of order $O(10^{-1}\text{m})$. The bit is viewed as a three-dimensional object at this length scale, which is thus used when deriving interaction laws between the bit and the rock formation. The second length scale, of order O(10m), corresponds to the length of the BHA segment with the first n stabilizers. Finally, the third one, of order $O(10^{3}\text{m})$, is concerned with the transmission of the axial force and torque along the drillstring, which is affected by the contacts between the drillstring and the borehole.

In summary, the borehole propagation model is constructed at the intermediate scale, with boundary conditions capturing the processes at the two other scales. At the lower boundary, the bit is collapsed onto a point, with the details of the bit/rock interaction encapsulated into interface laws consisting in relationships between the force and moment at the bit and the conjugated kinematic quantities (Detournay *et al*., 2008; Perneder *et al*., 2012). At the upper boundary, the action of the drillstring is replaced by assumed known forces, with the axial force being usually the only non-zero component (Johancsik *et al*., 1984; Ho, 1988; Aadnoy *et al*., 1998; Menand *et al*., 2006; Denoël, 2011).

All the dynamic and kinematic variables that are introduced in the borehole propagation model are quantities averaged over many revolutions. Indeed, the time scale associated with directional drilling is considerably larger than the period of revolution, itself larger than or of the same order as the period of vibrations of the bit and drillstring. Moreover, with the bit collapsed onto a point, the spatial resolution of the model cannot be less than the bit size, itself much larger than the bit penetration per revolution. This averaging thus implies that borehole propagation can be viewed as

a quasi-static process, with the dynamic effects possibly subsumed into parameters of the model. For example, the effects of bit whirl could be accounted for as an over-gauging of the borehole.

This review of the mechanics of directional drilling is structured into six Sections. Following the Introduction, Mathematical Formulation describes the different components of the mathematical model: namely, the kinematic relationships between the bit penetration and the borehole geometry, the bit/rock interface laws, and the elastic equations governing the BHA deformation. Next, Toy Model describes in geometrical terms the dynamical model of a propagating borehole for the simple case of a rigid BHA with one stabilizer. Borehole Trajectory formulates the delay differential equation that governs the evolution of the borehole inclination, and shows computed results of borehole trajectory following a change in the external loading. Stationary and Quasi-Stationary Solutions identifies the long-range asymptotic solutions of the borehole trajectory under constant loading. Finally, Stability and Borehole Spiraling analyzes the directional stability of the drilling system and computes the limit cycle corresponding to borehole rippling.

We have restricted the topics covered in this review to boreholes in a vertical plane. Extension of the model to three-dimensional borehole trajectories can be found elsewhere (Perneder, 2013; Perneder & Detournay, 2013; Marck, 2015; Marck & Detournay, 2016b).

2 MATHEMATICAL FORMULATION

2.1 Preamble

The directional evolution of the borehole results from the interaction between the borehole, the BHA, and the bit. The directional drilling model can thus be formulated by combining (i) the *kinematic relationships* between the bit penetrations and the parameters characterizing the evolving geometry of the borehole, (ii) the *bit/rock interface law* relating the reaction forces on the bit to its penetrations, and (iii) the *beam model of the BHA* providing relationships linking the generalized forces at the bit to the geometry of the borehole and other external loads acting on the BHA (Fig. 2). The resulting equations describe a dynamical system that can be used to predict the well path given the external forces acting on a drilling system of known characteristics, identify the stationary solutions of the system, analyze the stability of these equilibrium points, and eventually calculate, with the addition of a nonlinearity such as a saturation of the bit tilt, the limit cycle oscillations of the borehole if the dynamical system is unstable.

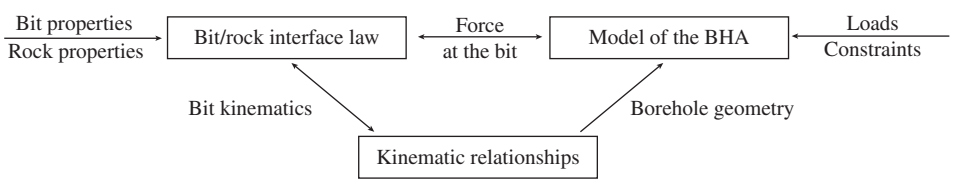


Figure 2 The three elements of the directional drilling model.

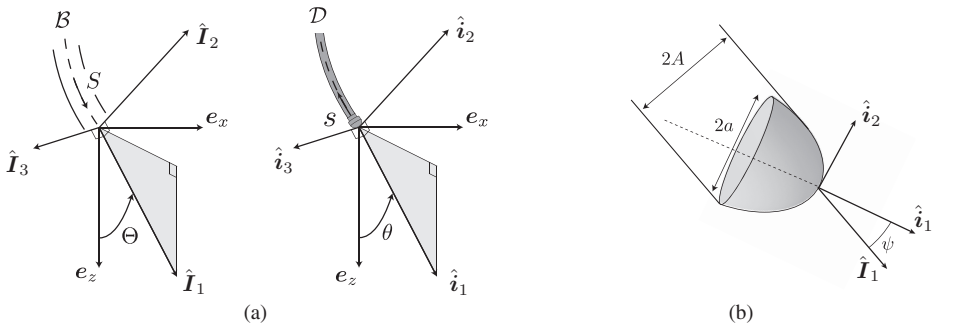


Figure 3 (a) Geometric description of the borehole and BHA. (b) The relative orientation of the bit with the borehole is measured by the tilt angle $\psi = \hat{\theta} - \hat{\Theta}$, which is here negative.

2.2 Geometry

The borehole geometry is referred to fixed basis $(\mathbf{e}_x, \mathbf{e}_y, \mathbf{e}_z)$, which has its origin at the rig and the $\mathbf{e}_z$-axis pointing in the direction of gravity (Fig. 3a).

The borehole is a growing cylinder-like object defined by its central axis $\mathcal{B}$ and its varying cross section, which is indirectly measured by the tilt of the bit with respect to $\mathcal{B}$. Axis $\mathcal{B}$, assumed here to be contained in a vertical plane, is described by $\mathbf{R}(S)$, a vectorial function of curvilinear coordinate S along the borehole, with $0 \leq S \leq L$; $S = 0$ at the surface and L is the increasing length of the borehole. If $\mathbf{R}$ is a smooth function, the tangent unit vector to the borehole is given by

$$\mathbf{I}_1 = \frac{d\mathbf{R}}{dS}. \tag{1}$$

Borehole axis $\mathcal{B}$ is completely defined by inclination $\Theta(S) \in [0, \pi]$, which is measured with respect to $\mathbf{e}_z$. Local borehole basis $(\mathbf{I}_1, \mathbf{I}_2, \mathbf{I}_3)$ is defined in such a way that $\mathbf{I}_2$ is in the same vertical plane as $\mathbf{I}_1$; $\mathbf{I}_3 = \mathbf{I}_1 \times \mathbf{I}_2$ is thus horizontal.

At the length scale of the BHA, axis $\mathcal{D}$ of the BHA is a small perturbation of $\mathcal{B}$. Like $\mathcal{B}$, axis $\mathcal{D}$ is assumed to be restricted to a vertical plane. It is parameterized by curvilinear coordinate s with origin at the bit and is described by vectorial function $\mathbf{r}(s; L)$. Here, length L of the borehole needs to be understood as the evolution variable, which enables the tracking of the evolving BHA deformation. Tangent vector $\mathbf{i}_1$ to $\mathcal{D}$ points in the direction of decreasing s; it is thus itself a small perturbation of tangent $\mathbf{I}_1$ to the borehole. Inclination $\theta(s; L) \in [0, \pi]$ of $\mathbf{i}_1$ defines the deformed configuration of the BHA at borehole length L. As for $(\mathbf{I}_1, \mathbf{I}_2, \mathbf{I}_3)$, local BHA basis $(\mathbf{i}_1, \mathbf{i}_2, \mathbf{i}_3)$ is defined in such a way that $\mathbf{i}_2$ is in the same vertical plane as $\mathbf{i}_1$ and $\mathbf{i}_3$ is horizontal.

The bit has a diameter 2a and a height 2b. Hereafter, a hat is attributed to variables evaluated at the bit; *e.g.*, $\hat{\Theta} = \Theta(L)$ is the borehole inclination at the bit, $\hat{\theta} = \theta(0; L)$ is the inclination of the bit axis, and $(\hat{\mathbf{i}}_1, \hat{\mathbf{i}}_2, \hat{\mathbf{i}}_3)$ is the bit basis. The relative orientation of the bit with respect to the borehole is measured by small angle ψ defined as

$$\psi = \hat{\theta} - \hat{\Theta}. \tag{2}$$

Bit tilt ψ thus measures the difference of inclination between $\hat{\mathbf{i}}_1$ and $\hat{\mathbf{I}}_1$ (Fig. 3b).

In principle, the overgauge of the borehole with respect to bit diameter 2a is affected by the tilt of the bit. This is particularly true for long-gauged bits. Hence, tilt angle ψ can be interpreted not only as a measure of the bit orientation relative to the borehole, but also as a measure of the borehole overgauge.

2.3 Kinematic relationships

The motion of the bit is defined by its velocity vector $\mathbf{v}$, its spin vector $\boldsymbol{\omega}$ orthogonal to bit axis $\hat{\mathbf{i}}_1$, and its angular velocity vector $\boldsymbol{\Omega}$ aligned with $\hat{\mathbf{i}}_1$ (Fig. 4a). With the bit motion restricted here to remain in a vertical plane, velocity vector $\mathbf{v}$ is in plane $(\hat{\mathbf{i}}_1,\hat{\mathbf{i}}_2)$ while $\boldsymbol{\omega}$ is orthogonal to $(\hat{\mathbf{i}}_1,\hat{\mathbf{i}}_2)$. The appropriate kinematic variables entering the interface laws are penetrations per revolution (Detournay *et al.*, 2008; Perneder *et al.*, 2012); namely, penetration vector $\mathbf{d}$ and angular penetration vector $\boldsymbol{\varphi}$, respectively defined as

$$\mathbf{d} = \frac{2\pi\mathbf{v}}{\Omega}, \qquad \boldsymbol{\varphi} = \frac{2\pi\boldsymbol{\omega}}{\Omega}, \tag{3}$$

where Ω is the magnitude of the angular velocity vector. In bit basis $(\hat{\mathbf{i}}_1, \hat{\mathbf{i}}_2, \hat{\mathbf{i}}_3)$, they reduce to axial penetration d_1, lateral penetration d_2, and angular penetration φ_3. The generalized penetration vector is defined as $\mathcal{P} = \{d_1, d_2, \varphi_3\}^{\mathrm{T}}$; it describes the motion of the bit/rock interface over one revolution of the bit. Also let β denote the relative orientation of penetration vector $\mathbf{d}$ with respect to bit axis $\hat{\mathbf{i}}_1$. Under normal drilling conditions, β is small, *i.e.*, penetration vector $\mathbf{d}$ is nearly aligned on $\hat{\mathbf{i}}_1$. Hence, β is given by

$$\beta \simeq \frac{d_2}{d_1}. \tag{4}$$

The propagation of the borehole is related to the bit kinematics, which are described by generalized penetration vector $\mathcal{P}$. For simplicity, we introduce the δ-operator to express the incremental change of a variable over one revolution of the bit. Penetration vector $\mathbf{d}$ is the incremental propagation of the borehole over a revolution, that is $\mathbf{d} = \delta\hat{\mathbf{R}}$, where $\hat{\mathbf{R}} = \mathbf{R}(L)$ gives the position of the bit relative to the origin of the fixed coordinate system. Hence, $\mathbf{d}$ is tangent to the borehole axis and $\mathbf{d} = d\hat{\mathbf{I}}_1$. The magnitude of the penetration vector, d, represents thus the incremental increase of the borehole length over one revolution, that is $d = \delta L$. An alternative definition of the delta operator is thus given by

$$\delta = d\frac{\partial}{\partial L}. \tag{5}$$

As tilt angle ψ measures the relative orientation of the bit with respect to the borehole (Fig. 3b), $\beta + \psi = 0$ or

$$\psi = -\beta = -\frac{d_2}{d_1}. \tag{6}$$

Angular penetration vector $\boldsymbol{\varphi}$ measures the rate of change of bit axis $\hat{\mathbf{i}}_1$ over one revolution: $\boldsymbol{\varphi} = \hat{\hat{\mathbf{i}}}_1 \times \delta\hat{\hat{\mathbf{i}}}_1$. Projection of this expression into the bit basis yields

$$\frac{\varphi_3}{d_1} = \frac{d\hat{\theta}}{dL}. \tag{7}$$

Strictly speaking, $d = d_1\sqrt{1+\beta^2}$, instead of d_1, should have been used in the above expression; however, as $\beta \ll 1$, no distinction is made here between d and d_1.

2.4 Bit/rock interface laws

The interface laws are relationships between generalized forces averaged over one revolution and penetration variables measuring the advancement of the bit/rock interface over a revolution, both measured at the reference point of the bit (Perneder *et al.*, 2012). It is generally assumed that the interface laws are rate-independent (Detournay *et al.*, 2008; Franca 2010; Perneder *et al.*, 2012). The assumption of rate-independence of the bit/rock interaction provides a simple, although not fundamental, argument to identify the penetrations per revolution as the appropriate kinematic variables in the interface laws.

The interaction forces are reduced to a force $\hat{\mathbf{F}}$, a moment $\hat{\mathbf{M}}$ orthogonal to bit axis $\hat{\mathbf{i}}_1$, and a torque $\hat{\mathbf{C}}$ acting along $\hat{\mathbf{i}}_1$ (Fig. 4a). Moment $\hat{\mathbf{M}}$ is directly related to the directional response of the bit, while torque $\hat{\mathbf{C}}$ is hardly influenced by this directional behavior.

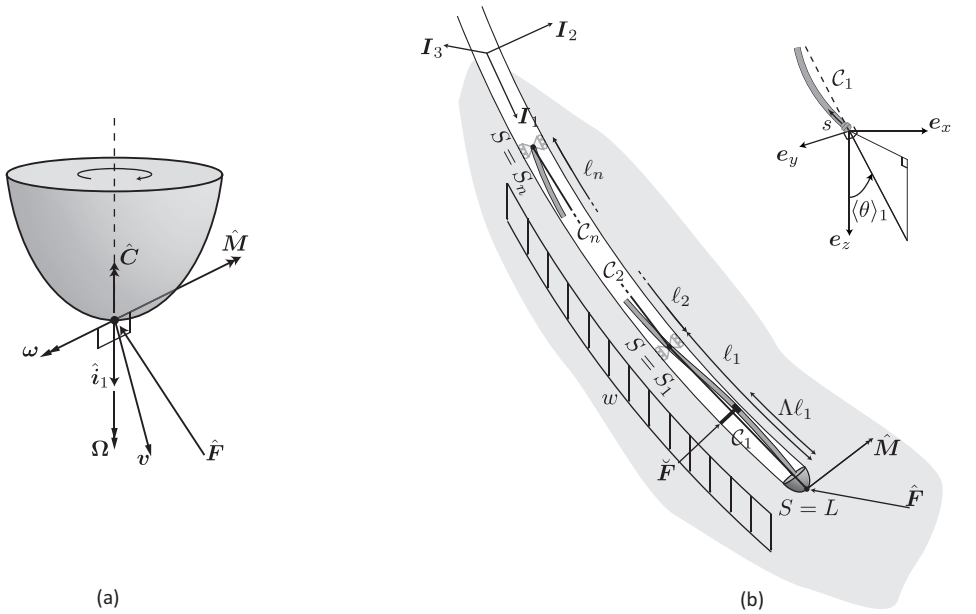


Figure 4 (a) Generalized forces $\{\hat{\mathbf{F}},\hat{\mathbf{M}},\hat{\mathbf{C}}\}$ and kinematics $\{\boldsymbol{\upsilon},\boldsymbol{\omega},\boldsymbol{\Omega}\}$ of the bit. Torque $\hat{\mathbf{C}}$ and angular velocity vector $\boldsymbol{\Omega}$ are aligned with bit axis $\hat{\mathbf{i}}_1$, while moment $\hat{\mathbf{M}}$ and spin vector $\boldsymbol{\omega}$ are orthogonal to $\hat{\mathbf{i}}_1$. Here, $\hat{\mathbf{M}}$ and $\boldsymbol{\omega}$ are assumed to be coaxial. (b) Beam model of the BHA. Chord C_i, $i = 1, \ldots, n$, link two successive contact points and have inclination $\langle\theta\rangle_i$.

Hence, in the following, torque $\hat{\mathbf{C}}$ is not taken into account in the interface laws. By assuming here that the penetration variables and the generalized forces are coaxial — a simplifying restriction on the structure of the interface laws, $\hat{\mathrm{F}}_3 = \hat{\mathrm{M}}_2 = 0$, on account that the borehole trajectory is planar. The remaining components of the generalized forces are represented by vector $\mathcal{F} = \{\hat{\mathrm{F}}_1, \hat{\mathrm{F}}_2, \hat{\mathrm{M}}_3\}^{\mathrm{T}}$.

When a cutter on a drag (PDC) bit is interacting with the rock, two basic processes take place: (i) penetration at the cutting face and (ii) contact at the cutter wearflat/rock interface (Detournay & Defourny, 1992). Experimental results suggest that, in a first regime associated with small depths of cut, the contact forces between the rock and the bit wearflats are not fully developed. In a second regime corresponding to depths of cut larger than a threshold, these contact forces reach saturation. These observations justify the use of bilinear interface laws between $\mathcal{F}$ and $\mathcal{P}$; similar laws also seem to hold for roller-cone bits (Franca, 2010).

Hereafter, the bit gauge is assumed to interact with the rock in the first regime, so that the gauge/rock interaction is dominated by contact forces. The interaction of the bit cutting structure with the rock is supposed to take place in the second regime and the magnitude of axial force $\hat{\mathrm{F}}_1$ is assumed to be greater than a threshold force G_1. This saturation force G_1 is the contact component of the weight on bit that is transmitted to the cutter wearflats. It is related to the state of wear of the bit; $\mathrm{G}_1 = 0$ for an ideally "sharp" bit. Finally, the reference point of the bit is selected in such a way that no moment acts on the bit if the angular penetration vanishes.

With the above assumptions, the bit/rock interaction laws can thus be formally expressed as (Perneder *et al.*, 2012)

$$\begin{Bmatrix} \hat{\mathrm{F}}_1 \\ \hat{\mathrm{F}}_2 \\ \hat{\mathrm{M}}_3 \end{Bmatrix} = -\begin{Bmatrix} \mathrm{G}_1 \\ 0 \\ 0 \end{Bmatrix} - \begin{bmatrix} \mathrm{H}_1 & 0 & 0 \\ 0 & \mathrm{H}_2 & 0 \\ 0 & 0 & \mathrm{H}_0 \end{bmatrix} \begin{Bmatrix} \mathrm{d}_1 \\ \mathrm{d}_2 \\ \varphi_3 \end{Bmatrix}. \tag{8}$$

Coefficients G_1, H_1, H_2, and H_0 are positive, a consequence of the components of the forces and moment on the bit being opposite to their conjugated kinematic variables on account that the drilling process is dissipative. Also, $\mathrm{H}_1 \ll \mathrm{H}_2$ as the bit ability to drill along its axis $\hat{\mathbf{i}}_1$ is greater than its ability to drill sideways.

The next step is to combine interface law (8) and kinematic relationships (6) and (7) to derive expressions for lateral force $\hat{\mathrm{F}}_2$ and moment $\hat{\mathrm{M}}_3$ at the bit. Recognizing that axial force on the bit $\hat{\mathrm{F}}_1$ is effectively known, the interface law can be rewritten as

$$\hat{\mathrm{F}}_2 = -\eta(\hat{\mathrm{F}}_1 + \mathrm{G}_1)\left(\hat{\theta} - \hat{\Theta}\right), \tag{9}$$

$$\hat{\mathrm{M}}_3 = \chi \ell_1^2 (\hat{\mathrm{F}}_1 + \mathrm{G}_1) \frac{\mathrm{d}\hat{\theta}}{\mathrm{dL}}. \tag{10}$$

The axial force reduced by the force transmitted by the wear surface of the bit, $\mathrm{W}_{\mathrm{a}} = -(\hat{\mathrm{F}}_1 + \mathrm{G}_1)$, is referred to as the active weight; it is directly responsible for the advance of the bit into the rock. The two numbers, η and χ, are the lateral and the angular steering resistances; they are defined as

$$\eta = \frac{\mathrm{H}_2}{\mathrm{H}_1}, \qquad \chi = \frac{\mathrm{H}_0}{\ell_1^2 \mathrm{H}_1}, \tag{11}$$

where ℓ_1 is the distance between the bit and the first stabilizer. Lateral and angular steering resistances measure the relative difficulty to impose, respectively, a lateral and an angular penetration to the bit relative to an axial one; they depend essentially on the characteristics of the bit gauge, *i.e.*, its height, geometry (full-gauged, undercut, tapered), and aggressiveness (passive, semi-active, active) (Dupriest & Sowers, 2009). Number η is of order $O(1 \sim 100)$ (Menand *et al.*, 2002; Perneder *et al.*, 2012), while χ is a small number of order $O(10^{-2} \sim 10^{-1})$ that also depends on the position of the first contact between the borehole and the BHA behind the bit. With the exception of Ho (1995), all other investigations have assumed that the bit is free to change its orientation; such an assumption implies that $\chi = 0$. Since all the coefficients H of the bit/rock interface laws are proportional to the downhole strength of the rock, the bit/rock interaction numbers η and χ only depend on the bit design (and on ℓ_1 for χ).

Equations (9) and (10) thus express proportionality between lateral force on the bit $\hat{F}_2$ and the tilt, and between moment at the bit $\hat{M}_3$ and the spatial rate of change of the bit inclination, under constant active weight W_a.

2.5 BHA model

The BHA consists of a connected set of heavy pipes called drill collars, stabilizers, and the RSS. At the intermediate scale of order O(10m) used to construct the model of directional drilling, the BHA is a slender elastic object subject to external forces and moments and constrained by the stabilizers to conform with the borehole geometry. Thus, at that scale, the BHA can in principle be modeled as a rod. Here it will be assumed that (i) the BHA is inextensible, (ii) the Euler-Bernoulli hypotheses apply, (iii) the properties are uniform, and (iv) there is no contact between the BHA and the borehole wall, other than those taking place at the bit, at the RSS, and at the stabilizers. Furthermore, the stabilizers are assumed to be centered on average in the borehole and to not transmit any moment between the borehole wall and the BHA. They are thus modeled as point supports of the BHA, and force BHA axis $\mathcal{D}$ and borehole axis $\mathcal{B}$ to intersect at these points. Also, since the velocity discontinuity at the borehole/stabilizer contact is essentially orthogonal to $\mathbf{I}_1$, the frictional forces are fully subsumed into a frictional torque at the stabilizer, and the reaction force at the contact can be assumed to be orthogonal to the borehole. In other words, the stabilizers can be assumed to slide frictionlessly along the axis of the borehole, a consequence of the rotation of the drillstring.

The model of BHA extends from the bit to the n^{th} stabilizer (with $n = 2$ or 3, usually). The RSS, located at a distance $\Lambda\ell_1$ from the bit, applies a transverse force $\breve{\mathbf{F}}$ on the BHA. The n stabilizers, which are numbered from 1 to n starting with the closest stabilizer to the bit, are treated as discrete geometrical constraints. They define n BHA segments of lengths $\ell_1, \ell_2, \ldots, \ell_n$ (Fig. 4b). On account of the assumed inextensibility of the BHA, curvilinear coordinate s_i of the i^{th} stabilizer is given by

$$s_i = \sum_{j=1}^{i} \ell_j, \; i = 1, \ldots, n. \tag{12}$$

On the other hand, position S_i of the i^{th} stabilizer in the borehole can be deduced from the isoperimetric constraint

$$\int_{S_i}^{S_{i-1}} \mathbf{I}_1 dS = \int_{s_{i-1}}^{s_i} \mathbf{i}_1 ds, \quad i = 1, ..., n, \tag{13}$$

where the index $i = 0$ has been assigned to the bit; *i.e.*, $S_0 = L$ and $s_0 = 0$.

In the following the distinction between bases $(\mathbf{i}_1, \mathbf{i}_2, \mathbf{i}_3)$ and $(\mathbf{I}_1, \mathbf{I}_2, \mathbf{I}_3)$ is blurred, on account that the angle between $\mathbf{i}_1$ (the tangent to BHA axis $\mathcal{D}$) and $\mathbf{I}_1$ (the tangent to borehole axis $\mathcal{B}$) is everywhere always very small, a consequence of the small clearance between the BHA and the borehole wall; in other words, at the scale of the BHA, $\mathcal{D}$ is the leading order approximation of $\mathcal{B}$. This simplification has several implications. First $s \simeq L - S$, meaning that the same curvilinear coordinate can be used as a measure of the arc length for both $\mathcal{B}$ and $\mathcal{D}$. This implies that the positions of the stabilizers on $\mathcal{B}$ are known; thus, $S_i = L - s_i$, $i = 1, ...,n$. Second, it can be assumed that RSS force $\breve{\mathbf{F}}$ is orthogonal to $\mathbf{I}_1$. Finally, the expressions for the bit generalized forces in basis $(\mathbf{i}_1, \mathbf{i}_2, \mathbf{i}_3)$ that embody the bit/rock interface laws can be interpreted as being valid in borehole basis $(\mathbf{I}_1, \mathbf{I}_2, \mathbf{I}_3)$. In other words the difference between the components of the bit forces expressed in these two different bases is disregarded. However, the distinction between the two bases is maintained in the bit/rock interface laws since the transverse force on the bit is related to the bit tilt.

As a consequence of ignoring the difference between bases $(\mathbf{i}_1, \mathbf{i}_2, \mathbf{i}_3)$ and $(\mathbf{I}_1, \mathbf{I}_2, \mathbf{I}_3)$, isoperimetric constraints (13) are approximated by writing that average inclination $\langle\theta\rangle_i$ of the BHA i^{th} segment is equal to average inclination $\langle\Theta\rangle_i$ of the borehole section between these two stabilizers

$$\langle\theta\rangle_i = \frac{1}{\ell_i}\int_{s_{i-1}}^{s_i} \theta(s; L) ds \simeq \langle\Theta\rangle_i = \frac{1}{\ell_i}\int_{S_i}^{S_{i-1}} \Theta(S) dS. \tag{14}$$

The equations governing the mechanical response of the BHA — the proportionality between the bending moment and the beam curvature and the equilibrium of the transverse forces and moments, can be expressed in terms of inclination $\theta(s)$. The moment-curvature relationship is

$$M_3 = -EI\theta', \tag{15}$$

where EI is the flexural rigidity of the BHA and the prime ($'$) denotes differentiation with respect to *s*. Combined with the moment equilibrium equation, (15) yields

$$F_2 = -EI\theta''. \tag{16}$$

Further substituting (16) in the transverse force equilibrium equation gives

$$EI\theta''' = w \sin\langle\Theta\rangle_1, \tag{17}$$

where w is the (buoyant) linear weight. In writing (17), we have assumed that the BHA has a uniform inclination $\langle\Theta\rangle_1$. Integrating (17) leads to the following expression for inclination $\theta(s)$ along each segment

$$EI\theta = A_0 + A_1 s + A_2 s^2 + \frac{1}{6} w \sin\langle\Theta\rangle_1 s^3. \tag{18}$$

The above expressions are valid along parts of the BHA comprised between points of singular loading. Indeed, coefficient A_2 is discontinuous at $s = \Lambda\ell_1$ where RSS force $\breve{\mathbf{F}}$ is applied, and at the internal stabilizers $s = s_i$, $i = 1, \ldots, n-1$ due to the reaction forces.

Finally consideration of the axial force equilibrium leads to

$$F_1' = w \cos \langle\Theta\rangle_1. \tag{19}$$

Equation (19) can be integrated to express the axial force at the bit in terms of the "imposed" axial force at the last stabilizer.

Once the deformed configuration of the BHA is determined, *i.e.*, $\theta(s)$ is known, the moment and transverse force at the bit are deduced from (15) and (16) evaluated at $s = 0$. In view of the linear nature of the Euler-Bernoulli beam theory, transverse force $\hat{F}_2(L)$ and moment $\hat{M}_3(L)$ can be expressed as a linear combination of the external loads and the kinematic constraints applied on the BHA:

$$\frac{\hat{F}_2}{F_*} = \mathcal{F}_b\left(\hat{\theta} - \langle\Theta\rangle_1\right) + \sum_{i=1}^{n-1}\mathcal{F}_i\left(\langle\Theta\rangle_i - \langle\Theta\rangle_{i+1}\right) + \mathcal{F}_w \sin\langle\Theta\rangle_1 \frac{w\ell_1}{F_*} + \mathcal{F}_r\frac{\breve{F}_2}{F_*}, \tag{20}$$

$$\frac{\hat{M}_3}{\ell_1 F_*} = \mathcal{M}_b\left(\hat{\theta} - \langle\Theta\rangle_1\right) + \sum_{i=1}^{n-1}\mathcal{M}_i\left(\langle\Theta\rangle_i - \langle\Theta\rangle_{i+1}\right) + \mathcal{M}_w \sin\langle\Theta\rangle_1 \frac{w\ell_1}{F_*} + \mathcal{M}_r\frac{\breve{F}_2}{F_*}, \tag{21}$$

$$F_* = \frac{3EI}{\ell_1^2}, \tag{22}$$

where F_* is a characteristic force, which can simply be interpreted as the reaction force induced at the end of a simply supported beam of length ℓ_1 and stiffness EI, in response to a unit inclination angle imposed at that end. For a BHA with uniform flexural rigidity and specific weight, $\mathcal{F}$ and $\mathcal{M}$ represent numbers of purely geometrical nature that only depend on the configuration of the BHA; *i.e.*, on the relative position of the stabilizers $\lambda_i = \ell_i/\ell_1$, $i = 2, \ldots, n$ and on the relative distance Λ between the bit and the RSS pads. While Λ is typically in the range [0.15,0.35], numbers λ_i are of order O(1). For a 2-stabilizer uniform BHA, these coefficients are listed in Table 1 below.

Table 1 Geometric coefficients $\mathcal{F}$ and $\mathcal{M}$ for a uniform BHA with 2 stabilizers. The coefficients for a 1-stabilizer BHA can be deduced by taking the limit $\lambda_2 \to \infty$. (Terms in λ_2^2 should be discarded in that case.)

Index	*Coefficient* $\mathcal{F}$	*Coefficient* $\mathcal{M}$
b	$-\dfrac{4\lambda_2+6}{4\lambda_2+3}$	$\dfrac{4(\lambda_2+1)}{4\lambda_2+3}$
w	$\dfrac{-3\lambda_2^3+10\lambda_2+6}{16\lambda_2+12}$	$\dfrac{\lambda_2^3-2\lambda_2-1}{16\lambda_2+12}$
r	$\dfrac{-2(\lambda_2+3)\Lambda^3+(6\lambda_2+9)\Lambda^2-4\lambda_2-3}{4\lambda_2+3}$	$\dfrac{(\Lambda-1)\Lambda((2\lambda_2+3)\Lambda-4\lambda_2-3)}{4\lambda_2+3}$
l	$\dfrac{6}{4\lambda_2+3}$	$-\dfrac{2}{4\lambda_2+3}$

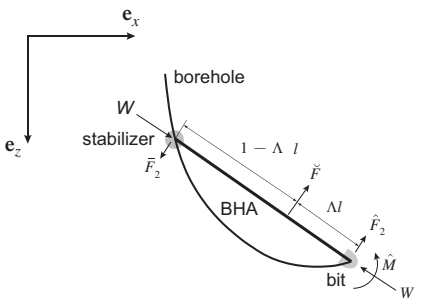


Figure 5 Forces acting on the rigid BHA with one freely tilting stabilizer ($\overline{\mathrm{M}} = 0$). Force $\breve{\mathbf{F}}$ corresponds to the reaction force on the RSS pads.

For more realistic BHA, the coefficients could be computed numerically using, for example, a finite-element discretization of the BHA. This approach is applicable as long as the linearity of the underlying model holds, which implies restrictions to the nature of the contacts between the BHA and the borehole, as well as to the borehole curvature (geometric linearity). The model description and the formulation of the propagation equations would remain completely similar.

3 TOY MODEL

It is illustrative to formulate first the dynamical model of a propagating planar borehole for the simple case of a rigid BHA with one stabilizer and a perfectly sharp bit. The BHA considered here consists of a drill pipe of length ℓ connecting the bit to a stabilizer that can freely tilt within the borehole. The forces acting on the BHA are the known (and possibly varying) weight on bit $\mathrm{W} = -\hat{\mathrm{F}}_1$ and transverse force $\breve{\mathbf{F}}$ applied by the pads of a RSS located at a distance $\Lambda\ell$ from the bit; the weight of the BHA is neglected (Fig. 5). By combining kinematic and mechanical considerations, an evolution equation for the borehole inclination is derived in terms of known geometrical and mechanical quantities. The equilibrium solution is then extracted from this dynamical model.

3.1 Kinematic considerations

Consider the borehole with varying curvature shown in Fig. 6a. Let $\overline{\mathrm{S}}$ and $\hat{\mathrm{S}}$ denote the current positions of the stabilizer and of the bit in terms of curvilinear coordinate S of the borehole. The corresponding position $\overline{\mathrm{S}}$ of the stabilizer relative to the bit is known as

$$\int_{\bar{\mathrm{S}}}^{\hat{\mathrm{S}}} \cos\Theta \, \mathrm{dS} = \ell\cos\,\theta, \qquad \int_{\bar{\mathrm{S}}}^{\hat{\mathrm{S}}} \sin\Theta \, \mathrm{dS} = \ell\sin\theta, \tag{23}$$

which results from the assumption of a rigid, inextensible BHA. Equations (23) can be solved for $\overline{\mathrm{S}}$ and BHA inclination θ, given the known inclination of the borehole $\Theta(\mathrm{S})$, $0 \le \mathrm{S} \le \mathrm{L}$.

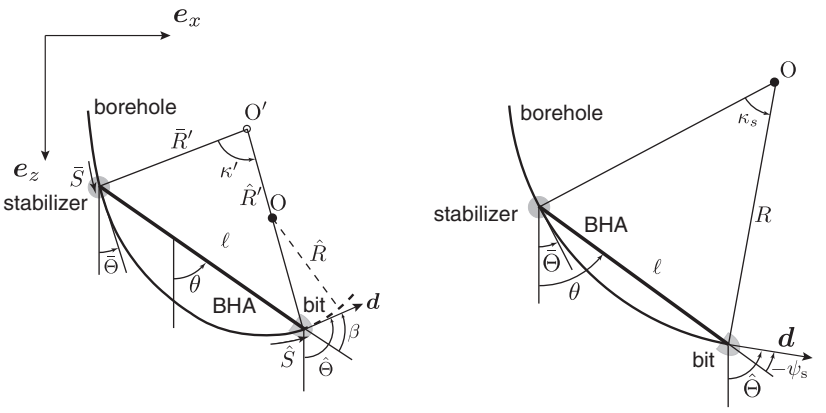


Figure 6 (a) Simplified directional drilling problem involving a rigid BHA with one freely tilting stabilizer. The instantaneous center of rotation of the BHA corresponds to O', while the center of curvature of the borehole at the bit corresponds to *O*. As O' is distinct from *O*, the borehole propagation is not stationary, *i.e.*, the borehole curvature is evolving. (b) Stationary solution for the hole propagation (constant curvature) for a rigid BHA with one stabilizer. The geometrical construction shows the relation $\kappa_s = -2\psi_s\,(= 2\beta_s)$ between steady-state borehole curvature κ_s and bit tilt ψ_s.

The rigid body motion of the BHA associated with bit penetration $\delta\hat{S} = d$, where $\delta\hat{S}$ denotes the variation of $\hat{S}$ over one bit revolution, is completely defined by integral constraints (23), the inclination of the borehole at the stabilizer and the bit, and inclination θ of the BHA. Indeed, applying the δ-operator to (23) yields a linear system of equations that can be solved for $\delta\bar{S}$ and $\delta\theta$. Thus,

$$\delta\bar{S} = \frac{\cos(\bar{\Theta} - \theta)}{\cos(\bar{\Theta} - \theta)}\,d, \qquad \delta\theta = \frac{\sin(\hat{\Theta} - \bar{\Theta})}{\cos(\bar{\Theta} - \theta)}\,\frac{d}{\ell}, \tag{24}$$

where $\hat{\Theta}$ and $\bar{\Theta}$ denote the inclination of the borehole at the bit and at the stabilizer, respectively, and where we have used $\delta\hat{S} = d$. The first Equation in (24) translates the BHA inextensibility condition; the second one expresses the BHA rigidity constraint. Linearization of (24) yields

$$\delta\bar{S} \simeq d, \qquad \delta\theta \simeq (\hat{\Theta} - \bar{\Theta})\,\frac{d}{\ell}, \tag{25}$$

with $\delta\bar{S} = d + O(\hat{\Theta} - \bar{\Theta})^2$.

The instantaneous center of rotation O' of the BHA is defined by the intersection of the two perpendiculars at $\hat{S}$ and $\bar{S}$ to the tangents $\boldsymbol{\delta}\hat{\mathbf{S}}$ and $\boldsymbol{\delta}\bar{\mathbf{S}}$ to the borehole, respectively. Angle κ' between the two line segments $O'\hat{S}$ and $O'\bar{S}$ is given by (Fig. 6a)

$$\kappa' = \hat{\Theta} - \bar{\Theta}. \tag{26}$$

We denote by *O* the center of curvature of the borehole at the bit. Let K and R denote the curvature and radius of curvature of the borehole, in general both a function of borehole curvilinear coordinate *S*, and let $\hat{\kappa} = \ell\hat{K}$ denote the scaled curvature at the bit.

Center of curvature O is located at a distance $\hat{\mathrm{R}}$ from the bit, on the perpendicular to $\boldsymbol{\delta}\hat{\mathbf{S}} = \mathbf{d}$ (Fig. 6a). The δ-variation of the borehole inclination at the bit, $\delta\hat{\Theta}$, is related to $\hat{\kappa}$ according to

$$\delta\hat{\Theta} = \frac{\hat{\kappa}\mathrm{d}}{\ell}. \tag{27}$$

3.2 Mechanical considerations

For a perfectly sharp bit, the bit/rock interface laws (9)–(10) can be expressed as

$$\frac{\hat{\mathrm{F}}_2}{\mathrm{W}} = -\eta\beta, \qquad \frac{\hat{\mathrm{M}}_3}{\mathrm{W}\ell} = -\frac{\chi\ell\varphi_3}{\mathrm{d}}, \tag{28}$$

where W is the weight on bit, $\hat{\mathrm{F}}_2$ is the transverse force on the bit, and $\hat{\mathrm{M}}_3$ is the moment at the bit. Also $\beta \simeq \mathrm{d}_2/\mathrm{d}_1$ and angular penetration $\varphi_3 = \delta\theta$.

Consider now the moment equilibrium with respect to the stabilizer

$$\hat{\mathrm{M}}_3 + \ell\hat{\mathrm{F}}_2 + (1-\Lambda)\ell\breve{\mathbf{F}} = 0. \tag{29}$$

In view of (28), this balance equation can be rewritten as

$$\frac{\chi\ell\varphi_3}{\mathrm{d}} + \eta\beta - (1-\Lambda)\breve{\Gamma} = 0, \tag{30}$$

where $\breve{\Gamma} = \breve{\mathbf{F}}/\mathrm{W}$ is the scaled force at the RSS pads. Equation (30) embodies all the information from the interface laws and moment equilibrium.

3.3 Borehole evolution

The direction of borehole propagation is given by penetration vector $\mathbf{d}$, which is tangent to the borehole. This condition is translated as

$$\beta + \psi = 0. \tag{31}$$

Furthermore, angular penetration φ can be expressed as

$$\varphi \simeq (\hat{\Theta} - \bar{\Theta})\frac{\mathrm{d}}{\ell}, \tag{32}$$

according to the definition $\varphi_3 = \delta\theta$ and (25). Using (31) and (32), with definition (2) of the bit tilt, the moment balance equation can equivalently be written as

$$(\eta+\chi)\hat{\Theta} = \eta\theta + \chi\bar{\Theta} + (1-\Lambda)\breve{\Gamma}. \tag{33}$$

Together with integral constraints (23) for the evaluation of θ, (33) can be used to propagate the borehole. Taking the δ-variation of (33) yields

$$(\eta+\chi)\delta\hat{\Theta} = \eta(\hat{\Theta} - \bar{\Theta})\frac{\mathrm{d}}{\ell} + \chi\delta\bar{\Theta} + (1-\Lambda)\delta\breve{\Gamma}, \tag{34}$$

which can be further rewritten as

$$(1+\epsilon)\eta\Theta'(\xi) = \eta\Theta(\xi) + \epsilon\eta\Theta'(\xi-1) - \eta\Theta(\xi-1) + (1-\Lambda)\breve{\Gamma}'(\xi), \tag{35}$$

where ϵ is a small parameter defined as

$$\epsilon = \frac{\chi}{\eta} \tag{36}$$

and where we have introduced scaled coordinate $\chi = \hat{S}/\ell$.

The borehole could be propagated either using delay algebraic Equation (33) and integral constraint (23), or delay differential Equation (36). Although (36) is equivalent to the two Equations (23) and (33), its consideration allows to account for the rigidity and inextensibility of the BHA via the differential form of the BHA rigidity and inextensibility constraints (25) rather than via integral constraints (23). This form of the evolution equation yields directly an expression for the borehole curvature at the bit.

3.4 Stationary solution

A necessary condition to reach stationarity is that both weight on bit W and force on the RSS pads $\breve{F}$ are constant, *i.e.*, $\breve{\Gamma} = \text{Const}$. The stationary solution is characterized by a constant bit tilt $\psi = \psi_s$ and by a constant borehole curvature $\kappa = \kappa_s$. Also $\delta\hat{S} = \delta\overline{S}$ and $\delta\theta = \delta\hat{\Theta} = \delta\bar{\Theta}$. It then follows that

$$\theta = \frac{1}{2}\left(\hat{\Theta} + \bar{\Theta}\right) \quad \text{or} \quad \psi_s = -\frac{1}{2}\left(\hat{\Theta} - \bar{\Theta}\right). \tag{37}$$

Hence

$$\kappa_s = \hat{\Theta} - \bar{\Theta}. \tag{38}$$

Furthermore, combining (34) and (38) yields the equilibrium curvature of the borehole

$$\kappa_s = \frac{2(1-\Lambda)\breve{F}}{\eta(1+2\epsilon)W}. \tag{39}$$

Equations (38) and $\kappa_s = -2\psi_s$ have a simple geometric interpretation upon recognizing that, at equilibrium, the instantaneous center of rotation of the BHA, O′, coincides with the center of curvature of the borehole O, *i.e.*, O′ ≡ O (see Fig. 6b).

4 BOREHOLE TRAJECTORY

4.1 Scaling

The equations governing the three elements of the directional drilling model form together a closed system of equations; that is, they are sufficient to describe the propagation of the borehole and the evolution of the deformed configuration of the BHA, given appropriate initial conditions. They are now transformed into an evolution equation for the borehole inclination, which is then integrated numerically. Before formulating this equation, we convert the physical quantities into dimensionless parameters.

Loading of the BHA is encapsulated in the following parameters

$$\Gamma = \frac{\breve{\mathrm{F}}_2}{\mathrm{F}_*}, \qquad \Pi = \frac{W_\mathrm{a}}{\mathrm{F}_*}, \qquad \Upsilon = \frac{\mathrm{w}\ell_1}{\mathrm{F}_*}. \tag{40}$$

Both Γ and Π are the control parameters for this system (strictly speaking, $\hat{\mathrm{F}}_1$ is the control parameter, as it depends directly on the magnitude of the hookload, the vertical force imposed at the top of the drillstring); Γ is generally of order $\mathrm{O}(10^{-3} \sim 10^{-2})$, while Π takes value ranging from 10^{-3} to 10^{-1}. Number Υ is also typically small, of order $\mathrm{O}(10^{-3} \sim 10^{-2})$.

Small parameter $\epsilon = \chi/\eta$ is preferred to χ, so that Π only manifests in group $\eta\Pi$; ϵ contrasts the dimension of the bit with the length of the first BHA segment as it is proportional to $(\mathrm{b}/\ell_1)^2$. This small parameter, generally of order $\mathrm{O}(10^{-3} \sim 10^{-1})$, affects the transient solution over a small distance that is often within the resolution of the model. In such a case it can be ignored, implying that the moment at the bit can actually be neglected.

Dimensionless group $\eta\Pi$ can be viewed as contrasting the resistance of the rock with the stiffness of the BHA, as the bit is tilted. Parameter $\eta\Pi$, typically of order $\mathrm{O}(10^{-2} \sim 1)$, depends on several properties of the system: lateral steering resistance η of the bit, axial force on the bit $\hat{\mathrm{F}}_1$, the combined state of wear of the drill bit and rock strength measured by G_1, distance ℓ_1 between the first stabilizer and the bit, and stiffness EI of the BHA.

Finally, $\xi = \mathrm{L}/\ell_1$ denotes the dimensionless length of the borehole; ξ is the independent variable of the differential equation governing the borehole inclination.

4.2 Borehole propagation

Given the description of the system in terms of (i) the n geometrical numbers (λ_i, $\mathrm{i} = 2, \ldots, \mathrm{n}$ and Λ) characterizing the configuration of the BHA, (ii) the two numbers essentially describing the bit/rock interface, η and ϵ, (iii) number Υ capturing gravity loading, and given the two forcing functions $\Pi(\xi)$ and $\Gamma(\xi)$, we seek to determine borehole inclination $\Theta(\xi)$ and bit inclination $\theta(\xi)$. For simplicity of notation, we are now dropping the hat characterizing a variable evaluated at the bit, as it is implicitly assumed that such a variable is a function of ξ. All the functions are in principle piecewise continuous functions of ξ.

The equations that govern the evolution of $\Theta(\xi)$ and $\theta(\xi)$ are deduced by equating expressions (20) and (21) for the lateral force and moment at the bit that were derived from considerations involving the deformable BHA, with (9) and (10) that were obtained from considerations involving the interface law

$$\eta\Pi(\theta - \Theta) = \mathcal{F}_\mathrm{b}(\theta - \langle\Theta\rangle_1) + \mathcal{F}_\mathrm{w}\Upsilon\sin\langle\Theta\rangle_1 + \mathcal{F}_\mathrm{r}\Gamma + \sum_{\mathrm{i}=1}^{\mathrm{n}-1}\mathcal{F}_\mathrm{i}\big(\langle\Theta\rangle_\mathrm{i} - \langle\Theta\rangle_{\mathrm{i}+1}\big), \tag{41}$$

$$-\epsilon\eta\Pi\theta' = \mathcal{M}_\mathrm{b}(\theta - \langle\Theta\rangle_1) + \mathcal{M}_\mathrm{w}\Upsilon\sin\langle\Theta\rangle_1 + \mathcal{M}_\mathrm{r}\Gamma + \sum_{\mathrm{i}=1}^{\mathrm{n}-1}\mathcal{M}_\mathrm{i}\big(\langle\Theta\rangle_\mathrm{i} - \langle\Theta\rangle_{\mathrm{i}+1}\big), \tag{42}$$

where differentiation with respect to ξ is denoted by a prime. These two equations can further be combined into a single delay differential equation (DDE) for $\Theta(\xi)$, by first differentiating (41) with respect to ξ, then eliminating θ' with (42), and finally dropping all the terms prefixed by small parameter ϵ except the terms containing Θ' and Γ'. Under the assumption of Π being constant, the DDE governing the evolution of borehole inclination $\Theta(\xi)$ reads

$$\begin{aligned}\epsilon\eta\Pi\Theta'(\xi) = &-\mathcal{M}_b[\Theta(\xi) - \langle\Theta\rangle_1] - \sum_{i=1}^{n-1} A_i(\eta\Pi)\left(\langle\Theta\rangle_i - \langle\Theta\rangle_{i+1}\right) \\ &+A_\Upsilon(\eta\Pi)\Upsilon \sin\langle\Theta\rangle_1 + A_\Gamma(\eta\Pi)\Gamma(\xi) - \epsilon\mathcal{F}_r\Gamma'(\xi),\end{aligned} \tag{43}$$

where $\langle\Theta\rangle_i$ is the averaged inclination of the i^{th} segment of BHA defined as

$$\langle\Theta\rangle_i = \frac{1}{\lambda_i}\int_{\xi_i}^{\xi_{i-1}} \Theta d\zeta. \tag{44}$$

and

$$\xi_i = \xi - \sum_{j=1}^{i}\lambda_j \tag{45}$$

with $\xi_0 = \xi$ corresponding to the position of the bit.

Coefficients $A_\Upsilon(\eta\Pi)$, $A_\Gamma(\eta\Pi)$, and $A_i(\eta\Pi)$ are given by

$$A_\Upsilon = \frac{\mathcal{F}_b\mathcal{M}_w - \mathcal{F}_w\mathcal{M}_b - \mathcal{M}_w\eta\Pi}{\eta\Pi}, \tag{46}$$

$$A_\Gamma = \frac{\mathcal{F}_b\mathcal{M}_r - \mathcal{F}_r\mathcal{M}_b - \mathcal{M}_r\eta\Pi}{\eta\Pi}, \tag{47}$$

$$A_i = \frac{\mathcal{F}_b\mathcal{M}_i - \mathcal{F}_i\mathcal{M}_b - \mathcal{M}_i\eta\Pi}{\eta\Pi}. \tag{48}$$

Borehole propagation Equation (43) does not only depend on the external loads and on the current borehole inclination, but also on the borehole past trajectory. The delays, corresponding to the positions of the stabilizers, capture the geometric feedback of the borehole geometry on the force and moment at the bit. The largest delay corresponds to the position of the last modeled stabilizer. Borehole inclination Θ along the entire BHA influences thus the drilling direction through secular terms $\langle\Theta\rangle_i$. This is clearly recognized from the first two terms on the right-hand side of (43).

Discontinuities in the borehole trajectory are generated by sudden changes in the weight on bit or in the RSS force, or by sudden change in rock properties. The discontinuities are of different order, however. While a sudden change in the RSS force induces a kink in the borehole trajectory, the crossing of an interface between two layers produces complex local perturbations in the borehole geometry, which, at the resolution of the model, are modeled as a shift in the bit position or equivalently as a jump in the averaged inclination of the first section (Boualleg *et al.*, 2006; Marck & Detournay, 2014). The magnitude and order of the

discontinuities can be obtained analytically in all cases. When a stabilizer encounters a trajectory discontinuity, it induces a discontinuity of one order higher in the borehole geometry at the bit, due to the smoothing effect of the *retarded* delay differential equations (Hale, 1977). For example, a stabilizer passing through a kink in the borehole trajectory induces a discontinuity in the borehole curvature at the bit.

4.3 Qualitative response

Three scales can be identified in the response of the borehole to a sudden change in control parameters Π and/or Γ: a short scale $O(10^{-1})$, an intermediate scale $O(1 \sim 10)$, and a large scale $O(10^2 \sim 10^3)$.

4.3.1 Short range

A short-range evolution is associated with fast dynamics controlled by small parameter ϵ multiplying Θ' in (43), which allows for fast changes in the bit and borehole orientations. Over this short range, secular terms in $\langle\Theta\rangle_i$, $i = 1, \ldots, n$, and the forcing term proportional to Υ is quasi-constant. In other words, these fast dynamics are at first order governed by a system of ODE obtained by freezing the magnitude of the secular and forcing terms.

Because it multiplies θ' in (42), small parameter ϵ also controls the short-range evolution of the bit inclination. In particular, it introduces a internal layer following any jump in the borehole inclination. If $\epsilon = 0$, the moment at the bit vanishes and the bit adapts instantaneously its orientation to any change in the load pattern. On the contrary if $\epsilon \neq 0$, it theoretically requires an *infinite* moment at the bit to impose a sudden change in its orientation.

As the drilling model has a resolution related to the bit dimensions, the internal layer is likely not relevant, except for cases involving a bit with a long gauge and a close stabilizer. Therefore, the internal layer should rather be collapsed onto a jump in both θ and Θ at the scale of the model. Beyond its strong influence close to discontinuities, parameter ϵ has been shown to weakly influence the intermediate- and long-range responses of the system (Perneder, 2013; Perneder *et al.*, 2016).

4.3.2 Intermediate range

Forcing parameters Γ and Υ are small so that the borehole inclination is expected to vary slowly, that is, borehole curvature κ is small. As a consequence, the gravity terms in Υ are quasi-constant forcing terms on a length scale that is at least an order of magnitude smaller than the radius of curvature of the borehole. The intermediate range is defined accordingly and is dominated by the secular influence of the borehole geometry on the deformation of the BHA, measured by $\langle\Theta\rangle_i$, $i = 1, \ldots, n$, in (43). In this respect, the intermediate dynamics are controlled by the position of the stabilizers along the BHA, by dimensionless group $\eta\Pi$ $\mathcal{F}$, $\mathcal{M}$. This transient behavior evolves, if the system is directionally stable, in such a way that the secular terms reach quasi-stationarity. The corresponding asymptotic solutions are

characteristic of a large scale behavior, whose evolution is now dominated by the small forcing parameters Γ and Υ.

4.3.3 Large range

The solutions corresponding to constant secular terms are such that the deformed configuration of the BHA in the borehole is stationary; in other words, the motion of the BHA axis is a rigid body motion. The solutions allowing for such an evolution are boreholes with a constant curvature. The large scale asymptotes are investigated after making the assumption that the variations of borehole curvature are negligible on a length of borehole equivalent to the length of the BHA. If control parameters Γ and Π are constant, borehole curvature $\kappa(\xi)$ slowly evolves according to

$$\kappa = A\Upsilon \sin \langle \Theta \rangle_1(\xi) + B\Gamma. \tag{49}$$

See Section 5.1 for details and for the expressions of coefficients A and B. This equation governs the slow dynamics on a length scale at least one order of magnitude larger than the length of the BHA. Finally, the large-scale asymptotes converge to stationary solutions if borehole inclination Θ reaches equilibrium, or equivalently, if curvature κ vanishes.

4.4 Simulations

4.4.1 1-stabilizer quasi-rigid BHA

First we examine the simple case of a very stiff BHA with one stabilizer. In order to be able to gracefully degenerate the system to a rigid BHA (corresponding to the toy model), the load parameters are rescaled using the alternate characteristic force $\overline{F}_* = w\ell_1$. The new dimensionless quantities are thus

$$\overline{\Pi} = \frac{W_a}{\overline{F}_*}, \qquad \overline{\Gamma} = \frac{\breve{F}}{\overline{F}_*}, \qquad \overline{\Upsilon} = \frac{\overline{F}_*}{F_*} = \frac{w\ell_1^3}{3EI}. \tag{50}$$

Thus $\overline{\Upsilon}$ is a small parameter for a stiff BHA, with the rigid case corresponding to the limit $\overline{\Upsilon} \to 0$.

Figure 7a shows the evolution of the borehole inclination for different stiffnesses of the BHA measured by $\overline{\Upsilon}$. Lateral steering resistance η has been set to 1, which is unrealistic in practice but is used here to accentuate the features of the response. The borehole and BHA are initially vertical and at $\xi = 0$, a constant RSS force is applied. A jump in the borehole inclination is induced at $\xi = 0$ whether the BHA is rigid or flexible. This initial discontinuity propagates into discontinuities of lesser order if the BHA is flexible, *i.e.*, if $\overline{\Upsilon} > 0$. On the contrary for the rigid BHA, whenever the stabilizer passes through a discontinuity, it induces a discontinuity of the same order but with an amplitude multiplied by $\epsilon/(1+\epsilon)$. Hence, the inclination for the rigid BHA is not only discontinuous at $\xi = 0$ but also at $\xi = 1, 2, \ldots$ (Fig. 7a). This is a consequence of the propagation

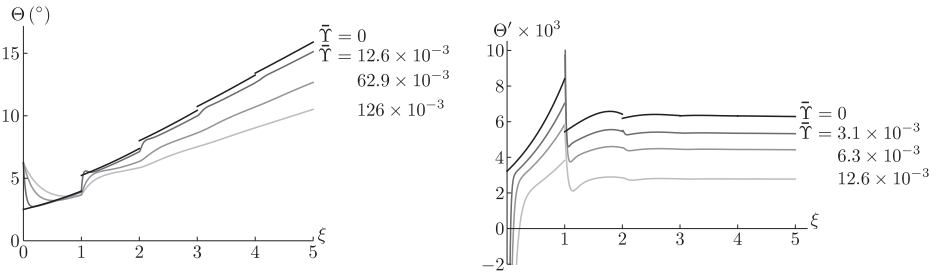


Figure 7 Evolution of a borehole evolving in a vertical plane for various stiffnesses of the BHA. The borehole and BHA are initially vertical. The system parameters are $\Lambda \simeq 0.29$, $\chi = 1, \overline{\Pi} = 6.49$, and $\overline{\Gamma} = 0.795$.

equation describing a rigid BHA being a *neutral* DDE. The borehole curvature is plotted in Figure 7b for the more realistic case of $\eta = 25$. The system is singularly perturbed with respect to the small parameter ϵ and an initial layer becomes apparent at $\xi = 0$.

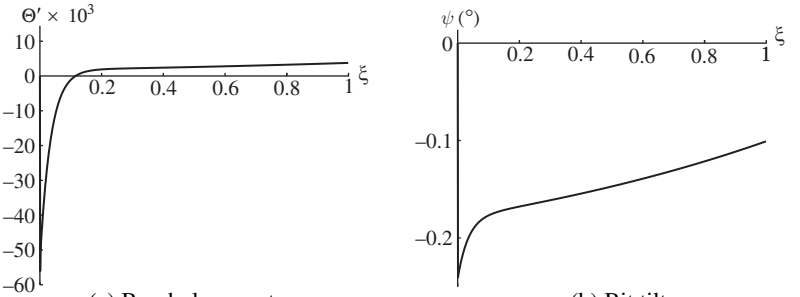
4.4.2 3-stabilizer BHA

Here we consider a $4^3/_4$" push-the-bit RSS. The BHA is equipped with three stabilizers, with the corresponding segment lengths given by $\ell_1 = 3.5$ m, $\ell_2 = 7$ m, $\ell_3 = 15$ m. The actuating pads of the RSS are 1 m away from the bit. The BHA is characterized by $w = 0.88$ kN/m and $EI = 2 \times 10^3$kNm^2. The weight on bit is fixed to $|\hat{F}_1| = 30$kN. The bit bluntness and rock properties are chosen so that $G_1 = 10$kN. The lateral and angular steering resistances are respectively selected to be $\eta = 25$ and $\chi = 1$. The initial conditions assume a straight vertical borehole and a straight undeformed BHA. At $\xi = 0$, a RSS force of magnitude $\breve{F} = 2.45$kN is applied and then kept constant. In view of the above description, $\Upsilon \simeq 6.3 \times 10^{-3}$, $\Gamma = 5 \times 10^{-3}$, $\Pi = 4.08 \times 10^{-2}$, and $\Lambda \simeq 0.29$.

The solution initially jumps to an inclination of $\Theta^+ = 0.0042^\circ$ and a curvature of $\Theta'^+ = -0.054$ at $\xi = 0^+$; in this case, the kink induced by the abrupt change in the RSS force is negligible for any practical purpose. At $\xi = 0$, the curvature is locally infinite. Follows a fast evolution of curvature Θ' and bit tilt ψ on the interval $\xi \in [0, 0.1]$ (Figs. 8a and 8b). These signs are interpreted as the emergence of a boundary layer due to small parameter ϵ.

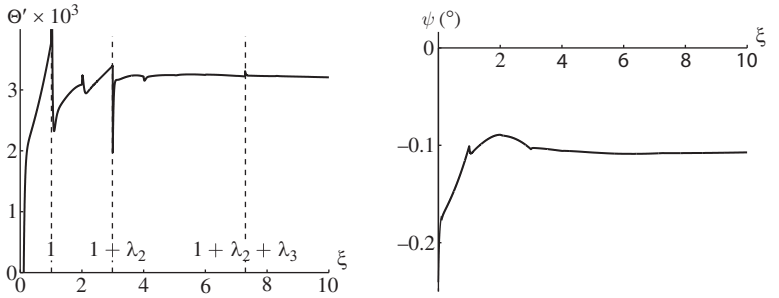
The intermediate-range evolution for the curvature and bit tilt is given in Figures 9a and 9b for $\xi \in [0, 10]$. At $\xi = 1$, $\xi = 1 + \lambda_2$, and $\xi = 1 + \lambda_2 + \lambda_3$, the borehole curvature varies locally rapidly. The effect of this quasi-discontinuous behavior appears to diminish quickly and the curvature seems to converge to a quasi-constant value.

The borehole inclination then varies slowly and converges here toward a stationary inclination as the system is stable (Fig. 10a). The curvature of the borehole Θ' slowly decays and appears to vanish at large ξ as the inclination stabilizes (Fig. 10b). This



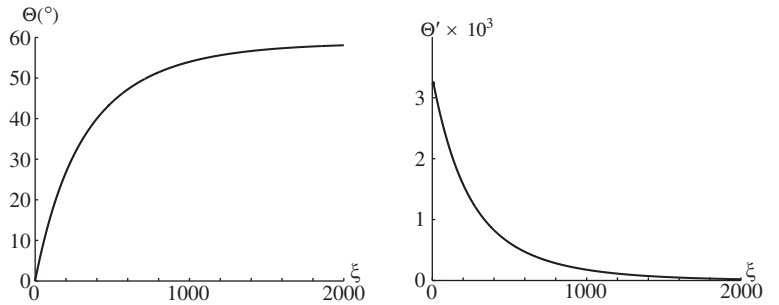
(a) Borehole curvature. (b) Bit tilt ψ.

Figure 8 Short-range 2D-simulation. The system parameters are $\lambda_2 = 2$, $\lambda_3 = 4.285$, $\Lambda \simeq 0.29$, $\eta = 25$, $\chi = 1$, $\Upsilon \simeq 6.3 \times 10^{-3}$, $\Pi = 4.08 \times 10^{-2}$, $\Gamma = 5 \times 10^{-3}$.



(a) Borehole curvature. (b) Bit tilt ψ.

Figure 9 Intermediate-range 2D simulation. The system parameters are $\lambda_2 = 2, \lambda_3 = 4.285, \Lambda \simeq 0.29$, $\eta = 25$, $\chi = 1$, $\Upsilon \simeq 6.3 \times 10^{-3}$, $\Pi = 4.08 \times 10^{-2}$, $\Gamma = 5 \times 10^{-3}$.



(a) Borehole inclination. (b) Borehole curvature.

Figure 10 Long-range 2D simulation. The system parameters are $\lambda_2 = 2$, $\lambda_3 = 4.285$, $\Lambda \simeq 0.29$, $\eta = 25$, $\chi = 1$, $\Upsilon \simeq 6.3 \times 10^{-3}$, $\Pi = 4.08 \times 10^{-2}$, $\Gamma_2 = 5 \times 10^{-3}$, and $\Gamma_3 = 0$.

behavior occurs on a large range, which is couple orders of magnitude greater than the length of the BHA.

In practice, the borehole is steered at the intermediate scale. Hence, the intermediate scale is the most important one for directional drilling applications. It is at that scale

that control algorithms are being designed to track a target trajectory of the borehole (Kremers *et al.*, 2015; van de Wouw *et al.*, 2015).

5 STATIONARY AND QUASI-STATIONARY SOLUTIONS

In the previous section we have shown that (i) under constant active weight Π and RSS force Γ, the long-range solution is characterized by a slowly changing curvature, due to the slow change of the BHA inclination with respect to gravity; and (ii) the solution tends toward a constant-inclination borehole, if such a stationary solution exists. These quasi-stationary and stationary solutions are of theoretical and practical relevance. A directed well path consists of building, holding, and dropping sections, which are respectively characterized by increasing, constant, and decreasing borehole inclinations (Inglis, 1987; Brusco *et al.*, 2004). For extended-reach wells, the straight section is slightly sloped or even horizontal over distances that can attain several kilometers (Rae *et al.*, 2005; Foster & Krepp, 2007).

Theoretical solutions can be found in the literature for straight boreholes (Lubinski and Woods, 1953; Bradley, 1975) and for boreholes of constant curvature in a vertical plane (Murphey & Cheatham, 1966; Fischer, 1974; Birades & Fenoul, 1988; Jogi *et al.*, 1988; Pastusek *et al.*, 2005; Downton, 2007; Studer *et al.*, 2007).

5.1 Quasi-stationary solutions: Constant-curvature boreholes

The long-range or quasi-stationary solution of the propagation Equation (43) is now derived after making the assumption that the variations of borehole curvature are negligible on a length of borehole equivalent to the length of the BHA. If the control parameters Γ and Π are constant, borehole curvature κ slowly evolves and the motion of the BHA axis is akin to a rigid body motion.

Under the conditions that both the RSS force Γ and active weight Π are constant (and thus that all the coefficients A_Υ, A_Γ, A_i, $i = 1, \ldots, n-1$ are constant in (43)), imposing a uniform borehole curvature $\kappa = \Theta'$ over the length of the BHA implies that

$$\kappa \simeq 2(\Theta - \langle\Theta\rangle_1) \simeq \frac{2\left(\langle\Theta\rangle_i - \langle\Theta\rangle_{i+1}\right)}{\lambda_i + \lambda_{i+1}}. \tag{51}$$

Hence (43) can be simplified to

$$A\kappa = 2A_\Gamma\Gamma + 2A_\Upsilon\Upsilon \sin\langle\Theta\rangle_1, \tag{52}$$

where

$$A = 2\varepsilon\eta\Pi + \mathcal{M}_b + \sum_{i=1}^{n-1} A_i(\lambda_i + \lambda_{i+1}). \tag{53}$$

Equation (52) governs the slow dynamics on a length scale at least one order of magnitude larger than the length of the BHA. These dynamics are driven by the slow change of the BHA orientation with respect to gravity. If curvature κ eventually

vanishes, this quasi-stationary solution converges to a stationary solution corresponding to an equilibrium inclination Θ_s given by

$$\Gamma = -\frac{A_\Upsilon}{A_\Gamma}\Upsilon \sin \Theta_s. \tag{54}$$

5.2 Stationary solutions: Straight boreholes

5.2.1 Equilibrium inclination

Expressions for lateral bit force $\hat{F}_2$ and bit tilt ψ as functions of distributed weight Υ and RSS force Γ can readily be derived from (20) and (21), under the conditions that the borehole inclination is constant, $\Theta(\xi) = \Theta_s$, and that the deflection of the BHA is invariant. Indeed, $\langle\Theta\rangle_i = \Theta_s$, $i = 1, \ldots, n$ and the absence of angular penetration at the bit causes the moment at the bit to vanish, in accordance with (10). Hence, (20) and (21) can be rewritten as

$$\frac{\hat{F}_2}{F_*} = \mathcal{I}_w \Upsilon \sin \Theta_s + \mathcal{I}_r \Gamma, \tag{55}$$

$$\psi = \mathcal{J}_w \Upsilon \sin \Theta_s + \mathcal{J}_r \Gamma, \tag{56}$$

where

$$\mathcal{I}_w = \mathcal{F}_w + \mathcal{F}_b \mathcal{J}_w, \qquad \mathcal{I}_r = \mathcal{F}_r + \mathcal{F}_b \mathcal{J}_r, \qquad \mathcal{J}_w = -\frac{\mathcal{M}_w}{\mathcal{M}_b}, \qquad \mathcal{J}_r = -\frac{\mathcal{M}_r}{\mathcal{M}_b}. \tag{57}$$

For a BHA with homogeneous properties, influence coefficients $\mathcal{I}$'s and $\mathcal{J}$'s are geometric factors that only depend on Λ and on length ratios λ_i, $i = 2,\ldots,n$. Using Table 1, the coefficients for a 2-stabilizer BHA are given by

$$\begin{aligned} \mathcal{I}_w &= \frac{3 + \lambda_2 - \lambda_2^2}{8}, \quad \mathcal{I}_r = \frac{(1-\Lambda)\left(-2 - 2\lambda_2 + \Lambda + \Lambda^2\right)}{2(1+\lambda_2)}, \\ \mathcal{J}_w &= \frac{1 + \lambda_2 - \lambda_2^2}{16}, \quad \mathcal{J}_r = -\frac{(1-\Lambda)\Lambda[3(1-\Lambda) + 2(2-\Lambda)\lambda_2]}{4(1+\lambda_2)}. \end{aligned} \tag{58}$$

The relationship between equilibrium inclination Θ_s of the borehole and scaled RSS force Γ is simply deduced by replacing the force and the tilt in interface law (9) by their expressions (55) and (56). Thus,

$$\Gamma = -\frac{\mathcal{I}_w - \mathcal{J}_w \eta \Pi}{\mathcal{I}_r - \mathcal{J}_r \eta \Pi} \Upsilon \sin \Theta_s. \tag{59}$$

It can be shown that (59) is equivalent to (54). In principle, the inclination of the borehole can vary between 0 and π so that, depending on the set of drilling parameters, either no solution to (59) exists (this is typically the case if the force Γ is too large) or two steady-state solutions coexist: a downward solution, $\Theta_s \in [0\,, \pi/2]$, and an upward one, $\Theta_s \in [\pi/2, \pi]$.

Equation (59) indicates further the existence of two particular values, $\eta\Pi|_\Upsilon$ and $\eta\Pi|_\Gamma$, of dimensionless group $\eta\Pi$

$$\eta\Pi|_\Upsilon = \frac{\mathcal{I}_w}{\mathcal{J}_w}, \qquad \eta\Pi|_\Gamma = \frac{\mathcal{I}_r}{\mathcal{J}_r}, \tag{60}$$

which correspond to two singular cases, referred to as Υ-Independent and Γ-independent, respectively. These two cases are discussed next.

5.2.2 Υ-independent case: Holding BHA

The system is able to hold the inclination of the borehole without any force at the RSS (or in the absence of a RSS) if $\eta\Pi = \eta\Pi|_\Upsilon$. For a BHA with 2 stabilizers,

$$\eta\Pi|_\Upsilon = \frac{6 + 2\lambda_2 - 2\lambda_2^2}{1 + \lambda_2 - \lambda_2^2}. \tag{61}$$

Under these conditions, equilibrium inclination Θ_s is undetermined; thus any inclination of the borehole can be maintained without applying a RSS force. Such a system is usually referred to as a holding assembly. The holding tendency of an assembly depends not only on the positions of the stabilizers, but also on the active weight on bit and on the bit selection.

The Υ-independent case can be explained by first considering the deflection of the BHA caused by gravity loading, without any reference to the bit/rock interface law. For a straight borehole, the transverse force at the bit and the bit tilt, induced by the deflection of the BHA, are both proportional to $\Upsilon \sin\Theta$ if $\Gamma = 0$. Hence their ratio is independent of $\Upsilon \sin\Theta$. Properly scaled, this ratio is in fact $\eta\Pi|_\Upsilon$. Thus enforcing $\eta\Pi = \eta\Pi|_\Upsilon$ ensures that ratio $\eta\Pi|_\Upsilon$ is in accordance with bit/rock interaction law (9). Figure 11a illustrates the deflection of a holding BHA with 3 stabilizers. The borehole inclination affects the magnitude of the transverse deflection, but not the deformed shape of the BHA; the transverse deflection at any point of the BHA is simply proportional to $\Upsilon \sin\Theta_s$.

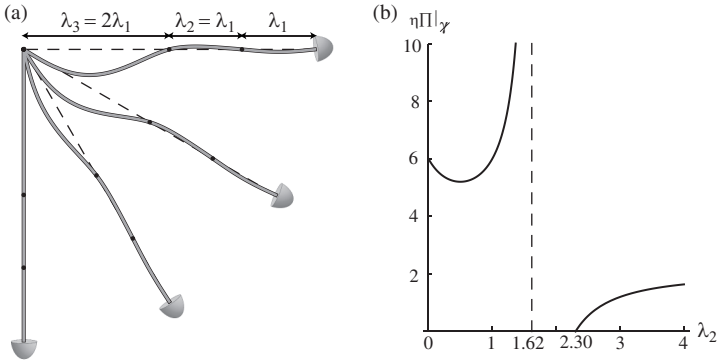


Figure 11 Υ-independent case: holding BHA. (a) Deformed configurations of a holding BHA for different equilibrium inclinations. The stabilizers are located at λ_1, $2\lambda_1$ and $4\lambda_1$ behind the bit, and $\eta\Pi$ = 4.3. (b) Values $\eta\Pi|_\Upsilon$ of the parameter $\eta\Pi$ necessary for a 2-stabilizer BHA to have a holding tendency.

Figure 11b plots the value of $\eta\Pi|_{\Upsilon}$ as a function of λ_2. As can be observed from this Figure, a 2-stabilizer BHA is unable to hold any inclination other than vertical, irrespectively of parameter $\eta\Pi$, if $1.62 < \lambda_2 < 2.30$.

5.2.3 Γ-independent case

If $\eta\Pi = \eta\Pi|_{\Gamma}$, the lateral force at the RSS no longer controls the inclination of the borehole. The equilibrium solution is a straight vertical borehole, due to the sole influence of distributed weight Υ. For a 2-stabilizer BHA, $\eta\Pi|_{\Gamma}$ is given by

$$\eta\Pi|_{\Gamma} = \frac{2\left(2 + 2\lambda_2 - \Lambda - \Lambda^2\right)}{\Lambda[3(1-\Lambda) + 2(2-\Lambda)\lambda_2]}. \tag{62}$$

The physical explanation is similar to the Υ-independent case. The RSS force deflects the BHA and tilts the bit, thus producing a lateral force at the bit; the ratio of this lateral force over the bit tilt — independent of Γ — is in fact $\eta\Pi|_{\Gamma}$.

5.2.4 $\eta\Pi$-independent case

The equilibrium borehole inclination is independent of dimensionless group $\eta\Pi$ if $\Pi|_{\Gamma} = \Pi|_{\Upsilon}$. There is $\eta\Pi$-independence if the tilt of the bit vanishes, meaning that bit axis $\mathbf{i}_1$ is aligned with the borehole and the bit does not penetrate the rock laterally ($d_2 = 0$). This case is made possible for $\Lambda = \Lambda_*$; for a 2-stabilizer BHA, Λ_* is only function of λ_2 and is given by

$$\Lambda_* = \frac{2\lambda_2^3 + \sqrt{9 - 8\lambda_2\left(\lambda_2^3 - 4\lambda_2 - 4\right)} - 8\lambda_2 - 5}{2\left(\lambda_2^3 - 4\lambda_2 - 4\right)}. \tag{63}$$

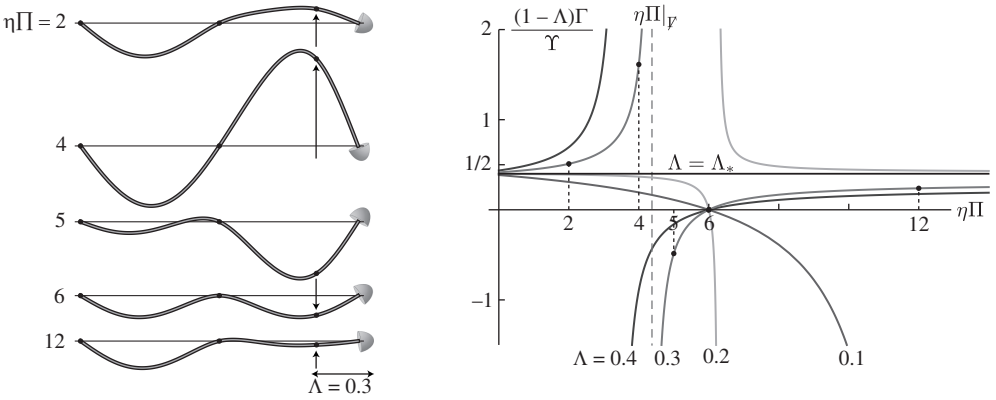
Because Λ may only vary between 0 and 1, the stationary solution may be $\eta\Pi$-independent only if λ_2 is less than the golden ratio $\left(1+\sqrt{5}\right)/2 \simeq 1.618$, for which $\Lambda_* = 0$.

5.2.5 Horizontal borehole

Ratio Γ/Υ required to drill a horizontal straight borehole ($\Theta_s = \pi/2$) is given in terms of $\eta\Pi$ in Fig. 12b for various positions Λ of the RSS and $\lambda_2 = 1$ (two BHA segments of same length). Depending on the value of $\eta\Pi$, the BHA takes various deformed configurations (Fig. 12a).

6 STABILITY AND BOREHOLE SPIRALING

Boreholes often exhibit a regular oscillating pattern (Sugiura & Jones, 2008), which, because of its shape similar to a corkscrew or helix, has been referred to as borehole spiraling. The wavelength of the oscillations is dominantly related to the distance between the bit and the first piece of equipment in contact with the wellbore — usually the first stabilizer (Gaynor *et al.*, 2001; Sugiura & Jones, 2008), and appears to be



(a) Exaggerated deformed configurations of the BHA for several values of $\eta\Pi$ ($\Lambda = 0.3$).

(b) Forcing term $(1 - \Lambda)\Gamma_2/\gamma$ as a function of $\eta\Pi$.

Figure 12 Horizontal borehole with a BHA consisting of two segments of equal length, $\lambda_2 = 1$.

independent of the rate of penetration and of the angular velocity (Stuart *et al.*, 2003). Spiraling affects negatively many aspects of drilling: lower-than-expected rates of penetration, reduction of bit life, decreased reliability of the measurement/logging-while-drilling tools, difficulty to clean the hole, increased wear of the stabilizers and pipes, increased torque and drag, issues in posing the casing, poor cementing conditions, and lower performances for push-the-bit RSSs (Gaynor *et al.*, 2001; Sugiura & Jones, 2008). To date, only a handful of papers have focused on analyzing borehole oscillations analytically (Pastusek & Brackin, 2003; Downton, 2007; Marck *et al.*, 2014; Marck & Detournay, 2016a; Marck & Detournay, 2016b; Perneder *et al.*, 2016).

6.1 Linear stability analysis

6.1.1 Evolution equation for the perturbation

The question of whether borehole spiraling occurs or not is formulated as the question of whether a perturbation in the borehole trajectory is progressively amplified or dampened along the borehole, due to the geometric feedback embedded in the system, until a limit cycle is reached. Stationary solutions and perturbations are not directly connected: spirals are observed around and along stationary solutions. The spiral or ripple can thus be seen as a perturbation of the stationary solution. Equation (43) is advantageously regarded as the superposition of two components: a quasi-stationary solution due to the quasi-constant loads on the BHA and the dynamics of the perturbation $\delta\Theta(\xi)$. Inserting this decomposition into (43) leads to the following equation governing the perturbation

$$\epsilon\eta\Pi\delta\Theta'(\xi) = -\mathcal{M}_b[\delta\Theta(\xi) - \langle\delta\Theta\rangle_1] - \sum_{i=1}^{n-1} A_i(\eta\Pi)\big(\langle\delta\Theta\rangle_i - \langle\delta\Theta\rangle_{i+1}\big). \tag{64}$$

The terms related to the constant RSS force naturally disappear as they only influence the quasi-stationary solution (if sufficiently smooth) and those associated with gravity are neglected, as their influence can be shown to be negligible on the onset of spiraling. The evolution of the perturbation is thus, at first order, purely geometric: the right-hand side of (64) is related only to the borehole trajectory. Equation (64) then propagates the perturbation around quasi-stationary solution $\Theta_s(\xi)$.

6.1.2 General considerations

The stability analysis relies on the observation that there exists a critical value of dimensionless group $\eta\Pi$, called $\eta\Pi|_s$, mostly a function of the BHA configuration, so that the system is always stable for $\eta\Pi > \eta\Pi|_s$. For a planar borehole and a BHA with uniform mechanical properties, $\eta\Pi|_s \simeq f(\lambda_i)$. This critical value corresponds to a Hopf bifurcation of equilibrium — *i.e.*, when the rightmost pair of complex-conjugate roots crosses the imaginary axis. The directional stability of any particular drilling system is assessed by comparing $\eta\Pi$, the dimensionless parameter that embodies the field conditions, with $\eta\Pi|_s$.

The importance of dimensionless group $\eta\Pi$ is directly related to the fundamental mechanism of borehole spiraling. For a given lateral force at the bit, a small $\eta\Pi$ induces a large bit tilt. Fluctuations in the lateral force at the bit, when the RSS pads or the stabilizers interact with a perturbation in the borehole, influence the bit tilt in a way inversely proportional to $\eta\Pi$, as $\psi = F_2/\eta\Pi F_*$. It results in an amplified perturbation in the borehole trajectory at the bit if $\eta\Pi$ becomes smaller than threshold $\eta\Pi|_s$.

6.1.3 Stability of a 2-stabilizer BHA

The stability diagram in the $\eta\Pi - \lambda_2$ plane is presented on Figure 13. For some positions of the second stabilizer, different stability transitions occur for different $\eta\Pi$: multiple marginally stable solutions characterized by different $\eta\Pi$ and wavelengths (but close to each other) coexist. In these particular cases, $\eta\Pi|_s$ is simply defined as the largest bifurcation value and the system is always stable for $\eta\Pi > \eta\Pi|_s$. The large-λ_2 asymptotic envelope to $\eta\Pi|_s(\lambda_2)$ is given by

$$\eta\Pi|_s \overset{\lambda_2 \gg 1}{\sim} \frac{1}{\pi}\lambda_2^{-3/2}. \tag{65}$$

Asymptote (65), which is represented by a dashed line in Fig. 13, is practically valid for $\lambda_2 \geq 4$. However if the second stabilizer is further away from the first one, additional contacts between the BHA and the borehole are likely. Because these contacts also influence the system stability (Marck *et al.*, 2014), this asymptote is of limited applicability.

For an infinitely rigid BHA ($\eta\Pi = 0$), the system is always unstable except when λ_2 is an integer; in which cases the system is marginally stable (Downton, 2007). The bit trajectory for a rigid BHA is kinematically determined and only straight or periodic boreholes (with a period in $1/k$, with $k \in N$) are admissible.

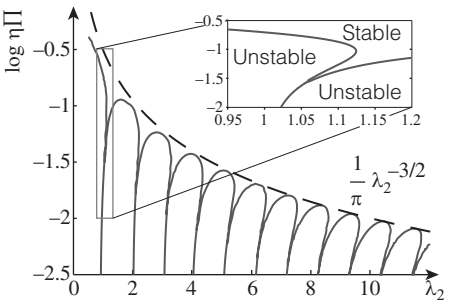


Figure 13 Variation of the bifurcation of stability with λ_2 for a 2-stabilizer BHA. The dashed line represents the asymptotic behavior for large λ_2 of the envelope to $\eta\Pi|_s(\lambda_2)$. Modified from Marck *et al.*, 2014.

Predictions of the stability analysis have been compared with field data from spiral holes pertaining to eight sections from four wells drilled with different bit types and BHA configurations (Marck *et al.*, 2014). This study shows that the propensity of a BHA to spiral can be estimated by the model by assuming reasonable values for parameters such as the lateral steering resistance and the active weight on bit. Moreover it provides confidence that the model can be used to optimize BHA designs and determine critical levels of weight on bit, both of which will mitigate the creation of spiraled holes.

6.2 Geometric approach to rippling

With $\varepsilon = 0$, the propagation Equation 43 reduces to

$$\mathcal{M}_b\Theta(\xi) = \mathcal{M}_b\langle\Theta\rangle_1 - \sum_{i=1}^{n-1} A_i\big(\langle\Theta\rangle_i - \langle\Theta\rangle_{i+1}\big) + A_\Upsilon\Upsilon\sin\langle\Theta\rangle_1 + A_\Gamma\Gamma(\xi). \tag{66}$$

and its perturbed form reads

$$\delta\Theta(\xi) = \langle\delta\Theta\rangle_1 - \sum_{i=1}^{n-1}\frac{A_i}{\mathcal{M}_b}\big(\langle\delta\Theta\rangle_i - \langle\delta\Theta\rangle_{i+1}\big). \tag{67}$$

Both (66) and (67) are functional delay algebraic equations.

The directional stability only depends on the averaged *perturbed* inclinations of the BHA sections, *i.e.*, it only depends on the position of the stabilizers relative to the bit. Equation (67) can readily be used to study the mechanism behind borehole rippling, by imposing a perturbed borehole trajectory of the form

$$\gamma(\xi) = A\sin\left(\frac{2\pi\xi}{\widetilde{\ell}}\right), \tag{68}$$

where A is the amplitude of the perturbation and $\widetilde{\ell}$ is the wavelength of the oscillations. The bit is assumed to follow this sinusoidal path as do the stabilizers.

The relative deflection of stabilizer i around the stationary solution relative to the bit is then given by

$$\Delta\gamma_i(\xi) = A\sin\left(\frac{2\pi(\xi-\xi_i)}{\widetilde{\ell}}\right) - \gamma(\xi), \tag{69}$$

from which the perturbed deflection of the BHA and the lateral force at the bit can be computed by solving the related beam problem. The bit inclination is obtained by ensuring that the moment at the bit vanishes ($\epsilon = 0$). The imposed sinusoidal trajectory is a physically acceptable solution only if at each point, drilling direction **d** at the bit is tangent to the prescribed borehole axis, or equivalently if the ratio of the scaled lateral force over the bit tilt is equal to $\eta\Pi$. This condition is satisfied only for some discrete combinations of dimensionless group $\eta\Pi$ and wavelength $\widetilde{\ell}$. These acceptable solutions correspond to pairs of complex-conjugate roots crossing the imaginary axis; strictly speaking such modes characterize marginally stable cases. By focusing on solutions where $\widetilde{\ell} \simeq 1$, critical $\eta\Pi$ and the corresponding wavelength are recovered, *i.e.*, $\eta\Pi = \eta\Pi|_s$ and $\Im(\alpha) = 2\pi/\widetilde{\ell}$.

This approach is illustrated here for a 3-stabilizer BHA with no RSS. The BHA is characterized by $\lambda_2 = 1.5$ and $\lambda_3 = 5$. Directional stability is defined by $\eta\Pi|_s \simeq 0.122$ and $\widetilde{\ell} \simeq 1.14$. As can be observed in Fig. 14, the fluctuations in the borehole trajectory actually betray oscillations of the bit tilt, because the orientation of the bit axis remains almost constant. The fact that the tilt drives the spiraling mechanism justifies further the central role of dimensionless group $\eta\Pi$ in evaluating the directional stability of the system. This fluctuation of the tilt results from to the relative positions of the stabilizers, which, as they follow the regular rippled trajectory, induce a similarly fluctuating lateral force at the bit (Fig. 14b). Measurement devices recording either the inclination of the BHA or of the bit then are likely to underestimate the actual micro-tortuosity of the borehole as well as its amplitude.

The deflection of the BHA and the lateral force at the bit are fully described by the positions of the stabilizers. (Unscaled lateral force F_2 is, however proportional to EI.)

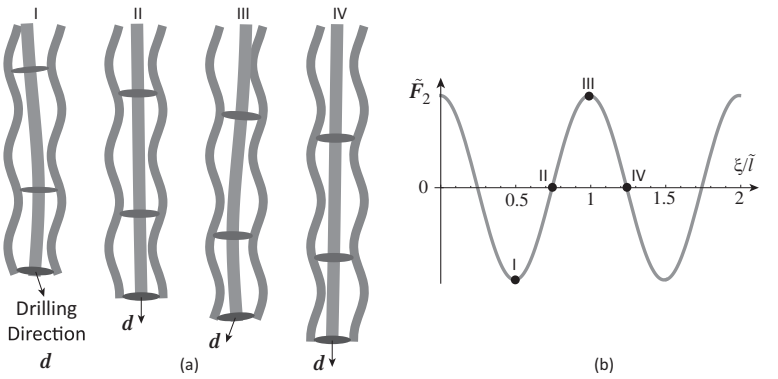


Figure 14 (a) Borehole rippling mechanism and (b) evolution of the lateral force at the bit in the rippled borehole.

Consequently, stabilizer positions that tend to induce a larger BHA deflection, when interacting with the prescribed perturbations in the borehole trajectory, require a larger $\eta\Pi$ to prevent the tilt from being too large.

6.3 Limit cycle

The previous linear stability analysis has provided information about the conditions under which a drilling system is prone to spiral. It is not able, however, to provide any information about the geometry and properties of the limit cycle. To do so a relevant nonlinearity is introduced: a saturation of the bit tilt, as observed experimentally (Pastusek *et al.*, 2005; Ernst *et al.*, 2007). Its origin is easily understood for some bit geometries: for tapered or undercut bits, there exists a critical tilt for which most of bit gauge theoretically starts interacting with the wellbore, suddenly limiting its lateral aggressiveness. The saturation value is of the order of $O(1^\circ)$.

6.3.1 Propagation equation with saturation of the tilt

Once the tilt has saturated, the lateral force at the bit does not affect the propagation of the borehole anymore (as long as its magnitude $|F_2|/F_*$ is larger than critical value $\eta\Pi\psi_c$). In order to derive the equation of propagation, expression (20) is then substituted by kinematic condition

$$\psi = \psi_c, \tag{70}$$

or equivalently

$$\theta = \psi_c + \Theta, \tag{71}$$

where ψ_c is the saturation value of the tilt.

The saturation of the bit tilt does not influence the lateral force and moment at the bit when computed from the BHA perspective. Consequently, the bit inclination always verifies

$$\mathcal{M}_b(\theta - \langle\Theta\rangle_1) + \mathcal{M}_w\Upsilon\sin\langle\Theta\rangle_1 + \mathcal{M}_r\Gamma + \sum_{i=1}^{n-1}\mathcal{M}_i\left(\langle\Theta\rangle_i - \langle\Theta\rangle_{i+1}\right) = 0, \tag{72}$$

which is deduced by setting to zero expression (42) for the moment at the bit. By substituting (72) into (41), a general expression for the lateral force at the bit is obtained to evaluate the saturation condition on the tilt.

The equation of propagation is given by Equation (66) when the tilt has not saturated, and by combining Equations (71) and (72), when it has, *i.e*,

$$\Theta'(\xi) = \theta'(\xi), \text{ if } \frac{|F_2|}{F_*} > \eta\Pi\psi_c. \tag{73}$$

6.3.2 Limit cycle for the perturbation

The limit cycle for the inclinations of the bit and the borehole is presented in Figure 15 for a BHA with three stabilizers located at distances 1, 3.5, and 6 behind the bit. Dimensionless group $\eta\Pi$ is equal to 5×10^{-2} as to make the system directionally unstable ($\eta\Pi|_s = 6.46 \times 10^{-2}$).

Following the geometric feedback embedded in the borehole geometry, the tilt oscillates between prescribed saturation values $\pm\psi_c$. Because of the absence of external loads on the BHA, *i.e.*, $\Gamma = \Upsilon = 0$, the resulting limit cycle is symmetric in terms of shape and amplitude. The amplitude of the oscillations in the borehole inclination is about equal to the saturation value of the tilt (Fig. 15a). (It is a bit smaller because of the opposition of phase between θ and Θ.) The borehole trajectory does not correspond to a sinusoidal path: the succession of fast transitions between pseudo-plateaus in the inclination induces a trajectory somewhat close to a triangular wave (Fig. 15b).

By approximating the oscillations in the borehole by a square signal of period $\widetilde{\ell}$ and extreme of $\pm\psi_c$, an upper bound for the amplitude of the ripple is given by

$$A_{max} \simeq \frac{\widetilde{\ell}\psi_c}{4}. \tag{74}$$

High frequencies thus create smaller oscillations. For the studied BHA, wavelength is $\widetilde{\ell} \simeq 1.09$, which leads to upper bounds of about 2.4×10^{-3}, 4.8×10^{-3}, and 9.6×10^{-3} for $\psi_c = 0.5°$, 1° and 2°, respectively. (Taking $\widetilde{\ell} \in [1 \sim 1.2]$ generally provides a fair estimate of the upper bound.) A lower bound is obtained by assuming a sinusoidal shape for the oscillations;

$$A_{min} \simeq \frac{\widetilde{\ell}\psi_c}{2\pi}, \tag{75}$$

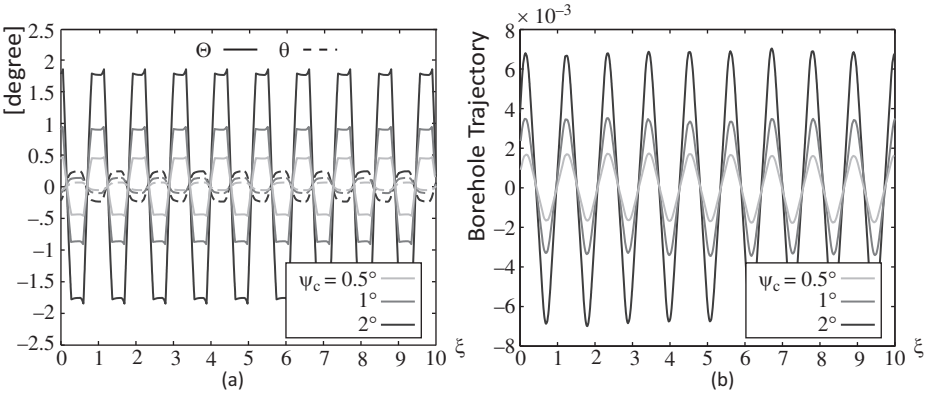


Figure 15 Limit cycle for different saturation values of the tilt ($\psi_c = 0.5°$, 1°, 2°). No external load is applied on the BHA ($\Gamma = \Upsilon = 0$). Other parameters for the simulation are $\lambda_2 = \lambda_3 = 2.5$ and $\eta\Pi = 0.05$. Modified from Perneder *et al.*, 2016.

providing amplitudes of 1.5×10^{-3}, 3×10^{-3}, and 6.1×10^{-3}, respectively. This lower bound is of limited application, however, as part of the tilt is generally mobilized by the (quasi-)stationary loads on the BHA in directional applications, see Marck (2015) for further discussion.

These approximations are to be compared with the *crooked-hole* formula, which defines the technological limit for the amplitude of the oscillations as half the over-gauge between the drill collars and the wellbore (Woods & Lubinski, 1954; Gaynor *et al.*, 2001). For small values of the saturation, the tilt drives the amplitude of the oscillations while it is limited by contacts between the drill collars and the wellbore for large saturation values. For tapered and undercut bits, it is likely that the saturation naturally limits the amplitude of the oscillations. This observation may explain field happenstances where the spiral amplitude was reported to be smaller than that predicted by the crooked-hole formula (Bellay *et al.*, 1996; Sugiura & Jones, 2008). Estimation of the ripple amplitude is central to estimate drift diameters or torque and drag.

ACKNOWLEDGMENTS

Financial support has been provided over the years by the Theodore W. Bennett Chair in Mining Engineering and Rock Mechanics and the Graduate School at the University of Minnesota, and also by CSIRO (Australia).

REFERENCES

Aadnoy, B. S., U. Stavanger, and K. Andersen (1998, March). Friction analysis for long-reach wells. In *IADC/SPE Drilling Conference*, Number IADC/SPE 39391, Dallas, Texas, U.S.A, pp. 819–834.

Bellay, G., H. Al-Waheed, and T. Audah (1996, October). Cyclic borehole effects in deviated wells. In *Abu Dhabi International Petroleum Exhibition and Conference*, Number SPE-36288-MS, Abu Dhabi, UAE. Society of Petroleum Engineers.

Birades, M. and R. Fenoul (1988, June). A microcomputer program for prediction of bottomhole assembly trajectory. *SPE Drilling Engineering 3*(SPE 15285), 167–172.

Boualleg, R., H. Sellami, S. Menand, and C. Simon (2006, February). Effect of formations anisotropy on directional tendencies of drilling systems. In *IADC/SPE Drilling Conference*, Number IADC/SPE 98865, Miami, Florida, U.S.A, pp. 1–10.

Bradley, W. B. (1975, June). Factors affecting control of borehole angle in straight and directional wells. *Journal of Petroleum Technology 27*(SPE 5070), 679–688.

Brett, J. F., J. A. Gray, R. K. Bell, and M. E. Dunbar (1986, February). A method of modeling the directional behavior of bottomhole assemblies including those with bent subs and downhole motors. In *IADC/SPE Drilling Conference*, Number IADC/SPE 14767, Dallas, Texas, U.S.A, pp. 365–376.

Brusco, G., P. Lewis, and M. Williams (2004). Drilling straight down. *Oilfield Review 16*(3), 14–17.

Callas, N. P. (1981, August). Predicting borehole trajectories. *Oil and Gas Journal 79*(34), 129–133.

Cheatham, J. B. and C. Y. Ho (1981, September). A theoretical model for directional drilling tendency of a drill bit in anisotropic rock. Technical report, Rice University, Houston, Texas, U.S.A.

Denoël, V. and E. Detournay (2011). Eulerian formulation of constrained elastica. *International Journal of Solids and Structures 48*(3), 625–636.

Detournay, E. and P. Defourny (1992, January). A phenomenological model for the drilling action of drag bits. *International Journal of Rock Mechanics and Mining Sciences and Geomechanics Abstracts 29*(1), 13–23.

Detournay, E. and L. Perneder (2011). Dynamical model of a propagating borehole. In *Proceedings of the 7th EUROMECH Nonlinear Oscillations Conference (ENOC)*.

Detournay, E., T. Richard, and M. Shepherd (2008, December). Drilling response of drag bits: Theory and experiment. *International Journal of Rock Mechanics and Mining Sciences 45*(8), 1347–1360.

Dogay, S., E. Ozbayoglu, and M. V. Kok (2009, January). Trajectory estimation in directional drilling using bottom hole assembly analysis. *Energy Sources Part A-Recovery Utilization and Environmental Effects 31*(7), 553–559.

Downton, G., A. Hendricks, T. S. Klausen, and D. Pafitis (2000). New directions in rotary steerable drilling. *Oilfield Review 12*(1), 18–29.

Downton, G. C. (2007, October). Directional drilling system response and stability. In *16th IEEE International Conference on Control Applications*, Volume WeC06.3, Singapore, pp. 1543–1550.

Downton, G. C. and M. Ignova (2011, September). Stability and response of closed loop directional drilling system using linear delay differential equations. In *IEEE International Conference on Control Applications*, pp. 893–898.

Dupriest, F. and S. Sowers (2009, March). Maintaining steerability while extending gauge length to manage whirl. In S. of Petroleum Engineers (Ed.), *SPE/IADC Drilling Conference and Exhibition*, Number SPE-119625-MS, Amsterdam, Netherlands.

Ernst, S., P. Pastusek, and P. Lutes (2007, February). Effects of RPM and ROP on PDC bit steerability. In *SPE/IADC Drilling Conference*, Number SPE/IADC 105594, Amsterdam, The Netherlands, pp. 1–11.

Fischer, F. (1974, October). Analysis of drillstring in curved boreholes. In *49th Annual Fall Meeting of the Society of Petroleum Engineers of AIME*, Number SPE 5071.

Foster, B. and T. Krepp (2007). Redefining the offshore ERD envelope: Techniques and technologies necessary for an expanding frontier. In *Offshore Technology Conference*, 30 April–3 May, Houston, Texas, U.S.A.

Franca, L. (2010, December). Drilling action of roller-cone bits: Modeling and experimental validation. *Journal of Energy Resources Technology 132*(4), 1–9.

Gaynor, T. M., D. C. Chen, D. Stuart, and B. Comeaux (2001, February–March). Tortuosity versus micro-tortuosity-why little things mean a lot. In *SPE/IADC drilling conference*, Number SPE-67818-MS, Amsterdam, The Netherlands. Society of Petroleum Engineers.

Genevois, J. M., J. Boulet, and C. Simon (2003, February). Gyrostab project: The missing link azimuth and inclination mastered with new principles for standard rotary BHAs. In *SPE/IADC Drilling Conference*, Number SPE/IADC 79915, Amsterdam, Netherlands, pp. 1–11.

Hale, J. K. (1977). *Theory of Functional Differential Equations*. Applied Mathematical Sciences (vol. 3). New York: Springer Verlag.

Ho, H.-S. (1986, October). General formulation of drillstring under large deformation and its use in BHA analysis. In *61st Annual Technical Conference and Exhibition of the Society of Petroleum Engineers*, Number SPE 15562, New Orleans, LA, U.S.A, pp. 1–12.

Ho, H.-S. (1987, September). Prediction of drilling trajectory in directional wells via a new rock-bit interaction model. In *62nd Annual Technology Conference and Exhibition of the Society of Petroleum Engineers*, Number SPE 16658, Dallas, Texas, U.S.A, pp. 83–95.

Ho, H.-S. (1988, October). An improved modeling program for computing the torque and drag in directional and deep wells. In *SPE Annual Technical Conference and Exhibition*, Number SPE 18047, Houston, Texas, U.S.A, pp. 407–418.

Ho, H.-S. (1995, October). Method and system of trajectory prediction and control using pdc bits.

Inglis, T. (1987). *Petroleum Engineering and Development Studies*, Volume 2: Directional drilling. Graham and Trotman.

Jogi, P. N., T. M. Burgess, and J. P. Bowling (1988, June). Predicting the build/drop tendency of rotary drilling assemblies. *SPE Drilling Engineering 3*(SPE 14768), 177–186.

Johancsik, C. A., D. B. Friesen, and R. Dawson (1984, June). Torque and drag in directional wells – prediction and measurement. *Journal of Petroleum Technology 36*(SPE 11380), 987–992.

Kremers, N., E. E. Detournay, and v. d. N. N. Wouw (2015). Model-based robust control of directional drilling systems. *IEEE Transactions on Control Systems Technology*.

Lubinski, A. and H. B. Woods (1953). Factors affecting the angle of inclination and dog-legging in rotary bore holes. In *Mid-Continent District*, Tulsa, U.S.A, pp. 222–250. American Petroleum Institute.

Maouche, Z. (1999, December). *Contribution a l'Amelioration de la Prediction en Inclinaison des Systemes de Forage Rotary Couplage Garniture-Outil de Forage*. Docteur de l'ecole nationale superieure des mines de paris, Ecole des Mines de Paris, Paris, France.

Marck, J. (2015). *A Nonlinear Dynamical Model of Borehole Spiraling*. Ph. D. thesis, University of Minnesota.

Marck, J. and E. Detournay (2014, June). Perturbation to borehole trajectory across a rock interface. In *48th US Rock Mechanics/Geomechanics Symposium*, Minneapolis, U.S.A.

Marck, J. and E. Detournay (2016a, February). Influence of rotary-steerable-system design on borehole spiraling. *SPE Journal*, 293–302.

Marck, J. and E. Detournay (2016b). Spiraled boreholes: An expression of 3d directional instability of drilling systems. *SPE Journal* (173156-PA). Published online.

Marck, J., E. Detournay, A. Kuesters, and J. Wingate (2014). Analysis of spiraled-borehole data by use of a novel directional-drilling model. *SPE Drilling & Completion 29*(03), 267–278.

Menand, S., H. Sellami, C. Simon, A. Besson, and N. d. Silva (2002, February). How the bit profile and gages affect the well trajectory. In *IADC/SPE Drilling Conference*, Number SPE 74459, Dallas, Texas, U.S.A, pp. 1–13.

Menand, S., H. Sellami, M. Tijani, O. Stab, and C. Simon (2006, February). Advancements in 3d drillstring mechanics: From the bit to the topdrive. In *IADC/SPE Drilling Conference*, Number IADC/SPE 98965, Miami, Florida, U.S.A, pp. 1–12.

Millheim, K., S. Jordan, and C. J. Ritter (1978, February). Bottom-hole assembly analysis using finite-element method. *Journal of Petroleum Technology 30*(SPE 6057), 265–274.

Millheim, K. K. (1982, March). Computer simulation of the directional drilling process. In *International Petroleum Exhibition and Technical Symposium*, Number SPE 9990, Beijing, China, pp. 483–496.

Murphey, C. E. and J. B. Cheatham (1966, March). Hole deviation and drill string behavior. *Society of Petroleum Engineers Journal 6*(SPE 1259), 44–54.

Neubert, M. and G. Heisig (1996). Mathematical description of the directional drilling process and simulation of directional control algorithm. *Zeitschrift für angewandte Mathematik und Mechanik 76*, 361–362.

O' Bryan, P. L. and C. W. Huston (1990, September). A study of the effects of bit gauge length and stabilizer placement on the build and drop tendencies of pdc bits. In *65th Annual Technical Conference and Exhibition of the Society of Petroleum Engineers*, Number SPE 20411, New Orleans, LA, U.S.A, pp. 67–76.

Pastusek, P. and V. Brackin (2003). A model for borehole oscillations. *Paper SPE 84448*.

Pastusek, P., V. Brackin, and P. Lutes (2005, October). A fundamental model for prediction of hole curvature and build rates with steerable bottomhole assemblies. In *SPE Annual Technical Conference and Exhibition*, Number SPE 95546, Dallas, Texas, U.S.A, pp. 1–7.

Perneder, L. (2013, January). *A Three-dimensional Mathematical Model of Directional Drilling*. Ph. D. thesis, University of Minnesota.

Perneder, L. and E. Detournay (2012). Equilibrium inclinations of straight boreholes. SPE 160335, *SPE Journal*, June, 18(3):395–405, doi:10.2118/160335-PA.

Perneder, L. and E. Detournay (2013, May). Steady-state solutions of a propagating borehole. *International Journal of Solids and Structures 50*(9), 1226–1240.

Perneder, L., E. Detournay, and G. Downton (2012, April). Bit/rock interface laws in directional drilling. *International Journal of Rock Mechanics and Mining Sciences 51*, 81–90.

Perneder, L., J. Marck, and E. Detournay (2016). A model of planar borehole propagation. SIAM Journal on Applied Mathematics. Submitted.

Rae, G., W. G. Lesso, and M. Sapijanskas (2005, February). Understanding torque and drag: Best practices and lessons learnt from the captain field's extended reach wells. In *SPE/IADC Drilling Conference*, Number SPE/IADC 91854, Amsterdam, Netherlands, pp. 1–11.

Rafie, S. (1988, February-March). Mechanistic approach in designing bha's and forecasting welbore position. In *IADC/SPE Drilling Conference*, Number IADC/SPE 17196, Dallas, Texas, U.S.A, pp. 161–170.

Rafie, S., H.-S. Ho, and U. Chandra (1986, February). Applications of a bha analysis program in directional drilling. In *IADC/SPE Drilling Conference*, Number IADC/SPE 14765, Dallas, Texas, U.S.A, pp. 345–354.

Stuart, D., C. Hamer, C. Henderson, T. Gaynor, and D.-K. Chen (2003, February). New drilling technology reduces torque and drag by drilling a smooth and straight wellbore. In *SPE/IADC Drilling Conference*, Number SPE-79919-MS, Amsterdam, The Netherlands. Society of Petroleum Engineers.

Studer, R., C. Simon, J. M. Genevois, and S. Menand (2007, November). Learning curve benefits resulting from the use of a unique bha directional behaviour drilling performances post-analysis. In *SPE Annual Technical Conference and Exhibition*, Number SPE 110432, Anaheim, California, U.S.A, pp. 1–11.

Sugiura, J. and S. Jones (2008). The use of the industry's first 3-d mechanical caliper image while drilling leads to optimized rotary-steerable assemblies in push-and point-the-bit configurations. In *SPE Annual Technical Conference and Exhibition*. Society of Petroleum Engineers.

van de Wouw, N., N. Kremers, and E. Detournay (2015). Output-feedback inclination control of directional drilling systems. *IFAC-PapersOnLine 48*(6), 260–265.

Woods, H. and A. Lubinski (1954). How to determine best hole and drill-collar size. *The Oil and Gas Journal 7*.



Taylor & Francis
Taylor & Francis Group
http://taylorandfrancis.com

Chapter 3

Challenges and issues for CO_2 storage in deep coal seams

A.S. Ranathunga[1], *P.G. Ranjith*[1] & *M.S.A. Perera*[1,2]

[1]*Deep Earth Energy Laboratory, Department of Civil Engineering, Monash University, Melbourne, Victoria, Australia*

[2]*Department of Infrastructure Engineering, The University of Melbourne, Melbourne, Victoria, Australia*

Abstract: Global warming is one of the most critical environmental issues facing the world today, and according to scientific reports, ignoring this issue will lead to severe economic and environmental costs to society. The increased greenhouse gas concentration in the atmosphere is the major cause of global warming, and the effect of CO_2 is critical. It is therefore necessary to use a rational combination of all the possible CO_2 mitigation strategies, such as the use of renewable fuels, improved energy efficiency, carbon sequestration and increased conservation to achieve a safer CO_2 level in the atmosphere with the rapidly increasing emissions. CO_2 sequestration is considered here.

CO_2 sequestration involves the capture of CO_2 released from anthropogenic sources and its secure storage in deep underground locations, either off- (ocean sequestration) or on-shore (geo-sequestration). However, in terms of safety, reliability and cost, onshore sequestration is more effective than offshore sequestration. Of the various potential CO_2 storage sinks in deep underground (*e.g.* depleted oil and gas fields, saline aquifers, shale beds and coal mines), CO_2 storage in deep coal seams offers unique advantages over the others, and the potential for offsetting CO_2 sequestration costs by producing a valuable energy product such as methane (coal seam gas). For nearly 20 years, CO_2 has been injected into coal seams to enhance the recovery of methane in a process known as enhanced coal bed methane (ECBM) recovery.

However, adsorption of the injected CO_2 into the coal mass causes it to swell, causing significant alterations in its internal rock mass structure, resulting in major modifications to its flow and strength properties. This CO_2 adsorption-induced coal matrix swelling process is dependent on the properties of both the seam and the injected CO_2, and swelling is reduced with increasing temperature due to the reduced sorption capacity. Furthermore, swelling exhibits inverted-U shaped variation with coal maturity or rank, due to the corresponding variation of the coal mass properties such as moisture, carbon content and pore space. On the other hand, the extent of swelling is largely dependent on the pressure and the physical state of the injected CO_2, and super-critical CO_2 creates much greater swelling than gas or liquid CO_2 due to its higher chemical potential. In addition, high- pressure injection of CO_2 causes the swelling process to be enhanced due to the higher flow ability of the injected CO_2 under reduced effective stress conditions at increased injection pressures. However, potential coal seams for CO_2 sequestration are available at extremely deep locations and there is a high possibility of phase change from gas/liquid to the super-critical state in the underground environment owing to changes in field conditions. This confirms the likely occurrence of high swelling rates in deep coal seams with CO_2 injection.

The effectiveness of the CO_2 storage process in any coal seam is greatly influenced by the flow ability of the injected CO_2 through the seam, which is dependent on a number of factors. These factors include i) coal matrix swelling that causes the internal coal seam pore space available for fluid/gas movement to be reduced, ii) CO_2 injecting pressure and seam depth, both of which change the effective stress on the coal seam and eventually, the seam's pore space, and iii) seam temperature that creates thermal expansion in the seam and leads to reduced sorption capacity with kinetic energy increment in injected CO_2 molecules. Importantly, the injected CO_2 phase condition critically influences its flow behavior in the seam, and super-critical, the form of CO_2 expected in deep coal seams, has significantly lower permeability than gas/ liquid CO_2, which causes unpredictable CO_2 injectibility into deep coal seams. Reduction of seam permeability over time after CO_2 injection is a common issue faced by many field-scale CO_2 sequestration projects. For example, there was around 50% reduction in CO_2 injectivity at the Allison unit CO_2 sequestration project in the San Juan basin, USA, during the first two years of injection.

Secure storage of injected CO_2 in the seam is critically important in CO_2 geo-sequestration in deep coal seams in terms of environmental safety and health. It is important to prevent the upward migration of CO_2, as this has potential to cause distress and on occasion death, and lateral migration into aquifers and surrounding more permeable geologic strata. These factors are mainly dependent on the coal mass strength properties. However, the fact that CO_2 adsorption-induced swelling creates a weakening effect in deep coal seams is well known. This strength reduction is greatly dependent on injecting CO_2 phase and pressure, it increases with increasing pressure, and super-critical CO_2 causes much greater strength reduction than gas/liquid CO_2. Furthermore, CO_2 adsorption into any coal seam mainly occurs through the walls of its natural cleat system that were formed during the coalification process. High rank coal seams, located deeper underground, are therefore likely to be subjected to a higher strength reduction with CO_2 injection, offering more numerous loci for CO_2 adsorption. However, it is generally accepted that the deeper the seam, the more secure the CO_2 storage. On the other hand, the likely super-critical nature of CO_2 in deep coal seams also causes greater strength reduction with CO_2 injection.

Existing government policies, public perceptions, and strict rules on coal mining affect the implementation of CO_2 sequestration in deep coal seams. For example, mines are generally required to have a maximum 3% CO_2 by volume in the mine air, and therefore injection of CO_2 into coal seams causes the mining environment to be polluted by the injected CO_2 and eventually, the seams become unsafe to mine forever. The current lack of knowledge related to coal seam CO_2 sequestration severely affects the implementation of this process in potential coal seams around the world. The complex heterogeneous nature of coal, which creates location-dependent coal seam properties, is the main reason for the limited knowledge of coal CO_2 sequestration.

1 INTRODUCTION

1.1 Global warming and the greenhouse gas effect

Emissions of greenhouse gasses (GHGs) will increase the average global temperature by 1.1 to 6.4 °C by the end of the 21st century (Pachauri & Reisinger, 2007) and exceeding

the current global average temperature by more than 2 °C would lead to serious consequences. Therefore, the International Panel on Climate Change (IPCC) has warned of the need for a 50-80% global GHG emissions reduction by 2050.

Carbon dioxide (CO_2) is one of the most significant greenhouse gases, and the anthropogenic CO_2 content (the CO_2 generated due to human activities) in the atmosphere is critical. In particular, the burning of fossil fuels such as coal, oil and gas has caused a substantial increase in the concentration of CO_2 in the atmosphere (Borah *et al.*, 2011; Pachauri & Reisinger, 2007; Perera & Ranjith, 2012; Ranathunga *et al.*, 2014; Stangeland, 2007; White *et al.*, 2005). According to Sundquist *et al.* (2003) this increase in atmospheric CO_2 concentration from around 280 to more than 380 ppm over the last 250 years has caused measurable global warming. The potential adverse impacts of global warming are sea-level rises; increased frequency and intensity of wildfires, floods, droughts, and tropical storms; changes in the amount, timing, and distribution of rain, snow, and run-off; and the disturbance of coastal marine and other ecosystems. Rising atmospheric CO_2 is also increasing the amount of CO_2 absorbed by seawater, causing the ocean to become more acidic, which potentially disruptively affects marine plankton and coral reefs (Sundquist *et al.*, 2008).

At the 16th United Nations Framework Convention on Climate Change (UNFCCC), held in Cancun, Mexico in 2010, the participants including Australia agreed to commit to a maximum temperature rise of 2 °C above pre-industrial levels, and to consider lowering that maximum to 1.5 degrees in the near future. Therefore, it is imperative to investigate possible CO_2 mitigation options and to implement them as soon as possible.

Some of the possible CO_2 mitigation options are carbon dioxide capture and storage or sequestration (CCS), energy efficiency improvements, the switch to less carbon-intensive fuels, nuclear power, renewable energy sources, enhancement of biological sinks, and reduction of non-CO_2 greenhouse gas emissions (Stangeland, 2007; Sundquist *et al.*, 2008; White *et al.*, 2005). Of those methods, CCS has the potential to reduce overall mitigation costs and increase flexibility in achieving greenhouse gas emission reductions (Gale, 2004; Metz *et al.*, 2005; Perera & Ranjith, 2012; White *et al.*, 2005).

1.2 CO_2 sequestration

Before human-caused CO_2 emissions began the natural processes that make up the global "carbon cycle" (see Figure 1), a near balance was maintained between the uptake of CO_2 and its release back to the atmosphere. However, existing CO_2 uptake mechanisms (sometimes called CO_2 or carbon "sinks") are insufficient to offset the accelerating pace of emissions related to human activities (Sundquist *et al.*, 2008). According to Sundquist *et al.* (2003), annual carbon emissions from burning fossil fuels in the United States are about 1.6 Gigatons, whereas annual uptake amounts are only about 0.5 Gigatons, resulting in a net release of about 1.1 Gigatons per year. Hence, controlling atmospheric CO_2 will require deliberate mitigation with an approach that combines reducing emissions and increasing storage.

CCS basically means the removal of CO_2 directly from anthropogenic sources (capture) and its disposal in geological or oceanic media, either permanently (sequestration), or for geologically significant time periods (storage) (Benson & Cole, 2008). The term "carbon sequestration" is used to describe both natural and deliberate processes by which CO_2 is either removed from the atmosphere or diverted from

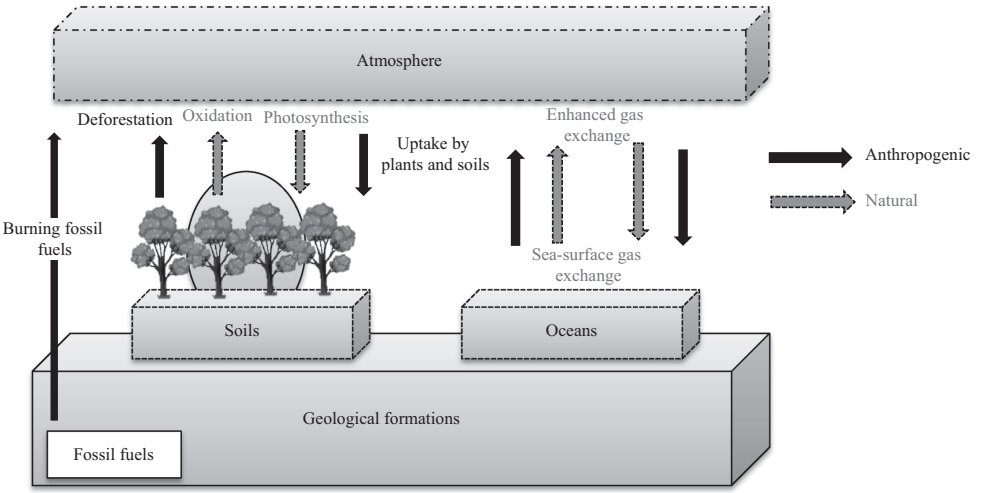


Figure 1 Global carboncycle (Benson & Cole, 2008).

emission sources and stored in the ocean, terrestrial environments (vegetation, soils, and sediments), and geologic formations. With over 60% of worldwide emissions coming from point sources that are potentially amenable to CO_2 capture, the prospects for CCS to significantly reduce CO_2 emissions are great (Sundquist *et al.*, 2008). Technical and economic assessments suggest that over the coming century, CCS may contribute up to 20% of CO_2-emission reductions, equivalent to the reductions expected from efficiency improvements and large-scale deployment of renewable energy resources (Benson & Cole, 2008; Metz *et al.*, 2005). Therefore, CO_2 sequestration becomes a more promising solution for the required outcomes of The United Nations Framework Convention on Climate Change (UNFCCC).

To significantly reduce global emissions to pre-industrial levels, huge volumes of CO_2 must be sequestered. For example, a large coal-fired power plant emits about 8 million tons of CO_2 annually. At the pressures and temperatures expected for sequestration reservoirs, the volume required to sequester CO_2 as a super-critical fluid is about 10 million cubic meters (Mm^3) per year. According to existing studies (Bachu, 2003; Benson & Cole, 2008; Metz *et al.*, 2005; Perera & Ranjith, 2012; Sundquist *et al.*, 2008; White *et al.*, 2005), several methods can be used in sequestrating CO_2, mainly on-shore and off-shore.

1.2.1 Off-shore CO_2 sequestration

Injecting CO_2 into off-shore marine sediments is one potential approach to the sequestration of CO_2 (see Figure 2), in which the CO_2 injected into off-shore sediments is stored deep beneath the ocean, avoiding the threats of direct ocean injection and effects on ocean ecology. There are several advantages in off-shore CO_2 sequestration compared to on-shore CO_2 sequestration. According to House *et al.* (2006), CO_2 is denser than seawater below 3000 m; therefore, off-shore reservoirs with suitable permeability in deep seawater make the cap rock less significant. Furthermore, marine sediments offer

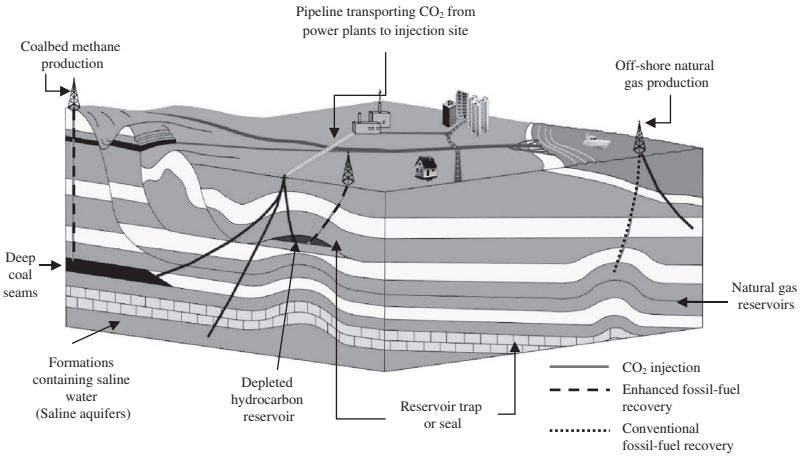


Figure 2 On-shore and off-shore CO_2 sequestration methods (Sundquist, 2008).

large storage potential. For example, the cretaceous sandstones of New Jersey have the capacity to store at least several hundred billion tons of CO_2, which is enough to dispose of all the CO_2 from power plants within 250 km of the coast near the reservoir for the next century (Schrag, 2009). Another advantage of off-shore CO_2 storage is the ability to manage pressure within the geologic formation by drilling additional wells to release pore fluid to the ocean, which avoids injected CO_2 back-migration to the atmosphere by the prevention of fractures (Archer & Brovkin, 2008). Moreover, the released pore fluid is similar to seawater, unlike the pore fluid released from on-shore CO_2 sequestration, and is more environmentally friendly (Vaughan & Lenton, 2011).

Although off-shore CO_2 sequestration acts as a large anthropogenic CO_2 storage pool, some researchers (Adams & Caldeira, 2008; Drange *et al.*, 2001; Sabine & Tanhua, 2010) have found a number of challenges in this process. In relation to the lack of secure storage life, high operational and transportation costs (most off-shore sites are located far away from the CO_2 trapping points) there are many environmental concerns, such as ocean acidification. Therefore, based on economic factors, the storage life and availability of sites, on-shore CO_2 sequestration has been identified as the most viable solution to the problem.

1.2.2 On-shore CO_2 sequestration

Another option to reduce anthropogenic CO_2 emissions to the atmosphere is to capture and store the CO_2 in porous rock masses (sedimentary rocks) available deep under the surface. Globally, the CO_2 storage capacity in sedimentary rocks is quite high, and recent estimates for the U.S. alone show a potential storage capacity of 2020 to 14,220 Gigatons of CO_2 ($GtCO_2$) (Orr, 2009). Depths below 800 to 1000 m, where the CO_2 density is high enough (500 to 700 kg/m^3) to limit the storage volume, are suitable for on-shore CO_2 sequestration. In this technique, the presence of low-permeability formations called cap rock above the storage zone is crucial in order to prevent the back-migration of stored CO_2 into the atmosphere (Ranjith & Perera, 2012).

Oil and gas reservoirs are one potential choice for on-shore CO_2 sequestration (see Figure 2). For example, for the purpose of enhanced oil recovery (EOR), around 30 megatons of CO_2 ($MtCO_2$) are injected into oil reservoirs in west Texas each year (Sundquist *et al.*, 2008). The potential for fuel recovery to offset the sequestration cost and the already available underground and surface infrastructure (wells, equipment and pipelines) make this method more attractive (Orr, 2009).

Injection of CO_2 into deep saline formations (see Figure 2) is also being tested on a commercial scale. CO_2 is typically in its super-critical phase at sub-surface temperatures and pressures, which is more dense than natural gas but less dense than brine or oil. The injected CO_2 interacts with the fluids and minerals present in the saline aquifers. CO_2 is relatively soluble in brine, and the resulting brine mixture is slightly denser than brine alone. Further, under typical sub-surface conditions, CO_2 is dissolved in brine at a proportion of 1:20 (CO_2: brine) by volume (Stevens *et al.*, 2001). Once a larger volume of CO_2 is dissolved, the driving force for upward migration of CO_2 is eliminated, and the CO_2 is immobilized while it continues to dissolve slowly, which will continue for a time scale of centuries (Bachu, 2000).

Deep unmineable coal seams are also possible storage locations, with international coal bed methane resources of 3010–7840 trillion cubic feet (Orr, 2009). When CO_2 is injected into coal seams, it adsorbs into the coal matrix and then desorbs the methane (CH_4) (developed during the coalification process) which migrates to the fractures and can be recovered. This process is known as enhanced coal bed methane (ECBM) recovery (Orr, 2009; Ranathunga *et al.*, 2014; White *et al.*, 2005). ECBM recovery is further discussed in the following sections.

2 CO_2 SEQUESTRATION IN DEEP COAL SEAMS

Coal is formed from the biodegradation of buried plants, and the process of forming coal from buried plants subjected to burial pressure and temperature is called the coalification process. Naturally-formed coal is composed of a solid matrix with well-defined networks of natural fracture systems called cleats, which formed during the coalification process. Therefore, the more mature the coal mass, the more developed the cleat system. Depending on the degree of coalification, coal can be categorized into several ranks, mainly high rank (bituminous coal and anthracite) and low rank (lignite and sub-bituminous coal), and rank increases with increasing coal maturity. Coal is composed of carbon (50%–98%), hydrogen (3%–13%), oxygen and smaller amounts of other elements, and the composition is dependent on the coal rank (see Table 1). For

Table 1 Chemical properties of different coal ranks (Durie, 1991).

Coal property / *Coal rank*	*Carbon (*db %)*	*Volatile matter (*db %)*	*Moisture content (%)*	*Specific energy (*db kJ g^{-1})*
Lignite	60–75	45–55	50–70	25–30
Sub-bituminous	75–80	40–45	25–30	28–32
Bituminous	80–90	20–40	5–10	30–35
Anthracite	90–95	5–7	2–5	35–38

Note: *db – dry basis

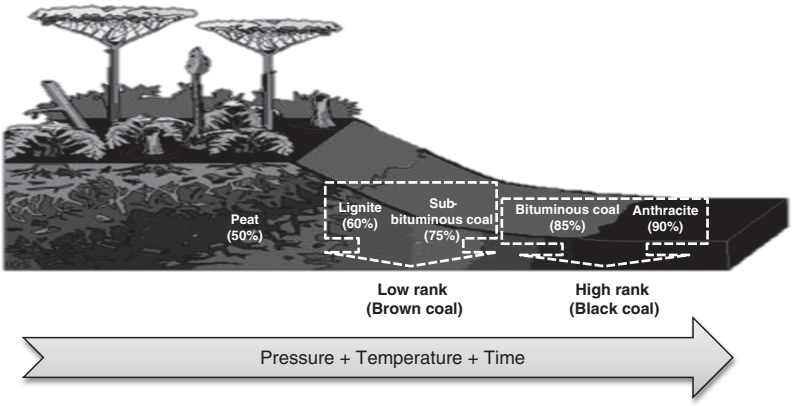


Figure 3 Coalification process of coal (Created by the authors using data from http://www.detectingdesign.com/fossilrecord.html).

example, high rank coal has greater carbon content than low rank coal. Generally, coal can be mainly separated into brown coal (lignite) and black coal (bituminous), depending on the carbon content (see Figure 3). According to Miedzinska *et al.* (2013), the characteristic surface morphology of a coal sample normally appears to be granular structure under scanning electron microscopy (SEM). There are many slots and free spaces between the grains with abundant storage of methane. Due to its chemical properties, coal has a greater affinity to absorb CO_2 than other gases like methane (CH_4) and nitrogen (N_2). This provides the basis for the CO_2 sequestration process to be on-going (White *et al.*, 2005).

2.1 Why store CO_2 in deep coal seams?

According to Shi *et al.* (2014), gases are stored in coal beds by three mechanisms:

- physically adsorbed compounds on the internal surfaces of coal
- adsorbed within the molecular structure; and
- within pores and natural structures.

Around 98% of CO_2 exists in an adsorbed phase on the walls of coal's micro pores, while the rest remains as free gas inside the cleats (Battistutta *et al.*, 2010; Perera & Ranjith, 2012; Shi & Durucan, 2005; White *et al.*, 2005). Therefore, CO_2 exists in a more stable form in coal, which will eventually decrease the risk of back-migration (Shi & Durucan, 2005). Moreover, during the coalification process, a large amount of methane (CH_4) is formed. When CO_2 is injected into a coal seam, it improves the recovery of CH_4 by directly displacing the methane from the coal, or by lowering the effective partial pressure of the CH_4 (Harpalani & Schraufnagel, 1990). This phenomenon is known as enhanced coal bed methane (ECBM) recovery, which will eventually offset the cost of sequestration of CO_2. Figure 4 illustrates a schematic diagram of the ECBM process.

Since coal has a larger surface area associated with the micro-pore structure compared with the conventional reservoirs of a given volume of rock, it can store

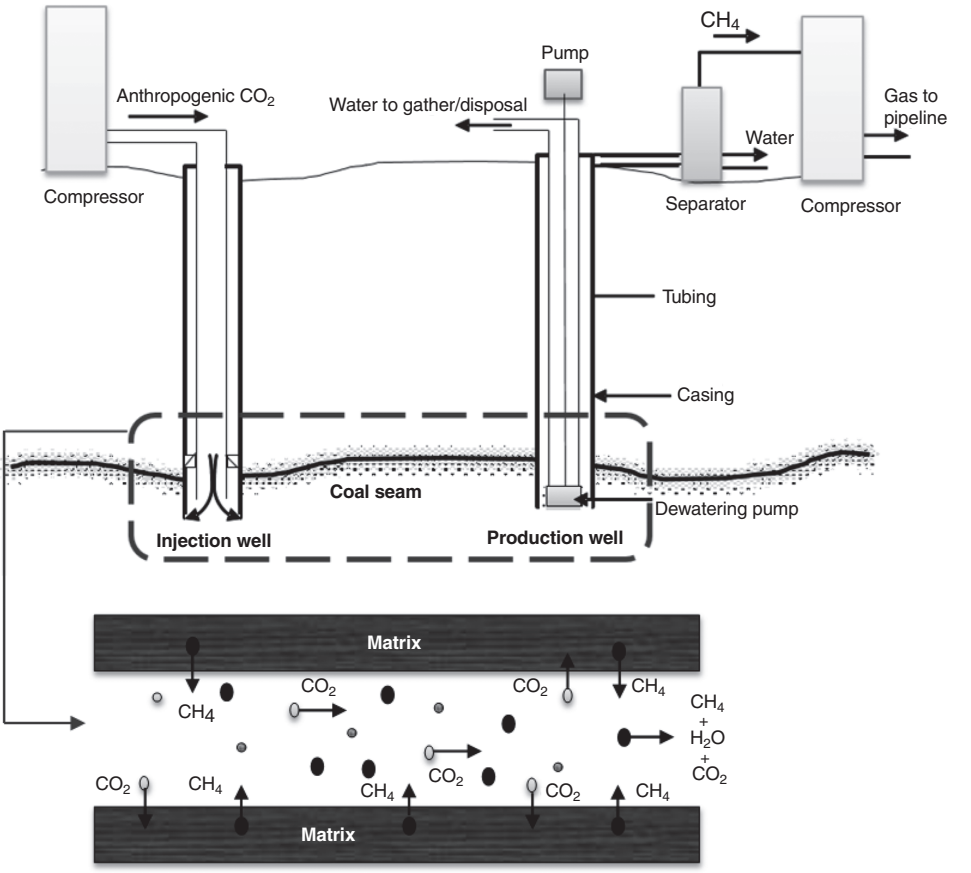


Figure 4 Enhanced coal-bed methane recovery process.

a substantial amount of CO_2 within the pore spaces (Perera & Ranjith, 2012; Stevens *et al*., 2001). For example, the combined Bowen and Sidney basins in eastern Australia can store about 11.2 gigatons of CO_2 (Stevens *et al*., 2001). According to Harpalani & Schraufnagel (1990), 5-15 gigatons of CO_2 in the world can be sequestered in coal beds by the profits gained from CH_4 production through the ECBM recovery process. These details demonstrate the prospective importance of CO_2 sequestration in deep unminable coal seams.

2.2 What happens when CO_2 is injected into coal seams?

As mentioned above, in coal beds, most gases exist in an adsorbed phase in the coal matrix and some as free gas in the fracture pore space. Generally, the coal mass natural cleat system formed during the coalification process governs gas movement through the coal matrix, unless a large joint exists (White *et al*., 2005). In the gas transport process in coal, first it moves through its natural cleat system and then adsorbs into the coal

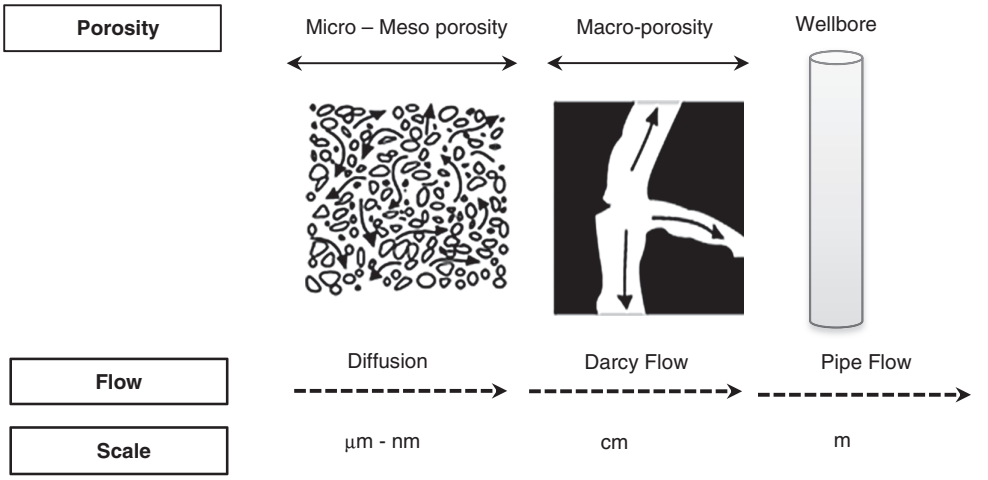


Figure 5 Gas transport process in coal (Bromhal *et al.*, 2005).

matrix along the cleat walls (White *et al.*, 2005) (see Figure 5). When the gas molecules reach the micro pores in the coal matrix, they follow the diffusion process (see Figure 5), as the mean flow path of the gas molecules is greater than the micro pore diameter. In contrast, when the gas molecules reach the cleats, flow is controlled by the coal mass permeability (Darcy flow), as the mean flow path of the gas molecules is smaller than the cleat width. However, the diffusion process is quite a slow process, and it therefore takes much greater time than the pressure-driven advection process in cleats.

According to existing findings, both CO_2 sequestration and ECBM recovery are dependent on the coal mass and adsorbing gas properties, such as coal rank, moisture content, temperature, depth, existing gas composition and adsorbing gas pressure, gas type and phase, and injection and production well operations (Gilman & Beckie, 2000; Perera & Ranjith, 2012; Sawyer *et al.*, 1990). Laboratory isotherm measurements demonstrate that medium- to high-rank coal can adsorb approximately twice as much CO_2 by volume as CH_4, and the common assumption is that, for higher rank coals, the ECBM process stores 2 moles of CO_2 for every mole of CH_4 desorbed (White *et al.*, 2005). However, some researchers have determined that some low rank coals may adsorb as much as 10 moles of CO_2 for every mole of CH_4 (Ranathunga *et al.*, 2014). Vishal *et al.* (2013) investigated the feasibility of CO_2 driven ECBM recovery in Indian coals (coal type – black coal) using a field-scale numerical model. These researchers found that approximately three times the volume of CO_2 can be sequestered in place of every volume of CH_4 for high rank coals. Field applications and laboratory experiments have shown that this ratio could be even larger at depths greater than 800 m, where gaseous CO_2 changes to super-critical CO_2 (White *et al.*, 2005).

However, according to Viete & Ranjith (2006), the injection of CO_2 into coal causes its chemical and physical properties to be greatly changed, resulting in unpredictable amounts of injectable CO_2 and producible CH_4 in coal seams. There has been much research conducted on this process, which has revealed that a great degree of swelling is

caused by CO_2 adsorption into the coal matrix that, in turn, can cause the permeability and the overall strength of the coal mass to be severely decreased (Fujioka *et al.*, 2010; Jasinge *et al.*, 2011; Perera & Ranjith, 2012; Wang *et al.*, 2011).

3 COAL MATRIX SWELLING

Coal matrix swelling occurs due to the lowering of the surface energy of the coal with gas adsorption. The decreased surface energy has the effect of lessening the strength of the chemical bonding in the atomic structure of the matrix, resulting in a volumetric expansion, or swelling, of the coal. Due to the fact that CO_2 adsorption is much greater than CH_4 and N_2 due to its higher chemical potential and adsorption capacity, the coal mass tends to swell significantly during CO_2 injection (Viete & Ranjith, 2006). According to Day *et al.* (2010), the amount of swelling in coal is directly related to the absolute adsorption capacity (Equation 1).

$$V_S = -0.0037 + 0.1596V_{abs} + 0.0101V_{abs}^2 \tag{1}$$

where V_s is the volumetric swelling percentage and V_{abs} is the volume of the absolute adsorption. Meanwhile, there is a direct relationship between amount of matrix shrinkage and desorbed gas volume at the standard pressure (Harpalani & Chen, 1995) (Equations 2 and 3).

$$\varepsilon_v = C\left(\frac{V_{LP}}{P_{L+P}}\right) \tag{2}$$

$$V_{des} = \left(\frac{V_{LP}}{P_{L+P}}\right) \tag{3}$$

where ε_v is the volumetric strain of the coal matrix; C is a constant depending on the coal mass properties; p is the pore pressure; V_{des} is the volume of gas desorbed from the coal matrix.

It should be noted that swelling does not occur homogeneously throughout the coal structure, but rather occurs more readily in the organic regions (macerals), which causes compression of the inorganic regions (minerals) of the matrix (Day *et al.*, 2010). This is due to the strength of the bonding within the minerals being much greater than that between the organic molecules within the coal matrix. According to Majewska *et al.* (2009), the degree of swelling is dependent on the moisture content, whereas the megascopic texture controls the swelling behavior with respect to bedding orientation. It has been noted that the degree of swelling is greater in a direction perpendicular to the bedding plane of the coal matrix than parallel to the plane (Karacan, 2007). This is caused by the heterogeneity of swelling between the organic and inorganic components within the coal matrix. As a result of this, and the inherent weaknesses found along bedding planes, it has been shown that cracks more readily develop along the face cleats, as opposed to across the bedding planes along the butt cleats (Anggara *et al.*, 2014). As mentioned previously, swelling of the coal matrix would definitely break the natural balance of the structure, with direct influences on permeability and strength reduction, which are the key factors in the CO_2 sequestration process.

3.1 Effective factors for CO_2 injection-induced coal matrix swelling

According to previous studies (Czapliński & Hołda, 1982; Day *et al*., 2010; Deevi & Suuberg, 1987; Jasinge *et al*., 2011; Majewska & Ziętek, 2007; Shi & Durucan, 2005), seam properties (coal rank and temperature) and injecting CO_2 properties (injecting CO_2 phase and pressure) are some effective factors for coal matrix swelling. These are therefore discussed in the following sections.

3.1.1 Seam properties

a) Coal rank
In general, the deeper the coal seam, the higher the rank, and this explains the effect of coal seam location on the CO_2 sequestration process. However, some contradictions can be seen in the research findings on the effect of coal rank on its swelling. Reucroft & Sethuraman (1987) found that there is an inverse correlation between coal rank and matrix swelling; high rank coal undergoes less swelling than lower-ranking coal under the same environmental conditions. These results have been confirmed by Ceglarska-Stefańska & Czapliński (1993) (see

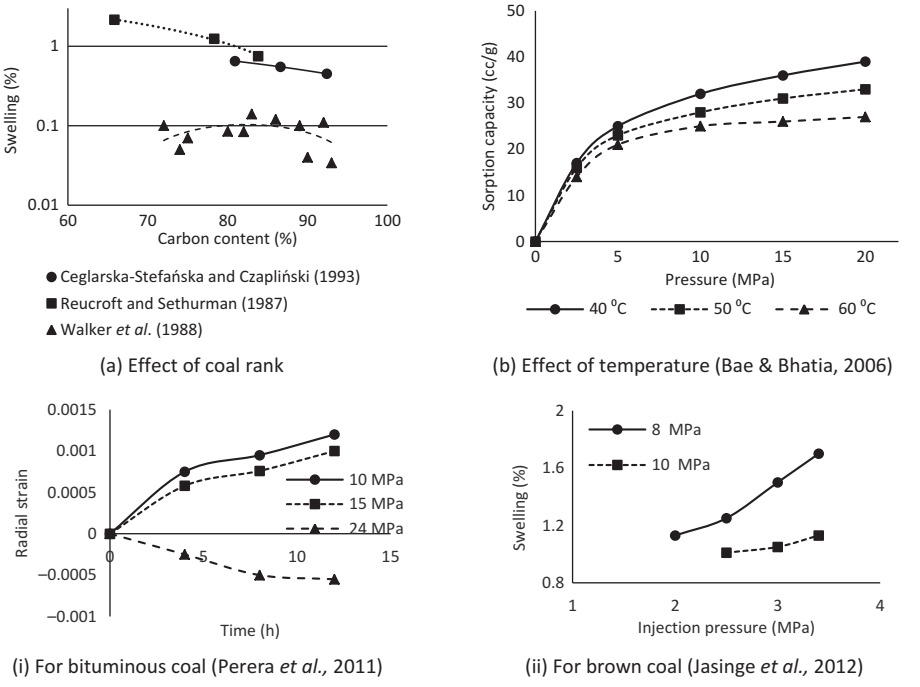


Figure 6 Effect of seam properties on swelling (Bae & Bhatia, 2006; Ceglarska-Stefańska & Czapliński, 1993; Jasinge *et al*., 2012; Perera *et al*., 2011; Reucroft & Sethuraman, 1987; Walker *et al*., 1988).

Figure 6(a)). This is thought to be due to the less mobile polymers present in high-ranking coal in contrast to low-ranking coal. This has the effect of preventing such a great deal of swelling at the molecular level, which transfers to less swelling present at the macromolecular level (Ceglarska-Stefańska & Czapliński, 1993). However, Walker *et al.* (1988) observed the increment only for lignite to highly volatile bituminous coals, and any further increase of rank causes the swelling effect to be reduced with increasing rank (in the anthracite region) (see Figure 6(a)).

b) Temperature
With increased temperature, gas adsorption capacity is reduced (Ceglarska-Stefańska & Czapliński, 1993), because with the temperature increment, gas molecules are released form the adsorbed phase as their kinetic energy is accordingly increased. According to Perera & Ranjith (2012), Bae & Bhatia (2006) and Kronimus *et al.* (2008), super-critical CO_2 is subjected to the temperature effect more significantly than sub-critical CO_2 (see Figure 6(b)). As discussed in the previous section, sorption capacity is directly proportional to the coal matrix swelling. Hence, similar behavior can be suggested for the temperature effect on swelling (Perera & Ranjith, 2012). According to the geothermal lines, underground temperature proportionally increases with depth. Therefore, according to both of these influences (rank and temperature), the CO_2 sequestration-created swelling effect should be clearly dependent on the location of the coal seam.

c) Depth (confining pressure)
When the depth is increased, CO_2 permeability in coal seams is reduced, since the pore space available for gas movement is shrunk considerably at greater depths, due to the higher confinement, resulting in higher tortuosity and consequently lower flow rate through the coal mass. This reduction of coal permeability for CO_2 causes less CO_2 adsorption into the coal matrix, resulting in less matrix swelling. This observation is irrelevant to coal rank, according to the studies by Jasinge *et al.* (2012) for brown coal (see Figure 6(c-i)) and Perera *et al.* (2011b) (see Figure 6(c-ii)), for bituminous coal. These studies reported similar observations of less coal matrix swelling at higher confinements.

3.1.2 *Injecting CO_2 properties*

Beyond 7.38 MPa pressure and 31.8°C temperature, CO_2 exists in its super-critical condition (see Figure 7) (Perera *et al.*, 2011a; Vishal *et al.*, 2013). It is well-known that the preferred coal seams for the ECBM production process are normally present beyond 1000 m from the ground surface, where the pressure and temperature are higher than the critical value of CO_2 (7.38 MPa and 31.8°C), and CO_2 is therefore present in the super-critical state (Figure 7). Therefore, Perera *et al.* (2011b) conducted a series of tri-axial experiments under sub-critical and super-critical CO_2 adsorption to investigate the CO_2 phase and pressure effect on coal swelling. They measured the radial strain increment in the coal samples during 15 hours of sub-critical and super-critical CO_2 adsorption, maintaining the system temperature above the critical temperature of CO_2 (31.8°C) (Figure 8(a)). According to the results, both sub-critical and

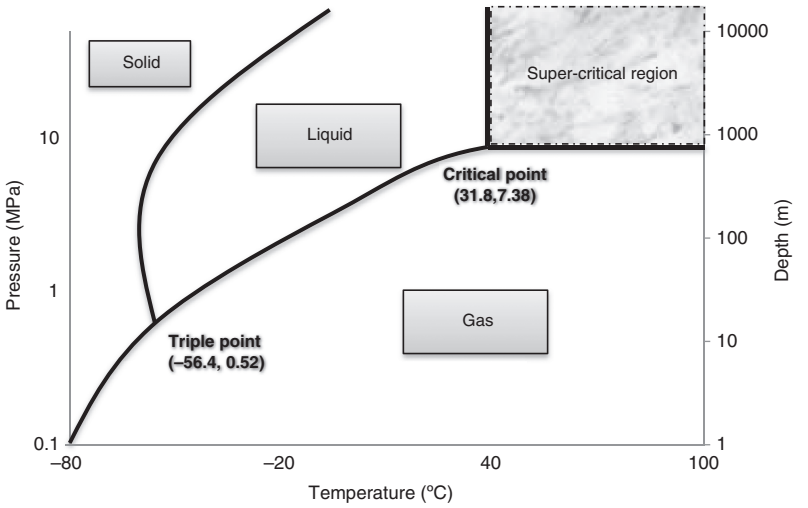
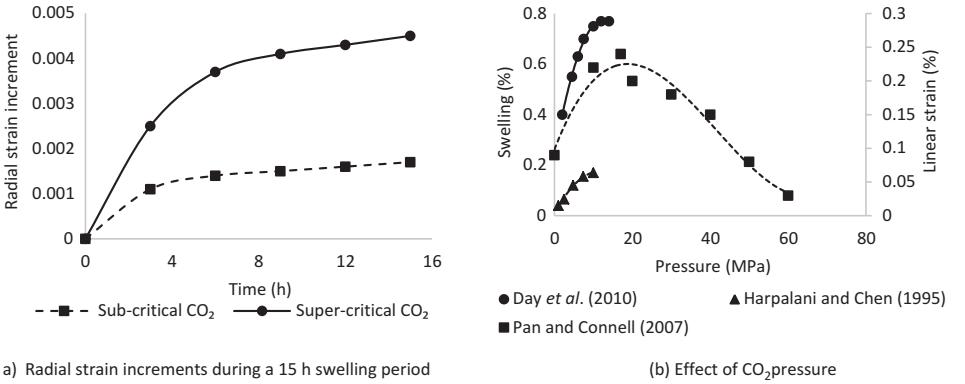


Figure 7 CO_2 phase diagram (Oldenburg, 2006).

super-critical CO_2 adsorptions induce a considerable swelling in coal, and the swelling created by super-critical CO_2 adsorption is more than three times greater than sub-critical CO_2 adsorption-induced swelling (Figure 8(a)). This is probably due to the highly chemically reactive nature of super-critical CO_2 compared to sub-critical CO_2. This implies that un-mineable coal seams are more vulnerable to the swelling effect. The effect of CO_2 pressure on coal swelling has also been studied by Day *et al.* (2010), Harpalani & Chen (1995) and Pan & Connell (2006), who have confirmed the increment of swelling with CO_2 pressure (see Figure 8(b)). In addition, Day *et al.* (2010: Figure 8(b)) and Pan & Connell (2006: Figure 8(b)) described the behavior at high pressures, where the swelling ratio may decrease after reaching a maximum swelling.



a) Radial strain increments during a 15 h swelling period

(b) Effect of CO_2pressure

Figure 8 Coal swelling with CO_2 injection (Day *et al.*, 2010; Harpalani & Chen, 1995; Pan & Connell, 2006; Perera *et al.*, 2011b).

Therefore, it is clear that not only gas injection pressure but also the adsorbing gas phase condition has a significant effect on coal matrix swelling.

4 CO_2 SEQUESTRATION EFFECT ON DEEP COAL-SEAM FLOW CHARACTERISTICS

Expansion of the coal matrix with swelling induced by CO_2 adsorption leads to the closure of cleats and fractures, as well as the reduction of the pore space available for gas movement, which eventually results in reduction of permeability. As the reduction of permeability would directly obstruct the injection of CO_2, it is necessary to have a comprehensive understanding of the process, to enable better control of CO_2 injection.

4.1 Does CO_2 sequestration create unpredictable CO_2 injectibilities?

Permeability is the term that provides a quantitative picture of the flow ability through any media. According to previous studies (Perera *et al*., 2011a; Perera & Ranjith, 2012; White *et al*., 2005), the permeability of natural coal seams varies with coal mass properties such as coal rank (carbon content and cleat structure), temperature and confining pressure, and injecting gas properties, such as phase and pressure.

Importantly, CO_2 injection into a deep coal seam causes its permeability to be altered, mainly due to CO_2 adsorption-induced coal matrix swelling. Existing research studies clearly show the significant swelling created by CO_2 injection into deep coal seams and the corresponding reduction of coal mass pore spaces and eventually the permeability (Viete & Ranjith, 2006; Perera *et al*., 2011b; Vishal *et al*., 2013). According to Perera *et al*. (2011a), this permeability reduction increases with increasing CO_2 injection pressure and CO_2 phase transition from sub- to super-critical (see Table 2). Moreover, as shown in Table 2, the temperature of the coal seam has a significant influence on the coal permeability alterations which occur with CO_2 injection, and CO_2 permeability in coal increases with increasing temperature only at higher CO_2 injection pressures (>10MPa). This is basically due to the fact that, with increasing temperature, the sorption capacity of and the swelling effect in coal are reduced, due to the increased kinetic movement of the CO_2 molecules (Bae & Bhatia, 2006), resulting in increased coal permeability at higher temperatures. This indicates the importance of selecting a coal seam with appropriate physical properties to achieve effective CO_2 sequestration in coal.

If the CO_2 sequestration process is considered, Durucan & Shi (2009) found some permeability reduction in deep coal seams due to methane adsorption. They also found that the reduction is partially recovered when permeability enhancement occurs with methane desorption (coal matrix shrinkage) during the CO_2 sequestration process. However, CO_2 creates much higher swelling effects in coal compared to methane or many other types of gas, and the effect is higher than the coal mass shrinkage effect during CH_4 desorption (Ranathunga *et al*., 2014). Therefore, the CO_2 sequestration process causes coal seam permeability to be significantly reduced over time. Therefore, the CO_2 sequestration process will require permeability enhancement treatments over time.

Table 2 Effect of CO_2 injection on coal seam permeability during CO_2 sequestration.

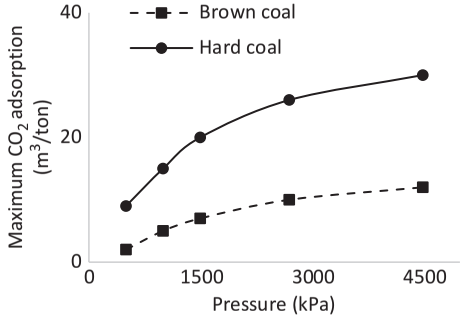
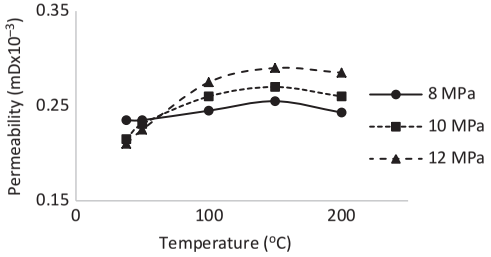
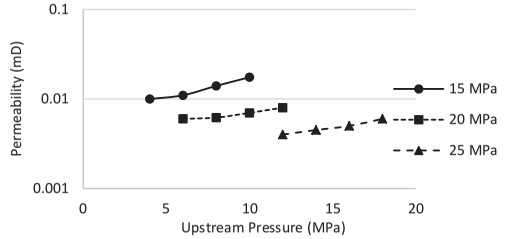
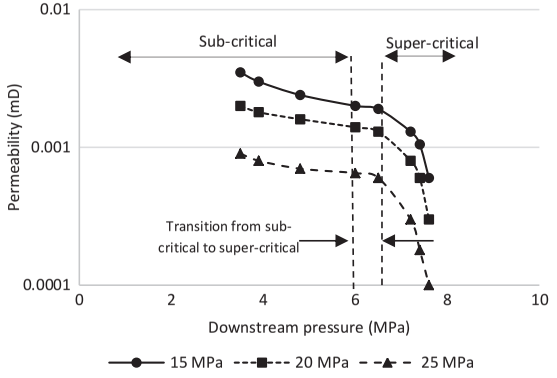
Effective factor	*Key observation*	*Figure*
Coal rank	– The CO_2 adsorption capacity is higher for high rank coal compared to low rank coal which leads to higher matrix swelling for higher rank coal and relatively lower permeability compared to low rank coal (Saghafi *et al*., 2007). – High rank coal has a higher surface area compared to low rank coal due to its cleat structure developed during the coalification process, which leads to higher adsorption capacities.	 Variation of gas adsorption capacity in coal with pressure (Saghafi *et al*., 2007)
Temperature	– A significant increase in coal permeability can be observed with increasing temperature for higher CO_2 injection pressures (>10MPa), and an insignificant effect on permeability at low CO_2 injection pressures (<9 MPa) (Perera & Ranjith, 2012) – Kinetic energy of gas molecules increases with increasing temperature. By the time the kinetic energy exceeds the intermolecular forces, the molecules tend to be released with random motion, which reduces the gas adsorption capacity in coal (Clarkson & Bustin, 1997).	 Temperature effects on CO_2 permeability at 20 MPa confinement (Perera & Ranjith, 2012)

Table 2 (Cont).

Effective factor	*Key observation*	*Figure*
Confining pressure	– Under the same experimental conditions, higher confining pressure induces lower permeability (Day *et al.*, 2010; Perera *et al.*, 2011a) – The compressive force created by higher confinements at greater depths causes the pore space available for gas movement to shrink considerably, resulting in higher tortuosity and consequently lower flow rate through the coal mass (Perera *et al.*, 2011a).	 Permeability for CO_2 movement with confining pressure (Perera *et al.*, 2011a)
CO_2 phase and pressure	– Permeability reduction increases with increasing CO_2 injection pressure and CO_2 phase transition from sub- to super-critical (Perera *et al.*, 2011a; Shi & Durucan, 2005). CO_2 tends to change from sub-critical to super-critical in deep coal seams with high temperature and pressure (approximately 7.38 MPa and 31.8^{0}C) (see Figure 7) – A drastic increment in coal adsorption is observed after 7.38 MPa up to around 9 MPa, with an indication of CO_2 adsorption increase in super-critical state. – The transformation of sub-critical to super-critical phase leads to different thermo-physical and transport properties, which may also influence the sorption capacity(Wang *et al.*, 2011).The greater swelling effect, as well as the higher increment in its viscosity, contribute to the high decline in permeability (Jasinge *et al.*, 2010)	 Permeability for CO_2 movement with injection pressure (Perera *et al.*, 2011a)

5 CO_2 SEQUESTRATION EFFECT ON DEEP COAL SEAM MECHANICAL PROPERTIES

Not only CO_2 injectibility into coal seams, also the overall strength of those seams is found to be altered with the CO_2 injection process, which is a greater threat in terms of long-term safety of the CO_2 storage process in deep coal seams as it may cause the back-migration of injected CO_2 into the atmosphere. Therefore, it is of great importance to have a comprehensive understanding of the effect of CO_2 sequestration to achieve better control of coal mass integrity during and after the CO_2 sequestration process.

5.1 Does CO_2 sequestration affect coal seam strength?

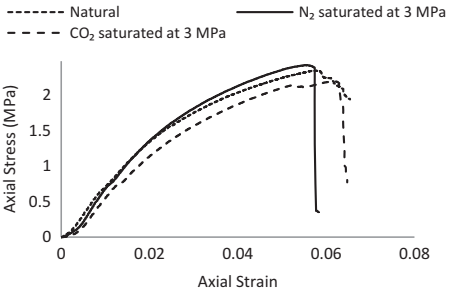
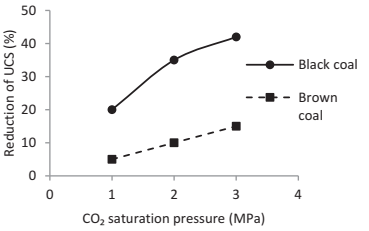
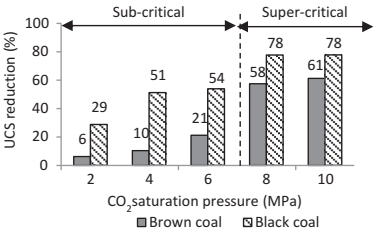
As proposed by Gibbs (1878) and Griffith (1921), material strength depends on the chemical potential of the adsorbate, and replacement of the existing adsorbate with one more chemically potent causes it to be weakened. CO_2 is clearly a more chemically potent gas compared to pre-adsorbed methane in coal seams (Gibbs, 1878; Griffith, 1921). This implies that the replacement of the CH_4 with CO_2 injection causes the coal seam strength to be reduced. The natural coal mass structure is a glassy, strained and cross-linked macro-molecular structure with high energy, which limits the freedom of coal molecules to move, resulting in a highly brittle structure (Larsen *et al.*, 1997; Majewska & Ziętek, 2007; Goodman *et al.*, 2005). When CO_2 is adsorbed, the coal mass polymer structure is rearranged with the increment of free volume in the coal matrix and the ductile properties of the coal structure are enhanced, affect the elastic modulus of the coal (Perera & Ranjith, 2012).

The reduction of coal strength with CO_2 injection into it is well known, and this strength reduction varies with seam location and injecting CO_2 properties (Aziz & Ming-Li, 1999; Czapliński & Hołda, 1982; Day *et al.*, 2010; Jasinge *et al.*, 2011; Perera & Ranjith, 2012). For example, the CO_2 adsorption-induced strength reduction is greater for high rank coal located at greater depths, and increasing the injecting CO_2 pressure causes greater brittleness reduction in the coal seam. Table 3 illustrates the current findings on this issue.

Importantly, the CO_2 sequestration and ECBM processes typically target deep coal deposits, and at such locations CO_2 may not exist in a sub-critical phase, as it does under standard laboratory conditions, but instead exists in a super-critical state. Therefore, Karacan (2007) and Aziz & Ming-Li (1999) found that when CO_2 pressure increases, so too do the strength losses. These additional strength losses are due to the greater adsorptive potential and dissolution ability of super- over sub-critical CO_2. In this way, super-critical CO_2 is able to access more of the coal matrix than sub-critical CO_2, which can cause more effects on the coal seam integrity (see Table 3).

While this CO_2 adsorption-induced strength reduction and crack formation cause the injected CO_2 to be back-migrated into the atmosphere, there is an additional concern related to the potential for fault instability located between the deposited CO_2 and the surface, leading to potential damage to infrastructure. Therefore, a better understanding of coal mass behavior is essential for the safe implementation of CO_2 sequestration at a field scale.

Table 3 Effect of CO_2 injection on coal seam strength during the CO_2 sequestration process.

Effective factor	*Key observation*	*Figure*
Adsorbing gas property	CO_2 (sub-critical) saturation decreases the strength of brown coal, while for N_2,the effect is the opposite. This is because N_2 is capable of replacing the existing CO_2 in the coal mass by reducing the partial pressure of the seam and consequently recovering the swelling areas to some extent (Kiyama *et al.*, 2011).	 Axial stress vs. Axial strain curves for different saturation mediums (Perera *et al.*, 2011c)
Coal rank	CO_2 saturation causes up to 4.5 times higher strength reduction in bituminous coal compared to lignite as there is a greater surface area in high density coal. High rank coal seams located deep underground offer greater loci for CO_2 adsorption due to their well-developed cleat system causing more swelling than low rank coal (Ranjith & Perera, 2012).	 Comparison of UCS strength reduction in bituminous and lignite coal (Ranjith & Perera, 2012)
CO_2 pressure and phase	• There is a linearly increasing trend for strength reduction with increased injection pressure (Perera *et al.*, 2013) • The increasing injection pressure has a significant negative effect on cleat performance with greater adsorption-induced swelling (Perera *et al.*, 2013) • A greater strength reduction (approximately 40%) in super-critical CO_2 compared to normal gaseous CO_2 due to the greater adsorptive potential for super-critical CO_2 (Perera *et al.*, 2013)	 Gaseous and super-critical CO_2 saturation effect on coal strength (Perera *et al.*, 2011c, 2013)

Although CO_2 sequestration is a promising method to reduce and control the greenhouse gas effect through the geological storage of anthropogenic CO_2, it still remains in the experimental stage, as many aspects need to be studied before being put into practice to avoid the risks associated with this process. Most of the possible coal seams for CO_2 sequestration are thin (0.5–5 m), contain many faults and are

much lower in permeability (0.001–0.005 Darcy) (Gale, 2004). Therefore, CO_2 adsorption-induced swelling in such seams may develop higher stresses on the top (overlying) and bottom (underlying) rock strata, which can create possible migration paths for injected CO_2 out of the coal mass through the faults generated.

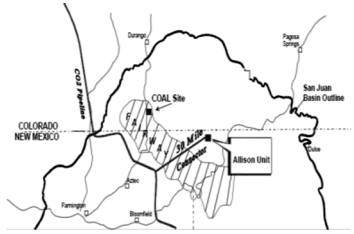
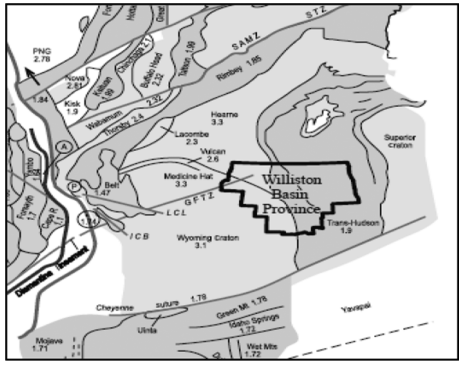
6 COAL CO_2 SEQUESTRATION FIELD PROJECTS

The USA, Canada, Poland, China, Australia, Japan and some other countries are using ECBM recovery via CO_2 sequestration at a field scale. Table 4 summarizes some of the main field-scale CO_2 sequestration projects in the world. In addition, initial testing for CO_2 sequestration in China has confirmed a large resource potential for CO_2 sequestration. There are two potential settings for CO_2storage within China's carboniferous coal deposits: the northeast China coal region and the Ordos basin in north central China. Of these, the northeast China coal region is heavily industrialized, with numerous coal-fired power plants that could provide cheap CO_2 for injection. The Ordos basin in north central China has superior reservoir quality, with minimal fracturing and higher permeability, and the potential for CO_2 sequestration is around 660 million tons in this basin (Stevens *et al*., 1999). In 2002, China initiated field-scale CO_2 sequestration with the collaboration of Canada, and during the first three years, the project was planned to perform three micro pilot tests before the selection of a suitable location meeting the requirements for a full-scale pilot test (White *et al*., 2005). According to Wong *et al*. (2007), the first micro-pilot test at the south Qinshui basin, Shanxi Province, China was successful and the field data were well-matched using a tuned reservoir model. Further, a multi-well pilot project was designed and planned to proceed (Wong *et al*., 2007).

However, most of the current field-scale CO_2 sequestration projects have faced the common issue of reduction of CO_2 injection capacity within 6 months to two years after initiation; due to coal matrix swelling (refer to Table 4). Interestingly, this matrix swelling-created CO_2 injectibility reduction has sometimes been recovered by the reduced effective pressure closer to the CO_2 injection well, and as a result considerable CO_2 injection capacity enhancements have been recorded (Fujioka *et al*., 2010; White *et al*., 2005). However, the combined influence has mostly had a negative influence on CO_2 sequestration and coal seam gas production. Therefore, various coal seam permeability enhancement techniques, including inert gas (N_2) injection and hydro fracturing, have been performed in the field.

Of these projects, the Ishikari basin and Fenn Big Valley basin projects have injected pure N_2 (Mavor *et al*., 2004; White *et al*., 2005; Fujioka *et al*., 2010) and the Fenn Big valley basin and Southern Bowen basin have injected a mixture of N_2 and CO_2 (flue gas) (Reeves & O'Neill, 1989; Mavor *et al*., 2004; White *et al*., 2005; Syed *et al*., 2013) into the coal seam to recover the CO_2 adsorption-induced swelled areas in the coal matrix to some extent. Although injecting an inert gas like N_2 (Mavor *et al*., 2004; White *et al*., 2005; Fujioka *et al*., 2010) or a mixture of CO_2 and N_2 (Reeves & O'Neill, 1989; Mavor *et al*., 2004;White *et al*., 2005) can increase coal seam permeability by a substantial amount, that increase is not sufficient for an economical CO_2 sequestration project. Therefore, more advanced approaches, such as hydro fracturing, have been required to enhance coal seam permeability to achieve an acceptable CO_2

Table 4 Field-scale CO_2 sequestration projects around the world.

CO_2 sequestration project	*Details of well configuration*	*Details of gas injection*	*Remarks*	*Figures*
Allison unit San Juan basin – USA (Clarkson & Bustin, 1997; Reeves, 2001, 2002a; Reeves, 2002b; Reeves *et al*., 2002; Reeves & Oudinot, 2005; White *et al*., 2005)	Has 4 CO_2 injection wells and 9, CH_4 production wells, drilled at 320-acre spacing	• CO_2 was injected at a maximum injection pressure of 17 MPa • Over 6 ½ years, 6.4 Bcf of CO_2 was injected	• The first experimental CO_2-ECBM recovery pilot project in the world, started in 1995 and the rank is medium to low volatile bituminous coal. • Initially, significant reduction in injectivity was observed due to coal matrix swelling and effective stress increment. • Gas production caused the overall reduction of pressure and reservoir volume and caused CO_2 adsorbed near the injection wells to be desorbed and migrate further from the wells. This increased permeability by reversing the swelling areas closer to injection wells.	 Allison Unit- San Juan basin, USA (Reeves, 2001)
Williston basin North Dakota – USA (Botnen *et al*., 2009; Perera & Ranjith, 2012; White *et al*., 2005)	Consists of five wells to around 340m depth	• Estimated CO_2 storage capacity is 10.3 TCU • Weakly developed cleat system was the main challenge for the injection of CO_2	• Second largest coal deposit in USA, consists of lignite coal deposit • 13 molecules of CO_2 can be sequestrated for each molecule of CH_4 • Due to coal mass swelling, 10-fold reduction was observed in first year	 Williston basin, North Dakota – USA (Peterson & Schmoker, 1995)

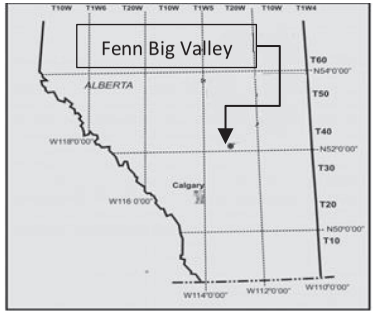
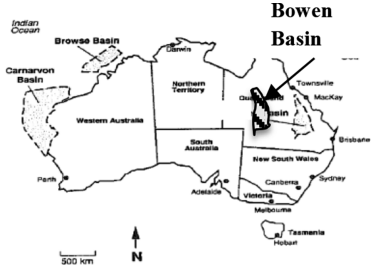
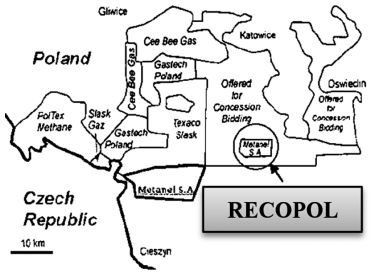
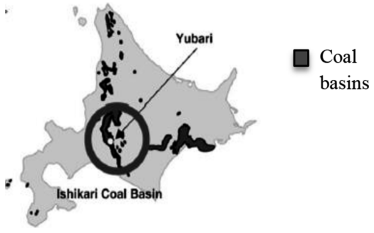
Fenn Big Valley basin Alberta – Canada (Mavor *et al*., 2004; Perera & Ranjith, 2012; White *et al*., 2005)	Consists of two wells	• Both CO_2 and flue gas were injected • In 1997, 12tons of CO_2 was injected and after a short process of CH_4 production, around 15 tons of CO_2 was injected. • Since the absolute permeability of the coal seam was very low (1 mad) during the pure CO_2 period, flue gas (13% CO_2, 87% N_2) was injected into the same injection wells in 2000. • Pure N_2 was injected to enhance the CO_2 injection rate and the absolute permeability of the coal seam was increased up to around 13.8 mad • Since the absolute permeability was reduced (1 mad) after 9 days, a mixture of CO_2 andN_2 (47% CO_2, 53% N_2) was injected, which increased the absolute permeability up to 5.6 mad	• Consists of 500 TCU out of 700 TCU coalbed methane resources in Canada • First pilot test of injecting flue gas in the world • Rank is high volatile B-bituminous	 Fenn Big Valley basin Alberta – Canada (Gentzis *et al*., 2008)

Table 4 (Cont).

CO_2 sequestration project	*Details of well configuration*	*Details of gas injection*	*Remarks*	*Figures*
Dowson river site Southern Bowen basin Australia (Perera & Ranjith, 2012; Reeves & O'Neill, 1989)	Three major phases 1 Micro pilot testing (one CO_2 injection well/ CH_4 production well) 2 Five-spot pilot testing (4 CO_2 injection wells and one CH_4 production well) 3 Nine-spot pattern field testing (16 CO_2 injection wells and 25 CH_4 production wells, drilled at 80–320acre spacing	• During first phase CO_2 is injected followed by a soak period, to allow the CO_2 to be adsorbed into coal • During second phase, both pure CO_2 and a mixer of CO_2 and N_2 is injected	• Estimated CBM resource base is 178 Tscf • The coals are high-volatile bituminous A and B • The timing of the demonstration is 4.3 years • If the project were to be successful, phase 3 would become a commercial operation	 Location of Southern Bowen basin, Australia (Source: Reeves & O'Neill, 1989)

Silesian basin, Poland (Reduction of CO_2 Emissions by Means of CO_2 Storage in the Silesian Coal Basin of Poland – RECOPL) (Perera & Ranjith, 2012; Reeves & Taillefert, 2002; White *et al*., 2005)	One CO_2 injection well and one CH_4 production well located 105 m from each other	• During first 6 months (in 2004) of CO_2 injection, permeability was reduced from 10–100 (CO_2 injection capacity – 1 ton/day) from the initial permeability (CO_2 injection capacity – 20 ton/day) • In mid-2005, a hydraulic fracture was created and CO_2 injection capacity increased up to 15 tons/day	• Small-scale project • 93% of the injected CO_2 was stored and 55-70% enhancement of CH_4 production was observed from the field tests	 Location of Silesian basin, Poland (Reeves & Taillefert, 2002)
Ishikari basin Yubari – Japan (Fujioka *et al*., 2010; Perera & Ranjith, 2012; White *et al*., 2005)	Two CO_2 injection wells and one CH_4 production well	• During the first year, without any gas production, a total of around 35.7 metric tons of $CO_2$was injected at a rate of 2.3 tons/day, which reduced to 11 metric tons in the second year • Due to decrease of effective pressure closer to the injection well, CO_2 injection was increased from 1.6 tons/day to 3.5 tons/day • The N_2 injection in 2005, enhanced the CO_2 injection up to 6.6 tons/day and gradually dropped again to the initial rate, and was then again increased because of effective stress variation.	• Small-scale project • Injection pressure was maintained at 15 MPa, which was slightly less than the cleat opening pressure of 15.8 MPa • A total of 480 tons of CO_2 was injected between 2004–2006	 Location of Ishikari coal basin, Japan (Fujioka *et al*., 2010)

injection capacity in the field (Ruehl, 1968; Mazza *et al.*, 1981; Puri *et al.*, 1991; Reeves & Taillefert, 2002).

Hydro fracturing techniques have already been tested in some field-scale projects, including the Silesian basin (Reeves & Taillefert, 2002; White *et al.*, 2005). However, there are some disadvantages to the hydro fracturing process, since the creation of hydraulic fractures may cause the coal seam to be weakened, and this may enhance the risk of injected CO_2 back-migration into the atmosphere. Therefore, creating hydro-fractures in coal seams, where they have already been weakened due to super-critical CO_2 injection, becomes a greater challenge and no extensive study has been conducted regarding this matter to date. Therefore, a far-reaching study is required, using comprehensive experiments under laboratory conditions or advanced numerical modeling approaches, before putting hydro fracturing into practice.

7 WHAT CAUSES THE LACK OF CO_2 SEQUESTRATION IMPLEMENTATION?

Basically, CO_2 sequestration in deep coal seams can be divided into two general sub-systems: operational and in situ. The operational sub-system includes components such as CO_2 capture, transportation, and injection. Once CO_2 is injected into coal beds, it enters an in situ sub-system. The past technological innovations and experiences have provided the tools and proficiency to handle and control CO_2 in the operational sub-system with adequate certainty and safety; however, in the in-situ sub-system knowledge is currently lacking, particularly of the environmental and human health risks. Furthermore, public perceptions, the economics of CO_2 sequestration and policy barriers are other challenges which discourage the use of CO_2-ECBM projects in spite of their multiple advantages (Bae & Bhatia, 2006; Holloway, 2005; Howard, 2002).

7.1 Complexity associated with coal heterogeneity

Some characteristics are required for effective and safe CO_2 sequestration in coal seams. These include i) sufficient capacity for storing large volumes of CO_2, ii) adequate CO_2 injectivity (permeability of at least 1–5 mD), iii) a minimally faulted and/or folded reservoir, and iv) a reservoir well confined with an overlying seal to prevent leakage of injected CO_2 into the atmosphere (Bachu, 2007; Gale & Freund, 2001). However, the satisfaction of all of these criteria is challenging and is made complex by the highly heterogeneous nature of coal. As discussed in Sections 4 and 5, the behavior of CO_2 permeability and coal seam strength vary with the seam and injecting CO_2 properties (coal rank, temperature, confining pressure, CO_2 phase and pressure). This leads to unpredictable CO_2 injectivity and coal seam integrity. In addition, the heterogeneous nature of coal increases the uncertainty in determining the properties representative of a whole seam (Day *et al.*, 2008; Ozdemir & Schroeder, 2009; Renzik *et al.*, 1978; Robertson, 2005; Saghafi *et al.*, 2007; Wang, 2007). Furthermore, there may be significant variations in properties within the same core sample or between different

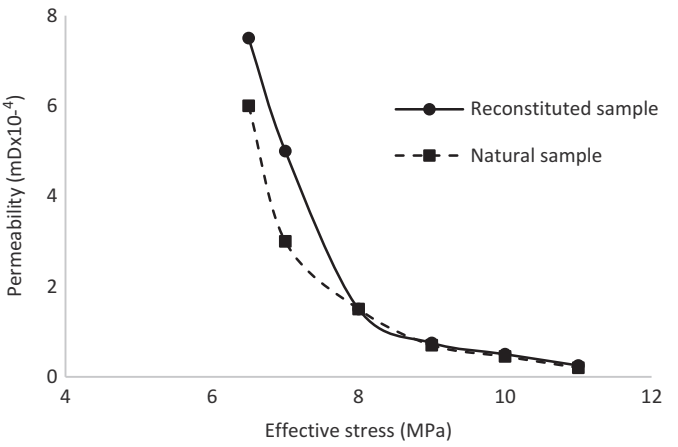


Figure 9 Permeability behavior with effective stress for natural and reconstituted coal samples (Jasinge *et al.*, 2011).

core samples obtained from the same coal seam. Therefore, the heterogeneous nature of coal has been a key hurdle to the confirmation of the effects of in situ coal properties on coal's behavior.

According to De Silva & Ranjith (2013) and Jasinge *et al.* (2011), homogenous reconstituted coal samples with reproducible properties can be used to overcome this problem. Figure 9 shows the variation of permeability with effective stress for reconstituted and natural samples of brown coal. The figure depicts very similar permeability behavior of CO_2 in the natural specimen and the reconstituted specimen (Jasinge *et al.*, 2011). Therefore, reconstituted coal samples can be used to avoid the complexities associated with coal heterogeneity. However, thorough investigation of the coal mass structure and its characteristics for different localities is crucial for the safe execution of CO_2-ECBM at a field scale.

7.2 Environmental and human health risks

The question of whether safe and stable storage of CO_2 in the sub-surface can be assured is probably the most important issue facing the underground storage of CO_2 at present, because this is likely to have a high impact on public acceptability. To protect the environment and the health and safety of the public, monitoring and verification of geologically-sequestered CO_2 is essential. Moreover, it is essential to satisfy the expected regulatory demands and to lessen any uncertainties associated with the long-term safety and the security of projects (White *et al.*, 2005). In-situ pressure gauges, chemical tracers, isotropic ratios, geophysical methods, visual inspection and the production response by nearby wells are some methods used for the detection of movement of stored CO_2 (Hall *et al.*, 1994). However, due to the limitations and uncertainties associated with those methods, it has become perplexed in fulfilling the monitoring process such as; (i) uncertainties that are due to wellbore storage effects in using pressure gauges, (ii) adsorptive nature of coal may irreversibly

sorb the compounds added as chemical tracers, and (iii) precision of the measurements during geophysical methods (Chikatamarla *et al.*, 2004; White *et al.*, 2005).

7.3 Policy, regulation and public perceptions of CO_2 sequestration using ECBM

For the operation of CO_2 sequestration in a safe and secure manner, the formation and application of sound regulatory and legal frameworks are essential. Public perceptions, policies, regulations and international conventions exist which may offer assistance or barriers to CO_2 capture and storage using ECBM recovery.

7.3.1 Policies, regulations and international agreements

The use of CO_2 sequestration will add to the cost of fossil fuel energy with some exceptions. Worldwide disposition of CO_2 sequestration could be encouraged by policies that address the added cost of CO_2 storage, not only in developed countries but also in countries where access to affordable energy is a key development priority. Some national governments have provided limited early inducements for CO_2 sequestration projects, while the United Nations Framework Convention on Climate Change (UNFCCC) and its Kyoto Protocol could both be used to encourage CO_2 storage. For example, the UNFCCC has accepted Norway's national inventory of greenhouse gas emissions, under which CO_2 from the Sleipner gas field that has been geologically stored does not contribute to Norway's emissions (Kheshgi *et al.*, 2005). To date, no CO_2 sequestration projects have been submitted for approval under the Clean Development Mechanism of the Kyoto Protocol (Kheshgi *et al.*, 2005). Within the European Union (EU) Emissions Trading System, CO_2 stored in geological formations can be deducted from Member States' inventories, based on the provisional monitoring guidelines of Member States, until succeeded by permanent EU monitoring guidelines (Kheshgi *et al.*, 2005). In the long term, the effective application of CO_2 storage will rely on economically efficient approaches to address the additional costs.

An effective legal and regulatory framework would facilitate good CO_2 sequestration practices without forming unintended barriers to the deployment of CO_2 sequestration. An expanded use of coal CO_2 sequestration would be accompanied by reductions in costs, improvements in technology, and improved understanding of risks and their management. A regulatory framework that encourages good practice and incorporates the evolving understanding of risk and its management could promote these improvements.

7.3.2 Public perception

Public acceptance and support is of great importance for coal CO_2 sequestration. At this stage the public is largely unaware of coal CO_2 sequestration. Early experience will leave a legacy for coal CO_2 sequestration in terms of public perceptions of it. Clear assessment of the merits of coal CO_2 sequestration and the competing technologies is a prerequisite for informed decisions. This would enable the merits of each option to be

weighed in the context of a broad range of priorities, including the long-term risks of climate change.

8 CONCLUSIONS AND SUGGESTIONS

8.1 Conclusions

- With the process of industrialization and modernization, carbon dioxide emission is becoming a major concern directly leading to global warming. Various approaches have been proposed to effectively address the problem by significantly reducing the amount of greenhouse gas (CO_2) in the atmosphere, including the use of renewable fuels, energy-efficient technology and carbon sequestration. Of these feasible methods, carbon dioxide sequestration in deep un-mineable coal seams is recognized as one of the most promising methods, for cost and safety considerations.
- CO_2 sequestration involves the capture of CO_2 released from anthropogenic sources and its secure storage in deep underground locations off-shore or on-shore. However, in terms of safety, reliability and cost, on-shore sequestration is more effective than off-shore sequestration. Of the various potential CO_2 storage sinks deep underground (*e.g.* depleted oil and gas fields, saline aquifers, shale beds, and coal mines), CO_2 storage in deep coal seams offers unique advantages, and the offsetting of CO_2 sequestration costs by the production of a valuable energy product like methane (coal seam gas) is critical. This process is known as enhanced coal bed methane (ECBM) recovery.
- However, adsorption of the injected CO_2 into the coal mass causes it to swell, leading to significant alterations in its internal rock mass structure, resulting in major modifications to CO_2 injectivity and coal mass integrity. This CO_2 adsorption-induced coal matrix swelling process is dependent on both seam (coal rank, temperature and confining pressure) and injected CO_2 properties (CO_2 phase and pressure), and the swelling reduces with increasing temperature due to the reduced sorption capacity. On the other hand, the amount of swelling is largely dependent on the pressure and the physical state of the injected CO_2, and super-critical CO_2 creates a much greater swelling effect than sub-critical CO_2, due to its higher chemical potential. Furthermore, high-pressure injection of CO_2 causes the swelling process to be enhanced due to the higher flow ability of the injected CO_2 under reduced effective stress conditions (difference of confining pressure and injection pressure) at increased injection pressures. However, potential coal seams for CO_2 sequestration process are available at extremely deep locations and there is a high possibility of phase change from sub- to super-critical state in the underground environment owing to changes in field conditions. This confirms the likely existence of high swelling rates in deep coal seams with CO_2 injection.
- The effectiveness of the CO_2 storage process in any coal seam is greatly influenced by the flow ability of the injected CO_2 through the seam, which is dependent on a number of factors, including coal rank, seam temperature, seam depth (confining pressure) and CO_2 injecting pressure and phase. Importantly, the injected CO_2 phase condition critically influences its flow behavior in the seam. In the she super-critical state, the expected form of the CO_2 in deep coal seams, CO_2 has

significantly lower permeabilities than sub-critical CO_2, which causes unpredictable CO_2 injectibilities into deep coal seams.

- Secure storage of injected CO_2 in the seam is critically important in CO_2 geo-sequestration in deep coal seams in terms of environmental health and safety. It is important to prevent the back-migration of CO_2, as this has potential to cause mine outbursts and lateral migration into aquifers and surrounding more permeable geologic strata. These factors are mainly dependent on the coal mass strength properties. However, it is well known that CO_2 adsorption-induced swelling causes weakening in deep coal seams. This strength reduction is greatly dependent on injecting CO_2 phase and pressure, and it increases with increasing pressure. In addition, super-critical CO_2 creates much greater strength reduction than sub-critical CO_2. High rank coal seams located deep underground are subjected to greater strength reduction with CO_2 injection, as they offer greater loci for CO_2 adsorption.
- Reduction of seam permeability over time (after CO_2 injection) is a common issue faced by many field-scale CO_2 sequestration projects. For example, there was around 50% reduction in CO_2injectivity at the Allison unit CO_2 sequestration project in the San Juan basin, USA, during the first two years of injection.
- Existing government policies, public perceptions, and strict rules on coal mining affect the implementation of CO_2 sequestration in deep coal seams. The lack of knowledge related to coal seam CO_2 sequestration has severely affected the implementation of this process in potential coal seams around the world. The complex heterogeneous nature of coal (which causes location-dependent coal seam properties) is the reason for the delay in, adoption of coal CO_2 sequestration.

8.2 Recommendations

- Extensive laboratory tests on different type of coals can be used to obtain a clearer view of the effects of CO_2 sequestration in coal mass in a controlled environment. These results can be used to support reservoir studies and then be extended to other advanced studies (risk assessment studies, economic optimization studies, project-screening models etc.).
- Numerous studies have been conducted on CO_2 sequestration in coal seams. However, knowledge regarding enhanced methane production remains limited. Therefore, more attention to enhanced methane production-related coal seam alterations is required.
- More demonstration projects of CO_2 storage in deep coal seams are required to increase knowledge of CO_2 sequestration-induced flow and mechanical property changes.
- A detailed monitoring system (near-surface monitoring and seam monitoring) is essential for the CO_2 sequestration projects to ensure the integrity of the CO_2 storage and CH_4 production process and to avoid the possible hazards related to CO_2 back-migration into the atmosphere. This would lead to higher confidence and improved public perceptions.

REFERENCES

Adams, E. E., & Caldeira, K. (2008). Ocean storage of CO_2. *Elements*, 4(5), 319–324.

Anggara, F., Sasaki, K., Rodrigues, S., & Sugai, Y. (2014). The effect of megascopic texture on swelling of a low rank coal in supercritical carbon dioxide. *International Journal of Coal Geology*, 125, 45–56.

Archer, D., & Brovkin, V. (2008). The millennial atmospheric lifetime of anthropogenic CO_2. *Climatic Change*, 90(3), 283–297.

Aziz, N. I., & Ming-Li, W. (1999). The effect of sorbed gas on the strength of coal – an experimental study. *Geotechnical & Geological Engineering*, 17(3–4), 387–402.

Bachu, S. (2000). Sequestration of CO_2 in geological media: criteria and approach for site selection in response to climate change. *Energy Conversion and Management*, 41(9), 953–970.

Bachu, S. (2003). Screening and ranking of sedimentary basins for sequestration of CO_2 in geological media in response to climate change. *Environmental Geology*, 44(3), 277–289.

Bachu, S. (2007). Carbon dioxide storage capacity in uneconomic coal beds in Alberta, Canada: Methodology, potential and site identification. *International Journal of Greenhouse Gas Control*, 1(3), 374–385.

Bae, J.-S., & Bhatia, S. K. (2006). High-Pressure Adsorption of Methane and Carbon Dioxide on Coal. *Energy & Fuels*, 20(6), 2599–2607.

Battistutta, E., van Hemert, P., Lutynski, M., Bruining, H., & Wolf, K.-H. (2010). Swelling and sorption experiments on methane, nitrogen and carbon dioxide on dry Selar Cornish coal. *International Journal of Coal Geology*, 84(1), 39–48.

Benson, S. M., & Cole, D. R. (2008). CO_2 sequestration in deep sedimentary formations. *Elements*, 4(5), 325–331.

Borah, R. C., Ghosh, P., & Rao, P. G. (2011). A review on devolatilization of coal in fluidized bed. *International Journal of Energy Research*, 35(11), 929–963.

Bromhal, G. S., Sams, W. N., Jikich, S., Ertekin, T., & Smith, D. H. (2005). Simulation of CO_2 sequestration in coal beds: The effects of sorption isotherms. *Chemical Geology*, 217(3), 201–211.

Chikatamarla, L., Cui, X., & Bustin, R. M. (2004). *Implications of volumetric swelling/shrinkage of coal in sequestration of acid gases*. Paper presented at the Coalbed Methane Symposium, Tuscaloosa, AL.

Clarkson, C. R., & Bustin, R. M. (1997). Variation in permeability with lithotype and maceral composition of Cretaceous coals of the Canadian Cordillera. *International Journal of Coal Geology*, 33(2), 135–151.

Czapliński, A., & Hołda, S. (1982). Changes in mechanical properties of coal due to sorption of carbon dioxide vapour. *Fuel*, 61(12), 1281–1282.

Day, S., Duffy, G., Sakurovs, R., & Weir, S. (2008). Effect of coal properties on CO_2 sorption capacity under supercritical conditions. *International Journal of Greenhouse Gas Control*, 2 (3), 342–352.

Day, S., Fry, R., Sakurovs, R., & Weir, S. (2010). Swelling of coals by supercritical gases and its relationship to sorption. *Energy & Fuels*, 24(4), 2777–2783.

De Silva, G. P. D., Ranjith, P. G., & Perera, M. S. A. (2015). Geochemical aspects of CO_2 sequestration in deep saline aquifers: A review. *Fuel*, 155(0), 128–143.

De Silva, P., & Ranjith, P. (2013). Advanced core flooding apparatus to estimate permeability and storage dynamics of CO_2 in large coal specimens. *Fuel*, 104, 417–425.

Drange, H., Alendal, G., & Johannessen, O. M. (2001). Ocean release of fossil fuel CO_2: A case study. *Geophysical Research Letters*, 28(13), 2637–2640.

Durie, R. (2013). *The science of Victorian brown coal: structure, properties and consequences for utilization*: Butterworth-Heinemann. Oxford, pp 103.

Durucan, S., & Shi, J.-Q. (2009). Improving the CO_2 well injectivity and enhanced coalbed methane production performance in coal seams. *International Journal of Coal Geology*, 77(1–2), 214–221.

Fujioka, M., Yamaguchi, S., & Nako, M. (2010). CO_2-ECBM field tests in the Ishikari Coal Basin of Japan. *International Journal of Coal Geology*, 82(3), 287–298.

Gale, J. (2004). Geological storage of CO 2: What do we know, where are the gaps and what more needs to be done? *Energy*, 29(9), 1329–1338.

Gentzis, T., Goodarzi, F., Cheung, F., & Laggoun-Défarge, F. (2008). Coalbed methane producibility from the Mannville coals in Alberta, Canada: A comparison of two areas. *International Journal of Coal Geology*, 74(3), 237–249.

Gibbs, J. W. (1878). On the equilibrium of heterogeneous substances. *American Journal of Science*(96), 441–458.

Gilman, A., & Beckie, R. (2000). Flow of coal-bed methane to a gallery. *Transport in porous Media*, 41(1), 1–16.

Goodman, A., Favors, R., Hill, M., & Larsen, J. W. (2005). Structure changes in Pittsburgh No. 8 coal caused by sorption of CO_2 gas. *Energy & Fuels*, 19(4), 1759–1760.

Griffith, A. A. (1921). The Phenomena of rupture and flow in solids. *Philosophical Transactions of the Royal Society of London. Series A, Containing Papers of a Mathematical or Physical Character*, 221, 163–198.

Hall, F., Chunhe, Z., Gasem, K., Robinson, R.Jr, & Dan, Y. (1994). *Adsorption of pure methane nitrogen and carbon dioxide and their binary mixtures on wet fruitland coal*. Paper presented at the SPE Eastern Regional Meeting.

Harpalani, S., & Schraufnagel, A. (1990). Measurement of parameters impacting methane recovery from coal seams. *International Journal of Mining and Geological Engineering*, 8 (4), 369–384.

Holloway, S. (2005). Underground sequestration of carbon dioxide—a viable greenhouse gas mitigation option. *Energy*, 30(11–12), 2318–2333.

House, K. Z., Schrag, D. P., Harvey, C. F., & Lackner, K. S. (2006). Permanent carbon dioxide storage in deep-sea sediments. *Proceedings of the National Academy of Sciences*, 103(33), 12291–12295.

Howard, H. (2002). *Carbon sequestration via mineral carbonation: overview and assessment*: MIT Laboratory for Energy and the Environment.

Jasinge, D., Ranjith, P., Choi, S.-K., Kodikara, J., Arthur, M., & Li, H. (2009). Mechanical properties of reconstituted Australian black coal. *Journal of geotechnical and geoenvironmental engineering*, 135(7), 980–985.

Jasinge, D., Ranjith, P., Choi, X., & Fernando, J. (2012). Investigation of the influence of coal swelling on permeability characteristics using natural brown coal and reconstituted brown coal specimens. *Energy*, 39(1), 303–309.

Jasinge, D., Ranjith, P. G., & Choi, S. K. (2011). Effects of effective stress changes on permeability of latrobe valley brown coal. *Fuel*, 90(3), 1292–1300.

Karacan, C. Ö. (2007). Swelling-induced volumetric strains internal to a stressed coal associated with CO_2 sorption. *International Journal of Coal Geology*, 72(3), 209–220.

Kheshgi, H., Stileman, T., Cappelen, F., Crookshank, S., Heilbrunn, A., Lee, A., Mikus, T., Robson, W., & Senior, B., (2005). *Carbon Dioxide Capture And Geological Storage: Contributing to Climate Change Solutions*. World Petroleum Congress.

Kiyama, T., Nishimoto, S., Fujioka, M., Xue, Z., Ishijima, Y., Pan, Z., & Connell, L. D. (2011). Coal swelling strain and permeability change with injecting liquid/supercritical CO_2 and N_2 at stress-constrained conditions. *International Journal of Coal Geology*, 85(1), 56–64.

Kronimus, A., Busch, A., Alles, S., Juch, D., Jurisch, A., & Littke, R. (2008). A preliminary evaluation of the CO_2 storage potential in unminable coal seams of the Münster Cretaceous Basin, Germany. *International Journal of Greenhouse Gas Control*, 2(3), 329–341.

Larsen, J. W., Flowers, R. A., Hall, P. J., & Carlson, G. (1997). Structural rearrangement of strained coals. *Energy & Fuels*, 11(5), 998–1002.

Majewska, Z., & Ziętek, J. (2007). Changes of acoustic emission and strain in hard coal during gas sorption–desorption cycles. *International Journal of Coal Geology*, 70(4), 305–312.

Mavor, M., Gunter, W., & Robinson, J. (2004). *Alberta multiwell micro-pilot testing for CBM properties, enhanced methane recovery and CO_2 storage potential*. Paper presented at the SPE Annual Technical Conference and Exhibition.

Mazza, R. L., Dahl, H. D., & Umphrey, R. W. (1981). Pretreatment for fracturing coal seams: U.S. Patent *No. 4,283,089*.

Metz, B., Davidson, O., De Coninck, H., Loos, M., & Meyer, L. (2005). *Carbon dioxide capture and storage*: IPCC Geneva, Switzerland.

Miedzińska, D., Niezgoda, T., Małek, E., & Zasada, D. (2013). Study on coal microstructure for porosity levels assessment. *Bulletin of the Polish Academy of Sciences: Technical Sciences*, 61 (2), 499–505.

Oldenburg, C. M. (2006). Geologic carbon sequestration: CO_2 transport in depleted gas reservoirs *Gas Transport in Porous Media* (pp. 419–426): Springer, pp. 419–426.

Orr, F. M. (2009). Onshore geologic storage of CO_2. *Science*, 325(5948), 1656–1658.

Ozdemir, E., & Schroeder, K. (2009). Effect of moisture on adsorption isotherms and adsorption capacities of CO_2 on coals. *Energy & Fuels*, 23(5), 2821–2831.

Pachauri, R., & Reisinger, A. (2007). Climate change 2007: synthesis report. Contribution of working groups I. *II and III to the fourth assessment report of the intergovernmental panel on climate change, IPCC, Geneva, Switzerland*, 104.

Pan, Z., & Connell, L. D. (2007). A theoretical model for gas adsorption-induced coal swelling. *International Journal of Coal Geology*, 69(4), 243–252.

Perera, M., Ranjith, P., Viete, D., & Choi, S. (2012). Parameters influencing the flow performance of natural cleat systems in deep coal seams experiencing carbon dioxide injection and sequestration. *International Journal of Coal Geology*, 104, 96–106.

Perera, M. S. A., & Ranjith, P. G. (2012). Carbon dioxide sequestration effects on coal's hydro-mechanical properties: a review. *International Journal of Energy Research*, 36(10), 1015–1031.

Perera, M. S. A., Ranjith, P. G., Airey, D. W., & Choi, S. K. (2011). Sub- and super-critical carbon dioxide flow behavior in naturally fractured black coal: An experimental study. *Fuel*, 90(11), 3390–3397.

Perera, M. S. A., Ranjith, P. G., Choi, S. K., & Airey, D. (2011). The effects of sub-critical and super-critical carbon dioxide adsorption-induced coal matrix swelling on the permeability of naturally fractured black coal. *Energy*, 36(11), 6442–6450.

Perera, M. S. A., Ranjith, P. G., & Peter, M. (2011). Effects of saturation medium and pressure on strength parameters of Latrobe Valley brown coal: Carbon dioxide, water and nitrogen saturations. *Energy*, 36(12), 6941–6947.

Perera, M. S. A., Ranjith, P. G., & Viete, D. R. (2013). Effects of gaseous and super-critical carbon dioxide saturation on the mechanical properties of bituminous coal from the Southern Sydney Basin. *Applied Energy*, 110(0), 73–81.

Peterson, J. A., & and Schmoker, J. W. (1995). *Geologic report, Williston Basin Province* [Online]. Available from: http://pubs.usgs.gov/dds/dds-069/dds-069-w/contents/REPORTS/069_W_CH_062.pdf. [Accessed on 26th March 2015].

Puri, R., Yee, D., Buxton, T. S., & Majahan, O. (1991). Method of increasing the permeability of a coal seam: U.S. Patent No. 5,014,788.

Ranathunga, A. S., Perera, M. S. A., & Ranjith, P. G. (2014). Deep coal seams as a greener energy source: a review. *Journal of Geophysics and Engineering*, 11(6), 063001.

Ranjith, P., & Perera, M. (2012). Effects of cleat performance on strength reduction of coal in CO_2 sequestration. *Energy*.

Reeves, S. (2001). *Geological sequestration of CO_2 in deep, unmineable coalbeds: An integrated research and commerical-scale field demonstration project*. Paper presented at the SPE Annual Technical Conference and Exhibition.

Reeves, S. (2002). *Coal-Seq project update: Field studies of ECBM recovery/CO_2 sequestration in coal seams*. Paper presented at the Proceedings of the 6th International Conference on Greenhouse Gas Control Technologies

Reeves, S. (2002). Field studies of enhanced methane recovery and CO_2 sequestration in coal seams. *World Oil*, 223(12), 56–60.

Reeves, S., Clarkson, C., & Erickson, D. (2002). Selected field practices for ECBM recovery and CO_2 sequestration in coals based on experience gained at the Allison and Tiffany Units, San Juan Basin *Topical Report*.

Reeves, S., & O'Neill, P. (1989). *Preliminary results from the broad meadow pilot, project Bowen basin Australia*. Paper presented at the Proc. 1989 Coalbed Methane Symposium, Univ. Ala. School of Mines and Energy Development and Gas Research Inst., Tuscaloosa, AL.

Reeves, S., & Oudinot, A. (2005). *The Allison Unit CO_2-ECBM Pilot–A reservoir and economic analysis*. Paper presented at the 2005 International Coalbed Methane Symposium, Paper.

Reeves, S., & Taillefert, A. (2002). Reservoir Modeling for the Design of the RECOPOL CO_2 Sequestration Project, *Poland* Topical Report.

Reucroft, P. J., & Sethuraman, A. R. (1987). Effect of pressure on carbon dioxide induced coal swelling. *Energy & Fuels*, 1(1), 72–75.

Robertson, E. P. (2005). *Measurement and modeling of sorption-induced strain and permeability changes in coal*: United States. Department of Energy.

Ruehl, W. (1968). *Method of degassing and fracturing coal seams:U.S. Patent No. 3,384,416*.

Sabine, C. L., & Tanhua, T. (2010). Estimation of anthropogenic CO_2 inventories in the ocean. *Annual review of marine science*, 2, 175–198.

Saghafi, A., Faiz, M., & Roberts, D. (2007). CO_2 storage and gas diffusivity properties of coals from Sydney Basin, Australia. *International Journal of Coal Geology*, 70(1), 240–254.

Sawyer, W., Paul, G., & Schraufnagel, R. (1990). Development and application of a 3D coalbed simulator. *CIM/SPE*, 90–119.

Schrag, D. P. (2009). Storage of carbon dioxide in offshore sediments. *Science*, 325(5948), 1658–1659.

Sean, P. D., & Pitman, M. D. (2012). *The Fossil Record*[Online]. Available from: http://www.detectingdesign.com/fossilrecord.html

Shi, J. Q., & Durucan, S. (2005). CO_2 Storage in Deep Unminable Coal Seams. *Oil & Gas Science and Technology*, 60(3), 547–558

Shi, J. Q., Durucan, S., & Shimada, S. (2014). How gas adsorption and swelling affects permeability of coal: A new modelling approach for analysing laboratory test data. . *International Journal of Coal Geology*, 128, 134–142.

Stangeland, A. (2007). A model for the CO_2 capture potential. *International Journal of Greenhouse Gas Control*, 1(4), 418–429.

Stevens, S. H., Kuuskraa, V. A., Gale, J., & Beecy, D. (2001). CO_2 injection and sequestration in depleted oil and gas fields and deep coal seams: worldwide potential and costs. *Environmental Geosciences*, 8(3), 200–209.

Stevens, S. H., Kuuskraa, V. A., Spector, D., & Riemer, P. (1999). CO_2 sequestration in deep coal seams: pilot results and worldwide potential (pp. 175–180): Pergamon Press, Oxford.

Sundquist, E.T., Burruss, R., Faulkner, S., Gleason, R., Harden, J., Kharaka, Y., Tieszen, L., & Waldrop, M. (2008). *Carbon sequestration to mitigate climate change*: US Department of the Interior, US Geological Survey.

Syed, A., Durucan, S., Shi, J. Q., & Korre, A. (2013). Flue gas injection for CO_2 storage and enhanced coalbed methane recovery: Mixed gas sorption and wwelling characteristics of coals. *Energy Procedia*, 37, 6738–3745.

Vaughan, N. E., & Lenton, T. M. (2011). A review of climate geoengineering proposals. *Climatic Change*, 109(3-4), 745–790.

Viete, D. R., & Ranjith, P. G. (2006). The effect of CO_2 on the geomechanical and permeability behaviour of brown coal: Implications for coal seam CO_2 sequestration. *International Journal of Coal Geology*, 66(3), 204–216.

Vishal, V., Ranjith, P., & Singh, T. (2013). CO_2 permeability of Indian bituminous coals: Implications for carbon sequestration. *International Journal of Coal Geology*, 105, 36–47.

Vishal, V., & Singh, T. (2013). *Development of reconstituted Indian coals to investigate coal response to carbon dioxide exposure*. Paper presented at the ARMA 47th US Rock Mechanics/Geomechanics Symposium 2013 (Laura J Pyrak-Nolte 23 June 2013 to 26 June 2013).

Vishal, V., Singh, L., Pradhan, S. P., Singh, T. N., & Ranjith, P. G. (2013). Numerical modeling of Gondwana coal seams in India as coalbed methane reservoirs substituted for carbon dioxide sequestration. Energy, 49(84), 384–394.

Wang, G. X., Zhang, X., Wei, X., Fu, X., Jiang, B., & Qin, Y. (2011). A review on transport of coal seam gas and its impact on coalbed methane recovery. *Frontiers of Chemical Science and Engineering*, 5(2), 139–161.

Wang, X. (2007). *Influence of coal quality factors on seam permeability associated with coalbed methane production*. University of New South Wales.

White, C. M., Smith, D. H., Jones, K. L., Goodman, A. L., Jikich, S. A., LaCount, R. B., DuBose, S. B., Ozdemir, E., Morsi, B. I., & Schroeder, K. T. (2005). Sequestration of carbon dioxide in coal with enhanced coalbed methane recovery: A review. *Energy & Fuels*, 19(3), 659–724.

Wong, S., Law, D., Deng, X., Robinson, J., Kadatz, B., Gunter, W.D., Jianping, Y., Sanli, F., & Zhiqiang, F. (2007). Enhanced coalbed methane and CO_2 storage in anthracitic coals—Micro-pilot test at South Qinshui, Shanxi, China. *International Journal of Greenhouse Gas Control*, 1(2), 215–222.



Taylor & Francis
Taylor & Francis Group
http://taylorandfrancis.com

Support Technology



Taylor & Francis
Taylor & Francis Group
http://taylorandfrancis.com

Chapter 4

Drift reinforcement design based on Discrete Fracture Network (DFN) modeling

J. Hadjigeorgiou[1] & *M. Grenon*[2]
[1]*University of Toronto, Toronto, Ontario, Canada*
[2]*Université Laval, Quebec City, Quebec, Canada*

Abstract: Discrete Fracture Networks (DFN) are a powerful technique in capturing the structural complexity of a rock mass. A design methodology is provided that employs DFN in the analysis and design reinforcement and support of drifts in hard rock. This is accomplished by the explicit representation of reinforcement and support in DFN models. This approach provides an evaluation and comparison of different support strategies for a given excavation.

1 INTRODUCTION

The design of excavations in rock requires an understanding of the way the ground acts in response to the rock mass conditions, acting forces and project related features, Palmstrom & Stille (2007). In this context, the first step lies in capturing the salient characteristics of the rock mass through field and laboratory investigations. The second step would be to employ this information to address specific requirements for a project such as type, geometry and size of an excavation. The design should also address operational requirements including design life. The third component of a design process is the identification of the forces acting on the excavation.

There are a multitude of engineering tools that can be used for assessing the stability of an excavation in rock and for providing recommendations for reinforcement and support to allow for an acceptable design, Choquet & Hadjigeorgiou (1993). These tools employ analytical solutions, rules of thumbs, empirical guidelines based on rock mass classifications and numerical modeling techniques, Hadjigeorgiou & Charette (2001). The advantages and limitations of these approaches have been addressed elsewhere, *i.e.* Milne *et al.* (1998), Palmstrom & Broch (2006), Lorig & Varona (2013). Dunn (2013) provided a comprehensive review of the uncertainty associated with the different methods used in ground support design.

This chapter provides a methodology for the design of reinforcement for drifts in hard rock. It does not address large scale excavations in operating mines such as production stopes, or large engineering structures such as large caverns in civil engineering. A major challenge in the design of reinforcement and support is the adequate representation of the rock mass. Empirical rock mass classification tools are by far the most popular techniques but they have inherent limitations in extrapolating from past experience to other ground conditions and accounting for the use of more recent reinforcement and surface support elements, Potvin & Hadjigeorgiou (2015).

This chapter focuses on the use of Discrete Fracture Networks (DFN) to capture the rock mass regime and subsequently, provides a methodology for the explicit representation of reinforcement in generated DFN models and quantifies their stabilization influence. This provides a more rigorous approach to the design of ground support and allows for further optimization of the design process.

2 DISCRETE FRACTURE NETWORKS (DFN)

A fundamental task in rock engineering is the characterization of rock mass geometry. This can be achieved through the use of Discrete Fracture Networks (DFN). It is important to note that the DFN terminology has evolved over time. Some of the early work by Dershowitz & Einstein (1988) refer to Rock Joint System (RJS) models, Grenon & Hadjigeorgiou (2003) used Discontinuity Network Modeling (DNM) while Einstein & Stephansson (2000) and Grenon & Hadjigeorgiou (2012) chose to use the term Fracture Systems Models (FSM). It is only in recent years that the term Discrete Fracture Networks (DFN) has become popularized to describe both deterministic and stochastic models that capture the variability of fracture geometry in space. The inconsistencies in terminology had the inadvertent effect that the technical literature has been segregated, thus hindering a broader understanding of DFN theory and awareness of reported rock engineering applications.

A DFN is defined by its geometric characteristics. Dershowitz & Einstein (1988) make a distinction between primary and secondary geometric characteristics. Primary characteristics, listed in Table 1, are used to describe the fracture system. Secondary fracture characteristics such as joint termination and correlation identify whether fractures terminate at the intersection with other joints, or terminate against intact rock.

2.1 DFN models

A DFN model can be constructed based on specific relationships between characteristics such as location of fracture sets, termination, and fracture shape. In effect, every generated DFN model is the result of a specific combination of the fracture system characteristics. The choice of the conceptual model is dependent on the general pattern of the natural fracture network and the objectives of the modeling. A DFN can be generated using any one of a series of conceptual models defined by the representation of the fracture characteristics. Some of the most popular DFN generating models are listed in Table 2.

It is the authors' opinion that the DFN models in Table 2 have been shown appropriate for rock mass characterization and for investigating the stability of excavations in rock. These models should not, however, be used as "black boxes" but employed with an understanding of their limitations. Mathis (2014) recommends that "one should not utilize a DFN model unless one understands not only the assumptions for discontinuity generation and interaction, but also how it references and utilizes the input discontinuity spatial characteristics".

Table 1 Geometric Fracture Characteristics, after Dershowitz & Einstein (1988).

Parameter	*Description*
Shape	Shape of joint boundaries can be polygonal, circular, elliptical or irregular. Joints can be planar or non-planar in space and shape should consider this fact also. Since joints are often planar, it is simpler to associate "shape" with the two-dimensional appearance and treat non-planarity separately.
Planarity	Character of the joint surface as related to an ideal plane. Deviations from planar surfaces can be on several scales :
Roughness	Deviation from planarity < 1 mm
Waviness	Deviation from planarity > 1 mm
Joint Size	Extent of jointing, generally expressed as trace length on two dimensional surfaces such as outcrops or as the surface area of individual joints
Persistence	An expression relating joint size to a reference size either the sum of trace lengths (l_i) relative to the length of a *colinear* scanline L: $\Sigma l_i/L$ or the sum of individual joint surface areas (a_i) to the surface of a *coplanar* reference plane A: $\Sigma \alpha_i/A$
Co-Planarity	Co-planarity expresses the fact that a number of joints can be located in the same plane
Location	The location of the joint surface in space; often only the relative joint location expressed through spacing or intensity is of interest
Spacing	Distance between intersection points produced by a line perpendicular to the joint mean attitude and the joints of a set where a set consists of joints that are parallel or subparallel to each other
Intensity	Number of joints per unit area or volume, or total joint trace length per unit area, or total joint area per unit volume
Attitude (orientation)	Orientation of the joint plane in space expressed by strike and dip, or dip direction and dip, or pole orientation with spherical coordinates

Table 2 Main features of different DFN models, modified from Staub et al. (2002).

Model	*Fracture characteristics considered in model*				
	Fracture Shape	*Fracture Size*	*Termination at intersection*	*Co-planarity*	*Orientation of sets*
Baecher	Circle Ellipse	Bounded	No	No	Stochastic
Enhanced Baecher	Polygon	Bounded	Yes	No	Stochastic
Baecher Algorithm, Revised Terminations (BART)	Polygon	Bounded	Yes	No	Stochastic
Nearest Neighbor	Polygon	Bounded	Yes	No	Stochastic
Veneziano	Polygon	Bounded	In fracture planes only	Yes	Stochastic
Levy-Lee Fractal	Polygon	Bounded	Yes	No	Stochastic

2.2 Data requirements of DFN models

Geomechanical data collection is a prerequisite for the construction of a geomechanical model. The limitations and issues of data have been addressed by several people including Hadjigeorgiou (2012). Developments in data collection technology can contribute to increased data quality and quantity and, if properly employed, can eventually result in greater confidence in the resulting data.

Geomechanical structural data can be collected in the field from using variations of mapping techniques as described in Hadjigeorgiou *et al.* (1995), borehole mapping, LiDAR (Light Detection and Ranging) and photogrammetry scanning data, for example Sturzenegger & Stead (2009), Fekete & Diederichs (2013). DFN modeling requires information on fracture orientation, size and intensity. Data collection can be challenging since the techniques are often constrained due to the limited access and exposure of the rock mass. This can result in incomplete data sets or sampling areas smaller than ideal for a given rock mass.

There are several procedures that can be used for the generation of DFN models, for example Hadjigeorgiou *et al.* (1995), Rogers *et al.* (2009). A procedure that describes the steps relating to the relevant components of an engineering geology model, data processing and modeling has been provided by Weir & Fowler (2014) and is reproduced in Figure 1.

2.2.1 *Fracture orientation*

Fracture orientation is determined from rock face mapping, or from oriented borehole data, and is defined by the dip and dip direction. It is recognized that linear surveys

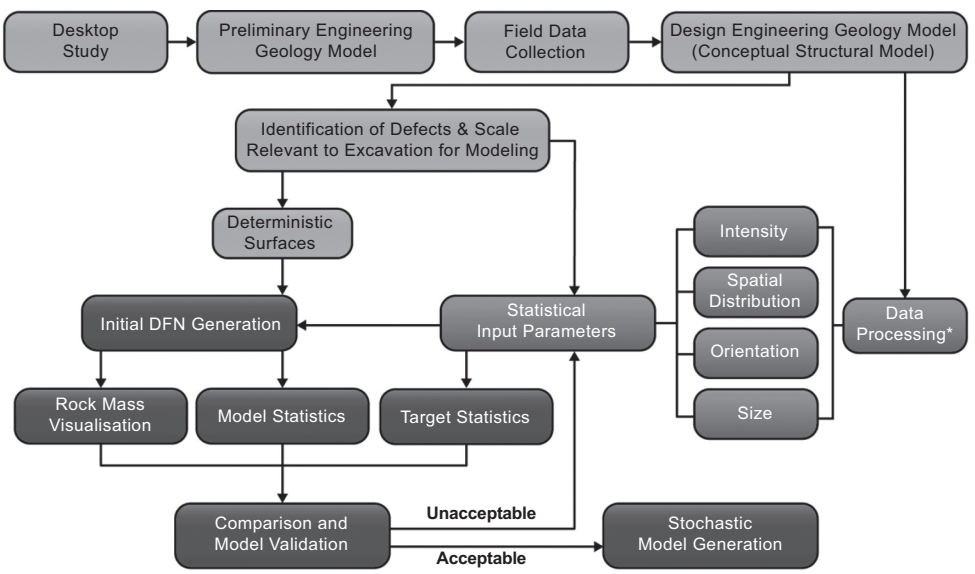


Figure 1 An overview of the DFN modeling process, after Weir & Fowler (2014).

introduce an orientation sampling bias. This has been addressed among others by Terzaghi (1965), Baecher (1983) and Priest (1995). The Fisher distribution provides a valuable model for fracture orientation data due to its simplicity and flexibility. Priest (1993) notes that it is a symmetric distribution, and consequently provides only an approximation for asymmetric data.

2.2.2 *Fracture size*

Fracture size or trace length is typically estimated from rock face mapping such as scanline or window mapping or from photogrammetry and LIDAR. Elmo *et al.* (2014) further differentiate between fracture trace length, as mapped along a rock face, and fracture radius. Fracture trace length is defined as an explicit measure of the trace that a fracture or fault makes with a rock exposure, while fracture radius is the radius of a circle of equivalent area to a polygonal fracture.

Trace length sampling is susceptible to four major biases: orientation bias, size bias, truncation bias, and censoring bias. Zhang & Einstein (1998) provided an analytical solution to determine a non-biased estimation of trace lengths for all joint sets. Alternatively it is possible to extrapolate from 2D data using a series of distributions as described in Dershowitz (1984).

2.2.3 *Fracture intensity*

Dershowitz & Herda (1992) provided a template for the consistent definition of fracture intensity measures based upon the dimension of the measurement region, and the dimension of the fracture. This system also referred to as the P_{ij} system has been updated by Mauldon & Dershowitz (2000) and has been accepted by the DFN community. In this nomenclature, P refers to "persistence" where the subscript i refers to the dimensions of the sample, and the subscript j refers to the dimensions of measurement, Table 3.

2.2.4 *Spatial distribution*

The spatial distribution of fractures is determined from spacing measurements along a sampling line. Staub *et al.* (2002) identify three stochastic approaches to extrapolate in 3D from 2D data: a) the Poisson process; b) a distribution of fracture centers such that fracture spacing along a sampling line follows a lognormal distribution, and c) a stationary correlated stochastic process where individual fracture location is correlated to the location of other fractures.

2.3 Selecting a DFN model

Although conceptually interesting, the majority of DFN models have not been extensively verified for rock engineering applications. A comprehensive review of the applicability, advantages of the various DFN models has been addressed by Staub *et al.* (2002). Table 4, is extracted from Staub *et al.* (2002) to identify DFN models that have been used in mining applications.

Table 3 Measures of Fracture Intensity, after Mauldon & Dershowitz (2000).

		Dimension of Feature				
		0	*1*	*2*	*3*	
Dimension of sampling region	0	P_{00} Length^0 Number of fractures				Point Measure
	1	P_{10} Length^{-1} Number of fractures per unit length of scanline (frequency of linear intensity)	P_{11} Length^0 Length of fractures intersects per unit length of scanline			Linear Measure
	2	P_{20} Length^{-2} Number of traces per unit area of sampling plane (areal density)	P_{21} Length^{-1} Length of fracture traces per unit area of sampling plane (areal intensity)	P_{22} Length^0 Area of fractures per unit area of sampling plane		Areal Measure
	3	P_{30} Length^{-3} Number of fractures per unit volume of rock mass (volumetric density)		P_{32} Length^{-1} Area of fractures per unit volume of rock mass (volumetric intensity)	P_{33} Length^{-2} Volume of fractures per unit volume of rock mass	Volumetric Measure

P_{32} provides a useful three dimensional measure of intensity which is independent of fracture size, and is not affected by the scale of the region analyzed. However, it cannot be determined in situ. Dershowitz & Herda (1992) have proposed a strategy to determine P_{32} from P_{10} (borehole) and P_{21} (areal mapping).

It is the authors' opinion that considerable thought be given to the selection of an appropriate DFN model for a particular case study. Otherwise, DFN software are used as "black boxes" making the interpretation of results extremely difficult.

Several proprietary and commercially available software tools can be used to generate DFN using a range of models, for example Kulatilake *et al.* (1993), Davy *et al.* (2014), Le Goc *et al.* (2014) and arguably the most widely used Fracman by Golder Associates (2014). Successfully calibrated DFN models provide good statistical agreement with field data and the models are considered acceptable. Grenon *et al.* (2016) demonstrated in a case study that the use of the Baecher, BART, Nearest Neighbor and Veneziano models had considerably different geometrical characteristics that had a significant impact on analysis and interpretation.

It is recognized that the use of DFN models is not appropriate in all cases for a variety of technical reasons, including lack of appropriate, verifiable, data, Mathis (2014). He suggests that "DFN models should not be utilized by those that are not fully cognizant of the biases and errors that can accrue within, and from the usage, of such models in design".

Table 4 Applicability of DFN models, modified from Staub et al. (2002).

Model	*Concept*	*Applicability*	*Advantages*	*Limitations*
Baecher	Generate fracture network from fracture centers that are distributed uniformly in space.	Homogeneous rocks.	Few field data available. Accurate in rock mechanics and hydraulics when a little is known.	Do not simulate terminations of fractures. Fractures must be planar. Do not account for complex features of fracture populations.
Enhanced Baecher	Generate fractures from fracture centers located at random points in space. Intersections are calculated with pre-existing fractures.	Fractured rock masses in which joint terminations are observed.	Suited for simulation of connectivity of natural fracture population. Multiple intersections per fracture are possible.	Fracture size distribution is not preserved. Joints must be planar.
BART	Same principle as for the Enhanced Baecher model, except that the center of fracture terminating at intersections is generated from point on fracture intersection	Fractured rock masses in which fracture terminations are observed.	Quick simulation. Fracture size distribution is preserved. Partial correlation in the simulated fracture population.	Fractures must be planar.
Nearest-neighbor	Fractures are organized into primary, secondary and tertiary groups, and are generated in this sequence.	Can account for the generation of fracture network according to the theory of fracture genesis.	Generate clusters of fractures around the primary group. More explicit than Levy-Lee model if fractures can be classified.	Must have enough data to assess the different groups and chronology.
Veneziano	Fracture network generated in 3 stochastic processes based on Poisson plane and Poisson lines.	Suited for 100% persistent and unbounded fractures.	Polygonal shapes are often observed in nature. More appropriate than orthogonal model for most cases, especially in case of coplanarity.	Often fail to construct blocks. Intersections of fractures do not often match joint edges. Complex 3-D model.
Levy-Lee Fractal	Generate clusters of smaller fractures around wider fractures.	In combination with geostatistical analysis: Hierarchical Fracture Trace Model.	Accounts for the chronology of fracture formation. Ability to generate a non-stationary fracture system with a set of parameters that remain constant throughout the generation system.	Do not consider the size and shape of the blocks delimited by the simulated fractures. Definition of the most appropriate fractal dimension.

2.4 Model calibration

The calibration process is an iterative process whereby a set of input data are adjusted or modified so that there is greater agreement with experimental data. A DFN model is generated for a particular zone or region, based on input data collected from rock exposures or boreholes. The DFN model is subsequently sampled to collect the same type of input information such as fracture orientation, P_{10}, P_{21}, trace length etc. A DFN model is considered to have been validated if the simulated parameters are statistically correlated to the in situ data. The calibration process may require a series of iterations before the model is accepted.

3 REINFORCEMENT AND SUPPORT USING DFN

The primary goal of ground support in mine drifts is to protect mine workers and equipment against rock falls. Despite the development of innovative ground stabilization techniques and the increasing use of mechanized and automated equipment, rock falls remain one of the major causes of injuries and fatalities in underground metal mines.

3.1 Key block analysis

Key block analysis relies on identifying the critical blocks created by intersections of discontinuities in a rock mass excavated along defined surfaces, Goodman & Shi (1985). It is then possible to determine the reinforcement strategy to stabilize removable blocks that have been identified as unstable. The inherent assumption is that fractures are of infinite length.

Esterhuizen & Streuders (1998) have employed JBlock to determine the probability of instability of keyblocks and the influence of support type and layout in stabilizing the excavation. Windsor (1999) has also relied on block theory to identify unstable blocks along an excavation and propose reinforcement strategies. The methodology was implemented in a software package SAFEX, Windsor & Thompson (1993). Dunn (2010) also demonstrated the use of probabilistic key block methods and the Point Estimate Method (PEM) in ground support design.

3.2 DFN applications in ground support analysis and design

The use of DFN in the design of reinforcement and support can be both implicit and explicit. Stacey *et al.* (2014) provide the background of the development of simple software in the mid 1980's used to generate and plot joint traces in 2D plates. They provided engineering applications where the 2D joint maps were used to determine appropriate rock bolt length and spacing for a contractual dispute on a tunneling project more than 30 years ago. Other implicit efforts include the work of Hadjigeorgiou *et al.* (1995) where they used field data to generate block size distributions to characterize the rock mass at an underground hard rock mine.

Explicit applications of DFN involve the generation of a 3D rock mass, the construction of a virtual excavation and the introduction of reinforcement and support elements. This is quite different from standard LEA and "Key block" approaches that assume that fractures are ubiquitous and have infinite length.

Dershowitz & Carvalho (1996) suggested that key block theory could be extended to employ 3D dimensional discrete fracture models of finite length specific to the tunnel location. Rogers *et al.* (2006) provided an example of the use of both deterministic and DFN limit equilibrium stability of excavations in rock suggesting that the DFN approach provides a better representation of the fracture network geometry.

Grenon & Hadjigeorgiou (2003) used Stereoblock to generate and validate 3-D DFN based on structural field data at three drifts at the Louvicourt Mine in Canada. Following a limit equilibrium analysis they determined the stability of individual wedges along the length of the excavations. The influence of different stabilization strategies on the stability of the excavations was quantified using safety factor distributions. Consequently, tests were undertaken to assure that the length of the reinforcement units was adequate and surface support, in this case mesh, would support smaller blocks between bolts.

Merrien-Soukatchoff *et al.* (2012) provide a series of applications using the RESOBLOCK software to investigate the stability of excavations and the impact of different rock bolting patterns. Graaf *et al.* (2014) used both deterministic analyses and DFN tools within FracMan to explore different support strategies at the Callie Underground Mine in Australia.

Nevertheless, DFN based tools have not gained wider acceptance as design tools for ground support. This could be attributed to a multitude of reasons including the accessibility to appropriate tools. Another factor is that at the green field stage there is limited data available. At more advanced stages in development, one has to consider that drift reinforcement is at a very local scale. This chapter focuses on DFN applications for structural control instabilities where stress plays limited role.

In constructing a DFN model for the design of reinforcement for a drift it is important to recognize that the local conditions are of importance, *i.e.* drift scale, as opposed to mine scale. The DFN model size is a function of the drift dimensions and length, geology and structural regime around the drift.

4 A CASE STUDY FOR THE DESIGN OF REINFORCEMENT AND SUPPORT USING DFN

The ground support design process is illustrated using an example from a Canadian underground hard rock mine in the arctic. The first step was the collection of structural data using photogrammetry mapping. This was followed by an analysis of the structural regime and the generation of DFN model. The stability analysis for typical drift dimensions focused on the generated structural wedges along the excavation. A reinforcement strategy, based on bolting pattern; was developed for the back of the drift and the sidewalls.

4.1 Data collection

A major challenge in an operating mine is collecting the necessary field data to characterize the rock mass. The collection of structural data, used in this analysis, has been described by Dubois *et al.* (2012). A photogrammetric approach was used to record 5 pairs of photos of rock exposures oriented at 90/160. The data were treated



Figure 2 Digital Structural Mapping.

using a commercial system, ShapeMetrix3D (2011). The 3D numerical models of the fractured rock mass were constructed using these photographs. A digital terrain model (DTM) was created for every pair and this was used to construct a synthetic surface. The digital images were subsequently superimposed on the surface.

The main geometrical components recorded through structural mapping are orientation, spacing, size and intensity of fractures. Digital or "virtual" structural mapping was conducted on the DTM and the fracture traces were identified on photographic images, Figure 2. All fractures were defined by their center coordinates, trace lengths and orientation.

4.2 Data analysis

4.2.1 Fracture orientation

All identified fractures were exported to Dips (Rocscience, 2012). In all, three dominant joint sets were identified from the stereonet plots (Figure 3). The mean orientations were determined for each joint set and the dispersion around the mean orientation values was quantified using the Fisher constant K (Table 5).

The use of photographic mapping allowed for the identification of sub horizontal fractures which are difficult to assess using scanline mapping. As summarized in Table 5 at this site the dip and direction for each joint set were : joint set 1 05°/349° (sub horizontal), joint set 2 41°/105° (inclined) and for joint set 3 89°/032° (sub vertical). Fisher's constant, K, is a measure of the dispersion of orientation within the

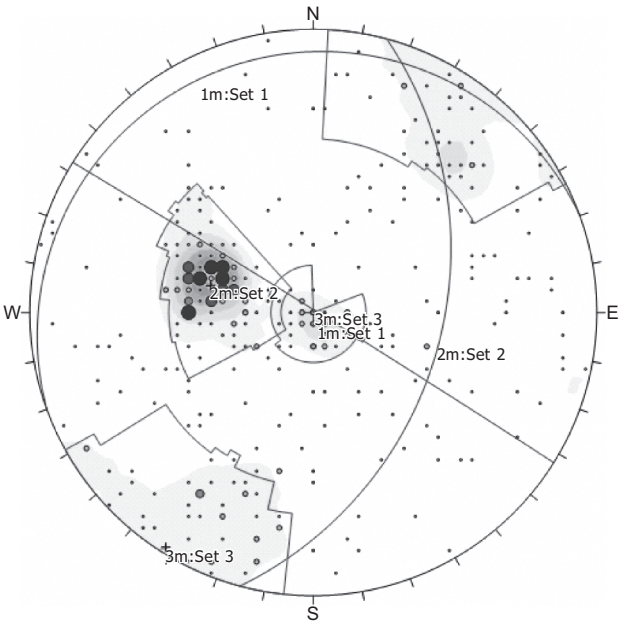


Figure 3 Stereonet representation of mapped fractures using photogrammetry.

Table 5 Reported fracture sets based on photogrammetry analysis relying on 5 pairs of photos, 363 joints mapped.

Fracture Set	*Number of traces*	*Dip*	*Dip Direction*	*Fisher's constant K*
1	38	5°	349°	56.63
2	114	41°	105°	34.76
3	83	89°	032°	17.62

joint population of a set. Fracture set 1 has the smallest dispersion around the mean value with joint set 3 the largest dispersion around the mean value.

4.2.2 Fracture trace length

Fracture trace lengths were determined from the constructed models using the sampling approach proposed by Zhang & Einstein (1998). This approach minimizes bias and allows for a non-biased estimation of trace lengths for all joint sets. The nonbiased trace length estimator was calculated using:

$$\mu = \frac{\pi(N + N_o - N_2)}{2(N + N_o - N_2)} C$$

where C is the radius of the circular sampling window, N is the total number of traces intercepting the window, N_0 is the number of traces with two extremities contained

Table 6 Estimated trace length for the recorded fracture sets.

Trace Length (m)		
Set 1	*Set 2*	*Set 3*
2.01	2.48	1.64

Table 7 Summary of structural field data.

	Set 1	*Set 2*	*Set 3*
Number of joints	38	114	83
Mean Orientation Dip/Dip Direction	$05^0/349^0$	$41^0/105^0$	$89^0/032^0$
K	57	35	18
Mean Trace Length (m)	2.01	2.48	1.64
P_{21}	1.07	3.38	1.66

within the sampling window, and N_2 is the number of traces with two extremities lying outside of the sampling window. The resulting mean trace length of the fractures is presented in Table 6.

4.2.3 Fracture intensity

Fracture intensity can be calculated by several qualitative and quantitate techniques. In this paper, in order to maximize the surface information available from the digital images, fracture intensity was calculated for every joint set based on the summation of trace lengths per unit area (P_{21}), as defined by Dershowitz & Herda (1992).

4.2.4 Summary of structural field data

The fracture properties obtained through the photogrammetry campaign are presented in Table 7. The scan planes orientation was $90^0/160^0$. The use of photogrammetry expedited the data collection process in an operating mine and provided the input data for the subsequent analysis.

5 DFN MODELING

5.1 DFN generation and calibration

The Enhanced Baecher model was selected to generate a series of DFN models. In this particular location and ground conditions, field observations did not support the presence of strong joint coplanarity as required by the Veneziano model. Furthermore, there was no evidence of joint termination on other joints as modeled by the BART model, nor strong joint clustering as modeled by the Nearest Neighbor model.

The forward modeling technique was used to calibrate the generated fracture systems. Scan planes were introduced in the DFN and the fracture properties on these

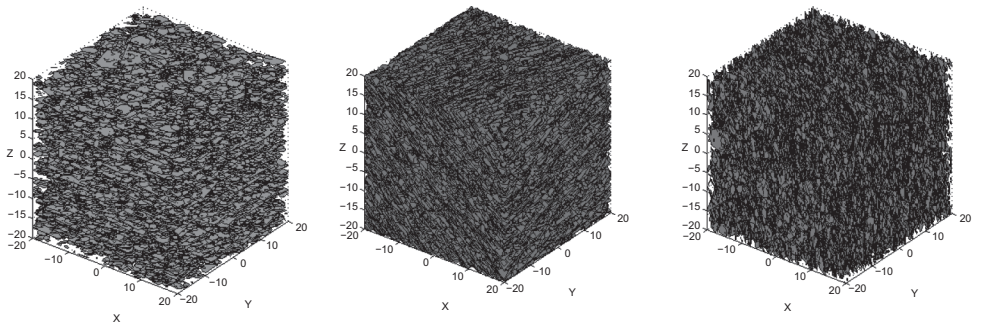


Figure 4 DFN models generated from fracture sets 1, 2 and 3.

planes were compared to photogrammetry results. In this case study, several DFN generations were necessary in order to achieve statistical agreement between the modeling results and the field data obtained using photogrammetry.

A typical calibrated DFN with a volume of 40 m x 40 m x 40 m had more than 160 000 fractures. To validate the DFN models, scan planes with the same orientation as the underground rock faces were simulated through the models. The intercepted fractures along these scan planes were calibrated until a good agreement was observed for mean orientation and dispersion for every set. Fractures were then also calibrated for their mean trace lengths. Several scan planes were introduced within every model, each containing five randomly located circular sampling windows, with a radius equal to the radius for the photogrammetry analysis, to sample the fractures. The DFN models were adjusted until a satisfactory statistical agreement was achieved between field and model data. Fracture intensities (P_{21}: total trace length of fractures per unit area) were then calibrated until satisfactory agreement was reached. The whole calibration process was greatly facilitated by enabling easy direct comparisons between field information provided by photogrammetry, and generated fractures. Figure 4 illustrates individual DFN models generated by each fracture set.

5.2 Stability analysis

Once an excavation is introduced in the generated 3D jointed rock mass, it is possible to identify all discontinuities intersecting a free face to define discrete blocks or wedges. The form of such defined blocks has an obvious impact on the stability of the excavation, with tetrahedral blocks being the most common type observed in the field. All tetrahedral blocks formed at a face of an excavation are defined by their base area, apex length (the distance between the base of a block and its summit) and volume. The resulting distributions for every block property are then calculated. At the same time, all fractures contributing to the creation of a wedge along the excavation were recorded. Consequently, it was possible to determine the most critical fracture sets for any given drift geometry and orientation. In this analysis, the Mohr-Coulomb criterion was employed to define the mechanical behavior of the fractures and the option was available to allow for variations in strength distributions.

To assess the potential for wedge creation along the drift 50 DFN models were generated and calibrated. A 5.5 x 5.5 m 35 m long drift in the EW direction was introduced in every one of the 50 DFN generated rock masses and all kinematically feasible wedges were identified. The individual stability of every tetrahedral wedge at the face of the excavation was determined based on a Limit Equilibrium analysis, as described in Grenon & Hadjigeorgiou (2003). In practice, it is convenient and common to provide different ground support recommendations for the back and side walls of a drift.

5.2.1 Stability analysis for the back of the drift

Along the generated fifty 35 m long drifts, 10769 wedges were created at the back. 1012 of these wedges were stable and 9757 unstable. Figure 5 provides a series of graphs defining the geometry and the stability of the formed wedges. In Figures 5a and 5b it is observed that the resulting wedges are small in size but the majority are unstable. The influence of the different fracture sets in the creation of the wedges at the back of the drift is illustrated in Figure 5c and 5d. As illustrated in Figures 5e and 5f fracture traces from the wedges on the excavations are in the same range as the traces measured on site. The largest wedges are formed by the interception of two joints from set 2 and/or 3 (Figure 5f). The cumulative plot of wedge size is shown in Figures 5g and 5h.

5.2.2 Stability analysis for the sidewalls of the drift

In all, 40078 wedges were created at the sidewalls of the fifty 35 m long drifts. 24720 of these wedges were stable and 15358 unstable. Figure 6 summarizes the salient statistics for the geometry and the stability of the formed wedges along the sidewalls of the drifts. A few larger wedges, greater than 3 tons were formed along the sidewalls than in the back. As illustrated in Figure 6f the number of stable wedges in the sidewalls is relatively higher than in the back. If one compares the results for the sidewalls of the drift with the results for the back (Figure 5), it is noted that different sizes of blocks are obtained for the same percentile. The more critical fracture set combinations in the sidewalls that produced the largest wedges was different than the back of the drift. As shown in Figure 6e the larger traces were mostly associated with unstable wedges.

6 REINFORCEMENT OF DRIFT USING DFN

In low-stress environments, in underground excavations close to the surface, it is the structural regime that quite often dictates the possible ground failure mechanism and consequently the choice and design of support necessary to mitigate such failure (Choquet & Hadjigeorgiou, 1993). The fundamental question is whether the objective is to reinforce individual wedges (spot bolting) or use a systematic reinforcement strategy (pattern bolting) aiming to provide support that will be adequate for multiple wedges. A DFN based approach is an attractive option for the evaluation of the stability

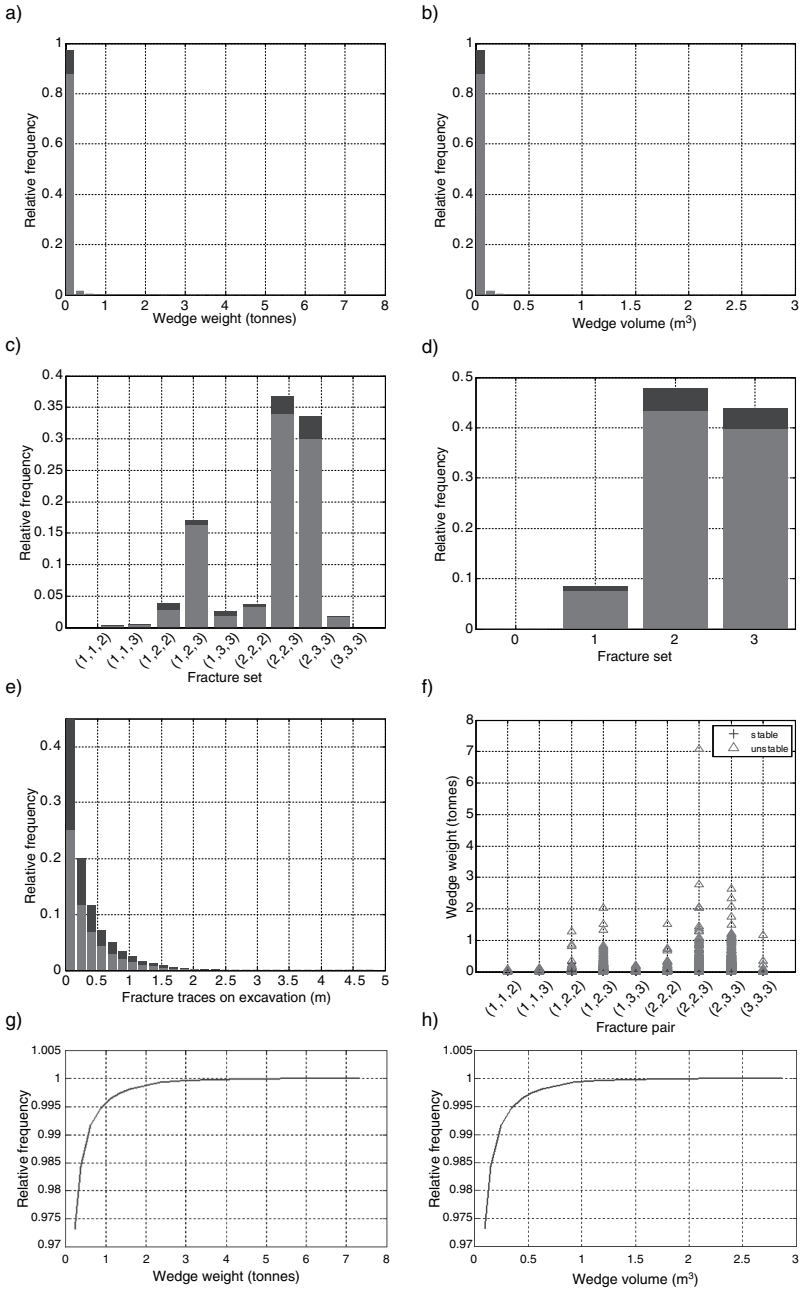


Figure 5 Geometric properties of wedges formed along the drift back of fifty 35m long drift. a) histogram of wedge weight, b) histogram of wedge volume, c) histogram of fracture combinations, d) histogram of sets creating wedges, e) histogram of fractures traces along the edges of wedges on drift surface, f) scatter plot of fracture pairs forming wedges versus wedge weight g) cumulative plot of wedge weight, h) cumulative plot of wedge volume.

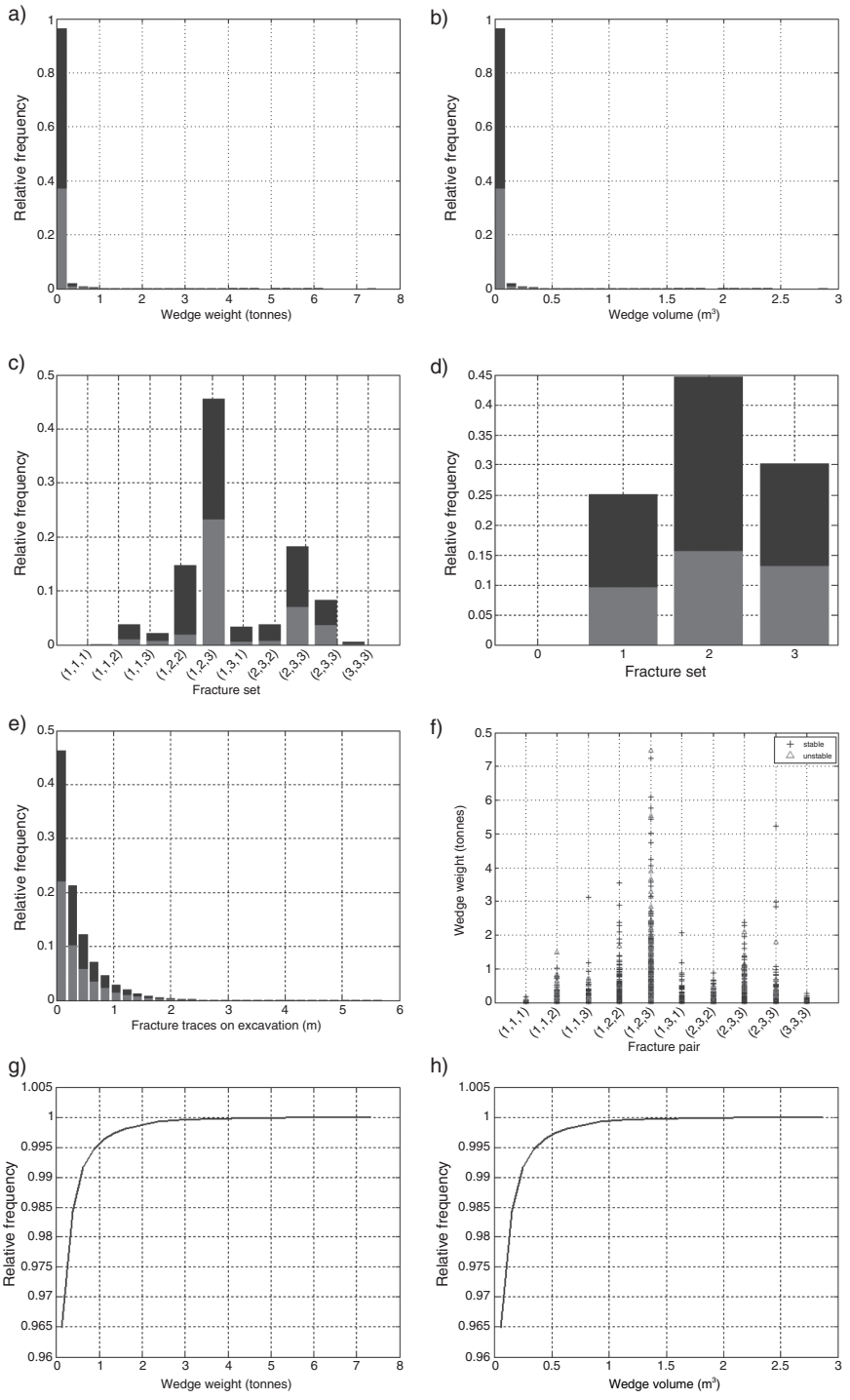


Figure 6 Geometric properties of wedges formed along the sidewalls of fifty 35m long drift. a) histogram of wedge weight, b) histogram of wedge volume, c) histogram of fracture combinations, d) histogram of sets creating wedges, e) histogram of fractures traces along the edges of wedges on drift surface, f) scatter plot of fracture pairs forming wedges versus wedge weight g) cumulative plot of wedge weight, h) cumulative plot of wedge volume.

of mining and tunneling excavations where it is not feasible or practical to evaluate the stability of individual wedges.

The choice of reinforcement elements is dependent on multiple parameters such as capacity, loading mode, deformation, long term performance and costs. In this case study, two types of bolts were investigated, point anchored mechanical bolts and friction bolts. The analysis can be extended to other types of bolts. As in most deterministic limit equilibrium analysis methods a point anchored bolt is defined by its anchored capacity, provided the bolt traverses the wedge. In a friction, or grouted rock bolt, the total resistance to support a wedge is defined by the embedment length of the bolt traversing the wedge and within the stable ground.

In a DFN-based analysis, the objective is to determine the gravity driven loads, geometry of wedges and the capacity provided by reinforcement units. The geometrical characteristics of a generated wedge include the base area, apex length and volume. Apex length is the perpendicular distance between the base of a block (delimited by the three summits located at back or the wall of a drift) and the peak of the block. The apex and wedge length can also be used as a criterion to ensure that the rock bolt is of sufficient length.

6.1 Single DFN analysis

A DFN model, presenting the largest wedge delineated at the back of the 35m long drift, along E-W was selected for further analysis. Of the 243 wedges created along the back of the drift only 22 were stable with 221 being unstable.

Figure 7 summarizes the results of the stability analysis. The wedges formed along the back of the drift for this DFN are shown in Figure 7a. The DFN with the largest wedge at the back of drift is 7 tons (Figure 7b). The scatter plot shows that very few wedges are stable, Figure 7c. The cumulative plot in Figure 7d may help in the design of reinforcement by providing an indication of the properties of the wedges to be stabilized. The factor of safety for the largest wedge along that drift is 0.43. In Figure 7e for this particular DFN, 5 wedges with apex higher than 1.5 m were created, the standard bolt length used at the site. Furthermore, from Figure 7d, all blocks are smaller than 10 tonnes. This suggests that block weight is not a major concern nor does it impose the need for high capacity rock bolts. Figures 7f and 7g illustrate the drift fracture traces and wedge area histograms for all wedges formed along the back of the drift. This is of particular use in the design of surface support.

6.1.1 Reinforcement scenarios

The first reinforcement strategy considered was the use of friction (expandable) bolts installed in a 1.2 × 1.2 m square spacing. The selected expandable bolts were 1.5 m long with tensile capacity of 10 tonnes and bond strength 12 tonnes per meter.

The stability results are presented in Figure 8 where it can be seen that this choice of reinforcement bolting pattern has limited impact on the resulting factor of safety. The main reason is that the generated wedges are small in size. For the larger wedge the

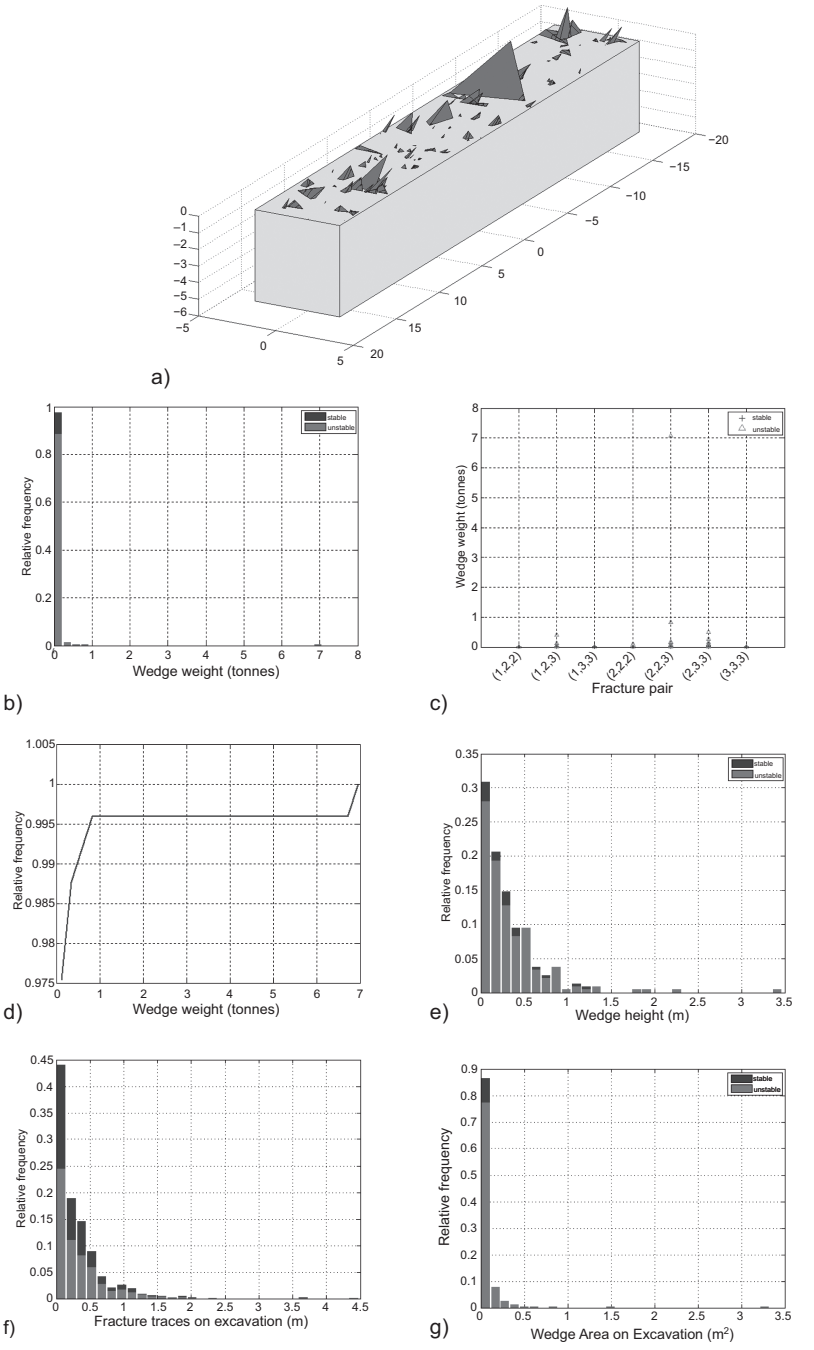


Figure 7 Wedges formed at the back for the most critical DFN. a) drift and wedges isometric view, b) histogram of wedge weight, c) Scatter plot of fracture pairs forming wedges versus wedge weight d) cumulative plot of wedge weight, e) histogram of wedge height (apex), f) histogram of fractures traces along the edges of wedges on drift surface g) histogram of fractures area along the edges of wedges on drift surface.

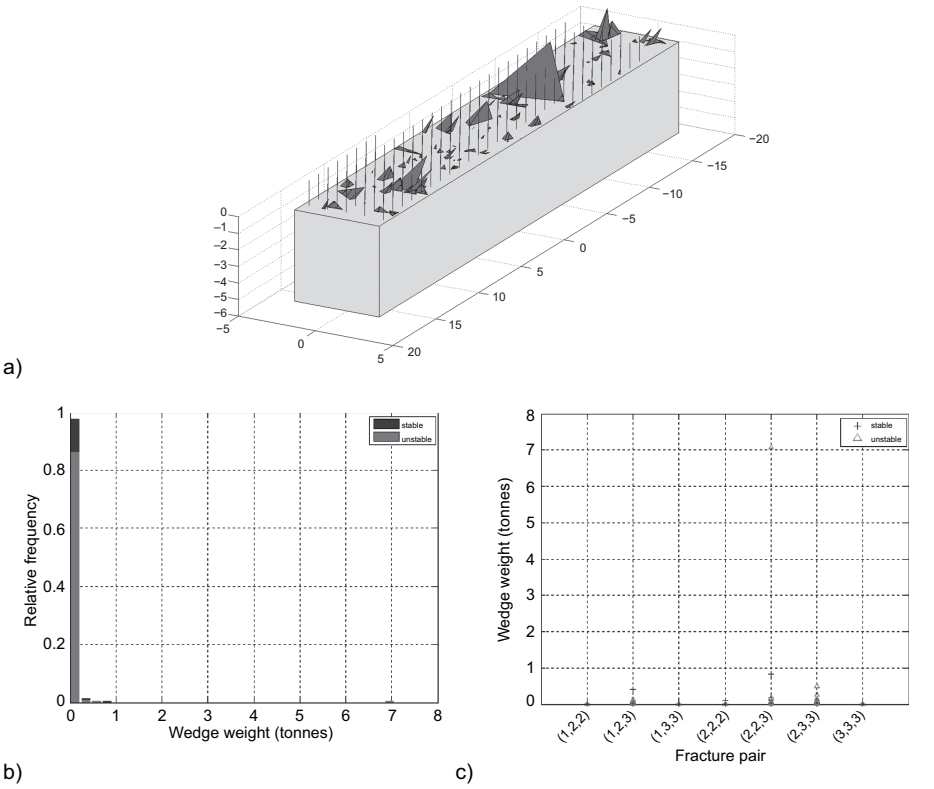


Figure 8 Wedge formed at the back for the most critical DFN supported by expandable bolts. a) drift and wedge isometric view, b) histogram of wedge weight, c) Scatter plot of fracture pairs forming wedges versus wedge weight.

factor of safety increased from 0.43 to 0.92. Two expandable bolts traverse the wedge. In this configuration there is only a small length of an expandable bolt through the wedge thus limiting its impact on the stability of the wedge.

The second explored reinforcement strategy was the use of point anchored mechanical bolts using a 1.2 × 1.2 m square spacing. The point anchored bolts have a capacity of 10 tons and a plate capacity of 5 tons. Figure 9 is a scatter plot of the wedges' weight versus the fracture pair and also shows if wedges are stable or not. It can be seen that the largest wedge associated with fracture combination (2, 2, and 3) is now stable.

6.1.2 Surface support

Surface support can be provided by liners such as shotcrete, mesh or thin pray on liners applied externally to the rock mass. To maintain the integrity of the sidewalls or back of the drift, the surface support should be capable of containing the bulking of the broken rock mass and deformations resulting from stress changes from further mining. The

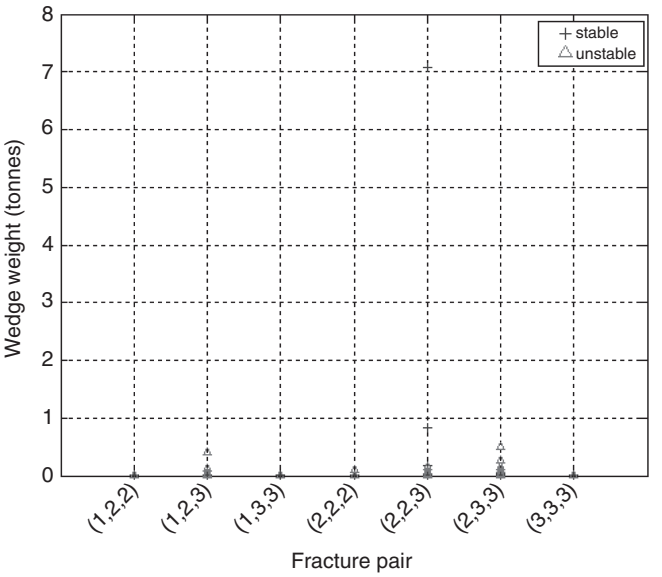


Figure 9 Scatter plot of fracture pairs forming wedges versus wedge weight when using point anchored mechanical rock bolts.

reinforcement and surface support are part of an integrated system that transfers and shares load until the excavation surface is stabilized or until the support system fails at its weakest link, Hadjigeorgiou & Potvin (2011).

An example application of the use of mesh in a DFN analysis has been reported by Grenon & Hadjigeorgiou (2003) and of support provided by a thin spray on liner by Hadjigeorgiou & Grenon (2004). The present case study investigated the impact of using 10 cm thick shotcrete, with shear strength of 100 t/m^2 and unit weight of 1 t/m^3 as a stand-alone support. The analysis was restricted, by assuming that the applied shotcrete would be only susceptible to shear failure. Under this assumption the shotcrete capacity is controlled by the base perimeter of every wedge at the back of the drift, the shotcrete thickness and its shear strength. It is recognized that this is in fact a simplification and the support mechanisms are in fact much more complex as outlined by Stacey (2001).

In this analysis all wedges could be supported by the application of shotcrete. The only geometrical properties needed for the wedge are the traces of the joints forming the wedge. Figure 10 identifies the fracture sets forming wedges versus wedge weight when using shotcrete as a stand-alone support. This analysis assumes that shotcrete has its full capacity upon installation and that the liner is only susceptible to shear failure.

7 CONCLUSIONS

The structural complexity of a rock mass can be captured by the use of Discrete Fracture Networks (DFN). A design methodology is provided that employs DFN in

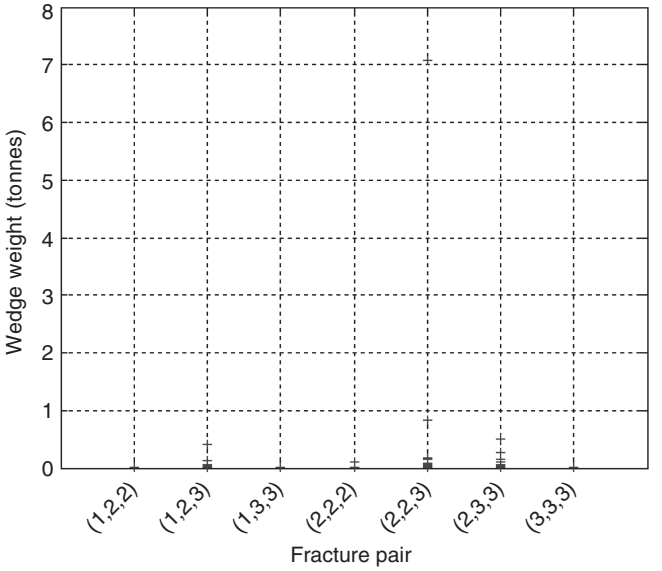


Figure 10 Scatter plot of fracture pairs forming wedges versus wedge weight when using shotcrete as a stand-alone support.

the analysis and design of reinforcement and support of drifts in hard rock. This is accomplished by the explicit representation of reinforcement and support in DFN models. This approach provides an evaluation and comparison of different support strategies for a given excavation. The described methodology is not software specific. It is important that there is a clear understanding of the theory and limitations of DFN and the availability of adequate geomechanical input data.

The use of DFN in the design of reinforcement and support of drifts was illustrated through a case study in an underground hard rock mine. In this particular case the structural data collection was facilitated by the use of photogrammetry. The joint set orientation, spacing and trace length distributions were used to generate 50 DFN. Following a validation process, whereby field input data were compared with the structural data resulting from the simulated 3-D networks, a drift was introduced in the simulated rock mass.

Following the stability analysis for 50 DFN generated models the influence of different stabilization strategies was quantified by means of safety factor distributions for the most critical DFN. Consequently, tests were undertaken to assure that the length of the reinforcement units was adequate and the mesh would capture smaller blocks between bolts. The undertaken analysis however does not account for other factors that may influence the choice of strategies. These may include quality control, long-term performance, etc.

The successful use of DFN for the design of reinforcement implies that there are sufficient quality structural data for input. It is also necessary that a judicious choice is made in selecting an appropriate DFN model for the prevalent ground conditions.

Furthermore, an adequate number of simulations is required. The stability analysis is based on structurally controlled gravity driven failure mechanisms of rigid blocks that are not allowed to rotate. Finally, it is assumed that the shear strengths of fractures are constant along their length. Provided these conditions are acknowledged, the use of DFN provides a powerful probabilistic tool that can investigate the potential of different reinforcement strategies and can provide a sound basis for cost benefit analysis of different options.

ACKNOWLEDGMENTS

The financial support of the Natural Science and Engineering Council of Canada (NSERC), Fonds de Recherche du Québec Nature et Technologies (FRQNT), and MITACS is gratefully acknowledged.

REFERENCES

Baecher, G.B. (1983) Statistical analysis of rock mass fracturing. *Mathematical Geology*, 15(2): 329–348.

Choquet, P. and Hadjigeorgiou, J. (1993) Design of Support for Underground Excavations. Chapter 12 in Vol. 4 of Comprehensive Rock Engineering. J. Hudson (Ed.). Pergamon Press, pp. 313–348.

Davy, P., Le Goc, R. and Darcel, C. (2014) A non-Poissonian, likely-universal, fracture model for hardrock. *International Discrete Fracture Engineering Conference*, *Vancouver, Canada*, DFNE 2014–141.

Dershowitz, W.S. (1984) *Rock joint systems*. PhD. Thesis. MIT, Cambridge, MA.

Dershowitz, W.S. & Carvalho, J. (1996) Key-block tunnel stability analysis using realistic fracture patterns. *North American Rock Mechanics Symposium, Montreal. (Aubertin et al. eds)*, pp. 1747–1751.

Dershowitz, W.S. & Einstein, H.H. (1988) Characterizing rock joint geometry with joint system models. *Rock Mechanics and Rock Engineering* 21, 21–51.

Dershowitz, W.S. & Herda, H.H. (1992) Interpretation of Fracture Spacing and Intensity. *Proc. 33rd U.S. Rock Mech. Symp., Santa Fe, NM.*

Dubois, E, Grenon, M. & Germain, P. (2012) Caractérisation structurale à l'aide de la photogrammétrie: mine Kikialik, Nunavik, Québec. *Conference TAC 2012*, *Montreal, Canada*. Octobre 2012.

Dunn, M.J. (2010) The application of probabilistic keyblock methods for support design in blocky rock masses. *In Proceedings 2nd Australasian Ground Control in Mining Conference, P. Hagan and S. Saydam (eds), 23–24 November 2010, Sydney, Australia*, The Australasian Institute of Mining and Metallurgy, Sydney, pp. 106–112.

Dunn, M.J. (2013) Uncertainty in ground support design and implementation in underground mining. *Ground Support 2013*. Y. Potvin and B. Brady (Eds), Australian Centre for Geomechanics, Perth, pp. 345–358.

Einstein, H.H. & Stephansson, O. (2000) Fracture systems, fracture propagation and coalescence. *ISRM International Symposium, 19–24 November*, Melbourne, Australia.

Elmo, D., Liu, Y. & Rogers, S. (2014) Principles of discrete fracture network modelling for geotechnical applications. *International Discrete Fracture Engineering Conference*, DFNE 2014 – 238.

Esterhuizen, G.S. & Streuders, S.B. (1998) Rockfall hazard evaluation using probabilistic key-block analysis. *Journal- South African Institute of Mining and Metallurgy* 98 (2), 59–63.

Golder Associates (2014) FracMan 7: Interactive Discrete Feature Data Analysis, Geometric Modeling, and Exploration Simulation, User Documentation.

Fekete, S. & Diederichs, M. (2013) Integration of three-dimensional laser scanning with discontinuum modelling for stability analysis of tunnels in blocky rockmasses. *International Journal of Rock Mechanics & Mining Sciences* 57 (2013), 11–23.

Goodman, R.E. & Shi, G.H. (1985) *Block Theory and Its Application to Rock Engineering*. Prentice Hall, New York.

Graaf, J.H, Barsanti, B.J., Doumis, K. & Rogers, S.F. (2014) Towards the Implementation of Discrete Fracture Network Modelling as a Geotechnical Design Tool – Case Study of Callie Underground Mine. *AUSROCK 2014: Third Australasian Ground Control In Mining Conference, Sydney, NSW, 5–6 November 2014*, pp. 399–408.

Grenon, M., Landry, A., Hadjigeorgiou, J. & Lajoie, P.L. (2016) Discrete Fracture Network based drift stability at the Éléonore mine. Mining Technology. http.dx.doi.org/10.1080/14749009.2016.119296

Grenon, M. & Hadjigeorgiou, J. (2012) Applications of fracture system models (FSM) in mining and civil rock engineering design. *International Journal of Mining, Reclamation and Environment* 26 (1, March), 55–73.

Grenon, M. & Hadjigeorgiou, J. (2003) Drift Reinforcement Design Based on Discontinuity Network Modelling. *International Journal Rock Mechanics and Mining Sciences* (40) pp. 833–845.

Hadjigeorgiou, J. (2012) Where do the data come from? Mining Technology 121, (4), 236–247.

Hadjigeorgiou, J. & Charette, F. (2001) Rock Bolting for Underground Excavations. Chapter 63 in Underground Mining Methods. Society of Mining Engineers. Hustrulid & Bullock (Eds), pp. 547–554.

Hadjigeorgiou, J. & Grenon, M. (2004) Towards a Rational Design Methodology for Thin Sprayed on Liners. *Chapter 3 In Surface Support in Mining. Australian Centre for Geomechanics*. pp. 65–70.

Hadjigeorgiou, J., Lessard, J.F., Villaescusa, E. & Germain, P. (1995) An Appraisal of Structural Mapping Techniques. *Second International Conference on Mechanics of Jointed and Faulted Rock*, Vienna. Balkema, pp. 191–198.

Hadjigeorgiou, J. & Potvin, Y. (2011) Hard Rock Ground Control with Screen and Shotcrete. *Chapter 8.6 in the SME Mining Engineering Handbook. Society of Mining Engineers*. pp. 573–594.

Hadjigeorgiou, J., Lessard, J.F. & Flament, F. (1995) Characterizing insitu block distribution using a stereological model. *Canadian Tunnelling*, pp. 201–211.

Kulatilake, P., Wathugala D. & Stephansson, O. (1993) Joint network modeling with a validation exercise in stripa mine, Sweden. *International Journal of Rock Mechanics and Mining Sciences & Geomechanics Abstracts* 30 (5), 503–526

Lorig, L.J. & Varona P. (2013) Guidelines for numerical modelling of rock support for mines. Ground Support 2013 — Y. Potvin and B. Brady (eds), Australian Centre for Geomechanics, Perth, pp. 81–105.

Le Goc, R., Darcel, C., Davy, P., Pierce, M. & Brossault, M. A. (2014) Effective elastic properties of 3D fractured systems. *International Discrete Fracture Engineering Conference*, DFNE 2014 – 142.

Mathis, J.I. (2014) To DFN or not to DFN –A Question of Circumstances. *International Discrete Fracture Engineering Conference*. DFNE 2014 – 106.

Mauldon, M. & Dershowitz, W.S. (2000) A multi-dimensional system of fracture abundance. In: *Geological Society of America Annual Meeting*, vol. 32 (7). Reno, Nevada, USA.

Merrien-Soukatchoff, V., Korini, T. & Thoraval, A. (2011) Use of an integrated discrete fracture network code for stochastic stability analyses of fractured rock masses. *Rock Mechanics and Rock Engineering* 44, 129–147.

Milne, D., Hadjigeorgiou, J. & Pakalnis, R. (1998) Rock mass characterization for underground hard rock mines. *Tunnelling and Underground Space Technology* 13 (4), 383–391.

Palmstrom, A. & Broch, E. (2006) Use and misuse of rock mass classification systems with particular reference to the Q-system. *Tunnelling and Underground Space Technology* (21), 575–593.

Palmstrom, A. & Stille, H. (2007) Ground behaviour and rock engineering tools for underground excavations. *Tunnelling and Underground Space Technology* 22 (2007), 363–376.

Potvin, Y. & Hadjigeorgiou, J. (2015) Empirical ground support design of mine drives. *In Proceedings Underground Design Methods, Australian Centre for Geomechanics, Perth, Australia*, pp. 419–430.

Priest, S. D. (1985) *Hemispherical Projection Methods in Rock Mechanics*. George Allen and Unwin: London, 124p.

Priest, S.D. (1993) *Discontinuity Analysis for Rock Engineering*. Chapman & Hall, London, p. 473.

Rocscience (2012) Dips Software, Version 6.0001 Beta, 1989–2012 Rocscience Inc, Toronto, Ontario, Canada.

Rogers, S., Elmo, D., Beddoes, R. & Dershowitz, W. (2009) Mine scale DFN modelling and rapid upscaling in geomechanical simulations of large open pits. *Proceedings International Conference on Large Open Pits*. Santiago, Chile.

Rogers, S.F., Moffitt, K.M. & Kennard, D.T. (2006) Probabilistic tunnel and slope block stability using realistic fracture network models. 41st US Rock Mechanics Symposium, Golden, Colorado, ARMA/USRM 06-1052.

ShapeMetrix3D (2011) *Measurement and assessment of rock and terrain surfaces by metric 3D images*. 3GSM GmbH, Graz, Austria.

Stacey, T.R. (2001) Review of membrane support mechanisms, loading mechanisms, desired membrane performance, and appropriate test methods. *The Journal of The South African Institute of Mining and Metallurgy*, October 2001, pp. 342–352.

Stacey, T.R., Armstrong, R. & Terbrugge, P.J. (2014) Experience with the development and use of a simple DFN approach over a period of 30 years. *International Discrete Fracture Engineering Conference*, DFNE 2014 – 103.

Staub, I., Fredriksson, A. & Outters, N. (2002) *Strategy for a rock mechanics site descriptive model*. R-02-02. Swedish Nuclear Fuel and Waste Management Company.

Sturzenegger, M. & Stead, D. (2009) Close-range terrestrial digital photogrammetry and terrestrial laser scanning for discontinuity characterization on rock cuts. *Engineering Geology*, 106 (3–4), 163–182.

Terzaghi, R. D. (1965) Sources of error in joint surveys. *Géotechnique*, 15, 287–304.

Weir, F. M. & Fowler, M. (2014) An Introduction to Discrete Fracture Network Modelling and its Geotechnical Applications. *AUSROCK 2014: Third Australasian Ground Control In Mining Conference*, Sydney, NSW, 5–6 November 2014, pp. 435–443.

Windsor, C.R. (1999) Systematic design of reinforcement and support schemes for excavations in jointed rock. *Proceedings International Symposium on Ground Support and Reinforcement Practice in Mining, Villaescusa et al. (eds), Kalgoorlie, WA*, Balkema, Rotterdam, pp. 35–58.

Windsor, C. & Thompson, W. (1993). *Safex-stability assessment for excavations in rock*. Rock Technology, Australia.

Zhang, L. & Einstein, H.H. (1998) Estimating the mean trace length of rock discontinuities. *Rock Mechanics and Rock Engineering* 31 (4), 217–235.

Chapter 5

The needs and technologies for measuring the in situ performance of rock bolts

A.J.S. (Sam) Spearing[1], *T.R. Kostecki*[2] & *K.V. Jessu*[1]
[1]*Western Australia School of Mines, Curtin University, Kalgoorlie, Western Australia, Australia*
[2]*Department of Mining and Mineral Resources Engineering, Southern Illinois University, Carbondale, Illinois, USA*

Abstract: The support system for underground excavations is vital for the safe and cost effective operation of mines and other underground installations. Understanding the interaction of the installed support with the stressed rock is important to ensure a safe and cost effective support and excavation design. Rock bolts are the most common component of any support system, and because they are installed into the rock, recording their performance is the most challenging. Testing the performance of the support is also an important quality control method. This chapter discusses the need for such testing and methods to achieve the appropriate results depending on the specific needs.

1 INTRODUCTION

This chapter explains why it is necessary to measure the performance of rock bolts underground and how to analyze and apply it. To date, very limited effective research, in regards to in situ roof bolt monitoring has been conducted. This is mainly due to four reasons; the lack of appropriate technology, instrumentation costs, the challenges of monitoring just after installation and the complexities of the data processing and conceptualization (Spearing *et al.*, 2013).

1.1 The need for measuring rock bolt performance

The need for underground support is dependent on the stress state around the excavation periphery (both during excavation and for the subsequent mine life, the excavation method (explosive or non-explosive),the shape and cross-sectional area of the tunnel, the presence of local and regional geological features and their properties, the presence of ground water and the in situ rockmass properties. Furthermore, the excavation shape, size and orientation are of particular importance as well as the number, orientation, frequency, length, and planarity of joints. Other important considerations are the potential mode of failure (dependent mainly on the rock properties and stresses) which can include:

1. Gravity induced key block failure (the most common)
2. Wedge shear failure
3. Plane shear failure
4. Toppling failure (common in ribs)

5. Buckling failure (in both roof and ribs)
6. Spalling
7. Bursting (sudden and violent)

The support design of the excavation must also take into account the "human factor", where design of a support system must make allowance for the following possibilities:

1. The tunnel may not always be adequately "made safe" (*i.e.* not all the loose rock may be removed after each blast)
2. The development crews may not always be able to identify potentially different and/or hazardous conditions
3. Unplanned over-break
4. Poorly trained and/or poorly equipped support installation crews.

Temporary support is also a major consideration as it provides essential protection for the workers and equipment working at, and near, the developing excavating face. However, temporary support will often not receive adequate focus from the support engineer, which can lead to expensive interruptions during excavation advance and injury or death to personnel.

The need for measuring rock bolt performance underground is necessary for various reasons including:

1. Having a fundamental and justifiable support design
2. Installation quality control and support effectiveness testing
3. Product development or optimization
4. Research and modeling

However, it must be considered that a zero risk situation is not possible, and a support design is only planned to control most, but not all, rock support conditions expected. Training the workforce to identify and report unusual conditions immediately is also essential.

1.2 Fundamental support design

In the majority of underground mines (especially coal mines), three types of support are installed.These types of support are primary, secondary and supplemental support. The most important is primary roof support. Primary support is installed as part of the production cycle and therefore represents the first line of defense against rock-related falls of ground in underground mines. The improper utilization and/or misunderstanding of the applicability and behavior of primary support can be serious from safety and cost standpoints. This is a major concern for underground mines as roof and rib support are a costly expense from a mining operational perspective and also frequently a production bottleneck, and should therefore be effectively designed and installed. As an example, from 2011 to 2015, rock-related accidents pertaining to fall of face, rib, highwall, roof or back, accounted for 50, 33, 28, 33 and 50% of the total underground fatalities in U.S. coal mines (MSHA, 2015).

The following basics should always be considered:

1. No support is required if the stresses do not exceed the strength of the rockmass and no significant blast damage (if applicable) has occurred.
2. The rockmass is weakened by geological features (faults, joints, bedding planes etc.) and water.
3. Support capacity and/or number of support elements need to be generally increased as mining depth increases and/or the excavation span increases. It should be noted that the relationship between span and support requirements is not linear. In Beam Theory the maximum normal stress increases with the square of the span.

There are several methods that can be used, and the selection should be made based on the complexity and uniqueness of the specific conditions.

1.2.1 Experiential method

This design approach uses experience gained from other similar situations and conditions.Experiential support design in mines is a very useful and justifiable design tool. It is generally fair to assume that if a certain support system worked under similar conditions previously then it should still work.

The main problems with this method are in the assessment of "similar conditions" and that "older methods" may be less technically effective and/or economic now. It tends to stifle improvement and innovation but is still a good initial design approach.

1.2.2 Empirical method

Rock mass classification methods, which are empirically determined, have been used for over 125 years after Ritter (1879) first attempted to develop a system for determining tunnel support. Classification methods are appropriate if used within the bounds of the case histories on which they are based, but they can be misleading if they are applied outside these design boundaries. Too frequently the designer is unaware of these boundaries.

Most mine related support and design methods are based on empirically determined relationships. The most commonly used methods are:

1. Rock quality designation (RQD) developed by Deere *et al.* (1969)
2. Q system developed by Barton *et al.* (1974)
3. Rock mass rating (RMR) that was later modified to include mining excavations by Bieniawski (1989).
4. Mine rock mass rating system (MRMR) introduced by Bieniawski (1989) and improvised by Laubscher & Taylor (1976).
5. Design Rock Mass Strength (DRMS) introduced by Laubscher (1990).
6. Coal Mine Rock Rating (CMRR) introduced by the US Bureau of Mines by Mark (1999).

The support engineer must always bear in mind that, apart from RQD, all the other methods need considerable interpretation and this can lead to a serious bias in the results. To reduce the effect of this, it is always useful to use the same person to conduct the rockmass classification. This is because while the other systems introduce important

and relevant parameters, the classification of these parameters is very open to individual bias. These parameters typically include the following:

1. Joint sets (the number of sets, the continuity, the roughness, the joint contact etc.)
2. Stress state
3. Presence of water
4. Rock properties

The details associated with these methods are not covered in this chapter as they are covered elsewhere in the book.

Two of the more commonly used failure criteria in mining are discussed in the following sections.They are the Mohr-Coulomb and Hoek Brown failure criteria.These failure criteria are simple methods to try and determine if the stress state exceeds the strength of a rock mass or joint set.

1.2.2.1 Mohr-Coulomb criteria

Mohr Coulomb's failure criterion is simple and a very useful if properly applied. Coulomb, in 1776, proposed that the shear strength of the soil/rockmass along the failure plane can be described as

$$\tau_f = c + \sigma \tan \varphi \tag{1}$$

Where:

τ_f is the absolute value of the shear strength on the failure plane
σ is the stress normal to the plane
c is the cohesion
ϕ is the internal friction angle of the soil

Equation 1 is expressed in the form of the total stress, and after Terzaghi's classical effective stress concept, the above equation was modified in terms of effective stress and was referred to as the Mohr-Coulomb failure criterion. Therefore, if the Mohr's circle for a state of stress at a point exceeds the coulomb failure loci, then that point is said to be in the state of failure. If only a portion of Mohr's circle overlaps the loci then failure only occurs on a specific set of failure planes. The failure loci are known as the failure envelopes as shown in the Figure 1. The only limitation of this theory is it applies to the materials for which compressive strength is far higher than the tensile strength.

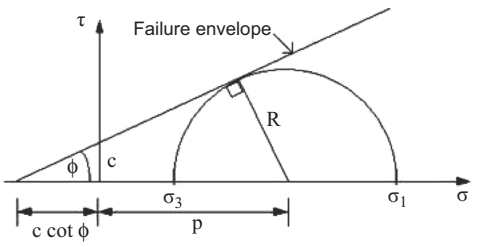


Figure 1 Mohr-Coulomb failure envelope.

1.2.2.2 The Hoek Brown criteria (Hoek & Brown, 1980)

Hoek-Brown proposed an empirical failure criterion in 1980. Since then, the criterion has been widely adopted for modeling the strengths of a wide range of rock types. The criterion was derived from the results of research into the brittle failure of intact rock by Hoek and studies on joint rock mass behavior by Brown. However, the Hoek-Brown criterion has its limitations. In particular, the controlling parameters and the empirical expressions that link these parameters to the observed mineralogy and rock structure. Despite these limitations, the Hoek-Brown criterion has been widely accepted by the international rock mechanics community. This criterion has been subject to modifications over the years. A recent version of the failure criterion, described by Hoek & Brown (1997) is as follows:

$$\sigma'_1 = \sigma'_3 + \sigma_{ci}\left(\mathrm{m_b}\frac{\sigma'_3}{\sigma_{ci}} + \mathrm{s}\right)^a \tag{2}$$

$$\mathrm{m_b} = \mathrm{m_i}\exp\left(\frac{GSI - 100}{28}\right) \tag{3}$$

Where:

σ_1 is the major principal stress at failure
σ_3 is the minor principal stress at failure
σ_{ci} is the uniaxial compressive strength of the intact rock material in the specimen
s and a are constants which depend upon the properties of the rock mass
m_b is rock mass strength characteristics
m_i is the value of the Hoek-Brown constant for the rock mass.
GSI is Geological Strength Index (GSI)

The Geological Strength Index (GSI) is a system of rock mass characterization that has been developed in engineering rock mechanics to meet the need for reliable input data related to rock mass properties required as input for numerical analysis or closed-form solutions for designing tunnels, slopes, or foundations in rock (Hoek *et al.*, 1998; Marinos & Hoek, 2000, 2001).

1.2.3 Analytical method

The three main analytical methods for mine support design are beam theory, plate theory and empirical support designs (such as that developed by the U.S. Corps of Engineers, 1980).

1.2.3.1 Beam theory

This is frequently used in room (bord) and pillar mines, especially in coal. The stress (σ_{xx}) on the roof increases in proportion to the square of the span. Beam theory shows that maximum normal stress is given by Equation 3:

$$\sigma_{xx(\max)} = \frac{\gamma L^2}{2t} \tag{4}$$

The maximum deflection (η_{max}) at the center of a beam is affected even more by an increase in the span as shown in Equation 4:

$$\eta_{max} = \frac{\gamma L^4}{32Et^2} \tag{5}$$

Where γ is the unit weight, L is the beam/room span and t is the beam thickness.

Beam theory assumes only gravity loading and in reality the horizontal stresses have a significant negative effect on the immediate roof stability. The immediate roof stability is also significantly dependent on the relative orientation of the rooms and the maximum horizontal stress.

1.2.3.2 Plate theory

Plate Theory can be, and is also often applied for coal mine intersections. Plate Theory utilizes a rectangular plate that is clamped at all corners and loaded. It is based on the following conditions:

1. The plate is a straight, flat structural element whose width is at least 4 times the thickness and whose length is equal to or greater than its width.
2. The material is elastic, homogeneous, and isotropic.
3. Maximum deflection is half the thickness.
4. All loads and reactions are normal to the plate.
5. When the plate deflects, the central plane remains unstressed.
6. Vertical straight lines before flexure remain straight but become inclined to the vertical.
7. The normal stresses in the plane of the plate are proportional to the distance from the central plane.

For such a plate clamped rigidly at four corners, the maximum deflection occurs at the center of the plate and is given by Equation 5:

$$\eta_{max} = \frac{\alpha q a^4}{Et^3} \tag{6}$$

Maximum normal stress, Equation 6, is found using the following equation:

$$\sigma_{xx(max)} = \frac{6\beta q a^2}{t^2} \tag{7}$$

Where q is the uniformly applied load per unit area, a is the cross-sectional area of the plate, α and β are coefficients for a uniformly loaded rectangular plate.

A typical intersection has a length to width ratio of 1.0, so the coefficients for α and β are 0.0138 and 0.0513 respectively for this equation when Poisson's ratio is equal to 0.3.

Reliance solely on Beam Theory and/or Plate Theory is not recommended due to uncertainties in the assumptions, as well as in the required input data (Bieniawski, 1983). Geological strata are unlikely to be elastic, homogeneous, and isotropic, and values of Young's modulus and immediate roof thickness can vary significantly locally throughout a deposit. The presence of discontinuities and water make it even more

unrealistic to deal with a rock mass using ideal engineering conditions. Rock Mass Classifications are therefore generally preferred.

1.2.3.3 Empirical design – U.S. Corps of Engineers support design

This method is straightforward and is outlined as follows (Anon, 1980).

Parameter	*Empirical Rule*
Minimum Length	Greatest of: – Bolt Spacing – Max Unstable Rock Thickness × 3 – Above the Springline* Spans < 6 m – 0.5 × Span Spans from 6 to 18 m –0.25 × span
Maximum Spacing	Least of: – Bolt Length × 0.5 – Max. Unstable Rock Thickness × 1.50 – 2.00 m maximum
Minimum Spacing	0.9–1.2m
Minimum Average Confining Pressure	Greatest of: – Above the Springline Pressure = 40 kN/m^2 – Below the Springline Pressure = 40 kN/m^2 – At Intersections Confining Pressures × 2

* this is typically interpreted as the point of deviation from vertical in the upper sidewall

1.3 Modeling method

Some elementary guidelines to successful modeling are:

1. The correct model selection based on experience and judgment and testing if applicable
2. The determination of representative input parameters
3. The setting of the model boundary conditions
4. Verification of the results by qualitative or quantitative means
5. Identifying in-situ horizontal and vertical stress magnitudes and principle stress orientations.
6. Understanding of the problem both in the pre- and post-failure states
7. When calibration to a theoretical problem is desired, knowing the assumptions of these problems and being able to recreate that scenario within the software
8. Experience with the program itself and understanding its idiosyncrasies
9. Calibration to in situ conditions, if necessary, using the model to extrapolate to other conditions.

The goal of any support system is to achieve the equilibrium of the rock mass around the excavation. A concept called the ground reaction curve has been used in the

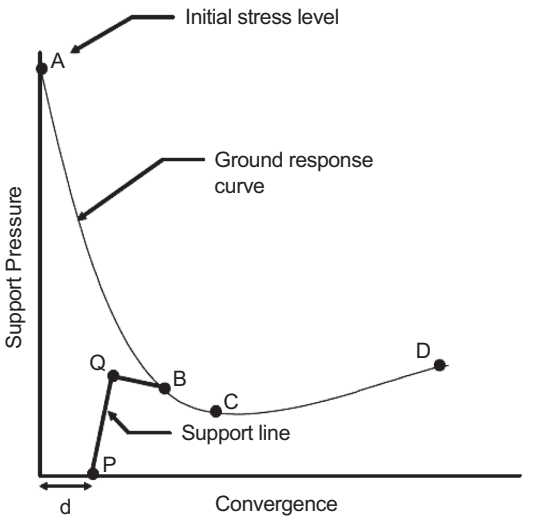


Figure 2 Illustration of a ground reaction curve (Barczak, 2006).

tunneling industry for many years (Brown *et al*., 1983) and can be utilized to estimate the number of support elements needed to achieve equilibrium. These curves plot the support pressure against the convergence, as shown in Figure 2.

Before excavation, the boundaries have stress equal to the in situ field stress (Point A in Figure 2). Once the excavation is developed, the reactive/support stress that is required to prevent additional convergence reduces as the rock structure begins self-supporting (Point B). A point is reached where serious rock failure and unraveling occurs (Point C), and the self-supporting capacity reduces significantly; the rock deformation/deterioration accelerates and the required reactive load to create stability increases significantly. Ultimately (near Point D), the installed support needs to carry deadweight (*i.e*. the failed ground). Equilibrium is essentially at Point B, where the support curve intersects the ground reaction curve. Using numerical modeling and in situ measurements of closure, these ground reaction curves and support interactions can be established to find the optimal method of support, and the appropriate time to install this support, for a particular roof geology and location (Speers & Spearing, 1996; Barczak, 2006).

1.4 Hybrid method

This involves a combination of methods with back analysis and is usually the best method.Any support design method must be continually reviewed (visually and with measurements) and amended as necessary.The method adopted must also meet the functional requirements of the excavation and also be cost effective. Engineering judgment based on available information is critical, and the design must be continually revisited and modified as more information becomes available.

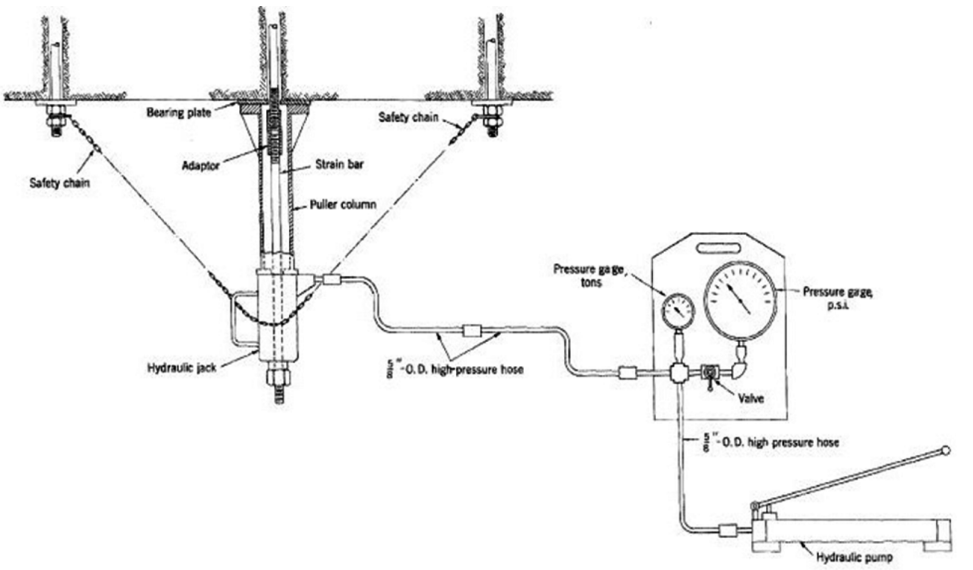


Figure 3 Rock bolt pull test equipment.

2 AN OVERVIEW OF ROCK BOLT INSTRUMENTATION METHODS

Following the success of mechanical shell anchors that replaced timber sets, posts and cribs (packs), Barry (1954) used a torque wrench to estimate the tension in rock bolts and introduced a pull test apparatus for rock bolts shown in Figure 3. The new equipment and its test procedure were developed to study rock bolt anchorage capacity in both sandstone and shale roof. Previously, this could not be satisfactorily determined using methods that existed at the time. Results from pull tests and tests using a torque wrench were compared with each other to form an effective analysis showing anchorage capacities.

Anchorage failure is one of the main failure mechanisms for fully grouted bolts. As roof deformation works its way upward, the mechanical key breaks down and most of the load is concentrated in the upper end of the bolt. If this load becomes more than the anchorage strength, bolts fail by pull-out. Based on thirty years of research, it is known that anchorage failure is the main reason for roof bolt failure where roof rock is weak and roof support is most critical. Data available in literature suggests that in soft shale or coal roof, 20–30 inches of resin anchorage may be required to achieve full bolt capacity. Pull-out tests are done in order to determine the effective rock bolt length needed in different strata.This is because certain lengths of the rock bolt need to provide good anchorage within weaker strata and this anchorage strength exceeds the ultimate strength of the rock bolt. Despite the importance in properly designing roof control systems, there is no widely accepted anchorage test for fully grouted bolts. Standard pull tests have sometimes been employed, but they provide little information on anchorage near the top of the bolt.

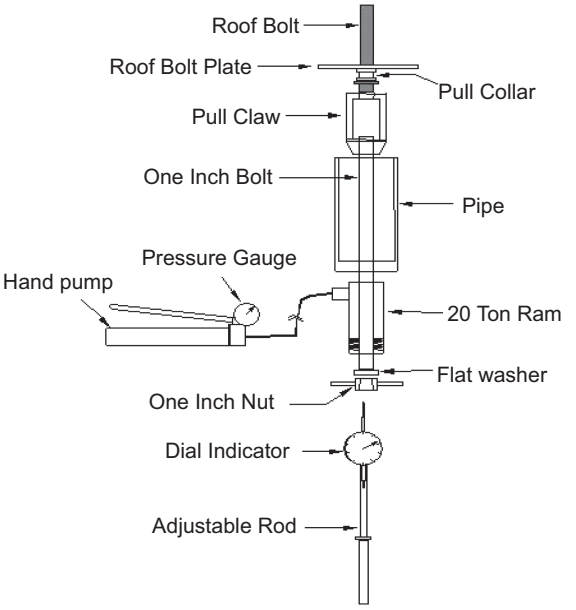


Figure 4 Schematic for SEPTfor lab or in situ rock bolts.

2.1 Short encapsulation pull-out tests

To overcome the short-comings discussed above, an alternative and standardized test method, first described more than 25 years ago in ASTM F432, is the Short Encapsulation Pull Test (SEPT). With this test, the bolt is installed with only a short (typically 0.30 cm/1 ft) encapsulation length of resin. A schematic of the SEPT method is shown in Figure 4.

This test method for rock bolt anchorage is useful and relatively quick, cheap and easy to conduct. The results can be used to:

1. Compare different anchoring systems
2. Compare different combinations of rock bolts (grade, diameter, bar surface texture/ribs etc.) and resin
3. Determine optimum installation parameters
4. Determine optimum bolting strata horizon in the immediate roof and rib
5. Quality control on the installation effectiveness
6. Design new rock bolt supports and test them initially in the lab using SEPT (or an appropriate modification).

This method is therefore a useful test that should be repeated at least three times. It can yield useful practical data that is adequate to answer many rock bolt support questions.

2.2 Short resistive strain gauges

Almost all attempts at monitoring rock bolt loads in the past have used short base-length (typically < 20 mm) strain gauges adhered into slots (about 3 mm wide and 3 mm

deep) machined along the length of the bolt. To attempt to record any bending or shear deformation, two diametrically opposed slots are populated with pairs of strain gauges. If the strain gauges are diametrically opposed as well, the axial strain can be given by:

$$\varepsilon_{axial} = (\varepsilon_A + \varepsilon_B)/2 \tag{8}$$

where ε_A and ε_B are the strain gauge reading on side A and side B of the rock bolt at the same distance along the bolt and is shown in Figure 6. The corresponding bending strain can be written as:

$$\varepsilon_{bending} \approx (\varepsilon_A - \varepsilon_B)/2 \tag{9}$$

where the inequality acknowledges that strain gauges in three grooves would be required to definitively determine the maximum magnitude of the bending strain vector.

In experimental studies using short base-length resistive strain gauges, less than 10% of the total bolt is monitored and the short gauge lengths are likely to be strongly influenced by errors related to any localized shear deformation. Although important, this may overshadow the overall axial performance of the rock bolt that is primarily of interest to researchers and engineers interested in the optimization of support design.

Figure 5 illustrates the typical two slotted configuration used and the short strain gauge configuration used (Serbousek & Signer, 1984).This approach is still useful where only the axial load determination is needed, but the instrument cost is becoming unjustified when compared to competing technologies.

2.3 Long base-length displacement sensors

According to Hyett *et al.* (2012) staggered instrumentation schemes for rock bolts involves a compromise between the number of gauges (*i.e.* cost) and the accuracy with

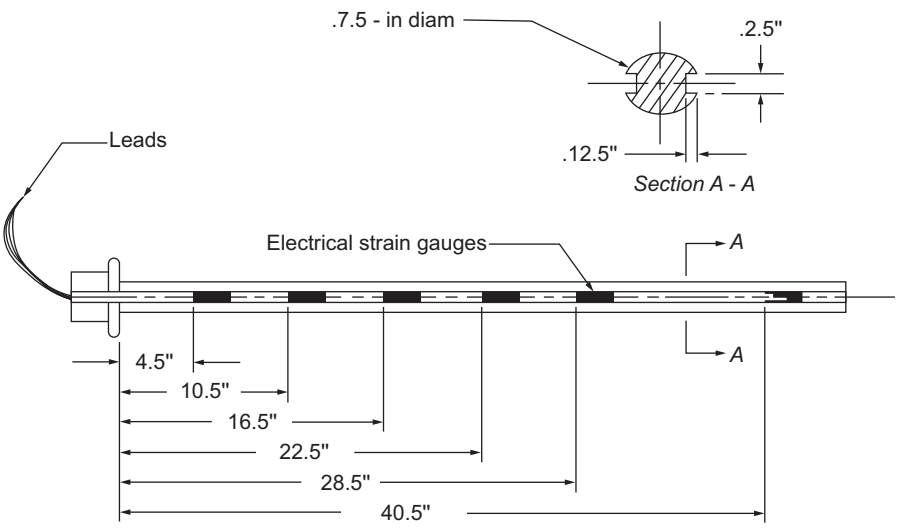


Figure 5 Short base-length resistive strain gauge technology.

which the strain profile along the bolt is resolved. Instrument cost is important since a percentage of instrumented bolts will be lost due to operational related attrition, firstly because the installation process involves spinning the grouted bolt in the resin, and thereafter, because at the production face, the proximity of mobile heavy machinery presents an on-going hazard. In addition they obviously cannot be re-used. The accuracy with which the load distribution along the bolt is measured using a discrete number of gauges depends on *(i)* the number of gauges, (*ii*) the base-length of the gauges, and (*iii*) the intrinsic accuracy and resolution of the gauges. Short base-length measurements will very accurately measure the load at specific locations but may be unrepresentative of the intervening bolt length especially if load concentrations occur at discontinuities. Long base-length measurements will capture localized deformation due to any discrete points of loading, but due to an averaging effect, will underestimate the extreme values, especially if the strain profile varies dramatically.

An alternative to the short strain gauge rock bolt monitoring approach was proposed by Spearing *et al*. (2011) based on an array of sub-micron resolution displacement sensors that measure the change in displacement or stretch (u^i) of the bolt. The end-points of the displacement sensor are attached to the bolt to define a base-length (L), typically in the range 200–500 mm; this gives more than an order of magnitude more coverage along a rock bolt than for a short resistive foil strain gauges. The corresponding strain (ε^i) for the ith sensor is determined from:

$$\varepsilon^i = u^i / L \tag{10}$$

The instrumented rock bolt has digital signal conditioning that transmits the strain values directly based on Equation 10. In order to limit the cost, the number of displacement sensors has been typically limited to six. The six strain gauges are then arranged with three in each diametrically opposed slot (sides A and B of the rock bolt) in an end-to-end arrangement shown on Figure 6 so that the entire length of the bolt is effectively monitored. Sensors denoted by i = 1, 3 and 5 are located on side A and sensors 2, 4

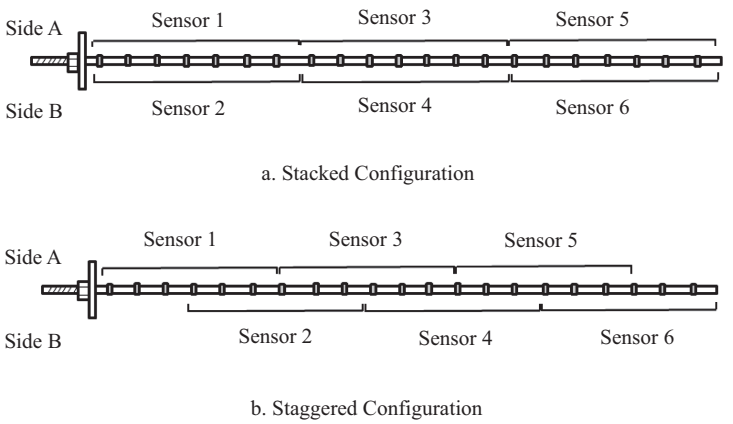


Figure 6 The two different long base-length displacement sensor configurations.

and 6 are on side B. The two different sensor configurations are termed *stacked* and *staggered* as shown in the Figure 6.

2.3.1 Stacked configuration

In the stacked configuration (Figure 6a), the axial strain and load at the three nodal points can be determined according to:

$$\varepsilon^{i}_{axial} = (\varepsilon^{2i-I} + \varepsilon^{2i})/2 \tag{11}$$

$$F^{i}_{axial} = EA\ \varepsilon^{i}_{axial} \tag{12}$$

with i = 1 to 3 (Figure 6a). This configuration provides only three points of lengthwise load determination, and therefore the load profile is somewhat crude. The corresponding bending strain is:

$$\varepsilon^{i}_{bending} = (\varepsilon^{2i-I} - \varepsilon^{2i})/2 \tag{13}$$

Since the gauges are arranged end-to-end and monitoring the whole length of the bolt the equivalent displacement profile can be written:

$$u^{i}_{axial} = \sum\nolimits_{n=1}^{n=i} (\varepsilon^{n}_{axial} \times \mathrm{L}) \tag{14}$$

This is graphically represented in Figure 7a. In other words, the bolt displacement, or stretch, relative to the toe of the bolt is calculated from the summation of the measured

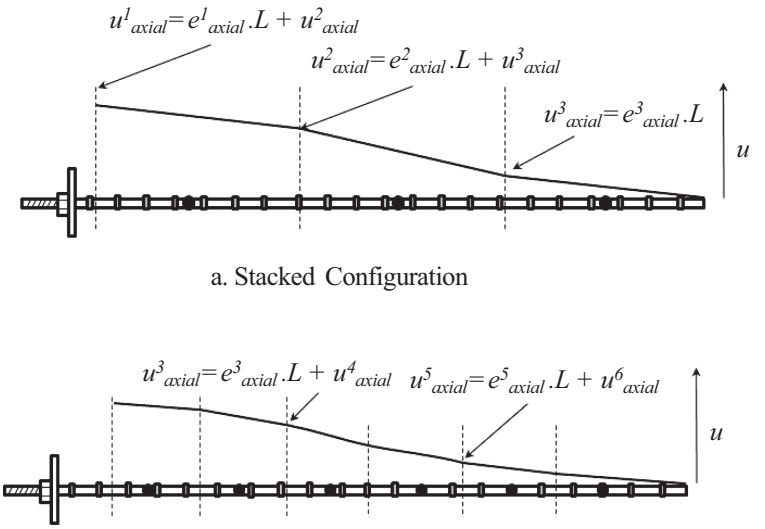


Figure 7 Displacement determination based on the accumulation of measured displacements along the bolt.

axial strains multiplied by the gauge length. It should be recognized that a distinction is made between the measured displacement, u^i, from each displacement sensor and the calculated axial displacement, u^i_{axial}, which accounts for any bending.

2.3.2 Staggered configuration

For the staggered configuration (Figure 6b), the gauges on Side A of the bolt are offset from those on Side B by one half the base-length of the sensor. In this case a data reduction scheme is implemented based on the central difference approximation to the second order governing differential equation for displacement variation along a grouted bolt (Farmer, 1975). The strains at the *i*th nodal point can be approximated as:

$$\varepsilon^i_{axial} = (\varepsilon^{i-1} + 2\varepsilon^i + \varepsilon^{i+1})/4 \tag{15}$$

$$\varepsilon^i_{bending} = (\varepsilon^{i-1} - 2\varepsilon^i + \varepsilon^{i+1})/2 \tag{16}$$

where ε^i is the strain measured by the displacement gauge centered at the *i*th nodal point and ε^{i-1} and ε^{i+1} are the two overlapping gauges on the opposite side of the bolt. At the ends of the bolt the following two approximations are used. For node 1:

$$\varepsilon^i_{axial} = (2\varepsilon^1 + \varepsilon^2)/3 \tag{17}$$

and for node 6, knowing that ε^i_{axial} must be zero at the toe end of the bolt:

$$\varepsilon^i_{axial} = (2\varepsilon^6 + \varepsilon^5)/4 \tag{18}$$

As for the stacked gauge configuration, since the staggered gauges are configured end-to-end and monitor the whole length of the bolt, the corresponding displacement profile at the *i*th nodal point can be calculated from the summation:

$$u^i_{axial} = \sum_{n=6}^{n=i} (\varepsilon^n_{axial} \times L) \tag{19}$$

The design using long base length strain gauges to monitor separate sections of the bolt, has two distinct advantages over the use of short strain gauges:

1. It is able to more accurately monitor both the strain and displacement of the bolt which can be compared with numerical and analytical models, and
2. The long base length tends to cancel out any local perturbations especially those related to localized lateral shearing movements which might otherwise have complicated the analysis.

Figure 8 shows contour plots of bolt displacement (in microns) and bolt strain (in μm – 153 μm being equivalent to 1 tonne) superimposed on the location of four rock bolts instrumented using long base-length strain sensors installed in the immediate roof of a coal mine over a period of time (Spearing & Hyett, 2012).

Figure 8 represents a contour map of bolt stretch (in microns) interpolated between the four instrumented bolts. A classical, almost symmetric, "arch" shape is defined, which migrates deeper into the immediate roof over the duration of the almost three month monitoring period.

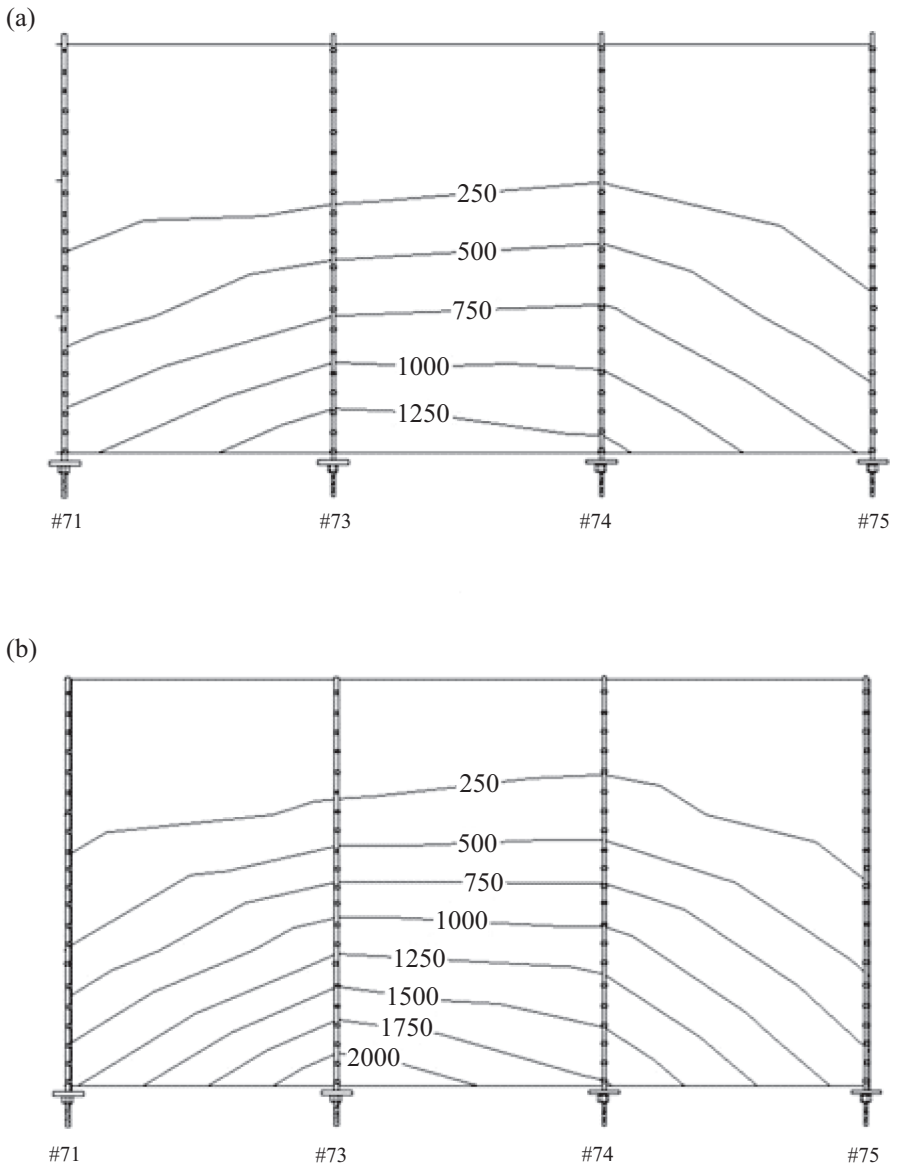


Figure 8 A contour diagram of the axial displacement (μ axial) during the experiment (a) first logged reading 08/28/2010 (b) last reading 11/11/2010.

2.4 Problems with the rock bolt instrumentation methods

The number of gauges and the gauge length are important in resin grouted rock bolts because typically a one foot resin column can hold over ten tons of axial load. This becomes significant because an induced parting (an opening along a discontinuity) in

the immediate roof strata, can cause a significant localized load that may be partially (or even totally) missed by the array of gauges as:

1. Short gauges may not be located near enough to the opening vicinity and the support generated by the resin column either side of the opening could mask the actual load
2. Long gauges that intersect the opening would record an average load over the gauge length and hence possibly miss the peak and the load shedding in the resin column

The design, which uses long base-length strain gauges (displacement sensors) to monitor separate sections of the bolt, has two distinct advantages which were mentioned previously.

Additionally, using two-slotted instrumented rock bolts can pose issues during in-situ installation as the two slots must be orientated in the direction of the maximum shear vector.This brings forth a number of issues, as the exact direction of maximum shear may not be known and it will often be difficult to spin a bolt into a particular orientation. In general, when installing using resin cartridges or mechanical shells, orientation of the slots is governed by a preferred direction, whereas a three-slot bolt can be spun in arbitrarily. The only alternative for two slot technologies is if the grout is pumped in.This allows orientation in the preferred direction but implies a bias to the installation procedure and may cloud the research findings.

It has also been found that both the short strain gauge and long base-length displacement sensors have significant shortcomings as neither capture the entire strain profile along the bolt. These strain gauge systems using only two slots can misrepresent any reactive loads in the bolt depending on where the load is applied relative to the two axially opposed slots. Consider that to obtain a strain tensor, three gauge rosettes are needed, and for the same reasons, three orientations of strain gauges along a bolt are also needed (*i.e.* 3 slots).

3 THE REQUIREMENTS FOR IN SITU ROCK BOLT MEASUREMENTS

3.1 Observational feed-back and monitoring

Observational feed-back and monitoring deals with mitigating instrument failures in the field by improving upon past design flaws as well as observing measured strains in situ and justifying those strains from local geology or observed local rock mass failures to improve the overall quality of an in situ monitoring study.

One of the key components of successful in situ monitoring is mitigating instrument failure and improving upon past practices. It's simple, the longer period of time, and the more instruments which are in operation, governs the amount of useable data and improves the overall quality of the field tests.

Take for example in 2009, an instrumented rock bolt study was conducted at three coal mines across the US where nearly two hundred instrumented bolts, extensometers and closure meters were installed as primary support at a coal face (Spearing & Gadde, 2011). Upon installation of the instrumented rock bolts, and at the early stages of the project, an oversight of the instrumented bolt design (*i.e.* an extended instrumented bolt head) led to multiple bolt failures due to heavy equipment clipping the extended bolt heads as the heavy equipment moved through the entry. This rendered the bolts inoperable which lost valuable data toward the project. In later field trials a new bolt

design which utilized a shorter bolt head effectively eliminated this problem. This is a good example of the importance in communication between the manufacturers, the end-users and the workforce at the mine can quickly compromise a costly instrumentation project.

Another key component of a quality in situ study is justifying how and why displacements or strains have accumulated in a series of rock bolts. This relies on close monitoring of local geology in the pillar, floor and immediate roof. When presenting results from an in situ study, it is quite difficult to determine how and why strains have accumulated in rock bolts without some sort of justification or observed local failures. For example, if an instrumented rock bolt is installed in the roof near a pillar rib, significant amount of strain can be accumulated by the rock bolt at a point in time during the monitoring period which can be justified by the pillar slough on the adjacent rib. Otherwise the rock bolt may be subjected to a local shear failure in the immediate roof.Point being, often times it is difficult to determine for sure, but providing justification,whether it is theorized or measured can really strengthen the results at the end of a project.

3.2 Remote monitoring

Remote monitoring of instrumented rock bolt systems is still very much in its infancy. Currently however, major strides are being made by leading instrumentation companies which offer data logging options for digital instruments with integrated telemetry. In the foreseeable future, it seems remote monitoring will become common place and supersede the current manual read methods for underground instrumentation. This is particularly evident as optical communications systems are now required for tracking purposes in underground mines, and with the development of optical rock bolt monitoring, bolting systems will be seamlessly incorporated into these communications systems. An example where telemetry solutions was used to monitor the blasting events in an underground mine is shown in Figure 9.

3.3 Data analysis and presentation of results

Data analysis and the clear presentation of the results is possibly the most critical process of in-situ monitoring studies. If results are not presented in an obvious, quickly comprehensible, interesting and conceptual manner the result is often wasted effort and misinterpretation.

In terms of rock bolt instrumentation studies, the database of observed strains is typically massive, and as technology progresses, is becoming larger and larger. Mainly because more strain values per length are being installed into the same size instrument. Because of this, data processing is typically cumbersome and leads to swathes of data which is hard to present, l*et al*one interpret, and can be overwhelming for new researchers. This is particularly evident for in situ studies, as the geology is not well known; displacements are often locally governed and predicting areas for high potential displacements are often too difficult. If sufficient laboratory tests have been conducted beforehand, the tests can at least be controlled to establish a solid foundation for data interpretation in the field. Some suggestions for data analysis and presentation are given below:

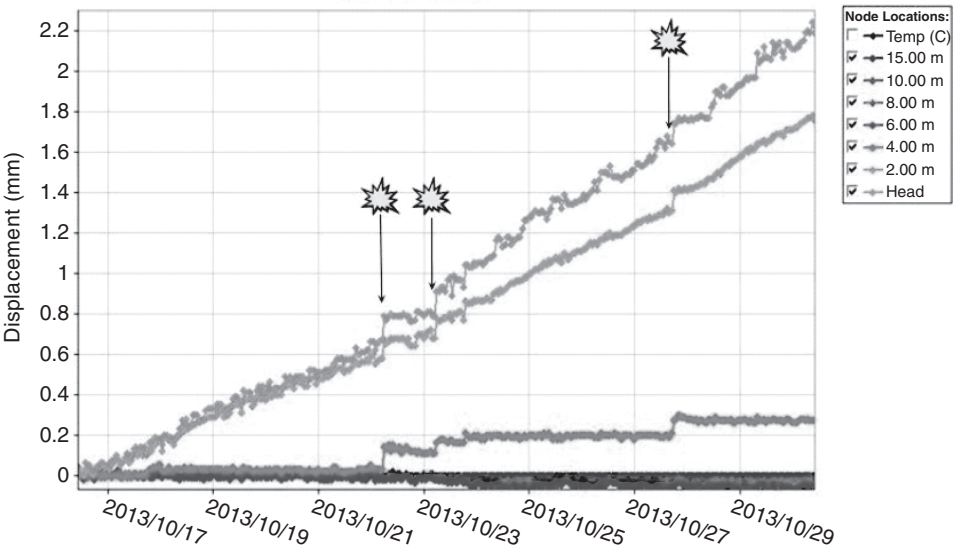


Figure 9 Displacements from blasting events observed at an underground mine using a remote monitoring solution (Hyett, 2013).

1. Begin early and plan – in terms of data analysis, be sure to have data sheets set up and ready for processing before testing begins – basically a plug and go scenario. Be consistent, by processing first and then thoroughly comparing results afterwards.
2. Work with a team – break up different duties to various people in a group. Assign data processing duties to one person, interpretation to another, laboratory setup and in-situ setup to another etc. Trying to accomplish large scale monitoring single handily is almost impossible.
3. Re-create expected in-situ measurements in the lab – laboratory studies such as axial and shear tests can be quite advantageous for understanding in situ behavior later on. These tests require several months to perfect, so preparation and setup should be conducted early in any research project.
4. Know the geology in-situ – when installing instrumentation in situ, knowledge of the local geology is critical – especially if the displacements are small (*i.e.* fractions of mm). This is particularly useful for conceptualization of results, as a visual rendering can give an idea of how to better understand the rockmass is behaving.
5. Measure displacements – in the laboratory, measuring displacements is probably the most critical to back calibrating numerical models or to understand how the test setup is behaving. Additionally, this gives an indication of the magnitude of displacements an in-situ rock mass has undergone in the field.
6. Be creative – be innovative and creative in terms of results presentation. Present the results in a manner that an observer who has zero knowledge of bolt research can understand.This is difficult at times, but can make, or break, an instrumented research project. A good example is shown in Figure 10.

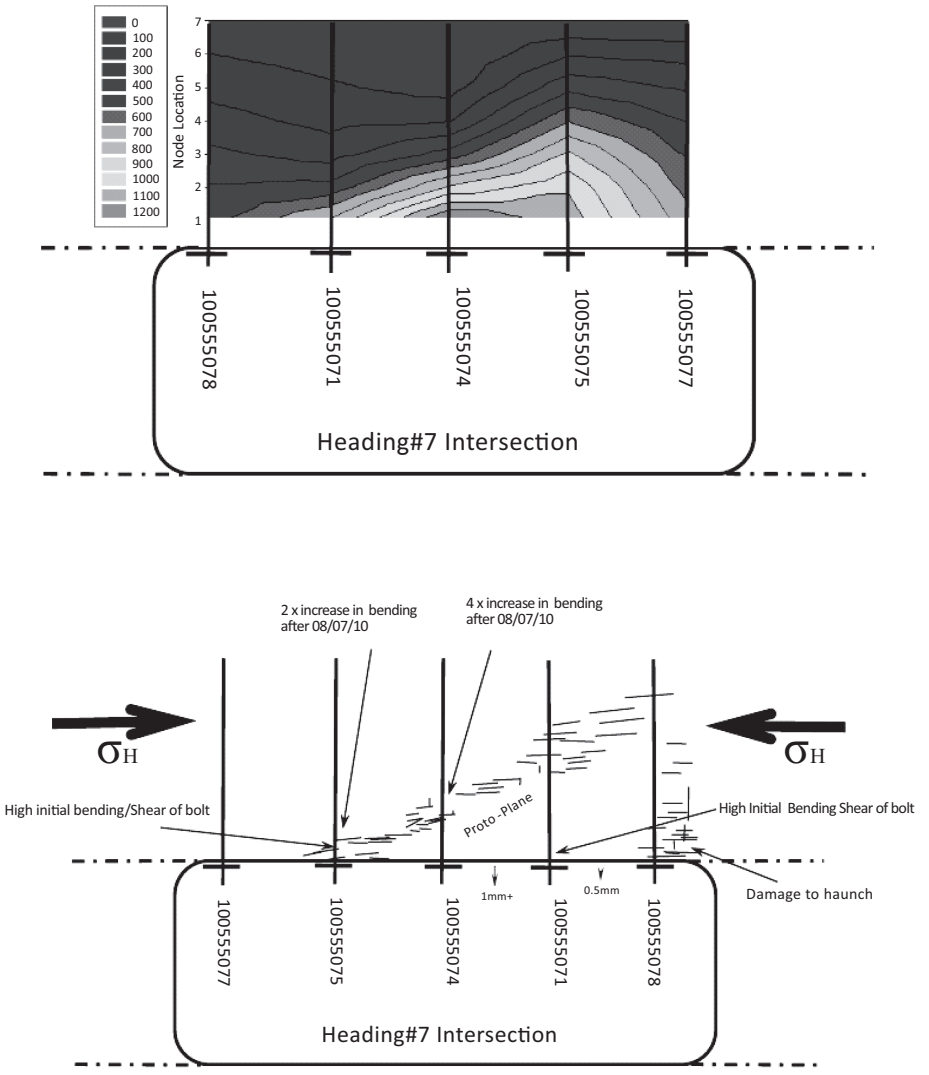


Figure 10 An example of creative means for presenting roof bolt instrumentation data. Axial bolt stretch contours (top), working hypothesis for the mechanism of roof instability based upon an instrumented entry (bottom) (Spearing *et al.*, 2013).

4. NEW INSTRUMENTATION APPROACHES AND TECHNOLOGY

4.1 The positioning of sensors on a rock bolt

Figure 11 shows a traditional two slot rebar to the new three slot rebar. The use of three slots (grooves) shows not only the axial loading but also captures the complete bending strain tensor along the bolt.

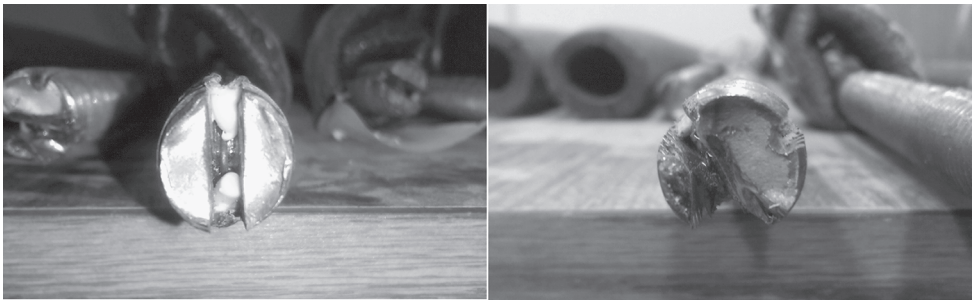


Figure 11 Comparison between a two and three slotted rock bolt.

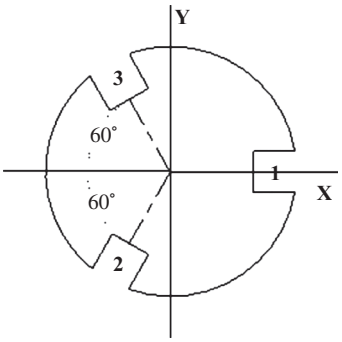


Figure 12 Cross-Sectional Area of three slotted rebar.

The three slot instrumented bolt involves populating triads of strains along the three slot rebar (Figure 12) to compensate for bending deformations in any direction. The axial strains are determined at every 5 mm along the bolt length, each based on the equation:

$$\varepsilon_{axial} = (\varepsilon_1 + \varepsilon_2 + \varepsilon_3)/3 \tag{20}$$

where ε_1, and ε_2 are the strain readings on Slot 1, 2 and 3 respectively at the same point length wise along the bolt.

The bending in the three slot rebar can be calculated individually, along the groove and perpendicular to that groove. The corresponding bending strain calculated with respect to slot one is:

$$\varepsilon_{x-\text{bending}} = (\varepsilon_1 - (\varepsilon_2 \cos 60^\circ + \varepsilon_3 \cos 60^\circ))/2 \tag{21}$$

$$\varepsilon_{y-\text{bending}} = (\varepsilon_2 \sin 60^\circ - \varepsilon_3 \sin 60^\circ)/2 \tag{22}$$

$$\varepsilon_{total-\text{bending}} = ((\varepsilon_{x-\text{bending}})^2 + (\varepsilon_{y-\text{bending}})^2)^{1/2} \tag{23}$$

$$\varphi = \tan^{-1}(\varepsilon_{y-\text{bending}}/\varepsilon_{x-\text{bending}}) \tag{24}$$

Where $\varepsilon_{x\text{-bending}}$ is the bending strain along the first slot and $\varepsilon_{y\text{-bending}}$ is the bending strain perpendicular to the first slot. The factor $\varepsilon_{total\text{-bending}}$ is the total bending strain along the angle φ from slot one direction Jessu *et al.* (2016).

4.2 Fiber Bragg Grating (FBG)

A Fiber Bragg Grating (FBG) is a distributed Bragg reflector constructed in short segments of optical fiber that reflects particular wavelengths of light and transmits all others. Fiber Bragg Gratings are sensitive to strain and temperature and thus are used as the sensing elements in the optical fibers. In the 1990s, FBG's were used to measure strain and temperature in the composite materials of the aircraft. The potential of sensitiveness of sensing the strain and temperature replaced the traditional strain gauges in numerous other applications such as seismology, oil and gas fields.

4.3 Distributed Optical Sensing (DOS)

Instead of making the measurements at discrete, predetermined points Distributed Optical Sensing (DOS) makes effectively continuous measurements over the full length of the fiber. DOS is capable of detecting changes in strain and temperature smaller than 0.1 micron and 0.01^0C, respectively. Distributed Optical Sensing technology using Rayleigh backscattering is now being used to obtain the complete strain profiles along the rock bolt with a spatial resolution on an order of 1.25 mm. An optical fiber of 100 microns diameter size is positioned and looped along the grooves and encapsulated with high strength epoxy resin by YieldPoint, Canada for example.

4.4 A comparison between the FBG and DOS technologies for instrumented rock bolts

Based upon the current state of the art, the FBG interrogators are less costly, are better suited for time dependent monitoring and are quantifiably a more reliable solution based on pilot data from a preliminary instrumentation study (discussed below). Additionally, FBG interrogators can multiplex anywhere from two to a several hundred FBG sensors per interrogator. On the other hand, the DOS technology provides significantly more readings per fiber, providing far better resolution and therefore a complete strain profile along the bolt length. With DOS, standard telecom fiber can be used for the instrument which is relatively inexpensive, whereas the FBGs can be quite costly (Hyett *et al.*, 2013). An illustration of the three instrumented bolt technologies is shown in Figure 13.

Undoubtedly, failures of instruments tend to occur in situ. This is not necessarily because of a design flaw, but has frequently more to do with the harsh environment instrumented rock bolts are subjected too. Take for instance, one of the harshest mining environments – coal mining.In this scenario, there is often dust, moisture, moving equipment and gas. This causes many issues, one of which being the most challenging, in that the instruments must be intrinsically safe. In hard rock mines this is not the case.

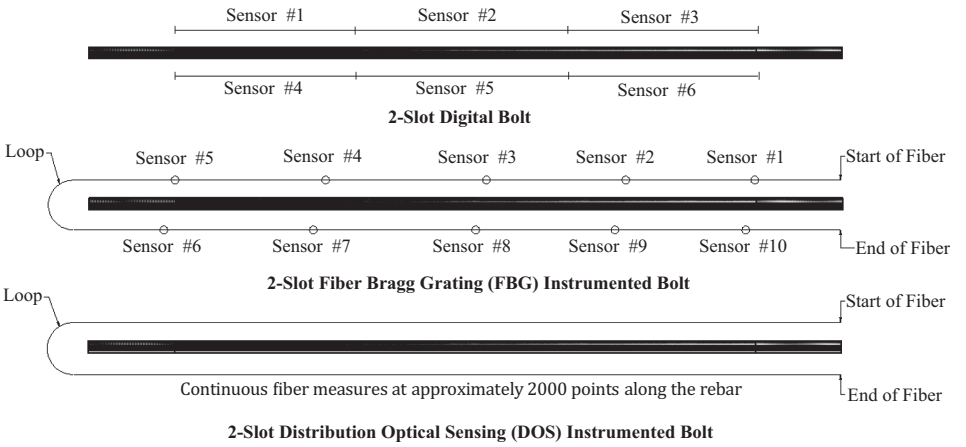


Figure 13 An illustration of the three instrumented bolt technologies for a four foot rock bolt.

As a result, manufacturers or researchers must be adaptive to these environments to increase instrument reliability overtime.

As mentioned previously, the reliability of the FBG and DOS bolts have been compared in an on-going pilot study of the two technologies. The following is a survival and cumulative hazard (risk) model developed based on underground testing at two US coal mines. These results provide a snapshot of the technologies reliability over time. Reiterating, this is the first time these technologies have been incorporated in an in situ scenario and the following results portray *only* the current state-of-the-art in terms of in situ mining studies. It is the researchers' responsibility to determine which monitoring solution is most suitable for their respective application.

Statistically reliability is defined as the probability that an item is functioning at time (t). This probability is given as a plot of a survival function S(t). Similarly the cumulative hazard function gives the cumulative *risk* at time (t), or in this case, the number of failures that have occurred by time (t).

The following charts are developed based on a Type I right censored data-set which was terminated at a time of 25 days. Twenty-five days was the end of each of the two in situ monitoring periods.The number of failures for the DOS and FBG instrumented rock bolts were logged,and the following is the given operation time in days:

	Operation Time (Days)																
Bolt #	1	2	3	4	5	6	7	8	9	10	11	12	13	14	15	16	17
FBG	25	25	25	25	25	25	8	1	25	25	1	–	–	–	–	–	–
DOS	7	7	1	3	1	25	25	25	25	9	25	17	10	24	25	25	15

The number of items on test for the DOS bolts was seventeen and eleven for FBG's.The number of failures was ten and three, respectively. Fitting an exponential survival

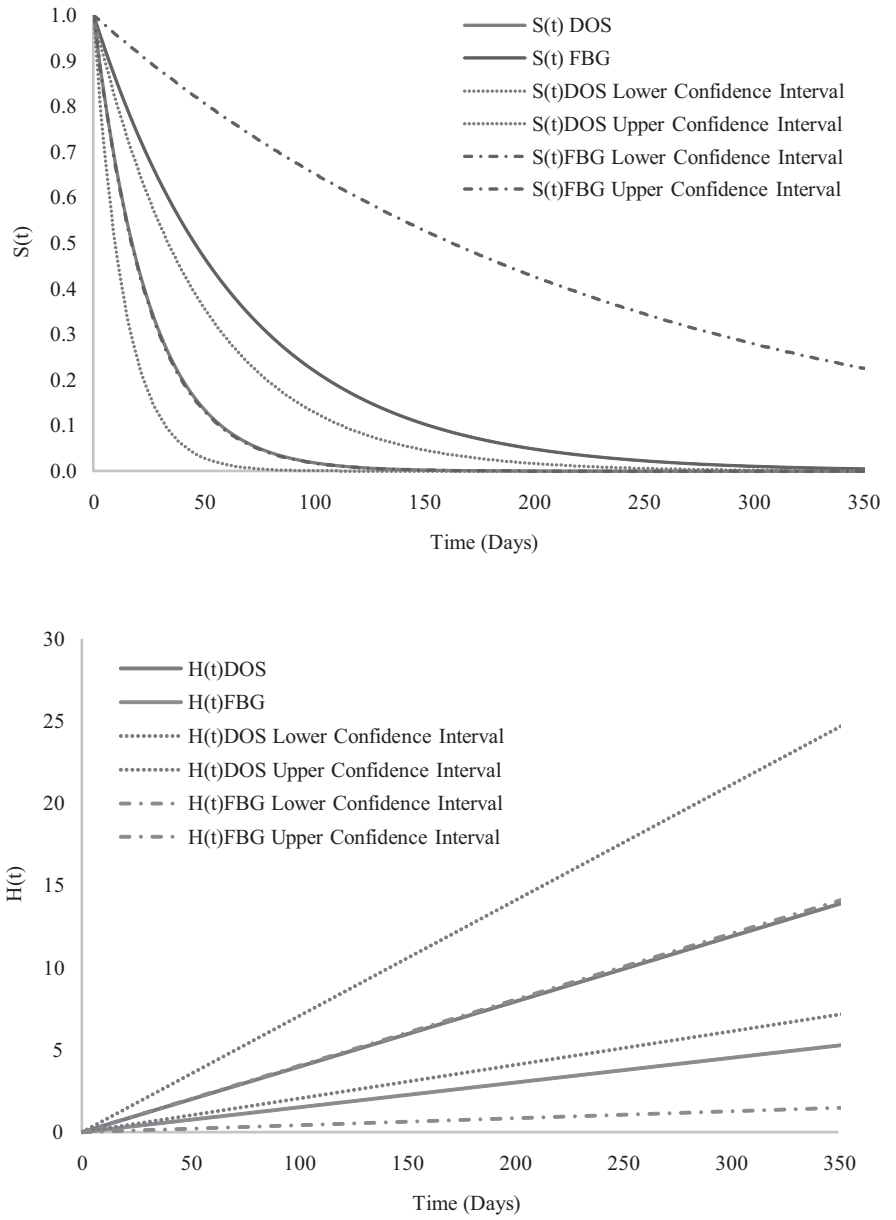


Figure 14 Plot of the survivor function and confidence intervals for FBG and DOS technologies (top) and the cumulative hazard function and confidence intervals for FBG and DOS technologies (bottom).

function to the data-sets, show that the survivor function can follow an exponential distribution given as:

$$S(t) = e^{-\lambda t} \tag{25}$$

If the survivor function is exponential, the cumulative hazard function is mathematically tractable, and is the negative of the natural log of the survival function which equates to the scale parameter (λ):

$$H(t) = -\log S(t) = \lambda \tag{26}$$

This is a standard statistical approach to calculating the cumulative hazard function from the survivor function.The details for calculating the magnitudes of λ, will not be covered here, as it is out of the scope of this chapter, but can be determined from any statistical survival software package relatively easily or analytically.

Based upon the results, the FBG technology shows a higher probability of operation over time. In fact, the predicted lower bound of failure follows the mean survival function for the DOS technology.From the cumulative hazard function it is easy to see that, under the current installation practices, and in terms of this particular underground coal mine study, the estimated number of failures per year, for DOS instruments (14.5) is nearly triple that of the FBG instruments (5.5).This does not indicate that the DOS technology is inferior to FBG's.Instead, based upon the current state of the art, the FBGs are certainly the more "field ready" optical monitoring solution.

4.5 Current shortcomings of the optical fiber technologies

The current shortcomings of this new optical sensing technologies are:

1. The data reader is currently costly and needs to be manually read. This means that manpower is needed at all times in order to collect data. This will hopefully change as the need and demand for such technology with rock bolts increases.
2. The data reader is delicate and not packaged for underground use.
3. Properties of the bolt are altered by slotting. This has always been the case with instrumentation along rock bolts, but a third slot is now recommended where shear and bending is anticipated to be even remotely significant.

4.6 The need for at least three slots

To illustrate the shortcoming of a two slot instrumented rock bolt and the effectiveness of a three slot instrumented rock bolt, simple bending tests were undertaken using a hydraulic press shown in Figure 15 (Kostecki *et al.*, 2016).

The following Figures clearly show the need for three slots where shear and bending is expected, as well as the potential for the new optical fiber technologies. The results from symmetric three-point bending tests were used for this, in addition to several other tests (including simple axial, cantilever and shear tests). Figure 16 illustrates the location of a force acting on the center of a two-slot instrumented bar. For two slot bolts the force was applied on-slot (Slot 1 or 2), or on the neutral axis.For three slot bolts, the force was applied on-slot (Slot 1, 2 or 3).

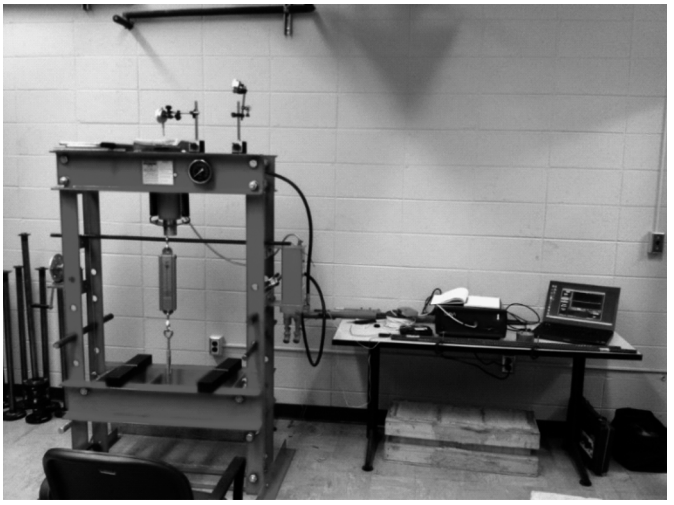


Figure 15 The laboratory test rig used.

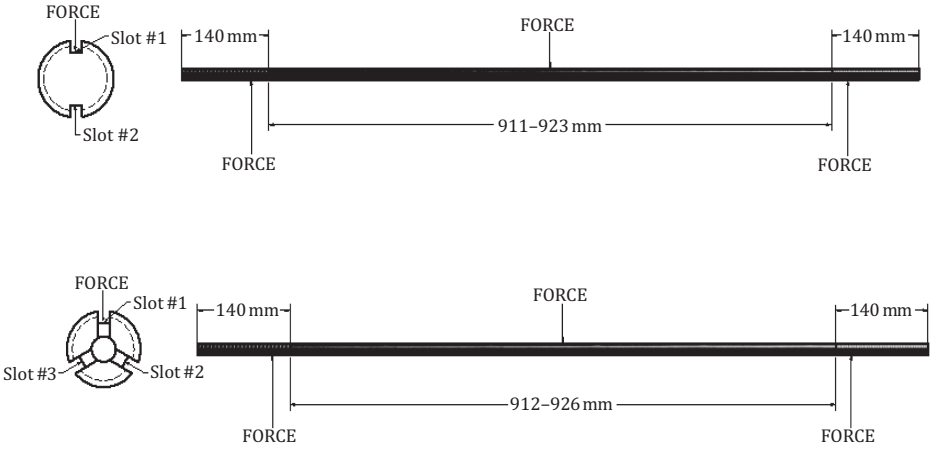


Figure 16 Representation of a force applied at the rebar center for a 2-slot three-point bending test (Top). Representation of a force applied at the rebar center for a 3-slot three-point bending test (Bottom).

Figures 17 to 19 give the results for simple three point bending tests on:

1. A two slot digital rock bolt where the load is applied directly on slot 1 (refer to Figure 16).
2. A two slot DOS rock bolt loaded on slot 1
3. A two slot DOS rock bolt loaded on the neutral axis (*i.e.* between the slots).

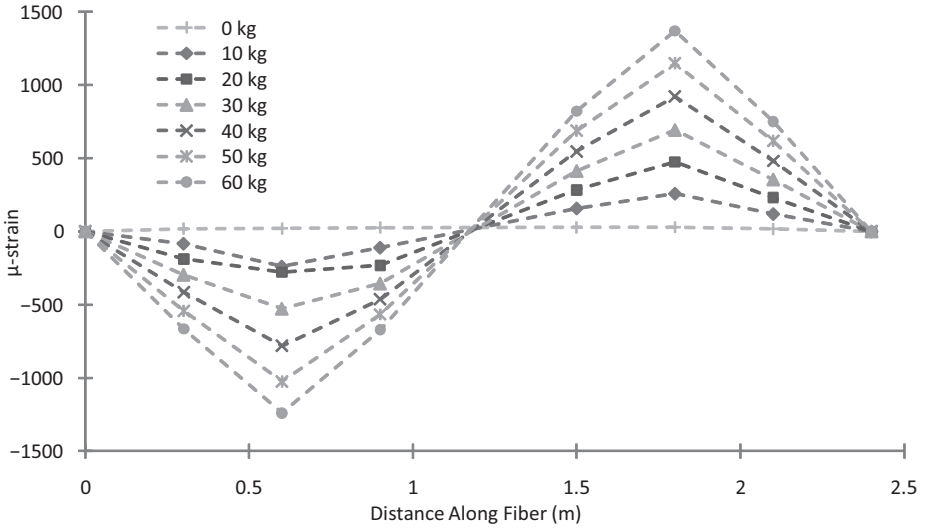


Figure 17 3-Point Bending Test of a 2 slot Digital Bolt Loaded Directly on Slot #1. Note that the strains are only recorded at discrete points along the rock bolt.

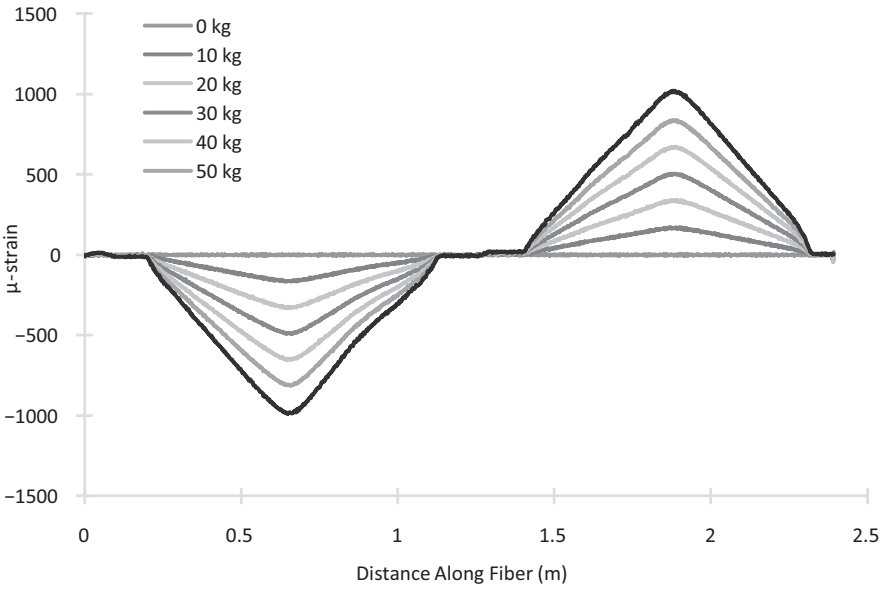


Figure 18 3-Point Bending Test of a 2 Slot DOS Bolt Loaded Directly on Slot #1. Note the basically continuous strain profile generated along the entire rock bolt by the DOS fibers.

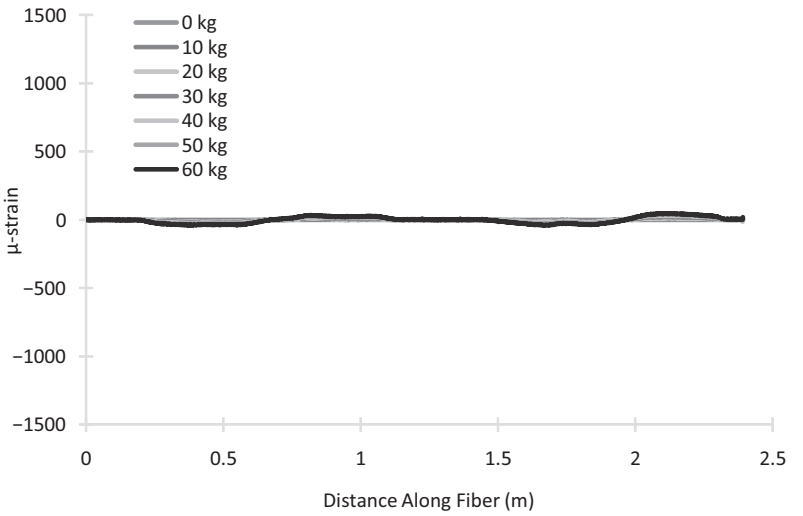


Figure 19 3-Point Bending Test of a 2 Slot DOS Bolt Loaded Directly on the Neutral Axis (Note that under the same loading conditions as in Figures 17 and 18, effectively no strain is recorded in the sensors).

Figure 19 clearly shows that when the bending force is applied on the neutral axis (90 degrees to the slots), the instrumentation is totally unable to record the bending strain. This has been a serious shortcoming with all previous instrumented rock bolt research where shear and bending are significant.

Figures 20 to 22 give the results for simple three point bending tests on:

1. A three slot DOS rock bolt where the load is applied directly on slot 1 (refer to Figure 16).
2. A three slot DOS rock bolt where the load is applied directly on slot 3.
3. A three slot FBG rock bolt where the load is applied directly on slot 3.

It is clear from these, and other repeated laboratory tests, that the use of two slotted rock bolts is not adequate, in terms of monitoring, magnitude and direction of bending and shear forces.

5 OVERCOMING THE CHALLENGES OF LABORATORY AND IN SITU INSTRUMENTATION

Instrumented rock bolt studies are accompanied by significant challenges in the laboratory and in situ. Projects require extensive planning, costs, labor and communication. In situ, it is often difficult to setup instrumentation sites, as it can be a hindrance to the mine. Not to mention, manufacturing and installing the instruments and processing the data. In which case, it becomes more effective to have a third party manufacturer develop the instruments for the researcher.This saves considerable time and effort and expedites the project as a whole. This however, creates a disconnect between the two

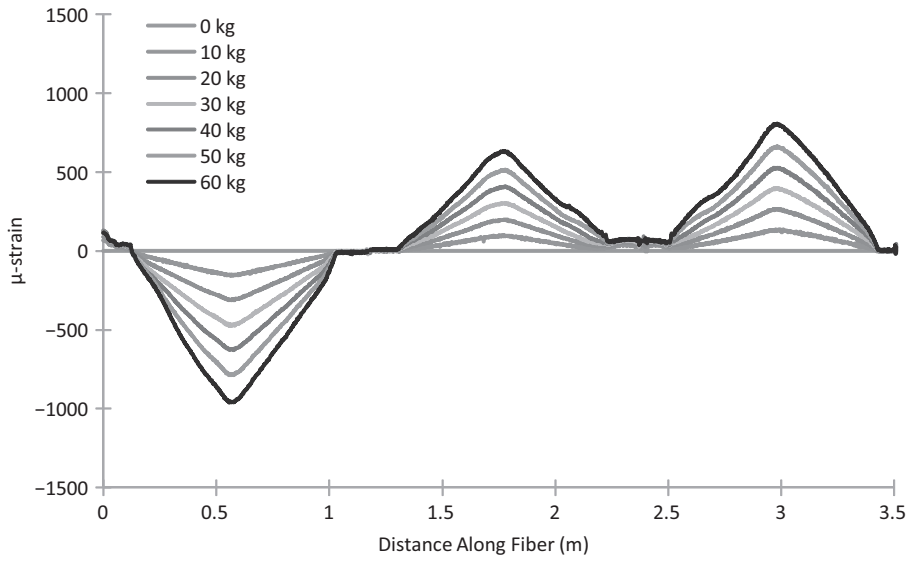


Figure 20 3-Point Bending Test of a 3 Slot DOS Bolt Loaded Directly on Slot #1 (Note that with the test configuration in Figure 19, no bending is actually recorded).

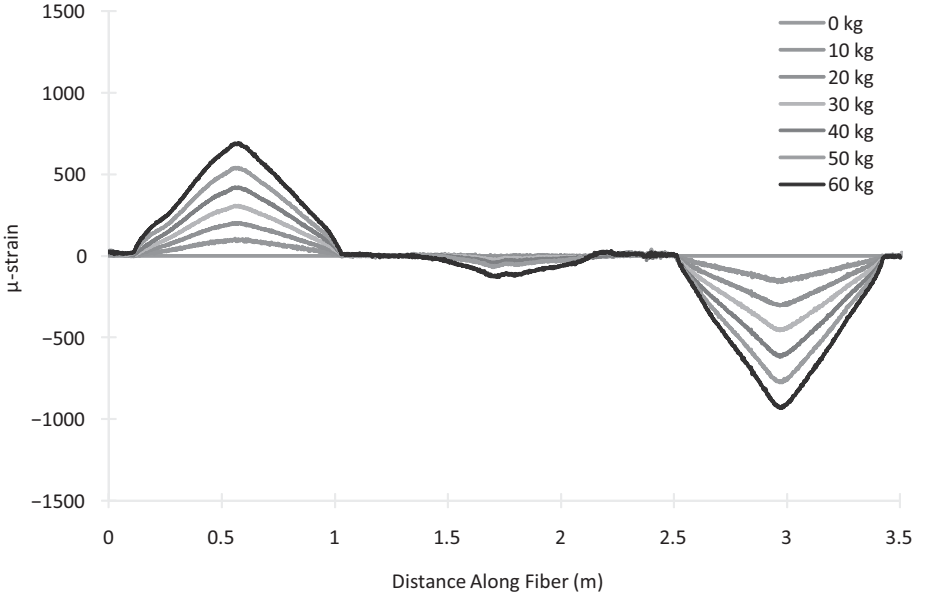


Figure 21 3-Point Bending Test of a 3 Slot DOS Bolt Loaded Directly on Slot #3 (Note: Slot #2 is not perfectly aligned at 120 degrees to the loading vector).

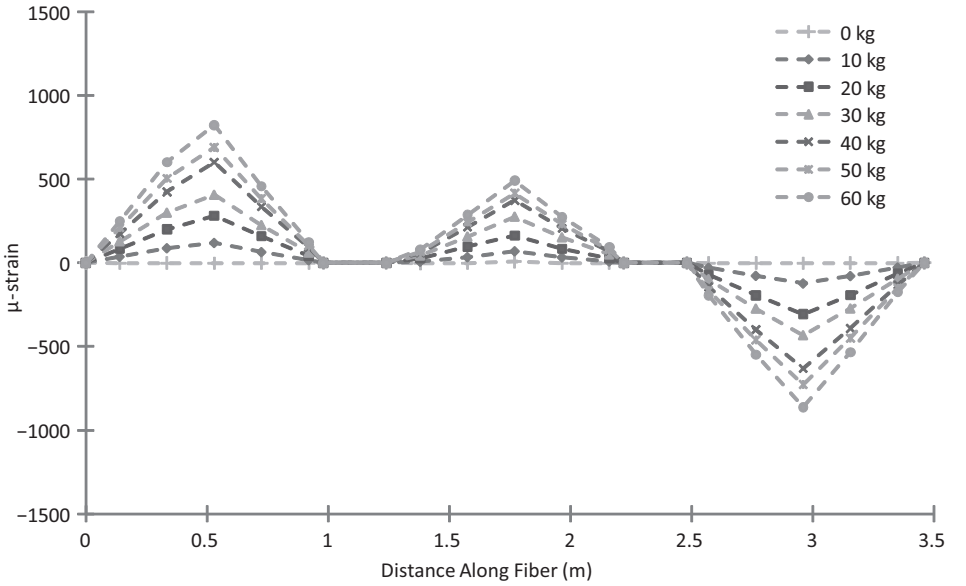


Figure 22 3-Point Bending Test of a 3 Slot FBG Bolt Loaded Directly on Slot #3.

parties, as part of understanding the rock bolt behavior requires some knowledge of how the instrumented bolts were manufactured as well as knowledge of the technologies capabilities. In the field, major difficulties arise:

- When trying to coordinate mine sites that are willing to take on the responsibility and added effort on top of their existing job duties to "cater" to the research group. This is often a major hurdle, as mine personnel must provide a bolter operator at the installation stage, as well as personnel to assist and take the researchers to the instrumentation site periodically. This is not an easy task as monitoring periods can sometimes extend for months at a time.
- The mine personnel must coordinate all safety training for those going underground. Researchers that monitor rock bolt instrumentation sites can be inexperienced in a mining environment. Therefore the safety coordinator must take on the huge responsibility to assure that they are aware of all of their surroundings and equipped with the proper safety equipment each and every trip underground. This can become quite tedious for the mine.
- Correcting design flaws on the fly. It is difficult to design the "perfect" instrument and requires much trial and error. Therefore, situations may arise where a design is not as perfectly suited for the situation as what was originally thought. The research team must be able to correct these flaws quickly as little time and high costs are at risk.
- Making sure that the research team is properly trained on operating the equipment underground. Once researchers are underground, most mines do not have the capabilities, or willingness, to call out for corrective action; and a ride out of the mine often only occurs at shifts end. Therefore, all researchers must be

knowledgeable and capable of equipment operation – especially if an instrument becomes inoperable and remedial action is needed.
- Additionally, understanding the rock movements in situ requires some validity in the lab. This also requires extensive planning and considerable thought, because recreating shearing and axial behavior in the lab requires innovation as standardized testing procedures for instrumented rebar are not yet developed.

6 INSTRUMENTATION SELECTION

The need and intended purpose for the use of instrumentation in general must be clearly defined before a selection can be even considered. The underground environment in general does not favor instrumentation mainly because:

1. There are physical access constraints.
2. There are manpower issues not only related to the installation of the instrumentation and data collection, but also in many countries, mine employees must always be in the close vicinity in case of an emergency situation and to take responsibility for the instrumentation team's safety.
3. The rockmass is discontinuous, making the placement of the instrumentation in a more representative location an additional challenge.
4. The underground environment is hostile to instrumentation typically being hot, humid and full of activities that often limit free and safe access to instrumentation sites especially if they are located close to active mining areas (which tend to be the preferred instrumentation sites).
5. It can be difficult to achieve accurate, reliable and repeatable results of instrumentation and justifying the cost of data loggers.

For all instrumentation the following are important, in order to draw conclusions based on the data obtained from any instrumentation program. The instrumentation should be:

1. Simple
2. Robust
3. Reliable
4. Cost effective (*i.e.* cheap but effective)
5. Judiciously placed
6. Repeated

Important considerations for rock bolt instrumentation are:

1. Multiple instrumented rock bolts should be installed in clusters, in case of damage during or after installation and to ensure consistent and reliable data.
2. The location of the instrumentation is always very critical. Considerations include: proximity to pillars or mid-spans, local geology etc.
3. Protecting the instrumentation from passing machinery and equipment.
4. Informing the workforce about the goals of the instrumentation project so they are less likely to damage it. The potential for better support systems (*i.e.* improving

their safety potentially) needs to be stressed to workers in the area on all shifts before any installation takes place.
5. Monitoring closure and differential rock strata movements are often helpful.
6. Ensuring that the instrumentation and data recorders are intrinsically safe, if required, and therefore situated in fresh air.

7 THE FUTURE OF IN SITU ROCK BOLT INSTRUMENTATION

Based on results to date, it would appear that at least three instrumented slots should always be used if more than the axial strain determination is needed. Alternatively, if only axial strain is needed, two slots are adequate, accepting that the neutral axis of the bolt will not capture shear and bending magnitude and direction, but costs can be reduced and reliability improved.

REFERENCES

ASTM (2013) DOI:10.1520/F0432. *Standard Specification for Roof and Rock Bolts and Accessories*. West Conshohocken, PA.

Barry, A. (1954) RI 5080, p. 20. *Use of Torque Wrench to Determine Load in Roof Bolts – Part 2. Expansion Type 3/4- Inch Bolts*. Washington D.C., US Bureau of Mines.

Barton, N.R., Lien, R. and Lunde, J. (1974) Engineering classification of rock masses for the design of tunnel support. *Rock Mechanics*, 6(4), 189–239.

"Coal Daily Fatality Report – July 1, 2015." *Coal Daily Fatality Report*. MSHA, n.d. Web. 03 July 2015.

Farmer, I.W. (1975) Stress distribution along a resin grouted anchor. *International Journal of Rock Mechanics and Mining Sciences & Geomechanics Abstracts*. (Online) 12, 347–351. Available from: http://www.sciencedirect.com/science/article/pii/0148906275901680.html (Accessed 24 February 2003).

Hoek, E., Marinos, P. & Benissi, M. (1998). Applicability of the geological strength index (GSI) classification for weak and sheared rock masses: the case of the Athens schist formation. *Bulletin of Engineering Geology and the Environment* 57(2), 151–160.

Hyett, A.J. & Spearing, A.J.S. (2012) New Technology for Measuring the In Situ Performance of Rock Bolts. *Proceedings of the 46th US Rock Mechanics / Geomechanics Symposium. ARMA 2012, 24–27 June 2012*, Chicago, Illinois. pp. 497–508.

Hyett, A.J., Mitri, H. & Spearing, A.J.S. (2012) Validation of Two New Technologies for Monitoring the In Situ Performance of Rock Bolts. *Proceedings of the 7th International Symposium on Rockbolting and Rock Mechanics in Mining. AIMS 2012, 30–31 May 2012, Aachen, Germany*. pp. 177–190.

Hyett, A.J., Forbes, B.J. & Spearing, A.J.S. (2013) Distributed Optical Sensing as Applied to Fully Grouted Rockbolts. *Proceedings of the 32nd International Ground Control Conference, 30 July – 1 August, 2013 Morgantown, West Virginia*. West Virginia University.

Jessu, K.V., Kostecki, T.R., Spearing, A.J.S. (2016) Measuring roof bolt response to axial and shear stresses: Laboratory and first in situ analyses. *CIM Journal* 7(1), 62–70.

Kostecki, T.R., Spearing, A.J.S., Forbes, B. & Hyett, A. (2016) New Instrumented Method to Measure the True Loading Profile Along Grouted Rockbolts. SME Transactions – January.

Laubscher, D.H. & Taylor, H.W. (1976) The importance of geomechanics classification of jointed rock masses in mining operations. In Exploration for rock engineering (ed. Z.T. Bieniawski) 1, pp 119–128. Cape Town: Balkema.

Marinos, P. & Hoek, E. (2000). GSI: a geologically friendly tool for rock mass strength estimation. *Proceedings of GeoEng 2000 at the International Conference on Geotechnical and Geological Engineering. GeoEng 2000, Melbourne, Victoria, Australia*. Lancaster, PA: Technomic Publishers, pp. 1422–1446.

Marinos, P. & Hoek, E. (2001). Estimating the geotechnical properties of heterogeneous rock masses such as flysch. *Bulletin of Engineering Geology and the Environment* 60, 82–92.

Ritter, W. (1879) *Die Statik der Tunnelgewölbe*. Berlin: J. Springer Publishing.

Serbousek, M.O. & Signer, S.P. (1984) Load Transfer Mechanics in Fully-Grouted Roof Bolts. *Proceedings of the 4th International Conference on Ground Control in Mining, 22–24 July 1985, Morgantown, West Virginia*. West Virginia University, pp. 32–40.

Spearing, A.J.S. & Gadde, M.M. (2011) Final report on NIOSH funded project "Improving underground safety by understanding the interaction between primary rock bolts and the immediate roof strata." *NIOSH Project*. BAA number 2008-N-10989.

Spearing, A.J.S., Hyett, A.J., Kostecki, T. & Gadde, M.M. (2013) New Technology for Measuring the In Situ Performance of Rock Bolts. *International Journal of Rock Mechanics and Mining Sciences*, 75, 153–166.

Terzaghi, C. (1925) Principles of Soil Mechanics. *Engineering News-Record*, 95, 19–27.

Chapter 6

Non-deformable support system in swelling and squeezing rocks

C.O. Aksoy[1] & *G. Gulsev Uyar*[2]
[1]*Mining Engineering, Dokuz Eylül University, Izmir, Turkey*
[2]*Mining Engineering, Hacettepe University, Ankara, Turkey*

Abstract: Swelling and squeezing rocks have different deformation mechanisms. However, significant deformations may occur in both rock types in rock engineering. Determining the most appropriate support system in swelling and squeezing rocks is one of the major challenges for rock engineers because there are many facts and issues to be considered, such as the type and performance of the support, the support elements, the rock mass parameters, the condition of the rock mass structure and the creation of an appropriate support strategy. Alongside all of these issues, parameters such as excavation geometry, round length (distance from face to the support) and excavation rate affect the support performance directly. The TH-type steel supports, developed by Toussaint and Heintzmann, that were first used in deep underground mine headings in the 1930s, have recently been used in tunnels as 'yield-control support systems'. However, the sliding capability of the TH steel support allows cross-section contractions. If the amount of convergence cannot be calibrated, reshaping studies have to be carried out at the excavated areas due to the occurrence of time-dependent creeps, especially in swelling and squeezing rocks. This situation increases the project costs and causes significant delays.

There are many support-system analysis techniques, including the convergence–confinement method, the yielding support system, and empirical and semi-empirical support analysis. The Non-Deformable Support System is one such support-system analysis method. It is typically seen as a numerical analysis and although numerical modeling is the key tool of this system, it is not the only one. Although the name of the system gives the impression that there is no deformation in the support system, this is not the case. The system contains some deformation but only to a certain tolerance determined by numerical analyses of the time-dependent deformation behavior of rock masses.

1 INTRODUCTION

Support design is one of the most important issues in tunneling. It is an analysis of process that includes complex 3D components. Correct solutions can only be produced by applying these 3D components with knowledge and understanding (Feng & Hudson, 2010). Bending moment, shear forces and axial forces acting on the supports affect the performance of support systems. The movement of the tunnel face, stresses occurring in front of the face, and the success of precautions for these effects can only be determined by 3D analysis (Aksoy & Onargan, 2010; Aksoy *et al.*, 2012; 2014). Design

of this complex structure in 2D brings many problems. Empirical or semi-empirical 3D solutions, however, take too much time. Numerical methods are the easiest way to perform 3D analysis. There are many methods in numerical modeling, the most popular being finite element (FEM), finite difference (FDM) and boundary element methods (BEM). The principles of numerical modeling are described in Figure 1 (Feng & Hudson, 2010). As can be seen from Figure 1, numerical modeling methods are relatively simple, but at the same time incorporate long-running observations.

It is possible to integrate many parameters (*e.g.* time, material model, failure criteria) into the model in 3D numerical modeling by which probable adverse effects on the support in front of the tunnel face, and in terms of excavation geometry and excavation amount, can easily be analyzed. Machine and operating conditions can easily be integrated into the model and precise analyses can be carried out, especially where tunnels are excavated by tunnel-boring machines (TBMs). In addition, support sensitivity can be analyzed by including the effects of dynamic forces such as earthquake and blast-induced vibration. For squeezing–swelling soil/rock mass, in particular, creeping behavior can be investigated (Barla, 1995), time-dependent deformation of supports can be detected, and early precautions can be provided (Aksoy *et al.*, 2012, 2014). There are many different approaches to support design. The most popular ones are convergence–confinement approaches (Eisenstein & Branco, 1991; Carranza-Torres & Fairhurst, 2000), passive support approaches (Barla *et al.*, 2011; Cantieni & Anagnostou, 2009), probability analysis (Chen *et al.*, 2007), rock-support interaction analysis (Shin *et al.*, 2011), and empirical and semi-empirical analysis (Singh *et al.*, 1995). These approaches have proved themselves in many important

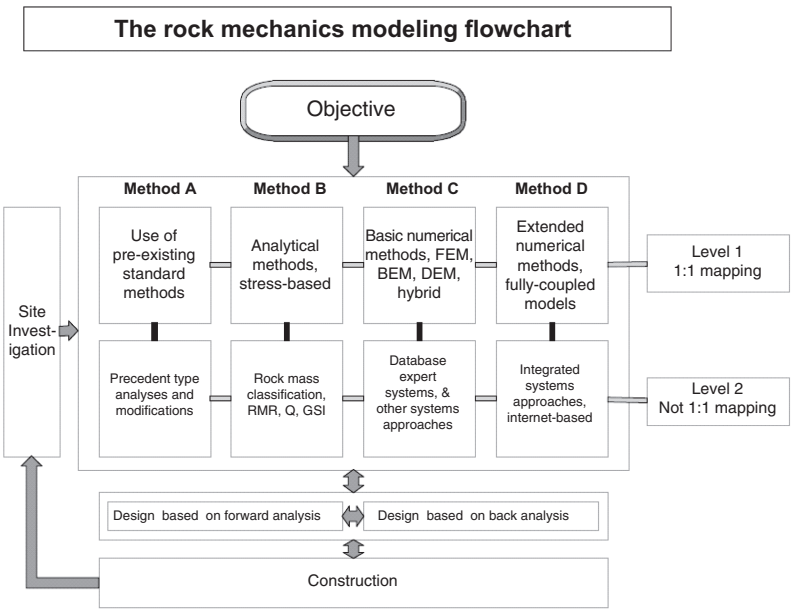


Figure 1 Flow chart of support design modeling (Adapted from Feng & Hudson, 2010).

projects. The Non-Deformable Support System (NDSS), still in the process of being developed, is a method based on numerical modeling.

2 PHILOSOPHY OF THE NON-DEFORMABLE SUPPORT SYSTEM

This section provides a brief introduction to the support design and aims of NDSS.

2.1 Brief introduction to support design

Two meanings for the term 'support' are usually found in a dictionary: first, military structures built for defensive purposes in a war (*e.g.* castles, ditches, ramparts, forts); second, wooden, iron or concrete reinforcement to keep underground cavities in safe and livable conditions. 'Support' has lost its initial meanings with the development of civilization, technology advancement and the development of weapons systems. The most important thing to ensure safety and stability within a desired timescale for the underground openings created during underground activities is an 'appropriate support system'. The basic principle of modern support systems is to help the rock to carry itsown load, instead of carrying the total load of the rock flowing through the openings in the rock.

2.2 Aim of NDSS

The main purpose of the support design is to keep underground openings stable during a given period. The main element in the design is the rock mass excavated. The behavior of the rock mass determines what type of design method should be used. Experience has shown that not every design method demonstrates the same success for a variety of rock mass behaviors, and different design methods should be used for different rock mass behaviors. For example, performing the same support design for a rock mass formed by blocky/disturbed basalt and a blocky claystone rock mass may present problems. The most important issue here is the behavior of basalt and claystone. Basalt is a strong rock and its time-dependent deformation behavior may be very limited. On the other hand, claystone is a weak rock and it occasionally shows high deformation properties. In support design, time-dependent deformation behavior may not be very important for the basalt. However, time-dependent behavior is of great importance both for the material and rock mass of claystone.

NDSS will be of great use at this stage. As previously mentioned, NDSS does not imply 'zero deformation'. Rather, it means, to 'not exceed the amount of deformation determined by analysis'. Time-dependent rock mass deformation parameters form the basis of NDSS. Using these parameters, the amount of deformation of underground openings can be predicted. Methods of 3D numerical modeling are used in these calculations, with the main objective being to solve the adversity of 2D solutions for underground openings because there are additional stresses as a result of the excavation face of underground openings and additional loads caused by these stresses. It is only possible to integrate all these loads to the design with 3D modeling. In addition, face stability is another important part of the design, especially for poor and very poor rock. Analysis of this type of support system in 2D will only define an approach, and not a solution.

3 DIFFERENCES OF THE NON-DEFORMABLE SUPPORT SYSTEM

Many factors, to different degrees, influence the squeezing ground conditions and the precautions taken in those kinds of conditions (Shrestha, 2006). These factors have been identified and recognized in different ways in many studies by researchers as follows: stress condition; strength and deformability of the rock mass; rock type; water pressure and porosity of rock mass; orientation of the geological structures; construction procedures and support systems.

3.1 Support design systems

The rock mass strength and deformability could make a direct contribution to the squeezing phenomenon. In particular, the ratio of rock mass strength to *in situ* stress plays an important role. Hence weak or strongly foliated rock may cause squeezing even when overburden is low. Low rock mass strength gives a low value to the ratio of rock mass strength to *in situ* stress and this causes an overstressing condition. In addition, high deformability gives rise to large deformation. Some of the different approaches proposed by various authors for analysis and support design are described below.

3.1.1 Empirical method

Empirical methods are based on experience and the comparison of different case histories (Shrestha, 2006). There are three approaches in empirical methods: the strength–stress ratio approach; the strain estimation approach; the rock mass classification approach. The Singh *et al.* (1992) approach and the Q-system (Grimstad & Barton, 1993) are examples of empirical methods.

3.1.2 Semi-analytical method

Kovari (1998) and Hoek & Marinos (2000) represent examples of the semi-analytical approaches used for the analysis of tunnel-squeezing phenomena.

3.1.3 Analytical method

The convergence–confinement method is an example of the analytical methods. Carranza-Torres & Fairhurst (2000) provide an example of its application.

3.2 Differences between NDSS and other systems

The support design methods used today contain static calculations that do not take into account the time-dependent deformation behavior of the rock mass. However, weak rocks show significant deformation properties over time as a result of exposure to stresses. In particular, in cases where there is tertiary stress, time-dependent behavior of the rock mass is very important. This is the most common problem in the industry. NDSS examines the time-dependent rock mass deformation behavior and contains dynamic cases in its construction. As a design method based on numerical modeling,

NDSS integrates parameters such as time, variable load and earthquake effect into the model in order to achieve a smooth support design.

The phenomenon is best illustrated with a small example. One of the parameters used in the numerical modeling studies is the rock mass deformation modulus, which is usually calculated with empirical equations. The deformation modulus is actually a parameter that defines the rock mass deformation behavior in numerical modeling, but it has been identified as a fixed value in modeling studies to date. However, we know that the deformation modulus will change as the load increases with time. When it is viewed from other angles, even under constant load, deformation behavior – and thus the deformation modulus – will change due to fatigue of the rock mass. In the example that follows, the formula of Sonmez *et al.* (2006) is used to calculate the deformation modulus (Equation 1).

$$E_{mass} = E_i 10^{[((RMR-100)(100-RMR)/4000 \quad \exp(-RMR/100))]} \tag{1}$$

In this case, a single value is used. This value includes the results of a deformability experiment conducted on a rock sample subjected to constant load (Figure 2). This value is the slope of the tangent of the curve obtained from deformability experiments.

The slope of the tangent at the beginning or at any specific time of the experiment will have an effect (see Figure 3). Therefore, the use of a single value of deformation modulus significantly limits the parameters in the analyses. NDSS eliminates this limitation. The empirical correlation evaluates the data obtained by deformability experiment within the concept of NDSS and accommodates the time-dependent change of the rock material and rock mass. Thus, NDSS is a support design method that integrates this function. The empirical equation used in the example above can be rewritten in the following manner (Equation 2).

$$E_{mass} = f(E_{i(t)}) 10^{[((RMR-100)(100-RMR)/4000 \quad \exp(-RMR/100))]} \tag{2}$$

NDSS is a design method based on 3D numerical modeling. This method not only serves the same purpose as other methods, but also takes into account the many complex parameters involved in support design.

Axial load	Axial Stress	Lateral Strain	Axial Strain
F	$\sigma = (F/A) \times 10^{-3}$	ε_1	ε_2
(kN)	(Mpa)	($\times 10^{-4}$)	($\times 10^{-4}$)
0.00	0.00	0	0
5.23	1.66	–7.91	92.02
8.02	2.55	–20.93	120.13
10.01	3.18	–22.61	140.32
14.42	4.58	–25.57	170.12
16.03	5.09	–28.24	190.14
17.16	5.45	–32.35	193.98
20.23	6.43	–40.89	213.19
25.54	8.11	–60.01	290.92
30.34	9.64	–75.97	320.23
51.03	16.21	–123.12	445.54

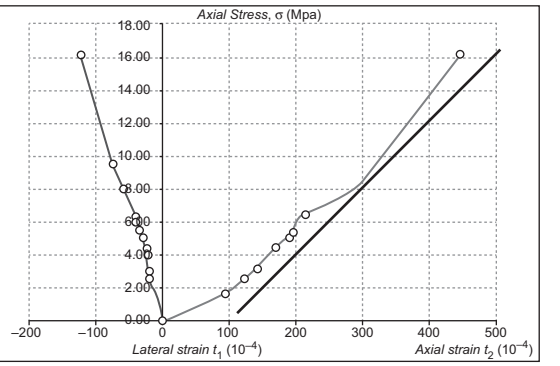


Figure 2 Sample of deformability test results.

Axial load	Axial Stress	Lateral Strain	Axial Strain
F	$\sigma=(F/A)x10^{-3}$	ε_1	ε_2
(kN)	(Mpa)	$(\times10^{-4})$	$(\times10^{-4})$
0.00	0.00	0	0
5.23	1.66	–7.91	92.02
8.02	2.55	–20.93	120.13
10.01	3.18	–22.61	140.32
14.42	4.58	–25.57	170.12
16.03	5.09	–28.24	190.14
17.16	5.45	–32.35	193.98
20.23	6.43	–40.89	213.19
25.54	8.11	–60.01	290.92
30.34	9.64	–75.97	320.23
51.03	16.21	–123.12	445.54

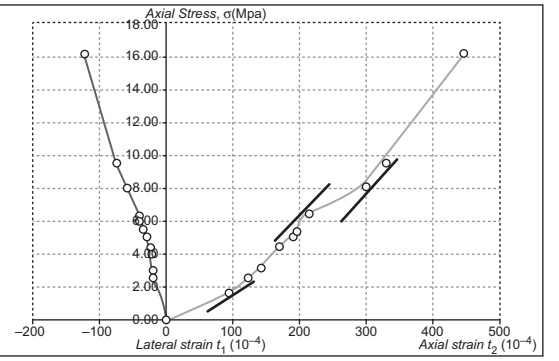


Figure 3 Time-dependent rock elasticity modulus lines that NDSS considers.

Any kinds of support elements and ground improvement methods may be a part of this design. In other words, it is possible to incorporate all the required elements for excavating a tunnel with a desired cross-section in any rock mass. The success of this system is valid for both conventional and mechanized tunnels. There is also the opportunity to integrate the operations in mechanized tunnels, which use TBMs, into the model.

Thus, well-defined rock mass behavior, time-dependent deformation behavior of the rock mass, and integration of excavation machine properties are all usual in this system. Significant advantages will be achieved in the opening of tunnels within very complex geological conditions. In addition, incorrect segment selections in the mechanized tunnels can be prevented by the results of correct calculations. The system also provides suitable TBM selection, especially for squeezing and swelling rocks.

One major part of NDSS, different from other methods, is its consideration of the effects of blasting on the rock mass and support performance. Other support design methods take into consideration blasting effects with a disturbance factor, which is in the empirical formula for calculating the parameters. In NDSS, however, the disturbance factor is accepted as '1' so that controlled blasting is predicted. The duration of vibration amplitudes at dominant frequencies, their effects on the support, and the resultant weakening of rock mass are all integrated into the NDSS model using actual data.

Although mechanized excavation is preferred in weak/very weak rock conditions, integrating the blasting effects in strong rock mass conditions within the NDSS model confers an additional advantage.

4 GEOTECHNICAL EVALUATION OF SWELLING AND SQUEEZING ROCKS

Swelling and squeezing are actually different from each other. However, the two continuously mix with each other. A volume increase is realized in swelling, but this is not the case in squeezing. On the other hand, the shear strength is typically exceeded in squeezing but this is rarely the case in swelling. Rocks are sensitive to the air causing

changes of water content. If there are clay minerals, anhydride or pyrite in the rocks, swelling occurs due to physico-chemical reactions in the environment involving water.

Swelling can be observed in rock or soil. The swelling process of rock masses can be examined in terms of subgroups: swelling of intact rocks, swelling of fault gouge and fillers in the discontinuities, and swelling of a combination of all of these.

Swelling rates and durations exhibit discrepancies over a wide range. For example, swelling rates in tunnel invert heave can differ by one meter or more per month (Einstein, 1994).

There are many difficulties in providing consistent estimates at the design stage of tunnelling in squeezing conditions. Such conditions are not easily projected during the excavation stage, when faced with specific geological formations that incorporate squeezing problems. Because rock heterogeneity and variations in the mechanical and hydraulic properties of the rock mass strongly affect the squeezing conditions, those conditions may vary even over a short distance. Therefore, the selection of the proper excavation construction method, that is, mechanized versus conventional tunneling, is highly challenging and requires great experience of squeezing problems. The fixed geometry and restricted flexibility of TBMs restrict the permissible space in which to accommodate ground deformations. However, to allow for large deformations a substantially greater profile can be excavated initially in conventional tunnelling. The conclusion to be drawn here is that, when serious squeezing conditions are anticipated in deep tunnels, conventional tunneling gives better performance than mechanized tunneling.

Although a slow rate of advance occurs in conventional tunneling within squeezing rocks, excavations continue – even in severe squeezing conditions – in those instances where face works are well-planned and suitable stability measures are taken. Mechanized tunnels, however, do not show tolerance to adverse effects; the excavation may be delayed and in many cases may come to a complete stop. Recent innovative technological developments have provided some methods to increase the rate of advance in conventional tunneling.

The rock mass properties, the geological and geotechnical conditions, the *in situ* state of stress relative to rock mass strength, the groundwater flow and pore water pressure all strongly affect the magnitude of tunnel convergence, the rate of deformation, and the extent of the yielding zone around the tunnel. Squeezing is therefore equivalent to yielding and time-dependence, and is often largely dependent on the excavation and support techniques being used. In cases in which the support installation is delayed, the rock mass moves into the tunnel and a stress redistribution occurs around it. However, in cases where the deformation is restrained, squeezing will lead to long-term load build-up on the support system. One of the most problematic situations during tunnel excavation is the squeezing behavior of rock mass. For many years, engineers have faced many difficulties in completing underground works during tunnel excavation. Squeezing problems may cause major delays in construction schedules and cost over-runs, and great effort should therefore be given to overcome this situation.

It is very difficult to prepare a tunnel project because of the complexity of the geometry, the load above, and the properties and interaction of rocks and support materials. The tunnel excavation must, therefore, be designed to ensure safety in the supports and minimum cost. The underground excavations in weak rock masses present great difficulties during tunneling. The stability of the tunnel scheduled to

open in such an environment should be examined by the use of detailed geological engineering studies in the design phase. Many researchers into the determination of the stability of underground excavation (Singh *et al*., 1992; Barla, 1995; Goel *et al*., 1995; Hoek *et al*., 1995; Bhasin & Grimstad, 1996; Carranza-Torres & Fairhurst, 2000) have proposed empirical equations and developed new numerical analysis methods thanks to rapid advances in computer technology such as FEM, FDM, BEM and the discrete element method (DEM).

The term 'squeezing rock', originating from the early days of tunneling though the Alps, refers to the decrease of tunnel cross-section when a tunnel is being advanced. The International Society for Rock Mechanics (ISRM, 2007) has defined squeezing rock and the mechanism that 'squeezing of rock' represents as large time-dependent convergence during tunnel excavation. This takes places when induced stresses and a particular combination of material properties causes yielding in some zones around the tunnel, surpassing the limiting shear stress at which creep starts. Deformations may either stop during construction or continue over a long period of time (Shrestha, 2006).

When an underground opening is excavated, the existing stress regime is disturbed and the stresses which cannot pass through the opening redistribute themselves around the tunnel opening (Bray, 1967; Panthi, 2006). Knowing that weak rocks such as shale, slate and phyllite, as well as weakness/fracture zones, behave very differently from isotropic and stronger rocks when subjected to tangential stresses, one can explain the concentration of the stress along the contour of the opening. In these kinds of weak rock mass, when the strength is less than the induced tangential stresses along the tunnel periphery, gradual formation of micro-cracks along the schistosity or foliation plane will take place. Thus, a viscoplastic zone of micro-fractured rock mass is generated deep into the walls. As defined by the ISRM, squeezing is time-dependent deformation, essentially associated with creep caused by exceeding a limiting shear stress. To predict the rock failure due to creep, the complete stress–strain curve can also be used. Figure 4 illustrates the horizontal line which is the locus of a creep test in a stress–strain graph. If the initial stress in the rock

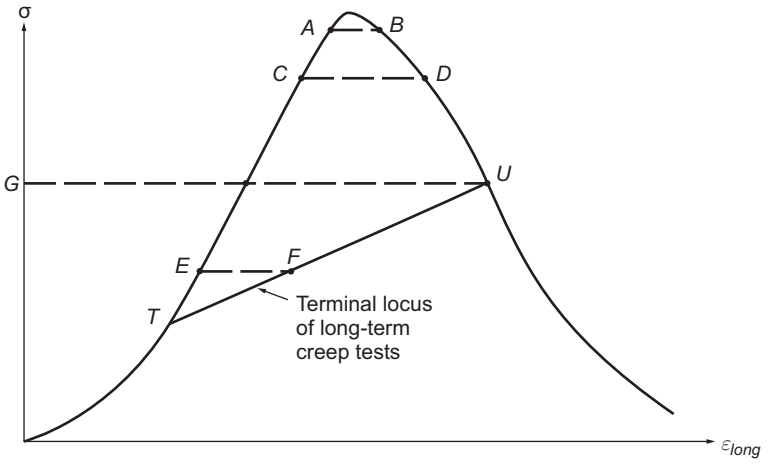


Figure 4 Creep in relation to the complete stress–strain curve (Goodman, 1989).

is close to the peak load, any creep will terminate in rupture when the accumulated strain intersects the falling part of the complete stress–strain curve.

Swelling behavior depends on the presence of water and air in the environment and on the mineral content of the rock. In general, the time-dependent swelling behavior of a rock is determined as given in Figure 5.

Squeezing, however, is actually a creep behavior. In the literature, momentary squeezing, creep-dependent squeezing and time-dependent squeezing behavior are expressed as in Figure 6 (Panthi, 2006).

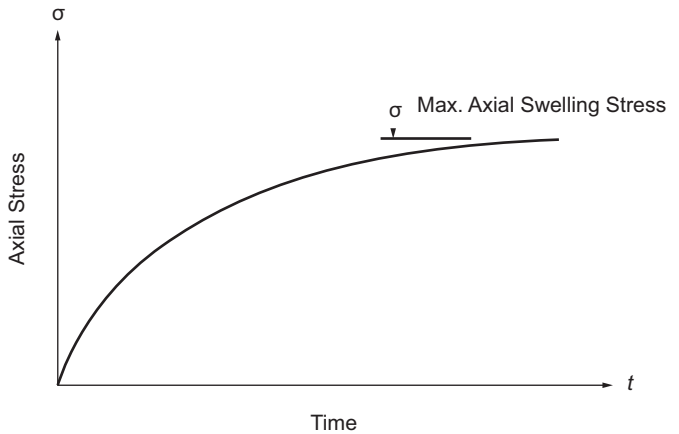


Figure 5 The time-dependent swelling behavior determined by oedometer test (Einstein, 1989).

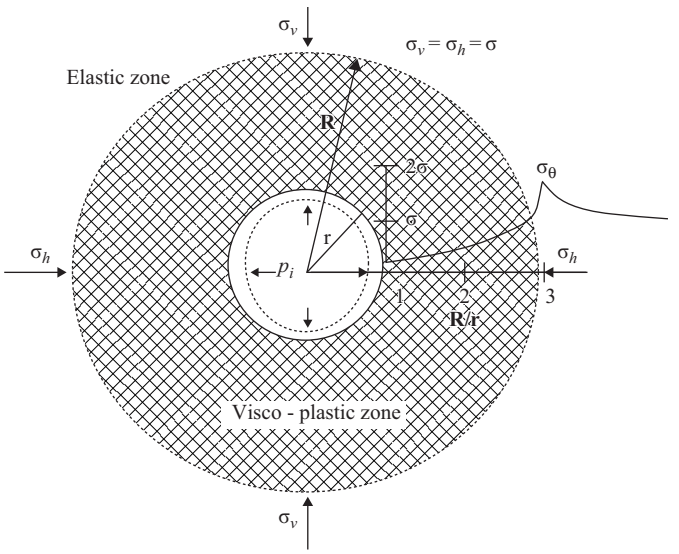


Figure 6 Squeezing behavior in a circular opening (Panthi, 2006).

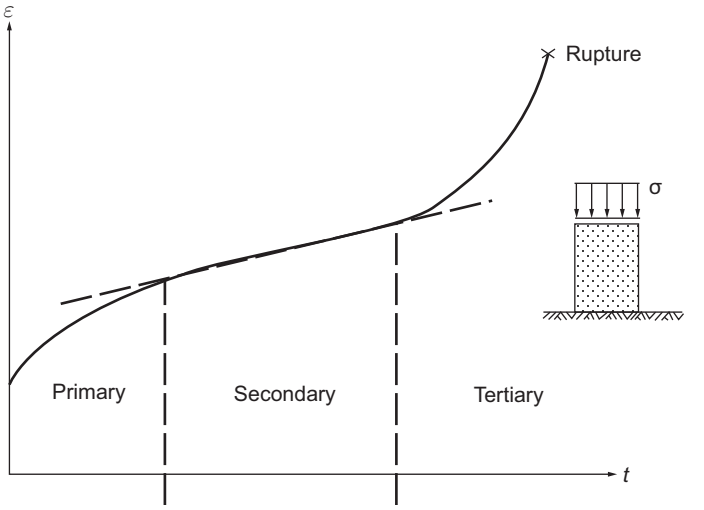


Figure 7 Creep behavior of rocks and the creep regions (Goodman, 1989).

To predict the rock failure owing to creep, the complete stress–strain curve is also valid. Figure 7 illustrates the creep behavior of rocks.

As Figure 7 implies, at first, rapid deformation occurs in the time-dependent deformation stages. This part is called the primary creep region. The amount of deformation over time is slower in the secondary creep region. Rocks are tired in this process. In the tertiary creep region, the deformation rate increases and rocks are moving to failure.

As already mentioned, swelling and squeezing are different phenomena. A volume increase is seen in swelling due to the presence of air and water, depending on the mineral composition of the rock. This is not the case in squeezing, in which there is a time-dependent deformation under constant load.

In swelling, the more clay minerals, anhydride or pyrite in the rock, the more the increase in volume. However, in squeezing, the rock structure and the amount of load applied is more important. When the load increases, shorter creep stages and faster failure are observed.

5 IMPORTANCE OF NUMERICAL MODELING IN ANALYSING SWELLING AND SQUEEZING ROCKS

5.1 Strategy of NDSS

Different methods can be used in the support design of underground openings. Experimental methods, geology and soil definitions, empirical classification methods and numerical modeling methods incorporate all of those methods that can be listed as contributing to rock mechanics design. Stille & Palmstrom (2003) describe their interaction in the form of a simple algorithm as shown in Figure 8.

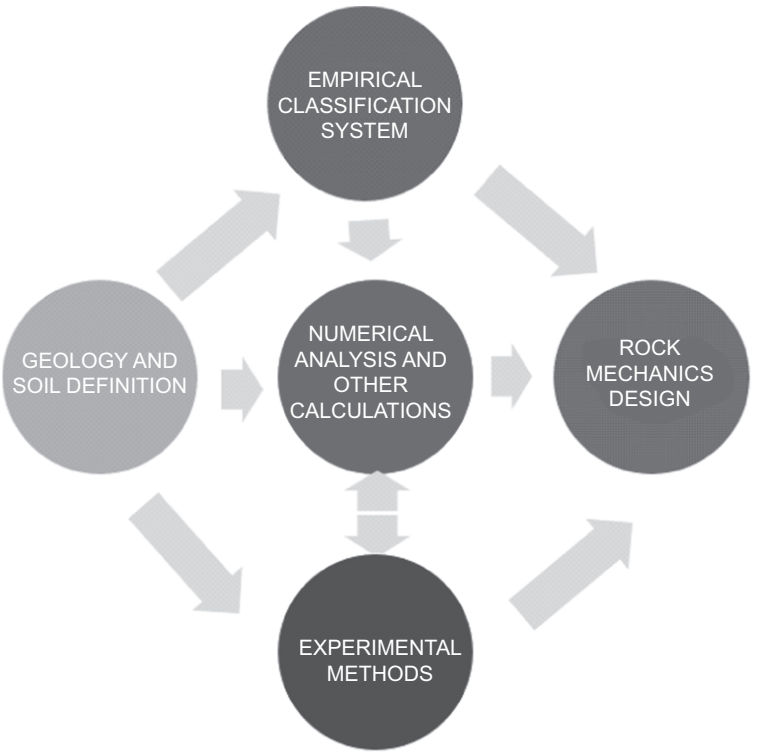


Figure 8 Rock mechanics design algorithm (Stille & Palmstrom, 2003).

At least two methods should be applied in any design work. The aim is to anticipate possible errors and make the design more realistic. It should be noted that in any of the design methods, the experience of the designer is very important.

Underground openings have a very complex structure. A complex systems including geological units, excavation geometry, excavation rate, the support elements and the support systems are all designed. Numerical models have the ability to accommodate solutions in which all those elements are integrated.

The most widely used numerical methods today are continuous methods (FDM, FEM & BEM), discontinuous methods (DEM and the discrete fracture network method), hybrid methods (hybrid FEM/BEM, hybrid FDM/DEM, hybrid FEM/DEM), and other hybrid models.

The primary reason for the difficulties in the modeling of rock mass is the prediction of its physical and engineering properties, rather than the definition of the rock mass through a production process.

It should be noted that rock mass classification systems are not final design tools. Rock mass classification systems should be used as a preliminary design tool. The performance of the support design generated by these systems must be analyzed with a more sophisticated method. Numerical modeling is one such advanced method. NDSS is a design method based on numerical modeling and incorporates the rock mass classification systems and experimental studies. As previously mentioned, the NDSS

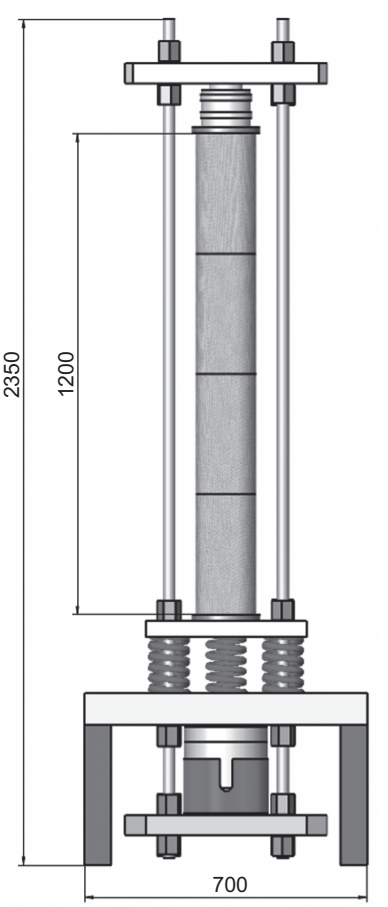


Figure 9 Servo-controlled deformation measurement apparatus (BESMAK, Turkey).

strategy, unlike that of other methods, has been based on the time-dependent deformation behavior of the rock mass. Another difference of NDSS from other methods is its ability to describe dynamic events (*e.g.* blasting, earthquake) in the model by defining them with formulas. These formulas can be used as input data to any software in the form of a '.dll' file.

Alternatively, the time-dependent deformation behavior of rock material can be obtained from servo-controlled deformation measurement test apparatus (see Figure 9) and can be used in the formulas to define rock parameters.

5.2 Decision of the parameters and definition of the true yielding criterion

A numerical modeling method is obliged to include field and laboratory measurements, observations and experiences in its body. This means that the raw data obtained from the field and the laboratory is available for use in empirical formulas and engineering

judgments. One of the most important elements in numerical modeling are the parameters. These parameters are expected to fully represent the rock mass and, therefore, one needs to be very sensitive in their selection.

Another principal topic in numerical modeling is the representation of the rock mass failure mechanisms. Many failure mechanisms can be identified in the existing software. For different rock masses, it is necessary to work with different failure mechanisms. For example, when working in a rock mass containing soft clay, the Mohr–Coulomb model should be used in the deformation and failure model, and when working in a strong and blocky rock mass, the Jointed Rock Mass model should be preferred. However, it should be remembered that the time-dependent deformation behavior of the rock mass is the main element of NDSS.

5.3 Importance of the results review

Field studies, observations and measurements, laboratory studies and the data bank formed after all those calculations are the main sources for NDSS. The results obtained after defining the geometry of underground openings, excavation size, shape, etc. must be examined in detail. This analysis requires significant experience for successful completion.

After modeling studies the time-dependent deformations in underground openings are examined. Thereafter, the support elements, which will withstand these deformations (depending on the type and geometry of excavation) are selected. Afterwards, interaction of the selected support elements with each other and with the rock mass are examined. At the end, all systems are integrated into the model and analysis is performed. After the final solutions, the performance of the support system is examined.

6 SUPPORT DESIGN PHASES OF THE NON-DEFORMABLE SUPPORT SYSTEM

The newly developed NDSS is a method based on 3D numerical modeling. This method, while serving the same purpose as other methods, also takes into account the many complex parameters involved in support design. Tunneling processes are 3D operations. In all three dimensions there are a number of changes and associated effects. A support design that only considers such effects immediately around the tunnel brings problems. Furthermore, the displacement occurring in the tunnel face varies for each rock mass. It is not appropriate to evaluate the displacement in the tunnel face on the basis of existing assumptions. Consideration of the 3D changes for the defined rock mass and tunnel sizes will give us more accurate results. The first step in this system is characterizing and interpreting the soil/rock mass and integrating them into the numerical model in the correct way. In this step, underground water and its fluid behavior can also be defined. This stage requires vital experience. The second step is to define the behavior of the rock mass in which the tunnel is to be excavated (using Hoek–Brown, Mohr–Coulomb, Soft Soil Creep, Hardening Soil and Jointed Rock Mass models as appropriate). This step, defining the behavior model of the rock mass and determining the time-dependent deformation characteristics of the rock mass, is the most critical

one. The difference between NDSS and other methods is that its working principle is based on the definition of time-dependent deformation of rock mass. The part of this method that is still being developed relates to the determination of time-dependent deformation behavior for different soil/rock masses. The third step in NDSS is to define the excavation geometry and support systems, and to integrate pre-determined *in situ* measurements to the model. From this point onwards, the capability of the software used takes on more significance. Figure 10 illustrates the stages of NDSS.

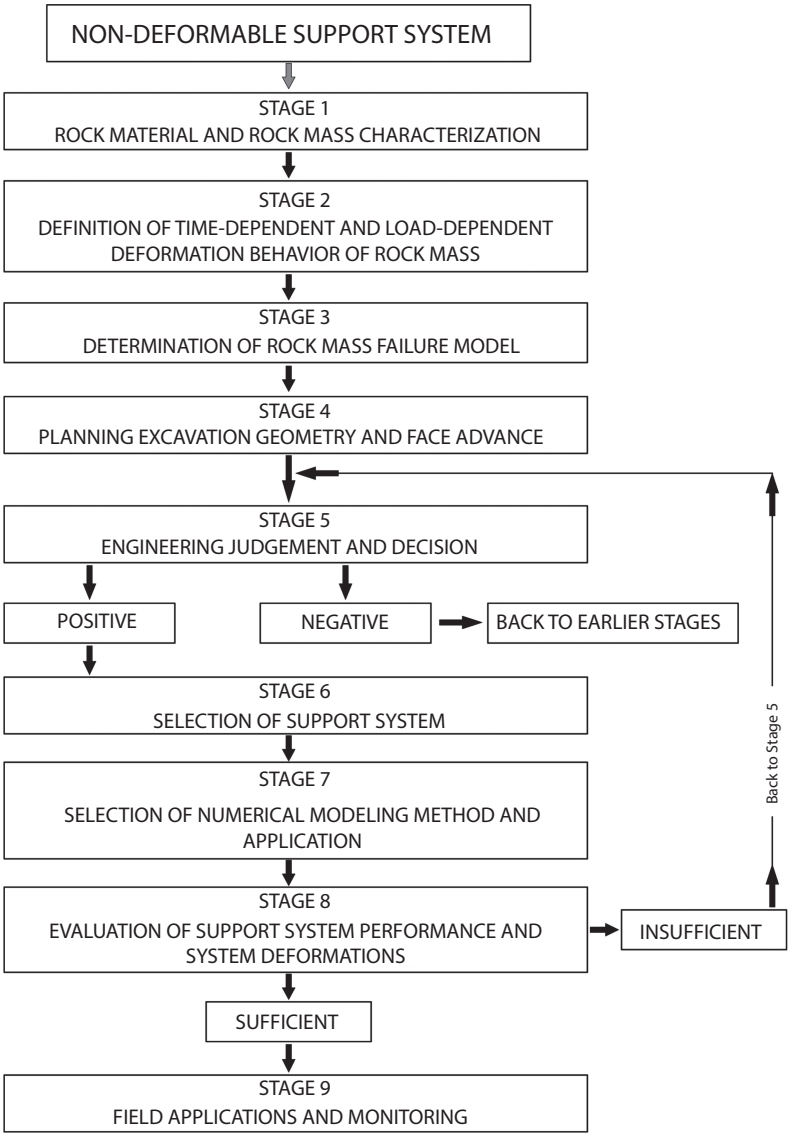


Figure 10 The stages of NDSS.

7 CASE STUDIES

Two case studies are outlined in this section. The first is the tunnel project of the Ankara–Istanbul High-Speed Railway project and the second is the support analysis of air inlet and outlet galleries for the Imbat Mining Company.

7.1 T-13 tunnel of the Ankara–Istanbul High-Speed Railway project

The objective of the Ankara–Istanbul High-Speed Railway project is to reduce the travelling time between Turkey's two largest cities, Ankara and Istanbul, and to increase the overall percentage of railway usage by creating a fast, comfortable and safe transportation facility. The route between Ankara and Istanbul is 576 km in length and all of it is electrified and signalized. When the project finishes, an electrified, signalized, two-line railway will have been constructed and the route from Ankara to Istanbul will shorten to 533 km. The current travelling time of 7 hours will reduce, with the 250 km/h speed of the train, to around 3 hours.

7.1.1 Geological and geotechnical conditions of the T13 tunnel

The T13 tunnel is planned to be 3580 m in length, starting at location 175 + 240 km and finishing at location 178 + 820 km. There are four main groups of rocks in this tunnel. Information about the rock formations passed in the T13 tunnel is given in Table 1. As illustrated in the table, both swelling and squeezing rocks are being excavated in the T13 tunnel.

Table 1 Geological and geotechnical definitions of the T13 tunnel.

Location (km)	*Lithology*	*Geotechnical information*
175 + 240 – 176 + 550	Graphite – schist	Grey/dark grey, often/very often jointed schistosity planes, slippery, shiny, partially disintegrated, weak/very weak, chlorite schist and greys in upper parts. (Squeezing condition)
176 + 550 – 177 + 900	Claystone – siltstone	Red, red/brown/greenish-black, grey often jointed, partially disintegrated, weak/medium strength, joints are open-close, slightly rough, wavy, clay and calcite fillings. (Swelling condition)
177 + 900 – 178 + 500	Brecciated limestone – gravelstone – sandstone	Grey-colored, coarse-grained, medium/rare jointed, medium/thick layered, slightly disintegrated, very strong and competent. Joints are rough, wavy, densely coated, calcite and clay fillings partially.
178 + 500 – 178 + 820	Gravelstone – sandstone – mudstone – claystone – siltstone	Yellowish/light brown, grey/greenish-grey, close-jointed, thin/medium layered, low/medium grade weathered, hard, high/medium strength. Joints are open, wavy, rough, colored with manganese oxide, and include clayed embankment in places.

(Adapted from Aygar *et al.*, 2010; Aksoy *et al.*, 2014)

Table 2 Laboratory test results.

Test	*Sample 1*	*Sample 2*	*Sample 3*
Elasticity modulus (Mpa)	1,240	1,199	870
Poisson's ratio	0.15	0.25	0.27
Liquid limit	56	65	187
Plastic limit	17	38	30
Plasticity index	39	27	157
Natural unit weight (kN/m^3)	22.84	19.12	19.63
Dry unit weight (kN/m^3)	20.69	14.67	15.57
Porosity (%)	20.70	44.19	40.09
Void ratio	0.26	0.79	0.67
Cohesion (kPa)	579	95	484
Internal friction angle (°)	19	18	0

(Adapted from Aygar *et al.*, 2010; Onalp & Yakut, 2010)

7.1.2 Laboratory tests on the samples from the T13 tunnel

The most important parameters of concern to rock engineers when designing support systems in highly deformable rocks are the swelling and squeezing indices of the rock, the liquid limit, the plastic limit, the plasticity index, cohesion, the friction angle, the elasticity modulus without drainage, and the porosity. Swelling index, squeezing index, and creep index are needed to determine creep behavior during tunneling works. Calculation of these indices and other necessary parameters will be outlined in the next section. The Atterberg limits, tri-axial tests, elasticity modulus and Poisson's ratio measurements and consolidation tests were conducted on samples taken from the T13 tunnel face. Information about these tests is given in Table 2.

7.1.3 Problem definition

During tunnel excavation, convergences of up to 63.4 cm occurred over time in the area of smectite group clays and high-deformable formations in the T13 tunnel. The most significant reason for this was that the elapsed time for closing the support ring was so long. As a result of this, reshaping works were necessary because these convergences were outside tunnel tolerances. Examples of deformations prior to the application of reshaping at the T13 tunnel are shown in Figure 11, and time-dependent vertical convergence measurements are illustrated in Figure 12.

7.1.4 Numerical modeling for NDSS with the soft soil creep model (modified cam-clay model)

Reshaping following these types of deformations in tunnel construction is extremely expensive and time-consuming. Analysing a non-deformable system for a support design in the same formation is therefore considered a fundamental requirement. Numerical modeling in 3D is the most convenient tool for partial excavation support analyses in formations which have high deformability properties (Aksoy & Onargan, 2010).

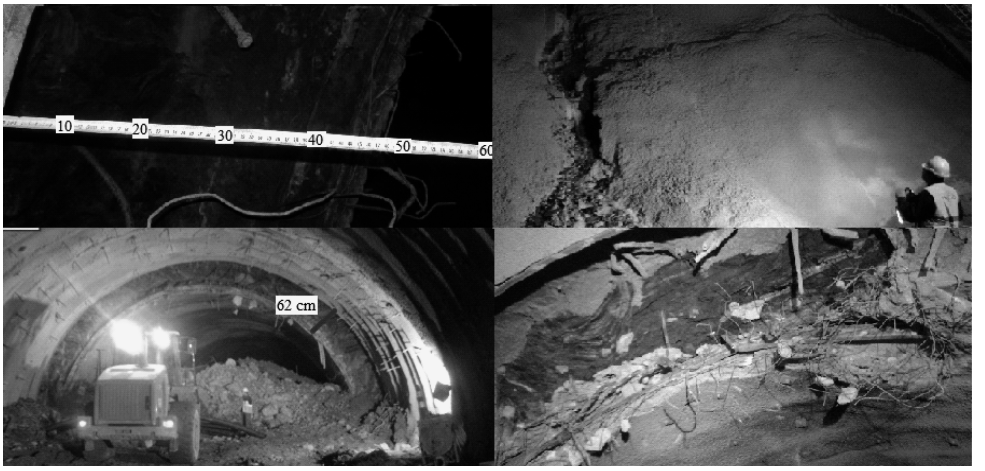


Figure 11 View of the deformed T13 tunnel.

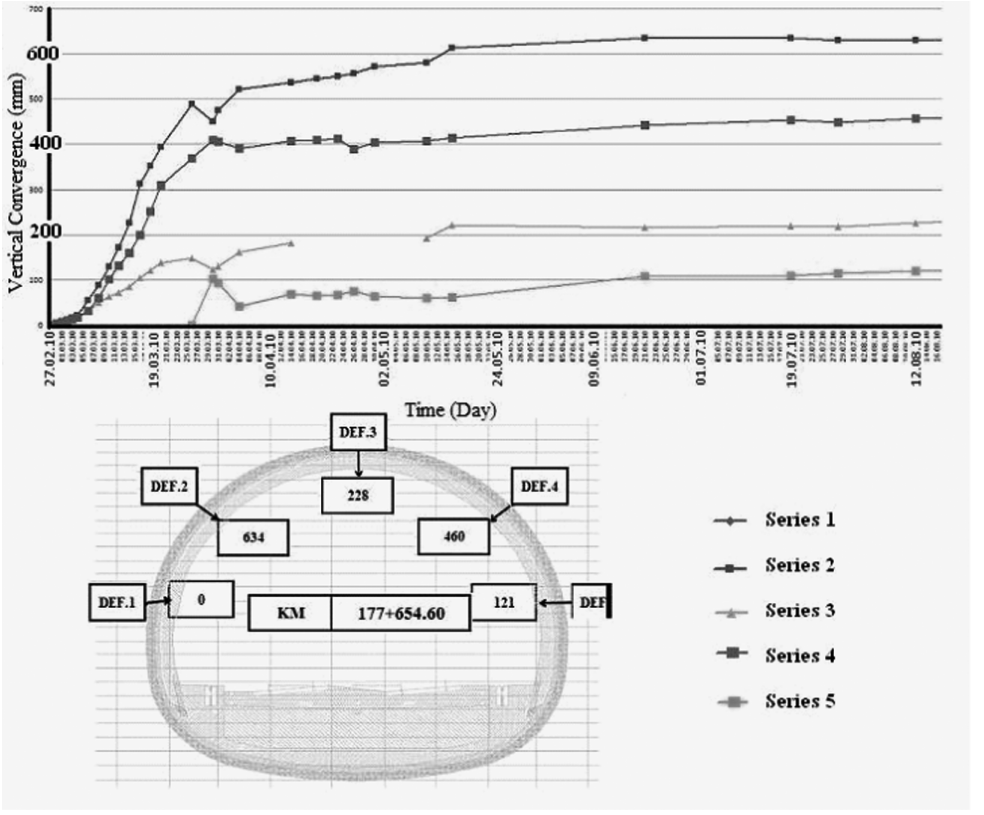


Figure 12 Time-dependent convergence measurement in T13 tunnel.

Table 3 NDSS and element properties.

Support element	*Properties*
Steel support	I-200 Profile (1 m)
Shotcrete	40 cm
Bolt	IBO (l = 8 m and 1×1 m)
Pipe	6 m (2 inches, overlap = 3 m)
Top heading temporary invert	40 cm
Face bolts	10 unit (12 m, overlap = 3 m)
Face shotcrete	10 cm
Invert concrete	3.15 m

(IBO: injection bore)

As mentioned above, high-deformable rocks are supposed to be represented within the Soft Soil Creep model (Modified Cam-Clay model). In this model, there must be Mohr–Coulomb parameters: cohesion, internal friction angle and dilatation angle. However, it is not possible to define the model with these parameters alone. For this reason, parameters representing the swelling and squeezing properties of the rock must be integrated into the model too. The Soft Soil Creep model includes all of these parameters.

The field studies (drilling, geotechnical investigations, etc.) and the designed support system elements, which were used for analysing a higher performance support system to address this problem, are illustrated in Table 3.

The main objective in developing this numerical model is the examination of the performance of the support system which must apply to the time-dependent creep properties of the rock. For this purpose, the numerical analysis was applied to a period of 816 days. Of this time, 700 days represent the full length of the development, and the remaining time includes the excavation and support stages. The integrated construction stages are as follows:

1. Installing the model
2. Reset displacement to zero
3. Defining the excavation of tunnel, steel pipe, temporary invert, face bolts, invert concrete, face concrete and injection bore (IBO) bolts
4. 1 m crown advance
5. Applying the support of crown
6. 1 m crown advance
7. Applying the support of crown
8. 1 m bench advance
9. Applying the support of bench
10. 1 m bench advance
11. Applying the support of bench
12. 1 m invert advance
13. Applying the support of invert
14. 1 m invert advance
15. Applying the support of invert
16. Applying 2 m invert concrete

This study includes the works in the T13 tunnel in the Eskisehir–Köseköy part of the Ankara–Istanbul High-Speed Railway project. This tunnel, which is located in clay containing a high percentage of oil, is one of 39 tunnels on this line. Time-dependent numerical modeling of the support systems in this tunnel was performed and the results were compared with *in situ* measurements. The following was used as a support system: steel I-200 support in every 1 m; 40 cm shotcrete; IBO bolt (length = 8 m; pattern:1×1m); steel pipe 6 m in length and two inches in diameter (overlapped by 3 m); 40 cm temporary invert; face bolt 12 m in length (overlapped by 3 m); 10 cm shotcrete to the face; 3.15 m concrete to the invert. The model was resolved using the Soft Soil Creep model and the results are shown in Figure 13. While the model results indicated deformations of 4.813 cm, the observed deformation was 7.8 cm.

7.2 Support analysis of air inlet and outlet galleries of the Imbat Mining Company

Longwall top coal caving is one of the methods used in thick coal seams. In coal mines where this method is used, some coal is left in place to be retrieved later in order to prevent damage to the main galleries. Stresses and strains created by roof layer caving of the panels advancing toward each other may put pressure on the main galleries. The amount of this pressure increases with time-dependent consolidation of roof layers. The sizes of the safety pillars gain importance in order to prevent this pressure and thus avoid damage to the supports of the main galleries. In this research, great deformations creating damage to the supports of the main galleries of the Imbat Mining Company were examined. Time-dependent deformation amounts were investigated both *in situ* and with time-dependent numerical modeling analysis (Aksoy *et al.*, 2015).

7.2.1 Problem definition

The main galleries serving both the D1 and D2 panels are located 25 m above the coal seam. These galleries are also used for the purpose of ventilation. Therefore, deformations in these galleries (see Figure 14) not only cause an increase in ventilation costs but also negatively affect the ventilation quality and coal transportation efficiency. When investigating the reasons for these deformations, the first topic of interest is the stage of the production at which support damage started.

In the scope of this research, time-dependent numerical modeling analysis was used in order to determine the sizes of the safety pillars. First, rock and rock mass properties were determined. Table 4 shows the rock mass parameters used in the numerical modeling.

Numerical modeling analysis using PLAXIS 3D TUNNEL V2 software (Plaxis, The Netherlands) was undertaken to predict the deformations due to caving in the Imbat Mining Company's Soma-Eynez underground coal mine. The size and production periods of the D1 and D2 panels were integrated into the model. A general view of the model is shown in Figure 15.

A total of 739 days of production progress of the D1 and D2 panels were integrated into the model. The time-dependent 3D numerical modeling analysis stages achieved for the production are listed below:

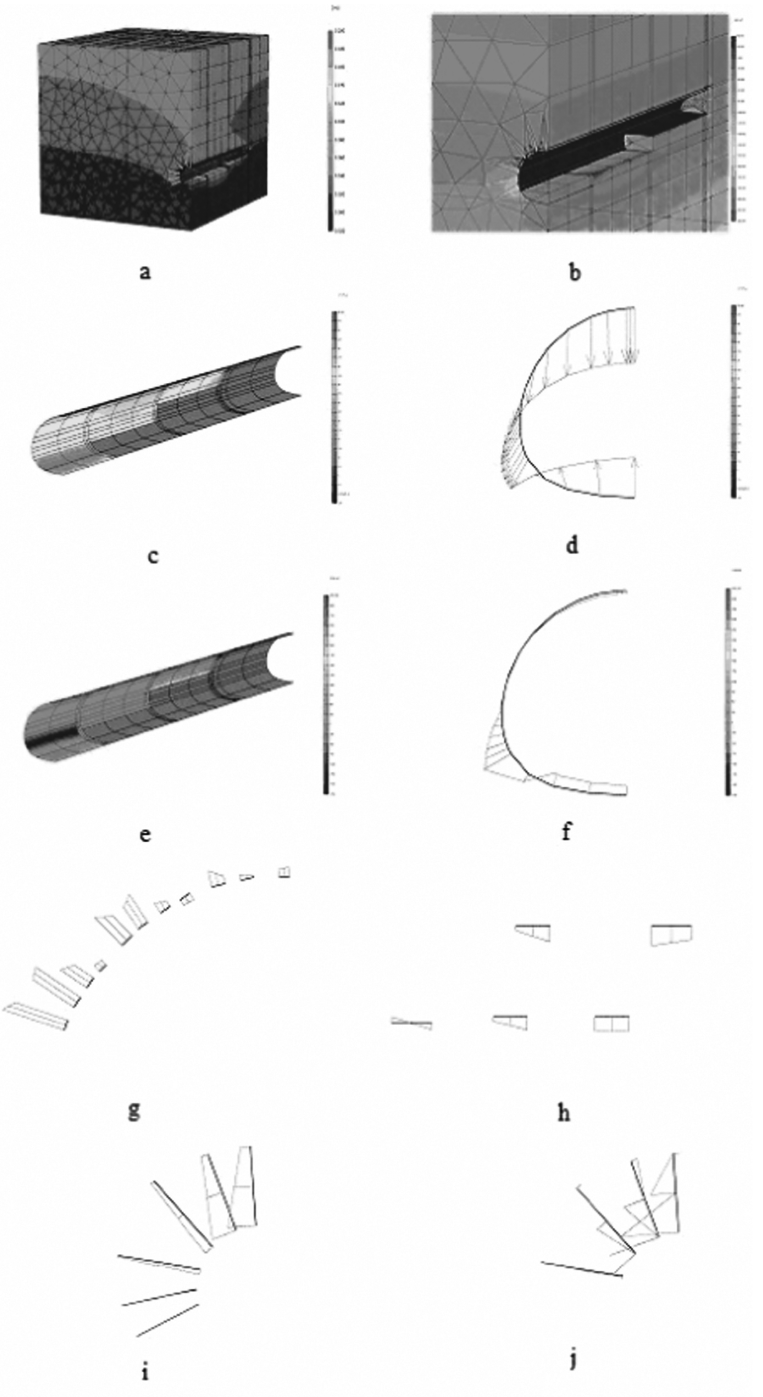
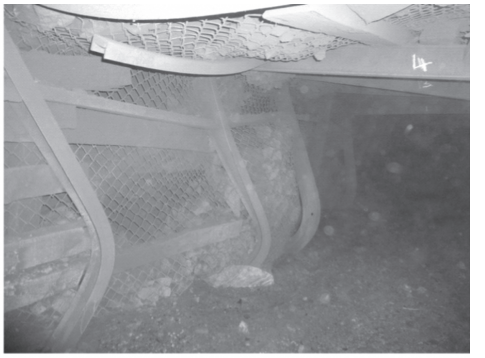


Figure 13 View of the results of numerical modeling studies: (a) total deformation; (b) total stress; (c) and (d) total deformation in the supports; (e) and (f) bending moment on the supports; (g) axial forces on steel pipes; (h) axial forces on face bolts; (I) axial forces on bolts and (j) shear forces on bolts (Adapted from Aksoy *et al*., 2012).



(a) before 60 m distances between D1 and D2 panel



(b) wall damage on right side main gallery after 60 m distance between D1 and D2 panels



(c) wall damage on left side main gallery after 60 m distance between D1 and D2 panels



(d) roof damage after 60 m distance between D1 and D2 panel

Figure 14 Support damage in the main galleries.

Table 4 Rock mass parameters used in numerical modeling.

Formation	*Elasticity modulus (E_i) (MPa)*	*Deformation modulus (E_k) (MPa)*	*Poisson ratio (v)*	*Density (kg/m^3)*	*Cohesion (MPa)*	*Internal friction angle (^{0})*
Marl (P2AB)	3,000	84.67	0.30	1,900	0.124	6.14
Limestone (P2)	23,000	4,925.23	0.24	2,650	3.600	27.47
Shale and claystone (P1)	5,000	609.12	0.33	1,900	1.022	15.90
Coal (KM3)	1,500	42.34	0.35	1,700	0.163	9.32
Marl (M3)	14,000	1,705.55	0.27	2,100	0.921	19.53
Marl (M2)	10,000	898.26	0.30	1,950	0.619	16.24
Coal (KM2)	2,000	223.60	0.33	1,650	0.436	12.94
Marl (M1)	15,000	2,450	0.25	2,200	0.885	19.58
Fractured zone	–	210,000	0.30	21	0.300	20.00

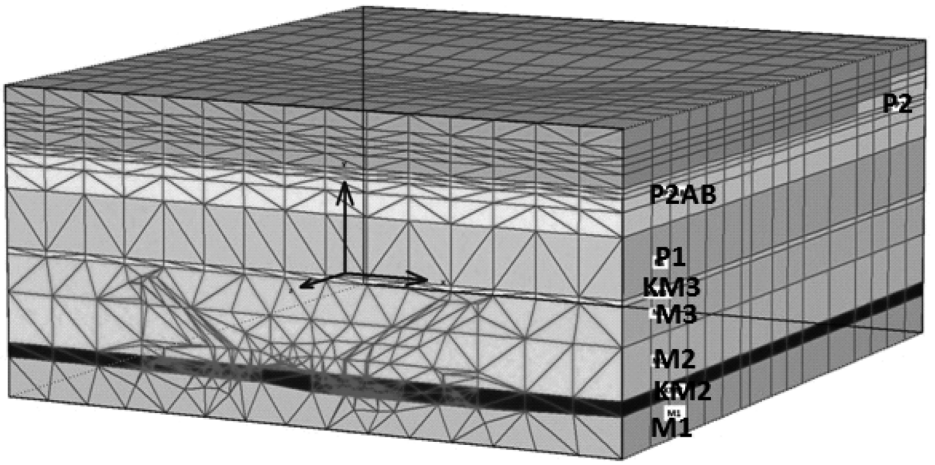


Figure 15 3D view of the model (labels reflect formations in Table 4).

1. Initial version of the model
2. Identification of the inlet and outlet ventilation galleries
3. Formation of the first three production faces at the D1 panel: t = 90 d, $\sum t = 90$
4. Formation of the first three production faces at the D2 panel: t = 90 d, $\sum t = 180$
5. The case in which the distance between the D1 panel and the safety pillar is 100 m: t = 260 d, $\sum t = 440$
6. The case in which the distance between the D1 panel and the safety pillar is 60 m: t = 90 d, $\sum t = 530$
7. The case in which the distance between the D2 panel and the safety pillar is 100 m: t = 61 d, $\sum t = 591$
8. The case in which the distance between the D1 panel and the safety pillar is 20 m: t = 30 d, $\sum t = 621$
9. The case in which the distance between the D2 panel and the safety pillar is 60 m: t = 30 d, $\sum t = 651$
10. The case in which the D1 panel affects the safety pillar: t = 13 d, $\sum t = 664$
11. The case in which the distance between the D2 panel and the safety pillar is 20 m: t = 45 d, $\sum t = 709$
12. The case in which the D2 panel affects the safety pillar: t = 30 d, $\sum t = 739$

7.2.2 Analysing the results

After final modeling, forces and moments affecting the main gallery support, according to time and production period, were obtained. The value of the forces and moments on the main gallery's supports are shown in Table 5.

Table 5 Forces and moments on the main gallery's supports according to time and excavation condition.

Step	Time (d)	Total time (d)	Distance between D1 panel and safety pillar (m)	Distance between D2 panel and safety pillar (m)	D1 side gallery			D2 side gallery		
					Axial force (kN/m)	Shear force (kN/m)	Bending moment (kNm/m)	Axial force (kN/m)	Shear force (kN/m)	Bending moment (kNm/m)
1	0	0	–	–	–	–	–	–	–	–
2	0	0	–	–	3,470	172.03	59.11	4,460	103.08	58.31
3	90	90	290	–	3,640	181.46	63.62	4,700	104.47	60.43
4	90	180	–	140	3,820	184.62	67.23	5,050	116.14	63.28
5	260	440	100	–	3,940	202.63	71.84	5,210	121.37	65.03
6	90	530	60	–	5,910	486.66	112.32	5,710	311.37	66.57
7	61	591	–	100	11,730	795.65	186.61	16,210	615.09	154.93
8	30	621	20	–	30,130	6070	704.76	30,260	1,380	346.57
9	30	651	–	60	38,960	6110	863.41	46,320	3,860	611.50
10	13	664	0	–	50,390	6,740	1,320	63,520	4,900	873.03
11	45	709	–	20	61,590	7,080	1,510	66,470	5,100	1,260
12	30	739	–	0	57,650	8,290	2,430	34,120	7,080	2,110

7.2.3 Evaluation of the results

After final modeling studies, the main source of the resulting deformation of the gallery supports has been detected as inefficient pillars. It is therefore proposed to decrease the distance between the supports and to use I-160 rigid steel supports following reshaping. In the next planning stage, it is suggested that pillars are left that are 2.5 times the thickness of the coal. The main reason is the starting distance of the deformation from the main galleries during production periods.

8 SUMMARY

NDSS is a support design methodology that has been newly proposed and continues to develop. This system is based on numerical modeling techniques of the type that have been used by many colleagues. It incorporates the field studies, and the measurements and observations made on site during the design phase. In addition, it includes the laboratory test results on the rock material. Within the system, there are data obtained from the various rock mass classification systems. In these respects, it is not significantly different to other systems. What distinguishes NDSS from these other systems is its ability to consider the time-dependent deformation behavior of the rock mass in designing the associated supports. Moreover, dynamic effects (*e.g.* explosion, earthquake, excavation vibration) are also taken into account.

From this perspective, especially in highly squeezing and swelling rocks, productive results are obtained.

REFERENCES

Aksoy, C.O. & Onargan, T. (2010). The Role of umbrella arch and face bolt as deformation preventing support system in preventing building damages. *Tunnelling and Underground Space Technology*, 25, 553–559.

Aksoy, C.O., Oğul. K., Topal, İ., Ozer, S.C., Özacar, V. & Posluk, E. (2012). Numerical modeling of non-deformable support in swelling and squeezing rock. *International Journal of Rock Mechanics and Mining Science*, 52, 61–70.

Aksoy, C.O., Oğul., K., Topal, İ., Poşluk, E., Gicir, A., Kucuk, K. & Aldas, G.G. (2014). Reducing deformation effect of tunnel with non-deformable support system by jointed rock mass model. *Tunnelling and Underground Space Technology*, 2, 218–227.

Aksoy, C.O., Kucuk, K. & Uyar, G.G. (2015). Safety pillar design for main galleries in multi-slice longwall top coal caving method. *International Journal Oil, Gas and Coal Technology*, 9(3), 329–347.

Aygar, E.B., Ertin, A. & Simsek, O. (2010). *Re-shaping project and C3 class support design report of T13 tunnel*. SIAL Geoscience Co Report.

Barla, G. (1995). Tunnelling Under Squeezing Rock Conditions. In: Kolymbas, D. (ed.) *Tunnelling Mechanics, Eurosummer School, Innsbruck*. Berlin, Logos Verlag. pp. 169–268.

Barla, G., Bonini, M. & Semeraro, M. (2011). Analysis of the behaviour of a yield-control support system in squeezing rock. *Tunnelling and Underground Space Technology*, 26, 146–154.

Barton, N. (1995). The influence of joint properties in modelling jointed rock masses. In: Fuji, T. (ed.) *Proceedings of 8th ISRM Congress, Tokyo*, Volume 3. Rotterdam, Balkema.pp. 1023–1032.

Bhasin, R. & Grimstad, E. (1996). The Use of Stress-Strength Relationship in the Assessment of Tunnel Stability. *Proceedings Recent Advances in Tunnelling Technology*. New Delhi, India. pp. 183–196.

Bray, J.W. (1967). A Study of Jointed and Fractured Rock – Part II. *Felsmechanik*, V(4), 197–216.

Cantieni, L. & Anagnostou, G. (2009). The interaction between yielding supports and squeezing ground. *Tunnelling and Underground Space Technology*, 24, 309–322.

Carranza-Torres, C. & Fairhurst, C. (2000). Application of the Convergence–Confinement method of tunnel design to rock masses that satisfy the Hoek–Brown failure criterion. *Tunnelling and Underground Space Technology*, 15, 187–213.

Chen, G., Li, H. & Zhou, W. (2007). Analysis of block removability in rock excavation by probabilistic approach. In: Eberhardt, E., Stead, D. & Morrison, T. (eds.) *Proceedings of the 1st Canada-US Rock Mechanics Symposium, Vancouver, Canada*. London: Taylor & Francis.pp. 159–166.

Einstein, H. (ed.) (1989). Suggested Methods for Laboratory Testing of Argillaceous Swelling Rocks. *International Journal of Rock Mechanics & Mining Sciences & Geomechanic Abstracts*, 26, 415–426.

Einstein, H. (ed.) (1994) Suggested Methods for Rapid Field Identification of Swelling and Slaking Rocks. *International Journal of Rock Mechanics & Mining Sciences & Geomechanic Abstracts*, 31, 547–550.

Eisenstein, Z. & Branco, P. (1991). Convergence-confinement method in shallow tunnels. *Tunnelling and Underground Space Technology*, 6, 343–346.

Feng, X.T. & Hudson, J.A. (2010). Specifying the information required for rock mechanics modelling and rock engineering design. *International Journal of Rock Mechanics and Mining Science*, 47, 179–194.

Goel, R., Jethwa, J. & Paithankar, A. (1995). Indian experiences with Q and RMR systems. *Tunnelling and Underground Space Technology*, 10, 97–109.

Goodman, R.E. (1989). *Introduction to rock mechanics*. New York, Wiley.
Grimstad, E. & Barton, N. (1993). Updating of the Q system for NMT. *Proceedings of the International Symposium on sprayed concrete – Modern use of wet mix sprayed concrete for underground support, Fagernes*. Oslo, Norwegian Concrete Association.
Hoek, E. & Marinos, P. (2000). Predicting tunnel squeezing problems in weak heterogeneous rock masses. *Tunnels and Tunnelling International*, November 2000, 45–51 (Part 1); December 2000, 34–36 (Part 2).
Hoek, E., Kaiser, P.K. & Bawden, W.F. (1995). *Support of underground excavations in hard rock*. Rotterdam, Balkema.
ISRM. (2007). The Quantitative Description of Discontinuities in Rock Masses. In: Ulusay, R. & Hudson, J.A. (eds.) *The Complete ISRM Suggested Methods for Rock Characterization, Testing and Monitoring: 1974–2006*. Lisbon, International Society for Rock Mechanics. pp. 25–45.
Kovari, K. (1998). Tunnelling in Squeezing Rock. *Tunnel*, 5, 12–31.
Onalp, A. & Yakut, S. (2010). Geotechnical test results of T13 tunnel, Geotechnic Laboratory Report, Istanbul Kultur University.
Panthi, K.K. (2006). Analysis of engineering geological uncertainties related to tunneling in Himalayan rock mass conditions, Doctoral Thesis, Norwegian University of Science and Technology, Trondheim, Norway.
Shin, Y., Song, K., Lee, I. & Cho, G. (2011). Interaction between tunnel supports and ground convergence–consideration of seepage forces. *International Journal of Rock Mechanics and Mining Science*, 48, 394–405.
Shrestha, G.L. (2006). Stress induced problems in Himalayan tunnels with special reference to squeezing, Doctoral Thesis, Norwegian University of Science and Technology, Trondheim, Norway.
Singh, B., Jethwa, J., Dube, A. & Singh, B. (1992). Correlation between observed support pressure and rock mass quality. *Tunnelling and Underground Space Technology*, 7, 59–64.
Singh, B., Viladkar, M.N., Samadhiya, N.K. & Sandeep Geotechnical Engineering Division (1995). A Semi-Empirical Method for the Design of Support Systems in Underground Openings. *Tunnelling and Underground Space Technology*, 3, 375–383.
Stille, H. & Palmstrom, A. (2003). Classification as a tool in rock engineering. *Tunnelling and Underground Space Technology*, 18, 331–345.



Taylor & Francis
Taylor & Francis Group
http://taylorandfrancis.com

Chapter 7

On-site visualization for advanced safety management in rock engineering

S. Akutagawa
Department of Civil Engineering, Kobe University, Kobe, Japan

Abstract: A new strategy for field measurement and safety management in rock engineering is proposed. In this method, specially designed sensors capable of 1) measuring arbitrary quantities and 2) visualizing them on-site, are used so that state of deformation, strain, inclination, etc., is grasped and shown visually to people nearby on a real-time basis. This "On-Site Visualization" strategy offers a new platform whereby visually shared information about structures in question would enable advanced safety management in rock engineering projects.

1 INTRODUCTION

Recent efforts in analyzing injury reports and accidents in workplaces have led to both national and global establishment of safety guidelines and risk management schemes. Enforcement of suggested methods to improve safety and reduce risks has achieved dramatic reduction in casualties at workplaces in the last several decades.

Monitoring has played one of the key roles in this process and is regarded as indispensable for tracking behavior of rock structures or associated infrastructures and managing safety both during construction and service time. Design of a monitoring project involves determination of 1) what needs to be measured, 2) at how many points, 3) by which instruments, 4) how information is managed, and is budget-dependent. A typical procedure in a traditional approach is shown in Figure 1 in which elapsed times between each step are shown. If Δt indicates time required for a safety officer (indicated as *S*) to recognize an occurrence of an original event, it would be $\Delta t = \Delta t_1 + \Delta t_2 + \Delta t_3 + \Delta t_{5a}$ with visual recognition through computer screen, and $\Delta t = \Delta t_1 + \Delta t_2 + \Delta t_3 + \Delta t_4 + \Delta t_{5b}$ with visual recognition through printed material. As far as the critical information on safety being received by workers with no delay while keeping Δt as small as possible, safety is expected to prevail.

There are, however, potential drawbacks in this procedure. A symptom for an undesirable event, thought it may be already detected, could go unnoticed for a while as Δt_{5a} and Δt_{5b} depend on how often the safety officer drops by a monitoring room for checking. For all workers (indicated as *W*) to be informed about the information, additional Δt_6 elapses. It is also of crucial importance to notice early symptoms for accidents might arise where no monitoring is performed. These facts reflect the fact that there still are casualties counted in thousands in coal mining industry alone (Association for Asian Research, 2015). Although detailed analyses may have difficulty to identify exact causes of those fatal incidents and other accidents of tunnel collapses

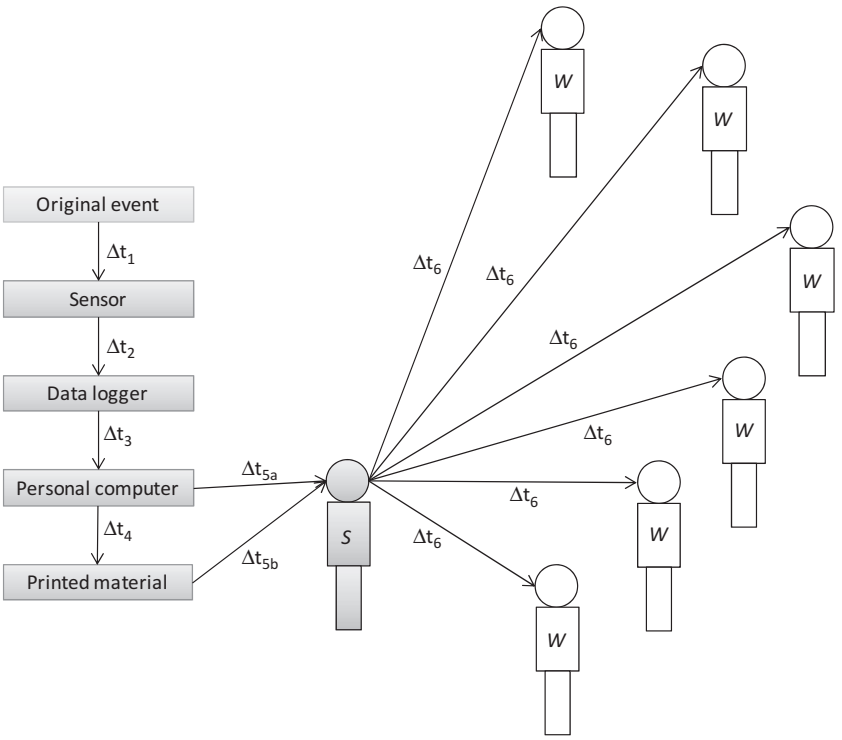


Figure 1 Procedures in a traditional monitoring approach.

(for example, Health and Safety Executive, 2000; Kitahara *et al.*, 2006), one could reasonably say some of them could have been prevented from happening if monitoring had been performed and crucial information leading to identification of early symptoms had been identified with no delay in time.

A new approach illustrated in Figure 2 is characterized by use of a new type of instrument which has the capability of not only processing data, but also visually outputting them for immediate recognition of measured information by one of the five human senses; namely, vision. Therefore, time required for all workers, skipping the safety officer, to notice occurrence of an event is expressed as $\Delta t = \Delta t_1 + \Delta t_2$. The speed of information processing in this method is literally identical to the theoretical speed limit, namely the speed of light. The core discussion given in this chapter is on how these instruments are designed and structured, and how they could contribute to further improvement of safety at workplaces for rock engineering communities.

2 METHODS FOR VISUALIZING MEASURED INFORMATION

Figure 3 shows process flows of six different methods for data collection and visualization discussed in this chapter. Strategic variations of these methods are in data collection scheme (electrical, optical or mechanical), data visualization scheme (as color of

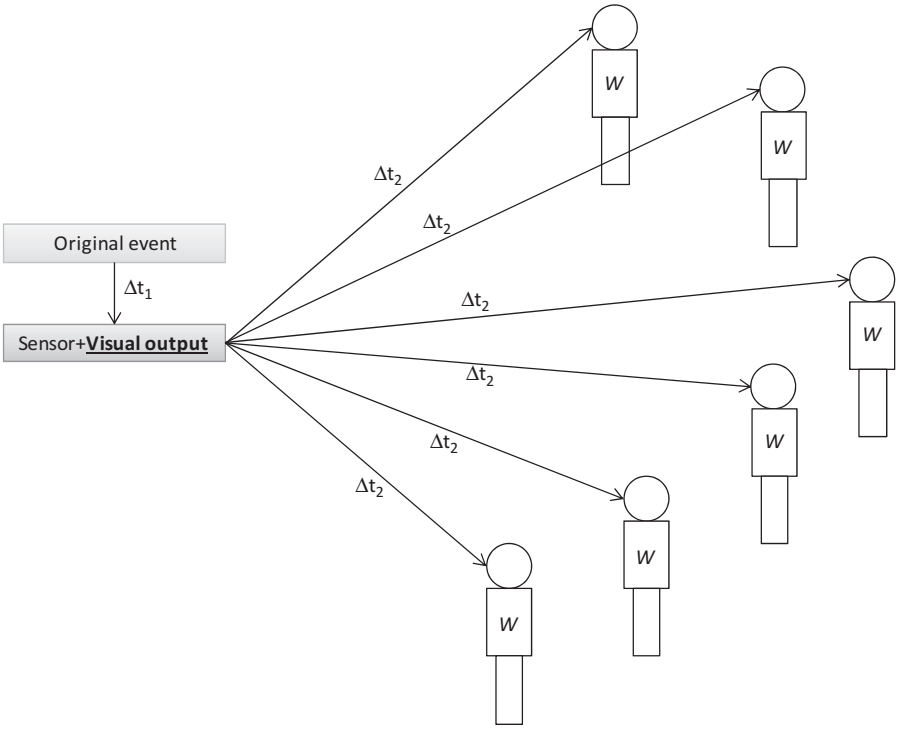


Figure 2 Procedures in On-Site Visualization.

light, as existence of light, as light patterns, as mechanical movement, etc.) and in degree of complexity or simplicity in each system, as described hereafter.

2.1 Visualization by using stand-alone electric device

The first method uses a stand-alone electric device called Light Emitting Deformation Sensor (LEDS) that can measure a relative deformation between two points by a simple mechanism and show the result by the color of LED (Akutagawa *et al.*, 2007, 2010). Figure 4 shows a schematic view of the fundamental structure of the sensor. Two points, A and B, are connected by a spring and a stiff wire. The spring is chosen in such a way that its stiffness is much smaller than that of the wire. Therefore, the relative displacement between A and B becomes approximately identical to the elongation of the spring. As a relative deformation occurs and the spring is elongated or contracted, the power supply needles prepared respectively for Red, Green, and Blue LED chips, slide on a specially designed panel switch, enabling arbitrary control of color depending on the magnitude of displacement.

LEDSs were applied in several field cases as shown in Table 1. Since this device can be used in a stand-alone mode with a battery box, installation is simple and visibility is satisfactory especially in underground construction sites. Similar ideas of transforming

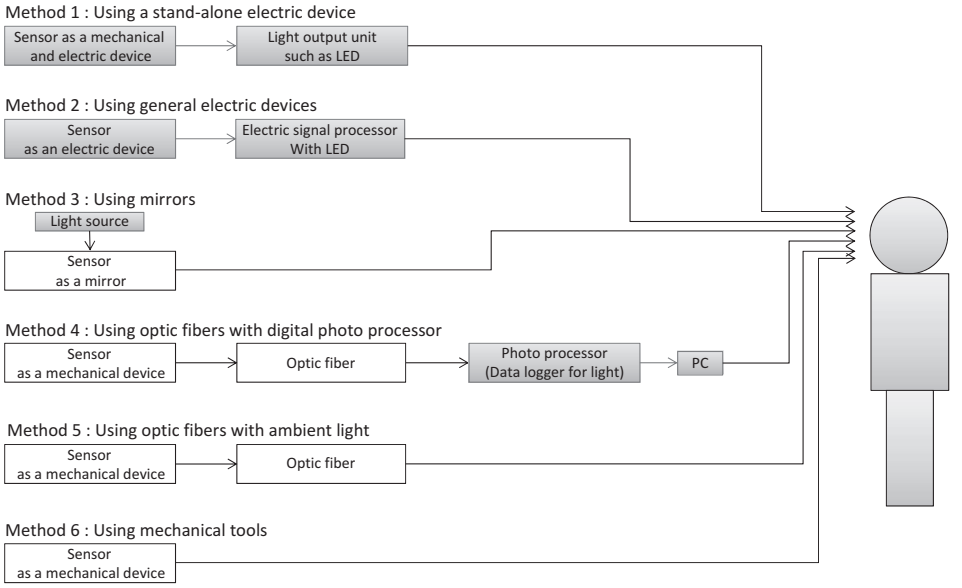


Figure 3 Various methods for data processing used in On-Site Visualization. Boxes in red indicate use of electricity.

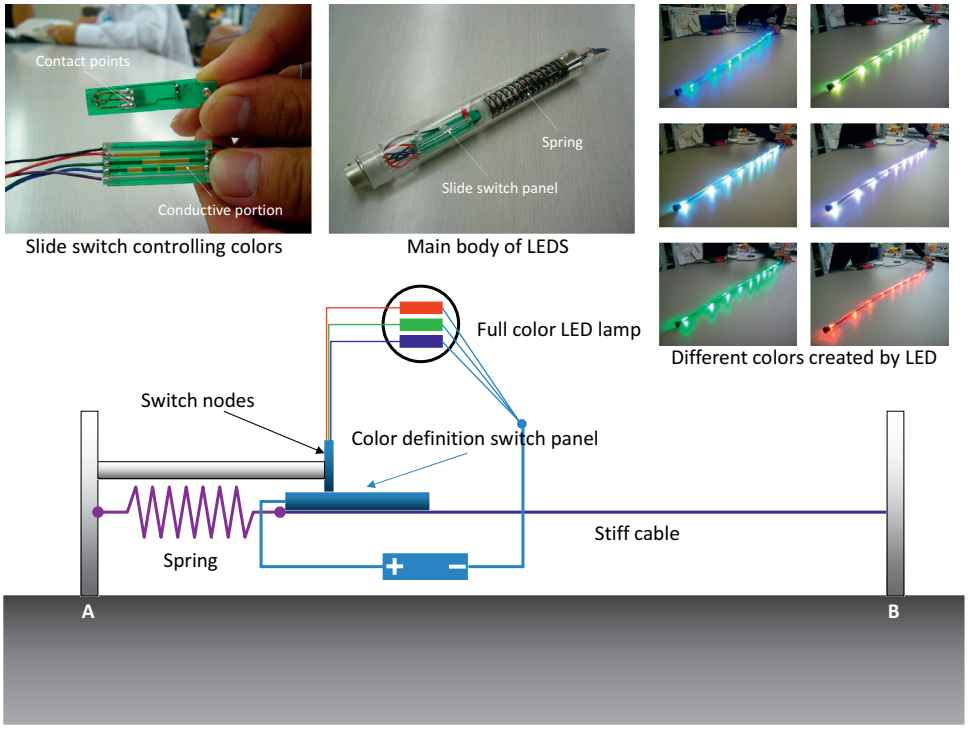


Figure 4 Basic structure of Light Emitting Deformation Sensor using a sliding switch.

Table 1 Application examples for Light Emitting Deformation Sensor.

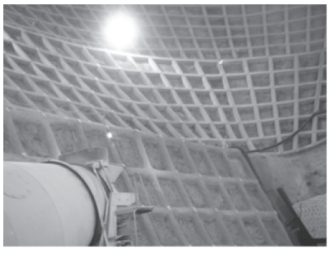
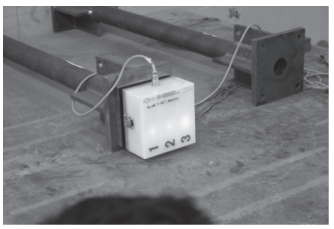
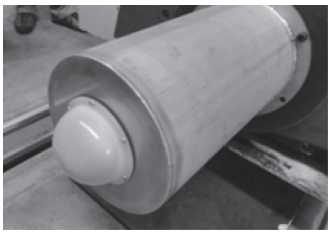
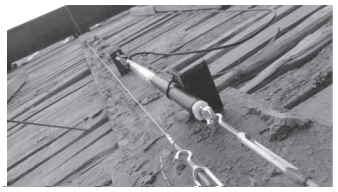
	**Laboratory simulation of landslide** Three LEDSs were used to monitor a simulated landslide. Four wood panels were used to represent moving blocks of the slope while three LEDSs were installed with the initial color of white. As one of the panels was moved, the induced displacements were picked up by the LEDS, and their color changed from white to blue. The very first On-Site Visualization experiment by the LEDS hand-made by students.
	**Safety monitoring at an open cut excavation site** Safety monitoring was performed at a late stage of a construction site. The tunnel was constructed by a cut and cover method and the LEDSs were installed between the retaining wall and steel columns to monitor what-they-call "unexpected small displacement". While a worker loosened an oil-jack of one of the strut beams, the closely positioned LEDS changed their colors showing to everyone around that the movement occurred just by a small amount within an assured safety.
	**Monitoring an aged shotcreted slope** An old shotcreted high slope was chosen as a test case to install LEDSs for the first time in field. Four LEDSs were installed, each measuring displacement between two points approximately 5m apart. As the site was by a national roadway with substantial traffic, lighting up of LEDS was only allowed during limited time in the evening time. However, the visibility of the LEDSs installed in the range of 100m or more was excellent. This was a good example to demonstrate how the use of LEDS could help maintenance works since the safety over a wide area can be checked by one sight.
	**Monitoring tunnel convergence** LEDSs having 1m long light emitting part were used to monitor extra convergence displacement of a tunnel in which soft and squeezing ground conditions were observed occasionally. LEDSs were installed on its side wall to ensure the further displacement after extra reinforcement of shotcrete was confined to its minimum level.
	**Monitoring of a high slope at a tunnel portal** Stability of a high slope just outside of a tunnel portal was monitored by two LEDSs. To ensure additional visibility of the LEDS, an optional LED unit cabled from the original sensor was hung on the side wall of the tunnel entrance.

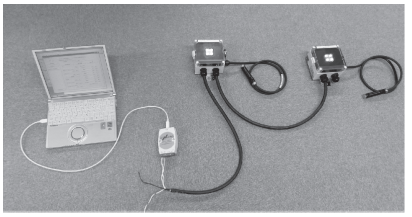
Table 1 (cont.)

	**Monitoring reinforced soil wall during road tunnel construction** An LEDS was installed between the reinforced soil wall and a steel column to ensure the construction works nearby did not affect the reinforced ground. As this site was right in the middle of heavily populated area with heavy traffic in Tokyo, the maximum care had to be paid to achieve safety throughout the construction just beneath the road.
	**LEDS for rockbolt** The modified LEDS for rockbolt was developed and tested in a lab. In this example, three relative displacements were measured from one rockbolt and their colors were shown in the LED unit box outside rock mass. Further cost down and simplification of the device is awaited for field application.
	**LEDS for ground anchor** The modified LEDS for ground anchor was developed and tested in a lab. Generally, estimation of axial force of a ground anchor requires use of oil jack and considerable manpower, and it is a costly practice. Once the newly developed LEDS for a ground anchor is installed, its axial force in a usual condition, or after heavy rain, earthquake, etc. can be simply visualized by the color of LED attached on its cap. (Akutagawa *et al.*, 2011)
	**LEDS for measuring wall closure** LEDS was installed to measure wall closure displacement at an open excavation site in New Delhi, 2010. A special attachment device was used so that a closure displacement was transferred to the LEDS as elongation. (Akutagawa, 2010)

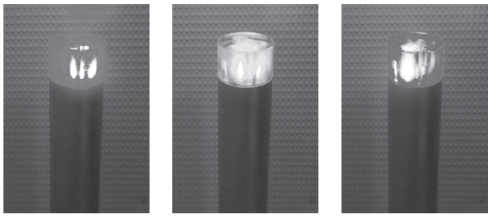
deformation into LED color can be extended for visualization of forces in rock bolts and ground anchors (Akutagawa *et al.*, 2011; QUALIROCK, 2015).

2.2 Visualization by using electric device

The second method employs a general-purpose electric device for visualization of arbitrary data. A fully integrated monitoring and visualization system may be arranged where multiple sets of sensors with visual output function are controlled and operated by a PC. It is also possible to use a laser pointer, for example, as a stand-alone device with which inclination can be visualized easily. Figure 5 summarizes various arrangements for monitoring and visualization of arbitrary data using electric devices.



LEC system controlled by a PC.



Stand-alone inclination sensor



LEIS system controlled by a PC.



Stand-alone laser pointer



Laser based deformation sensor

Figure 5 Examples of electricity-powered sensors with visual output function.

Light Emitting Converter (LEC) is a compact data logger that is capable of 1) converting analog signal from an arbitrary sensor connected to it into digital one, 2) showing it by the color of LED based on a pre-defined color scheme and 3) storing data on an SD card. A sensor to be connected to LEC can be chosen from a family of available sensors for measurement of deformation, strain, inclination, pressure, temperature, etc. The color scheme can be defined and changed later, if necessary, for each LEC-sensor pair by the control software installed on a PC. Five colors of choice can be used to visualize the measured data of arbitrary type with respect to properly defined threshold values (Akutagawa, 2010).

Acceleration sensors used in automobile industry is utilized to form a Light Emitting Inclination Sensor (LEIS). LEIS is equipped with a heater and automatic temperature control function such that the temperature inside the sensor box is kept at 50 degrees centigrade at all times to stabilize inclination reading (Izumi *et al.*, 2014c). The LEIS has two acceleration sensors positioned at orthogonal directions and the maximum gradient computed from them is calculated and compared with pre-defined threshold values to determine the corresponding color of rotation lamps. Laser pointers could be used as easy-to-handle inclination sensors. For example, a laser pointer that experiences rotation of 0.01 degree can be identified as the movement of its projected beam spot by 8.7mm on a screen 50m away from the pointer. If greater magnification is needed, the screen can be placed further. Laser based deformation sensor can also be used to identify deformation occurring at a point of installation by reading position of laser beam projected from a Total Station at a distance (Enzan Kobo, 2015). Table 2 includes

Table 2 Application examples for electricity-powered devices.

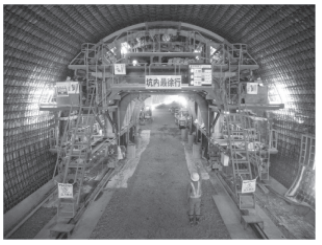
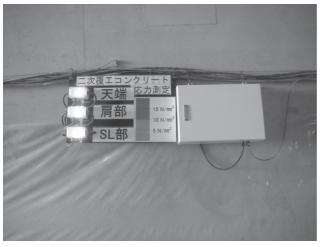
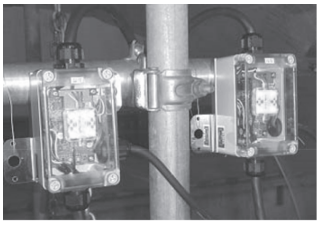
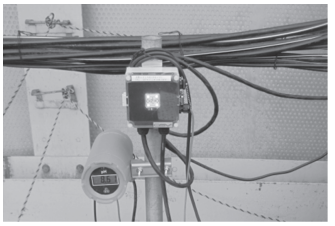
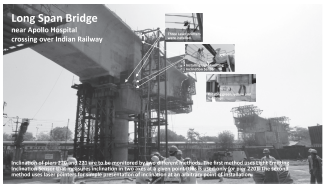
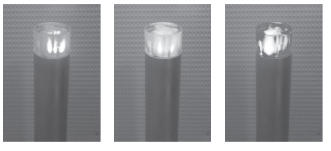
	**Visualizing safety during tunneling under special condition** A NATM tunnel had to be constructed with an overburden of only 30cm due to the constraints of the project. After the top thin layer was completed as a reinforced concrete structure sitting on reinforced ground, the tunnel was driven while allowing daily traffic above. Three displacement sensors were used with LECs to make sure that the traffic load during tunnel construction was within the expected range and the tunnel structure remained safe.
	**Visualizing pressure of fresh concrete for tunnel lining** A portion of a NATM tunnel had to be heavily reinforced in the concrete lining. To ensure and visualize how fresh concrete is poured into the steel form through re-bars reaching to far corners, LECs were used jointly with pressure sensors so that a confirmation could be visually identified when the fresh concrete reached the pre-installed pressure sensors at the far corners in the form.
	**Visualizing stresses in tunnel lining** LECs were connected to stress sensors embedded in secondary concrete lining. This type of operation may be of benefit if continuing pressure on the lining is expected in squeezing ground.
	**Visualizing temperature and moisture** Temperature and moisture were visualized during concrete curing process. To optimize moisture and temperature during concrete aging process, LECs were used together with moisture and temperature sensors. Workers were able to use visualized information to control their work.
	**Visualizing axial forces in ground anchors** Some movement was observed for a slope near a highway construction site. To stop its movement, additional anchors were installed while monitoring axial forces in existing anchors.
	**Visualizing tower inclination during bridge construction** Temporal structures during construction require careful management for their safety. Since they are not permanent structures, less attention is paid usually. Visualization of inclination of main towers of a temporal cable suspended bridge helped improve safety monitoring a great deal.

Table 2 (cont.)

	**Visualizing acid content in underground water** Water quality can also be monitored by OSV. Injection for soil reinforcement uses materials with various chemical ingredients. A pH sensor can be connected to LEC to monitor and present acid content of underground water.
	**Visualizing safety at Delhi metro construction site** An open cut site with 10m depth was monitored by using LECs. Inclination of retaining walls, boundary walls, forces in strut beams, etc. were monitored for visualization of safety to workers and citizens nearby. (Nakamura *et al*., 2010; Izumi *et al*., 2014b)
	**Visualizing inclination with high precision** LEIS uses two MEMS sensors to measure inclinations θ_x and θ_y in the sensor box kept at 50 °C throughout measurement period. $\theta=SQRT(\theta_x^2+\theta_y^2)$ is then compared with two threshold values I_1 and I_2, such that; green light is turned on if $\theta<I_1$, yellow light is turned on if $I_1 \leqq \theta < I_2$, and red light is turned on if $I_2 \leqq \theta$.
	**Visualizing inclination of girder beam during bridge construction** Three LEISs were installed to monitor inclination of bridge girder beam with construction stages. Data were stored on a hard disk of the PC at a selected time interval. Also, the data were uploaded on an FTP server every hour so that they can be accessed from a remote office. (Nakamura *et al*., 2010)
	**Visualizing inclination with a portable inclination sensor** Light Emitting Inclination Sensor / Pocket is a stand-alone and portable inclination sensor that uses a MEMS sensor, with its maximum resolution of 0.01 degree, to measure inclinations θ_x and θ_y to compute $\theta=SQRT(\theta_x^2+\theta_y^2)$. θ is then compared with two threshold values I_1 and I_2, such that green, yellow and red LED flashes to visualize inclination.
	**Laser based deformation sensor** Laser beam is projected from a Total Station to each deformation sensor with a fixed time interval. Multiple optical sensors installed on the deformation sensor reads horizontal and vertical positions of the laser beam and determine LED colors. This picture shows an initial condition at a test tunnel (Enzan Kobo, 2015).

field application examples using these devices. Use of these devices with properly defined threshold values, defining relationships between measured data and color of light, helps improve safety management a great deal.

2.3 Visualization by using mirrors

In general, open visualization of measured information is favored by all concerned. However, some owners show concern over responsibility of handing visualized information concerning safety of a project. For this reason, a new optical method for measuring and real-time visualization of inclination in a general rock engineering projects is proposed. A key feature in this method is the use of a mirror. It is generally the case that many geo-hazards, such as slope failure, rock wall collapse, landslide, etc., induce inclination at arbitrary points within the rock mass in question. It is therefore a great interest from monitoring point of view, that magnitudes of the inclination be measured and visualized at as many points as possible at low cost.

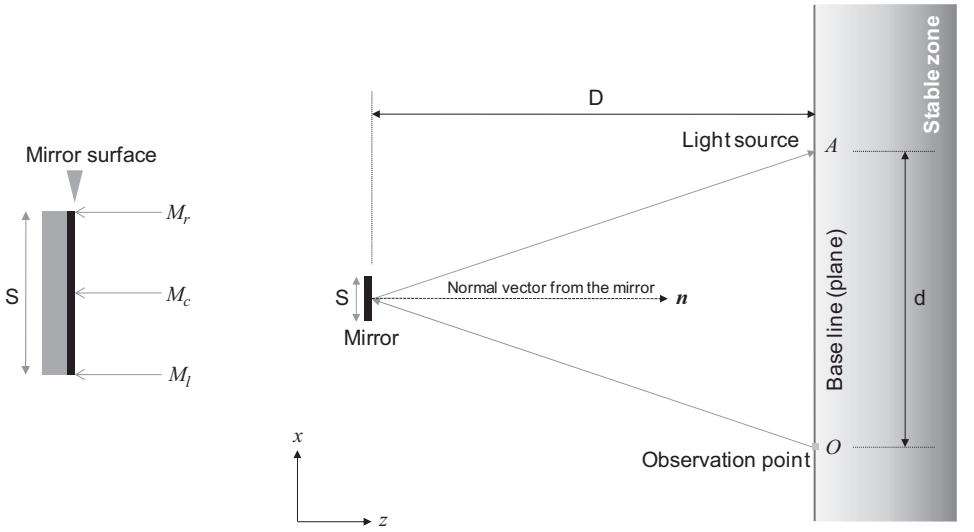
In the proposed method, a mirror is placed at a monitoring point M such that a light source placed at another point A can be visually identified through that mirror by an observer standing at point O. Points A and O are assumed to be in a stable zone where ground movement is believed to be zero. Monitoring point M is assumed to be in the region where one could expect some movement due to land slide, and so on, that includes arbitrary magnitude of inclination θ. As θ changes, the observer can visually identify the reflected image of the light source moving away from the mirror center and eventually losing its sight, knowing the inclination has exceeded the critical value which is determined from mirror size and distances between M, A and O. If inclination needs to be measured and visualized at many points, one can install as many mirrors as possible while still using just one point O where real-time visual identification can be made. For this reason, the proposed method is called "Single Observation Point" method (Akutagawa *et al.*, 2014c).

First, key positions on a mirror having a width of S are defined in Figure 6(a) in which left edge, center and right edge points are shown as M_l, M_c and M_r.

The mirror is installed at a distance D from a base line where the ground is assumed to be stable. It is positioned there so that the normal vector $\boldsymbol{n}$ becomes perpendicular to the baseline and the observer can visually identify the light source at M_c on the mirror. The collimation line in this case is therefore OM_cA. Note that the distance d between the observation point O and the location of a light source, A, is usually very small compared to D, but exaggerated in this figure.

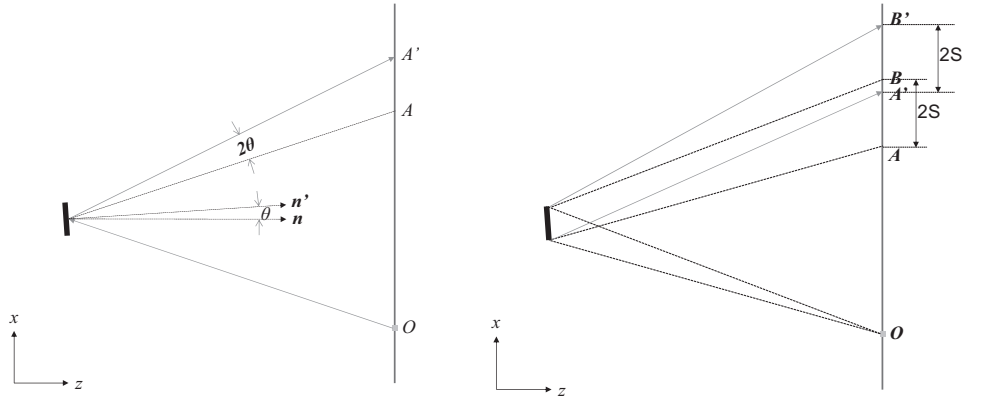
Assume that the mirror rotates by an angle θ, then the collimation line is forced to rotate as much as 2θ, as shown in Figure 7(a). The observer eventually sees a new point A' which is 2θD apart from A at M_c in the mirror. Based on this principle of collimation line rotation, one could find the shift of the initially mirrored zone AB to a new zone $A'B'$ due to the mirror rotation of θ, as shown in Figure 7(b). Note that the width of the mirrored zone before and after the rotation is 2S in this case.

If presented in xy plane, the shift of mirrored zone can be represented as shown in Figure 8, provided that the mirror is circular and the light source with diameter L is initially at the center of the mirrored zone. Actual visions for the observer looking at the mirror is given in Figure 9 where real dimensions 2S and L are given over the mirror whose diameter is S. The initial vision Figure 9(a) has the light source at the center.



(a) Key positions. (b) Locations of the mirror, an observation point and a light source.

Figure 6 Definition of key parameters to be addressed in the Single Observation Point method.



(a) Shift of collimation line. (b) Shift of mirrored zone.

Figure 7 Rotational shifts of mirrored image due to mirror rotation.

As the mirror rotation angle increases, the observer recognizes that the light would shift away from the center (Figure 9 (b)). It will then eventually go completely off the mirror (Figure 9 (c)) when the rotation angle becomes a critical value of θ_c =(S+L/2)/2D (rad).

If a circular mirror of diameter 10cm is installed 100m away from the base line to capture a light source, for example an LED light of diameter 5cm, at its center, one would lose its vision when the rotation angle reaches 0.035 degrees. If one needs the

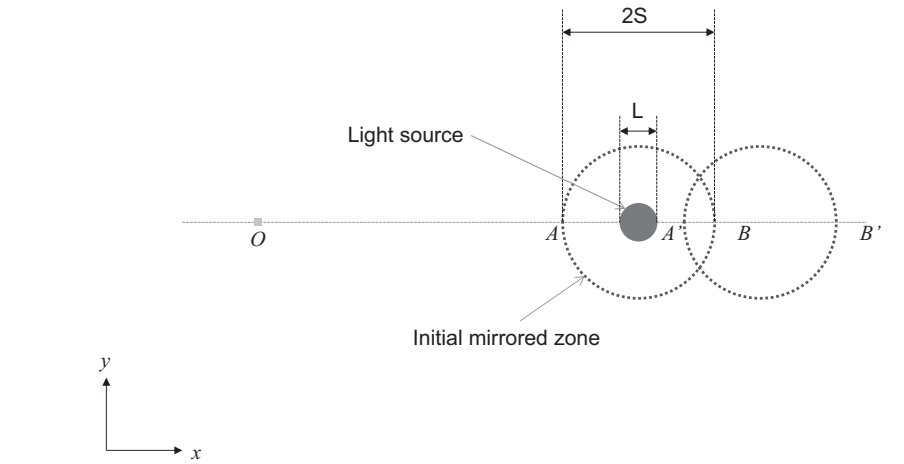
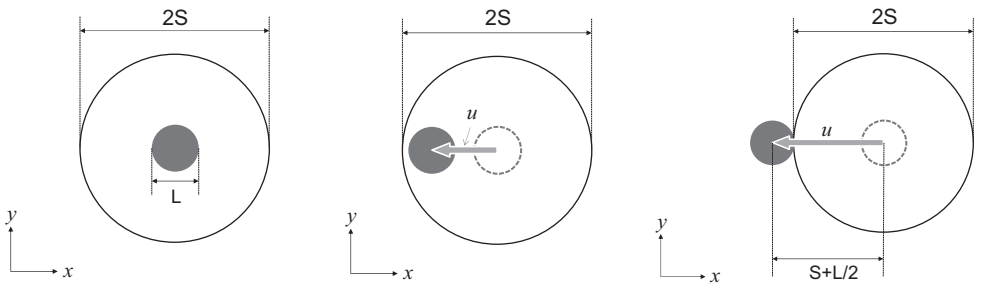


Figure 8 Shift of mirrored zone in x-y plane.



(a) Light is at the center. (b) Light starts to move. (c) Light disappears.

Figure 9 Shift of light source in the mirror.

critical rotation angle θ_c of 0.01 degrees to lose the light off the mirror, S and L can be 3.48cm and 1cm, respectively, for example. Likewise, one could employ arbitrary arrangement of D, S and L to conduct measurement of rotation angle at very high precision. As shown in Figure 10, it is possible to install as many mirrors as required so as to perform monitoring of rotation angles and simultaneous visualization from one point, using just one light source. As all the visual information is gathered at this unique point only, it is called the Single Observation Point (SOP). Some field application examples are given in Table 3.

2.4 Visualization by using optic fibers with digital photo sensor

Geotechnical engineers need to address a problem at hand from various angles at varying scales to get a full understanding of the situation. For the case of a landslide,

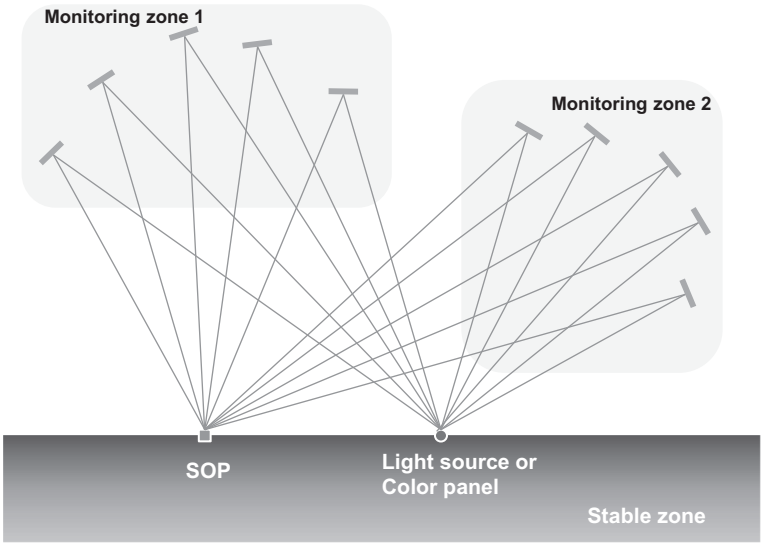


Figure 10 Measurement of rotation angles at multiple points from a Single Observation Point.

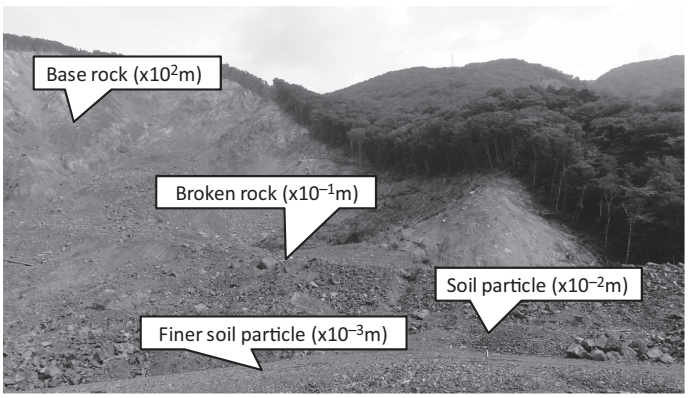


Figure 11 Various natural scales at which a problem needs to be addressed.

safety factor is computed considering an area in the order of hundreds of meters or more. As you observe a site of landslide, such as the one in Figure 11, you would find a bare face of the base rock, large pieces of broken rock, mass of gravels, soil mass of varying degree of water content, and so on, all on different scales. Although, safety factor or stability of a slope is usually discussed on a large scale, it is equally important to understand and evaluate state of geo-materials at a small scale since all large scale failures start, fundamentally, from instability of granular soil particles measured in the order of "mm".

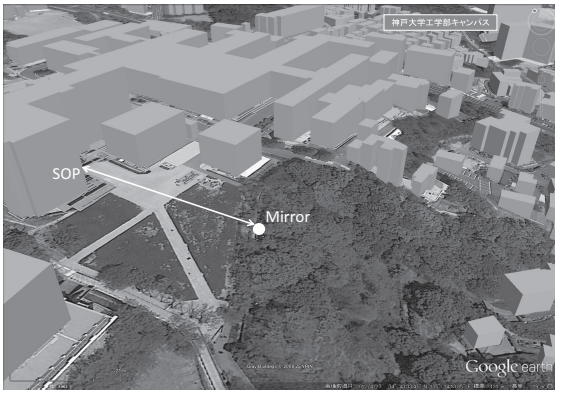
Table 3 Application examples for Single Observation Point method.

<table>
<tr>
<td></td>
<td><u>Landslide zone</u>

Three mirrors (M1, M2, M3) were installed in a landslide zone at distances 148m, 127m, 110m, respectively from the observation point. It was found that daily fluctuation of rotation angle by as much as 0.02～0.03 degrees tends to occur when the ground was not expected to be moving. Also, it was found that the M1 had undergone rotation angle change greater than 0.07～0.08 degrees before the slope reinforcement was completed.

</td>
</tr>
<tr>
<td></td>
<td><u>Slope above a tunnel portal</u>

Three mirrors (M1, M2, M3) were installed on a tunnel portal slope surface at distances, approximately 150m, respectively from the observation point. It was found that the M3 had undergone rotation angle change greater than 0.019 degrees over the tunnel construction period.

</td>
</tr>
<tr>
<td>
</td>
<td><u>Embankment movement</u>

One mirror was installed on an embankment slope surface at a distance of approximately 50m from the observation point. It was found that the mirrored image did not change at all over the monitoring period of 12 months, indicating that the slope had not moved and was safe.

</td>
</tr>
</table>

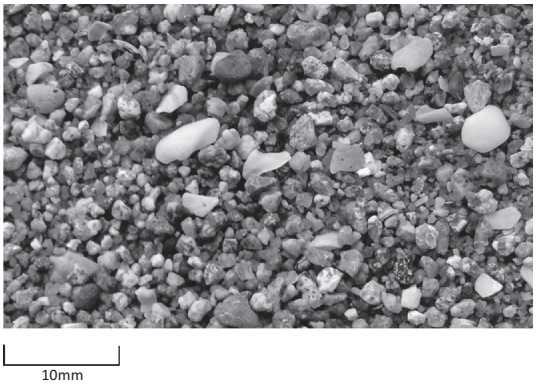


Figure 12 Randomness of size and shape of sand particles sampled at a beach.

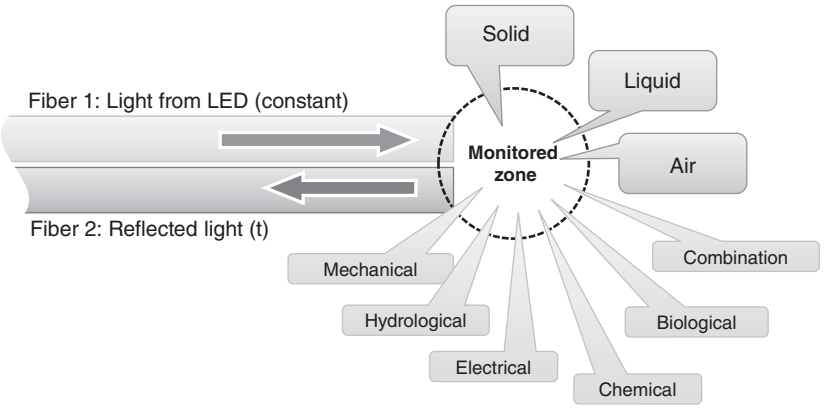
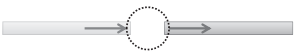
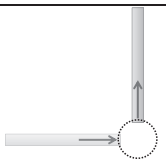


Figure 13 Factors affecting intensity of reflected light at the tip of plastic optical fibers.

The main theme discussed in this section is a method of observing changes of various factors occurring in granular geo-material such as the one shown in Figure 12. Special attention is paid to how light travels, bounces, and gets reflected in a highly complex 3D geometry that is sensitive to deformation of granular materials and to alteration of any quantity affecting paths of light (Matsumoto *et al*., 2012; Akutagawa *et al*., 2014b).

To perform the task at a given point, two plastic optical fibers having diameter of 1mm are used. Fiber-1 is used to supply light to the point of observation. Fiber-2 collects light reflected back from surfaces of nearby particles and so on, and carries it back to a photo sensor. Therefore, the area of observation at the tip of fibers is in the order of mm. In a natural geo-environment, a monitored zone ahead of the fibers would be crowded with soil particles of varying sizes, liquid containing arbitrary substances in it, and possibly air of arbitrary contents. Exact geometry of these solid particles, liquid and air

Table 4 Positioning variations of two fibers.

		
Twin fiber	**Gap**	**Random alignment**
Light once out of the 1st fiber, hits surfaces of nearby particles and gets scattered. Part of the scattered light gets into the 2nd fiber which is digitally recorded. The properties of the returning light (intensity and color) are affected by many factors telling the story of what is happening at the tip of the fibers.	By aligning the 2nd fiber in the line of the 1st fiber, a slightly different type of fiber sensor is formed. The Gap sensor is conveniently used to identify existence and properties of arbitrary materials between the two fibers.	Aligning of the 2nd fiber could be at an arbitrary angle with respect to the 1st fiber depending on geometrical boundary conditions near an observation point.

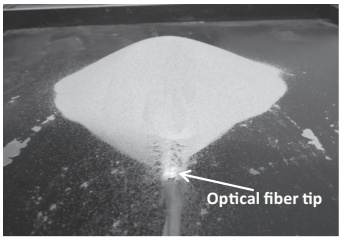
is extremely complex since they are also affected by meniscus force of water. If absolutely none of these factors changes over time, the intensity (=brightness) or color of reflected light remains constant. If, on the other hand, any single or more factors change, the properties of the reflected light are changed declaring that "something is happening over here". In the terminology of On-Site Visualization, the local zone ahead of fibers is "On-Site" and visualized information is available there. However, it is impossible to see it by human eyes, the information is sent to "Off-Site" location, namely the other end of fibers, where the returned light can be observed by naked eyes or digitally processed by photo sensors. As far as geometrical arrangement of fibers at an observation point, arbitrarily arrangements may be chosen depending on the nature of a problem as shown in Table 4. This method therefore is characterized by the use of optic fiber as one pixel camera, and is fundamentally different from the other methods in which grated fibers are used (for example, Meltz *et al.*, 1989; Hill *et al.*, 1978).

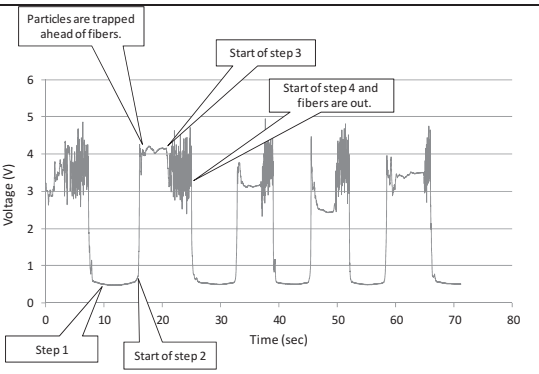
Figure 14 shows an instrumentation scheme including several sets of photo sensors and optical fibers to conduct measurement at multiple points. Light is supplied by LED lamps from which fibers (shown in blue) carry white light to observation points. Another set of fibers (shown in red) carry reflected light back to photo sensors for digital processing of data. Photo sensors may be chosen from library of available products depending on if you seek only for brightness of returning light, or full color nature of returning light including brightness. Light is lost to some extent as it travels through fibers; therefore, one needs to take this into consideration when long fibers are to be used during monitoring. Table 5 shows some examples of applying this technology.

The new method described here uses light as the key signal transmitter. As the path and intensity of light is affected by many factors originating from mechanical, hydrological, electrical, chemical and biological phenomena happening near the fiber tip, an interpretation of the obtained signal to identify exact causes is not straightforward. However, on the other hand, there is a situation in which knowing that "something rather than nothing is happening right there" matters.

For the same reason, changes in obtained light intensity matters, rather than its absolute values. If large number of fiber sensors are installed, a zone in which "something is happening" could be identified easily, directly and instantaneously. This

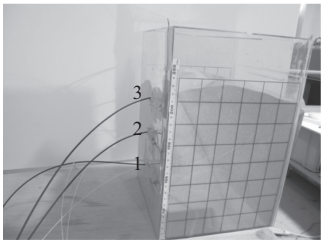
Table 5 Application examples of optical fibers.

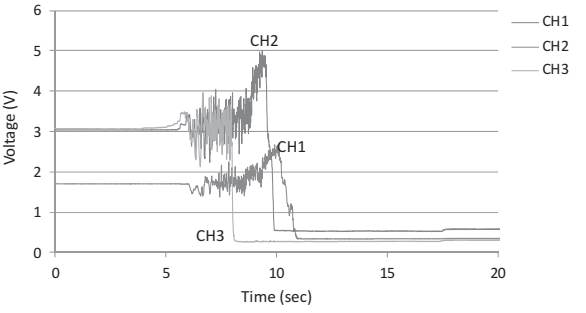




Moving a twin fiber sensors in dry sand

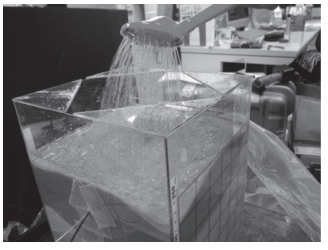
A twin fiber sensor was moved within a small mountain of fine and dry sand. A mountain of approximately 5cm high was made on a black plate. The fiber sensor was then inserted into and pulled out from the mountain several times. The intensity of the reflected light before insertion was fairly low because while the fiber tip was in the air outside the mountain, there wasn't anything that could reflect light back into Fiber-2. As the fiber tip got closer to the mountain surface, the intensity grew quite rapidly until the tip was in first contact with sand particles. As the fibers were forced into the mountain, a limited number of fine sand particles were believed to be trapped at the fiber tip as the intensity remained more or less constant for a while. As the fibers were pulled back, new space left behind the leaving fibers dragged sand particles producing random variation of light intensity until the fiber tip got out of the mountain. This cycle repeated in a very consistent way. Considering the geometric complexity of all the dynamic events that were happening in these processes, the repetition of the very consistent patterns of intensity of reflected light was remarkable and of value in terms of building a new methodology of reading what is happening at the tip of the fibers.





Four twin fiber sensors in collapsing sand mass

Three points of observation were set at different depths in a plastic box(30cm*30cm*40cm) containing dry sand. After the completion of the set-up, one side of the box was removed causing the sand mass to collapse naturally. The first signal was captured for CH3 located at the highest point. The other two followed in the order of heights as were expected rationally.



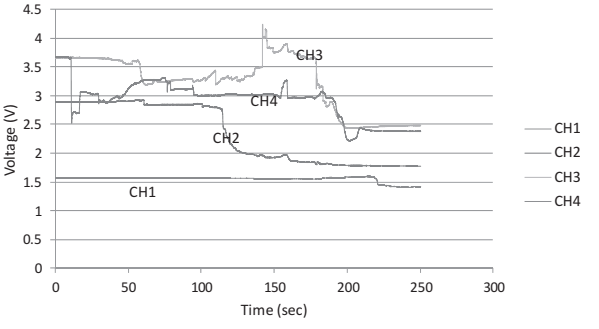
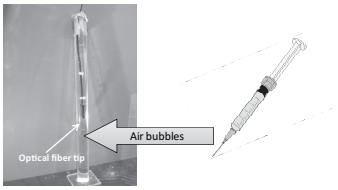
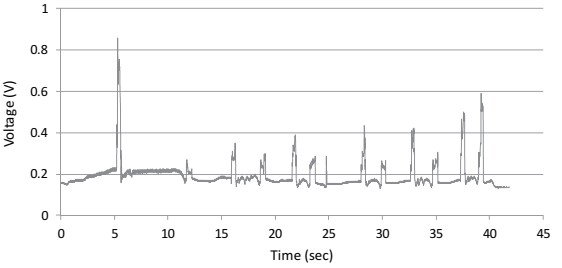


Table 5 (cont.)

Monitoring a wetting process

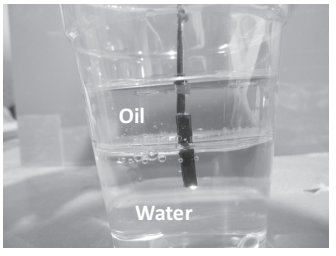
After a box of dry sand was prepared, water was sprinkled from above, wetting the sand mass until it was saturated. As the water was supplied from above, CH4 positioned at the highest point picked up the first signal indicating that the water reached the CH4 fibers at that moment. The wetting process seemed to have propagated downward in the correct order. The first sign of water reaching each point could be identified by the first disturbance observed for each light intensity.

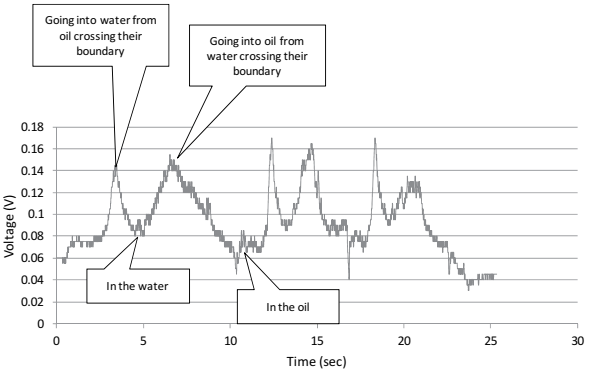




Monitoring air bubbles

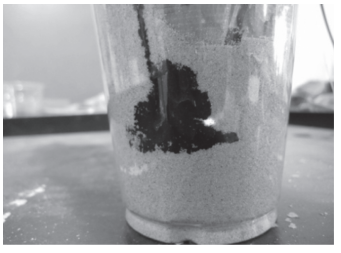
A twin fiber sensor was positioned at the mid height of a cylinder (50cm tall) and a syringe was used to supply air bubbles from just beneath the fiber tip. As air bubbles traveled upwards near and across the fiber tip, abrupt changes of light intensity were recorded, since light path was strongly affected as dynamically moving boundary surfaces between water and air passed in front of the fiber tip.





Monitoring boundary planes between two different types of liquid

A boundary plane between two substances having different refractive indices acts as a mirror. For the case of a dual liquid system, a boundary plane between oil and water acted as the mirror. As a fiber tip was moved across this boundary surface several times, the light intensity peaked as it got closer to the boundary every time, while it showed a lower value in oil and higher value in water in response to their respective liquid color.



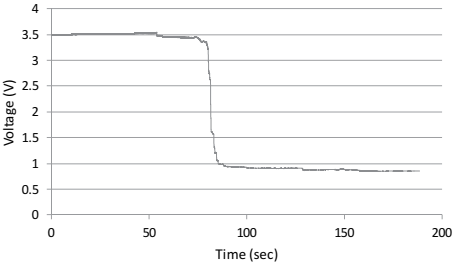
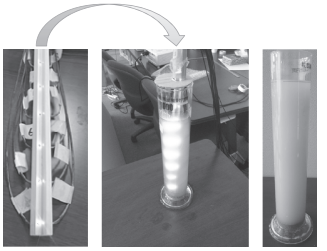


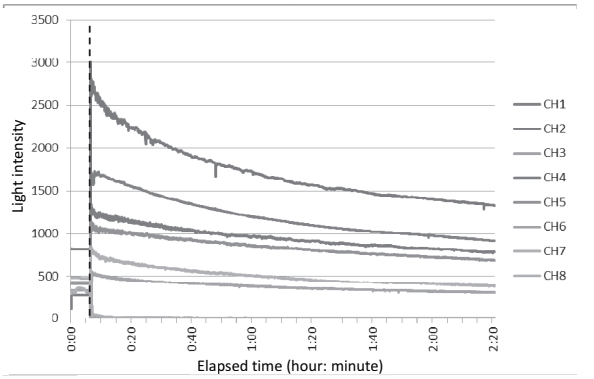
Table 5 (cont.)

Monitoring movement of alien liquid in a host medium

Black ink was injected into a cup filled with Toyoura sand (Zhang *et al.*, 2013). As the ink got closer to the fiber tip, the light intensity dropped rapidly, since the new alien material that arrived was the black ink. The similar process of injection (such as cement grouting) could be easily monitored in the same manner.



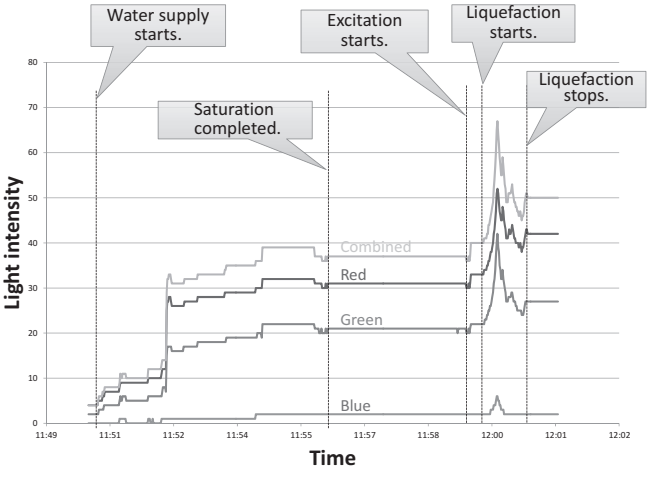
(a) Unit with 8 gap sensors (b) Initial condition with the unit installed in a cylinder (c) Final state



Monitoring turbidity

A wooden frame with L-shape cross section was prepared to house 8 units of fiber gap sensors which were installed at 90 degrees apart. This apparatus was placed in a glass cylinder (30cm in height and approximately 7cm in diameter) filled with muddy water. The water was initially fully stirred so that distribution of soil particles was fairly uniform throughout the volume of water. During monitoring, light emitted from 1st fibers would simply get scattered, go out of the cylinder, or hit soil particle and get reflected back into the 2nd fibers. Since the amount of light coming back to 2nd fibers is dependent on density of soil particle, the properties of returning light become a function of turbidity. Immediately after starting monitoring, the test set up was fully covered in a card board box to shut out external light. At the 7th minute, the apparatus was placed in the cylinder. Differences in initial values in water come from inconsistent placement of fibers (distance between fiber tips, roughness of fiber tip, etc. due to manual preparation of the test device). As the time elapsed, the light intensities (brightness of returning light representing density of soil particles) decreased gradually for all active sensors, perfectly describing time-dependent nature of turbidity in still muddy water.





Monitoring liquefaction

A 500cc glass container was filled with dry Toyoura Sand and two twin fiber sensors were installed at mid-height and bottom of the container. This test specimen was later saturated, given artificial excitation (by hitting the container with a light hammer) to simulate liquefaction. Light intensities, from the one at the mid height, varied in the preparation stage while the specimen was gradually saturated. They were kept constant when there was no external disturbance. As the excitation kept giving energy into the specimen, the liquefaction started just before 12:00 lasting for about 90 seconds while more hammering continued. The light intensities stopped fluctuating and were kept constant after the hammering was stopped.

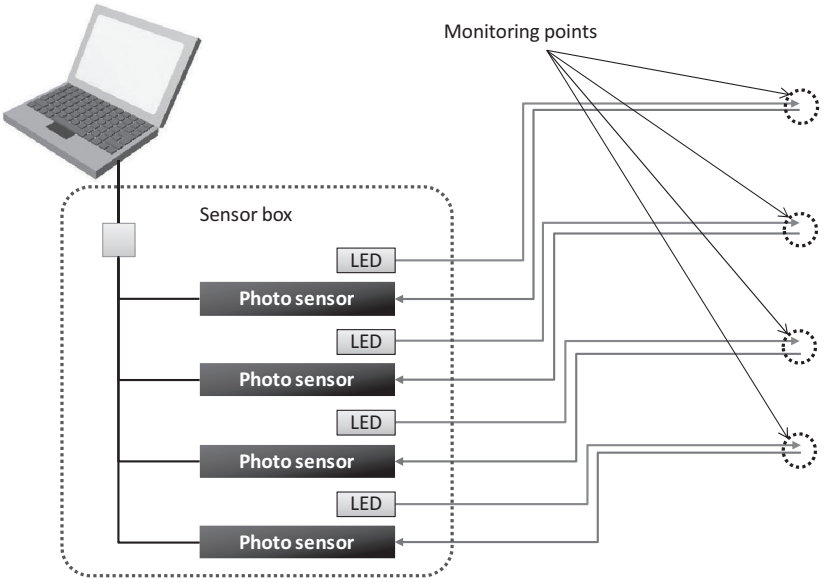


Figure 14 A measurement system including four photo sensors.

presents a clear contrast to geo-physical survey that is used to identify a zone of "problem" indirectly by analyzing obtained data consuming finite amount of time.

Plastic optical fibers used in this investigation are thin (diameter=1mm). Even if coated fibers were used, a pair of twin fibers (Fiber-1 to send light and Fiber-2 to receive reflected light) to conduct measurement at one point can be braced in the cross sectional space of approximately 5mm. This is an immense advantage that these fiber sensors could be installed at arbitrary positions within a geo-structure (man-made or natural) without disturbing its inherent structural performances.

To execute this type of monitoring using light, one needs a set of photo sensors, a light source and optical fibers. Electricity-dependent parts (photo sensors and light source) can be placed in a secured place. The other parts for sending light, sensing and carrying reflected light are all electricity-independent, lightning protected, hard-to-break-down, and low in cost.

2.5 Visualization by using optic fibers with ambient light

If monitoring is required for a long period, say 10 years or more, or when budget is low to perform it, choice of electric devices would be rather avoided and a simpler yet robust method is needed. This section deals with such methods as would require no power to run, cost less to produce and install compared to most other methods, reliable for a long duration of time and be literally free of running cost. The concept is shown in Figure 15 in which an optic signal created by an arbitrary filter is transported to an observer using ambient light given by, for example, the Sun, headlights of

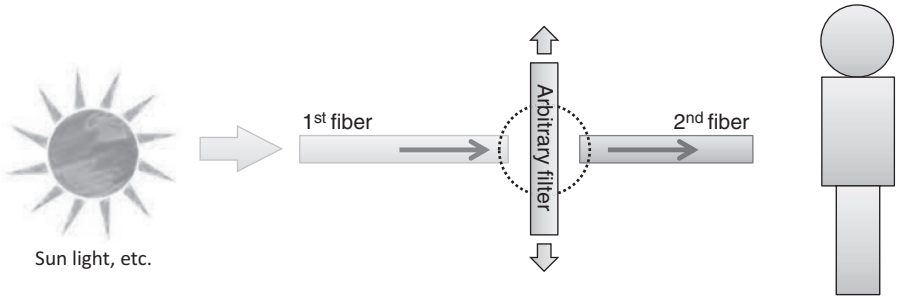


Figure 15 Use of ambient light to enable a zero-running-cost method.

automobiles, street lights, torch lights, etc., that are available for free or could be thought of as external elements from the core monitoring system. The monitoring system in this illustration is made of optic fibers (the first one is not necessarily required) and a filtering device and works without electricity. The filtering mechanism may be designed in such a way that it is functional according to the nature of problems at hand. A color filter responding to deformation, sun shade plate responding to land slide deformation, etc., would do the job. Table 6 shows several examples in which these zero-running-cost methods were successfully applied in various situations.

2.6 Visualization by using mechanical tools

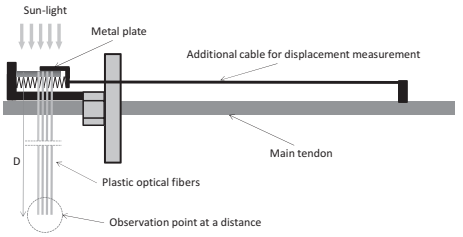
Mechanical devices used to measure and visualize engineering quantities have been around a while in various fields. One good example is use of a uniquely designed deformation sensor capable of visualizing roof deformation of coal strata (Conover *et al.*, 2010). In this section, a type of device to magnify small displacement into rotation of needle is presented with some application examples. As shown in Figure 16, an elongation of u occurring between Points 1 and 2 is indicated as rotation of a needle as much as u/r radian (approximately), provided that the elongation is correctly transferred from a thread to a pulley with no slip. By selecting a pulley of desired radius, one can set up a device of any precision. Some application examples are explained in Table 7.

3 PLANNING AND OPERATION

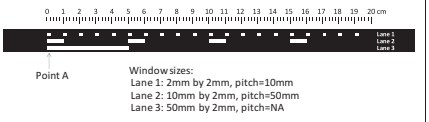
3.1 Optimized planning

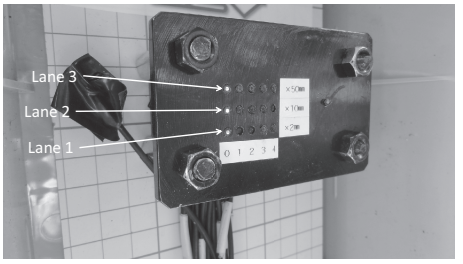
Having defined various methods for data collection and visualization, it is important to design an effective monitoring project based on OSV under a given budget. Characterization of the project usually starts from identification of general factors such as those given in Figure 17(a). These factors are common for all monitoring

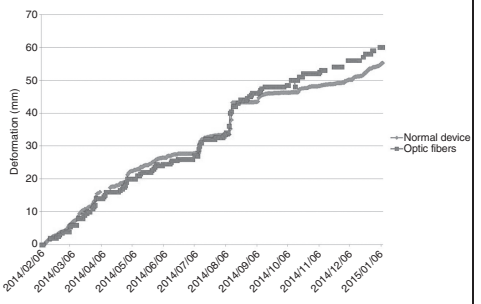
Table 6 Examples of using optic fibers with ambient lights.

<table>
<tr>
<td>
</td>
<td><u>Visualizing axial force in anchor</u>

In the new scheme for visualizing axial force by the Sun light, a metal plate is attached to the spring and the plate moves to right (in a relative sense) when the axial force increases, and to left otherwise. Just beneath the metal plate, several optical fibers are placed in such a way that sun-light can go into those fibers if their ends are exposed to the sun. An observer at distance can then count the number of fibers receiving the sun-light, can identify the position of the plate, and therefore identify the approximate value of the anchor force. The distance from the metal plate to the observation point can be in hundreds of meters. This scheme works, off course, during the day time only. An additional advantage of this method is that the monitoring can be conducted without using any electrical device. (Akutagawa et al., 2012)</td>
</tr>
<tr>
<td></td>
<td><u>Visualizing landslide deformation</u>

Slow, but non-converging deformation in landslide area needs to be monitored and visualized with a large measuring range. The device on the left was designed to measure deformation of up to 200mm and has a glass filter plate (below) with specially designed windows to take in sun light.


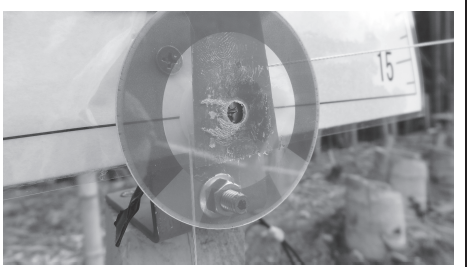
In the first lane, 2*2mm windows are arrayed at 10mm interval. These are for reading displacement increment of 2mm. In the second lane, 2*10mm windows are arrayed at 50mm interval. These are for reading displacement increment of 10mm. In the third lane, there is only one 2*50mm window. This is for reading displacement increment of 50mm.</td>
</tr>
<tr>
<td>


</td>
<td>There are five optic fibers placed at 2mm interval, in terms of center-to-center distance below the first lane. Below the second lane, five fibers are placed at 10mm interval. Likewise, below the third lane there are five fibers placed at 50mm interval.

As the filter plate is made to displace according to the landslide deformation, the sun light reaches different optic fibers depending the positions of windows printed in the filter plate. By decoding light patterns on a monitoring board, one can determine current level of deformation. The record of measurement over a 12 month period shows that the device functions very well for zero running cost.</td>
</tr>
</table>

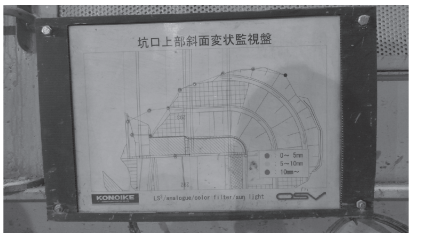
Table 6 (cont.)





Visualizing deformation of slope just above a tunnel portal

Deformation of two arbitrary points is translated into rotation by a pulley which is indicated as a rotating needle. The needle is also attached to a circular transparent color filter plate behind which an optic fiber is awaiting ambient light to come in. As the sunlight is colored when it goes through the filter and into the fiber, the color, and therefore deformation, can be visually identified at the monitor board placed in a tunnel. The similar method can be used to visualize deformation ahead of tunnel face, as well (Akutagawa *et al.*, 2013).



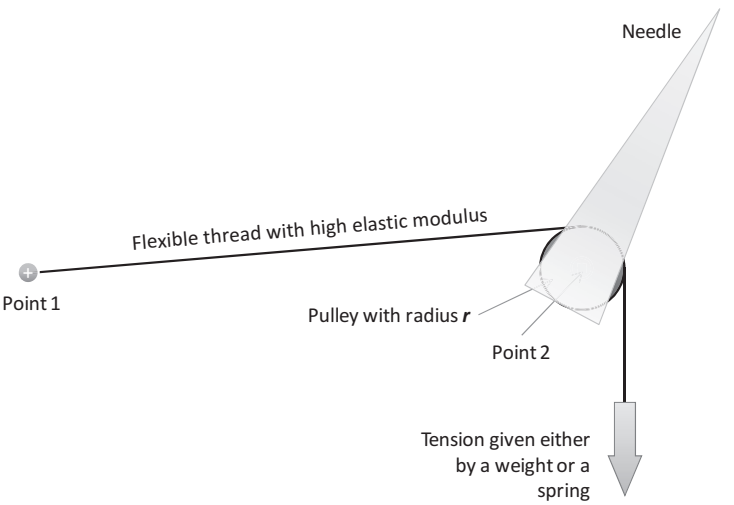
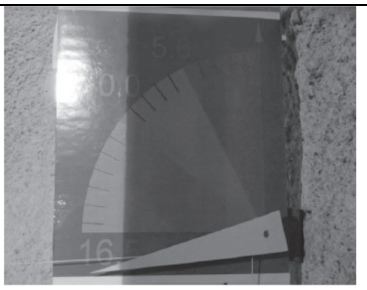


Figure 16 Translation of displacement into rotation.

projects with or without use of OSV sensors. Factors listed in Figure 17(b) are directly associated with the use of sensors built on the OSV concept. It is seen from the list of factors that there is no single and unique design solution for a given OSV monitoring project.

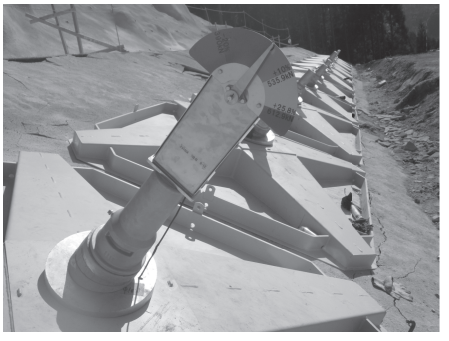
Table 7 Application examples of using mechanical devices.

<table>
<tr>
<td>
</td>
<td><u>Convergence measurement in a tunnel</u>

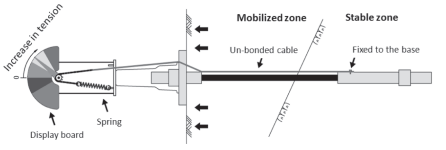
Mechanical sensor can be used to measure and indicate deformation across a crack in shotcrete, tunnel convergence and any other locations of interests. Photos on the left show examples of using pulley with radius of 10.5mm (Akutagawa et al., 2014d).

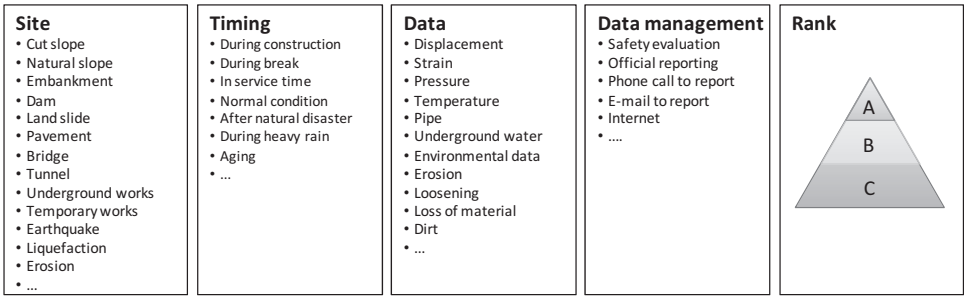
</td>
</tr>
<tr>
<td></td>
<td><u>Sliding rock slope</u>

In this field example, several mechanical sensors were installed on a rock slope that had been sliding at every heavy rain fall over the last several years. Monitoring conducted over a 3 month period in 2013 revealed that a maximum deformation of 30mm was observed. Pulley with radius of 10.5mm was used in this case, too (Izumi et al., 2014a).

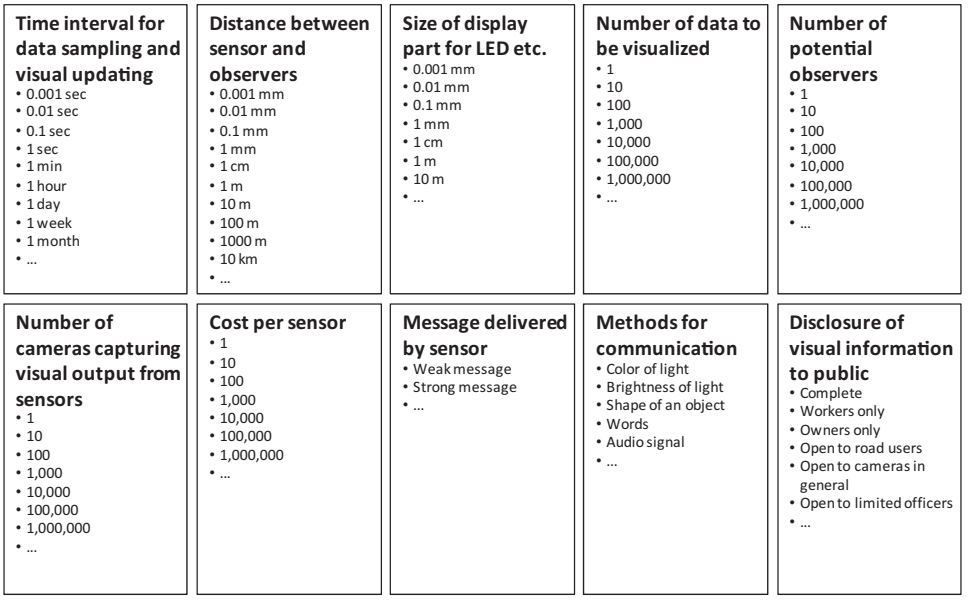
</td>
</tr>
<tr>
<td></td>
<td><u>Ground anchor</u>

A specially designed ground anchor with a mechanical sensor on the anchor cap was installed. The sensing part is connected to an un-bonded cable fixed at the end. Change in anchor force can be easily visualized from distance with zero running cost. In this example, the pulley has a radius of 15.27mm (Saito et al., 2014).

</td>
</tr>
</table>



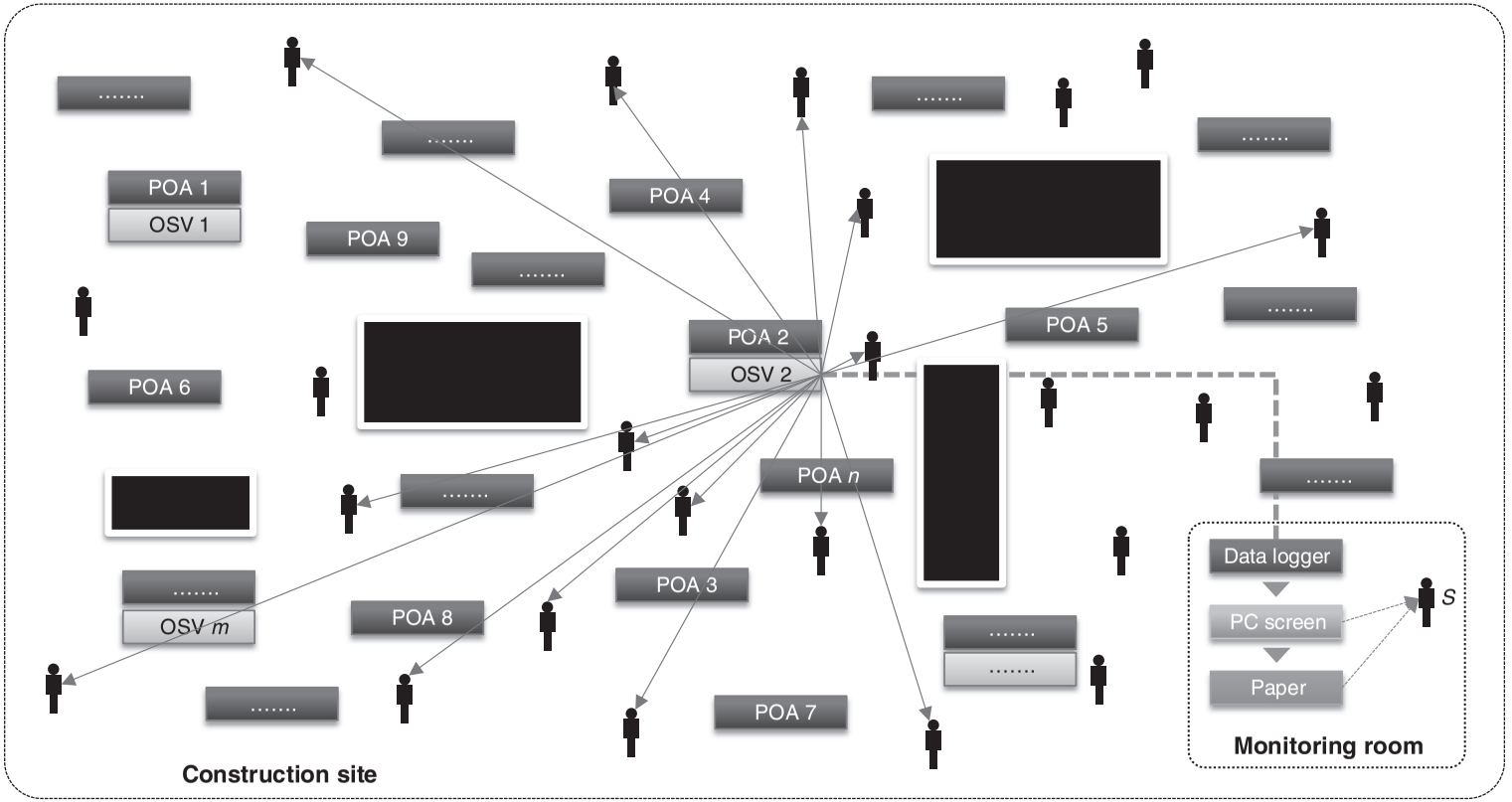
(a) General factors associated with a monitoring project.



(b) OSV-related factors associated with a monitoring project.

Figure 17 Design factors associated with a monitoring project using OSV sensors.

Figure 18 shows an illustrative example of what a planning of an OSV monitoring project involves. Black areas represent buildings or sight-blocking-objects in a construction site. There could be as many as n Potential Origin of Accident (POA) of which m are monitored by OSV sensors. An ideal case is that the ratio m/n is 1. Solid arrows show light travelling from a sensor "OSV 2" to workers. Thick dashed line indicates cabled connection between the sensor and data logger in a monitoring room. Designers need to fully understand a situation, prioritize areas to be monitored, select best combination of OSV sensors under a given budget while systematically analyzing how people move around and see these sensors in the site. There is no Golden Rule as such to automatically come up with a best solution; however, a strong research interest has to be paid to this optimization problem.



POA = Potential Origin of Accident

Figure 18 An illustrative example of planning an OSV monitoring project.

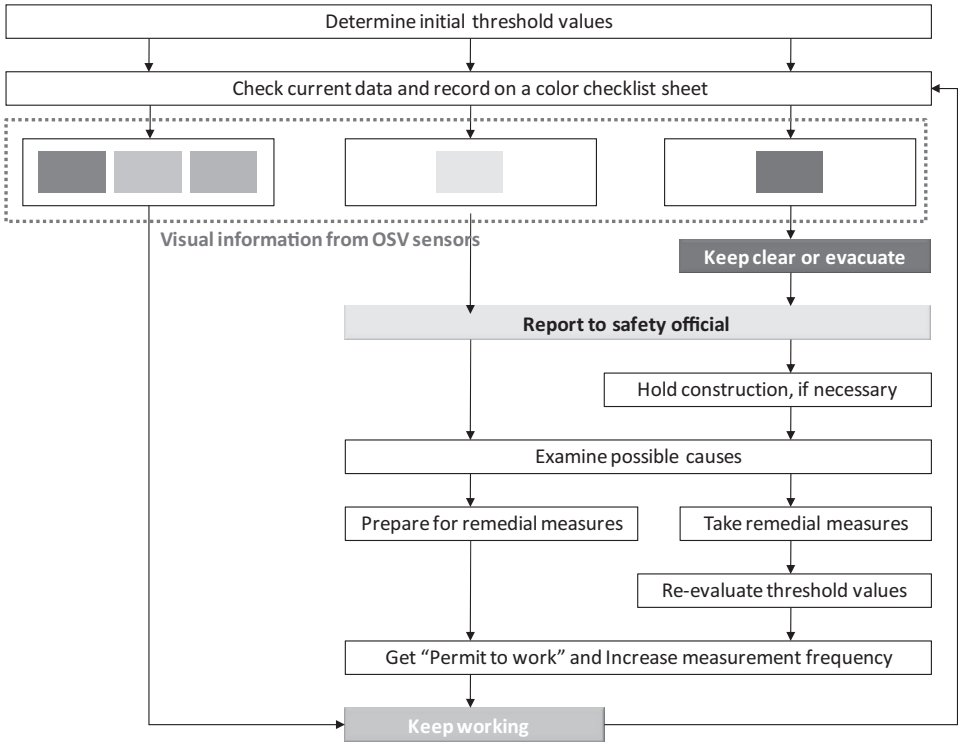


Figure 19 An example flow of actions associated with employment of OSV.

3.2 Operation

Figure 19 shows an example flow of actions to be taken when a monitoring based on OSV is employed. Determination of threshold values must be conducted carefully among engineers and owners while considering timing of device installation with respect to progress of construction.

As the new visual scheme is brought into action, the concept and purpose of the OSV monitoring and action guidelines need to be explained in plain words to workers, general contractors, safety management officers and citizens nearby. In order to inform them about how to respond to visualized information, a safety education seminar need to be conducted on site.

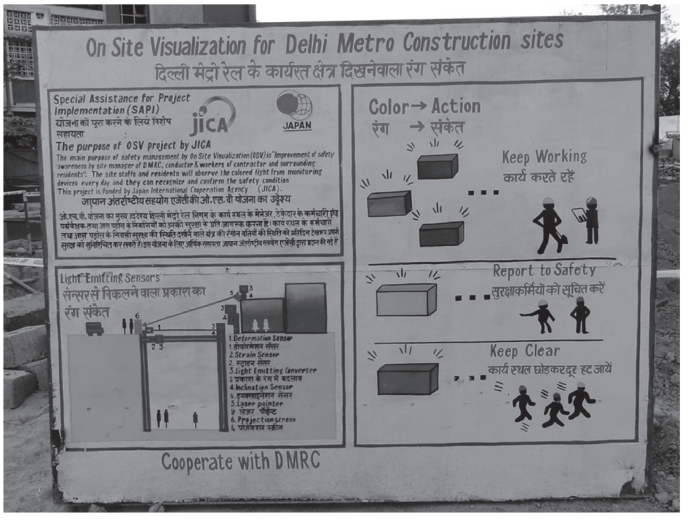
Figure 20 shows examples of a safety education seminar, a board explaining actions to be taken and questionnaires conducted for workers at the OSV monitoring site in New Delhi.

4 CONCLUSIONS

This chapter introduced a new monitoring scheme called On-Site Visualization. A cleverly designed monitoring based on the concept of OSV is expected to improve



(a) Safety education seminar for workers.



(b) Big board showing actions to be taken for each color.



(c) Questionnaires for workers.

Figure 20 Safety education and operation of monitoring based on OSV (Nakamura *et al.*, 2010).



(a) Open cut excavation site.



(b) Underground construction site.

Figure 21 Ideal design examples of OSV monitoring for advanced safety management.

safety and reduce risk with the best use of visualized information shared by all concerned. Further hardware improvement in terms of cost, durability, function and inter-connectivity with ICT helps more advanced design of an OSV project for limited budget, as illustrated in Figure 21. In terms of public acceptance, there shall be more test cases in which messages in the form of visualized information shall be utilized to raise quality of life, in terms of safety, not only for workers, but also for citizens. Once the cost required for installation of these devices is reduced down to a critical level, and

standard operational guidelines be explicitly documented, safety management practices in rock engineering communities would advance to a new stage.

REFERENCES

Akutagawa, S., Takano, K. & Takenaka, T. (2007) Development of a new device to translate relative deformation into color of light and its application. *Proceedings of the General Convention for Japan Society for Civil Engineers, Hiroshima, CD-ROM 3–01. (In Japanese)*

Akutagawa, S. (2010) On Site Visualization as a new paradigm for field measurement in rock engineering. *Proceedings of the 6th Asian Rock Mechanics Symposium*, New Delhi, pp. 34–45.

Akutagawa, S., Kusui, A. & Nomura, M. (2010) Light emitting sensors as new visual tool for rock structure monitoring. *Proceedings of the International Symposium of the International Society for Rock Mechanics*, EUROCK 2010, Lausanne, pp. 609–612.

Akutagawa, S., Minami, Y., Haba, T., Hiroshima, T. & Nozawa, T. (2011) A new method for visualizing stresses in rock support measures by using a light emitting sensor. *Proceedings of the 9th ISRM Congress*, Beijing.

Akutagawa, S., Nishio, A., Takeya, K., Ishizuka, Y. & Katayama, T. (2012) A new method for visualizing force in ground anchor by using plastic optical fiber and sun light. *Proceedings of the 7th Asian Rock Mechanics Symposium*, Seoul, October 15–19.

Akutagawa, S., Zhang, H., Terashima, M. & Tsujimura, K. (2013) Measurement and real-time visual presentation of the ground deformation ahead of mountain tunnel face using optical fibers. *Proceedings of Sinorock Symposium for the 3rd International Society for Rock Mechanics*, Shanghai, pp. 759–762.

Akutagawa, S., Zhang, H., Terashima, M. & Tsujimura, K. (2014a) Simple mechanical methods for monitoring and data-visualization during NATM tunnel construction. *Proceedings of the 42nd Symposium for Rock Mechanics*, *Tokyo*, *CD-ROM*.

Akutagawa, S., Nishio, A., Matsumoto, Y. & Machijima, Y. (2014b) A new method for reading local deformation of granular material by using light. *Proceedings of the 48th US Rock / Geomechanics Symposium, Minneapolis*, Paper 7723.

Akutagawa, S. Nakata, K., Nishio, A. & Yamada, H. (2014c) Single Observation Point method for measurement and real-time visualization of inclination using a mirror for rock engineering projects. *Proceedings of the 8th Asian Rock Mechanics Symposium, PDF file RHM-4*, Sapporo, Japan.

Akutagawa, S., Zhang, H., Terashima, T. & Tsujimura, K. (2014d) A mechanical method for monitoring and visualization of deformations of tunnel structures. *Proceedings of the 8th Asian Rock Mechanics Symposium, PDF file FMT2-5*, *Sapporo, Japan*.

Association for Asian Research. (2015) *Safety Challenges in China's Coal Mining Industry*. [Online] Available from: http://www.asianresearch.org/articles/2997.html [Accessed 1st June 2015].

Conover, D., Ross, T. & Bigby, D. (2010) Recent experience using Telltale Roof Monitoring Systems. *Proceedings of the 29th International Conference on Ground Control in Mining*, *July 27–29*, *Lakeview Resort*: *Golf & Spa*, *Morgantown, WV, USA*.

Enzan Kobo. (2015) Product pamphlet for A-Flash-α. *(In Japanese)*

Health and Safety Executive (2000) The collapse of a NATM tunnels at Heathrow airport – a report of the investigation by the Health and Safety Executive. *HSE books, Sudbury Suffolk, ISBN 0717617920*.

Hill, K.O., Fujii, Y., Johnson, D. C. & Kawasaki, B. S. (1978) Photosensitivity in optical fiber waveguides: Application to reflection fiber fabrication. *Applied Physics Letters* 32 (10), p. 647.

Izumi, C., Akutagawa, S., Zhang, H. & Tsujimura, K. (2014a) The development of low cost Mechanical OSV (On Site Visualization) and its application on Bai Chay Bridge approach road in Vietnam. *Proceedings of the International Conference on Life-Cycle of Structural Systems* – Furuta, Frangopol & Akiyama (Eds), Waseda University, pp. 649–656.

Izumi, C., Akutagawa, S., Tyagi, J., Abe, R., Sekhar, Ravi & Kusui, A. (2014b) Application of a new monitoring scheme "On Site Visualization" for Safety management on Delhi Metro Project. *Tunnelling and Underground Space Technology 44*, pp. 130–147.

Izumi, C., Akutagawa, S., Sekhar, Ravi, Kataria, R., Abe, R. & Haga, H. (2014c) On-site visualization monitoring for long span bridge on Delhi Metro Project. *Current Science* 106, (09), pp. 1280–1290.

Kitahara, S., Ohta, T., Kawagoe, T. & Nagai, S. (2006) Geological factor of the Ushikagi tunnelling collapse. *Proceedings of Japan Society of Engineering Geology*, *pp. 89–92. (In Japanese)*

Matsumoto, Y., Nishio, A., Machijima, Y., Takahashi, A. & Akutagawa, S. (2012) Fundamental experiments for detecting arbitrary changes occurring in granular materials by measuring intensity of reflected light. *Proceedings of a Symposium on Geo-environment and Monitoring, Kansai Branch of Japanese Geotechnical Society. (In Japanese)*

Meltz, G. *et al.* (1989) Formation of Bragg gratings in optical fibers by a transverse holographic method. *Optics Letters* 14 (15), p. 823.

Nakamura, N., Abe, R., Akutagawa, S., Takahashi, A. & Kusui, A. (2010) Final Report, Special Assistance for Project Implementation (SAPI) applying the monitoring method by On Site Visualization at Delhi Metro construction sites. *SAPI for Delhi Metro Phase II Project utilizing Japanese ODA, Japan International Cooperation Agency (JICA)*, March to June, 2010.

QUALIROCK (2015) ROCKTALE [Online] Available from: http://www.rocktale.co.za/ [Accessed 2nd June 2015].

Saito, H., Kobayashi, R., Takeya, K. & Akutagawa, S. (2014) Development of a new method to grasp axial force variation in ground anchor. *Proceedings of the 53rd Symposium for Japan Society of Landslide*, *pp. 114–115*. (*In Japanese*)

Satou, J., Tamaru, K., Kusumoto, T. & Nishimura, K. (2014) Empirical research of the curved tunnel face and early invert installing, Japan Society of Civil Engineers. *Tunnels and Underground* 45 (1), pp. 49–59. (*In Japanese*)

Zhang, F., Ye, B. & Ye, G. (2013) A unified description of Toyoura sand. *Constitutive Modeling of Geomaterials, Springer Series in Geomechanics and Geoengineering*, *pp. 663–674*.



Taylor & Francis
Taylor & Francis Group
http://taylorandfrancis.com

Chapter 8

Longer-term performance of grouted bolts in different lithologies in Illinois mines

Yoginder P. Chugh, H. Gurley & W. Bell
Mining and Mineral Resources Engineering, Southern Illinois University, Carbondale, Illinois, USA

Abstract: This contribution assesses longer-term anchorage performance of fully grouted bolts in different lithologies in two coal mines in Illinois using the Short Encapsulation Pull Test (SEPT) studies. These tests were done at three different times after bolt installation; 0 days, 125–140 days, and 188–270 days. A borehole was also drilled in each test area about 2.6 m above the coal seam prior to bolts installation and examined with a borehole camera to document changes in de-laminations. Load cells monitored changes in few selected bolts. In addition to Grip Factor (GF), anchorage stiffness data for bolts were also developed that provided additional insights. GF values for all lithologies were similar to those reported in the literature. GF values typically increased with time but anchorage stiffness typically decreased. This was a significant finding affecting longer-term performance of bolts and ground control in coal mines in southern Illinois.

1 INTRODUCTION

Chugh *et al.* (2009) analyzed the US Mine Safety and Health Administration (MSHA) reportable roof-falls database of 642 falls for Illinois mines for the period 2004 to 2008. The data accounted for almost 100% of the underground coal production in Illinois. Although normalization of data was not possible, three highly relevant observations were made: 1) Some primary supports widely used in Illinois (conventional, partially grouted tension, double-lock, and longer bolts) may not be effective in controlling roof falls; 2) About 35% of the falls had stand-up time less than 90 days, and 40% less than 120 days; 3) Longer fully-grouted bolts (beyond 1.8 m length) should be avoided; 4) Fall height is typically larger than bolt length by 0.3–0.6 m for all types of bolts used. The above established the need to evaluate longer-term performance of different types of bolts in typical lithologies associated with Herrin (No. 6) and Springfield (No. 5) coal seams in Illinois. A roof fall database, for the period January 1, 2005 through May 15, 2010, was developed for the two mines involved in this study to further establish the need for longer-term performance of primary supports. At Mine 1, most falls occurred in 4-way intersections with stand-up times of either less than 60 days or greater than 120 days. Mine 2 experienced most falls in 3- and 4-way intersections in isolated areas of transitional lithologies and they occurred either between 0 and 90 days or after 180 days. These included shear zones, compressional faults, clay dikes, and lithofacies changes, etc. In transitional roof lithologies areas around the channels, time-dependent performance

of primary roof supports becomes important since rock mass deformations occur due to preexisting discontinuities and degradation of rock mass properties due to moisture absorption and migration. Additionally, coal mine roof rating (CMRR) values for most sites evaluated ranged 30–45. Most falls were associated with geologic anomalies rather than to CMRR or other rock mass classification indices. These coupled with well-documented studies on moisture sensitivity of shales associated with Illinois coal seams established the need for this study whose goal was to assess the longer-term performance of different bolts used as primary supports in several different lithologies above coal seams. Short Encapsulation Pull Test (SEPT) studies were used to assess the longer-term performance of bolts. Grip factor and anchorage stiffness data for bolts were developed in different lithologies at the two mines immediately after installation and at 125–140 days and 188–270 days after installation.

2 Mining conditions in Illinois

Underground mining conditions in Illinois are generally favorable with persistence of thick, relatively parting-free coals; gentle pitch (~1.0%); relatively dry conditions; low methane liberation; and generally good roof conditions. The only widespread undesirable characteristic is the relatively weak floor immediately beneath the coal seams. Significant depositional variations involving competent and non-competent roof strata are present on regional and local scales. Room-and-pillar mining with about 60% extraction ratio was the primary mining method until 2005 but longwall mining has increased over the last 10 years in areas with surface subsidence rights. Currently, seven (7) longwall faces are operating in southern and central Illinois. Two general roof types overlie the coal seams. Over most of the basin, the coals are overlain by up to 1.5 m of hard, black, "slaty" shale which is overlain by a limestone unit of similar thickness above No. 6 coal seam and generally less than 0.6 m for No. 5 seam. Both units contain marine fossils. The second general roof type is silty, gray shale which may be 18.3 m (occasionally 31 m) thick. This shale is associated with a large fluvial/deltaic complex characterized by extensive channel sandstone deposits, split coal, and "washouts". A brief description of the characteristics of two Illinois mines that cooperated in this study is given below.

Mine 1 extracts No. 5 seam coal averaging 1.3 to 1.5 m in thickness at average mining depth of 88.4 m and maximum depth of 130 m. The coal seam is typically overlain by sandy shale and/or laminated shale described as "stack rock" and one or more bands of limestone that are 0.15 to 0.3 m thick. In localized areas, limestone thickness can vary or disappear. Very hard ball-shaped concretions are sometimes found immediately above the coal seam. The immediate mine floor strata consist of claystone underlain by competent shale. The mine uses room-and-pillar mining methods with average mining height of about 2 m. Entry width averages 6.1 m and entry/crosscut spacing (center-to-center distance) ranges from 24.4 to 30.5 m in main entries and 18.3 to 20 m in panels. Many roof control problems are associated with the "stack rock" roof. Some of the mapped roof fall areas involve "stack rock" while others are in the transition lithology zone that is encountered when approaching this feature.

Mine 2 extracts No. 6 seam coal at an average depth of 183 m. Borehole data within about 200 m of an underground test area revealed 188 m of overburden overlying the 1.8 m thick coal seam with immediate roof lithology consisting of black shale (Anna),

limestone (Brereton), dark gray shale, coal (Jamestown), and sandy shale. Roof lithology at this mine can change rapidly. Limestone can thin or disappear suddenly and water-bearing sandstone can approach the coal seam. In these areas, water typically drips or flows from the mine roof and/or roof bolts. The immediate mine floor is a claystone underlain by competent shale. The mine uses longwall mining methods with panels mined in the east-west direction. Entry widths in gate roads and mains are typically 5.8 m and crosscut spacing (center-to-center distance) ranges from 30.1 to 45.7 m.

2.1 Overall approach and roof fall experience at study mines

This research started by meeting with a Mine Safety and Health Administration (MSHA) District Roof Control Specialist to discuss roof control issues, long-term roof bolt performance, seasonal-effects on bolt tension, roof deterioration over time, horizontal stresses, and mining practices. Then roof fall locations and geologic data were collected at each mine. SEPT studies experimental areas were identified in cooperation with the mining company based on roof lithologies and roof fall experience.

A roof fall database for the period January 1, 2005 through May 15, 2010 was developed. At Mine 1 most falls occurred at 4-way intersections and had stand-up time of either less than 60 days or greater than 120 days. Most falls with stand-up time of over 180 days were supported by 1.8 m long fully-grouted, passive No. 6 (18 mm) rebar, Grade 40 bolts. Lower number of falls for the same time period supported by 1.2 m long fully-grouted passive bolts was most likely due to the presence of substantial limestone in the immediate roof. Mine 2 experienced most falls in 3- and 4-way intersections in isolated areas of transitional lithologies and they occurred either between 0 and 90 days or after 180 days. Very few falls occurred where limestone was present within 1.8–2.5 m above the coal seam.

3 FIELD BOLT INSTALLATION AND SEPT STUDIES

Mark *et al.* (2003) provided a good discussion of field performance testing of fully grouted bolts. The anchorage of a fully-grouted bolt is measured by "grip factor" or GF, which is defined as resistance to pull-out force per inch or mm of grouted length. It is measured by loading the upper portion of the grouted bolt in SEPT. The anchorage capacity of a fully grouted bolt may exceed the tensile strength of the bolt resulting in yielding of the bolt rather than the anchorage bond. To lower anchorage capacity and resistance to the pull out test to below the nominal tensile strength of a roof bolt, the resin column is shortened and confined to the upper 0.3 m to 0.6 m of the bolt length depending on the strength of the host rock. This length provides enough area to ensure adequate mixing, but more importantly it minimizes the possibility of the bolt yielding prior to bond failure. GF is calculated as (load to slippage)/(resin anchor length) and is stated in units of N/mm. Increasing GF and increasing roof bolt response to loading or "stiffness" can significantly improve its ability to resist rock movement.

A pertinent research review revealed that most, if not all, SEPT studies had been conducted immediately or soon after bolt installation. In this study, SEPT studies



Figure 1 Laboratory calibration setup with DDAS data collection system.

were performed in the field according to guidelines outlined by Mark *et al*. (2002) to determine changes in the "grip factor" over an extended time period. An electronic digital data acquisition system (DDAS) and a bolt pull test frame were constructed (Figures 1 and 2) to calibrate test equipment prior to performing field studies (Chugh, 2010). The DDAS consisted of a pressure transducer, string extensometer, data acquisition module with power supply, and laptop computer. The pressure transducer and analog pressure gage mounted on the hydraulic hand pump were calibrated using a Humboldt proving ring. Data collected manually using the analog pressure gage and dial indicator was then calibrated with the DDAS data. Figure 2 provides a schematic of the SEPT equipment setup and shows equipment being tested at the SIUC Materials Test Laboratory in Carterville, IL.

A typical SEPT was conducted by installing a roof bolt equipped with a pull collar, which fits around the shaft of the roof bolt and is located between the roof bolt head and roof bolt plate. A pull claw is threaded onto a pull rod that is inserted through a bolt bell housing and a hollow cylinder hydraulic jack shown in Figure 2. The pull rod then receives a bearing plate held in place by two jam nuts. The latter assembly is attached to the roof bolt using the pull claw to engage the pull collar. The bolt bell housing between a second bearing plate and the roof bearing plate allows the hydraulic cylinder to apply load to the roof bolt pull collar by pushing against the roof bolt bearing plate. A dial indicator measures the distance between the two plates. During laboratory testing of equipment, roof bolts were installed into 25 mm diameter steel pipe using procedures that are

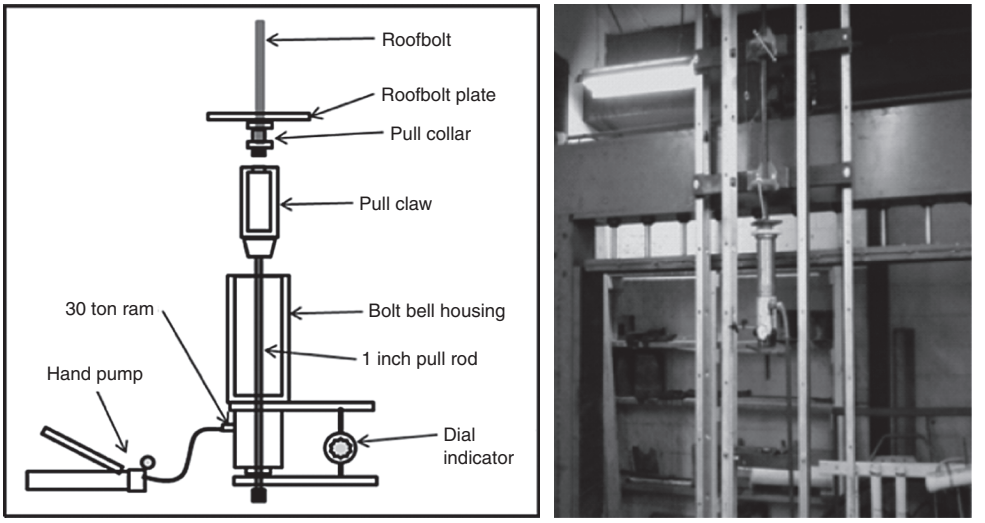


Figure 2 SEPT studies equipment schematic (left) and laboratory test frame (right).

typically used during underground installation. The bolt/pipe assembly was securely clamped in a test frame shown in Figure 2. Then the hydraulic cylinder, bolt bell housing, and pull claw assembly were attached and data was collected using both manual and DDAS systems.

Load cells designed at SIUC were used to determine the amount of load applied to mine roof strata during and after roof bolt installation. The load cell consisted of a composite material disk housed between two 1.3-mm thick steel plates and calibrated for load-deformation. They were installed by inserting a roof bolt through a 25.4-mm diameter hole in the center of the load cell assembly and tightening the roof bolt against the load cell and mine roof bolt plate.

Tension rebar (TR) bolts were installed to the specified torque range as required by the MSHA-approved roof control plan. Torque is a good indicator of the amount of load applied to the roof bolt and can change over time. It was monitored using a CDI Model 6004 LD SNSS torque wrench with a range of 162.7 to 813.5 N-m and resolution of 6.8 N-m.

SEPT analyses typically focus on reporting peak load (PL) and GF values. This study also developed "Anchorage Stiffness around 50% of the Failure Load" designated as AS-50. It was computed by: 1) Plotting load-displacement data for a SEPT, 2) Subtracting the value of un-grouted bolt length deformation at each load from (1) above, 3) Plotting modified load-displacement data from (2) above, and 4) Computing AS-50 as the slope of the curve in (3) above around 50% of the anchorage capacity +/– 1.8 tonnes. The authors thought that AS-50 was more important than GF since it represented the rock reinforcement potential while GF represented only the load carrying potential. The important variables identified for SEPT were: 1) Bolt length-three bolt lengths (1.2 m, 1.8 m, and 2.4 m) extending into different lithologies were tested; 2) Time duration-tests were done over three time intervals (0 days, 125–140

days, and 188–270 days after installation); and 3) Test bolts were installed in two drill hole diameters (25 mm and 35 mm) resulting in two annulus sizes.

3.1 Mine I studies

Site 1 – It was located in the "stack rock" area. Thirty-eight (38) roof bolts were installed at Site 1 designated as 1–1 (Figure 3). Before installation, a bore hole was drilled about 2.7 m into the roof. A borehole camera was used to observe lithologic changes and delaminations or cracks present in the immediate roof strata. The camera had "fish eye" lens to provide 180 degree view of the interior of the drill hole. Images on Day 0 revealed no discernible lithologic changes and only two small cracks that extended approximately 90 to 120 degrees around the circumference of the borehole. Similar data were collected during the next SEPT cycle after 140 and 273 days.

Thirty-three (33), No. 6 (18 mm diameter) Grade 40, bolts were installed for SEPT with 30 cm grout length. Three (3) different bolt lengths (1.2, 1.8 and 2.4 m) were installed in two (2) different diameter drill holes, 25 mm and 35 mm. Six (6) roof bolts of each length were installed in 25 mm diameter holes. The mean diameter of the drill bits was 26.08 mm. Six (6) bolts, three (3) each of 1.2 m and 1.8 m lengths, were installed in 35 mm diameter drill holes with mean drill bit diameter of 34.98 mm. Only three (3), 2.4 m long bolts could be installed in 35 mm diameter holes. Depth of each hole was 25 mm deeper than the installed bolt length. This was determined by measuring the distance from the roof bearing plate, when installed on the roof bolt, to the end of the bolt. Resin used was Minova, Fast Set 23 mm A23-6-M35LIF, Facility code G, expiration date of 7/11/11. Resin cartridges were cut into appropriate lengths, based on annulus size, to achieve encapsulation of the top 30 cm of roof bolt. The cut-lengths of resin were resealed using 3 mm plastic "zip ties". To help confine the resin to the top 30 cm of the roof bolt, tape was wrapped around the bolt around this location to increase its diameter to create a seal. The bolt and resin cartridge were inserted into the hole until the bearing plate was 25 mm from roof contact. The bolt was then rotated for 5–7 seconds with upward pressure maintained against the bearing plate and mine roof for 45 seconds. SEPT was run 1-hour after installation. Two (2), 1.8 m tension-rebar bolts were also installed near the test area at 339 N-m torque for monitoring changes in it over time. To monitor bolt load changes over time, the developed load cell consisting of a composite material sandwiched between two steel plates was installed between the roof bolt head and roof bearing plate. Load cells were installed on one roof bolt of each length. The changes in load were correlated to change in the thickness of the composite material measured with resolution of 0.00127 mm.

Site 2 – This site was located in an area with shale and limestone in the immediate roof. At this site designated as 1–2 (Figure 3), two 2.7 m deep holes were drilled and located near each end of the test area for viewing with a digital camera. Only two (2) identifiable roof separations less than 3.175 mm wide intersected the hole at about 90 to 120 degrees around the circumference. Six (6), SEPT bolts (No. 6 size (18 mm) rebar, grade 40 each of 1.2, 1.8, and 2.4 m length) were installed in 25 mm diameter holes. The mean drill bit diameter was 26.03 mm. These bolts used the same resin and installation procedures as at Site 1.

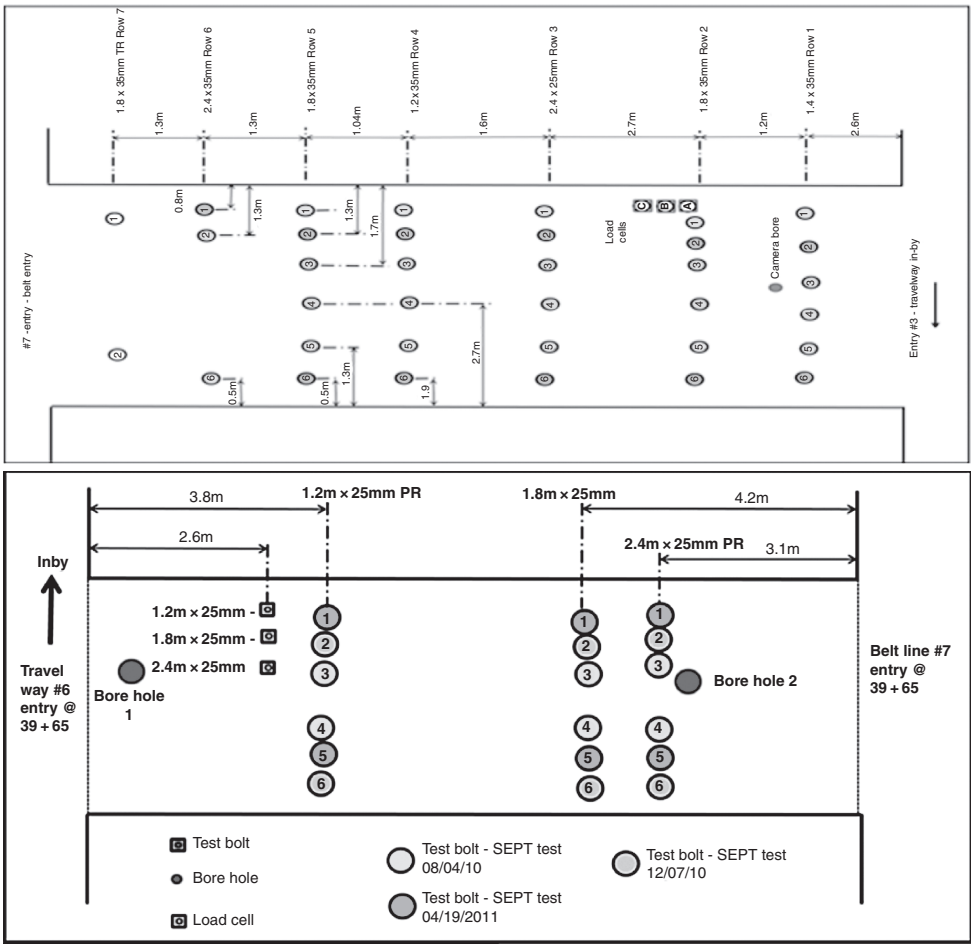


Figure 3 Roof bolt installation layout- Site 1-1 (top) layout- Site 1-2 (bottom).

3.2 Mine 2 studies

Site 1 – Twenty-seven (27) bolts No. 7 rebar (22 mm diameter), Grade 60 bolts were installed at Site 1 designated as 2–1 (Figure 4). Lithology and delaminations were monitored through a 3.4 m deep borehole above the coal seam. The immediate roof strata consisted of 0.45 m of black shale, 1.37 m of limestone, and sandy shale above it. An exploration core hole from the surface was located about 150 m north of Site 2–1. The lithology in this hole consisted of 0.27 m black shale, 1.68 m limestone, 0.37 m dark gray shale, 0.15 m rider coal seam, 0.67 m dark gray shale and 2.4 m of sandy shale. The mining height was 2.1 m, entry width was 5.3 m, and the area was dry with competent ribs. At this site, 22 bolts were installed for SEPT and five (5) for monitoring load changes over time. All bolts were installed in 35 mm diameter drill

holes with 60 cm resin encapsulation length as recommended by the roof bolt and resin manufacturer. The mean diameter of drill bits was 35.1 mm. The resin used was JennMar FastSet dated 28 September, 2010 – 18:33:20. The resin spin time was 5–6 sec and the hold time was 20–25 sec. All holes were drilled 25 mm longer than the bolt length.

Site 2 – Eleven (11) bolts were installed at Site 2, and designated as Site 2–2 (Figure 4). Nine (9) bolts were installed for SEPT and two were installed for monitoring load changes with time. An observation hole 3.4 m deep was drilled. The immediate roof strata at this site consisted of 0.20–0.25 m of black shale, 1.15–1.2 m of limestone, and sandy shale above it. The exploration core hole indicated in Site 2–1 is about

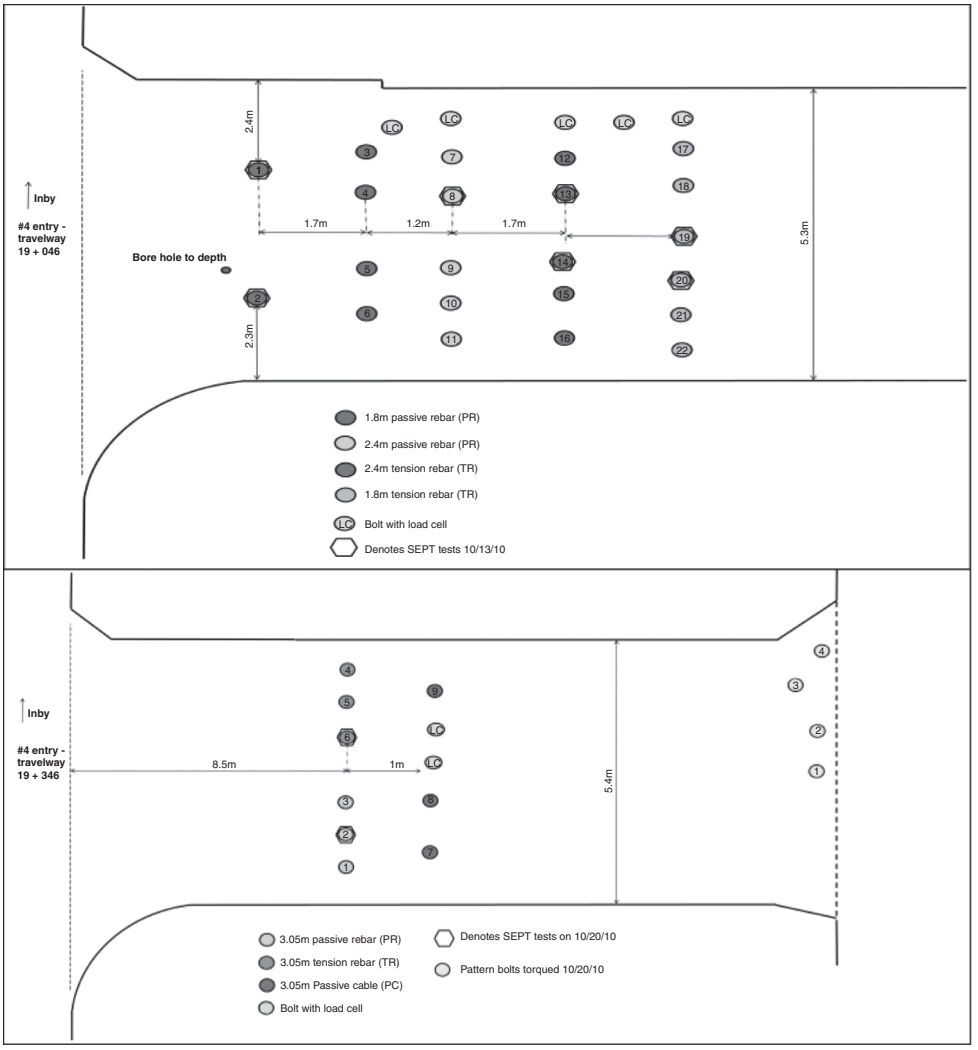


Figure 4 Roof bolt installation layout- Site 2-1 (top) and Site 2-2 (bottom).

60 m north of this site. At this site, three (3), 3 m long bolts were installed for SEPT-one grouted, one passive rebar, and one tension-rebar. In addition, one passive cable for SEPT and two (2), 3 m long tension rebar bolts with load cells were installed. The resin used was JennMar FastSet dated 29 Sept 10 – 05:56:40. In addition, four (4), 2.4 m long tension rebar bolts were installed as part of the primary roof support pattern for monitoring changes in installed average bolt torque of 389 N/m.

4 RESULTS AND DISCUSSION

4.1 Mine 1

SEPT studies at Site 1 were conducted one hour after installation on July 20, 2010, (Day 0), on December 7, 2010 (Day 140), and on April 19, 2011 (Day 273). At Site 2, SEPT studies were conducted one hour after installation on August 4, 2010 (Day 0), on December 7, 2010 (Day 125), and on April 19, 2011 (Day 258). Table 1 shows GF and AS-50 values from these tests.

On April 19, 2011, several bolts that had been pulled as much as 2.54 cm from the roof contact by earlier testing were again found tight against the roof. This is attributed to additional roof strata movement. At Site 2, Hole 2 (borescope hole nearest the No. 7 belt entry) became partially blocked around 21.6 cm above the coal seam due to a portion of the roof moving in the southwest direction along a joint plane.

1.2-m Passive Rebar Bolts: On each test date, two bolts in 25 mm holes and two bolts in 35 mm holes at Site 1 and two bolts in 25 mm holes at Site 2 were tested. At Site 1,

Table 1 Grip Factor and Anchorage Stiffness– Mine 1.

Bolt Length/Drill Hole Diameter/ Bolt Type (meter/mm)	*GF (N/mm)*	*AS-50 (N/mm)*	*GF (N/mm)*	*AS-50 (N/mm)*	*GF (N/mm)*	*AS-50 (N/mm)*
	Site 1					
	Day 0		*Day 140*		*Day 273*	
1.2 / 25 / PR	356	19250	335	19092	321	17125
1.2 / 35 / PR	318	21922	342	32014	257	16264
1.8 / 25 / PR	325	16768	355	25244	333	18597
1.8 / 35 / PR	145	2290	231	6935	163	26114
2.4 / 25 / PR	195	8952	296	15404	288	13362
2.4 / 35 / PR			263	10658	194	16856
	Site 2					
	Day 0		*Day 125*		*Day 258*	
1.2 / 25 / PR	296	13317	341	96289	352	38925
1.8 / 25 / PR	320	14776	333	120151	337	92396
2.4 / 25 / PR	302	14673	336	34156	290	33268

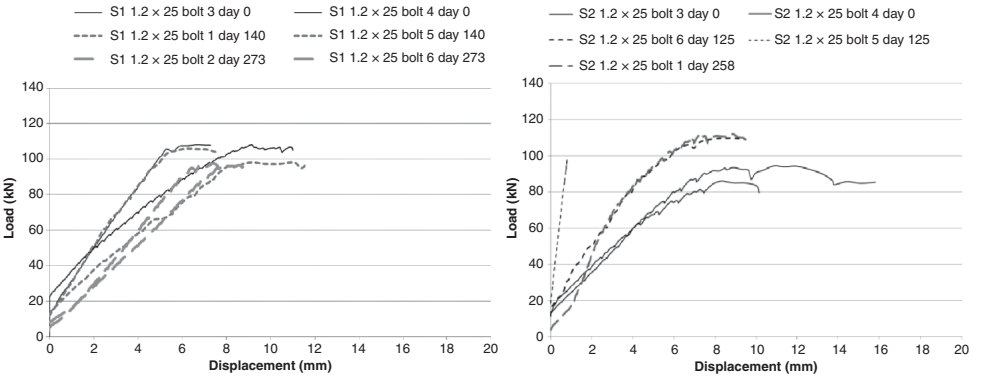


Figure 5 1.2m x 25mm bolt length/hole dia. SEPT results- Site 1-1 (left) and Site 1-2 (right).

1.2-m long bolts in 25 mm diameter holes progressively lost GF and AS over the 273-day test period. The AS-50 loss was only 0.8% over the first 140 days, but 10.3% over the last 133 days resulting in a total decrease of 11.0% over the entire period. GF loss was 8.9% for the entire 273-day period. At Site 2, GF and AS-50 values for 1.2-m bolts in 25 mm holes increased 15.5% and 623%, respectively, over the first 125-day period. During the second 133-day period, AS-50 decreased by about 59.6%, but for the overall 258-day test period, both values showed an increase. Results of SEPT tests for Sites 1 and 2 are seen Figure 5.

At Site 1, 1.2 m long bolts in 35 mm holes showed increases in GF and AS-50 of 7.5% and 46.0%, respectively, over the first 140 days, but decreases of 25.1% and 49.2%, respectively, over the last 133 days, for overall decreases of 19.5% and 25.8%, respectively. No bolts were installed in 35 mm holes at Site 2 due to production constraints. Decrease in GF and AS-50 values were significantly less for 1.2-m bolts in 25 mm holes than for 1.2-m bolts in 35 mm holes. While AS-50 was initially higher for bolts in larger holes and it increased during the first 140 days, by the end of the 273-day test period, it was less than for bolts in smaller holes. SEPT results for these bolts are shown in Figure 6.

1.8-m Passive Rebar Bolts: On each test date, two bolts in 25 mm holes and two bolts in 35 mm holes at Site 1 and two bolts in 25 mm holes at Site 2 were tested. At Site 1, 1.8 m long bolts in 25 mm holes gained GF and AS during the first period, then lost roughly half of that gain during the second period, but overall there was an increase in both values. Results were similar at Site 2; however, GF did not decrease during the second period but remained about the same. The behavior of 1.8 m bolts in 25 mm holes at Site 2 was quite similar to that of 1.2 m bolts in 25 mm holes. At Site 1, 1.8 m bolts in 35 mm holes showed increases in GF and AS-50 during the first 140 days, similar to the same length bolts in 25 mm holes; however, during the second 133-day period, while GF decreased as seen with bolts in 25 mm holes, AS-50 continued to increase. Overall, increases in GF and AS-50 were greater for 1.8 m bolts in 35 mm holes than for 1.8 m bolts in 25 mm holes. Results are presented in Figure 7 for 1.8 m × 25 mm bolts at Sites 1 and 2. Results for 1.8 m × 35 mm bolts at Site 1 are shown in Figure 8.

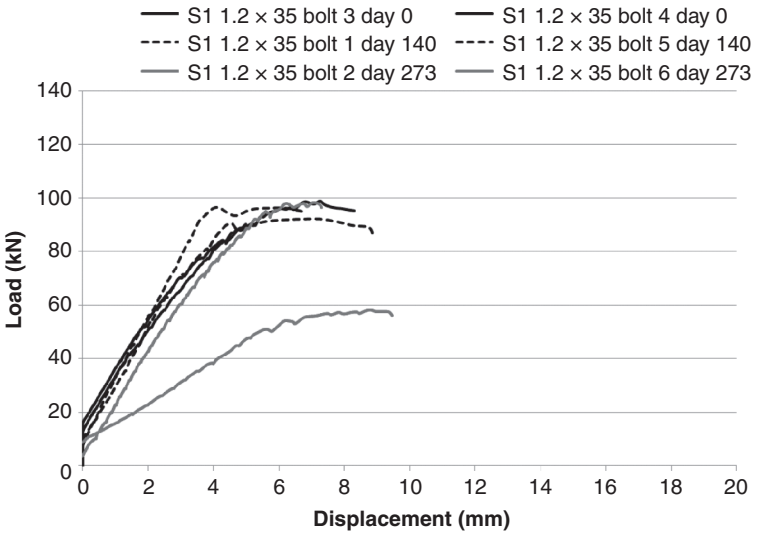


Figure 6 1.2m x 35mm bolt length/hole dia. SEPT results- Site 1-1.

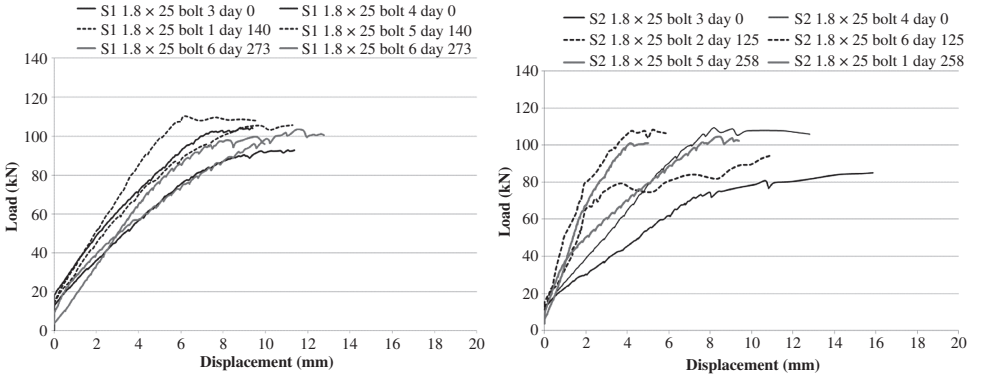


Figure 7 1.8m x 25mm bolt length/hole dia. SEPT results- Site 1-1 (left) and Site 1-2 (right).

2.4-m Passive Rebar Bolts: On each test date, two bolts in 25 mm holes at Site 1 and two bolts in 25 mm holes at Site 2 were tested. Because of the limited number of 2.4 m bolts in 35 mm holes at Site 1, two bolts were tested at 140 days and one bolt was tested at 273 days. For 2.4 m bolts in 25 mm holes, both sites showed increases in GF and AS-50 during the first period followed by decreases during the second period. With the exception of GF for 2.4 m bolts in 25 mm holes, decreases during the second period were less than increases during the first period. With limited capability to test 2.4 m bolts in 35 mm holes, results indicate a decrease in GF of 26.6% and an increase in AS-50 of 58% during the last 133-day period of SEPT work. It is important to

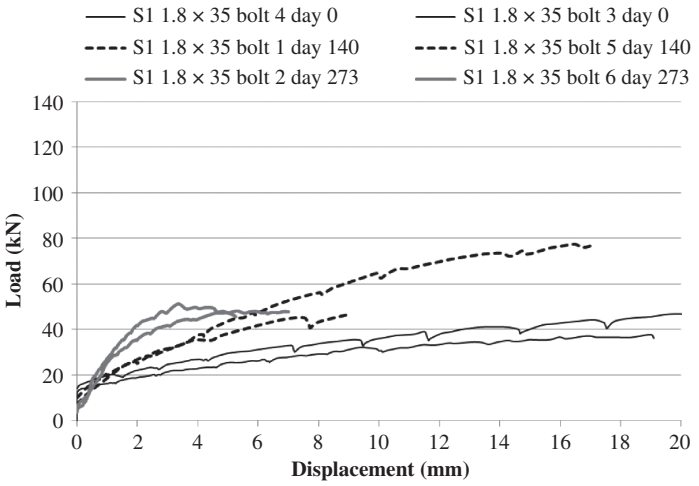


Figure 8 1.8m x 35mm bolt length/hole dia. SEPT results – Site 1-1.

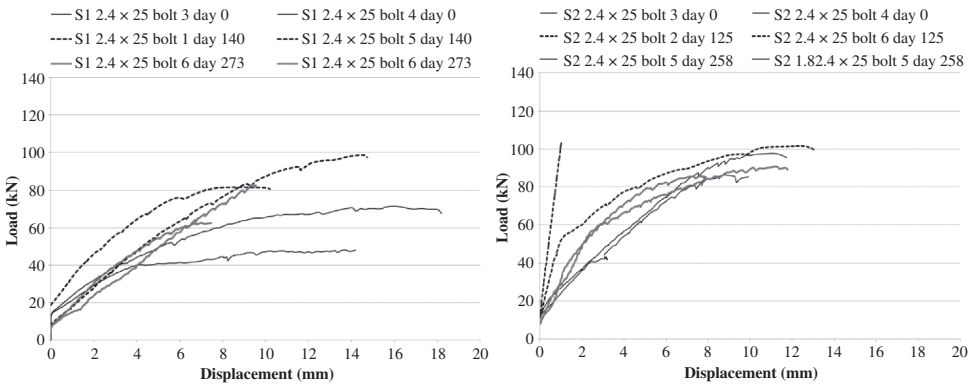


Figure 9 2.4m x 25mm bolt length/hole dia. SEPT results- Site 1-1 (left) and Site 1-2 (right).

mention that the observed increase or decrease in GF and AS-50 for all bolt lengths and hole sizes are within the testing variability. SEPT test results for 2.4 m × 25 mm and 35 mm bolts at Sites 1 and 2 are presented in Figures 9 and 10.

Load Cell Data: Bolts with load cells installed are identified in Figure 3. Load cells were monitored initially one hour after installation and again on December 7, 2010 and April 19, 2011 with results shown in Table 3. At Site 1, measurements indicate only a slight increase in load on bolts over the 273-day period. The 1.2 m long bolt in the 25 mm hole saw the largest increase equaling 3.79 kN of load. At Site 2, measurements indicate a large increase in load during the 258-day period. The increase was similar for 1.2 m and 1.8 m bolts and slightly higher than the highest value at Site 1, but the 2.4-m bolt saw 15.1 kN increase in load at Site 2.

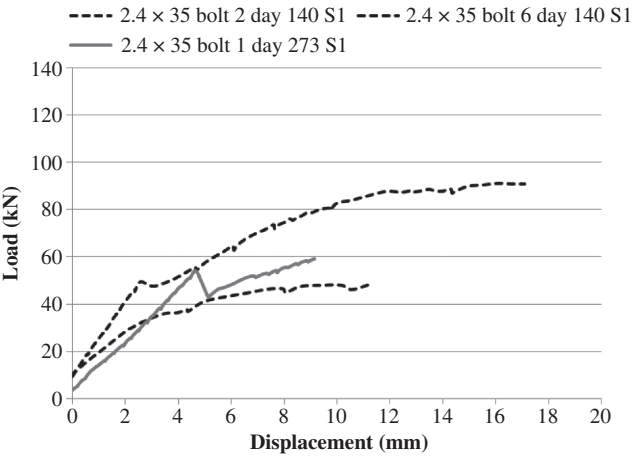


Figure 10 2.4m x 35mm bolt length/hole dia. SEPT results- Site 1-1.

4.2 Summary results-mine 1

The GF and AS (50) results for Mine 1 Sites 1–1 and 1–2 on Day 0 and Days 125–140, and 258–273 were presented in Table 1 and in Figures 5–10. The results for each bolt type and installation are based on the average of two tests. A summary of observations is given below.

- The GF values for shorter length bolts (1.2 m to 1.8 m) in Black Shale range about 220 to 260 N/mm at both sites. These values are typical for load carrying capacity in Illinois mines.
- The No. 6 (18 mm) rebar in 35 mm diameter borehole can exhibit significantly lower GF values than in 25 mm diameter borehole (Table 1). This is consistent with previous scientific findings.
- The 1.8 m and 2.4 m long bolts in 25 mm and 35 mm holes at Site 1–1 show poor GF values and range 110 to 145 N/mm.
- GF values seem to be less dependent on the lithology and much more on the annulus between the bolt size and the bolt hole.
- The GF values are similar or slightly higher after 120 or 140 days. Borehole observations showed no additional laminations or opening up of previous laminations.
- Incremental changes in bolt loads after 24 hours indicated by load cells at Site 1–1 were small and vary only 1.12 to 3.36 kN. At Site 1–2 the bolt loads increase varied 16 to 23.6 kN for different length bolts after 140 days.
- AS values at both sites after 120 or 140 days are generally higher than Day 0 values. After 273 days at Site 1, AS values decrease for all bolts with the exception of the 1.8 m and 2.4 m long bolts installed in 35 mm boreholes which saw a significant increase in AS values at Day 273. Thus, it appears that the curing of the resin continues after installation for a period but may deteriorate over a long time for small resin annulus. For larger annulus this may not be the case.

- The AS values for longer bolts (1.8 m and 2.4 m long bolts) on Day 0 both in 25 mm and 35 mm holes were generally low with mean of 11.3 kN/mm and 11.8 kN/mm, respectively while the mean for 1.2 m long bolts was 18.16 kN/mm or about 36% increase. Even with limited data this is a critical finding and may corroborate field observations that longer bolts are not effective in controlling roof falls.
- Overall, 1.2 m long bolts provide better GF and AS values than 1.8 m or 2.4 m bolts. These results are consistent with observations at the mine that 1.2 m bolts are most effective.

4.3 Mine 2

SEPT studies at Site 1 were conducted one hour after installation on October 13, 2010 (Day 0), on February 11, 2011 (Day 121), and on April 26, 2011 (Day 195). Site 1 had 1.8 m and 2.4 m bolts. At Site 2, which had only 3.1 m long bolts, SEPT studies were conducted one hour after installation on October 20, 2010 (Day 0), on February 11, 2011 (Day 114), and on April 26, 2011 (Day 188). Table 2 shows GF and AS-50 values from these tests.

1.8-m Passive and Tension Rebar Bolts: GF decreased 16.8% and AS-50 increased 1.5% during the first 121 days for PR bolts while during the second 74-day period, GF increased 15% and AS-50 decreased 15%. For TR bolts, the GF and AS-50 values were 3.3% and 25% lower, respectively, after 121 days. During the second 74-day period, GF and AS-50 increased 2.4% and 8%, respectively. SEPT test results for the three collection periods are shown in Figure 11.

2.4-m Passive and Tension Rebar Bolts: GF and AS-50 values were 23% and 9% lower, respectively, after 121 days for PR bolts. During the second 74-day period, GF and AS-50 values increased 26.8% and 29.5%, respectively. For TR bolts, the GF

Table 2 Grip Factor and Anchorage Stiffness – Mine 2.

Bolt Length/Drill Hole Diameter/ Bolt Type (meter/mm)	*GF (N/mm)*	*AS-50 (N/mm)*	*GF (N/mm)*	*AS-50 (N/mm)*	*GF (N/mm)*	*AS-50 (N/mm)*
	Site 1					
	Day 0		*Day 121*		*Day 195*	
1.8 / 35 / PR	317	17326	263	17592	303	14901
1.8 / 35 / TR	305	41012	295	30726	302	33199
2.4 / 35 / PR	295	18039	227	16386	287	21235
2.4 / 35 / TR	234	416834	263	32748	252	72782
	Site 2					
	Day 0		*Day 114*		*Day 188*	
3.1 / 35 / PR	315	31668	79	3099		
3.1 / 35 / TR	242	10867			101	8549
3.1 / 35 / PC					163	4143

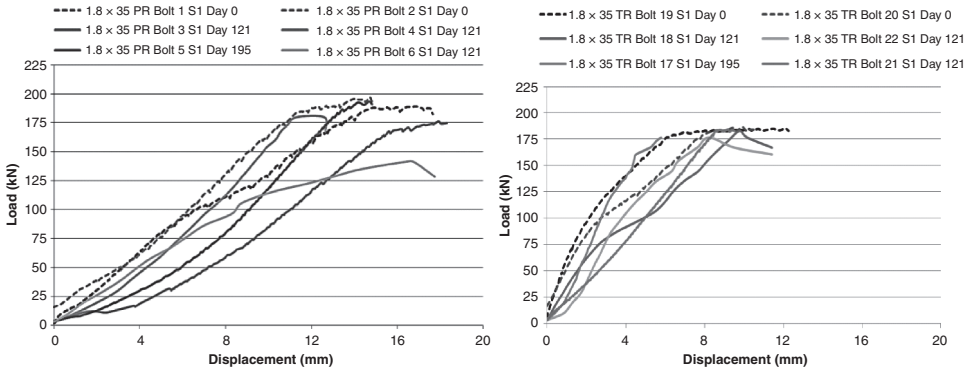


Figure 11 1.8m x 35mm PR SEPT data (left) and 1.8m x 35mm TR SEPT data (right) Site 2-1.

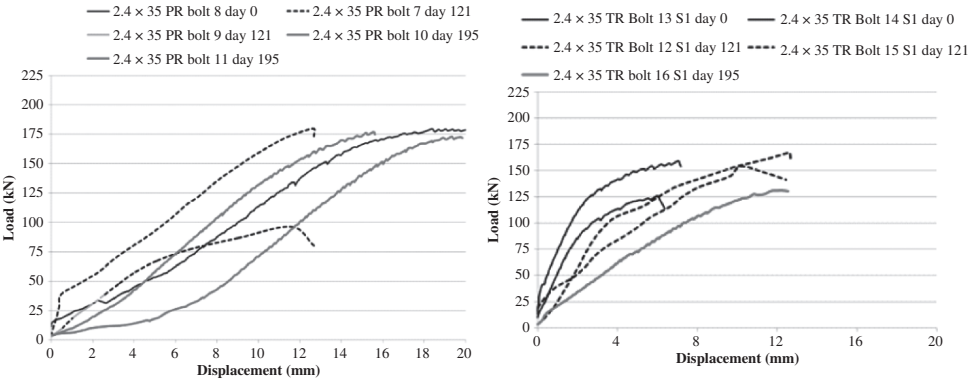


Figure 12 2.4m x 35mm PR SEPT data (left) and 2.4m x 35mm TR SEPT data (right) Site 2-1.

increased 12.6% and AS-50 decreased 92% during the first 121 days. During the second 74-day period, GF decreased 4.2% and AS-50 increased 122%. SEPT test results are shown in Figure 12.

3.1-m Passive and Tension Rebar Bolts: GF and AS-50 values decreased 75% and 90%, respectively, after the first 114-day period for PR bolts. The GF and AS-50 values decreased for TR bolts by 58.4% and 21.3% after 188 days. SEPT test results are seen in Figure 13.

3.1-m Passive Cable Bolts: During testing on Day 114, the hydraulic cylinder malfunctioned and data from Bolt #7 was considered invalid. Therefore, only data for tests on Day 188 could be obtained. The mean GF value of 163 N/mm and the AS-50 value of 4.14 N/mm are extremely low. All 3.1 m long bolts at Site 2 were completely anchored in sandy/limey-shale that overlies the 1.22–1.27 m of limestone present at Site 2. This may have affected GF and AS-50 values for these bolts when compared to shorter bolts at Site 1 where 1.8 m bolts were anchored totally in limestone and 2.4 m bolts were anchored at the interface of limestone and sandy/limey-shale. SEPT test results are shown in Figure 14.

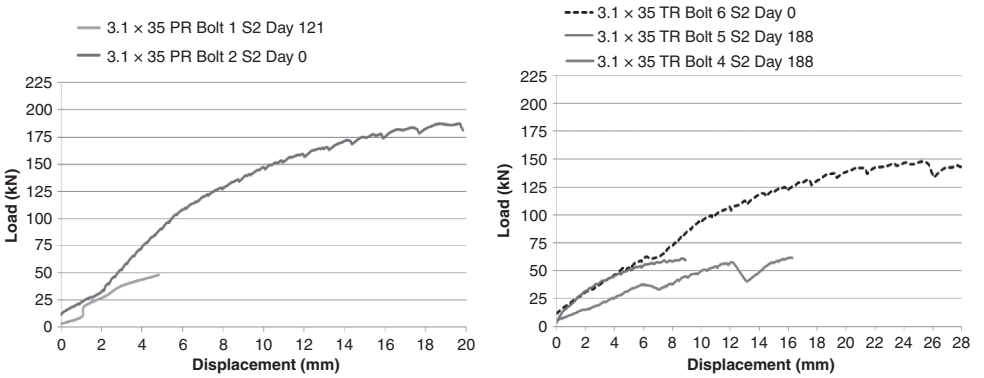


Figure 13 3.1m x 35mm PR SEPT data (left) and TR SEPT data (right) Site 2-2.

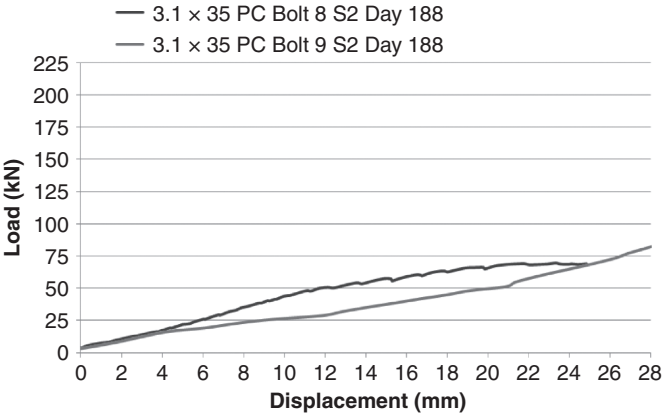


Figure 14 3.1m x 35mm PC SEPT data Site 2-2.

Torque Monitoring of Tension Rebar Bolts: Torque measurements reported in Table 4 indicate a mean torque of 388.8 N-m on Day 0 and 362.7 N-m on Day 121, a 6.6% loss.

Load Cell Data: An increase in load was seen over the 195-day test period for all bolts, with 1.8-m and 2.4-m TR bolts experiencing the largest increases of 11.96 kN, and 11.3 kN, respectively.

4.4 Summary results-mine 2

- The GF and AS values for Sites 2–1 and 2–2 based on Day 0 through Day 195 data (Table 2 and in Figures 10-13) are similar to those at Mine 1.
- GF values at Site 2-1 for different lithologies range 227 to 317 N/mm and are similar to Mine 1. Longer bolts seem to have smaller GF values than shorter bolts. Similar data for AS-50 is non-conclusive.

Table 3 Load cell data collected from Mine 1 – Sites 1 and 2.

Load Cell ID	*Bolt length (m)*	*Increase in load Day 0 to Day 140 (kN)*	*Increase in load Day 0 to Day 273 (kN)*
		Site 1	
A	2.4	2.22	2.45
B	1.8	1.78	1.78
C	1.2	1.33	3.78
		Site 2	
1	1.2	16.0	4.9
2	1.8	18.7	4.7
3	2.4	23.6	15.1

Table 4 Torque data collected from Mine 2 – Site 1.

Bolt ID	*Day 0 torque (kN)*	*Day 121 torque (kN)*	*Percent (%) loss*
1 – 1.8TR	400.0	386.4	3.4
2 – 1.8TR	339.0	325.4	4.0
3 – 1.8TR	413.5	393.2	4.9
4 – 1.8TR	402.7	345.7	14.1
Mean	388.8	362.7	6.6

- Tensioned-rebar bolts tend to have lower GF values. This is consistent with field observations that such bolts are not typically effective for roof control.

A comparison of the performance of 1.8 long PR bolts installed in 35 mm drill holes at Mines 1 and 2 is given in Figure 15. At Mine 1, No. 6 (18 mm) rebar bolt in 35 mm hole has poor GF averaging 145 N/mm, 231 N/mm, and 163 N/mm for Days 0, 140, and 273, respectively. At Mine 2, the GF for No. 7 (22 mm) with 60 cm of grout length was 317 N/mm, 263N/mm, and 303 N/mm for Days 0, 121, and 195, respectively. The mean AS value for the three data collection periods at Mine 1 was 11.8 kN/mm while at Mine 2 it was 16.6 kN/mm. The No. 7 bolts achieved peak loads ranging from about 180 to 195 kN. This difference may be attributed to annulus at Mine 1 of 9.53 mm for No. 6 bolts and 6.53 mm for No. 7 bolts at Mine 2.

5 CONCLUDING REMARKS

This contribution has presented limited longer-term performance data of currently used primary roof support systems at two mines. The performance data include both

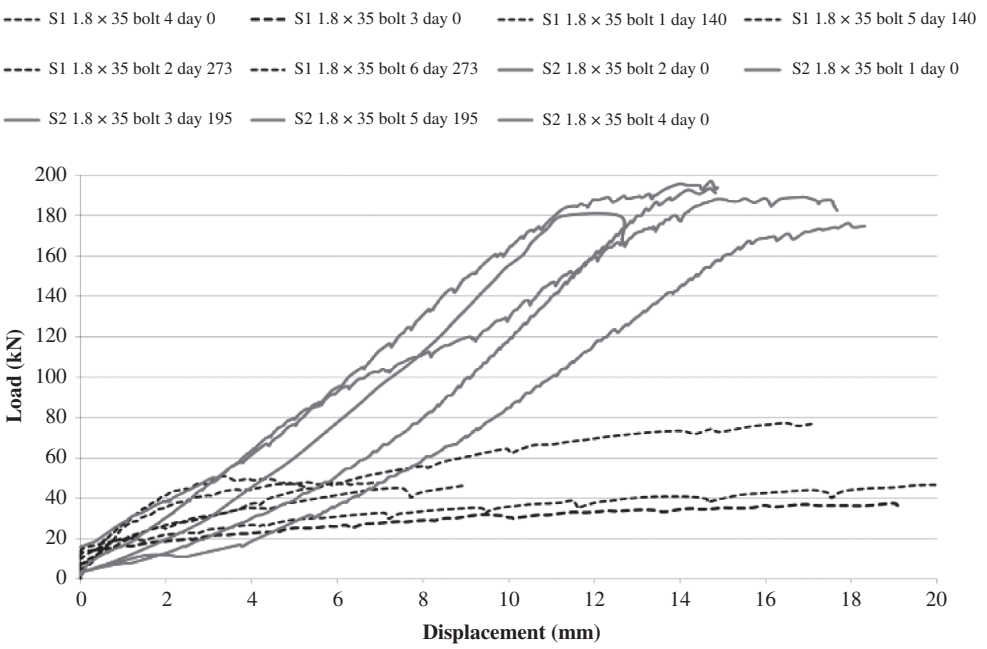


Figure 15 Comparison of No. 6 (18 mm) 1.8 long bolts in 35 mm boreholes at Mine 1 (dotted lines) and No. 7 (22 mm) 1.8 long bolts in 35 mm boreholes Mine 2 (solid lines).

"Grip Factor" or GF and "Anchorage Stiffness around 50% of the failure load or AS (50)". The result show that: 1) GF and AS-50 values in different lithologies at Mine 1 are similar even for different types of bolts, 2) GF and AS-50 data show that annulus diameter is most important in determining bolt performance and drill bit wear should be constantly monitored to obtain the best results, 3) # 6 (18mm) rebar installation in 35 mm boreholes should be avoided, 4) Longer bolts show lower AS-50 values, 5) Larger diameter PR bolts at Mine 2 show higher AS-50 values than smaller bolts at Mine 1. The longer 3.1-m bolts at Mine 2 had low GF and AS-50 values and therefore there is a need to reassess bolting practices at Mine 2, and 6) The effect of time on GF and AS-50 is variable and within experimental data variability limits, no firm conclusions can be drawn. Authors think that performance testing of grouted bolts should be based both on GF and AS values because AS values represent the rock mass reinforcement potential while GF values represent the load carrying potential.

ACKNOWLEDGMENTS

The authors acknowledge the financial support of Illinois Clean Coal Institute of the Illinois Department of Commerce and Economic Opportunity. Additional thanks are due to Minova and JennMar bolt manufacturers and the mining companies for their assistance in installation of bolts. Thanks are also due to MSHA professionals for making very useful suggestions.

REFERENCES

Chugh, Y.P., Kollipara, V.K., and H. Gurley, 2009. An analysis of roof fall data base for Illinois coal mines. International Symposium on Rock Mechanics and Geo-Environment in Mining and Allied Industries, February 12–14, 2009, Varanasi, BHU, India.

Chugh, Y.P. 2009. Development of Improved Roof Support Systems for Illinois Underground Mines, Illinois Clean Coal Institute ICCI Project No. 07-1/3.1 B-2.

Chugh, Y. P. 2010. Improved Artificial Supports around Mining Areas for Enhanced Productivity, Progress report, Project 10/3-A, Illinois Clean Coal Institute, October 2010.

Mark, C., C.S. Compton, Dolinar, D.R, and D.C. Oyler, 2003. Field Performance Testing of Fully Grouted Roof Bolts, SME Annual Meeting Preprint 03-138.

Mark, C., C.S. Compton, Oyler, D.C., and D.R. Dolinar, 2002. Anchorage pull testing for fully grouted roof bolts. In Proceedings of the 21st International Conference on Ground Control in Mining, Morgantown, WV, 105–113.



Taylor & Francis
Taylor & Francis Group
http://taylorandfrancis.com

Chapter 9

Tunnel support in South African mines

L. J. Gardner
Mining Projects Department, Impala Platinum Limited, Rustenburg, North West Province, South Africa

Abstract: South Africa is famous for its abundance of mineral resources; and mining forms a significant part of the economy. While most other mining countries have similar large open pits and underground mines for massive orebodies, South Africa's narrow-reef tabular gold and platinum mines are unique. Similarly, the development and support of smaller-dimension access tunnels using hand-held pneumatic jackhammers is not widely practiced in mining. This chapter focuses on the support of these tunnels.

1 INTRODUCTION

South Africa is famous for its abundance of mineral resources, which represent a significant proportion of both current international production and reserves. It hosts the largest known reserves of manganese and platinum group metals (PGMs), as well as some of the largest reserves of gold, diamonds, vanadium and chromite ore. The country's economy has been built on mining, and South African mining companies play a key role in the global industry.

South African mines can be classified into four main types, namely:

- Underground mines for tabular hard rock deposits (includes most gold, platinum and chrome mines).
- Underground mines for tabular soft rock deposits (includes most coal mines).
- Underground mines for massive deposits (includes copper, base metals and diamondiferous mines).
- Surface mines (includes strip mining for tabular deposits, as well as larger pits for near-surface base metal deposits and diamond pipes).

Many other mining countries boast similar mining operations; particularly for coal seams, massive underground mines and large open pits, but the South African gold and platinum mines are unique in terms of their orebody characteristics, depth, layout and complexity. This chapter will focus of the support of tunnels in these mines.

2 GEOLOGICAL AND GEOTECHNICAL BACKGROUND

2.1 Gold mining

Gold is mostly mined from the Witwatersrand Basin, an immense arc-shaped and largely underground geological formation which holds the world's largest known

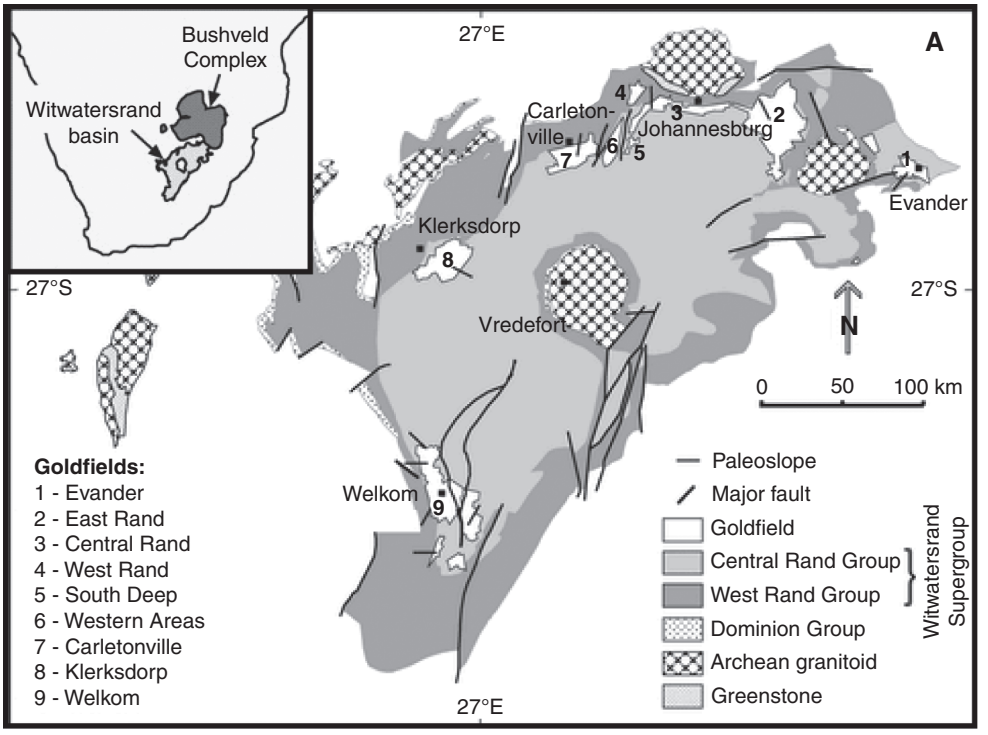


Figure 1 Location and details of the Witwatersrand Basin.

gold reserves. As shown in Figure 1, the basin covers an elliptical area with a 300 km long major axis from Evander in the north-east to Theunissen in the south-west, and 150 km wide stretching from Steynsrus in the south-east to Coligny in the north-west, with a small subsidiary basin at Kinross. It consists of a 5000–7000 m thick layer of Archean, mainly sedimentary rocks laid down over a period of about 260 million years, starting about 3000 million years ago.

The entire series of rocks, known as the "Witwatersrand Supergroup" consists of quartzites, banded ironstones, mudstones, tillites, conglomerates and some marine lava deposits. Most of the basin is buried deep under younger rocks, but some outcrops do occur. Gold occurs at 6 sites along the northern and western margins of the Witwatersrand basin, where Archean rivers from the north and west formed fan deltas with many braided channels. These flowed into the "Witwatersrand Sea" to the south, where the earlier sediments that form the older rocks of the Witwatersrand Supergroup had been deposited. Some of these gold bearing fan deltas extend to more than 4000 meters below the surface.

Gold mining is concentrated around five main centers, namely Evander, Johannesburg (split into the East, Central and West Rand), Carletonville (the far West Rand), Klerksdorp and Welkom. Although many of the older mines around Johannesburg are now nearly exhausted, the Witwatersrand Basin still produces most of South Africa's gold and much of the world output.

A variety of economic horizons are mined across the various areas, including:

- The Kimberley Reef in the Evander area,
- The Kimberley Reef and Black Reef in the East Rand,
- The Main Reef, Main Reef Leader, Bird Reef and South Reef in the Central Rand,
- The Main Reef, South Reef, Bird Reef, Kimberley Reef and Elsburg Reefs in the West Rand,
- The Ventersdorp Contact Reef and Carbon Leader reef in the Carletonville area,
- The Vaal Reef in the Klerksdorp area, and
- The Basal Reef, Elsburg Reefs, Leader Reef, Middle Reef, Beatrix Reef and Kalkoenkrans Reef in the Welkom area.

Despite the number of different reefs, the vast majority of these can be characterized as being tabular, narrow (less than 1.2m high) and shallow-dipping (less than 35 degrees above the horizontal). These orebodies are currently mined underground at depths ranging from 150 meters (shallow) to more than 4000 meters (ultra-deep) below the surface.

Rock densities typically range from 2.4 t/m^3 for shale to more than 3.0 t/m^3 for lava. Uniaxial Compressive Strengths for the different rock types vary between 80 MPa for shale to more than 300 MPa for siliceous quartzite and hard lava. The lower strength rock types (shale, argillaceous quartzite) generally behave in a ductile manner when loaded, whereas the stronger rock types (siliceous quartzite and hard lava) behave in a brittle fashion.

Virgin vertical stress levels are in the order of 27.5 MPa/km of depth. The major principal stress is normally near-vertical, and average k-ratios vary from more than 1.5 at shallower depths to approximately 0.5 at 3000 meters below surface (Jager & Ryder, 1999).

2.2 Platinum mines

The world's largest known reserves of Platinum Group Metals (PGMs) exist within the Bushveld Complex, an extremely large, 2-billion year-old saucer-shaped layered igneous intrusion located in the northern part of South Africa. In plan, the complex has a clover-leaf shape, consisting of four compartments or limbs, as shown in Figure 2. It is unique both in its size (it covers some 66 000km^2) and in the economic importance of its minerals.

Two PGM-rich horizons are typically exploited – the Merensky economic horizon and UG2 chromitite seam. The PGMs recovered include platinum, palladium, rhodium, ruthenium and iridium, together with quantities of gold, nickel, copper and several other metals and compounds. The complex comprises a diversity of igneous rocks, with compositions varying from ultramafic to felsic. Typical rock types include norites, anorthosites, felspathic pyroxenite, pegmatoidal pyroxenite and chromitite.

The majority of underground mining occurs in the Western and Eastern limbs. The geological sequence across the Western and Eastern limbs dips at between 5 and 30 degrees towards the center of the complex. In the West, the Merensky and UG2 ore bodies are separated by between 18 and 150 meters, with this middling increasing across the Western limb from North to South. In the East, the middling increases to more than 400 meters. Economic mining widths range from 1.2 to 1.5

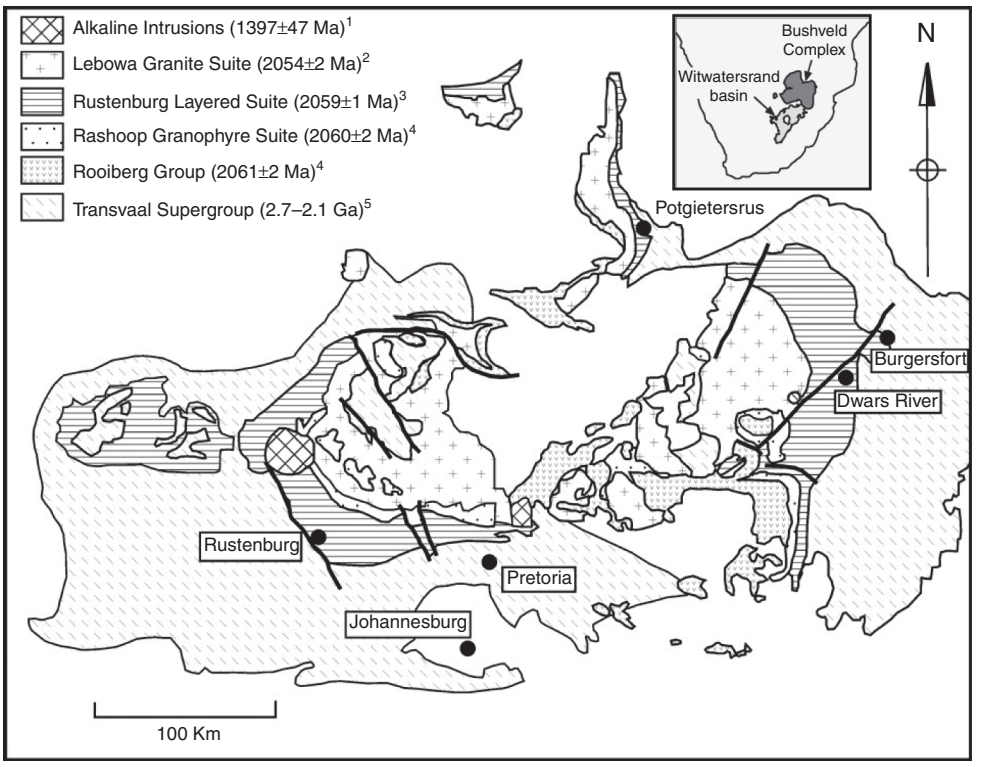


Figure 2 Location and details of the Bushveld Complex.

meters for the Merensky reef horizon and from 0.8m to 1.8 meters for the UG2 chromitite seam.

Average rock densities range from 2.7 t/m^3 for the noritic and anorthositic rock types to more than 4.1 t/m^3 for the chromitite rocks. Uniaxial Compressive Strengths for the different rock types vary between 80 MPa for chromitite to more than 160 MPa for the more brittle anorthosites. The lower strength rock types (chromitite, pegmatoidal pyroxenite) generally behave in a ductile manner when loaded, whereas the stronger rock types (norites and anorthosites) behave in a more brittle fashion.

Virgin vertical stress levels are in the order of 28 to 30 MPa/km of depth. The major principal stress is normally horizontal and oriented along the ore bodies' strike direction, the intermediate principal stress is horizontal and dip-orientated and the minor principal stress is near-vertical. Average k-ratios vary from more than 3.0 at shallow depths to approximately 1.0 at 1500 meters below surface (Gardner, 2003).

3 MINING PROCESS

Orebody access normally begins with the sinking of a shaft – a decline shaft for shallow-depth orebodies (typically less than 350 meters below surface), alternatively one or more vertical shafts for deeper orebodies. Landings or stations are cut from the

shaft barrel at regular intervals, with the vertical interval between stations being governed by the dip of the orebody (the steeper the dip, the greater the interval).

From the shaft stations, the orebody is opened up by a regular grid of tunnels (normally flat, but sometimes together with more inclines / declines). A series of off-reef haulages are developed, initially crosscutting through the country rock (main or station crosscuts), then turning 90 degrees to run at a reasonably constant distance below the orebody (footwall drives). The footwall drives are connected to the orebody or reef horizon at regular intervals (typically 150 m to 200 m) by a combination of stope crosscuts and inclined travelling ways. On the reef horizon, dip-aligned raises and winzes are developed to establish infrastructure for stoping operations.

Until recently, most tunnel development was conducted using manual labor (although small railbound drill rigs have recently been introduced). A team of between two and six rock drill operators uses hand-held pneumatic rock drills and airlegs to drill holes for tendon support and shot holes for blasting. Other members of the team install columns for ventilation and pumping, pipes for compressed air and service water, as well as tracks for railbound equipment in flat development ends. Rock broken by the blast is cleaned either by rocker shovel (off-reef flat ends) or by scraper winch (on-reef inclined ends). Blast advance rates are typically 2.0 m/blast for flat ends and 1.5 m/day for inclined ends.

Typical tunnel sizes are as follows (equipped dimensions):

- Vertical shafts – 6.0 m to 12.0 m in diameter.
- Inclines / declines – 6.0 m wide × 4.0 m high.
- Station crosscuts – 3.5 m high × 3.5 m wide.
- Footwall drives – 3.2 m high × 3.0 m wide.
- Stope crosscuts – 3.0 m high × 3.0 m wide.
- Travelling ways – 2.0 m high × 1.5 m to 3.0 m wide.
- Raises and winzes – 2.8 m high × 1.5 m wide.

Although some trackless room-and-pillar mining takes place, underground stoping (*i.e.* orebody extraction) operations generally follow traditional, labor-intensive mining practice. This process involves a team of between 7 and 15 people excavating stopes averaging 30 m long and between 80 cm and 1.5 m wide. The team uses hand-held drilling and manual charging-up of shot holes, to achieve a daily blast advance of approximately 1.0 m. Blasted rock is removed by means of scraper winches, while tendon and timber support (elongates and/or matpacks) is manually installed to maintain the stability of the excavated area.

4 TUNNEL SUPPORT DESIGN PROCESS

When designing the support system for an excavation, the geotechnical engineer must consider and evaluate a number of parameters, often in an iterative manner. These include:

- The intended purpose and planned lifetime of the excavation.
- The depth below surface and attendant rock mass response.
- Block size – large vs. small vs. fractured.
- Excavation height – safe examination and support installation.
- Maintaining long-term stability.

4.1 Relating tendon length to excavation purpose and dimension

When designing an appropriate support system, the dimensions, purpose and anticipated lifespan of the excavation need to be taken into consideration. There is a vast difference between the support requirements for a main shaft station (large, long-term, used by many people), as opposed to those of an in-stope re-development end (small, short-term, limited personnel access).

To assist with the process, particularly with respect to tendon lengths and spacing, geotechnical engineers have at their disposal a number of options. These range from the crudest rules of thumb, though design based on rock mass classification, to sophisticated numerical modeling. Two of the approaches used are listed below:

- Designing tendon length and support resistance criteria based on fallout heights determined by an analysis of historical fall of ground data. This approach was originally proposed by Dr. M K C Roberts and is described by Jager & Ryder (1999). It is normally used in established mines, which have a large database of falls of ground. Typically, the primary support system must provide sufficient support resistance to cater for at least 95% of all potential falls within the specific geotechnical area.
- Following the approach proposed by Barton, Lien & Lunde (1974), which makes use of a concept termed the Excavation Support Ratio (ESR). An appropriate ESR value is allocated to each typical type of excavation, based on the purpose of the individual excavation, its anticipated life expectancy and the actual excavation width or span. Excavations are thus allocated into classes based on risk level, for example:
    - Critical excavations (ESR of 1.3) *e.g.* shafts, shaft station breakaways, loading boxes and pump stations – the loss of such excavations would have a serious, long-term effect on production, or result in the stoppage of the shaft or mine for a significant period.
    - Long-term excavations (ESR of 1.6) *e.g.* shaft tip areas, inclines / declines, station crosscuts, footwall strike drives and main rock passes – the loss of such excavations would have a serious, medium-term effect on production.
    - Production excavations (ESR of 2.0) *e.g.* stope crosscuts, travelling ways and stope panels – the loss of such excavations would have a minor, short-term effect on production.

  Obviously, critical ends present a higher risk to both production and safety; hence the support requirements in areas with an ESR of 1.3 are more stringent than those in areas with an ESR of 1.6 or 2.

The Barton approach is typically adopted for new projects, where there is no historical data available for the area in question. On a practical level, typical tendon length requirements for long term excavations range from 2.4 m long solid steel tendons to 6.0 m long pre-stressed cable anchors, depending on the width of the excavation.

4.2 Depth below surface and attendant rock mass response

South African gold and platinum mines operate at depths ranging from 30m to nearly 4000 m below surface. Over this wide range of depths, the rock mass response to mining undergoes several changes, as shown in Figure 3.

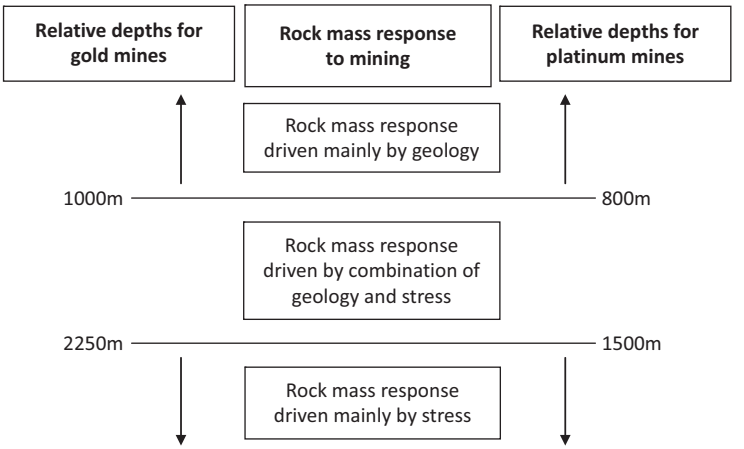


Figure 3 Rock mass response to mining at different depths.

- At shallow depths, the rock mass response is geologically-controlled – *i.e.* falls of ground tend to originate along geological structural boundaries (*e.g.* joints, faults, dikes, veins, etc.).
- At greater depths, the rock mass response is stress-driven, with all rock types fracturing to some degree, even under virgin stress conditions.
- In the zone between these two depths, fracturing takes place selectively. In platinum mines, the brittle "whiter" anorthositic rock types fracture first, followed by the "grayer" noritic rock types. In gold mines, the brittle siliceous quartzites also show signs of fracturing earlier than the more ductile argillaceous quartzites.

4.3 Block size – large vs. small vs. fractured

To prevent falls of ground in tunnels, potentially-loose individual blocks of rock need to be kept in place. In shallow conditions in the Bushveld Complex, rock block sizes (as dictated by near-vertical joint spacing) are typically in the order of 1.5m × 1.5m. This implies that they can be pinned in place by tendons installed on a 1.0m × 1.0m pattern, as shown in Figure 4. Additional tendons are however required to pin odd blocks that may occur when the excavations traverse abnormal geological structures (*e.g.* faults, dikes, veins, etc.). Similar conditions are found in some intermediate depth gold mines, as shown in Figure 5.

Where joint frequency increases, block sizes reduce to the point where individual blocks can no longer be pinned in place without substantially reducing the tendon spacing, shown in Figure 6. Ground conditions are typically classified as "blocky ground" when the block size is less than 0.5 m × 0.5 m. Such situations generally require some form of area coverage, installed together with the primary support tendons, such as strapping, shotcrete or wire mesh.

In fractured conditions, the fracture slab size also varies at depth in the Western limb of the Bushveld Complex. The "whiter" anorthositic rock types, with a higher feldspar content, tend to fracture in thin "plates" (see Figure 7) while the "grayer" noritic rock



Figure 4 Ground conditions in a platinum mine tunnel (courtesy of Northam Platinum).



Figure 5 Ground conditions in a South African gold mine tunnel (source: Harmony Gold).



Figure 6 Typical "blocky ground" conditions found at shallow depth in the Bushveld Complex.



Figure 7 Thin "plate"-type stress-fracturing in anorthositic rock type at depth.

types tend to fracture in larger slabs (see Figure 8). If not confined, the rock continues to slab, often to more than 1.0 m from the original excavation perimeter. In these situations, tendons alone do not provide adequate support.

4.4 Excavation height, safe examination and support installation

The face area of most tunnels developed using hand-held drilling (particularly for railbound traffic) has traditionally been examined, barred and made safe manually. This is normally done at the start of the cleaning shift, working off the muck pile to



Figure 8 Thick "slab"-type stress-fractured block in noritic rock type at depth.

attain a working height of 2.0 m to 3.0 m. Once the broken rock has been removed, the working height becomes excessive and hazardous for safe barring at the start of the drilling shift, and for support installation (whether only tendons or with some form of area coverage). To ensure a safe working height, it is essential to bring in a portable drill carriage or construct a working platform.

Also, in ends supported only by tendons, once the face has advanced and the end has been equipped, safe subsequent examination and barring / dressing of loose rocks is limited by several issues. These include the practical height which a manual pinch bar can reach without placing the user beneath the rock being barred, potential damage to equipment or machinery in the excavation and the need to keep traffic (people, vehicles or rock) moving through the area.

In light of the above, several strategies are typically employed to minimize risk:

- Where increased height is required, multiple mining cuts are typically employed (the top cut being fully mined and supported first), full area coverage is normally specified for the hanging wall and sidewalls and additional cable anchors are installed in the hanging wall and sidewalls.
- In areas with non-typical ground conditions (whether due to block size or fracturing), sidewall tendons are specified to within a maximum of 2.0 m above the footwall.
- Tunnels supported using tendons only are limited to a maximum of 3.5 m high (equipped height) to allow safe subsequent dressing with a 3.0 m long aluminum pinch bar.

4.5 Maintaining long-term stability

A primary support system is initially intended to safeguard the development team against potential falls of ground. It must also assist in maintaining the integrity and stability of the tunnel over many years, often with little or no additional secondary or tertiary support installation. For this reason, the geotechnical engineer should attempt to predict the events and conditions that may affect the tunnel over its lifetime, then design and specify the support system accordingly. In some cases, it is impossible to ensure tunnel stability without secondary and tertiary support.

Common events and conditions typically include:

- Stress changes due to the tunnel being overstoped/overmined by mining the orebody above it. This process results in stress increasing as the stope face approaches the tunnel, followed by a stress drop as the stoping passes over and the tunnel is left in the de-stressed "shadow". At depth, the net effect in strong brittle rock types is that as stress increases, the tunnel rock walls fracture. Unless supported, the fractured blocks and slabs are then prone to fall out once the stress levels reduce.
- In weaker and more ductile country rocks, such as shales and argillaceous quartzites, the effect of stoping-induced stress inevitably results in deformation and "squeezing" of the tunnel. Deformation is unlikely to be stopped, but attempts must be made to control the rate of deformation, so that the tunnel remains open and stable throughout its intended operating lifetime.
- The harsh climatic environment in underground mines inevitably corrodes steel objects, including support elements. In some cases, this takes place inside the tendon support hole, but in most situations the corrosion begins within the confines of the tunnel. Tunnels subjected to emissions from diesel engines and return airways are usually the worst affected. Support units most affected are wire mesh and/or strapping, plus protruding portions of tendons and cable anchors. Where possible, galvanized or coated support material should be specified. If this is not possible, protective coatings should be applied after installation.
- Tunnels at depth are often subjected to mining-induced seismic activity, ranging from localized strain bursting through shakedown from nearby seismic events to actual bursting of the tunnel walls. Where this is the case, yielding capability and full area coverage needs to be built into the mine's tunnel support strategy.

5 TUNNEL SUPPORT PHASES, TYPES AND COMBINATIONS

5.1 Tunnel support phases

Tunnel support is typically split into primary, secondary and tertiary support phases.

- Primary support is installed at the working face by the development team, to protect them from localized rockfalls and provide immediate stability.
- Secondary support, if required, is typically installed by specialist contractors some distance behind the face, to ensure long-term tunnel stability.
- Tertiary support, if required, is also typically installed by specialist contractors. It is normally only installed as a last resort *i.e.* if the tunnel stability is likely to be compromised due to stress and/or ground conditions.

5.2 Tunnel support types

Tunnel support types can be grouped into at least four classes, namely tendons and cable anchors, surface coverage elements, artificial support and volume filling materials. A number of different support units are used during various phases of tunnel support, in many cases the support types overlap the different phases. Some of the more common unit types are listed below:

5.2.1 Tendons and cable anchors

- Friction stabilizers (*e.g.* Split Sets™).
- Pressurized friction-type stabilizers (*e.g.* Swellex™, Hydrabolt™).
- Mechanically-anchored rockstuds and rockbolts, normally post-grouted.
- Cement-grouted tendons, either rockbolts or shepherds' crooks, normally rebar.
- Resin-anchored rockbolts, typically using different resin cartridges to achieve a fast setting time combined with full-column grouting.
- Cables, anchored using resin, cementitious grout or a mechanical shell.

Detailed explanations of these units are provided by Hutchinson & Diederichs (1996) and Hoek (2012).

5.2.2 Surface coverage elements

- Narrow-width strapping (*e.g.* Osro / Oslo straps).
- Safety nets (only for temporary protection of the development team).
- Mesh, including welded mesh, diamond mesh and chain-link mesh.
- Thin Sprayed Liners.
- Shotcrete or sprayed concrete.

5.2.3 Artificial support

- Sets, constructed from timber and/or steel.
- Steel arches, profiles include square, horseshoe and circular.

5.2.4 Void filling materials

- Timber laggings.
- Aerated concrete.
- Cemented tailings.

5.3 Examples of tunnel support combinations

5.3.1 Primary support

- Example 1: A footwall drive in a shallow platinum mine, with good ground conditions. The major rock-related hazard is from large, joint-bound blocks. Typical primary support consists of 1.8 m long X-Pandabolt™ pressurized friction stabilizers, spaced at 1.0 m intervals in a block pattern and installed in the hanging wall only. A safety net combines with the tendons to protect the crew against smaller rocks that may fall during the shift.
- Example 2: A 5 m high × 5 m wide incline being developed using trackless machinery at shallow depth in blocky ground conditions. The major rock-related hazards are blocks falling from between the tendons and the inability to make safe after excavation due to the excavation height. The primary support system consists of 2.4 m × 1.4 m sheets of welded mesh for area coverage, pinned in place by 2.4 m long friction anchors spaced 1.2 m × 1.2 m apart and installed by the drill rig. This system is illustrated in Figure 9.



Figure 9 Incline support system of mesh and friction stabilizers.

- Example 3: A station crosscut being developed on a platinum project shaft at 1500 meters below surface. The major rock-related hazards are from slabs of anorthositic host rock, as well as wedges created by parting planes between different rock layers. Here primary support consists of a 50 mm thick layer of fiber-reinforced shotcrete, followed by 2.1 m long resin-anchored rockbolts, spaced 1.0 m apart in a block pattern, installed on the hanging wall and down both sidewalls, to within 1.5 m of the footwall. This is followed by 4.5m long × 38 ton cable anchors installed into the hanging wall only to pin the possible wedges, spaced 1.5 m × 2.0 m and kept within 6.0 m of the advancing face. This system is illustrated in Figure 10.
- Example 4: A decline shaft being developed in a gold mine at 4000 meters below surface. The major rock-related hazard is stress-induced fracturing during development, followed by shakedown damage from mining-induced seismicity during stoping operations. Primary support consists of an 8 mm thick layer of Thin Sprayed Liner, combined with 2.4 m long friction stabilizers spaced 1.0 m apart in a block pattern, installed on the hanging wall and down both sidewalls to within 1.0 m of the footwall. This is followed by 3.5 m long × 38 ton cable anchors, installed around the perimeter of the tunnel, spaced 1.5 m × 2.0 m and kept within 6.0 m of the advancing face. Given the stress regime at this depth, the primary support system has to be backed up by secondary support within 50 m of the advancing face.



Figure 10 Station crosscut support system of shotcrete and resin-anchored rockbolts.

5.3.2 Secondary support

- Example 1: Mesh-reinforced shotcrete – typically applied in areas where full area coverage is required, but tunnel deformation is likely crack unreinforced shotcrete. An initial 50 mm thick layer of shotcrete is applied to the rockwalls, followed by a layer of diamond mesh which is nailed to the shotcrete. Finally, a second 50 mm thick layer of shotcrete is sprayed over the mesh.
- Example 2: The commonly-termed "meshing and lacing" – diamond mesh, criss-crossed with de-stranded hoist rope and pinned in place by cement-grouted shepherds' crooks. This system is illustrated in Figure 11. Depending on local conditions, the length and thickness of the shepherds' crooks can be altered, the lowest row of lacing can be installed higher or lower on the sidewalls, the lacing pattern can be reduced in size and the mesh type and thickness can be varied. Also, the rebar shepherds' crooks can be replaced by yielding versions such as the "cone bolt" or "wiggle bar" to provide energy absorption in case of rockbursts or rockwall deformation.

5.3.3 Tertiary support

- Example 1: Straps and anchors – applied where tunnel deformation is likely, often installed over existing meshing and lacing. A regular pattern of 4.5 m or even 6.5 m long cable anchors are installed around the perimeter of the tunnel spaced approximately 1.5 m apart in a block pattern. The anchor cables are threaded through multi-strand narrow straps (Osro / Oslo straps) which are installed over



Figure 11 "Meshing and lacing" secondary support (source: Harmony Gold).

the anchor pattern prior to the anchors being tensioned, thus locking the straps under the anchors' load-spreading washers. The straps provide a load-spreading function between the different cable anchors.

– Example 2: Steel arches or ring sets, combined with void filling – used in extreme cases, such as where the ground conditions do not allow reinforcement of the rockwalls using tendons or cable anchors, or where deformation of the tunnel cannot be contained by other methods. The arches or ring sets are passive support, so the void between the support and the adjacent rockwalls must be filled to provide some form of support and impact resistance. An example of steel arches being used to support the entrance of a chairlift excavation from surface is shown in Figures 12 and 13.

5.4 Tunnel stability and damage

Even very well supported tunnels are not indestructible – given an adequate level of stress, deformation or fracturing, rock will eventually close any excavation. Figures 14 to 17 show different supported tunnels at various stages of failure.

6 SUPPORT FOR NON-TYPICAL TUNNEL DEVELOPMENT

6.1 Shaft sinking and shaft station cutting

The sinking of vertical shafts to access deeper orebodies is a highly specialized form of tunnel development. The world's deepest single-drop vertical shaft is the South Deep shaft complex in South Africa, which extends to 2995 meters below surface. Most gold



Figure 12 Steel arches being installed (courtesy of Two Rivers Mine).



Figure 13 Steel arches with void filling material (courtesy of Two Rivers Mine).



Figure 14 Damage to tunnel supported by steel arches and timber cribbing (courtesy of J.D. Bosman).

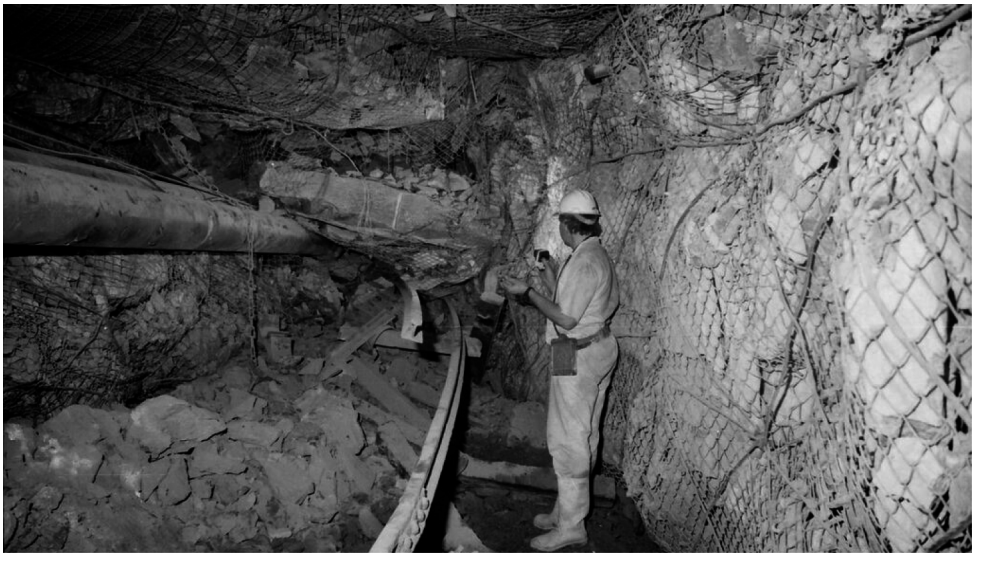


Figure 15 Damage to a tunnel supported by tendons, meshing and lacing (courtesy of J.D. Bosman).

mine shafts are more than 1500 m deep; often two, or even three sequential shafts are needed to access the deepest workings. Older timber shafts were either square or rectangularly-shaped, while today's shafts are either circular or oval in profile, with all shaft infrastructure manufactured from steel.



Figure 16 Timber sets destroyed by combined effects of stress and deformation (courtesy of J.D. Bosman).



Figure 17 Deformation causing hanging- and sidewall bulging and footwall heave (courtesy of J.D. Bosman).

Shafts are classed as critical excavations; if the shaft is not stable and safe for hoisting people, material and rock, the mine cannot operate. For this reason, the shaft barrel is permanently supported by a monolithic concrete lining at least 300 mm thick. The concrete lining is cast in rings, with the shuttering being kept between 24 m and 30 m from the bottom of the shaft.

Most of the activities associated with the sinking process, *e.g.* cleaning, drilling and charging up, take place at the shaft bottom, below the lined section. Primary support thus protects the crew working at the shaft bottom from rocks that may slide or fall from the shaft barrel perimeter between the lining and the shaft bottom. The support is installed by the shaft sinking crew, directly after the rock broken by the previous blast has been cleared.

The primary support comprises blast-resistant cladding in the form of welded mesh or expanded metal sheeting. This is pinned in place by friction stabilizers installed on a block pattern, as shown in Figure 18. Where large prominent blocks and/or potential wedges are identified, these are pinned by cable anchors. Shotcrete or Thin Sprayed Liners are occasionally used to consolidate areas of friable ground in conjunction with the cladding. The lifetime of the primary support is typically not longer than 10 days, after which it is covered by the concrete lining.

Shaft landings or stations are created by blasting an inclined brow out of the shaft perimeter and creating a catwalk around the shaft. From the catwalk, tunnels are broken out to form the basis for the development to open up the orebody. The horizontal span across the catwalk excavation can extend to as much as 20 m, so careful planning and sequencing of operations is required to ensure that the excavation is carried out safely.

Like the shaft barrel, the station brow, catwalk and immediate station area is classed as a critical excavation. This area is supported by a combination of cable anchors, steel



Figure 18 Primary shaft barrel support system (courtesy of Worley Parsons).



Figure 19 Shaft station development and support (courtesy of Worley Parsons).

tendons and cladding, with area coverage being provided by fiber reinforced shotcrete. An example of station cutting is shown in Figure 19 – the catwalk has been created and rock broken in the access tunnel development is being loaded into kibbles by the grab before being hoisted to surface.

6.2 Developing though special areas

The term "special area" covers a wide variety of situations, but it is generally recognized that a special area is one which presents a higher level of rock-related risk. For mining development, one of the most difficult special area situations is trying to traverse friable ground, such as a major shear zone, water-bearing fault or a "running" dike. These require a cautious approach, reduced advance rates and extensive support measures. Two examples are described below:

– Example 1: A 30 m wide shear zone adjacent a major fault on a platinum mining project. The ground conditions varied significantly within the shear zone, ranging from blocky to friable. To develop through the area, advance rates were reduced to 1.0 m per blast, with smaller inter-hole burdens and lighter explosive charges to minimise blast damage. The primary support consisted of spaced frame mesh (a "mattress" of two wide-aperture mesh sheets, spaced 50 mm apart), pinned into place by resin-anchored rockbolts and covered by a 75 mm thick layer of shotcrete. Cable anchors were installed where required to supplement the rockbolts. Tunnel dimensions were increased by approximately 1.0 m to accommodate the later installation of steel sets, should they be required.



Figure 20 Ring sets provide access through a "running" dike (source: Wimico).

– Example 2: A 40 m wide "running" dike separating two major ore blocks on a gold mine in the Klerksdorp area, as reported by Oelofse & Judeel (1999). The dike material has weathered and altered over time, resulting in millimeter-size fragments that collapse into any void, hence the term "running" dike. Developing through the dike required spiling and chemical resin injection ahead of the face, for consolidation of the dike material. The tunnel was excavated by hand scaler, with advances in the order of 1.0 m per shift. Heavy duty steel ring sets were installed at 1.0 m intervals, as close to the face as possible. Mine poles were used as lagging outside the sets, and any further void between sets and dike material was filled by aerated cement. Despite several setbacks, the 40 m wide dike was successfully traversed in 10 months. A similar example is shown in Figure 20.

7 CONCLUSION

The dimensions, development method and support of tunnels in South African gold and platinum mines may differ from that employed in large, mechanized mines, but the support philosophy, design approach and support units employed are essentially similar. This chapter has presented aspects of the design process, as well as examples of support types and combinations currently in use for different mining tunnels.

REFERENCES

Barton N., Lien R. and Lunde J. (1974) Engineering Classification of Rock Masses for the Design of Tunnel Support, *Rock Mechanics Journal*, Vol. 6, No. 4, pp. 189–236.

Gardner L.J. (2003) *Optimising the location of footwall haulages below the reef horizon for the No 16 shaft complex at Impala Platinum Limited*, *Masters' degree in Engineering investigational project*, University of the Witwatersrand, Johannesburg, pp. 17–20.

Hutchinson, D.J. and Diederichs, M.S. (1996) *Cablebolting in Underground Mines*, *BiTech publishers*, Pennsylvania State University, Pennsylvania.

Jager, A.J. and Ryder, J.A. (1999) *A Handbook on Rock Engineering Practice for Tabular Hard Rock Mines*, *Published by the Safety in Mines Research Advisory Committee*, Creda Communications, Johannesburg, pp. 11 and 149.

Oelofse, M.J. and Judeel, G. (1999) *Tunnelling through the running dyke on Tau Lekoa Mine – Vaal River Operations*. In Hagan, T.O. (ed.) *SARES 99: Proceeding of the second South African Rock Engineering Symposium, SARES 99, 13–15 September 1999, Johannesburg, South Africa*. Johannesburg, Creda Communications, pp. 101–107.

Rocscience Incorporated. (2012) *Education section: Hoek's Corner Chapter 14 – Rockbolts and Cables* [Online], Available on: www.rocsience.com/hoek/corner/14_Rockbolts_and_cables.pdf [Accessed 05 November 2012].

Chapter 10

Design of rockburst support systems for deep hard rock mines

B.P. Simser
Principal Ground Control Engineer, Sudbury Integrated Nickel Operations, a Glencore Company, Sudbury, Ontario, Canada

Abstract: A generally well accepted methodology for rockburst support design is to consider the energy absorption capacity of the support system and compare that to the energy released during a rockburst. The reality is that both the demand and capacity can only be estimated, and are not precise calculations. Mining support systems typically consist of various types of rock bolts (tendons), coupled with various types of surface support such as mesh or shotcrete. Invariably there is a sharp stiffness contrast between the internal rock reinforcement and the surface support. The component capacities are not strictly additive: for example softer wire mesh may take several hundred millimeters of deformation to reach peak capacity while many tendons reach their peak at a few 10's of millimeters. Other complications include: pre-loading of the ground support using up some of its capacity prior to the rockburst event; shearing of the tendons where most of the design capacity numbers come from pure axial loading tests; the difficulty of transferring high dynamic loads to tendons with small cross sectional area (loading regime of several square meters transferred to tendons typically in the order a few hundred mm^2); complexities during support installation such as irregular rock surfaces, and installation quality.

Despite these limitations many advances have been made in the last few decades, with several examples of mining support systems successfully containing substantial rockbursts. A review of some Canadian Hard Rock mining experience is given dating back to the late 1990s where the development of a rockburst support system began at the now closed Brunswick lead/zinc mine. More recent experience from other Canadian Mines is also discussed. Examples of rockburst support demand and estimated capacity are given, as well as thoughts on possible future improvements.

1 INTRODUCTION

Rock bursting, the sudden violent failure of rock, is one of the core hazards for deep hard rock mining. Conventional ground support systems are designed for static or quasi static loading conditions. Rockbursts can have ejection velocities in the several meters per second range and transient deformations can be in the order of 10's of centimeters (figure 1 below).

The cause of rockbursting in deep mines can be varied and is often complex. Several different mechanisms or combinations are possible. For example a highly loaded pillar

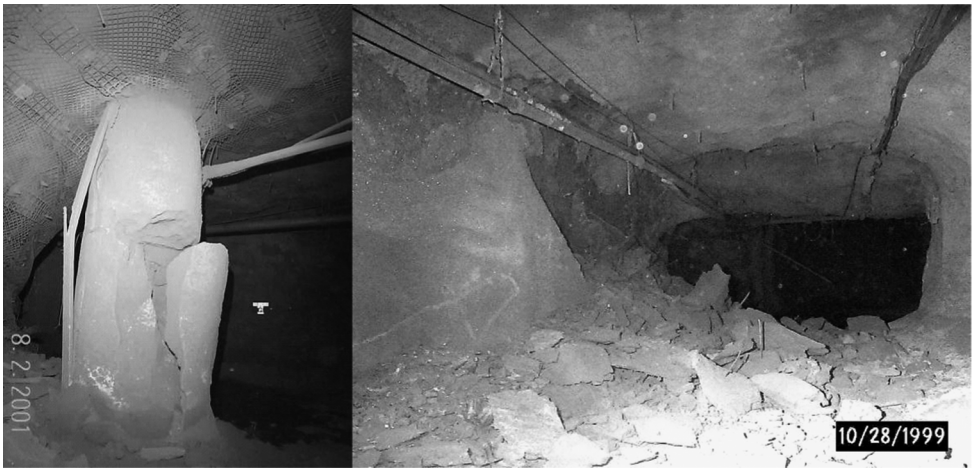


Figure 1 Left – 1.8m diameter shotcrete post dynamically failed after a large seismic event. An estimated 14 cm of vertical convergence occurred (measured by comparing the full length of the timber segments shown on the left hand side of the photo to the new back to floor distance). Right – Violently ejected material caused by a rockburst (Simser *et al*., 2002). Ejection velocities were estimated to be in the 4 to 5m/s range for a large portion of the material.

may burst, but the triggering mechanism could be a large seismic event generated by fault slip or the dynamic ground motion caused by large mine blasts. Furthermore the localized loading on ground support systems can be a combination of tensile, shear, bending, and compression forces. *"The design of rock support for these conditions is therefore problematic, since neither the demand imposed on the support, nor the capacity of the support systems under dynamic loading can be defined." (Stacey, 2012)*. There are however techniques to estimate both the demand and capacity, which at least give the engineer an appropriate range to design for. Conservatism in the support design is required due to the inherent uncertainties and the unavoidable simplifications that need to be made. Empirical experience (Morissette *et al*., 2014) from historic and existing mining operations remains one of the best ways to vet rock burst support design.

Figure 1 (right-hand photo) is an example of a wall bursting caused by seismic activity following a 160000 tonne stope blast 50m away. Approximately 114 tonnes of material was ejected including 12 tonnes of steel fiber reinforced shotcrete. The fibrecrete was sprayed at an average thickness of 10cm and the wall was bolted with a combination of splitsets and resin grouted rebar. Approximately 75% of the bolts did not break; the stress fracture zone around the opening had been expelled and generally un-raveled around the bolts. Some observations from the burst were clear: more deformation capacity was needed; and a better way to transfer dynamic load to the tendons was also required.

In general, the more fractured and dilated the rockmass is around an opening, the more difficult it will be to get good load transfer to the tendons. This creates a quandary for support design: elements that inhibit dilation of fractured rock such as grouted rebar and shotcrete, are inherently stiff and have insufficient deformation capacity to withstand

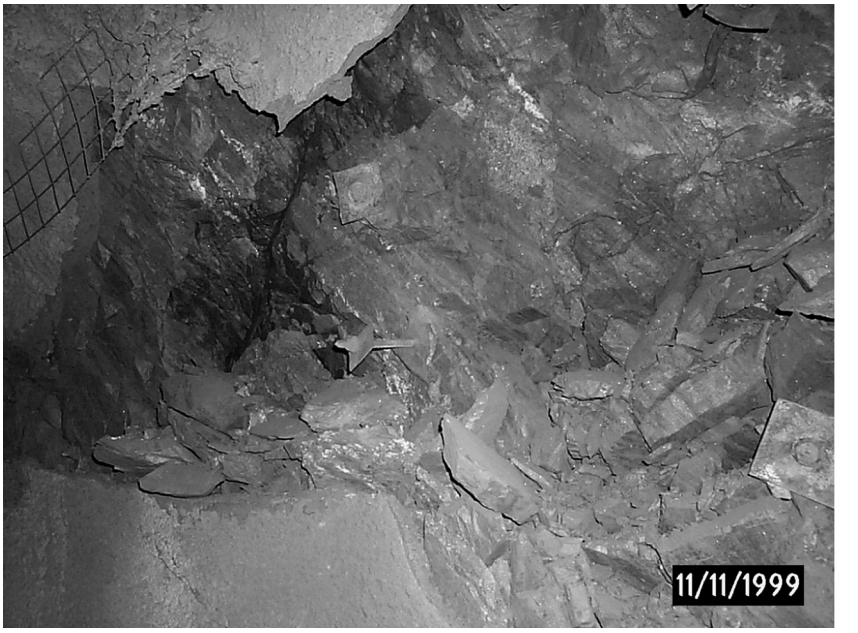


Figure 2 Close up view of the rockburst shown in Figure 1 above. The exposed rebar and splitsets are distorted but relatively intact with the ejected material un-raveling around them. The mesh squares in the upper left corner are 100 × 100mm for scale.

large rockbursts. Energy absorbing elements such as chain link mesh and yielding rock bolts allow deformation but may not inhibit the rockmass loosening, which makes it more likely to have rock un-ravel around tendons when dynamically loaded.

2 ROCKBURST MECHANISMS

Rockburst mechanisms can be separated into two main areas: source mechanisms; and damage mechanisms. Ortlepp & Stacey (1994) put rockburst source mechanisms into the following categories: strain-burst; buckling; face crush burst and pillar burst; shear rupture; and fault-slip type events. Stacey (2012) noted that the first three mechanisms have coincident damage and source locations. The shear rupture and fault slip type events may have seismic sources located significant distances from the damage, in some cases hundreds of meters. There are also cases where significant fault slip events have source locations very close to the observed damage (Counter, 2014); mine design changes rather than ground support improvements may be required to mitigate this type of risk.

2.1 Source mechanisms

Most burst prone mines employ seismic monitoring systems. It is often noted that the source of a large event is offset from the actual damage location, and that the damaged area may be further away than some un-damaged excavations.

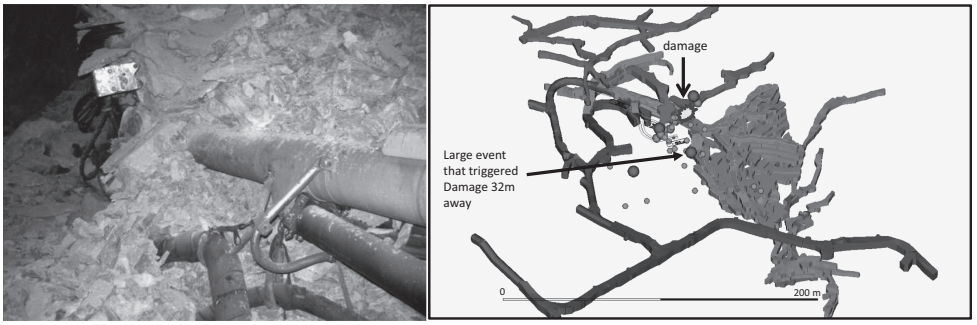


Figure 3 Left – Narrow vein jumbo with the drilling boom buried in rockburst fly rock. Right – Isometric view of the mining area showing the large event locating 32m away from the damage area.

The damage noted in figure 3 did not have a recorded seismic event at the damage location. The seismic system deployed at the mine was capable of locating events down to Richter Magnitude –1.5 or smaller with location accuracies in the 5 to 15m range. This was a close call event with an operator in the heading, so the timing of the damage was clearly associated with a Richter Magnitude 1.7 event that located 32m away. In this case it was interpreted to be a local strain energy build up around the development heading that had a triggered release; the ground motion from the large event being the trigger. A quirk of seismic monitoring systems is that a small triggered event would likely be buried in the seismogram of the larger event and thus not be clearly identified. For example a P wave velocity of 6260m/s travelling 32m would take about 5.1 milliseconds, while the triggered waveform for the large event occurred over approximately 200 milliseconds in the relatively dense mine wide seismic array. In the Ortlepp & Stacey mechanism classification, this would have been a fault slip event that triggered a local pillar burst. Mixed mode source mechanisms are not widely reported, and are often explained by site response factors such as stress accumulation around openings at the damage site.

2.1.1 Fault slip events

The influence of geological structure is often a key element in observed bursting. The strict definition of a "fault" in the geological sense may be misleading. Large mechanical contrast in material properties can behave similar to a fault with displacement (figure 4).

In figure 4 left, a relatively weak copper vein (unconfined compressive strength u.c.s. ~ 60 MPa) was attempting to dynamically squeeze out into an overhand cut and fill drive. The granitic country rock has a u.c.s. of around 240 MPa. The weaker vein material takes the brunt of the displacement, and in this case was contained by 75 × 75mm aperture weld mesh and 8mm wire diameter weld mesh straps. The damage was concurrent with a Richter Magnitude 1.1 seismic event locating several meters from the photo location. Figure 4 right shows an inclusion of the country rock, in this case metasediments, within fine grained massive sulfides (Simser & Andrieux, 2013). A similar material strength contrast to the copper example existed, and the mine had several rock

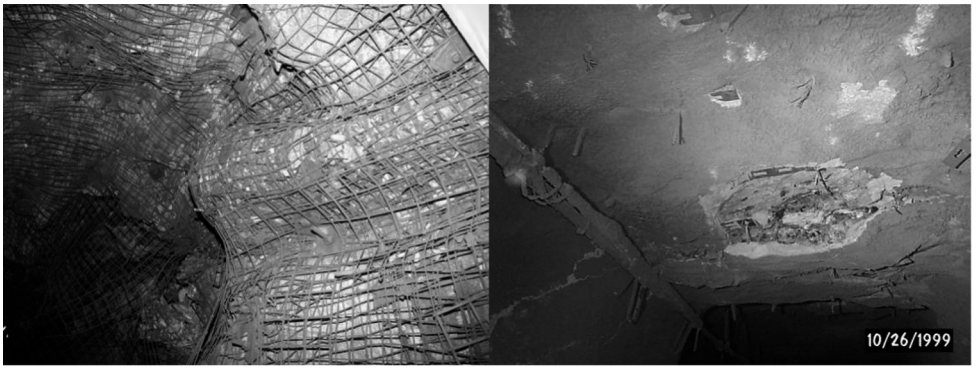


Figure 4 Example of different geological structures exhibiting "fault" like movement.

bursting and high deformation related failures related to this type of inclusion. In both cases the geological features would not be classified as "faults" but under mining induced stresses, the relatively narrow inclusion of weaker material deforms in a fault-like manner.

More conventional faulting, in the geological sense is also a well known seismic and rockburst risk. The 3D nature of faults is often complex and difficult to characterize. *"Rock tends to deform in shear – it is simply the easiest way for rock to deform since it requires no volume change"* (Van Aswegen, 2013). Mining induced deformation is often taken up by faulting, especially when the structures day light into mine openings.

Increased and asymmetrical seismicity is often recorded following mine blasts near faults (figure 5). A homogenous rockmass/stress field would have mining induced fracturing in a more or less symmetrical pattern. Rockmasses are often not homogenous, and the presence of geological structure can influence both the local stress field and the local rockmass strength.

Significant rockmass weaknesses such as faults will allow both aseismic creep and seismic fault slip type movement. The recorded seismicity may be a combination of rock fracturing near the fault as it displaces, or from "fault slip" type events. Faults can lock up due to asperities such as geometric jogs, offsets by younger faults, or mining induced clamping stresses. A sudden release on an asperity can produce relatively large magnitude seismic events. Crustal seismology may consider a Richter 2 or 3 events as a small earthquake, but in the mining world, excavations may be close by, and these are considered very large and potentially dangerous occurrences. For most mining layouts the fault slip risk increases with increasing extraction. The fault simply has more room to displace, over a larger area as mining progresses near the structure. The potential for an asperity lock up and subsequent large events increases.

In figure 6 below (Simser, 2013), the first year of mining (2009) has one stoping line crossing a significant fault. In this layout there are two panels per stoping line, typically 30000 tonnes per panel. By the end of 2012 five stoping lines pierce the same fault. Even with cemented tailings backfill, the fault can creep into the stopes as mining induced stresses both clamp and add shear displacement along various portions of the fault. By definition, seismic moment is:

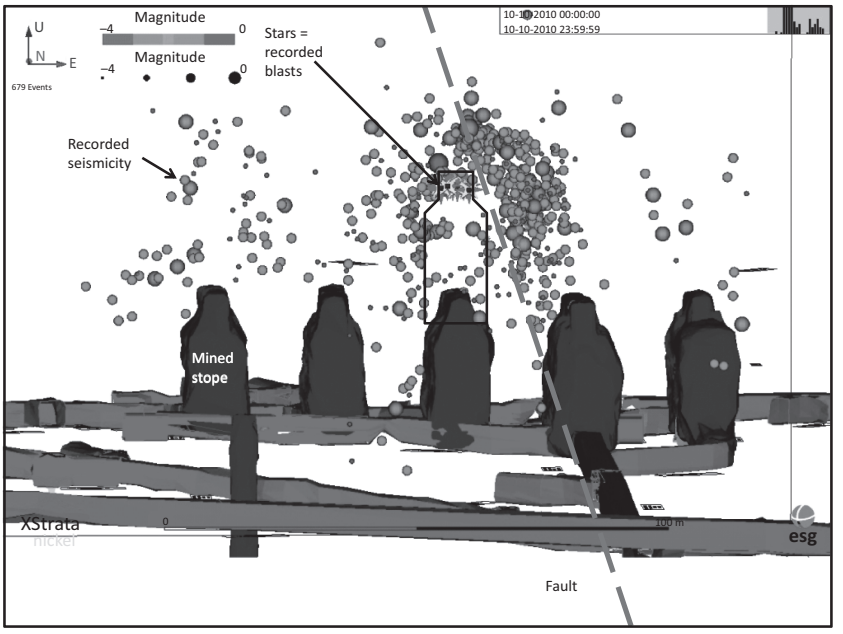


Figure 5 Example of asymmetric seismicity following a stope blast (outline in center of second tier of mining). The response was greater in terms of event rate than similar sized blasts in that time period of mining due to the presence of a significant fault (dotted line).

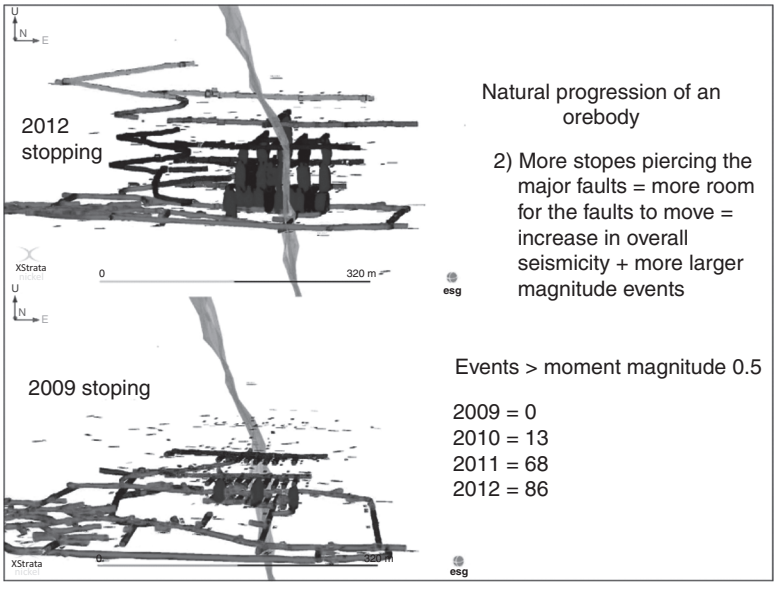


Figure 6 Mining layout shown in isometric view at different stages of extraction. The bottom image shows mine development (5 × 5m tunnels) with three stope lines having been mined (rectangular shapes). The top image shows the progression of mining over time. The fault is shown as an undulating, steeply dipping planar feature.

$$M = A\ d\ G$$

Where A = slip area d = slip displacement and G = shear modulus of the host rock.

As the fault is given more degrees of freedom (more stopes to creep into), the potential moment magnitude of seismic events will increase. This is clearly shown in the example by the number of larger events in the area increasing with time. Other factors such as increased mining induced stresses also contribute to the increase in larger events. De-clamping a fault, rather than increasing shear stresses across it can also be the source of large fault slip seismicity.

2.1.2 Dikes

Dikes are also a well known burst prone geological structure. In some cases the dike contact may be faulted, allowing fault slip type movement. Some dike material is very fine grained, and very strong (>300 MPa), so its' capacity to store local strain energy may be the root cause of bursting. Figure 7 shows both examples of dike related rockbursts, fault-slip on dike contact (left) and sudden release of strain energy (right).



Figure 7 Left – dike burst in development ramp – fortunately no injuries occurred. The support system consisted on 100mm aperture weld mesh with 4.9mm diameter wire strands and 22mm resin grouted rebar on approximately a 1×1m pattern. Most of the rebar were necked and snapped. The dike had an overall folded geometry and a local altered slip along the contact. Right – strain burst from dike material in upper shoulder of a tunnel. The support system consisted on 50mm of fiber reinforced shotcrete and 2.4m long resin grouted rebar.

2.1.3 Pillar bursts

Pillar geometries are also well known to increase rock burst risk. Several scales of strain energy accumulation in a pillar are possible for conventional mining layouts. For example it is often necessary to create multiple mining fronts to achieve suitable production rates, especially for narrow vein geometries. The converging fronts or "sill pillars" can store large amounts of energy, and in the narrow vein mining case can become very squat with high confinement. A rule of thumb is if the width to height ratio of the pillar is less than 2/3, it will likely yield relatively benignly, but >2/3 it can store significant strain energy (Simser & Jalbout, 2014). For example Swan (2013) noted bursting problems in a sill pillar for a narrow vein copper mine starting around 1999 when the overall width to height ratio was nearing a critical state. At the time the sill was relatively wide (multiple veins, some flat dipping veins). By 2015 some remnant areas of this sill were still being mined, but with no stress problems. The wider areas had effectively yielded, and gravity failures became the prime ground control concern (the overall width to height ratio of the pillar has become very slender). However in the same mine, where narrow sill pillars were left, very high stresses could result (squat geometry leading to high confinement) and in some cases areas were abandoned or large scale destress blasts used to reduce risk.

The burst shown in figure 8 was in a sill pillar, the damage locating in the widest span area of the cut and fill development. The wider span (~6m versus normal mining span of 3m) was due to a fattening in the vein, in this case weaker material, which also led to deeper stress fracturing around the opening. The local widening effectively reduced the width to height ratio of the sill pillar. The narrower portions of the area were essentially un-damaged. Smaller spans meant lower depth of stress fracturing and a stronger



Figure 8 Sill pillar burst after a Richter magnitude 1.9 seismic event. The drive was an undercut for a longhole extraction of a highly stressed remnant.

portion of the overall sill pillar. Simple elastic 3D numerical modeling gave a strong correlation between the overall geometry and the locally derived failure line (σ_1, σ_3 criterion based on several back analyses). This is collaborative evidence that the burst was likely a stress driven "pillar burst" type. If a simple model which mainly accounts for mining geometry can correlate well with observed damage, then geometry is likely the main factor. In other areas, the geometry may not have reached an apparently critical state, but rockmass weaknesses such as faults may be the main factor for burst damage. Generally speaking the 3m wide cut and fill mining shown in figures 3, 4 left and 8 can manage high stress until 2 or 3 cuts are left. When only one cut is left, the rock is sufficiently yielded to dramatically lower the rock burst risk (Simser *et al.*, 2015). Where possible the mine switches mining methods to non entry blasthole for sill extractions. In flatter vein areas (too flat for gravity flow of blasted rock) innovative methods such as large scale destress blasting are required to extract the last 2 to 3 cuts. Rockburst prone support is routinely installed, but this may not reduce risk adequately. The support has to be safely installed in a high stress area; and if even if the support holds, workers may be exposed to large ground motions causing anxiety. For the narrow vein case, limited mechanized equipment options are available to remotely install support, so a design change is by far the preferred choice to reduce risk.

Pillar bursts have also been observed for smaller dimension rib pillars, for example between draw points in blasthole or caving operations and for room and pillar layouts. Although the potential energy storage may be significantly less than a larger sill pillar, smaller bursts with workers nearby is also a serious safety concern. This type of pillar failure is often a creeping risk; it slowly increases with time and overall extraction. For example in a room and pillar layout, the overall extraction footprint will slowly increase the tributary load on the pillars. In blasthole layouts, the pillars may initially be at an acceptable stress state, but as mining progresses, the overall wrap around stress state slowly increases and can eventually overload the pillar. In the example shown in figure 9 below, the pillar was formed after the first sub levels had been partially mined



Figure 9 Draw point pillar burst from a blasthole operation.

out. It remained stable with minimal ground support in the walls until the third and fourth sub levels above started being extracted. Restricting access or backfilling the crosscuts after mining is completed are other accepted risk mitigation techniques for localized failures.

The pillar burst shown in figure 9 was recorded as a local Richter Magnitude 0.0 seismic event. Approximately 5 tonnes of material was ejected up to a distance of 5m from the wall. The pillar dimensions were 7m along strike, 15m in the transverse direction, and 5m high. Even moderate sized seismic events can cause significant local damage if they occur close to the skin of an opening.

2.1.4 Seismically induced falls of ground

Recognizing rock ejection versus gravity fall is not always trivial. For example in figures 1, 3, and 9 it was clear that gravity could not account for how the failed material ended up where it landed. Bursting from the roof or back of an excavation is not always obvious. Fine fragmentation, "rock flour" (finely ground up rock material), and damage to ground support may offer clues to distinguish between gravity and rock-burst failures. Seismically induced falls of ground occur when a significant ground motion from seismic activity or blasting is enough to overcome a marginally stable support system. The main component of the failure may be gravity driven, but the "straw that broke the camel's back" was the ground motion.

The vibrations from blasting vary and are typically higher frequency relative to natural seismic events of similar magnitude. The seismic monitoring network recorded the blast that triggered the fall in figure 10 as a Richter Magnitude 1.6 when multiple

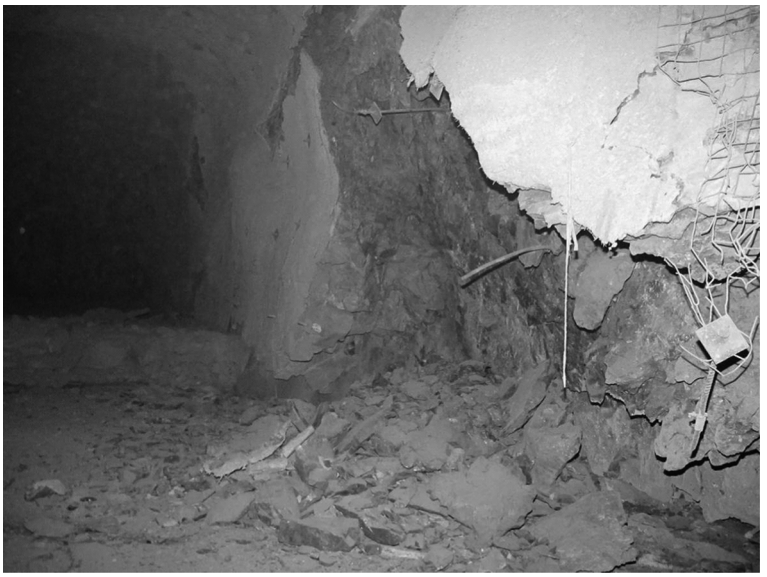


Figure 10 Fall of ground triggered by a stope blast 12.5m away. The wall had been heavily stress fractured and undercut by local mining. The failure is resting on top of a backfilled stope.



Figure 11 Seismically induced fall of ground after a Richter Magnitude 2.1 seismic event.

holes were firing, the shots leading up to the main portion of the blast were recorded as magnitude 1.0 events. In this case the failure area was over top of a filled stope and no man entry was required. The original support had been installed 1.5 years beforehand and survived the development cycle stress changes and the mining of a 30000 tonne stope directly below. The support was 50mm of synthetic fiber reinforced shotcrete and 22mm diameter resin grouted rebar on a 1.3 × 1.3m pattern. Support system fatigue prior to rockburst or strong ground motion loading can be an important factor.

Figure 11 shows an example of heavily stress fractured material being violently shaken down during a seismic event. In this case the area was planned for support rehabilitation and was not open for man entry. The original support (rebar and weld mesh) had been compromised by both corrosion and rockmass dilation over time.

2.1.5 Other burst mechanisms

Detailed rockburst mechanisms can be complex and varied. Some work in the field of mine seismology can help identify the causes, for example focal mechanism studies. However these can be complicated by waveform scattering and reflections around the mined out areas. Face crush bursts from the Ortlepp & Stacey (1994) classification are more commonly associated with longwall mining where a relatively large area is excavated inducing very high stresses ahead of the advancing face. South African gold reef mining is a classic example. Buckling mechanisms have been reported (White *et al.*, 2002) where steeply dipping, relatively closely spaced jointing sub parallel to excavation walls can violently fail. It such cases in may be possible to re-orientate the

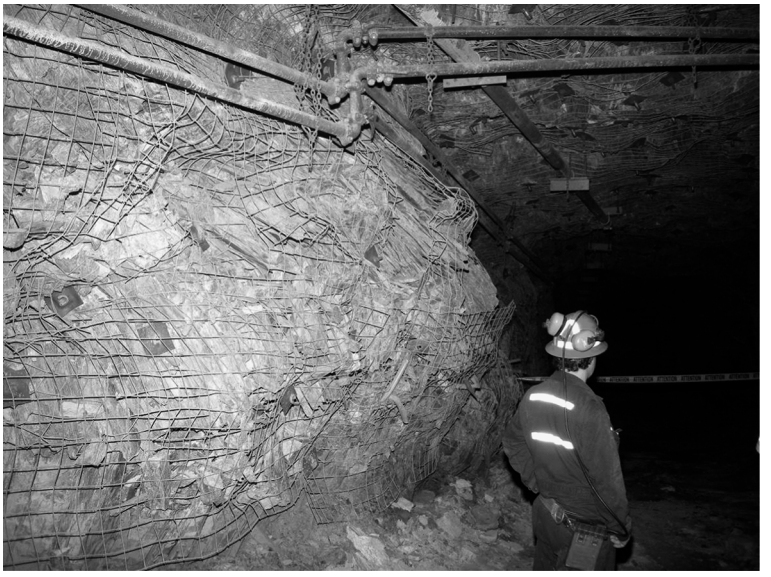


Figure 12 Buckled layers of laminated rock contained by splitsets, mesh and hybrid bolts (Mercier-Langevin & Turcotte, 2007). The hybrid bolts have a rebar installed within the splitset to limit shear failure, increase pullout resistance, and double plate the bolt collar. The original orientation of the layering was dipping at 70^0 and striking parallel to the tunnel wall.

tunnel to cross the stiff lamination layers at a more favorable angle. Similar deformation but at a much slower rate can cause squeezing ground conditions (Mercier-Langevin & Turcotte, 2007).

2.1.6 Burst mechanism general remarks

The engine driving many bursts is closure; deep excavations are not natural and will eventually close. This process is normally accommodated by rockmass creep, with jumps in the deformation rate as mining progresses. Many deep level gold mines in South African utilize stabilizing pillars to reduce the overall amount and rate of closure as rockburst mitigation. The risk of rockbursting slowly increases as the mining extraction increases and the overall closure increases.

Short term stress redistribution events are generally more predictable than fault slip type. Numerical models, seismic monitoring of blast response, and proactive workplace closures can all be used to help manage the risk due to over loading the rockmass. Fault slip type events are more random, and not as closely associated with blasting. This is partly because geological structures are difficult to characterize, both geometrically and by variations in strength. The nature of fault slip seismicity will vary from mine to mine, but in one example 20 large events were analyzed (Simser, 2008) with 40% of them being related to mine blasting, 30% having some potential precursory seismic activity before the large event, and with 30% of them having no precursory activity. In

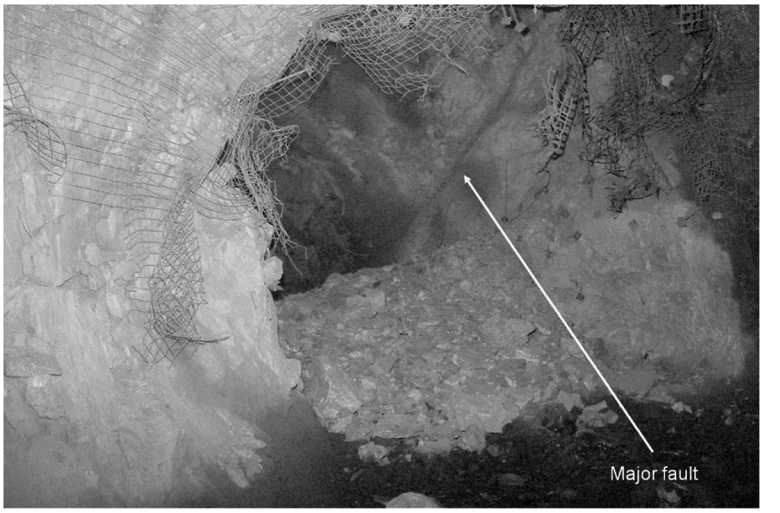


Figure 13 From Simser (2008). A fault intersecting a vent raise periodically "slipped" causing large seismic events and hundreds of smaller aftershocks. The raise had to be remotely mucked out on several occasions to maintain sufficient air flow.

the no precursory activity cases, the area was quiet, sometimes for days, and then the first recorded event was the large one and located on a known fault.

More complete work on seismic source and damage mechanisms can be found in Ortlepp (1997), Van Aswegen (2013), and Kaiser *et al.* (1996). However it is clear that regardless of the detailed mechanics, rockburst support systems require deformation capacities in the tens of centimeters and must survive loading rates of several meters per second.

2.2 Damage observations

Damage mechanisms can be very complex and are not necessarily well understood. Amplification of seismic waves occurs at the solid rock/fracture zone interface and the free surface of the excavation (Van Sint & Alvina, 2008). It often appears as though the fracture zone around an opening is the material that gets ejected. Other complications include: local stored strain energy around openings released by far field event; pre-loading and/or shearing of the rock support prior to the rockburst; support installation quality including corrosion; local opening geometry especially span; and variations of rockmass strength and structures. However complex the damage mechanics are, simple observations allow for some key conclusions.

The photo in figure 14 left is of a wall supported with a 1.3 × 1.3m pattern of 2.4m long 22mm diameter resin grouted rebar and a 2 × 2m pattern of 5m grouted cable-bolts. The cables were not plated, and the support was installed over 50mm of fiber reinforced shotcrete. No failures occurred along the tendons, some plates were torn off a few of the rebar. The vast majority of the failure was due to the fracture zone around the original opening being dynamically shaken out during the stope blast. Load transfer to the tendons clearly was inefficient. The right hand photo is an example of typical



Figure 14 Left – Wall failure viewed after blasthole stope backfilled. The majority of the stress fractured material around the blasthole overcut access was dislodged into the open stope prior to filling. Right – stress fracturing observed in a post pillar cut and fill stope. The fracture zone developed in the back of the previous cut and is exposed while breasting through the current cut.

stress fractures exposed by cut and fill mining. This is often the sort of material that gets expelled during a rockburst.

Recent drop weight testing on full scale test panels, where both bolts and surface retainment elements could be tested as a system showed a dramatic difference between dynamically loading "intact" rock versus "fractured" rock (Roth *et al.*, 2014). For the simulated intact rock, approximately 75% of the impact energy was absorbed by the bolts. The stiffer elements see the load first, and then the remaining 25% of the energy was absorbed by the mesh. For the simulated fractured rockmass, the ratio was about 70% energy absorption from the mesh, and only 30% by the bolts. This is more representative of the type of dynamic loading one could expect in a deep hard rock mining scenario.

Another common rockburst observation is the failure of weak links (Simser, 2007). Sharp edged plates can guillotine the mesh, which in turn may peel open at the seams, so the full potential capacity of the system is not utilized. Load transfer to the tendons is difficult; the use of double plates or mesh straps can make a large difference in the survivability of the support system (snow shoe effect).

Figure 16 highlights several key issues; this wall survived a substantial rockburst. The heavier mesh with double plating clearly helped despite some plates breaking some of the 8.4mm diameter strands in the mesh strap plates. The deformation incompatibility of the soft mesh versus the relatively stiff bolts is also obvious. In this case steel stretch style yielding bolts were used (Li, 2010), and although they presumably displaced during the burst, virtually all tendon types are still much stiffer than the mesh. The bulging between the bolts is a direct result of this.

Very large seismic events can cause wide spread damage, in part due to the large ground motion travelling through the mine, and to a large part the local site vulnerability. Ortlepp (1997) listed the factors impacting site response as: excavation

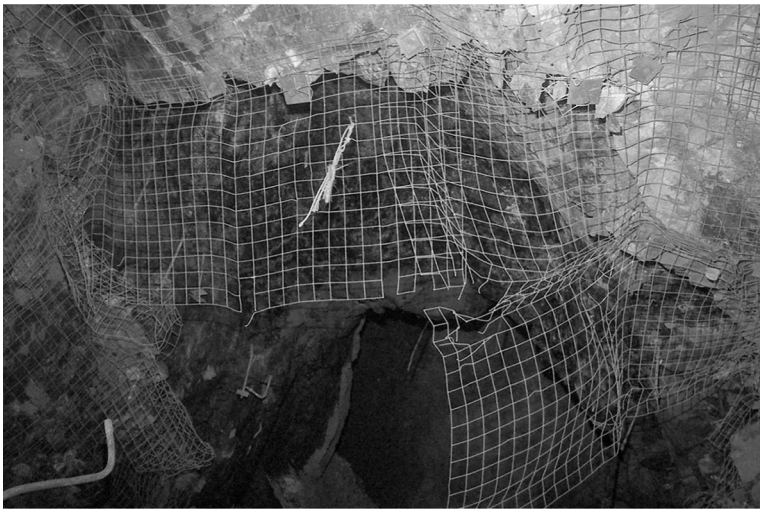


Figure 15 Brow failure next to a blasthole open stope. The weld mesh sheets peel open at the seams after square edged 125×125mm (6.4mm thick) plates guillotine the 4.5mm diameter wires.

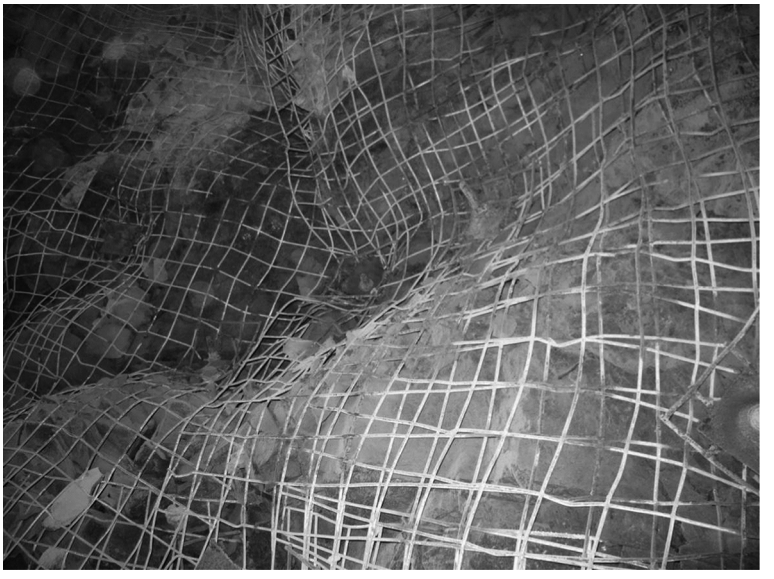


Figure 16 Wall support containing a rockburst. In this case the plates are 150×150mm (6.4mm thick and domed), the weld mesh has 5.7mm diameter strands, and the mesh strap plates are 300 × 300mm with 8.4mm diameter wires.

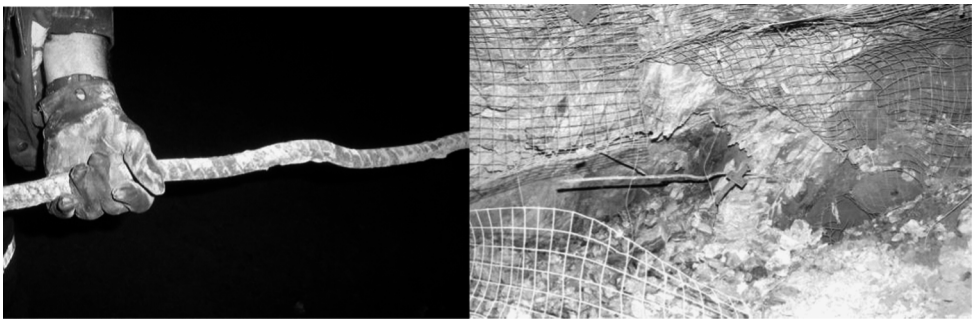


Figure 17 Sheared rebars – left – bar taken from a rock burst damage location. Right – rebar exposed in drift and fill mining process.

geometry, shape, and size; characteristics of existing support, local rockmass conditions, intensity of induced fracturing; site amplification; and stress intensity around the opening. For example in the case sited by Counter (2014), a Richter Magnitude 3.5 event caused widespread damage ranging from: seismic shake down (typically wide span areas); lower wall blowouts below the existing support system; failure of rigid support systems (shotcrete and rebar); localized failure of burst prone support ("ground zero" near the source of the large shear rupture); and successful containment of heavy damage where rockburst prone support was installed (typically modified conebolts, weld mesh and weld mesh straps over the original rebar and shotcrete support and a little further from the source of the shear rupture). Several examples of heavy shearing in exposed rebar were also noted. The mine upgraded several hundred meters of tunnel support to full "burst-prone" and experienced another Richter Magnitude 3.5 event a few years later. The damage containment was remarkable, showing that well designed support systems can dramatically impact the local site response.

The observation of sheared tendons exposed by burst damage is not unique (figure 17). The support capacity implication is twofold: most design numbers are sited from pure axial testing; and the shearing may have caused pre-event lockup or support capacity loss. For example many yielding tendon types rely on a predominantly axial sliding, such as conebolts[1], or steel stretch bolts rely on a length of free bar to absorb energy. Lockup along the bolts axis will lower the potential energy absorption capacity.

Heal *et al.* (2006) quantified "excavation vulnerability potential" by studying a large database of rockburst case histories. They listed the four main factors as: stress conditions; ground support system capacity; excavation span; and influence of geological structure.

3 ESTIMATING ROCKBURST SUPPORT SYSTEM DEMAND

There are several approaches to estimate the demand required from a support system under rock bursting conditions. An observational approach, based on past case

1 For further information: South African conebolts www.avengman.com; modified conebolts www.mansouringmining.com

histories is often used. This will not directly translate to new projects with no prior excavation history, but provides a reasonable band width to design for. The Canadian Rockburst Support Handbook (Kaiser *et al.*, 1996) outlines several techniques to estimate ejection velocity. One of the most useful ones is based on ballistics. Wall bursting is best suited to this method, as gravity can't explain how ejected material landed far from the wall.

3.1 Ballistics approach

Ejection velocity (V_e)

$$V_e = d(g/(2hcos^2\theta + sin2\theta))^{0.5}$$

The method can be applied on individual fragments or the center of mass of ejected material. A couple of examples are given below. The burst shown in figure 1 right had the center of mass eject from approximately 1.8m high, and flew approximately 2.5m. The calculated ejection velocity assuming it flew out horizontally would be 4.1m/s. This is clearly only an estimate, and can be further refined by considering sub zones of material rather than just the overall center of mass. Some of the fragments went across the 6m wide opening to the far wall, which would have ejected faster than 4.1 m/s, and some of the material could have heaved out and fallen under gravity. Individual fragments such as the one shown in figure 19 below can also be used for an ejection velocity estimate.

The figure 19 fragment travelled approximately 3m from a height of 2.25m, yielding an ejection velocity of about 4.4m/s. Using the simple kinetic energy formula an estimate of the total energy released can be made. The kinetic energy is very sensitive to the ejection velocity estimate as this term is squared. The bulk of the burst material weighed about 75.25 tonnes over a 28.2m^2 ejection area. Assuming a 4.1m/s ejection velocity the energy absorption requirement would be 22.4 kJ/m^2. This does not account

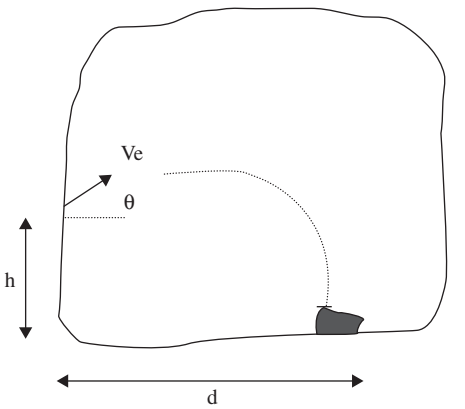


Figure 18 Ballistics approach for wall ejection rock bursting (Kaiser *et al.*, 1996). The ejection velocity can be estimated by measuring the height the material came from (h), the distance it flew (d) and the angle it flew out at. The angle may be difficult to determine. Occasionally bolts will bend in the trajectory direction but assuming a flat trajectory may be required. "g" is the gravitational constant.

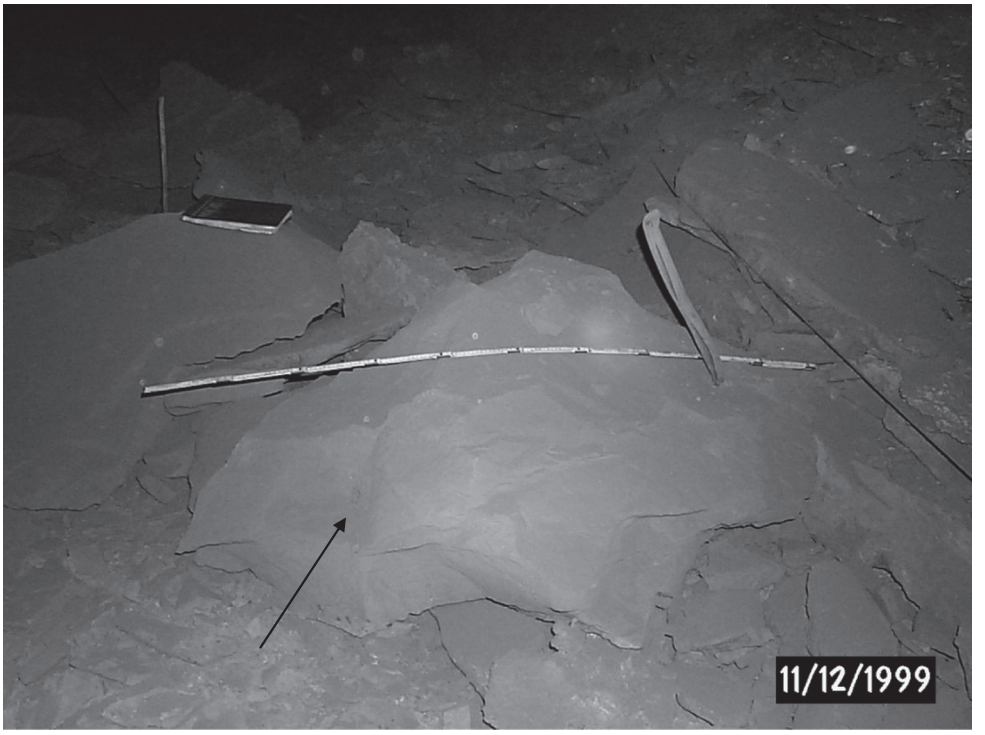


Figure 19 A large ejected fragment from the same rockburst shown in Figure 1 (Simser *et al.*, 2002). Note two broken splitsets, one flush to the rock surface indicated by the arrow, the other sticking out but necked and sheared.

for the energy absorbed by the failed support. Figure 2 shows that many of the tendons did not break, and the rock flew out around them. Discounting the energy absorbed by the bolts is reasonable in this case. The fibrecrete would have absorbed some energy, likely in the order of a few kJ's (Kaiser *et al.*, 1996).

3.2 Burst energy lower bound estimated by considering the failed support capacity

Another method for estimating the burst energy is to consider the failed support elements, and the lower bound energy would be greater than the energy absorption capacity of the support (Ortlepp *et al.*, 1997). The fragment in figure 19 weighed approximately 1350 kg (4.3 t/m^3 density material – massive lead-zinc sulfide). The energy absorption capacity of the splitsets is listed in Kaiser *et al.* as 5 to 15 kJ. For simplicity assuming they absorbed 10 kJ each, then the energy balance would be: kinetic + potential energy of the fragment > energy absorbed by the support elements.

$$1/2\, mv^2 + mgh = 20kJ$$

The fragment came from the wall, so discounting the potential energy, the resultant ejection velocity becomes: ½ (1350)(v^2) = 20000 or velocity was about 5.4m/s. If the splitsets only absorbed 5 kJ each, then the velocity would have been about 3.8 m/s.

3.3 Magnitude – distance (PPV) approach

Another method to estimate burst velocity is to use a magnitude-distance scaling relationship. For example Hedley (1992) derived the following equation from several Ontario hard rock mines:

$$V = 4000(R/10^{M/3})^{-1.6}$$

Where velocity is in mm/s, R = distance in meters, and M = Nutli Magnitude (Richter Magnitude + 0.3).

This is also a crude estimate because the distance is calculated as though the seismic event were a point source. Large events will have volume or areal extent, and seismic systems will have some inherent location error. For example the burst shown in figure 8 was triggered by a Nutli Magnitude 2.2 seismic event locating 11.5m away. The Hedley formula predicts a ground motion of 1.2m/s. The damage appears to be from a larger ejection velocity, but the distance of 11.5m could easily be less with limitations on source location accuracy (normally +/–10m in this example).

Kaiser *et al.* (1996) outline similar ground motion scaling laws, also based on distance and seismic magnitude relationships. Unless the event was extremely close to the damage location, this type of approach typically yields ground motions in the cm/s range while damage observations are typically in the m/s range. Waveform amplifications around openings and fractures zones can be in the order of 6 to 12 times that of the incident wave (Van Sint, 2008) which could easily account for the discrepancy. Local strain energy can also be triggered like the sudden release of a coiled spring as the seismic wave passes through.

3.4 Assuming the fracture zone gets ejected at 3m/s

The South African Chamber of Mines guide (1988) recommended design energy absorption capacities based on 3m/s ejection velocities. No doubt higher velocities have been observed from actual rockbursts, but the bulk of ejected material typically lies within this guideline. Smaller fragments (with low mass and sometimes higher ejection velocities) will not add a large proportion of the required energy absorption (joules). A relatively common observation for hard rock bursting is that the pre-existing fracture zone is the material that gets ejected. This isn't universal, but provides a method for estimating the required dynamic capacity of a support system. For example the burst shown in figures 20 and 21 below was damaged over an area of $9m^2$ to an average depth of about 0.5m (the dilated portion of the stress fracture zone). Assuming it was ejected at 3m/s, this would be an energy absorption requirement of:

$$1/2\ mv^2 = 1/2\left(9m^2\ x\ 0.5m\ x\ 3t/m^3\right)(3)^2 = 60.75\ kJ\ or\ 6.75\ kJ/m^2.$$



Figure 20 The stress fracture zone around a deep opening (Simser, 2007) ejected out after support system weak link failures. In this case the main weak link was sharp edged plates guillotining 4.5 mm diameter weld mesh and peeling open at the mesh sheet seams.

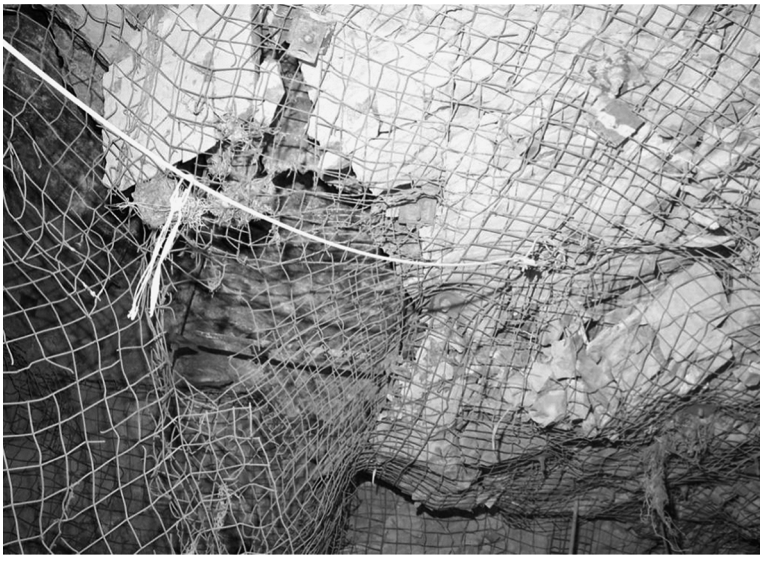


Figure 21 Edge of the burst shown in figure 20 showing the failure stopping at a line of 8.4mm wire diameter mesh straps. Yielding bolts (modified conebolts) were installed over the strapping. The ejected portion of the burst had conventional rebar, weld mesh and cablebolts but was missing the "snow shoe" effect of the strapping and the yielding capacity of the conebolts.

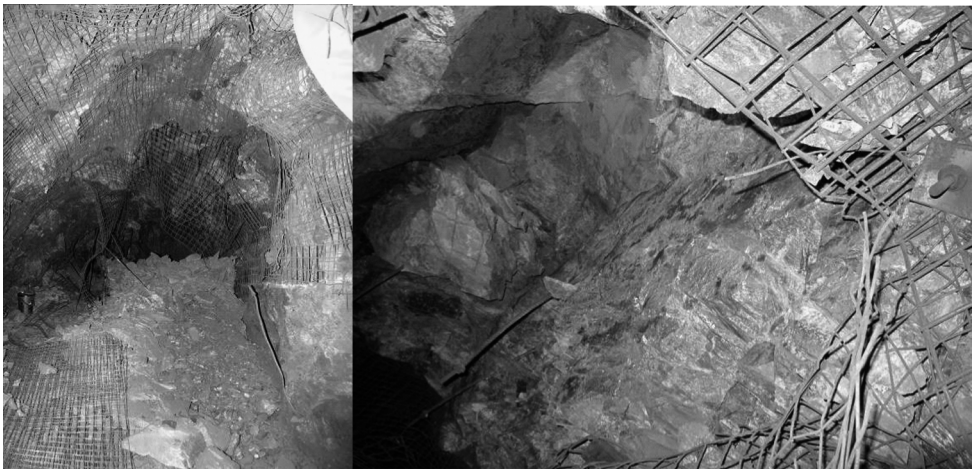


Figure 22 The stress fracture zone between two altered contacts was dynamically expelled during a Richter Magnitude 1.1 seismic event. The bolt length was 2.1m and depth of failure was slightly less (some snapped bolt ends were visible in the back of the failure). The fracture zone likely "road up" the slips and was more than normally expected for this area.

In this case the failure of weak links is essential to consider, and the support system had experienced deformation prior to the seismic event which lowered its overall capacity.

For newer projects where empirical observational evidence does not exist or is lacking, a reasonable approach is to use numerical models to estimate the depth of fracturing around the openings. If an assumed ejection velocity of 3m/s is used, then a conservative energy absorption target would be the mass of the fracture zone being shot out at this velocity. The depth of fracturing is equally important for static ground support design, and can be measured by test hole drilling. For example in high stress ground, newly drilled boreholes won't squeeze/notch in failed ground, but will once the high stress zone it intersected. This is an accurate measure of the depth of fracturing and can be verified with diamond drill holes where borehole camera or visual observations can clearly see the stress fractures. Physical observations can be important as the depth of fracturing can be anomalously deep in certain situations. Figure 22 shows a rock burst where the fracture zone was deeper than normal for the area. The failure was bounded by two copper veins with altered (chloritized) contacts. The slips allow the stress fractures to dilate, which in turn lowers the confinement allowing the next stress fracture to form more easily.

3.5 Measured ejection velocities

The crudeness of the above methods is difficult to overcome. There are cases of measuring ground motion with heavily damped geophones (Milev *et al.*, 2000) or by high speed photography (Heal *et al.*, 2006). In the heavily damped geophone monitoring, ground motions up to 3 m/s were recorded in some Deep South African gold mines during large seismic events. High-speed cameras have been used to monitor fly rock

velocities for simulated rockbursts and in rare instances have captured actual rockbursts. Personnel communication with a tunneling contractor indicated that they filmed a small burst with calculated ejection velocity of 3.2m/s. The burst was from the back of the tunnel, and only the skin ejected, followed by a gravity fall after the key block spit out.

4 ESTIMATING ROCKBURST SUPPORT CAPACITY

The example shown in figure 20 arguably had enough capacity to stop the burst; however most of the rebar and cablebolts did not break. Some plates were stripped off, and some plates even remained more or less intact. From Kaiser *et al.* (1996) the 20mm rebar might have absorbed 3 kJ each, the mesh about 3kJ/m^2 and the cables about 6 kJ each. The rebar was installed roughly on a 1 × 1m pattern and the cables on a 2 × 2m pattern. The cumulative system capacity is difficult to estimate because the elements have different stiffness, but keeping a simple additive approach 3 + 3 + 6/4 = 7.5 kJ/m^2. In figure 21 the addition of heavy mesh strapping reduced the plate guillotining and the addition of yielding bolts that could go along with the ride was enough to contain the same burst.

Any calculation of dynamic support system demand and capacity for rock bursting can only be considered an estimate and some logical considerations must be made. For example a rockbolt that can absorb 100 kJ and installed at 2m spacing could mathematically contain a rockburst of 25kJ/m^2. However if the distance between the bolts is excessive dangerous fly rock will eject freely.

4.1 Support element testing

Since the Canadian Rockburst Support Handbook (Kaiser *et al.*, 1996) was first published in 1996 there have been several notable dynamic support element testing programs. Some of the early data was extrapolated from static pull testing; now a fairly comprehensive catalog of element testing is becoming available. The CANMET Bell Corners dynamic testing rig has produced technical data sheet for many rockbolts (Doucet & Voyzelle, 2012). Another well known support testing program is from the Western Australian School of Mines (Player *et al.*, 2004; Villaescusa, 2014). Generally speaking grouted bolts are tested by dropping a weight onto a bolt installed into a thick walled steel tube. Various methods have been tried to test friction bolts including in situ testing by Carlton *et al.* (2013). Roth *et al.* (2014) and pioneering work by Ortlepp & Stacey (1997) have tested complete support systems under dynamic load. The lab results offer design numbers for various elements or support systems but it is acknowledged that many other complicating factors occur in situ. Support installation quality, support capacity lost over time as mining induced deformation takes places, nature of the support loading (shear, tension, compression) are a few key examples. However lab results offer repeatability and when reality is complex, a simplified model can be used to gain critical understanding of key parameters.

Hadjigeorgiou & Potvin (2011) have summarized a lot of the current and historic dynamic testing programs. With the proliferation of new rockbolts (*e.g.* Li, 2010) and even mesh options (*e.g.* Geobrugg Mesh (Roth *et al.*, 2004), high energy absorption

mesh (Potvin, 2008)) a comprehensive list of support elements and their corresponding static and dynamic capacities is not included here. Most suppliers can provide both static and dynamic capacities often from the testing programs listed above. Good engineering judgment is still required, for example in principle a mechanically anchored rockbolt should be able to stretch between the plate and the anchor over the entire length of the bolt. During a dynamic ground motion, tension in the plate is often lost due to rock un-raveling, and in practice mechanical rockbolts perform poorly during rockbursts (Hedley, 1992). Thin walled friction bolts will tear in shear and not mobilize the full cross sectional area of the steel (Simser, 2007). Both are also prone to corrosion problems which can also lower their real in-situ capacity dramatically. Conversely some bolt types often perform better than implied by lab testing. A fully encapsulated rebar can deform in multiple places along the bar, such as at each closely spaced stress fracture plane. Split tube testing whereby the drop weight impacts the midpoint of the installed bolt will differ from plate impact testing which is heavily influenced by the threads (weakened). Underground observations can vary considerably, for example in figure 7 left, the strain in the failed rebar was localized along a slip plane, which necked and snapped all the bars in tension. In this case a split tube test result would be representative of the energy capacity. In many cases rebar failure does occur at the threads, so a plate impact test would be more representative.

Combining different material may have unintended consequences. For example mesh can deform 100's of millimeters before reaching peak load capacity (figure 23).

When shotcrete is sprayed over mesh, it stiffens up the overall displacement capacity and can only deform several centimeters instead of 10's of centimeters (figure 24). Round determinate panel (RDP) tests (ASTM, 2005) can be used as a proxy for the behavior of reinforced shotcrete underground. Figure 25 below shows test results from plain shotcrete, fiber reinforced shotcrete and weld mesh embedded in shotcrete. Although many different fiber types and dosages exist and embedded mesh performance will depend on where the mesh is relative to the sample thickness (RDP samples are 800mm diameter and 75mm thick cast or sprayed shotcrete panel centrally loaded in the lab), it is clear that there is an overall displacement limit (<100mm in the example shown). For "heavy" rockbursting this simply is not enough and the shotcrete can become part of the fly rock as shown in figure 1 right.

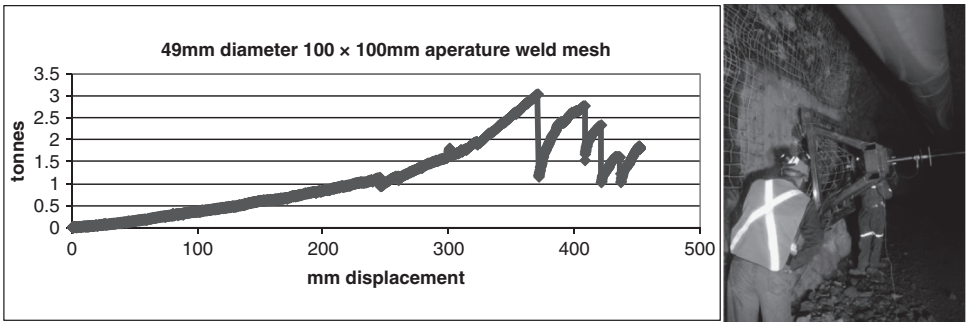


Figure 23 In situ pull test of weld mesh. Different testing configurations will vary the results, but mesh is passive ground support and doesn't reach peak capacity until several hundred mm of displacement.



Figure 24 Close up view of shotcrete cracking after a rockburst event. In this location the support held but the embedded 8mm wire mesh strands are necked and failed in tension at the crack location. Scale is in inches.

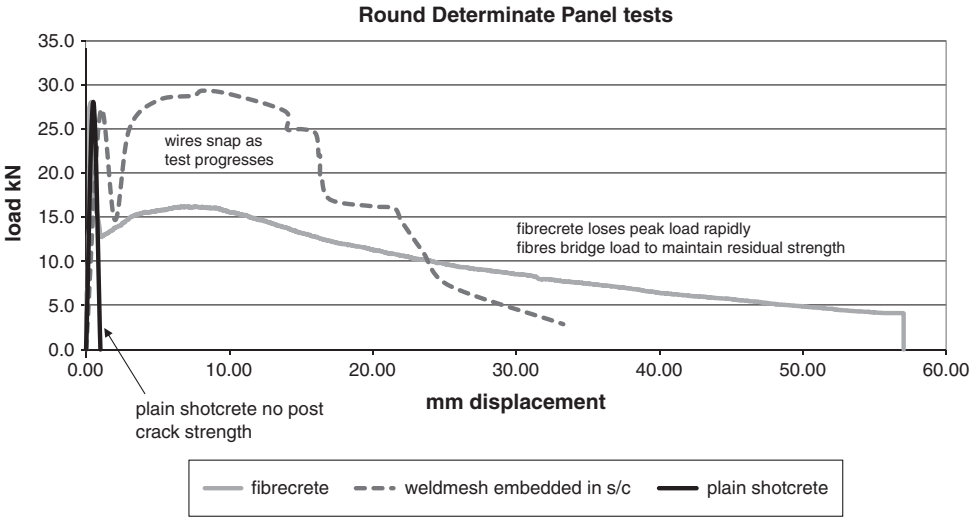


Figure 25 Relative performance of round determinant shotcrete panels. The toughness[2] of various shotcrete reinforcement types can be varied according to fiber type, length, and dosage or mesh type but it is very difficult to get enough displacement capacity for large rockbursts with inherently brittle shotcrete.

2 Area under the load displacement curve

The capacity used for support elements is only an estimate when extrapolating lab data to the real in situ performance during a rockburst event.

4.2 Support system capacity

A few important principals need to be adhered to for a successful rockburst support system design: adequate static load capacity; substantial deformation capacity (often 10's of centimeters); energy absorption capacity (a product of the load bearing and deformation capacities); adequate length of reinforcing elements and areal coverage; it is often only as good as its' weakest link; and it has to be practical and economic to install. Deformation capacity is often over looked, in figure 1a an example of over 10cm transient displacement occurred during a large seismic event. A system that allows too much displacement, may lead to heavy bulking between the tendons and pre-mature failure around plate edges. Villaescusa *et al.* (2014) recommended 300mm as a practical maximum deformation for design purposes. Allowing more deformation will create large "ballooning" of broken rock and challenge plate connections to the bolts or snap wire strands.

Support elements have varying stiffness and do not sustain dynamic loads in perfect harmony. Figure 26 does indicate that mesh can "bag" to close to its' full capacity so long as weak links don't fail first. Load transfer to tendons is often difficult and it is difficult to determine how much load bolts really take during a burst. Instrumented rockbolts or cables with real time data logging may eventually provide enough data to derive some empirical guidelines, but with localized rockburst damage this will take time.



Figure 26 Bagged mesh near the brow of an open stope.



Figure 27 Cable lacing used over expanded metal mesh in a deep Canadian Mine.

Local support practice will vary between region and even mine sites. Traditional South African Gold Mines use chain link mesh and cable lacing with 16mm diameter cement grouted rebar. The deformation capacity comes mainly from the retainment system. Ortlepp & Stacey (1997) showed the value of the cable lacing with dynamic testing, despite the labor intensive method used to install it; it remains one of the better methods to absorb rockburst energy. Potvin (2008) design a crinkled mesh fabric with lacing incorporated in the mesh sheets for improved mechanized installation. Figure 4 left shows the use of heavy gauge mesh straps, which at that specific mine are carefully installed over the mesh sheet seams. The straps aid transfer load to the tendons, help bolts work together in a system, and improve the overall retainment capacity. They do not cover 100% of the area, so some assumptions are required to calculate their overall impact on a ground support system.

Given the complexities observed underground, an exact support system design for rockbursting is not possible. A reasonable estimate is to simply add the component capacities of the main system components to calculate the required kJ/m^2. The system requires good bolt plates with sufficient areal coverage to transfer load to the bolts, weak links such as mesh sheet seams need to be reinforced with good bolting practice (sheet overlaps, straps over the seams….), shotcrete as the outer layer will limit the overall displacement capacity, etc. As long as the practical considerations are adhered to, the simple additive approach provides a support system capacity estimate that can be used to compare different systems and crudely estimate factors of safety.

Table 1 shows an example of estimating support system capacity. To estimate a factor of safety an example for estimating demand is given below using a narrow rib pillar layout (transverse blasthole mining draw point pillars). Figure 28 shows a 2D simulation of three stope crosscuts with 5 × 5m profiles and 7.5 m pillars in-between. The pillars have a 2.3 m thick fracture zone next to a highly stressed pillar core. If this

Table 1 Idealized dynamic support capacity table. Note that the 1.5×1.5m spacing with yielding bolts and heavy mesh has a higher kJ/m2 rating than the 1×1m rebar with heavy mesh. However the wider pattern may allow too much deformation between the bolts so it might not perform as well in situ.

Support element	*kJ*	*Retainment*	*kJ/m2*
fully grouted rebar	5	thin wire weld mesh	2
steel stretch yielding bolt	25	heavy wire weld mesh	5
support system	kJ/m2	comment	
1.5×1.5m rebar + thin wire mesh	4.2	minor strain bursting	
1.5×1.5m yielding + thin wire mesh	13.1	wide bolt pattern for bursting!	
1×1m rebar + heavy wire mesh	7.0	moderate strain bursting	
1×1m yielding + heavy wire mesh	30.0	significant rockburst	

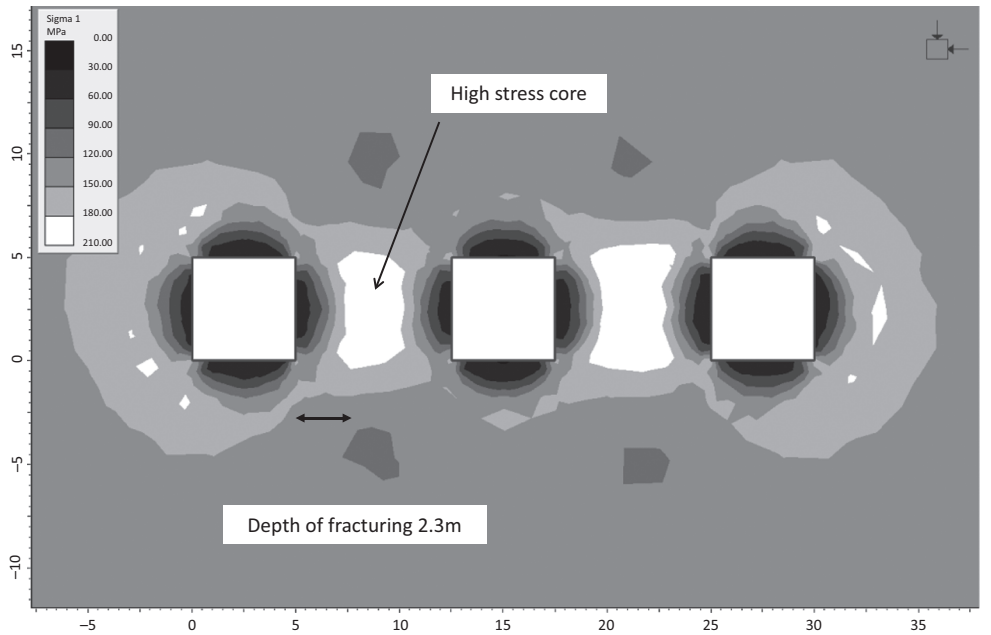


Figure 28 2D non linear simulation of draw point pillars showing a 2.3m thick fracture zone next to a 5 × 5m tunnel and a highly stressed pillar core.

fractured material is blown out at 3m/s, then the estimated demand per linear meter of tunnel would be (for density = 2.7 tonnes per m^3):

$$1/2mv^2 = {}^1/_2(5 \times 2.3 \times 1)(2.7)(3)^2$$
$$= 139.7\text{kJ over a } 5 \times 1 \text{ m portion of the tunnel} = 27.9\text{kJ/m}^2$$

The estimated safety factor would be capacity/demand 30 /27.9 or 1.1 assuming a 1 × 1m pattern of yielding bolts and heavy mesh was used as the support system.

5 SUMMARY

Despite complications observed in the field, the use of rockburst resilient support systems has become wide spread for deep hard rock mines. Many examples of successfully supporting substantial dynamic loads exist. A simplified approach to the design, both demand and capacity still gives a reasonable estimate and can narrow down the range of practically installed support options.

Ground support is often the last line of defense or the "*PPE of the mine*[3]" and should not be used as a substitute for poor mine design. Care needs to be taken installing the ground support especially if the tunnel development is in high stress to start with. Remote procedures such as Australian jumbo bolting, or automated boom style bolters with carousels may be required. In many cases the rockburst support installation is in anticipation of forthcoming mining induced stress changes. Mining projects often underestimate the impact of future mining and the rockburst support is installed as an upgrade after damage incidents.

Conflicting opinions exist on the value of shotcrete as part of a rockburst support system. Early application on well prepared rock surfaces (high pressure water scaling) can inhibit rockmass dilation, reinforcing natural or mining/blasting induced fractures. This in turn can help later load transfer to rockbolts and reduce the amount of rock unraveling. The brittle nature of shotcrete is abundantly clear when it is hit by dynamic loading. Mesh on the outer layer, despite equipment damage, blast fly rock and corrosion, is a requirement to sustain 10's of centimeters of deformation.

The influence of strain energy around openings is often under-estimated. Large seismic events triggering seemingly far field ejection damage are often a case of dynamically pushing a pre-loaded tunnel over the edge. Recent advances in ground motion modeling (Malovichko & Basson, 2014) are improving understanding of wave amplification around openings. Adoption of mountain highway engineering products to take the impact of falling rocks in underground applications offers the potential to greatly improve retainment capacity (high tensile strength chain link mesh).

A lot of focus has been on the dynamic capacity of tendons and other ground support elements. The programs at the Western Australian School of mines and CANMET (Bells Corners, Canada) have added a lot to the dynamic capacity database and helped suppliers develop new and innovative products now widely available to the industry.

The depth of fracturing around openings can be a key element of both dynamic and static ground support design. The required energy absorption capacity is strongly related to the actual ejection velocity, which varies within a rockburst. The example of the skin of a tunnel ejecting at 3.2m/s followed by gravity failure offers some promise. If the key blocks can be maintained, and the rock mass dilation kept to reasonable limits, then this helps preserve the inherent rockmass strength. The dilemma of double supporting (operators hate the idea of multi pass systems for cost and productivity reasons) with a stiff inner layer (shotcrete) and an outer flexible layer (mesh or possibly thin spray on liners) is still the "best" off the shelf approach for typical mechanized mining.

3 Personnel Protective Equipment of the mine – Dave Counter – Deep and High Stress Mining 2014

REFERENCES

An industry Guide to Methods of Ameliorating the Hazards of Rockfalls and Rockbursts. Chamber of Mines Research Organization. South Africa. 1988.

ASTM 1550-05 (2005) Flexural Toughness of Fiber-Reinforced Concrete (Using Centrally Loaded round Panel). ASTM, West Conshohocken, PA.

Carlton, R., Darlington, B. & Mikula, P. (2013) In situ dynamic drop testing of the MDbolt at Mt Charlotte Gold Mine. Ground Support 2013. Proceedings of the 7th International Symposium on Ground Support in mining and Underground Construction, Perth, Australia.

Counter, D.B. (2014) Kidd mine – Dealing with the issues of deep and high stress mining – past, present, and future. Proceedings of the Seventh International Conference on Deep and High Stress Mining. Sudbury, 2014.

Doucet, C. & Voyzelle, B. (2012) Technical Information Data Sheets. Dynamic Ground Support Testing. CANMET. Natural Resources Canada.

Hadjigeorgiou, J. & Potvin, Y. (2011). A critical assessment of dynamic rock reinforcement and support testing facilities. Rock Mechanics and Rock Engineering, Published online. Springer-Verlag.

Heal, D., Potvin, Y. & Hudyma, M. (2006) Evaluating Rockburst Damage Potential in Underground Mining. 41st U.S. Symposium on Rock Mechanics. Golden Colorado.

Heal, D. & Potvin, Y. (2007) In-situ Dynamic Testing of Ground Support Using Simulated Rockbursts. Fourth International Conference on Deep and High Stress Mining, 7–9 November 2007, Perth, Australia.

Hedley, D.G.F. (1992) Rockburst Handbook For Ontario Hardrock Mines. Mining Research Laboratories, CANMET Special Report SP92-1E.

Kaiser, P.K., McCreath, D.R. & Tannant, D.D. (1996) Canadian Rockburst Support Handbook. Geomechanics Research Centre, Sudbury, Ontario, Canada.

Li, C. (2010) A new energy-absorbing bolt for rock support in high stress rock masses. International Journal of Rock Mechanics & Mining Sciences 47, pp. 396–404.

Malovichko, D. and Basson, G. (2014). Simulation of mining-induced seismicity using the Salamon-Linkov Method. Proceedings of the Seventh International Conference on Deep and High Stress Mining. Sudbury.

Mercier-Langevin, F. & Turcotte, P. (2007). Evolution of ground support practices at Agnico Eagles's LaRonde Division: innovative solutions for high stressed ground. Rock Mechanics: Meeting Society's Challenges and Demands. Eberhardt, Stead, Morrision (eds). pp. 1497–1504.

Milev, A.M., Spottiswoode, S.M., Murphy, S.K. & Geyser, D. (2003) Strong Ground motion and Site Response Recorded Underground During Mine Induced Seismic Events. ISS International Seminar on Seismic Monitoring in Mines. March 2003. Stellenbosch, South Africa.

Morissette, P., Hadjigeorgiou, J. & Thibodeau, D. (2014) Investigating the dynamic load-demand on support systems using passive monitoring data. International Journal of Rock Mechanics & Mining Sciences 67, pp. 115–126.

Morissette, P., Hadjigeorgiou, J., Punkkinen, A. & Chinnasane, D., (2014). The influence of change in mining and ground support practice on the frequency and severity of rockbursts. Deep Mining 2014. Sudbury, Canada. Hudyma, M. and Potvin, Y. (eds). Australian Centre for Geomechanics.

Ortlepp, W.D. & Stacey, T.R. (1994) Rockburst Mechanisms in tunnels and shafts. Tunneling and Underground Space Technology, 9, 1, pp. 5–65.

Ortlepp, W.D. (1997) Rock Fracture and Rockbursts an Illustrative Study. The South African Institute of Mining and Metallurgy, Johannesburg.

Ortlepp, W.D., Durrheim, R.J., Handley, M.F., Haile, A. & Roberts, M.K.C. (1997) Rockburst Damage to Tunnels in a Deep South African Gold Mine Caused by a M=3.6 Seismic Event. 4th international Symposium on Rockbursts and Seismicity in mines, Krakow, Poland.

Ortlepp, W.D. & Stacey, T.R. (1997) Testing of Tunnel Support: Dynamic Load Testing of Rock Support containment Systems. SIMRAC GAP Project 221, 1997, South Africa.

Player, J.R., Villaescusa, E. & Thompson, A.G. (2004) Dynamic testing of rock reinforcement using the momentum transfer concept. Ground Support in Mining and Underground construction, Proceedings form the 5th International Symposium on Ground Support, Perth, Australia.

Potvin, Y. (2008) HEA Mesh – High Energy Absorption Mesh. Australian Centre for Geomechanics Newsletter. Vol. 31. December 2008.

Potvin, Y., Wesseloo, J. & Heal, D. (2010) An interpretation of ground support capacity submitted to dynamic loading. Deep Mining 2010. Santiago, Chile.

Roth, A., Windsor, C., Coxon, J. & de Vries, R. (2004). Performance assessment of high tensile wire mesh ground support under seismic conditions. Proc. Ground Support in mining and underground construction. Villaescusa and Potvin (eds.), 589–594, Leiden, Balkema.

Roth, A., Cala, M., Brandle, R., & Rorem, E. (2014) Analysis and numerical molelling of dynamic ground support based on instrumented full-scale tests. Seventh International Conference on Deep and High Stress Mining, 16–18 September 2014, Sudbury, Canada.

Simser, B. (2007) The Weakest Link: Ground Support Observations at Some Canadian Shield Hard Rock Mines. Fourth International Conference on Deep and High Stress Mining, 7–9 November 2007, Perth, Australia.

Simser, B. (2008) Mining in a Seismically Active Fault Zone: A case Study from Xstrata's Craig Mine, Sudbury, Ontario. Strategic Versus Tactical Approaches in Mining. Quebec City, Canada.

Simser, B. (2013) Seismic Monitoring at Nickel Rim South Mine. Engineering Seismic Group (ESG) – Seismic Monitoring Seminar. June 2013. Kingston, Ontario, Canada.

Simser, B., and Andrieux, P. (2013) Rockburst Case Histories – Brunswick Mine. Rockburst Case Histories 1985, 1990, 2001 & 2013. Deep Mining Research Consortium. CAMIRO Mining Division.

Simser, B. & Jalbout, A. (2014) Rock Mechanics tools for mining in high stress ground conditions at Nickel Rim South Mine. Proceedings of the Seventh International Conference on Deep and High Stress Mining. Sudbury.

Simser, B., Andrieux, P. & Gaudreau, D. (2002) Rockburst Support at Noranda's Brunswick Mine, Bathurst, New Brunswick. 4th American Rock Mechanics Symposium. Toronto, Ontario, Canada.

Simser, B., Deredin, R., Jalbout, A. & Butler T. (2015) Use of Microseismic monitoring Data as an Aid to Rock Mechanics Decision Making and Mine Design Verification. 49th US Rock Mechanics / Geomechanics Symposium, San Francisco.

Stacey, T.R. (2012) Support of excavations subjected to dynamic (rockburst) loading. Harmonising Rock Engineering and the Environment – Qian & Zhou (eds). Taylor & Francis Group, London, ISBN 978-0-415-80444-8.

Swan, G., Rockburst Case Histories – Fraser Copper Mine (2013). Rockburst Case Histories 1985, 1990, 2001 & 2013. Deep Mining Research Consortium. CAMIRO Mining Division.

Van Aswegen, G. (2013) Forensic Rock Mechanics, Ortlepp Shears and Other mining Induced Structures. 8th International Symposium on Rockbursts and Seismicity in Mines. Russia, September 2013.

Van Sint, J.F. & Alvina, N. (2008) Ground motion amplification around underground excavations. Australian Centre for Geomechanics Newsletter. Vol. 31. December 2008.

Villaescusa, E. (2014) Geotechnical design for Sublevel Open Stoping. Western Australian School of Mines. CRC Press.

Villaescusa, E., Player, J. & Thompson, A. (2014) A reinforcement design methodology for highly stressed rockmasses. Ground Support Subjected to Dynamic Loading Workshop. Deep Mining 2014. Sudbury, Canada.

White, B., Williams, T. & Whyatt, J. (2002) Mechanics of a large, strain-type rock burst and design for prevention. NARMS-TAC 2002, "Mining and Tunnelling Innovation and Opportunity," Proceedings of the 5th American Rock Mechanics Symposium and the 17th Tunnelling Association of Canada Conference, July 7–10, 2002, Toronto, Ontario, Canada. Hammah, R, Bawden, W, Curran, J, Telesnicki, M, eds., Toronto, Ontario, Canada: University of Toronto Press, 2002 July, 2: 1095–1101.

Yao, M., Sampson-Forsythe, A. & Punkkinen, A. (2014) Examples of ground support practice in challenging ground conditions at Vale's deep operations in Sudbury. Deep mining 2014. Sudbury, Canada.



Taylor & Francis
Taylor & Francis Group
http://taylorandfrancis.com

Chapter 11

Energy-absorbing rockbolts

C.C. Li
Department of Geology and Mineral Resources Engineering, NTNU – Norwegian University of Science and Technology, Trondheim, Norway

Abstract: The modern concept of rock support is to dissipate a part of the energy released from the rock mass in order to achieve a stable status in underground excavations. This is particularly true in high-stress rock masses. In this chapter, the loading conditions and the requirements for rockbolts are first discussed in order to understand why energy-absorbing support devices are needed in high-stress rock conditions. Testing methods for examining the performance of rockbolts are also briefly presented to facilitate the reading of the test results of the rockbolts in the subsequent sections. Seven types of energy-absorbing rockbolts, which are either used for dynamic rock support in practice or still in the stage of trials, are introduced. All energy-absorbing bolts are characterized by their high load and displacement capacities compared with conventional rockbolts such as fully encapsulated rebar bolts. They dissipate energy either through ploughing/slippage in the grout or auxiliary elements such as anchors and sleeves (cone bolt, Garford bolt, Durabar, Yield-Lok, Roofex and He bolt) or through stretching of the bolt steel (D-Bolt). The dynamic load of an energy-absorbing rockbolt based on ploughing/slippage is usually smaller than its static load, while the static and dynamic loads of the stretching-based rockbolt (D-Bolt) are approximately the same.

1 INTRODUCTION

Rockbolts are installed in boreholes to provide support and reinforcement functions for rock masses. They are classified into three categories according to their anchoring mechanisms: *discrete-point anchored bolt*, *fully encapsulated bolt* and *frictional bolt* (Windsor, 1997; Li & Stillborg, 1999; Li *et al.*, 2014). A *discrete-point anchored rockbolt* refers to a bolt that is anchored in a borehole at one or more positions along the bolt length in addition to the anchor point at the face plate and bolt thread on the rock surface. Mechanical bolts with an expansion shell and the D-Bolt with multi-anchors belong to this category of rockbolt. The mechanical bolt is anchored in the borehole through the mechanical locking of the expansion shell at the far end of the bolt. The D-Bolt is fully grouted in the borehole and it mechanically interacts with the grout and the rock at the anchor positions after hardening of the grout. The *fully encapsulated rockbolt* usually refers to a rebar bolt that is grouted in a borehole along its entire length, either with cement mortar or resin. The rebar bolt is integrated with the grout and the rock through the tightly spaced ribs on the cylindrical surface of the

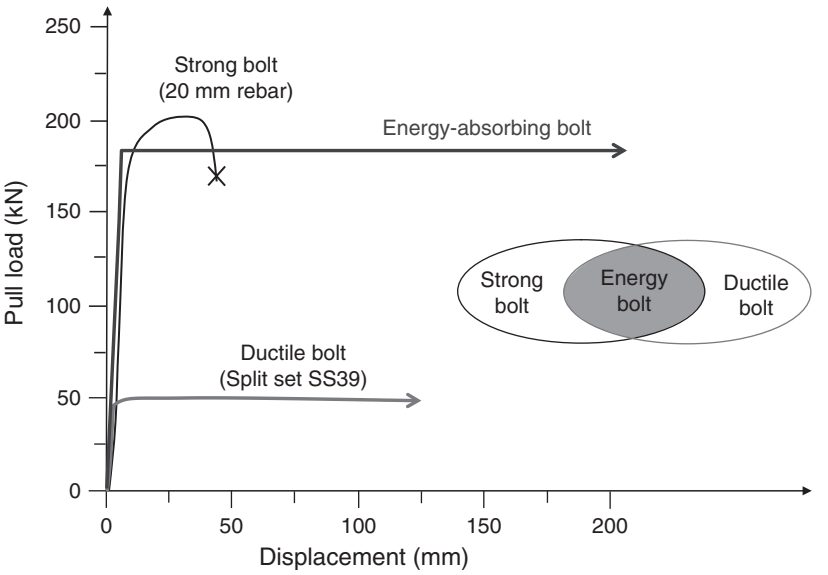


Figure 1 Performance of rockbolts subjected to pull loading.

rockbolt. A *frictional rockbolt* is anchored in the borehole through the friction at the bolt–rock interface. The Split set and inflatable rockbolts (such as Swellex) belong to this category of rockbolt. According to their performance, on the other hand, rockbolts can be classified into categories of *strong*, *ductile* and *energy-absorbing bolts* (Li, 2010), Figure 1. A *strong rockbolt* is characterized by its high load capacity but low deformability. Fully grouted rebar bolts belong to this category of rockbolt. A *ductile rockbolt* can accommodate large rock displacements, but its load capacity is low. The Split set is such a type of rockbolt. *Energy-absorbing rockbolts* are not only strong but also deformable, so that they are capable of absorbing a significant amount of energy prior to failure.

The stability of an underground opening, such as a tunnel, is mainly governed by three factors: the quality of the rock mass, the primary in situ stress state and the size and geometry of the opening. Of the three factors, the in situ stress state plays a crucial role in the stability of the rock mass. Low in situ stresses may lead to loosening (*i.e.* de-stressing) of the country rock and thus the rock falls under gravity, while high in situ stresses would result in rock failure owing to stress concentration. The loading condition of rockbolts is thus associated with the in situ rock stresses. In shallow locations, the in situ rock stresses are usually low and the major instability issue is falls of loosened wedge blocks from the roof. In this case, the load on the rockbolts is the deadweight of the potentially falling blocks (Figure 2). It is required that the rockbolts must be strong enough to bear the deadweight of the blocks. Thus, the strength of the rockbolts is more important than the displacement capacity in this type of rock condition. In other words, strong rebar bolts are appropriate support devices in low-stress rock masses.

In deep locations, for instance at a depth of 1000 m below the surface, the in situ rock stresses are so high that rock failure usually is unavoidable. The high stresses can lead to

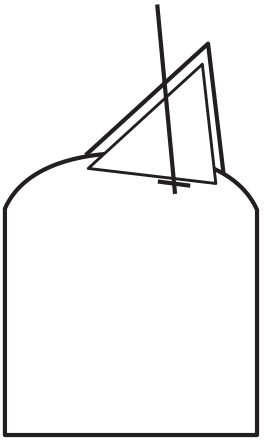


Figure 2 Deadweight loading on a rockbolt in low-stress rock masses.

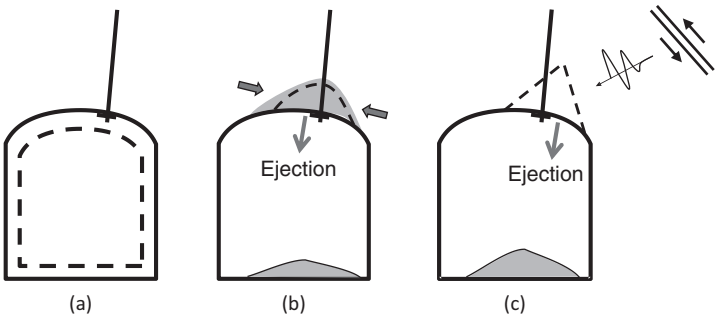


Figure 3 Loading conditions on rockbolts in high-stress rock masses. (a) Rock squeezing, (b) Strain rockburst, (c) Fault-slip rockburst.

two consequences in underground openings: rock squeezing in soft and weak rock and rockburst in hard rock (Figure 3). It is well known that the ductile rockbolt Split set has been used in many mines to deal with rock squeezing. The main function of such a ductile support device is to avoid disintegration of the fractured rock parties, but it is not capable of effectively restricting the rock displacement because of the low load capacity of the device. Both rock squeezing and rockburst are related to the strain energy released from the rock mass. In such a rock condition, the rockbolts, together with other types of support devices, have to be capable of absorbing a part of the released strain energy instead of simply equilibrating the ground load because the ground load is not constant, rather it is correlated with the deformation. Take a rockburst event as an example. A certain amount of strain energy stored in the stressed rock mass is transformed to kinetic energy when the rockburst event occurs. The rockbolts, together with other support devices, must be capable of absorbing the kinetic energy in order to retain the failed rock in place. The stronger the bolts are, the less the failed rocks displace. Obviously, strong rockbolts are preferred in this case because they effectively restrict

the rock displacement. In other words, strong energy-absorbing rockbolts are appropriate support devices in high-stress rock masses.

It can be said that energy-absorbing rockbolts with high load capacities are the ideal rockbolts for rock support, particularly in high-stress rock masses. This chapter gives an introduction to the energy-absorbing rockbolts that are available today. The criteria for selection of the rockbolts for presentation in this chapter are either that they have been used for rock support in practice or they have been publicized in detail through scientific articles and presentations at international symposia. The history of the development of energy-absorbing rockbolts is first given a brief review. The underground loading conditions and the design demands on rockbolts are then introduced. The testing methods to examine the static and dynamic performances of rockbolts are also briefly presented for the purpose of helping readers to read the test results of individual rock bolts. Finally, individual energy-absorbing rockbolts are presented in the aspects of structure, work principle and static and dynamic performances. The terminology "yield" is used in some literature to express the concept of energy-absorbing capacity of a rockbolt. Yield and energy-absorbing are synonyms in this paper.

2 DYNAMIC LOADING AND DESIGN REQUIREMENTS

2.1 Dynamic loading

Rockburst is a phenomenon where brittle and hard rock fails suddenly and the failed rock is thrown away in a certain ejection velocity. All rockburst events are related to high in situ stresses in the rock mass. A rockburst event is either classified as *strain burst* (Figure 3b) or *fault-slip burst* (Figure 3c) depending on the triggering mechanism. Strain burst refers to a burst event that is directly related to stress concentration in the rock surrounding an underground opening, while fault-slip burst refers to a burst event triggered by seismic waves caused by fault slippage. It is thought that the kinetic energy of the ejected rock comes from the potential strain energy stored in the rock mass as well as the dynamic energy brought by the seismic waves. The study by Li (2013) demonstrates that the ejection velocity of the ejected rock is mainly associated with the potential strain energy stored in the rock prior to rockburst. The seismic waves only play a role of triggering the rockburst in most cases.

2.1.1 Strain rockburst

After excavation, the tangential stress in the superficial rock becomes elevated. The rock fails when the tangential stress is beyond a certain limit and the elastic strain energy stored in the rock is released suddenly, which leads to strain rockburst. Strain rockburst is characterized by superficial rock failure in the form of spalling or slabbing with the rock being burst down like onion skins.

Strain rockburst does not involve any seismic activity prior to the occurrence of the rockburst event. It is simply due to the energy release after rock failure. In other words, the strain energy stored in the rock is transformed into kinetic energy as the rockburst

event occurs. The elastic strain energy (*i.e.* the potential energy) stored in the rock party to be ejected is expressed by:

$$\text{Potential energy} = \frac{m}{2\rho E}\sum \sigma_i^2 \tag{1}$$

where m is the mass of the rock party, ρ the density of the rock, E the Young's modulus of the rock and σ_i are the average principal stresses in the rock party (i = 1, 2 and 3). The kinetic energy of the ejected rock is expressed by

$$\text{Kinetic energy} = \frac{1}{2}mv_1^2 \tag{2}$$

where v_1 is the ejection velocity. The right-hand sides of the above two expressions should be equal according to the law of energy conservation. Thus, the ejection velocity of a strain rockburst event is obtained as:

$$v_1 = \sqrt{\frac{1}{\rho E}\sum \sigma_i^2}. \tag{3}$$

2.1.2 *Fault-slip rockburst*

Underground excavation changes the stress state in such a manner that the tangential stress around the opening is elevated but the radial stress is reduced. The reduction in the radial stress may lead to a decrease in the normal stress on some pre-existing faults nearby and in turn the shear resistance of the faults is reduced. Slippage, therefore, may occur along those faults. Such fault slippage will generate seismic strain/stress waves (*i.e.* P and S body waves) that propagate spherically outward from the hypocenter of the slippage (Figure 3c). In highly stressed rock masses, the country rock surrounding an underground opening is usually already fractured because of elevation in the tangential stress. When the seismic waves reach the free surfaces of the opening, rockburst events may be triggered so that the fractured wall bursts down. This is the so-called *fault-slip rockburst*. The kinetic energy of the ejected rock after a fault-slip rockburst event is equal to the sum of the elastic strain energy stored in the rock prior to the burst and a portion of the seismic wave energy. The ejection velocity contributed by the seismic wave energy is determined via the analysis below.

Assume that a fault-slip event generates a sinusoidal seismic wave (Figure 4), which is expressed by:

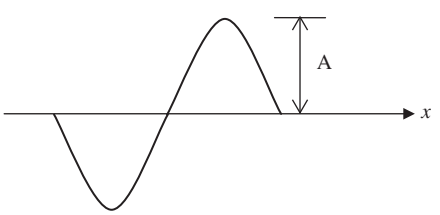


Figure 4 A sinusoidal seismic wave pulse.

$$u_x = A \sin(\omega t - kx) \tag{4}$$

where u_x = particle displacement at position x,
A = displacement amplitude,
f = frequency,
ω = angular frequency, $\omega = 2\pi f$,
t = time,
C = wave velocity
k = wave number, $k = \omega/C$ and
x = position.

The seismic wave induces particle vibrations in the rock it passes through. The vibrations bring about a strain and stress in the rock so that a static strain energy density, w_s, is induced in the rock by the seismic wave. On the other hand, the wave propagation means that a kinetic energy component, w_k, is also induced by the seismic wave. Therefore, the total energy induced by the seismic wave, w, is the sum of the two components w_s and w_k, that is, $w = w_s + w_k$.

In the case of a longitudinal wave (*i.e.* the P wave), the normal strain induced by the wave is $\varepsilon_x = \partial u_x/\partial x$ and the normal stress is $\sigma_x = E\varepsilon_x$. The static wave strain energy density is expressed as $w_s = \sigma_x \varepsilon_x/2$. The average static strain energy density of the seismic wave is then obtained as

$$\overline{w}_s = \frac{1}{4}\rho(PPV)^2, \tag{5}$$

where ρ is the density of the rock and PPV represents the peak particle velocity, $PPV = A\omega$. The particle velocity is expressed by $\dot{u}_x = \partial u_x/\partial t$. The kinetic energy density is calculated as $w_k = \rho \dot{u}_x^2/2$. The average kinetic energy density is then obtained as

$$\overline{w}_k = \frac{1}{4}\rho(PPV)^2. \tag{6}$$

The total energy density in the rock, which is caused by the seismic wave, is thus

$$w = \overline{w}_s + \overline{w}_k = \frac{1}{2}\rho(PPV)^2. \tag{7}$$

Let v_2 represent the wave-induced velocity of the ejected rock. The following equilibrium must exist:

$$\frac{1}{2}m{v_2}^2 = wV, \tag{8}$$

where V is the volume of the ejected rock, $V = m/\rho$. The ejection velocity v_2 is then obtained as:

$$v_2 = PPV. \tag{9}$$

The total ejection velocity is then obtained as

$$v = \sqrt{v_1^2 + v_2^2} = \sqrt{\frac{1}{\rho E}\sum \sigma_i^2 + PPV^2}. \tag{10}$$

In the case of a pure strain rockburst, the ejection velocity of the ejected rock is simply determined by the stresses in the rock to be ejected, as expressed by Equation 3. Assume that a strain rockburst occurs in the tunnel wall where the vertical stress (σ_1) is 60 MPa, the wall-parallel horizontal stress (σ_2) is 20 MPa and the wall-perpendicular stress (σ_3) is zero. Let the Young's modulus of the rock be E = 60 GPa and the density of the rock ρ = 2700 kg/m^3. Substituting these data into Equation 3 yields v_1 = 5 m/s, that is, the average ejection velocity of the ejected rock would be 5 m/s when the strain rockburst occurs. This is a quite reasonable ejection velocity for a strain rockburst event in hard rock.

The study by Yi & Kaiser (1993) showed that it is reasonable to assume the rock ejection velocity is equal to the peak particle velocity (PPV) under typical mining and seismicity conditions. The theoretical solution in Equation 9 is in agreement with their conclusion if we only talk about the seismicity-induced ejection velocity. In the case of a fault-slip triggered rockburst event, the ejection velocity is actually composed of two components as expressed by Equation 10: the velocity due to the release of the static strain energy in the rock to be ejected, v_1, and the velocity due to the seismic wave, v_2. Using the example above, the ejection velocity v_1 is 5 m/s. The near-field PPV of a strong fault-slip seismic event (Nuttli magnitude 3–4) is approximately 3 m/s (Kaiser *et al.*, 1995). The ejection velocity due to the seismic event is thus v_2 = PPV = 3 m/s according to Equation 9. The total ejection velocity, according to Equation 10, is 5.8 m/s. That is, the total ejection velocity is slightly increased by the seismic wave. This implies that the main function of seismic waves is probably to trigger rockburst events. The ejection velocity is mainly dependent on the static stress state of the rock.

In conclusion, the fault-slip seismic event may mainly play the role of trigger in a fault-slip rockburst event. It does not contribute much to the ejection velocity of the ejected rock. The ejection velocity is mainly dependent on the stresses in the ejected rock prior to the rockburst event.

2.2 Performance requirements on rockbolts

As stated previously, the basic requirement for rockbolts is the energy absorption capacity, either in squeezing rock or burst-prone rock. In the case of a rockburst event, a part of the released energy tends to become kinetic energy, ejecting the failed rock. The rockbolts, together with other support devices in the support system, have to absorb the kinetic energy to prevent the rock from being ejected. It requires that the energy absorption capacity of the rockbolts has to be higher than the kinetic energy of the potentially ejected rock. On the other hand, strong rockbolts can stop the rock movement after a small displacement after absorbing the kinetic energy and thus provide more satisfactory support than weak rockbolts.

In the case of rock squeezing, the interaction between the rockbolts and the rock mass can be illustrated with the help of the so-called Ground Response Curve (GRC) in Figure 5 (Brown *et al.*, 1983; Carranza-Torres & Fairhurst, 2000). The GRC at time t_0 describes the relationship between the radial displacement of the tunnel wall and the support pressure on the wall immediately after excavation of the tunnel. The tunnel wall may be self-stabilized after a certain amount of displacement in a competent rock mass without need of rock support. However, in squeezing rock, the displacement may increase with time so that the GRC moves rightward in the diagram to the position marked by t_1 after a certain time. Stiff rockbolts will collapse immediately after

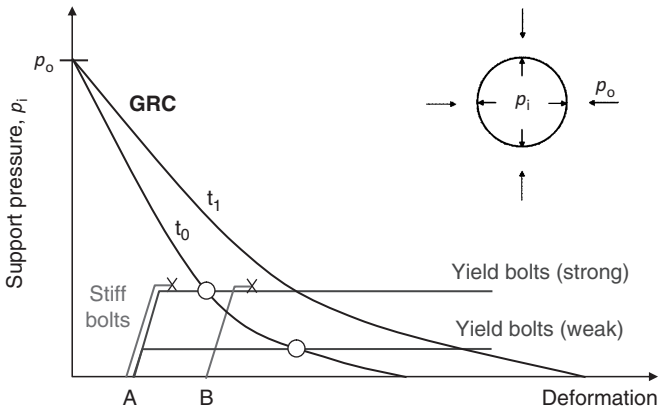


Figure 5 The ground response curves and the performances of stiff and yield rockbolts.

excavation of the tunnel if they are installed too early at position A. They may survive the excavation if installed at B, but will collapse after a while when the GRC moves to position t_1. Yield rockbolts can stabilize the tunnel wall after a certain displacement, even though they are installed at A. They still provide the designed support load until their displacement capacity is used up when the squeezing rock displacement increases with time. The difference between strong and weak yield rockbolts is also illustrated in Figure 5. The rock becomes stabilized after a smaller rock displacement with strong yield rockbolts than with weak yield rockbolts. Therefore, it is desired that yield rockbolts should be both strong and deformable, that is, strong and energy absorbent.

2.3 Design parameters

The factor of safety (*FS*) is a parameter that has been used in rock-support design for a long time. It is defined by the following general formula:

$$FS = \frac{\text{Resistance}}{\text{Driving force}}. \tag{11}$$

In shallow tunnels, where loosened wedge blocks tend to fall under gravity, the rockbolts have to be capable of providing a resistant load higher than the deadweight of the falling blocks in order to prevent the blocks from falling. This is a load-controlled condition. The "driving force" is the deadweight of the blocks and the "resistance" is the strength of the rockbolts. Such a strength–load defined safety factor is appropriate for support design in low-stress rock masses.

In high-stress rock masses, rock failure is unavoidable after excavation. Either squeezing deformation in weak rock or rockburst in hard rock is attributed to the energy release from the rock mass. In these cases, therefore, the safety factor of a rock support design should be calculated on the basis of the released energy to be absorbed by the support devices and the energy absorption capacity of the support devices. Such an energy-based factor of safety is expressed as:

$$FS = \frac{\text{Energy absorption of support devices}}{\text{Released energy to be absorbed}}. \quad (12)$$

As stated above, a strong rockbolt is more effective than a weak one in restricting rock deformation. Therefore, both the energy absorption capacity and the load capacity of rockbolt should be taken into account in rock support design.

3 A BRIEF HISTORY

The earliest publication that introduced the concept of yield rockbolt might be the one by Cook & Ortlepp in 1968 in the Bulletin of the Chamber of Mines of South Africa Research Organization. One year later, Ortlepp (1969) published the results of his field testing of yield rockbolts in a symposium in Oslo, Norway. Ortlepp was probably the first person to carry out dynamic field tests of rock support. His field tests were summarized by himself (Ortlepp, 1992) and others, for instance Stacey (2012) recently. Ortlepp carried out the tests on two rockbolt and mesh support systems installed in a tunnel, one with fully grouted conventional rockbolts and the other with the yield rockbolts that he had developed (Ortlepp, 1968). The rockburst loading was simulated by blasting, with blast-holes 430 mm apart drilled parallel to the tunnel axis about 600 mm outside the tunnel perimeter. The first test failed because of the high blast intensity. The second one with reduced blast intensity proved that the support system, consisting of yield rockbolts and a double layer of wire mesh, could contain the energy of the blast. Figure 6 shows a sketch of the tunnel profile after the test. The tunnel wall to the right that was reinforced with the yield rockbolts was retained, while the

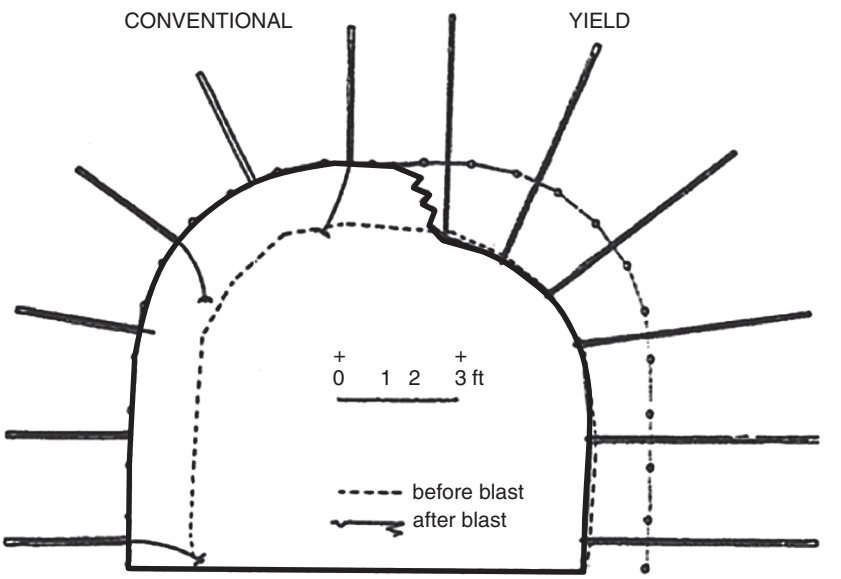


Figure 6 Profile of the tunnel after the blasting test (Ortlepp, 1969; Stacey, 2012).

wall to the left side that was reinforced with the conventional rockbolts collapsed. Ortlepp's field tests demonstrated that the support system incorporating yield rockbolts successfully prevented the rock wall from collapsing but the conventional support system did not. In spite of the success of the tests, the progress in development of yield support devices was slow, not only in other countries but also in South Africa where the first type of yield rockbolt was tested in field. The first commercial yield rockbolt, the so-called cone bolt, was not introduced to the public until approximately 20 years later in the beginning of the 1990s (Jager, 1992; Ortlepp, 1992).

A comprehensive rockburst research program was conducted in the 1990s in Canada (CAMIRO Mining Division, 1996). Dynamic rock support with yield rockbolts was one of the topics in the program. Engineers like fully grouted rockbolts, possibly because of their reliability in anchoring. Grouted rockbolts were installed almost 100% with resin in Canadian metal mines. The Southern African cone bolt was originally designed for cement grout. To adapt to resin grout, a modified version of the cone bolt was developed in the early 2000s in Canada (Simser, 2001; Gaudreau *et al.*, 2004). Since the beginning of the 2000s, a number of other yield rockbolts, for example Garford bolt, D-Bolt and Yield-Lok, have appeared.

4 TESTING METHODS

4.1 Static pull test

The ultimate load and displacement are two parameters that describe the static performance of a rockbolt. In laboratory, the load and displacement capacities of a rockbolt are usually evaluated through static pull tests (Figure 7). When tested, the rockbolt is installed in concrete blocks (or steel tubes). The displacement of the joint between the two blocks is registered when the bolt is pulled. Figure 7b shows one example of test facilities for static tests of rockbolts. The NTNU/SINTEF rockbolt test rig is equipped with two pieces of high strength concrete blocks with dimensions of 950 × 950 × 950 mm^3 each. A hole is drilled through the blocks in place and the bolt is then installed in the borehole. For pull test, the pull load is applied to the concrete block to the right

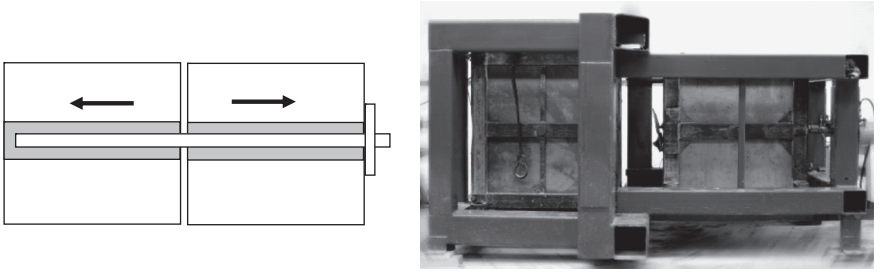


Figure 7 Static pull test of rock bolts. (a) Work principle, (b) the NTNU/SINTEF rockbolt test rig.

through two hydraulic jacks, while the left block is fixed in the frame. Shear tests of rockbolts can also be carried out on the rig. The load capacity of the test rig is 600 kN for pull and 500 kN for shear.

4.2 Dynamic drop test

The dynamic performance of a rockbolt can be described in terms of the energy absorption capacity and the ultimate displacement. These two parameters can be determined through drop tests. In a drop test, the rockbolt is grouted either with cement mortar or resin in split steel tubes and a dynamic load is applied to the rockbolt via the split tubes so that the rockbolt is stretched in the position of the tube split. There are two options for application of the dynamic load: by free mass fall or by momentum transfer. With the free mass fall method, a mass falls freely onto the impact plate attached to the lower tube of the rockbolt assembly (Figure 8a). The kinetic energy of the drop mass is transferred to the rockbolt via the plate and the lower tube. The test facility at CANMET in Ottawa, Canada, employs this principle to apply the dynamic load (Figure 8b). With the momentum transfer method, the mass and the rockbolt assembly fall together until the beam reaches the buffers (Figure 9a). After that, the velocity of the beam is quickly de-accelerated to zero and the momentum is transferred to the rockbolt assembly and the mass on the rockbolt. The kinetic energy in the beam and rockbolt assembly system is then absorbed by the rockbolt. The test facility at the Western Australian School of Mines (WASM) employs this principle to apply the dynamic load (Figure 9b).

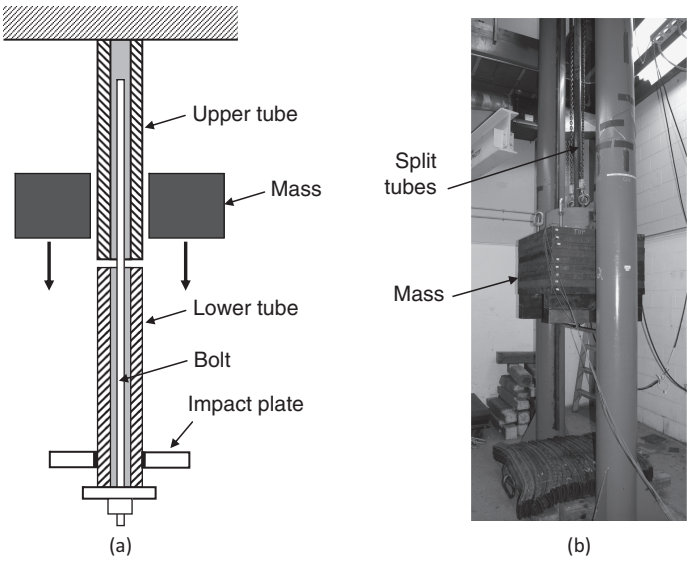


Figure 8 Dynamic test of rockbolts based on mass free fall. (a) The principle, (b) the CANMET testing facility.

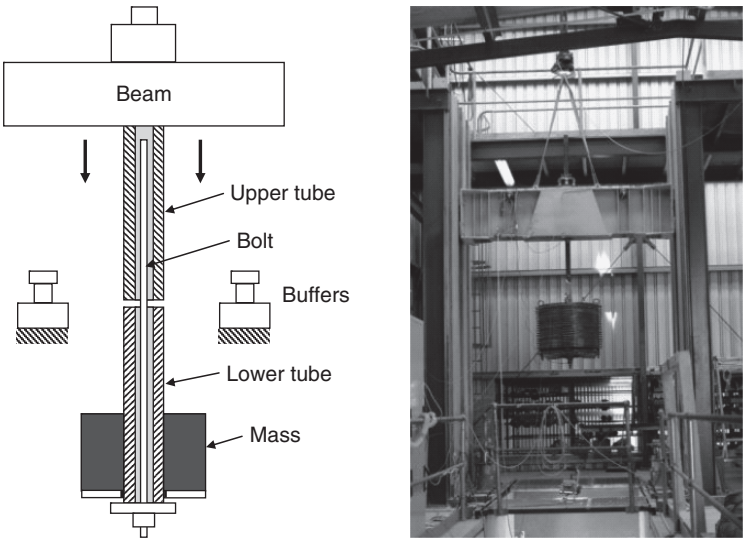


Figure 9 Dynamic test of rockbolts based on momentum transfer. (a) The principle, (b) the WASM testing facility (Villaescusa *et al.*, 2013).

The testing facilities that have been used for dynamic rockbolt tests was thoroughly reviewed by Hadjigeorgiou & Potvin (2011).

5 ENERGY-ABSORBING ROCKBOLTS

5.1 The cone bolt

The cone bolt was invented in the 1990s in South Africa, aiming to combat rockburst in deep mines (Jager, 1992; Ortlepp, 1992). The bolt consists of a smooth steel bar and a flattened conical flaring forged at the far end of the bolt shank. It has two versions, the original one for cement grout (Figure 10a) and a modified one for resin grout (Figure 10b). A blade is added at the end of the modified cone bolt for the purpose of resin mixing. The cone bolt is fully grouted in a borehole. Rock dilation will induce a load on the face plate, which then transfers the load to the bolt shank and the cone at the bolt end. The grout facing the conical side of the cone is crushed when the pull load is high enough and the cone then ploughs in the grout to do work. The mechanics of the cone bolt is described by the following expression:

$$P = \frac{\pi}{4}\left(D^2 - d^2\right)k\sigma_c, \tag{13}$$

where P is the ultimate load, D the diameter of the cone, d the diameter of the bolt shank, σ_c the uniaxial compressive strength (UCS) of the grout and k is a scale factor for

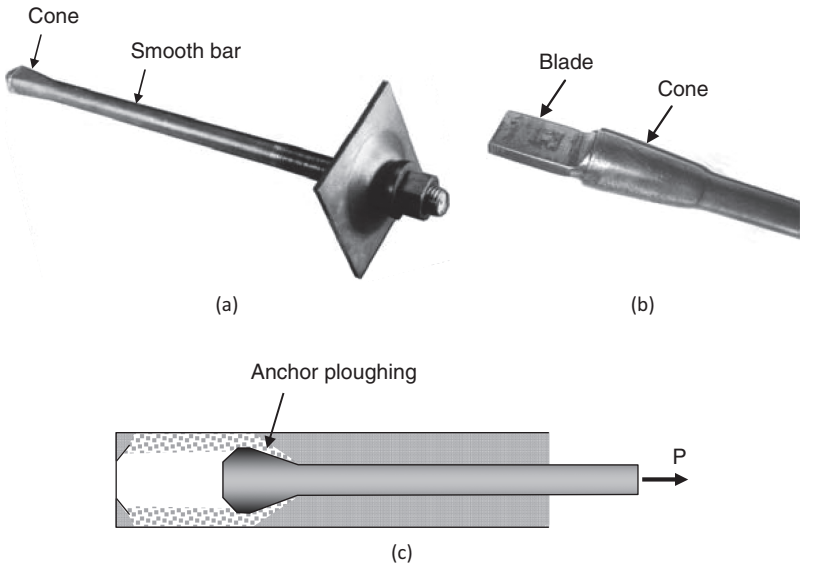


Figure 10 The cone bolt. (a) The original version for cement grout, (b) the modified version for resin grout (Simser, 2001), (c) the work principle.

the UCS taking into account that the grout is crushed under the cone instead of simple shear failure.

A cone bolt can displace for a considerable distance if it ploughs as desired. Lindfors (2000) carried out a series of pull tests on cement-grouted cone bolts in an underground mine in Sweden. The bolts displaced up to 900 mm at a pull load of approximately 170 kN. In order to achieve the desired ploughing mechanism, the shape of the cone and the crushing strength of the grout must have a satisfactory match. In reality, the strength of the grout varies because of variations in the type of grout material and the water–cement ratio or the mixing quality in the case of using resin grout. This leads to significant variations in the yield load of the cone bolts. Many static pull and dynamic drop tests have been carried out both in fields and in laboratories over the past decades. Figure 11 shows representative results of such tests. The static yield load varies from approximately 60 kN to 150 kN (Figure 11a). The drop test results shown in Figure 11b are for 22 mm cone bolts tested with a kinetic energy input of 33 kJ. The dynamic yield load of those bolts is 150–175 kN for the 40 MPa resin grout, but drops to approximately 100 kN for the 20 MPa resin grout. Lindfors (2000) and Simser *et al.* (2006) observed in their tests that the cone of the bolts might plough little or not at all in some cases, so that the displacements were purely coming from the stretching of the bolt shanks. In those cases, the yield load of the bolts was equal to the yield limit of the bolt steels. Such a large spread in the load capacity could cause uncertainties for rock support design.

The cone bolt has been used for rock support in many metal mines in Canada and Australia in the past decade.

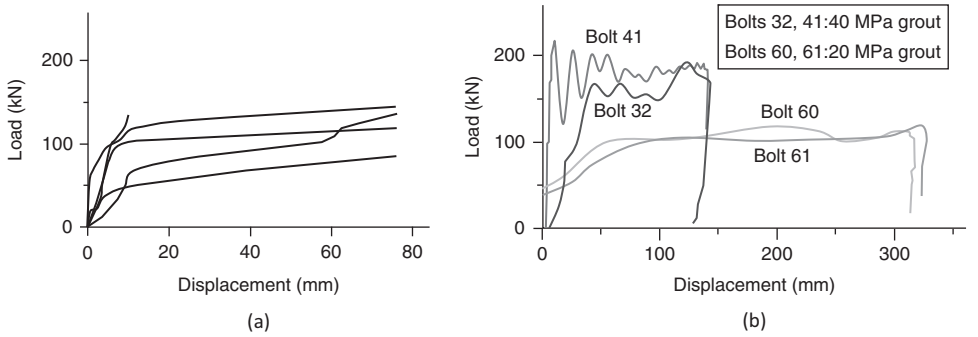


Figure 11 Static and dynamic test results of modified cone bolts with resin grouts. (a) Static pull tests, redrawn after Simser *et al.* (2006), (b) dynamic drop tests, redrawn after Varden *et al.* (2008).

5.2 The Garford solid bolt

The Garford solid bolt, invented in Australia, consists of a smooth solid steel bar, an anchor and a coarse-threaded sleeve at the far end (Figure 12). This bolt is characterized by its engineered anchor, the inner diameter of which is smaller than the diameter of the solid bolt bar. The bolt is spun into the borehole, which is filled with resin cartridges. The resin is mixed by the threaded sleeve at the bolt end. The anchor is resin encapsulated in the borehole after installation. When the rock dilates, the pull load in the solid bar forces the solid bar to be extruded through the hole of the anchor. The yield load is determined by the difference in the diameters of the anchor hole and the solid bar. The ultimate displacement of the bolt is determined by the length of the bar tail contained within the threaded sleeve. The ultimate load of the Garford bolt are related to the strength of the steel and the geometric parameters of the bolt as follows:

$$P = \frac{\pi}{2} d\Delta d k \sigma_s, \tag{14}$$

where d is the diameter of the bolt shank, Δd is the difference between the diameter of the bolt shank and the anchor hole diameter, σ_s the yield strength of the bolt steel and k is a factor for the extruding process.

Figure 13 shows the dynamic test results of two 20 mm bolts, which were loaded with a kinetic energy input of 33 kJ (Varden *et al.*, 2008). The Garford bolts are used in some Australian metal mines for dynamic rock support.

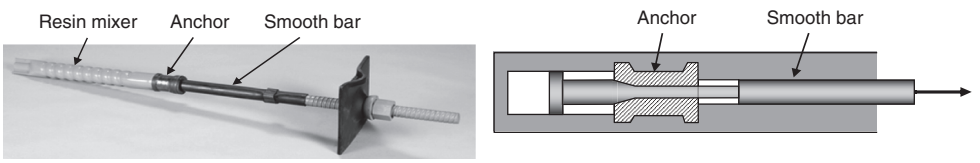


Figure 12 The Garford solid bolt.

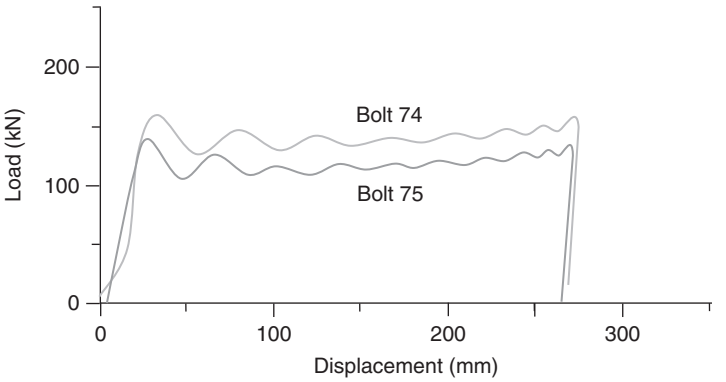


Figure 13 Dynamic test results of 20 mm Garford bolts with impact input of 33 kJ. Redrawn after Varden *et al.* (2008).

5.3 The D-Bolt

The D-Bolt, invented in Norway, comprises a smooth steel bar and a number of integrated anchors along the bolt length (Figure 14) (Li, 2010). The bolt is either cement or resin encapsulated in a borehole. The short anchors are firmly fixed in the grout, while the long smooth bar sections between the anchors elongate upon rock dilation. The bolt absorbs energy through full mobilization of the strength and deformation capacity of the bolt steel. The ultimate load of the D-Bolt is simply related the tensile strength of the bolt steel:

$$P = \frac{\pi}{4} d^2 k \sigma_t, \tag{15}$$

where σ_t is the tensile strength of the bolt steel and k is a factor taking into account the hardening of the steel. A reasonable value for k is 0.9.

Static and dynamic test results for D-Bolts are presented in Figure 15. The bolt sections tested are 22 mm in diameter and 1.5 m in length between the anchors. The ultimate static load and displacement are 260 kN and 165 mm, respectively (Figure 15a), and the ultimate dynamic load and displacement are 285 kN and 220 mm, respectively

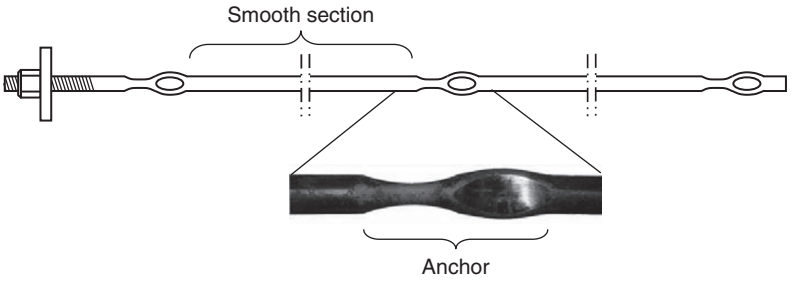


Figure 14 The D-Bolt.

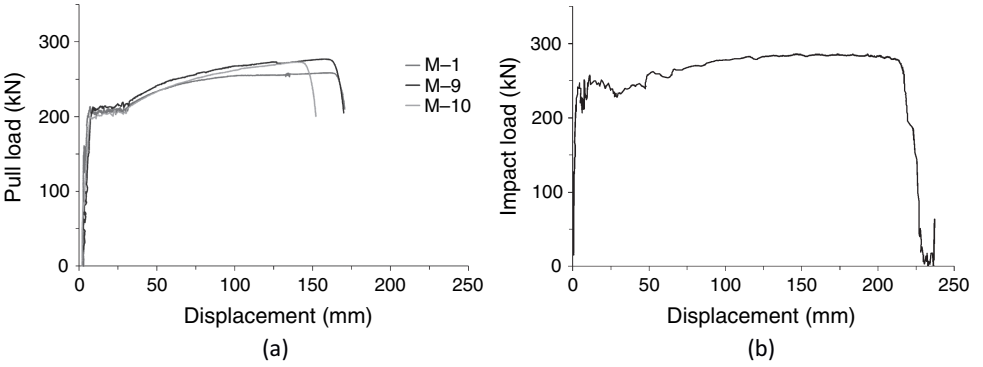


Figure 15 Test results of the D-Bolt sections of 22 mm × 1.5 m (Li, 2012; Li & Doucet, 2012). (a) Static pull test results, (b) dynamic drop test result (drop mass 2897 kg, drop height 1.97 m and input energy 56 kJ).

(Figure 15b). The bolt section absorbs approximately 60 kJ of energy prior to failure under dynamic loading. Every section of the bolt works independently; failure of one section does not result in the loss of the entire bolt, with the remaining sections continuing to provide rock reinforcement. In general, the ultimate load of the D-Bolt is equal to the tensile strength of the steel and the ultimate displacement is approximately 15% of the bolt length.

D-Bolts have been used in metal mines for dynamic rock support in many countries, for instance Sweden, Canada, USA, South Africa, Chile and Australia.

5.4 The Yield-Lok

The Yield-Lok bolt consists of a round steel bar of 17.2 mm in diameter (Figure 16). The anchor, or Upset, of the bolt is encapsulated in an engineered polymer coating. The bolt is encapsulated in the borehole with resin grout. The Upset ploughs within the polymer coating when the pull load exceeds the predefined load limit. The mechanics of the Yield-Lok is similar to the cone bolt, which is described by Equation 13, where D is the diameter of the Upset. Static and dynamic test results of the bolt are shown in Figure 17. The dynamic load is in general lower than the static load. Yield-Lok bolts are used in some metal mines for dynamic rock support in Canada.



Figure 16 The Yield-Lok (Wu & Oldsen, 2010).

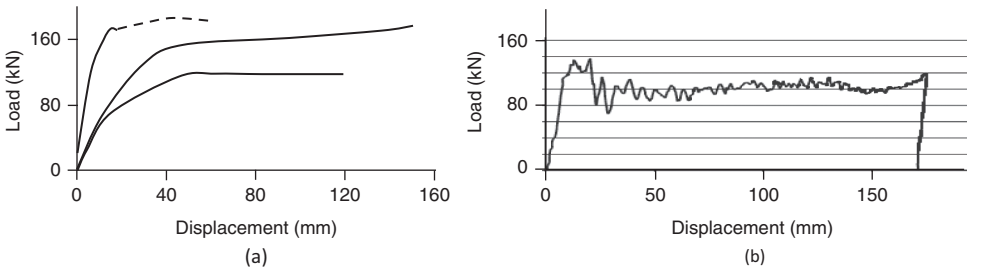


Figure 17 Test results of the Yield-Lok bolts. (a) Static pull test results, (b) dynamic test result (drop mass 1115 kg, drop height 1.5 m and input energy 16.4 kJ). Redrawn from Wu & Oldsen (2010).

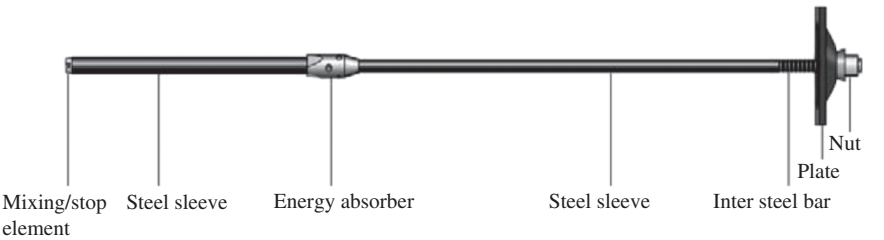


Figure 18 The Roofex rockbolt.

5.5 Roofex

Roofex is composed of an engineered anchor and a smooth bar (Figure 18) (Charette & Plouffe, 2007; Galler *et al.*, 2011). Its work principle is similar to the Garford solid bolt, that is, the smooth solid steel bar is extruded through the hole of the anchor at a designed load level. The bolt is spun into a borehole that is filled with resin cartridges and the resin mixer at the end of the bolt mixes the resin. It is required that the anchor must be fully encapsulated in the resin grout. The smooth steel bar slips through the anchor to dissipate the energy and accommodate the rock displacement. The mechanics of the Roofex is similar to that of the Garford bolt, as described by Equation 14, but the factor k would have a different value for Roofex because of the different shape of its anchor. Figure 19 shows static pull and dynamic drop test results for Roofex rockbolts. The results indicate that the dynamic load of the Roofex bolt is much smaller than its static load.

5.6 Durabar

Durabar is another yield rockbolt invented in South Africa (Ortlepp *et al.*, 2001). The bolt is composed of a smooth bar and a sinusoidally waved portion as well as the face plate and the nut (Figure 20). The bolt has a smooth tail in the far end, which determines the maximum displacement capacity of the bolt. The bolt is fully grouted

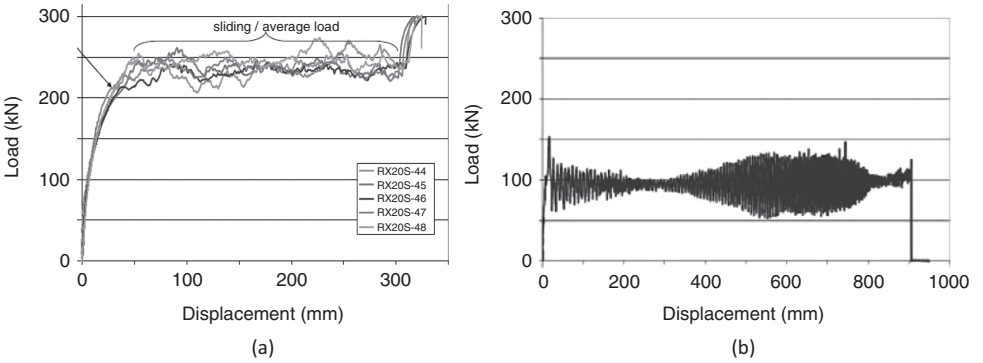


Figure 19 Laboratory test results of Roofex Rx20 rockbolts (Galler *et al*., 2011). (a) Static pull test results, (b) dynamic test result.

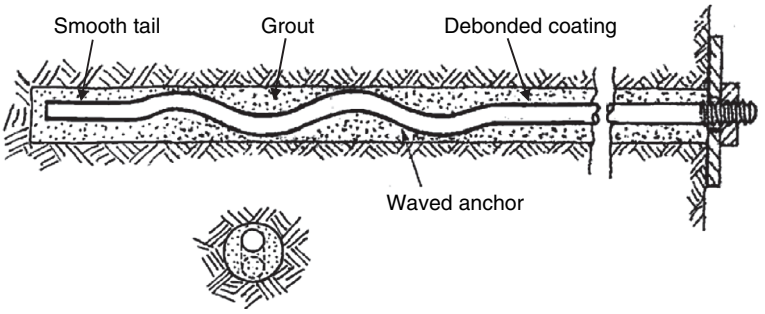


Figure 20 Durabar (Ortlepp *et al*., 2001).

into a hole in the rock. It is required that the shape of the waved portion must be carefully formed and the full length of the bar is de-bonded from the grout in order that the desired performance of the bolt is achieved. The Durabar is able to yield by sliding through the hardened cement grout. As the load on the Durabar reaches the designed load limit, it starts to slip through the wave path in the grout. The friction in the wave path is the main energy dissipation mechanism. The ultimate load of the Durabar is related to the slope angle of the wave portion and the frictional coefficient between the bolt shank and the grout. A normal load is induced on the wave portion as a pull load is applied to the bolt. The magnitude of the normal load is associated with the slope angle i that is represented by the ratio of the amplitude of the wave to the half-wave length. The ultimate load can be related to the relevant parameters as follows:

$$P = \frac{h}{l} Nkf, \tag{16}$$

where h is the amplitude of the wave portion, l the half-wave length, N the number of half waves, f the frictional coefficient and k is a constant.

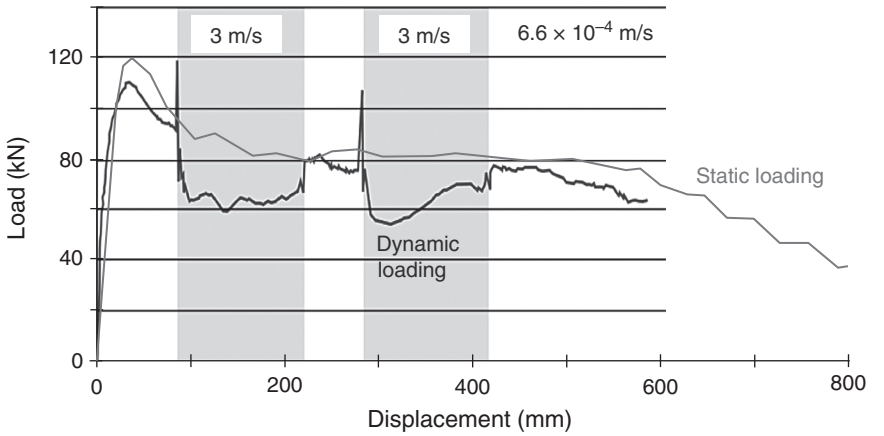


Figure 21 Static and dynamic performances of Durabar. Redrawn from the Durabar brochure.

The performance of Durabar is mainly dependent on the properties of the steel and requires that the strength of the grout exceeds a minimum value of about 25 MPa. A Durabar of 16 mm in diameter and 2.2 m length can dissipate 45 kJ over a 500 mm displacement under a static pull load according to Ortlepp *et al.* (2001). The static load of the 16 mm Durabar stabilizes at a level of 80 kN, while its dynamic load drops to approximately 60 kN for a drop velocity of 3 m/s (Figure 21).

5.7 The He bolt

The He bolt, invented in China, is composed of a solid bar, a cone-shaped piston, a sleeve, a face plate and a nut (Figure 22). The far end of the solid bar is groove threaded, which is the anchor of the bolt. The diameter of the cone-shaped piston is slightly smaller than the inner diameter of the sleeve so that it is tightly assembled in the sleeve, which is attached to the face plate and the nut. The bolt is fully grouted in a borehole with either cement mortar or resin. Both the threaded anchor of the bolt at the far end and the sleeve are encapsulated in the grout according to the authors (He *et al.*,

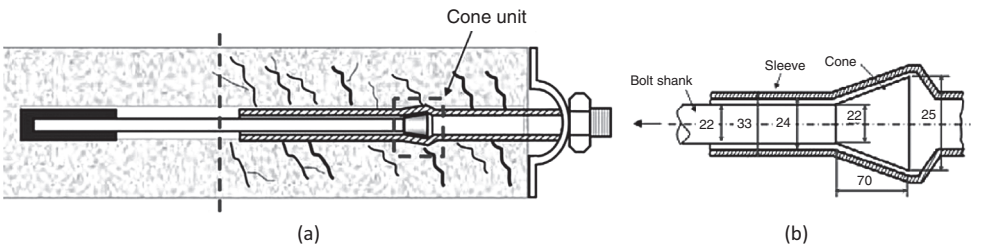


Figure 22 The He bolt (He *et al.*, 2014). (a) The work principle, (b) a close-up sketch of the match between the cone and the sleeve.

2014). The cone slips in the sleeve to accommodate the rock dilation, Figure 22a. In accordance with the drawing illustrating the match between the cone and the sleeve during slippage (Figure 22b), it seems that the sleeve is radially expanded when the conical piston slips. Therefore, the pull resistance load of the bolt is not simply due to the friction between the cone and the sleeve wall, but also to the plastic deformation of the sleeve. The ultimate load of the He bolt is described as (He *et al.*, 2014):

$$P = 2\pi f I_s I_c, \tag{17}$$

where f is the frictional coefficient at the cone–sleeve interface, I_s a constant describing the behavior of the sleeve and I_c a constant describing the geometry of the cone.

The bolt was both statically and dynamically tested in the laboratory. The diameter of the solid bars of the bolt specimens was 22 mm and the outer and inner diameters of the sleeves were 33 and 24 mm, respectively. The diameter of the conical piston was 0.7–1 mm larger than the inner diameter of the sleeve, that is, varying from 24.7 to 25 mm. Figure 23a shows the static test result of the bolt specimen with a cone diameter of 24.9 mm. The stick–slip phenomenon occurred during slippage of the cone in the sleeve, with a load oscillation between 140 and 180 kN. The mean values of the static load were 108, 125 and 106 kN, corresponding to cone diameters of 24.7, 24.8 and 24.9 mm, respectively. It seems that the load capacity of the bolt is sensitive to the cone diameter.

Three He bolts were drop tested with a drop mass of 1000 kg and a drop height of 0.5, 0.7 or 1 m (He *et al.*, 2014). The average load of the bolts varied from 67 to 88 kN, which is smaller than the static load. Figure 23b shows the dynamic test result of a He bolt tested with a drop mass of 1000 kg and a drop height of 0.7 m. It is seen that the amplitude of the load oscillations in the dynamic test is much larger than that in the static tests. It is noticed that all of the rockbolts were tested in open air instead of in real or simulated boreholes. It is not clear how the encapsulation affects the behavior of the bolt when the bolt is installed in a borehole.

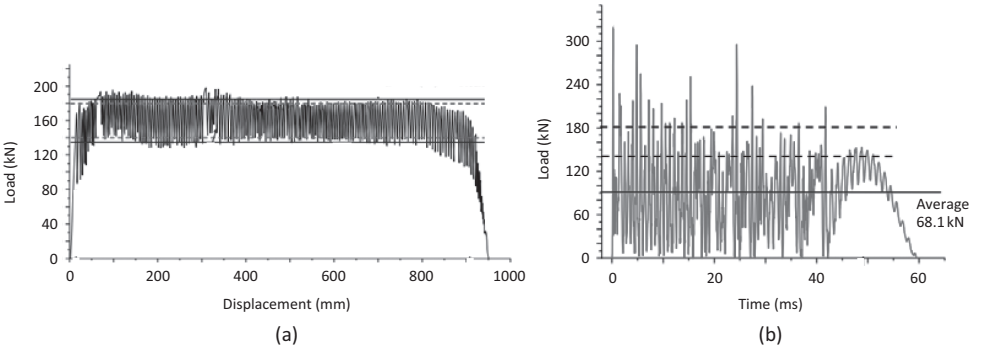


Figure 23 Laboratory test results of the He bolts (He *et al.*, 2014). (a) The static pull test result of the bolt with a cone diameter 24.9 mm, (b) the drop test result of the bolt (drop mass 1000 kg, drop height 0.7 m).

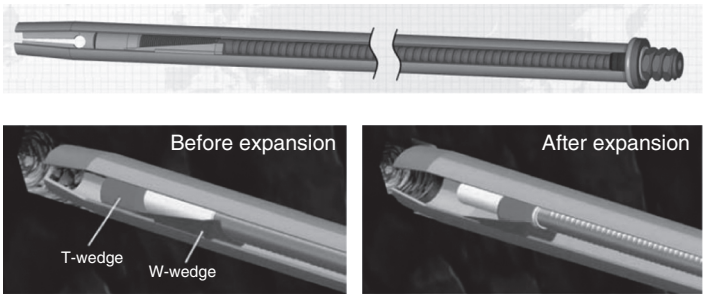


Figure 24 The Sandvik MD bolt (Darlington, 2014).

5.8 The MD bolt

The Mechanical Dynamic (MD) bolt was recently developed by Sandvik Australia (Darlington, 2014). The bolt is composed of a tube of 47 mm in diameter (similar to the standard Split set), a threaded bar and a set of wedges at the far end of the threaded bar. The threaded bar together with the wedges are contained in the tube (Figure 24). The bolt is installed in a hole drilled with 42.5–45 mm drill bit, typically using Jumbo. The T-wedge is pulled to the W-wedge during rotation of the threaded bar so that the tube is expanded and pressed onto the hole wall. When subject to strata load, the bolt slips in the strata. It seems that the aim of the expansion is to increase the friction between the tube and the rock. The ultimate load of the MD is simply equal to the frictional resistance along the bolt–rock interface:

$$P = (N_o + N_w)f, \tag{18}$$

where N_o is the normal force at the bolt–rock interface, purely contributed by the elastic matching between the Split set and the rock, N_w is the extra normal force applied onto the borehole wall after tightening up the wedges and f is the frictional coefficient.

On-site dynamic trials show spreading displacements for input energy from 12 to 25 kJ (Figure 25).

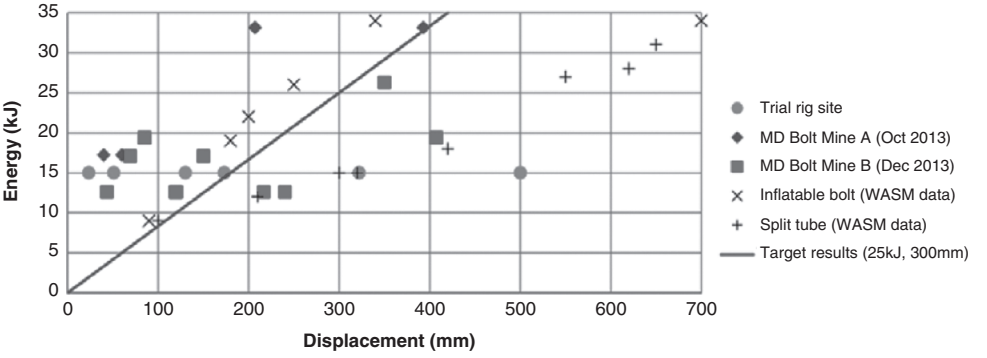


Figure 25 Dynamic test results of the MD bolts (Darlington, 2014).

6 DISCUSSION

The energy-absorbing bolts introduced above dissipate energy either through stretching of the bolt steel (D-Bolt), frictional slippage (cone bolt, Durabar, Yield-Lok, He bolt and MD bolt) or through steel extruding (Garford bolt and Roofex). Based on the test results, the dynamic load capacity of a slippage-based rockbolt is smaller than its static load capacity, but its displacement capacity is high. The static and dynamic load capacities of the stretching-based D-Bolt are similar.

The performance of an energy-absorbing bolt is characterized by its energy absorption and displacement capacity. When absorbing a given amount of energy, the bolt displacing less is better than the one displacing more because the former is more powerful to restrict rock movement. Table 1 lists the energy absorption, displacement capacity and average dynamic load capacity of a few types of energy-absorbing. Note that the average dynamic load of the listed bolt devices is calculated from the energy absorption and ultimate displacement of the bolts, with the exception of those marked by stars. Energy absorption refers to the total energy absorbed by the bolt prior to failure. It is seen in Table 1 that the average dynamic load of the cone bolts varies in the range from 50 to 216 kN. The spreading in the dynamic load is possibly attributed to different displacement mechanisms involved (ploughing, steel stretch or a combination of the two). The average load is 120–156 kN for the Garford solid bolt, 81–99 kN for the Yield-Lok, 68–88 kN for the He bolt and approximately constantly at 280 kN for the D-Bolt. The energy absorption capacities of several types of conventional rockbolts are also listed in the table. Most of them have remarkably low energy absorptions compared with the energy-absorbing rock bolts.

The energy-absorbing rockbolts are anchored in boreholes either at two points (all of the bolts in the list except for the D-Bolt) or at several points (the D-Bolt). Figure 26 depicts the loading models for these two types of anchoring mechanisms. The axial load is constant in the entire bolt section between the anchor and the face plate for two-point anchored rockbolts (Figure 26a), while the axial loads are different in different sections for the D-Bolt (Figure 26b). The shear stress is of course zero on the shank of all of the rockbolts because of the de-bonding nature at the bolt–grout interface.

7 CONCLUDING REMARKS

All rock support devices essentially should be energy absorbent, that is, not only strong but also deformable, for underground rock support. The requirement of energy absorption on rockbolts has been acknowledged in the practice of rock support in high-stress rock conditions. Eight energy-absorbing rockbolts were introduced in this chapter, most of which were developed in the past decade. An energy-absorbing bolt is characterized by both its high load and displacement capacities, and it can dissipate a large amount of energy prior to failure compared with conventional rockbolts such as fully encapsulated rebar bolts. The current energy-absorbing rockbolts dissipate energy either through ploughing/slippage in the grout or auxiliary elements such as anchors and sleeves (cone bolt, Garford bolt, Durabar, Yield-Lok, Roofex and He bolt) or

Table 1 Energy absorption, ultimate displacement and average load of energy-absorbing, as well as conventional, rock bolts under dynamic loading.

Bolt type	*Diameter (mm)*	*Kinetic energy (kJ)*	*Absorbed energy (kJ)*	*Drop mass (kg)*	*Ultimate displ. (mm)*	*Average load (kN)*	*References*
Energy-absorbing rockbolts						Note: * Readings on load-displacement curves	
Cone bolt	22,0		33		190	150–174*	Varden *et al.* (2008)
			33		320	100*	
Cone bolt MCB33 new	17,2	26,3		1184	520–640	62–53	Cai & Champaigne (2010)
		32,8		2229	465	92	
		16,4		1115	280–420	70–50	
Cone bolt MCB33 old	17,2	16,4		1115	80–245	216–78	Cai & Champaigne (2010)
Garford solid bolt			33		270	120*–140*	Varden *et al.* (2008)
			21		170	124	Player *et al.* (2008), Hadjigeorgiou & Potvin (2011)
			28		180	156	
			27		195	138	
			53		425	125	
Roofex Rx20		16		893	182	98	Galler (2011)
		32		1783	412	100	
		43		2229–2897	592–703	95–94	
		51–57		2897	785–840	103–108	
D-Bolt (0.9-m section)	22	26		2452	140	281	Li & Doucet (2012)
D-Bolt (1.5-m section)	22	56		2897	225	277	
Yield-Lok	17,2	16,4		1115	175– 230	99–81	Wu *et al.* (2010)
He bolt	22	4,9		1000		88*	He *et al.* (2014)
	22	6,9		1000		68*	
	22	9,8		1000		85*	
Conventional rockbolts							
Resin encapsulated rebar	19		1–4		10–30	100–170	Kaiser *et al.* (1995).
Mechanical bolt (2 m long)	16		2–4		20–50	–	
De-bonded cable (4 m long)	16		4–8		30–50	–	
Split set	–		5–15		80–200	40–80	
Super Swellex	38/54		18–25		100–150	180–190	

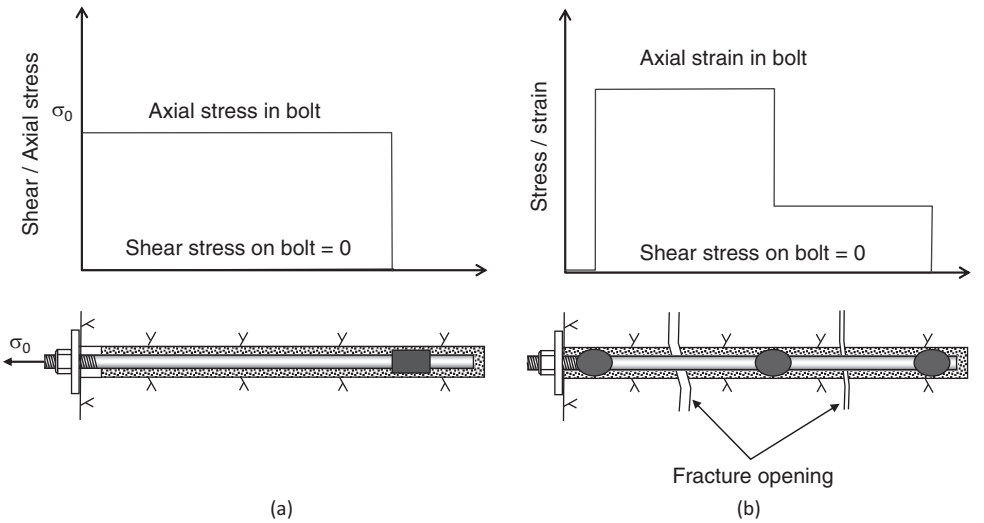


Figure 26 Stress/strain distributions along energy-absorbing bolts when subjected to pull loading. (a) For two-point anchored bolts, (b) for the multi-point anchored D-Bolt.

through stretching of the bolt steel (D-Bolt). The dynamic load of an energy-absorbing rockbolt based on ploughing/slippage is usually smaller than its static load, while the static and dynamic loads of the stretching-based rockbolt (such as the D-Bolt) are approximately the same.

REFERENCES

Brown, E.T., Bray, J.W., Laydanyi, B. & Hoek, E. (1983) Ground response curves for rock tunnels. *Journal of Geotechnical Engineering*, 109(1), 15–39.

Cai, M. & Champaigne, D. (2010) Development of a fully debonded cone bolt for rockburst support. In: Jan, M.V.S. and Potvin, Y. (eds.) *Deep Mining 2010 – Proceedings of the 5th International Seminar on Deep and High Stress Mining*. Australian Centre for Geomechanics, pp. 329–342.

Cai, M. & Champaigne, D. (2012) Influence of bolt-grout bonding on MCB conebolt performance. *International Journal of Rock Mechanics and Mining Sciences*, 49, 165–175.

CAMIRO Mining Division (1996) *Canadian Rockburst Research Program 1990–1995*.

Carranza-Torres, C. & Fairhurst, C. (2000) Application of the convergence-confinement method of tunnel design to rock masses that satisfy the Hoek-Brown failure criterion. *Tunnelling and Underground Space Technology*, 15(2), 187–213.

Charette, F. & Plouffe, M. (2007) Roofex – results of laboratory testing of a new concept of yieldable tendon. In: Potvin, Y. (ed.) *Deep Mining 07 – Proceeding of the 4th International Seminar on Deep and High Stress Mining*. Australian Centre for Geomechanics, pp. 395–404.

Cook, N.G.W. & Ortlepp, W.D. (1968) A yielding rockbolt. *Chamber of Mines of South Africa Research Organisation Bulletin*, No. 14, 6–8.

Galler, R., Gschwandtner, G.G. & Doucet, C. (2011) Roofex bolt and its application in tunnelling by dealing with high stress ground conditions. In: *ITA-AITES World Tunnel Congress*, Helsinki, Finland. 11p.

Gaudreau, D., Aubertin, M. & Simon, R. (2004) Performance assessment of tendon support systems submitted to dynamic loading. In: Villaescusa, E. and Potvin, Y. (eds.) *Proceedings of the Fifth International Symposium on Ground Support*. Taylor & Francis, pp. 299–312.

Hadjigeorgiou, J. & Potvin, Y. (2011) A critical assessment of dynamic rock reinforcement and support testing facilities. *Rock Mechanics and Rock Engineering*, 44, 565–578.

Jager, A.J. (1992) Two new support units for the control of rockburst damage. In: Kaiser, P.K. and McCreath, D.R. (eds.) *Proceedings of the International Symposium on Rock Support*. Rotterdam: Balkema, pp. 621–631.

Kaiser, P.K., McCreath, D.R. & Tannant, D.D. (1995) Rockburst support. *Rockburst Research Handbook*, volume 2. Canadian Rockburst Research Program 1990–1995. Mining Research Directorate.

Li, C. & Stillborg, B. (1999). Analytical models for rockbolts. *International Journal of Rock Mechanics and Mining Sciences*, 36(8), 1013–1029.

Li, C.C. (2010) A new energy-absorbing bolt for rock support in high stress rock masses. *International Journal of Rock Mechanics and Mining Sciences*, 47(3), 396–404.

Li, C.C. (2012) Performance of D-bolts under static loading conditions. *Rock Mechanics and Rock Engineering*; 45(2), 183–192.

Li, C.C. & Doucet, C. (2012) Performance of D-bolts under dynamic loading conditions. *Rock Mechanics and Rock Engineering*, 45(2), 193–204.

Li, C.C. (2013). Relationship of fault-slip rockburst with seismic waves. In: Zhao, J. and Li, J. (eds.) *Proceedings of RocDyn-1: Rock Dynamics and Applications – State of the Art*. CRC Press, Boca Raton, 347–352.

Li, C.C., Stjern, G. & Myrvang, A. (2014) A review on the performance of conventional and energy-absorbing rockbolts. *Journal of Rock Mechanics and Geotechnical Engineering*, 6, 315–327.

Ortlepp, W.D. (1969). An empirical determination of the effectiveness of rockbolt support under impulse loading. In: Brekke, T.L. and Jorstad, F.A. (eds.) *Proceedings of the International Symposium on Large Permanent Underground Openings*. Oslo: Universitats-forlaget, pp. 197–205.

Ortlepp, W.D. (1992) The design of support for the containment of rockburst damage in tunnels – an engineering approach. In: Kaiser, P.K. and McCreath, D.R. (eds.) *Rock Support in Mining and Underground Construction*. Rotterdam: Balkema, pp. 593–609.

Ortlepp, W.D., Bornman, J.J. & Erasmus, N. (2001) The Durabar – a yieldable support tendon – design rationale and laboratory results. In: *Rockbursts and Seismicity in Mines—RaSiM5*. South African Institute of Mining and Metallurgy, pp. 263–264.

Player, J.R., Thompson, A.G. & Villaescusa, E. (2008) Dynamic testing of reinforcement system. In: *Proceedings of the 6th International Symposium on Ground Support in Mining and Civil Engineering Construction*. SAIMM Symposium Series S51, pp. 581–595.

Roth, A., Cala, M., Brändle, R. & Rorem, E. (2014) Analysis and numerical modelling of dynamic ground support based on instrumented full-scale tests. In: *Deep Mining 2014*. Australian Centre for Geomechanics, pp. 151–163.

Simser, B. (2001) *Geotechnical Review of the July 29th, 2001. West Ore Zone Mass Blast and the Performance of the Brunswick/NTC Rockburst Support System*. Technical report, 46p.

Simser, B., Andrieux, P., Langevin, F., Parrott, T. & Turcotte, P. (2006) Field behaviour and failure modes of modified Conebolts at the Craig, LaRonde and Brunswick Mines in Canada. In: *Deep and High Stress Mining*. Quebec, 13p.

Stacey, T.R. (2012) A philosophical view on the testing of rock support for rockburst conditions. *The Journal of the Southern African Institute of Mining and Metallurgy*, 112, 703–710.

Varden, R., Lachenicht, R., Player, J., Thompson, A. & Villaescusa, E. (2008) Development and implementation of the Garford Dynamic Bolt at the Kanowna Belle Mine. In: *10th Underground Operators' Conference*. Launceston, 19p.

Villaescusa, E., Thompson, A.G. & Player, J. (2013) A decade of ground support research at the WA School of Mines. *Proceedings of the 7th International Symposium on Ground Support in Mining and Underground Construction*, Perth, Australia. Australian Centre for Geomechanics, pp. 233–245.

Windsor, C.R. (1997) Rock reinforcement systems. *International Journal of Rock Mechanics and Mining Sciences*, 34(6), 919–951.

Wu, Y.K. & Oldsen, J. (2010) Development of a New Yielding Rock Bolt – Yield-Lok Bolt. In: *Proceedings of the 44th US Rock Mechanics Symposium*, Salt Lake City, USA. Paper ARMA 10–197, 6p.

Yi, X. & Kaiser, P.K. (1993) Impact testing of rockbolt for design in rockburst conditions. *International Journal of Rock Mechanics and Mining Sciences & Geomechanics Abstracts*, 31, 671–685.

Monitoring Technology



Taylor & Francis
Taylor & Francis Group
http://taylorandfrancis.com

Chapter 12

Microseismic monitoring technologies for deep mining

R.J. Durrheim
Natural Resources and the Environment Unit, Council for Scientific and Industrial Research, South Africa & School of Geosciences, University of the Witwatersrand, South Africa

Abstract: Earthquakes triggered or induced by mining may cause damage to underground and surface infrastructure, loss of production, and injury to mine workers and the public. As shallow ore bodies are exhausted, mining depths are destined to increase, giving rise to situations where the stress exceeds the strength of the rock mass and making rockbursts more likely. Microseismic monitoring and analysis is used to mitigate the risk posed by rockbursts by enabling rescue efforts, guiding the design and implementation of mining layouts and rock support systems, and assessing seismic hazard. Current practice is reviewed, and standards, procedures and guidelines for the design and operation of a microseismic monitoring system are provided.

1 INTRODUCTION

Seismicity associated with deep mining can pose a significant risk, exemplified by incidents in South Africa, Australia and the USA during the past decade that caused significant human and financial losses and received widespread coverage in the media. On 9 March 2005 some 40 mine workers were trapped for about 8 hours in a deep gold mine in the Klerksdorp mining district following a M5.3 seismic event that damaged the shaft and tunnels and caused falls of ground in working places. Two miners were fatally injured, the mine was shut for over six months, and many buildings suffered damage (Durrheim *et al.*, 2006; Figure 1a). On 5 August 2014 the same region was struck by a M5.5 event, the largest earthquake ever to occur in a mining district in South Africa. The damage to mine workings was relatively small, although many dwellings in nearby towns were damaged. On 25 April 2006 three mine workers were trapped in a Tasmanian gold mine following a fall of ground associated with a M2.2 event; one mine worker perished, while the others were rescued some 14 days later (Hills, 2012). On 6 August 2007 six mine workers perished when a section of Crandall Creek coal mine in Utah collapsed following a M_L3.9 seismic event; three members of the rescue team were killed by a subsequent collapse (Pechmann *et al.*, 2008).

Earthquakes may be triggered or induced in situations where the stress, amplified by mining activities, exceeds the strength of the rock mass. The ejection of rock and shaking of the ground may cause damage to underground and surface infrastructure, loss of production, and injury to mine workers and the public (Figure 1). As shallow ore bodies are exhausted, mining depths and the size of excavations are likely to increase, and greater efforts will have to be made to reduce the risk posed by rockbursting. Microseismic monitoring is one of the technologies that is used to mitigate the risk posed by mining-related seismicity by enabling rescue efforts, guiding the design and implementation of mining layouts and rock support systems, and assessing seismic



(a) (b)

Figure 1 (a) Apartment block in Stilfontein, South Africa damaged by a M_L=5.3 tremor on 9 March 2005, (b) Tunnel in a deep South African gold mine damaged by M_L=3.5 tremor.

hazard. It is estimated that more than 200 mines worldwide were operating seismic networks in 2015. Although most of the technology has been supplied by a handful of manufacturers and service providers, there is a large range in practice owing to the specific problem being tackled (which impacts on the design of the network) and the vintage of the system. This chapter reviews the state-of-the-art of microseismic monitoring in deep mines; provides standards, procedures and guidelines for the design and operation of a system; and concludes with a selection of case studies.

Seismology started to emerge as a quantitative science in the last decade of the nineteenth century, and its methods were soon used to investigate mining-related tremors. The first deployment of seismographs specifically to monitor mining-related seismicity was in 1910 when tremors related to the extensive mining of gold-bearing reefs caused alarm in Johannesburg (Durrheim, 2010). Ben-Menahem (1995), in his concise history of seismology, describes developments in theory (*e.g.* continuum mechanics), technology (*e.g.* the invention of the mechanical seismograph and digital computer), and earthquake observations (*e.g.* those produced by the World-Wide Standard Seismograph Network, WWSSN) that led to quantum advances in the understanding of earthquakes. Not only has mine seismology drawn on these advances in science and technology, but deep mines have also provided a "laboratory" where the physics of earthquakes can be studied at close range.

Knowledge and experience regarding mine seismology and rockburst phenomena is shared at various international conferences, notably the *Rockbursts and Seismicity in Mines* (RaSiM) symposia, held at approximately quadrennial intervals in South Africa (1982, 2001), USA (1988), Canada (1993), Poland (1997), Australia (2005), China (2009) and Russia (2013). The work presented at the first four symposia was reviewed by Ortlepp (2005). In addition, the biennial seminars on *Deep and High Stress Mining*, which cover a broader range of topics including rock engineering, cooling, ventilation and mechanization, have been held in Australia (2002, 2007, 2012), South Africa (2004), Canada (2006, 2014) and Chile (2010). The book *Challenges in Deep and High Stress Mining* (Potvin *et al.*, 2007) contains a selection of papers presented at the first three seminars. Several important reports and books dealing with mine seismology

have been published since the 1980s, notably *An Industry Guide to Methods of Ameliorating the Hazards of Rockfalls and Rockbursts* (Anon, 1988), the *Rockburst Handbook for Ontario Hardrock Mines* (Hedley, 1992), *An Introduction to Mining Seismology* (Gibowicz & Kijko, 1994), *Seismic Monitoring in Mines* (Mendecki, 1997), *Rock Fracture and Rockbursts* (Ortlepp, 1997), *A Handbook on Rock Engineering Practice for Tabular Hard Rock Mines* (Jager & Ryder, 1999), *A Textbook on Rock Mechanics for Tabular Hard Rock Mines* (Ryder & Jager, 2002), and *Rockbursts: Case Studies from North American Hard-rock Mines* (Blake & Hedley, 2003).

2 SEISMIC MONITORING OBJECTIVES

In order to design and operate a mine seismic system, it is necessary to define clearly the objectives of a particular system. Seismic monitoring is carried out for several purposes:

1. Rapid response to a seismic event that may have caused damage. Firstly, to direct rescue teams to areas where miners may be trapped or injured, thereby limiting the loss of life. Secondly, to halt hoisting until the shaft infrastructure has been examined. Thirdly, to evacuate parts of the mine that may be struck by aftershocks.
2. Seismic hazard assessments (SHA) are performed in an effort to mitigate the risks associated with rockbursts. Hazard refers to the likelihood of occurrence of a seismic event. The consequence of an event depends on many factors, such as the location and size of the event, the vulnerability of excavations to shaking, and the exposure of workers and equipment. Risk is an attempt to quantify the loss, and is given by the product of the hazard and the consequence. To synchronize SHA with typical mining cycles, SHA procedures are often described as short, medium and long term, with time spans of minutes to hours, weeks to months, and years, respectively.
3. Back analysis of large and/or damaging seismic events, whether associated with casualties or not, in order to determine the cause of the event(s) and to explain the severity and distribution of damage. This understanding is essential for developing strategies to reduce seismic hazard and minimize rockburst risk.
4. Monitoring the mining process, for example the progression of the cave front in a block cave mine, or the response of the rock mass to a large blast.
5. Research and experimental development to improve knowledge of the rockbursting phenomena and to develop technologies (*e.g.* improved ground support elements and systems) to mitigate the hazard.

3 NETWORK DESIGN

A schematic of a typical microseismic system is shown in Figure 2. Vibrations produced by mining-related events are recorded on sensors installed underground and on the surface. The data is received at a central office for real time processing and analysis.

3.1 Performance criteria

The primary output of microseismic monitoring is the time, location and size of seismic events. The desired sensitivity of the network (M_{min}), location accuracy and processing

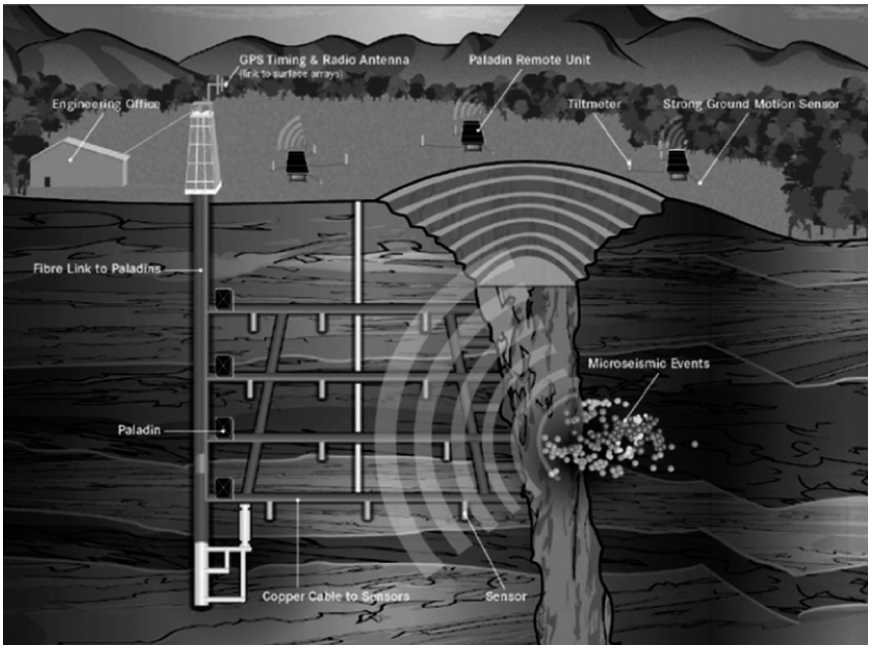


Figure 2 A typical microseismic system (Collins *et al*., 2014, p. 682).

Table 1 Suggested performance criteria for microseismic networks.

Monitoring objective	*Sensitivity (M_{min})*	*Location accuracy (in plan)*	*Processing speed*
Rapid response to potential rockbursts	0.5	200 m	2 minutes
Long-term SHA*	1.0	200 m	days
Medium-term SHA*	0.0	30 m	days
Short-term SHA*	−1.0	30 m	10 minutes
Back analysis of large events (sufficient sensitivity to detect aftershocks)	0.0	30 m	hours

* SHA – Seismic Hazard Assessment. The proposed network sensitivities and location accuracies are necessary to perform SHA, but do not guarantee success. In most cases, the same data set is used for long-, medium- and short-term SHA, thus the location accuracy of most events used for long-term SHA is better than 200 m.

speed depends on the monitoring objectives. These may differ for various parts of the mine (*e.g.* mined-out areas, active mining sections, shaft pillar) and may change with time as some areas are mined out and new stopes established. Suggested performance criteria for seismic networks are presented in Table 1.

3.2 System specifications

The selected performance criteria can only be met if a seismic network is designed appropriately. However, there are inevitable tradeoffs between cost and performance.

Table 2 Guidelines for the design of seismic networks.

	RECOMMENDED MINIMUM SYSTEM CHARACTERISTICS	
APPLICATION	**MINE-WIDE**	**RESEARCH/SPECIAL AREAS**
Scale	300 m – 5 km	100 m – 1 km
Sensitivity	M_{min}= 0 for mined-out areas M_{min} =−1 for active mining areas	M_{min}=−2
PARAMETERS		
Sampling rate	1 kHz for mined-out areas 2 kHz for active mining areas	10 kHz
Sensor density	5 sites within 1 km of source	5 sites within 300 m of source
Sensors	Tri-axial sets of geophones or accelerometers.	Accelerometers
Dynamic range	120 dB	110 dB
Resolution at all levels	10 bits	10 bits
Event rate	1–1000 events/day	1000–10,000 events/day
Sustained event rate	250 per hour	2500 per hour
Communication rate	9.6 kb/s	115 kb/s
Communication method	Dual twisted pair or optical fiber	Coaxial copper cable or optical fiber
Timing	GPS	GPS

The geometric configuration and spacing of the sensors are the primary factors that determines the sensitivity and location accuracy of a network. A rule-of-thumb is that any event above M_{min} should be recorded clearly by at least five tri-axial sites or on 15 valid seismograms. Guidelines for the design of seismic networks are presented in Table 2.

When designing the network, long-term mine plans should be taken into account and new sensors should be installed routinely as the mine expands. Data acquisition units may be relocated from sites in areas where mining activity has terminated. The effect on network performance should any sensor fail should also be considered.

4 NETWORK OPERATION

4.1 Calibration of the velocity model and magnitudes

The accurate estimation of P- and S-wave velocities is fundamental to obtaining reliable locations. Factors that affect seismic velocities include the rock type, the presence of mining excavations, stress variations and fracturing. An error of 3% in the velocity translates to an error of 30 m for a source-sensor ray path of 1000 m. It is recommended that calibration blasts be detonated at several locations spanning the mine to perform a crude survey of the seismic velocities. It is recommended that velocity variations of more than 3% are taken into account in the event location procedures, for example, by excluding data recorded at sensor sites in the "shadow" of excavations from the calculation, or by the development of a more detailed velocity model and the use of ray-tracing algorithms to determine locations. Guidelines for performing calibration blasts are provided in Table 3.

Table 3 Guidelines for the design and measurement of calibration blasts.

Blast location	The coordinates of the blast should be determined to better than a meter. Both the position of the collar of the blast holes and the extrapolated position of the explosives should be recorded and marked clearly on the mine plan. If the blast is to be recorded at several sensor sites, it is desirable that the ratio (largest distance)/(smallest distance) should be greater than 3. Short holes should be used for short distances, as a blast hole with explosives over a 10 m length could translate to a location error of up to 2% at a hypocentral distance of 500 m.
Blast time	If possible, the blast time should be recorded by means of a temporary geophone near the collar of the blast hole connected to the seismic system. If this is not possible, the time of detonation should be recorded to the nearest 10 seconds. If the origin time is not accurately recorded, the blast should be situated to give as wide a range of distances to the various sensor sites as possible.
Charge size	A low gas, high velocity of detonation (VOD) explosive such as Energex, Powergel or Dynagel should be used. The seismic coupling must be good. The hole should be well tamped. The blast should be well confined, *i.e.* no rock should be ejected by the blast. The size of the charge depends on the distance from the calibration blast to the most distant geophone. From past experience, the following charge sizes are recommended: **Distance to sensor site (m)** — **Charge size (kg)** 200 — 5 500 — 10 1500 — 50 The exact size of the charge is less critical than the coupling with the rock, as the efficiency of converting chemical to seismic energy varies much more widely (say 0.1 to 2%) than the variation in chemical energy density in explosives.
Examples	To detonate a 50 kg charge, it is recommended that 3 BX size holes be drilled, each hole at least 10 meters in length. The holes should be close to each other (say 1 meter apart). About 16 kg should be loaded in each hole. Assuming a density of the explosive of 1.5 g/cc and a hole diameter of 60 mm, the explosive should fill about 4 m of each hole. The remainder of the hole should be firmly tamped. Alternatively, one large diameter (*e.g.* 90 mm) hole should be drilled for the entire 50 kg charge. Simultaneous detonation must be achieved. Use Cordtex, and detonate at the toe and middle of each hole.

The methods used to calculate magnitudes are quite variable. In some instances, magnitude is based on measurements of the radiated energy, in other instances on the seismic moment, and in yet other cases on a combination of energy and moment. It is recommended that the methods used to calculate local magnitude should be standardized between networks, and the magnitudes harmonized with those calculated by the national seismological network.

4.2 System management

"What gets measured, gets done" is a precept that applies as much to the management of a seismic network as to any other management function. The performance of the network and sensors must be tracked; all software upgrades and changes in system settings must be logged; data must be backed up regularly; and a record kept of all

emergency response notifications, containing information such as the quick and final location, the person(s) notified and the actions taken.

A power failure may disable an entire seismic network. Power failures are sometimes caused by large seismic events, resulting in the loss of critical data. It is recommended that mines take measures to prevent the loss of data, *e.g.* by installing uninterruptible power supply units. A sensor site may be disabled by a power failure, break in the data transmission line, or failure of electronic components. These faults may have many causes, ranging from fires and falls of ground, to power surges and cable theft. A prior assessment should be made of the impact of the loss of any site on network performance so that repair work can be prioritized. A tri-axial sensor may operate with one or two disabled geophones/accelerometers. The remaining transducer(s) may be used for locations, although the determination of other source parameters may be compromised. It is desirable that at least 80% of the sites should be fully functional.

Consistency in the methods and parameters used to calculate source parameters is especially important when performing seismic hazard assessments, or trends in the data may by masked by processing artifacts. New versions of processing software and parameters are implemented from time to time, either to fix bugs or to incorporate advances in theory and technology. This may make it necessary to recalculate the source parameters of all events in the seismic database.

5 ESTIMATION OF SEISMIC SOURCE PARAMETERS

5.1 Location and origin time

The location and origin time are the most basic source parameters. As a rule of thumb, it should be possible to reduce the location error to less than 3% of the average hypocenter-site distance provided high quality data from at least five sites of reasonable configuration is available. The easiest way to improve the accuracy of locations would thus seem to be to increase the density of sensor sites. However, the installation of additional sensor sites is an expensive option. Sophisticated mathematical methods, such as joint hypocentral determination and double difference techniques, may also be used to improve accuracy.

An example set of seismograms with arrival picks and theoretical arrival times is shown in Figure 3, the difference providing an indication of the accuracy of the arrival picks, the reliability of the velocity model, and the uncertainty in the source location. The accuracy with which P- and S-wave arrival times can be picked can be improved by rotating the seismograms to radial and transverse components, and by filtering the seismograms to reduce noise. If a seismogram has an exceptionally large time residual, reconsider the pick and check for multiple events on the seismogram. “If in doubt, leave it out” is a sound maxim. It is generally better to have fewer, but more reliable picks.

5.2 Quantification of source parameters and mechanisms

An accurate description of the seismic source is considered vital for meaningful back analysis and effective seismic hazard assessment. The fundamental source parameters of a seismic event are its time, location, radiated seismic energy and scalar moment (a

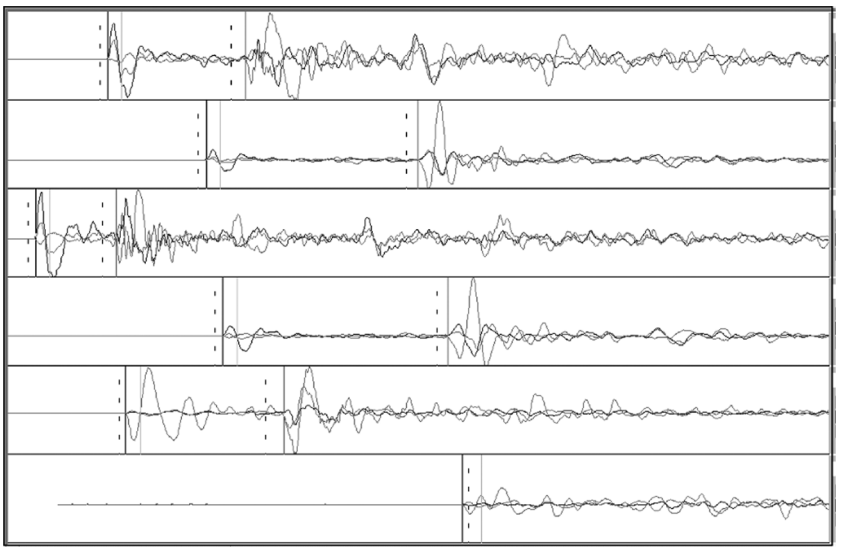


Figure 3 A M_L 1.2 event recorded at six three-component stations in Impala platinum mine, South Africa (Courtesy Impala Platinum). Solid lines indicate the picks of P- and S-waves; dashed lines the theoretical arrival times produced by the optimum source location; seismogram duration is 0.554 s.

measure of the co-seismic deformation), from which many other parameters may be derived. Some parameters require further analysis of the seismograms *e.g.* the calculation of the Fourier spectrum to determine the frequency content, especially the dominant frequency on the velocity seismogram (the "corner frequency"), or the estimation of the polarization direction of the body wave. Commonly used source parameters include:

- Stress change associated with the event, described by the stress drop or apparent stress;
- Dimensions of the source, described by the radius, area or volume;
- Slip on the fault, described by the displacement and velocity of slip, and the orientation of the slip vector; and
- Source mechanism, described by the Energy Index (for a given moment, a comparison of the observed energy and average energy), the ratio of energy in the S- and P-waves (E_S/E_P), and the moment tensor (a vector representation of source kinematics). Moment tensor solutions may be unreliable if the focal sphere is not well covered *e.g.* the event is external to the network, or the network has a planar geometry.

Source parameter calculations (*e.g.* Figure 4) are affected by the same factors as location calculations (geometry of the seismic sensors, the seismic velocity model, complex ray paths caused by fracturing and extreme stress variations around stopes, etc.), as well as several additional factors such as the frequency range of the recording instrumentation, and the material and mechanical properties of the medium (*e.g.* density, elastic and shear moduli, attenuation and scattering). Simplifying assumptions are made regarding the source model (*e.g.* the Brune (1970) model assumes that the rupture resembles a "penny-shaped crack"). Many of the mathematical techniques that are used during data processing and analysis require intelligent choice of parameters

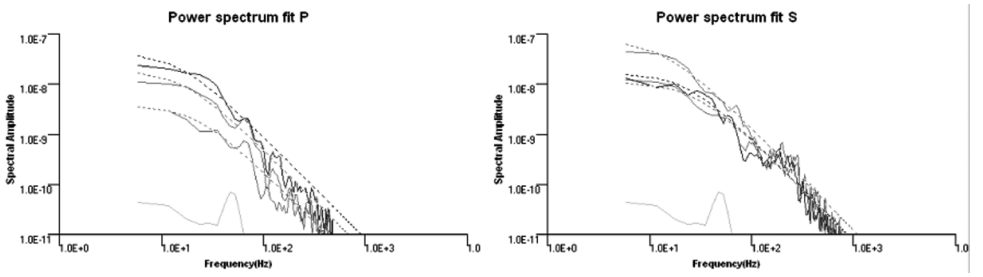


Figure 4 Fourier power spectra for P- and S-wave windows of the displacement seismogram are used to calculate source parameters such as the scalar moment and the corner frequency. (Courtesy Impala Platinum).

Table 4 Practical tips for determining source parameters.

Network design	Insufficient frequency range is generally the factor that contributes most to uncertainty in the calculation of source parameters. In the case of very large events (say M_L>3.0), the geophone's lower cut-off frequency may be close to or even above the corner frequency, thus making estimation of seismic moment unreliable. To ensure proper calculation of source parameters for these very large events, mines should have at least one 1 Hz geophone in the network. In the case of very small events (say M_L<-2.0) the upper cut-off frequency of the sensor may be close to or below the corner frequency. In these cases the moment can be calculated, but other parameters will be unreliable. As the upper cut-off frequency depends primarily on the sampling rate and the kind of sensor, acquisition units with sufficient sampling rate and geophones with high natural frequency should be selected.
Processing	Magnitude should be based on the scalar seismic moment, and not on combinations of moment and energy. Scalar seismic moment is usually very robust and is not significantly affected by the method used to estimate it. A problem only occurs when events with M_L>3.5 are recorded. In these cases, the seismic moment and magnitude are underestimated if the event is recorded by 4.5 Hz sensors. Spectral analysis for the purpose of calculating primary source parameters energy and moment should be based on at least 4 P- and 4 S-spectra. Velocity and displacement spectra should be complete in the upper frequency range with a recognizable corner frequency and high-frequency drop-off.
Quality control	Exclude or flag blast events so that the database used for seismic hazard assessment is not contaminated.

(*e.g.* Fourier analysis, digital filtering, curve fitting). Some practical tips for source parameter calculations are provided in Table 4.

6 STANDARD OPERATING PROCEDURES FOR MICROSEISMIC MONITORING

6.1 Emergency response to rockbursts

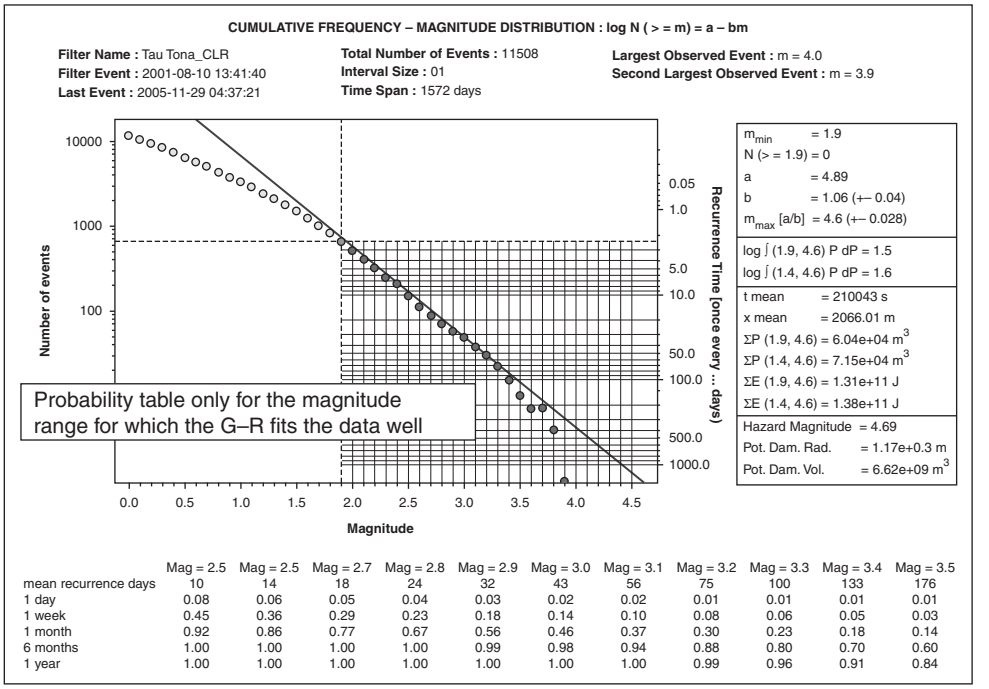
The primary objective of seismic monitoring in rockburst-prone mines is to limit the loss of life and/or damage to infrastructure following a seismic event. This is achieved

through (i) the rapid identification of areas that may have suffered damage so that rescue efforts may be initiated as quickly as possible; and (ii) the halting of hoisting operations, should damage to the shaft barrel or steelwork be suspected; and (iii) the determination of the section of the mine that should be evacuated. These procedures can be broken down into several steps:

1. Determination of notification thresholds. A comprehensive rockburst database should be compiled, and the relationship between the event magnitude, the distance of the source from the working place, and the intensity of rockburst damage should be determined. The emission source (*e.g.* face bursts, fault slip) and areas of the mine (*e.g.* stopes, tunnels, shafts) should be taken into account. A threshold should be selected that ensures a notification is issued for, say, 95% of the cases where rockburst damage that poses a risk to safety occurs.
2. Quick location of potential areas of rockburst damage. The working places closest to the hypocenter of the seismic event, or most vulnerable to damage, must be identified as quickly as possible. This requires that the seismic event should be located with an accuracy of 200 m or better in plan, and that the hypocentral coordinates can easily be used to identify the names and/or numbers of nearby working places. The severity of rockburst damage is dependent on many factors in addition to the distance from the seismic event. Thus it is more important to identify quickly the area in which damage could possibly have occurred, rather than to conduct detailed seismogram analysis to identify the panel closest to the hypocenter.
3. Rapid notification of the control room. In order to enable medical attention to be given within the "golden hour", the location of the event and a list of the working places most likely to have sustained damage should be transmitted to the mine control room and other designated personnel within a few minutes of the occurrence.
4. Determination of the evacuation zone and period, if any.

6.2 Long-term seismic hazard assessment

Long-term seismic hazard assessment refers to a time scale of months to years, and supports annual and longer-term mine planning. A well-maintained seismic database allows hazardous geological structures and mine layouts to be recognized, and can also be used to calibrate numerical models so that standard rock engineering design tools can be applied appropriately. In new mining areas, data from geologically similar areas may be used for model calibration. Long-term seismic hazard trends may be used to assess the effectiveness of the mining strategies that have previously been applied. For example: the analysis of the relationship between the frequency and magnitude of earthquakes (the b-value) in different parts of a mine, or for different mining methods (Figure 5). This can be used to determine the mean recurrence rate of potentially damaging earthquakes and the maximum credible magnitude M_{max}, both important factors in the assessment of the seismic hazard.



	Mag = 2.5	Mag = 2.5	Mag = 2.7	Mag = 2.8	Mag = 2.9	Mag = 3.0	Mag = 3.1	Mag = 3.2	Mag = 3.3	Mag = 3.4	Mag = 3.5
mean recurrence days	10	14	18	24	32	43	56	75	100	133	176
1 day	0.08	0.06	0.05	0.04	0.03	0.02	0.02	0.01	0.01	0.01	0.01
1 week	0.45	0.36	0.29	0.23	0.18	0.14	0.10	0.08	0.06	0.05	0.03
1 month	0.92	0.86	0.77	0.67	0.56	0.46	0.37	0.30	0.23	0.18	0.14
6 months	1.00	1.00	1.00	1.00	0.99	0.98	0.94	0.88	0.80	0.70	0.60
1 year	1.00	1.00	1.00	1.00	1.00	1.00	1.00	0.99	0.96	0.91	0.84

Figure 5 Monthly analysis of the frequency-magnitude relationship (Courtesy of TauTona mine).

6.3 Medium-term seismic hazard assessment

Medium-term seismic hazard assessment (SHA) refers to a time scale of days to weeks. Most mines review production and planning on a monthly basis. SHA is a key input, enabling mining strategies to be developed that minimise the seismic hazard and exposure. Seismicity is the quantitative description of the space, time and magnitude distribution of seismic events occurring within a given volume ΔV in a time interval Δt. Seismicity can be quantified using the following four largely independent quantities: average time between consecutive events; average distance between consecutive events; sum of seismic moments, $\sum M$; and sum of radiated energies, $\sum E$. Many parameters can be derived from the basic quantities to describe the statistical properties of co-seismic deformation and the associated changes in stress, strain and rheology. Appropriate seismic analyses allow the relationship between seismic hazard and mining layouts, mining rates and local geological features to be established and monitored, and actions can then be taken to mitigate the rockburst risk. Medium-term SHA can be broken down into several steps:

1. Determine the required sensitivity and location accuracy.
2. Delimit datasets in space and time. This is not a simple matter, as there is an inevitable trade-off between statistical significance and resolution: the larger the area considered and the longer the time window, the greater the number of events analyzed and the greater the statistical stability, but the poorer the resolution in

space and time. Furthermore, the locus of seismic events migrates as mining progresses, and the effective sensitivity and location accuracy of the network changes accordingly. Lastly, the rate of mining may vary from month to month, complicating comparisons.

3. Select the seismic parameters to be analyzed. No general procedure for medium-term SHA has emerged. Practice is largely based on experience and local knowledge, and varies considerably between mines, service providers and even between different areas on a single mine. An example of a monthly report is shown in Figure 6.
4. Select the non-seismic parameters to be analyzed. Many mines have implemented in-house customized rockburst/rockfall hazard assessment systems that incorporate geotechnical and mining parameters *e.g.* proximity of geological structures, face shape, ground conditions, compliance with support standards, and the outputs of numerical modelling such as Energy Release Rate (ERR) and Excess Shear Stress (ESS) (Jager & Ryder, 1999).
5. Identify signals that might indicate a change in seismic hazard. A variety of methodologies have been implemented, including spatial analysis, clustering, ΣE-ΣM diagrams, stiffness diagrams, seismic response parameter, time-of-day distribution, and various integrated methods (see, for example, Van Aswegen, 2003, 2005).

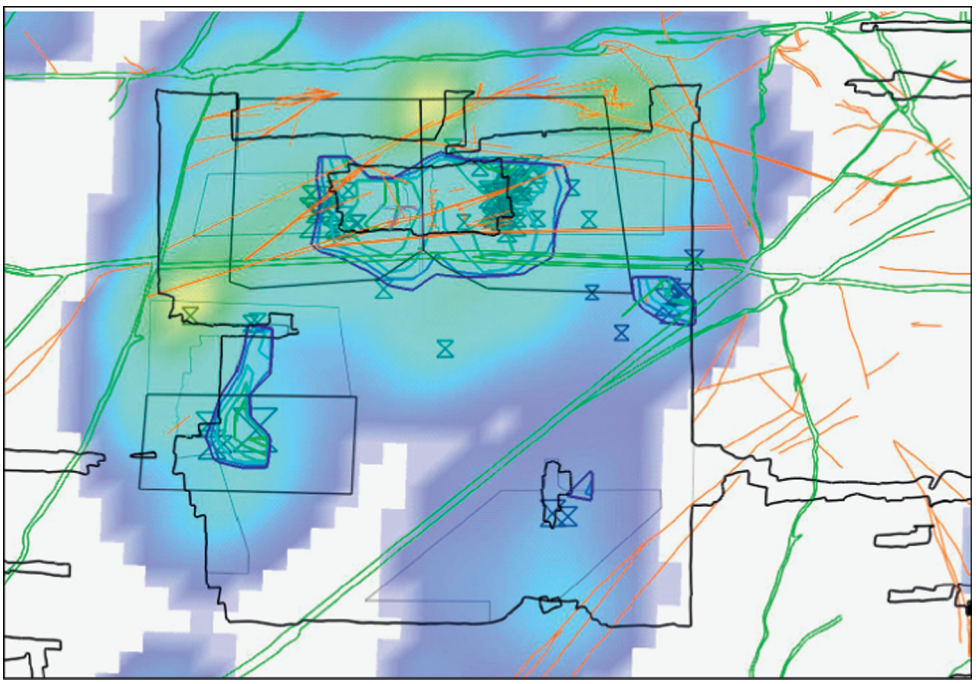


Figure 6 Monthly report showing the seismic response to mining of a shaft pillar: long term seismic displacement (colors), cumulative apparent stress over past 100 days (contours), and events with M>0 during the preceding month (symbols) (courtesy of TauTona mine).

6.4 Short-term seismic hazard assessment

Short-term seismic hazard assessment (SHA) refers to a time scale of minutes to a day. Short-term SHA can be broken down into several steps:

1. Determine the required sensitivity and location accuracy.
2. Delimit datasets in space and time.
3. Select the seismic parameters to be analyzed. Many parameters may be used, such as the seismic activity, b-value, Energy Index and Cumulative Apparent Volume. Since the removal of rock at depth is the driving force of mine seismicity, seismic activity is closely correlated with mining activity and thus should be taken into account when analyzing the seismicity data.
4. Select the non-seismic parameters to be analyzed. These are similar to those used for medium-term SHA.
5. Identify signals that might indicate a change in seismic hazard. An example is shown in Figure 7.
6. React to a warning. Usually an audit is conducted to ensure that support and escape ways meet standards. In some cases, part or all the mine may be evacuated or re-entry delayed until the hazard subsides
7. Quantify the SHA success rate. The "success" of an SHA method can only be determined if the objective of the exercise is clearly stated. Earthquake and mine seismologists have made strenuous efforts to develop methods to predict the location, time and magnitude of a seismic event. While some success has been achieved in predicting instabilities and the duration of aftershock sequences, the

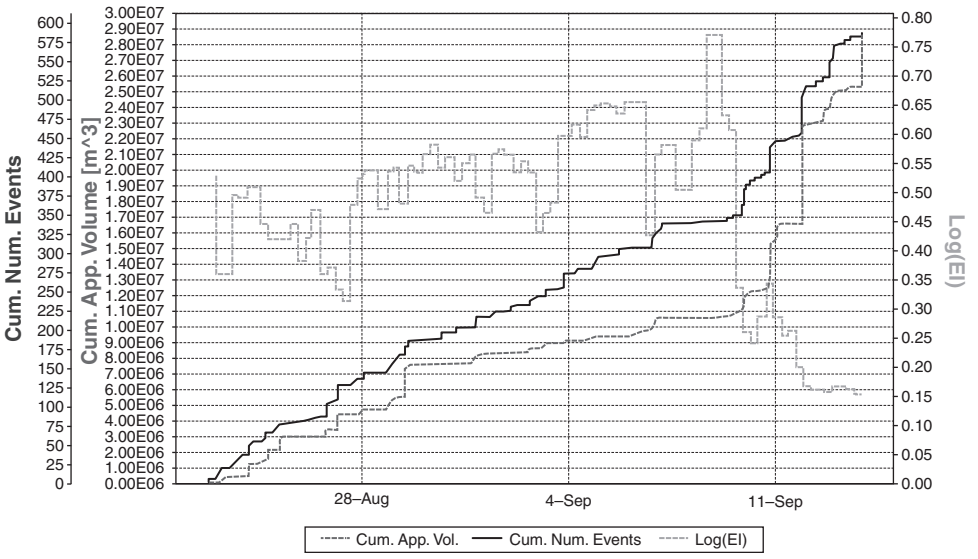


Figure 7 Example of short-term seismic hazard assessment in a section of a deep South African mine. The time history of the Cumulative Number of Events, Cumulative Apparent Volume (CAV) and Energy Index (EI) is shown. A large event on 9 September was preceded by a drop in EI and acceleration in the CAV (Rebuli & Kohler, 2014).

reliable prediction of earthquakes remains an elusive and perhaps impossible goal. Hence the objective of short-term SHA is often defined in broad terms, *e.g.* "to raise awareness", "to check on ground conditions and ensure compliance with support standards", or "to select areas for visits by safety, production or rock engineering personnel".

6.5 Back analysis

Back analyses should be carried out in the case of any seismic event or series of events that were exceptionally large or in unusual locations, or any rockburst that has caused injury, significant damage or loss of production. Back analyses are performed in an effort to understand the immediate and contributory causes of the seismic event and/or rockburst, so that measures may be taken to mitigate the risk and prevent recurrence in the future. Several examples are presented in the case history section below.

7 ROCKBURST RISK MANAGEMENT

The management of risk is an integral part of mining. The risks include the injury of workers, damage to equipment, loss of production, loss of reputation, failure to fulfill contractual obligations, fall in commodity prices, and industrial action. The risk of a fatality occurring is probably the most sensitive risk faced by mining companies. While most companies proclaim a "zero tolerance" approach, Stacey *et al.* (2006) argue that this unrealistic, and propose an approach that uses comparative fatality statistics to define a level of acceptable risk, noting that there is a fundamental difference between civil and mining engineering projects. The design requirements for a civil engineering project (*e.g.* a road tunnel or dam) are usually clearly defined, and usually require a conservative design as the projects are usually of a long-term nature and are open to the public; while many mining excavations are temporary or short term, not open to the public, and the viability of a project is usually critically sensitive to costs. The level of risk that is regarded "acceptable" is a necessary and significant consideration in any mining project or operation and is inextricably linked to ethics, and thus requires input from executive management. Corporate strategies should stipulate the levels of risk that are acceptable to the mining company, and this will form the basis of the criteria for all mine design and operational activities, including the environmental and health risks (*e.g.* pollution, dust) associated with mining.

The balanced scorecard, a concept for measuring a company's activities in terms of its vision and strategies, was introduced in the early 1990s. The key new element was the focus on the human issues that drive the financial outcomes, to enable organizations to focus on the future and act in their long-term best interest. Implementation of a scorecard typically includes four processes: (i) Translating the vision into operational goals; (ii) Communicating the vision and linking it to individual performance; (iii) Business planning; and (iv) Getting feedback and learning and adjusting the strategy accordingly. Since the original concept was introduced, balanced scorecards have become a fertile field of theory and research, and many practitioners have adapted the original concept to other fields of endeavor. A "seismic monitoring scorecard" could be a useful tool to assist a rockburst-prone mine to continuously improve its system to manage rockburst

Table 5 Elements of a Seismic Monitoring Scorecard.

System design according to monitoring objectives	**30%**
Mine subdivided into zones of varying seismic hazard	
Monitoring objectives defined per hazard district	
Monitoring objectives translated into required network performance	
Network design according to desired performance (within constraints of access)	
Network installed according to design	
Calibration blasts carried out for velocity model and location accuracy	
Seismic system operation and data collection	**40%**
Station days lost below 20% for past year, no deterioration over time	
80% of sensors fully functional	
Adequate resources for system maintenance and upgrade	
Seismic raw data are quality controlled	
Minimum of 5 stations per event, 8 picks, 8 spectra	
Data back-up procedures in place	
Magnitude relation adjusted to national catalog; time base calibrated	
System operation & maintenance procedures documented	
Annual review performed (internal or external)	
Seismic data analysis procedures	**30%**
Emergency event location	
Back-analysis of large events	
Short-term seismic hazard procedure(s) – description and evaluation	
Medium-term seismic hazard procedure(s) – description and evaluation	
Long-term seismic hazard procedure(s) – description and evaluation	
Exchange of information with other disciplines (rock engineering, geology, safety, production)	
Needs of recipients of seismic information assessed	
Written procedures for communication, roles and responsibilities	
Performance of methods assessed, improvements planned and implemented	
External review of procedures every two to three years, with the findings documented and evidence that the recommendations were implemented.	

risk. The main elements of the scorecard are described in Table 5. The overall score should be a reflection of a mine's efforts to optimize the design and operation of its seismic network, thereby reducing the risk and complying with legal requirements.

8 CASE STUDIES

8.1 Back analysis of a Mn2.6 event, Kidd Mine, Canada

Kidd Mine in the deepest base metal mine in the world, using open hole stoping to mine copper-zinc ore at depths of up to 2900 m (9500 level) below surface. An account of the assessment of seismic hazard and the management of the rockburst risk is provided by Disley (2014). Seismic monitoring commenced in the mid-1980s, and since then various systems have been installed. In 2014 the microseismic system consisted of 13 six-channel Engineering Seismology Group (ESG) Viper seismic stations supporting a mixture of triaxial and uniaxial accelerometers and 4.5 Hz and 15 Hz geophones; complemented by a strong ground motion system located in mined out areas, calibrated

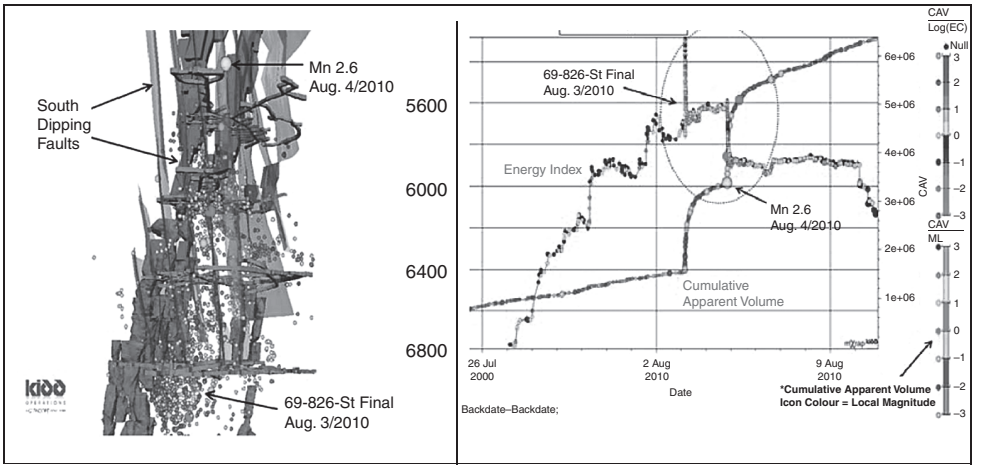


Figure 8 Microseismic monitoring and analysis in Kidd Mine (Disley, 2014). (a) Seismicity following a blast on 6800 level, (b) Log Energy Index / Cumulative Apparent Volume Instability graph.

to the Nuttli magnitude scale (Mn) of the Geological Survey of Canada. Waveform data is manually processed on site and imported into the Mine Seismicity Risk Analysis Program (mXrap, Australian Centre for Geomechanics, 2014) for sorting into clusters.

Seismicity following a large stope blast on 6800 level and back analysis of a Mn2.6 event is shown in Figure 8. The redistribution of stress following a blast in the 69–826 stope produced an immediate response in the surrounding rock mass, revealed by the cluster of seismicity and a sudden increase in the Cumulative Apparent Volume (CAV) in the following 24 hours. The first event above 6000 level was a Mn2.6 event some 40 hours later that caused some damage. Back analysis did not provide evidence of any precursory events in the area, although the widespread seismicity following the blast suggested activation of the south-dipping regional faults.

8.2 Simulation of the seismicity at Renison Mine, Australia

Mine design options are routinely assessed by numerical modelling. However, this requires a range of input parameters such as the virgin stress and rock failure criteria, which are seldom accurately known. Comparison of modeled and observed seismicity can be used to validate the input parameters. A method of simulating seismicity is presented by Malovichko & Basson (2014). Essentially, the Indirect Boundary Element Software (developed by the Institute for Mine Seismology) places a 3D grid over the model domain and searches for possible planes of failure by identifying lobes of positive Coulomb Failure Stress (CFS), using the largest lobes as flaws *i.e.* points where failure may initiate. Modeled input parameters include the mining steps, virgin stress, rock mass properties and mining steps. The outputs are two catalogs: seismic events with origin times (related to the mining steps), size and mechanism; and aseismic events.

The seismicity simulation method is demonstrated by applying it to a narrow vein area in Renison mine in Tasmania, the largest operating tin mine in Australia

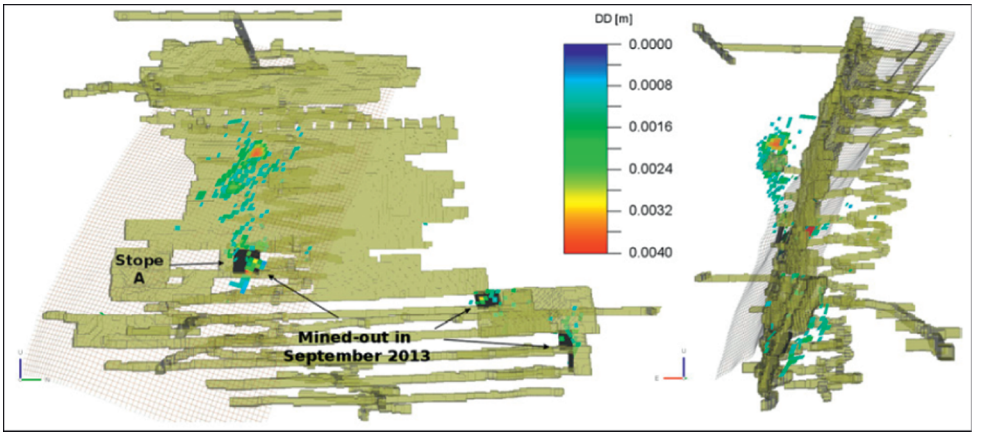


Figure 9 Simulation of seismicity at Renison Mine, Australia (Malovichko & Basson, 2014). The weak dike is displayed as a mesh. New and reactivated displacement discontinuities associated with the 27th mining step are shown, with mined out stopes colored black.

(Malovichko & Basson, 2014). This part of the mine has a number of triaxial geophones installed away from the stopes and declines that provide high quality data, enabling source parameters and mechanisms to be calculated reliably. A Boundary Element model was built, consisting of 33 monthly steps and ultimately 183,000 elements. Initially a single Mohr-Coulomb failure criterion was used for the entire rock mass, but this produced seismicity that was clustered close to the excavations, contrary to the observed data. The cohesion and friction angle were then reduced to simulate greater scattering, and specific failure criteria were introduced to model the response of a joint set and weak dike. The 33 mining steps produced 3400 seismic and 100 aseismic events (Figure 9).

The modeled aseismic events were distributed along the weak dike. The modeled seismicity compared reasonably well with the larger observed seismic events, but did not reproduce the smaller events as the minimum flaw size was set at 5 m. Malavichko & Basson (2014) note several shortcomings of their method, notably the approximate modelling of the stress field and the neglect of tensile failure. Advances in computational techniques and computing power have led to significant advances in the modelling of the response of the rock mass to mining that can be usefully applied to mine design. However, the intrinsic heterogeneity of the rock mass makes it unlikely that actual seismicity will ever be perfectly predicted.

8.3 Back analysis of damaging events at Kiruna Mine, Sweden

Kiruna Mine uses sublevel caving to exploit a continuous body of iron ore that is 4 km long, 80 m wide and a known depth extent of 1500 m. An account of seismicity and microseismic monitoring is provided by Dahnér (2015). A large damaging seismic event occurred in 2007, and since then several other large events have caused damage in production areas. These large events were thought to be associated with large faults that intersect the ore body. An Institute for Mine Seismology microseismic system was

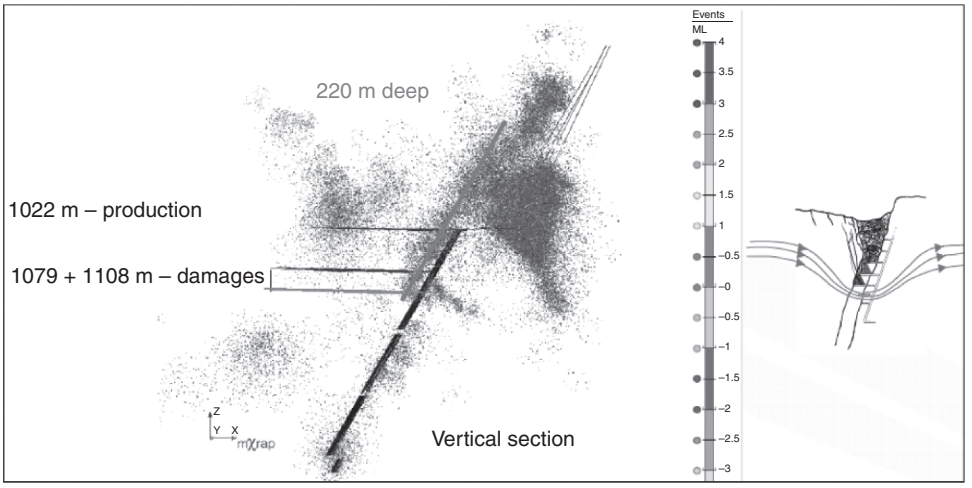


Figure 10 Seismicity in Kiruna Mine, Sweden (Dahnér, 2015).

installed in 2009, subsequently expanded, and in 2015 supported about 220 sensors. Seismic events are spatially clustered automatically using the MS-RAP software supplied by the Australian Centre for Geomechanics. The clusters are then manually grouped based on the E_S/E_P ratio, b-value and Energy–Moment relation.

Back analyses were performed of two damaging events that occurred in 2013 and 2014 with local magnitudes of 2.2 and 2.1, respectively. Damage, joints and factures were mapped and compared with the observed seismicity (Figure 10). No large faults were found to intersect the orebody, although a set of smaller faults and fractures parallel to the ore body was identified and is believed to be associated with the observed seismicity.

The large events were analyzed in detail by Malevichko *et al.* (2015). The event of July 2013 is taken as an example (Figure 11). The waveforms recorded at 166 sites were used to perform a full moment tensor inversion, which yielded two possible slip planes, one gently dipping to the west, the other steeply to the east. A range of studies were performed to resolve the ambiguity: the Excess Shear Stress was calculated on both nodal planes and compared with the location of the point of initiation of the main event; the source dimension was estimated for Brune and Madariaga models and compared with the aftershock distribution, near-field body wave polarization and far-field source spectra; and the slip amplitude, propagation of the rupture, and slip velocity was simulated and compared with the observed strong ground motions.

8.4 Analysis of seismicity following blasting to determine re-entry protocols

Seismically active mines generally experience an increase in seismic hazard due to rock mass instability following blasting. Limiting the spatial and temporal exposure of personnel to increased seismic hazard induced by blasting is one of the tactical measures employed by management to manage risk, and commonly forms a component of re-entry protocols. The mining practice of blasting at designated

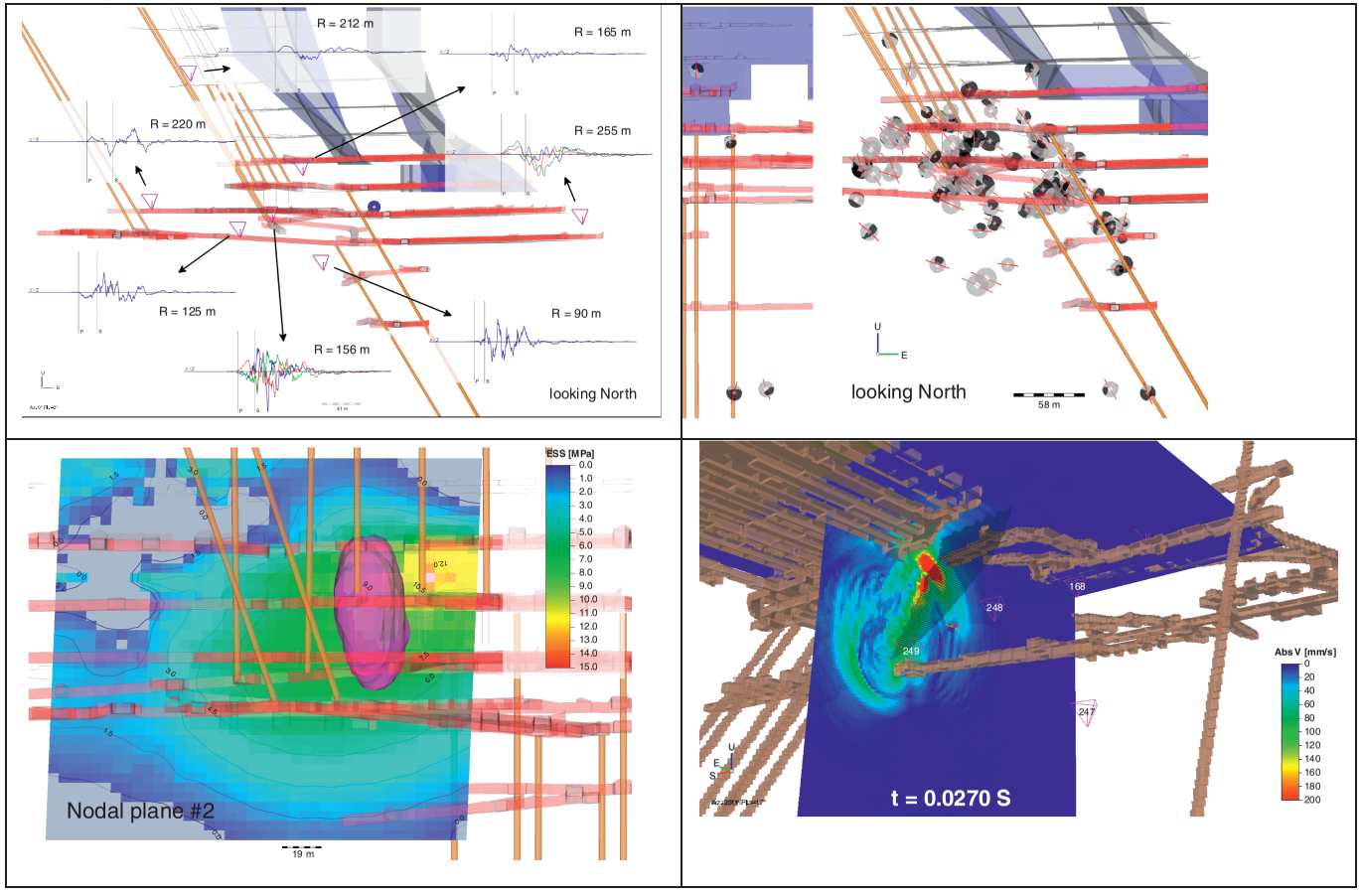


Figure 11 Seismological analysis of a M_L2.2 event in Kiruna Mine, Sweden (Malevichko *et al*., 2015). Top left: Mine layout and seismograms. Top right: Source mechanisms of aftershocks. Bottom left: ESS modelling on a nodal plane, the ovoid indicating the location of the event with 95% confidence. Bottom right: Simulation of the propagation of the rupture.

times (typically at the end of working shifts) inevitably results in seismic sequences that overlap in time while separated in space. Furthermore, blasting in similar spatial locations may result in sequences that overlap in space but not in time. Additionally, stress redistribution mechanisms may result in a significant degree of variability in the space-time response.

Woodward & Wesseloo (2015) developed an algorithm that automatically assesses the timing, location, and quantity of seismicity to identify seismic sequences, represented by the time of the first event and mean location of all events in the sequence. The method identifies events that have triggered a sequence of aftershocks by searching through the earthquake catalog with a series of space and time windows; and then models the identified sequences using the Modified Omori Law. The method distinguishes between sequences that are local and immediate, local and delayed, remote and immediate, and remote and delayed (Figure 12).

8.5 Observational studies in South African mines to mitigate seismic risks

The collaborative research project entitled "Observational studies in South African mines to mitigate seismic risks" drew on over a century of study of mining-related and tectonic earthquakes by South African and Japanese researchers, respectively (Ogasawara *et al.*, 2009; Durrheim, 2010; Durrheim *et al.*, 2010; Utsu, 2003). The project had four main aims: (i) to learn more about earthquake preparation and triggering mechanisms by deploying arrays of sensitive sensors within rock volumes where mining is likely to induce seismic activity, (ii) to learn more about earthquake rupture and rockburst damage phenomena by deploying robust strong ground motion sensors close to potential fault zones and on stope hanging walls, (iii) to upgrade the South African surface national seismic network in the mining districts, and (iv) to develop human capacity and research infrastructure in South Africa. The five-year project (2010–2015) was conducted under the auspices of the Science and Technology Research Partnership for Sustainable Development (SATREPS), funded by the Japanese Science and Technology Agency (JST) and the Japanese International Cooperation Agency (JICA).

Research sites were established at three deep gold mines in the Witwatersrand basin: Cooke #4, Hlanganani and Moab Khotsong (Durrheim *et al.*, 2012). Boreholes were drilled to accurately locate faults that were considered capable of producing mining-induced seismicity. Acoustic emission (AE) sensors, strain- and tilt meters, and controlled seismic sources were installed to monitor the quasi-static deformation of the rock mass, the accumulation of strain and damage during the earthquake preparation phase, and changes in dynamic stress produced by the propagation of the rupture front. Here we describe some of the work at Cooke #4 led by Masao Nakatani (Earthquake Research Institute at Tokyo University). A network of 28 acoustic emission (AE) sensors was installed in a volume spanning 95 m x 50 m x 30 m at a depth of about 1 km, sufficiently sensitive to locate events as small as M_w-5 (Figure 13).

Naoi *et al.* (2014) investigated the frequency-magnitude distribution (FMD) of acoustic emissions (AEs) that occurred between 8 August 2011 and 10 August 2011. A data set comprising 365,237 events that had at least 10 P-wave traveltime readings

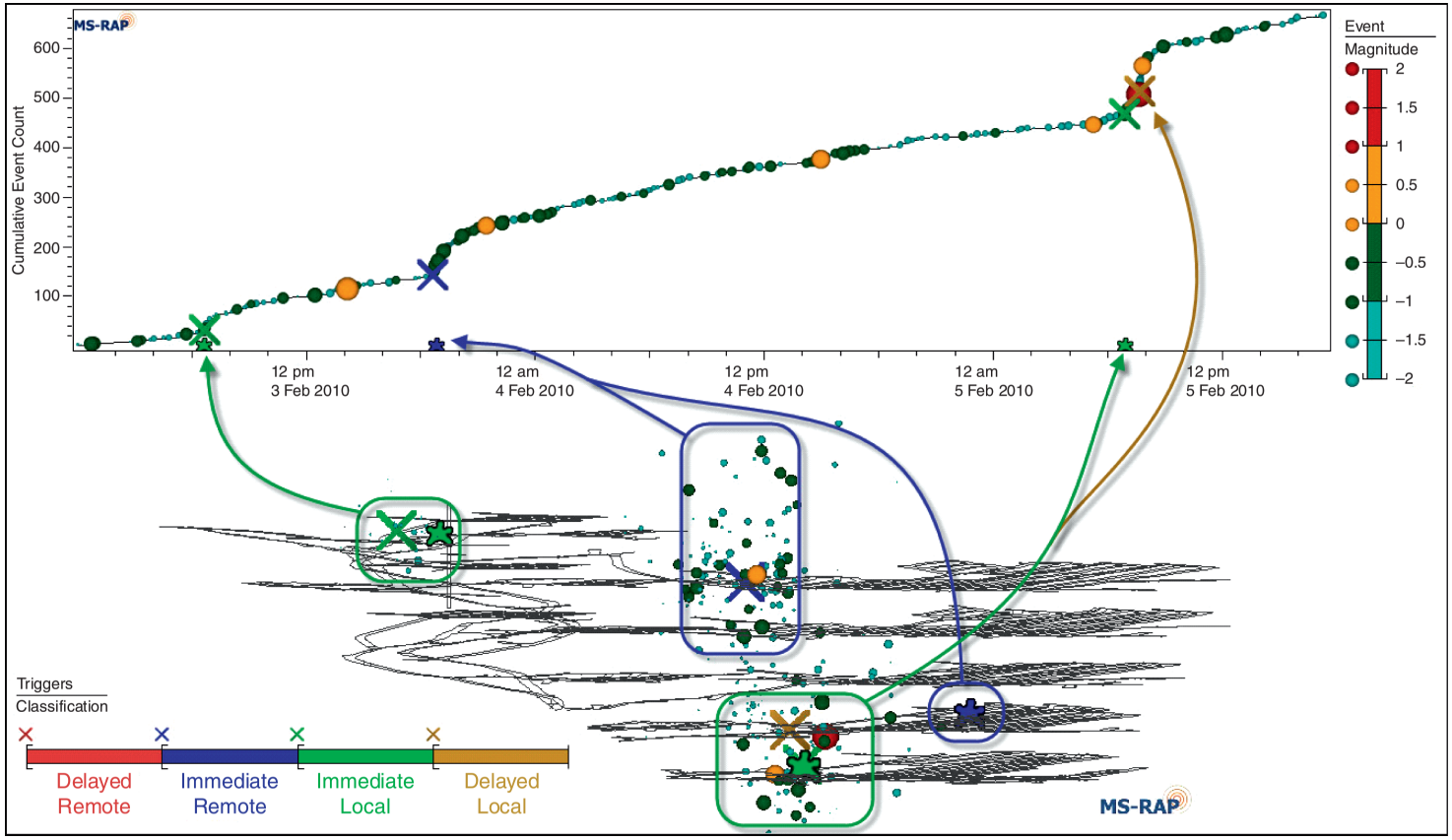


Figure 12 Cumulative count plot (top) and a perspective view of seismicity (bottom). Data over this short period illustrates the variable space time relationship between sequences and blasting (Woodward & Wesseloo, 2015).

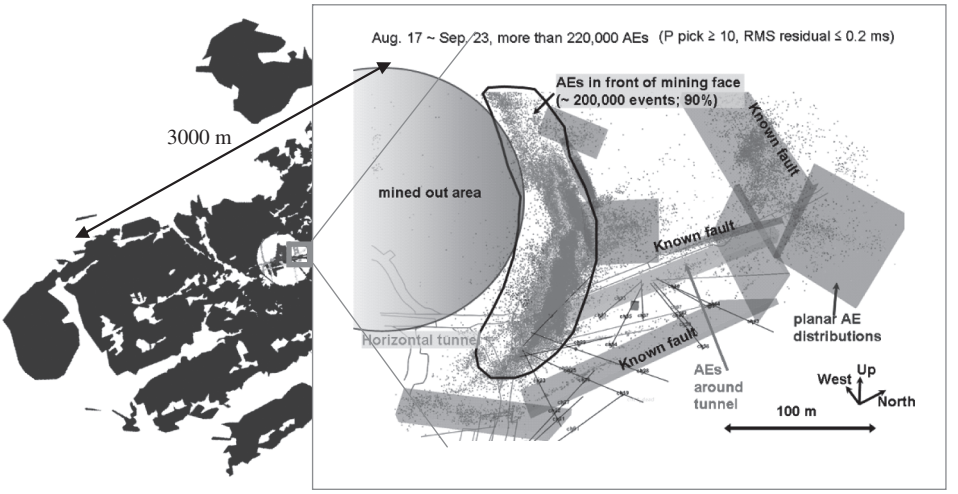


Figure 13 Research site at Cooke #4 mine. The shaft pillar (white circular area in the middle of the left figure) is about 1 km deep and surrounded by old stopes that were not back-filled. The location of the AE network of Nakatani (2013) is shown by a small rectangle. Seismicity associated with the mining face and planar structures is shown on the right. A sophisticated automatic location algorithm (Horiuchi *et al.*, 2011) was used because the number of AEs was too large to process manually.

and root-mean-square (rms) arrival-time residuals of 0.2 ms or less were used in the analysis. Once the events due to the blasts were removed, the FMDs of AEs were found to obey a Gutenberg-Richter (GR) law. The b-value was found to be independent of time from 1 minute to more than 30 hours after the blast. This result suggests that even the very small seismic events that occur immediately after blasting, which are thought to be mostly produced by the generation of new fractures in the intact rock, have the same FMD as events that occur several tens of hours after blasting, which are thought to be mainly events caused by slip on pre-existing weak planes. The AE catalog showed that the GR law with b~1.2 was valid between M_W –3.7 and M_W 0 for AEs around the mining front. The range of the b~1.2 law was extended to M_W 1 by the seismic catalog produced by the mine-wide network, which covers the same area but over a longer time period.

The monitoring system automatically located 40,555 AEs that occurred in the period 30 September to 5 October 2011, some of which were located by Moriya *et al.* (2015) using the joint hypocenter location and the "collapsing" method. Moriya *et al.* (2015) applied multiplet and the double-difference analysis to determine the orientation of eight structural planes characterized by similar AE events. The structural planes are sub-parallel to the mining front and dip steeply (>70°). In the eastern part of the stope the structural planes were found to expand downwards; while in the western part of stope the structural planes were found to expand upwards.

9 SUMMARY

Rockbursts are a major risk of deep and high-stress mining, causing damage to infrastructure, loss of production, and injury to mine workers and even the public. Mine owners and managers have the responsibility to ensure that the working environment is healthy and safe when a mine is designed, constructed, equipped, operated and decommissioned. Microseismic monitoring, analysis and interpretation are key components of the risk management system on rockburst-prone mines.

Microseismic monitoring has been implemented on a routine basis for nearly three decades. During this time there have been major improvements in data capture, processing and interpretation as a result of advances in electronics, computing, applied mathematics and rock mechanics. There remains considerable variation in seismic hazard assessment and risk management procedures and practice, as these depend on many factors that vary between mines and countries. Hazard assessment and risk management methods rely, to a greater or lesser extent, on the incorporation of non-seismic information, local experience and subjective judgment. In many cases this tacit knowledge still has to be translated into explicit guidelines and standard procedures based on rigorous evaluation and validation. Fortunately, vigorous attempts efforts to advance the science and technology of microseismic monitoring continue. Conferences are regularly held where mine seismology researchers, practitioners and service providers share their knowledge and experience, to the ultimate benefit of those who work or invest in deep mines.

REFERENCES

Australian Centre for Geomechanics. (2014) *mXrap*, [Online], Perth, Australian Centre for Geomechanics. Available from: http://www.mxrap.com.

Anon. (1988) *An Industry Guide to Methods of Ameliorating the Hazards of Rockfall and Rockbursts*. 2nd edition. Johannesburg, Chamber of Mines Research Organization.

Ben-Menahem, A. (1995) A concise history of mainstream seismology: Origins, legacy, and perspectives. *Bulletin of the Seismological Society of America*, 85, 1202–1225.

Blake, W.E. & Hedley, D.G.F. (2003) *Rockbursts: Case Studies from North American Hardrock Mines*. Lyttleton, CO, Society for Mining, Metallurgy, and Exploration, Inc. (SME).

Brune, J.N. (1970) Tectonic stress and the spectra of seismic shear waves from earthquakes. *Journal of Geophysical Research*, 75, 4997–5009.

Collins, D.S., Toya, Y., Pinnock, I., Shumila, V. & Hosseini, Z. (2014) 3D velocity model with complex geology and voids for microseismic location and mechanism. In: Hudyma, M. & Potvin, Y. (eds.), *Deep Mining 2014: Proceedings of the Seventh International Conference on Deep and High Stress Mining*. Perth, Australian Centre for Geomechanics. pp. 681–688.

Dahnér, C. (2015) A rock mechanical analysis of seismic and geological data for two large events at Kiruna Mine. Institute for Mine Seismology Seminar, Stellenbosch, 20–21 April 2015.

Disley, D.V. (2014) Seismic risk and hazard management at Kidd Mine. In: Hudyma, M. & Potvin, Y. (eds.), *Deep Mining 2014: Proceedings of the Seventh International Conference on Deep and High Stress Mining*. Perth, Australian Centre for Geomechanics. pp. 107–121.

Durrheim, R.J. (2010) Mitigating the risk of rockbursts in the deep hard rock mines of South Africa: 100 years of research. In: Brune, J. (ed.), *Extracting the Science: A Century of Mining Research*. Littleton, CO, Society for Mining, Metallurgy, and Exploration, Inc. pp. 156–171.

Durrheim, R.J., Anderson, R.L., Cichowicz, A., Ebrahim-Trollope, R., Hubert, G., Kijko, A., McGarr, A., Ortlepp, W.D. & Van der Merwe, N. (2006) The risks to miners, mines, and the public posed by large seismic events in the gold mining districts of South Africa. In: Hadjigeorgiou, J. & Grenon, M. (eds), *Proceedings of the Third International Seminar on Deep and High Stress Mining*, Université Laval, Canada, Section 30.

Durrheim, R.J., Ogasawara, H., Nakatani, M., Yabe, Y., Milev, A., Cichowicz, A., Kawakata, H., Moriya, H & the JST-JICA SA research group. (2010) Observational Study to Mitigate Seismic Risks in Mines: A new Japanese – South African collaborative project. In: Van Sint Jan, M. & Potvin, Y. (eds.), *Proceedings of the Fifth International Seminar on Deep and High Stress Mining*. Perth, Australian Centre for Geomechanics. pp. 215–225.

Durrheim, R.J., Ogasawara, H., Nakatani, M., Yabe, Y., Kawakata, H., Naoi, M., Ward, A.K., Murphy, S. K., Wienand, J., Lenegan, P., Milev, A.M., Murakami, O., Yoshimitsu, N., Kgarume, T., Cichowicz, A. & the SATREPS research group. (2012) Establishment of SATREPS experimental sites in South African gold mines to monitor phenomena associated with earthquake nucleation and rupture. In: Potvin, Y. (ed.), *Deepmining 2012: Proceedings of the Sixth International Seminar on Deep and High Stress Mining*. Perth, Australian Centre for Geomechanics. pp. 173–187.

Gibowicz, S.J. & Kijko, A. (1994) *An Introduction to Mining Seismology*. San Diego: Academic Press.

Hedley, D.G.F. (1992) *Rockburst Handbook for Ontario Hardrock Mines*. CANMET Special report SP92-1E, Energy, Mines and Resources Canada.

Hills, P.B. (2012) Managing seismicity at the Tasmania Mine. *Mining Technology*, 121(4), 204–217.

Horiuchi, S., Horiuchi, Y., Iio, Y., Sawada, Y., Sekine, S., Nakamura, H., Okada, T., Nakatani, M. & Naoi, M. (2011). Automatic P and S wave arrival time picking compared to manually picking, Abstracts, *IUGG General Assembly*, Melbourne, # 3430.

Jager, A.J. & Ryder, J.A. (ed.) (1999) *A Handbook on Rock Engineering Practice for Tabular Hard Rock Mines*. Johannesburg, Safety in Mines Research Advisory Committee.

Malovichko, D. & Basson, G. (2014) Simulation of mining-induced seismicity using the Salamon-Linkov method. *Deep Mining 2014: Proceedings of the Seventh International Conference on Deep and High Stress Mining*. Perth, Australian Centre for Geomechanics. pp. 667–680.

Malovichko, D., Lötter, E. & Meyer, S. (2015) Seismological analysis of two large damaging events in the Kiruna Mine. Institute for Mine Seismology Seminar, 20–21 April 2015, Stellenbosch, South Africa.

Mendecki, A.J. (ed.) (1997) *Seismic Monitoring in Mines*. Chapman and Hall, London, p. 262.

Moriya, H., Naoi, M., Nakatani, M., Van Aswegen, G., Murakami, O., Kgarume, T., Ward, A. K., Durrheim, R., Philipp, J., Yabe, Y., Kawakata, H. & Ogasawara, H. (2015). Delineation of large localized damage structures forming ahead of an active mining front in the Cooke 4 Mine, South Africa, by using advanced acoustic emission mapping techniques, *International Journal of Rock Mechanics & Mining Sciences*, *International Journal of Rock Mechanics & Mining Sciences*, 79, 157–165.

Nakatani, M. (2013) Microfractures on natural faults stressed by mining. In: *International Summer School on Earthquake Science "Diversity of Earthquakes"*, Earthquake Research Institute of the University of Tokyo and the Southern California Earthquake Center, 25 September 2013, Hakone, Japan.

Naoi, M., Nakatani, M., Philipp, J., Horiuchi, S., Otsuki, K., Kgarume, T., Morema, G., Khambule, S., Masakale, T., Miyakawa, K., Watanabe, A., Moriya, H., Murakami, O., Yabe, Y., Kawakata, H., Yoshimitsu, N., Ward, T., Durrheim, R. & Ogasawara, H. (2014) Frequency-magnitude distribution of $-3.7 < M_W < 1.3$ mining-induced earthquakes and b-value invariance with post-blast time, *Pure and Applied Geophysics*, 171, 2665–2684.

Ogasawara, H., Durrheim, R.J., Nakatani, M., Yabe, Y., Milev. A., Cichowicz, A., Kawakata, H. & Moriya, H. (2009) JST-JICA SA Research Group, a Japanese-South African collaboration to mitigate seismic risks in deep gold mines. In: Van der Westhuizen, J. (ed.), *Proceedings of the First Hard Rock Safe Safety Conference*, 28–30 September 2009, Sun City, South Africa. Johannesburg: South African Institute of Mining and Metallurgy. pp. 115–134.

Ortlepp, W.D. (1997) *Rock Fracture and Rockbursts: An Illustrative Study*. Monograph Series M9, Johannesburg, South African Institute of Mining and Metallurgy.

Ortlepp, W.D. (2005) RaSiM comes of age: A review of the contribution to the understanding and control of mine rockbursts. In: Potvin, Y. & Hudyma, M. (eds.), *Proceedings of the Sixth International Symposium on Rockbursts and Seismicity in Mines*. Perth: Australian Centre for Geomechanics. pp. 9–11.

Pechmann, J.C., Arabasz, W.J., Pankow, K.L., Burlacu, R., & McCarter, M.K. (2008) Seismological report on the 6 August 2007 Crandall Canyon mine collapse in Utah. *Seismological Research Letters*, 79(5), 620–636.

Potvin, Y., Hadjigeorgiou, J. & Stacey, D. (eds) (2007). *Challenges in Deep and High Stress Mining*. Perth: Australian Centre for Geomechanics.

Rebuli, D.B. & Kohler, S.J. (2014). Using clustering algorithms to assist short-term seismic hazard analysis in deep South African mines. In: Hudyma, M. & Potvin, Y. (eds.), *Deep Mining 2014: Proceedings of the Seventh International Conference on Deep and High Stress Mining*. Perth, Australian Centre for Geomechanics. pp. 699–708.

Ryder, J.A. & Jager, A.J. (eds.) (2002) *A Textbook on Rock Mechanics for Tabular Hard Rock Mines*. Johannesburg, Safety in Mines Research Advisory Committee.

Stacey, T.R., Terbrugge, P.J. & Wesseloo, J. (2006). Risk as a rock engineering design criterion. In: Hadjigeorgiou, J. & Grenon, M. (eds.), *Proceedings of the Third International Seminar on Deep and High Stress Mining*. Université Laval, Canada, Section 27.

Utsu, T. (2003). Centennial Report of Japan. Part 2. Historical development of Seismology in Japan. In: Lee, W., Jennings, P., Kisslinger, C. & Kanamori, H. (eds.), *International Handbook of Earthquake & Engineering Seismology*, Part B, Academic Press, Chapter 79.33, pp. 1–19.

Van Aswegen, G. (2003) Applications of seismic hazard assessment methods in mines. In: *Proceedings of the Tenth Congress of the International Society for Rock Mechanics*, The South African Institute of Mining and Metallurgy, Symposium Series S33, pp. 1261–1268.

Van Aswegen, G. (2005) Routine seismic hazard assessment in some South African mines. In: Potvin, Y. & Hudyma, M. (eds.), *Proceedings of the Sixth International Symposium on Rockbursts & Seismicity in Mines*. Perth, Australian Centre for Geomechanics, pp. 437–444.

Woodward, K. & Wesseloo, J. (2015) An iterative approach to the assessment of the spatial and temporal relationship between seismic responses and blasting. *Journal of the South African Institute Mining and Metallurgy*, 115(11), 1045–1056.



Taylor & Francis
Taylor & Francis Group
http://taylorandfrancis.com

Chapter 13

Large landslides with seismicity

Ewald Brückl
Department of Geodesy and Geoinformation, Technische Universität Wien, Vienna, Austria

1 INTRODUCTION

The global distribution of earthquake hypocenters maps the pattern of plate boundaries, and indeed this pattern was one part of the observational data that led to the theory of plate tectonics. Relative velocities between neighboring plates range from 0.001 m/year to 0.1 m/year. Plate boundaries separating oceanic lithosphere are sharp and clearly recognizable in the seafloor topography. On continents, plate boundaries manifest themselves in fault systems with widths of several 100 km. Most earthquakes occur in the upper crust, the schizosphere, which extends from near the surface to about 20 km depth, whereas some earthquakes follow subducting lithospheric slabs down to depths of around 600 km. Deformation during earthquakes may represent most of the total tectonic deformation, however segments of plate boundaries may also deform to a high percentage silently, *i.e.* by more or less steady creep.

Large rapid landslides exert substantial reaction forces on the bedrock and are sources for earthquakes detectable by global seismic networks. However, this is not the theme of this essay and we refer to Ekström & Stark (2013) as an excellent study on this theme. Here we will concentrate on large landslides that are actively moving but still accessible by men or even vehicles. There are many similarities between the deformation style of these landslides and inter- and intraplate tectonic deformations linked to earthquakes. As an example, we refer to a study of the seismic signature of a large landslide where the authors (Gomberg *et al.*, 2011) test the hypothesis that this "landslide is a useful natural laboratory for observing fault slip, specifically that slip along its basal and side-bounding strike-slip faults occurs with comparable richness of aseismic and seismic modes as along crustal- and plate-scale boundaries".

In addition, without reference to global plate tectonics, one may expect deeper insight into the deformation style and the rheological processes involved in the movement of large landslides by monitoring the seismic activity. The use of geophones, installed at an active mass movement as part of a geotechnical warning system, dates back at least half a century. Seismicity generated by the unstable slope at Mt. Toc was observed by one nearby seismic station before this mass movement developed into the catastrophic rockslide into the Vajont hydropower reservoir on 9th October 1963. As described by Kilburn & Petley (2003), it was found that the acceleration of the mass movement was not accompanied by seismic activity increasing in the same way. In order to achieve a deeper understanding of the relation between the geodetically

observable displacements and the hydro-meteorological parameters of a large landslide and the temporal and spatial pattern of seismicity, monitoring by dedicated seismic networks deployed on and around active landslide masses started after the year 2000 (*e.g.* Brückl & Parotidis, 2005; Roth & Blikra, 2005; Mertl & Brückl, 2007). These campaigns concentrated on large mass movements in crystalline hard rocks of the European Eastern Alps and Norway. Seismic monitoring of soft rock landslides began in the European Eastern Alps in 2005 (Walter & Joswig, 2008).

In this essay on large landslides with seismicity, or rather the seismic activity of active large landslides, we start with a consideration of possible source mechanisms and their physical description in section 2. The following section 3 on relevant seismic monitoring techniques includes instrumentation, signal detection, a diversity of methods for the location of individual seismic events and monitoring of seismic noise produced by the activity of the landslide. Thereafter, in section 4 we present seismic data and analysis from selected examples, exemplary for different landslide types. In section 5 we set seismicity generated by large landslides into a more general seismological context. We try to correlate waveforms with source mechanisms and summarize the complex relationship between hydro-meteorological parameters, seismicity, and geodetically observable displacements. This leads additionally to a consideration of the potential of seismic monitoring for supporting prediction of landslide evolution and early warning. A brief résumé including recommendations for future work concludes this essay. We will use the general term LME (Landslide Micro-Earthquake) for seismic events produced by the movement of a landslide. More specific terms like "slidequake" should be reserved for events with a corresponding source mechanism.

2 SOURCE MECHANISMS

Most earthquakes in a plate tectonic regime occur at plate boundaries and crustal fault systems. They are driven by the diverse movements of the individual plates and the buildup of tectonic stress and strain along the active faults. According to the elastic rebound theory, stress and strain are released by an earthquake, *i.e.* by a sudden failure along the focal area. Stick-slip behavior of the material at the fault is a precondition for an earthquake otherwise stress and strain would be released by silent and more or less continuous creep with a creep rate determined by the large scale plate tectonic movements. We may also say that one or several earthquakes restore stability in the area where they occur, however the plate tectonic movement is not influenced by the stress and strain released around the focal area.

Generally we may expect that earthquakes also occur at the border of moving landslide masses and their internal deformation zones, downscaled by several orders of magnitude according to the different scales of tectonic plates and landslide masses. We will treat possible fault mechanisms of these earthquakes (slope-tectonic earthquakes) in paragraph 2.2. However, there is a completely different type of earthquake in landslides corresponding to the failure of parts or the whole landslide mass. For this type of landslide earthquake, no stress and strain release is achieved by a relatively small displacement along the sliding surface and stability is restored only after a larger movement, which could also be a catastrophic slide. This type of earthquake is impossible on a plate tectonic scale, however, earthquakes comparable with this new

type have been reported from large landslides but also large ice sheets and outlet glaciers in particular (Eckström *et al.*, 2003). We will examine the fundamentals of this new earthquake type, the bulk instability, generated by partial or complete slope instabilities in the following.

2.1 Bulk instability

We simplify the landslide as a block of mass B resting on a potential sliding surface inclined by an angle α and the friction coefficient μ. The driving force is $F_d = B\, g \sin\alpha$, where g is the gravitational acceleration. The retaining force caused by the basal friction is $F_f = B\, g\, \mu \cos\alpha$. In the case of $F_d > F_f$, the block reacts with an acceleration $a = g(\sin\alpha - \mu\cos\alpha)$. The reaction force to the subsurface, which represents the seismic source, is $F = -a\, B$. If the inclination α or the friction coefficient μ varies along the travel path, the acceleration varies equivalently with time and travel distance. The acceleration may also be negative until the block comes to rest. In the case of a large landslide mass, the whole process corresponds to a catastrophic slope collapse with more or less large runout.

Kanamori & Given (1982) and Kanamori *et al.* (1984) analyzed the seismic recordings from the Mt Saint Helens landslide initiated by the eruption of 1980. A landslide mass of about 2.8 km^3 slid down approximately 25 km and generated an earthquake of magnitude M = 5.6, radiating seismic waves with very long periods (>100 s), much higher than expected for tectonic earthquakes of similar magnitude. The analysis of the surface wave radiation pattern brought the authors to the conclusion that a single force F(t) acting on the surface and varying in time is the proper seismic source. The displacement u_n at a distant seismic station is therefore given by

$$u_i = F_j G_{ij} \tag{1}$$

where G_{ij} is the Green's tensor (*e.g.*, Aki & Richards, 1980).

Kawakatsu (1989) showed that the total seismic event caused by a slope collapse or a similar process can be characterized by a centroid single force CSF =–B D, with D as the total travel distance. Eckström & Stark (2013) detected and evaluated the long period signals of 29 large and catastrophic landslides. Their analysis provides information on the force history, CSF, and surface wave magnitude. The product CSF was broken into its factors B and D by the additional inspection of satellite images or other in-situ information. The following relation between Ms and CSF (given in SI units) can be derived from the data of Eckström & Stark (2013):

$$M_s = 0.2758\ \mathrm{LOG10}(|\mathrm{CSF}|) + 1.1832. \tag{2}$$

This relation has a value of $R^2 = 0.58$ for the given data range $4.6 \le M_s \le 5.6$.

Brückl *et al.* (2015) applied a rotational slider block model of the collapsing landslide mass to the data provided by Eckström & Stark (2013). The landslide is simplified as a mathematical pendulum with the total mass concentrated in one point. The kinematics of the movement is therefore determined by the location of the center of rotation, the length of the pendulum L and the rotation angle α.

It can be shown (Brückl *et al.*, 2015) that to a first order approximation of the trigonometric functions the first half period of the movement of the rotational slide can be described by a mathematical pendulum which is in rest for the elongation $\alpha = \Phi_d$,

with Φ_d the angle of dynamic friction. The duration T of the source function equals the first half of the pendulum period and is given by Equation 3.

$$T = \pi \,\mathrm{sqrt}\,(L/g). \tag{3}$$

The travel distance D, the angle of dynamic friction Φ_d, and the peak acceleration a_{Peak}, respectively peak force F_{Peak} are given by Equations 4, 5, and 6. The symbols are defined in figure 1.

$$D = CSF/B = L(\alpha_0 - \alpha_1) \tag{4}$$

$$\Phi_d = (\alpha_0 + \alpha_1)/2 \tag{5}$$

$$F_{Peak} = B\,g(\alpha_0 - \Phi_d) = gCSF/(2L) \tag{6}$$

The Köfels rockslide (Ötz valley, Austria) with an estimated total mass of ~9 Gt and a travel distance of ~2 km is recognized as the largest rockslide in the crystalline region of the European Alps (Brückl *et al.*, 2001). It took place around 8700 radiocarbon years B.P. Pumice and fused rock, generated by the sliding process, was found at the basal sliding surface and an internal deformation zone (*e.g.*, Erismann & Abele, 2001). Figure 2 shows a rotational slider block fitted to the pre- and post-failure topography of the Köfels rockslide. The length of the corresponding mathematical pendulum is L ~ 6.5 km and for the duration of the slide follows T ~ 80 s. A magnitude M ~ 5.7 earthquake was generated by this gigantic rockslide according to Equation 2.

Gomberg *et al.* (2011) invoke varying pore pressure p as the physical parameter controlling the acceleration or deceleration of a planar slider block. The frictional force F_f per unit area of the failure surface is given by Equation 7, with σ the total normal force. The friction angle Φ does not change between static and dynamic conditions.

$$F_f = (\sigma - p)\tan(\Phi) \approx (\sigma - p)\Phi \tag{7}$$

Precipitation, snowmelt, or even air pressure induced groundwater flow (Schulz *et al.*, 2009a; Schulz *et al.*, 2009b) increase p and reduce F_f below the driving gravitational force, leading the slide to accelerate. Dilatancy (Iverson *et al.*, 2005) generated by shear deformation at slip zones increases the pore volume and, depending on the time and length scales of dilatancy and the groundwater diffusion parameters, p decreases leading to a stabilization of the slide. Like for the rotational slider block model, the planar slider block model controlled by pore pressure is non-linear and irreversible, upslope movements are not possible.

The rotational and the planar slider block models, which control the movement of a slide either by decreasing driving force due to the decreasing slope or by increasing resistive force due to decreasing pore pressure, should be considered as end members of real slides where both factors interact.

2.2 Local elastic strain and stress release

In analogy to plate tectonic earthquakes, we may assume that the more or less steady state movement of the bulk landslide mass is controlled by processes not influenced by individual LMEs. Elastic strain and stress is built up at some locations by the large scale movement of the bulk landslide mass. After reaching the ultimate stress at a pre-given

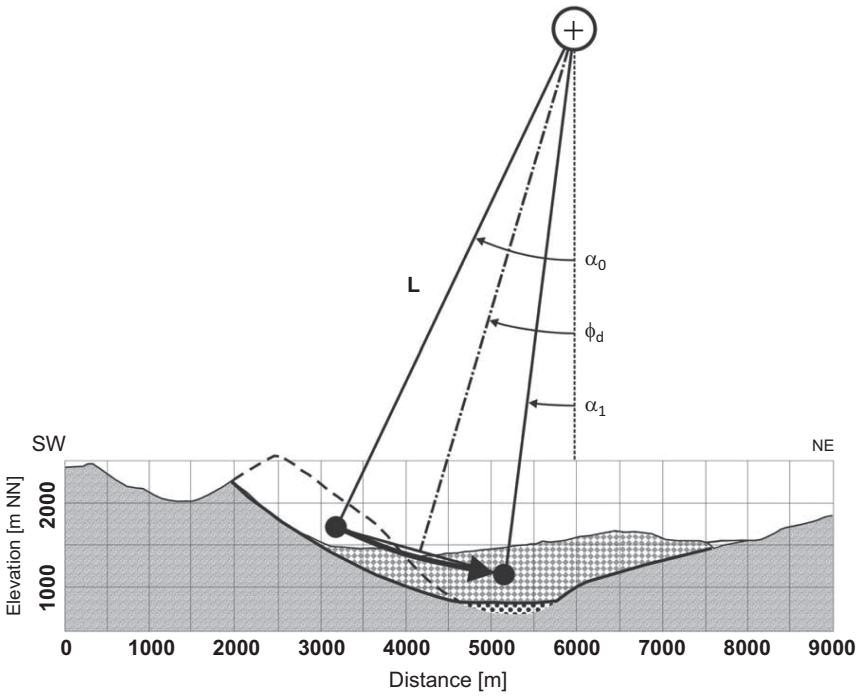


Figure 1 Rotational slider block fitted to the pre- and post-failure structure (Brückl *et al.*, 2001) of the Köfels rockslide; L… length of equivalent mathematical pendulum, α_0… start elongation, Φ_d… angle of dynamic friction, α_1… stop elongation.

fault zone, a fracture occurs and elastic rebound (Reid, 1910) represents the earthquake source mechanism. The description of seismic source mechanisms is a widely studied field and we refer to standard text books (*e.g.*, Aki & Richards, 1980; Stein & Wysession, 2003; Lay & Wallace, 1995) for comprehensive overviews and treatise of the underlying theory. The seismic displacement field u caused by discontinuous displacement at a fault can be described as follows in a 3D Cartesian coordinate system:

$$u_i = M_{jk} G_{ij,k} \tag{8}$$

M_{jk} is the 3x3 seismic moment tensor. This tensor is symmetric due to the conversion of torque. The index "k" in $G_{ij,k}$ means the spatial derivative of G_{ij} in the direction with the index k. We first consider the shearing and tearing strike-slip fracture modes. In case the normal to the fault plane is n = (0, 0, 1) and the mean slip vector u = (u_s, 0, 0), the moment tensor is with G the shear modulus and A the area of the fracture plane:

$$M = \begin{pmatrix} 0 & 0 & Gu_sA \\ 0 & 0 & 0 \\ Gu_sA & 0 & 0 \end{pmatrix} \tag{9}$$

In seismology this mechanism is known as the DC (double couple) seismic source. The scalar seismic moment of a DC is $M_0 = G\, u_s\, A$. This quantity is related to the magnitude by the following empirical relation (Hanks & Kanamori, 1979):

$$M_s = 1.5\mathrm{Log10}(M_0) - 9.1 \tag{10}$$

The seismic wave radiation pattern of most tectonic earthquakes can be explained by this source type. The DC is valid for strike-slip earthquakes at normal faults, reverse faults, and strike-slip faults. Comparable earthquakes on the slope-tectonic scale could happen in the scarp area and areas of longitudinal tension and compression. These slope tectonic earthquakes at the sliding surface could be an analog to the occurrence of earthquakes at low dip subduction zones. The overriding plate would correspond to the landslide mass. Gomberg *et al.* (2011) inferred the term "slidequake" for this type of earthquake expected and observed on landslide masses.

At different states in the development of a mass movement, especially during an early state, we expect that tensional fractures should also occur. The moment tensor of a tension crack, again occurring in a plane with the fault plane normal $n = (0, 0, 1)$, the mean displacement in the direction of the fault normal u_n, and λ the first Lamé constant are given by:

$$M = \begin{pmatrix} \lambda u_n A & 0 & 0 \\ 0 & \lambda u_n A & 0 \\ 0 & 0 & (\lambda+2G)u_n A \end{pmatrix} \tag{11}$$

The displacements in the far field of a seismic moment source are determined by the time derivative of the seismic moment (*e.g.*, Aki & Richards, 2002), therefore silent / continuous slip will not generate ground motion at distant observation points in an amplitude and frequency range observable by seismic instruments. In contrast to silent / continuous slip at fault and fracture zones, stick-slip behavior of the motion is an additional condition for the occurrence of tectonic and slop-tectonic earthquakes. For shear failures a drop of the static friction coefficient μ_s to a lower dynamic friction coefficient μ_d must occur.

In order to get an idea about the extent of low magnitude focal areas we use the expression for the scalar seismic moment $M_0 = G\, u_s\, a^2$ and Equation 10 to estimate the edge length, a, of quadratic focal areas for the magnitudes M = –3, –2, –1, 0. With conventional values for the shear modulus of compact rock $G = 30\ 10^9$ Pa, and taking the average slip along the focal area $u_s = 10^{-4}$ a, we get a = 0.24m, 0.74m, 2.4m, and 7.4m. Using $G = 1\ 10^9$ Pa, which is more appropriate for near surface layers we get a = 0,74m, 2.3m, 7.3m, and 23m.

3 SEISMIC MONITORING TECHNIQUES

3.1 Data acquisition

The frequency range of seismic signals generated by LMEs is in the range of 5 – 100 Hz (*e.g.* Spillmann *et al.*, 2007; Helmstetter & Garambois, 2010). For some special event types and at small epicentral distances this may reach up to ~150 Hz (*e.g.*, Walter *et al.*, 2012). Usually short period seismometers (natural frequencies 1 – 2 Hz) or geophones with natural frequencies of 4.5 – 10 Hz are used. The use of geophones with higher natural frequencies may be justifiable in special cases, especially if the geophones are mounted in boreholes. Generally, 3-component (3C) seismometers or geophones are

used, although sometimes only vertical (Z) geophones or a combination of both are used.

We cannot exclude that LMEs also generate signals with dominating periods above the amplitude maxima of the ubiquitous micro-seismic noise with spectral amplitude maxima at between 0.1 – 0.2 Hz (*e.g.*, Stein & Wysession, 2003). Broad band (BB) seismometers with natural periods above 20 s are adequate to record these seismic signals. Such BB seismometers have already been installed at some landslide monitoring sites. However, to the authors knowledge, LMEs with dominating frequency content below the micro-seismic noise have so far not been observed, therefore BB seismometers should be seen as a supplement to the short period seismometers and the substantially less expensive geophones because the instrument noise of BB seismometers exceeds that of geophones at higher frequencies.

A variety of single and multi-channel recorders suitable for the recording of LMEs are available on the geophysical market. Central multi-channel recording systems usually need long sensor cables that must be protected against electric lightning impulses. Modern seismic recorders have state of the art 24-Bit A/D conversion and sample rates of up to 1 KHz should be possible, however for most LMEs a sample rate of 200 Hz fulfills the conditions for correct sampling. Seismic data are stored on internal disks either continuously or as events fulfilling specific trigger criteria. The power supply is usually a 12V battery. For longer monitoring, the battery must be recharged by a photovoltaic system or a wind generator. The implementation of a seismic monitoring system into an early warning system is an important issue, in which case seismic data should be available in real time or at least near real time. For this to be realized, data transmission to a central server by a radio link or a router using the mobile network is required.

As an example of a well-documented seismic monitoring system (http://www.norsar.no/seismology/Projects/AKN/), we refer to the Åknes rockslide in Norway. A local seismic network has been operating on this unstable slope since 4th November 2005. It is equipped with 8 3C geophones (natural frequency 4.5 Hz), which are connected by cables to a locally installed 24-Bit recording unit. The recording unit operates in the event trigger mode with a sample rate of 125 Hz. Data are transmitted by radio link to the 13 km distant village of Hellesylt, and from there via a secure VPN connection to NORSAR. The latest data are visualized and available on the internet.

Different concepts for possible network geometries were realized during LME monitoring campaigns. The preference of one of these concepts was not determined by the scientific goal alone, but also by the available equipment, project budget, and duration of the monitoring campaign. Three different concepts have been realized in the past:

- **Standard micro-seismic network**: More than 3 stations equipped with 3C sensors are deployed more or less irregularly over the target area. The locations of the stations are selected mostly as a compromise between accessibility, favorable recording conditions, and the geometrical aspects of location methods. Additional deployment of sensors in boreholes or galleries improves LME detection and location substantially (*e.g.*, Spillmann *et al.*, 2007; Helmstetter & Garambois, 2010).

- **Clustering sensors in mini-arrays:** A minimum of 3 vertical sensors surround a central 3C sensor at distances of few to several tens of meters. The mutual distances of sensors within one mini-array are significantly lower than those to the center of another mini-array. (*e.g.*, Helmstetter & Garambois, 2010; Walter *et al.*, 2012).
- **Regular grid:** A large number of (vertical) sensors is deployed in a grid as regularly as possible under the constraints of the landslide morphology (*e.g.*, Sumgullion location; Gomberg *et al.*, 2011). A dense rectangular grid, which fulfills the requirements of correct special sampling (grid spacing < half wave length of seismic signal), represents the optimum from a theoretical point of view. However, because of its high technical effort it has not been utilized for long-term monitoring so far.

3.2 Event detection

STA/LTA event detection is a standard method based on the amplitudes of a seismic signal (Allen, 1978). STA is the short time average of the rectified amplitudes or the envelope, LTA the long term average of the same data. STA/LTA is also implemented as an event trigger method in recording systems. For example, at the Randa monitoring site STA and LTA durations of 0.04 s and 0.50 s has been set up. A STA/LTA = 40 threshold was set to trigger an 8s long record (Spillmann *et al.*, 2007).

Event detection based on STA/LTA can also be applied to continuously recorded data. Refined methods for the calculation of LTA, developed for general seismological purposes, can be applied. STA still represents an average of the envelope or the absolute amplitudes of the short time, but LTA can be defined more adaptively to the data with the following recursive formula (Schweitzer *et al.*, 2002):

$$\mathrm{LTA}(t) = a\mathrm{STA}(t - b) + (1 - a)\mathrm{LTA}(t - 1). \tag{12}$$

Parameter b is needed to prevent a too early influence of emergent signals on LTA. Parameter a controls the update rate of LTA with new data.

In order to detect low S/N events, the STA/LTA trigger level should be set quite low. This usually results in a large number of insignificant events. Setting a minimum number of stations in a LME network with simultaneous triggering effectively reduces the number of detections.

A refined detection of low S/N ratio signals can be achieved using / analyzing spectrograms instead of only traces. The spectrogram is the power spectral density computed in tapered time windows sliding over the seismic trace. Using this process, the 1D seismic trace x(t) can be expanded to a 2D representation S(f, t). Of course, this expansion is achieved only through a reduction of temporal resolution limited by the window length used for FT and the time step of successive windows. Joswig (1990, 1995) developed the algorithm for the transformation of a spectrogram to a sonogram, whereby a quasi-stationary noise level is subtracted from the spectrogram in order to enhance low amplitude seismic events (Figure 2).

Spectrograms, sonograms or, generally, spectrograms after logarithmic scaling and removal of a noise model can efficiently support interactive event detection by an expert or can also represent the starting point for automatic pattern recognition (*e.g.* Joswig, 1990, 1995; Spillmann *et al.*, 2007). The main steps of an automatic pattern

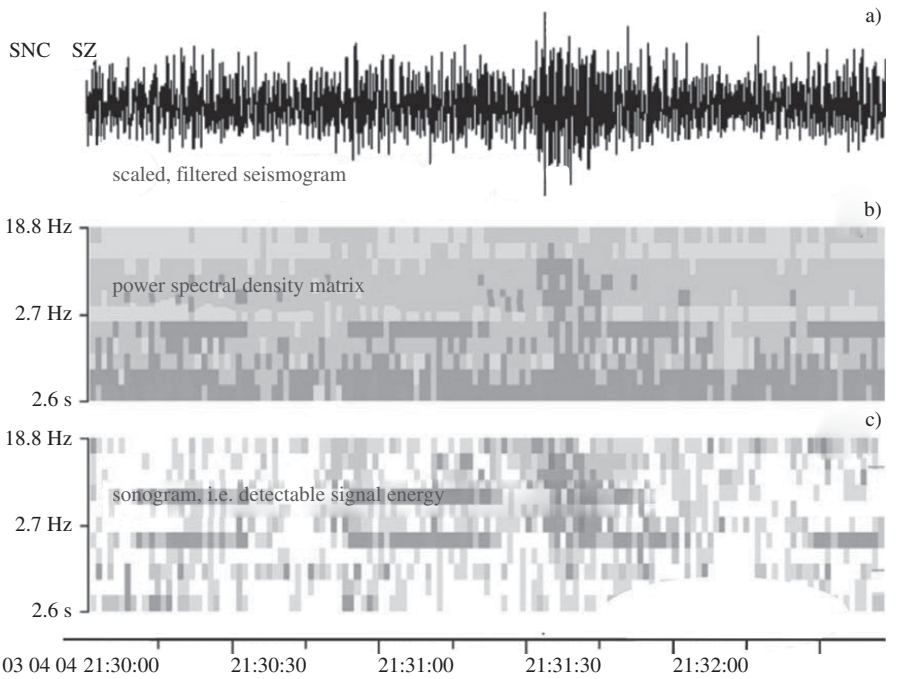


Figure 2 Transformation of a spectrogram to a sonogram (modified after Joswig, 2008); a) trace, b) spectrogram, c) sonogram.

recognition method (Mertl, 2015) using image processing tools extensively (*e.g.*, Gonzales *et al.*, 2004; Matlab Toolbox) are shown in Figure 3. The data are from the Gradenbach LME – monitoring site (see section 4.4).

Due to the sensitivity of the image processing method based on single trace spectrograms, a large number of events can be detected. Similarly to the STA/LTA method, the number of significant events can be effectively reduced if simultaneous detections are considered (Figure 4). "Simultaneous" infers that different travel times from possible source locations are taken into account.

3.3 Event screening

After event detection by STA/LTA or methods based on the analysis and processing of spectrograms or sonograms, events that do not represent signals from LMEs still remain and should be excluded from further evaluation. Detections of electronic noise usually have a very specific signature and should be identified by an expert. Earthquakes recorded by seismic observatories can be excluded by an inspection of the bulletins. Low magnitude local earthquakes (Figure 5a), quarry blasts or other natural or artificial seismic sources with comparable energy not reported by the bulletins could be identified in the recordings of a nearby seismic observatory, or an extra reference seismic station a few kilometers apart from the LME network. As a rule of thumb, all events with comparable (equal) or higher amplitudes on the reference

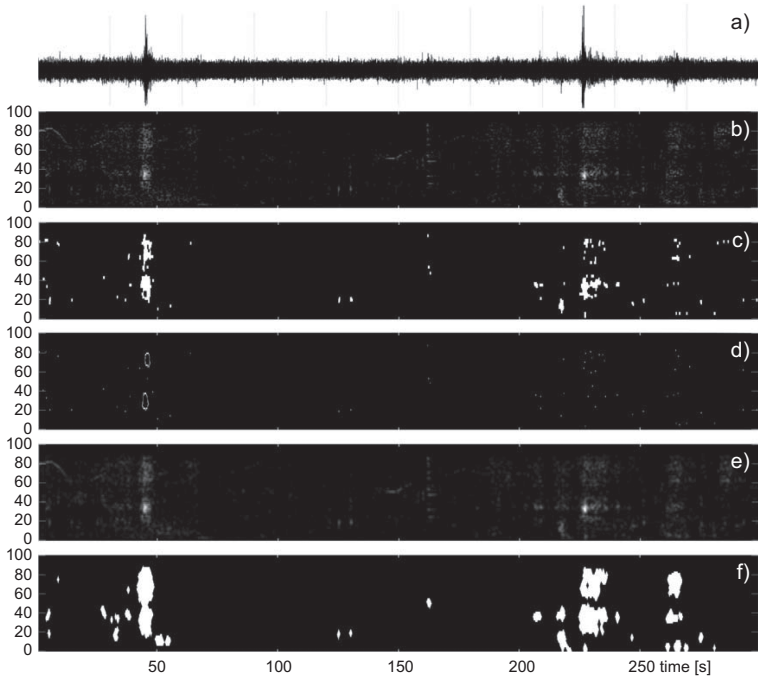


Figure 3 Processing of the spectrogram of a single trace (modified after Mertl, 2015).

a) trace;
b) spectrogram after logarithmic scaling and removal of the noise model;
c) after setting intensity to 1 or 0 by a defined threshold, and removal of speckle noise by the repeated application of the "opening" and "closing" process;
d) extraction of seed points or rings by "shrink";
e) 2D low pass filtered version of b), after contrast stretching in order to enhance contrast;
f) final pattern generated by "region growing" in e) starting from seed points and rings in d); the resulting binary image is further cleaned from speckle noise using "opening" and "closing".

station than on the stations installed on the mass movement can be excluded as LMEs generated by the monitored mass movement.

Another class of seismic events detected by the automatic procedure and to be excluded from further analysis is signals generated by atmospheric processes or transmitted mainly by air. The sources of these signals can be thunder (Figure 5a), an aircraft or helicopter (Figure 5b) or traffic on a nearby road (Figure 5c). Additional recording of sound pressure by a microphone effectively supports the identification of these events.

3.4 Location of seismic sources

3.4.1 Use of travel times

Standard earthquake location methods are based on the arrival times of seismic waves (P- or S-waves). The unknown focal coordinates are longitude and latitude (or X and Y) of the epicenter, the focal depth Z, and the focal time t0. These methods represent the

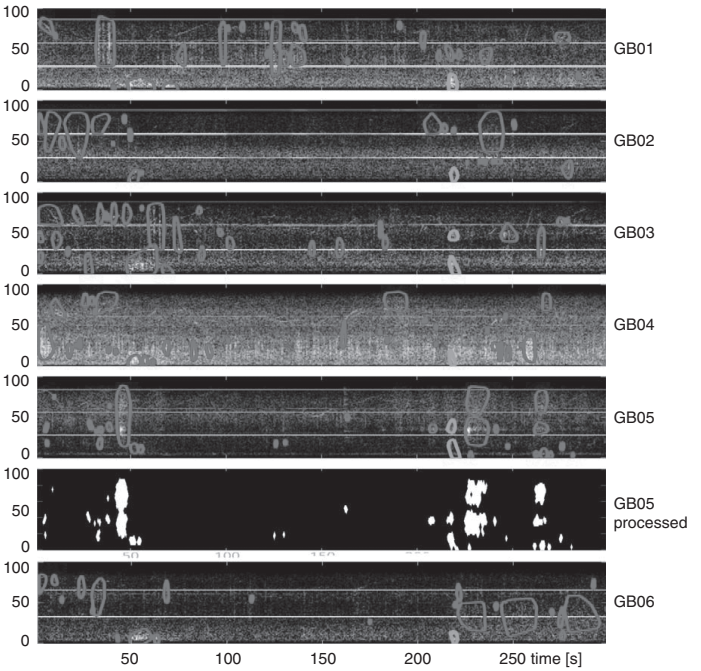


Figure 4 Figure 3f (GB05, processed) together with the corresponding results at all other stations on the Gradenbach DSGSD. The red polygons mark the extracted patterns on each station. The green polygons highlight the patterns which have been linked to a common event recorded on 6 stations GB01–GB06 (after Mertl, 2015).

optimization of an objective function where the arguments are the geometry of the seismic network, the observed arrival times of seismic waves, $tobs_i$, at the stations, and the calculated travel times, $tcalc_i$, from a hypothetical hypocenter (X, Y, Z, t0) to station i. Generally it is also possible to invert the parameters of the seismic structure in the area spanned by the sources (earthquakes) and receivers (seismic stations) simultaneously with the focal coordinates of individual earthquakes. Here we assume that either a seismic velocity model for the monitoring area already exists, or at best a reliable 3D model of Vp and Vs has been derived from a dense local seismic survey. Reliable travel times $tcalc_i$ for each seismic station with index i to all nodes of a closely spaced grid in the potential focal area can be calculated in advance.

The focal time t0 can be calculated from a weighted mean of all differences ($tobs_i - tcalc_i$) (Moser *et al.*, 1992). The most common objective functions, whose minimization or maximization allow for the determination of the other focal coordinates, are the L2 Norm (Equation 13) and the relative probability density function PDF(X, Y, Z) (Equation 14), which is based on Bayesian statistics (Tarantola & Valette, 1982).

$$L2(X,Y,Z) = \sum (tobs_i - tcalc_i - t0)^2/\sigma_i^2 \tag{13}$$

$$PDF(X,Y,Z) \approx \exp\left[-1/2 \sum (tobs_i - tcalc_i - t0)^2/\sigma_i^2\right] \tag{14}$$

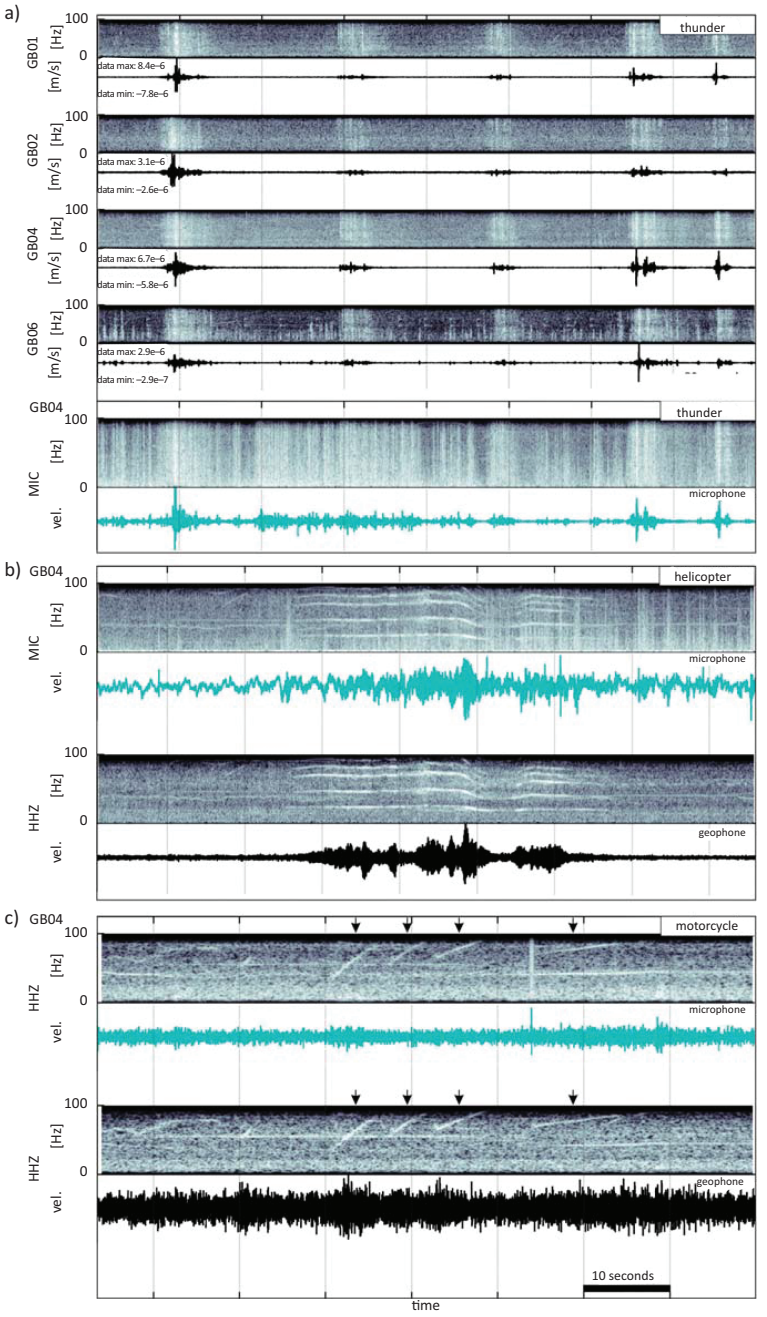


Figure 5 Seismic signals recorded at the Gradenbach DSGSD and excluded from further analysis (after Mertl, 2015).

a) Thunder: spectrograms and traces of the data from the Z-geophones at stations GB01, GB02, GB04, GB06, on top, black; spectrogram and trace of the data from the microphone at station GB04, on bottom, turquoise;

b) Helicopter: spectrogram and trace of the data from the microphone at station GB04, on top, turquoise; spectrogram and trace of the data from the Z-geophones at stations GB04, GB02, GB04, GB06, on bottom, black;

c) Motorcycle: spectrogram and trace of the data from the microphone at station GB04, on top, turquoise; spectrogram and trace of the data from the Z-geophones at stations GB04, GB02, GB04, GB06, on bottom, black.

The sum Σ is over all stations i. The standard deviations σ_i take the uncertainties of $tobs_i$ and $tcalc_i$ into consideration.

Both methods assume a Gaussian error distribution and are sensitive to outliers in variable $tobs_i$. The use of the L1 Norm could make solutions more robust. Another path was taken by Joswig (2008) with the introduction of so-called nanoseismic monitoring. This method aims to achieve reliable location of earthquakes by making recordings with a S/N near to 1. The total dataset is subdivided into subsets that define a mathematically exact solution. Using this procedure and with support from an instructive GUI, an expert can instantaneously check the reliability of individual travel time picks. This method would preferentially be applied to mini-arrays with 4 – 6 stations.

3.4.2 Beam forming

Some minimum quality of P- or S-wave arrivals must be guaranteed for reliable travel time picking, which is a precondition for the application of location based on arrival times. This precondition is frequently not fulfilled for the signals generated by LMEs. This is not only caused by a low S/N but is also due to the emergent character of the signal strength, in which P- and S-waves cannot be distinctly identified. Beam forming is a method that allows for a location without the necessity of travel time picking, and it can be applied to the data of one array or mini-array. It is assumed that the distance to the epicenter significantly exceeds the dimensions of the array. By beam forming, the back azimuth to the epicenter (direction from the array center to the epicenter) can be determined. The epicenter may be determined using the intersection of beams derived from separate arrays. Further information that can be obtained by beam forming is the apparent slowness of the dominant seismic waves. In case the epicenter distance is not large compared to the dimensions of the array, the curvature of incident wavefronts could be used to gain information on the epicenter distance (Almendros *et al.*, 1999).

In the following we review beam forming under the assumption of a homogeneous medium below the array and incident plane waves. Figure 6 shows the geometry of an array and the incident plane wave in map view and along a vertical section of the ray path through the center of the array. The incident plane wave is defined by the constant ray vector [sx0, sy0, sz0]. This vector has the direction of the tangential vector of the ray and the magnitude of the slowness s=1/v0, with v0 the velocity of the seismic wave.

$$[sx0,\ sy0,\ sz0] = 1/v0[tx0,\ ty0,\ tz0] \tag{15}$$

The extent of the array is usually small compared to the epicentral distance and we expect the waveform of the seismic signal to be the same at all sensor locations, but with time shifts taking into account the different travel distances. Thus the signals w_i at the different stations i of the array can be described by Equation 16, where $\boldsymbol{s0}$ is the ray vector, $\boldsymbol{r}_i$ the position vector and w(t) the waveform at the origin of the local coordinate system.

$$w_i(t + s0 * r_i) = w(t). \tag{16}$$

Beam forming is performed by the application of phase corrections with varying ray vectors s, stacking all traces after phase correction and calculation of the power $E_{beam}(s)$ according to Equation 17

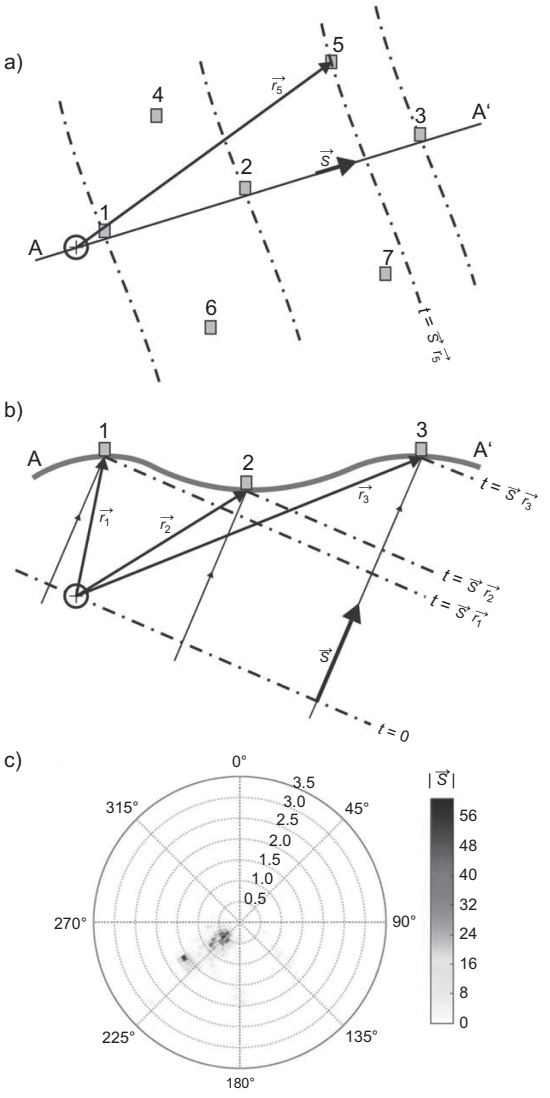


Figure 6 Beam forming: plane wave front arriving at a mini-array; a) map view; b) vertical section along A – Á; c) polar diagram of beam energy $E_{beam}(\boldsymbol{s})$; 1 – 7… seismometers, $\boldsymbol{r}_i$… location vectors, $\boldsymbol{s}$…slowness vector (projected in a)), dash-dot lines represent wave fronts, thin straight lines in b) represent rays.

$$E_{beam}(s) = 1/N * \int \left[\sum w_i(t + (s0 - s) * r_i)\right]^2 dt \tag{17}$$

E_{beam} has a maximum for s = s0, because for this case all time shifted waveforms are in phase. The location of this maximum defines direction and magnitude of the incident ray vector. Besides the formulation of beam forming in the (x, y, z, t), space beam forming can also be applied in the wavenumber – frequency domain (*e.g.*, Schweitzer

et al., 2002). In the case where all sensors are coplanar, the determination of s0 is reduced to the determination of the component of the ray vector in this plane. The result can be presented in an azimuth – slowness diagram (Figure 6c)

In case the mini-array contains also one 3C-geophone or seismometer, the analysis of particle motion and a polarization analysis can further constrain the azimuth of the incoming wave and provide information about the wave type.

3.4.3 Use of amplitudes

Since the introduction of an intensity scale by Mercalli, isoseismal maps have been derived from macro-seismic observations, which allow for a reliable determination of the epicenter and can even achieve estimates of the focal depth. This method can also be applied to instrumental data on ground motion, using general or locally valid amplitude – distance relations for seismic waves. Kanamori (1993) used accelerometer data and a peak acceleration – distance relation to fit the data recorded during earthquakes at or near the San Andreas Fault. He used a least squares method to determine magnitude and epicenter location, and emphasizes the simplicity of the method, the ability for real time applications, and the reasonable accuracy that could be achieved.

Kanamori's method can be adapted to the location of LMEs in a straight-forward manner. Different from Kanamori's method, we consider ground velocity instead of ground acceleration. Analog to the definition of the local magnitude M_L we define pseudo-magnitudes derived from the recordings of individual seismic stations in a local grid according to Equation 18.

$$\mathrm{pseudoM}^{k}_{i,j} = \log10\left(A^{k}\right) + n\ \log10\left(\Delta^{k}_{i,j}\right) + C^{k} \tag{18}$$

$\mathrm{pseudoM}^{k}_{i,j}$ … pseudo magnitude derived from station k for grid point (i, j)

A^{k} …amplitude observed at station k (*e.g.*, maximum value of the resultant ground velocity in a selected time window)

n …exponent of an amplitude – distance power law

$\Delta^{k}_{i,j}$ …hypocentral distance from station k to grid point (i, j)

C^{k} …correction for station k considering local coupling to ground

The distance term of Equation 18 can be pre-calculated for a local network on a mass movement. The exponent n can be taken from M_L definitions or derived from LMEs located by other methods or controlled source experiments on the mass movement of interest. Of course, apart from power law amplitude – distance relations, other relations can be used. In order to account for local seismometer coupling to ground stations, corrections C_k should be applied. They are usually considered constant for all LMEs. Local earthquakes (*e.g.*, in the epicenter distance range 10–100 km) may have roughly the same frequency content as LMEs. Differences in the amplitude – distance correction are negligible for these local earthquakes and station corrections C_k can be derived from the observed amplitudes.

Pseudo-magnitudes $M^{k}_{i,j}$ back-projected from the stations k to the grid points (i, j) can be calculated from one LME. The minimum standard deviation of all pseudo-magnitudes defines the grid point closest to the epicenter.

3.5 Magnitude

3.5.1 Moment magnitude

The moment magnitude Mw is related to the seismic moment M_0 by Equation 19, and M_0 can be estimated from the long-period amplitude determined from the displacement spectra of isolated P-waves Ω_0 according to Equation 20 (Hanks & Kanamori, 1979).

$$M_w = 2/3 \quad LOG10(M_0) - 6.06 \quad [\text{SI units}] \tag{19}$$

$$M_0 = 4\pi\rho Vp^3 R\Omega_0/Up \tag{20}$$

The other parameters in Equation 20 are ρ the density, Vp the P-wave velocity, R the hypocenter distance, and Up = 0.52, a correction for the mean radiation pattern of P waves (*e.g.*, Aki & Richards, 1980). An equivalent equation exists for S waves. The factor R in Equation 20 only compensates for geometrical spreading, and other processes reducing the amplitudes with distance are not taken into account.

The low frequency spectral amplitude Ω_0 must be determined from the P-waveform alone, therefore the derivation of magnitudes from seismic moment can only be applied to impulsive waveforms that allow for a separation of the P-wave (or S-wave) phase from other overlapping phases.

3.5.2 Local magnitude M_L

Networks deployed on landslides also provide a further opportunity to record local earthquakes recorded by nearby seismic observatories. This offers the opportunity to calibrate magnitudes derived from data recorded at the landslide with local magnitudes M_L provided by the national seismic services. For example, the Austrian seismological service can calculate M_L using Equation 18, with A the maximum value of horizontal components [nanom/s], bandpass 1 – 10 Hz, the exponent in amplitude-distance power relation n = 1.66, Δ the epicenter distance [degree], and C= –0.304.

The value of exponent n in the amplitude-distance power relation for different ranges of epicenter distances presents an issue. Beyond 10km epicenter distance, a value of n ~ 1.6 relies on the experiences of the national seismological services. For epicenter distances in the range of the network dimensions, the exponent n could be derived from seismic data recorded at the landslide. Wust-Bloch & Joswig (2006) found that for epicenter distances R < 1km an exponent n=1 is appropriate, while the epicenter range ~1km < D < ~10 km remains experimentally indefinite. They pragmatically assume a change from n =1.6 to n=1.0 at a distance of 3km.

3.6 Noise monitoring

Seismic noise observed at a mass movement may not only be ground motion induced by external sources, as discussed in section 3.3. Seismic noise can also be caused by frequent LMEs below the detection level of individual events. McNamara & Buland (2004) used the power spectral density (PSD) to quantify the background noise at seismic observatories in the USA. This quantity can be calculated automatically and in

real time, which means it can be easily implemented into a permanent seismic monitoring system.

Given a time series x_j (j = 0 … N–1; N … number of samples, even), the power spectral density PSD_k for the frequency f_k is defined as follows:

$$f_k = k/N\Delta t \qquad k = 1\ldots N/2 - 1;\ \Delta t\ldots\text{sample interval} \tag{21}$$

$$X_k = \sum X_j \exp(-i2\pi jk/N) \quad \text{summation } j = 0 \ldots N - 1 \tag{22}$$

$$PSD_k = 2\Delta t/N\,|X_k|^2 \tag{23}$$

The number of samples used for the FFT, the window function, and the amount of overlap of successive windows determine the calculation of the PSD. A factor compensates for the weighting of the data within one window (*e.g.* cosine window). To make different sensor and recording systems comparable, the frequency response must be compensated for. Furthermore, whether the PSD is calculated for ground acceleration, velocity or displacement must be taken into consideration.

Figure 7a shows the PSD of a one week recording with a 4.5 Hz vertical geophone and 24-Bit recording system at the Gradenbach mass movement (see chapter 4.4). The window length for the PSD computation was 300 seconds with a 50% overlap. The number of spectral bins used for the FFT was 8192. This leads to spectrogram images containing 576 spectra per day. The daily variation of the noise due to nearby traffic, narrow frequency band noise probably generated by PV power supply, and the increase of noise below 0.5 Hz due to micro-seismic noise and the limitations of frequency compensation of the 4.5 Hz geophone can clearly be identified. The distinct low frequency burst in the second half of the time window was generated by a regional

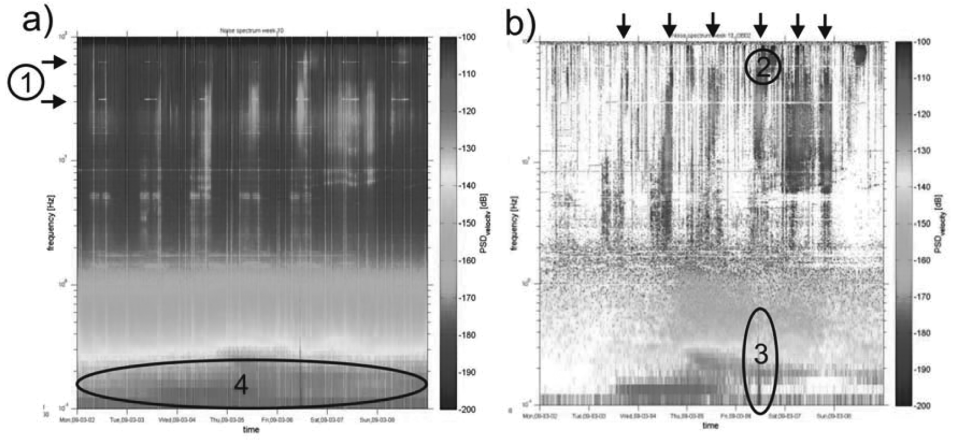


Figure 7 Ambient noise recording at the Gradenbach DSGSD; a) PSD (Power spectral density) for week 10, 2009; b) Enhancement of the ambient seismic noise pattern shown in a) by the removal of the average daily noise from the spectrograms; 1… electronic noise induced by PV power supply, 2… variations in daily noise, 3… regional earthquake, 4… microseismic noise + electronic / digital noise at low frequencies due to imperfect frequency compensation of 4.5 Hz geophone (after Draxler, 2013).

earthquake. To better highlight the patterns that stand out against the general ambient seismic noise, the average daily noise for each week was computed and removed from the spectrograms, resulting in differential PSDs highlighting daily and irregular variations from the general ambient seismic noise (Figure 7b).

4 SEISMIC SIGNALS FROM DIFFERENT LANDSLIDE TYPES

We expect that different mass movements or landslide types exhibit different patterns of seismic activity. There are several well established landslide classification schemes (*e.g.*, Cruden & Varnes, 1996). Distinctive features are among others geometry, material (rock or soil), velocity, and failure mechanism. In this essay we will generally maintain these classifications, however we will attempt to group mass movements in a way that may be associated with typical patterns of seismic activity. Although the Mohr-Coulomb failure criterion does not determine the ultimate stability of all failure mechanisms, we take the ratio of the average slope angle to the effective angle of friction (either peak or residual) as a characteristic parameter of a mass movement with respect to its temporal evolution and, possibly, to its seismic activity.

Figure 8 shows a schematic diagram of the average displacement over time of different types of mass movements. This diagram has some similarity to the concept of primary, secondary, and tertiary creep with a transition to ultimate failure. We allocate 3 groups of mass movements or landslides to the displacement – time diagram, which we describe in the following.

The first group represents **pre- and post-failure processes on steep slopes** (referred to in the following as "**steep slopes**"). Under the term "steep" we consider a mountain slope steeper than the effective angle of friction or, as a proxy, the inclination of talus built up by the same rock material. Cohesion is needed to balance the gravitational forces along a potential sliding surface steeper than the angle of effective internal friction. In the case of cohesion dropping to zero after a process of progressive damage, the slope will immediately transit to dynamic failure. Besides stick-slip processes along discontinuities, we also expect tensional crack initiation and growth as possible seismic

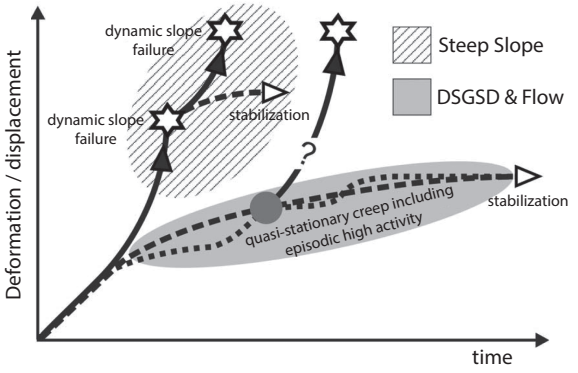


Figure 8 Schematic deformation / displacement – distance diagrams for instable steep slopes, DSGSD, and flow-type mass movements.

sources. As indicated in Figure 8, the slope remaining after a major rockslide may still be termed a steep slope, which either trends toward stabilization during a period of stress relaxation or further progressive failure leading to the next major rockslide.

As a second group of active landslides with potential seismic activity, we consider **deep-seated gravitational slope deformation (DSGSD)**. DSGSD is a phenomenon frequently observed in the hard rock slopes of the alpine regions (*e.g.*, Bisci *et al.*, 1996). Typically the deformation comprises the whole flank of a valley with ~1000 m difference in elevation. The maximum thickness of the deformed rock mass usually exceeds 100m, and the total volume may significantly exceed 0.1 km^3.The average slope of the DSGSD examples we are going to present in section 4.3 varies between 27° and 37°. Other examples from the Austro Alpine nappes of the Eastern Alps show inclinations of ~28° (Brückl & Parotidis, 2005). There is no example where the average inclination exceeds that of the local talus.

The term DSGSD covers manifold deformation styles and failure processes. "Bergzerreißung", "Talzuschub", sagging or Sackung (Zischinsky, 1969) and kink band slumping (Goodman & Kieffer, 2000; Preh & Poisel, 2004) can be summarized under DSGSD. For most slopes affected by DSGSD, the retreat of the ice age glaciers around 15000 years ago (*e.g.*, van Husen & Reitner, 2011) and as a consequence the loss of lateral support by the ice pressure is considered to be the initiation of the slope instability (*e.g.*, Prager *et al.*, 2008). However, this conception implies a long initial phase of the mass movement, during which progressive damage degrades the rock strength almost to its residual value (*e.g.*, Brückl & Parotidis, 2005), because many DSGSDs are still active today, or even exhibit the most significant displacements in historic times.

Although elements of the original rock structure are still preserved in a DSGSD, damage to the rock mass affects the whole landslide mass and is not only concentrated in isolated deformation zones. Evidence for this conclusion comes, among other things, from seismic data on several DSGSD in the European Eastern Alps that suggest a general power law for the increase of Vp with depth (Brückl & Parotidis, 2005), given by Equation 24.

$$V_p = V_{1m} * D^n \tag{24}$$

V_{1m} is V_p at 1m depth and varies between 394 m/s and 523 m/s. The exponent n varies between 0.26 and 0.46 at the four DSGSDs Brückl & Parotidis (2005) investigated.

According to the time – deformation diagram (Figure 8), active DSGSDs may deform or slide by stationary creep with velocities of some mm/year to cm/year or undergo episodic high deformation rates in parts of the slope or its entirety, which may reach velocities of up to tens of mm/d.

Large **flow** –type mass movements cover a wide range of their longitudinal extent and total volume. Their width is usually bounded by the cross-section of the valley. The flow-type mass movements are fed from a steep scarp area. The average inclination of the actual flow is lower than that of a DSGSD, usually significantly lower. Flow may overlap in the qualitative displacement – time diagram (Figure 8) with DSGSD but it does not evolve from DSGSD.

The flow-type mass movements we are going to present here started in historic times. Even though they occur in areas glaciated during the ice age, their initiation does not date back to the retreat of the ice age glaciers. In a further contrast to DSGSD, the original rock

structure is completely destroyed and brittle rock material has been transformed to loose rock or granular soil. On a large scale, the deformation style suggests plastic or viscous behavior, so at a first glance one would not expect seismic activity at flow-type landslides.

Displacement rates of flows exceed those of DSGSD significantly. Flow-type landslides exhibit steady movements that are modulated, most likely by the pore pressure in the landslide mass and at the basal sliding surface / zone. Evidence for triggering via the daily variations in air pressure has also been provided for (Schulz *et al*., 2009a). We cannot exclude that exceptionally high percolation of rain and / or melt water, erosion in the toe area, or accumulation of material in the source area can result in a catastrophic acceleration.

In this essay we are going to present one example of seismic activity of a steep slope, three examples of a DSGSD, and two examples of flow-type mass movements, five of which are from the European Alps and one from the Rocky Mountains (Figure 9). Pre- and post-failure processes on steep slopes, DSGSD, and flow differ significantly with respect to their geometry. Figure 10 shows a) cross plots of the average slope inclination α, and b) the ratio of average vertical thickness H to the horizontal extent L in the direction of the slope gradient over the ratio of the average displacement D to H.

Rockfall is a common phenomenon occurring on steep slopes and DSGSDs. It can also occur on parts of a flow-type mass movement if the inclination locally exceeds the

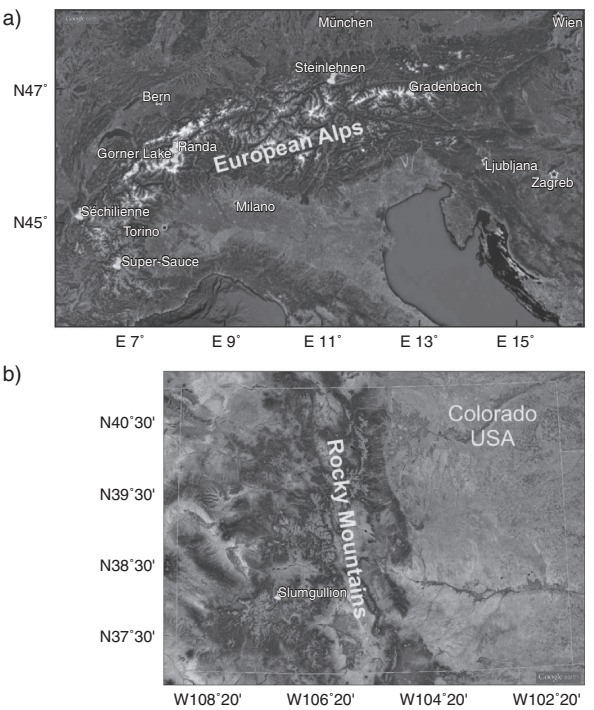


Figure 9 Location maps landslide examples presented; a) Randa, Séchillienne, Steinlehnen, Gradenbach, and Super Sauce, European Alps; b) Slumgullion, Rocky Mountains.

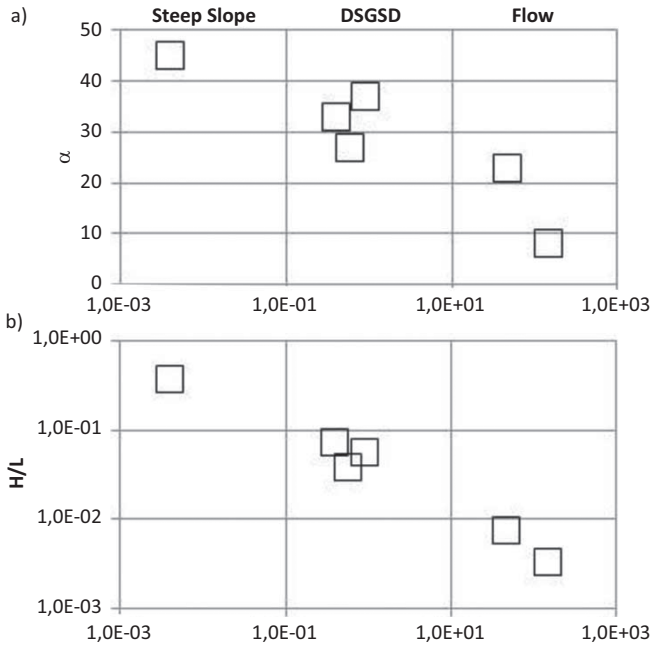


Figure 10 Characteristic geometric quantities of landslide examples presented. a) α over D/H; b) H/L over D/H; α… average surface inclination, D…average displacement of center of mass, H… average thickness of the landslide.

slope of talus. Even if it is not, per se, a large landslide, it is frequently associated with the movement and particularly the acceleration phases of large landslides. With this in mind we start in section 4.1 with a short presentation of typical seismic patterns associated with rockfall. In the following sections 4.2 – 4.4 we present examples of seismic activity on steep slopes, DSGSDs, and flow-type landslides.

4.1 Rockfall

The term rockfall covers a wide range of rock volume. For safety reasons, even rock volumes <0.001 m^3 may be of interest and monitoring systems have been developed by the consulting companies (*e.g.*, Collins *et al.*, 2014). At the upper limit, volumes of up to 10^4 m^3 or 10^5 m^3 (*e.g.*, Hungr *et al.*, 2001) are designated as rockfall. The seismic characteristics of these larger volumes were studied *e.g.* by Deparis *et al.* (2008) using recordings of a regional network. Here we restrict ourselves to rockfalls, which accompany the movements of a large landslide. Volumes may be in the range of several m^3 but also significantly less. These rockfalls may be the consequence of chemical weathering, freezing and thawing, high precipitation, but could also be an indication of increased activity in a landslide.

Based on the rockfall observations made at the Super-Sauce mudflow, Walter *et al.* (2012) differentiated between rockfalls built by one single or a few boulders jumping down the slope and rockfalls that resemble a small rock avalanche. A well documented example of the first type was observed at the Gradenbach DSGSD (Brückl *et al.*, 2013), as shown in Figure 11. The seismic signature is an irregular sequence of impulsive

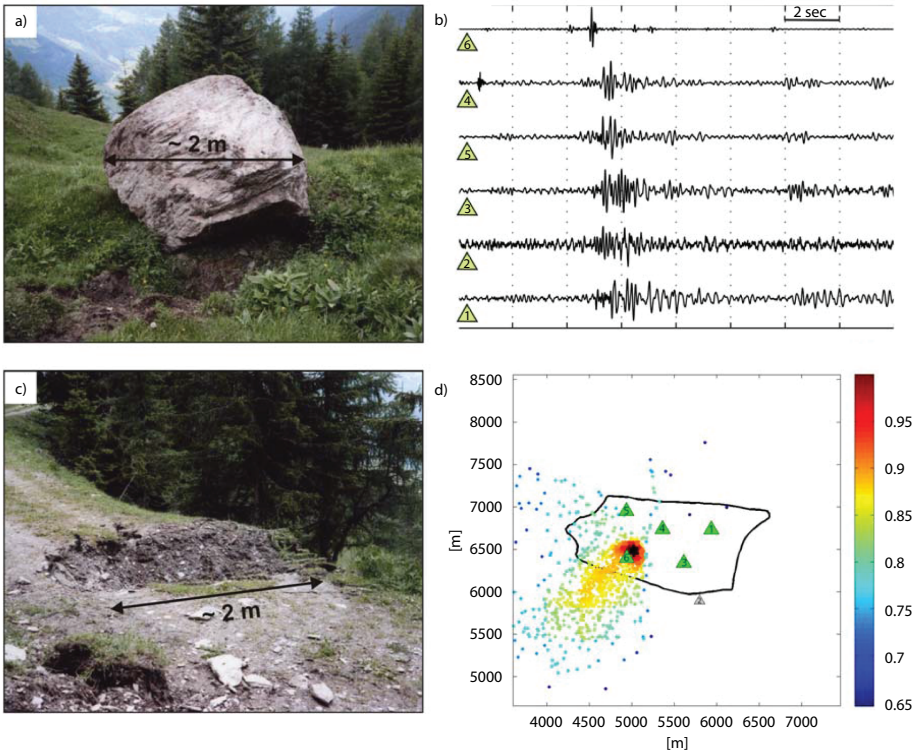


Figure 11 Single bolder rockfall at the Gradenbach DSGSD; a) the bolder; b) seismic records; c) effect of the strongest impact to the ground; d) seismic network and location of the strongest impact on ground by the use of first arrival times (Brückl *et al.*, 2013).

signals moving down the slope. The strongest impact could be well located by the use of first arrival times and the epicenter agrees well with the location of the main impact. The boulder had a diameter of roughly 2m.

As a second example, we present a rockfall at Steinlehnen (Figure 12) observed both by the local seismic network and ground based InSAR (Weginger, 2012). This rockfall belongs to the avalanche type rockfall. It lasted around 30s and showed a more continuous seismic signature. The path of this rockfall was traced by the InSAR images as well as by the seismic data when applying the amplitude location technique. There is fair agreement between both tracing methods.

4.2 Post-or pre-failure seismic activity on a steep rock slope

On the 18th April and 9th May 1991, two successive rockslides took place near **Randa** in the Matter Valley, Swiss Alps (for location see Figure 9). The failure volumes involved rock masses of about 20 and 10 10^6 m^3 respectively, which dropped on average between 400 and 600 m. These events produced Ms 4.9 and 4.8 earthquakes recorded by seismic stations on a global scale (Eckström & Stark, 2013).The rock-slide occurred in massive Para- and Orthogneiss (Eberhardt *et al.*, 2004) of the

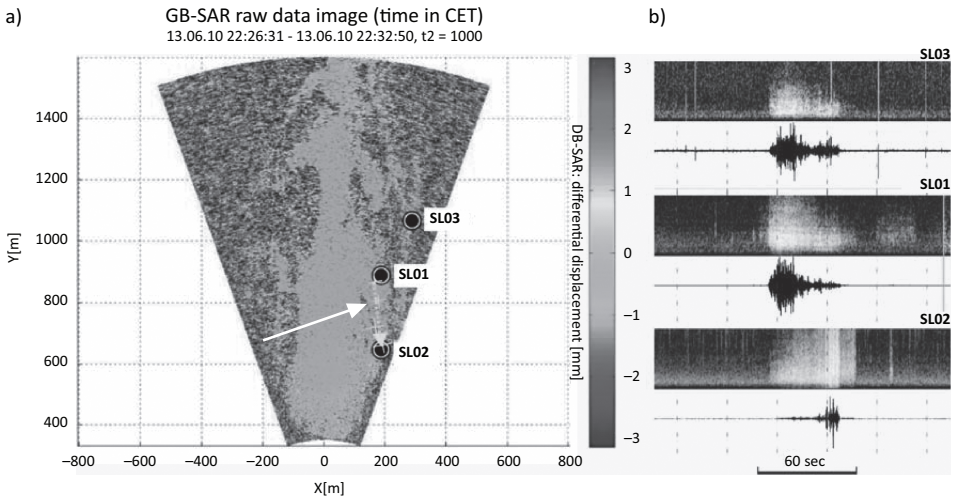


Figure 12 Avalanche type rockfall observed by the seismic network and GB-SAR on the Steinlehnen DSGSD (after Weginger, 2012); a) GB-SAR interferogram showing the trace of the avalanche-type rockfall (black arrow), the location of the seismic stations SL01, SL02, SL03, and the trace of the avalanche-type rockfall as determined from the seismic data (white crosses and arrow): b) spectrograms and traces recorded at SL01, SL02, SL03.

Penninic nappes of the Valais. The average gradients of the slope before the rockfalls was about 60° and 50°, thus significantly higher than the angle of internal friction. The foliation dipped about 20° into slope favorable for stability. The rupture surface developed along a combination of ~45° and ~75° downslope dipping discontinuities. The failure process could have initiated through the development of tensile rock mass damage following deglaciation.

The area behind the main scarp of the second large rockslide represents a steep slope. It could either be an area of stress relaxation and stabilization over a longer period, or could be in preparation of a third rockslide in geologically short times. For this reason the fracture system of the slope above the actual scarp was extensively explored using aerial photography, mapping of outcrops, and 3 boreholes. Based on optical televiewing, geophysical logs and borehole radar data geology, the major fracture and fault system was mapped down to a depth of 75 m (Willenberg, 2004; Eberhardt *et al.*, 2004; Spillmann *et al.*, 2007). Deformation of the slope above the actual scarp continued after the rockfall sequence of the year 1991 with ~10–20 mm/year (2004–2008). An annual variation of the deformation observed by crack extensometers and inclinometers has been superimposed on this trend. The downslope dip of the velocity vectors is around 30° and significantly lower than a potential sliding plane of a third rock fall. The deformation could be related to deep-reaching thermo-mechanical processes (Gischig *et al.*, 2011). At present it cannot be predicted if the ongoing movements will lead to stabilization of the rock mass behind the actual scarp, or if it will turn into a progressive failure and a third catastrophic rockfall event. The volume of a potential third rockfall is estimated to be about 6 10^6 m^3.

Seismic monitoring of an area of roughly 25 10^3 m^2 above the actual scarp was carried out from January 2002 to July 2004 (Spillmann *et al.*, 2007). Figure 13 provides

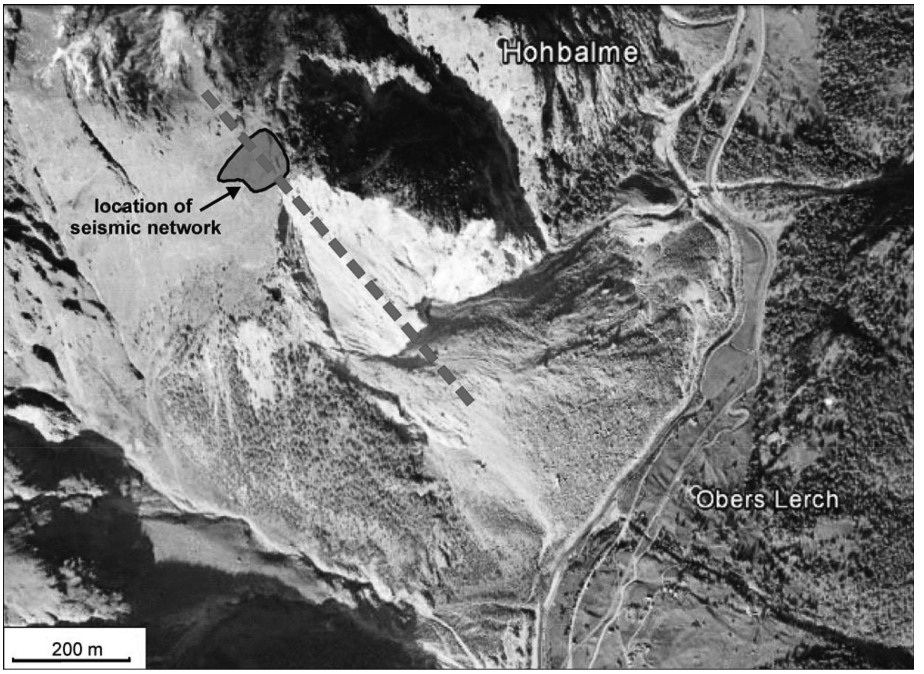


Figure 13 Overview of the Randa unstable steep slope; dotted line represents the vertical profile shown in Figure 15.

a view looking toward the monitoring site. The seismic network included nine 3C geophones (8 Hz) deployed in shallow pits or holes and three 3C borehole geophones (28 Hz) mounted in three boreholes at depths between 42 m and 114 m. The geophones were connected by cables to a central 24-bit recording unit, which was powered by solar panels and a wind generator. The recording system operated in the event trigger mode, with 8000 Hz sample rate. Data were stored temporarily on an on-site computer and then transferred to a PC in the valley and transmitted to the processing laboratory.

A total of 66 409 events were recorded. Data screening with identification of transients, recognition of sonogram patterns and manual classification reduced this large number to 223 events classified as LMEs or micro-earthquakes. The LMEs were then classified into two groups based on the duration and amplitude – time characteristics of the waveforms, namely single events and multiple events. 42% of the observed waveforms were single events with waveforms comparable to the recordings of small detonations with durations no longer than ~1sec. The rest were classified as multiple events with a more complex source time function. Frequency content of the signals above the background noise reached up to 100 Hz for the surface sensors and up to 200 Hz for the borehole sensors (Figure 14).

The rather impulsive source functions and the good S/N ratios allowed for accurate first arrival travel time picking. A 3D seismic refraction survey utilizing the data from the local seismic network in addition was carried out in order to generate a high resolution P-wave velocity model. On the basis of this velocity model and the high

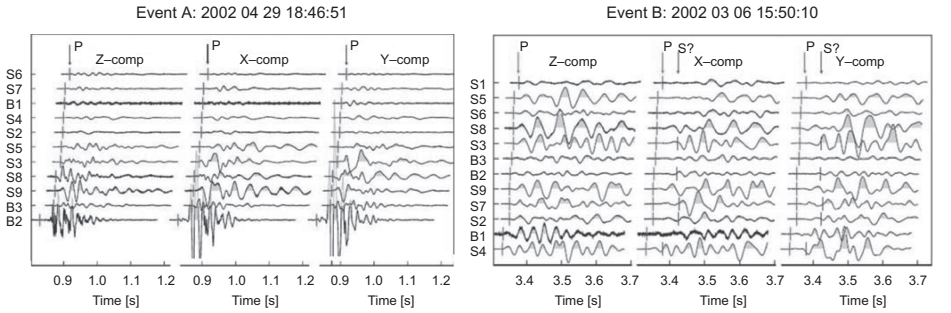


Figure 14 LME waveforms recorded at the Randa unstable steep slope (after Spillmann *et al.*, 2007).

quality first arrival travel times, accurate determination of hypocenters was possible. The determination of the focal depths benefitted substantially from the data of the borehole geophones. Figure 15 shows the cumulative PDF of the different hypocenters in longitudinal cross section. Most of the seismic activity is concentrated in the surficial zone of low P-wave velocities (< 1500 m/s) and intensive fracturing, however increased seismicity also reaches far along a steeply dipping zone, which could possibly outline the scarp of a future rock slide.

Neither snow melt nor high precipitation had an impact on the seismic activity. This is no surprise as the top 40 m of the three boreholes were usually dry.

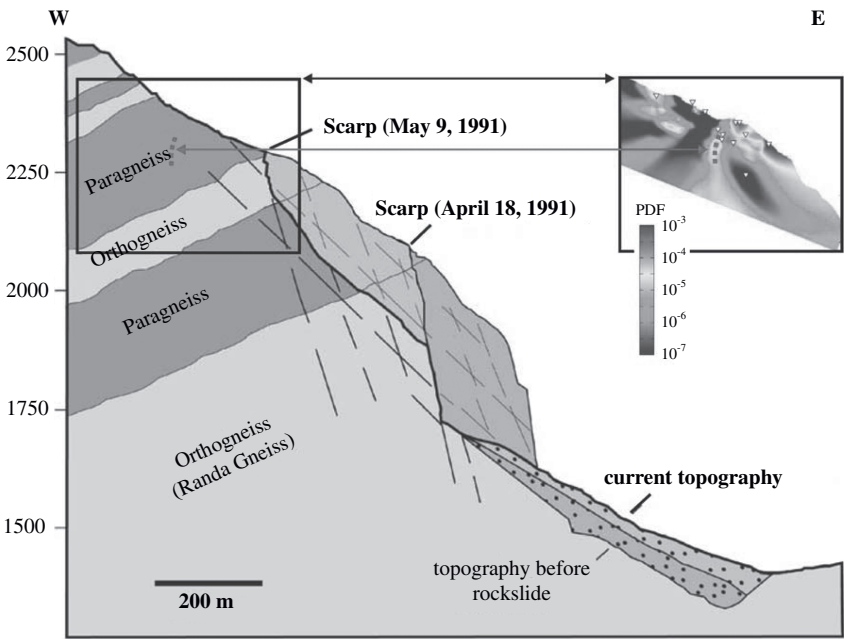


Figure 15 Geological cross section of the Randa unstable steep slope (after Eberhardt *et al.*, 2004); cumulative PDF of hypocenters (Spillmann *et al.*, 2007) shown in insert; dotted line (red arrow) marks possible next scarp.

Seismic moments were derived from P-wave arrivals using Equation 20, and the magnitudes were calculated using Equation 19 Most magnitudes were in the range -2.0 < Mw < 0.5. During 2002, the monthly rate of micro-earthquakes reached 23-25, whereas in 2004 this rate did not exceed 7. Only long term seismic and geodetic observations could affirm that this reduction can be correctly interpreted as a post-failure relaxation process and exclude the possibility that the present scarp area is in an initial phase of a third large rockslide.

4.3 DSGD – deep seated gravitational slope deformation

As a first example, we look at the **Séchilienne** DSGSD (Helmstetter & Garambois, 2010) located in the Belledonne Massif of the French Alps (Figure 9). The slope mainly consists of mica-schists with interbedded quartz-feldspar-rich layers. At the top, between an elevation of 1030 – 1110 m, the DSGSD is delimited by a 20 – 40 m high scarp. The toe at the valley floor is at 330m. The lateral extent of the DSGSD is not clearly defined and the area is estimated to be between 0.5 -1.0 km^2. A 240 m long gallery was driven into the DSGSD landslide in its central part. A succession of rigid block movements and normal faulting was observed but a basal sliding surface or zone was not explored. The maximum depth of the DSGSD likely exceeds 150 m. Cosmic ray exposure dating applied to the rock of the main scarp supports the theory of an initiation of the Séchilienne DSGSD processes caused by the retreat of the ice age glacier (Le Roux *et al.*, 2009).

The slope of the Séchilienne DSGSD is divided into a more gentle upper part and a steeper lower part but is on average about 33°. A presently very active zone comprising 3 – 5 million m^3 is located on top of the steeper part of the slope (Figure 16). The velocity of the active zone reached 1.4 m/year in 2008, about twice the value of 2000. This highly active zone has been the main target of seismic monitoring in the Séchilienne DSGSD (Helmstetter & Garambois, 2010).

The installation of a seismic network at the Séchilienne DSGSD started in May 2007 with the deployment of two mini-arrays (THE and RUI in Figure 16). These mini-arrays consisted of one 3C 2Hz geophone and six vertical 2Hz geophones installed in a typical distance around the central 3C geophone. The geophones were later replaced by 0.05 Hz seismometers. In addition, 21 vertical 4.5 Hz geophones and one 3C 4.5 Hz station were deployed in the 240 m long gallery with a station interval of 20 m, including an area outside the gallery portal. The data acquisition has been operating with a sampling rate of 500 Hz since April 2008.

Since the installation in May 2007, several thousand events have been recorded. Semi-automatic software was developed to detect and separate LMEs from local or regional earthquakes and industrial or natural noise. Normalized spectrograms of the data from all sensors of one mini-array were stacked in the frequency range 1 – 50Hz. An event was identified when the stacked amplitude exceeded 3. Most detected signals lacked impulsive first arrivals, thus reliable travel time picking was not possible. Beam-forming using data from the mini-arrays was applied in order to locate the source locations in the velocity range of 1000 – 4000 m/s. The source depth was constrained to zero. Perhaps because of the location uncertainties, the authors abstain from providing an estimate of magnitudes, but instead provide logarithmic plots of cumulative frequency over the maximum event amplitudes (in counts).

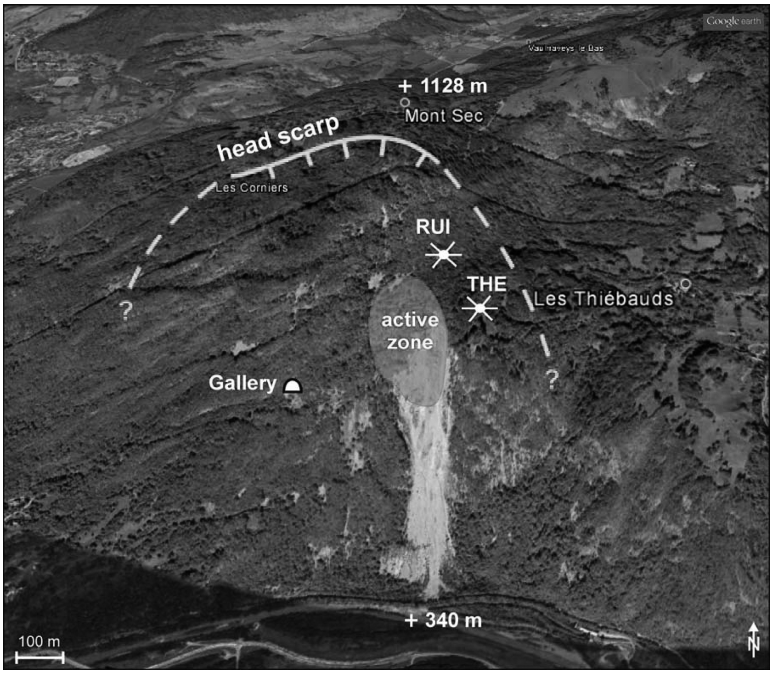


Figure 16 Overview of the Séchilienne DSGSD; locations of seismic mini-arrays are labeled RUI and THE; active zone is highlighted.

Until April 2009, rockfalls were the most frequent seismic sources related to the dynamics of the Séchillienne DSGSD. Based on the data from an artificially induced rockfall with known volume, the maximum volume of natural rockfalls during the monitoring period was estimated to about 4 m^3.

Figure 17 depicts typical waveforms of LMEs at the Séchilienne DSGSD. They show large variability in signal waveform and duration. The main frequency content is below 50 Hz with maxima around 20 Hz for smaller events and below 10 Hz for the stronger events. Compared to nearby tectonic earthquakes, the frequency content is significantly lower. It cannot be clearly determined if the lower frequency content of the LMEs is caused by different source locations and source-time functions or rock mass properties responsible for the damping of the seismic wave. Similar to the scarp area of the Randa rockslide, one type of LME corresponds to the impulsive type (Figure 17a). Small explosions fired near the active zone produced similar waveforms (Figure 17b). Another event type shows mostly emergent onsets and represents source-time functions lasting ~5 s. These events may be either relatively broad-band like the impulsive events (Figure 17c) or low frequency (Figure 17d). Only a fraction of all detected LMEs could be located with sufficient accuracy. They clustered either in the high creep velocity area or the head scarp. Helmstetter & Garambois (2010) do not exclude that some hypocenters are located at or near a basal shear zone.

An analysis of rockfall and LME frequencies (events / day), precipitation and displacement rate of the active zone of the DSGSD shows a strong correlation

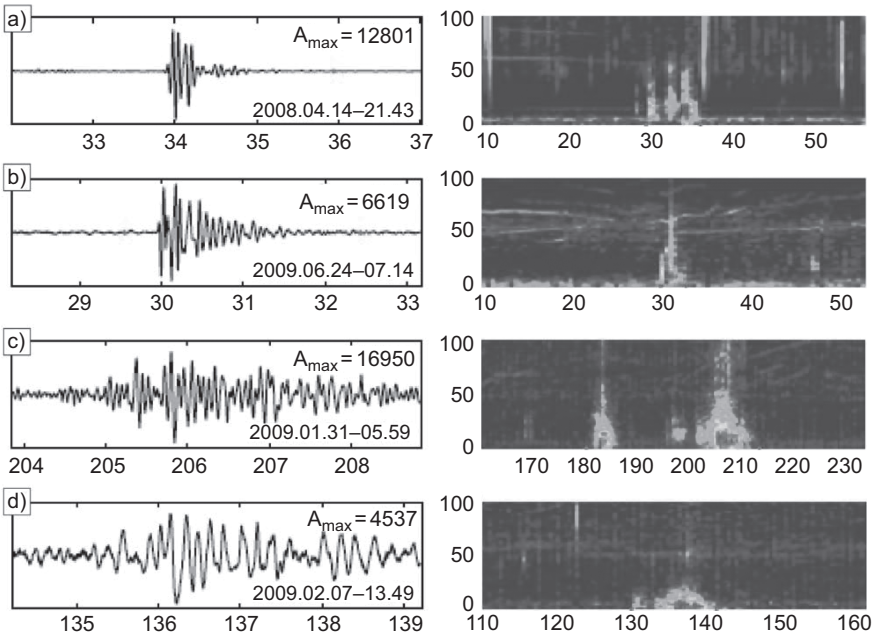


Figure 17 LME waveforms including spectrograms recorded at the Séchilienne DSGSD (after Helmstetter & Garambois, 2010); a) and b) short impulsive LMEs; c) emergent LME, broad band; d) emergent LME, low frequency.

between these parameters. However, even these relationships are not obvious from a quick look at the data. Some but not all rainfall events trigger increased rockfall and seismic activity (Helmstetter & Garambois, 2010). Daily precipitation, rockfall and micro-seismic activity precede increased displacement rates by about 4-5 days. During the monitoring period, the displacement rates of the active zone varied between 2 mm/day to 7 mm/day.

Next we consider the **Steinlehnen** mass movement (for location see Figure 9) as an example where seismic monitoring covers a phase of significant acceleration of an active zone of more than 20 times the quasi-continuous normal creep velocity without an apparent trigger. The Steinlehnen slope clearly shows the signature of a DSGSD (Figure 18). It is located in Gries in Sellrain, Northern Tyrol, Austria (Zangerl *et al.*, 2007). The unstable slope consists of paragneisses, amphibolites and granodiorite-gneisses. As in Randa, the lithological contacts dip gently into the slope and should support stability.

The head scarp exposes the basal sliding plane over a vertical distance of nearly 100 m. The lateral borders of the landslide mass can be traced clearly from morphology. The top scarp has an elevation of ~ 2100 m and the toe in the valley is at ~ 1250 m. The average inclination of the slope is ~ 37°. Talus covers great portions of the slope. A cross section of the Steinlehnen landslide is shown in (Figure 18b). The maximum thickness of 150 m is an estimate based on geological and geomechanical or kinematic considerations (Mayr am Trinkhof *et al.*, 2010). Other estimates based on the dip of displacement vectors come to a maximum depth of 70 – 100m (Zangerl *et al.*, 2007).

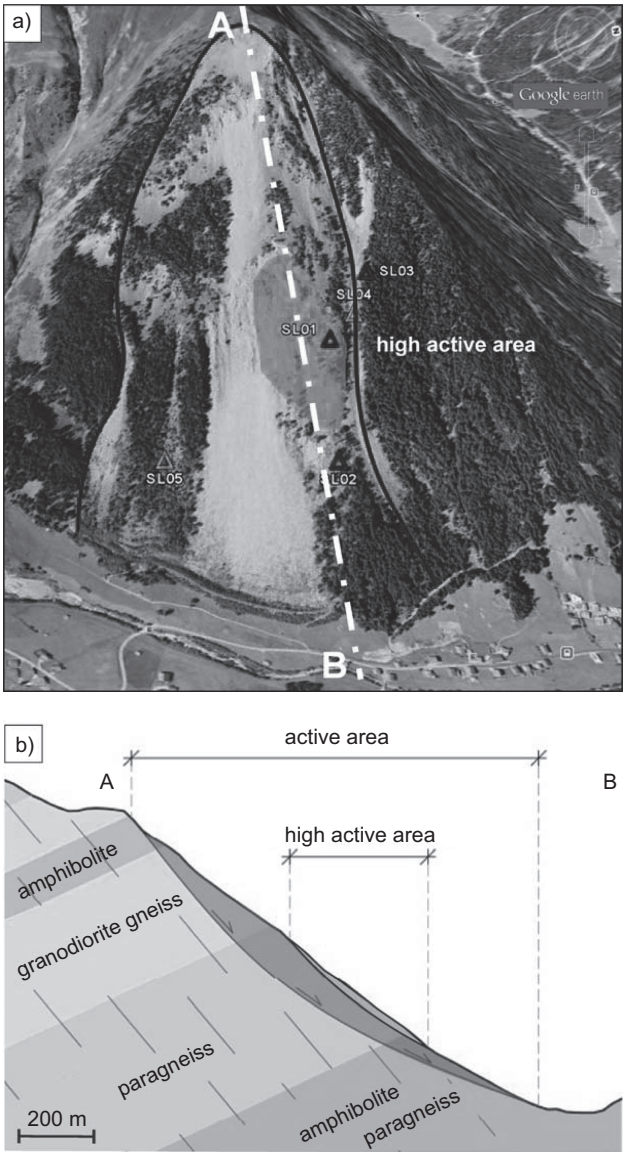


Figure 18 Steinlehnen DSGSD. a)overview with outline of the whole DSGSD (black line), high active area (hatched), location of seismic stations SL01 – SL05 and location of profile (white dash-dot line) shown in b); b) geological cross section (after Mair am Trinkhof *et al*., 2010).

The DSGSD is separated into several sliding masses bounded by additional scarps at about 1900m and 1650m.

In the summer of 2003, a slab in the central part of the landslide (colored spot in Figure 18a) of 10 – 20 m thickness accelerated and reached a total displacement of ~24m over a period of a month. A second acceleration phase of the same slab took place

during the spring of 2004 with a total displacement between 1.0 – 2.5 m (Zangerl *et al.*, 2007). During the acceleration phase, displacement rates of up to 40 mm/day were observed, whereas these rates dropped down to <0.5 mm/day during the quiet phases. The summer of 2003 was extraordinary warm and dry and no rainfall events likely to trigger the acceleration were reported. The second acceleration was also not triggered by unusually high levels of precipitation during this phase.

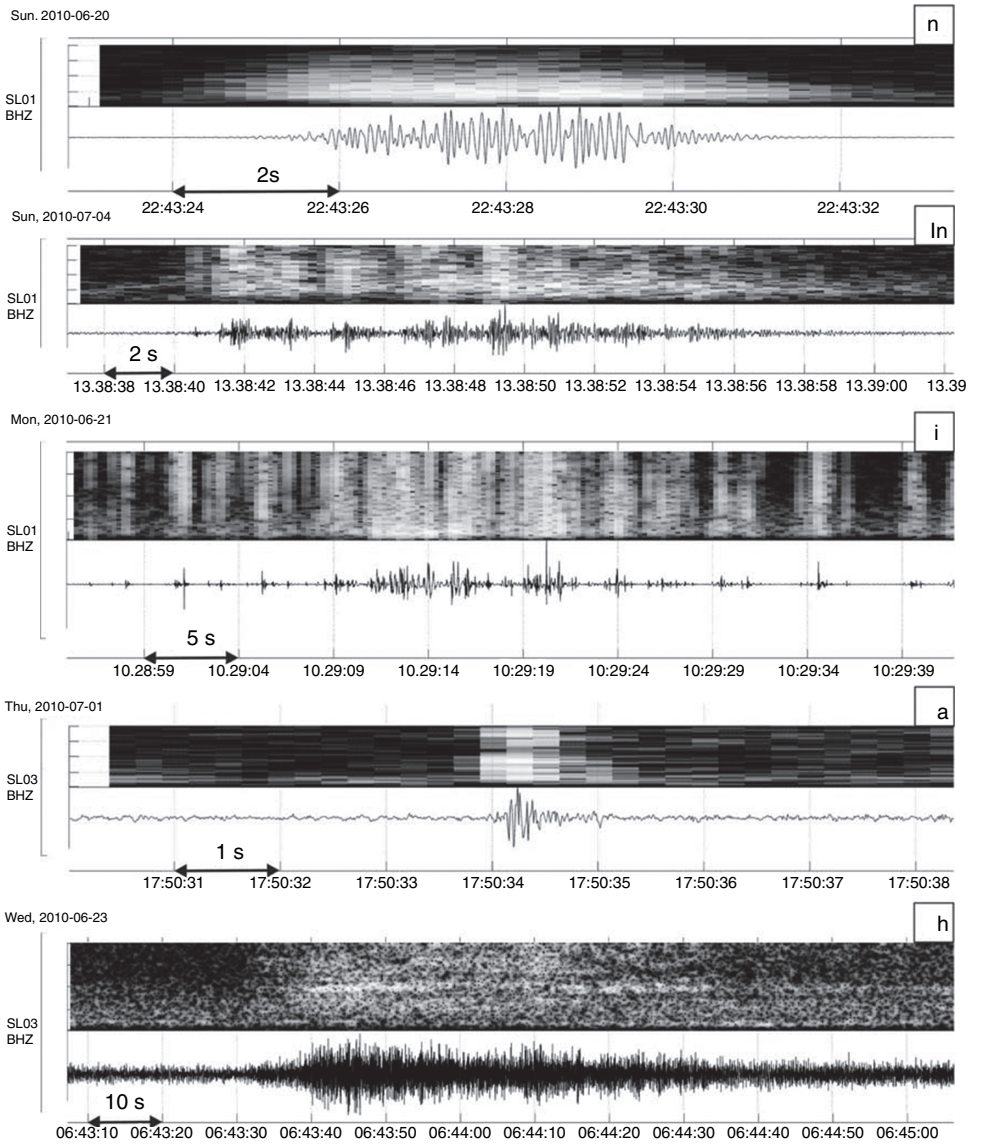


Figure 19 Waveforms (Z-component) including spectrograms recorded at the Steinlehnen DSGSD (Weginger, 2012); event types n, In, and i were classified as LMEs.

Between 10th and 28th June 2010, the Steinlehnen DSGSD was monitored by a GB-InSAR (ground based interferometry synthetic aperture radar) system installed opposite the Steinlehnen DSGSD. A third, less pronounced acceleration phase of the active slab was observed, with total displacements reaching up to 0.09 m and maximum displacement rates of ~0.05 m/day. Up to 5 seismic monitoring stations, each equipped with one 3C 4.5 Hz geophone, were operating at the Steinlehnen slope during this period (Figure 18a). Besides rockfall displaying the clear characteristic of a moving source (see Figure 12), Weginger (2012) identified 5 further classes of seismic events from or near from the DSGSD. Record samples of the different seismic event classes (n, ln, i, a, h) are shown in Figure 19. On the basis of 7 event parameters derived from duration, amplitudes, polarization, ACF and CCF of the signal and its envelope and the temporal development of the cumulative amplitudes of the envelope, Weginger (2012) was able to objectify his subjective classification using a Fuzzy logic classification method. Figure 20 shows the cumulative frequencies, normalized to 100% for the whole observation period of these events, derived using the interactive and the Fuzzy logic classification schemes. The high quantitative conformity of both methods supports the reliability and relevance of the classification.

Source location based on amplitudes was applied to the different event classes. The event types n, ln, i with significant increases in the cumulative amplitudes between

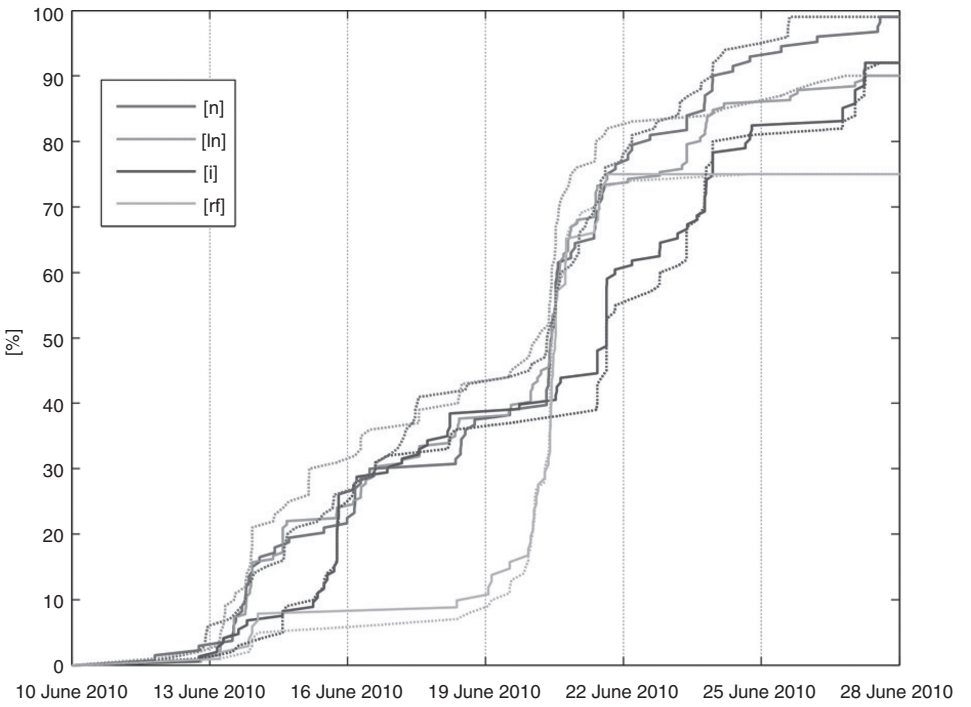


Figure 20 Steinlehnen cumulative frequencies of event types n, ln, i, and rf (rockfall); solid lines represent interactive classification, dotted lines represent automatic classification based on Fuzzy logics (Weginger, 2012).

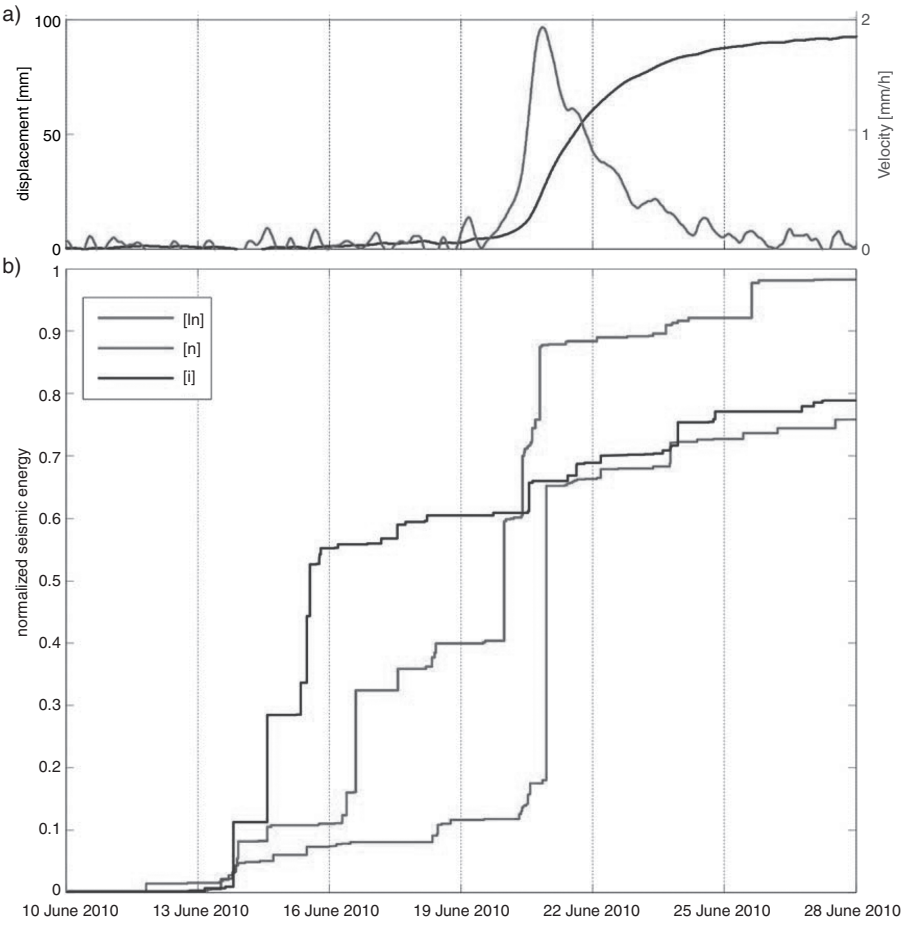


Figure 21 Temporal development of displacement rate and seismicity at the Steinlehnen DSGSD; a) displacement and displacement rate; b) cumulative frequencies of energy released by event types ln, n, i (Weginger, 2012).

13–17 June 2010 and 20–22 June 2010 were located at the active slab and classified as LMEs. The event types h and a, which showed monotonously increasing cumulative amplitudes, were located outside the active slab or the whole DSGSD. They were not classified as LMEs.

Figure 21 shows the normalized cumulative energy of the event types n, ln, i and the cumulative rockfall frequency together with the temporal development of displacement and velocity of the active slab derived from the GB-InSAR data for the period of 10th – 28th June 2010. The high velocity phase starts on 20th June and lasts until 25th June with a maximum velocity of nearly 2 mm/h. The initial value and the maximum of the high velocity phase correlate well with significant increases of the cumulative energy of event types ln and n and the increase of rockfall activity. The increase of the seismic and rockfall activity between 13th and 17th June was not accompanied by a significant increase of the velocity, nor was extraordinary rainfall reported to precede or

accompany the period of high velocities of the active slab. No external trigger of this phase has been determined thus far.

As a third example of a seismically active DSGSD, we present the **Gradenbach** mass movement (*e.g.*, Brückl *et al.*, 2013) which is located in the central Eastern Alps at the southern edge of the Penninic Tauern window (see Figure 9). A melange of phyllitic Bündner-schists, carbonates, and Alpine Verrucano constitute the rock mass of the Gradenbach DSGSD. The phyllitic Bündner-schists in particular are less competent and more susceptible to mass movements in comparison to the para- and orthogneisses to the south and prasenites and amphibolites to the north (*e.g.*, Fügenschuh *et al.*, 1997). The Gradenbach mass movement involves an area of ~ 1.7 km^2, the volume of which was estimated to be around 0.12 km^3 using refraction seismic measurements and borehole data (Brückl & Brückl, 2006).

Highly active phases of the Gradenbach DSGSD in 1965 and 1966 caused massive erosion at its toe and catastrophic debris flows. Another acceleration of the whole slope was observed during the period 1974–75 (Kronfellner-Kraus, 1980). A reconstruction of the geodetically and photogrammetrically observed deformation history since 1965 is provided by Brückl *et al.* (2013). An analysis of this data led to the result that the actual kinematics of the mass movement can be approximately described as block movement (Brückl *et al.*, 2006). It is also interesting to note that about 50% of the total displacement along the head scarp occurred after 1965 (Brückl *et al.*, 2013). Figure 22 provides an overview of morphology, structure and displacement history of the DSGSD. All significant accelerations of the Gradenbach DSGSD correlate with exceptionally high precipitation, partly enhanced by snow melt.

The seismic activity of the last and less pronounced acceleration phase in 2009 was monitored by a network consisting of 6 seismic stations on the mass movement and one reference station on solid rock nearby (Figure 22). All stations were equipped with 3C 4.5Hz geophones and a router for data communication using the mobile phone network. Event detection based on spectrogram analysis by image processing was carried out (see Figure 3) and LMEs were classified into 5 different LME classes. Figure 23 shows the four more frequent types (A, B, D, and tremor). Criteria comparable to those applied to the data from the Steinlehnen site were applied to interactively perform this classification. Signals from rockfall could also be clearly detected and classified as such (*e.g.*, Figure 11).

A 3D-model of the P-wave model of the whole Gradenbach DSGSD was derived from data summarized by (Brückl & Brückl, 2006) and built the basis for travel time location of sufficient S/N ratio data of each class (Mertl, 2015). All examples from the 5 event classes were located at or near the boundary of the DSGSD. The lower S/N ratio examples from each class that were not located are expected to also originate from the mass movement.

The four LME types (A, B, D, tremor) and rockfall show a very characteristic relation to displacement rate, snowmelt and discharge (Figure 24) for the year 2009. With the onset of snowmelt in the beginning of April, the discharge of one gauge (Berchtoldsgraben) at the Gradenbach slope rises dramatically. Simultaneous tremors occur very strongly and only during this period. Class D events and the less frequent class A events also start around this time. After about 6 weeks of seismic quiescence, seismic activity starts again with rockfall and, most significantly, with class B LMEs. At that time the acceleration of the whole Gradenbach DSGSD can be clearly seen in the geodetic data. This phase of seismic activity lasts until the maximum velocity is reached

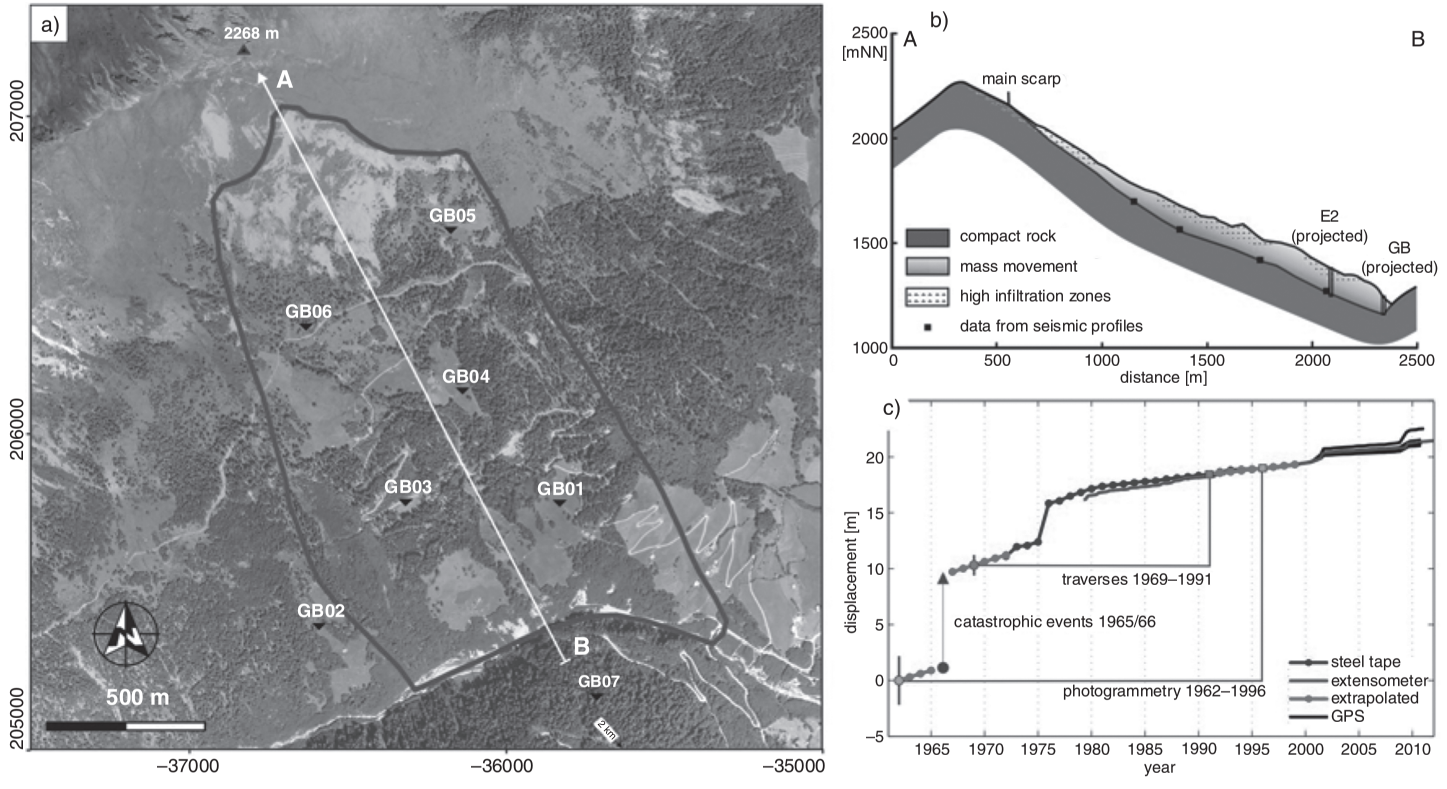


Figure 22 Gradenbach DSGSD (Brückl *et al.*, 2013); a) orthophoto with outline of the DSGSD, location of the seismic stations GB01 – GB07, trace of the cross section shown in b); b) geophysical – geological cross section of the Gradenbach DSGSD; c) temporal development of the average displacement from 1962–2012.

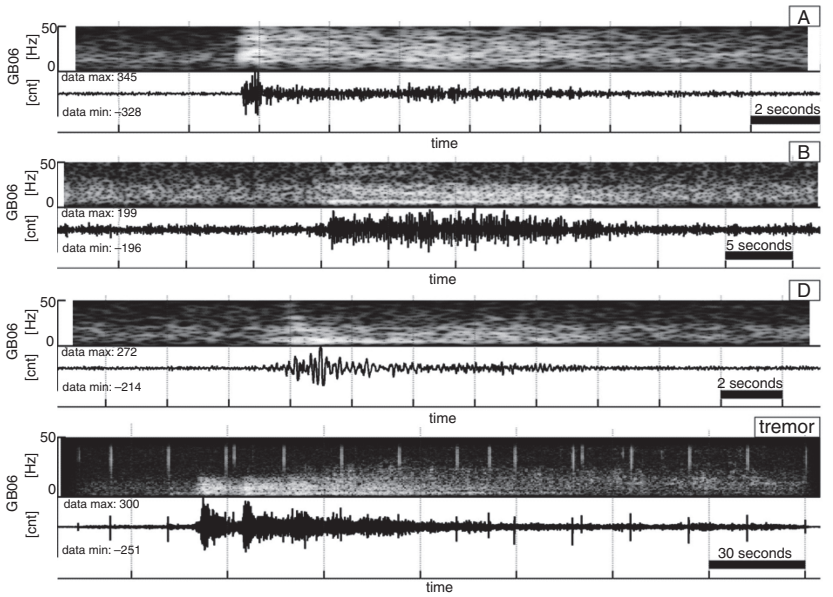


Figure 23 LME waveforms (Z-component) including spectrograms recorded at the Gradenbach DSGSD (after Brückl *et al.*, 2013, Mertl, 2015).

at the beginning of June. Thereafter, the type B events and rockfall ceases nearly completely. From its maximum in June, the displacement rate decreases continuously heading into August, accompanied by type A and D seismic activity.

The available data from the seismic network Gradenbach was used for the computation of PSDs of the ambient noise (Draxler, 2013). The spectrograms of the years 2008 to 2010 were computed using the method described in section 3.6. The visualization of the spectrograms together with the displacement, hydrological and meteorological data revealed two distinct patterns: the occurrence of increased seismic energy in the ambient noise at certain frequency bands with the beginning of the snowmelt and recurrent ambient noise patterns after precipitation peaks. Both patterns are more significant in 2009 than in 2008 and 2010.

Figure 25 shows the PSD observed at seismic station GB02 from week 13 – 24 in 2009 together with snow cover equivalent, discharge at the Bechtoldhang gauge and displacement rate. The power spectral densities of the ambient noise increase in the frequency range ~20 – 50 Hz with the start of infiltration in spring. At the beginning of the geodetically observable acceleration of the Gradenbach DSGSD, this noise grows and its frequency range widens to deeper frequencies below 10 Hz. The general pattern of these two phases agrees well with the frequency of the different LME types shown in Figure 24.

Besides this seasonal trend, the ambient noise spectra also react to individual rainfall events. Figure 26 shows a stack of 11 single ambient noise spectra covering 40 h after the onset of a strong, short period of rainfall in 2009. Before stacking, the long term noise was removed from the spectra and the time axes were related to the onset of each rainfall event. After ~12h event time, a high amplitude band develops between 4 – 100 Hz. The maximum occurs at 8 Hz and 26 h after precipitation peak. A second high amplitude

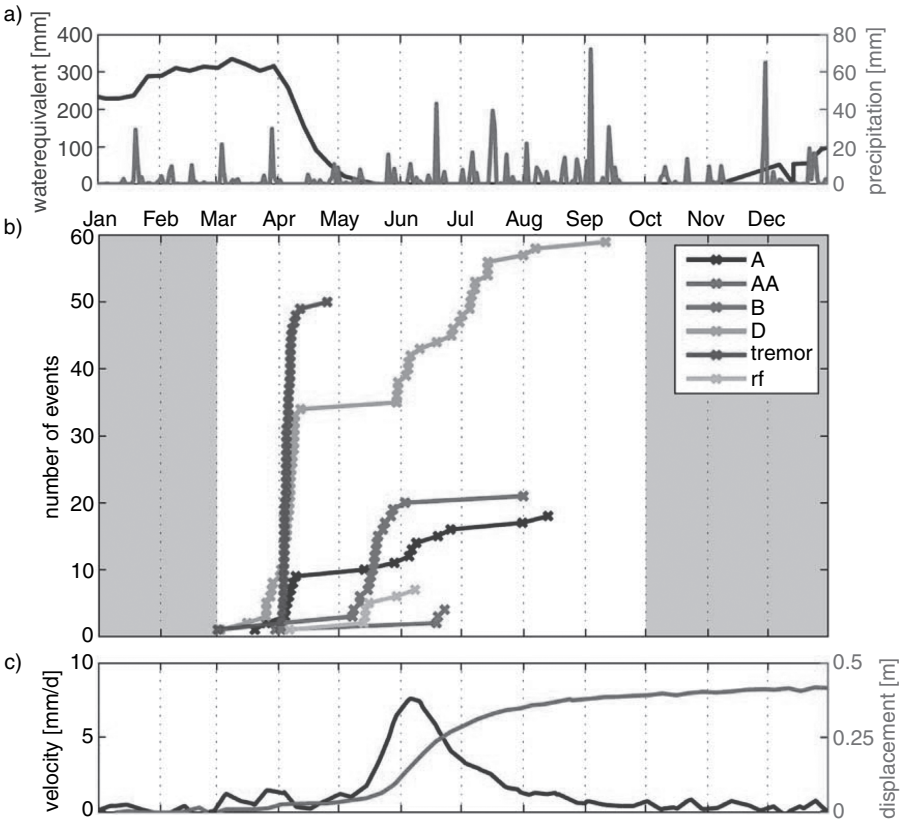


Figure 24 Temporal development of a) snowmelt and precipitation, b) cumulative frequency of LMEs and rockfall, c) displacement and velocity at the Gradenbach DSGSD (after Brückl *et al.*, 2013; Mertl, 2015).

band starts after ~16h in the frequency range 0.3 – 0.9 Hz and reaches the maximum at 0.5 Hz and 30h after precipitation peak. Both bands end at ~ 48h. This pattern emphasizes the importance of percolating water, which destabilizes the landslide mass at different depth levels and delay times (Draxler, 2013). The slope reacts more sensitively to single rainfall events the more active the slope is on a seasonal time scale.

4.4 Flow

The first flow-type mass movement we will look at is the **Super-Sauce** landslide. It is located on the north-facing slopes of the Barcelonette Basin, Alpes-de-Haute province, France (Figure 9). It developed from the Jurassic "Terres-Noires" (black marls) of the Ubaye valley, an area known for the development of numerous active landslides. The Super-Sauce earthflow originates from the steep slope of the Brec Second crest (Figure 27), and the crown of the source area is at 2105 m, the actual toe at 1740m (July 2008). The flow has a length of 850m and an average width of 135 m. The average

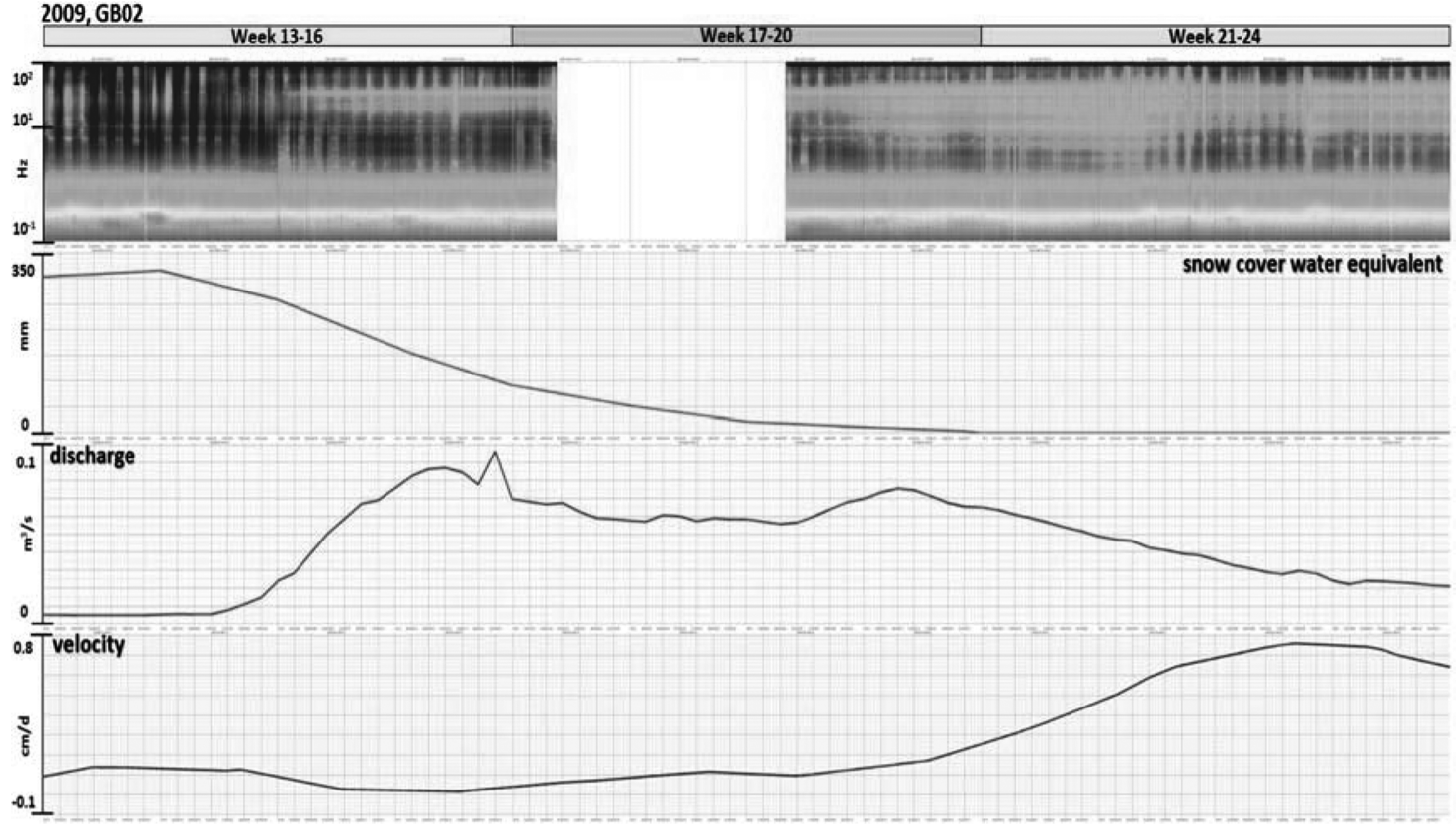


Figure 25 Gradenbach ambient noise monitoring – seasonal pattern (after Draxler, 2013); PSD data of station GB02 available for weeks 13–24, 2009 together with snow cover water equivalent, discharge of gauge located at mass movement, and velocity.

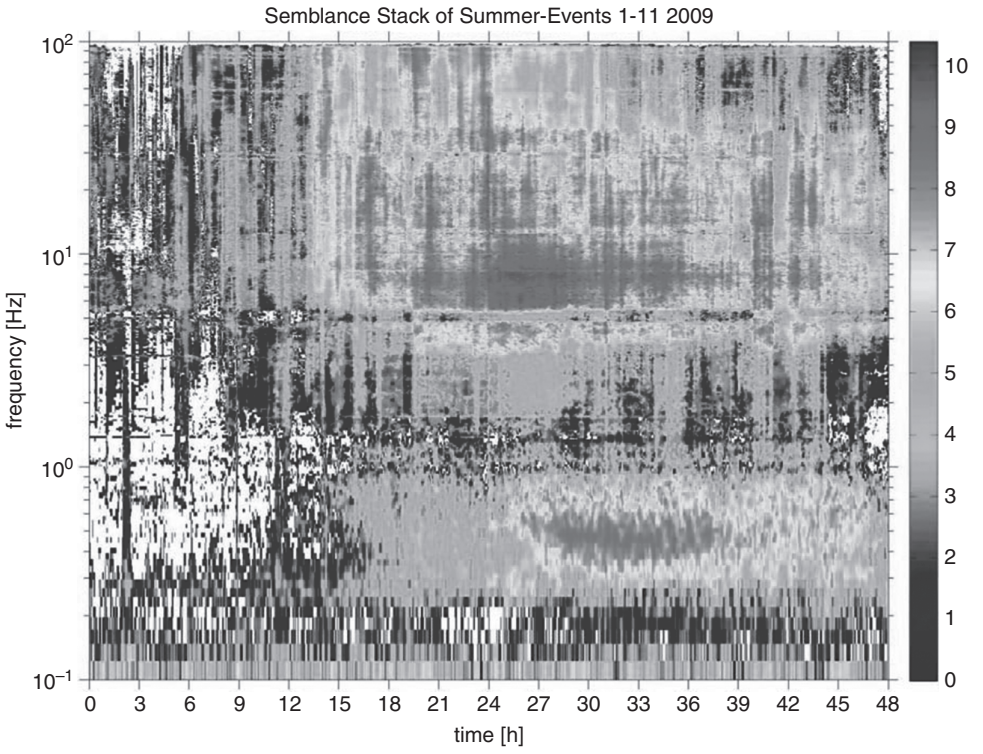


Figure 26 Gradenbach ambient noise monitoring – precipitation related pattern (after Draxler, 2013); stack of 11 single ambient noise spectra covering 40 h after the onset of strong, short periods of rainfall in 2009.

slope of the flow, with the uppermost part excluded, is ~23°. The volume has been estimated at 750 000 m^3 (Walter *et al.*, 2012 and references therein). The mean thickness of the flow is 6.5 m or <1% of the length. The original rock mass decomposed completely into a granular mass with ~ 20% clay (Malet *et al.*, 2005) and an internal friction angle of 32° (Van Asch & Malet, 2009). This relatively high friction angle compared to the average slope of the flow requires either high pore-water pressure or a lower internal friction angle at the basal sliding surface, or both. The landslide triggered around 1960, ruling out a causal connection to the retreat of ice age glaciers. From 1996 – 2007 the velocities covered the range of 2 – 30 mm/day.

A seismic monitoring campaign at the Super-Sauce landslide was carried out between 14th and 24th July 2008 (Walter *et al.*, 2012). Four small arrays (called seismic navigation system SNS by the authors) were deployed along the more active zone of the flow (see Figure 27). Each array consisted of one 3C short period seismometer in the center and three vertical short period seismometers surrounding the sensor in the center at distances of 25 – 30m. Data were recorded in continuous mode with 400 Hz sampling rate.

Data analysis and event detection was carried out interactively on the basis of a visualization of waveforms and sonograms. Besides rockfalls, 34 LMEs were detected

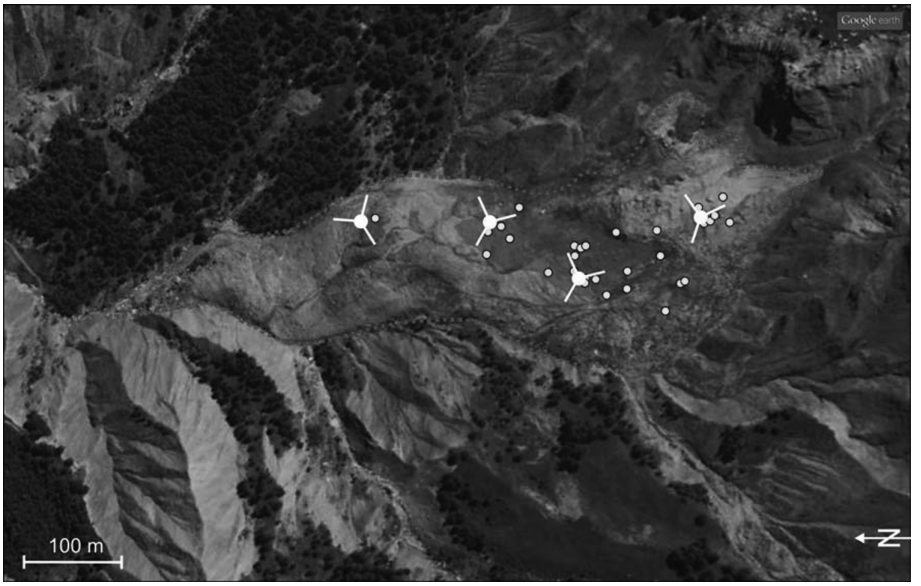


Figure 27 Overview of the Super Sauce flow (after Walter *et al.*, 2012); a dotted line outlines the flow, the highlighted area is the most active part, white symbols show the location of the seismic mini-arrays, LME (slidequake) epicenters are shown as white circular areas.

and labeled as "slidequakes". They have impulsive onsets, last 2–5 s, and cover a wide frequency band (10–80 Hz). Subsequently arriving phases have lower frequencies between 10 – 30 Hz (Figure 28a). The frequency content of these events is similar to that of low magnitude local earthquakes. They were interpreted as the result of stress relief, most likely at internal shear surfaces. The location of epicenters based on travel times could be applied to events detected by at least two mini-arrays within a distance of 200 m. A simple velocity model was derived from data gained from calibration shots. Location accuracy could be checked by location of these known sources. Focal depth was not well constrained by the sparse data, and it is assumed to be very shallow and not at the basal sliding surface. The slidequakes occurred mostly in the more active area (> 0,01 m/day) in the middle of the mudflow, near an emergent in-situ crest in the central part, and a few occurred in the hard rock of the source area. Magnitudes of the detected slidequakes were in the range $-3.2 \leq Ml \leq -1.3$. The highest magnitudes of slide quakes were observed a few hours following a strong rainfall event. The temporal distribution was otherwise uniform.

Single mini-arrays also detected low energy and very high frequency events (5–150 Hz) with durations of 2–20s (Figure 28b). These events must have been either within or near the area covered by one mini-array due of an observed amplitude decay in one mini-array with a factor of 30. The main source area of these events was concentrated around a stable crest within the high-velocity zone of the flow. Fissure development in the uppermost layer of the flow was assumed to be the source mechanism. This assumption was confirmed by the simultaneous recordings of an extensometer installed over an existing fissure and a seismometer installed within the fissure.

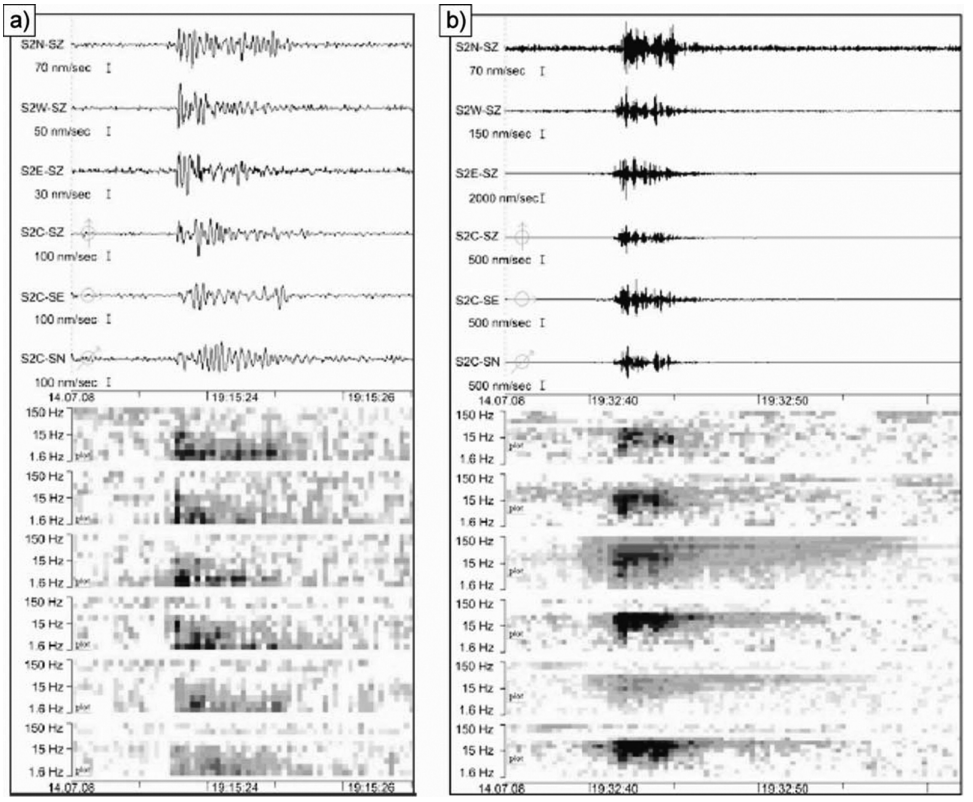


Figure 28 LME waveforms including spectrograms recorded at the Super Sauce flow (after Walter *et al.*, 2012); a) slidequakes; b) fissure development.

Slidequakes and fissure development at Super-Sauce are explained by brittle behavior of the landslide mass. Macroscopically, Super-Sauce is a typical flow and one would therefore expect ductile deformation without seismic activity, however shear strength analysis of the landslide material shows that the water content is in a range where the material deforms in a brittle manner (Walter *et al.*, 2012).

The second example of a flow is the **Slumgullion** landslide (Gomberg *et al.*, 2011). It is located in San Juan Mountains, a large early-Tertiary volcanic center in southwest Colorado (Figure 9, Figure 29). The landslide formed as a result of the collapse of hydrothermally altered volcanic materials in the rim of the Lake City Caldera (Lipman, 1976). An older, now inactive part developed from the crown at 3650 m and reached a total length of 6.8 km. The old flow covers an area of 4.6 km^2 and ends at an elevation of 2750m. This older movement became active 800 – 900 years ago according to radiocarbon dating of trees (Madole, 1996), and around 700 years ago it dammed the Gunnison River and created Lake San Cristobal (Crandell & Varnes, 1961).

Today most of the landslide is inactive, but a significant part within the boundaries of the older slide reactivated roughly 300 years ago (Varnes & Savage, 1996). The active part ends at an elevation of 2750 m, has a length of 3.9 km and is about 300 m wide.

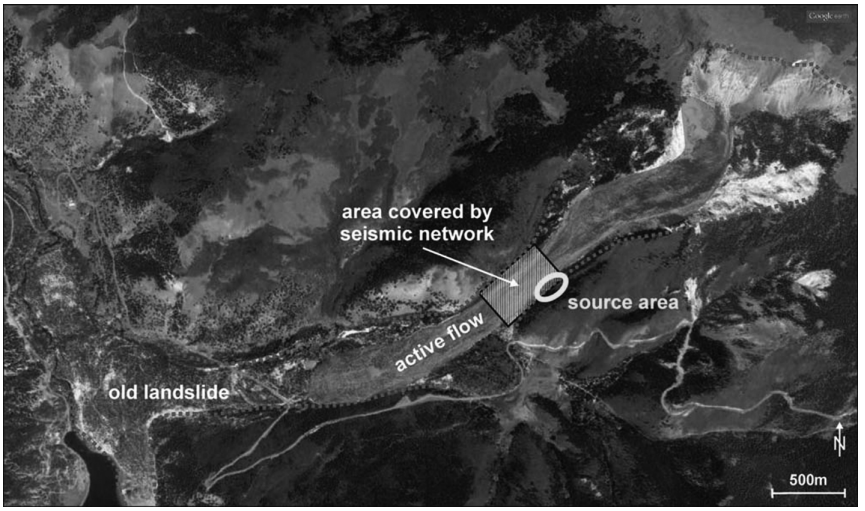


Figure 29 Overview of the Slumgullion flow (after Gomberg *et al.*, 2011); the dotted line outlines the old flow, the shaded area the currently active part, the hatched rectangle symbolizes the area of the seismic network, the most probable source area of LMEs is marked by a oval.

The average thickness is ~17m. Bedrock surrounding the landslide consists of volcanic rocks ranging in composition from rhyolite to basalt. The landslide mass itself comprises sandy, silty clay with scattered patches of boulder debris, clay and pond and stream sediments. The clay content is 10 -50% Smectite and some kaolinite with high swelling potential (Schulz *et al.*, 2009b). The average slope of the active part is 8°.

The Slumgullion landslide moves primarily by sliding along discrete bounding faults (Fleming *et al.*, 1999). Additionally, differential internal processes take place at faults and fractures within the landslide body. Between 1958–1968, velocities up to 6 m/year were reached in the central part of the landslide and the toe advanced by ~1 m/year. Currently (year 2011), individual kinematic elements move at long-term average annual velocities of 0.5-7 m/year. Extensometers across one of the two bounding strike-slip faults were used to document correlations between daily variations in landslide velocity and atmospheric pressure (Schulz *et al.*, 2009b).

During the period 18–26 August 2009, a seismic monitoring campaign was carried out at the Slumgullion landslide (Gomberg *et al.*, 2011), where 88 single channel recorders were deployed along an approximately 450 m long section of the central part of the active landslide in a nearly regular grid (Figure 29). Geodetic and hydrometeorological monitoring supplemented the campaign. Throughout the monitoring campaign, the displacement rate averaged 9.5 mm/day. One stronger period of rainfall occurred during the observation period.

Almost all seismic data were scanned visually. Cross correlation with a "template" for each signal type derived from clear and high S/N ratio records was used to detect and characterize seismic events. An event was considered confirmed if a correlation coefficient above some threshold and time delays between recordings consistent with a reasonable velocity model was found.

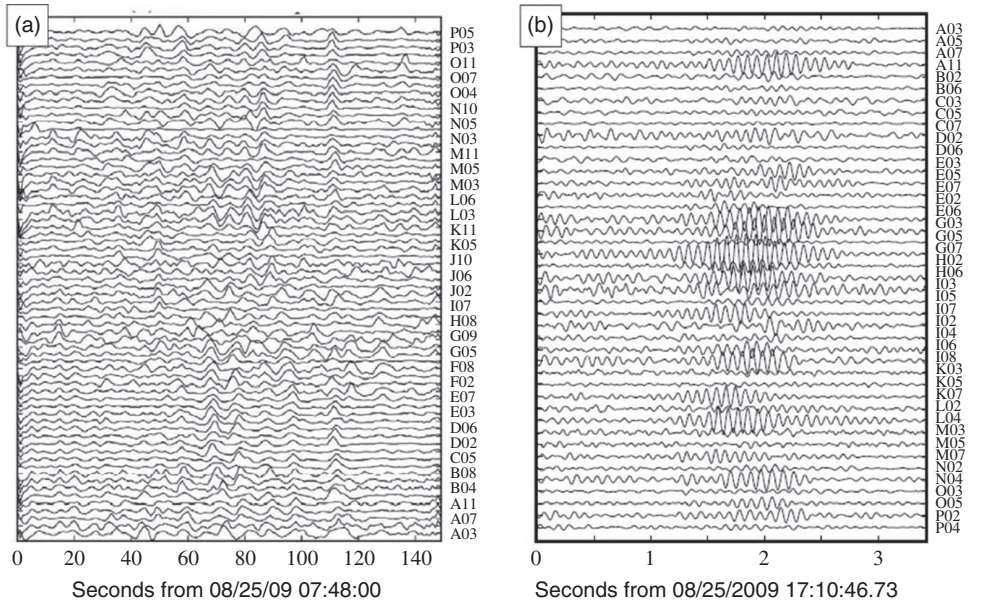


Figure 30 LME waveforms recorded at the Slumgullion flow (after Gomberg *et al.*, 2011); a) tremor (envelopes); b) harmonic slide quakes.

Several types of seismic signals were detected and related to LMEs: "tremors" and "harmonic slide quakes". The dominant energy of a tremor is distributed broadly above 30-50Hz and diminishes toward the Nyquist frequency (125Hz). High amplitudes of tremor envelopes last <10s and follow irregularly in intervals of several tens of seconds over a period of about 2 minutes (Figure 30a). Harmonic slide quakes last 2-3 s with 90 – 180 repeats. Depending on the threshold of cross-correlation, their fundamental frequency is ~12 Hz and no harmonics are visible throughout the whole duration (Figure 30b). This LME-type occurs more frequently during daytime, and an increase in sliding velocity is also observed during the day. Daytime lower atmospheric pressure may modulate fluid flow, decrease basal friction and thus induce the velocity variation (Schulz *et al.*, 2009a).

Beam-forming with an apparent velocity of 400 m/s consistent with S-wave velocities for the depth interval 5 – 25 m (Williams & Pratt, 1996) along with maps of observed amplitudes were used to locate seismic events. Hypocenters of tremor signals were at the left side-bounding strike-slip faults of the landslide within location error. As with tremors, harmonic slide quakes most probably originate at the left side-bounding strike-slip faults of the landslide. Trapping of seismic energy in a low velocity channel at the boundary is assumed to explain the harmonic character of this type of seismicity.

The stick-slip behavior of the side-bounding strike-slip faults is explained by a transient dilatancy strengthening until some steady porosity is reached (Gomberg *et al.*, 2011). Similar harmonic quakes were also observed on Antarctic ice sheets, with their sources located in the basal highly sheared till layer (*e.g.*, Winberry *et al.*, 2013).

5 GENERAL EVIDENCE OF SEISMICITY GENERATED BY LARGE LANDSLIDES

5.1 Seismic efficiency

The seismic efficiency of an earthquake is the ratio of the energy radiated by the seismic waves to the total work done by frictional forces along the rupture surface during the earthquake (*e.g.*, Aki & Richards, 1980). In analogy to this definition of seismic efficiency, we calculate the ratio of the cumulative radiated seismic energy E_S to the potential energy release E_P of the whole landslide mass during the same monitoring period. E_S can be calculated using Equation 25 (*e.g.*, Stein & Wysession, 2003) with the magnitude – frequency data shown in Figure 31a, c, d.

$$E_s = \sum 10^{(4.8+1.5M)} \text{Joule} \tag{25}$$

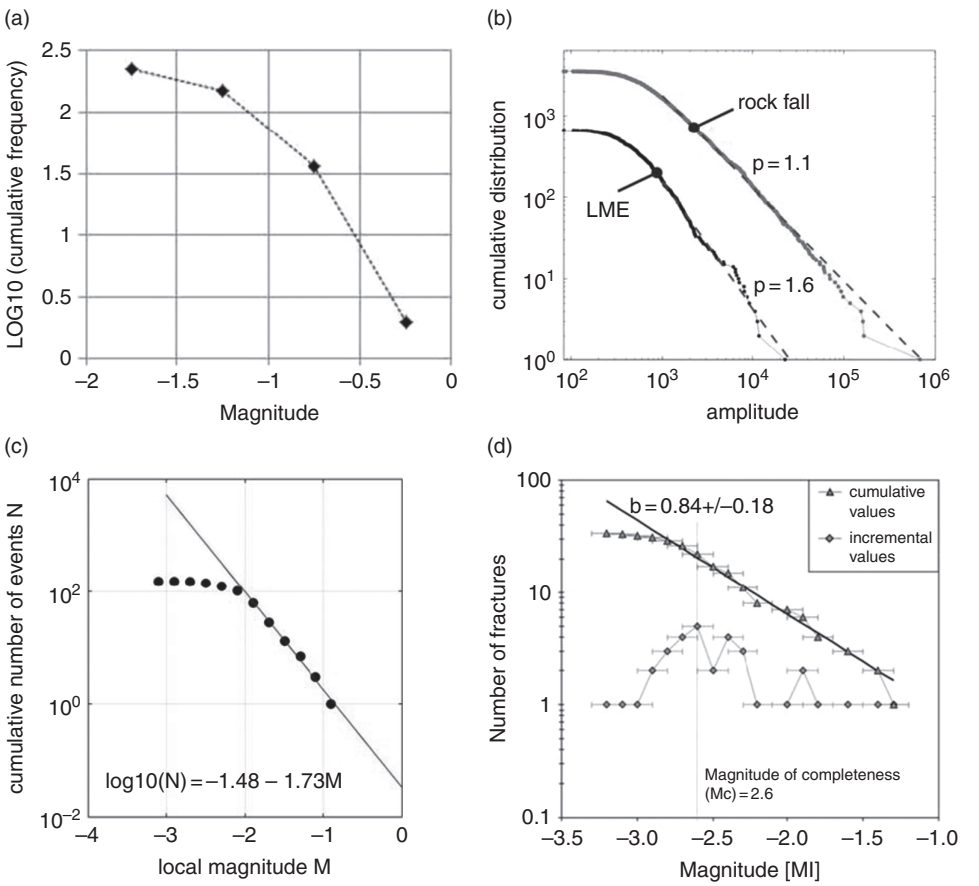


Figure 31 Magnitude – cumulative frequency plots (Gutenberg -Richter diagrams) of LMEs for: a) Randa (Spillmann *et al.*, 2007), b) Séchilienne (Helmstetter & Garambois, 2010), c) Gradenbach (Mertl, 2015), d) Super Sauce (Walter *et al.*, 2012).

Table 1 Radiated seismic energy Es versus total potential energy release E_P.

	Landslide type	E_S *[Joule]*	*volume* $[m^3]$	*density* $[kg/m^3]$	*dZ [m]*	E_P *[Joule]*	E_S/E_P
Randa	steep slope	$3.2\ 10^5$	$6\ 10^6$	2500	0.013	$1.9\ 10^9$	$\mathbf{1.7\ 10^{-4}}$
Gradenbach	DSGSD	$2.1\ 10^4$	$1.2\ 10^8$	2300	0.016	$4.3\ 10^{11}$	$\mathbf{4.9\ 10^{-8}}$
Super Sauce	flow	$2.1\ 10^3$	$4.5\ 10^5$	2200	0.098	$9.5\ 10^8$	$\mathbf{2.2\ 10^{-6}}$

The summation in Equation 25 is over all LMEs. The potential energy release E_P can be calculated from published data on the landslide mass (total or representative of the observation area), estimates of the average density, and the average vertical displacement during the monitoring period. Input data and results are compiled in Table 1.

The ratio E_S/E_P can be seen as an index number for the ratio of seismic active deformation (*e.g.*, stick-slip) to total deformation including seismo-inactive silent creep. According to Table 5.1, the ratio E_S/E_P changes dramatically between the different landslide types. On the basis of the presently available data, we cannot determine if Randa, Gradenbach, and Super Sauce are representative of the different landslide types or if this ratio changes during the evolution of a landslide. More examples and long term data are necessary to evaluate the significance of the ratio E_S/E_P.

5.2 Magnitude – frequency statistics

The magnitude frequency distribution of tectonic earthquakes worldwide, also including those in restricted tectonic areas or fault systems, follows the Gutenberg-Richter relation (*e.g.*, Lay & Wallace, 1995):

$$\mathrm{Log10N_M} = \mathrm{a} - \mathrm{bM} \tag{26}$$

N_M is the cumulative frequency of earthquakes with magnitudes greater or equal to the magnitude M. It has yet to be tested if the GB relation also holds for slope tectonic earthquakes at different types of active large mass movements.

Magnitudes of LMEs and their frequencies were determined in order to analyze the Gutenberg – Richter statistic for **the Randa steep slope** (Spillmann *et al.*, 2007), the **Gradenbach DSGSD** (Brückl *et al.*, 2013; Mertl, 2015) and the **Super Sauce flow** (Walter *et al.*, 2012). For the **Séchilienne DSGSD** (Helmstetter & Garambois, 2010), these statistics are only available for the maximum amplitudes and not for the magnitudes. However, as most epicenters are clustered in a relatively narrow active zone, the logarithms of the maximum amplitudes can be taken as a proxy for the magnitudes. The four Gutenberg-Richter diagrams are compiled in Figure 31.

The b-values for tectonic earthquakes in different seismo-tectonic zones are usually in the range of 0.8 – 1.2, depending on the stress regime (Schorlemmer *et al.*, 2005). Three of the four plots (Sechillienne, Gradenbach, Super Sauce) show linear relations from which the magnitudes of completeness M_C and the b-values can be derived. The b-values vary between 0.84 and 1.7. Further studies are necessary to clarify whether these different b-values are typical for the different landslide types, indicative for their actual state of activity or related to particular source mechanisms.

For the Randa steep slope, a reasonable b-value of b = 1.3 fits only between the magnitude range [–1,5, –0.5]. According to this b-value, one would expect 8–9 earthquakes in the magnitude interval [–0.5, 0.0], but only 2 were observed. A possible explanation for this deviation from the Gutenberg-Richter law at higher magnitudes will be given in the next subsection.

In the subsections 5.2 and 5.3 we present arguments for the correlation of different LME waveforms with the moment tensor source type or single force source type. These different source types may by associated with different b-value ranges, however with the present state of available data we wish to only emphasize this possibility.

5.3 Slope tectonic earthquake

In seismology, the source mechanisms of tectonic earthquakes are described by moment tensors, therefore we use the term "slope tectonic earthquakes" for LMEs with source mechanisms describable by moment tensors. This term is more general than the term "slidequakes" inferred by Gomberg *et al.* (2011) and Walter *et al.* (2012) because it comprises tension cracks in addition to slip.

The duration of source time functions of tectonic as well as slope tectonic earthquakes is limited by the dimensions of the focal area and the rupture velocity, respectively the shear wave velocity (*e.g.*, Stein & Wysession, 2003) In subsection 2.2 we estimated that the linear dimension of the focal area for a magnitude M = 0 slope tectonic earthquake is either 7.4 m in compact rock or 23 m in a fractured near surface layer. Reasonable values for the shear wave velocities for these two rock classes are 3500 m/s and 700 m/s. It follows that the length of the source time function is then in the range 0.001 s– 0.016 s, assuming a rupture initiation in the center of the focal area. Green's functions representative of seismic structure and extension of the usual monitoring areas are not longer than around 1s and impulsive in most propagation directions. Convolution with the source time function does not lengthen the seismic signal and limit the frequency bandwidth noticeably, therefore we deem the impulsive single events observed at Randa, Sechillienne, Steinlehnen, Gradenbach and Super Sauce as slope tectonic earthquakes. Their focal mechanism should be describable by a moment tensor, either a double couple (shearing or tearing fracture mode) or a tensional crack. Multiple impulsive events should also be explained by the same source mechanisms in the case where their waveforms are clearly separated in time. Waveforms generated by fissure development at the Super Sauce flow partly overlap (Walter *et al.*, 2012), but represent fracture mode I (tensional crack) and are also classified as slope tectonic quakes.

The steep slope at Randa, which is either in the state of stress relaxation after the rockslides in 1991 or in a preparatory phase for a next major failure, is a highly fractured rock mass. Typical distances of major faults are in the range of 50 m. However, many minor faults are separated by much smaller distances. We may hypothesize that this fault system limits the maximum linear dimension of the seismic fault plane to 5 – 10 m, thus explaining the deficiency of slope tectonic earthquakes above M ~ –1.

5.4 Bulk instability and tremor

Snowmelt at the Gradenbach DSGSD started at the beginning of April 2009. During May 2009, when the slope became accessible for vehicles, several morphological signs

of slope deformation became visible at or near the road. Figure 32a shows one scarp with a lateral extent of about 30m and downslope displacements of about 0.2 m.

Even though these slides are only minor movements, one would expect that they produce seismic signals observable by the local seismic network. Figure 33b shows the

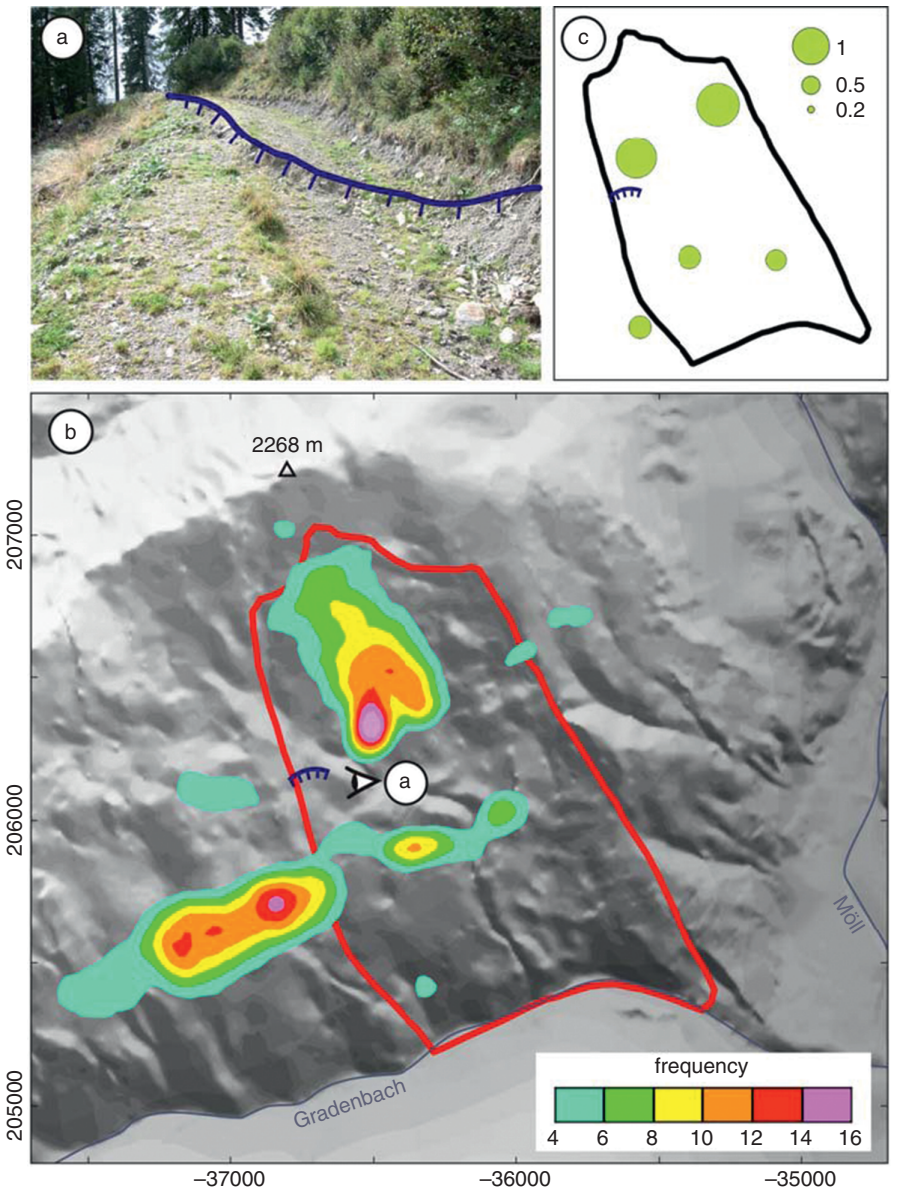


Figure 32 Minor slides on the Gradenbach DSGSD as possible single force sources for tremor-type LMEs; a) view to the scarp of a minor slide which occurred probably after the onset of snowmelt 2009; the location of this scarp is marked in b) and c); b) cumulative frequency of PDF above a threshold for located LMEs; c) mean normalized PGVs of tremor-type LMEs at seismic stations.

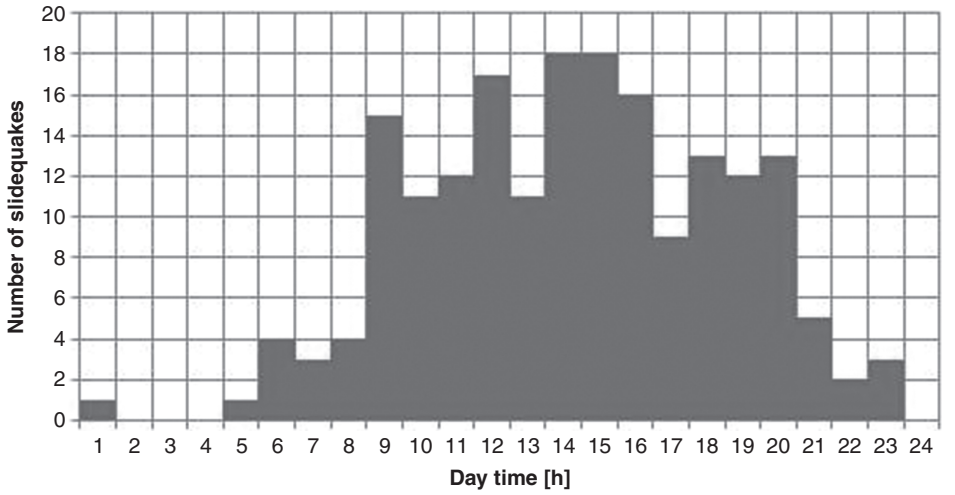


Figure 33 Daily variation of harmonic slide quakes at the Slumgullion flow (after Gomberg *et al.*, 2011).

spatial frequency of possible epicenters with PDF>0.7. This cumulative distribution shows seismic activity due to LMEs with interpretable first arrivals. However, there was apparently no epicenter located at these slides. In the following we interpret the minor slides as seismic sources due to bulk instabilities in order to check if they were detectable by the local seismic network.

In order to estimate the dominating period and magnitude of these bulk instabilities, we apply the rotational slider block model. The linear dimensions of the slide shown in Figure 33a are about 1/30th the size of those of the whole Gradenbach DSGSD. According to Brückl and Parotidis (2005), the pendulum length of the Gradenbach DSGSD is R = 5178 m. Assuming similarity of the geometry of the smaller rotational slides, their pendulum length is approximately R = 173 m. The duration of the source time function of the seismic signal then follows from Equation 3 to be T = 13 s.

Scaling the volume of the whole Gradenbach DSGSD of 0.12 km^3 down by a factor of $(1/30)^3$, we get a volume of 4.4 10^3 m^3 and a mass of B = 8 10^6 kg, assuming a density of $\rho = 1800$ kg/m^3. The displacement at the head scarp is roughly D = 0.2 m. We take this as an estimate of the displacement of the center of mass of the slide. The centroid single force, representing the equivalent seismic source of such a minor slide, is $|CSF| = B\,D = 1.6\ 10^6$kgm. Equation 2 provides an empirical relation between centroid single force CSF and the magnitude Ms. However, this relation is only supported by data (Ekström & Stark, 2013) in the range 10^{13}kgm< |CSF| < 10^{17}kgm, therefore we derive an estimate of the local magnitude (Equation 17 with n = 1.66 and C = -0.304 from the peak ground displacement produced by the S-wave at a distance of d = 3 km (0.027 deg) by the use Equation 27:

$$U_s = 1/(4\pi\rho V_s^2 d) * F_{peak} \tag{27}$$

Equation 27 is the scalar part of the tensor equation for the S-wave radiation (Aki & Richards, 1980) and represents the U_S radiated in directions normal to F_{peak}. In

order to calculate the local magnitude with Equation 18, the peak ground velocity V_s in the frequency range 1 – 10 Hz is required. It is derived by multiplying U_s by a factor $2\,\pi\,10\,s^{-1}$. Using this data and our estimates, we get a local magnitude of M_L = –0.7. Given this magnitude, it is not surprising that the local network equipped with 4.5 Hz geophones was not able to catch the fundamental mode (T ~ 13s) of the corresponding single force seismic source.

Experience from large landslides (*e.g.*, Yamada *et al.*, 2012) shows that higher frequency signals are superimposed on the dominating long period seismic signals of large landslides due to particular processes beyond the general acceleration of the landslide mass followed by deceleration until a halt. The amplitudes of these signals are in the range or below that of the fundamental mode and may have the character of tremor lasting as long as the fundamental mode.

The temporal development of the seismic activity during the acceleration phase at the Gradenbach DSGSD in the spring of 2009 shows about 50 tremors at the begin of snowmelt in April 2009. After mid-April, tremor activity ceased completely. We speculate that these tremors were generated by the movement of the minor slide shown in Figure 33a and more similar events. The spatial distribution of the cumulative PGV (peak ground velocities) of tremor suggests that most of the sources are located in the upper third of the mass movement (Figure 33c). Considering the very incomplete information about the number, size and temporal development of these minor slides, we leave the given explanation of tremor generation by minor slides during an active phase of large landslides as a hypothesis to be checked by future investigations.

Seismic activity was observed at the **Slumgullion flow** only at or near the left (with respect to the flow direction) boundary with waveforms described as tremor and harmonic slide quakes. During the 9-day seismic monitoring period in August 2009, displacement rate, which was observed by extensometers across the left boundary of the flow, and the seismic activity show a significant daily variation. The latter is depicted in Figure 33. An average number of harmonic slide quakes per day of ~ 40 can be derived from this data when also taking the actual operating times of the monitoring network into account. The average displacement rate during the seismic monitoring period was 9.5 mm/d. Neglecting slip events (or bulk instabilities) of the whole landslide mass in the area of the seismic network associated with tremor, the displacement per harmonic slidequake is D = 0.24 mm. If we assume that the whole landslide volume below the network (~ 300m x 450m x 17m) is involved in one bulk instability, we get a centroid single force CSF ~ 10^6 kg m when using a density of d~2000 kg/m^3. This value is in the same range as we estimated for the minor rotational slides on the Gradenbach DSGSD. As is to be expected, higher frequency seismic activity like tremor and harmonic slide quakes may be sufficiently excited to be recorded by the local seismic network. As with the minor slides at Gradenbach, the low fundamental periods associated with bulk instability were not detected at the Slumgullion flow.

5.5 Precipitation /snowmelt–seismic activity –displacement rate

Neither the seismic activity nor displacement rates at the Randa steep slope were influenced by precipitation or snowmelt between 31-month observation time (Spillmann *et al.*, 2007). As described in Gischig *et al.* (2011), rock instability at the Randa steep slope is driven by thermomechanical forcing. This would imply seasonally variable slip along

critically stressed discontinuities, however the extent to which this effect modulates the seismic activity has not yet been investigated and cannot be determined from a study of the data provided by Spillmann *et al.* (2007) and Gischig *et al.* (2011) alone.

Variations of the displacement rates of the two flow-type landslides, Super Sauce and Slumgullion, are linked to variations in groundwater level or precipitation during the relatively short monitoring periods in the summer. At Super Sauce (Walter *et al.*, 2012), the only slidequakes with magnitudes $M_L > -1.5$ were observed after the strongest rainfall. Increased fissure development coincided with a rise in groundwater level and increased displacement rate once. Seismic activity at the Slumgullion flow shows a daily period with an activity high during daytime. This runs in parallel with significantly higher displacement rates. According to Schulz *et al.* (2009a), these higher displacement rates are due to groundwater level changes caused by the diurnal air pressure variation.

In contrast to the flow type landslides Super Sauce and Slumgullion, significant seismic activity occurring before an increase in displacement rates was observed at the DSGSD type landslides Steinlehnen, Sechillienne, and Gradenbach. At Steinlehnen, LMEs precede acceleration by about 6 days, and rockfall intensity increases significantly in time with the acceleration. It is the only example where neither precipitation nor snowmelt triggers the acceleration. At Séchillienne, LME and rockfall frequency immediately follow precipitation, whereas an increase of displacement rates is delayed by about 4 days.

In the year 2009, seismic activity at Gradenbach with tremor and other LME types coincided with snowmelt. After about 5 weeks of silence, the acceleration phase of the slope started together with LME and rockfall activity. About 4 months after snowmelt, the seismic activity ceased together with the displacement rates. The seismic noise analysis by PSD revealed a response of noise amplitudes to heavy precipitation events with delays of about 12h and 26h. As already addressed in section 4.3, the temporal evolution of seismic activity at Gradenbach before a significant acceleration is controlled by percolation of snowmelt and rain at two levels. The upper level consisting of soil and highly disintegrated rock is destabilized by percolating water and increased pore water pressure for about one week after onset of snowmelt. The sources of increased noise after heavy precipitation are also located in this upper level. The following 5 weeks of seismic inactivity indicated that percolating water does not trigger LMEs at deeper levels of the landslide mass. The restart of seismic activity and the start of increasing displacement rates roughly 6 weeks after onset of snowmelt are interpreted to coincide with a sufficient increase of pore water pressure at the level of the sliding surface or zone by the percolating snowmelt. The sensitive seismic reaction of the upper level of the Gradenbach DSGSD implies that not only is the basal sliding zone near an ultimate limit state, but the uppermost layers are also always near an ultimate stress state. The observed minor slides (like that one shown in Figure 32a) further support this assumption.

5.6 Potential for prediction and early warning

Besides the intention of learning more about the deformation mechanisms of landslides, seismic monitoring of landslides is expected to support the prediction of the long term evolution of a landslide and complement early warning systems. On the basis of the data reviewed in this chapter, conclusions are currently only speculative but may focus future seismic monitoring efforts upon essential tasks. We restrict our examples to

those of steep slopes and DSGSD, Randa and Gradenbach, which have E_S/E_P ratios differing by more than 3 orders (Table 1).

To the author's knowledge, neither a rupture of a large and steep slope nor a catastrophic acceleration of a DSGSD has been monitored by a local seismic network thus far. However, data are available for a steep slope on a much smaller scale from a cliff collapse near Mesnil-Val on the Normandy coast, France. Amitrano *et al.* (2005) report seismic monitoring of such an event, including the precursory phenomena. The frequency N(t) and the seismic energy E(t) obey inverse Omori's laws. The generalized form of Omori's law (*e.g.*, Utsu, 1961), describes the temporal evolution of aftershock frequency after a major earthquake (Equation 28), however, with different parameters k, c, p, and the time t taken as time to the slope failure or major earthquake it can be applied to model foreshocks (*e.g.*, Peng *et al.*, 2007; Schmid & Grasso, 2012) or LMEs preceding slope failure.

$$N(t) = k/(c + t)^p \tag{28}$$

The data from the Mesnil-Val site suggest that a warning based on increased activity could be given ~10 min before the collapse and a reliable prediction of the rupture time about 1 min in advance, provided data acquisition and continuous updating of calculations are done in real-time.

The following arguments support the assumption that an inverse Omori law would also apply to the transition of the seismo-active scarp area at Randa to a third catastrophic rockslide:

- The relatively high ratio E_S/E_P indicates a coupling of deformation and seismic activity.
- LMEs at Randa are slope tectonic earthquakes indicating the decrease of cohesion at shear planes or tensional strength at steeply dipping discontinuities.
- The slope failure happens immediately after reduction of cohesion at shear planes and tensional strength at steeply dipping discontinuities.

  The ratio E_S/E_P of the Gradenbach DSGSD is only 0.03% of the ratio for the Randa steep slope. This low ratio is in line with the findings that the kinematics of the Gradenbach DSGSD approximately matches those of a block movement, but silent sliding prevails at the basal surface. Long term data on variations, in particular a temporal decrease of E_S/E_P, could be diagnostic for the evolution of the basal sliding surface.

  A close look to Figure 24 shows that rockfall and one LME type (labeled B) start together with the geodetically observable activation of the mass movement. This seismic data may therefore support the interpretation of the geodetic data with regard to the near future development of the sliding process.

  Significant seismic precursors occurred at the Gradenbach DSGSD about 6 weeks before the geodetically observable acceleration together with the onset of snowmelt. It has been shown that accelerations of the Gradenbach DSGSD are significantly controlled by the cumulative input of snowmelt and precipitation (Brückl *et al.*, 2013 and references therein). Presently, a question of interest is if the precursory seismic activity is only a consequence of the infiltration or if its intensity also tells us something about the general state of stress of the slope and its readiness for a dangerous acceleration.

6 RÉSUMÉ / CONCLUSION

On the basis of general and well accepted landslide classification schemes, we grouped examples of large landslides with seismicity into unstable steep slopes, where pre- or post-failure processes may occur, slopes with deep seated gravitational slope deformation (DSGSD) in crystalline rock and flow-type mass movements, where original rock structures are completely destroyed and transformed into a granular material.

Seismic data acquisition and analysis methods used in the observation of seismicity generated by the movement of large landslides can build on general seismological concepts. Considering different schemes of field geometries, the deployment of several mini-arrays appears to be the best compromise between effort / costs and resolution of LMEs (Landslide Micro-Earthquakes), at least for larger network areas. Seismic sensors mounted in deep boreholes (*e.g.*, > 30m) substantially support the location of hypocenters, especially the determination of the focal depth. Event detection, discrimination of signals unrelated to landslide related seismicity and event classification are issues. We refer to methods based on spectrograms, sonograms and their processing by image processing tools. Many LMEs have low S/N ratios and emergent arrivals of seismic phases. Location based on travel times is therefore frequently not possible and alternative methods such as beam forming are successfully applied. We also emphasize the potential of methods based on the decay of seismic amplitudes with distance.

LMEs generated by these different landslide classes show a variety of waveforms, which can be classified interactively but also automatically on the basis of parameters like signal duration, frequency content or the pattern of the envelope. These waveforms range from impulsive events similar to those generated by small explosions to tremor lasting several tens of seconds. Rockfall can be clearly identified and distinguished from the recordings of LMEs. Seismic efficiency, the ratio between the seismic energy radiated by LMEs and the total potential energy release during the same time interval, varies by more than 3 orders between examples for a steep slope (highest), a flow and a DSGSD (lowest).

Seismic sources are usually represented by their scalar seismic moment or, if the radiation pattern of seismic waves is taken into account, by the seismic moment tensor. LMEs have magnitudes below M = 0. The corresponding dimensions of the focal area and rupture velocities suggest that source times are in the range of 0.01 s or below. Thus the source of impulsive and short seismic events may be described by a moment tensor and a very short source time function. Due to its physical similarity to tectonic earthquakes, we termed this LME type "slope tectonic earthquake". The other extreme in the manifold LME waveforms is tremor. Significant occurrence of tremor was observed on a DSGSD-type (Gradenbach) and a flow-type (Slumgullion) landslide. We associated tremor with the single force mechanism and termed the source process "bulk instability". The observed tremors were interpreted as the higher frequency seismic signals generated during long period (> 10 s) instability of a fraction of the whole landslide mass. The bulk instability comes to rest because of the decreasing diving gravitational force during a rotational slide, or because of shear deformation causing dilatancy and decreasing pore pressure. The fundamental period of bulk instability has not been observed so far. Observation by broad band seismometers would be necessary to observe these signals.

Whereas seismicity at the steep slope (Randa) showed no correlation with precipitation, snowmelt, and displacement rates, the DSGSD examples show significant patterns. At one example (Steinlehnen), a significant geodetically observed acceleration of an active slab was preceded by LMEs by about six days. No hydro-meteorological trigger could be identified. The high velocity phase was accompanied by rockfall. At the two other examples (Séchillienne and Gradenbach), LME activity increased or even started with high precipitation and / or the beginning of snowmelt. In one case (Séchillienne), the geodetically observable acceleration started roughly four days later, while at another (Gradenbach) it started six weeks later. This delay is interpreted as the time required for precipitation or snowmelt to accumulate at the level of the main sliding surface and to increase pore pressure there. The frequencies of some LME types also correlated with the geodetically observed acceleration or the episodic high velocity phase. One flow-type landslide (Slumgullion) exhibits an extremely high sensitivity to pore pressure at the sliding surface. Pore pressure variations at the sliding surface, induced by the diurnal air pressure variations, trigger small bulk instabilities observable by geotechnical devices and the associated LMEs (tremor and so-called harmonic slidequakes).

Seismic efficiency and the temporal development thereof, the prevailing LME-types and their spatial distribution, and especially the relations to hydro-meteorological parameters as well as displacement and deformation by no doubt have the potential to support early warning systems. However, we must admit that the study of seismic signals generated by large landslides and their relation to the landslide type and kinematics, the state of evolution, hydro-meteorological parameters, and displacement rates is still a young discipline. Long term multidisciplinary monitoring covering phases of both low and high activity would improve our understanding. Comparative studies could benefit from the simultaneous observation of landslides of the same type in different states of activity. Methodological progress should be achieved by the determination of the source mechanisms (either moment tensor or single force) and the extraction of the source time function. The monitoring of long period signals would also be very interesting, and to this end broad band seismometers have already been installed at some landslides.

REFERENCES

Aki K, Richards PG (1980) *Quantitative Seismology Theory and Methods*, Vol 1, W.H. Freeman and Company, San Francisco, pp. 557.

Aki K & Richards PG (2002) *Quantitative Seismology Theory and Methods*, Vol 1, W.H. Freeman and Company, San Francisco, pp. 557.

Allen RV (1978) Automatic earthquake recognition and timing from single traces: *Bulletin of the Seismological Society of America*, 68, no. 5, pp. 1521–1532.

Almendros J, Ibáñez JM, Alguacil G, Del Pezzo E (1999) Array analysis using circular-wavefront geometry: An application to locate the nearby seismo-volcanic source. *Geophysical Journal International* 136, pp. 159–170. doi:10.1046/j.1365-246X.1999.00699.x.

Amitrano D, Grasso JR, Senfaute G (2005) Seismic precursory patterns before a cliff collapse and critical point Phenomena. *Geophysical Research Letters* 32, L08314. doi:10.1029/2004GL022270

Bisci C, Burattini F, Dramis F, Leoperdi S, Pontoni F, Pontoni F (1996) The Sant'Agata Feltria landslide (Marche Region, central Italy): a case of recurrent earth flow evolving from a deep-seated gravitational slope deformation. *Geomorphology* 15, pp. 351–361.

Brückl E, Brückl J, Heuberger H (2001) Present structure and prefailure topography of thre giant rockslide of Köfels. *Zeitschrift für Gletscherkunde und Glazialgeologie*, 37/1, pp. 49–79.

Brückl E, Parotidis M (2005) Prediction of slope instabilities due to deep-seated gravitational creep. *Natural Hazards and Earth System Sciences*, 5, pp. 155–172. SRef-ID: 1684-9981/nhess/2005-5-155.

Brückl E, Brückl J (2006) Geophysical models of the Lesachriegel and Gradenbach deepseated mass movements (Schober range, Austria). *Engineering Geology* 83, pp. 254–272.

Brückl E, Brunner FK, Lang E, Mertl S, Müller M, Stary U (2013) The Gradenbach Observatory-monitoring deep-seated gravitational slope deformation by geodetic, hydrological, and seismological methods. *Landslides*. doi: 10.1007/s10346-013-0417-1.

Brückl E, Binder D, Mertl S (2015) Seismic Sources from Landslides and Glaciers. *Encyclopedia of Earthquake Engineering*. DOI 10.1007/978-3-642-36197-5_385-1, Springer-Verlag Berlin Heidelberg.

Collins DS, Toya Y, Hosseini Z, Trifu CI (2014) Real time detection of rock fall events using a micro-seismic railway monitoring system. In: GeoHazards 6, Kingston, Canada.

Crandell DR, Varnes DJ (1961) *Movement of the Slumgullion earthflow near Lake City*, Colorado. Geological Survey Research, 1961, U.S. Geol. Survey Prof. Paper 424-B, art. 57, pp. 136–139.

Cruden DM, Varnes DJ (1996) Landslide types and processes. In: Turner AK, Schuster RL (eds.), *Landslides: Investigation and Mitigation. Transportation research board special report* 247, pp. 36–75.

Deparis J, Jongmans D, Cotton F, Baillet L, Thouvenot F, Hantz D (2008) Analysis of rock-fall and rock-fall avalanche seismograms in the French Alps. *Bulletin of the Seismological Society of America* 98 (4), pp. 1781–1796.

Draxler AM (2013) *Seismic Noise Analysis at the Gradenbach Landslide*. Diploma Thesis, TU Wien. pp. 108.

Eberhardt E, Stead, D, Coggan JS (2004) Numerical analysis of initiation and progressive failure in natural rock slopes–the 1991 Randa rockslide. International Journal of Rock Mechanics and Mining Sciences, 41, 1, pp. 69–87.

Ekström G, Nettles M, Abers GA (2003) Glacial earthquakes. *Science* 302, pp. 22–624. doi:10.1126/science.1088057.

Ekström G, Stark CP (2013) Simple Scaling of Catastrophic Landslide Dynamics. *Science* 339 (6126), pp. 1416–1419. doi: 10.1126/science.1232887

Erismann TH, Abele G (2001) *Dynamics of Rockslides and Rockfalls*, Heidelberg, Springer. pp. 316.

Fleming RW, Baum RL, Giardino M (1999) *Map and description of the active part of the Slumgullion Landslide*, Hinsdale County, Colorado. U.S. Geological Survey Miscellaneous Investigation Series Map I-2672.

Fügenschuh B, Seward D, Mancktelow N (1997) Exhumation in a convergent orogen: The western Tauern Window. *Terra Nova* 9, pp. 213–217.

Gischig V, Moore JR, Evans KF, Amann F, Loew S (2011) Thermomechanical forcing of deep rock slope deformation: 2. The Randa rock slope instability. *Journal of Geophysical Research* 116, F04011. doi:10.1029/2011JF002007.

Gomberg J, Schulz W, Bodin P, Kean J (2011) Seismic and geodetic signatures of fault slip at the Slumgullion Landslide Natural Laboratory. *Journal of Geophysical Research* 116, B09404.

Gonzalez RC, Woods RE, Eddins SL (2004). *Digital Image Processing Using Matlab*. Pearson Prentice Hall.

Goodman RE & Kieffer DS (2000) Behavior of Rock in Slopes. Journal of Geotechnical and Geoenvironmental Engineering 126(8), pp. 675–698.

Hanks, TC, Kanamori H (1979) A moment magnitude scale. *Journal of Geophysical Research* 84, pp. 2348–2350.

Helmstetter A, Garambois S (2010), Seismic monitoring of Séchilienne rockslide (French Alps): Analysis of seismic signals and their correlation with rainfalls, *Journal of Geophyical Research* 115, F03016. doi:10.1029/2009JF001532.

Hungr O, Evans SG, Bovis M, Hutchinson JN (2001) Review of the classification of landslides of the flow type. *Environmental and Engineering Geoscience* VII, pp. 221–238.

Husen vD, Reitner JM (2011) An outline of the Quaternary stratigraphy of Austria. *Quaternary Science Journal* 60 (2–3), pp. 366–387.

Iverson RM (2005) Regulation of landslide motion by dilatancy and pore pressure feedback. *Journal of Geophysical Research*, Vol. 110, F02015, doi:10.1029/2004JF000268

Joswig M (1990) Pattern recognition for earthquake detection, Bull. Seism.Soc. Am., 80, pp. 170–186.

Joswig M (1995) Automated classification of local earthquake data in the BUG small array, Geophys. J. Int. 120, pp. 262–286.

Joswig M (2008) Nanoseismicmonitoring fills the gap between microseismic networks and passive seismic. *First break* 26, pp. 121–128.

Kanamori H, Given JW (1982) Analysis of long-period seismic waves excited by the May 18, 1980, eruption of Mount St. Helens – a terrestrial monopole? *Journal of Geophysical Research B*, 87 (B7), pp. 5422–5432. ISSN 0148-0227.

Kanamori H, Given JW, Lay T (1984) Analysis of seismic body waves excited by the Mount St. Helens eruption of May 18, 1980. *Journal of Geophysical Research B*, 89 (B3). pp. 1856–1866. ISSN 0148-0227.

Kanamori H (1993) Locating earthquakes with amplitude – Application to Real-Time Seismology. *Bulletin of the Seismological Society of America (BSSA)*, 83, pp. 264–268.

Kawakatsu H (1989) Centroid single force inversion of seismic waves generated by landslides. *Journal of Geophysical Research* 94. doi: 10.1029/89JB01118. issn: 0148-0227.

Kilburn CRJ & Petley DN (2003) Forecasting giant, catastrophic slope collapse: lessons from Vajont, Northern Italy. Geomorphology, 54, 1–2, 21–32. 10.1016/S0169-555X(03)00052-7.

Kronfellner-Kraus G (1980) *Neue Untersuchungsergebnisse in Wildbächen – Der Talzuschub in Abhängigkeit von Niederschlägen*. International Symposium Interpraevent. Bad Ischl, 1, pp. 179–192.

Lay T, Wallace TC (1995) *Modern Global Seismology*, Academic Press, San Diego, pp. 521.

Le Roux O, Schwartz S, *et al.* (2009) CRE dating on the head scarp of a major landslide (Séchilienne, French Alps), age constraints on Holocene kinematics. *Earth and Planetary Science Letters* 280, pp. 236–245.

Lipman PW (1976) Caldera-collapse breccias in the western San Juan Mountains, Colorado. *Geological Society of America Bulletin* 8, pp. 1387–1410.

Madole RF (1996) Preliminary chronology of the Slumgullion landslide, Hinsdale County, Colorado. In Varnes, D.J., Savage, W.Z., eds., The Slumgullion earth flow: a large-scale natural laboratory. U.S. Geological Survey Bulletin 2130, pp. 5–8.

Mair am Tinkhof K, Buhl V, Schmalz T (2010) Instabile Talflanken: ein interdisziplinärer Ansatz zur Analyse. *Vortragsreihe Seminar Geowissenschaften*, Vienna University of Technology.

Malet JP, Laigle D, Remaitre AO, Maquaire O (2005) Triggering conditions and mobility of debris flows associated to complex earthflows. *Geomorphology* 66, pp. 215–235.

McNamara DE, Buland RP (2004) Ambient Noise Levels in the Continental United States, *Bulletin of the Seismological Society of America* 94, (4), pp. 1517–1527.

Mertl S & Brückl E (2007) Observation of fracture processes in creeping rock masses by seismic monitoring. Proceedings at 11th Congress of the International Society for rock Mechanics, Lisbon, Portugal, 9–13 July 2007.

Mertl S (2015) *Characterization of local seismic events on the deep-seated events gravitational slobe deformation Gradenbach*. Phd. Thesis, TU Wien, pp. 176.

Moser TJ, Eck TV, Nolet G (1992) Hypocenter determination in strongly heterogeneous earth model using the shortest path method. *Journal of Geophysical Research* 97, pp. 6563–6572.

Peng Z, Vidale JE, Ishii M, Helmstetter A (2007) Seismicity rate immediately before and after main shock rupture from high-frequency waveforms in Japan. *Journal of Geophysical Research*, VOL. 112, B03306, doi:10.1029/2006JB004386, 2007.

Prager C, Zangerl C, Patzelt G, Brandner R (2008) Age distribution of fossil landslides in the Tyrol (Austria) and its surrounding areas. *Natural Hazards and Earth System Sciences* 8, pp. 377–407.

Preh A, Poisel R (2004) A UDEC model for "Kink Band Slumbing" type failures of rock slobes. In: *Numerical Modeling of Discrete Materials in Geotechnical Engineering, Civil Engineering and Earth Sciences*, Proceedings of the 1 st UDEC/3DEC Symposium, Bochum, Germany, Balkema, pp. 243–247.

Reid HF (1910) *The Mechanics of the Earthquake, The California Earthquake of April 18, 1906, Report of the State Investigation Commission*, Vol.2, Carnegie Institution of Washington, Washington, D.C.

Roth M & Blikra LH (2005) Seismic monitoring of the unstable rock slope site at Åknes, Norway. Ber.Geol. B.-A., 82, ISSN 1017-8880-Landslide Monitoring Technologies & Early Warning Systems.

Schmid A, Grasso JR (2012) Omori law for eruption foreshocks and aftershocks. *Journal of Geophysical Research*, vol. 117, B07302, doi:10.1029/2011JB008975.

Schorlemmer D, Wiemer S, Wyss M (2005) Variations in earthquake-size distribution across different stress regimes. *Nature* 437, pp. 539–542, doi:10.1038/nature04094.

Schulz WH, Kean JW, Wang G (2009a) Landslide movement in southwest Colorado triggered by atmospheric tides. *Nature Geoscience, Letters*, DOI:10.1038/NGEO659.

Schulz WH, McKenna JP, Kibler JD, Biavati G (2009b) *Relations between hydrology and velocity of a continuously moving landslide—evidence of pore-pressure feedback regulating landslide motion? Landslides* 6, pp. 181–190.

Schweitzer *et al*., NMSOP (2002) Seismic Arrays. in: *Instrumentation in Earthquake Seismology. Chapter 9*. Jens Havskov, Gerardo Alguacil (eds.) Springer Science & Business Media

Spillmann T, Maurer H, Green AG, Heincke B, Willenberg H, Husen S (2007) Microseismic investigation of an unstable mountain slope in the Swiss Alps. *Journal of Geophysical Research* 112, B07301. doi: 10.1029/2006JB004723.

Stein S, Wysession M (2003) *An Introduction to Seismology, Earthquakes and Earth Structure*, Blackwell Publishing, Oxford, pp. 498, ISBN 0-86542-078-5.

Tarantola A, Valette B (1982) Inverse problems = quest for information. *Journal of Geophysics* 50, pp. 159–170.

Utsu T (1961) A statistical study of the occurrence of aftershocks. *Geophysical Magazine* 30, 521, 605.

Van Asch TW, Malet JP (2009) Flow-type failures in fin-grained soils: an important aspect in landslide hazard analysis. *Natural Hazards and Earth System Sciences* 9, pp. 1703–1711.

Varnes DJ, Savage WZ (eds) (1996) The Slumgullion earth flow: a large-scale natural laboratory. *U.S. Geological Survey Bulletin* 2130.

Walter M, Arnhardt C, Joswig M (2012) Seismic monitoring of rockfalls, slide quakes, and fissure development at the Super-Sauze mudslide, French Alps. *Engineering Geology* 128, pp. 12–22.

Weginger S (2012) *Detektion und Lokalisierung seismischer Signale zur Überwachung der Massenbewegung Steinlehnen*. Master thesis, TU Wien. pp. 96.

Willenberg H (2004) Geologic and kinematic model of a complex landslide in crystalline rock (Randa, Switzerland), Ph.D. Thesis, 184 pp, ETH Zürich.

Winberry JP, S. Anandakrishnan S, Wiens DA, Alley RB (2013) Nucleation and seismic Tremor associated with the glacial earthquakes of Whillans Ice Stream, Antartica. *Geophysical Research letters* 40, pp. 312–315. doi: 10.1002/grl.50130.

Walter M & Joswig M (2008) Seismic monitoring of fracture processes generated by a creeping landslide in the Vorarlberg Alps, First Break 26(6), pp. 131–135.

Wust-Bloch GH, Joswig M (2006) Pre-collapse identification of sink-holes in unconsolidated media at Dead Sea area by "Nanoseismic Monitoring" (graphical jackknife-location of weak sources by few, low-SNR records). *Geophysical Journal International* 167, pp. 1220–1232.

Yamada M, Matsushi Y, Chigira M, Mori J (2012) Seismic recordings of landslides caused by Typhoon Talas (2011), Japan. *Geophysical Research Letters*, vol. 39, L13301, doi:10.1029/2012GL052174.

Zangerl C, Eberhardt E, Schönlaub H, Anegg J (2007) Deformation behaviour of deep-seated rockslides in crystalline rock. In: Rock mechanics: proceedings of the 1st Canada-US rock mechanics symposium, Vancouver, 27–31 May 2007. doi: 10.1201/NOE0415444019-c112.

Zischinsky U (1969) Über Sackungen. *Rock Mechanics* 1, pp. 30–52.

Chapter 14

Seismic monitoring of geological CO_2 storage

S. Lüth & A. Liebscher
Section 6.3 Geological Storage, GFZ German Research Centre for Geosciences, Potsdam, Germany

Abstract: Carbon capture and geological storage (CCS) has been discussed as one of several options contributing to the reduction of greenhouse gas emissions related to human activities for about two decades now and many countries have developed first projects investigating all aspects of the CCS process chain. The geological storage of carbon dioxide (CO_2) is and has been investigated at a number of sites of various scales. Small scale pilot sites (storing less than 100,000 tons of CO_2) provide ideal laboratory conditions for testing various monitoring approaches, including seismic methods. Demonstration and full scale storage sites (storing CO_2 in the order of up to several million tons) show feasibility at large scale and demonstrate the performance of large scale 4D seismic measurements in tracking the CO_2 plume in the reservoir. The ability of seismic measurements to image CO_2 distribution in a storage formation depends on the contrast between the elastic properties of the storage formation before injection and with CO_2 injected. Saline aquifers within sedimentary basins are almost ubiquitous over the globe and are therefore regarded as most prospective storage formations. They also, particularly at shallow to intermediate depth levels (down to around 1,500 m), provide favorable conditions for seismic monitoring due to the large impedance contrast between brine and free phase CO_2. This has been demonstrated by pilot and full scale storage projects at Ketzin and Sleipner. Laterally heterogeneous geological conditions and greater depths pose larger challenges for surface based seismic monitoring and in these cases, borehole based observations become crucially important as shown at the Nagaoka site. Depleted oil and gas reservoirs are candidate structure for CO_2 storage as well, but even with extremely high levels of repeatability, seismic monitoring of CO_2 stored in such formations is hardly feasible from the surface, and still difficult using borehole based methods, due to a very small elastic contrast between initial reservoir conditions and those after starting CO_2 injection. But also at sites where a direct seismic monitoring of CO_2 in the primary reservoir is hardly possible, often saline aquifers at shallow to intermediate depth are potential areas of secondary CO_2 accumulation after leakage, and in this case, seismic measurements are an indispensable tool for above reservoir monitoring assuring safe storage and the absence of leakage out of the storage complex.

1 INTRODUCTION TO GEOLOGICAL CO_2 STORAGE

1.1 Motivation

The emissions of anthropogenic greenhouse gases (GHG) due to the combustion of fossil fuels have strongly increased since the onset of Industrial Revolution and they are commonly considered the main reason for global warming. The most important GHG in terms of their contribution to the greenhouse effect are water vapor and clouds (H_2O), carbon dioxide (CO_2), methane (CH_4), and ozone (O_3) (Kiehl & Trenberth, 1997). Most greenhouse gases have natural sources and sources related to human activities the like, but after about 1750, human activities have caused a substantial increase in atmospheric GHG concentration. Atmospheric CO_2 concentration rose from 280 ppm before 1750 to presently 395 ppm (Blasing, 2014). Methane concentrations rose from 722 ppb (before 1750) to about 1800 ppb at present. CO_2, relative to other GHG, has low global warming potential (GWP) (*e.g.* relative GWP = 1 for CO_2, GWP = 72 for methane for 20 years, GWP = 16,300 for sulfur hexafluoride (IPCC, 2007a)), but due to its relatively high atmospheric concentration, it is the main contributor to global warming (except for water vapor which, however, is not affected much on the global scale by human activity). The reduction of anthropogenic CO_2 emissions is therefore considered to be a crucial measure in order to limit the increase in global mean temperature to two degrees Celsius above pre-industrial levels (IPCC, 2013).

The portfolio of measures to mitigate CO_2 emissions comprises enhanced energy efficiency, renewables, nuclear energy, coal to gas substitution, and the capture and geological storage of carbon dioxide (CCS). The availability of fossil fuels is finite, but still oil and gas reserves (including unconventional resources) have been proven to last for decades (IPCC, 2007b), and the reserves of coal will even last much longer (Thielemann *et al.*, 2007) although there is an on-going debate concerning the expected long-term world production (Rutledge, 2011). For the next decades, which will see persistent use of fossil fuels combustion as well as significant CO_2 emissions related to, *e.g.* cement or steel production, CCS can significantly contribute to reducing GHG emissions (IPCC, 2005; Volkart *et al.*, 2013).

1.2 Pilot, demonstration and full scale storage sites

Geological CO_2 storage is the last link of the CCS chain. Previously captured carbon dioxide is injected into appropriate geological formations where it is to remain safely stored over hundreds to thousands of years until the reservoir has reached a stable state due to dissolution and mineralization of the free gas phase. Formations suitable for CO_2 storage are deep saline formations, mature oil and gas fields, and unminable coal seams (ECBM, enhanced coal bed methane). Furthermore, CO_2 storage may be combined with enhanced oil or gas recovery (CO_2-EOR, CO_2-EGR; IPCC, 2005). In order to investigate the potential of different geological formations to serve as CO_2 storage reservoirs, CO_2 was injected at several sites of various characteristics and intensive efforts were made in monitoring the storage related processes at these sites. It is far beyond the scope of this review to provide a complete overview of all CO_2 storage projects but it should be noted that the projects can be subdivided into three different

classes which can be ranked according to the amount of carbon dioxide stored in the respective project. We distinguish pilot, demonstration and commercial scale projects (Michael *et al.*, 2010).

Pilot sites are typically characterized by injection rates in the order of 10,000 tons CO_2 per year, with an injection phase lasting a few weeks up to several years. The total amount of stored carbon dioxide is less than 100,000 tons. The Frio project injected 1,600 tons of CO_2 into the Frio Formation, underlying large areas of the United States Gulf Coast (Hovorka *et al.*, 2006). At Nagaoka (Japan), 10,400 tons of CO_2 were injected into a thin permeable sandstone layer at 1,100 m depth (Saito *et al.*, 2006). At Ketzin (Germany), the first European onshore pilot site was operated and 67,000 tons of CO_2 were injected into a saline aquifer formation at 630–650 m depth (Martens *et al.*, 2014). A depleted gas reservoir was used for the storage of more than 65,000 tons of naturally occurring CO_2 mixed gas within the Australian Otway project at a depth of 2,050 m (Underschultz *et al.*, 2011).

Demonstration projects are commonly regarded as the next step after successful completion of pilot projects on the path towards full scale storage sites. Typically, about one million tons of CO_2 are injected at a rate of a few hundred thousand tons per year. In the Illinois Basin (USA), as of late summer 2014, about 900,000 tons of CO_2 have been injected at 2,000 m depth into the Mt. Simon Sandstone within the DECATUR project (Gollakota & McDonald, 2012; Streibel *et al.*, 2014). The Secarb Cranfield project (Mississippi, USA) was initially designed as a demonstration scale project. After injecting more than 3 million tons of CO_2 into the more than 3 km deep Tuscaloosa Formation, the project has already reached commercial scale (Hovorka, 2013).

Full (or commercial) scale storage sites are typically characterized by injection rates in the order of a few hundred thousand to some million tons of CO_2 per year. Total capacities reach several tens of million tons. The first commercial scale project of CO_2 storage commenced in 1996 at Sleipner in the Norwegian North Sea (Torp & Gale, 2004). The saline Utsira Formation has been used for the injection of CO_2 co-produced with natural gas from the Sleipner field since then. More than 15 million tons of CO_2 have been injected since 1996 (Global CCS Institute, 2014). Further commercial scale projects are related to gas production (In Salah, Algeria), or an LNG plant (Snøhvit, Norway, see Eiken *et al.*, 2011). More large scale projects are currently under development, *e.g.* Gorgon in Australia (Malek, 2009) or in China (Li *et al.*, 2013).

2 GEOPHYSICAL PROPERTIES OF ROCKS AND CO_2

The density of CO_2 is characterized by high variability, depending on the pressure and temperature conditions. Above critical pressure and temperature conditions (31° Celsius, 7.4 MPa), CO_2 reaches supercritical conditions. For typical pressure-temperature gradients in sedimentary basins, this is accompanied by a significant increase in CO_2 density and CO_2 storage typically targets at reservoirs below 800–1000 m depth in order to ensure CO_2 remains supercritical and thus utilizes the available pore space efficiently. Figure 1 shows the density-temperature function of CO_2 depending on pressure conditions, and the CO_2 density depending on reservoir depth (assuming hydrostatic conditions and various temperature gradients with depth). For low to

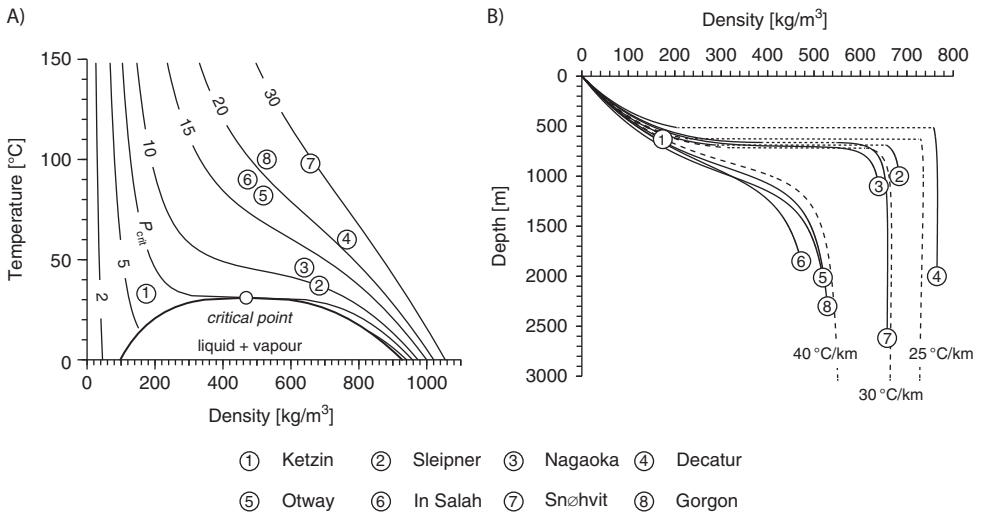


Figure 1 Density-temperature-pressure (A) and density-depth (B) relations for pure CO_2 as calculated with the EOS of Span & Wagner (1996). Isolines in (A) refer to pressure given in MPa. Circles refer to initial reservoir conditions for exemplary CO_2 storage sites. CO_2 density as function of depth (B) is calculated assuming linear temperature increase with depth and hydrostatic pressure conditions. Dotted lines indicate phase transition from vapor to liquid CO_2 and stippled lines refer to hypothetical geothermal gradients of 25, 30 and 40 °C/km.

intermediate temperature gradients, CO_2 density rapidly reaches high density values (> 600 kg/m^3) below 700–800 m depth, for high temperature gradients, density remains low down to ca. 1000 m and then gradually increases to higher density values (~500 kg/m^3) between 1500 and 2000 m depth. Thus, the optimal storage depth depends on the geothermal gradient and is below 800 m for "cold" regions and below 1500 m for "warm" regions. Reservoir conditions of various storage projects are indicated showing projects in "warm" environments are at 2000 m depth or deeper, whereas projects in "cold" environments may be as shallow as 1000 m. The Ketzin pilot site is characterized by exceptionally shallow reservoir depth where CO_2 in the reservoir can be expected to reside in gaseous state and to cause a stronger seismic response than if the CO_2 were present as a supercritical fluid under higher pressure conditions (Kazemeini *et al.*, 2010).

2.1 Rock physics models

When CO_2 is injected into a porous reservoir formation it will replace the initial pore fluid which may be brine, oil or gas. The seismic signature of CO_2 injected into a storage formation depends on the contrast between elastic properties of reservoir rocks before CO_2 injection and reservoir rocks with partial or full saturation of CO_2. The elastic properties of porous rocks with multi-phase pore fluids depend on the saturation relation of the pore fluids and also on the distribution of the pore fluids. We distinguish between uniform saturation (all pores in the rock are

considered to have the same saturation) and patchy saturation (multiple fluids are distributed as patches of one single fluid, respectively). Biot-Gassmann substitution theory is commonly used to estimate the effect of fluid changes on elastic properties of rocks for low frequencies (Gassmann, 1951; Biot, 1956). The effective bulk modulus of rock with pore fluid (K_{sat}) can be expressed using the effective bulk modulus of dry rock (K_{dry}), the bulk modulus of the mineral material making up the rock (K_0), the effective bulk modulus of the pore fluid (K_{fl}) and porosity (Φ) (Mavko *et al.*, 1998):

$$K_{sat} = K_{dry} + \frac{(1 - \frac{K_{dry}}{K_0})^2}{\frac{\Phi}{K_{fl}} + \frac{1-\Phi}{K_0} - \frac{K_{dry}}{K_0^2}} \tag{1}$$

This equation is valid under the assumption of homogeneous mixture of pore fluids involved, such as CO_2 and brine, or CO_2 and methane or oil. Further assumptions are porous, isotropic, and homogeneous rocks which are elastic and have entirely connected pore spaces (Kazemeini *et al.*, 2010 and references therein). Generally, the Biot-Gassmann equation can be assumed to be valid at seismic frequencies (below about 100 Hz), where wavelength is usually large enough to consider the porous rock as effectively homogeneous. For higher seismic frequencies which are used in sonic logging or in laboratory experiments, heterogeneous saturation patches need to be considered which do not equilibrate while being passed by a seismic wave. The effective bulk modulus for patchy saturation distribution (K_{patchy}) is described by Hill's equation (Kazemeini *et al.*, 2010):

$$K_{patchy} = \left[\sum_{i=1}^{n} \frac{x_i}{K_i + \frac{4}{3}G}\right]^{-1} - \frac{4}{3}G, \tag{2}$$

where n is the number of distinct fluid filled patches, x_i is the volume fraction of the *i*th patch, K_i is the bulk modulus of the rock saturated with the *i*th fluid (which for fluid mixtures is again calculated based on the Biot-Gassmann equation), and G is the rock's shear modulus. In Figure 2, seismic impedance (P-wave velocity * density), and P-wave velocity are shown for an exemplary case of a typical sandstone reservoir, initially filled with brine as a pore fluid, and CO_2 replacing brine (S_{gas}). For the uniform saturation case (Biot-Gassmann), seismic impedance and P-wave velocity are highly sensitive at low CO_2 saturation values, whereas for the patchy saturation distribution, seismic impedance and P-wave velocity show approximately linear behavior relative to CO_2 saturation.

In most cases, at frequencies commonly used in surface seismic surveys, the uniform saturation case will be applicable, whereas at the laboratory scale and in sonic logging applications, the patchy saturation model will be applicable for heterogeneous reservoirs. Time-lapse sonic log measurements and CO_2 saturations, derived from pulsed neutron gamma logs, were investigated at the Nagaoka pilot site. Comparison with rock physical models showed that the observations were best explained by a patchy saturation model, modified to take into account irreducible water saturation (Azuma *et al.*, 2013).

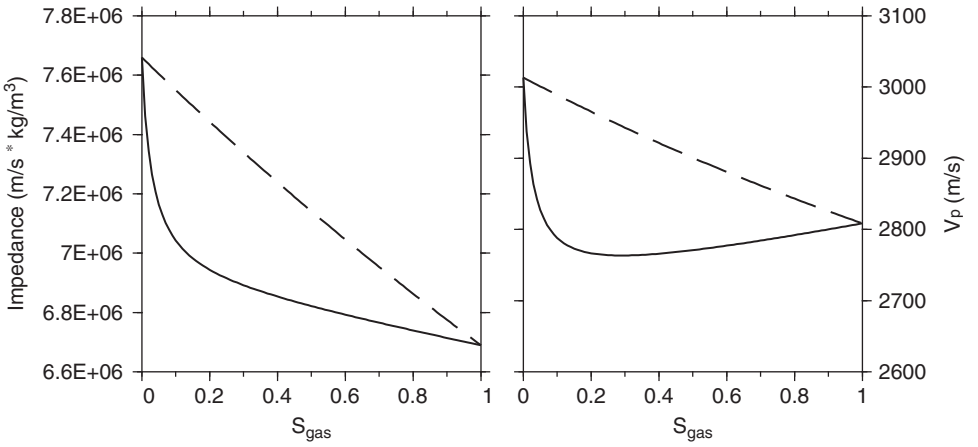


Figure 2 Seismic impedance (P-waves) and P-wave velocity versus CO_2 saturation in a typical sandstone reservoir with brine as initial pore fluid. The solid lines show the uniform saturation model (Biot-Gassmann, Equation 1), the dashed lines show the patchy saturation (Equation 2). As a reservoir, an initially brine filled sandstone at 1,500 m depth is assumed.

2.2 Laboratory measurements

In addition to mere fluid mixing, the injection of CO_2 into a storage formation will disturb the previously existing physico-chemical equilibrium between the rock matrix and the pore fluid (Nover *et al.*, 2013). The following changes may occur in the storage formation which may directly or indirectly affect the elastic and hydrological properties of the formation: decrease in pH, pore pressure increase, and dissolution and precipitation of mineral phases. In order to understand these processes of fluid-solid interaction, laboratory tests under reservoir conditions are an important contribution providing important base data for geophysical monitoring.

CO_2 flooding experiments in order to support the interpretation of reservoir monitoring results were performed about two decades ago already (Wang *et al.*, 1998). A focus of these measurements was on the response of V_p and V_s to changes in CO_2 saturation and pressure increase. V_p decreased due to increasing CO_2 saturation and increasing pressure. The effects of CO_2 saturation on V_s were negligible and V_s decreased, mainly due to increasing reservoir pressure.

Core materials from real storage sites are rarely available, but several studies have been performed using surface outcrop or core samples from shallow wells, and some also used samples from deep storage formations (Zemke *et al.*, 2010; Ivanova *et al.*, 2012; Hangx *et al.*, 2013; Gurevich *et al.*, 2014). Long-term batch experiments were performed on sandstone samples. When brine was replacing CO_2 as a pore fluid, 14% of V_p increase was observed. When CO_2 was flooded into the sample to replace the brine again, only a slight decrease of V_p was observed (3%) which was interpreted as an indication of irreducible water saturation in the order of ~50% (Zemke *et al.*, 2010).

Kummerow & Spangenberg (2011) simulated the injection of pure CO_2 and of CO_2 with minor amounts of SO_2 into a saline aquifer using a reservoir sandstone sample of the Ketzin CO_2 storage pilot site. A strong dependency of the results on the purity of the

CO_2 was observed. While the sample flooded by pure CO_2 showed V_p-saturation behavior according to the "patchy saturation model", injection of SO_2 contaminated CO_2 resulted in a V_p-saturation function according to the uniform saturation model. Critical reservoir properties such as permeability and porosity changed considerably due to CO_2-SO_2 injection into the reservoir sandstone sample.

Seismic velocity and attenuation tomography was performed with porous sandstone samples during CO_2 injection experiments (Lei & Xue, 2009). Difference tomography imaged changes in velocity and attenuation due to partial replacement of water by CO_2. P-wave velocity reduction and increased attenuation were observed due to partial CO_2 saturation. The experimental results were in good agreement with the White and Dutta-Odé theory for partial saturation (Dutta *et al.*, 1979). This implied that fluid diffusion played a major role in velocity dispersion and energy loss at ultrasonic frequencies.

3 3D REFLECTION SEISMIC MEASUREMENTS

Repeated 3D seismic measurements (commonly referred to as "4D seismic" or "time-lapse seismic" measurements) generally provide the most comprehensive insight into the distribution of the CO_2 injected into the storage formation, including also potential signatures of CO_2 which may have leaked into shallower formations above the cap rock. 3D seismic measurements are the most broadly applied geophysical method in the oil and gas industry in the search for new hydrocarbon reservoirs and in exploiting existing reservoirs. Seismic measurements consist in the controlled operation of seismic sources (explosives, vibrator trucks, accelerated weight drops and others) on a pattern of distributed source point locations, and the recording of the resulting elastic wavefield using seismic receivers (geophones, hydrophones, seismometers or fiber optic cables, a recent development gaining importance in borehole seismic measurements). The seismic wavefield is reflected at heterogeneities of the seismic impedance (the product of P- or S-wave velocity and density) in the underground which may be related to stratigraphic layer boundaries or variations in the pore fluids in the respective geological formations. If sources and receivers are distributed along profiles on the Earth's surface, we commonly call these 2D seismic measurements, as these measurements aim at imaging a 2D section of the Earth's interior. If sources and receivers are distributed in an area on Earth's surface, the measurements aim at imaging a 3D cube of the Earth's interior below this area and are referred to as 3D seismic measurements. 4D seismic refers to repeated 3D surveys involving time as fourth dimension.

3.1 Acquisition

The acquisition concepts for 3D seismic surveys depend strongly on the environment in which the surveys are performed. In the marine environment, 3D data acquisition is relatively fast and simple, compared to onshore environments, in particular in remote areas with little infrastructure and rough topography. The "transition zone", defined by areas of low water depths, under the influence of tidal depth variations, or swamps, poses particular challenges, and technologies applied here can be described by a combination of marine and land seismic approaches. Standard marine acquisition

uses a boat to tow one or more seismo-acoustic sources ("airguns") and one or more cables, equipped with pressure sensitive receivers ("streamers"). For 3D acquisition, the boat tows arrays of airguns and streamers. Modern vessels are able to tow 12 or more streamers, with typical line separations of 25 to 75 m. The length of the streamer cables depends on the depth of the acquisition target and is in the order of a few kilometers for typical exploration surveys. Surveys, covering thousands of square kilometers, can be acquired within a few weeks (Bacon *et al.*, 2003).

Land seismic surveys typically consist of a seismic source (or a group of seismic sources) moving over a pattern of source point locations and exciting seismic wavefields on each of these source points. An array of seismic receivers (vertical or three-component geophones) is deployed along profiles recording the wavefields emitted at the source point locations. Wherever possible, vibrator trucks are used as sources, having little environmental impact and allowing for relatively fast acquisition progress, but in areas of limited accessibility, explosives shot in shallow boreholes are used as an alternative. The receiver arrays typically consist of several lines with altogether several hundreds to thousands of single geophones. In areas with few obstacles and good infrastructure, several hundred source points may be acquired per day. This is still far beyond the efficiency of a marine seismic acquisition and is significantly reduced in topographically and logistically complicated areas (*e.g.*, sand dunes, jungles, high mountains or densely populated areas).

A particular challenge for seismic monitoring surveys (repeated acquisition on a site in order to detect potential changes in the underground by comparing the baseline data with data from the monitoring surveys) is to ensure an optimum of repeatability in order to avoid misinterpretations of time-lapse differences in the data. Ideally, the acquisition conditions of repeat surveys should be as much as possible identical to those of the baseline survey. The following factors may affect the repeatability of time-lapse data and should be considered:

1. Deviations in source and receiver geometry.
2. Usage of different types of seismic sources and receivers.
3. Variations in weather conditions affecting acquisition noise and (in land acquisition) causing changing seismic properties in the shallow weathering layer.

3.2 Processing and interpretation

The seismic data which have been acquired according to the approaches described in the previous chapter contains the signature of the wavefield reflected at geological boundaries in the underground, but these signals are usually (one should rather say always) overlain by components of the seismic wavefield which are not related to reflections from layer boundaries at depth. These components, which are not useful for standard reflection seismic interpretation (but may be useful for other approaches such as seismic tomography or surface wave analysis) comprise direct compressional (P-) and shear (S-) waves, surface waves, air blast, as well as ambient noise not related to the operation of the seismic source. The data processing aims at removing or suppressing wavefield components not useful for reflection imaging and at enhancing the reflected wavefield for subsequent imaging of the subsurface. A comprehensive overview of seismic data processing is given by Yilmaz (2008). The final processing result is provided as a 3D cube of migrated reflectivity distribution indicating the true

location of reflecting layer boundaries at depth. The processing of 4D seismic data has to tackle additional challenges related to the suppression of time-lapse noise unrelated to the monitoring target. The standard approach to solve this is to process the single 3D seismic data using similar processing chains and parameters to produce 3D cubes of reflectivity which then undergo an additional processing flow of cross-equalization (*e.g.* Rickett & Lumley, 2001; Ivandic *et al.*, 2015). After cross-equalization, the subtraction of monitoring and baseline data then may reveal amplitude changes in the reservoir level, related to reservoir processes such as the injection of CO_2, or the production of oil or gas. Examples of such time-lapse signatures of CO_2 injection are presented in Section 6 (Case studies).

4 SURFACE-BOREHOLE SEISMIC MEASUREMENTS

Surface-based seismic monitoring of CO_2 storage is commonly complemented by additional downhole acquisition (Daley *et al.*, 2008; Götz *et al.*, 2014; Gurevich *et al.*, 2014). Borehole-based seismic measurements are only able to image structures in close vicinity to the boreholes used for the acquisition and are therefore unable to provide a comprehensive image of the extent of a CO_2 plume in the storage formation. However, the added value of borehole-based seismic acquisition consists in several aspects:

- Direct observation of seismic traveltimes with depth, enabling to perform reliable time-to-depth conversion of surface-based seismic measurements.
- Enhanced signal-to-noise ratio resulting in better imaging quality, in particular for time-lapse surveys.
- Shorter ray paths for reflections from the reservoir level for higher depth resolution of the measurements compared to surface seismic acquisition.

Seismic **Crosshole Tomography** uses two observation boreholes located close to each other in order to image the section between the boreholes. The typical distance between the boreholes is between 50 m and 100 m. A seismic borehole source is operated in one borehole, and the seismic wavefield is acquired in the other borehole using a multi-level borehole receiver chain. At the Nagaoka pilot site, the injected CO_2 was successfully imaged by a reduction of P-wave velocity (Saito *et al.*, 2006). The P-wave velocity reduction observed by crosshole tomography was 3.0% and 3.5% for two surveys, being significantly less than P-wave velocity reduction measured by sonic logging (more than 20% after CO_2 breakthrough). This result demonstrates a major challenge for any traveltime based tomographic investigation. Thin low-velocity layers are difficult to resolve as the commonly interpreted directly travelling P-waves tend to propagate preferably through high-velocity rock masses surrounding the low-velocity anomaly.

Vertical Seismic Profiling (VSP) uses a seismic source operating at the surface, and seismic receivers in at least one observation borehole. The specific acquisition geometry depends on the acquisition task defined by the site operator. For zero offset VSP, a seismic source operates close to the well head of the observation borehole. Seismic receivers are used at a large depth range from the well head down to the bottom hole to record the wavefield over the full depth range of the well. The acquired data are used for an analysis of seismic velocity with depth, and for providing a reflectivity image along

the trace of the observation well. Offset VSP is acquired using a seismic source operating on a source location at a certain distance from the observation well and by acquiring the seismic wavefield over are large depth interval in the well. 2D and 3D VSP measurements consist of a seismic source operating along profiles or within a 2D array of source point locations on the surface and the acquisition of the wavefields by a limited amount of borehole receivers at fixed depth levels in the borehole. This approach is also referred to as Moving Source Profiling (MSP). Examples of borehole seismic surveys acquired for monitoring CO_2 storage are presented in Section 6.

5 USING SEISMIC MEASUREMENTS TO ASSURE SAFE AND SUSTAINABLE STORAGE

5.1 Baseline site characterization

Once a storage site has passed the assessment phase, as a basis for site development, comprehensive characterization has to be performed in order to assure the site is actually suitable for large scale storage and the injection and monitoring infrastructures are deployed according to the geological setting. Baseline site characterization activities fulfill several purposes:

- Provide supporting data for a structural understanding of the storage complex, including the reservoir formation and overlying caprock and aquifer systems.
- Provide baseline data for later evaluation of rock properties changes during the active injection phase ("time-lapse mode").
- Provide detailed subsurface information in particular in the area surrounding the expected injection location in order to support planning the drilling of injection and monitoring wells (Juhlin *et al.*, 2007).

The key investigations which form typical site characterization are summarized, with particular focus on storage in saline aquifers, by Chadwick *et al.* (2008). The key elements for a detailed geological site characterization are a regular grid of 2D seismic data over a broad area, sufficient to characterize broad reservoir structure and extents, and high quality 3D seismic data over the injection site and the adjacent area (Chadwick *et al.*, 2008). The 3D seismic data, ideally, are tuned to resolve the reservoir as well as its overburden. The surface seismic data need to be complemented by well data permitting to characterize reservoir and overburden elastic and hydrogeological properties. For a regional scale characterization, vintage seismic exploration data (typically 2D sections) may be available which are sufficient for the large scale model, whereas the high resolution characterization around the injection site demands for high quality 3D data acquired using state of the art technology. As an example, for the full scale Sleipner storage site, a regional grid of 2D seismic profiles (~16,000 line km) and 3D seismic data around the injection point (770 km^2) were used for a detailed assessment of the reservoir structure (Chadwick *et al.*, 2008). A detailed structural model was built including the topography of the reservoir top. This was used to estimate the extent of storage footprint (extent of free phase CO_2 in the reservoir and of the pressure signature) by reservoir simulation. A detailed characterization of lateral heterogeneities in the storage formation and its overburden is critical for pre-injection risk assessment and

subsequent establishment of a monitoring plan for the operational phase. Faults in the reservoir and caprock may be acting as seals, resulting in a compartmentalized reservoir structure, or may provide pathways for CO_2 migration and are therefore structures to be characterized with particular focus and to be considered for subsequent monitoring in the operational and post injection phases of a CO_2 storage site.

5.2 Long-term monitoring technologies

Full scale CO_2 storage sites will typically be designed for an operational period of a few decades, with annual injection rates of a few hundred thousand to some million tons of CO_2. The injection (operational) period will be followed by the post injection or closure phase (Plasynski *et al.*, 2011; Kühn *et al.*, 2013) during which the site operator needs to demonstrate that the site is evolving towards a state of long-term stability. This demonstration is a major requirement the operator has to fulfill before being able to transfer responsibility for the site's safety to the public. Long-term storage safety relies on four storage mechanisms, which are (in the order of increasing long-term stability) structural trapping, residual trapping, dissolution of CO_2 in brine, and finally mineralization (Frykman, 2012). Coupled reservoir simulations for the Ketzin pilot scale and the full scale Sleipner site have shown that the quantitative contributions of the different stabilization processes are site dependent and also characterized by uncertainties related to assumptions related to reservoir properties as well as to geochemical parameterization (Estublier *et al.*, 2013; Klein *et al.*, 2013). A common result of the coupled long-term reservoir simulations is that the stabilization of the reservoir in terms of dissolution and mineral trapping is a process lasting over several centuries to millennia. The risk of CO_2 leakage out of the storage complex is highest in the late operational and early post-injection phases, when reservoir pressure has reached a maximum and most of the stored CO_2 is still in the structural trapping stadium (Benson & Cole, 2008). Subsequently, due to dissolution and mineralization, reservoir pressure will decrease. It is in the early post-injection phase when the site operator has to demonstrate that the site is evolving towards a state of stability and that there is no detectable leakage. This requirement implies that reservoir monitoring needs to include the post-injection phase for a period during which the absence of detectable leakages needs to be assured and which is long enough to provide sufficient data assuring a stabilization of the reservoir. This period has to be defined according to previous risk assessment for the storage site and its duration may be in the same order as has been the active operational (injection) phase. Long-term stability and repeatability as well as economic efficiency are requirements for monitoring methods applied in the post-injection phase. Further repeats of 3D seismic measurements may be required but will be reduced in terms of the repetition rate and potentially concentrated onto areas previously identified as potential leaking structures, such as fault zones. Permanent deployment of seismic sources (Kasahara *et al.*, 2011) and/or receivers (Arts *et al.*, 2013), but also highly mobile small scale seismic sources (Sopher *et al.*, 2014) for a fast and efficient surveying of shallow structures identified as target formations for leakage, may be considered for monitoring in the post closure phase.

6 CASE STUDIES

6.1 Ketzin

6.1.1 Site characteristics

The Ketzin pilot site is located near Berlin (Germany). Until 2000, seasonal underground storage of natural gas had been performed at the location close to the town of Ketzin (Havel). The development of the site for CO_2 storage started in 2004. Sandstone layers of the Triassic Stuttgart Formation at 630 m – 650 m depth were used as a storage formation (Figure 3). The topography of the reservoir formation is dominated by an east-west striking double anticline, formed by salt tectonic uplift. The injection site is located on the southern flank of this anticline, and the uppermost main sandstone horizon, a saline aquifer, has a thickness of about 10 m to 20 m. The injection lasted from June 2008 to August 2013. In total, slightly more than 67,000 tons of CO_2 were injected during this period (Martens *et al.*, 2014).

Operational and reservoir monitoring has been performed during the injection period and the early post-injection phase. Operational monitoring comprised primarily flow rate, temperature, and pressure monitoring (Liebscher *et al.*, 2013b). For reservoir

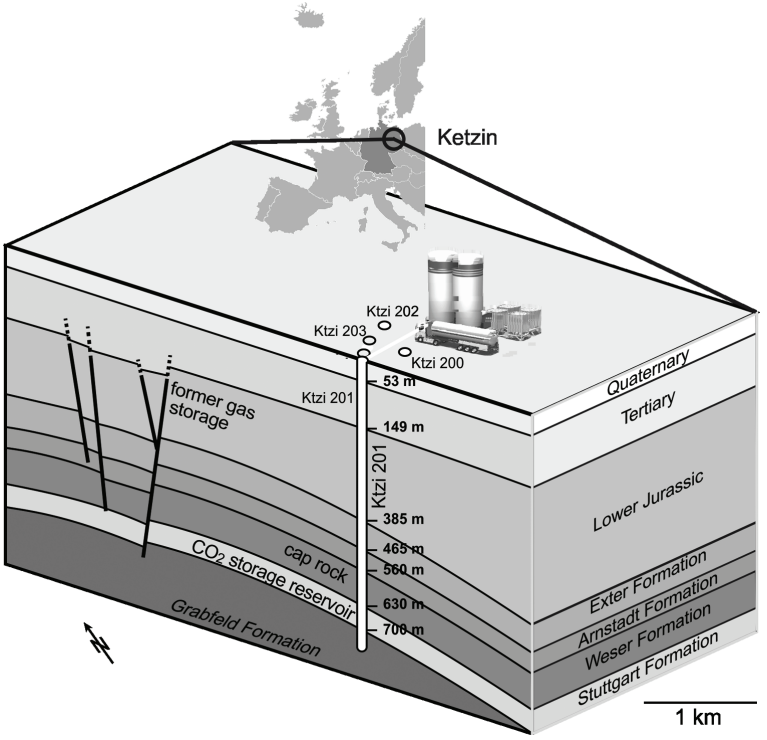


Figure 3 Vertically exaggerated block diagram of the storage complex at the Ketzin pilot site (modified from Liebscher *et al.*, 2013a).

monitoring, a multi-disciplinary concept had been designed comprising geophysical, geochemical and microbial methods (Giese *et al.*, 2009).

6.1.2 Seismic monitoring

The seismic monitoring concept of the Ketzin pilot site was designed to enable imaging the propagation of the injected CO_2 in the reservoir at various spatial and time scales (Lüth *et al.*, 2011). It consists of crosshole tomographic surveys, VSP (vertical seismic profiling) and MSP (moving source profiling) observations, and repeated 2D and 3D surface seismic measurements. For the crosshole tomographic surveys, the monitoring wells Ktzi 200 and Ktzi 202 were used (Figure 3). These two monitoring wells are located at 100 m distance from each other. One baseline survey was acquired before the start of injection, and two repeat surveys were acquired during the first two months after injection started. The section imaged by the crosshole tomographic measurements is located at a lateral offset of ~50 m with the injection well (Ktzi 201) and during the first two months of CO_2 injection, only a small quantity of CO_2 had migrated into the area between monitoring wells Ktzi 200 and Ktzi 202. Therefore, faint indications of P-wave velocity reduction due to partial CO_2 saturation in the initially brine saturated reservoir were resolved by waveform inversion analysis of the acquired data (Zhang *et al.*, 2012).

Surface-downhole VSP and MSP measurements were acquired in order to image the CO_2 propagation in the vicinity of the injection and monitoring wells at better resolution as would have been possible by using surface seismic measurements alone. The acquisition was performed using a seismic source operating at the surface and downhole receivers (3-component geophones) deployed in the monitoring well Ktzi 202 (see Figure 3). Time-lapse zero offset VSP measurements consist of one baseline survey, acquired before the start of CO_2 injection, and one repeat survey, acquired in February 2011, after 46,000 tons of CO_2 were injected (Götz *et al.*, 2014). A clear time-lapse amplitude signature of a part of the CO_2 plume close to the monitoring well Ktzi 202 was observed, and this amplitude signature was used for a wedge modelling study in order to derive the thickness of the CO_2 plume around the well Ktzi 202. The result is shown in Figure 4. An optimal fit between the measured repeat data and modeled data, based on a one-dimensional model with varying thickness of the CO_2 plume, was reached for a plume thickness of 6 m, which is 2 m below the thickness of the reservoir sandstone layer at the monitoring well Ktzi 202. This may be interpreted as an indication that the CO_2 plume is concentrated to the upper 6 m of the sandstone layer of the storage formation and the lower part of this sandstone layer is still brine saturated.

While the borehole based seismic measurements provided high resolution information from the reservoir close to injection and monitoring wells, they did not enable to image the full extent of the injected CO_2 in the reservoir. Repeated 3D seismic surveys (4D seismic) were acquired, covering an area of 12 km^2 around the injection site. As of spring 2015, three 3D seismic surveys have been acquired: 2005 – baseline measurements before the drilling of injection and monitoring wells (Juhlin *et al.*, 2007); 2009 – first repeat survey after 14 months and 22,000 tons of CO_2 injection (Ivanova *et al.*, 2012); 2012 – second repeat survey after 50 months and 61,000 tons of CO_2 injection (Ivandic *et al.*, 2015). In order to ensure the highest possible degree of repeatability, all surveys were attempted to be acquired under identical environmental and logistical conditions: They were acquired

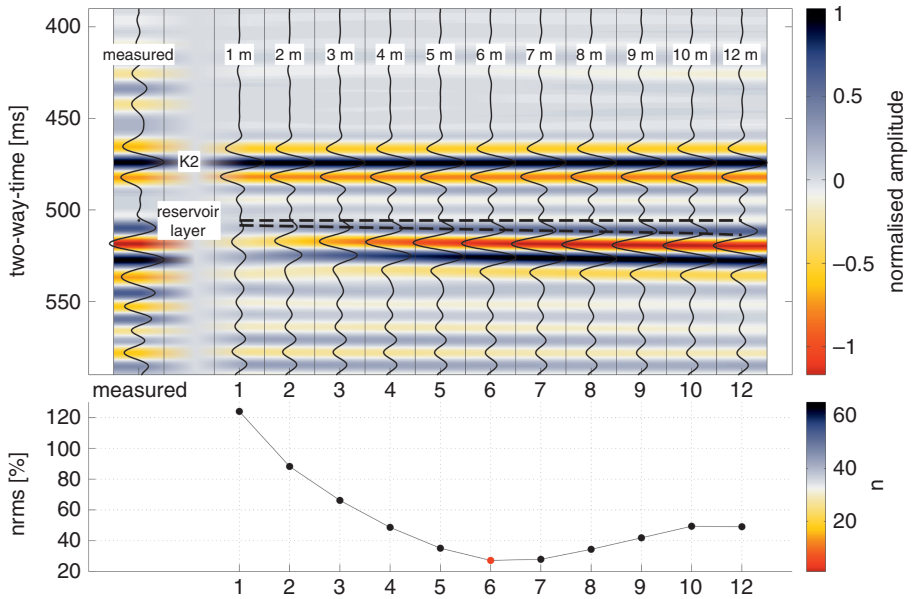


Figure 4 Result of wedge modeling for zero offset time-lapse VSP data at the Ketzin pilot site. Top left: the corridor-stacked trace of the measured repeat survey. The colored amplitudes are overlain by the wiggle trace. Top right: the result of wedge modeling, from left to right for 1 m to 12 m reservoir thickness. The top and bottom of the reservoir are plotted as dashed black lines. Bottom: NRMS error between the modeled and measured traces (Figure from Götz *et al.*, 2014).

in the same season of the year (late summer, early autumn). Identical acquisition equipment (geophones, recording equipment) and identical seismic sources were used. Source and receiver points as defined for the 2005 baseline survey were used for the repeat surveys wherever possible. Even though significant efforts were made to ensure repeatability of the monitoring surveys, various factors affected the reproduction of initial conditions defined by the baseline survey. The main factors affecting repeatability were the following: The surveys were acquired under varying precipitation conditions which influenced P-wave velocities in the near surface low velocity layer and strongly affected static corrections and frequency contents of the acquired data (Bergmann *et al.*, 2014). Weather conditions during the repeat surveys, and also construction activities, affected accessibility of source and receiver locations, reducing the reproducibility of the initial acquisition geometry. These conditions are typical for land-seismic acquisition and can be expected to occur at other potential monitoring projects as well. Still, careful processing of the baseline and repeat data, including a cross-correlation workflow reducing non-reservoir-related time-lapse effects (Ivandic *et al.*, 2015) enabled to detect variations of the reflection amplitudes in the depth level of the top reservoir formation which can be attributed to the effect of CO_2 replacing brine as initial pore fluid in the storage formation (Figure 5). The lateral extent of the CO_2 in the storage formation as detected by seismic measurements is shown for the first repeat survey 2009 and the second repeat survey 2012. Initial reservoir simulations performed in the development phase of the pilot storage

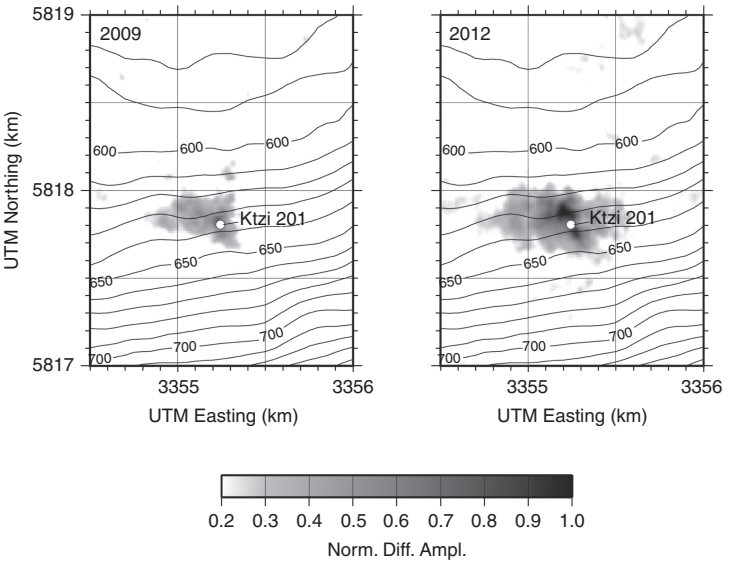


Figure 5 Map view of normalized differential amplitudes at the top Stuttgart Formation extracted from 3D difference cubes (left: Repeat 2009 – Baseline; right: Repeat 2012 – Baseline). The location of the CO_2 injection well (Ktzi 201) is indicated by a circle. Amplitude differences at the top of the storage formation higher than 0.2 are indicated by gray scales, showing the lateral extension of the CO_2 in the storage formation detected by seismic measurements. Depth isolines indicate the topography of the storage formation (Norden *et al.*, 2010). Depth values are given in meters below ground level.

site had predicted mainly northward directed migration of the CO_2 injected into the storage formation, driven by gravitational forces pushing the CO_2 up-dip towards the top of the anticlinal structure of the reservoir (Frykman *et al.*, 2009). Seismic monitoring results as shown in Figure 5 however indicate a predominantly westward migration of the injected CO_2, running parallel to depth isolines, and obviously driven more strongly by anisotropic permeability conditions within the storage formation than by gravitational forces.

6.2 Nagaoka

6.2.1 Site characteristics

The Japanese pilot project for CO_2 storage is located at the Iwanohara Base, near the town of Nagaoka. Injection lasted from July 2003 through January 2005. In this period, 10,400 tons of CO_2 have been injected into a saline aquifer in the Pleistocene Haizume Formation at 1,100 m depth (Mito & Xue, 2011). After the active injection period, well logging campaigns (neutron logging, sonic logging and induction logging) have been continued, providing the longest post injection time-series of monitoring data at CO_2 storage sites. The research infrastructure of the Nagaoka pilot site consists mainly of four wells, the injection well (IW1), and three observation wells (OB2-4). Two of these

observation wells (OB2 and OB3) are located so that the crosswell tomography between these wells covers the injection depth interval of IW1 (Sato *et al.*, 2011).

6.2.2 *Seismic monitoring*

Apart from continuous well logging measurements, seismic crosshole tomography and sonic logging were repeated during and after CO_2 injection in order to image the CO_2 plume propagation in the reservoir formation (Sato *et al.*, 2011). Time-lapse 3D surface seismic data was acquired at the Nagaoka site as well, but these measurements did not detect seismic amplitude changes due to CO_2 storage (Xue & Matsuoka, 2008). A baseline crosshole tomography survey was acquired six months before the injection started, and six monitoring surveys were acquired during and after the injection period (Sato *et al.*, 2011). Two exemplary velocity difference tomograms are shown in Figure 6. The tomograms show the relative velocity difference between the baseline survey and the respective monitoring survey. The velocity difference tomograms show a slight decrease of P-wave velocity close to the injection interval along IW1, in the order of 4 %. The area of decreased P-wave velocity, detected by crosshole tomography, was interpreted as an approximate macro-scale distribution of the CO_2 injected into the aquifer, but the tomographic measurements failed to indicate the presence of CO_2 at the observation well OB2, as had been proved by time-lapse well logging (Sato *et al.*, 2011). Sonic logging measurements were acquired periodically in the three observation wells, and after 247 days of injection, a notable decrease of P-wave velocity was detected in OB2 at the reservoir level. Sonic P-wave velocity decreased from the baseline value of 2.47 km/s to 1.92 km/s, equivalent to a reduction of more than 20 %, which differs significantly from the P-wave velocity reduction detected by crosshole tomography between OB2 and OB3. The comparison of crosshole tomography and

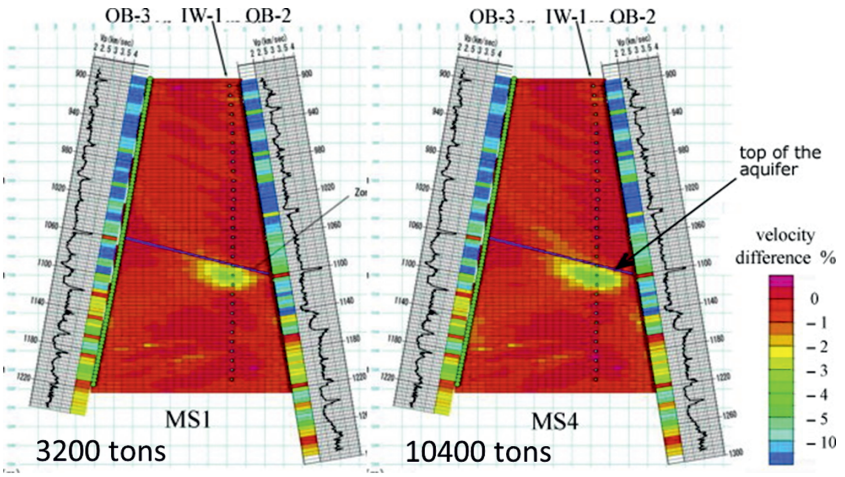


Figure 6 Velocity difference tomograms from the Nagaoka site for monitoring survey (MS) 1 with 3,200 tons of CO_2 injected (left) and for MS 4 with 10,400 tons of CO_2 injected (right). Reprinted from Sato *et al.* (2011), with permission from Elsevier.

sonic logging results represents an impressive example of possible pitfalls in the interpretation of crosshole tomographic surveys. The seismic wavefield, emitted from a seismic source in a borehole and propagating directly to receivers deployed in a second borehole, tends to be refracted through rock mass regions characterized by comparatively high seismic velocities and to avoid propagating through low-velocity regions. Thus, seismic traveltime crosshole tomography usually tends to underestimate seismic low-velocity anomalies within the investigated rock mass in terms of the degree of velocity reduction relative to the surrounding rock mass and also in terms of the lateral extent of the low-velocity anomaly.

6.3 Otway

6.3.1 Site characteristics

In the Australian Otway basin, the first Australian pilot project for CO_2 storage has been established. The Otway project is located in the south-east of Australia, approximately 150 km west of Melbourne. CO_2-rich gas from the Buttress-1 supply well was used for the demonstration of CO_2 storage after drying and compression. Via the injection well CRC-1, it was injected into the Waarre C formation unit, a depleted gas field at 2 km depth (Underschultz *et al.*, 2011). Between March 2008 and August 2009, 65,445 tons of CO_2 rich mixed gas was injected. Recently, the Otway project has entered a second phase ("Stage 2"), aiming at the investigation of small CO_2 quantities in a saline aquifer (Pevzner *et al.*, 2013). Figure 7 shows schematically the design and geology of the Otway project ("Stage 1"). The depleted gas reservoir is located in a tilted fault block structure. Its small size (0.5 km^2), relatively large depth of around 2 km and thickness of less than 25 m on average, present a challenge for detailed reservoir characterization as well as for any geophysical monitoring method (Urosevic *et al.*, 2011). In addition, the CO_2 rich gas mixture was injected into a depleted gas reservoir, and according to reservoir simulations, the injected CO_2 was expected to mix with the residual CH_4 in the reservoir and to accumulate under the remaining gas cap as a thin layer. Due to the low impedance contrast between CH_4 and CO_2 mixed with CH_4, small seismic time-lapse signals were expected which would have been detected by land seismic time-lapse measurements only under highly favorable conditions (Urosevic *et al.*, 2011). In order to enhance the ability of the monitoring program to detect a seismic signature of the injected CO_2, the seismic monitoring program was designed to combine surface based and borehole measurements, using the Naylor-1 monitoring well (Figure 7).

6.3.2 Seismic monitoring

The seismic monitoring program at the Otway site consists of 3D surface seismic surveys and zero offset as well as 3D VSP surveys. The 3D seismic surveys were acquired three times, a baseline, prior to CO_2 injection, and two monitor surveys, after CO_2 injection of 33 ktons and 65 ktons, respectively (Urosevic *et al.*, 2011). The borehole seismic data consists of a baseline survey and one monitor survey, acquired after the end of the injection period. Apart from attempting to image the propagation of the CO_2 injected into the Waarre C formation at 2 km depth, the measurements were

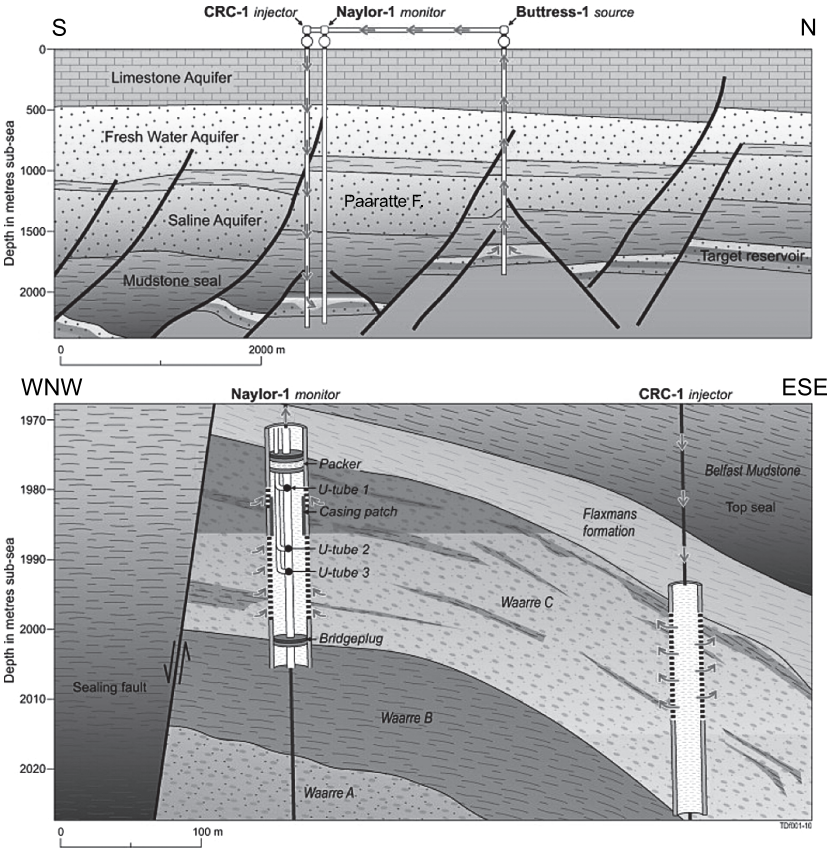


Figure 7 Schematic cross-section diagrams of the CO_2CRC Otway Project field site showing the pilot test well configuration and geology. Reprinted from Underschultz *et al.* (2011), with permission from Elsevier.

also expected to assure the absence of leakage into the shallower saline aquifer, the Paaratte formation. This was done by combining reservoir simulation results and seismic modelling involving realistic noise conditions. It could be shown that already small accumulations of CO_2 in the Paaratte Formation would generate strong changes in the elastic properties of the host rock which would have been detected by the seismic measurements (Urosevic *et al.*, 2011).

Figure 8 shows results from the 3D surface seismic monitoring. The surveys had been designed with very high nominal fold (over 100, meaning that each subsurface point was imaged by stacking more than 100 traces from different source-receiver pairs), and as a result, very high repeatability was achieved. This can be recognized in the high similarity of the seismic data, shown in Figure 8 (left), and in the low normalized root mean square difference amplitudes (around 20 %), shown in Figure 8 (right). Despite this very high level of repeatability, at the reservoir level (at 1.5 s in the time-migrated sections in Figure 8), no significant time-lapse amplitude changes due to CO_2 injection into the Waarre C formation were detected.

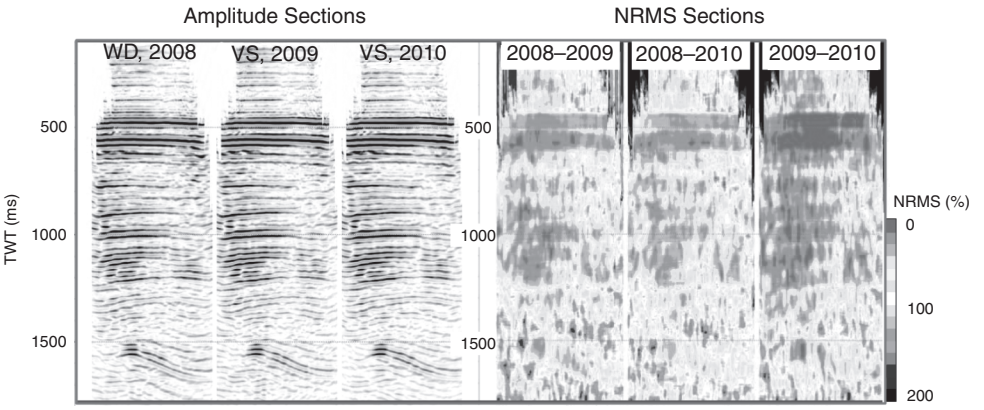


Figure 8 Left: Sections selected from 3D reflection cubes acquired in 2008 (baseline, weight drop source (WD)), 2009 (first monitor, vibro source (VS)), 2010 (second monitor, vibro source (VS)). Right: Normalized root mean square (NRMS) difference sections for the data shown on the left. NRMS values of 0 % indicate perfect correlation, 200 % indicates anti-correlation. At the reservoir level (1.5 s), an NRSM of around 20 % can be regarded as very good for time-lapse land seismic data (Figure modified from Urosevic *et al.* (2011), published under a Creative Commons License).

In Figure 9, raw corridor stacks of zero-offset VSP baseline and monitoring surveys are shown. The high repeatability of the surveys is obvious, visible in the similarity of traces labeled A, B, and C. The difference data, shown in traces D and E in Figure 9, show that in spite of this high degree of repeatability, only a very weak time-lapse signature of injected CO_2 can be seen in the depth level of the storage formation. These

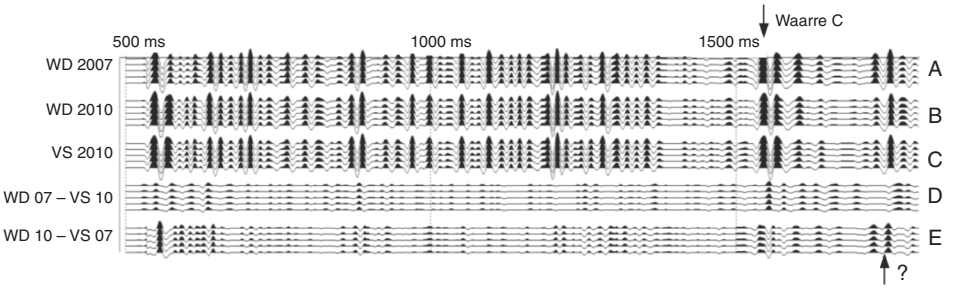


Figure 9 Zero offset VSP corridor stacks indicating reflectivity along the monitoring well Naylor-1. A: Baseline survey, weight drop source; B: Post injection repeat survey, weight drop source; C: Post injection repeat survey, vibro source; D: Difference between baseline (weight drop) and post injection (vibro); E: Difference between baseline and post injection surveys for weight drop sources. The reservoir zone is indicated by arrow ("Waarre C"). The difference seismograms (D and E) show time-lapse amplitudes of the CO_2 signature just above noise threshold. In E, strong difference amplitudes below the reservoir ("?") may be caused by attenuation effects within the reservoir level (Figure modified from Urosevic *et al.* (2011), published under a Creative Commons License).

results show impressively that seismic monitoring of CO_2 storage in depleted gas reservoirs is an extremely challenging task, if it is possible at all. Nevertheless, in the case of potential migration of stored CO_2 into shallower formations, typically consisting of brine saturated aquifers, modeling studies performed for the Otway site, as well as experiences from saline aquifer pilot projects, have shown that seismic monitoring is an indispensable tool in delineating the potential distribution of CO_2 which may have migrated upward into shallower formations.

6.4 Sleipner

6.4.1 Site characteristics

CO_2, captured from gas production from the Sleipner field in the central Norwegian North Sea, has been injected into the saline aquifer Utsira Formation since September 1996 (Torp & Gale, 2004). The Utsira Formation lies 1,000 m below sea bottom, water depth is approximately 80 m (Eiken *et al.*, 2011). The injection rate has been 1 Mton CO_2 per year, and as of 2014, more than 15 Million tons have been injected. The Utsira Formation is an elongated sand reservoir, extending for more than 400 km from north to south and between 50 and 100 km from east to west. The top of the Utsira Formation shows rather smooth topography with a local high close to the Sleipner field, and a second one around 200 km north of Sleipner. The thickness of the Utsira Formation reaches up to 200 – 300 m at these local highs (Torp & Gale, 2004). Within the Utsira Formation, which consists mainly of uncemented fine grained sand, thin shale layers are intercalated, which form local intra-reservoir barriers. Due to these thin shale layers, the injected CO_2 is prevented from accumulating at the top Utsira Formation but is rather distributed over multiple horizontal layers at various depth levels within the reservoir.

6.4.2 Seismic monitoring

3D seismic monitoring data have been acquired at Sleipner on an annual to bi-annual basis. A baseline survey was acquired in 1994, and between 1999 and 2008, six repeat surveys were acquired. A clear time-lapse amplitude difference could be observed in the 3D cubes allowing to delineate the lateral extent of the CO_2 plume by the cumulated reflection amplitude (Figure 10) and also demonstrating the vertical distribution of the injected CO_2 on depth sections (inlay in Figure 10).

The seismic data clearly imaged the lateral migration and vertical distribution of the CO_2 plume which is around 200 m in height and elliptical in plan view (Chadwick *et al.*, 2009). The seismic image of the plume shows several bright sub-horizontal reflections which are interpreted to originate from discrete CO_2 layers, each several meters thick. Comparison of seismic data from early campaigns with more recent data has shown that the discrete layers formed early after injection started (by 1999) and have remained visible ever since (Chadwick *et al.*, 2009). The lower layers of the plume have remained stable whereas the upper layers continue to spread laterally and increase in brightness. The detailed seismic observations have been used for an extensive assessment of the plume development using reservoir simulations. As an example, an axisymmetric model has been used, with thin intra-reservoir mudstones separating the

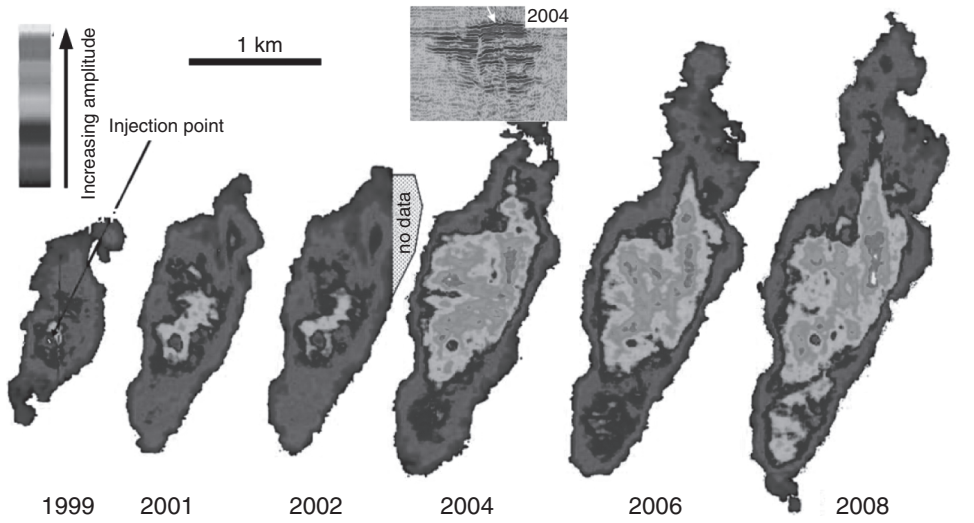


Figure 10 Time-lapse seismic difference reflection amplitude maps at Sleipner, cumulative for all layers. Expansion of the plume in all directions is observed, as well as intensified reflections in the central part of the plume (Figure modified from Eiken *et al.* (2011), published under a Creative Commons License). For the 2004 monitor survey, the amplitude differences with the baseline survey are shown in an east-west section for the central part of the plume, close to the injection point (Chadwick *et al.*, 2009).

discrete CO_2 layers as imaged by the seismic measurements (Boait *et al.*, 2011). Flow simulations have confirmed that the CO_2 spreads laterally under each of the intra-reservoir mudstones. The simulations have also indicated that during more or less continuous CO_2 injection, the upper layers grow more rapidly with time than the lower layers, which actually decrease in thickness and lateral extent with time.

7 SUMMARY AND CONCLUSIONS

The growth of greenhouse gas emissions related to human activities is commonly regarded as a major factor of global warming, and all major economies currently strive to reduce their greenhouse gas emissions in order to restrict global warming to a scenario which is expected to avoid most devastating effects of unrestricted emissions. Carbon capture and geological storage (CCS) is part of the portfolio for emissions reduction, at least for the next approximately 100 years, as long as fossil energy sources continue to be used globally. For the geoscientific community, the need to assure safe long-term operation of CO_2 geological storage poses challenges in terms of storage complex characterization, monitoring, and long-term simulation of reservoir behavior. Most approaches which are applied to CO_2 storage sites have been adapted from hydrocarbon exploration, including the intensive application of surface and borehole based seismic surveys for reservoir characterization and monitoring, by performing repeated (time-lapse) surveys and comparing the data with baseline observations.

If geological CO_2 storage is supposed to contribute significantly to reducing global warming, a large number of full scale projects would need to be implemented, with several 10 million tons of CO_2 stored per site, and the long-term safety of these sites for several 1,000 years would need to be assured until the reservoir can be assumed to have reached a stable state. Experiences gained from the monitoring of hydrocarbon reservoirs mostly cover the operational phase of a reservoir which does not go beyond a few decades and where seismic time-lapse monitoring is usually not explicitly required to assure operational safety, but rather applied to optimize reservoir management. Large scale CO_2 storage reservoirs will reach the post injection or closure period after a few decades of injection, when the reservoir will have reached a certain overpressure in relation to the initial state of the reservoir. Diffusion and dissolution of the stored CO_2 will slowly result in an equilibration of the reservoir, but this is a slow process which needs to be monitored in order to assure the behavior of the reservoir conforms to the expectations and no leakage out of the storage complex occurs.

In order to gain practical experience and to enhance the scientific understanding of the processes related to CO_2 storage, pilot, demonstration and full scale storage projects have been established over the globe. In many of these, seismic methods were and are being applied to characterize the reservoir and to track the injected CO_2, with particularly successful results for shallow to intermediately deep saline aquifers, whereas direct seismic monitoring of CO_2 stored in complex deep structures and in depleted gas reservoir has proven to be highly challenging, as demonstrated at the Otway site. At deep large scale sites with complex geology and a small impedance contrast between the initial state and the state after CO_2 injection started, it may be difficult, if not even impossible, to track the stored CO_2 in the primary storage formation. Still, repeated 3D seismic observations are of high importance at such sites, assuring no CO_2 has leaked into shallower formations, which will be saline aquifer formations in many cases.

Surface based seismic monitoring of saline aquifers has demonstrated the ability of the seismic method to detect relatively small amounts of CO_2 and to image large reservoirs comprehensively as shown, *e.g.*, at Ketzin and Sleipner. In the case studies shown above, we have concentrated on the detection and imaging of CO_2 reservoirs, without further discussing attempts to perform quantitative interpretations aiming at a description of the saturation distribution within the plume. The quantification of CO_2 distribution, as imaged by seismic methods, is based on the determination of elastic parameters (V_p, V_s) and density which may be used to infer CO_2 saturation. As shown in chapter 2.1, there is significant uncertainty as for the relation between elastic properties and CO_2 saturation, depending on the applied petrophysical model. The validity of petrophysical models depends on the wavelength of the geophysical signal in relation to the dimension of heterogeneity within the considered rock mass. The Biot-Gassmann model applies for "homogeneous" CO_2 distribution, *i.e.*, the seismic wavelength is significantly larger than reservoir internal heterogeneities of CO_2 distribution. In this case, at saturations larger than ~20 %, elastic properties show very low sensitivity for variations in CO_2 saturation. Therefore, particularly surface seismic observations, characterized by rather large wavelengths, will enable quantitative interpretations only with high uncertainty. Observations performed at very high seismic frequencies (and small wavelengths), such as sonic logging, or laboratory measurements using ultrasonic frequencies, can rather be interpreted using the Gassmann-Hill model of

"patchy" CO_2 distribution, which is characterized by an almost constant sensitivity for saturation changes over the full range of possible values. For a quantitative description of CO_2 distribution in a reservoir, logging measurements and laboratory experiments, as demonstrated at the Nagaoka site, are therefore an indispensable component, together with surface based large scale observations from the surface.

REFERENCES

Arts, R.J., Zhang, X., Verdel, A.R., Santonico, D., Meekes, J.A.C., Noorlandt, R.P., Paap, B.F., & Vandeweijer, V.P. (2013). Experiences with a permanently installed seismic monitoring array at the CO_2 storage site at Ketzin (Germany) – A status overview. *Energy Procedia*, 37, 4015–4023, doi:10.1016/j.egypro.2013.06.301.

Azuma, H., Konishi, C., & Xue, Z. (2013). Introduction and application of the modified patchy saturation for evaluating CO_2 saturation by seismic velocity. *Energy Procedia*, 37, 4024–4032, doi: 10.1016/j.egypro.2013.06.302.

Bacon, M., Simm, R., & Redshaw, T. (2003). *3D Seismic Interpretation*. Cambridge University Press, Cambridge, UK.

Benson, S.M. & Cole, D.R. (2008). CO_2 sequestration in deep sedimentary formations. *Elements*, 4 (5), 325–331, doi: 10.2113/gselements.4.5.325.

Bergmann, P., Kashubin, A., Ivandic, M., Lüth, S., & Juhlin, C. (2014). Time-lapse difference static correction using prestack crosscorrelations: 4D seismic image enhancement case from Ketzin. *Geophysics*, 79 (6), B243–B252, doi: 10.1190/geo2013-0422.1.

Biot, M.A. (1962). Theory of propagation of elastic waves in a fluid-saturated porous solid. Part 1: low frequency range. *Journal of the Acoustical Society of America*, 28, 168–178.

Blasing, T.J. (2014). *Recent Greenhouse Gas Concentrations. Carbon Dioxide Information Analysis Center*. [Online] Available from: http://cdiac.ornl.gov/pns/current_ghg.html [Accessed 10 Dec 2014.], doi: 10.3334/CDIAC/atg.032.

Boait, F., White, N., Chadwick, R.A., Noy, D., & Bickle, M. (2011). Layer spreading and dimming within the CO_2 plume at the Sleipner Field in the North Sea. *Energy Procedia*, 4, 3254–3261.

Chadwick, R.A., Arts, R., Bernstone, C., May, F., Thibeau, S., & Zweigel, P. (2008). *Best Practice for the Storage of CO_2 in Saline Aquifers*. Keyworth, Nottingham: British Geological Survey Occasional Publication No. 14, ISBN: 978–0–85272–610–5.

Chadwick, R.A., Noy, D., Arts, R., & Eiken, O. (2009). Latest time-lapse seismic data from Sleipner yield new insights into CO_2 plume development. *Energy Procedia*, 1, 2103–2110.

Daley, T.M., Myer, L.R., Peterson, J.E., Majer, E.L., & Hoversten, G.M. (2008). Time-lapse crosswell seismic and VSP monitoring of injected CO_2 in a brine aquifer. *Environmental Geology*, 54 (8), 1657–1665.

Dutta, N.C., Odé, H., & Seriff, A.J. (1979). On White's model of attenuation in rocks with partial gas saturation. *Geophysics*, 44, 1806–1812.

Eiken, O., Ringrose, P., Hermanrud, C., Nazarian, B., Torp, T.A., & Høier, L. (2011). Lessons learned from 14 years of CCS operations: Sleipner, In Salah and Snøhvit. *Energy Procedia*, 4, 5541–5548.

Estublier, A., Fornel, A., Parra, T., & Deflandre, J.-P. (2013). Sensitivity study of the reactive rransport model for CO_2 injection into the Utsira saline formation using 3D fluid flow model history matched with 4D seismic. *Energy Procedia*, 37, 3574–3582.

Frykman, P. (2012). Review of relevant trapping mechanisms based on site portfolio. *CO_2 Care Publications*, 39, doi: http://doi.org/10.2312/GFZ.CO2CARE_D3.1.

Frykman, P., Nielsen, C.M., Norden, B., & Förster, A. (2009). *Modelling and predictions in the Ketzin CO_2 storage experimental site. 13th Annual Conference of the International Association of Mathematical Geosciences IAMG09* (Stanford, CA, USA), CD-ROM.

Gassmann, F. (1951). Über die Elastizität poröser Medien. *Vierteljahresschrift der Naturforschenden Gesellschaft in Zürich*, 96, 1–23.

Giese, R., Henninges, J., Lüth, S., Morozova, D., Schmidt-Hattenberger, C., Würdemann, H., Zimmer, M., Cosma, C., Juhlin, C., & CO_2SINK Group (2009). Monitoring at the CO_2SINK Site: A concept integrating geophysics, geochemistry and microbiology. *Energy Procedia*, 1, 2251–2259.

Global CCS Institute (2014). *Sleipner CO_2 Storage Project* [Online]. Available from: http://www.globalccsinstitute.com/project/sleipner%C2%A0co2-injection [Accessed 11 Dec 2014].

Gollakota, S. & McDonald, S. (2012). CO_2 capture from ethanol production and storage into the Mt Simon Sandstone. *Greenhouse Gases: Science and Technology*, 2 (5), 346–351.

Götz, J., Lüth, S., Krawczyk, C.M., & Cosma, C. (2014). Zero-Offset VSP monitoring of CO_2 storage: Impedance inversion and wedge modelling at the Ketzin pilot site. *International Journal of Geophysics*, Volume 2014, Article ID 294717, 15 pages, http://dx.doi.org/10.1155/2014/294717.

Gurevich, B., Pevzner, R., Urosevic, M., Kepic, A., Shulakova, V., Caspari, E., & Lebedev, M. (2014). 2D and 3D seismic investigations for stages 1 and 2C. In: Cook, P. (ed.) *Geologically Storing Carbon: Learning from the Otway Project Experience*. CSIRO Publishing, Melbourne.

Hangx, S., van der Linden, A., Fons, M., & Bauer, A. (2013). The effect of CO_2 on the mechanical properties of the Captain Sandstone: Geological storage of CO_2 at the Goldeneye field (UK). *International Journal of Greenhouse Gas Control*, 19, 609–619, doi: 10.1016/j.ijggc.2012.12.016.

Hovorka, S.D. (2013). Three-million-metric-ton-monitored injection at the Secarb Cranfield Project – Project Update. *Energy Procedia*, 37, 6412–6423.

Hovorka, S.D., Benson, S.M., Doughty, C.K., Freifeld, B.M., Sakurai, S., Daley, T.M., Kharaka, Y.K., Holtz, M.H., Trautz, R.C., Nance, H.S., Myer, L.R., & Knauss, K.G. (2006). Measuring permanence of CO_2 storage in saline formations – The Frio experiment. *Environmental Geosciences*, 13, 103–119.

IPCC (2005). Summary for Policymakers. *In:* IPCC Special Report on Carbon Dioxide capture and Storage, Prepared by Working Group III of the Intergovernmental Panel on Climate Change (Metz, B., Davidson, O., de Coninck, H.C., Loos, M., & Meyer, L. (eds.)). Cambridge University Press, 3–16.

IPCC (2007a). *Climate Change 2007: The Physical Science Basis*. Contribution of Working Group I to the Fourth Assessment Report of the Intergovernmental Panel on Climate Change (Solomon, S., Qin, D., Manning, M., Chen, Z., Marquis, M., Averyt, K.B., Tignor, M., & Miller, H.L. (eds.)). Cambridge University Press, Cambridge, United Kingdom and New York, NY, USA, 996pp.

IPCC (2007b). *Climate Change 2007: Mitigation*. Contribution of Working Group III to the Fourth Assessment Report of the Intergovernmental Panel on Climate Change (Metz, B., Davidson, O.R., Bosch, P.R., Dave, R., & Meyer, L.A. (eds.)), Cambridge University Press, Cambridge, United Kingdom and New York, NY, USA.

IPCC (2013). *Climate Change 2013: The Physical Science Basis*. Contribution of Working Group I to the Fifth Assessment Report of the Intergovernmental Panel on Climate Change (Stocker, T.F., Qin, D., Plattner, G.-K., Tignor, M., Allen, S.K., Boschung, J., Nauels, A., Xia, Y., Bex, V., & Midgley, P.M. (eds.)). Cambridge University Press, Cambridge, United Kingdom and New York, NY, USA, 1535pp.

Ivandic, M., Juhlin, C., Lüth, S., Bergmann, P., Kashubin, A., Sopher, D., Ivanova, A., Baumann, G., & Henninges, J. (2015). Geophysical monitoring at the Ketzin pilot site for CO_2 storage: New insights into the plume evolution. *International Journal of Greenhouse Gas Control*, 32, 90–105, doi: 10.1016/j.ijggc.2014.10.015.

Ivanova, A., Kashubin, A., Juhojuntti, N., Kummerow, J., Henninges, J., Juhlin, C., Lüth, S., & Ivandic, M. (2012). Monitoring and volumetric estimation of injected CO_2 using 4D seismic, petrophysical data, core measurements and well logging: a case study at Ketzin, Germany. *Geophysical Prospecting*, 60, 957–973, doi: 10.1111/j.1365-2478.2012.01045.x.

Juhlin, Ch., Giese, R., Zinck-Jørgensen, K., Cosma, C., Kazemeini, H., Juhojuntti, N., Lüth, S., Norden, B., & Förster, A. (2007). 3D baseline seismics at Ketzin, Germany: The CO_2SINK project. *Geophysics*, 72 (5), B121–B132, doi: 10.1190/1.2754667.

Kasahara, J., Hasada, Y., & Tsuruga, K. (2011). Imaging of ultra-long term temporal change of reservoir(s) by accurate seismic source(s) and multi-receivers. *In: „Extended Abstracts of EAGE Workshop on Permanent Reservoir Monitoring (PRM)"*, Trondheim, Norway, pp. 40–44.

Kazemeini, S.H., Juhlin, C., & Fomel, S. (2010). Monitoring CO_2 response on surface seismic data; a rock physics and seismic modeling feasibility study at the CO_2 sequestration site, Ketzin, Germany. *Journal of Applied Geophysics*, 71 (4), 109–124, doi:10.1016/j.jappgeo.2010.05.004.

Kiehl, J.T. & Trenberth, K.E. (1997). Earth's annual global mean energy budget. *Bulletin of the American Meteorological Society*, 78 (2), 197–208, doi:10.1175/1520-0477.

Klein, E., De Lucia, M., Kempka, T., & Kühn, M. (2013). Evaluation of long-term mineral trapping at the Ketzin pilot site for CO_2 storage: An integrative approach using geochemical modelling and reservoir simulation. *International Journal of Greenhouse Gas Control*, 19, 720–730, doi: 10.1016/j.ijggc.2013.05.014.

Kühn, M., Wipki, M., Durucan, S., Korre, A., Deflandre, J.-P., Boulharts, H., Lüth, S., Frykman, P., Wollenweber, J., Kronimus, A., Chadwick, A., Böhm, G., & CO_2CARE Group (2013). Key site abandonment steps in CO_2 storage. *Energy Procedia*, 37, 4731–4740.

Kummerow, J. & Spangenberg, E. (2011). Experimental evaluation of the impact of the interactions of CO_2–SO_2, brine, and reservoir rock on petrophysical properties: A case study from the Ketzin test site, Germany. *Geochemistry, Geophysics, Geosystems*, 12 (5), doi: 10.1029/2010GC003469.

Lei, X. & Xue, Z. (2009). Ultrasonic velocity and attenuation during CO_2 injection into water saturated porous sandstone: Measurements using difference seismic tomography. *Physics of the Earth and Planetary Interiors*, 176, 224–234.

Li, L., Zhao, N., Wei, W., & Sun, Y. (2013). A review of research progress on CO_2 capture, storage, and utilization in Chinese Academy of Sciences. *Fuel*, 108, 112–130, doi: 10.1016/j.fuel.2011.08.022.

Liebscher, A., Martens, S., Möller, F., & Kühn, M. (2013a). On-shore CO_2 storage at the Ketzin pilot site in Germany. In: Gluyas, J. & Mathias, S. (eds.) *Geoscience of Carbon Dioxide (CO_2) Storage*. Woodhead Publishing Limited, ISBN-13: 978 0 85709 427 8; doi: 10.1533/9780857098924.3.278.

Liebscher, A., Möller, F., Bannach, A., Köhler, S., Wiebach, J., Schmidt-Hattenberger, C., Weiner, M., Pretschner, C., Ebert, K., & Zemke, J. (2013b). Injection operation and operational pressure-temperature monitoring at the CO_2 storage pilot site Ketzin, Germany – Design, results, recommendations. *International Journal of Greenhouse Gas Control*, 15, 163–173.

Lüth, S., Bergmann, P., Cosma, C., Enescu, N., Giese, R., Götz, J., Ivanova, A., Juhlin, C., Kashubin, A., Yang, C., & Zhang, F. (2011). Time-lapse seismic surface and down-hole measurements for monitoring CO_2 storage in the CO_2SINK project (Ketzin, Germany). *Energy Procedia*, 4, 3435–3442, doi:10.1016/j.egypro.2011.02.268.

Malek, R. (2009). Results of due diligence study phase 3.5 on feasibility of Gorgon CO_2 sequestration. *Petroleum in Western Australia*, September 2009, Western Australian Department of Mines and Petroleum, 13–17.

Martens, S., Möller, F., Streibel, M., Liebscher, A., & the Ketzin Group (2014). Completion of five years of safe CO_2 injection and transition to the post-closure phase at the Ketzin pilot site. *Energy Procedia*, 59, 190–197, doi: 10.1016/j.egypro.2014.10.366.

Mavko, G., Mukerji, T., & Dvorkin, J. (1998). Gassmann's Relations in: *The Rock Physics Handbook—Tools for Seismic Analysis in Porous Media*. Cambridge University Press, 168–177.

Michael, K., Golab, A., Shulakova, V., Ennis-King, J., Allinson, G., Sharma, S., & Aiken, T. (2010). Geological storage in saline aquifers – a review of the experience from existing storage operations. *International Journal of Greenhouse Gas Control*, 4, 659–667.

Mito, S. & Xue, Z. (2011). Post-Injection monitoring of stored CO_2 at the Nagaoka pilot site: 5 years time-lapse well logging results. *Energy Procedia*, 4, 3284–3289.

Norden, B., Förster, A., Vu-Hoang, D., Marcelis, F., Springer, N., & Le Nir, I. (2010). Lithological and petrophysical core-log interpretation in CO_2SINK, The European onshore research storage and verification project. *SPE Reservoir Evaluation Engineering*, 13, 179–192, http://dx.doi.org/10.2118/115247-PA.

Nover, G., von der Gönna, J., Heikamp, S., & Köster, J. (2013). Changes of petrophysical properties of sandstones due to interaction with supercritical carbon dioxide – a laboratory study. *European Journal of Mineralogy*, 25, 317–329, doi: 10.1127/0935-1221/2013/0025-2295.

Pevzner, R., Urosevic, M., Casparia, E., Galvin, R.J., Madadia, M., Dance, T., Shulakova, V., Gurevich, B., Tcheverda, V., & Cinar, Y. (2013). Feasibility of time-lapse seismic methodology for monitoring the injection of small quantities of CO_2 into a saline formation, CO_2CRC Otway Project. *Energy Procedia*, 37, 4336–4343.

Plasynski, S.I., Litynski, J.T., McIlvried, H.G., Vikara, D.M., & Srivastava, R.D. (2011). The critical role of monitoring, verification, and accounting for geologic carbon dioxide storage projects. *Environmental Geosciences*, 18 (1), 19–34.

Rickett, J.E. & Lumley, D.E. (2001). Cross-equalization data processing for time-lapse seismic reservoir monitoring: A case study from the Gulf of Mexico. *Geophysics*, 66 (4), 1015–1025.

Rutledge, D. (2011). Estimating long-term world coal production with logit and probit transforms. *International Journal of Coal Geology*, 85 (1), 23–33.

Saito, H., Nobuoka, D., Azuma, H., Xue, Z., & Tanase, D. (2006). Time-lapse crosswell seismic tomography for monitoring injected CO_2 in an onshore aquifer, Nagaoka, Japan. *Exploration Geophysics*, 37, 30–36.

Sato, K., Mito, S., Horie, T., Ohkuma, H., Saito, H., Watanabe, J., & Yoshimura, T. (2011). Monitoring and simulation studies for assessing macro- and meso-scale migration of CO_2 sequestered in an onshore aquifer: Experiences from the Nagaoka pilot site, Japan. *International Journal of Greenhouse Gas Control*, 5 (1), 125–137.

Sopher, D., Juhlin, C., Huang, F., Ivandic, M., & Lüth, S. (2014). Quantitative assessment of seismic source performance: Feasibility of small and affordable seismic sources for long term monitoring at the Ketzin CO_2 storage site, Germany. *Journal of Applied Geophysics*, 107, 171–186, doi: 10.1016/j.jappgeo.2014.05.016.

Streibel, M., Finley, R.J., Martens, S., Greenberg, S., Möller, F., & Liebscher, A. (2014). From pilot to demo scale – Comparing Ketzin results with the Illinois Basin-Decatur Project. *Energy Procedia*, 63, 6323–6334.

Thielemann, T., Schmidt, S., & Gerling, J.P. (2007). Lignite and hard coal: Energy suppliers for world needs until the year 2100 – An outlook. *International Journal of Coal Geology*, 72 (1), 1–14.

Torp, T. & Gale, J. (2004). Demonstrating storage of CO_2 in geological reservoirs: The Sleipner and SACS projects. *Energy*, 29 (9–10), 1361–1369.

Underschultz, J., Boreham, C., Dance, T., Stalker, L., Freifeld, B., Kirste, D., & Ennis-King, J. (2011). CO_2 storage in a depleted gas field: An overview of the CO_2CRC Otway Project and initial results. *International Journal of Greenhouse Gas Control*, 5 (4), 922–932.

Urosevic, M., Pevzner, R., Shulakova, V., Kepic, A., Caspari, E., & Sharma, S. (2011). Seismic monitoring of CO_2 injection into a depleted gas reservoir – Otway Basin Pilot Project, Australia. *Energy Procedia*, 4, 3550–3557.

Volkart, K., Bauer, C., & Boulet, C. (2013). Life cycle assessment of carbon capture and storage in power generation and industry in Europe. *International Journal of Greenhouse Gas Control*, 16, 91–106, doi: 10.1016/j.ijggc.2013.03.003.

Wang, Z., Cates, M.E., & Langan, R.T. (1998). Seismic monitoring of a CO_2 flood in a carbonate reservoir: A rock physics study. *Geophysics*, 63 (5), 1604–1617.

Xue, Z. & Matsuoka, T. (2008). Lessons from the First Japanese Pilot Project on saline aquifer CO_2 storage. *Journal of geography (Chigaku Zasshi)*, 117 (4), 734–752 (Japanese, English abstract).

Yilmaz, Ö. (2008). *Seismic Data Analysis: Processing, Inversion and Interpretation of Seismic Data*. In: Doherty, Stephen M. (ed.), Investigations in Geophysics, no. 10. Revised edition of: Seismic data processing (1987). Society of Exploration Geophysicists, Tulsa, USA.

Zemke, K., Liebscher, A., Wandrey, M., & the CO_2SINK Group (2010). Petrophysical analysis to investigate the effects of carbon dioxide storage in a subsurface saline aquifer at Ketzin, Germany (CO_2SINK). *International Journal of Greenhouse Gas Control*, 4, 990–999, doi: 10.1016/ j.ijggc.2010.04.008.

Zhang, F., Juhlin, Ch., Cosma, C., Tryggvason, A., & Pratt, G. (2012). Cross-well seismic waveform tomography for monitoring CO_2 injection: a case study from the Ketzin Site, Germany. *Geophysical Journal International*, 189 (1), 629–646, doi: 10.1111/j.1365-246X.2012.05375.x.



Taylor & Francis
Taylor & Francis Group
http://taylorandfrancis.com

Chapter 15

Observation-based design of geo-engineering projects with emphasis on optimization of tunnel support systems and excavation sequences

M. Sharifzadeh[1], *M. Ghorbani*[2] & *S. Yasrobi*[3]

[1]*Department of Mining Engineering, Western Australian School of Mines, Curtin University, Kalgoorlie, Western Australia, Australia*

[2]*Department of Mining & Metallurgical Engineering, Amirkabir University of Technology, Tehran, Iran*

[3]*Pazhoohesh Omran Rahvar (P.O.R.) Consulting Engineers Company, Tehran, Iran.*

Abstract: The geomaterial in engineering design rarely shows uniform distribution of its properties and behavior. Geotechnical investigation does not detect all possible design parameters accurately and some uncertainties always remain. In such conditions, preliminary design with simplifying assumptions, and detailed design using observational methods during construction, are recommended. Back analyses are very powerful tools for interpreting the results of field measurements. They should be used not only to determine material properties but also to generate a mechanical model of soils and rocks. A brief review of back analysis procedures is presented, including comparisons, problems, recent advances and further development. A classification of different back analysis methods, considering those deterministic and non-deterministic aspects applicable in geotechnical engineering problems, is proposed. The application of observational methods to a large urban tunneling project is illustrated as a case study. The importance of geotechnical/structural/geodetic instrumentation as a practical engineering tool for systematic monitoring of tunnels and buildings in urbanized areas is shown, together with details of how the Niayesh tunnel monitoring plan, taking into consideration all requirements, was created and implemented. Based on the monitoring results, probable alerts, possible countermeasures and several design optimizations were identified. In sequential excavation methods, for reasons of safety and cost, it is essential to fully understand the influence on tunneling performance of both a given excavation sequence, and the trailing distance and face-advancing sequences of different excavation stages in soft ground urban tunneling. Different excavation sequences employing the side drift method were planned and modeled using a three-dimensional finite element method and the optimal excavation sequence was selected. Finally, the trailing distance between different excavation stages was analyzed numerically and the optimal distance for minimum surface settlement was determined.

1 INTRODUCTION

Tunnel and underground excavations are increasingly used for civil, mining and energy purposes. From the civil point of view, because of the rapid development of urbanization, tunneling has become a preferred construction method for transportation and underground utility systems. From the mining point of view, because of limitations in surface resources, the development of underground mining has increased and existing underground mines are getting deeper and deeper.

Given the vast requirement for underground excavation, tunneling technology has significantly advanced in the past few decades. Previously, tunnels were designed in detail before construction. However, because of various ground-related uncertainties, construction methods in which detailed design was done before tunnel excavation could not cover all aspects of real ground conditions and several failures were reported in such design procedures. To minimize risks and uncertainties, observational approaches were introduced and applied. Based on the observational approach, tunnel design was firstly performed by preliminary geotechnical investigation and instrumentation, followed by the use of monitoring systems. By considering monitoring results from full-scale projects and back analysis, real ground behaviors were obtained. During the early stages of construction, the preliminary design could be modified and adjusted using the observed real-world ground behavior data obtained from back analysis. The potential benefits of such observational methods are illustrated in Figure 1.

In this chapter, first the tunnel design procedures involving observational methods are described, which illustrates the key roles of instrumentation, monitoring and back analysis in tunnel design, data update and subsequent design modification. Second, an

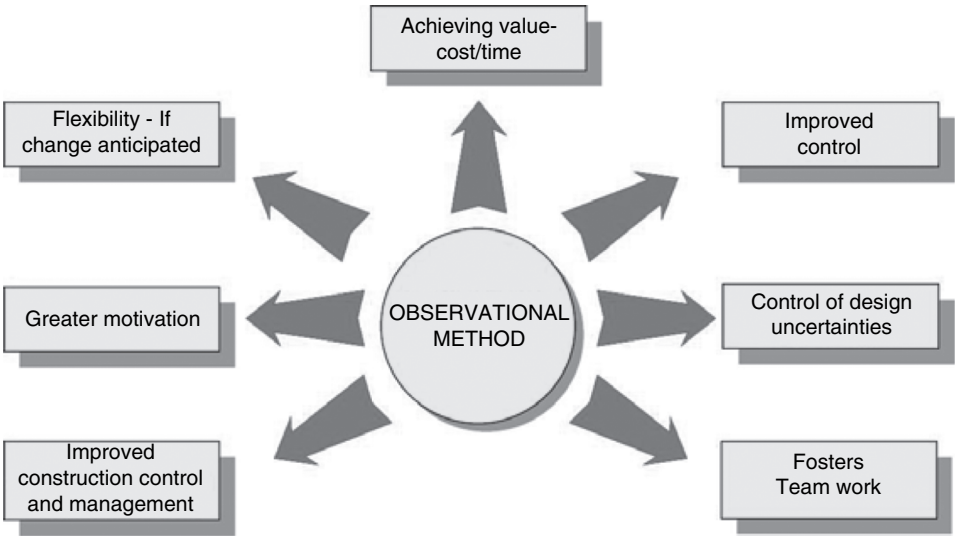


Figure 1 Some potential benefits of the observational methods in geotechnical engineering (Adapted from CIRIA, 1999).

insight into details of geotechnical instrumentation and the planning of monitoring in underground constructions is presented. Third, broad reviews of back analysis methods to derive ground mechanical parameters at full-scale are discussed. Then the applications of the observational approach in the special case of large urban tunnel project are illustrated and the benefits of such an approach in design optimization are explained. Finally, the efficiency of the observational approach is summarized and conclusions are discussed.

2 DESIGN UNCERTAINTIES AND OBSERVATION-BASED GEOTECHNICAL DESIGN PROCEDURE

2.1 Ground investigation and its uncertainties

Geomaterial rarely shows uniform distribution of its properties and, consequently, of behavior. This is because it is formed naturally and its materials are spatially distributed and vary from one point to another, yet only a limited number of geotechnical explorations can be conducted. The nature of its creation causes complexity and different material behavior at different locations – so-called site-specific factors. Geotechnical investigations such as field mapping, geophysical methods, boreholes and core logging, and field and laboratory tests cannot detect all possible variability in material properties and parameters. In most cases, therefore, obtaining the accurate geotechnical parameter values is extremely difficult or even impossible. This leads geotechnical design to explicitly involved assumptions and uncertainties in a project. Einstein and Baecher (1982) have been defined three main sources for uncertainties and errors in engineering geology and rock mechanics:

1. Innate, spatial variability of geological formations, where wrongly made interpretations of geological setting may be a significant consequence, as already described.
2. Errors introduced in the measurement and estimation of engineering properties, often related to sampling and measuring.
3. Inaccuracies caused by modeling physical behavior, including incorrect types of calculation or inappropriate models.

In any engineering study, one can never know what has been left out of an analysis. Thus, in addition to the three major uncertainties above, there is also uncertainty due to omission. The real world has variations and properties that cannot entirely be included in a characterization or an analysis. According to Einstein and Baecher (1982), most of the major failures of constructed facilities have been attributable to omissions.

The variation in material type and complexity in each site-specific case, and in project dimension and construction method on the neighboring ground disturbance, make it difficult to explore all uncertain parameters and conditions. Such high levels of uncertainty make it impossible to design in full detail prior to construction. Thus the development of investigations during construction using the observational method, and the updating of the design accordingly, remarkably enhance the project from both the technical and the economic point of view.

2.2 Observation-based geotechnical design procedure

In the process of designing an underground excavation, there are parameters with varying degrees of uncertainty that must be taken into account. These uncertainties are often related to subsurface conditions and other site-specific factors. Issues of safety and economy were key considerations when the basis for the observational method was formulated. The observational method approach is designated as active design. The basis of this approach is to establish a preliminary design, devise contingency actions for those cases in which the structural behavior deviates from the expected, select and execute relevant observations during construction, and conduct modification of design to suit the ground conditions encountered.

The geotechnical design procedure involving an observational approach is illustrated in Figure 2. As shown, each geotechnical engineering project first performs a preliminary geotechnical investigation and site characterization to identify ground conditions and associated hazards that may threaten the project. In this stage of geological and engineering investigation, engineering experiences and judgment can greatly facilitate the derivation of appropriate design parameters and the visualization of a ground geomechanical model using appropriate assumptions that reflect real-world conditions.

A preliminary design for the project is prepared, together with detailed instrumentation and monitoring plans for the various geotechnical units using limited data and existing norms and standards. Based on the preliminary design report, the construction sequences commence and are followed by excavation, instrument installation and the recording of monitoring data. During this stage, the measured data, such as displacement and stress, are processed and compared to those calculated during preliminary design. Considering the project is implemented at full scale, the ground's real behavior can be monitored and compared with the predictions of the early design stage. If big discrepancies between predicted and observed ground behavior are seen, then back analysis based on monitoring results and the practical evidence from construction can be engaged to derive more realistic ground parameters. Based on these newly calculated parameters, the design reports can be adjusted and updated, and the next construction sequences will be implemented using these updated reports. This cycle of parameter modification is repeated to achieve the most suitable design parameters for each geotechnical unit. Finally, the detailed or final design is established based on the most realistic ground behavior and design parameters. Further details regarding the acquisition of site investigation data can be found in several references (Bieniawski, 1984; Brady & Brown, 2004; Villaescusa, 2014).

3 GEOTECHNICAL INSTRUMENTATION AND MONITORING

3.1 Instrumentation and monitoring concepts

Instrumentation, monitoring and back analysis are the main components of the observational method. The main purpose of the instrumentation and monitoring is to monitor the performance of the geo-engineering projects and the behavior of the confining ground during the construction process, in order to provide safety and to optimize the ground parameters and design.

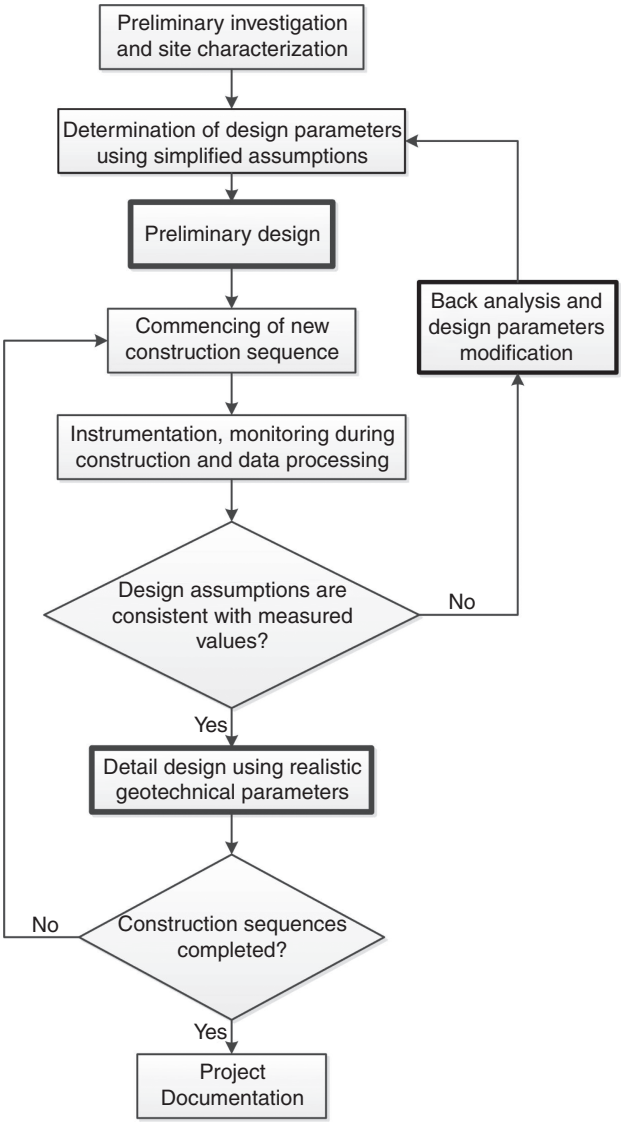
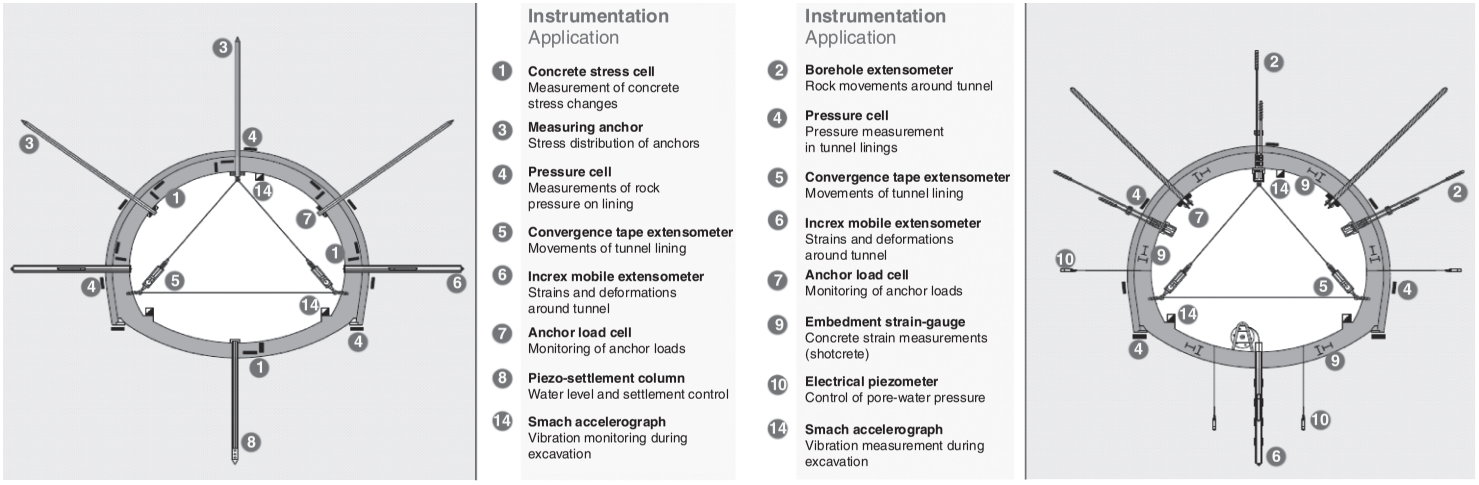


Figure 2 Observation-based design procedure for geotechnical projects.

Instrumentation involves the use of measuring devices to monitor both tunnel structure and its confining ground. The various types of instruments used for different parameter measurements in underground excavation are illustrated and annotated in Figure 3. The type of instrument is selected according to the parameter that must be measured. Force and displacement measurements make up the most popular monitoring applications in projects. The objectives of instrumentation during construction will change, depending on the size and type of construction, the geotechnical conditions and the project schedule. The use of geotechnical, structural or geodetic measurements – or a combination of them – depend



(a) (b)

Figure 3 Various instrumentation systems in an underground excavation (Adapted from Geokon, 2012).

on several factors, such as ground type, expected ground behavior, the importance of the tunneling influence zone, and the level of available measurement technologies.

The purpose of monitoring is to scrutinize and control the project through the collection of evidence such as instrument data and visual observation, followed by the processing and analysis of the evidence gathered. Data and evidence is collected using data acquisition systems and stored in appropriately designed databases. The data is manipulated, analyzed and presented in a technical way to represent the ground's response to project construction and enable the prevention of potential problems. By integrating the monitoring results in back analysis, the ground geotechnical parameters can be derived and used for design updates. The most important physical quantities to be monitored can be subdivided into deformations, stresses, piezometric levels and temperatures. The most common monitoring method is the measurement of displacements, for example, convergence of the underground openings or ground surface settlements. From a mathematical point of view, displacement measurements are not greatly influenced by typical local effects. By comparison, stresses and strains are differential quantities, whose validity is limited to local regions (Ghorbani & Sharifzadeh, 2009). It is therefore necessary to observe stress and strain at several successive points in order to obtain a distribution over a sufficiently large area.

3.2 Design monitoring plan

The task of planning a monitoring program should be a logical and comprehensive engineering process that begins with defining the objectives and ends with planning how the measurement data will be applied. Dunnicliff (1993) defines the steps involved in planning a monitoring program as follows:

1. Define the project conditions
2. Predict mechanisms that control behavior
3. Define the geotechnical questions that need to be answered
4. Define the purpose of the instrumentation
5. Select the parameters to be monitored
6. Predict magnitudes of change
7. Devise remedial actions
8. Assign tasks for design, construction, and operation phases
9. Select instruments
10. Select instrument locations
11. Plan recording of factors that may influence measured data
12. Establish procedures for ensuring reading correctness
13. List the specific purpose of each instrument
14. Prepare budget
15. Write instrument procurement specifications
16. Plan installation
17. Plan regular calibration and maintenance
18. Plan data collection, processing, presentation, interpretation, reporting and implementation
19. Write contractual arrangements for field instrumentation service
20. Update budget.

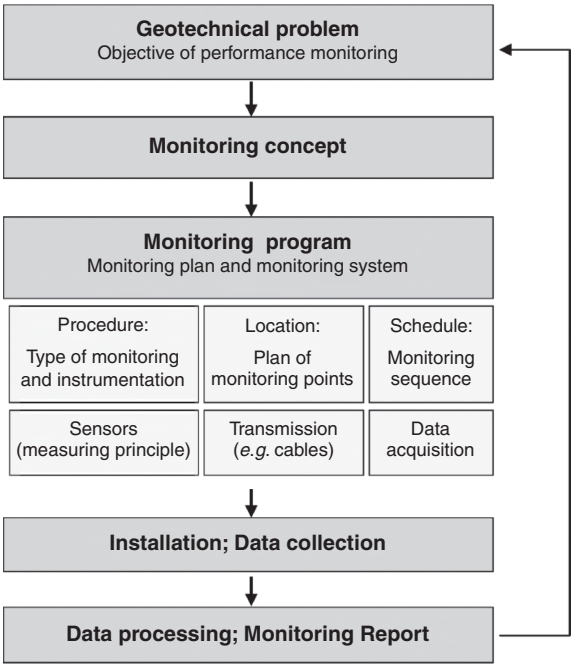


Figure 4 Content and course of a geotechnical monitoring program (Adapted from DIN, 2011).

Geotechnical monitoring should be planned, carried out and evaluated in conjunction with the geotechnical design. Geotechnical monitoring should take all features (both content and course of action) into consideration as shown in Figure 4.

3.3 Trigger criteria and trend rate

The comprehension and critical reading of the monitoring data has the same importance as the measure itself. Part of the comprehension process is the verification of the threshold values. These limits are defined with reference to the design values and, based on these, it is necessary to define some countermeasures. The threshold limits which are defined for each monitored quantity are as follows:

- Alert limit: the exceeding of this value requires an increase to the frequency of readings, both for underground instruments and those on the surface or in buildings, in order to better (and more rapidly) monitor the evolution of the unforeseen phenomenon so as to avoid potentially uncontrollable situations.
- Alarm limit: the exceeding of this value requires the immediate intervention of the engineer in order to apply appropriate countermeasures.

The countermeasures are necessary to bring the situation within acceptable limits or to reinforce the structure to increase its resistance. Countermeasures may include (but shall not necessarily be limited to) increased monitoring frequency, ground treatment, additional support measures, modifications to the excavation/support sequencing.

Monitoring is the basis of a flexible design approach in which the design hypotheses are systematically checked through monitoring results on site, and mitigation measures are those actions predefined at the design stage that form the reaction if and when the encountered conditions are different from the reference scenarios. Furthermore, the reference scenario of the section already excavated is systematically back analyzed to match it to the reality, which is then used to update the predictions of the reference scenario for the next tunnel section to be excavated. Mitigation measures to avoid the dangerous potential migration of the cavity to the surface are related to actions carried out from the surface or from inside the tunnel itself.

Tunneling-induced settlements in urban areas could affect buildings and other surface or subsurface structures. Thus, before constructing new underground structures in urban areas, an analysis of the possible induced effects and selection of appropriate mitigation measures – including the treatment of the ground, reinforcement of existing structures and changes to tunnel specifications – are necessary.

The collected monitoring data can be used in two ways. Initially, all observations and evidence is integrated into rapid diagnosis to prevent possible abnormal behavior, such as excessive displacement or load which may cause failure. In the case of an abnormal condition, immediate action such as changes in support patterns or excavation sequences may be required. At the second stage, the collected data are analyzed in detail: data trends are extracted and compared with the values predicted by the design. If there are big discrepancies between measured and predicted results, then back analysis to calculate the most realistic geotechnical parameters for the ground is recommended, followed by design review and modification with the updated parameters.

4 DESIGN REVIEW AND BACK ANALYSIS

The engineering design and construction of underground openings and surface structures requires *in situ* input parameters such as stress, rock and soil strength and deformation parameters, and porewater pressure. These parameters are essential for stability analysis and ground support system design for these geostructures. Without them, the process of engineering design is not possible.

Despite the availability of several experimental means for determining the parameters at the site, if the geological conditions are complex, it will be very difficult for the engineer to carry out the task in hand. In other words, because the mechanical parameters at various locations around the site vary greatly due to the complexity of the geological conditions, a large number of field tests may be required to describe the ground parameters adequately. In addition, if we conduct a large number of field tests at the site, then there is a large cost in money and time which is an intolerable burden for most projects. However, it is often not feasible to obtain a complete geotechnical characterization of the ground from the preliminary geological studies or from the geotechnical and geophysical explorations along the tunnel axis. Only during the construction of the tunnel itself, or of a pilot tunnel, is it possible to obtain a complete evaluation of the behavior of the ground. Thus, new approaches are needed to address these issues. One of these approaches, back analysis, was put forward in the 1970s and received much attention because of its obvious practical value.

Back analysis is generally defined as a procedure developed for solving system identification (or characterization, back calculation or calibration) problems, which can provide the controlling parameters of a system by analysis of its output behavior. The system is simulated in a model, and the input parameters of the model are identified through the output information. The term 'back analysis' well reflects the backward nature of this calibration procedure and, together with the basic concepts and methods of identification theory, it was introduced to geotechnical engineering in the design and construction of underground engineering, slope engineering, water conservancy and hydroelectric power engineering (Gioda & Maier, 1980; Cividini *et al.*, 1981; Sakurai, 1982; Gioda & Sakurai, 1987; Sakurai *et al.*, 2003).

In general terms, two 'tools' are necessary to perform a back analysis. The first is a stress analysis procedure using analytical or numerical methods, for determination of the stress, strain and displacement distributions for the problem at hand. The second is a suitable optimization algorithm that minimizes the discrepancy between the data measured in the field and the corresponding results obtained by the stress analysis (Cividini *et al.*, 1981). This discrepancy is commonly expressed as the error function and described below (Equation 1):

$$\varepsilon(P) = \left\{ \sum_{i=1}^{n} [u_i^* - u_i(P)]^2 \} \right\} \tag{1}$$

In this equation, u_i^* and $u_i(P)$, $i = 1, 2, ..., n$ are the normalized measured and corresponding analysis results, respectively. Obviously, $u_i(P)$ depends on the unknown model parameters collected in the vector P.

The various techniques for solving such a error minimization problem can be divided into two groups, comprising gradient-free and gradient-based parameter identification methods that are explained by Pichler *et al.* (2003) as follows:

- 'Gradient-free parameter identification methods' such as fuzzy logic, artificial neural network methods, genetic algorithms or probabilistic (stochastic) search techniques. In this type of method, the entire parameter space is searched for an optimal solution, and error function values are evaluated sequentially and compared for different parameter sets. This method requires a large amount of numerical analysis to find optimal parameters.
- 'Gradient-based parameter identification methods': these methods seem to be robust and efficient only if the error function shape is relatively smooth or if the chosen initial point is very close to the solution. They are, therefore, limited to the identification of a small number of parameters for which the influence on the error function will be important. Unfortunately, for geotechnical studies, problems are often complex and the solutions are not unique. To have information about the uniqueness of the solution, several minimizations need to be computed and compared. Gradient-based methods can then become an exhaustive process to identify parameters without a guarantee of reaching a good description of the solution set (Levasseur *et al.*, 2007). These methods employ the gradient of ε (*i.e.* the derivation of ε with respect to parameter vector P). In the case of elastic material behaviors, the gradient of ε can be computed analytically (Ohkami & Ichikawa, 1997; Ohkami & Swoboda, 1999). However, for other cases, especially non-linear or

elastoplastic problems, computation of the analytical expression of the gradient of ε is a challenging task, which makes major modifications of the analysis tool (*e.g.* finite element software) unavoidable (Mahnken & Stein, 1995). These methods are characterized by a local search for a minimum of the error function and do not search for optimal solutions in the entire parameter space. This local search starts from an initial choice for the unknown parameters. Since results depend highly on these initial choices, such algorithms may get trapped in a local minimum of the error function.

The back analysis method has been applied to: the identification of *in situ* stress fields (Cai & Chen, 1987; Kaiser *et al.*, 1990); the characterization of rock and soil parameters (deformation and strength characteristics) using field measurements in test galleries (Gioda & Maier, 1980; Sakurai & Takeuchi, 1983); rock mass hydraulic properties; rock mass zoning; boundary conditions (Tonon *et al.*, 2001); loads acting on tunnel linings; the predicted behavior of a geotechnical structure at an early stage of construction (Asaoka & Matsuo, 1984); evaluation of rock and soil mechanics field tests (Gioda & Maier, 1980; Cividini *et al.*, 1981); calibration of laboratory tests (Iding *et al.*, 1974; Imre, 1994). Application has involved closed-form solutions and numerical methods among others. Simultaneous evaluation of several parameters is achievable.

In the field of underground construction, the measurements that are most frequently carried out usually correspond to one of the following groups of parameters, according to the particular problem: strains, relative and absolute displacements, stresses in linings and in the surrounding material, support pressures (steel arches and rock bolts), forces in the rock anchors, and groundwater pressures. Preference is usually given to displacement measurements as they represent, from the mathematical point of view, parameters that are not greatly influenced by typical local effects. Stresses and strains are, by comparison, differential parameters that can result in values that are very different from point to point. Their mean value should therefore be calculated over a sufficiently large base of data to provide representative values (Oreste, 2005). On the other hand, because displacements of rock and soil induced by excavation can be measured easily and reliably, displacement-based back analysis techniques have been a hot research topic since the 1970s, and extensive studies have been conducted to develop different models of displacement-based back analysis (Kirsten, 1976; Jurina *et al.*, 1977; Sakurai & Abe, 1979; Gioda & Jurina, 1981; Sakurai & Takeuchi, 1983; Yang *et al.*, 1983, 2000; Wang *et al.*, 1987; Yang, 1990; Zhao & Lee, 1996; Sakurai, 1997; Gioda & Locatelli, 1999; Gioda & Swoboda, 1999; Swoboda *et al.*, 1999; Feng *et al.*, 2004; Zhang *et al.*, 2006). Back analysis based on field measurements of strains or stresses has also been used (Kaiser *et al.*, 1990; Zou & Kaiser, 1990). These models range from linear elastic to non-linear models – such as elastoplastic, viscoelastic (Ohkami & Swoboda, 1999) and viscoplastic models (Mahnken & Stein, 1995) – from two-dimensional to three-dimensional models (Swoboda *et al.*, 1999; Hisatake & Hieda, 2007), and from deterministic to non-deterministic (uncertain) models.

4.1 Back analysis techniques

Several back analysis techniques were developed in past few decades which is categorized and illustrated in Figure 5. In general, there are two fundamental approaches to the

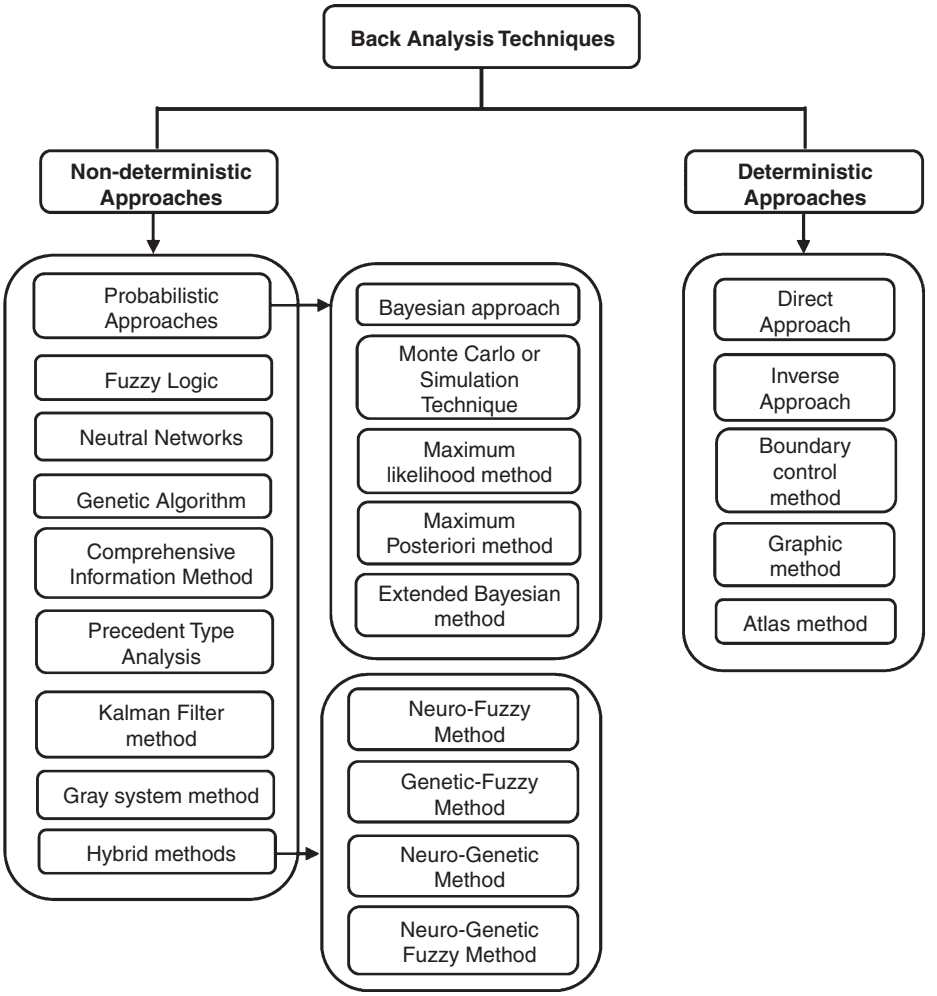


Figure 5 Classification of back analysis methods in geotechnical engineering.

back analysis problem, namely, deterministic and non-deterministic approaches. In deterministic identifications, the discrepancy between the system and the model variables is simply seen as a (deterministic) signal to be minimised according to a suitably defined loss function. Back analysis based on deterministic methods includes the inverse approach (Cividini *et al*., 1981), the direct approach (Cividini *et al*., 1981), the graphic method, the atlas method and the boundary control method (Ichikawa & Ohkami, 1992). In non-deterministic identification, the discrepancy between the system and the model is considered as a non-deterministic signal. Back analysis based on non-deterministic methods includes the probabilistic (statistical) methods, fuzzy logic (Liang *et al*., 2003), artificial neural networks (Pichler *et al*., 2003), genetic algorithms (Lavasseur *et al*., 2007), the precedent type analysis method (Li *et al*., 1998), the Kalman filter method (Kosmatopoulos *et al*., 1995; Rubio & Yu, 2007), the grey

system method, and the comprehensive information method. Probabilistic methods can be subclassified into the Bayesian method (Cividini *et al*., 1981), Monte Carlo simulation techniques (Cividini *et al*., 1981), the maximum likelihood method, the maximum a posteriori method and the extended Bayesian method. Today's hybrid of soft computing techniques (most of which incorporate fuzzy logic) – such as the neuro-fuzzy (Gokceoglu *et al*., 2004), genetic fuzzy, neuro-genetic and neuro-fuzzy-genetic methods – are extensively used for parameter identification in geotechnical engineering problems.

4.1.1 Deterministic approaches

In relation to classical stress analysis problems, two alternative approaches for back analysis, referred to as 'inverse' and 'direct' approaches respectively, are described here in a deterministic context.

In the inverse approach, the system of equations governing the stress analysis problem is rewritten in such a way that material parameters appear as unknowns, and measured values (displacements or stresses) appear as input data. Since the number of available measurements usually exceeds the number of unknown parameters, the final system contains more equations than unknowns and the solution has to be based on a suitable optimization algorithm. The first inverse algorithm based on the finite element method (FEM) was proposed by Kavanagh & Clough (1971) for structural problems, and subsequently Jurina *et al*. (1977) developed the first inverse approach applicable to parameter identification in geotechnical problems. Gioda (1980) used this approach to search for elastic material parameters B (bulk modulus) and G (shear modulus), and it can be modified to calculate the earth pressure acting on a tunnel lining. Using the inverse algorithm suggested by Sakurai & Takeuchi (1983), it is possible to compute both Young's modulus and the initial state of stress simultaneously. Here, the Poisson's ratio and the initial vertical stress are assumed as known. An inverse algorithm for parameter identification of non-linear elastic solids was suggested by Iding *et al*. (1974).

The direct approach adopts the same numerical model used for stress analysis, within the framework of an iterative procedure; hence no formulation of the inverse problem is required. The direct approach employs the trial values of the unknown parameters as input data in the stress analysis algorithm, until the discrepancy between measurements and corresponding quantities obtained from a numerical analysis is minimised. Based on the error function described in Equation 1, back analysis aims at determination of the absolute minimum of ε, which provides the best agreement between measured and computed values.

In geotechnical engineering, most analyses are performed by means of the FEM. Unfortunately, the computational effort of such analyses is usually rather high. Moreover, realistic modeling of geotechnical problems requires consideration of different types of non-linearities. These arise from, for example, non-linear boundary conditions and/or non-linear material behavior. Consequently, the error function (Equation 1) may have several local minima, making back analysis a challenging task. In order to minimize this error function, which is highly non-linear and, in most cases, an analytical expression of its gradient cannot be determined easily, algorithms known in mathematical programming as direct search methods are used (Himmelblau,

1972). The simplex method, Rosenbrock's algorithm (Rosenbrock, 1960) and Powell's method (Powell, 1964), which are iterative procedures that perform the minimization process only by successive evaluation of the error function, were recommended by Gioda & Maier (1980) for this purpose.

An inverse back analysis procedure can demonstrate smooth, fast-converging and stable behavior, if measured data are well-selected (Gioda, 1985). This is because boundary control is built into the algorithm. Points where both the nodal forces and nodal displacements are known basically control the error minimizing procedure. This ensures quick convergence for data of good quality, but can cause divergence of the procedures in the case of ill-selected measurement data (Swoboda *et al*., 1999).

Direct formulation is very flexible; applying such a procedure for complex constitutive models is easier, where the inverse relations cannot be derived in the simple direct way. Furthermore, development of the direct back analysis code is much less difficult than development of the code based on an inverse algorithm. The only work involved is appending a module to an existing program, which does the minimization of errors between measured and predicted data (Cividini *et al*., 1981).

It is not straightforward to work out a general criterion for choosing the most convenient algorithm for back analysis. However, it should be observed that inverse techniques are particularly convenient when dealing with a relatively large number of unknown parameters and when the finite element mesh has a small number of nodal variables. On the other hand, the direct procedures are preferable when a few parameters are back analyzed using large finite element meshes (Cividini & Gioda, 2003). However, the course of convergence is highly dependent on the number of unknown parameters, the quality of their initial guess and on the optimization strategy chosen. The direct method can give an insufficient solution, especially in cases where Young's modulus and Poisson's ratio are to be identified simultaneously (Swoboda *et al*., 1999).

The boundary control method suggested by Ichikawa and Ohkami (1992) combines the advantages of both approaches. In the inverse portion of this algorithm, the equilibrium equation is coupled together with observational boundary conditions and the direct part of the algorithm improves convergence of a Newton's iteration process.

When using a deterministic optimization strategy based on gradient evaluations, it is not guaranteed that the global minimum of the problem is obtained. However, a more systematic approach would be to use a hybrid method, that is, a combination of deterministic and stochastic strategies.

4.1.2 Non-deterministic approaches

Today, soft computing techniques (most of which incorporate fuzzy logic) are extensively used for parameter identification in rock and soil engineering problems. An interesting and, perhaps, the most attractive characteristic of fuzzy models compared with other conventional methods commonly used in geosciences, such as statistics, is that they are able to describe complex and non-linear multivariable problems in a transparent way (Setnes *et al*., 1998). Moreover, fuzzy models can cope with non-probabilistic (*i.e*. semantic) uncertainties.

In the back analysis problem of rock engineering, in order to identify physical parameters, the displacements of the surrounding rock should be measured, but a

particular precision of displacement may be required and sometimes may be beyond the available precision of measurement. Intricate experimental measurements or complicated numerical computations are often needed in conventional methods. This is time-consuming and costly. Therefore, a simple but sensitive analysis method for the identified parameters is needed. The neural network model is an ideal candidate to resolve this kind of identification problem. Neural network methods need only a few data measurements from any single place, provided that the data cover the area in which the physical parameters of interest are identified (Liang *et al*., 2003).

In the engineering literature, genetic algorithms are well-known for their ability to solve complex optimization problems. The method is robust and highly efficient but does not guarantee an exact identification of the optimum solution. However, it does permit the localization of an optimum set of solutions close to this optimum (Gallagher & Sambridge, 1994). This property is interesting in relation to the idea of back analysis in geotechnical studies. The genetic algorithm is a new and efficient optimization method for geotechnical back analyses (Levasseur *et al*., 2007).

The use of probabilistic (statistical) instruments for the calibration of numerical models is common in geotechnical contexts because of the large uncertainties in the initial estimation of the parameters of the rock mass, and because of the field measurements that represent the data of the back analysis, which are in general affected by errors that depend, for example, on the nature of the measured quantities, on the characteristics of the adopted devices, and on the field conditions. Various techniques have been proposed to evaluate the influence of these errors on the computed mechanical parameters. Some of them are described here.

A first approach is based on the so-called Monte Carlo simulation technique. In following this method, the influence of the measurement error, and of the number of input data, is evaluated through a series of numerical tests (Cividini *et al*., 1981). Each of these consists of a set of back analyses based on suitable generated input measurements (*e.g*. displacements). The input data are obtained by adding a disturbance term, representing the experimental 'errors', to the 'exact' measurements. Independent random number generators, with chosen probability distributions and zero mean value, are used to work out these errors. The number of generators coincides with that of the input measurements. Their probability distributions depend on the characteristics of the measuring devices and of the measured quantities (Cividini & Gioda, 2003).

The 'exact' displacements can either be evaluated on the basis of actual field measurements or be simulated through a preliminary stress analysis of the problem at hand, in which reference values of the material parameters are introduced (Cividini *et al*., 1981). This procedure permits establishment of a probabilistic correlation between the resolution of the measuring device, the number of measurements and the accuracy of the computed parameters characterizing the soil/rock mass.

The simulation technique offers the advantage of an extremely simple implementation, but requires a computational effort that rapidly increases according to the number of free variables in the numerical model and the number of unknown parameters.

A typical feature of the Bayesian approach is that a priori information on the unknown (uncertain) parameters can be introduced in the back analysis, together with the data deriving from *in situ* measurements. In most cases, the a priori information consists of an estimation of the unknown parameters based on the engineer's judgment or available general information. This leads to a numerical calibration

procedure that combines the knowledge deriving from previous, similar problems with the results of the *in situ* investigation in order to obtain a mean value for the uncertain parameters and their variance. From this, it is possible to derive a final probabilistic distribution. It is worthwhile observing that the Bayesian approach is also applicable when the number of unknown parameters exceeds the number of *in situ* measurements, if a reliable initial guess on the parameters can be formulated (Cividini *et al.*, 1983).

Both approaches lead, in practical terms, to the same results, with regard to the relationship between the resolution of the measuring devices and the uncertainty of the estimated parameters. However, the computer time required by the (Monte Carlo) simulation process is much larger than that required by the Bayesian approach (Cividini & Gioda, 2003).

The Kalman filter (KF) was formulated in the 1960s as an algorithm for the analysis of linear discrete stochastic processes. The KF methodology is apt for solving parameter identification (inverse) problems in a statistical context, through a sequence of estimations, which starts from an a priori estimation by an 'expert' (Bayesian approach) and exploits a time-stepping flow of experimental data until convergence is empirically ascertained. The KF algorithm was incorporated into Gioda's inverse algorithm by Murakami and Hasegawa (1993). This probabilistic procedure allows us to use the measurement error information in the inverse calculation and to evaluate the influence of measurement error on the result of back analysis.

Grey system theory uses a black-grey-white color spectrum to describe a complex system whose characteristics are only partially known or known with uncertainty. White is used to denote a completely known system, and black represents a completely unknown system. Geotechnical systems are, by their nature, complex and usually heterogeneous, and it is very rare for such systems to be completely understood in all their complexity. Grey system theory generally includes: (a) grey incidence analysis, which compares and evaluates a system's factor behaviors; (b) system modeling, which predicts the behavior of the system (Deng, 1986).

4.2 Difference between parameter identification and back analysis

In much of the preceding discussion, the word 'identification' was used, rather than 'back analysis'. In parameter identification, the input data used in the computations are checked after the field measurement results have been analyzed, and can be modified if needed, but the model remains the same the whole time. In back analysis, the modeling should also be checked with field measurements as well as the material properties. Nevertheless, it is common that, in the observational methods, the input data used in the computation are usually checked during the excavation, with the modeling being fixed (Sakurai, 1997).

It is extremely important in any geotechnical engineering problem that the models should not be assumed, but rather should be determined by a back analysis. If a model is fixed all the time during observational procedures, the results are not only inadequate but also misleading in their interpretation, in that they provide incorrect information to the decision making in relation to modification of design and construction methods. In fact, after Sakurai (1997), the following three different procedures can be distinguished (Tonon *et al.*, 2001):

1. In a forward analysis, once a mechanical model is assumed, and the values of the mechanical parameters are determined, then displacements, stresses and strains can be calculated.
2. In an identification procedure, displacements, stresses and strains are measured, a mechanical model is assumed, and then the values of the mechanical parameters are calculated.
3. In a back analysis, displacements, stresses and strains are measured, and then the model as well as the values of the mechanical parameters are determined.

While the first two approaches are primarily inductive, the third approach is deductive. This means that the rules of thinking that we follow in the forward analysis and parameter identification are difficult to make explicit. By contrast, the mathematical theory of logic (completed with probability theory) seems to apply quite well to back analysis (inverse analysis) (Tarantola, 2005).

4.3 The main issues in back analysis

4.3.1 Uniqueness, identifiability and stability

The most significant problem of inverse analysis may be characterized by three key words: the uniqueness, identifiability and stability of the solution. The uniqueness of the solution relates to the idea that a given formulation of an inverse analysis has only one set of unique parameter values for a given observational data set. The identifiability, on the other hand, means a purely mathematical relationship, irrespective of any inverse analysis formulation, as to whether a distributed parameter system (*i.e.* a partial differential equation) is capable of mapping a unique set of parameter values from a set of observational data. The stability of the solution, in turn, is defined such that when an objective function converges at a point in a parameter hyperspace, a set of parameter values would also converge to a point at the same rate. One can easily imagine that the instability is associated with an objective function that is very flat near the optimum, so that most minimization algorithms converge slowly to this point (Honjo *et al.*, 1994).

4.3.2 Model identification

The other significant aspect that is often problematic in geotechnical inverse analysis is that of model identification. This relates to selection of the optimum model from many alternative models of varying sophistication and complexity. There are generally two types of error in inverse analysis: one is system modeling error, which can be evaluated by the goodness of fit of the calculated results to the observed data, and the other is the error associated with parameter uncertainty. An increase in parameter numbers generally improves the system modeling error, although the parameter uncertainty is increased, and vice versa. It should be recognized that an increase in the parameter uncertainty reduces the prediction reliability, which is the most important output of an inverse analysis. Therefore, a sophisticated model (*i.e.* a model with more parameters) may not give better prediction, and it all depends on the quantity and quality of the data. Apparently, there is a trade-off between these two components, and the best model is the one that balances these two, which is the essence of model identification (Honjo *et al.*, 1994).

4.4 Important considerations on the use of back analysis

To ensure the uniqueness of back analysis solutions and increase the speed of back analysis, Sakurai (1997) described a number of principles to follow in order to choose the parameters that must be identified:

1. Select parameters that are of greatest influence on the stability of underground openings;
2. Select parameters that are very difficult to obtain accurately enough by other methods;
3. Reduce the number of unknown parameters to be identified as much as possible.

The rock mass parameters that are most difficult to estimate from the preliminary investigations and that rely heavily on back analysis results include: (a) the relationship between the horizontal and vertical stresses in the rock mass; (b) the dilatancy of the rock mass; (c) the strength parameters of the rock mass in a plastic field (Oreste, 2005).

The minimization of the error function alone does not always guarantee a correct back analysis. The qualitative trend of the displacements on the wall of the excavations, for example, should be the same in the calculation as in reality, as a confirmation of the validity of the calculation model and of the simplified assumed hypotheses.

5 APPLICATION OF GEOTECHNICAL MONITORING IN THE CASE OF A LARGE URBAN TUNNEL (NIAYESH)

The Niayesh road tunnels were constructed in the urban area between the Niayesh and Sadr highways in Tehran, Iran. This project is one of the biggest tunneling projects in the Middle East, with a total length of over 8 km, and cross-sectional areas ranging from 87 to 470 m^2 (see Figure 6).

The major characteristics and limitations of the Niayesh road tunnel project include (Ghorbani *et al.*, 2012):



Figure 6 A plan of the Niayesh road tunnels in Tehran, Iran.

1. Heavy traffic along the highways and connecting roads above the tunnel
2. High building intensity in several areas of the tunnel alignment
3. Sewers and pipes above the tunnel route and old sewers with unknown locations
4. Highway bridges crossing the alignment of the tunnel
5. Low overburden in some areas with soft ground and man-made features with high water inflow in some regions
6. Passes beneath Mellat Park Lake
7. Many bifurcations with large cross sections along the tunnel route
8. Limitations on instrument installation along the tunnel route and on buildings and other surface structures
9. Inadequate site investigations due to a lack of permission, especially in residential areas.

5.1 Tunnel geology

According to the geology map of Tehran prepared by the Geological Survey of Iran – based on results from boreholes, test pits and trenches along the tunnels' routes and geological mapping during tunnel construction – the tunnels passed through A and B formations (Figure 7). The groundwater table was well below the tunnel level.

5.2 Construction procedure and emergency plan

The Niayesh tunnels were excavated according to the principles of the sequential excavation method (SEM), taking into consideration the following factors (after ITA, 2009):

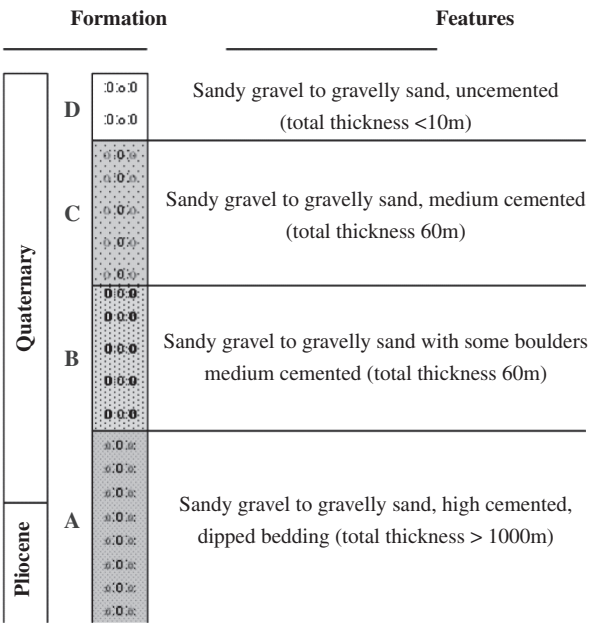


Figure 7 Stratigraphy of Tehran alluviums (Adapted from P.O.R., 2008).

1. Difficult and complex ground with changeable geological formations
2. Greater variability in the choice of excavation methods according to the ground conditions
3. Highly variable shapes of cross sections
4. Greater variability in the choice of excavation sequences according to the ground conditions (change from top-heading advance to side-heading advance and vice versa)
5. Easier optimization of the primary support using the observational method in special cases
6. Difficult access to the main tunnels (given that tunneling is in a densely populated urban area)
7. Many bifurcations and intersections with large cross sections along the tunnels' routes.

According to the SEM contract documents in the Niayesh road tunnel project, longitudinal profiles were defined along the tunnel's alignment, which was termed ground advance classification. In longitudinal profiles, the tunnels were divided into different sections based on depth of overburden, tunnel geometry and geotechnical specifications. Using this data, appropriate excavation class and support systems were defined for different sections and the values of tunnels' deformations and surface settlements were computed (Table 1).

The geometry, excavation classes and support elements for different cross sections of the Niayesh road tunnel project are presented in Table 2.

5.3 Monitoring system

Monitoring is an essential part of SEM (also known as the New Austrian Tunneling method (NATM)). Based on the special characteristics of the Niayesh tunnel, an extensive monitoring programmer was developed for this project, especially in residential areas and at junctions and bifurcations with large cross sections. The monitoring plan for the Niayesh tunnel project had the following objectives (Ghorbani *et al.*, 2012):

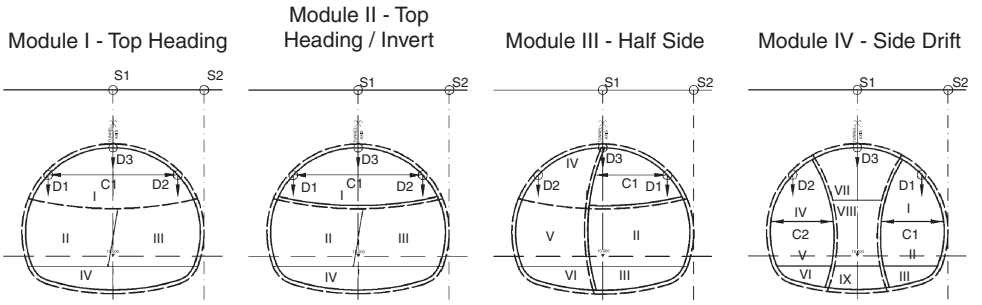
1. To prevent unexpected phenomena in order to avoid critical situations for tunnels, buildings, highways, roads and bridges in terms of safety. Monitoring enables appropriate mitigation measures to be taken as soon as measurements reflect a need for action.
2. To check the design assumptions and improve the design solutions through back analysis and further interpretation of the behavior of the ground during excavation.

A typical instrumentation array for a 3.5-lanes cross section is illustrated in Figure 8. As shown in Figure 6, the tunnels pass through densely populated urban areas with high-rise buildings with commercial, residential, governmental and political applications. Taking into account several factors of buildings, tunnels and ground conditions – such as buildings' characteristics, position of buildings relative to tunnels, and tunnel dimension – all the buildings at the tunnel route were classified into three categories: (a) critical buildings (red buildings – 29%); (b) buildings that needed more assessment (yellow buildings – 65%); (c) non-critical buildings that are not affected much by tunneling (green buildings – 6%). In Table 3, the type and total number of instruments

Table 1 Ground advance classification of 2.5-lanes cross section at Niayesh tunnel (P.O.R. Consulting, Iran & D2 Consult, Austria).

	Location	Main Tunnel											
	Lane Number	2+1											
	Type	2A				2B				2C			
	Ground Advance Classification	2AI	2AII	2AIII	2AIV	2BI	2BII	2BIII	2BIV	2CI	2CII	2CIII	2CIV
	Overburden [m]	8-15				15-30				>30			
	Total Length [m]	see Zoning Plan				see Zoning Plan				see Zoning Plan			
Geotechnic Specification	Description	High Cemented Clayey Sand or Gravel											
	Internal Friction	40	35	34.5	34	40	38	34.5	34	40	35,5	34,5	34
	Cohesion [kg/cm²]	55	42	38	35	55	45	40	30	55	45	40	30
	Permeability [cm/s]	1E-5--1E-4	1E-5--1E-4	1E-5--1E-4	1E-5--1E-4	1E-5--1E-4	1E-5--1E-4	1E-5--1E-4	1E-5--1E-4	1E-5--1E-4	1E-5--1E-4	1E-5--1E-4	1E-5--1E-4
	Density [gr/cm³]	1.7--2.4	1.7--2.4	1.7--2.4	1.7--2.4	1.7--2.4	1.7--2.4	1.7--2.4	1.7--2.4	1.7--2.4	1.7--2.4	1.7--2.4	1.7--2.4
Construction	Module	I	II	III	IV	I	II	III	IV	I	II	III	IV
	Initial Lining Thickness [cm]	30	30	30	30	30	30	30	35	35	35	35	40
	Temporary Initial Lining Thickness [cm]	-------	-------	15	15	-------	-------	15	20	-------	-------	20	30
	Temporary Invert Lining Thickness [cm]	-------	20	20	-------	-------	20	20	-------	-------	20	25	-------
	Sealing Thickness [cm]	2.0	2.0	2.0	2.0	2.0	2.0	2.0	2.0	2.0	2.0	2.0	2.0
	Invert Type	Arch	Arch	Arch	Arch	Arch	Arch	Arch	Arch	Arch	Arch	Arch	Arch
	Lattice Girder Spacing	1.7--2.2	1.3--1.7	1.3--1.7	1.0--1.3	1.7--2.2	1.3--1.7	1.3--1.7	1.0--1.3	1.7--2.2	1.3--1.7	1.3--1.7	1.0--1.3
	Length of Round TH	1.7--2.2	1.3--1.7	1.3--1.7	1.0--1.3	1.7--2.2	1.3--1.7	1.3--1.7	1.0--1.3	1.7--2.2	1.3--1.7	1.3--1.7	1.0--1.3
	Length of Round Bench (=F x TH) **)	2.0	2.0	2.0	2.0	2.0	2.0	2.0	2.0	2.0	2.0	2.0	2.0
	Length of Round Invert (=F x TH) **)	3.0	3.0	3.0	3.0	3.0	3.0	3.0	3.0	3.0	3.0	3.0	3.0
	Initial Lining Lattice Girder Bars	Φ25 & 2*Φ18	Φ25 & 2*Φ18	Φ25 & 2*Φ18	Φ25 & 2*Φ18	Φ25 & 2*Φ18	Φ25 & 2*Φ18	Φ25 & 2*Φ18	Φ28 & 2*Φ20	Φ28 & 2*Φ20	Φ28 & 2*Φ20	Φ28 & 2*Φ20	Φ28 & 2*Φ20
	Temporary Initial Lining Lattice Girder Bars	-------	Φ20 & 2*Φ18	Φ20 & 2*Φ18	Φ20 & 2*Φ18	-------	Φ20 & 2*Φ18	Φ20 & 2*Φ18	Φ20 & 2*Φ18	-------	-------	Φ20 & 2*Φ18	Φ20 & 2*Φ18
	Wire Mesh *)	Φ8@200*200 (2 Layer)	Φ8@200*200 (2 Layer)	Φ8@200*200 (2 Layer)	Φ8@200*200 (2 Layer)	Φ8@200*200 (2 Layer)	Φ8@200*200 (2 Layer)	Φ8@200*200 (2 Layer)	Φ8@200*200 (2 Layer)	Φ8@200*200 (2 Layer)	Φ8@200*200 (2 Layer)	Φ8@200*200 (2 Layer)	Φ8@200*200 (2 Layer)
Settlement	S1 Surface Settlement [mm]	-27	-28	-17	-16	-29	-31	-22	-19	-33	-35	-26	-23
	S2 Surface Settlement [mm]	-22	-22	-14	-13	-28	-28	-21	-18	-31	-34	-25	-23
Deflection	D1 First Excavated Side Drift [mm]	-18	-17	-13	-7	-30	-34	-29	-13	-45	-52	-41	-19
	D2 Second Excavated Side Drift [mm]	-18	-17	-3	-5	-30	-34	-5	-9	-45	-52	-7	-12
	D3 Middle Drift [mm]	-17	-17	-20	-6	-27	-28	-38	-9	-38	-41	-51	-11
	C1 First Excavated Side Drift [mm]	-5	-6	-13	-2	-11	-14	-29	-5	-15	-23	-46	-9
	C2 Second Excavated Side Drift [mm]	-------	-------	-------	-5	-------	-------	-------	-5	-------	-------	-------	-14

TH.....Top Heading
F.....Factor
Module means Excavation Concept
*).....2 Layers - 1 Layer earthside, 1 Layer airside
**).....In case of maximum settlement and ground deflection length of round bench and length of round invert shall be reduced.



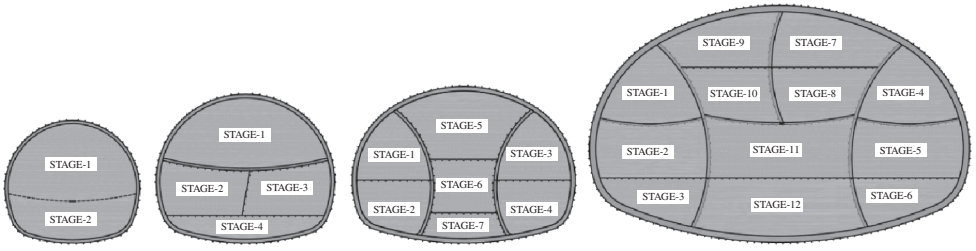
for the monitoring of tunnels, surrounding ground and buildings in the Niayesh tunnel are presented.

5.4 Design of sequential excavation method

The construction of tunnels in urban areas encounters many problems, such as face stability, ground surface settlement, tunneling-induced building damage and high

Table 2 Geometry, excavation classes and support elements of the Niayesh road tunnel project (Ghorbani *et al.*, 2012).

Excavation class	*1.5 lanes*	*2.5 lanes*	*3.5 lanes*	*Bifurcation*
Tunnel geometry				
Area (m^2)	87	136	186	470
Width/Height (m)	10.80/9.80	14.40/11.90	18/12.60	30.60/19.60
Number of traffic lanes	1	2	3	4
Total length of main tunnels (m)	8100			
The height of tunnel overburden	Maximum: 40m; Minimum: 4.7m; Average: 18m			
Maximum longitudinal slope (%)	4.5			
Transverse slope (%)	Maximum: 6%; Minimum: 1%			
Excavation and support				
Shotcrete (C25/30) (cm)				
Main wall	25	Based on ground	35	45–55
Temporary wall	–	advance classification	25	25
Temporary invert	25	(Table 1)	–	20
Main invert	25		35	45–55
Excavation round length in crown (m)	1–1.5		1–1.5	1
Excavation round length in bench (m)	3–4.5		3–4.5	2
Pre-support measures	Forepoling was arranged in the roof area of the tunnels in loose grounds in the form of a fan (Ls = 6 m and φ = 76 mm)			
Excavation method	Sequential excavation method (SEM) using mechanical tunnel excavator			
Tunnel shape	Modified horseshoe shape for 1.5- and 2.5-lanes cross sections, and mouth shape for 3.5- and 4- lanes cross sections			



costs. In many countries, sequential excavation is currently applied where soft ground tunneling without a TBM is indicated (Romero, 2002). A great variety of excavation techniques have been developed (Geisler *et al.*, 1985; Pottler, 1992), which apply different methods to excavation and support. It is therefore important to investigate and compare the effect of these methods on ground disturbance and surface settlement. Given the low strength of the ground and the large span of the Niayesh tunnels, a full-face excavation was not possible. Therefore, SEM was selected for this project. This

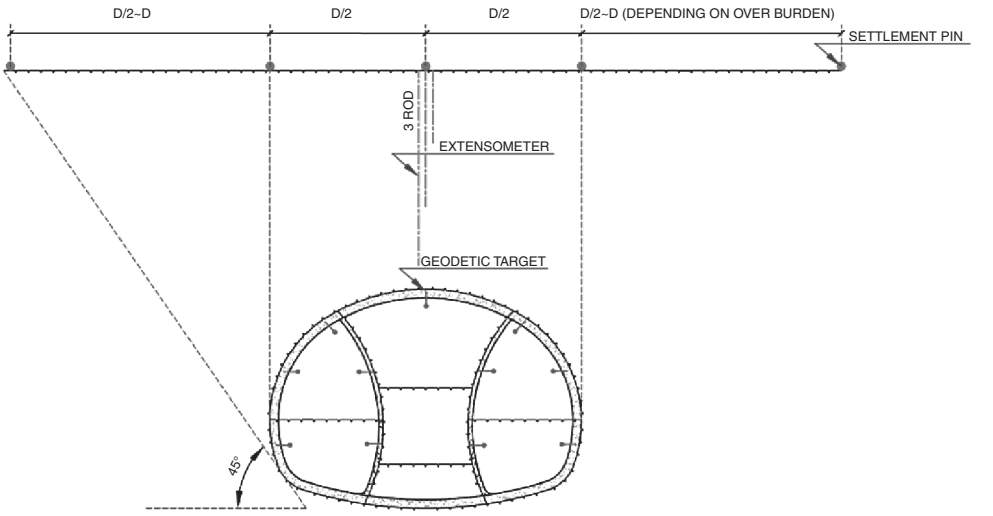


Figure 8 A typical instrumentation array for a 3.5-lanes cross section.

Table 3 The type and total number of instruments for monitoring the tunnels, surrounding ground and buildings in the Niayesh road tunnel project.

Instrument type	*Number*	*Instrument type*	*Number*
Total station (TM30, Leica 1201, …)	8	In-place MEMS bi-axial tiltmeter	107
Bi-reflex target	3,000	Portable tiltmeter	3
Digital convergence meter	4	Tilt plates	276
Tunnel convergence pin	1,500	Leveling instrument	7
Multiple Point Borehole Extensometer (MPBX)	8	Building settlement pins	396
Vibrating wire embedment strain gauge	81	Pavement settlement pins	1,000
Pressure cell	8	Deep settlement pins (2 m depth)	70
Crackmeter	75	Green field settlement pins	500

method is well-suited to tunneling in difficult, complex and rapidly changing geological formations.

5.4.1 Finite element model of Niayesh tunnel

The simulation of the SEM tunneling process for the Niayesh 3.5-lanes cross section tunnels started with the selection of the model geometry in three dimensions, and plane strain analysis was incorporated. Given the asymmetry of the excavation sequences in the assumed excavation methods, the entire domain was considered in the model (Figure 9). Given the constitutive modeling, the soil layers were assumed to be a Hardening Soil material, while the shotcrete lining was assumed to behave in a linear elastic manner. Table 4 summarizes the geotechnical properties used in the analyses. The shotcrete lining properties which were used in the modeling are presented in

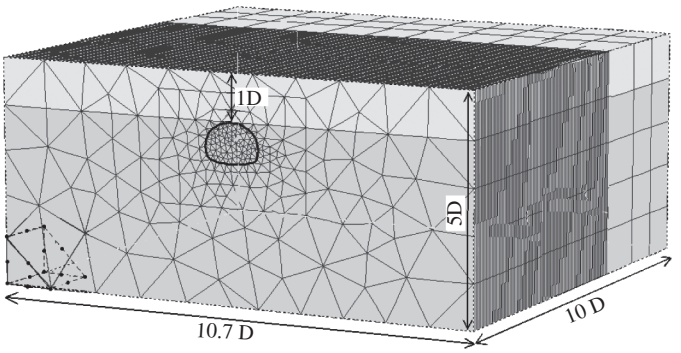


Figure 9 Finite element model of Niayesh 3.5-lane cross section tunnels (D = 15 m).

Table 4 Geotechnical properties of soil layers.

Depth (m)	*Unsaturated density* γ_{unsat} *(kN/m^3)*	*Saturated density* γ_{sat} *(kN/m^3)*	*Elasticity modulus unloading* E_{ur}^{ref} *(kN/m^2)*	*Elasticity modulus secant* E_{50}^{ref} *(kN/m^2)*	*Elasticity modulus oedometer* E_{Oed}^{ref} *(kN/m^2)*	*Cohesion C (kN/m^2)*	*Poisson ratio* υ_{ur}	*Internal friction angle* φ *(°)*	K_0^{nc}*
0–15	16	17	2.423×10^5	8.077×10^4	8.077×10^4	30	0.2	34	0.44
<15	18	19	2.827×10^5	9.423×10^4	9.423×10^4	40	0.2	36	0.41

* K_0 Value based on Jaky's formula for various layers of soil: ($K_0 = 1 - \sin \varphi$)

Table 5 Shotcrete lining properties used in modeling.

Lining type	*Poisson ratio* (υ_{ur})	*Weight W (kN/m/m)*	*Equivalent thickness d (m)*	*Element*	*Flexural rigidity EI (kNm^2/m)*	*Normal stiffness EA (kN/m)*
Temporary wall	0.2	5.35	0.25	Elastic	2.73×10^4	5.25×10^6
Permanent wall	0.2	7.5	0.35	Elastic	7.5×10^4	7.35×10^6

Table 5. Prior to the analysis, numerical models were developed and verified, based on the measured data from the Niayesh road tunnel.

5.4.2 Selection of tunnel excavation method

Tunnel design and construction requires the use of appropriate techniques and technologies during all phases of a tunnel project. In the main, a distinct rule does not exist to facilitate decision making about the selection of an appropriate excavation method.

This decision is mostly influenced by engineering experiences rather than theoretical calculations. The excavation method and sequencing schemes for a tunnel that is located in an urban area would typically be based on the complex interactions occurring between several factors, such as safety, cost and schedule (Hoek, 2001). Other significant factors that affect the selection of excavation method are the surrounding material properties (including geotechnical characteristics), the size and shape of the tunnel section, underground hydrology, in situ and induced stresses, regional geology, structural geology and weak-zone characteristics (Yu & Chern, 2007). Subdividing the excavation area is necessary for large-span tunnels in order to minimize ground disturbance and surface settlement. The structural integrity of the tunnel-surrounding material can thus be largely maintained.

After plotting the location of the Niayesh tunnel on the diagram proposed by Yu and Chern (2007) in Figure 10, side (or sidewall) drift (SD) and central diaphragm (CD) methods were shown to be the most suitable for the excavation. Thus, these excavation methods, based on the proposed excavation sequences shown in Figure 11, were

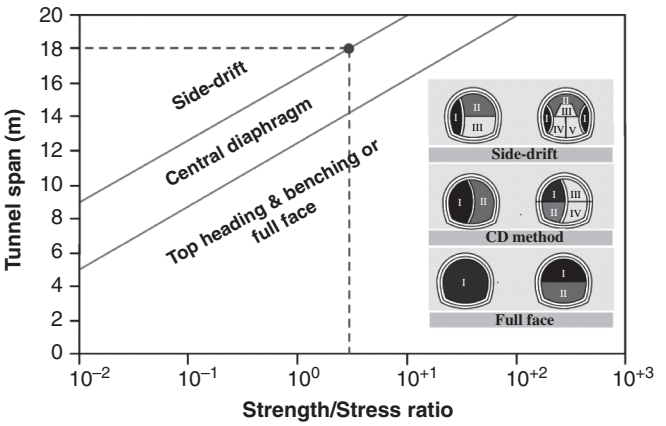
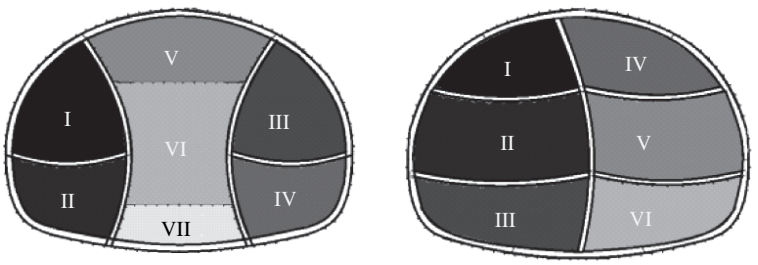


Figure 10 Empirical determination of excavation method based on three parameters of span size, compressive strength and vertical stress on tunnel.



a) Side Drift (SD) method

b) Central Diaphragm (CD) method

Figure 11 Excavation sequences of (a) the side drift method and (b) the central diaphragm method.

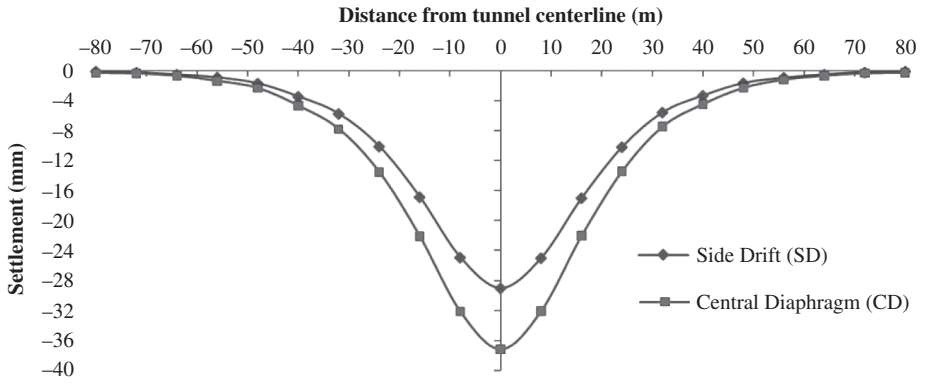


Figure 12 The computed transverse surface settlement profiles for CD and SD excavation methods.

simulated using a numerical FEM, in order to select the appropriate excavation method based on its potential for minimization of ground surface settlement. It was assumed that the final concrete lining would be placed at sufficient distance from the excavation face for it not to need consideration in the numerical simulations.

The results obtained from the 3D FEM models are relative to the final situation after completion of excavation and initial lining. In Figure 12, the computed surface settlement profiles for both CD and SD excavation methods are illustrated. As seen in Figure 12, for both SD and CD methods, the maximum value of surface settlements (about 29.4 mm and 37 mm respectively) were computed over the tunnel center line. Based on these modeling results, the CD method induces more surface settlement than the SD method. The SD method was, therefore, preferred over the CD method for the Niayesh urban tunnel excavation, given its better capability in limiting ground surface settlements as well as tunnel deformations. It should be noted that partitioning the face through staged excavation typically results in reduced face-advance rates, more stages of temporary support installation, and additional underpinning and delayed closure of the tunnel liner.

5.4.3 Optimal excavation sequence for side drift method

For economic execution of a SEM, it is essential to fully understand the influence of a given face-advancing sequence on the tunneling performance. The main factor in the selection of optimal excavation sequences is limitation of surface settlement values. The selection of excavation sequences depends, for example, on tunnel geometry, ground properties and the groundwater table. Limited research has been conducted in the field into the effects of different face-advancing methods on tunneling performance (Bowers, 1997; Karakus & Fowell, 2003; Farias *et al.*, 2004). These studies have provided valuable information but they are limited to specific tunneling cases; the 3D effects of various face-advancing methods on tunneling performance have been considered in very few studies. As discussed more extensively by Szechy (1967), the arrangement of underground openings and their excavation sequences depend on the operations that must be conducted in them (excavation method, installation and

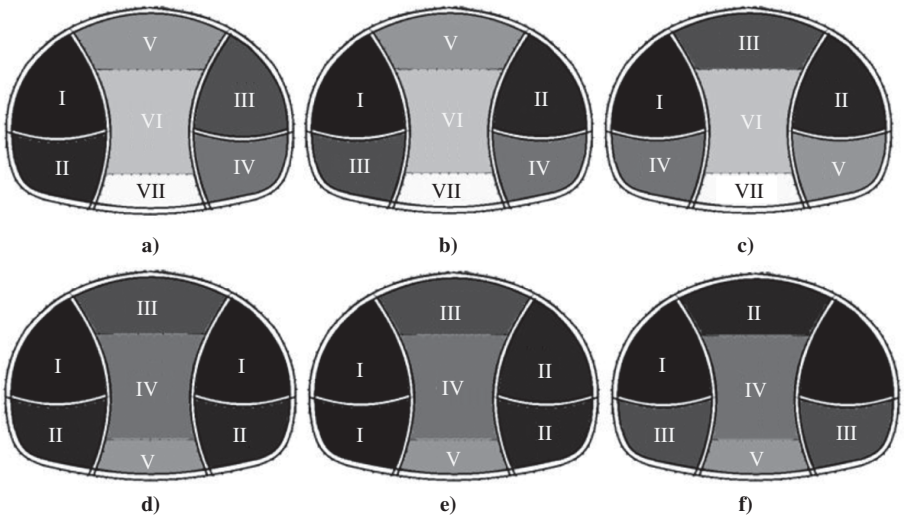


Figure 13 Proposed excavation sequences for the Niayesh tunnel using side drift method.

construction of temporary and permanent support, short-term and long-term use, etc.), the nature of the ground, and the in situ stress conditions encountered. There is, therefore, a practical need to simulate the different phases of tunnel construction and find the optimal construction procedure.

In order to find the optimal excavation sequences for the Niayesh tunnel, six excavation schemes based on the SD method were proposed and numerically analyzed, taking into consideration tunnel geometry and properties of soil layers (Figure 13). During selection of excavation sequences, principal factors such as ring closure time, number of excavation stages, subdividing area, and stage of central gallery excavation were considered.

Transverse surface settlement profiles for six excavation sequences are illustrated in Figure 14. Based on the numerical modeling results, the excavation scheme labeled (a) had the lowest surface settlement value and it was selected as the optimal scheme for the excavation of the Niayesh urban tunnel project. Results shows that rapid closure of the supporting ring and the excavation stage of the central gallery (middle drift) are the most important factors in controlling tunnel deformations and surface settlements in soft ground tunneling. Figure 12 indicates that conducting excavation of the central gallery in later stages reduces the extent of surface settlement.

The excavation volume of each stage has bilateral effects on surface settlement. A smaller excavation volume leads to less displacement and surface settlement. However, a smaller excavation volume also increases the number of excavation stages and delays support ring closure, which serves to increase surface settlement. Closing the support ring in soft ground must be done in fewer steps; delaying the ring closure results in large deformations and settlements. If face stability is adequately maintained, rapid ring closure through the adoption of a larger excavation volume is more effective than adopting a smaller excavation volume when it comes to limiting the

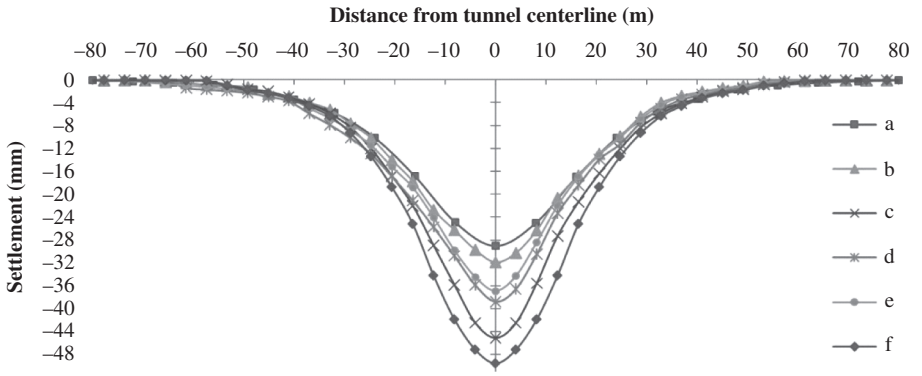


Figure 14 Transverse settlement profiles of the proposed excavation schemes (see) for the Niayesh tunnel.

tunnel crown and surface settlements in soft ground tunneling at shallow depths (Sharifzadeh *et al.*, 2013b).

5.4.4 Optimal trailing distance between excavation stages

Tunnel excavation causes a disturbance of the initial state of stress in the ground and creates a stress regime in the form of a bulb around the advancing tunnel face. The extent of the stress disturbance around an active heading depends mainly on ground conditions, distance between different excavation stages, and excavation round length. While a large disturbance zone will be produced when using a full-face excavation method, this zone can be reduced by adopting SEM and an appropriate trailing distance between different faces, thereby limiting surface settlement. Depending on the size of the opening and the quality of the ground, a tunnel cross section may be subdivided into multiple drifts (DTFHA, 2009). If the different excavation faces are close together, disturbance zones around faces will interfere with one another and lead to more displacement of the tunnel crown and greater surface settlement. Therefore, a trailing distance must be retained between different faces, so that critical disturbance zones will not interfere with or affect each other. During tunneling in soft ground conditions, the support ring closure behind the face should be executed as quickly as possible to create a load support ring, thus requiring the trailing distance between different faces to be kept as short as possible (Sharifzadeh *et al.*, 2013a).

In order to identify the optimal trailing distance between different faces, side galleries were simulated at distances of 6 m (0.4 D), 10 m (0.67 D), 15 m (1 D), 22 m (1.47 D) and 30 m (2 D) in front of the central gallery face (Figure 15). The excavations were simulated according to excavation scheme (a) (from Figure 13) in 1 m round length, with right and left side drifts excavated simultaneously.

Transverse surface settlement curves for different trailing distances between the central gallery and side drifts are illustrated in Figure 16, which shows that by increasing trailing distances, the disturbance zones of different stages do not

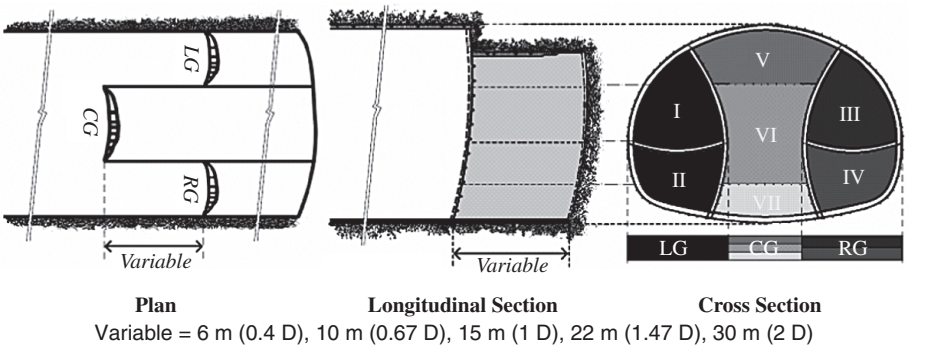


Figure 15 Plan view, longitudinal and transverse sections with variable distance between side drifts and middle drift faces.

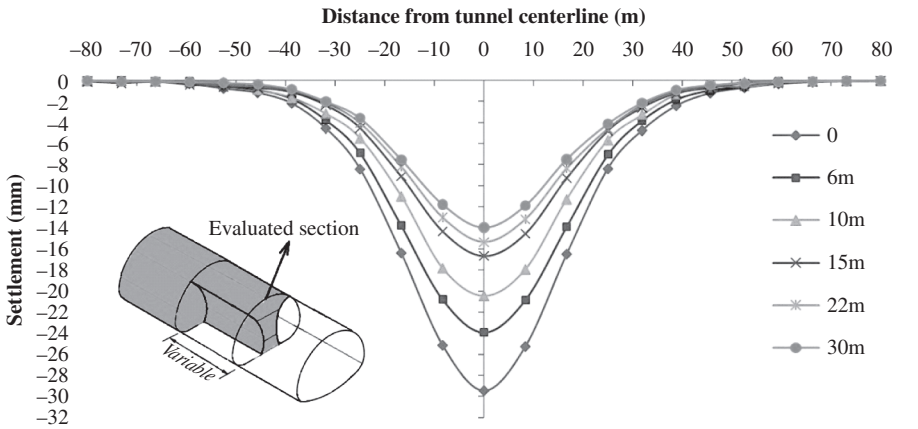


Figure 16 Transverse surface settlement curves for different trailing distances between side drifts and middle drift faces.

interfere with each other as much, leading to a reduction in the degree of surface settlement.

According to Figure 16, the optimum trailing distance was computed to be 15 m or more. This result is consistent with the statements of Yoo (2009), who reported that the best tunneling performance can be achieved by keeping the trailing distance greater than one tunnel diameter (D).

In the Niayesh project, given the urban environment, ground conditions, tunnel dimensions and value of the overburden in the tunnel route, the trailing distances between excavation faces were designed to be in the range 15–25 m, in order to reduce surface settlement. This example demonstrates that trailing distances derived using numerical simulation are in good accordance with operational results.

In order to minimize interference between disturbance zones and maintain efficient control of surface settlements, it is better to excavate side drifts separately. Thus, the

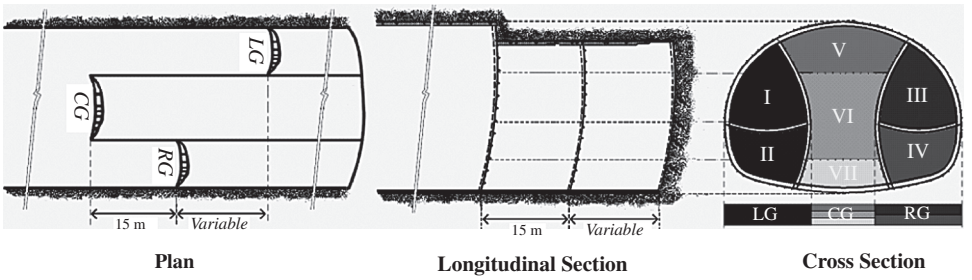


Figure 17 Plan view, longitudinal and transverse sections with variable distance between faces of side drifts.

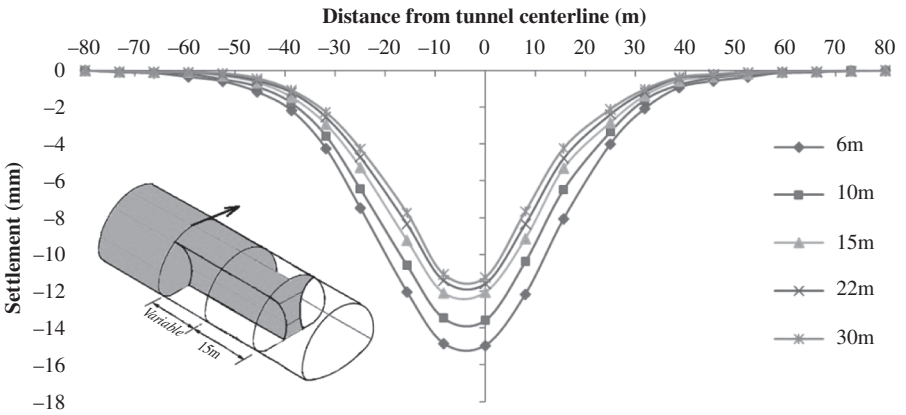


Figure 18 Transverse surface settlement curves for left gallery section at different trailing distances between side drifts.

excavations of three galleries (left, right and central) were simulated with different trailing distances from each other. Tunnel excavation procedures were simulated with trailing distances between the two side drifts of 6 m (0.4 D), 10 m (0.67 D), 15 m (1 D), 22 m (1.47 D) and 30 m (2 D), as shown in Figure 17. The minimum optimal trailing distance of 15 m between side drift faces and the middle drift face, derived in the previous step, was applied to all of the models.

Transverse surface settlement curves for left and right drift sections at different trailing distances between lateral galleries are illustrated in Figures 18 and 19 respectively. As expected, increasing the trailing distance between side drifts leads to a decrease in surface settlements.

As seen in Figures 18 and 19, surface settlement variations are larger as trailing distance increases from 6 m (0.4 D) to 15 m (1 D), but it has gentler variation once trailing distance is greater than 15 m (1 D). Based on these results, the optimal trailing distance between side drifts should be not less than 15 m (1 D).

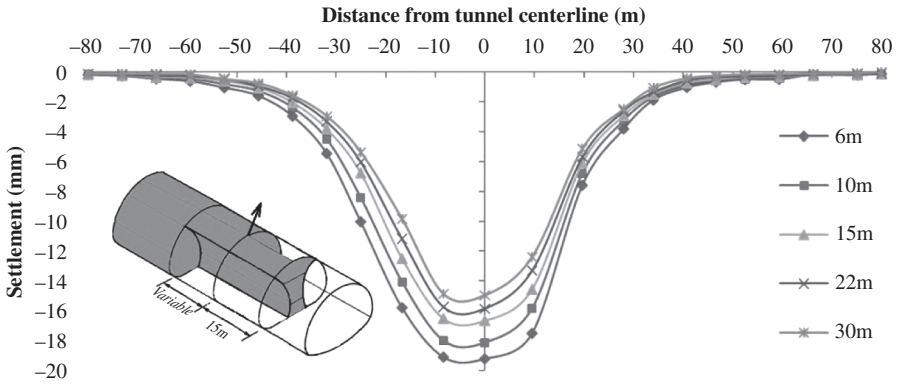


Figure 19 Transverse surface settlement curves for right gallery section at different trailing distances between side drifts.

5.5 Design optimization based on observational method

In the process of tunnel design, several parameters with varying degrees of uncertainty must be taken into account. These uncertainties are mostly related to tunnel-hosting ground conditions and tunnel construction performance. Thus, the real ground behavior around a tunnel's axis could not be accurately predicted at the design stage. This becomes even more important where a tunnel passes through an urban area and directly affects infrastructure and buildings. Therefore, for several reasons – such as safety, economy and understanding of the ground's real behavior – the use of the observational method as a practical engineering tool is necessary. A fundamental component of the observational method in tunneling is the use of monitoring data to assess the adequacy of the chosen design and the safety margins of the design.

In the Niayesh road tunnel project, given the technical and design requirements, the project's geological and geotechnical conditions, the results of monitoring, and the experiences gained during construction, the excavation activities and support elements were continuously adjusted to suit the ground conditions.

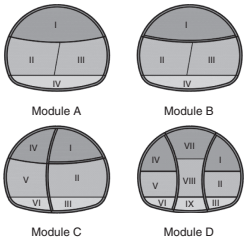
5.5.1 Modification of the excavation activities

During the preliminary design phase, excavation modules were selected for every section of the tunnels according to their longitudinal profile (ground advance classification). The real ground classes were defined on site, directly at the face, by mutual agreement between the geotechnical engineer and the resident engineer and based on the geotechnical monitoring results. Depending on the conditions of the ground encountered and these monitoring results, appropriate excavation modules were applied at different sections of the tunnels.

Modifications applied to the Niayesh tunnel excavation activities included: (a) modification of the pre-defined excavation modules; (b) modification of the length of excavation rounds for each stage; (c) modification of the trailing distance between excavation stages in different modules.

Table 6 Comparison of the costs of the designed and constructed modules for 2.5-lanes cross section in the Niayesh tunnel.

Designed module	*Constructed module*	*Cost ratio of constructed module to designed module*
Module A	Module A	1
Module B	Module A	0.71
Module C	Module A	0.62
	Module B	0.87
Module D	Module B	0.61
	Module C	0.70



Note: The excavation rate of Module A is approximately 65 percent greater than Module B

Comparisons between the costs of the modules as designed and the modules as constructed are presented in Table 6.

5.5.2 Modification of the support elements

Based on the NATM concept, the ground around the tunnel not only acts as a load, but also as a load-bearing element. In the Niayesh tunnel, depending on the project conditions and monitoring results, the requirements for a specific support were determined. Contractual arrangements were flexible to ensure that the most economical type and amount of support was used.

Modifications applied to the Niayesh tunnel support elements included: (a) modification of the tunnel's initial support elements (*i.e.* the thickness of shotcrete and the distance between lattice girders); (b) modification of the pre-support elements (*i.e.* forepoling, pre-grouting); (c) modification of the initial support elements around the ramps and portals (*i.e.* number, diameter and depth of the reinforced piles, number and length of the soil nails).

In all of the design modifications described above, the major concern was limiting the ground settlements induced by tunneling and limiting any potential damage to the existing structures and utilities above the tunnel.

6 SUMMARY

We have presented a brief review of back analysis procedures, including comparisons, problems, recent advances and further development. Different back analysis methods according to those deterministic and non-deterministic aspects applicable in geotechnical engineering problems were introduced. Because back analysis is a practical engineering tool that can bridge field measurement, design and construction, further efforts are required to make the best use of developing technologies and also to raise the level of conceptual understanding of the back analysis procedures in current use. Back analysis is, and will continue to be, a key to achieving scientific tunnel construction in the future.

Back analyses are very powerful tools for interpreting the results of field measurements. Back analysis should not only be used to determine material properties but also to generate a mechanical model of soils and rocks.

Solutions of geotechnical inverse problems are neither identifiable nor unique in a strict sense. Furthermore, the limitations in quantity and quality of available data, together with the multicollinearity, tend to make solutions unstable. However, these issues do not prevent us from adopting the inverse analysis method to identify models and estimate parameters.

When constructing a system for a given purpose, our ultimate goal is to obtain a system that is as useful as possible for that purpose. This means, in turn, constructing a system that can handle a proper blend of the three most fundamental characteristics of systems: credibility, complexity and uncertainty. Ideally, we would like to obtain a system with high credibility, low complexity and low uncertainty. Unfortunately, these three criteria conflict with one another and to achieve a high level of usefulness from any system, we need to find the right trade-off among them.

There are many reasons why back analysis techniques are being used more frequently. The two most important are, first, the development of numerical calculation methods for the analysis of the stresses and strains in a rock mass, and second, the availability of quick and simple personal computers with which the large amounts of data – which are necessary to resolve the numerical modeling and error minimization (parametric analyses) – can be produced in the shortest possible time, at the lowest possible cost. However, the use of back analyses has not become as popular as previously expected. There are several reasons for this: (a) there are few engineers who can manage both on-site practice and the execution of back analyses in computer rooms; (b) back analyses are not included in the specifications of contracts for tunnel construction works; (c) practical methods for applying back analysis results to the design of tunnel supports and construction procedures have not been developed to a level that would be regarded as satisfactory for industry acceptance (Sakurai *et al.*, 2003).

Leroueil and Tavenas (1981) prepared guidelines for the correct use of back analysis techniques, the most important of which are:

- It is wrong to undertake back analysis of the same problem by carrying out uncoupled analysis on only a few limited phenomena – all of the uncertain parameters of the rock should be considered in the back analysis, and all of the physical phenomena should be simultaneously included;
- If the measurements carried out in situ are available, it is necessary to first of all look at their qualitative interpretation on the basis of known case histories in order to fully understand the physical phenomenon that governs the problem;
- Unrealistic conclusions of a back analysis should be rejected – if necessary, one should add the original hypotheses to the modification and the back analysis should be repeated with a new calculation model.

For economic execution of SEM, it is essential to fully understand the influence of a given face-advancing sequence on the tunneling performance. Improper selection of an excavation sequence could have a destabilizing effect on the tunnel, and the influence of excavation sequences on ground settlements must be taken into account, particularly in the case of large-span urban tunnels in shallow depths.

REFERENCES

Asaoka, A. & Matsuo, M. (1984). An inverse problem approach to the prediction of multi-dimensional consolidation behavior. *Soils and Foundations*, 24, 49–62.

Bieniawski, Z.T. (1984). *Rock Mechanics Design in Mining and Tunneling*. Rotterdam, Balkema.

Brady, B.H.G. & Brown, E.T. (2004). *Rock Mechanics for Underground Mining* (3rd edn). Netherlands, Springer.

Bowers, K.H. (1997). An Appraisal of the New Austrian Tunnelling Method in Soil and Weak Rock. PhD Thesis, The University of Leeds, 240p.

Cai, M. & Chen, X. (1987). Back-analysis of initial stress field in rocks by the simplex method. In: *Proceedings of First National Conference on Geomechanics*. pp. 217–222.

Cai, M., Morioka, H., Kaiser, P.K., Tasaka, Y., Kurose, H., Minami, M. & Maejima, T. (2007). Back-analysis of rock mass strength parameters using AE monitoring data. *International Journal of Rock Mechanics and Mining Sciences*, 44(4), 538–549.

CIRIA. (1999). *The observational method in ground engineering: Principles and applications, REP R 185*. London, Construction Industry Research and Information Association.

Cividini, A. & Gioda, G. (2003). Back analysis of geotechnical problems. In: Bull, J.W. (ed.) *Journal of Numerical Analysis and Modelling in Geomechanics*. London, Spon Press. pp. 165–196.

Cividini, A., Jurina, L. & Gioda, G. (1981). Some aspects of characterization problems in geomechanics. *International Journal of Rock Mechanics and Mining Sciences and Geomechanics*, 18, 487–503.

Cividini, A., Maier, G. & Nappi, A. (1983). Parameter estimation of a static geotechnical model using a Bayes' approach. *International Journal of Rock Mechanics and Mining Sciences and Geomechanics*, 20, 215–226.

Deng, J.L. (1986). *Grey Prediction and Decision Making*. Wuhan, China, Huazhong University Press.

DIN. (2011). *Geotechnical Measurements, DIN 1407*. Berlin, Beuth Verlag.

DTFHA. (2009). *Technical Manual for Design and Construction of Road Tunnels – Civil Elements*. Washington, DC, US Department of Transportation Federal Highway Administration.

Dunnicliff, J. (1993). *Geotechnical Instrumentation for Monitoring Field Performance*. New York, John Wiley.

Einstein, H.H. & Baecher, G.S. (1982). Probabilistic and statistical methods in engineering geology. 1. Problem statement and introduction to solution. *Rock Mechanics*, Supp. 12, 47–61.

Feng, X.T., Zhao, H. & Li, S. (2004). A new displacement back analysis to identify mechanical geo-material parameters based on hybrid intelligent methodology. *Numerical and Analytical Methods in Geomechanics*, 28(11), 1141–1165.

Farias, M.M., Moraes, A.H. & Assis, A.P. (2004). Displacement control in tunnels excavated by the NATM: 3-D numerical simulations. In: *Tunnelling and Underground Space Technology*, 19, 283–293.

Gallagher, K. & Sambridge, M. (1994). Genetic algorithms: A powerful tool for large-scale nonlinear optimization problems. *Computers and Geosciences*, 20(7/8), 1229–1236.

Geisler, H., Wagner, H., Zieger, O., Mertz, W. & Swoboda, G. Practical (1985). Theoretical aspects of the three dimensional analysis of finally lined intersections. In: *Proceedings of the 5th International Conference on Numerical Methods in Geomechanics*, Nagoya. pp. 1175–1183.

Geokon: http://www.geokon.com/content/posters/Tunnelling_Instrumentation.pdf.

Ghorbani, M. & Sharifzadeh, M. (2009). Long term stability assessment of Siah Bisheh power-house cavern based on displacement back analysis method. *Tunnelling and Underground Space Technology*, 24(5), 574–583.

Ghorbani, M., Sharifzadeh, M., Yasrobi, S. & Daiyan, M. (2012). Geotechnical, structural and geodetic measurements for conventional Tunnelling Hazards in Urban Areas – The case of Niayesh road tunnel project. *Tunnelling and Underground Space Technology*, 31, 1–8.

Gioda, G. (1980). Indirect identification of the average elastic characteristics of rock masses. In: Pells, P.J.N. (ed.) *International Conference on Structural Foundations on Rock, Sydney, Australia*. Rotterdam, Balkema. pp. 65–73.

Gioda, G. (1985). Some remarks on back analysis and characterization problems in geomechanics. In: Sakurai, S. & Ichikawa, T. (eds.) *Proceedings of the 5th International Conference on Numerical Methods in Geomechanics, Nagoya, Japan*. Rotterdam, Balkema. pp. 47–61.

Gioda, G. & Jurina, L. (1981). Numerical identification of soil structure. *Numerical and Analytical Methods in Geomechanics*, 5, 33–56.

Gioda, G. & Locatelli, L. (1999). Back analysis of the measurements performed during the excavation of a shallow tunnel in sand. *Numerical and Analytical Methods in Geomechanics*, 23, 1407–1425.

Gioda, G. & Maier, G. (1980). Direct search solution of an inverse problem in elastoplasticity: identification of cohesion, friction angle and in situ stress by pressure tunnel test. *International Journal for Numerical Methods in Engineering*, 15, 1832–1848.

Gioda, G. & Sakurai, S. (1987). Back analysis procedures for the interpretation of field measurements in geomechanics. *Numerical and Analytical Methods in Geomechanics*, 11, 555–583.

Gioda, G. & Swoboda, G. (1999). Developments and applications of the numerical analysis of tunnels in continuous media. *Numerical and Analytical Methods in Geomechanics*, 23, 1393–1405.

Gokceoglu, C., Yesilnacar, E., Sonmez, H. & Kayabasi, A. (2004). A neuro-fuzzy model for modulus of deformation of jointed rock masses. *Computers and Geotechnics*, 31, 375–383.

Himmelblau, D.M. (1972). *Applied nonlinear programming*. New York, McGraw-Hill.

Hisatake, M. & Hieda, Y. (2007). Three-dimensional back-analysis method for the mechanical parameters of the new ground ahead of a tunnel face. *Tunnelling and Underground Space Technology*, 23, 373–380.

Hoek, E. (2001). Big tunnel in bad rock. *Journal of Geotechnical and Geoenvironmental Engineering*, 127(9), 726–740.

Honjo, Y., Tsung, L.W. & Sakajo, S. (1994). Application of Akaike information criterion statistics to geotechnical inverse analysis: the extended Bayesian method. *Structural Safety*, 14, 5–29.

Ichikawa, Y. & Ohkami, T. (1992). A parameter identification procedure as a dual boundary control problem for linear elastic materials. *Soils and Foundations*, 32(2), 35–44.

Iding, R.H., Pister, K.S. & Taylor, R.L. (1974). Identification of nonlinear elastic solids by a finite element method. *Computer Methods in Applied Mechanics and Engineering*, 4, 121–142.

Imre, E. (1994). Model validation for the oedometric relaxation test. In: *Proceedings of the 13th International Conference on Soil Mechanics and Foundation Engineering, New Delhi, India*. Rotterdam, Balkema. pp. 1123–1126.

ITA. (2009). *General Report on Conventional Tunnelling Method*, ITA Report No. 002. Lausanne, Switzerland, International Tunnelling and Underground Space Association.

Jurina, L., Maier, G. & Podolak, K. (1977). On model identification problems in rock mechanics. In: *Proceedings of the International Symposium on the Geotechnics of Structurally Complex Formations, Capri*. Vol. 1. pp. 287–295.

Karakus, M. & Fowell, R.J. (2003). Effect of different tunnel face advance excavation on the settlement by FEM. *Tunnelling and Underground Space Technology*, 18, 513–523.

Kaiser, P.K., Zou, D. & Lang, P.A. (1990). Stress determination by back analysis of excavation-induced stress changes – A case study. *Rock Mechanics and Rock Engineering*, 23(3), 185–200.

Kavanagh, K.I. & Clough, R.W. (1971). Finite element application in the characterization of elastic solids. *International Journal of Solids and Structures*, 7, 11–23.

Kirsten, H.A.D. (1976). Determination of rock mass elastic moduli by back analysis of deformation measurement. In: Bieniawski, Z.T. (ed.) *Proceedings of Symposium on Exploration for Rock Engineering, Johannesburg*. Cape Town, Balkema. pp. 1154–1160.

Kosmatopoulos, E.B., Polycarpou, M.M., Christodoulou, M.A. & Ioannou, P.A. (1995). High-order neural network structures for identification of dynamical systems. *IEEE Transactions Neural Networks*, 6(2), 422–431.

Leroueil, S. & Tavenas, F. (1981). Pitfalls of back analyses. In: *Proceeding of the 10th International Conference On Soil Mechanics and Foundation Engineering*, Stockholm, pp. 185–190.

Levasseur, S., Malecot, Y., Boulon, M. & Flavigny, E. (2007). Soil parameter identification using a genetic algorithm. *Numerical and Analytical Methods in Geomechanics*, 32, 189–213.

Li, S.H., Wu, X.Y. & Ma, F.S. (1998). Application of precedent type analysis (PTA) in the construction of Ertan Hydroelectric Station, China. *International Journal of Rock Mechanics and Mining Science*, 35, 787–795.

Liang, Y.C., Zhang, D.P., Liu, G.R., Yang, X.W. & Han, X. (2003). Neural identification of rock parameters using fuzzy adaptive learning parameters. *Computers and Structures*, 81, 2373–2382.

Mahnken, R. & Stein, E. (1995). Parameter identification for viscoplastic models based on analytical derivatives of a least-squares functional and stability investigations. *International Journal of Plasticity*, 12(4), 451–479.

Murakami, A. & Hasegawa, T. (1993). Application of Kalman filtering to inverse problems. *Theoretical and Applied Mechanics*, 43, 3–14.

Ohkami, T. & Ichikawa, Y.A. (1997). Parameter identification procedure for visco-elastic materials. *Computers and Geotechnics*, 21(4), 255–275.

Ohkami, T. & Swoboda, G. (1999). Parameter identification of viscoelastic materials. *Computers and Geotechnics*, 24(4), 279–295.

Oreste, P. (2005). Back-analysis techniques for the improvement of the understanding of rock in underground constructions. *Tunnelling and Underground Space Technology*, 20(1), 7–21.

Pichler, B, Lackner, H. & Mang, H.A. (2003). Back analysis of model parameters in geotechnical engineering by means of soft computing. *International Journal for Numerical Methods in Engineering*, 57, 1943–1978.

Pottler, R. (1992). Three-dimensional modeling of junction at the channel tunnel project. *International Journal for Numerical and Analytical Methods in Geomechanics*, 16, 683–695.

POR. (2008). *Geotechnical Investigations & Foundation Report for Niayesh Tunnel Project*. Tehran, Pazhoohesh Omran Rahvar Consulting Engineers.

Powell, M.J.D. (1964). An efficient method of finding the minimum of a function of several variables without calculating derivatives. *The Computer Journal*, 7, 155–162.

Romero, V. (2002). NATM in soft-ground: A contradiction of terms. *World Tunnelling, NATM & Shotcreting Focus, Jacobs Associates, USA*, 338–343.

Rosenbrock, H.H. (1960). An automatic method for finding the greatest or least value of a function. *The Computer Journal*, 3, 175–184.

Rubio, J.D.J. & Yu, W. (2007). Nonlinear system identification with recurrent neural networks and dead-zone Kalman filter algorithm. *Neurocomputing Journal*, 70, 2460–2466.

Sakurai, S. (1982). Monitoring of caverns during construction period. In: Wittke, W. (ed.) *Rock Mechanics: Caverns and Pressure Shafts, Proceedings of the ISRM Symposium, Aachen*. Rotterdam, Balkema. pp. 433–441.

Sakurai, S. (1997). Lessons learned from field measurements in tunneling. *Tunnelling and Underground Space Technology*, 12, 453–460.

Sakurai, S. (1997). Monitoring and performance in tunneling. In: *Proceedings of the 14th International Conference on Soil Mechanics and Foundation Engineering, Hamburg, Germany*. Rotterdam, Balkema. pp. 2409–2412.

Sakurai, S. & Abe, S. (1979). A design approach to dimensioning underground opening. In: *Proceedings of the 3rd International Conference on Numerical Methods in Geomechanics, Aachen, Germany*. Balkema Publications, Rotterdam, The Netherlands. pp. 649–661.

Sakurai, S., Akutagawa, S., Takeuchi, K., Shinji, M. & Shimizu, N. (2003). Back-analysis for tunnel engineering as a modern observational method. *Tunnelling and Underground Space Technology*, 18(2–3), 185–196.

Sakurai, S. & Takeuchi, K. (1983). Back analysis of measured displacements of tunnels. *Rock Mechanics and Rock Engineering*, 16(3), 173–180.

Setnes, M., Babuška, R. & Verbruggen, H.B. (1998) Rule-based modeling: Precision and transparency. *IEEE Transactions on Systems, Man, and, Cybernetics Part C*, 28(1), 165–169.

Sharifzadeh, M., Ghorbani, M. & Masoudi, R. (2009). Displacement based back analysis of Siah Bisheh pumped storage powerhouse cavern by means of distinct element method. *Sharif: Engineering*, 47, 49–57.

Sharifzadeh, M., Darai, R. & Sharifi, M. (2011). Design of sequential excavation tunneling in weak rocks through findings obtained from displacements based back analysis. *Tunnelling and Underground Space Technology*, 28, 10–17. doi:10.1016/j.tust.2011.08.003

Sharifzadeh, M., Kolivand, F., Ghorbani, M. & Yasrobi, S. (2013a). Design of sequential excavation method for large span urban tunnels in soft ground – Niayesh tunnel. *Tunnelling and Underground Space Technology*, 35, 178–188.

Sharifzadeh, M., Tarifard, A. & Moridi, M.A. (2013b). Time-dependent behavior of tunnel lining in weak rock mass based on displacement back analysis method. *Tunnelling and Underground Space Technology*, 38, 348–356.

Swoboda, G., Ichikawa, Y., Dong, Q.X. & Zaki, M. (1999). Back analysis of large geotechnical models. *International Journal for Numerical and Analytical Methods in Geomechanics*, 23, 1455–1472.

Szechy, K. (1967). *The Art of Tunnelling*. Akademiai Kiado, Budapest.

Tarantola, A. (2005). *Inverse Problem Theory and Methods for Model Parameter Estimation*. Philadelphia, Society for Industrial and Applied Mathematics.

Tonon, F., Amadei, B., Pan, E. & Frangopol, D.M. (2001). Bayesian estimation of rock mass boundary conditions with applications to the AECL underground research laboratory. *International Journal of Rock Mechanics and Mining Sciences*, 38(7), 995–1027.

Villaescusa, E. (2014). *Geotechnical Design for Sublevel Open Stoping*. Boca Raton, FL, CRC Press.

Wang, S., Yang, Z. & Lin, X. (1987). The back-analysis method from displacements for visco-elastic rock mass. In: *Proceedings of the Second International Symposium on Field Measurements in Geomechanics, Kobe, Japan*. Rotterdam, Balkema. pp. 1059–1068.

Yang, L. (1990). Advance in back analysis approaches and application in engineering. In: *Engineering Application of Numerical Method in Rock Mechanics*. Shanghai, Tongji University Press. pp. 60–65.

Yang, Z.F., Liu, Z.H. & Wang, S.J. (1983). A practical back analysis's method from displacements to estimate some parameters of a rock mass for design of an underground opening. In: *Proceedings of International Symposium on Field Measurements in Geomechanics, Zurich, Switzerland*. Rotterdam, Balkema. pp. 1267–1276.

Yang, Z.F., Lee, C.F. & Wang, S.J. (2000). 3-D back analysis on one trial adit in three gorges, China. *International Journal of Rock Mechanics and Mining Science*, 37, 525–533.

Yoo, C. (2009). Performance of multi-faced tunnelling – A 3D numerical investigation. In: *Tunnelling and Underground Space Technology*, 24, 562–573.

Yu, C.W. & Chern, J.C. (2007). Expert system for D&B tunnel construction. In: *Underground Space the 4th Dimension of Metropolises*, London, England.

Zhang, L.Q., Yue, Z.Q., Yang, Z.F., Qi, J.X. & Liu, F.C. (2006). A displacement-based back-analysis method for rock mass modulus and horizontal in situ stress in tunneling – Illustrated with a case study. *Tunnelling and Underground Space Technology*, 21(6), 639–649.

Zhao, J. & Lee, K.W. (1996). Construction and utilization of rock caverns in Singapore, part C: planning and site selection. *Tunnelling and Underground Space Technology*, 11, 81–86.

Zou, D. & Kaiser, P.K. (1990). Determination of in situ stresses from excavation-induced stress changes. *Rock Mechanics and Rock Engineering*, 23(3), 167–184.

Chapter 16

Moment tensor evaluation of acoustic emission sources in rock

G. Manthei
Department of Mechanical Engineering, THM·University of Applied Sciences, Gießen, Germany

Abstract: This chapter will review applications of the moment tensor method on acoustic emission events in rock of greatly differing scales of some hundred meters down to several centimeters. These are acoustic emission measurements in underground laboratory and parts of a mine (large-scale applications), during underground hydraulic fracturing tests in rock (intermediate-scale applications), as well as in laboratory studies on rock specimens (small-scale applications). The moment tensor method pointed out that deviatoric stress induced acoustic emission shows high proportion of volumetric source components, while hydraulically induced acoustic emission shows shear mechanisms without significant volumetric source components.

1 INTRODUCTION

This chapter will review applications of the moment tensor (MT) method on acoustic emission (AE) events in the fields, mine monitoring, hydraulic fracturing in rock, and testing of rock specimens in the laboratory, that means in much differing scales of some hundred meters down to several centimeters. Nevertheless, the principal mechanism does not depend on the scale: The rapid release of elastic energy by processes of crack growth or deformation within the rock generates transient pulses of elastic wave energy as AE events. In an even larger scale, the same is true for earthquakes. Therefore, most of the theory of earthquakes can be transferred to AE sources. The frequency range of AE phenomena in the broadest sense extends from the infrasonic range (less than 16 Hz) far into the ultrasonic range (higher than 16 kHz). The largest and therefore longest events as well, namely earthquakes, are found at the lowest end of the frequency scale (Fig. 1).

The focus length and displacement of an earthquake can amount to more than several hundred kilometers and up to several meters, respectively. The frequencies used in seismology extend to some Hertz (left-hand side of Fig. 1). On the other side, the highest ultrasonic frequencies may be generated by AE events in the microscopic region, for instance by dislocation movement. In this case the source area may extend to some micrometers and the displacement (Burgers vector) is to be measured in nanometers (right-hand side of Fig. 1). The range of AE measurements in rock as used for mine monitoring or laboratory testing lies between the frequency ranges of 1 kHz up to 1 MHz.

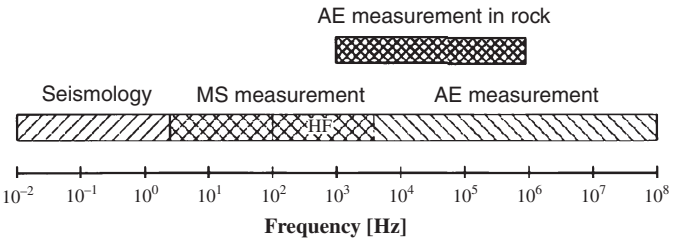


Figure 1 Frequency range of acoustic emission (AE) measurement as compared with seismology and microseismic (MS) measurement (HF: high frequency, Manthei & Eisenblätter, 2008).

In analogy to earthquakes, AE sources (such as microcracks) radiate acoustic energy, and, consequently, it is possible to investigate them by similar techniques as used in seismology. The mechanisms of earthquakes and AE sources are in principal the same, in spite of the fact that strengths and frequencies differ by orders of magnitude (Eisenblätter, 1980; Rice, 1980). Therefore, it is possible to apply the MT inversion, which describes mechanisms of general seismic sources, to these events, whose frequencies range between 20 kHz and 1 MHz.

The "microseismic method" and thereby the "AE method" was discovered by Obert (1938) from the U.S. Bureau of Mines, Denver/Colorado, rather by chance. An experiment was being conducted in a lead-zinc mine in order to determine whether the seismic velocity in mine pillars was dependent on stress. These measurements were often disturbed by signals, which obviously were generated by the pillar itself. Obert and Duvall carried out an extensive study of AE in nine mines including two deep mines in Canada. Using multi-channel recording systems they were able, by comparison of amplitudes and coincidences, to roughly locate zones of higher acoustic activity.

In rock, AE is generated by crack formation under high stress. This phenomenon provides the basis for the AE method, which is able to detect zones of microcracking or macrocracking or highly stressed zones in rock without any knowledge of the mechanical properties or the state of stress. In the case of geomechanical investigations on rock formations in mines and on rock specimens in laboratory under uniaxial or triaxial compressional load, volume changes in the source play an important role. This fact has been confirmed in many laboratory experiments on rock samples under compressional deviatoric stress conditions. The experiments demonstrate that microcracking leads to a nonreversible increase of the rock volume, or dilatancy (Brace *et al.*, 1966; Scholz, 1968; Lockner & Byerlee, 1977; Miller *et al.*, 1998; Hunsche & Hampel, 1999). Dilatancy can be explained as volume expansion caused by tensile opening.

Figure 2 shows two prominent examples of AE measurements in highly stressed zones in hard rock (left-hand side) and salt rock (right-hand side). In both cases nearly all AE events were found in zones close to the sidewalls of the gallery. These so-called excavation disturbed zones (EDZ) was formed by many small dilatant microcracks, which occurred during and immediately after excavation. It may be recognized that most of the events are located in a small layer about 1 m width along the wall profile. The extension of the EDZ depends among others on depth of the cavity.

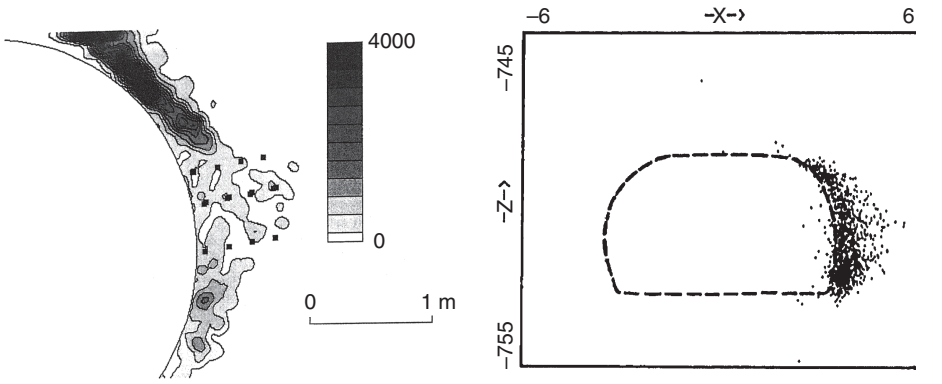


Figure 2 Left-hand side: Event density of acoustic emission (AE) activity recorded in the sidewall of the Mine-by tunnel during excavation in hard rock. The AE sensor locations are shown as black squares (Falls & Young, 1998). Right-hand side: Located AE events in horizontal projection parallel to the gallery axis in a salt mine. The measured gallery profile is marked by dashed line (Eisenblätter *et al.*, 1998).

The topic of this paper is to show the capability of the MT method, which was applied to AE events detected in rock. The MT method is capable of describing sources with volumetric components such as tensile cracks, deviatoric sources such as shear cracks, or a mixture of both source types. The volumetric source components can be easily obtained using the isotropic part, or one-third of the MT trace. With the MT method, the source mechanisms are estimated by a least-squares inversion calculation from amplitudes of the first motion as well as from full waveforms of compressional (P) and shear (S) waves. This method requires additional knowledge about the transfer function of the medium (the so-called Green's function) and sensor response.

In AE applications to rock, double-couple (DC) mechanisms are not prevalent. Very often sources of mixed mode or of pure tensile type are found by MT analysis (Ohtsu, 1991; Read & Martin, 1991; Niitsuma *et al.*, 1993; Cai *et al.*, 1998; Manthei *et al.*, 1998; Manthei *et al.*, 2001). The MT method has most commonly been applied to events generated during laboratory tests on specimens (for instance of fracture mechanical type) of different materials with well-defined defects of known type and size (Wadley *et al.*, 1981; Scruby *et al.*, 1983; Ohtsu & Ono, 1986; Kim & Sachse, 1988; Kishi & Enoki, 1988). In most applications the number of investigated events was small enough for individual processing.

Many examples of the application of the MT method on AE events in rock, as found in the literature are given in Table 1 and 2 for field and laboratory measurements, respectively.

Table 1 shows the monitored are (site), the rock type, the linear dimension of the covered area, the number of investigate events, the upper limit of the frequency region of the AE sensors (corner frequency), and the source mechanisms, which are obtained by the MTs.

These applications can be classified in AE measurements in underground laboratories, in mines, and during hydraulic fracturing tests in rock. The frequency of AE measurements in rock begins with applications in mines of about 1 kHz up to 100 kHz. In this frequency range accelerometers or typical piezoelectric AE sensors are used for

Table 1 Overview on application of moment tensor (MT) method on acoustic emission (AE) events in underground laboratories and mines and during hydraulic fracturing tests in rock.

Reference	*Site*	*Rock type*	*Typical distances*	*Number of investigated events*	*Corner frequency*	*Source type*
Application of MT method on AE events in underground laboratories and mines						
Young & Martin (1993)	Underground research laboratory, Canada	Granite	100 m	Approximately 40 AE events	10 kHz	Non-shear events with volume change
Baker & Young (1997)	Underground research laboratory, Canada	Granite	10 m	20 AE events	10 kHz	Mixed mode events of implosion/shear, tensile shear, and shear
Collins *et al.* (2002)	Underground research laboratory, Canada	Granite	10 m	34 AE events in three Clusters	400 kHz	Shear mode events and tensile mode events
Young *et al.* (2004)	Underground research laboratory, Canada	Granite	100 m	Cluster of 12 AE events	10 kHz	Shear- and closure events
Manthei *et al.* (1998)	Salt mine Asse, Germany	Rock salt	100 m	2.200 AE events	100 kHz	Shear- and mixed mode events
Dahm *et al.* (1998)	Salt mine Asse, Germany	Rock salt	50 m	43 AE events in two clusters	100 kHz	Shear mode events
Manthei *et al.* (2001)	Salt mine Morsleben, Germany	Rock salt	100 m	68 AE events	100 kHz	Mixed mode of shear and tensile events
Manthei *et al.* (2008)	Salt mine Morsleben, Germany	Rock salt	150 m	53 AE events in three clusters	100 kHz	Tensile mode events
Application of MT method on AE events during hydraulic fracturing tests						
Ohtsu (1991)	Underground tunnel, Japan		10 m		100 kHz	Shear and tensile mode events
Niitsuma *et al.* (1993)	Laboratory, Japan	Granite	10 m	32 AE events	10 kHz	Tensile, shear, and mixed mode events
Niitsuma *et al.* (1993)	Kamaishi mine, Japan	Granite	30 m	37 AE events	10 kHz	Shear mode events
Dahm *et al.* (1999)	Salt mine Bernburg, Germany	Rock salt	10 m	187 AE events in two clusters	250 kHz	Shear mode events
Manthei *et al.* (2001)	Salt mine Bernburg, Germany	Rock salt	10 m	263 AE events	250 kHz	Shear mode events

Table 2 Overview on application of moment tensor (MT) inversion on acoustic emission (AE) events in rock specimens.

Reference	*Specimen size*	*Rock type*	*Loading*	*No. of investigated events*	*No. of AE sensors, Frequency range*	*Source type*
Shah & Labuz (1995)	90 mm high, 48 mm thick, 48 mm long	Charcoal granite	Unconfined compression	150 AE events	8 AE sensors, not available	Shear mode events
Carvalho & Labuz (2002)	100 mm high, 40 mm thick, 100 mm long	Red Wildmoor sandstone	Biaxial compression	290 AE events	8 AE sensors, 100 kHz to 1 MHz	Shear mode events
Fakhimi *et al.* (2002)	100 mm high, 40 mm thick, 100 mm long	Berea sandstone	Biaxial compression	497 AE events	8 AE sensors, 100 kHz to 1 MHz	Mixed mode events
Sellers *et al.* (2003)	242 mm high, 96 mm diameter	Elsburg quartzite	Uniaxial compression	35 clustered AE events	9 AE sensors, 100 kHz to 1 MHz	Shear and tensile mode events
Chang & Lee (2004)	100 mm high, 50 mm diameter	Hwangdeung granite, Yeosan marble	Triaxial compression	Not available	6 AE sensors, 100 kHz to 1 MHz	Shear and mixed mode events
Manthei (2005)	300 mm high, 150 mm diameter	Salt rock	Triaxial compression	12,500 AE events	12 AE sensors, 20 kHz to 1 MHz	Tensile mode events
Thompson *et al.* (2009)	190.5 mm high, 76.2 mm diameter	Westerly granite	Triaxial compression	40 AE events	13 AE sensors, 800 kHz	Shear mode events
Graham *et al.* (2010)	125 mm high, 50 mm diameter	Aue granite	Triaxial compression	Not available	11 AE sensors, 100 kHz to 2 MHz	Tensile and shear mode events
Kao *et al.* (2011)	73 mm high, 32 mm thick, 217 mm long	Charcoal granite	Three-point bending	400 AE events	8 AE sensors, 100 kHz to 1 MHz	Mixed mode events with dominant shear mode
Aker *et al.* (2014)	127 mm high, 50.8 mm diameter	Vosges sandstone	Triaxial compression	162 AE events	12 AE sensors, 50 kHz to 1.5 MHz	Mixed mode events of shear and tension
Kwiatek *et al.* (2014)	100 mm high, 150 mm diameter	Vosges and Bentheim sandstone	Triaxial compression	1,717 AE events	16 AE sensors, 300 kHz to 800 kHz	Implosion mode events with CLVD components

long term AE. The distances between sensors are up to 150 m. About one order of magnitude smaller (5 m to 10 m) is the length of travel paths of AE measurements during hydraulic fracturing tests in mines. In this case the frequencies range predominantly from 10 kHz to 250 kHz. In such experiments the AE events are hydraulically induced in order to determine the orientation of the macroscopic fracture planes. An overview of the application of the MT method on AE events on rock specimens in laboratory studies is given in Table 2.

Because of the much smaller travel paths of a view decimeters in rock specimens it is expected that in rock samples much smaller events with significantly higher frequencies (up to 1 MHz) and lower energy were registered. After the lists of various applications (Table 1 and 2) found in the literature, an introduction into the theory of the MT, and its decomposition (Section 2) a total of six applications of the MT method at different scale will be presented in Section 3. These are AE measurements in underground laboratory and parts of a mine (large-scale applications), during underground hydraulic fracturing tests in rock (intermediate-scale applications), as well as in laboratory studies on rock specimens (small-scale applications). Section 4 of this chapter will summarize the main results of the MT inversion.

2 THEORY

2.1 Moment tensor representation

The observed displacement $\vec{u}_n(\vec{x},t)$ at an observation point is given with the MT representation of a seismic point source as:

$$\vec{u}_n(\vec{x},t) = \int_{-\infty}^{+\infty} M_{pq}(\tau)\frac{\partial}{\partial\xi_q}G_{np}\left(\vec{x},t-\tau,\vec{\xi},0\right)d\tau. \tag{1}$$

In this Formula 1 u_n is the displacement, M_{pq} the seismic MT, G_{np} the Green's function tensor, $\vec{\xi}$ and $\vec{x}$ are space coordinates. Equation 1 can be used to describe the excitation, which is caused not by external forces, but by crack formation in the material itself. In AE testing an external force can generate by a pencil lead break or in fracture of a glass capillary on the surface of an elastic body. In case of internal cracks, the forces and its moments in the source region must be self-equilibrating. If each of the components M_{pq} shares the same time function $\dot{S}(t)$, Equation 1 becomes in the far field

$$\vec{u}_n(\vec{x},t) = [M_{pq}\cdot\dot{S}(t)] * G_{np,q}. \tag{2}$$

The asterisk denotes the convolution in the time domain and $\dot{S}(t)$ is the time derivative of the source time function. In practice the near-field term and the intermediate-field term are found to be small in several wavelengths away from the source. In the ray-theoretical limit, the Green's function tensor in Equation 2 can be further simplified. For this, a local coordinate system is introduced with origin at the source location with coordinates x_0, y_0, and z_0 (see Fig. 3). The azimuth angle φ (angle in horizontal plane) is measured clockwise from north and θ is the angle between the normal vector of the

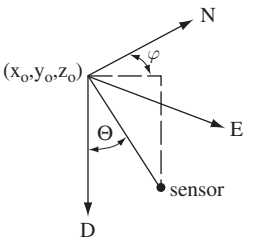


Figure 3 Orientation of the local coordinate system with origin at source coordinates x_0, y_0, z_0. The azimuth angle φ is measured clockwise from north, and the take-off angle θ is zero when z_0 points downwards.

Table 3 Coefficients a_{ik}^n in Equation 3 for P-wave, SV-wave, and SH-wave modes (Box 9.12 in Aki & Richards, 2002).

	$n = P$	$n = SV$	$n = SH$
$a_{j,1}$	$\sin^2\theta \cdot \cos^2\varphi$	$\frac{1}{2}\sin^2\theta \cdot \cos^2\varphi$	$-\frac{1}{2}\sin\theta \cdot \cos^2\varphi$
$a_{j,2}$	$\sin^2\theta \cdot \cos^2\varphi$	$\frac{1}{2}\sin^2\theta \cdot \sin^2\varphi$	$\sin\theta \cdot \cos^2\varphi$
$a_{j,3}$	$\sin^2\theta \cdot \sin^2\varphi$	$\frac{1}{2}\sin^2\theta \cdot \sin^2\varphi$	$\frac{1}{2}\sin\theta \cdot \sin^2\varphi$
$a_{j,4}$	$\sin^2\theta \cdot \cos\varphi$	$\cos^2\theta \cdot \cos\varphi$	$-\cos\theta \cdot \sin\varphi$
$a_{j,5}$	$\sin^2\theta \cdot \cos\varphi$	$\cos^2\theta \cdot \sin\varphi$	$\cos\theta \cdot \cos\varphi$
$a_{j,6}$	$-\sin^2\theta + 1$	$-\frac{1}{2}\sin^2\theta$	0

horizontal plane and radius vector of source and sensor (Aki & Richards, 2002). For source No. i and Sensor No. j in n direction we obtain the displacement components:

$$u_{ij}^n = I_j^n \sum_{k=1}^{6} m_{ki} \cdot a_{jk}^n. \tag{3}$$

With $m_{1i} = M_{11}, m_{2i} = M_{12}, m_{3i} = M_{22}, m_{4i} = M_{13}, m_{5i} = M_{23}$, and $m_{6i} = M_{33}$ are the MT components and I_j^n are the so-called elementary seismograms which correspond to scalar Green's functions for a given wave mode and displacement component. In the case of a uniaxial sensor, which has radial symmetry (what is true for AE sensors), the radial (SV) and transversal (SH) shear wave components are added to one component. Table 3 shows the coefficients a_{jk}^n in Equation 3 for the P-wave, SV-wave, and the SH-wave modes.

2.2 Absolute method

For the application of the absolute MT method using the first motion amplitudes and their polarities we calculate Green's function of the homogeneous full space (Aki & Richards, 2002). In the case of a single-source MT method using first motion amplitudes the index for source i in Equation 3 is dropped and Equation 3 leads to

$$u_{ij}^n = I_j^n \sum_{k=1}^{6} m_k \cdot a_{jk}^n. \tag{4}$$

In the case of full waveform MT method we write Equation 2 as

$$u_j^n(t) = \left\{ \sum_{k=1}^{6} m_k \cdot a_{jk}^n \cdot I_j^n(t) \right\} * S\Big(t\Big). \tag{5}$$

Thus, the inverse problem requires the determination of a common source time function $S(t)$ and the MT components m_k. The method is described in a paper of Michaels & Pao (1985). An iterative algorithm is applied on the basis of two linear subproblems. First, the m_k components are set to arbitrary nonzero initial values. Using these m_k the source time function $S(t)$ is calculated from Equation 5. Next, $S(t)$ is used to improve m_k. This procedure of alternately calculating $S(t)$ and m_k can be continued until convergence is reached. An improved source time function is obtained by averaging over all sensors after each iteration step. The final solution is the one, which has the smallest sum over squared residuals between observed and predicted waveforms. To avoid convergence to a local minimum MT components as initial values can be found by a grid search method or can be found by the absolute method using first motion amplitudes.

2.3 Relative methods

The relative MT methods applied here are described in detail in the papers of Dahm (1996). In this paper we will give only a brief summary of the methods. The relative method is applicable to clustered sources from a small area. The area's extension should not exceed the dominant wavelength of the used signals. Input data are the amplitudes of P and S waveforms from at least two sources, recorded at several sensors. Azimuths and take-off angles of the ray must be calculated in the same manner as for the absolute methods. No Green's functions have to be calculated. The method is preferable to an absolute method when attenuation along the travel path and site effects near the sensor location are poorly known. The simplest version is the relative method with reference mechanism. This is a robust relative method because the moment of a second event is estimated relative to a known MT of a first event. The equation can be written as (index n is dropped in the following equations):

$$u_{1j} \sum_{l=1}^{6} m_{l2} \cdot a_{jl} = u_{2j} \sum_{l=1}^{6} m_{k2} \cdot a_{jk}. \tag{6}$$

With m sensors, we can write

$$\begin{pmatrix} f_1 \\ \vdots \\ f_m \end{pmatrix} = \begin{pmatrix} u_{11}a_{11} & \rightleftharpoons & u_{11}a_{16} \\ \vdots & \ddots & \vdots \\ u_{1m}a_{m1} & \rightleftharpoons & u_{1m}a_{m6} \end{pmatrix} \begin{pmatrix} m_{11} \\ \vdots \\ m_{62} \end{pmatrix}, \tag{7}$$

where

$$f_1 = u_{2j} \sum_{k=1}^{6} m_{k1} a_{jk}.$$

The MT components of the second source are linearly dependent on those of the first source. The unknown MT can be estimated by a least-square calculation. The algorithm is flexible to work with more than one reference mechanism. The relative inversion using reference mechanism is a robust approach as long as the reference mechanism is accurate.

Using an extension of the method, the radiation patterns of all sources under investigation are estimated simultaneously, without the demand for a reference mechanism. When two sources have different radiation patterns, it is also possible to estimate the MT of the first source. The matrix formulation for m observations from two sources follows from Equation 6.

$$\begin{pmatrix} 0 \\ \vdots \\ 0 \end{pmatrix} = \begin{pmatrix} -A_2 & A_1 \\ 1 & 1 \end{pmatrix} \begin{pmatrix} S_1 \\ S_2 \end{pmatrix} \tag{8}$$

with

$$A_i = \begin{pmatrix} u_{i1}a_{11} & \rightleftharpoons & u_{i1}a_{16} \\ \vdots & \ddots & \vdots \\ u_{im}a_{m1} & \rightleftharpoons & u_{im}a_{m6} \end{pmatrix},$$

$$l = (1, 1, 1, 1, 1, 1),$$

$$S_K = (m_{1k}, m_{2k}, m_{3k}, m_{4k}, m_{5k}, m_{6k})^T,$$

and with an additional constraint

$$\sum_{i=1}^{2} \sum_{k=1}^{6} m_{ki} = C \neq 0.$$

In this case we call source one reference event (not to be confused with reference mechanism). With an increasing number of events the estimated errors of the MT components of the reference event decrease. In this case, the reference event has higher weight than the other ones. When the data of all events are of the same quality, it makes sense using each source as a reference event. This leads to an enlarged equation system (see Dahm, 1996). Based on Dahm's work, Anderson (2001) developed the hybrid MT method to enhance the accuracy of the MT components by correcting iteratively the input data.

2.4 Moment tensor sources

The seismic MT quantitatively describes a seismic point source and it characterizes all information about the source. The MT (3×3 matrix) is symmetric, *i.e.* it consists of six independent components. The diagonal elements represent linear vector dipoles, the off-diagonal elements represent the force couples with arms. The MT can be visually

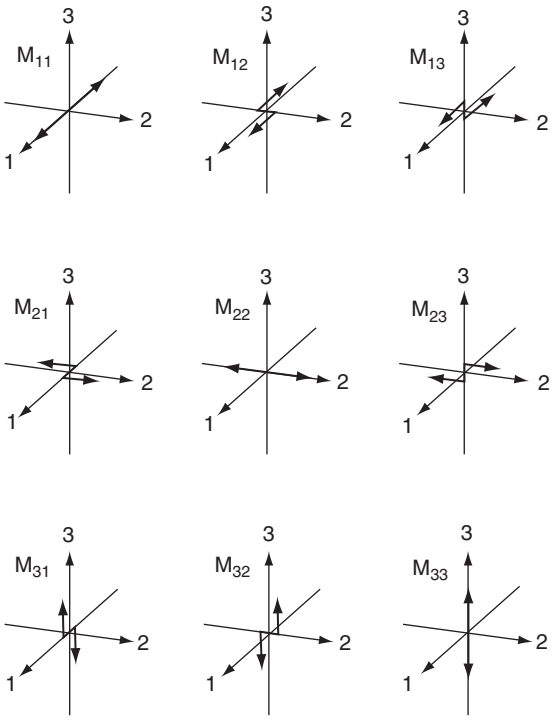


Figure 4 Representation of the moment tensor (MT) in the "force-couple model" with the nine force couples and the appropriate MT components (Aki & Richards, 2002).

represented by the "force-couple model" and mathematically represented by the "displacement model". The force-couple model consists of two pairs of forces acting at a point source. In Figure 4 the first index indicates the direction of the force and the second index indicates the arm direction. Each pair consists of forces with equal magnitude and opposite directions, so that the total force is equal to zero. In addition, the torque of each couple about the origin of the axes is of equal magnitude and opposite to one another so that the total torque is zero. The figure shows three dipoles without moment, namely the components with the same indices M_{11}, M_{22}, M_{33}. Because of the equilibrium in the source region the six other dipoles with moment are composed to three double couples without moment.

In the displacement model the MT for an isotropic medium can be written as:

$$M_{pq} = \lambda \cdot v_k n_k \delta_{pq} + \mu \cdot \left(v_p n_q + v_q n_p\right) \quad k, p, q = 1 \ldots 3. \tag{9}$$

In Equation 9, λ and μ are elastic constants, known as the Lamé moduli, v_k is the displacement vector at the fault plane of the source, and n_k is the normal vector of the fault plane. δ_{pq} is the Kronecker symbol. Figure 5 shows four source types, in the displacement model (left-hand side) and the force-couple model (right-hand side). In the case that both vectors perpendicular to each other, it is a pure shear source (Fig. 5a). On the other hand if both vectors antiparallel to each other, it is a pure tensile source (Fig. 5b).

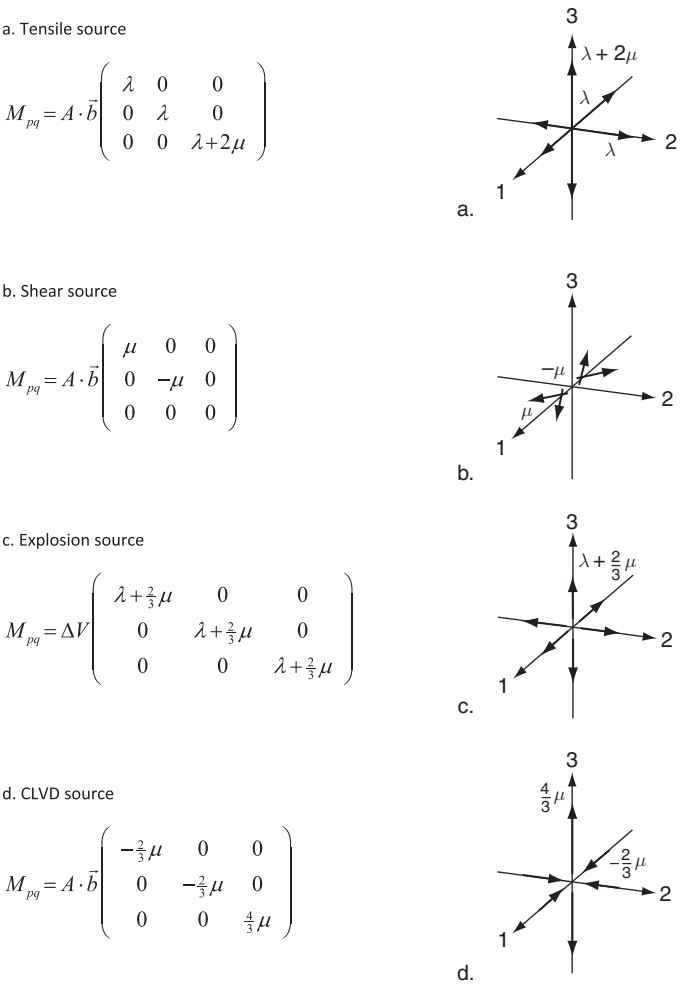


Figure 5 Representation of the moment tensor (MT) in the "force-couple model" with the nine force couples and the appropriate MT components (Aki & Richards, 2002).

Eisenblätter (1980) introduces three types of AE source as shown in Figure 6. This figures shows three models together with the direction of slip or fracture (black filled arrows) and the forces involved (double arrows), which are the cause of slip propagation. The dislocation vector $\vec{b}$ (Burgers vector) is also shown together with the slip or fracture surface in each case (shaded are). Types 1 and 2 not only contain the various forms of shear fracture (known as Mode II and Mode III in fracture mechanics) but also the sources of tectonic earthquakes and both the basic forms of plasticity sustainers in metals (edge and screw dislocations). These two types contain friction on existing cracks and rock bursts as well.

Slip with Type 1 and 2 is caused by a force couple and the rotational moment due to this is compensated by a second force couple which acts perpendicular to the first, as

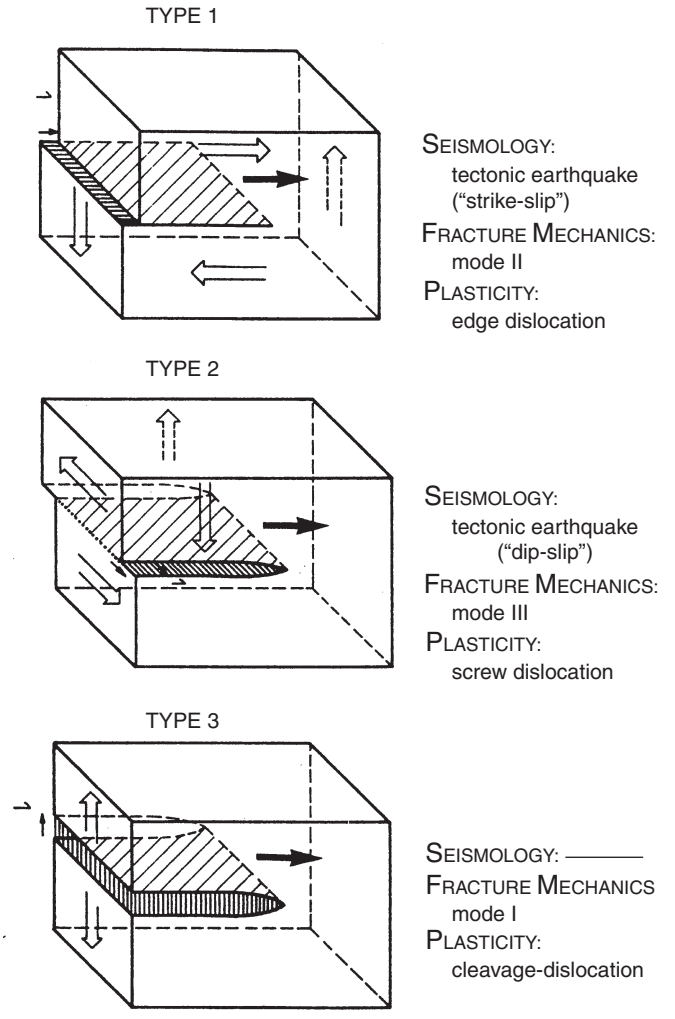


Figure 6 Types of AE sources (Eisenblätter, 1980).

expected in solid bodies. Type 3 shows crack growth as caused by tensile load. This type of crack loading is the most dangerous and is responsible for brittle fracture in metals. It is known as Mode I in fracture mechanics.

2.5 Decomposition of the moment tensor

2.5.1 Standard decomposition into DC, ISO, and CLVD mechanisms

However, the interpretation of the MT by physical models is not unique. In the literature, a number of proposals of the decompositions of the MT can be found. A good overview about the decomposition is given in the student's guide published by

Jost & Herrmann (1989). According to the results of the eigenvalue analysis, a general decomposition of the MT is defined as:

$$M = \frac{1}{3}\begin{pmatrix} tr(M) & 0 & 0 \\ 0 & tr(M) & 0 \\ 0 & 0 & tr(M) \end{pmatrix} + \begin{pmatrix} m_1^* & 0 & 0 \\ 0 & m_2^* & 0 \\ 0 & 0 & m_3^* \end{pmatrix} \tag{10}$$

where $tr(M) = m_1 + m_2 + m_3$ is the trace of the entire MT and $m_i^* = m_i - 1/3 \cdot tr(M)$ are deviatoric eigenvalues. The first term in Equation 10 describes the isotropic part of the MT, which is important for quantifying the volume change in the source. The isotropic source component in percent is defined by the ratio of the tensor norms of the isotropic and total MT (Silver & Jordan, 1982):

$$ISO\% = M_{ISO}^2 / M_{TOT}^2 \cdot 100\% \text{ with } M_{ISO} = tr(M)/\sqrt{6} \text{ and}$$
$$M_{TOT} = \|M\|/\sqrt{2}.$$

The second term describes the deviatoric part of the MT. The deviatoric part can be further decomposed by various methods. In the field of AE decomposition double-couple (DC) and compensated linear vector dipole (CLVD) is frequently used. The double-couple component is $DC = \left(1 - 2m_{min}^*/2m_{max}^*\right) \cdot 100\%$. The CLVD is given by $CLVD = (100 - DC)\%$. Note that DC + CLVD + ISO is larger than 100%, since DC and CLVD refer to the tensor with isotropic component removed.

2.5.2 Decomposition in DC and tensile mechanisms

Dahm *et al.* (1999) additionally find it promising to introduce for AE sources in rock salt an optional "general-dislocation-source" constraint (shear and tension dislocation on the same failure plane), leading for dislocation sources to a faster convergence of source parameters. When applied, the MTs in Equation 2 are replaced by:

$$\begin{aligned}
M_{11} &= -\mu C\left(\sin 2\phi \sin\delta \cos\eta + \sin^2\phi \sin 2\delta \sin\eta\right) + D\left(\lambda + 2\mu \sin^2\phi \sin^2\delta\right) \\
M_{12} &= \mu C\left(\sin 2\phi \sin\delta \cos\eta + \frac{1}{2}\sin 2\phi \sin 2\delta \sin\eta\right) - D\mu \sin 2\phi \sin^2\delta \\
M_{22} &= \mu C\left(\sin 2\phi \sin\delta \cos\eta - \cos^2\phi \sin 2\delta \sin\eta\right) + D\left(\lambda + 2\mu \cos^2\phi \sin^2\delta\right) \\
M_{13} &= -\mu C(\cos 2\phi \cos\delta cos\eta + \sin\phi \sin 2\delta \sin\eta) + D\mu \sin\phi sin2\delta \\
M_{23} &= -\mu C(\sin\phi \sin\delta cos\eta - \cos 2\phi \cos 2\delta \sin\eta) - D\mu \cos\phi sin2\delta \\
M_{33} &= \mu C \sin 2\delta \sin\eta + D\left(\lambda + 2\mu \cos^2\delta\right)
\end{aligned} \tag{11}$$

ϕ and δ denote strike and dip of the crack surface, respectively, η is the rake of the shear dislocation vector, C and D are the magnitudes of the shear and tension dislocation multiplied by the crack area, respectively, and again λ and μ are Lamés constants. The Equation system 11 is solved with respect to C, D, ϕ, δ, and η. This leads to a nonlinear inversion problem, which can be iteratively solved by *e.g.* gradient method. To avoid the convergence to a local minimum several inversion runs are useful. In order to find appropriate start values an equidistant grid on the focal sphere is recommended. The final solution is the one with the smallest sum over squared residuals between observed

and predicted first motion amplitudes. Unfortunately Dahm's decomposition method was not continued and applied to AE events in rock.

2.5.3 Decomposition in DC, ISO, and tensile mechanisms

Ohtsu (2000) developed the so-call SIGMA (Simplified Green's functions for Moment tensor Analysis) code, which is embedded in a commercially available AE measuring system. The code has been applied routinely to signals generated in concrete by crack formation. The classification of a crack in the SIGMA code is performed by the eigenvalue analysis of the MT. Setting the ratio of the maximum shear contribution as X, three eigenvalues for the shear crack become X, 0, -X. Likewise, the ratio of the maximum deviatoric tensile component is set as Y and the isotropic tensile as Z. It is assumed that the principal axes of the shear crack are identical to those of the tensile crack. Then, the eigenvalues of the MT for a general case are represented by the combination of the shear crack and the tensile crack. Because relative values are determined in the SiGMA, three eigenvalues are normalized and decomposed,

1.0	$= X + Y + Z,$
intermediate eigenvalue/maximum eigenvalue	$= 0 - Y/2 + Z,$
minimum eigenvalue/maximum eigenvalue	$= -X - Y/2 + Z,$

where X, Y, and Z denote the shear ratio, the deviatoric tensile ratio, and the isotropic tensile ratio, respectively. In the present SiGMA code, AE sources of which the shear ratios are less than 40% are classified into tensile cracks. The sources of X > 60% are classified into shear cracks. In between 40% and 60%, cracks are referred to as mixed mode events.

2.5.4 Decomposition in DC, ISO, CLVD, and tensile mechanisms

Hudson *et al.* (1989) proposed another decomposition method. They distinguish different source types only with two parameters T and k. First, the eigenvalues of the MT m_i are sorted according to their relative values, so that $m_1 \geq m_2 \geq m_3$. Then the deviatoric eigenvalues m_i^* are formed in the same way as in Equation 9 when the isotropic part is subtracted from MT. The parameter T, which describes the deviatoric part of the MT is defined as:

$$
\begin{aligned}
T &= -\frac{2m_3^*}{m_2^*} \quad for \quad m_3^* > 0; \quad 0 < T \leq 1 \\
T &= 0 \qquad for \quad m_3^* = 0 \\
T &= \frac{2m_3^*}{m_1^*} \qquad for \quad m_3^* < 0; \quad -1 \leq T < 0.
\end{aligned}
$$

At $T = 0$ the MT characterizes a pure double-couple source mechanism and for $T = \pm 1$ the source mechanism is a positive and negative CLVD source mechanism, respectively. The second parameter k with $-1 \leq k \leq 1$ describes the volumetric source component and is defined as:

$$k = \frac{m_{ISO}}{(|m_{ISO}| - m_2^*)} \quad for \quad m_3^* > 0$$
$$k = \frac{m_{ISO}}{(|m_{ISO}| + m_1^*)} \quad for \quad m_3^* \leq 0.$$

For k = 0 the volume change in the source is equal to zero. For k = ± 1 the source mechanism is a purely isotropic that means an explosion or implosion source mechanism. For the visualization of these two parameters the so-called T-k plot, as seen in Figure 7, was suggested. While parameter k is plotted at the axis of ordinate (y axis) and parameter T is plotted at the axis of abscissae (x axis).

Remarks: The DC mechanism is realistic for both, microcracks and tectonic earthquakes. In seismology, significant CLVD mechanisms can be found for deeper earthquakes or earthquakes with two or more sub-events at a fractal geometry of the fault plane (Frohlich, 1994; Miller *et al.*, 1998). In AE, the CLVD component has no significance as a mechanism of microcracks. In combination with a mayor positive isotropic component it can be interpreted as tensile crack (Mode I). According to the definitions above, the isotropic component of a pure tensile source is 75% (for rock with Poisson ratio of 0.25) with a 100% CLVD component where the DC source component equals zero. In a broader sense, CLVD source components can be interpreted as the deviatoric part of a tensile source in the case of microcracks.

The volume change in the source can be estimated from the isotropic source components of the entire MT. In the literature, two relationships between the isotropic MT M_{ISO} and the volume change are given. Müller (2001) has noted an apparent inconsistency between the two relationships used to calculate the volume change of a seismic source from the isotropic part of the MT. Following Müller, the frequently used relation of Aki and Richards (2002, Equation 3.35) $M_{ISO} = (\lambda + 2/3\mu)\Delta V$ is applicable

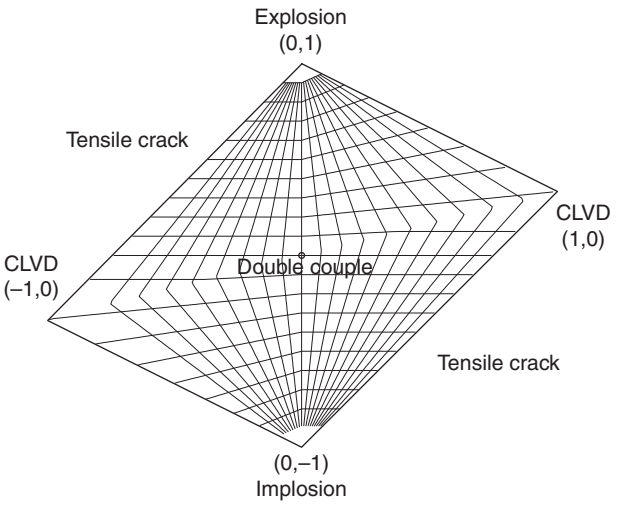


Figure 7 Hudson diagram in the *T–k* plot to with various event mechanisms (Hudson *et al.*, 1989).

only to plane cracks with tensile source components. This source type is expected for microcracking in rocks as in our investigations. The second relation $M_{ISO} = (\lambda + 2\mu)\Delta V$ applies to spherically symmetric sources such as explosions or implosions (Müller, 1973) and gives significantly lower values for the volume change. This discrepancy was considered in the new edition of the textbook of Aki and Richards (2002, see Problem 3.8). It should be mentioned that isotropic source components could be feigned through high noise and signal offset of the registration system (preamplifier or power supply). Except from underground explosions, isotropic source components below 10% are often not considered in earthquake seismology to be significant. This cannot be presupposed for microcracks in rock. The author suggests a check of the significance of isotropic source components by the application of the statistical tests *e.g.* the F test (Manthei, 2005).

3 APPLICATIONS OF THE MOMENT TENSOR METHOD

3.1 Moment tensor method in mines

3.1.1 Granite

The first example on MT method in mines refers to crack formation in granite caused by stress redistribution around newly excavated tunnel. A research program has been undertaken by the Atomic Energy of Canada Limited to develop the technology needed for the safe and permanent disposal of nuclear waste. The main objectives were to investigate the response of a rock mass to excavation and to study the long-term stability of underground openings.

After the so-called mine-by experiment in the Underground Research Laboratory (URL) located in Pinawa, Manitoba, a sealing experiment was conducted to observe the integrity of different sealing technologies subjected to high hydraulic pressures in June 1997. Two bulkheads had been constructed and keyed into the tunnel to create a chamber in granite (Room 425 in Fig. 8), which was pressurized to ambient pore pressure of about 4 MPa. Stresses and displacements as well as microseismicity (MS) were monitored around the tunnel and the keys with a 16-channel MS system (MS 1 to MS 16 in Fig. 8). The MS system operates in the low-frequency range of 0.5 to 10 kHz. The volume of the monitored area is approximately 10^6 m^3. Within this volume an AE system monitors a 10^3 m^3 region in the high-frequency range of 40 to 400 kHz. The AE measurements have been carried out utilizing 16 borehole transducers around one quadrant of a clay key to give highly detailed cracking information (AE 1 to 16 in Fig. 8).

The AE events have been recorded during excavation of a 40 m long tunnel segment in direction of the maximum principal stress σ_1 (see insert at the bottom of the right-hand side in Fig. 8). The system monitored the AE activity in time periods where no excavation work took place.

Figure 9 shows the location of approximately 15,350 AE events in four successive stages a to d within a time period of about 5 months. The Figures 9a-d show a lateral view (at top of each figure), a plan view (below), and a cross-sectional view along the tunnel axis together with the contour of the tunnel and the key before and during excavation of the clay key. The events are marked by black dots.

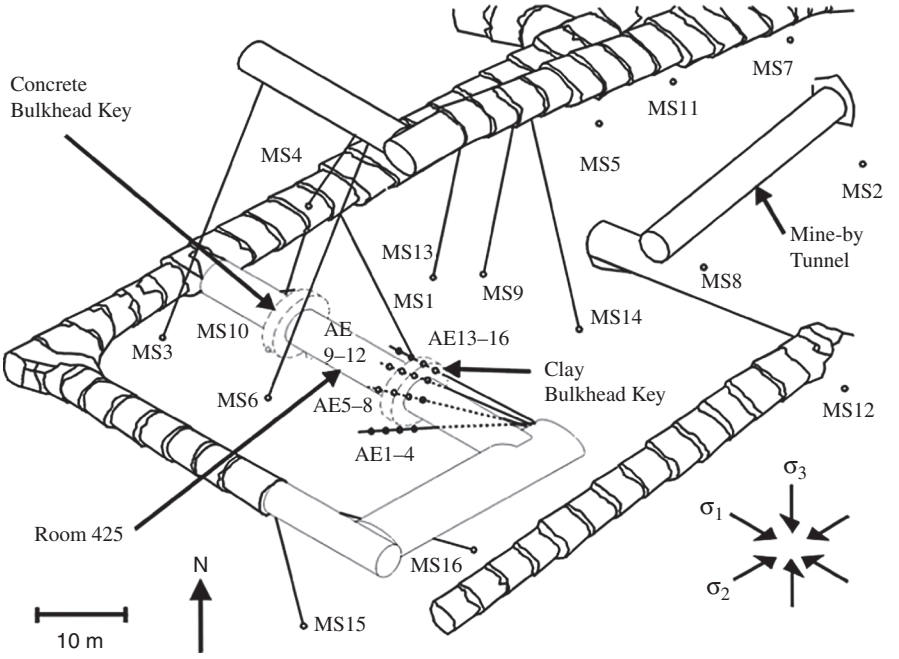


Figure 8 Test site of the sealing experiment with locations of the AE network (AE1 to A16) and microseismic network (MS1 to MS16). The orientation of the principal stresses is given in the insert at the bottom of the right-hand side (Collins *et al.*, 2002).

All events are located in a 15 m long region in zones close to the tunnel floor. Only those parts are indicated by events, which are orientated toward the sensor array. The opposite part of the floor is acoustically shaded by the tunnel itself. Before excavation of the clay key 1,119 AE events were located within a time period of 9 days (see Fig. 9a). The majority of the events were located in a time period of 3.5 months. In this time the clay key and the floor segment were completely excavated (see Fig. 9b and c). The locations cluster around the bottom of the key. Figure 9d shows the events occurring in the time interval directly following the key excavation in the floor region and concentrated around the corners of the key. The gap in AE activity of about 1 m around the clay key in the tunnel floor correlates with low-stress regions as predicted from geomechanical modeling results. From the location of the AE events it can be concluded that the EDZ is limited to within 1 m around the clay key. In some regions it is less than 1 m wide (Collins *et al.*, 2002).

In order to determine the source mechanisms of 155 well located AE events (Collins *et al.*, 2002) applied the MT method on three clusters. Figure 10 shows the location of the three clusters in (a) plan view, (b) side view, and (c) section view. The 16 AE sensors are shown as black dots. Clusters 1 and 2 occur before the excavation of the clay key, and locate just below the floor of Room 425. Cluster 3 occurs when the clay key has been approximately three-fourths excavated and locates at the 90° angle of the lower part of the key.

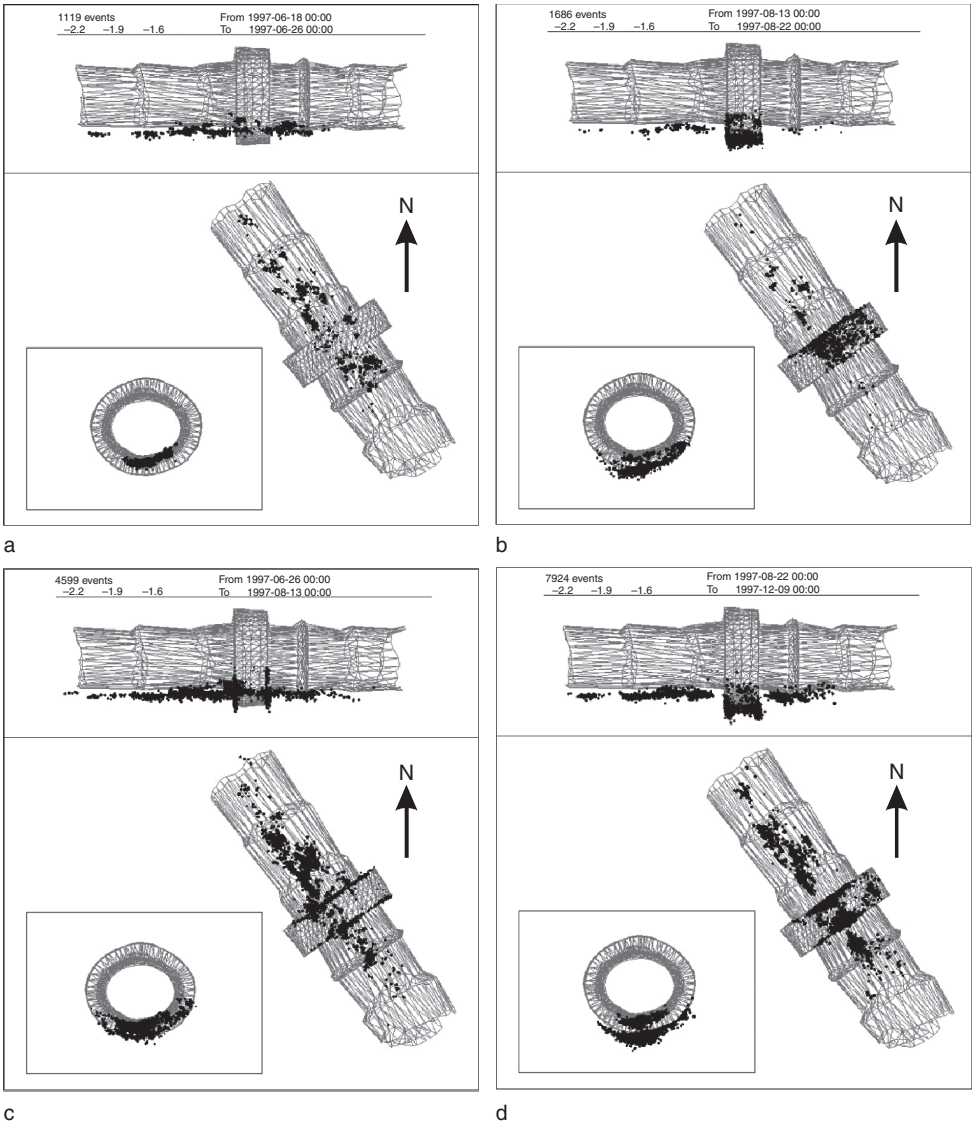


Figure 9 Located AE events in four successive stages a to d in top view and lateral view parallel to the tunnel axis. a: before excavation of the clay key; b to d: during excavation of the clay key (Young & Collins, 2001).

Figure 11 shows the *T-k* plot of all three clusters (middle) and at the right-hand side and left-hand side the P-wave radiation pattern of the investigated events of Cluster 1, 2, and 3. The investigation using the MT method pointed out, that single low frequency MS events are found to be spatially associated with clusters of higher frequency AE events.

The MTs of the clustered AE events and the single MS events were determined with all three of the clusters having MS events showing dominantly deviatoric mechanisms.

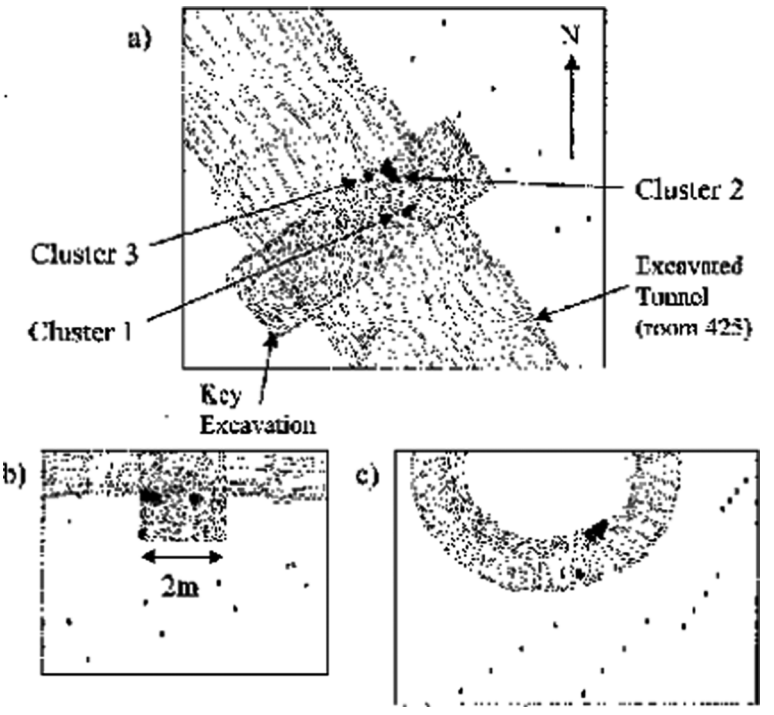


Figure 10 The locations of the three AE clusters in (a) plan view, (b) side view, and (c) section view. The 16 AE sensors are shown as black dots (Collins *et al.*, 2002).

On the T-k source type plot, two of the MS events (MS1 and MS3 in Fig. 11) are nearly positive CLVD sources while the other MS event (MS2a in Fig. 11) is considered to be a dominantly DC source.

The direction of the slip vector of the DC event agrees with the temporal movement of the associated AE event cluster locations. The majority of the AE events have deviatoric mechanisms, which are interpreted as cracks, which are sub-parallel to the tunnel circumference orientated. Additionally each cluster had at least one AE event with significant positive volumetric components, which is interpreted as tensile opening. Four AE events were recorded with significant crack closure mechanisms possibly relating to the crushing of asperities on the fracture. Collins *et al.* (2002) concluded, that the AE/MS relationship are showing the initial AE events as foreshocks which occur in highly stressed regions along the eventual MS (main shock) fracture plane. Subsequent AE events are considered as aftershocks, which are generated over the restabilising fracture in the surrounding region.

3.1.2 Rock salt

The following examples of field studies originate from two sections of the underground repository of Morsleben in a salt mine in northern Germany. Originally, each section was monitored by a network of 24 AE sensors since 1995 and 1997, respectively. Each

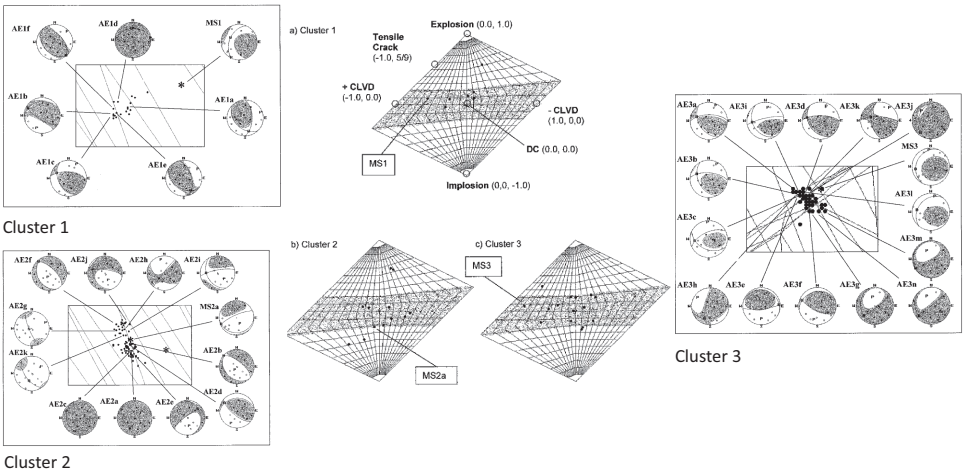


Figure 11 P-wave radiation pattern of the investigated events in an equal-area, lower hemisphere projection (so-called beach balls) of AE and MS events from Cluster 1, 2 (left-hand side) and Cluster 3 (right-hand side). Middle: *T–k* plot of events in Cluster 1 to 3 after Hudson *et al.* (1989) (Collins *et al.*, 2002).

network covers an area of 150 m × 100 m × 120 m (Spies *et al.*, 2004; Manthei *et al.*, 2007). The MT method has been applied on AE events in the central and southern section of the repository (Manthei *et al.*, 2001, 2007). In this paper the results in the southern section will be presented. In the southern section, long-term AE measurements have been carried out with the aim to investigate the micro- and macrofracturing processes in a region of a high degree of excavation. For more than fifteen years, the AE events were located by a network of 24 borehole sensors. Their mean rate is in the range of 60 to 100 events per hour. In order to get information about the source mechanisms, the MT method has been applied to strong events, which were localized with good accuracy using more than 29 compressional-wave and shear-wave onsets. The selected events originated in a pillar between huge underground cavities.

Figure 12 shows a plan view (horizontal projection) of the site. In this projection, the contours of the rooms and the main drift are marked by continuous lines (Rooms 2 and 3) and dashed lines (Rooms 9s and 9n). This mine section was excavated about 70 years ago in rock salt. Nuclear waste is stored in the two lower Rooms 2 and 3. A drift is located at a level between the upper and lower rooms. The average depth level of the cavities is about 500 m. 24 AE sensors (black dots) equipped with piezoelectric transducers are installed in boreholes of up to 30 m length, which were drilled from the drift (gray area) because the rooms are not accessible anymore. The central unit of the measuring system consists of a transient recorder monitoring the signals of the sensors (frequency range of 1 to 100 kHz), a computer controlling all actions of data acquisition and in-situ evaluation, and a modem for telecommunications.

Figure 13 shows in a perspective view of the cavities and the main drift (Rooms 9n and 9s and Disposal Rooms 2 and 3) 41,521 very strong events (light dots), which were located in a time period of approximately 5 years.

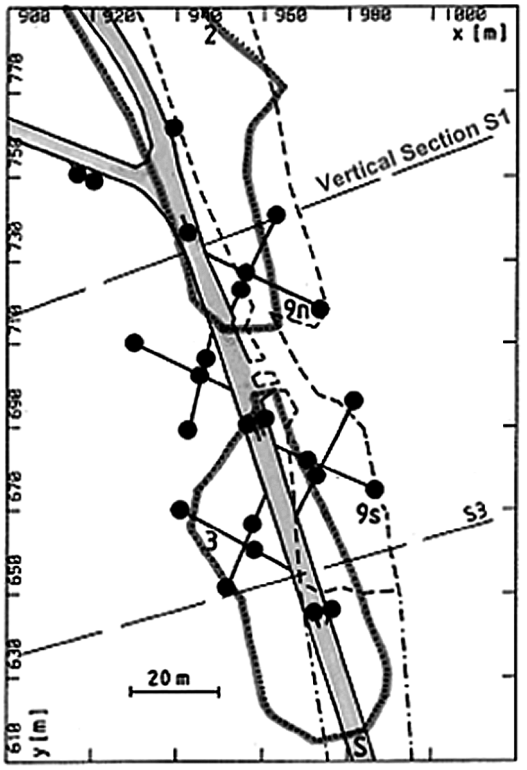


Figure 12 Plan view of the two levels with Rooms 9n and 9s (bold continuous line) and Room 2 and 3 (dashed line) and the access drift (gray). The position of the borehole sensors are marked by black dots (Manthei *et al.*, 2007).

Figure 14 shows windowed time traces aligned at the times of the first motion of the P wave. The numbers at the end of the traces refer to the incidence angle, the peak amplitude in Volt, and the length of the travel path. The following steps outline the treatment of data before MT inversion calculations:

- Data were corrected for the measured sensor sensitivity and directivity.
- Geometrical wave attenuation and damping were considered.
- Traces where the incidence angle was greater than 80° were eliminated.

Traces where the wave radiation is disturbed by large rooms or drifts are eliminated too. After the data treatment, the over-determined equation system was solved for the six MT components using SVD. Figure 15 displays the results of the MT calculations of 53 events with stable MT solutions in a perspective view in northeast direction together with the cavities and the main drift without the upper Room 9s (compare with Fig. 13). The events (light dots) are located in three separate regions. 18 events are located in Region I beneath the floor of the main drift. 20 and 15 events are located in Region II and III at the western wall and below the floor of Room 9n, respectively. This figure shows for each region the calculated P-wave radiation pattern in an equal-area, lower

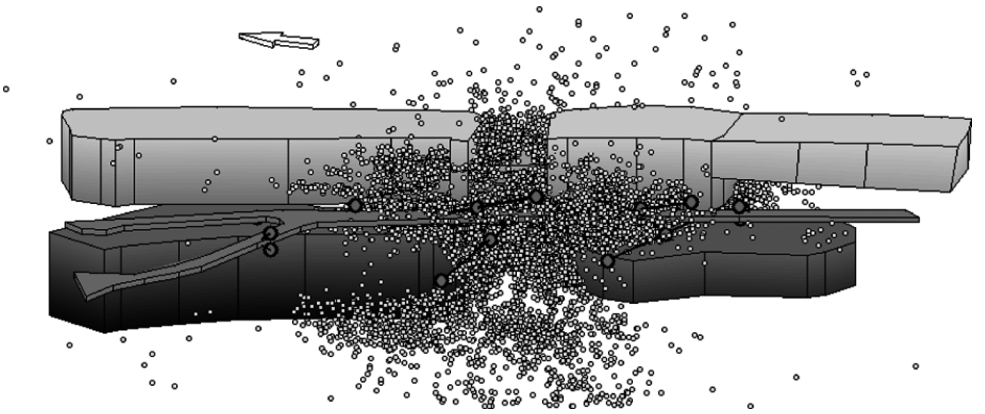


Figure 13 Perspective view of cavities and the main drift at two levels (Rooms 9n and 9s and Disposal Rooms 2 and 3). The black dots indicate the AE sensors in boreholes, the light dots represent the locations of 41,521 AE events (Manthei *et al*., 2007).

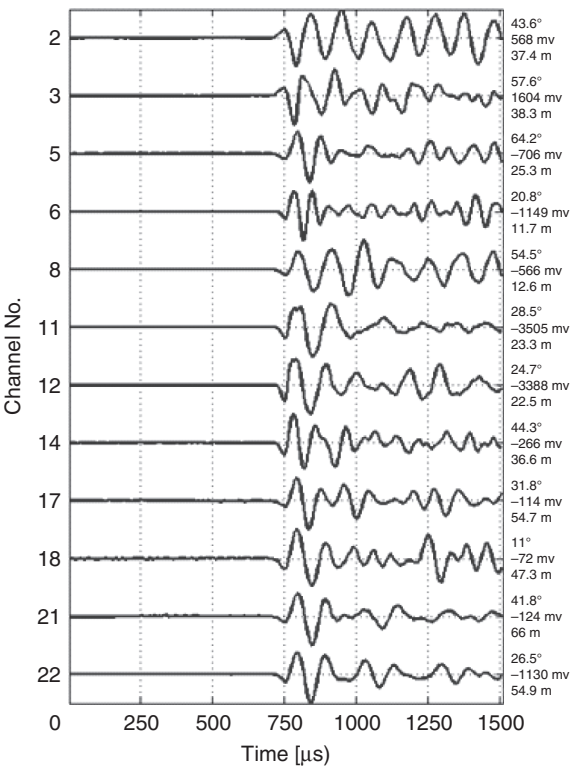


Figure 14 Aligned P-wave onsets of a located AE event in rock salt (Manthei *et al*., 2007).

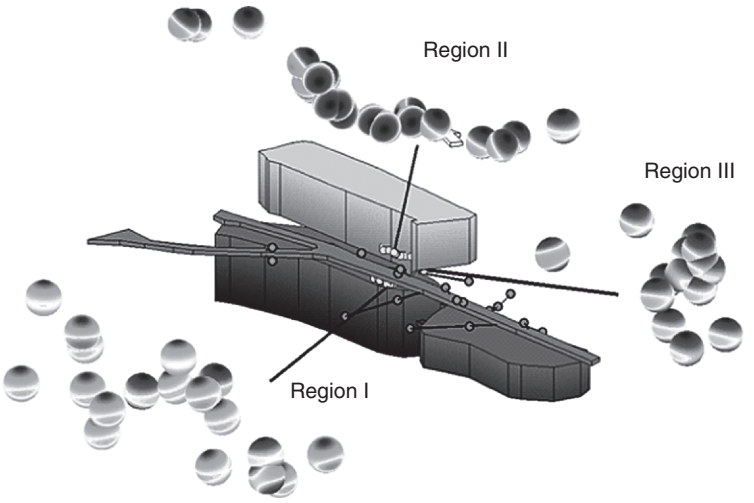


Figure 15 Perspective view of cavities and the main drift at two levels (without Room 9s) with the P-wave radiation pattern of the investigated events in an equal-area, lower hemisphere projection (beach balls). The light and dark areas are indicating the dilatational and compressional first motion, respectively (Manthei *et al.*, 2007).

hemisphere projection (beach balls). The red and blue areas indicate zones of dilatational and compressional first motion, respectively.

The white lines in the beach balls indicate the nodal line. A closer look to Figure 15 points out that adjacent events show similar radiation patterns. This means, that the source mechanisms and source orientations are the same. Furthermore, the radiation patterns of events in Region I show an extended area of dilatational first motion (red area) compared with events in Region II and III, which is an indication for an increased volumetric source component or tensile mechanism. Except some events in Region II, the nodal lines of the events in Region II and III are nearly identical.

Generally, all events show two clearly discernible nodal lines, which enclose a flat angle below 90°. This result is an indication for more or less mixed mode mechanisms of both shear and tensile components, whereas an angle of 90° would indicate a pure shear source mechanism. The decomposition of the MT into volumetric and deviatoric parts confirms this result. Whereas events in Region I and III show 20 to 25% lower shear source components and 20% higher volumetric source components than in Region II, events in Region II show high shear source components (approximately 50%) and low volumetric source components (below 20%). Apart from a few events, most of the T (or tensional) axes tend to have approximately vertical direction in the range between 60° and 90° (measured from horizontal direction). The P (or compressional) axes have nearly horizontal direction.

All evaluated events are located in zones of the highest AE activity in the northern part of the monitored area. In these zones, the AE events occur in "bandlike" structures between the corners of the upper and lower Rooms 9n and 2, respectively, as shown in Figure 16 in a projection of all events, which include the smaller ones, within a 20-m

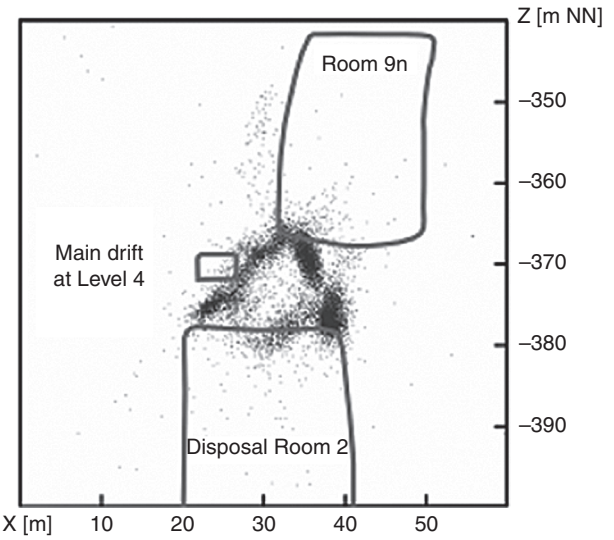


Figure 16 Located AE events in vertical cross Section S1 (see Fig. 12) (Manthei *et al.*, 2007).

interval to vertical Section S1 (see Fig. 12). This figure shows a more complete picture of the highly active zones (10,000 events in one month). Geomechanical finite element calculations (Spies *et al.*, 2004) pointed out that the highest shear stresses and deformations exist in these zones. In addition, the calculations showed also that in these zones tensile stresses are to be expected. This combination of shear and tensile stresses will explain the observed high shear and volumetric source.

3.2 Moment tensor method during hydraulic fracturing test

A second topic of this paper is the application of MT method to hydraulic fracturing tests in rock. The typical linear dimension of the covered region is about 10 m. Those tests are used for in-situ stress measurements in mines. Examples are shown from measurements in siliceous sandstone and rock salt. These measurements were used to find the orientation of the macroscopic crack plane and to determine the source mechanism (tensile crack or shear crack).

3.2.1 Underground working tunnel Imaichi, Japan

A lot of papers show the application of AE during hydraulic fracturing tests on rock samples as well as in the field for example Lockner & Byerlee (1977), Eisenblätter (1988) and Niitsuma *et al.* (1993), respectively. One of the first who applied the MT method on AE events, which were detected during in-situ AE measurements in rock, was Ohtsu (1991). Ohtsu carried out AE measurements during in-situ hydraulic fracturing tests at an underground working tunnel in Imaichi/Japan. The test site was composed of siliceous sandstone. In order to monitor AE events a total number of 34 AE sensors were installed in boreholes in a distance of one meter from the injection

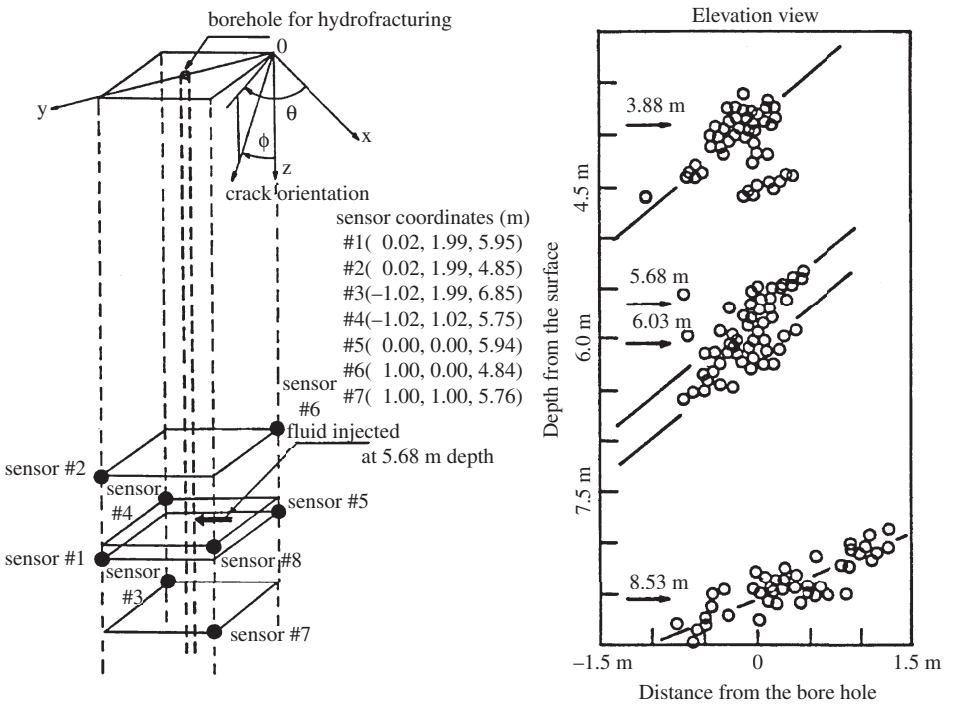


Figure 17 Left-hand side: Configuration of the hydraulic fracturing test site in siliceous sandstone. Eight acoustic emission (AE) transducers (indicated by filled circles) were located in four boreholes around the central injection well for the injection test in 5.68 m. Right-hand side: Located AE events in the elevation view for hydraulic fracturing tests in 3.88 m, 5.68m, 6.03m and 8.53m (location of the injection is marked by means of horizontal arrows) (Ohtsu, 1993).

well. The sensors were 17 accelerometers with resonance frequency of 25 kHz and piezoelectric transducers with resonance frequency of 65 kHz. Left-hand side of Figure 17 shows the configuration of only eight AE sensors. During four hydraulic fracturing tests at 3.88 m, 5.68 m, 6.03 m, and 8.53 m borehole depths approximately 200 AE events were located. Right-hand side of Figure 17 shows that clustered events appear periodically along the injection well, which were attributed to the fracture planes.

The events from the injection test in 5.68 m depth overlap those of the injection test at 6.03 m. The solid lines indicate the fracture planes found by AE locations. The fracture planes are oriented transverse to the injection well and inclined approximately by angles of 40° to 45° with respect to the horizontal direction. The deepest cluster is inclined by an angle of 25°. According to visual inspection of the injection well prior to hydraulic fracturing, the orientation of existing natural joints varied from 40° to 60°. Ten AE events, which were recorded during the fracturing test in 5.68 m borehole depth, were analyzed by using SIGMA. The MT analysis pointed out that the orientation of microscopic crack planes was in good agreement with the direction of the macroscopic fracture plane. AE events of shear type occurred more in the center of the macroscopic fracture planes whereas those of tensile type are located farther from

the injection well near the crack tip. From these AE measurements it was concluded, that at first tensile cracks were generated at the week seam of joints, and then shear cracks occurred on the open joints. The orientation of tensile cracks was perpendicular to the macroscopic fracture plane and the events of shear type were parallel to the macroscopic fracture plane.

3.2.2 *Salt mine Bernburg, Germany*

The test site of the hydraulic fracturing tests was located in the salt mine Bernburg, Germany, at the 420-m level in the Leine rock salt. Let-hand side of Figure 18 shows the test site in a perspective view. The western sidewall of a huge chamber of 120 m length, 25 m width, and 30 m height is approximately 20 m away from the access drift. The horizontal injection well (diameter 42 mm, length approximately 12 m) had been made from the side of the access drift, which cuts the barrier pillar. Due to the high degree of excavation the barrier pillar is under high compressional and differential stresses with maximal and minimal principal stresses of approximately 25 and 10 MPa, respectively. Six hydraulic fracturing tests and additional refracturing tests with an injected oil volume of 100 and 300 cm^3, respectively, and injection time intervals of 15 min have been carried out in the injection well, at depths of approximately 1.3, 2.0, 3.4, 5.8, 7.0, and 8.8 m. Eight AE borehole sensors (right-hand side of Fig. 18) were placed in four boleholes (10 m length, 100 mm diameter) around the central injection well. The AE events were located using P- and S-wave arrival times.

Figure 19 shows an AE event recorded by eight channels during the hydraulic fracturing test in 5.8 m borehole depth. The signals are low-pass filtered with a corner frequency of 17 kHz which is below the resonance frequency of the sensor. The signals show clearly discernible P and S wave onsets, which are very easy to pick automatically, and the onsets show similar wavelets. During six fracturing and refracturing tests, 735 AE events could be precisely localized with a residual error below 10 cm. The orientations of the macroscopic fracture planes as indicated by AE measurement were

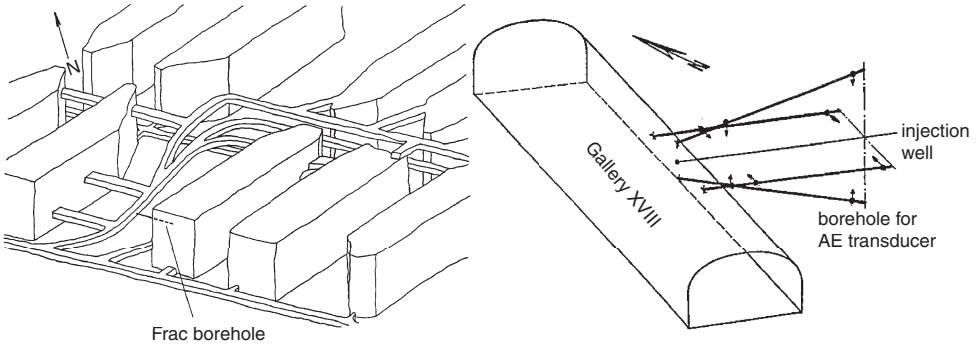


Figure 18 Left-hand side: Test site of the hydraulic fracturing test series at the 420-m level in the vicinity of huge chambers. Right-hand side: Boreholes for the acoustic emission (AE) sensors around the 12 m long horizontal injection well. Arrows mark the direction of maximal transducer sensitivity (Manthei *et al.*, 2001).

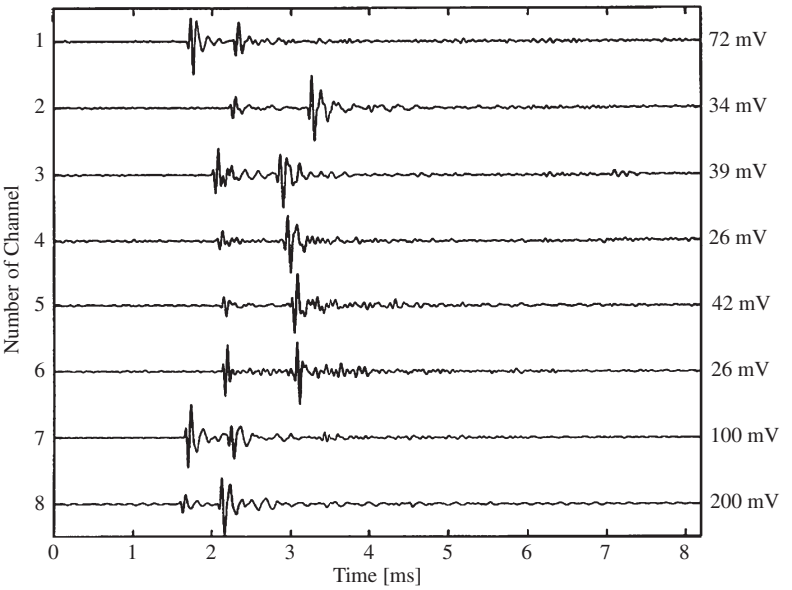


Figure 19 Typical signals for a source from hydraulic fracturing test in 5.8 m borehole depth with clearly discernible P- and S-wave onsets (Manthei *et al.*, 2001).

compared with independent stress calculations. These FEM calculations based on long-term surface subsidence measurement and measurement of underground convergence.

Figure 20 shows the result of these stress calculations in a vertical cross-section through the test site (upper figure). The horizontal line represents the injection well. A part of the contour line of the huge chamber can be seen at the right-hand side. At the left-hand side, the contour line of the access gallery is indicated. The crosses represent the orientations of the calculated principal stresses around the test site. It can be seen that in the vicinity of the free surfaces of the rooms (wall, floor and roof) only the stress component parallel to the surface exists. In a larger distance from the surface the second stress component appears.

Figure 20 shows at the bottom the orientation of the principal stresses along the injection well and the located events in the enlarged projection to the y-z plane (side view). The orientation of the fracture planes as measured by AE agrees remarkably well with the orientation of the calculated principal stresses. It can be seen that the direction of the fracture planes appears to coincide with the maximum principal stress. Whereas in smaller borehole depths up to 2 m the macroscopic fracture planes are parallel to the gallery wall and perpendicular to the horizontal injection well, the fractures in greater depths are striking in y-direction at approximately 63°. This fact is observed for all fractures. These results confirm that fractures are oriented normal to the minimum principal stress (Manthei *et al.*, 2001).

Manthei *et al.* (2001) studied 263 well-located clustered events, which occurred during fracturing and refracturing tests in 1 to 9 m borehole depths. The characteristic diameter of the source volume of each cluster is approximately 0.4 m, which is nearly

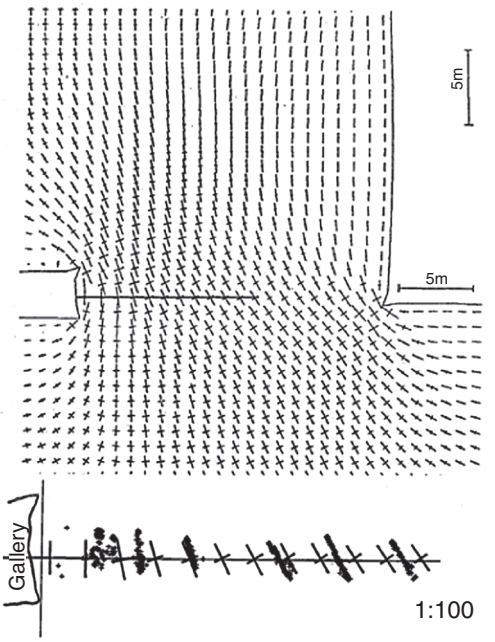


Figure 20 Calculated stress field (top) around the test site together with the contours of the access drift (left-hand side) and the huge chamber (right-hand side). Enlarged view (bottom) of the stress field (crosses) along the injection well and the located AE events (Manthei *et al.*, 2001).

one P wavelength at the dominant frequency of filtered wavelets at approximately 10 kHz. The number of events ranges from 11 (fracturing test in 8.8 m) up to 33 events (refracturing test in 1.3 m). One cluster (refracturing test in 2.0 m) contains 51 events. Because of the excellent waveforms four various MT methods were applied. The first two methods are the absolute MT methods using peak-to-peak amplitudes and its polarities and full waveform of compressional and shear wave. The second two methods are relative methods with reference and without reference mechanism as described in Section 2. Figure 21 shows an example of inversion calculation using the full waveform MT method for one single event. The figure shows the calculated P-wave radiation pattern in a projection to the lower hemisphere. The dotted are comprises of compressional first motion, the white area those of dilatational motion. The directions of the calculated maximal compressional and dilatational radiation, called P and T axes, are indicated by black and white triangles, respectively. Experimental values in this diagram are the directions of the rays from source to sensor. They are indicated as circles. Black and open circles correspond to compressional and dilatational first motion, respectively. Prerequisite for conformity of experimental and calculated data is that black circles lie in the dotted area and open circles in the white area, which is the case in the present example.

In addition, the detected P-wave signals at the eight sensors (the number indicates the channel) are plotted in Figure 21. The traces are scaled to a common maximum. It can be seen, that the polarities of the P-wave first motion are negative for Channels 1 and 5.

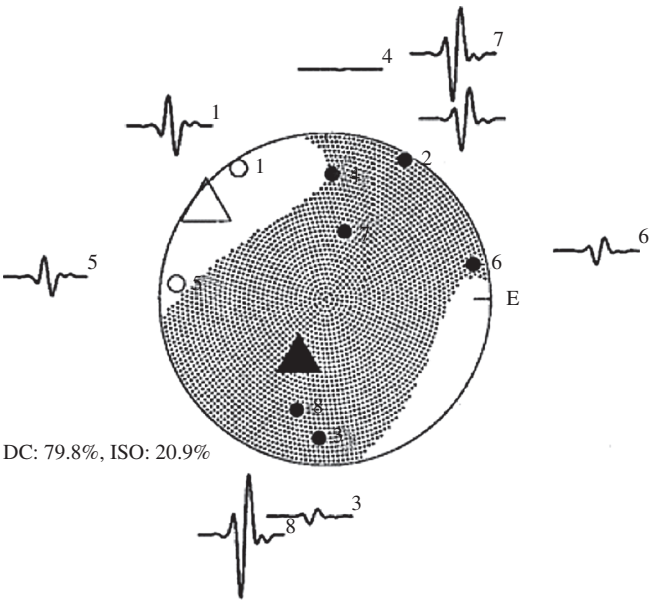


Figure 21 P-wave radiation pattern in projection to the lower hemi-sphere (equal area projection, north is at the top) and the detected P waveforms at the eight sensors. P and T axes are given with black and white triangles, respectively. Projected rays are plotted as circles. Black and white circles indicate compressional and dilatational first motion, respectively (Manthei *et al.*, 2001).

The biggest and smallest amplitudes were measured at Sensors No. 8 and 4, respectively. Sensor No. 8 is very close to the P axis. Sensor No. 4 lies within a few degrees of the nodal lines. In direction of nodal lines no waves are radiated. This example shows good agreement between the observed and calculated radiation pattern. The decomposition leads to a double-couple component of approximately 79% and to an isotropic component of approximately 21%. It was found that the events show similar radiation patterns with a major double-couple component, and that the orientations of the microscopic crack planes found by MT do not coincide with the macroscopic fracture planes indicated by source locations. Dahm *et al.* (1999) assumed that shear failure occurred on horizontal, preexisting planes of weakness indicated by horizontal layers, which are observed within the salt rock at the test site.

3.3 Application of the MT method on rock samples

3.3.1 Mechanical properties of rock

Well performed laboratory deformation tests were used to develop the constitutive equations which are prerequisites for the computer analysis of the coupled thermal, mechanical, and hydraulic processes in rock and for the prediction of the long-term behavior of a rock formation especially for underground repositories or storage caverns (*e.g.* storage of gas and oil).

Pusch & Alkan (2002) investigated the gas permeation through cylindrical rock salt specimens under triaxial compression in relation to dilatancy development under deviatoric stress conditions. Similarly to previous studies, they observed a spontaneous increase in permeability by some orders of magnitude shortly after the so-called dilatancy boundary (DB) was exceeded. The DB separates the elastic compression phase with volume decrease from the dilatant deformation phase with volume increase. They attributed this permeability increase to the percolation of gas along the extended grain boundaries of the rock salt. Simultaneous AE measurement demonstrated that the percolation begins simultaneously throughout the specimen.

The following two examples present the application of the MT method on rock samples in order to investigate failure and dilatation of rock. The MT is an adequate method of describing sources with volumetric components such as tensile cracks. Tensile cracks are mainly responsible for dilatancy. Thus, it is possible to recognize zones of higher permeability for fluids, which plays an important role for use of a rock formation as radioactive waste disposal. Due to the higher sensitivity in laboratory experiments the number of detected AE events is much higher compared with measurements in mines. Besides the high sensitivity of AE event detection, laboratory measurements provide an opportunity of very good sensor coverage of the focal sphere, which is necessary for a precise source location and stable MT solutions.

3.3.2 Sandstone sample

Aker *et al.* (2014) studied the variety of source mechanisms of AE events associated with crack initiation, healing, and macroscopic failure of a rock sample during triaxial stress. The experimental setup consists of a rock sample mounted inside a triaxial load cell controlling the axial (vertical) stress, the radial confining pressure, and the pore pressure of the fluid inside the rock (Fig. 22a). The rock sample is a cylindrical specimen of Vosges sandstone with 50.8 mm diameter and 127 mm length. A small cylindrical borehole of 5.2 mm was horizontally drilled at mid-height through the sample (Fig. 22b). An array of twelve piezoelectric AE sensors (pinducers with resonance frequency of about 1 MHz) was mounted at the surface of the sample (Fig. 22c). Additional, ultrasonic measurements of compressional-(P) and shear-(S) wave velocities in axial and radial directions was carried out.

In total, 1,072 AE events could be located using at least six P-wave onsets. The location of a subset of 305 AE events, which was located using at least ten P-wave onsets are shown in Figure 23a overlaid on a cross-sectional X-ray CT image. It can be seen, that the location of the events match well the macroscopic fractures developed during the experiment. A set of 162 AE events was considered having high quality waveforms for the MT inversion. The location of these events is shown in Figure 23b and 23c. In these figures the events are colored according their origin time and according to different stages of the experiment, respectively.

The MTs were calculated using at least six manually picked P-wave first motion amplitudes. The results of the MT inversion are shown in the Hudson T–k plot in Figure 24. Figure 24a displays the Hudson plot subdividing the coordinate space into different source mechanisms. Figures 24b to 24d display the solutions for all 162 events colored according to their distance from the borehole, their origin time, and their seismic moment, respectively.

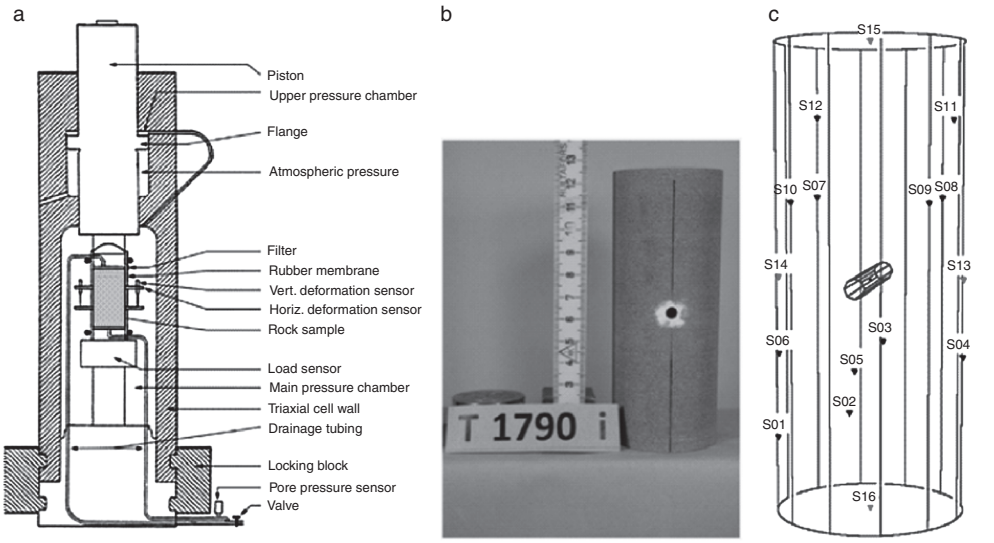


Figure 22 The principle of the triaxial load cell (a), the cylindrical sandstone specimen with the 5.2 mm diameter central borehole (b), position of twelve pinducers (S01 to S12), and four ultrasonic transducers (S13 to S16) (c) (Aker *et al.*, 2014).

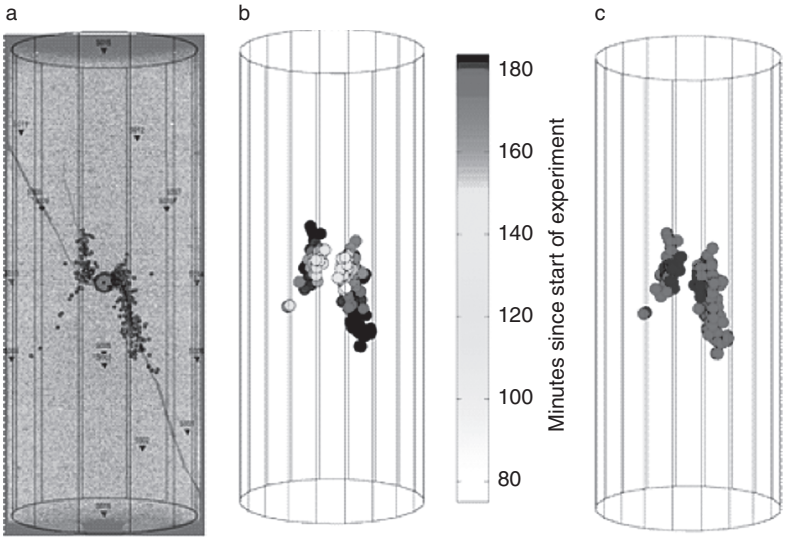


Figure 23 (a) Locations of 305 AE events overlaid on a 2D-longitudinal cross sectional cut of the 3D X-ray CT image. (b) Location of 162 events selected for MT inversion, colored according to origin time in minutes after start of the experiment. (c) The same events as shown in (b) colored according to the stage of the experiment (Aker *et al.*, 2014).

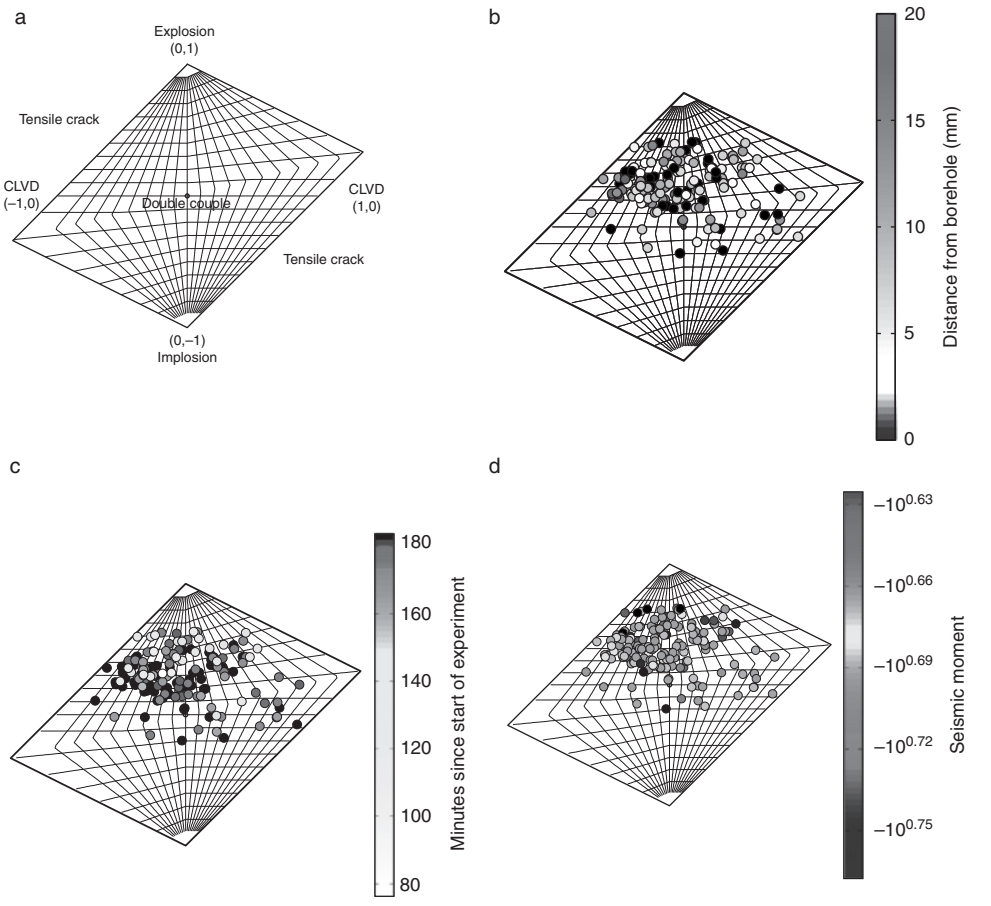


Figure 24 Hudson diagrams of the events. Top left: Interpretation of *T–k* coordinates. Top right: *T–k* plot of 162 events shaded according to distance from the borehole. Bottom left: *T–k* plot of 162 events shaded according to origin time since start of the experiment. Bottom right: *T–k* plot of 162 events shaded according to relative seismic moment (Aker *et al*., 2014).

The seismic moments of the analyzed events as well as their double-couple percentages increase in time (and thus with increasing the deviatoric stress); the isotropic components decrease in time. The majority of events are situated in the upper half of the Hudson plot indicating a tendency of fractures to be opened. Aker *et al*. (2014) observe that events with small seismic moments are related to more tensile mechanisms, whereas events having large seismic moments are close to pure shear mechanisms.

It can be concluded, that events close to the borehole show a higher portion of isotropic percentage in MT compared to events occurring in the macroscopic fracture featuring higher DC percentages. The horizontal borehole interferes with the applied load and forms a strong spatially dependent anisotropic stress field, focusing the crack initiation into both shear and tensile failures.

3.3.3 Rock salt sample

A compression experiment on a cylindrical rock salt specimen (diameter 150 mm, length 300 mm, Fig. 25) from the Asse salt mine was carried out in the laboratory of the Department for Waste Disposal Technology and Geomechanics at the Technical University of Clausthal, Germany. During the test the axial displacement and axial force, the radial pressure, and the volume change (dilatancy) of the specimen were measured and stored.

AE measurements were carried out using an array of 12 AE wide-band sensors (Fig. 25, E1 to E12), which were glued to the surface of the specimen. The positions S1 to S3 were used for separate senders for ultrasonic transmission measurements during the compression test in axial and at two height levels in radial direction. The AE measuring system included three four-channel transient recorder cards in a personal computer. These cards (sampling rate 10 MHz, resolution 14 bit, storage capacity 512 kByte per channel) were read each time when at least two channels were hit. The digitized signals were stored on the hard disk of the personal computer. Starting at an isotropic pressure of 5 MPa, an increasing axial compression load was applied in such a way that a constant axial strain rate of $8.33 \cdot 10^{-6}$ sec^{-1} was produced. The maximum and minimum principal stresses were in radial and axial direction, respectively. The ultimate axial stress was approximately 55 to 60 MPa. During the experiment (duration 4.5 hours) about 100,000 events were recorded. The location of the events was made off-line after the test. As the signals showed a surprisingly good signal-to-noise ratio (Fig. 26) automatic location was possible. Approximately 57% and 30% of these events were locatable using at least 8 and 16 consistent P- and S-wave onsets, respectively.

Manthei (2005) demonstrates the application of the MT method to analyze automatically this huge amount of AE events. The source mechanisms could be evaluated on

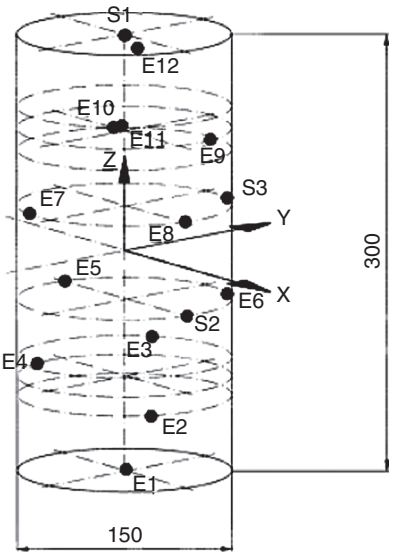


Figure 25 Geometry of the rock salt specimen and AE sensor positions (Manthei, 2005).

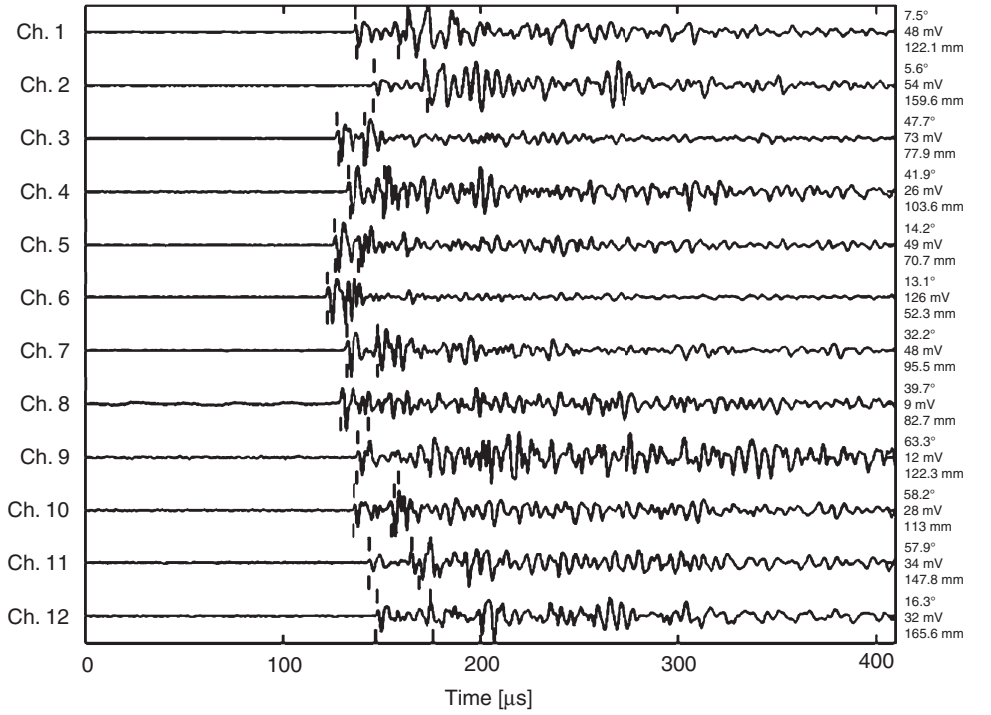


Figure 26 Event originated from the lower half of the specimen. The onsets of the picked and calculated P- and S-wave arrivals are marked by ticks above and below the signal trace, respectively (Manthei, 2005).

about 15% the detected events, and stable MT solutions were obtained on 12.5% on the detected events, whereas 2.5% of the events did not fulfill the stability criteria. This means that the events showed too large misfit between measured and calculated first-motion amplitudes.

Figure 27 displays in its upper part the position of tension axes (T axes) in a vertical coordinate plane (x-z-plane) and in its lower part the density of T axes in an equal-area projection to the lower hemisphere in five stages. The figure shows at top the T axes by means of small dashes, which were rotated in such a way that the axes lie in the vertical coordinate planes. The z axis corresponds to the loading direction. The shape of the contour of the rock specimen at the end of each stage is plotted as a box. Apart from few events, which were recorded at the beginning of the test (figure at the left-hand side) most of the T axes are nearly horizontal orientated. The T axes are distributed around the focal sphere at plunge below 30°. One accumulation of events has been formed in direction of approximately 54° in azimuth (measured clockwise from top) and of 15° in plunge which becomes stronger with increasing axial stress.

In order to study the distribution of the volumetric and double-couple components the events were separated into two fractions: events with exclusively compressional first motions and events with dilatational first motion at least at one channel. The latter

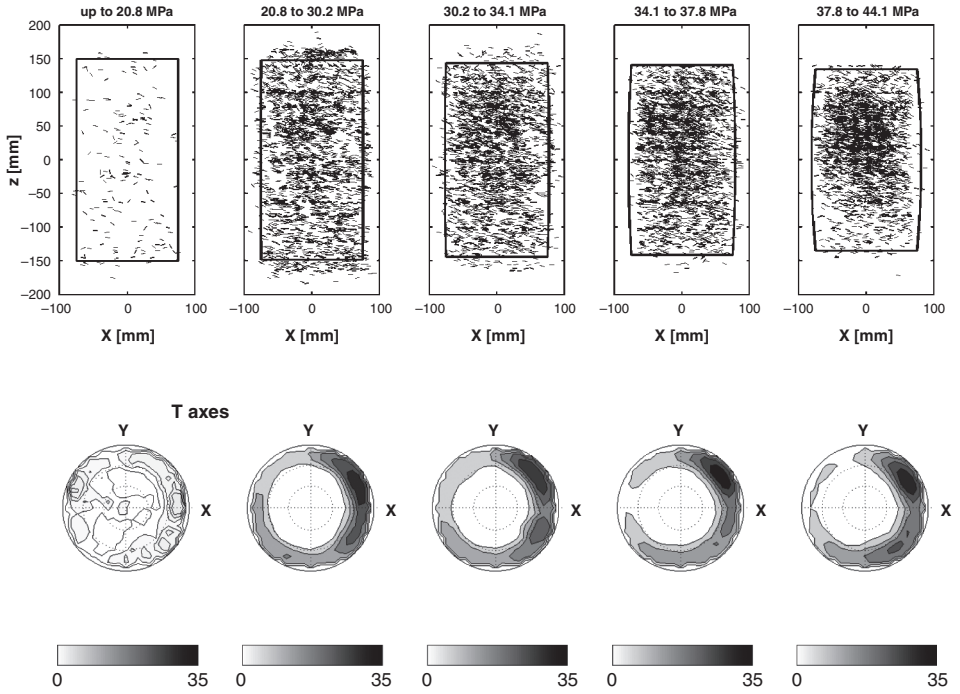


Figure 27 At top: position of T axes marked by small dashes, which are lying in the vertical x-z-projection plane in five successive stages. The black boxes are the contour of the specimen after reaching the final stress at each stage. At bottom: distribution of the T axes in an equal-area projection on the lower hemisphere (Manthei, 2005).

fraction includes only about 2.5 per cent of all events. The histograms of the volumetric and double-couple components of both fractions are shown in Figure 28. The distribution of the fraction with compressional first motion is indicated by unfilled bars, the other with partly dilatational first motion is indicated by filled bars.

At top of Figure 28 shows the distribution of the R value of all evaluated events. The R value defined by Feignier & Young (1992) as the ratio of the isotropic component to the sum of the isotropic and deviatoric component. Additionally, the specific R values of a pure implosional source at -100%, pure explosional source at 100%, pure shear source at R = 0 per cent, and pure tensile source at 67% are marked by arrows. The R values show a peaked distribution with maximum at 54% close to the R value of a pure tensile source. At higher values the distribution quickly tails off. At lower R values the tail reaches down to negative values indicating the presence of few events with partly implosional source components. It can be seen that the predominant source mechanism is of tensile type. Pure explosional sources do not occur.

The distribution of the volume change (at bottom of Fig. 28) shows that most of the events have volume changes below about 50 mm^3 with a pronounced increase to very small values. The total amount of dilatancy calculated from the MTs by adding up the volume change of all events is about 150 ml. The survey of the rock specimen after the

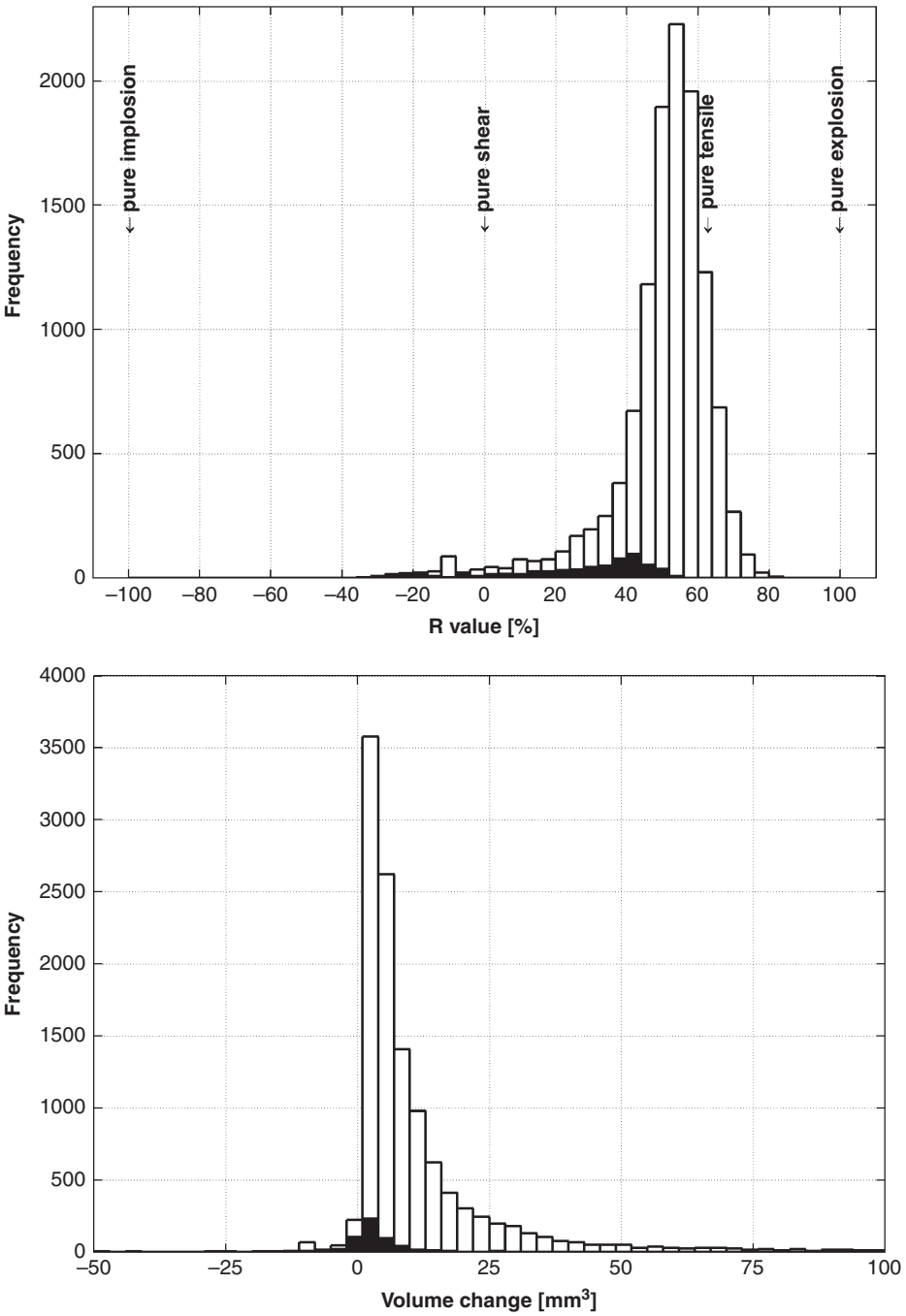


Figure 28 Top: Histogram of R values of all 12,500 evaluated events. The R values of pure explosion sources, pure implosion sources, pure shear sources, and pure tensile sources are marked by arrows. Bottom: Histogram of the volume change (in mm3) in the acoustic emission (AE) sources (Manthei, 2005).

test pointed out that the average diameter of the rock specimen had increased from originally 150 mm to 158.2 mm and that the final axial deformation was about 26.4 mm. According to these dimensions the actual dilatancy of the specimen was about 75,6 ml. That means, that the calculated dilatancy is two times higher than the measured one. It can be even more, because small events, which are not considered in the MT evaluation, contribute to the volume, but with much smaller amount than the big events. This discrepancy between measured and calculated dilatancy can be explained by the fact that open cracks were partly closed due to the applied confining pressure. This suggests that some of the opened cracks close during further loading of the specimen.

Manthei (2005) concluded, that two types of microcracks are observed in rock salt under dilatant loading. Cracks of Type 1 are inter-crystalline cracks, which cause tensile opening at grain boundaries and cracks of Type 2 are intra-crystalline cracks or transcrystalline cracks on crystallographic planes (cleavage planes) within a grain. The latter kind of cracks causes no opening of crack surfaces.

During loading, cracks of Type 1 are formed at grain boundaries, which are favorably orientated in direction of the maximum principal stress, this is in the experiment in axial direction of the cylindrical specimen. With increasing load neighboring cracks become more frequent and grow together to one jointed crack, which may extend even over several neighboring grains. The direction of opening is perpendicular to maximal compression. Consequently, crack Type 1 is responsible for dilatancy and an increase of permeability for fluids.

4 SUMMARY

This chapter reviews applications of MT method of AE events in three fields, mine monitoring, hydraulic fracturing tests in rock, and testing of rock specimens in the laboratory. That means in much differing scale of some hundreds meters down to several centimeters. The MT method pointed out, that events, which were detected during mine monitoring, show high proportion of volumetric components, which are to be expected in EDZ under deviatoric stress in areas near the cavity contours or layer boundaries in the mine. The dominant mechanism is mixed mode mechanism of shear and tensile cracking. Tensile cracks are mainly responsible for dilatancy. Thus, it is possible to recognize zones of higher permeability for fluids, which plays an important role *e.g.* for use of a rock formation as underground disposal.

Similar results are observed on AE events, which were generated during triaxial compression tests of rock samples. Most of the events showed significant isotropic source components, which is in good agreement with dilatation of the rock during compressional loading. Due to the higher sensitivity in laboratory experiments the number of detected AE events is much higher compared with measurements in mines. In order to process all detected events, it is essential to evaluate the AE events in various automatic procedures such as registration of events, location of events, determination of source mechanisms, and automatic stability check of the MT solutions. Besides the high sensitivity of AE event detection, laboratory measurements provide an opportunity of a very good sensor coverage of the focal sphere which is necessary for a precise source location and stable MT solutions.

An entirely different character have source mechanisms of the events from hydraulic fracturing tests in rock. According to the results of the MT inversion shear fractures without significant volumetric source components primarily occur. It was found by the MTs, that the orientations of the microscopic crack planes do not coincide with the macroscopic fracture planes indicated by source location. The direction of the macroscopic fracture planes appears to coincide with the maximum principal stress and perpendicular to the minimum principal stress. It was assumed that shear failure occurred on preexisting planes of weakness like on geological layers in rock salt or joints in hard rock.

Conditions for the practical application of the MT method can be derived from the examples as described. With respect to the practical application it can be remarked that a sufficient large number of sensors should be arranged in such a way that the focal sphere is well covered in all directions, which is essential for the use of only P-wave first motions for location and MT inversion. This is a question of accessibility for drilling wells for sensor installation in mines or underground laboratories. The sensors should be installed far enough from excavations and galleries, so that the wave propagation will not be disturbed ("shaded") by excavated rooms and galleries.

In order to deduce a physical description of AE sources from recorded waveforms, a well-characterized AE sensor is required. Only the knowledge of physical quantity measured by the AE sensor the seismic moment can be derived from the entire MT. It is interesting to compare various relationships between seismic moment and magnitude. In literature many relationships were derived from earthquakes. Usually, the seismic magnitude is calculated from seismological empirical formulas like the famous Gutenberg-Richter relation (Gutenberg & Richter, 1956). Also admitting that only a correlation of orders of magnitudes is needed, this approach seems to be uncertain.

REFERENCES

Aker, E., Kühn, D., VavryÊuk, V., Soldal, M. & Oye, V. (2014) Experimental investigation of acoustic emissions and their moment tensors in rock during failure. *International Journal of Rock Mechanics & Mining Sciences*, 70, pp. 286–295.

Aki, K. & Richards, P.G. (2002) *Quantitative Seismology*, Second Edition, University Science Books, Sausalito, California.

Alkan, H. & Pusch, G. (2002) *Definition of the dilatancy boundary based on hydro-mechanical experiments and acoustic detection. SMRI Fall Meeting*, Bad Ischl, Austria.

Andersen, L.M. (2001) *A relative moment tensor inversion technique applied to seismicity induced by mining. Ph.D Thesis, University of the Witswatersrand*, Johannesburg.

Baker, C. & Young, R.P. (1997) Evidence for extensile crack initiation in point source time-dependent moment tensor solutions. *Bulletin of the Seismological Society of America*, 87 (6), pp. 1442–1453.

Brace, W.F., Paulding, B.W. & Scholz, C. (1966) Dilatancy in the fracture of crystalline rocks. *Journal of Geophysical Research*, 71 (16), pp. 3939–3953.

Cai, M., Kaiser, M. & Martin, P.K. (1998) A tensile model for the interpretation of microseismic events near underground openings. *Pure Applied Geophysics*, 153, pp. 67–92.

Carvalho, F.C.S. & Labuz, J.F. (2002) Moment tensors of acoustic emissions in shear faulting under plane-strain compression. *Tectonophysics*, 356, pp. 199–211.

Chang, S.-H. & Lee, C.-I. (2004) Estimation of cracking and damage mechanisms in rock under triaxial compression by moment tensor analysis of acoustic emission. *International Journal of Rock Mechanics & Mining Sciences*, 41, pp. 1069–1086.

Collins, D.S., Pettitt, W.S. & Young, R.P. (2002) High-resolution Mechanics of a Microearthquake Sequence. *Pure Applied Geophysics*, 159, pp. 197–219.

Dahm, T. (1996) Relative moment tensor inversion based on ray theory: theory and synthetic tests, *Geophysical Journal International*, 124, pp. 145–257.

Dahm, T., Manthei, G. & Eisenblätter, J. (1998) Relative moment tensors of thermally induced microcracks in salt rock, *Tectonophysics*, 289, pp. 61–74.

Dahm, T., Manthei, G. & Eisenblätter, J. (1999) Automated moment tensor inversion to estimate source mechanisms of hydraulically induced micro-seismicity in salt rock, *Tectonophysics*, 306, pp. 1–17.

Eisenblätter, J. (1980) *The origin of acoustic emission – Mechanisms and models*. In: *Acoustic Emission*, Conference in Bad Nauheim, Deutsche Gesellschaft für Metallkunde e.V., pp. 189–204.

Eisenblätter, J. (1988) *Localisation of fracture planes during hydraulic fracturing experiments in a salt mine*. In: *Acoustic Emission*, Deutsche Gesellschaft für Metallkunde e.V., Oberursel, pp. 291–303.

Eisenblätter, J., Manthei, G. & Meister, D. (1998) *Monitoring of Microcrack Formation around Galleries in Salt Rock*. In: Hardy, H.R. (ed.) Acoustic Emission/Microseismic Activity in Geologic Structures and Materials: Proceedings of the Sixth Conference, Trans Tech Publications, Clausthal-Zellerfeld, pp. 227–243.

Fakhimi, A., Carvalho, F.C.S., Ishida, T. & Labuz, J.F. (2002) Simulation of failure around circular opening in rock. *International Journal of Rock Mechanics & Mining Sciences*, 39, pp. 507–515.

Falls, S.D. & Young, P.R. (1998) Acoustic emission and ultrasonic-velocity methods used to characterise the excavation disturbance associated with deep tunnels in hard rock. *Tectonophysics*, 289, pp. 1–15.

Feignier, B. & Young, R.P. (1992) Moment Tensor Inversion of Induced Microseismic Events: Evidence of Non-Shear Failure in the -4<M<-2 Moment Magnitude Range, *Geophysical Research Letters*, 19 (14), pp. 1503–1506.

Frohlich, C. (1994) Earthquakes with non-double-couple mechanisms. *Science*, 264, pp. 804–809.

Graham, C.C., Stanchits, S., Main, I.G. & Dresen, G. (2010) Comparison of polarity and moment tensor inversion methods for source analysis of acoustic emission data. *International Journal of Rock Mechanics & Mining Sciences*, 47, pp. 161–169.

Gutenberg, B. & Richter, C.F. (1954) Seismicity of the Earth, *Princton University Press*.

Hudson, J.A., Pearce, R.G. & Rogers, R.M. (1989), Source type plot for inversion of the moment tensor. *Journal of Geophysical Research*, 94 (B1), pp. 765–774.

Hunsche, U. & Hampel, A. (1999) Rock Salt – the mechanical properties of the host rock material for a radioactive waste repository. *Engineering Geology*, 52, pp. 271–291.

Jost, M.L. & Herrmann, R.B. (1989) A student's guide to a review of moment tensors. *Seismological Research Letters*, 60, pp. 37–57.

Kao, C.-S., Carvalho, F.C.S. & Labuz, J.F. (2011) Micromechanisms of fracture from acoustic emission. *International Journal of Rock Mechanics & Mining Sciences*, 48, pp. 666–673.

Kim, K.Y. & Sachse, W. (1988) Study of brittle fracture by acoustic emission from indention cracks. *Journal of Applied Physics*, 65 (11), pp. 4234–4244.

Kishi, T. & Enoki, M. (1988) *Three Dimensional Location, Dynamic Green's Function and Source Moment Tensor in Acoustic Emission Signal Analysis*. In: *Acoustic Emission*, Conference in Bad Nauheim, Deutsche Gesellschaft für Metallkunde e.V., pp. 25–36.

Kwiatek, G., Charalampidou, E.-M., Dresen, G. & Stanchits, S. (2014) An improved method for seismic moment tensor inversion of acoustic emissions through assessment of sensor coupling

and sensitivity to incidence angle. *International Journal of Rock Mechanics & Mining Sciences*, 65, pp. 153–161.
Lockner, D. & Byerlee, J. (1977) Hydrofracture in Weber Sandstone at high confining pressure and differential stress. *Journal of Geophysical Research*, 82 (B14), pp. 2018–2026.
Manthei, G., Eisenblätter, J. & Salzer, K. (1998) *Acoustic Emission Studies on Thermally and Mechanically Induced Cracking in Salt Rock*. In: Hardy, H.R. (ed.) Acoustic Emission/ Microseismic Activity in Geologic Structures and Materials: Proceedings of the Sixth Conference, Trans Tech Publications, Clausthal-Zellerfeld, pp. 245–265.
Manthei, G., Eisenblätter, J., Spies, T. & Eilers, G. (2001) Source parameters of acoustic emission events in salt rock. *Journal of Acoustic Emission*, 19, pp. 100–108.
Manthei, G., Eisenblätter, J. & Dahm, T. (2001) Moment tensor evaluation of acoustic emission sources in salt rock. *Construction and Building Materials*, 15, pp. 297–309.
Manthei, G. (2005) Characterization of Acoustic Emission Sources in a Rock Salt Specimen under Triaxial Load. *Bulletin of the Seismological Society of America*, 95, pp. 1674–1700.
Manthei, G., Eisenblätter, J. & Spies, T. (2007) *Source Mechanisms of Acoustic Emission Events between huge Underground Cavities in Rock Salt*. In: Advances in Acoustic Emission 2007, Proceedings of the Sixth International Conference on Acoustic Emission, Lake Tahoe, Nevada, USA, pp. 288–293.
Manthei, G. & Eisenblätter, J. (2008) *Acoustic Emission in Study of Rock Stability*. In: Grosse, C.U. & Ohtsu, M. (eds.) *Acoustic Emission Testing*, Springer-Verlag Berlin Heidelberg, pp. 239–310.
Michaels, J.E. & Pao, Y.H. (1985) The inverse source problem for an oblique force on an elastic plate. *Journal of the Acoustic Society of America*, 77, pp. 2005–2011.
Miller, A.D., Foulger, G.R. & Julian, B. R. (1998) Non-double-couple earthquakes. 2. Observations. *Reviews of Geophysics*, 36, pp. 551–568.
Müller, G. (1973) Seismic moment and long-period radiation of underground nuclear explosions. *Bulletin of the Seismological Society of America*, 63, pp. 847–857.
Müller, G. (2001) Volume Change of Seismic Sources from Moment Tensors. *Bulletin of the Seismological Society of America*, 91 (4), pp. 880–884.
Niitsuma. H., Nagano, K. & Hisamatsu. K. (1993) Analysis of acoustic emission from hydraulically induced tensile fracture of rock. *Journal of Acoustic Emission*, 11, pp. S1–S18
Obert, L. (1977) *The Microseismic Method: Discovery and Early History*. In: Hardy, R.H. & Leigthon F.W. (eds) Acoustic Emission/Microseismic Activity in Geologic Structures and Materials: Proceedings of the first Conference, Trans Tech Publications, Clausthal-Zellerfeld, pp. 11–12.
Ohtsu, M. & Ono, K. (1986) The Generalized Theory and Source Representation of Acoustic Emission. *Journal of Acoustic Emission*, 5 (4), pp. 124–133.
Ohtsu, M. (1991) Simplified Moment Tensor Analysis and Unified Decomposition of Acoustic Emission Sources: Application to In Situ Hydrofracturing Test. *Journal of Geophysical Research*, 96 (B4), pp. 6211–6221.
Ohtsu, M. (2000) *Moment Tensor Analysis of AE and SiGMA Code*. In: Kishi, T., Ohtsu, M. & Yuyama, S. (eds.), *Acoustic Emission – Beyond the Millennium*, Elsevier, pp. 19–34.
Read, R. S. & Martin, C. D. (1991) *Mine-by experiment final design report*. Atomic Energy of Canada Limited internal report. Report number AECL–10430.
Rice, J.R. (1980) Elastic wave emission from damage processes. *Journal of Nondestructive Evaluation*, 1, pp. 215–224.
Scholz, C.H. (1968) Microfracturing and the Inelastic Deformation of Rock in Compression. *Journal of Geophysical Research*, 73 (4), pp. 1417–1432.
Scruby, C.B., Wadley, H.N.G. & Hill, J.J. (1983) Dynamic elastic displacement at the surface of an elastic half-space due to defect sources. *Journal of Applied Physics*, 16, pp. 1069–1083.

Sellers, E.J., Kataka, M.O. & Linzer, L.M. (2003) Source parameters of acoustic emission events and scaling with mining-induced seismicity. *Journal of Geophysical Research*, 108 (B9), pp. 2418–2430.

Shah, K.R. & Labuz, J.F. (1995) Damage mechanisms in stressed rock from acoustic emission. *Journal of Geophysical Research*, 100 (8), pp. 15,527–15,539.

Silver, P.G. & Jordan, T.H. (1982) Optimal estimation of scalar seismic moment. *Geophysical Journal of the Royal Astronomical Society*, 70, pp. 755–787.

Spies T., Hesser J., Eisenblätter J. & Eilers, G. (2004) Monitoring of the rockmass in the final repository Morsleben: experiences with acoustic emission measurements and conclusions. In: Proceedings DisTec 2004, Berlin, pp. 303–311.

Thompson, B.D., Young, R.P. & Lockner, D.A, (2009) Premonitory acoustic emissions and stick-slip in natural and smooth-faulted Westerly granite. *Journal of Geophysical Research*, 114 (B2).

Wadley, H.N.G., Scruby, C.B. & Shrimpton, G. (1981) Quantitative Acoustic Emission characterization during low temperature cleavage and intergranular fracture. *Acta Metallurgica*, 29, pp. 399–414.

Young, R.P. & Martin, C.D. (1993) Potential Role of Acoustic Emission/Microseismicity Investigations in the Site Characterization and Performance Monitoring of Nuclear Waste Repositories. *International Journal of Rock Mechanics & Mining Sciences*, 30, pp. 797–803.

Young, R.P., Collins, D.S., Reyes-Montes, J.M. & Baker, C. (2004) Quantification and interpretation of seismicity. *International Journal of Rock Mechanics & Mining Sciences*, 41, pp. 1317–1327.



Taylor & Francis
Taylor & Francis Group
http://taylorandfrancis.com

Chapter 17

Fiber-optic monitoring in underground rock engineering

*H.F. Wang & J.R. Gage**
Department of Geoscience, University of Wisconsin – Madison, USA
**currently at Chevron Energy Technology Company, Houston, Texas, USA*

Abstract: Fiber-optic sensing of deformation and temperature has characteristics that make it a promising, emerging technology for applications in underground rock engineering. In general, there are two main types of fiber-optic sensors, discrete and distributed. Discrete sensors respond to strain and temperature, by changes in spacing of a diffraction grating in the fiber or in a cavity between two ends of fiber that are micrometer-scale. In distributed sensing, the fiber optic cable itself is the strain and temperature sensor. Distributed sensors are based on Rayleigh, Raman, and Brillouin scattering of light from the fiber-optic cable itself. The backscattered light can be analyzed for strain and/or temperature with a spatial resolution of one meter. In this chapter, the physics underlying Fiber Bragg Gratings (FBG), SOFO, Distributed Temperature Sensing (DTS), Distributed Strain and Temperature (DST), and Distributed Acoustic Sensing (DAS) are described. Several prototype case studies of fiber-optic monitoring in underground mines, recent developments in fiber-optic extensometers, and fiber-optic sensing in boreholes in the oil and gas industry are reviewed.

1 INTRODUCTION

This chapter describes the state-of-the-art in fiber-optic sensing for underground structures from the perspectives of geomechanics, geophysics, and Structural Health Monitoring (SHM). The organization of this chapter is first to describe the principles of discrete and distributed fiber-optic sensing systems and their associated technologies. Next, several research projects are described that provide proof-of-concept case histories that utilize discrete fiber-optic sensors and distributed temperature sensing for underground applications. Third is a discussion of how and when fiber-optic sensing can be combined with conventional deformation sensors. Fourth, applications of fiber-optic sensing in oil and gas wells are described. Then, the review closes with a section that summarizes the pros and cons of fiber-optic sensing in comparison with conventional techniques, but with the general conclusion that future advances are likely to lead to increasing adoption.

The words 'fiber optic' conjure up its ubiquitous presence in telecommunications and the internet. Because the fused silica and wave-guide construction of fiber-optic cables have very low attenuation, they can transmit information over distances of tens of kilometers. Also, because light carries the information, fiber-optic cables are immune to interference from electromagnetic radiation. Therefore, fiber-optic sensors can be

installed adjacent to power lines, or be subjected to very high electric fields associated with high magnetic fields in physics accelerators. As a practical example, electrical strain sensors were routinely damaged by lightning strikes on the bare granite face of Mt. Rushmore before Fiber Bragg Grating (FBG) strain sensors were substituted for Linear Variable Differential Transformers (LVDTs) (Micron Optics, 2010).

Another aspect that makes fiber optics a robust technology for underground monitoring is the fiber-optic cable itself. The fused silica core of the fiber is chemically inert, lightweight, and has a reasonable strength for long-term durability under ambient conditions typical in underground facilities. At high temperatures, considerations need to be made with regard to the cable jacket material, and at very high temperatures, such as in geothermal wells, diffusion of hydrogen into glass produces fiber darkening. Operating temperatures between –20 to +60 °C, which are required for fiber-optic interrogation equipment, are similar to that of most electronic components and computers. Fiber-optic cable itself responds to environmental variables of stress and temperature, which makes it a distributed environmental sensor in addition to being the medium for transmitting the information.

Applications of fiber-optic sensing in Structural Health Monitoring (SHM) have increased rapidly (Glišić & Inaudi, 2007). In SHM, measurements of load, deformation, and temperature are recorded over both long and short time periods (Kincade, 2006) to give information concerning the condition and performance of structures (Glišić & Inaudi, 2007). SHM not only provides a warning of imminent failure of a structure, but in the best case scenario, the data from SHM can be used to plan maintenance activities to prevent failure from being reached, thus increasing the safety, performance, and longevity of civil structures.

Many of the techniques developed in SHM for bridges, buildings, rail, and pipelines are directly applicable to deep, large underground facilities. Tunnels are already generally considered to be within the purview of SHM (Glišić & Inaudi, 2007). The high stress fields experienced in underground openings and their anticipated lifetimes of years to decades to centuries require the ability to predict rock mass stability under loading. Monitoring and predicting deformation in the rock mass are critical to ensure the safety of human occupants and the longevity of the underground space. Tunnels, mines, pumped storage facilities, nuclear waste storage facilities, deep boreholes, and underground physics laboratories are built at depths up to 5000 meters, in different geologic environments, and hence in different stress regimes requiring different monitoring systems and techniques.

The constantly changing geometry of underground openings in mines presents special challenges for monitoring. Although not the focus of this review, boreholes for hydrocarbon or heat extraction or for fluid injection are another category of underground engineered space in which strain and temperature are measured and monitored. Rock heterogeneity and complex geometry of underground spaces mean that the spatial variability of deformation occurs from the grain-scale of millimeters to the facility-scale, which can be tens of kilometers in dimension. The time variability of deformation also can occur over several orders of magnitude. It can be sudden in the case of a rock burst or it can be slow squeezing over decades.

Beginning with the design phase, deformation prediction is typically based on finite element models using available or estimated rock properties. As with most geoengineering problems, much of the difficulty of prediction lies in the inability to characterize

adequately the rock properties, especially discontinuities. As a consequence, semi-quantitative measures, such as Rock Mass Rating (RMR) or the Hoek-Brown Geological Structure Index (GSI) (Hudson & Harrison, 1997), are used to characterize the rock mass together with empirical charts for design criteria such as rock bolt spacing for ground control.

During and following construction, validating model predictions is necessary to assess their performance. Parameter adjustment, or even the physics incorporated within the model, can be revised using back analysis. Thus, monitoring should be a continuous or periodic process over the life of the facility, which requires systems with inherent longevity and durability. For civil structures, the post-construction era will be measured in decades. With the inherent uncertainties and high stresses associated with the deep underground environment, the potential for rock failure must always be borne in mind. Mitigating the risk is prudent, but a formal cost-benefit analysis may be precluded by the uncertainties. Keeping abreast of the condition of the facility through Structural Health Monitoring (SHM) is gaining acceptance for underground construction (Bhalla *et al*., 2005).

One reason for the growth in research in underground monitoring is that maturing technologies, like fiber-optic sensors and their associated instrumentation, can collect data that were not previously achievable. Fiber-optic sensors are robust and geometrically flexible, possess long-term stability, are cost effective, extend coverage in spatial extent with improved resolution, and provide data at a higher sampling rate than many traditional strain monitoring technologies. In addition to fiber-optics, a host of new technologies with potential for underground geotechnical applications exist, including LIDAR, wireless "smart dust", piezoelectric sensors, and high resolution electrical and seismic imaging (Gochioco, 2000; Warneke *et al*., 2001; Haneberg *et al*., 2005; Barbosa *et al*., 2009; Sloan *et al*., 2007). All these options should be considered when designing a monitoring program.

Duncliffe (1998) was one of the first to recognize the potential for fiber-optic sensors for geotechnical monitoring. Currently, fiber-optic sensors are used for several geotechnical applications such as monitoring convergence in underground tunnels (Inaudi *et al*., 1998b), monitoring temperature and strain at thousands of points over 300 kilometers of pipeline (Glišić & Inaudi, 2007), and monitoring deformations caused by the construction of tunnels (Klar & Linker, 2010). Additionally, most fiber-optic sensors have a conventional counterpart. For example, a discrete FBG "patch" gauge with a gauge length up to a few centimeters provides data similar to an electrical resistance foil gauge. Thus, substituting fiber-optic strain sensors for traditional monitoring techniques in underground structures is appealing.

Sensors range from bare fiber-optic filaments (125-500 μm in diameter) to gauge lengths of 1 cm to 10 m to distributed cables measuring strain or temperature along their lengths continuously for over tens of kilometers. Thus, possibilities exist to instrument a single rock bolt with several gauges, a pillar face with tens of centimeter-long gauges, and even entire lengths of drifts and shafts in an underground mine. Additionally, once installed, fiber-optic sensors can be monitored remotely, which reduces the number of personnel underground, making any mining operation safer.

In general, fiber-optic sensors can have several advantages over traditional SHM methods, which make them ideal for monitoring intact rock in a subsurface setting. They are relatively inexpensive, lightweight, versatile, and long-lasting (Zhang *et al*.,

2006). Measurements that are based on frequency-shifts are stable over time. Because glass is an inert substance, fiber-optic sensors are resistant to most chemicals and they are immune to electromagnetic interference, and they show small-to-no creep deformation. Many types of sensors can be incorporated in a single data-acquisition cable, and the promise is that the methods will become even better, cheaper, and faster in the future.

2 PHYSICS OF FIBER-OPTIC SENSING TECHNOLOGIES

Fiber-optic sensors consist of two main types: discrete and distributed. Discrete fiber-optic sensors are similar to electrical resistance strain gauges. They have a finite gauge length and measure displacement or strain between the endpoints of the gauge. Discrete fiber-optic sensors are attached directly to the rock mass by embedding them in a grouted borehole or anchoring them to the rock surface (Gage *et al.*, 2010). They can be highly miniaturized as implemented in their medical applications (Rao *et al.*, 1998). Or they can be manufactured into a fiber that is part of an assembly that has a larger gauge length. These different gauge lengths lead to classifying discrete fiber-optic sensors as 'long-gauge' or 'point' sensors (Glišić & Inaudi, 2007). Discrete fiber-optic sensors include Structural Monitoring by Fiber Optics (SOFO)[1] and Fiber Bragg Grating (FBG) sensors.

In distributed fiber-optic sensing, the fiber itself is the sensor. Distributed fiber-optic sensing, whether strain or temperature, has a spatial and temporal resolution over which the measurement is averaged and measurements are taken over the entire length of the cable. The three main types of distributed sensing are Distributed Temperature Sensing (DTS), Distributed Strain and Temperature (DST) and Distributed Acoustic Sensing (DAS). Typical spatial resolutions in distributed sensing are one meter and sampling rates range from one kilohertz to one sample per second or lower depending on the application. The spatial sampling and continuous profile for DST, DTS, and DAS lead to the monikers "thermometer per meter", "strain gauge per meter", and "seismometer per meter", respectively. The total length of a distributed fiber-optic sensor can be tens of kilometers. A so-called 'quasi-distributed' sensor can be made of daisy-chained discrete FBG sensors manufactured in a single, continuous fiber. Tradeoffs between cost, sensitivity, and measurement range must all be considered when choosing the type of fiber-optic sensor and configuration to employ.

2.1 Discrete sensors

Practical, highly-sensitive, discrete fiber-optic sensors are part of a system that includes not only the sensor itself but also appropriate exposure or coupling to the environment or medium for the variable of interest (strain, temperature, pressure, etc.) and the measurement instrument. The micrometer-scale precision required is often based in the two most common techniques of optical interferometry - the Michelson interferometer and the Fabry-Perot interferometer –which are used for the measurement in the FBG and SOFO sensors described below.

1 SOFO is the French acronym of "Surveillance d'Ouvrages par Fibres Optiques" (or structural monitoring by optical fibers) (Inaudi *et al.*, 1998a).

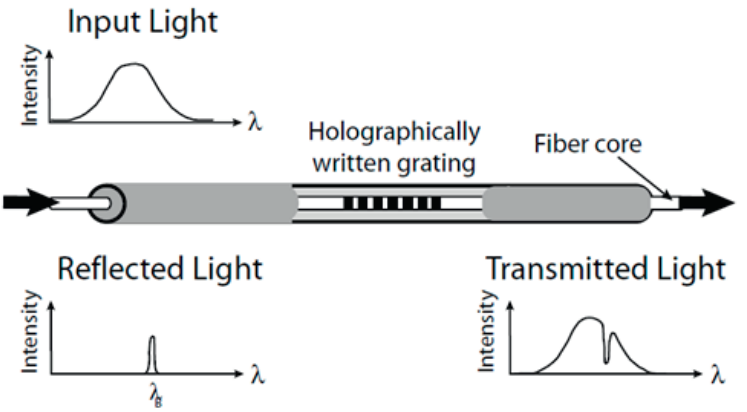


Figure 1 Diagram of a Fiber Bragg Grating with input, reflected and transmitted light spectra. Light with the wavelength of the Bragg grating (λ_B) is reflected. The Bragg wavelength changes with strain and temperature. After Hasse (2007), from Gage *et al.* (2010).

2.1.1 Fiber Bragg Grating (FBG) sensors

FBG sensors consist of a single-mode fiber surrounded by a cladding and protective coating. A periodic refractive index grating corresponding to a specific Bragg wavelength λ_B is written into the core of the fiber to form the sensor. Broad-spectrum light or a tunable laser is transmitted down the fiber from a laser interrogation box. The grating reflects a specific wavelength of light corresponding to its Bragg wavelength back to the interrogation box, and all other light is transmitted down the fiber (Figure 1) (Kersey *et al.*, 1997).Changes in strain and temperature elongate or shorten the fiber causing changes in the spacing of the diffraction grating and thus the wavelength of the reflected light. The change in the reflected wavelength of light from the FBG sensor corresponds to changes in strain and temperature (Kersey *et al.*, 1997).

Strain monitoring with FBG sensors requires a separate FBG strain gauge and temperature sensor at each measurement location. Both the FBG strain gauges and FBG temperature sensors are constructed using the same basic fiber with inscribed refraction grating as described above. In FBG strain gauges, the fiber is anchored at each end of the diffraction grating, which allows the gauge to measure the mechanical strain between the endpoints of the FBG strain gauge. However, the strain gauge is also subject to shortening and elongation from thermal strain, which requires that the effect of the environmental temperature changes be subtracted to measure the mechanical strain. In contrast, in FBG temperature sensors, the fiber and diffraction grating are fixed only at one endpoint, allowing the other end to move freely and thus only measure the shortening and elongation of the fiber due to temperature change.

In the FBG strain gauge, the change in wavelength of the reflected light is converted into raw strain (which is a sum of both the thermal and mechanical strain) using the following equation:

$$\varepsilon_{raw} = \frac{\Delta\lambda/\lambda_o}{F_G} \tag{1}$$

where ε_{raw} is the total strain measured by the change in the Bragg wavelength of the FBG sensor and $\Delta\lambda$ is the change in the Bragg wavelength. λ_0 is the reference Bragg wavelength for the sensor and F_G is the gauge factor, which is a constant that is a function of the physical properties of the materials used to construct the FBG gauges. Reference wavelengths are in the range 1500–1600 nm where light absorption is at a minimum.

In order to determine the mechanical strain measured by the FBG sensor, the thermal strain must be subtracted from ε_{raw}. Temperature change affects the shift in wavelength of the FBG stain sensors by inducing thermal strain in the fiber as well as changing the refractive index of the fiber. Thus, in order to examine mechanical strain it is necessary to apply a thermal correction to Equation 1. The thermal strain is calculated as Gage *et al.* (2012):

$$\varepsilon_{thermal} = \Delta T[(C_1/F_G) + CTE_s - C_2] \tag{2}$$

where C_1, C_2, and F_G are constants based on the gauge construction, CTE_S is the coefficient of thermal expansion of the test specimen, and ΔT is the change in temperature. Temperature (T) is calculated from the FBG temperature sensor using a manufacturer-calibrated equation.

2.1.2 Fabry-Perot sensors and wavelength analyzers

The Fabry-Perot interferometer accurately measures the distance between two mirrors whose spacing is on the order of the wavelength of light (Figure 2). An (inexpensive) incoherent, white light source multiply reflecting in the cavity returns only light that is at a wavelength of some multiple of the cavity spacing. As a measurement device, the cavity spacing in the Fabry-Perot interferometer is controlled using a piezoelectric crystal to find the peak intensity. The voltage applied to the crystal is calibrated to the cavity spacing.

A tunable Fabry-Perot interferometer is used in some commercial fiber-optic interrogation units for finding wavelength peaks of FBG sensors (*e.g.*, the Micron Optics SM125 interrogator). When a string of FBG sensors, each with its unique diffraction grating spacing, is connected on a single fiber, the SM125 can read all the spacings as the tunable laser across the entire wavelength range.

Fabry-Perot interferometry is also the basis of a strain sensor. Two glass fibers whose ends are perfectly flat oppose each other with a gap of a few microns to form the cavity (Pinet, 2009). A microcapillary glass tube anchors each fiber at a point a few millimeters from the cavity. Gluing or embedding the capillary point sensor into a material means that changes in the cavity spacing due to mechanical deformation or temperature can be converted to a measured strain.

2.1.3 SOFO sensors

SOFO sensors are extensometers containing two fibers inside a protective tube whose ends are anchored to the measurement points (Inaudi *et al.*, 1998a). Inside the tube one fiber is connected to measurement anchors and a second is a loose reference fiber (Figure 3). The change in distance between the two anchors is obtained from the

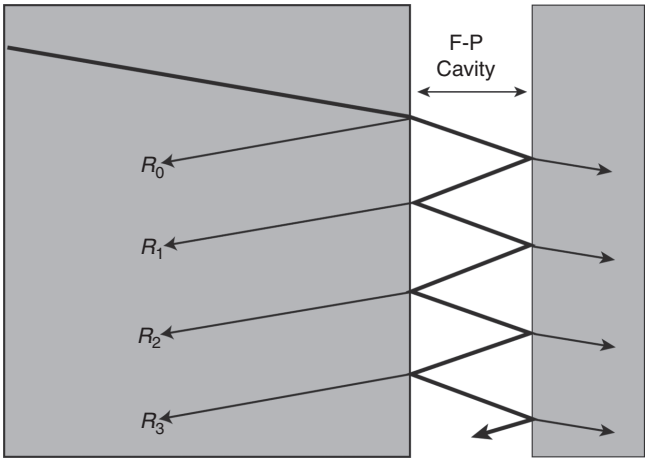


Figure 2 Schematic sketch of a Fabry-Perot sensor whose cavity is between the ends of fiber-optic cable that is anchored on both sides. As a measuring device the cavity spacing is adjustable using a piezometric device. From Pinet *et al.* (2009).

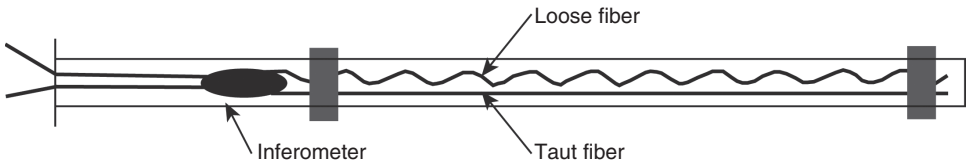


Figure 3 Schematic cross section of a SOFO sensor. One fiber is held taut between two anchors (gray bars) and the second is loose. A Michelson interferometer measures the difference in path length. From Inaudi *et al.* (1998a).

displacement of a moving mirror in one arm of a Michelson interferometer. For a near-infrared light source, whose wavelength is 1550 nm, the measurement accuracy is around 2 micrometers, regardless of gauge length. Typical gauge lengths between 20 cm and 20 m lead to strain accuracy between 0.1 and 10 microstrains. Michelson interferometry has also been used over path lengths of a hundred meters and longer in geophysical and gravity-wave applications for monitoring vertical strains in a borehole (Zumberge *et al.*, 2003) or horizontal strains in tunnels (Takemoto *et al.*, 2006). Because of the long baseline and being in a vacuum tube, strains can be measured to 10^{-13}.

2.2 Distributed sensing principles

In distributed sensing the fiber-optic cable itself is the strain and temperature sensor. A distributed sensing system sends an outgoing light pulse and then records the back-scattered light from tiny imperfections, sound waves, and molecular interactions along the entire length of the fiber. Three types of backscattering occur: Rayleigh, Raman, and Brillouin (Figure 4). The location of the backscattering event is calculated from the

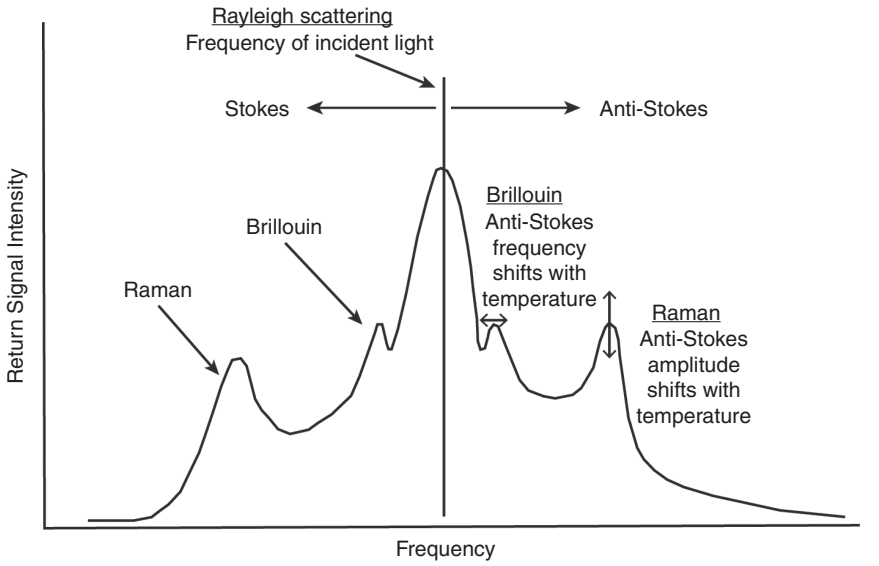


Figure 4 Schematic spectrum of backscattered light from an optical pulse in fiber-optic cable (not to scale). The center peak is due to Rayleigh backscattering at the frequency of the incident light. The Raman peaks are due to interaction between the incident light and molecular vibrational states in fused silica. Raman frequency shifts are determined by the molecular structure but the anti-Stokes intensity is a function of temperature. Brillouin frequency shifts are due to interaction between the incident light and phonons (sound waves) in the fused silica. The frequency shift is dependent on the density of the fused silica, and hence, strain and temperature. From Selker *et al.* (2006).

roundtrip travel-time of the signal while the physics of each type of backscattering is exploited for measurement information.

In the technologies discussed in this chapter, Rayleigh scattering will be associated with recording dynamic strain of seismic waves (Distributed Acoustic Sensing or DAS), Raman scattering with temperature (Distributed Temperature Sensing or DTS), and Brillouin scattering with strain and/or temperature (Distributed Strain and Temperature Sensing or DST). In Raman scattering temperature is recorded as changes in the intensity of the backscattered light whereas in Brillouin scattering temperature and/or strain is recorded as changes in the frequency of the backscattered light.

A fiber-optic sensing cable is constructed of three concentric layers (Figure 5). The innermost layer is the fiber core of fused silica. Its diameter is 9 μm in single-mode fiber and either 50 or 62.5 μm in multimode fiber. The names are derived from the number of modes of light that can be carried within the core.

The next layer is the cladding, which is glass of a different index of refraction that traps light within the core of the fiber. The cladding diameter is 125 μm. The dimensions of core and cladding in single-mode and multimode fiber are designated by 9/125 and 50/125 or 62.5/125, respectively. The larger diameter of multimode fiber supports multiple modes of light trapped within the core and hence can carry

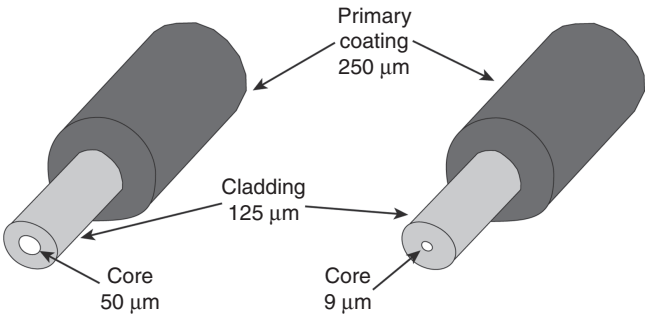


Figure 5 Cross section of multimode and single mode fiber-optic cable. From Aminossadati *et al.* (2010).

more information. The tradeoff is that the shorter distance between reflections at the core/cladding interface leads to greater attenuation, and, hence shorter maximum sensor lengths.

The outermost layer of a fiber-optic sensing cable is the sheath that protects the core and cladding and adds rigidity to the cable. The core and cladding are protected from the environment in various ways. For temperature sensing, the fiber must be insulated from mechanical strain. Hence it is surrounded by a buffer tube (loose tube construction) and then protected and toughened with jackets and an outer sheath. Strain sensing cable is tight buffered so that strain on the jacket is transferred without slippage to the core (Noni *et al.*, 2011). The choice of outer jacket is based on resistance to environmental conditions, such as temperature or rodents. Cable weights vary from 18 kg/km for polyamide to 142 kg/km for stainless steel (AFL, 2015) with corresponding differences in ease of handling and deploying. The cable diameter is typically a few millimeters, and multiple fibers can be enclosed within a single sheath. While all fiber-optic cables are built on the same principles, hundreds of different specialty cables are available.

2.2.1 Distributed Temperature Sensing (DTS)

The most widely used method for DTS measurements utilizes the Raman backscattering effect in which the intensity of the anti-Stokes backscattered light (Figure 4) is proportional to temperature (Glišić & Inaudi, 2007; Culshaw & Kersey, 2008). The distributed nature of DTS provides a *de facto* spatial resolution of one meter over long distances, but, in addition, the profile can be repeatedly sampled to view temporal changes along the cable. The sampling interval can be as frequent as a few seconds to as long as a minute, depending upon the length of the cable and the amount of stacking needed to overcome noise. With appropriate calibration, temperature sensitivity is between 0.1 and 1°C.

DTS is used widely in environmental hydrology (Tyler *et al.*, 2010), the petroleum industry (Smolen & Van der Spek, 2003), and the geothermal energy industry (Jaaskelainen, 2010). For example, temperature variations in DTS cable laid in a stream or in a water or oil well can delineate where inflow or outflow

occurs (Denney, 2010). DTS can also be used for fire detection in tunnels and mines and has potential for monitoring ventilation in a mine (Aminossadati *et al.*, 2010).

In a DTS monitoring system, a Class 1M laser in the interrogator unit sends out a 10-ns light pulse at a near-infrared frequency of 1550 nm into multimode fiber. A typical index of refraction of fused silica is n = 1.5, which means light travels at two-thirds its speed in vacuum or 2×10^8 m/s. Thus, light travels approximately 2 meters in 10 ns, which sets the spatial resolution of one meter for locating the distance of a scattering site. The maximum pulse repetition rate depends on the total length of the installation. If, for example, it is 10 km in length, then the roundtrip travel time is 10^{-4} s. Therefore, the repetition rate of laser pulses must be less than 10 kHz. In practice, the launch frequency is smaller because of time required to process the returned signal. Obtaining the location of the back-scattered light uses the time-of-flight method known as Optical Time Domain Reflectometry (OTDR), which is used in the telecommunications industry for determining attenuation in fiber-optic lines (Tanaka *et al.*, 1996).

The Raman backscattering effect is the inelastic interaction between scattered light and molecular vibrational energy states in the glass. It accounts for less than one percent of the Rayleigh scattered light, which itself is 0.1% of the incident light energy. In a Stokes process, the incident light adds energy to the lattice. The interaction of the incident light and the imperfection in the fiber raises a vibrational mode from the ground state to an excited state, which then immediately drops down to a lower energy state but above the energy of the incident photon (Figure 6). Because the incident light adds energy to the lattice, the backscattered frequency, ν_1, is smaller than the frequency of the incident light ν_o. The Raman shift of the scattered light is calculated from the difference in the quantized energies of the incident light and backscattered light, $h\nu_o$ and $h\nu_1$, respectively, where h is Planck's constant. This frequency difference corresponds to a wavelength difference of 40 nm for an incident wavelength of 1064 nm (Smolen & Van der Spek, 2003). The location of the Raman peak in Figure 4 is known as the Stokes line.

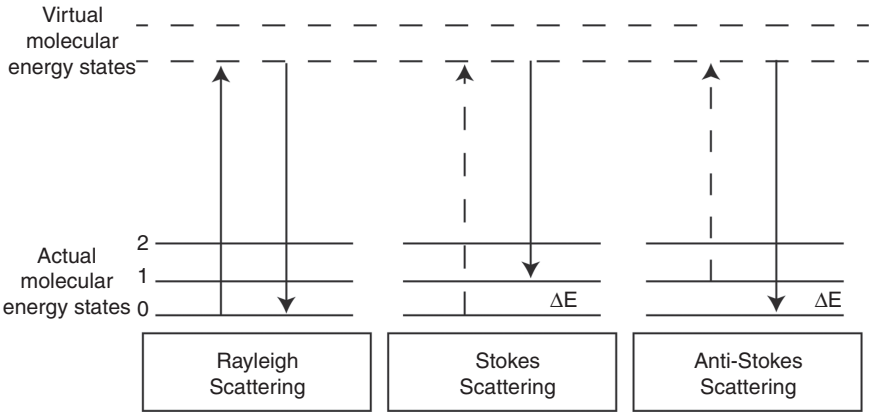


Figure 6 Schematic of drawing of molecular energy states of the Rayleigh, Stokes, and Anti-Stokes Processes. From Suarez et *al.* (2011).

In an anti-Stokes process, the interaction drops an electron from the excited state back to the ground state, decreasing the lattice energy, and adding energy to the backscattered light. Therefore, the resulting anti-Stokes line is at the sum of the frequencies. Because the Stokes and anti-Stokes lines are the energies of excitation or absorption of a particular vibrational mode, the two lines are symmetrical about the incident light's frequency and are independent of the frequency of the incident light.

Because most molecules are in their ground state at room temperature, relatively few scatterers contribute to the anti-Stokes peak. However, the basis of DTS is that the number of molecules in the excited state follows a Boltzmann distribution because excitation from the ground state is a thermally-activated process, which means that the intensity of the anti-Stokes peak is a strong function of temperature (Dakin *et al.*, 1985). The amplitude of the Stokes line is largely independent of temperature. The initial ratio of the intensity of the anti-Stokes (aS) to Stokes (S) backscattered light is given by

$$\frac{I_{aS}^{o}}{I_{S}^{o}} = \left(\frac{\lambda_S}{\lambda_{aS}}\right)^4 \exp(-\Delta E/kT) \tag{3}$$

where λ_S and λ_{aS} are the wavelengths of the Stokes and anti-Stokes peaks, respectively, ΔE is the energy of the vibrational state, k is Boltzmann's constant, and T is the temperature in °K. Thus, the intensity of the anti-Stokes peak increases exponentially with increasing temperature.

In addition to the temperature mediated effect on the ratio of the intensity of the anti-Stokes and Stokes lines, light is attenuated with distance along the fiber path according to Beer's law:

$$I(z) = I_0 \exp(-\alpha z) \tag{4}$$

where α represents the attenuation coefficient of the appropriate wavelength in m^{-1}. The attenuation coefficient is often specified in units of dB/km typically, 1 dB/km. Combining the two equations leads to the DTS equation:

$$T(z) = \frac{\Delta E/k}{\ln\left(\frac{C_S\lambda_S^4}{C_{aS}\lambda_{aS}^4}\right) + (\Delta\alpha)z - \ln\left(I_{aS}(z)/I_S(z)\right)} \tag{5}$$

where $\Delta\alpha = \alpha_{aS} - \alpha_S$ and C_S/C_{aS} is a calibration factor (Suarez *et al.*, 2011). Thus, Equation 5 contains the measurement, $I_{aS}(z)/I_S(z)$, and three parameters: $\Delta E/k$, C_S/C_{aS}, and $\Delta\alpha$. They are usually obtained by using (1) a calibration bath in which several meters of cable are placed, (2) double-sided measurement in which the laser light is launched from two directions within a cable containing two multimode fibers, and (3) the ratio $\Delta E/k$ is taken to be 600°K as applicable to most DTS fiber.

2.2.2 *Distributed Strain and Temperature Sensing (DST)*

Brillouin scattering is the interaction between a propagating light signal and thermally excited acoustic waves (phonons) present in the silica core of the fiber. Phonons are the

sound equivalent of photons, that is, quantized sound waves. The scattering follows the same principles just described for Raman scattering. The Stokes and anti-Stokes lines are associated with creating or annihilating a phonon, respectively. The Brillouin frequency shift, v_B, is the frequency of the acoustic wave associated with the phonon. As for Raman scattering, the frequency shift is negative for a Stokes process, and the frequency shift is positive for an anti-Stokes process. The quantized phonon energy is hv_B.

The phonon as a sound wave produces a periodic variation of the index of refraction within the fiber, like an FBG grating, whose spacing d is the acoustic wavelength. A constructive interference condition for the first reflection is $d = \lambda_o/n$, where the wavelength of the incident light in the fiber is λ_o/n. The acoustic wavelength, d, is related to the acoustic velocity, V_a, and v_B by the usual relation between wavelength, wave speed, and wave frequency: $d = V_a/v_B$. Combining these expressions leads to the Brillouin frequency shift:

$$v_B = \frac{2nV_a}{\lambda_o} \tag{6}$$

Using the values $V_a = 5800$ m/s, $n = 1.5$, and $\lambda_o = 1550$ nm, gives $\nu_B \sim 10$ GHz. Typically ν_B is between 10 and 12 GHz, considerably smaller than the Raman frequency shift because energies of phonons are much smaller than that of vibrational states.

The acoustic velocity, V_a, is a function of the density of the fused silica, which, in turn, is a function of the strain and temperature. Hence, the Brillouin frequency shift can be used to measure those two variables.

$$\Delta v_B = C_T \Delta T + C_\varepsilon \Delta \varepsilon \tag{7}$$

Where the coefficients $C_T \approx 1.2$ MHz/°C and $C\varepsilon \approx 505$ MHz/% (Thévenaz, 2010). Therefore, 20 με of deformation is equivalent in frequency shift to about 1 °C temperature change. Temperature stability or a separate loose cable paralleling the strain cable is critical to accurate strain measurement. An accuracy of 1 MHz in measuring the Brillouin frequency shift leads to a strain accuracy of about 20 με and/or 1 °C (Thévenaz *et al.*, 1998). As Equation 7 shows, Brillouin scattering has the potential for measuring either strain or temperature changes, with the problem of distinguishing between the two. Originally, the Brillouin effect was first proposed to measure temperature (Culverhouse *et al.*, 1989).

The measurement of the frequency shift of the spontaneous Brillouin scattered light can be made using a technique called Brillouin Optical Time Domain Reflectometry (BOTDR) (Thévenaz, 2010). In BOTDR the incident laser frequency, v_o, is optically mixed with the backscattered signal, $v_o - v_B$, in the case of the Stokes wave, to produce beat frequencies that are the difference and sum of the two frequencies.

The beat signal is then electronically mixed with a local oscillator, which is stepped across the range of Brillouin frequencies in small megaHertz frequency increments, enabling the peak of the frequency distribution of the backscattered signal to be reconstructed at each position. BOTDR utilizes the stronger Stokes, rather than anti-Stokes, backscattered light, because more Brillouin interactions are associated with phonon creation than annihilation.

Because BOTDR uses spontaneous, backscattered Brillouin light, it requires only one end of the fiber-optic cable both for sending the probe pulse and analyzing the returned

signal. However, the spontaneous Brillouin backscattered intensity is only 0.01% of the Rayleigh intensity and, hence, is quite weak (Ohno *et al*., 2001). The low intensity has given rise to another measurement technique, Brillouin Optical Time Domain Analysis (BOTDA) (Diaz *et al*., 2007), which has much greater signal strength through Stimulated Brillouin Scattering (SBS). SBS is the non-linear amplification of the back-scattered Brillouin light when it interacts with a counter-propagating, continuous-wave (CW), probe wave whose frequency is equal to the difference between the high-powered incident light (pump pulse) frequency and the Brillouin frequency. This amplification produces the Brillouin Gain Spectrum (BGS) (Figure 7), which is recorded at every position along the fiber.

3 RESEARCH PROJECT CASE STUDIES

Most fiber-optic sensing in underground facilities have been SHM applications in tunnels and some mines. In general, the SHM techniques used for bridges, roadways, dams, and pipelines can be readily transferred to underground facilities (Glišić & Inaudi, 2007). The websites of commercial vendors of equipment and cable (*e.g.* Micron Optics, SmartTec, Omnisens, AFL, Oz Optics, Brugg Cable) are another valuable resource for case studies. The case studies presented in this section represent a selection of research projects. Two studies involve the use of FBG sensors for measuring strain and characterizing rock-mass properties. They illustrate how commercially available fiber-optic technology can be adapted to existing sensors (Gage *et al*., 2010, 2011, 2013) and how FBG sensitivity can be greatly improved via field emplacement techniques and new photonic measurement methods (Tokunaga *et al*, 2011; He *et al*., 2013). The third study utilizes DTS for detecting anomalous temperatures that might signal fire hazard (Aminossadati *et al*., 2010). The DTS study highlights the benefits of distributed sensing in terms of whole-mine monitoring. The fourth study describes a pilot 25-meter-scale experiment to monitor strain and displacement in a pillar at a depth of 1000 meters as mining occurred in a nearby stope (Valley *et al*., 2012).

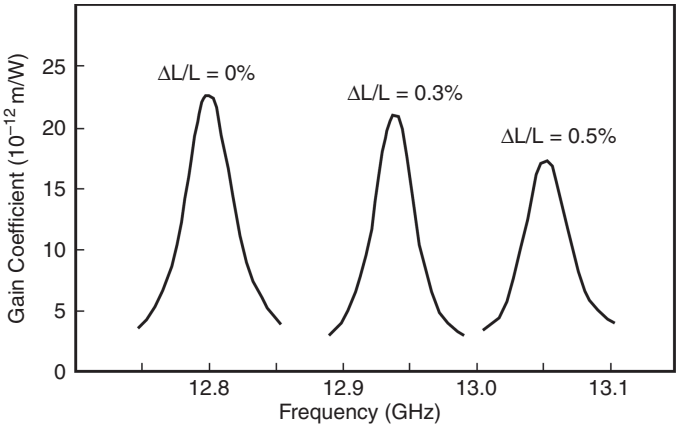


Figure 7 Brillouin Gain Spectrum showing change of peak due to strain. From Thévenaz (2010).

3.1 Monitoring rock deformation using FBG strain and temperature sensors

3.1.1 FBG installation techniques for measuring deformation in a deep mine in Lead, South Dakota (USA)

With any fiber-optic monitoring array for intact rock masses, installation techniques and attachment to the rock mass are critical to ensure robust and valid strain data. Gage *et al.* (2010, 2011) provide details of an FBG installation where they used two types of FBG sensors, different gauge lengths, and different installation methods. The FBG sensor arrays were installed ~1250 m underground on the 4100-level of the Sanford Underground Research Facility (SURF) at the site of the former Homestake gold mine in South Dakota, USA. The rock mass is composed of crystalline metamorphic rock that contained several pervasive joint sets including mineralized veins (Gage *et al.*, 2014).

Gage *et al.* used two main types of FBG sensors manufactured by Micron Optics Inc. Both types are FBG sensors and have a sensitivity of 1με and 0.1 °C. The first type, called a "tube gauge", consists of an FBG strain gauge housed in a 1 m long plastic tube where the strain sensing FBG is mounted on a thin steel rod that is anchored to the two ends of the tube (Gage *et al.*, 2010). One end of the tube gauge contains the temperature compensation FBG that is mounted on a metal tab that is anchored to one end of the tube and the other end is not attached. These tube gauges measure one-dimensional shortening and elongation between the ends of the sensor with an effective gauge length of 1 m (Gage *et al.*, 2010).

The second type of FBG sensors employed by Gage *et al.* (2011, 2013) was a "patch gauge" with an effective gauge length of 10 mm. These patch gauges were built into arrays of six strain gauges in series each with its own external, co-located temperature compensation FBG sensor. The FBG arrays were installed on Fiber-optically instrumented ROck STrain Strips (FROSTS), which are modified ROck Strain Strips (ROSS) developed by Signer & Sunderman (2003). ROSS were developed as an alternative to instrumented rock bolts, to measure rock movement and the performance of roof supports in mines. The ROSS is cut from a thin (1.5 mm) sheet of stainless steel. The shape of the ROSS is similar to that of a dog-bone consisting of narrow (1.27 cm wide) straight strips of metal between two sets of wider (3.18 cm wide) areas with teeth cut into the edges of the strip (Figure 8). The twisted sections of the ROSS with the teeth are designed to center the strain strip in the borehole and grip the grout to ensure sufficient coupling between the ROSS and the rock mass. The strain gauges are installed on the narrow straight portions of the ROSS (Figure 8).

The ROSS is typically instrumented with electrical-resistance strain gauges at 30 cm intervals along its length (Signer & Sunderman, 2003). In contrast, to construct the FROSTS, fiber-optic FBG strain and temperature gauges were chosen to replace the electrical resistance strain gauges for several reasons: (1) the incorporation of highly accurate temperature gauges with the strain gauges provides a detailed thermal profile with depth into the rock mass; (2) FBG gauges are easily read in the field using off-the-shelf interrogation boxes and manufacturer-supplied software rather than a specially designed and built data acquisition system (Signer & Sunderman, 2003) or time-consuming campaign-style readings; (3) the FBG gauges are arranged in series with

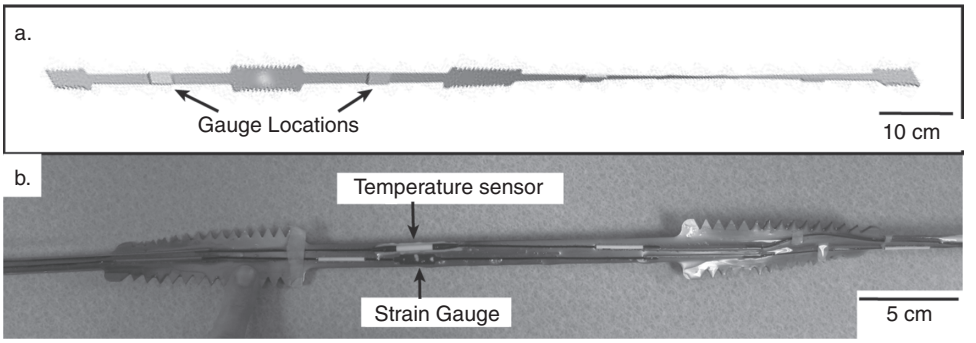


Figure 8 (a) Sketch of a rock strain strip. Light gray patches denote strain gauge locations. From Signer & Sunderman (2003). (b) Photograph of fiber-optic strain and temperature sensors on FROSTS from Gage *et al.* (2012).

12 gauges operating off a single fiber-optic cable and interrogation channel, which creates a slimmer design than each resistance gauge with its own set of wires; and (4) FBG gauges require no calibration and do not have drift over time so an FBG array could be installed with its interrogation box in another location and run indefinitely without any on-site interaction.

Both the tube gauges and FROSTS were installed into an alcove in the underground laboratory adjacent to the main drift. The alcove measured 2-m deep by 3-m wide and 2-m tall. The tube gauges were installed in two different ways: surface mounted and embedded. The two ends of each surface mounted sensor sit in steel u-shaped brackets welded to the heads of rock bolts (Figure 9). The embedded sensors were grouted into the rock mass in holes drilled ~2-m deep. The embedded sensors have a manufacturer-supplied 5-cm-diameter disk-shaped bracket on each end to help the sensor grip the rock mass (Figure 9). The tube gauges were installed in sets of three with two perpendicular surface-mounted sensors and one sensor embedded perpendicular to the surface of the rock (Figure 9) (Gage *et al.*, 2010).

Two FROSTS were embedded into the rock mass in the alcove. One FROSTS was installed vertically into a drill hole in the roof of the alcove. The second FROSTS was installed horizontally into a wall of the alcove. Both FROSTS were grouted into the rock mass (Gage *et al.* 2013).

All FBG sensors performed within the expected standards (Gage *et al.*, 2010, 2013). However, the FROSTS were the preferred installation method, yielding high-quality, detailed strain and temperature measurements within an intact rock mass (Gage *et al.*, 2014). The tube gauges that were installed on the surface of the rock mass (Figure 9) experienced large temperature changes due to the mine ventilation. These temperature swings where much higher than any mechanical strain measured by the sensor, and although a temperature correction was applied, the environmental temperature changes masked any strain measured by the surface-mounted sensors (Figure 10) (Gage *et al.*, 2010).

The embedded tube gauges were insulated from the large air temperature changes that affected the surface-mounted tube gauges (Figure 10). However, the 1-m gauge length was too large to detect and monitor accurately the magnitude of mechanical strain in the

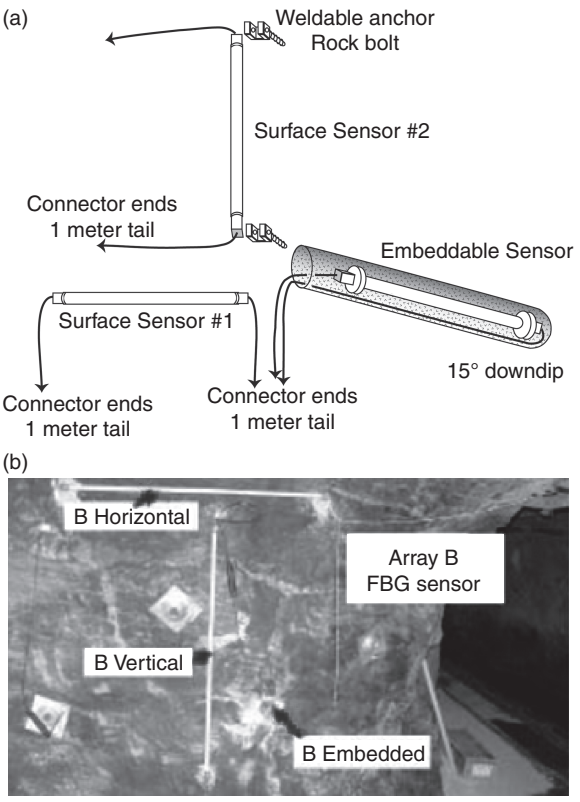


Figure 9 (a) Sketch of "tube" gauge array installation at the SURF laboratory in Lead, South Dakota, USA. The two surface-mounted gauges are oriented vertically and horizontally. They sit in metal u--shaped brackets welded to the surface of rock bolts. The embedded sensor is grouted into a borehole drilled perpendicular to the rock surface. (b) Photograph of Array B's two, 1-m-long surface-mounted tube gauges and drill hole for the embedded sensor. From Gage *et al.* (2010).

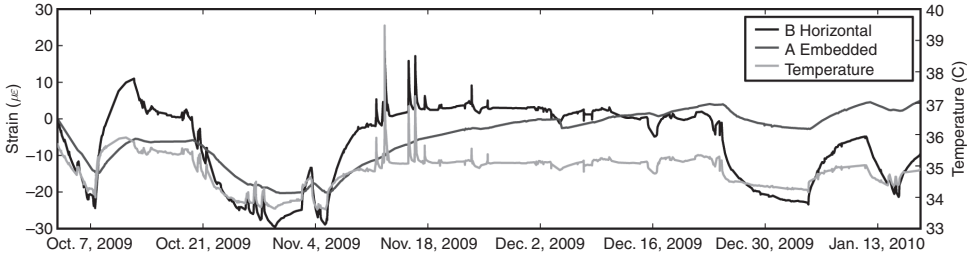


Figure 10 Example of raw strain data collected from the FBG "tube" gauge arrays (Figure 9) in the SURF laboratory. The plot shows data for correlative sensors from the two arrays: the surface-mounted sensor from one array (black) and the embedded sensor from the other (medium gray). Both sensors should be measuring similar magnitude strain in the same horizontal direction. Also plotted (light gray) is the surface temperature. Notice how the strain measured by the surface-mounted sensor (black) responds to environmental temperature change (light gray). From Gage *et al.* (2010).

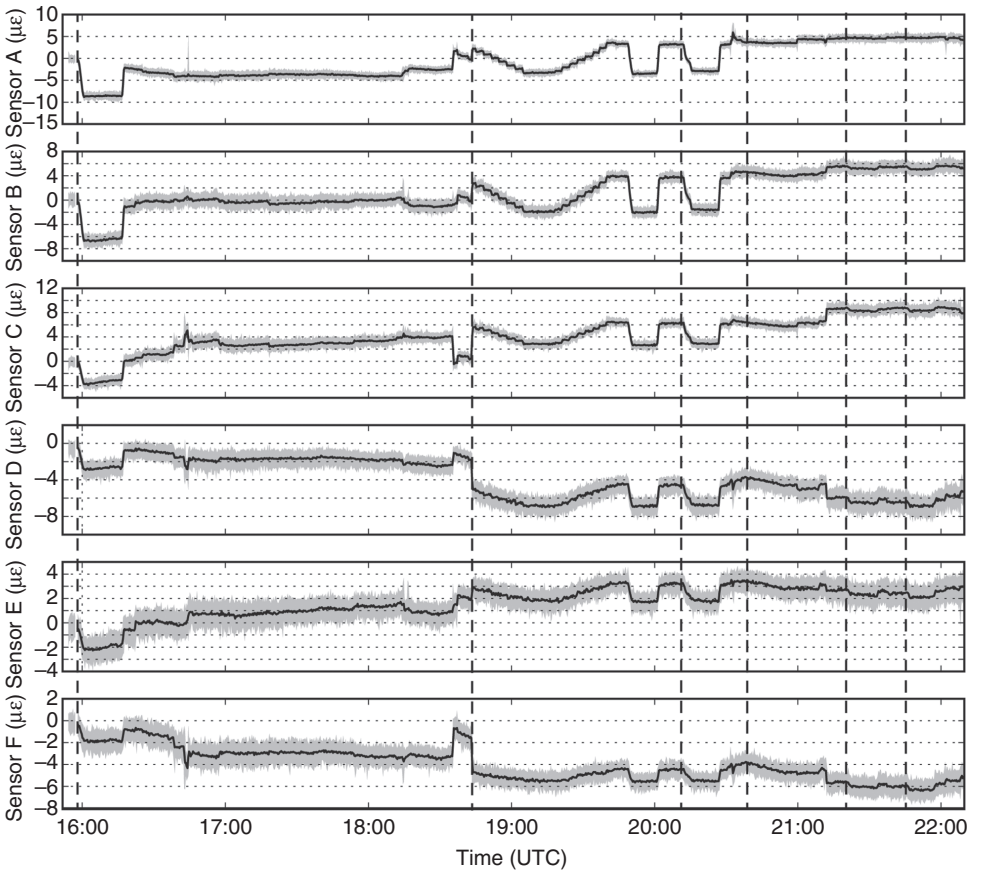


Figure 11 Example strain data collected from the six FBG "patch" gauges on a FROSTS installed at the SURF laboratory. Dashed vertical lines correspond to the application of an external 100-ton (890 kN) load. Shortening is negative and elongation is positive. Sensor A is closest to the surface of the rock mass (0.62 m) and sensor F is the deepest (2.14 m). Data were collected at 5 Hz. The black line is one's moving-average of the raw strain data (gray area). From Gage *et al.* (2014).

intact rock mass (Gage *et al.*, 2010). The FROSTS provided the most accurate and detailed measurement of strain (Gage *et al.*, 2014). In an effort to measure the mechanical properties of an intact rock mass, Gage *et al.* (2014) applied a 100-ton load to the roof of the alcove with a hydraulic jack. The FBG sensors on the FROSTS recorded each loading event and measured a strain profile with depth into the intact rock mass that helped to characterize a mechanical profile from the damage zone into the stress-relieved zone (Figure 11) (Gage *et al.*, 2014).

The work of Gage *et al.* demonstrates that discrete fiber-optic strain and temperature sensors are a viable and effective tool for monitoring deformation in intact rock masses and the structural health of underground structures. Gage *et al.* also show the importance of fiber-optic sensor installation methods and the geometry of the sensor array relative to the expected mechanical strain.

3.1.2 Ultrahigh resolution FBG system for measuring rock deformation due to tides in an underground vault at Aburatsubo Bay, Japan

Matsui *et al.* (2009) first used FBG strain gauges to measure rock deformation due to tidal loading and earthquakes in Japan. In order to reliably measure earth strains on the nanometer scale, they subsequently developed an ultrahigh-resolution FBG strain sensor and measurement technique (Liu *et al.*, 2012; He *et al.*, 2013). Their work shows that FBG sensors can record strain comparable to 38-meter-long quartz-tube strain meters.

Two FBG "tube gauges" from Micron Optics Inc. were mounted on the floor of a vault 10m underground in the Aburatsubo Crustal Movement Observatory in Japan. Additionally, in the same underground space, Japan's Earthquake Research Institute had installed 38-m-long silica-tube extensometers, which have been monitoring continuously since 1976. Like Gage *et al.* (2010), the Micron Optics tube gauges had a resolution of 1 με and 1 °C, and each had a gauge length of 1 m. The ends of the sensors were attached to two stainless steel rods grouted in 30-cm-deep holes drilled into the rock mass. The data from the first installation were too sensitive to temperature fluctuations inside the unventilated vault to record accurately deformation from tidal loading (Liu *et al.*, 2012).

In order to insulate better the FBG sensors, the two tube gauges were later mounted across two steel anchors in a 15-cm-deep trench in one of the vaults of the observatory. The trench was then filled with soil sprayed with an additional 15-cm thickness of polystyrene foam (Liu *et al.*, 2012). Even with the second installation, the recorded strain was still unacceptably noisy, although tidally induced strain was visible in the data (Matsui *et al.*, 2009).

Liu *et al.* (2011, 2012) and He *et al.* (2013) developed a technique that improved the resolution of the FBG gauges by two orders of magnitude, making them capable of measuring strain on the nanometer scale. The three main elements of the ultrahigh resolution FBG sensor were 1) a sensor configuration that provides precise measurement of the environmental noise, 2) a highly stable, narrow linewidth, tunable laser for sensor interrogation, and 3) a cross-correlation algorithm to remove the environmental noise due to temperature fluctuations (Liu *et al.*, 2011).

In the new sensor configuration, each measurement location has two identical FBG sensors installed – one is used for strain sensing and the other for reference (Liu *et al.*, 2012). The sensing FBG is installed coupled to the rock mass. The reference sensor is installed "strain-free" or not attached to the rock mass so that it can distinguish any environmental disturbances from the mechanical strain of interest (Liu *et al.*, 2012). Then a narrow linewidth tunable laser interrogates the FBGs.

Liu *et al.* (2012) use a cross correlation technique to determine the Bragg wavelength difference from the measured spectra to compute the mechanical strain. The cross correlation approach was found to be the most efficient algorithm at suppressing random noise and yielded very good resolution (He *et al.*, 2013).

With the new FBG sensor configuration and cross correlation algorithm, Liu *et al.* (2012) were able to record accurately earth strains. Strain data were recorded continuously for 52 days and compared to strain measured by the silica-tube extensometers (Figure 12). Strain caused by the daily and diurnal tides was recorded by the FBG sensors as the changes in strain correlated to the daily changes in tide level (Figure.

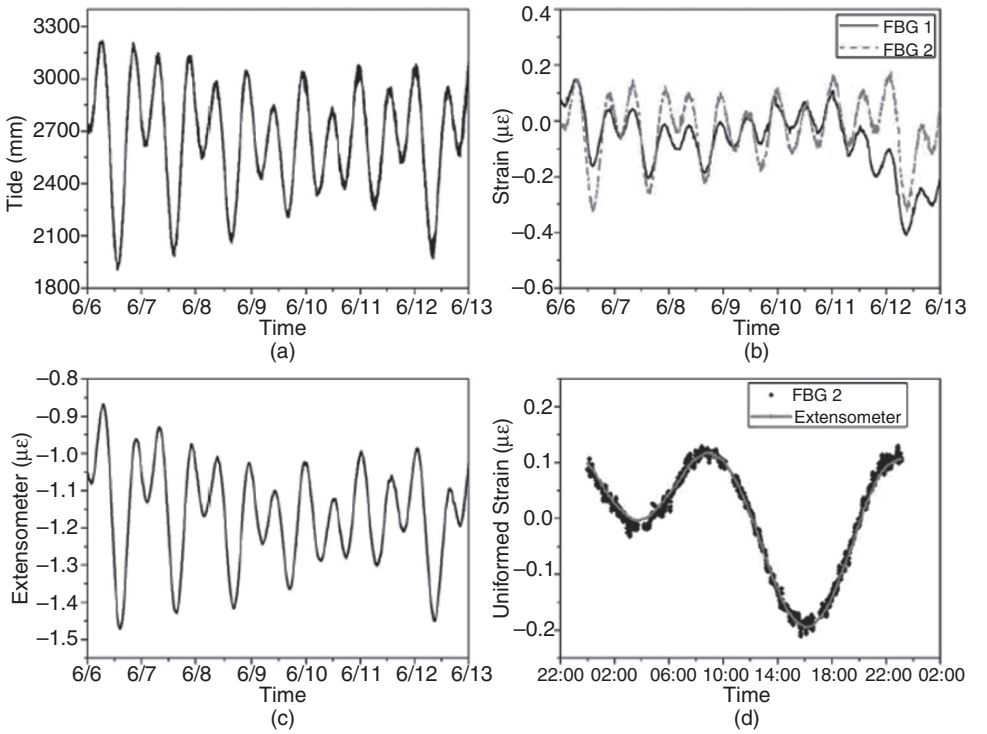


Figure 12 Tide and strain data from FBG and silica-tube extensometers installed in Aburatsbo Bay, Japan. (a) Oceanic tide level. (b) Strain measured by the FBG sensors. (c) Strain measured by the silica-tube extensometers. (d) Comparison of measured strain from the FBG and the silica-tube extensometer. From Liu *et al.* (2012).

12). Further, Liu *et al.* (2012) showed that the data recorded by ultrahigh resolution FBG strain gauges were in very good agreement with the measurements of the long-running silica-tube extensometers (Figure 12).

The ultrahigh resolution FBG strain gauges were able to measure a co-seismic response to the M = 7.2 Sanriku Earthquake of 10 July, 2011. Both the ultrahigh-resolution FBG sensors and the silica-tube extensometers show clear temporal responses, but of different character (Figure 13). Although theoretical co-seismic strain should be on the order of 10^{-9}, below the resolution of even the ultrahigh resolution FBG sensors, the FBG sensors at Aburatsubo recorded co-seismic compressional strains of -1.5×10^{-7} and -2.5×10^{-7} (Figure 13). Meanwhile, the silica-tube extensometers recorded Love waves.

The study at Aburatsubo Bay, Japan further demonstrates the validity of FBG strain gauges for use in measuring mechanical strain in rock masses. The development of an ultrahigh resolution FBG sensor shows that there is still room for the technology to develop and become more accurate. The gauge length of one meter adds to the range of measurement scale in crustal observatories.

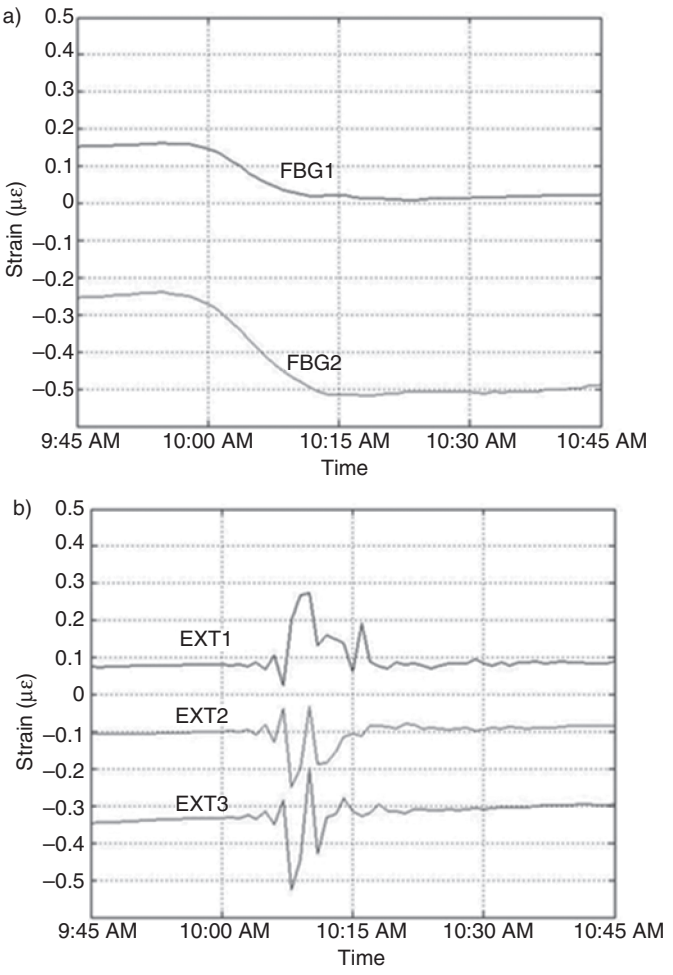


Figure 13 Comparison of strain data from the FBG sensors (a) and the silica-tube extensometer (b) at the time of the Sanriku (Mw = 7.2) earthquake on 10 July 2011 (unpublished data, U. of Tokyo Earthquake Research Institute).

3.3 Employing DTS temperature monitoring to enhance mine safety

Distributed Temperature Sensing shows great potential for increasing safety in mines. Localized, elevated temperature within a mine is considered to be an early indicator of potentially hazardous situations such as fire. Thus, a fast, precise, and reliable means of temperature monitoring, which in itself does not constitute a fire hazard, can enhance mine safety. Real-time temperature monitoring can assist to control ventilation, manage escape routes, and minimize the potential damage caused by hazards (Aminossadati *et al.*, 2010).

Aminossadati *et al.* (2010) installed three different DTS arrays in a coal mine in Queensland, Australia to test the accuracy and effectiveness of DTS as an underground temperature monitoring technique. They used a multimode fiber with a sensitivity of 1 °C and a 1-m spatial resolution, and capable of measuring over a 10-km distance. They installed the optical fiber in all working areas of the mine with a focus on real-time monitoring of temperature change in two heat chambers.

Aminossadati *et al.* (2010) installed both unidirectional and double-ended DTS configurations, both of which use Optical Time-Domain Reflectometry (OTDR) technology. The unidirectional arrays consisted of single-line and dual-line configurations. For the single-line configuration the fiber-optic sensing cable makes one traverse through the mine and one end is connected to the multiplexer and the other is terminated. In the dual-line configuration, the sensing cable is laid out in a loop so that it makes two identical traverses through the mine. Similar to the single-line array, one end is connected to the multiplexer and the other end is terminated. The main advantage of the dual-line configuration is that there are two sensing fibers measuring the temperature at any point. However, both the single-line and dual-line configurations become inoperable if the fiber were to break anywhere along its length (Aminossadati *et al.*, 2010).

Aminossadati *et al.* (2010) also installed a dual-loop, double-ended configuration. In the dual-loop array the fiber-optic sensing cable is measured from both ends. The cable makes a loop through the mine, similar to the dual-line configuration, but both ends are attached to the multiplexer. The dual-loop configuration has two advantages: it provides two temperature measurements at any point along its length, and if the optical fiber is damaged, the system is still capable of recording temperature measurements (Aminossadati *et al.*, 2010). If the fiber breaks, the dual-loop essentially becomes a dual-line configuration with the termination occurring at the break.

In order to assess the accuracy of the DTS measurements, Aminossadati *et al.* (2010) compared the DTS data to measurements from digital thermometers at 12 locations in the mine. They found that the DTS was extremely accurate and there was a maximum absolute difference of 0.52 °C between the DTS and digital thermometers.

Aminossadati *et al.* (2010) also ran several experiments where they heated and cooled a chamber and compared the temperature data measured by the DTS to theoretical temperature models based on air flow and heat generation. They found that the results of the DTS measurements and theoretical results agreed reasonably well for several locations within the mine. Overall, Aminossadati *et al.* (2010) showed that the DTS system could scan the entire underground mine with precision and accuracy and locate any thermal anomalies. DTS is an effective technology for use in mines to monitor temperature in real-time and potentially mitigate hazards.

3.4 Employing distributed strain monitoring to enhance mine safety

A field trial of distributed strain sensing was conducted by Valley *et al.* (2012) in a 25-meter-thick sill pillar at a depth of 1000 meters in an active mine. Distributed strain cables (Smartec SMART profile cable) were grouted into five, 10-cm diameter boreholes that went through the pillar (Figure 14). The cables were centered and slightly pretensioned by hanging a 2-kg weight on the end. An Omnisens BOTDA interrogator was used with a 0.1-MHz scanning step and a 5-ns pulse length. The spatial resolution

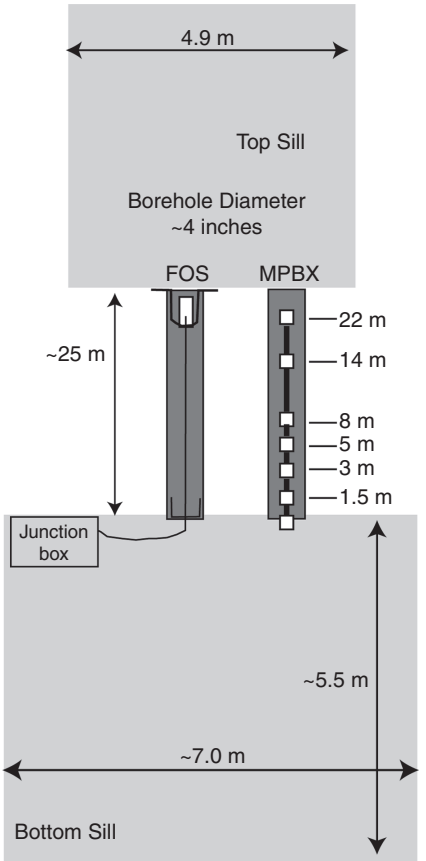


Figure 14 Schematic diagram of DST and MPBX installation from Valley *et al.* (2012).

was considered to be 0.1 m. Prior to the field experiment, one-meter lengths of cable were tested with weights up to 5 kg. Noni *et al.* (2011) performed similar laboratory testing using the same Omnisens interrogator but Brugg BruSteel cable over distances of about 4 meters. The two sets of laboratory experiments were over similar strain ranges between a few tenths and 1%. Both investigations found that strain profiles have a qualitatively linear relationship with the Brillouin frequency shift.

The five grouted DST cables were in holes parallel to traditional MPBXs (Figure 16). The strain profiles from DST were integrated over the pillar thickness to obtain displacement. The two sets of data were processed for equivalent times and locations and profiles (Figure 15). The fiber-optic system recorded the sharp extension by August 11 while it did not become as apparent in the MBPX response until August 21. The displacement event recorded by the two systems differed, however, with it being about 2 mm for MPBX versus about 0.4 mm for DST. Valley *et al.* attribute the discrepancy to the difference in compliance of the grout-sensor system in the boreholes. The displacement event occurred where a fracture had been located by borehole televiewer. If extension

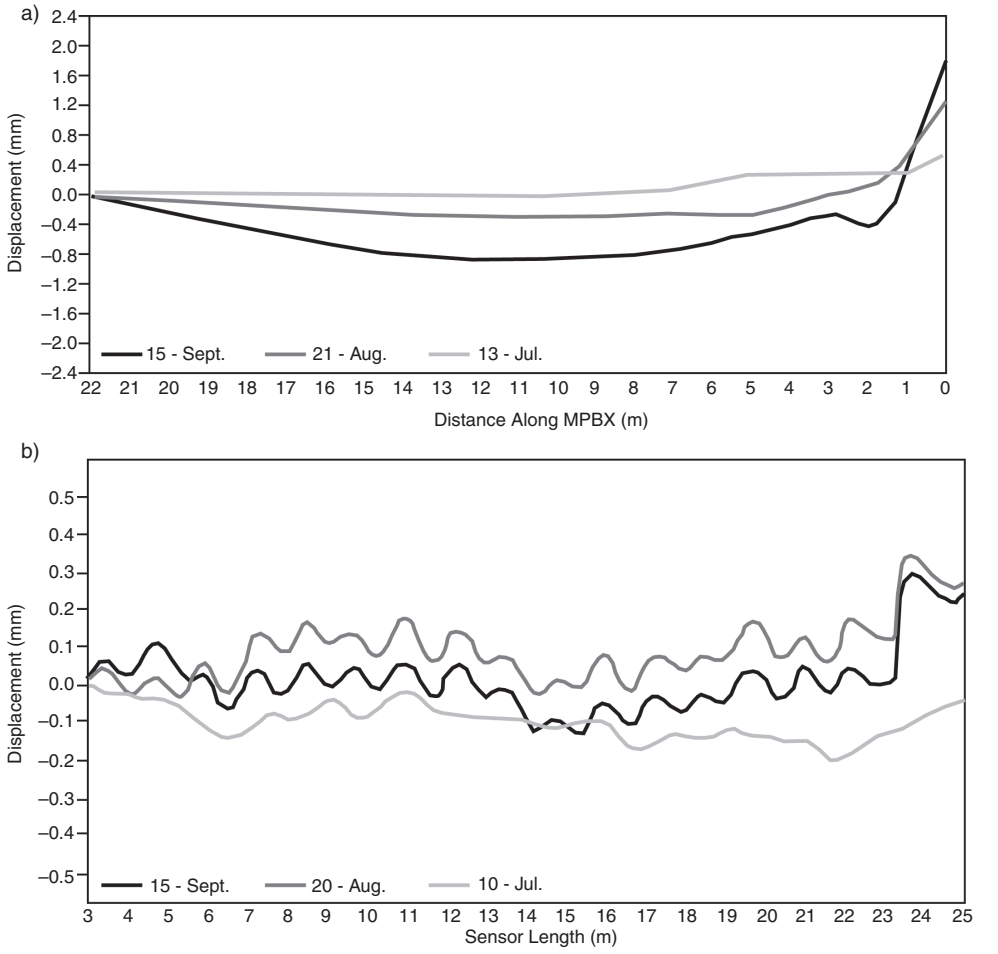


Figure 15 Comparison of displacement profiles at different times from (a) MPBX and (b) DST. DST oscillations are believed to be an artifact of cable construction. Data from Valley *et al.* (2012).

took place on this fracture, then DST can localize the event despite a spatial resolution that is much larger.

4 OVERVIEW OF FIBER-OPTIC EXTENSOMETERS

Measuring displacement or strain is one of the most basic sensing requirements in geomechanics. The longevity of an underground structure, its size, and requirements for spatial and temporal sampling and measurement accuracy or precision are factors that go into the design of a geomechanical monitoring and characterization program. Further engineering considerations include the implementation of the design in terms of installation, sensor type and associated instrumentation, and reliability. For example, the interrogator for a fiber-optic sensor can be hundreds of meters away from the

measurement site because of the low attenuation, which allows the instrument to be located where power, access, and a more hospitable environment exist. Finally, availability and cost of the monitoring array are necessary and practical considerations. Build and delivery time are shorter for commodity sensors than for specialized sensors or sensors based on new technology. Although commercially available fiber-optic sensors have been on the market for more than a decade, their adoption follows a pattern typical for emerging technologies. In this section, the characteristics of several developmental fiber-optic instruments for measuring deformation are described and the importance of anchoring both discrete and distributed sensors is discussed.

As the description of FROSTS shows, FBG gauges can replace traditional electrical resistance strain gauges in a one-to-one fashion (Gage *et al.*, 2013). Another example of hybrid sensors are borehole extensometers developed by Clemson University for characterizing fracture mechanics and flow properties (Schweissinger *et al.*, 2007; Skawski, 2012; Skawski *et al.*, 2011; Murdoch *et al.*, 2014). The extensometers lie between packers in a borehole and are anchored to the borehole wall, but are easily retrieved and relocated. Water is injected or removed using techniques typical of hydraulic well tests, and the transient signals of pressure and displacement are analyzed for mechanical and hydrologic properties. The 5DX will measure relative movement of two points in three orthogonal displacements and two rotations. Both LVDT and DVRT as well as FBG gauges have been used for measuring the movement. The RMS noise level at a 2-Hz sampling rate is less than 30 nm axially and 250 nm in transverse directions. The sensitivity is such that displacements of a fractured biotite gneiss were shown to be driven by barometric pressure fluctuations (Murdoch *et al.*, 2014).

For longer gauge lengths, the Micron Optics OS3600 tube gauge comes in lengths between 0.5 and 2 meters, and SOFO comes in lengths between 0.5 and 20 meters. The long SOFO gauge length becomes comparable to that of conventional borehole extensometers, which are anchored deep in a borehole and at the collar.

Any displacement or strain measurement, however, is meaningful only if the sensors are measuring the true rock-mass behavior. The availability of suitable anchoring devices or methods is of central importance to achieving solid coupling. A variety of anchors have been developed for conventional extensometers (*e.g.*, Geokon) and for the Micron Optics tube gauge. Additionally, the ability of any displacement sensor to measure in both tension and compression requires it to be pre-tensioned, if installed in a borehole (*e.g.* Gage *et al.*, 2013), and the anchor at the collar must be set after pre-tensioning. The OS3600 tube gauge, which contains the FBG as a short length of fiber between steel rods attached to anchors at both ends, is pre-tensioned. Another consideration is that the compliance of the gauge itself be as small as possible when measuring strain in a stiff rock mass.

The coupling of DST cable to the surface of a rock mass can be achieved by either continuous grouting of the cable to the rock mass or in a point-to-point configuration using rock bolts as anchors. Laboratory experiments were conducted in which tight-buffered, fiber-optic cable was wrapped around and epoxied to rock cylinders and compared with continuously grouted cable (Noni *et al.*, 2011). The radius of curvature must typically be larger than 30 mm in order not to attenuate light. Alternatively, an anchor through which the fiber is clamped could be fastened to the rock bolt, or directly

to the rock. Specialty fiber-optic anchors have even been developed for soil (Iten *et al.*, 2009).

If fiber-optic cable is anchored point-to-point at a series of rock-bolt anchors, then it functions like optical convergence tape. Uniform strain will be recorded from anchor to anchor. The fiber sheathing must not slip relative to the cladding or core and must be firmly clamped to the anchor as well. Preliminary laboratory tests using a tight-buffered cable and clamp manufactured by Brugg AG in Switzerland gave confidence that the sheath does not slip over distances of a few meters (Noni *et al.*, 2011).

Hyett *et al.* (2013) recognized the potential to instrument rock bolts with distributed stain sensing technology. Their instrumentation involves cutting grooves on opposite sides of the rock bolt rebar to house the fiber-optic cable. Although Hyett *et al.*'s instrumentation technique performed well in their laboratory testing, they did not test the DST-instrumented rock bolts *in situ* and did not develop an installation technique that is suitable for the instrumented rock bolts they propose.

5 GEOMECHANCAL APPLICATIONS OF FIBER-OPTIC SENSING IN OIL AND GAS WELLS

While the emphasis in this review has been on underground facilities like tunnels and mines, a few examples of fiber-optic sensing in geomechanical and geophysical applications are worth mentioning from the oil and gas industry because of their potential transferability. The general interest in fiber-optic sensing in the oil and gas industry is indicated by news stories in the *Journal of Petroleum Technology* (JPT) (Rassenfous, 2012; Jacobs, 2014). A driving concept is the idea of the "smart well" in which fiber-optic sensors play the role of a central nervous system.

Maintaining well integrity during production is a significant economic concern. In a joint study by Baker-Hughes and Shell, deformation of well casing was monitored using a quasi-distributed string of FBG sensors (Figure 16) (Pearce *et al.*, 2009). A fiber-optic cable with embedded FBGs every one centimeter was spiral wound and cemented in a groove inside the casing. The spiral geometry enabled axial strain, bending, and hole ellipticity to be determined. Axial strains in testing could be obtained to 0.1%. The system is offered by Baker Hughes (2010) as the Real Time Compaction Monitoring (RTCM) System. While RTCM is based on thousands of FBG sensors, Baker Hughes has also developed a distributed strain monitoring system that uses a Rayleigh backscatter and a Swept Wavelength Interferometer (SWI) (Duncan, 2014). More than one fiber-optic cable can be fastened to casing and in different orientations, *e.g.*, axial or spiral.

Another important fiber-optic sensing technology that is increasing in application is Distributed Acoustic Sensing (DAS). The fiber-optic cable senses the passage of elastic waves with a spatial resolution of one meter. The backscattered Rayleigh wave is signal processed for dynamic strain (Shatalin *et al.*, 1997; Mestayer *et al.* 2011; Miller *et al.*, 2012; Parker *et al.*, 2014). The amount of data acquired can be large. At its maximum sampling rate of 10 kHz, a spatial resolution of one meter, and a cable length of one kilometer, sixty seconds of recording would produce over 2 GB of data. As useful seismic information is contained within frequencies below 1 kHZ, the data quantity can be one or two orders of magnitude smaller than DAS' capability.



Figure 16 Fiber optic strain gauges are protected in the metal casing that spirals inside this grate. Signals from thousands of points along that path are assembled to create a 3D view of the force on the reservoir on the bottomhole assembly. From Rassenfous *et al.* (2012).

The primary application of DAS in the energy industry has been Vertical Seismic Profiling (VSP) and flow detection. Trials have been conducted through partnerships between instrument companies and energy companies or government laboratories (Cox *et al.*, 2012; Mateeva *et al.*, 2014; Daley *et al.*, 2013; Parker *et al.*, 2014). A VSP profile comparing geophones and DAS is shown in Figure 17. Several advantages accrue to using DAS for VSP. It obviates the need to install geophones into an active well, there is no length limit to the DAS array, and the fiber-optic cable can be permanently cemented between casing and the borehole wall to allow repeat VSP surveys.

DAS can also be deployed in near-surface arrays (Daley *et al.*, 2013; Wang *et al.*, 2014; Castongia *et al.*, 2017; Baldwin, 2015) to provide high-spatial density along the cable. An enclosed geometric configuration combined with active sources can be used for a subsurface velocity profile and travel-time tomography. At the present time, DAS has not been employed in the mining industry, but, in concept, DAS arrays could piggyback, with appropriate ground-motion coupling, on other fiber-optic monitoring to characterize rock property variations or to detect and locate rock bursts induced by mining activity.

6 SUMMARY AND CONCLUSIONS

Sensors, light source, data analysis, and interpretation are the key components in any fiber-optic monitoring system. The two primary types of fiber-optic sensors are discrete and distributed. Discrete sensors are based on the Fiber Bragg Grating (FBG) or micrometer-scale optical cavity using Fabry-Perot interferometry, or SOFO using

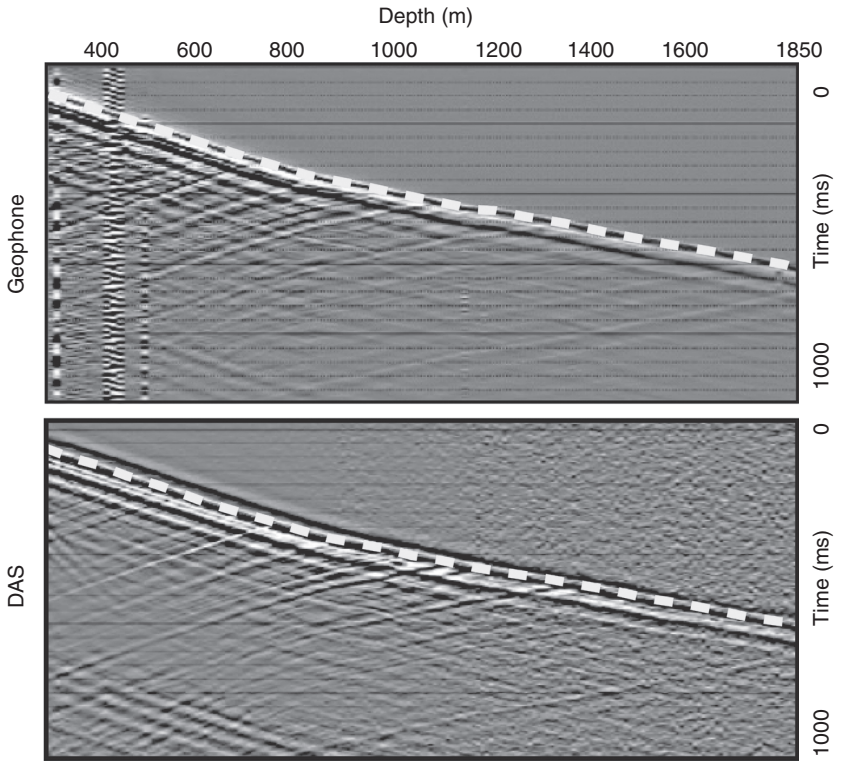


Figure 17 Comparison of VSP recorded by DAS (10-m channel spacing) and a co-located geophone array (7.5-m spacing) (Cox *et al.*, 2014). The first arrival picks are denoted by black dashed lines.

Michelson interferometry comparing two optical paths over gauge lengths between 0.5 and 20 meters. Accuracies of discrete sensors are on the order of one microstrain or 0.1° C. In principle, FBG accuracies are stable over long times because the reference grating spacing is known and glass is chemically stable. Distributed systems based on multi-mode fiber and Raman scattering are most common and measure temperature accurately to a few degrees Celsius with careful calibration. Distributed systems based on single-mode fiber and Brillouin scattering measure strain and/or temperature and have accuracies on the order of 30 microstrains, or two degrees Celsius. Distributed Acoustic Sensing (DAS), based on Rayleigh scattering, records ground motion like a one-component geophone in the direction of the cable.

Additional research and development is needed to validate fiber-optic measurements in rock masses. The greatest need is to establish case studies in different underground settings to encourage further development and deployment, as is often the case for the adoption of new technologies. The research and development can occur most usefully through cooperative programs between several communities: fiber-optic instrument and cable companies, the construction and mining industry, and academic and government laboratories. One particular need is enhanced methods of anchoring discrete and distributed fiber-optic cable to the rock mass, either along the surface of drifts or

embedded in boreholes. Further development is also needed for validating fiber-optic methods to monitor rock bolts and cable supports and to record rock bursts throughout a mine.

In conclusion, fiber-optic sensors have special attributes that make them potentially transformative for monitoring and characterizing rock masses in underground facilities. They can sense strain and temperature over spatial scales ranging from centimeters to tens of kilometers and temporal scales ranging from milliseconds to decades. Large-scale deployment of fiber-optic sensors appears to be an ideal technology for multi-spatial and multi-temporal measurements of rock-mass response to loading.

ACKNOWLEDGMENTS

Many colleagues have participated in our research on fiber-optic sensing. Participants from the University of Wisconsin-Madison were Dante Fratta, Neal Lord, Matt Kogle, Josh Roberts, Ashley Meulemans, Chelsea Lancelle, Ethan Castongia, and Alex Baldwin; from Montana Tech were Noni and Mary MacLaughlin; from the U. of Tokyo were T. Tokunaga, K. Mogi, Z. He, and Q. Liu. Other participants from Japan were Y. Kashiwai and H. Matsui. Alan Turner, Rich Barry, and Steve Gabriel contributed extensively to underground experiments at SURF. Michael Mondanos and Athena Chalari were invaluable partners in DAS field trials. This collaborative research project was supported by National Science Foundation grants to H. Wang and D. Fratta (CMMI-0900351), M. MacLaughlin (CMMI-0821788 and 0900663), and L. Murdoch (CMMI-0900163 and EAR-0609960) and by a Japan Science and Technology Agency grant to T. Tokunaga and Z. He.

REFERENCES

AFL (2015) Specialty Fiber Optic Cable, https://www.aflglobal.com/productionFiles/resources/catalogs/AFL-Specialty-Fiber-Optic-Cable.pdf.

Aminossadati, S.M., Nayeemuddin, M.M. & Shemshad, J. (2010) Distributed temperature measurements using optical fibre technology in an underground mine environment. Tunnelling and Underground Space Technology, 25, 220–229.

Baker Hughes Incorporated (2010) Optical reality: Fiber-optic technology monitors sand screen deformation in real time. *Connexus*, 1 (1), 20–23.

Baldwin, J.A. (2015) Developing a Multichannel Analysis of Surface Waves (MASW) Method for Application to Distributed Acoustic Sensing (DAS) Array and Co-Located Seismometers at Garner Valley, California, M.S. Thesis, University of Wisconsin-Madison, 50pp.

Barbosa, G.A., Lanceros-Mendez, S., Campos, J., Pamplona, J., Zamith, M., Almeida, A.M., Cabral, J.M. & Rocha, J.G. (2009) Piezoelectric sensor for acoustic wave detection in anisotropic systems. *Industrial Electronics, 2009. IECON '09. 35th Annual Conference of IEEE, 3–5 November, pp. 1905–1910.*

Bernini, R., Minardo, A. & Zeni, L. (2009) Dynamic strain measurement in optical fibers by stimulated Brillouin scattering. *Optics Letters*, 34 (17), 2613–2615.

Bhalla, S., Yang, Y.W., Zhao, J. & Soh, C.K. (2005) Structural health monitoring of underground facilities – Technological issues and challenges. *Tunneling and Underground Space Technology*, 20, 487–500.

Castongia, E., Wang, H. F., Lord, N., Fratta, D., Mondanos, M. & Chalari, A. (2017) An Experimental Investigation of Distributed Acoustic Sensing (DAS) on lake Ice. *J. of Env. & Eng. Geophysics*, 22 (2), in press.

Cox, B., Wills, P., Kiyashchenko, D., Mestayer, J., Lopez, J., Bourne, S., Lupton, R., Solano, G., Henderson, N., Hill, D. & Roy, J. (2012) Distributed acoustic sensing for geophysical measurement, monitoring and verification. *CSEG Recorder*, 7–15.

Culshaw, B. & Kersey, A. (2008) Fiber-optic sensing: A historical perspective. *Journal of Lightwave Technology*, 26 (9), 1064–1078.

Culverhouse, D., Farahi, F., Pannell, C.N. & Jackson, D.A. (1989) Potential of simulated Brillouin scattering as sensing mechanism for distributed temperature sensors. *Electronic Letters*, 25 (14), 913–915.

Dakin, J.P., Pratt, D.J., Bibby, G.W. & Ross, J.N. (1985) Distributed optical fibre Raman temperature sensor using a semiconductor light source and detector. *Electronics Letters*, 21 (13), 569–570.

Daley, T.M., Freifeld, B.M., Ajo-Franklin, J., Dou, S., Pevzner, R., Shulakova, V., Kashikar, S., Miller, D.E., Goetz, J., Henninges, J. & Lueth, S. (2013) Field testing of fiber-optic Distributed Acoustic Sensing (DAS) for subsurface seismic monitoring. *The Leading Edge*, 32 (6), 699–706.

Denny, D. (2010) Combining distributed-temperature sensing with inflow-control devices for improved injection profile. *Journal of Petroleum Technology*, 62, 2pp.

Diaz, S., Mafang, S.F., Lopez-Amo, M. & Thévenaz, L. "High performance Brillouin distributed fibre sensor," in *Proceedings of the European Workshop on Optical Fibre Sensors*, Naples, 2007.

Duncan, R. (2014) Well monitoring using coherent detection of Rayleigh scatter. U.S. Patent Application 13/886,929, Filed 3 May 2013.

Duncliffe, J. (1988) *Geotechnical Instrumentation for Monitoring Field Performance*. New York, Wiley Publishing.

Gage, J.R., Fratta, D., Turner, A.L., MacLaughlin, M.M. & Wang, H.F. (2013) Validation and implementation of a new method for monitoring *in situ* strain and temperature in rock masses using fiber-optically instrumented rock strain and temperature strips. *International Journal of Rock Mechanics & Mining Science*, 61, 244–255.

Gage, J.R., Noni, N., Turner, A., MacLaughlin, M. & Wang, H.F. (2010) Fiber optic strain and temperature monitoring in crystalline rock at the Sanford Underground Science and Engineering Laboratory (SUSEL), Lead, South Dakota. *44th U. S. Rock Mechanics Symposium and 5th U.S- Canada Rock Mechanics Symposium, 27–30 June, Salt Lake City, Utah, USA*, 8pp.

Gage, J.R., Wang, H.F., Fratta, D.O. & Turner, A.L. (2014) *In situ* measurements of rock mass deformability using fiber Bragg grating strain gauges. *International Journal of Rock Mechanics and Mining Sciences*, 71, 350–361.

Gage, J.R., Wang, H.F., MacLaughlin, M., Turner, A. & Fratta, D. (2011) A new method for measuring in situ strain in intact rock masses: Fiber optically instrumented rock strain and temperature strips (FROSTS). *45th US Rock Mechanics Symposium, San Francisco, CA, 26–29 June 2011*;, 10 pp.

Glišić, B. & Inaudi, D. (2007) *Fibre Optic Methods for Structural Health Monitoring*. 1st ed. Sussex, Chichester, John Wiley & Sons, Inc., Chichester, UK.

Gochioco, L.M. (2000) High-resolution 3-D seismic survey over a coal mine reserve area in the U.S. – A case study. *Geophysics*, 65 (3), 712–718.

Haneberg, W.C., Creighton, A.L., Medley, E.W. & Jonas, D.A. (2005) Use of LiDAR to assess slope hazards at Lihir gold mine, Papua New Guinea. In: Hungr, O., Fell, R., Couture, R. & Eberhardt, E. (eds.) *Landslide Risk Management, Conference on Landslide Risk Assessment, Vancouver, Canada, 31 May–3 June 2005, Vancouver, Canada*. Philadelphia, PA, Taylor and Francis. 10 pp.

Hasse, K. (2007) Strain sensors based on Bragg gratings. *IMEKO 20th TC3, 3rd TC16 and 1st TC22 International Conference Cultivating MetrologicalKknowledge, 27–30 November 2007.*

He, Z., Liu, Q. & Tokunaga, T. (2013) Ultrahigh resolution fiber-optic quasi-static strain sensors for geophysical research. *Photonic Sensors*, 3, 295–303.

Hudson, J.A. & Harrison, J.P. (1997) *Engineering Rock Mechanics: An Introduction to the Principles*. Oxford, Pergamon Publishing.

Hyett, A.J., Forbes, B.J. & Spearing, A.J.S. (2013) Enlightening Bolts: Using Distributed Optical Sensing to Measure the Strain Profile along Fully Grouted Rock Bolts. In *Proceedings of the 32nd International Conference on Ground Control in Mining, Morgantown, WV, 30 July – 1 August 2013*, 107–112.

Inaudi, D., Casanova, N., Steinmann, G., Mathier, J. & Martinola, G. (1998a) SOFO: Tunnel monitoring with fiber optic sensors. *Reducing Risk in Tunnel Design and Construction*, 7 (8), 1–12.

Inaudi, D., Conte, J.P., Perregaux, N. & Vurpillot, S. (1998b) Statistical analysis of under-sampled dynamic displacement measurements. *SPIE Symposium on Smart Structures and Materials*, 3325, 105–110.

Iten, M., Ravet, F., Niklès, M., Facchini, M., Hertig, T., Hauswirth, D. & Puzrin, A.M. (2009) Soil-embedded fiber optic strain sensors for detection of differential soil displacements. *4th International Conference on Structural Health Monitoring of Intelligent Infrastructure (SHMII-4) 2009, 22–24 July 2009, Zurich, Switzerland.*

Jacobs, T. (2014) Downhole fiber-optic monitoring: An evolving technology. *Journal of Petroleum Technology*, 66, 40–50.

Jaaskelainen, M. (2010) "Temperature monitoring of geothermal energy wells", *Proc. SPIE* 7653, Fourth European Workshop on Optical Fibre Sensors, 765303 (September 08, 2010); doi:10.1117/12.868156; http://dx.doi.org/10.1117/12.868156.

Kersey, A., Davis, M., Patrick, H., LeBlanc, M., Koo, K. & Askins, C. (1997) Fiber grating sensors. *Journal of Lightwave Technology*, 15, 1442–1463.

Kincade, K. (2006) Optoelectric applications: Fiberoptic sensing – Fiber sensors lay groundwork for structural health monitoring. *Laser Focus World*, 42.

Klar, A. & Linker, R. (2010) Feasibility study of automated detection of tunnel excavation by Brillouin optical time domain reflectometry. *Tunnelling and Underground Space Technology*, 25, 575–586.

Liu, Q., Tokunaga, T. & He, Z. (2011) Realization of nano static strain sensing with fiber Bragg gratings interrogated by narrow linewidth unable lasers. *Optics Express*, 19 (21), 20214–20233.

Liu, Q., Tokunaga, T., Mogi, K., Matsui, H., Wang, H. F., Kato, T. & He, Z. (2012) Ultrahigh resolution multiplexed fiber Bragg grating sensor for crustal strain monitoring. *IEEE Photonics Journal*, 4, 996–1003.

Mateeva, A., Lopez, J., Potters, H., Mestayer, J., Cox, B., Kiyashchenko, D., Wills, P., Grandi, S., Hornman, K., Kuvshinov, B., Berlang, W., Yang, Z. & Detomo, R. (2014) Distributed acoustic sensing for reservoir monitoring with vertical seismic profiling. *Geophysical Prospecting*, 62, 679–692.

Matsui, H., Kashiwai, Y., Sano, O., Tokunaga, T., He, Z., Mogi, K. & Wang, H.F. (2009) Evaluation of the applicability of optical fiber strain sensors for monitoring rock deformation caused by ocean tide – A case study at the Aburatsubo site, Japan. *EOS Transactions American Geophysical Union. 90: Fall Meeting Suppl.*, Abstract H23E-1010.

Mestayer, J., Cox, B., Wills, P., Kiyashchenko, D., Lopez, J., Costello, M., Bourne, S., Ugueto, G., Lupton, R., Solano, G., Hill, D. & Lewis, A. (2011) Field trials of Distributed Acoustic Sensing for geophysical monitoring. *SEG San Antonio Annual Meeting*, 4253–4257.

Micron Optics Incorporated (2010) Case Study – Mount Rushmore Rock Block Monitoring System. http://www.micronoptics.com/document_library/case_studies/civil_structures/MicronOptics-Mt_Rushmore_2010.pdf, accessed on 12 July 2015.

Murdoch, L., Moysey, S., Germanovich, L., Ozan, C., Kim, S., Skawski, G., Ebenhack, J. & Smith, J. (2014) Proof-of-feasibility of using Wellbore deformation as a diagnostic tool to improve CO_2 sequestration. https://www.netl.doe.gov/File%20Library/Events/2014/carbon_storage/4--Larry- Murdoch.pdf, accessed on 12 July 2015.

Noni, N., MacLaughlin, M.M. & Wang, H.F. (2011) Validation of fiber-optic strain-sensing cable for deep underground installation. *45th US Rock Mechanics Symposium, San Francisco, CA, 26–29 June 2011*, 10 pp.

Ohno, H., Naruse, H., Kihara, M. & Shimada, A. (2001) Industrial applications of the BOTDR optical fiber strain sensor. *Optical Fiber Technology*, 7 (1), 45–64.

Parker, T., Shatalin, S.V. & Farhadiroushan, M. (2014) Distributed acoustic sensing – a new tool for seismic applications. *First Break*, 32 (2), 61–69.

Pearce, J., Legrand, P. Dominique, T., Childers, B., Rambow, F. & Dria, D. (2009) Real-time compaction Monitoring with fiber-optic Distributed Strain Sensing (DSS). *SPWLA 50th Annual Logging Symposium, 21–24 June 2009*, 11pp.

Pinet, E. (2009) Fabry-P´erot fiber-optic sensors for physical parameters measurement in challenging conditions. *Journal of Sensors*, 2009, 1–9.

Rao, Y.P., Webb, D.J., Jackson, D.A., Zhang, L. & Bennion, I. (1998) Optical in-fiber Bragg Grating sensor systems for medical applications. *Journal of Biomedical Optics*, 3 (1), 38–44.

Rassenfoss, S. (2012) Fiber Optic Sensing – Learning How It Really Feels Downhole. *Journal of Petroleum Technology*, 64, 36–43.

Schweisinger, T., Murdoch, L. & Huey, Jr., C. (2007) Removable borehole extensometers for measuring axial displacements during well tests. *Geotechnical Testing Journal*, 30 (3), 202–211.

Selker, J.S., Thévenaz, L., Huwald, H., Mallet, A., Luxemburg, W., van de Giesen, N., Stejskal, M., Zeman, J., Westhoff, M. & Parlange, M.B. (2006) Distributed fiber optic temperature sensing for hydrlogic systems. *Water Resource Research*, 42, W12202.

Shatalin, S.V, Treschikov, V.N. & Rogers, A.J. (1997) Interferometric optical time-domain reflectometry for distributed optical-fiber sensing. *Applied Optics*, 37, 5600–5604.

Signer, S. & Sunderman, C. (2003) New Tools for rook Support Evaluation and Design. *22nd International Conference on Ground Control in Mining*, 5–7 August, 2003; Department of Mining Engineering, West Virginia University, Morgantown, WV, 114–118.

Skawski, G. (2012) Hydromechanical well testing using a 3D fiber optic extensometer. *M.S. Thesis, Clemson University, USA*, 141pp.

Skawski, G.M., Tokunaga, T., Ito, Y., Mogi, K., Cho, A., Germanovich, L.N., Hisz, D.B., Ebenhack, J., Wang, H.F. & Murdoch, L. (2011) Development of a 3d FBG extensometer for hydromechanical well testing. *American Geophysical Union, Fall Meeting 2011*, abstract #H21B-1107.

Sloan, S.D., Tsofliasa, G.P., Steeples, D.W. & Vincent, P.D. (2007) High-resolution ultra-shallow subsurface imaging by integrating near-surface seismic reflection and ground-penetrating radar data in the depth domain. *Journal of Applied Geophysics*, 62 (3), 281–286.

Smolen, J.J. & van der Spek, A. (2003) *Distributed Temperature Sensing: A DTS Primer for Oil & Gas Production*. The Netherlands, Shell International Exploration and Production.

Suárez, F., Hausner, M.B., Dozier, J., Selker, J.S. & Tyler, S.W. (2011) Heat transfer in the environment: Development and use of fiber-optic distributed temperature sensing. In: dos Santos Bernardes, M.A. (ed.), *Developments in Heat Transfer*. Intech, pp. 611–636.

Takemoto, S., Momose, H., Araya, A., Morii, W., Akamatsu, J., Ohnashi, M., Takamori, A., Miyoki, S., Uchiyama, T., Tatsumi, D., Higashi, T., Telada, S. & Fukuda, Y. (2006) A 100 m laser strainmeter system in the Kamioka Mine, Japan, for precise observations of tidal strains. *Journal of Geodynamics*, 41 (1–3), 23–29.

Tanaka, K., Tateda, M. & Inoue, Y. (1996) Measuring the individual attenuation distribution of passive branched optical networks. *Photonics Technology Letters*, 8 (7), 915–917.

Thévenaz, L. (2010) Brillouin distributed time-domain sensing in optical fibers: State of the art and perspectives. *Frontiers of Optoelectronics in China*, 1–9.

Thévenaz, Niklès, M, Fellay, A., Facchini, M., & Robert, P. (1998) Truly distributed strain and temperature sensing using embedded optical fibers, SPIE Proceedings vol. 3330, Smart Structures and Materials 1998: Sensory Phenomena and Measurement Instrumentation for Smart Structures and Materials, Richard O. Claus; William B. Spillman; Eds., pp. 301–314, 1998.

Tokunaga, T., Liu, Q., He, Z., Mogi, K., Matsui, H., Wang, H.F. & Kato, T. (2011) Application of an ultra-high-resolution FBG strain sensor for crustal deformation measurements at the Aburatsubo Bay, Japan. *American Geophysical Union, Fall Meeting 2011*, abstract #H13H-07.

Tyler, S.W., Selker, J.S., Hausner, M.B., Hatch, C.E., Torgersen, T. & Schladow, S. (2010) Environmental temperature sensing using Raman spectra DTS fiber-optic methods. *Water Resources Research*, 4 (187), 673–679.

Valley, B., Madjdabadi, B.M., Kaiser, P.K. & Dusseault, M.B. (2012) Monitoring mining-induced rock mass deformation using distributed strain monitoring based on fiber optics. *ISRM International Symposium – EUROCK 2012*, 28–30 May, Stockholm, Sweden, 14pp.

Wang, H.F., Lord, N.E., Chalari, A., Lancelle, C., Baldwin, J.A., Castongia, E., Fratta, D., Nigbor, R.L. & Karaulanov, R. (2014), Field Trial of Distributed Acoustic Sensing Using Active Sources at Garner Valley, California, Abstract NS41C-07 presented at 2014 Fall Meeting, AGU, San Francisco, CA, 15–19 December.

Wang, H.F., Tokunaga, T., He, Z., Liu, Q., Kashiwai, Y., Matsui, H., Mogi, K. & Kato, T. (2014) Measuring earth strain induced by ocean tides using Fiber Bragg Grating extensometers at Aburatsubo Bay, Japan, unpublished, 35pp.

Warneke, B., Last, M., Liebowitz, B. & Pister, K. (2001) Smart dust: Communicating with a cubic-millimeter. *Computer*, 34, 44–51.

Zhang, W., Gao, J., Shi, B., Cui, H. & Zhu, H. (2006) Health monitoring of rehabilitated concrete bridges using distributed optical fiber sensing. *Computer Aided Civil and Infrastructure Engineering*, 21, 411–424.

Zumberge, M.A., Berger, J., Hedlin, M.A.H., Husmann, E., Nooner, S., Hilt, R. & Widmer-Schnidrig, R. (2003) An optical fiber infrasound sensor: A new lower limits on atmospheric pressure noise between 1 and 10 Hz. *Journal of Acoustical Society of America*, 113, 2474–2479.

Chapter 18

A 3D laser scanning technique and its application to rock mechanics and rock engineering

Q. Feng[1], *G. Wang*[1] & *K. Röshoff*[2]
[1]*MultiInfo 3D Laser Scan Solution AB, Skarpnäck, Stockholm, Sweden*
[2]*Kobus AB, Hässelby, Stockholm, Sweden*

Abstract: The 3D laser scanning technique emerged in the late 1990s and has developed rapidly in recent years, becoming increasingly popular for rock mechanics applications. The technique enables us to scan an object at a distance (from a few centimeters to several kilometers) with high resolution (up to a few millimeters) and high scanning speed (up to one million points per second). The results of the scan are point clouds (a set of points with x, y and z coordinates in a spatial system) and panoramic images in greyscale or color. The scanning data are the integration of both spatial (coordinate) and visual (image) information in three dimensions, enabling the creation of a new way to solve problems in rock mechanics with several advantages. In recent years, specific efforts have been made in application to rock mechanics, such as on-site documentation and measurement for rock exposure mapping, monitoring of deformation for slope stability analysis, detection of water leakage, and quality control of blasting in relation to conditions such as overbreak and underbreak.

In this chapter, state-of-the-art 3D laser scanning techniques are first introduced and then application examples are presented, including the results from various projects and case studies contributed by different groups. Finally, the limits of current capabilities are discussed and recommendations made for further development of the techniques.

1 INTRODUCTION

The 3D laser scanning technique emerged at the end of the 1990s for 3D digital measurement, documentation and visualization in several fields, including 3D design in the processing industry, and documentation and surveying in architecture and infrastructure. In recent years, with the development of electronics and computer technology, scanning techniques have developed rapidly in terms of both hardware and software, and so more applications have become possible.

By using a 3D laser scanner, a tunnel or underground construction can be scanned at a distance (from a few centimeters to several kilometers) with high resolution (up to a few millimeters) and high scanning speed (up to one million points per second or more). The results of the scanning are point clouds (a set of points with x, y, and z coordinates in a spatial system) and panoramic images in greyscale or color. The scanning data are the integration of both spatial (coordinate) and visual (image) information in three dimensions, which can be transformed into a global coordinate system by controlled survey. Thus, a rock engineering object in its as-built situation can

be quickly recorded in 3D digital and visual formats in a real-coordinate system. In this case, it provides the potential for application of 3D measurement, documentation and visualization with high resolution and accuracy, making possible the creation of a new way to solve problems in rock mechanics with several advantages.

In practice, the typical set of parameters often captured include fracture orientation, spacing, trace length and aperture (Brown, 1981; Hudson, 1989; Priest, 1993). However, in current practice, much of this data is still obtained by hand through, for example, the use of compass and inclinometer for fracture mapping, measurement with a ruler, and documentation by recording information in a notebook and photographing with a camera. The most well-known drawback of traditional methods is that too many man-hours are involved in the *in situ* data acquisition procedures, which are time-consuming, not accurate enough, and sometimes difficult and dangerous when physically accessing rock faces. Recently, it has been realized that applying a new method for *in situ* data acquisition is the key to solving this bottleneck problem and improving rock face mapping data in both quality and quantity.

In order to avoid these problems, a new method should offer the following benefits: (a) rapid capture of data in the field; (b) digital collection of the data in order to exploit modern computer resources and speed up the procedure of data capturing and processing; (c) the facility to visually direct the data capture so that the operator's background knowledge and experience can be fully used to observe the complicated phenomena at a jointed rock mass and then obtain the required information for rock engineering applications; (d) operation at an appropriate level of accuracy for different rock engineering applications; (e) the ability to capture the data in 3D without physically contacting rock faces from a range of distances.

Recently, there have been efforts in rock mechanics applications, such as on-site documentation and measurement for rock exposure mapping (Feng, 2001; Slob & Hack, 2004; Slob *et al*., 2005; Feng & Röshoff, 2004), detection of water leakage through laser imaging (Feng *et al*., 2006), identification of rock types based upon image analysis (Wang, 2005; Feng *et al*., 2006), the capture of input data for numerical modeling (Jonsson *et al*., 2009), deformation monitoring (Hesse & Stramm, 2004; Schneider, 2006), 3D roughness analysis (Fardin *et al*., 2004), and quality control of blasting in relation to conditions such as overbreak or underbreak. These examples clearly demonstrate the potential benefits for rock mechanics application.

In the rest of this chapter, the following will be considered: (a) the current state of development of hardware and software for 3D laser scanning; (b) examples of application to rock mechanics; (c) an evaluation of the benefits of laser scanning to rock mechanics, compared to other methods; (d) the limitations of the current techniques and the need for further development.

2 CURRENT DEVELOPMENT OF 3D LASER SCANNING TECHNIQUES

Laser scanning, sometimes referred to as lidar (light detection and ranging), is a relatively new technique for obtaining the digital data of an object: rather than making a single measurement like a laser rangefinder, it captures millions of measurements, called point clouds, by rotating mirrors (or the entire unit) to cover a large area of an object's surface. A 3D scanner is a type of device that records the as-built situation

of an object in terms of data about its shape, and possibly its appearance (*i.e.* intensity or color), by emitting light and detecting the reflection of that light in order to accurately determine the distance to the reflecting object. Nowadays, it is widely applied to different fields for 3D measurement, surveying, documentation and modeling for architecture and archaeology, 3D design, and 3D surveying. As an entire solution, 3D laser scanning techniques consist of both hardware and software, which involves not only the capture of scanning data with a scanning device, but also the processing of the captured data and generation of useful results.

2.1 State of the art in laser scanning hardware

The first set of scanning devices were developed in the late 1990s in several countries in Europe and North America. Subsequently, some of the developers were purchased by manufacturers of surveying instruments. In the current market, there are many different types of laser scanning systems available from many more countries. However, these scanning devices are designed and developed for many different purposes, suitable to different cases of different applications. It is important, therefore, to select a scanner suitable to your particular application.

2.1.1 Different scanning systems

There are different scanning systems available in the current market, capturing different sizes of object (*e.g.* from a small tool to a large building) at a wide range of scales (*e.g.* from a few millimeters to tens of hundreds of meters), and they can be divided into different categories based upon different standards, according to scanning platform as shown in Figure 1, as follows: airborne laser scanning (ALS), terrestrial laser scanning (TLS) and micro-laser scanning (MicroLS).

In airborne laser scanning (ALS), the scanning system is loaded on an aircraft to capture 3D data about large areas. Terrestrial laser scanning (TLS) involves standing on the ground with different ranges of scanning distance, which is currently the practice most commonly applied to rock engineering projects. Micro-laser scanning (MicroLS) covers 3D scanning devices able to scan an object from a short distance (from a few millimeters to a few meters) that are either handheld or desk-mounted, which are mainly applied to fields such as reverse engineering and prototyping, quality control/inspection and documentation of cultural artifacts.

In terms of scanning range, the scanners can be classified as follows: long-range (up to several kilometers), mid-range (up to several hundred meters) and short-range (up to few meters).

Scanners can also be divided into three different types according to their scanning principles, summarized below:

- Pulse-based scanner. The pulse-based scanner is also called a time-of-flight (TOF) scanner, and is an active scanner that uses laser light to probe the subject. At the heart of this type of scanner is a TOF laser rangefinder. This finds the distance to a surface by timing the round-trip time of a pulse of light, as shown in Figure 2a. Clearly, the accuracy of a TOF 3D laser scanner depends on how precisely we can measure the time t. The laser rangefinder only detects the distance of one point in its direction of view.

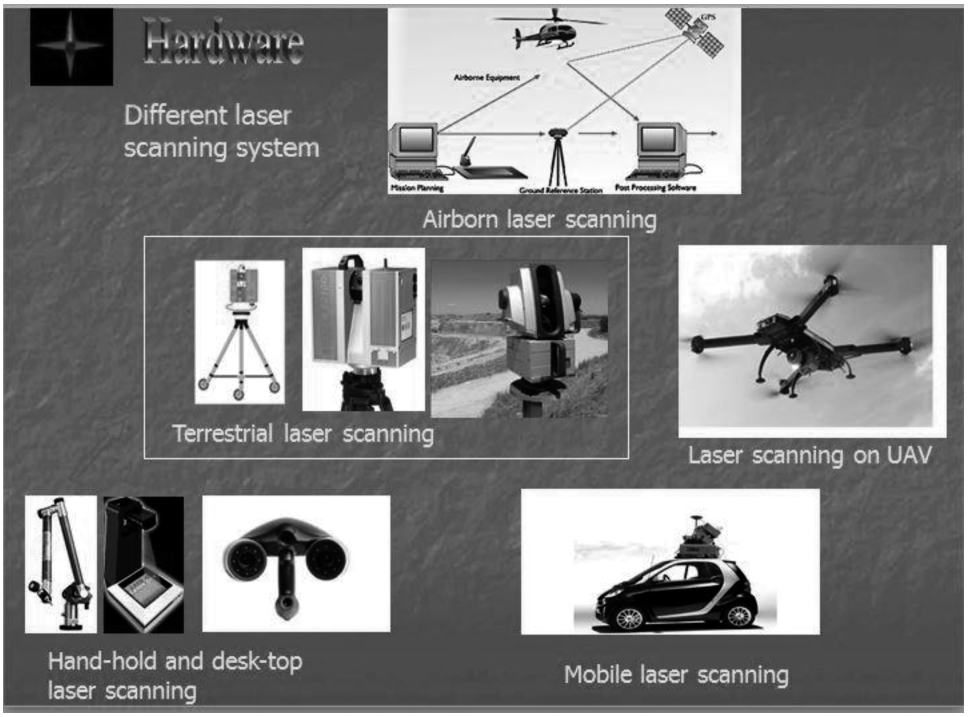


Figure 1 Different types of 3D laser scanning systems available in current market.

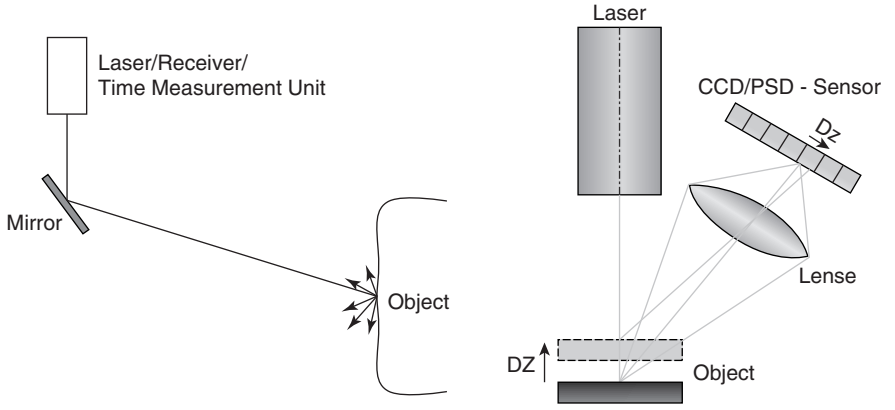


Figure 2 (a) Principle of time-of-flight laser scanner; (b) Principle of triangulation sensor (Adapted from Boehler & Marbs, 2002).

- Phase-based scanner. In comparison to the pulse-based scanner, this type of scanner has a high-speed scanning rate and better accuracy. Here, the transmitted beam is modulated by a harmonic wave and the distance is calculated using the phase difference between the transmitted and received waves. The phase-based scanner has higher

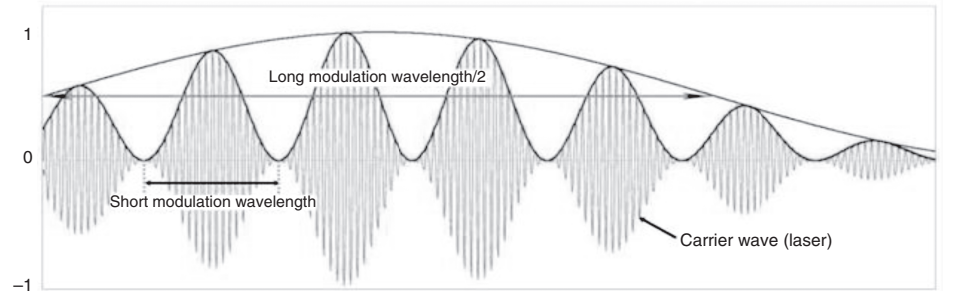


Figure 3 Schematic drawing of two modulation wavelength and carrier wave for phase-based laser ranging.

Table 1 Typical features of different scanners.

Type Features	*Pulse-based*	*Phase-based*	*Triangulation*
	ALS & TLS	*TLS*	*MicroLS*
Range	Long (km)	Middle (100s of m)	Short (m)
Resolution	Low–Middle (cm)	High (mm)	High (mm)
Accuracy	Low–Middle (cm)	High (mm)	High (mm)
Scanning speed	Low–Middle	High	Low

precision, and higher measurement rates of up to one million points per second can be obtained applying the phase shift measurement principle, illustrated in Figure 3.

- Triangulation-based scanner. Triangulation-based 3D laser scanners are also active scanners that use laser light to probe the environment. This technique, shown in Figure 2b, is called triangulation because the laser dot, the camera and the laser emitter form a triangle.

Table 1 shows some typical features of different types of scanners, which are summarized according to their technical specifications.

2.1.1 New trends in hardware development

3D laser scanning hardware has developed rapidly in recent years because of the development of electronics and computer technology. The principal trends in scanning hardware development are set out in the following subsections.

2.1.1.1 Improvement of scanner function in terms of usability and quality

The scanner itself has been improved in several ways in order to be more user-friendly in terms of its handling, with better quality in both the scanner and the scanning data captured. Some of the improvements are outlined below:

- Simpler operation. The scanner has become a standalone device, incorporating an internal computer, battery, camera, global positioning system (GPS), compass and inertial measurement unit (IMU). It is now designed in a more compact way with

lighter weight and smaller dimensions so that it is easily transported and carried. Scanners can be remotely controlled with a smart phone or tablet computer via Wi-Fi. Scanning data can be stored on an internal hard disk with a large storage capacity, and then copied via a USB port for further processing. The scanner's status can be intelligently diagnosed and adjusted.

- Better data. Scanning can now be conducted over longer distances, up to six kilometers, and wider viewing angles, rotating 360 degrees both vertically and horizontally, with increased scanning speeds of one million points per second or more, so that a large amount of scanning data can be captured very quickly. The resolution and accuracy of scanning data can be at millimeter-level for phase-based scanners. Noise can be filtered first by hardware, and then also by software. With a good quality of internal camera, a series of high-resolution images can be automatically captured in conjunction with the scanning, so that scanning images with true color can be obtained.

2.1.1.2 Development of scanners for robust applications

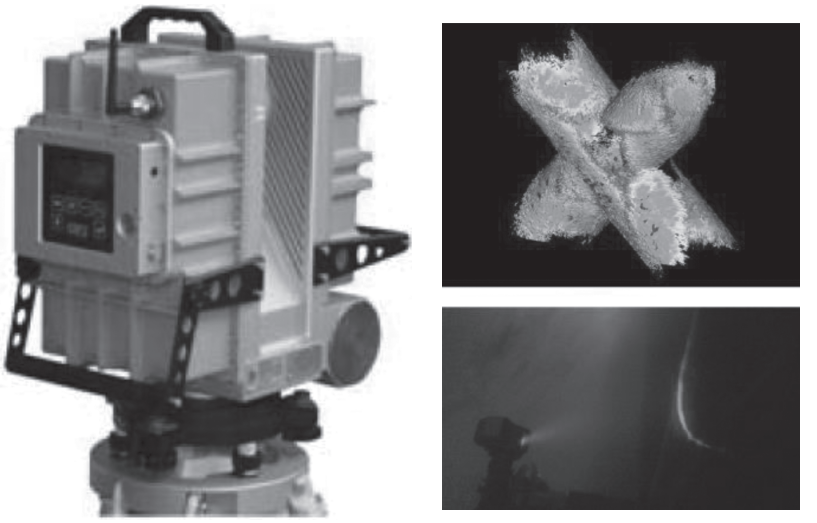
Some applications have led to the development of scanners capable of operating under more extreme conditions, for example:

- Explosion-proof scanner. In a chemical plant, on an oil platform, or in underground coal mining, where combustible or explosive gases are present, the scanner needs to be explosion-proof and scanners, such as that shown in Figure 4a, have been developed accordingly.
- Underwater scanning. It is now possible for scanning to be conducted in water for applications such as subsea inspection (see Figure 4b) and inspection inside the cooling water of nuclear plants (Newton Labs, 2016).

2.1.1.3 Coordination with other devices to capture integrated data

For some applications, scanning data needs to be integrated with other data, such as the distribution of radioactivity, temperature and stress in 3D. In addition, 3D scanning can only record the surface information and cannot penetrate the surface of an object, so there is a requirement to combine the scanned surface information with subsurface data. Scanners can now be plugged into other devices, such as thermal cameras, ground-penetrating radar (GPR) and radioactivity meters (*e.g.* gamma camera/meter) in order to capture multiple data for more applications. The following integrations have been developed:

- GPR. This is a geophysical method that uses radar pulses to image the subsurface. It can now be integrated with a scanning system to obtain both geometrical data and geophysical data about an object from both its surface and beneath its surface. For example, a combination of scanning and GPR is now used for inspection of underground pipelines.
- Thermal imaging. Temperature can vary significantly around some objects, and by combining the data from both a scanner and a thermal camera, the 3D temperature distribution of an object can be visualized. A scanner integrated with a thermal camera



(a) (b)

Figure 4 (a) Explosive-proof laser scanner (Zoller + Fröhlich, Wangen, Germany); (b) Underwater scanning (2GRobotics, Waterloo, Canada).

is now available on the market (see Figure 5) for use in applications such as the forensic investigation of crime scenes and the monitoring of pipelines in power plants.

- Radioactivity measurement. In the nuclear industry, radioactivity is the subject of greatest concern. By combining scanning data with radioactivity measurement, the distribution of radioactivity in a nuclear facility can be quantitatively analyzed in 3D. As a result, a scanner integrated with a gamma camera has now been developed for use in the nuclear industry to record both 3D geometrical data and radioactivity distribution for projects such as nuclear decommissioning and radioprotection (Createc, 2016).

2.1.1.4 Scanning from multiple platforms

One of the most recent developments in scanning hardware is the availability of a series of scanning systems on different platforms, such as scanning underwater, on boats, on the ground, on mobile vehicles, integrated into planes or unmanned aerial vehicles (UAVs), by hand using a handheld scanner, and even while walking with a bag-based scanner on your back. In fact, it is now possible to perform 3D scanning in many different ways and further details of some examples follow:

- Mobile scanning systems. A mobile scanning system, illustrated in Figure 6, is an integrated system, including a laser scanner, digital video camera, GPS and IMU, which is loaded on a car or some other type of mobile vehicle. In this case, 3D scanning data and images of an object (*e.g.* a tunnel or a road) can be quickly recorded while a mobile vehicle is travelling.



(a) (b)

Figure 5 (a) Scanner with thermal camera; (b) Scanning data with temperature (Zoller + Fröhlich, Wangen, Germany).

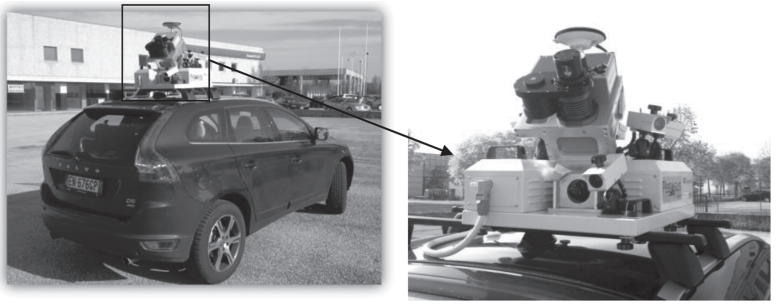


Figure 6 Scanning system on a car.

- Airborne scanning systems. A scanner with a camera, GPS and IMU can also be loaded on a plane, helicopter or unmanned aerial vehicle (UAV) to scan an object from the air. The increasing popularity of this approach means there are now many different airborne systems on the market.
- Personal scanning systems. A scanning system including a scanner, one or more video cameras, GPS and IMU can also be loaded onto a small trolley or into a backpack so that scanning can be undertaken while walking around.

2.2 Development status of data processing software for laser scanning

The data recorded by a scanning system contains a large amount of different types of data, including point coordinates and images, together with some associated

parameters such as indexes to link calibration of scanner and camera. For a mobile scanning system, additional parameters from the GPS, IMU and odometer are also attached. It is important, therefore, to develop a suitable software package to control the hardware and process the large amount of recorded data.

In a typical laser scanning project, this software needs to carry out several steps, including field scanning, preprocessing of the recorded raw data, post-processing of the data to generate the results required by the specific application, and export and transformation of the data and results to a suitable user-defined system, for example, a computer-aided design (CAD) system, geographical information system (GIS) or virtual reality system. In this case, one piece of software is not enough, and a series of software packages are developed for different applications. In considering the entire procedure of a scanning project, from data collection to the final model, a rough distinction can be made between the software packages as follows:

- Software for scanning control in the field. This type of software is developed by the scanner manufacturer, and is mainly used to control the hardware as it captures the scanning data.
- Software for preprocessing of the recorded raw data. The raw data recorded by the scanning system needs to be preprocessed before any further interpretation can be carried out in order to address several issues including: (a) terrestrial scanning can be derived from more than one station, not yet georeferenced into the same predefined coordinate system; (b) data noise needs to be filtered out; (c) scanning points need to be colorized with the images collected at the same time. Software to solve these problems is mainly developed by the hardware manufacturers, but some is also provided by the software developers.
- Software for post-processing. After preprocessing, scanning data is registered in user-defined or georeferenced coordinate systems. All of the scanned objects are thereby reconstructed in 3D digital format with their correct geometry and spatial location. The aim of the post-processing is to generate results from the scanning data for further application, for example: (a) to reconstruct 3D model from point clouds as either standard geometrical or free-form mesh models; (b) to generate lines (*e.g.* cross sections of a building or a tunnel) from point clouds; (c) to calculate the volume of a stone or coal heap; (d) to create an orthophoto from the scanning data; (e) to calculate the deformation of a tunnel. This type of software is mainly created by third-party developers.
- Software for linking and converting scanning data into other systems. Scanning data are normally large in volume because the data is in raster format as point clouds or images. Special software must be developed to process large amounts of scanning data and link it to other software, such as CAD or GIS, for further processing. In some cases, 3D data must be transformed to 2D images or drawings, and scanning data in specialized and/or proprietary formats needs to be converted into a neutral or standard format such as ASCII. This type of software is created either by third-party developers or by the companies which have developed the receiving software (*e.g.* CAD or GIS developers).
- Software for special applications. The software described thus far is generally applicable to all scanning and modeling. However, for very specific applications, software needs to be developed with professional background knowledge of the

speciality in question. The results can be specific parameters for specific contexts with a specific data format and standards. Examples could include software for tunneling to evaluate the overbreak and underbreak from blasting, and software for blasting design through the use of scanning data. This type of software is mainly developed by software developers in conjunction with experts in the particular speciality.

The development of all of this software is moving very fast, and gaining more and more attention from users because the quality of these software modules has a considerable influence on the quality of the final modeling results, and also on the time needed to achieve the results. Thus, a smoothly performing software product is a basic precondition for the widescale acceptance of 3D laser scanning techniques.

3 CAPTURE PROCEDURE AND FEATURES OF SCANNING DATA

3.1 Typical procedure for scanning data capture

The stages of a typical scanning procedure are described in the following subsections.

3.1.1 Control surveying

Reference surveying is often carried out by using a total station to set up a local coordinate system around the scanning area, and linking the local coordinate system to a global coordinate system.

3.1.2 Scanning

The operation of different scanning systems varies according to the requirements of the scanning software and the reference surveying. However, some basic parameters must be correctly selected for most applications: (a) scanning resolution; (b) scanning range; (c) position of each scan; (d) number and location of reference targets. In addition, some scanning systems are also sensitive to environmental factors, such as temperature, moisture, the density of particles in the air, and even the reflectivity of the object. These parameters and factors must be carefully considered in order to obtain a good quality of scanning data.

The typical raw data from laser scanning is the so-called point cloud, which is a set of vertices in a 3D coordinate system. These vertices are usually defined by x, y and z coordinates and are typically intended to be digitally representative of the external surface of the object (*e.g.* rock mass).

For most phase-based scanners, the raw scanning data combines both point and intensity, so that the corresponding intensity image in both 2D and 3D can be obtained, which is useful for documentation and identification of objects in detail. Figure 7 shows the raw scanning data typically captured from a phase-based scanner.

The true color scanner is still under development, and at present it is possible to scan some small objects but not possible, in practice, to scan a rock mass over a large area. However, another alternative in which scanning data is combined in software with color photos is now possible. During scanning, color photos are captured by a digital

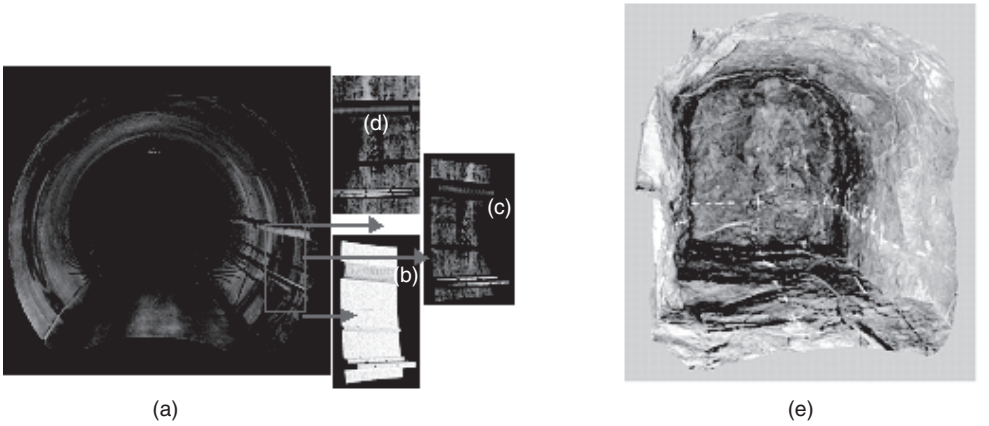


Figure 7 (a) Presentation of raw scanning data; (b) Point cloud; (c) 3D laser image; (d) 2D laser image; (e) 3D color model of scanning data in tunnel.

camera at the same time, and then the color photos are registered to the scanning data in software, so that a true color 3D model of a rock mass can still be obtained, as shown in Figure 7e.

3.1.3 Preprocessing data

The scanning data captured on site, also called raw scanning data, must be preprocessed before any further modeling or calculation can be carried out. The reasons are:

1 Each individual scan positions the scanning data in a local coordinate system, and several scans are generally needed to cover the whole object. As a result, each individual scan then needs to be registered into a common, shared coordinate system.
2 Not all points in the raw scanning data can be used because there are always noise points captured, particularly when using a phase-based scanner. The noise points have, therefore, to be filtered out of the raw scanning data.

In consequence, the raw scanning data generally needs to be preprocessed in two steps: (a) register each individual scan into a common coordinate system; (b) filter out noise points from the raw scanning data.

In addition, different scanner producers generate different data formats for the raw scanning data, so it is sometimes necessary to convert the raw scanning data into another format, depending upon which modeling software is to be used for the post-processing.

3.1.4 Post-processing data

After preprocessing of the raw scanning data, the point clouds have been positioned and oriented in a given coordinate system, and all scanning points are correctly located

in a known coordinate system, so the post-processing can be performed. This is typically handled by one of two different approaches:

- Use of specially developed software. Because the scanning data are large in volume, compared to other data, and also have a special data format, special software has been developed. This software can process the large amounts of scanning data and create different results as required, including CAD models, mesh models and cross sections. These, in turn, can be exported into other existing application systems, such as CAD, GIS or other user-familiar systems.
- Direct input into existing software packages. Such integration proved difficult in the earlier stages of 3D scanning development, but now many so-called plug-in software modules have been developed, and these make it possible to import large scanning data files into more user-familiar software, such as CAD and GIS. In addition, the many more hardware producers now in the market will attract more users, and will increasingly allow their special data formats to be converted into a neutral format, the ASCII format, making scanning data more readily available for post-processing in a wider range of different software packages.

3.2 Special features of scanning data

In general, 3D laser scanning techniques offer several advantages:

- A revolutionary technique for measurement and surveying. It enables us to measure an object in terms of a single point through to a cloud of points, so that it is possible to measure the area of a free-form surface or the volume of a stone heap.
- Integration of visual and orientation information. Traditionally, visual information like images from a camera or video camera have been recorded separately from the orientation information provided by GPS or a total station. In 3D laser scanning, both visual and orientation information are integrated with one another, which enables us to ensure that what we measure is what we see.
- From 2D plane design to 3D visual design. Traditionally, design has involved drawing in a 2D plane. By using 3D laser scanning data – both 3D point clouds and panoramic images (or bubble views) – visual design in 3D now becomes possible, which allows virtual designing within a 3D digital model.

These features have great potential for rock mass characterization in a rock mechanics project. Compared to traditional methods for rock mass characterization, the following features of laser scanning represent significant advantages: (a) capture of a large coverage of a rock surface at high resolution (up to millimeters) in a short time (a few minutes depending on the resolution selected); (b) all the data are in digital format and in 3D, both image and coordinates; (c) following reference surveys, all scanning data are registered in a global coordinate system, and a rock mass can be assigned its real position in space; (d) a rock mass can be recorded by remote control with minimal dangers to personal safety; (e) there is no need for illumination, yet high-resolution digital images can be obtained; (f) the combination of scanning and photography in software makes it possible to record a rock mass in real color. Thus, laser scanning can avoid the drawbacks of traditional methods, and also improve the quality and quantity of the data for rock mass mapping. Based upon laser scanning, a rock mass can be

quickly recorded and the following useful information obtained: (a) position of a rock mass with 3D coordinates in a global coordinate system; (b) geometrical features, for example, length between points or orientation of a fracture; (c) visual information, for example, 2D and 3D digital images, and 3D virtual models; (d) physical features, for example, water leakage and differentiation of rock type by virtue of different intensities.

4 APPLICATION EXAMPLES

To evaluate the potential application of laser scanning to rock face mapping, it is important to understand the typical procedure for site mapping in a rock engineering project, and then establish whether laser scanning can help to improve or solve the problems of traditional methods.

Thus, for a site mapping project, the typical procedure is:

1. Collect the raw data in the field. The raw data consists of different types, dependent upon the nature of the project, but all projects must collect basic data, such as location, geometry (of fracture, rock surface etc.) and site-specific phenomena, through measurement, photography and observational note-taking. Digital methods can make this step much faster and more accurate than traditional approaches, and a more detailed description will follow in a subsequent section.
2. Calculate and analyze the raw data. After the field data collection, the raw data must be processed for a range of different purposes, such as calculation of fracture orientation, plotting into the stereo diagram for fracture analysis and stability analysis, import of the fracture parameters for numerical modeling, and also for the design of a dam or tunnel. All such data processing is now computer-driven, so any input data must be digitalized, which is time-consuming for traditional recordings.
3. Present and transform the processed data. The processed data and results, either in tabular or graphic form, should either be presented in an appropriately useful way, or exported to other software for further analysis, modeling or design, all of which are likely to be digital in format and computer-driven.
4. Store and archive the raw data and results. With the development of computer science, the data are now mostly stored and archived in a digital way on external or internal hard disk, so it is important to convert all data to digital format.

Thus, in order to avoid the drawbacks of traditional methods, a new approach must have the following important features: (a) rapid capture of data in the field; (b) digital collection of the data in order to use computing resource to speed up both data capture and processing; (c) visual control of all operations so that the operator's background knowledge and experience can be fully utilized in observing the complicated phenomena at a jointed rock mass, and the required information for rock engineering applications is obtained; (d) maintenance of given levels of accuracy for different rock engineering applications; (e) the ability to capture data in 3D without physically contacting rock faces, from a range of distances.

Some typical examples of applications are summarized in this section.

4.1 Site characterization of a rock exposure

The most typical application for 3D laser scanning is the site characterization of a rock exposure. Currently, rock surface mapping is still mainly performed using traditional methods, which are well-known as the use of a geological compass with inclinometer to measure dip and strike, the taking of notes in a notebook, and the taking of photos for documentation. These traditional methods have some obvious drawbacks, including:

- The need for personal contact with the rock face, which frequently leads to problems such as rock faces that are inaccessible or dangerous to reach, making it difficult or impossible to obtain the mapping data;
- Uncertainty and inaccuracy – mapping results can be heavily dependent upon personal experience, and it is difficult to ensure or validate that the mapping data are reliable or if it is wrong, how it became wrong;
- Time-consuming – not only in terms of the fieldwork but also the large amounts of time to transfer data into a computer for further modeling and analysis.

3D laser scanning offers great potential to avoid some of the drawbacks of traditional methods, and also improve the quantity and quality of the raw data and the results. Based upon a review of the literature and our own project experiences, the specific benefits of laser scanning when it comes to rock surface mapping can be summarized as follows:

- Laser scanning is a non-contact technique, so it is not necessary to reach the rock surface, and there is no consequent risk to the individual.
- It can capture the rock surface, in terms of its geometry and position, much more quickly and accurately than traditional methods.
- It collects the data in digital and 3D formats, making 3D digital mapping possible, and the raw data can be directly and rapidly processed by computer. Both semi-automatic (Feng & Röshoff, 2004) and fully automatic methods (Slob *et al.*, 2005) of measurement are possible and have been tested for fracture mapping.
- All of the data, from the raw data to the processed results, can be stored and archived within the digital medium, and also transferred (*i.e.* input and output) among other software packages.
- In particular, it is possible to verify the data and the results because the raw data is retrievable and the processing methods are repeatable, which makes the data quality more reliable and controllable.

To characterize the features of exposed rock faces, the International Society for Rock Mechanics (ISRM) proposed ten parameters (Brown, 1981) – namely, orientation, spacing, persistence (or trace length), roughness, aperture, wall strength, filling, seepage, number of fracture sets and block size – to describe the geometrical, mechanical and hydraulic features of fractures.

In order to adequately characterize the features of a rock surface, the new methods must provide enough information to replace the personal observation and measurement of the traditional ones, and better them in some ways. In general, the information required is:

- Geometrical information. It is necessary to obtain some geometrical parameters, that is, fracture orientation (dip and strike), block size, spacing, roughness and aperture. Digital methods are able to capture 3D digital data, and can provide 3D geometrical information for rock face mapping.
- Physical information. Information such as rock types, mechanical properties of a rock, wall strength and mineral fillings must also be obtained. It is possible to identify the rock types, and perhaps also the mineral fillings, from color photos and intensity laser images, but the ability to measure mechanical properties (*e.g.* wall strength) is limited.
- Visual information. Photographs and images are needed for a mapping mission in order to identify the rock types, discontinuity set and water leakage (seepage). Again, color photos and intensity laser images make this possible.
- Spatial information. This provides the location and orientation of the rock surface in space. It can be captured through digital methods by measuring a number of reference points and then transforming them into a global coordinate system.

The literature review reveals that laser scanning techniques have been applied to several different situations at the rock exposure, including road cuts, open pits, tunnels and even a borehole.

When site mapping a rock exposure, it is possible to apply laser scanning to a range of very specific purposes, some examples of which are described below.3

4.1.1 Fracture orientation

Orientation of a fracture plane is traditionally measured by a compass and inclinometer. By using laser scanning, fracture orientation can be measured semi-automatically (Feng & Röshoff, 2004) or fully automatically (Slob *et al.*, 2005).

In the semi-automatic method, orientation of a fracture plane (*e.g.* dip and strike) can be determined interactively or semi-automatically from the 3D laser scanning data. The method aims not only to take advantage of modern computer techniques, but also enables operators to employ their geological background knowledge to control the mapping results. A typical mapping procedure with this method not only involves computer software acting as a virtual mapping platform, but also involves interaction between the operator and the computer: (a) the operator selects a portion of the rock surface from the whole 3D scanning model; (b) the operator selects a fracture exposed on the scanned rock surface and marks the exposed fracture surface interactively; (c) the computer automatically calculates the best-fit fracture plane and then calculates the fracture orientation. Figure 8 shows an example of fracture mapping based on 3D laser scanning data from an exposed rock face.

The fully automatic method (Slob *et al.*, 2005) is based upon segmentation approaches to the processing of scanning point clouds, after which the best-fit plane of fracture surfaces can be automatically calculated and the fracture orientation is determined, as shown in Figure 9.

4.1.2 Roughness

Fracture roughness is mostly characterized in the laboratory on small specimens of a natural fracture surface. *In situ* determination of fracture roughness at a large scale is

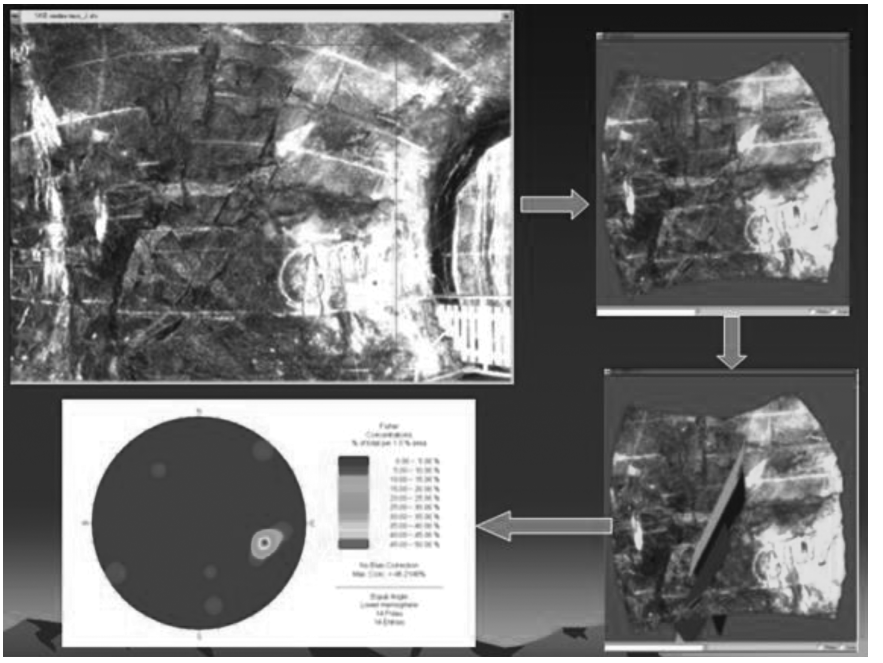


Figure 8 Semi-automatic fracture mapping.

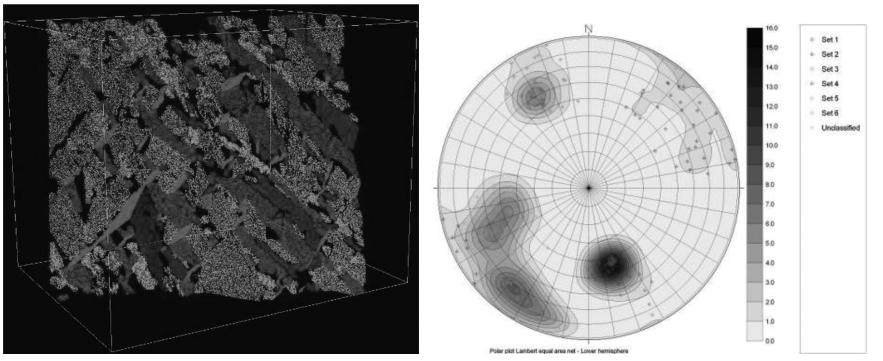


Figure 9 Fully automatic fracture mapping (Adapted from Slob *et al*., 2005).

very important to understand the scale effect of fracture roughness, the large-scale deformation of rock masses and the hydromechanical behavior of fractured rocks. By using laser scanning, fracture roughness can be quantitatively described in several different ways, conferring a number of advantages:

- Triangulated mesh. A triangulated mesh of a fracture can be created from scanning point clouds (DTFHA, 2008). If the orientation of each triangle is plotted on

a stereonet, then the scatter about the mean orientation of the fracture gives information on the dilatation angle. In the classic sawtoothed fracture analyzed by Patton (1966), the dilatation angle is defined as the rise angle of the sawteeth compared with the mean orientation. The dilatation angle is directly related to the additional friction angle as a result of roughness (Goodman, 1989), and the dilatation angle can be directly determined on a stereonet from the angle between the mesh triangle orientation and the mean orientation of the fracture.

- Directional cross section profile. A cross section profile is created from cross sections taken through a fracture at different angles as appropriate (a cross section in the direction of the dip vector, for instance, would be relevant for slope stability purposes) in order to provide information about roughness (DTFHA, 2008).

Compared to traditional methods, laser scanning not only describes the fracture roughness quantitatively, but also provide information about its orientation once the scanning area is registered within a known coordinate system. This is important for rock mechanics because it not only allows calculation of the shear strength, but also determines the slipping direction.

4.1.3 Length and spacing

Fracture exposure lengths and the spacing between different fracture sets can also be measured either via laser image or in 3D point clouds.

4.1.4 Rock type

Laser scanning not only measures the position but also the reflective intensity at every point, so that the laser image created is based upon the intensity difference between different objects. Because different rocks have different intensities, the intensity laser image has been studied in order to identify different rock types. In this study, several image processing methods were tested, such as texture analysis and image classification. Figure 10 shows different rock types in a pseudo-color laser image created by these methods.

4.1.5 Water leakage identification

Water leakage is an important hydrological parameter in site characterization. Based upon the reflective intensity difference between damp and dry rocks, laser imagery can not only detect the position and area of a water leakage, but also quantify the amount of water involved, as illustrated in Figure 11.

4.2 Quality control of tunnel construction

4.2.1 Quality control of tunnel blasting

For a new tunnel under construction, it is important to control the overbreak or underbreak by comparison to the theoretical design. By using full-coverage laser scanning data, the quality of the blasting can be accurately presented in either a 3D model, a cross section or a difference model (see Figure 12).

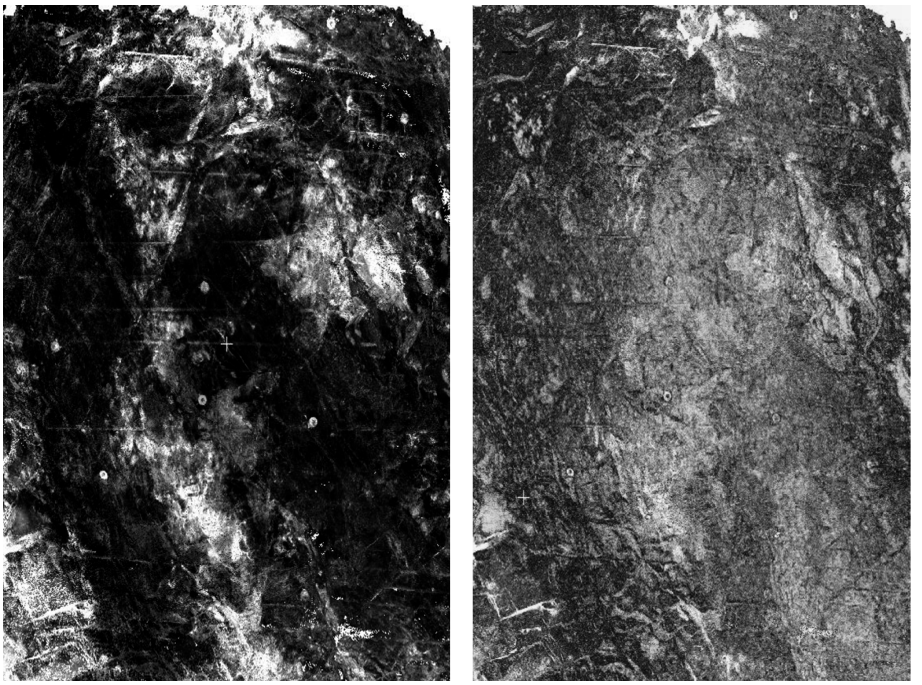


Figure 10 Rock type comparison between laser image (left) and pseudo color image (right) (Wang, 2005).

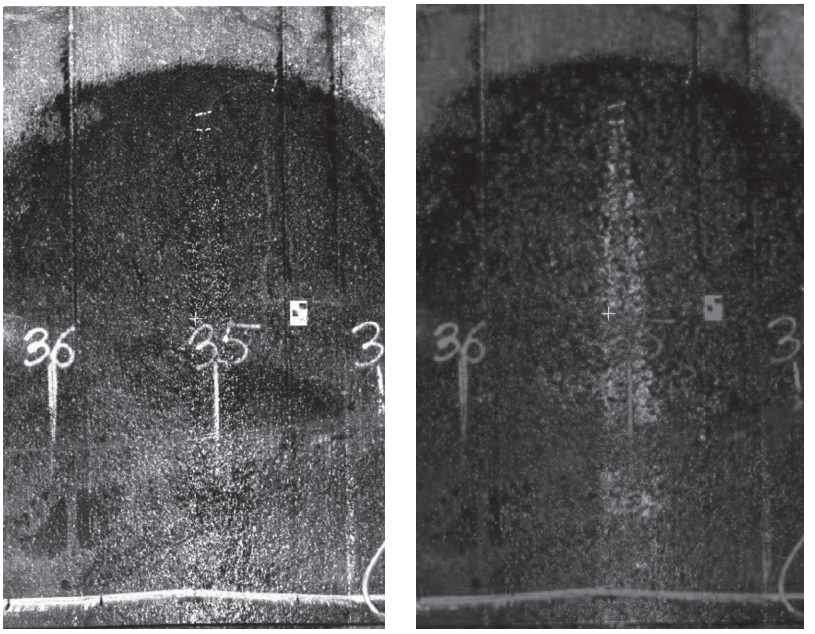


Figure 11 Identification of water leakage from laser image processing analysis (Wang, 2005).

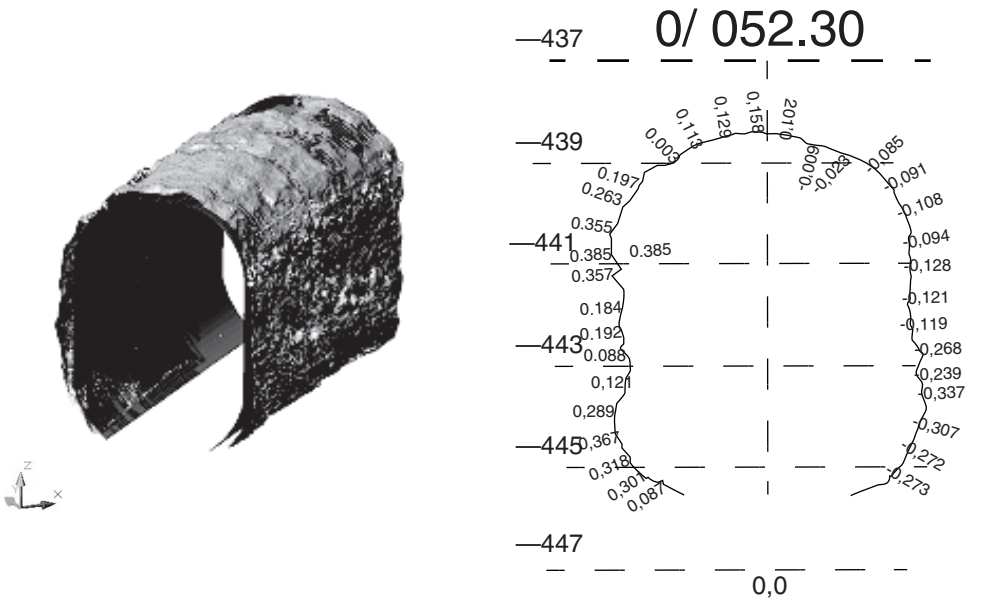
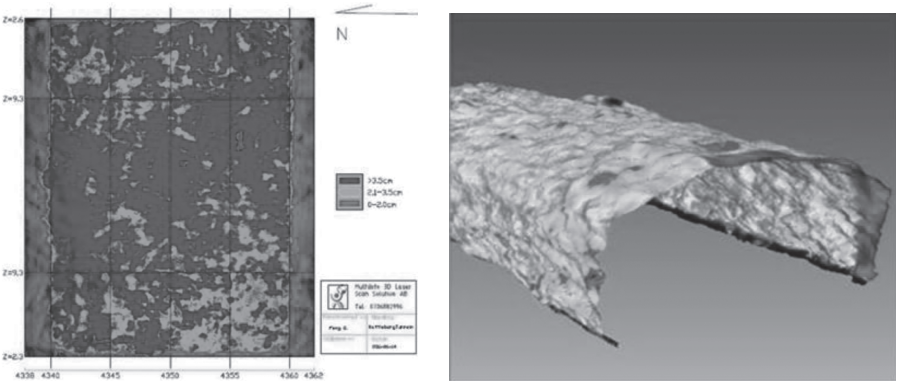


Figure 12 Difference model (left) and profile (right) comparisons between designed and blasted tunnel.



(a) (b)

Figure 13 Thickness of sprayed concrete in an unfolded tunnel map (left) and 3D model (right).

4.2.2 Thickness control of sprayed concrete

The thickness of the sprayed concrete is important to tunnel reinforcement. Traditionally, it is just tested with a spike at a number of randomly selected points. However, using full-coverage laser scanning data, the thickness of the sprayed concrete

can be accurately calculated and presented in an unfolded tunnel map or even in a 3D model, as shown in Figure 13.

4.3 Deformation monitoring

A rock mass can be deformed by both artificial and natural forces, such as tunneling, mining and earthquake, which may result in a disaster for both human beings and facilities. One of the most important concerns for rock mechanics is, therefore, to monitor the deformation of a rock mass.

Traditionally, the rock mass is monitored by measuring the displacement of several points at a defined position, such that the monitoring is only effective at those selected points, and offers no insight into the rock mass as a whole. There is an obvious risk of missing one or more unstable portions of the rock.

With laser scanning, the surface of a rock mass can be scanned in full coverage with a high density of scanning points, so that the rock mass can be monitored as a whole. Compared to traditional methods, laser scanning offers two significant advantages in this application:

1. Full coverage of the entire object, not limited to selected points. Traditionally, the deformation is monitored by the relative displacement between a selection of points, but with laser scanning the disturbed parts can be fully covered and quickly scanned at high resolution, without risk of missing those parts ignored in a traditional approach.
2. Deformation can be visualized in 3D and identified in a laser image. As already described, 3D scanning data consists of both point clouds and intensity laser

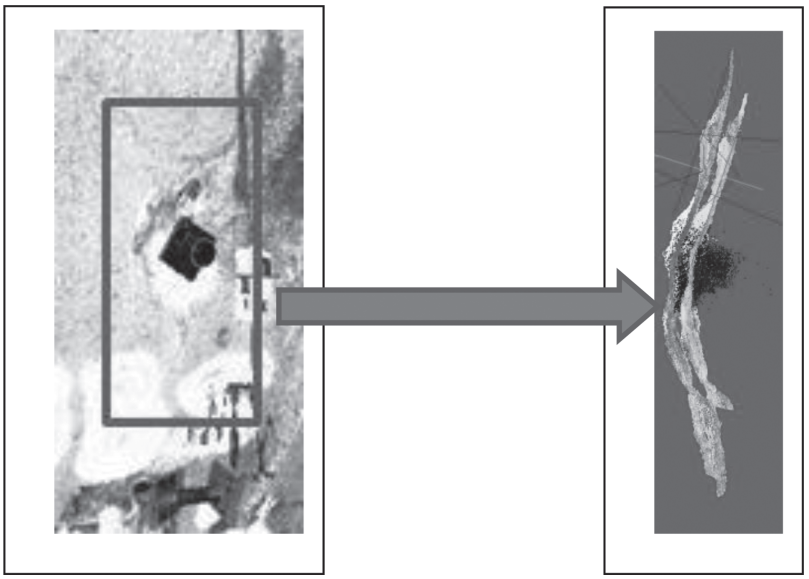


Figure 14 Identifying deformation of an object in both laser image and 3D model.

images, so if specific aspects are of particular interest, then the deformation and its corresponding objects can be visualized in both 3D and laser image. Figure 14 shows the location of a special object and its deformation after blasting.

Problems and uncertainties exist in relation to deformation monitoring, so additional consideration should be given to some of these:

- Accuracy of control surveying relative to the real deformation. In order to monitor the absolute movement of a rock mass, control surveying is important. This involves relating the deformed part to a stable part, or transforming details of the deformed area into a global coordinate system. In either case, it is important to know the accuracy of the control surveying with respect to the real deformation. In many publications and case studies, the accuracy of control surveying is not mentioned, creating uncertainty as to whether the displacement derives from an error of control surveying or from the real deformation.
- Resolution of a scanner relative to the accuracy of deformation measurement. In general, a high-resolution scan is capable of identifying the minor deformation of an object. However, scanning an object with a high-resolution scanner may not automatically provide a high accuracy of deformation measurement. This is a misunderstanding often made in practice. As previously mentioned, a rock mass sometimes needs to be scanned from several positions, or a large area of a rock mass need to be covered by several scans. In this case, all of the scans must be registered into a common coordinate system. Normally, the more scans registered, the more errors will be propagated at registration.
- Accuracy of the parameters created from scanning points. In laser scanning, the deformation can be evaluated through different parameters, such as changes of volume, surface area, rotation and profile lengths. However, it is also necessary to analyze the accuracy of creation from scanning points for those parameters. If the error in creating the parameters is larger than the deformation, any movement of a rock mass may be obscured, and any deformation may remain undiscovered.

4.4 Improvement of input data for numerical modeling

In rock mechanics, numerical modeling is often used to estimate and simulate the behavior of a rock mass under certain conditions at geometrical, geological and hydrological boundaries. It is important in numerical modeling that the parameters that are input closely describe the real conditions of a rock mass. Such input data can be improved with laser scanning, so that the results of numerical modeling can be brought closer to the reality. Several studies have tested laser scanning techniques for the creation of input data for numerical modeling.

A case study by Bäckström *et al.* (2009) applied the input data from laser scanning (*i.e.* the as-built 3D model and profile of a tunnel) to evaluate the factors that affect and control the excavation disturbance zone (EDZ), and compared the results with the design data. By using the irregular as-built profile of the tunnel, the stress distribution around the tunnel shows interesting results (Figure 15). It shows that the irregular shape of the tunnel walls in the as-built sections, as well as their bumpiness, generates

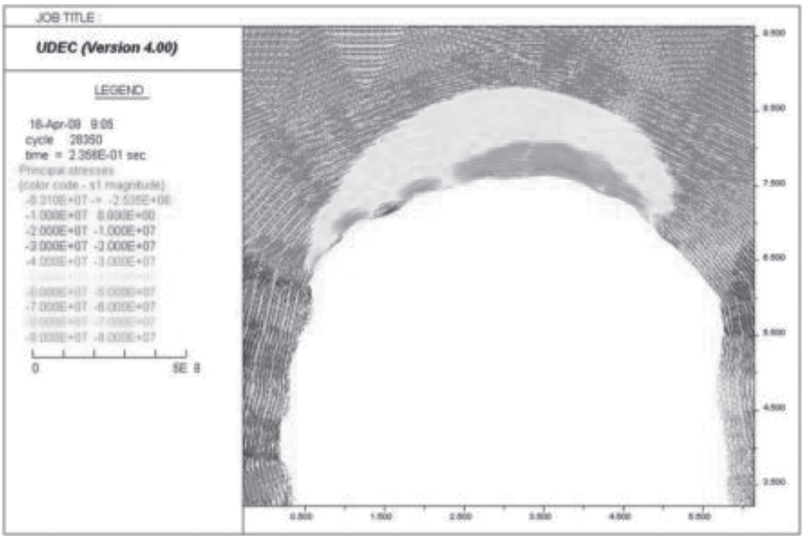


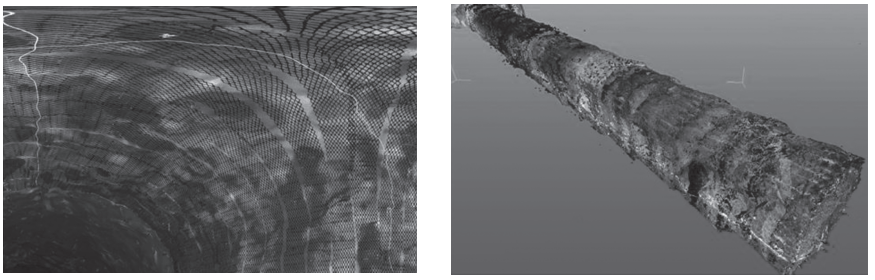
Figure 15 Stress tensor plots at section 47 with the borehole seismic data after excavating the heading; model with E = 65 GPa; maximum compressive stress = 83 MPa (Adapted from Bäckström *et al.*, 2009).

asymmetry in the redistribution of stress around the tunnel. Bump-type (convex) irregularities tend to distress the area, being able to generate high tension locally. In contrast, cavity-type irregularities (concave) tend to increase the compressive stress locally. The larger the irregularity of the tunnel contour, the larger the heterogeneity found in the boundary stresses of the tunnel contour. The high localized stresses near the tunnel wall irregularities could induce local fracturing and asymmetry in the EDZ. The same study also shows that the current software developed for numerical modeling has some limits when it comes to inputting a 'heavy' 3D model and profile with a high resolution of a few millimeters. Nevertheless, it shows the potential application of laser scanning data to numerical modeling. Further development of the numerical modeling software may reveal more interesting results, which may prove unobtainable from traditional methods.

4.5 Documentation and visualization

In rock engineering, *in situ* documentation and visualization is important in observing the situation around rock exposure. Traditionally, a notebook with some drafts or drawings, together with a camera, is a common basis for on-site documentation. This has some drawbacks:

- The notes and drawings made by the person can be incorrect or subjective, and difficult to validate.
- Pictures taken by a standard camera usually require illumination and have small coverage.



(a) (b)

Figure 16 (a) Laser intensity image; (b) Color model for documentation in a tunnel.

- In particular, the pictures taken by a camera are not measurable. Although photogrammetry techniques are available, extra work is needed.
- All of this information is separately recorded, making it difficult to combine one with any other in terms of absolute position, and thus difficult to understand the relationship between them.
- At least some of the information is not digital, so extra work is needed if the information has to be processed by a computer.

By comparison with traditional methods, laser scanning techniques provide some advantages to the practice of on-site documentation, as described in the following subsections.

4.5.1 High-resolution intensity images can be recorded without illumination

The best resolution of a high-speed scanner is now less than one millimeter in an intensity image. As the scanner operates via an infrared laser, illumination is not necessary. Figure 16 shows documentation of a sensor cable and colorized point clouds in a tunnel.

A high-speed laser scanner with a high dynamic range color camera is the best solution for documentation of an underground excavation, as illustrated in Figure 16b. With good illumination or the use of Smart Light (Smart Light allows the capturing of high-quality images without an external light source), scanning data can be displayed in true color for 3D visualization of a tunnel.

4.5.2 Enables integration of visualization and measurement

As already described, laser scanning data consists of both position information in the coordinates of each scanning point and visual information in the form of the intensity image. Thus, the object in a laser scanning intensity image is not only visualized but can also be measured in 3D.

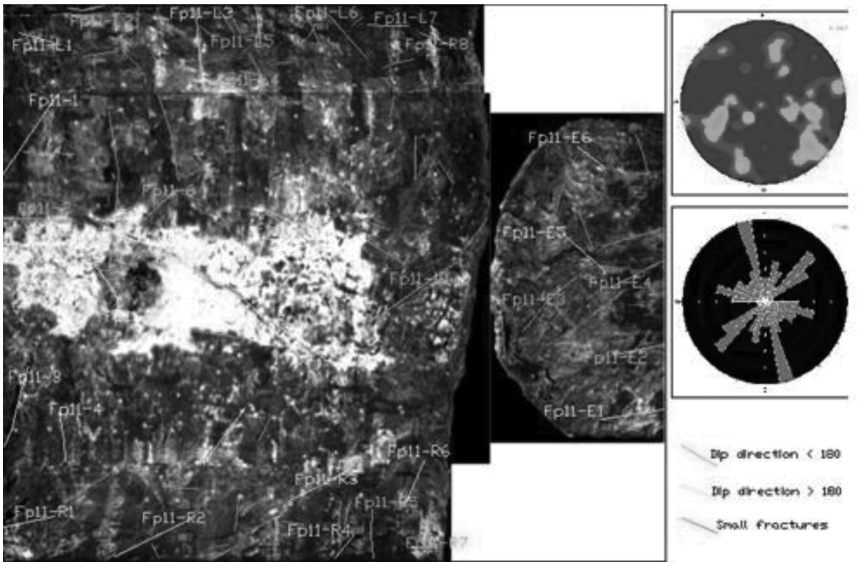


Figure 17 Fracture line trace map created from laser scanning intensity image (Adapted from Wang *et al.*, 2009).

4.5.3 Provides relationship information

As we know, on-site documentation by traditional methods does not provide exact position information. With laser scanning, the scanning data can be registered into a common coordinate system, so that any objects captured in the image can be accurately positioned in space, and the relationship between them can be defined.

An example is a trace map of fractures overlaid on a laser scanning image, as seen in Figure 17. Compared to a traditional trace map, it is easy to see what is represented by the fracture trace line, and each trace line can also be tracked to its position in a 3D model. In addition, it is also possible to obtain a 3D trace line, and it is interesting to consider how a 3D trace line might be used in rock mechanics in the future. In addition, when a scanner is scanning, it can rotate in 360 degrees both horizontally and vertically. Thus, a rock face is often recorded together with its surroundings. Moreover, even an entire tunnel (*e.g.* a tunnel 42 km in length) can be scanned and registered in the same coordinate system, and each scan – together with laser images – will show the exact position in space. Again, the relationship between a rock face and its surroundings can be obtained, which suggests the potential for application to future design and project planning in both rock mechanics and rock engineering.

4.5.4 Retrievability

With laser scanning, a rock face or tunnel can be accurately recorded in a given coordinate system, and made visible in a laser scanning image, which means the rock mass can be virtually stored in a computer in 3D. This offers potential

application to rock mechanics in at least two ways. First, if something is uncertain or wrong, it is possible to trace it back to the original virtual model and discover the reasons. For example, if the measurements of the on-site mapping (*e.g.* fracture orientation and slope geometry) are uncertain, it is possible to study the scanned 3D virtual model and establish a correction. Second, if information is found to be missing, it may be possible to obtain it from the virtual model without any need to revisit the site. Even if the original rock face has disappeared, for example, a tunnel section has been blasted out, the required data can still be retrieved from the scanned virtual model. This is useful for both quality control and accident investigations.

4.5.5 Large and wide coverage

Compared to a camera, laser scanning has a large and wide coverage, even in the dark. Because each scan can be registered into the same coordinate system, a large 3D model, for example, of a tunnel tens of kilometers in length, can be obtained, together with a large laser scanning image, which is impossible with a camera. In addition, a high resolution laser image can be captured in difficult conditions, such as in a narrow (about half a meter in diameter) vertical borehole.

4.5.6 Multiple views from the same data sources

Based upon the same captured scanning data, a rock surface or a tunnel can be visualized in several different ways, including: (a) an unfolded 2D laser image in the same format as photos from a camera (*e.g. jpg* or *tiff* files); (b) a 3D panoramic image; (c) a video film or movie in a standard format (*e.g.* an *avi* file), which can be created so that one might fly or walk through a tunnel in a 3D virtual space; (d) a 3D model, created by conversion of the scanning data (*e.g.* point clouds).

4.6 Application to mining

The laser scanning technique has also been applied in the mining industry for safety control, design and planning. For example, safety control in underground coal mining in China is a major concern because many accidents occur every year. For this reason, the Chinese government has applied some of these techniques to set up monitoring systems (*e.g.* gas monitoring) linked to alarms. Understanding the as-built situation underground is very important not only for monitoring but also for emergency rescue planning. Laser scanning has been applied to capture the as-built data in 3D for this purpose, and Figure 18 shows a scan of a tunnel in an underground coal mine in China.

For the open-pit mining industry, deformation monitoring of tailings dams is important, and laser scanning techniques were also tested in the province of Sichuan, southwestern China, to monitor the stability of a tailings dam, and also to provide some basic information, such as a 3D digital terrain model (DTM) and a measure of the tailings volume, in order to improve the existing design (see Figure 19).

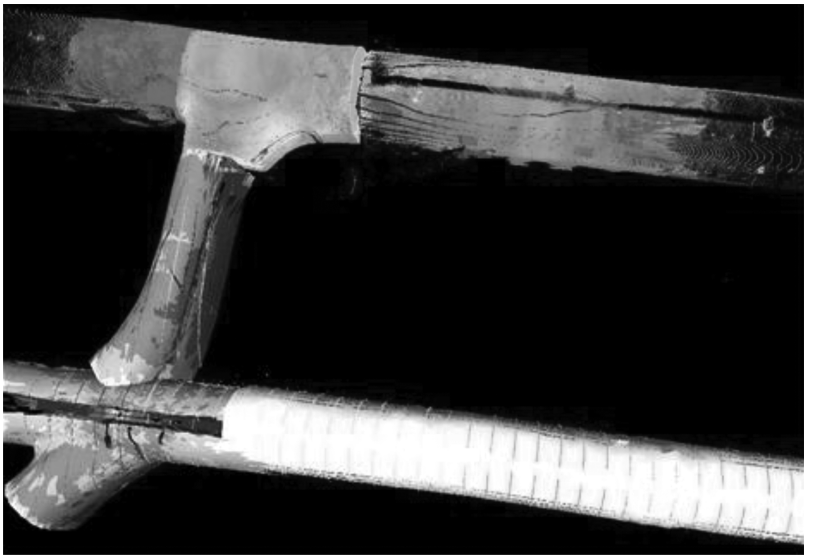
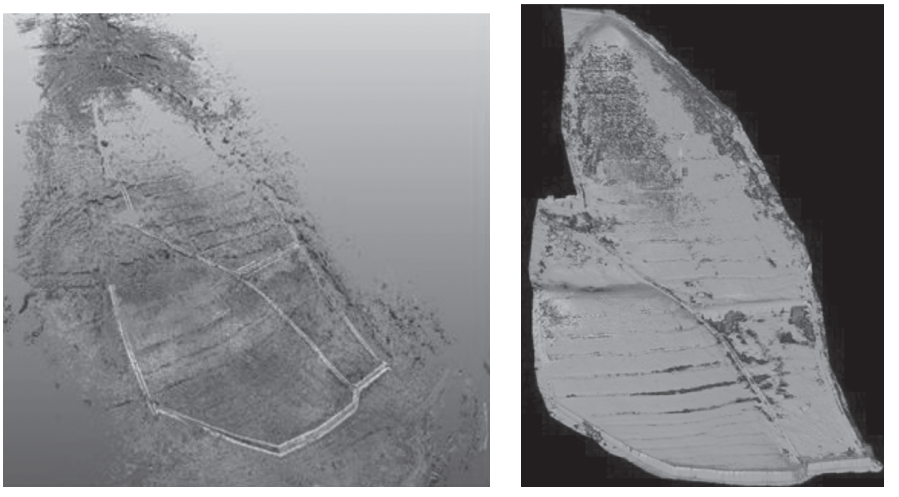


Figure 18 3D point cloud of a coal mine tunnel with pseudo-color and grayscale (Courtesy of Sichuan Province Academy of Safety Science and Technology).



(a) (b)

Figure 19 (a) 3D point cloud with color; (b) 3D DTM model of deformation with color scale (Courtesy of Sichuan Province Academy of Safety Science and Technology).

5 DISCUSSION

Laser scanning techniques have undergone more than 15 years of development since the late 1990s. The technique has many potential applications in rock mechanics and

rock engineering, but it is important to clarify some points in order that this method is applied correctly and effectively in practice.

5.1 Select the most suitable type of laser scanner for the application

There are many different types of 3D laser scanners on the market, many of them developed with pulse-based techniques, and a small proportion with phase-based techniques. They can be very different in their specifications, such as scanning speed, maximum scanning range, resolution, accuracy, and range of working temperature. For each different application in rock mechanics, it is important to select a suitable scanner in order to make correct use of the technique.

5.2 Understand how to use the specification parameters of the scanner

Each scanner has a list of its specification parameters, and it is important to understand exactly what the real meaning and significance is for each of them. For example, the maximum scanning range is related to the reflective intensity. If the object has very low or very strong reflectivity, the scanner cannot receive the return signal, so scanning data cannot be acquired. In addition, the maximum scanning range can be affected by other factors. For example, the scanning range of a pulse-based scanner can be affected by weather. Whether it is cloudy or sunny makes relatively little difference, although strong sunshine will slightly shorten the range. Fine rain, mist and fog can affect the scanning range, depending on droplet size. Whether it is day and night may also affect the scanning range: when scanning at night, there is less noise, the scanning spot is bigger and scanning range is longer. For a phase-based scanner, it is difficult to obtain a return signal if an object has a reflectivity of less than 5% or more than 95%.

5.3 Do understand the difference between resolution and accuracy

Through the use of scanning control software, scanning resolution can be selected according to the particular requirements of a project. Different scanners also have different maximum resolutions. However, the scanning resolution of an object is not only dependent upon the resolution parameters chosen while scanning, but is also related to other factors, including the distance and incidental angle to the scanned object and the reflective intensity of the object (or rock surface, etc.). Even the transformation between different coordinate systems by software can affect the final resolution. So, the effective resolution of the scanning data can be quite different from the resolution parameters configured in the scanner. On the other hand, even if the object can be scanned with a high resolution, it does not automatically mean that one can achieve the same high level in the accuracy of the final results. For example, the accuracy of deformation monitoring of a rock mass depends upon several factors, including the accuracy of control surveying between the stable area and the deformed area, the resolution of each individual scan, the accuracy of registration into a common coordinate system of each scan, and also the calculation accuracy of parameters or

models in monitoring the deformation. Thus, users are often confused by the difference between resolution and accuracy, and this is not so easy to verify in practice.

5.4 Do not confuse the accuracy of the scanner specification with that of the final results

Manufacturers often provide a specification of a scanner under different parameters. It is quite common for some users to treat the instrument's accuracy as the accuracy of their final results. In practice, this is quite dangerous. The instrument accuracy is often carefully (or simply) described by the manufacturer under some very specific conditions, for example, within a certain distance and incidental angle, for a particular type of object surface, or at some precise working temperature. Moreover, the instrument accuracy is often given separately in terms of its linear and angular accuracy, which is quite different from the accuracy of the coordinates of a point, or of a 3D model. The accuracy of the final result of a project depends upon many factors, such as: (a) control surveying; (b) instrument accuracy and scanning parameter settings; (c) the methods and procedures for registration of scanning point clouds in different software packages; (d) the presentation format of the final results, for example, the use of a cross section with a point line or a polyline, or a 3D model with a mesh or solid model.

5.5 Use an appropriate data format

There are many different data formats in use. They can be categorized into three main groups according to the stage in which the data is generated.

5.5.1 Raw data from a scanner

The raw scanning data is captured by different scanners in several different file formats (*e.g. fls*, *fws*, *zfs*, *zfc*, *ixf*, *3dd*, *rsp*, *ptb* and *ptg*). In the early days of the development of laser scanning techniques, many of the raw data formats could only be handled by software specific to each type of scanner, but the situation is now much better and many of these formats can be imported directly into generic third-party software created for different applications.

5.5.2 Data from processing the raw data

The raw data can be processed by different software and is typically exported in the form of point clouds and laser images. Point clouds can be held in many different file formats (*e.g. xyz*, *pts*, *ptx*, *dxf* and *asc* files), and laser images likewise (*e.g. bmp*, *tiff*, *jpg*, *png* and *coe* files). These data formats are often more neutral than the raw data, and can be imported and processed in many application software packages.

5.5.3 Final data models or parameters for further applications

The 3D model or parameters generated from the scanning data can be saved and then exported in a number of different file formats, which are compatible with the particular application software being used for design and further analysis (*e.g. sat*, *dwg*, *dxf* and *stl*).

In practice, it is often necessary to convert between these different data formats throughout the entire lifecycle of a laser scanning project. The situation is much improved in comparison to that at the beginning of the development of this technique. However, it is still not fully open. Information can be lost in converting from one format to another, and conversions are often not fully bidirectional. In addition, even the same data file formats can be displayed in different ways once imported into other software packages because, for example, of the different structure of layers in different CAD products.

5.6 Store and backup data securely

The safety of the data storage and backup is important for a laser scanning project because of the significance of data reuse and retrieval, and because it is sometimes impossible to go back to scan again if, for example, a section of a tunnel has disappeared through blasting, or a rock surface has been covered by shotcrete. Two questions are frequently asked: which media provides the safest method of backup? How long can the data be stored? In laser scanning, significantly large amounts of data can be generated, from many gigabytes to several terabytes. At present, it is unclear exactly how long data can be stored and which storage medium is the best for laser scanning data. However, scanning data stored on a CD for ten years is still readable if the CD is kept with care. Alternatively, extra work will be necessary to check the data integrity and make backups in different media on a regular basis.

6 CONCLUSION

Traditional methods for site characterization of rock exposure have a number of drawbacks, which can affect the further analysis, numerical modeling and design of rock mechanics. In the past, many efforts have been made to improve the quality and quantity of site mapping and documentation. 3D laser scanning has been developing for more than 15 years since the late 1990s, and has shown good potential application for site mapping and documentation in rock mechanics, thus generating more interest in recent years.

The review of the state of the art for 3D laser scanning techniques has revealed much development and improvement in both hardware and software since the late 1990s, and the latest developmental trends are focused on: improving scanning quality (*e.g.* scanning speed, resolution and accuracy, and scanning with color); easier and simpler operation for the users of the hardware; increasing compatibility and standardization of data formats and processing, especially in relation to the interface and integration with existing application software, which in turn makes the data from laser scanning more compatible with other data for even more applications.

3D laser scanning has several advantages in comparison to other methods, and can quickly capture an object in 3D with large coverage, high resolution and without illumination. The scanning data consists of several different types of information:

geometrical, spatial, visible and physical. In particular, the data can be retrieved and reused, which make it possible to improve quality control and reduce the costs of site investigation. In contrast to the photos and videos from a camera or video camera, laser scanning images in both 2D and 3D can be both visualized and measured, which highlights the application potential for site characterization in rock mechanics and rock engineering.

The various case studies illustrate the potential applications in rock mechanics of using scanning data with both coordinates and images, which make it possible to view and measure the rock surface in 3D with high resolution and accuracy. Thus, in recent years, laser scanning techniques have been applied to diverse projects in rock mechanics and rock engineering, including site characterization of rock exposure (*e.g.* fracture mapping, identification of water leakage, and rock type classification from laser images), monitoring of overbreak and underbreak in tunnel blasting, quality control of shotcrete spraying, deformation monitoring, improvement of input data for numerical modeling, and documentation and visualization. These case studies demonstrate the great potential in the application of laser scanning techniques to rock mechanics and rock engineering.

7 RECOMMENDATIONS

3D laser scanning techniques have already demonstrated great potential for application to rock mechanics and rock engineering. In order to further improve their application to rock mechanics, the ongoing development of both hardware and software needs to continue. Some particular aspects of potential benefit are recommended below, based upon user feedback and our investigation of the current state of the art.

7.1 Development of software specific to rock mechanics applications

Specialized software in support of laser scanning for rock mechanics applications is not well-developed. In particular, some existing software, for example, software for numerical modeling, needs to be improved in terms of both data format compatibility and capacity to handle large amounts of data.

7.2 Standardization of data formats

There are still too many types of data format in the entire lifecycle of a scanning project, and these frequently require extra work to convert from one to another. Standardization of data formats within the different scanning functions is necessary for more useful and productive applications.

7.3 Evaluation of the accuracy of rock mechanics applications

Laser scanning has potential application to many different types of project (*e.g.* site mapping, deformation monitoring, quality control of tunneling). However, users are often confused about the difference between the accuracy of the measuring instrument and that of the final result, and with so many different uses it is not so simple to

evaluate the actual accuracy and the factors that influence it. More case studies are needed to establish the influential factors in different rock mechanics applications for the future.

ACKNOWLEDGMENTS

This report is extended from the results of an ISRM-Swedish national task, which was stimulated by ISRM and Professor John Hudson during his presidential period from 2007 to 2011, and funded by BeFo, the Swedish Rock Engineering Research Foundation, with the support of Mikael Hellsten, Managing Director of BeFo. The authors would like to acknowledge those who gave us the opportunities to test these techniques in different projects related to rock mechanics applications, including SKB (Swedish Nuclear Fuel and Waste Management Company), Trafikverket (Swedish Road and Railway Authority), Fortum, Vattenfall, SP Technical Research Institute of Sweden, Besab, RTC (Rock Tech Centre in Sweden), SL (Stockholm Local Traffic Management Company). Thanks to BBK and ÅF for the time to carry out some parts of this study. We are indebted to the reference group, including Professor John Hudson (ISRM), Mikael Hellsten (BeFo), Anders Boberg (Tyrens), Ulf Håkansson (Skanska), Tommy Ellison (Besab), Peter Lund (Trafikverket) and Peter Hultgren (SKB), for their suggestions and critical inputs to improve both the content and language of this report.

REFERENCES

Bäckström, A., Jonsson, M., Christiansson, R. & Mas-Ivars, D. (2009). Analysis of factors that affect and controls the excavation disturbance/deformation zone in crystalline rock. In: Ribeiro, L. (ed.) *Proceedings of the ISRM-Sponsored International Symposium on Rock Mechanics: 'Rock Characterisation, Modelling and Engineering Design Methods' (SINOROCK2009)*. London, Taylor & Francis.

Boehler, W. & Marbs, A. (2002). 3D scanning instruments. In: *Proceedings of the CIPA WG 6 International Workshop 'On Scanning for Cultural Heritage Recording', Corfu*. pp. 9–12.

Brown, E.T. (ed.). (1981). *Rock Characterization Testing and Monitoring: ISRM Suggested Methods*. London, Pergamon Press.

Createc. (2016). *Radiation Imaging*, https://www.createc.co.uk/challenging-problems/radiation-imaging/, accessed 27 May 2016.

DTFHA. (2008). *Ground-Based LiDAR: Rock Slope Mapping and Assessment*. Lakewood, CO, US Department of Transportation Federal Highway Administration.

Fardin, N., Feng, Q. & Stephansson, O. (2004). Application of a new in situ 3D laser scanner to study the scale effect on the rock joint surface roughness. *International Journal of Rock Mechanics and Mining Sciences*, 41, 329–335.

Feng, Q. (2001). Novel methods for 3-D semi-automatic mapping of fracture geometry at exposed rock surfaces, Doctoral Thesis, Royal Institute of Technology, Stockholm, Sweden.

Feng, Q. & Röshoff, K. (2004). In-situ mapping and documentation of rock faces using full coverage 3D laser scanning technique. *International Journal of Rock Mechanics and Mining Sciences*, 41(3), 139–144.

Feng, Q., Wang, G. & Röshoff, K. (2006). Detection of water leakage using laser image from 3D laser scanning data. In: Ribeiro, L. (ed.) *Proceedings of IAEG 10th Congress, Nottingham,* London, Taylor & Francis.

Goodman, R.E. (1989). *Introduction to Rock Mechanics* (2nd edn). New York, Wiley.

Hesse, C. & Stramm, H. (2004). Deformation measurements with laser scanners – Possibilities and challenges. In: *Proceedings of International Symposium on Modern Technologies, Education and Professional Practice in Geodesy and Related Fields, Sofia, Bulgaria*. pp. 228–240.

Hudson, J.A. (1989). *Rock Mechanics Principles in Engineering Practice*. London, CIRIA/ Butterworths.

Jonsson, M., Bäckström, A., Feng, Q., Berglund, J., Johansson, M. & Olsson, M. (2009). Aspo Hard Rock Laboratory: Studies of Factors That Affect and Controls the Excavation Damage/ disturbed Zone, SKB Report R-09-17. Stockholm, Swedish Nuclear Fuel and Waste Management Co.

Newton Labs. (2016). *Underwater Laser Scanners Accurately Measure As-Built Features*, http:// www.newtonlabs.com/laser.html, accessed 27 May 2016.

Patton, F.D. (1966). Multiple modes of shear failure in rock. In: *Proceedings of the 1st Congress of International Society of Rock Mechanics, Lisbon*. pp. 509–513.

Priest, S.D. (1993). *Discontinuity Analysis for Rock Engineering*. London, Chapman & Hall.

Schneider, D. (2006). Terrestrial laser scanner for area based deformation analysis of towers and water dams. In: *Proceedings of the 3rd IAG Symposium of Geodesy for Geotechnical and Structural Engineering and 12th FIG Symposium on Deformation Measurements,* Baden, Austria.

Slob, S. & Hack, H.R.G.K. (2004). 3D terrestrial laser scanning as a new field measurement and monitoring technique. In: Hack, R., Azzam, R. & Charlier, R. (eds.) *Engineering Geology for Infrastructure Planning in Europe. A European Perspective*. Berlin, Springer Verlag. pp. 179–190.

Slob, S., Hack, H.R.G.K., van Knapen, B., Turner, K. & Kemeny, J. (2005). A method for automated discontinuity analysis of rock slopes with three-dimensional laser scanning. *Transportation Research Record*, 1913(1), 187–208.

Wang, G. (2005). Applications of 3D laser scanning data for tunnel geological mapping, Master of Science Thesis, Royal Institute of Technology, Stockholm, Sweden.

Wang, G., Feng, Q. & Röshoff, K. (2009). A new approach to tunnel digital geological mapping using 3D terrestrial laser scanning technique. In: Ribeiro, L. (ed.) *Proceedings of the ISRM-Sponsored International Symposium on Rock Mechanics: 'Rock Characterisation, Modelling and Engineering Design Methods' (SINOROCK2009)*. London, Taylor & Francis.

Chapter 19

Review of GPS displacement monitoring in rock engineering

N. Shimizu & S. Nakashima
Department of Civil and Environmental Engineering, Yamaguchi University, Ube, Japan

Abstract: The Global Positioning System (GPS) has been widely used for monitoring the displacements of slopes, open pit mines, dams, etc. in various rock engineering projects. This article begins by outlining GPS and then reviews the procedure for the displacement monitoring method together with error correction methods based on the ISRM suggested method. Practical applications for monitoring landslides, cut slopes, quarries, dams, etc. are illustrated to verify this technology.

1 INTRODUCTION

Monitoring rock displacements is important for assessing the stability of rock masses, for confirming the validity of the design and the construction work, and for understanding the in-situ rock behavior. In order to achieve successful monitoring, various instruments and systems have been developed.

The Global Positioning System (GPS) has the potential to continuously realize three-dimensional displacement monitoring over an extensive area with high accuracy in real time. It has become an effective tool for field monitoring in Rock Engineering.

GPS began to be used for displacement monitoring in the mid-1980s in the fields of Civil and Mining Engineering as well as other related fields (*e.g.*, Chrzanowski & Wells, 1988; Burkholder, 1988, 1989). Since then, practical applications have been performed by many researchers (*e.g.*, Hudnut & Behr, 1998; Gili *et al.*, 2000; Malet *et al.*, 2002; Kim *et al.*, 2003; Tasci, 2008), and guidelines have been published for displacement monitoring (*e.g.*, US Army Corps of Engineering, 2002; Vermeer, 2002; Bond, 2004). ISRM has also approved the suggested method for monitoring rock displacements using GPS (Shimizu *et al.*, 2014).

This article outlines GPS and reviews the procedure for the displacement monitoring method together with error correction methods based on the ISRM Suggested Method. Practical applications for monitoring slopes, landslides, tunnels, dams, etc. are illustrated to verify this technology.

2 OUTLINE OF GPS

The Global Positioning System (GPS) is a satellite-based positioning system that was developed by the US Department of Defense. It was firstly designed as a navigation

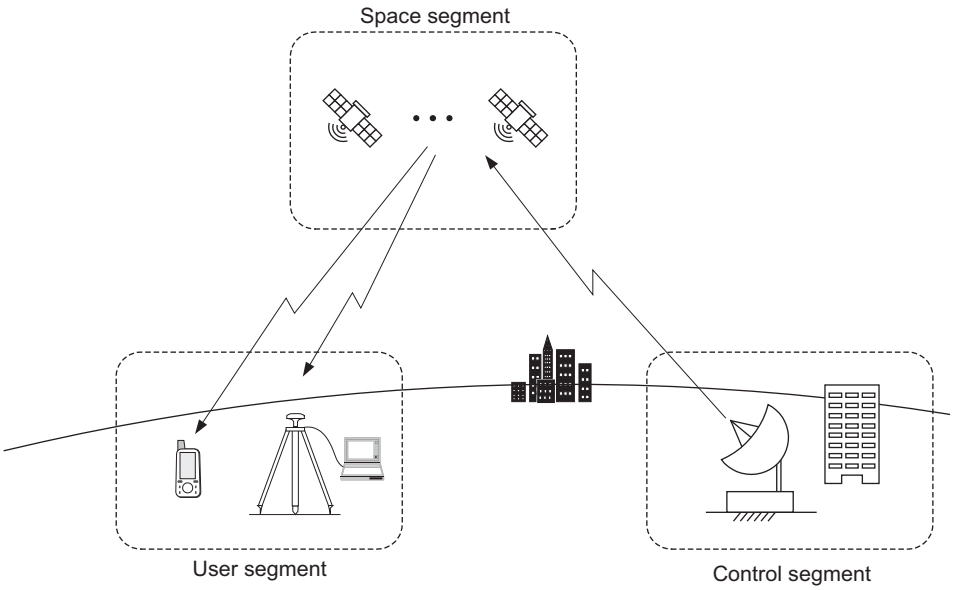


Figure 1 System architecture of GPS (Shimizu *et al.*, 2014).

system in the early 1970s, and then began to be used as a method for precise long baseline surveying from the late 1970s to the early 1980s (Hoffman-Wellenhof *et al.*, 2001; Misra & Enge, 2006).

GPS is composed of three segments, namely, (1) the space segment, (2) the control segment, and (3) the user segment (Figure 1). The space segment is composed of artificial satellites. Currently, 31 satellites are in operation. The satellites fly in nearly circular orbits for periods of sidereal hours (11 hours and 58 minutes). Each satellite continuously transmits the signals for positioning. The control segment consists of a worldwide network of ground facilities. Its tasks are to track the satellites in orbit, to time the synchronization of the satellites, to upload the data messages from the satellites, etc. Both the space and the control segments are managed by the USA. The user segment consists of receiver equipment and a related system. Anyone who prepares the receiver equipment can use GPS at any time.

There are two methods for using GPS. The first method is point positioning for navigation. The three-dimensional absolute coordinates of a measurement point, namely, latitude, longitude, and height, are obtained instantaneously. The accuracy of point positioning is approximately a few meters to ten meters or more. The second method is relative positioning. Relative positioning uses carrier phase measurements and was established for precise surveying. It provides the three-dimensional relative coordinates in latitude, longitude, and height between two points with the accuracy of millimeters to centimeters.

Therefore, relative positioning can be used for monitoring rock displacements. By continuously observing the coordinates of measurement points, the displacements are obtained as changes in the coordinates. The standard deviation of the

measurements can be just a few millimeters when the baseline length is less than one kilometer and the installation and data corrections are conducted carefully.

Nowadays, similar systems are being developed or are in the planning stages in Russia, the EU, China, and Japan. Those including GPS are collectively called the Global Navigation Satellite System (GNSS). GNSS will be used for monitoring rock displacements in the future.

3 DISPLACEMENT MONITORING USING GPS

When users conduct relative positioning for monitoring rock displacements, one antenna with a receiver is set on the reference point and a second antenna with a receiver is set on a measurement point (Figure 2). If users set these antennas at a number of measurement points, the displacements at each point can be simultaneously obtained. The static method, which is one method of relative positioning, will yield the most reliable and precise results in GPS positioning. The kinematic method, which is also a method of relative positioning, can be used for monitoring displacements. The accuracy of the kinematic method is generally lower than that of the static method; and thus, the static method is recommended here for monitoring rock displacements.

In this section, the standard procedure for monitoring and the recommended procedure for error corrections of the measured results, based on the ISRM Suggested Method (Shimizu *et al.*, 2014), are described.

3.1 Monitoring procedure

The outline of the procedure for monitoring displacements by the static method is given as follows:

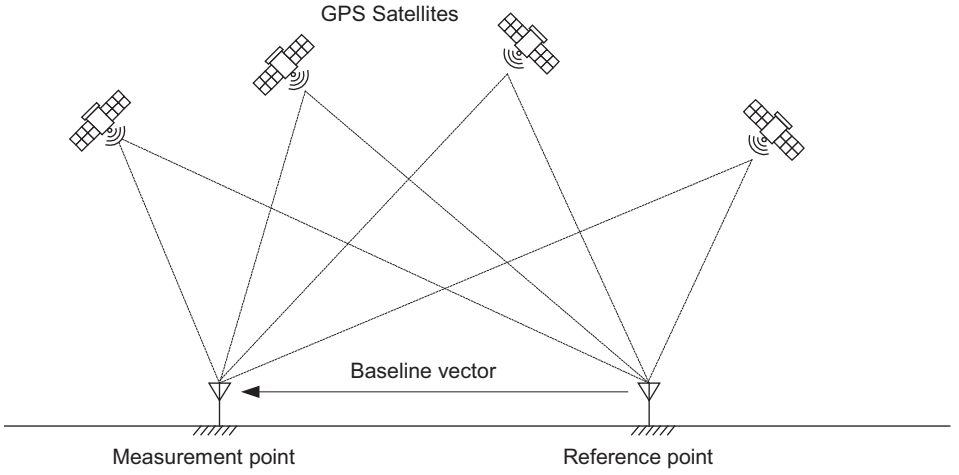


Figure 2 Relative positioning of GPS (Shimizu *et al.*, 2014).

1. Set up the receiver(s) at the measurement point(s) and the reference point (Figure 2).
2. Measure the carrier phase of the signal every epoch interval and receive the navigation data at each measurement point and the reference point from the same satellites simultaneously. The measured carrier phase and the data are saved automatically in the memory of the receivers. The receivers perform this process automatically.
3. Download the data from all the receivers to a computer.
4. Collect the downloaded data of the reference point and the measurement point(s) at which the user would like to know the displacements, and conduct a baseline analysis to obtain the relative coordinates of the measurement point(s) from the reference point.
5. Repeat Steps 3 and 4 for the succeeding observation session.
6. Calculate the changes in the coordinates at each measurement point between the two sessions, and then obtain the displacements.

Software for downloading, logging, and processing the GPS data, and for the baseline analysis, is generally provided by the manufacturer of the receiver.

When standard receivers for surveys are employed to monitor displacements, the users are usually required to download the GPS data from the receivers, to analyze the data in order to obtain the coordinates of the measurement points, and to calculate the displacements for each session. If such a process is conducted manually, it is inconvenient and ineffective for continuous monitoring. In order to overcome this troublesome process, automatic monitoring systems can be designed and applied for monitoring displacements.

The author and his associates developed a GPS displacement monitoring system using an L1 signal, as illustrated in Figure 3 (Iwasaki *et al.*, 2003; Masunari *et al.*, 2003; Shimizu & Matsuda, 2002, 2003). Sensors, composed of an antenna and a terminal

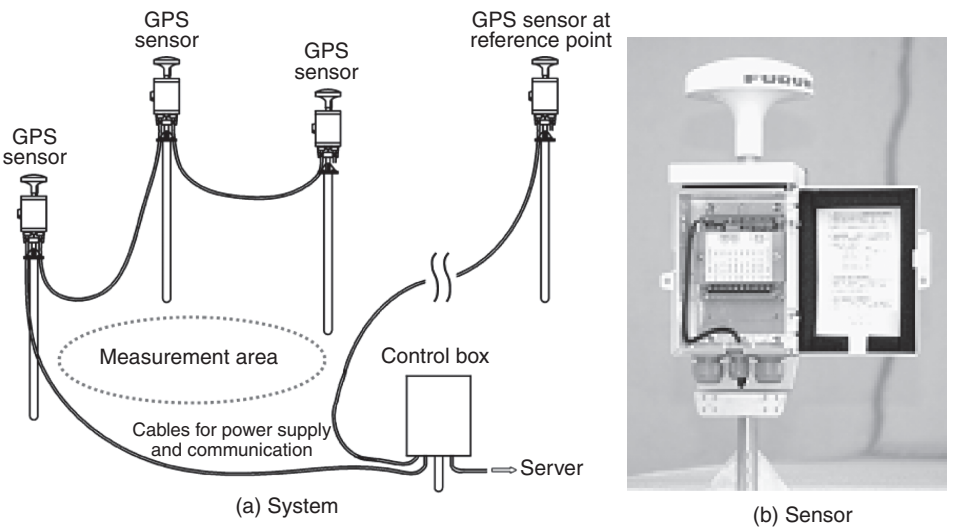


Figure 3 GPS displacement monitoring system (Shimizu *et al.*, 2011).

box, are set on measurement points and a reference point. They are connected to a control box into which a computer, a data memory, and a network device are installed. The data emitted from the satellites are received at the sensors and then transferred to the control box through cables. The server computer, which is located in an office away from the measurement area, automatically controls the entire system to acquire and then analyze the data from the control box. Then, the three-dimensional displacements at all the monitoring points are obtained. The monitoring results are provided to users on the web through the Internet in real time. The users only need to access the home page to see the monitoring results.

3.2 Improvements in accuracy-error corrections

Standard deviations in the conventional GPS survey are 5 mm in the horizontal direction and 10 mm in height when the baseline length is less than one kilometer. Precise monitoring for practical use, however, often requires higher accuracy than this. The most important issue in the practical use of GPS is how to improve the measurement accuracy.

Measurement results generally include random errors (noise) and bias errors. Random errors arise from random fluctuations in the measurements. On the other hand, typical bias errors in GPS monitoring are tropospheric delays and other signal disturbances due to obstructions above the antennas and multipath effects. Since both random and bias errors affect the monitoring quality, it is recommended that appropriate error correction methods be applied to reduce such errors.

Generally, the measurement value y is composed of exact value u, bias errors ε_p and ε_T, and random error ε_R, as follows:

$$y = u + \varepsilon_p + \varepsilon_T + \varepsilon_R \tag{1}$$

where ε_p is an error due to a signal disturbance caused by obstructions above the antennas, ε_T is an error due to tropospheric delays, and ε_R is a random error due to receiver noise. Tropospheric delays occur when signals from the satellite reflect in the atmosphere due to meteorological conditions (Hoffman-Wellenhof *et al.*, 1997; Misra & Enge, 2006).

Both bias errors ε_p and ε_T can be reduced and corrected by methods described in the next section. After removing the bias errors from the measurement value, an appropriate statistical model is applied to estimate the exact displacement.

3.2.1 Bias errors

Tropospheric delays

Tropospheric delays occur as a result of refractive effects, due to air density, when signals propagate through the troposphere extending from a height of about 0 to 11 km above the earth. The air density is a function of the pressure of dry gases and water vapor. This means that the measurement results are subject to the influence of the meteorological conditions along the signal propagation path. When the difference in height between the reference and measurement points is more than a few tens of meters,

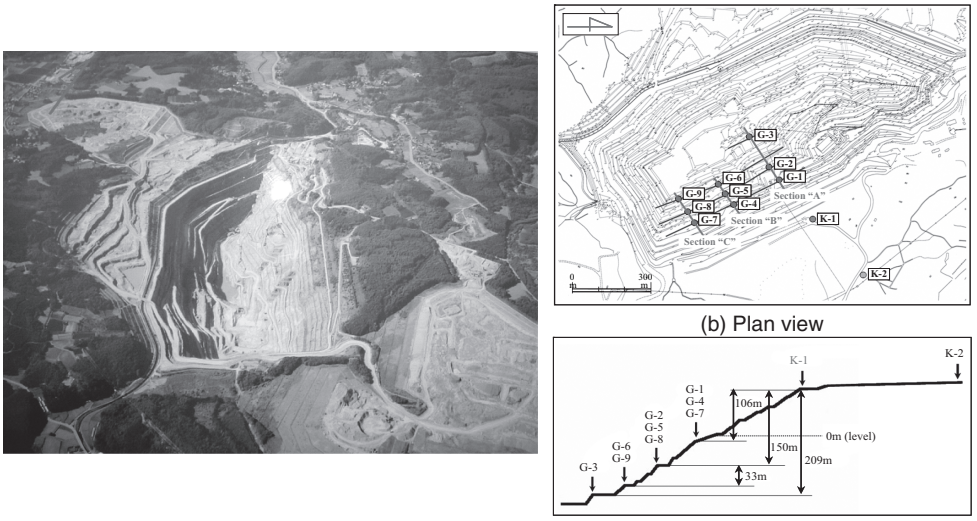


Figure 4 Limestone quarry (Nakashima *et al.*, 2012).

it may not be possible to ignore the bias of the tropospheric delays in precise monitoring with an accuracy of millimeter level, even for short baseline lengths. An appropriate model, like the modified Hopfield model, the Saastamoinen model, etc. (Hoffman-Wellenhof *et al.*, 2001; Misra & Enge, 2006), can be employed to correct such tropospheric delays. Tropospheric models are usually installed in the baseline analysis software. The meteorological data (atmospheric pressure, temperature, and humidity) should be measured as input data for it.

Figure 4 is a limestone quarry where displacements are monitored by GPS. Figure 5 shows the three-dimensional displacements at a monitoring point G-1 for a year without any error corrections. The baseline length and the difference in height between the two antennas were 252 m and 106 m, respectively. The epoch interval (measurement interval or logging rate of the carrier phase) and the session length (the observing duration of the carrier phase measurements) were 30 seconds and 1 hour, respectively. The displacement in height increased from May to August and then decreased from August to October, although the monitoring area was stable and there must not have been any displacements during the monitoring period. The above phenomenon is usually seen in cases where the difference in height between the reference and the measurement points is large.

Figure 6 shows the measured temperature, the relative humidity, the atmospheric pressure, the estimated partial pressure of the water vapor, and the zenith tropospheric delay (per unit height difference) using the modified Hopfield model. It is found that the transition in tropospheric delay over a year is quite similar to one of the displacements in height. This might indicate that tropospheric delays affect displacements in height.

Actually, the bias of the displacement in height, caused by the tropospheric delay, tends to be proportional to the difference in height between the reference and the

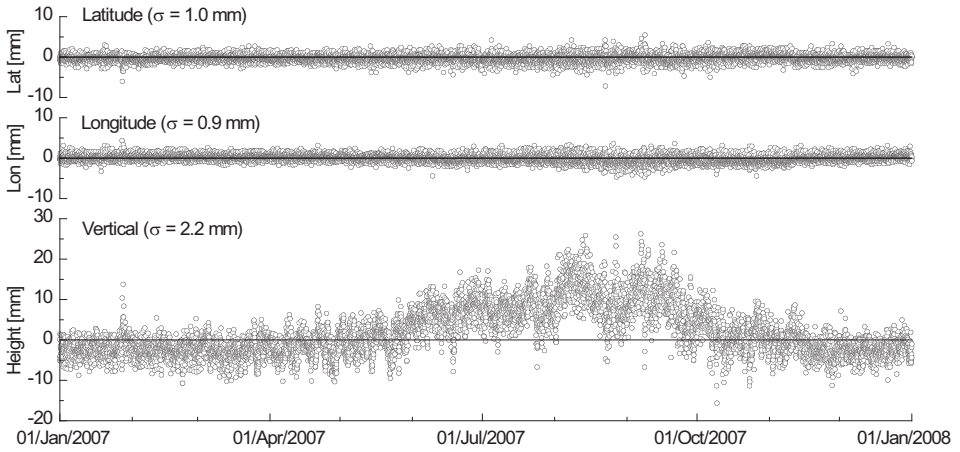


Figure 5 Displacement monitoring results affected by tropospheric delay at G-1 (baseline length: 252m and height difference: 106m) (Nakashima *et al.*, 2012).

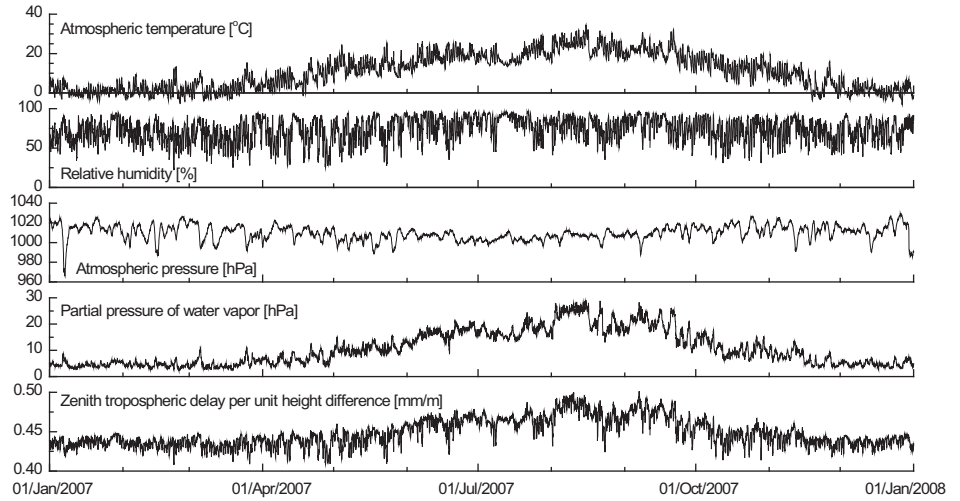


Figure 6 Measured temperature, relative humidity and atmospheric pressure, and estimated partial pressure of water vapor and zenith tropospheric delays (Nakashima *et al.*, 2012).

measurement points. The amount of bias is 10–20 mm for a height difference of about 100 m during a one-year period, as shown in Figure 5. On the other hand, the horizontal displacements are hardly subjected to the influence of the tropospheric delay (see Figure 5).

In order to correct the tropospheric delay, the modified Hopfield model was adopted for the baseline analysis using the measured temperature, the relative humidity, and the atmospheric pressure. The corrected results are shown in Figure 7. Figure 8 presents

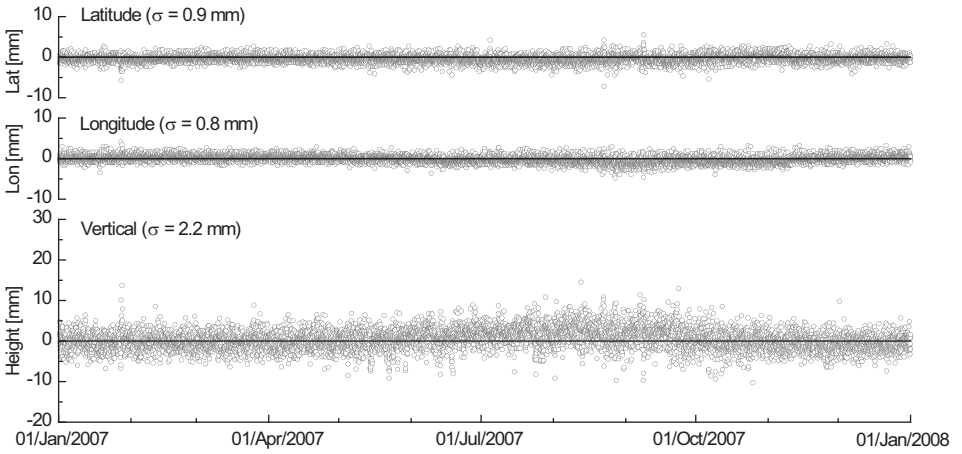


Figure 7 Displacement monitoring results corrected by tropospheric delays using modified Hopfield model (Nakashima *et al.*, 2012).

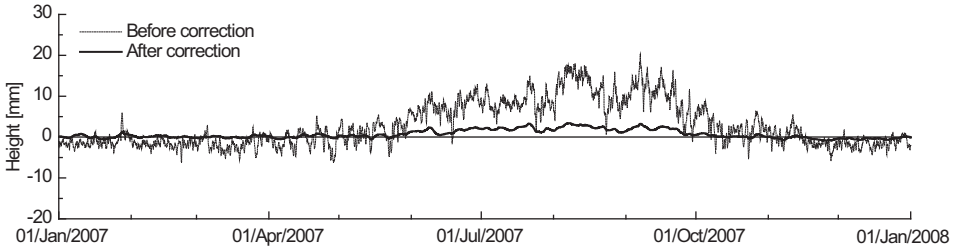


Figure 8 Comparison between original and corrected monitoring results for tropospheric delays (Nakashima *et al.*, 2012).

a comparison between the original and the corrected monitoring results, which are smoothed by the trend model (see 3.2.2). It is clear that the movement in the original displacements in height from May to November 2007, as well as the daily scatters, have been almost eliminated.

Signal disturbance due to obstructions above antennas

Obstructions above an antenna (trees, slopes, etc.) may block the antenna signal reception or may cause a disturbance to the signals; these overhead obstructions become error sources in GPS displacement monitoring. Antennas should be located in areas with a sufficiently open sky. When there are unavoidable obstructions above the antennas, it is a good practice to analyze the data without the signals transmitted from the satellites behind the obstructions.

Figure 9 shows the monitoring results at a point on a slope where trees on the upper parts of the slope were obstructions. The baseline length and the difference in height

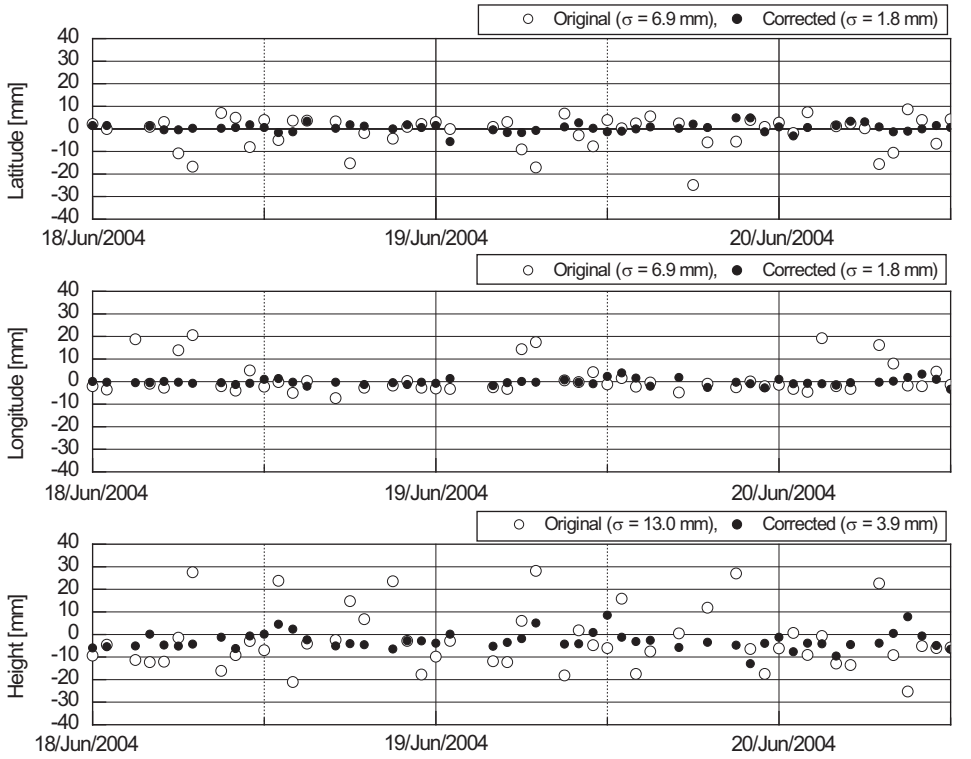


Figure 9 Example of original and corrected monitoring results without using the data from the satellites moving behind the trees (baseline length: 266m and height difference: 7m) (Shimizu *et al.*, 2011).

were 266 m and 7 m, respectively. The epoch interval and the session length were 30 seconds and 1 hour, respectively. The circles in Figure 9 represent the original results obtained from the baseline analysis. They are seen to scatter periodically.

Figure 10 shows satellite paths over one hour, drawn in the sky photo above the antenna, for a session in which the monitoring results were largely scattered. The numerals represent the satellite numbers. The antenna received signals from all the satellites, except No. 24, which was moving behind a slope (its signal couldn't reach the antenna). The signals of satellite Nos. 4 and 20 came through trees and were disturbed. Therefore, the baseline analysis was conducted without using the data from satellite Nos. 4, 20, and 24, which were moving behind trees during the whole monitoring period.

The corrected results were obtained as the bullets shown in Figure 9. The scattered results were significantly improved. The standard deviations in the horizontal and height displacements improved from 6.9 mm and 13.0 mm to 1.8 mm and 3.9 mm, respectively. It is clear that the analysis without the data from the satellites moving behind the obstructions is effective in reducing errors and in improving the accuracy of the GPS displacement measurements.

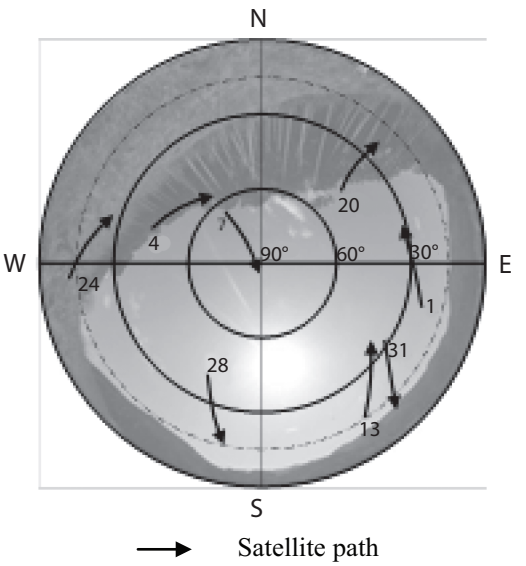


Figure 10 Satellite paths on sky photo above antenna during a session (one hour) for scattered results (Shimizu *et al.*, 2011).

The other error source is multipath signals, which is the phenomenon of a signal reaching an antenna via two or more paths. This is mainly caused by signal reflections from objects (buildings, walls, fences, etc.) and from the ground surface in the vicinity of the antennas. Naturally, the primary defense against multipath signals is to position the antennas away from any reflective objects and to set a mask angle for cutting multipath signals.

3.2.2 Random errors

After removing the bias errors from the measurement value, Equation 1 can be written as follows:

$$\tilde{y} = y \; - (\varepsilon_p + \; \varepsilon_T) = \; u \; + \; \varepsilon_R \tag{2}$$

In order to estimate the exact value u from the corrected measurement result $\tilde{y}$ with random errors, it is recommended that an adequate statistical method be adopted. The author used "*the trend model*" (Kitagawa & Gersch, 1984) for this purpose (Shimizu, 1999; Shimizu & Matsuda, 2002).

This model is composed of a system Equation 3 and an observation Equation 4, as follows:

$$\Delta^k u_n = v_n \tag{3}$$

$$\tilde{y}_n = u_n + w_n \tag{4}$$

where u_n represents the estimates for the exact values of the displacements and $\tilde{y}_n$ is the corrected measurement results represented by Equation 2. The measurement interval is Δt and subscript n denotes progressing time t ($t = n\Delta t$). Δ is the operator for the finite difference ($\Delta u_n = u_{n-} - u_{n-1}$) and Δ^k means the rank "k" difference. Equation 3 is a kind of probability finite difference equation for rank k. v_n and w_n are white noises with an average value of 0, a standard deviation of τ, and an observation error with a standard deviation of σ.

The trend model can yield good estimates for exact displacements. Through many experiments and practical applications, it was proven that the system can detect displacements of 1–2 mm and displacement velocities of 0.1 mm/day (Shimizu and Matsuda, 2002).

Figure 11 shows the three-dimensional displacements measured at a point of a slope behind a tunnel entrance represented in the local coordinate system, *i.e.*, the horizontal X (longitudinal axis of the tunnel) and Y (orthogonal axis with the longitudinal axis) directions, and the height direction. The results denoted by the circles are scattered due to random errors. The standard deviations (denoted by σ in Figure 11) are 2.4 mm, 1.2 mm, and 3.5 mm in the directions of X, Y, and height, respectively. The baseline length and the difference in height between the two antennas were 142 m and 13 m,

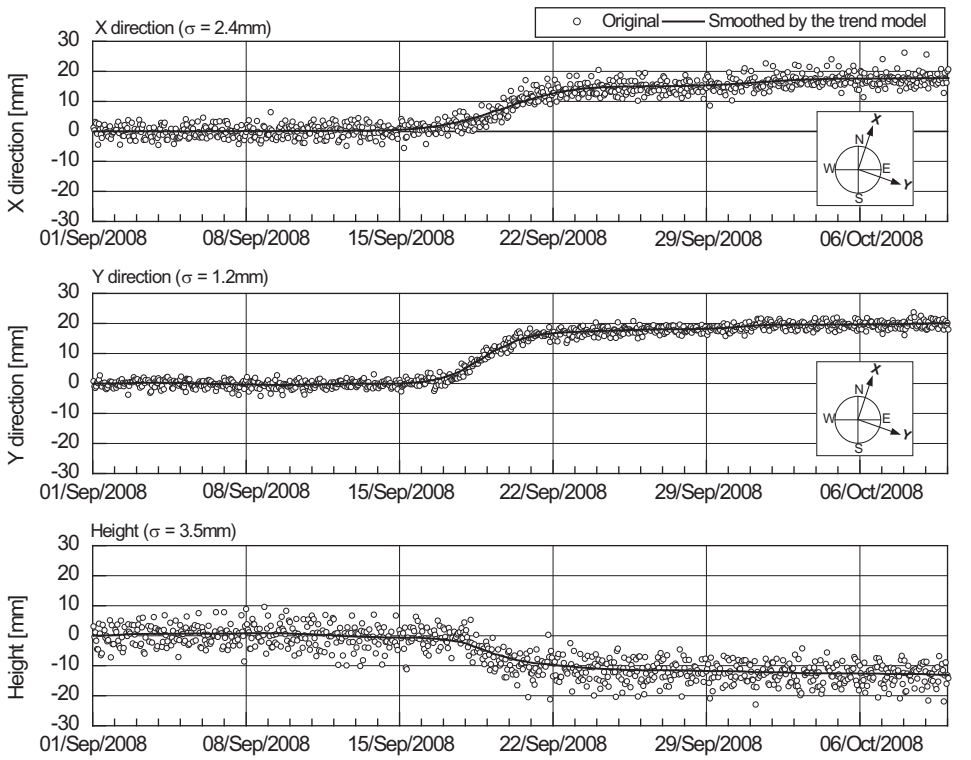


Figure 11 Example of original monitoring results and estimated displacements using the trend model (baseline length: 142m and height difference: 13m) (Matsuda *et al.*, 2012).

respectively. The epoch interval and the session length were 30 seconds and 1 hour, respectively.

The solid lines are drawn as smoothing results, which were obtained by applying the trend model to the original results. It is found that the trend model can yield good estimates from the original measurement results including random errors.

The fundamental equations for relative positioning and the tropospheric models are described in the ISRM Suggested Method (Shimizu *et al.*, 2014).

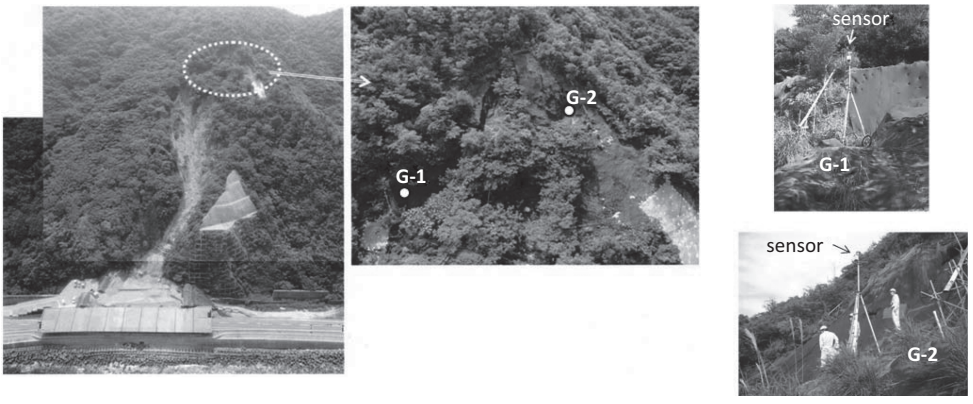
4 PRACTICAL APPLICATIONS OF GPS DISPLACEMENT MONITORING

4.1 Unstable steep slope

The GPS displacement monitoring system (see Figure 3) is applied to monitor the displacements of an unstable steep slope along a national road in Japan. Since local slope failures have occurred several times over the last 20 years, displacement monitoring has been conducted by borehole inclinometers and surface extensometers. Some of the instruments, however, have occasionally not worked well due to large deformations, and it has been difficult to perform the monitoring continuously. In order to overcome such trouble, the GPS monitoring system has been applied for continuous monitoring (Furuyama *et al.*, 2014).

4.1.1 Monitoring site

Figure 12 presents photographs of the slope and the monitoring area. The slope is composed of mainly tuff and sandstone, and its bedrock is granite. The surface is covered with a colluvial deposit. The left side of the slope, as seen in the photograph in Figure 12(a), has been gradually failing over the last 20 years, and a concrete rock-shed tunnel has been constructed to cover the road and to protect it.



(a) Slope and monitoring area

(b) GPS Sensors at G-1 and G-2

Figure 12 Monitoring site; slope beside road (Furuyama *et al.*, 2014).

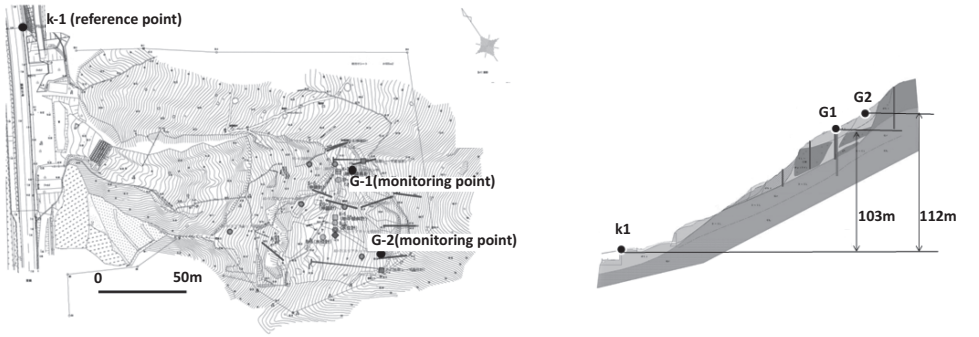


Figure 13 Monitoring points and reference point (Furuyama *et al.*, 2014).

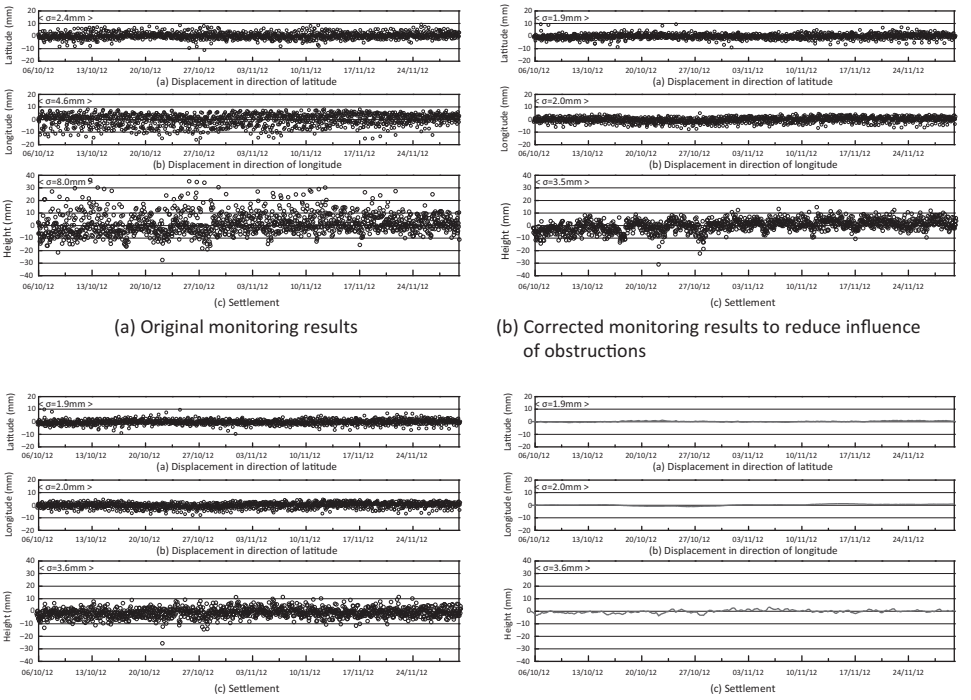
Two antennas were set at the top of the slope to monitor displacements, and another antenna was set at a fixed point in a stable area as a reference point, denoted by K-1, beneath the slope (see Figure 13). The monitoring points, denoted as G-1 and G-2, were set on the left and right sides of the slope, respectively. Three-dimensional displacements were continuously measured every hour using the static method of GPS. The distance between monitoring point G-1 and reference point K-1 was 221 m, while that between monitoring point G-2 and the reference point was 258 m. The differences in height between the two points and the reference point were 103 m and 112 m, respectively.

4.1.2 Effects of error corrections

Since both differences in height between reference point K-1 and monitoring points G-1 and G-2 were more than 100 m, the error due to the tropospheric delays of the signal wave from the satellite could not be ignored. In addition, since the trees around the monitoring points have grown and become obstructive above the antennas, they will cause a disturbance to the signals and a decline in the measurement accuracy. In order to correct these types of errors, the error-correction methods described in 3.2 were applied.

Figure 13(a) shows the original monitoring results obtained from a baseline analysis using the observed wave phase. Although the slope did not move at all during this period, the results were rather wavy and scattered.

As the first step of correction, the signals obtained from the satellites located behind the obstructions above the GPS antenna were not used when analyzing the data (see 3.2.1). Figure 14(b) presents the corrected results. Comparing the original and the corrected results (Figures 14(a) and 14(b)), the scattering that appeared in the original results has been significantly improved; *i.e.*, the standard deviations of the displacements in the direction of latitude, longitude, and height were improved from 2.4 mm, 4.6, and 8.0 mm to 1.9 mm, 2.0, and 3.5 mm, respectively. Some periodic behavior, however, still remains.



(a) Original monitoring results

(b) Corrected monitoring results to reduce influence of obstructions

(c) Corrected monitoring results to reduce influence of both obstructions and tropospheric delays

(d) Monitoring results after error corrections

Figure 14 Effects of error-corrections for GPS displacement monitoring results (Furuyama *et al.*, 2014).

As the second step of correction, an appropriate model was employed to correct the tropospheric delays. The modified Hopfield model was adopted to estimate the amount of tropospheric delays (see 3.2.1). Figure 14(c) shows the results after correcting both the obstructions and the tropospheric delays. Comparing the original and the corrected results (Figures 14(a) and 14(c)), the scattering and the periodic behavior appearing in the original results have been clearly improved.

Finally, as the third step of correction to reduce random errors, the trend model was applied to estimate the exact displacement from the monitoring results. The solid lines in Figure 14(d) show the final results. Although some small scattering still exists, it is found from these results that no displacement occurred during this period.

Comparing the original and the corrected monitoring results (Figures 14(a) and 14(d)), it can be seen that the original results have been significantly improved through the above error-correction procedure.

4.1.3 Monitoring results

The displacement monitoring results at monitoring point G-1 are shown with an hourly amount of rainfall in Figure 15. Monitoring was started in the middle of March 2013.

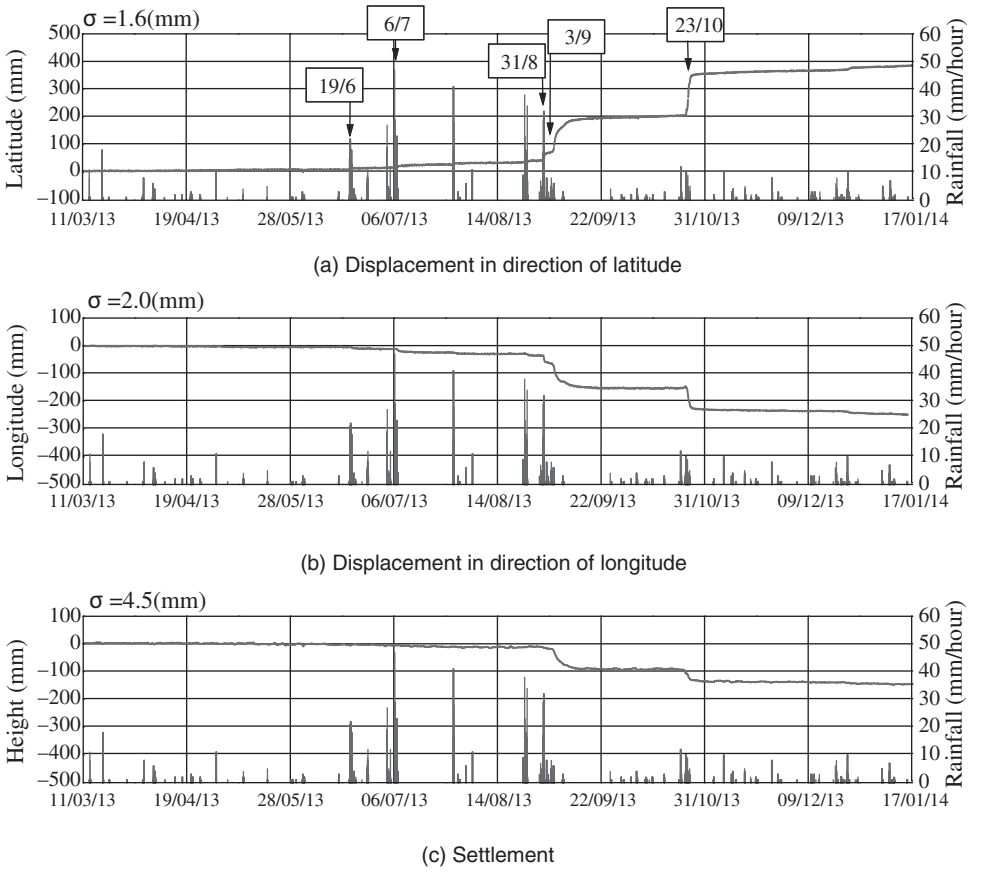


Figure 15 Displacement monitoring results at point G-1 (Furuyama *et al.*, 2014).

The three-dimensional displacements in the direction of latitude, longitude, and height have been continuously measured every hour.

The standard deviations of the measurements at G-1 and G-2 are shown in Table 1. Since the standard deviations of the conventional GPS are 5 mm and 10 mm in the horizontal and vertical directions, respectively, it is shown that the GPS monitoring system and the correction method used here have been successful. Actually, the monitoring results have been obtained continuously and smoothly without missing any results.

Table 1 Standard deviations in measurement.

Meas. Point	*Latitude(mm)*	*Longitude(mm)*	*Height(mm)*
G-1	1.6	2.0	4.5
G-2	1.9	1.6	3.6

(Monitoring duration; March 2013 to January 2014)

Small displacements of less than 2-3 mm/month were generated at monitoring point G-1 during the low rainfall period from March to early June. Whenever heavy rain fell from July to October, the displacement gradually increased. Eventually, it reached 355 mm in the north direction, 234 mm in the west direction, and 137 mm in settlement by the end of October. However, displacements at G-1 gradually converged and became stable after this rainfall period.

On the other hand, no remarkable displacements were measured at G-2 in this period. The right-hand side of the slope is seen to be more stable than the left-hand side.

Figure 16(a) shows the displacement vectors in the plan view of the slope, while Figures 16(b) and 16(c) show the vertical sections including G-1 and G-2, respectively. Both directions of vectors for G-1 and G-2 almost coincided with the steepest direction of the slope in the plan view. The direction of the displacement at G-1 was toward the front of the slope in the vertical section until the middle of August. After heavy rainfall at the end of August and early September, the direction changed to be parallel to the slip

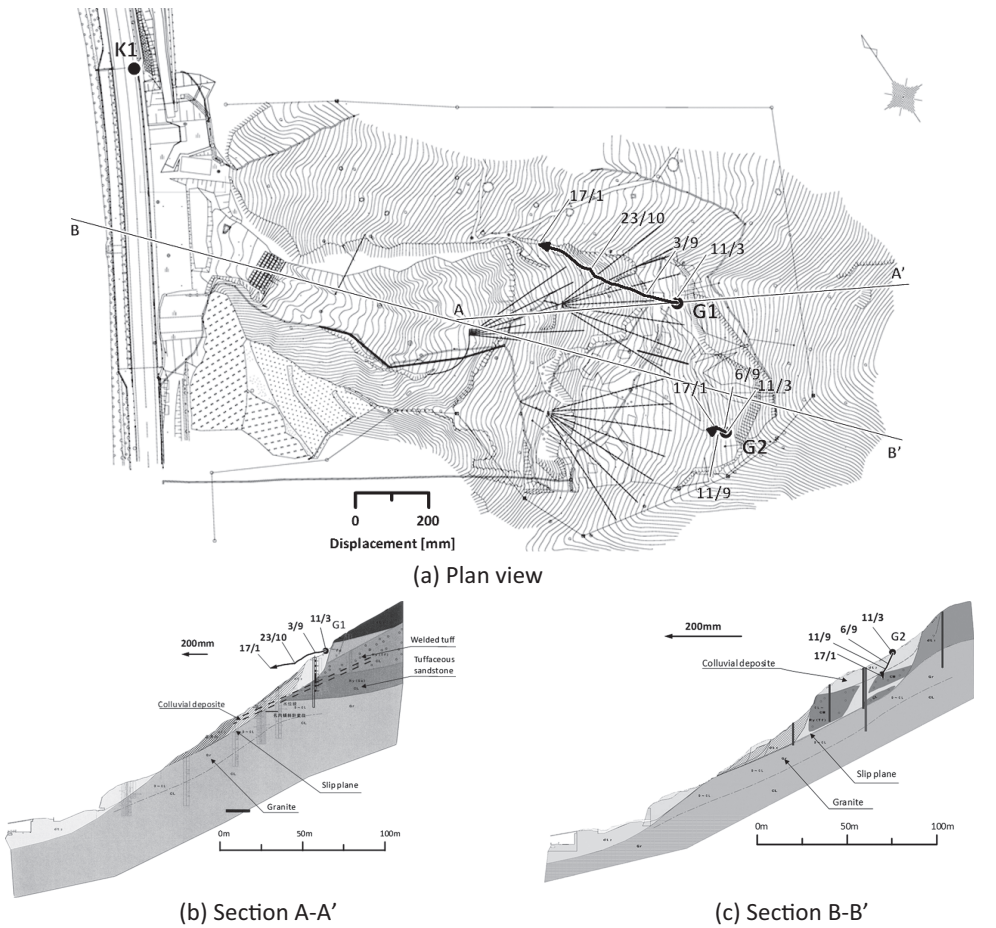


Figure 16 Transitions of displacement vectors (Furuyama *et al.*, 2014).

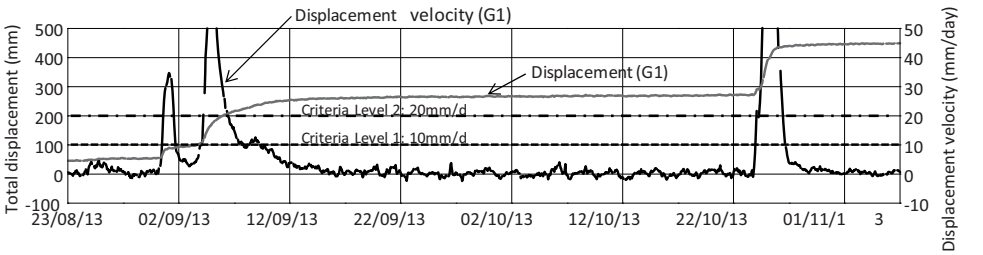


Figure 17 Displacement and velocity (mm/h) at G-1.

plane of the slope, and it was toward the front of the slope again after the last large displacement of October 23. On the other hand, the direction of the displacement at G-2 is parallel to the slip plane at the top of the slope in the vertical section.

Figure 17 shows the velocity of the displacement (mm/day) calculated from the monitoring displacements. Regulations (criteria) for traffic safety along this road have been given by the government as follows. When the displacement velocity (mm/day) is beyond 10 mm/day and the total amount of continuous rainfall exceeds 100 mm, one lane of the roadway is temporarily closed. And when the displacement velocity (mm/day) is over 20 mm/day and the total amount of continuous rainfall exceeds 200 mm, both lanes of the road are temporarily closed.

The GPS monitoring results are seen to have provided effective information for managing traffic safety, comparing them with the above criteria.

4.2 Landslide dam caused by heavy rain

A large-scale slope failure occurred in a mountainous area of Western Japan due to a heavy rainfall brought about by a typhoon. The huge volume of colluvial deposit blocked a river channel and created a landslide dam. Then, a debris flow occurred due to the erosion of part of the deposit. In order to prevent the collapse of the landslide dam and the occurrence of further debris flows, disaster recovery works were carried out. The GPS monitoring system was applied to monitor the behavior of the unstable colluvial deposit (Sato *et al.*, 2014).

4.2.1 Monitoring site

The slope failure occurred over an area that was 650 m long, 410 m wide, and 60 m deep (Figure 18). The volume of the colluvial deposit was estimated to be 4.1 million m^3. The slope was formed by alternating beds of sandstone and mudstone.

GPS sensors were set at 11 measurement points on the slope of the colluvial deposit (denoted by the bullets; G-1, G-2, …, and G-8) and at a reference point outside of the area (Figure 19) in order to perform the safety management of disaster recovery works. The distance between the measurement points and the reference point was about 100 m – 700 m. Electric power was supplied to the monitoring system by means of

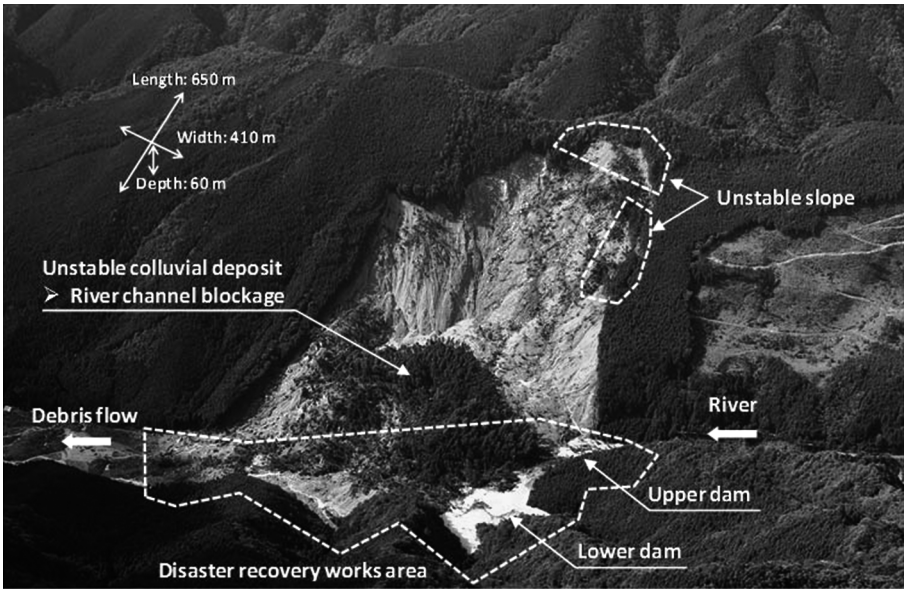


Figure 18 Landslide dam and unstable colluvial deposit (Sato *et al.*, 2014).

a solar panel, and the measurement data were transmitted via a cellular phone to a computer at the control office. Extensometers, denoted by S-1 to S-4, were also set in the upper area of the unstable slope (Figure 19).

4.2.2 Monitoring results

The displacement vectors and the monitoring results of G-5 over three years are presented in Figure 20. These results show that the total amount of displacement in the lower area of the slope (G-1 to G-8, except for G-5 in Figure 20(b)) was not large and ranged from a few millimeters to 34 mm.

On the other hand, the displacements in the upper area of the unstable slope (G-5, and S-1 to S-4 in Figure 20(b)) increased up to 540 mm to 3353 mm. The displacements often exceeded the criteria for the suspension of disaster recovery work (10mm/day for caution and 25mm/day for warning; see Figure 21). At those times, the monitoring office issued a warning for unstable slope conditions to the engineers and workers at the site and the work was suspended. The people in that vicinity were evacuated to a safe area several times over the three years.

GPS monitoring is useful for the safety management of disaster recovery works.

4.3 Landslide with a high velocity

A landslide occurred in a portion of a hill covered with snow located in the north-west part of Japan a few days after the temperature suddenly increased. The mass was

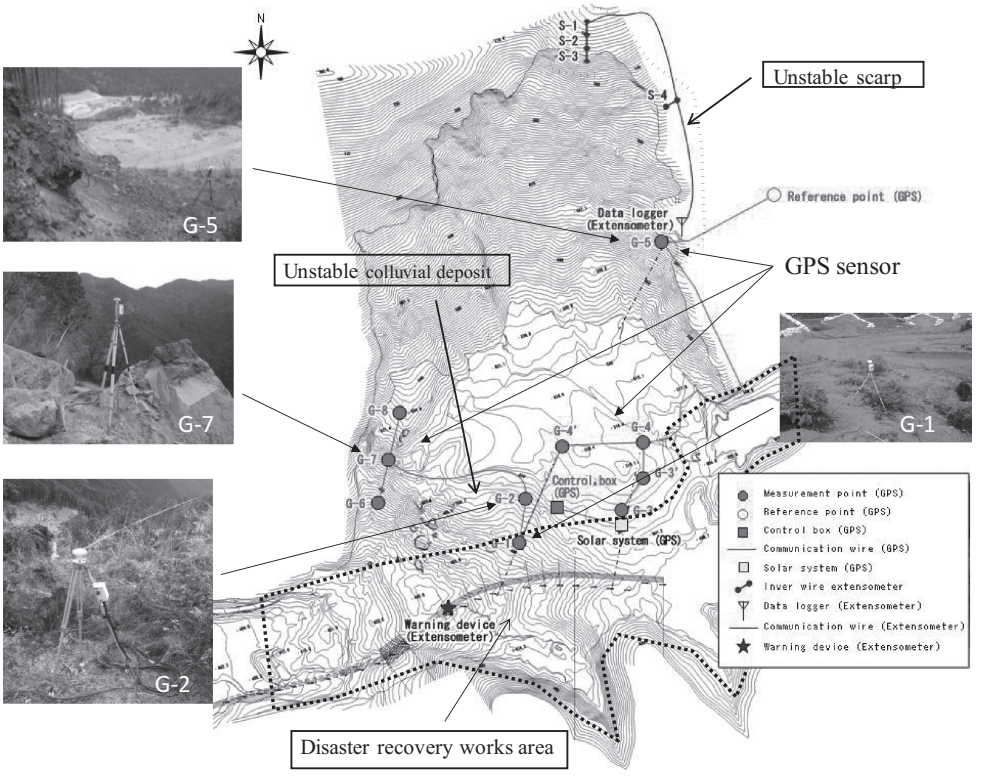


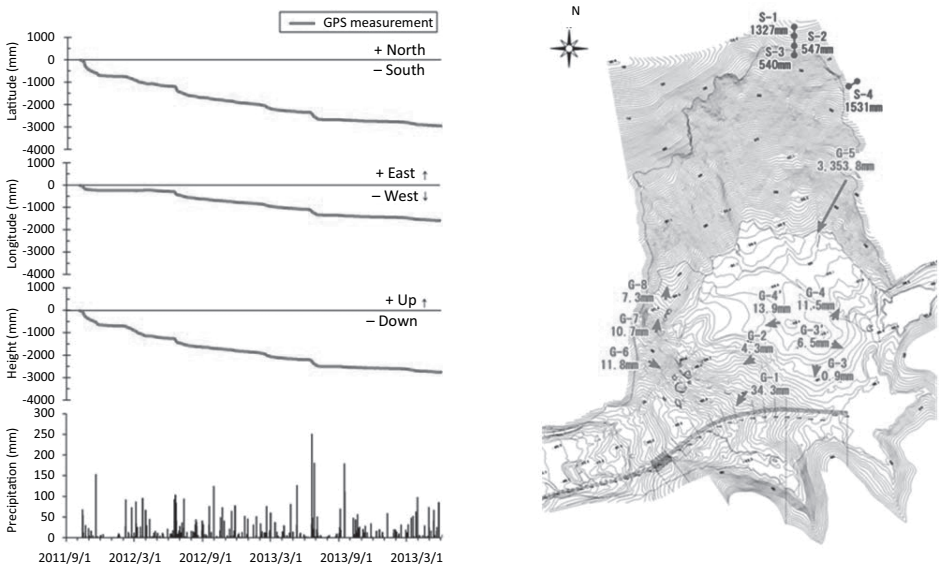
Figure 19 Plan view of monitoring site and location of GPS sensors (Sato *et al*., 2014).

500m in length, 150 m in width, and 20 m in depth, and moved down with a high velocity, namely, a maximum value of 20 m per day, to an alluvial fan with a village. The GPS displacement monitoring system was applied to continuously monitor the movement in order to issue an evacuation advisory or to give orders to the local residents (Tosa *et al*., 2014).

4.3.1 Monitoring site

The upper and lower areas of the hill are composed of mainly unconsolidated conglomerate and massive mudstone, respectively. The mass of the slope moved down along the ground surface (alluvial fan) with an inclination of only 2 degrees (Figure 22).

The landslide occurred on March 7, 2012. In order to monitor such a mass movement, the total station was used immediately after the movement began at the points denoted by T1 and T4 in Figure 23. A drainage system using surface drains and boring was applied to drain water from the landslide area after March 11 together with countermeasures consisting of concrete blocks to resist the movements.



(a) Monitoring displacements and rainfall at G-5 (b) Displacement vectors in plan view

Figure 20 Monitoring results (Sato *et al.*, 2014).

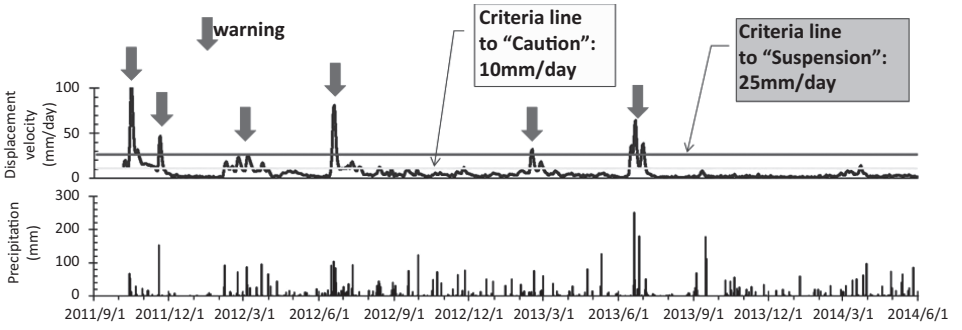


Figure 21 Displacement velocity at G-5 and criteria (Sato *et al.*, 2014).

However, the velocity of the movement was still large, and thus, some other system, available for continuously monitoring 24 hours a day, was required for obtaining displacements in real time to protect the local area and its residents from damage and injury. For this purpose, the GPS displacement monitoring system was installed on March 14 and 15, one week after the occurrence of the movement.

The four monitoring points, G-1 to G-4, were set on the inside of the landslide area (Figure 23) and the other points were set on the outside of the area. A reference point was fixed 200 m north of the landslide area.

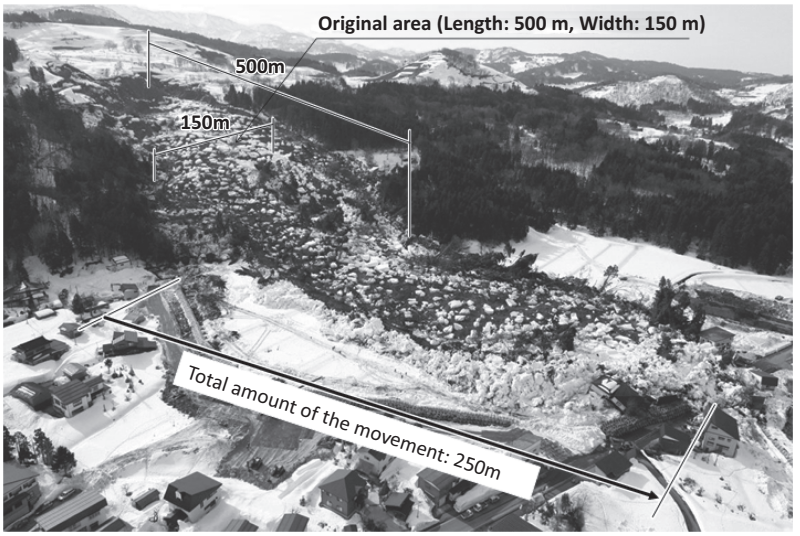


Figure 22 Landslide with a high velocity (Tosa *et al*., 2014).

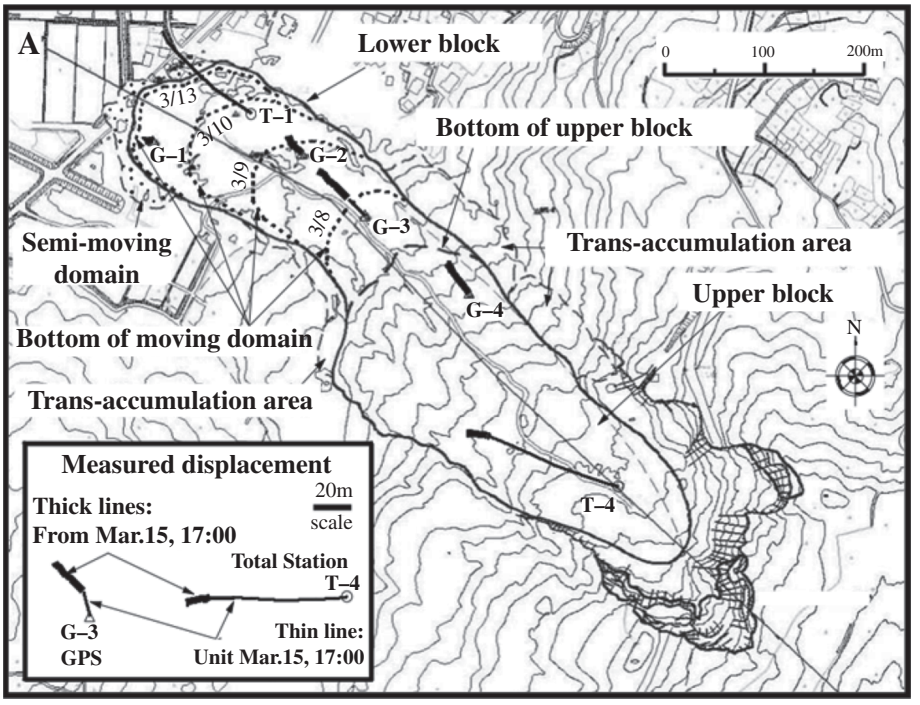


Figure 23 Plan view of landslide area and trace of displacements at Monitoring points (Tosa *et al*., 2014).

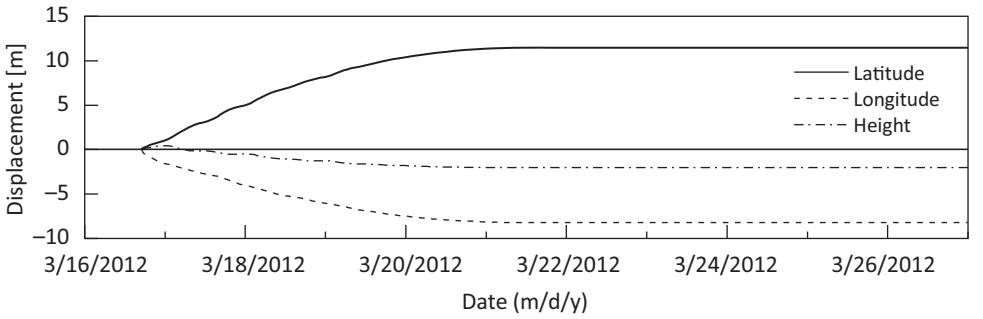


Figure 24 Displacement monitoring results at G-4.

4.3.2 Monitoring results

The trace of the horizontal displacements at T-1 and T-4 by the total station and at G-1, G-2, G-3, and G-4 by GPS are presented in Figure 23. The displacement velocity of the upper area of the slope rose to the maximum on March 9 to 13, and it reached 20 m/day from March 11 to 12. The toe of the lower area of the slope moved down 100m during the 15-hour period from 16:00 on March 8 to 7:00 on March 9.

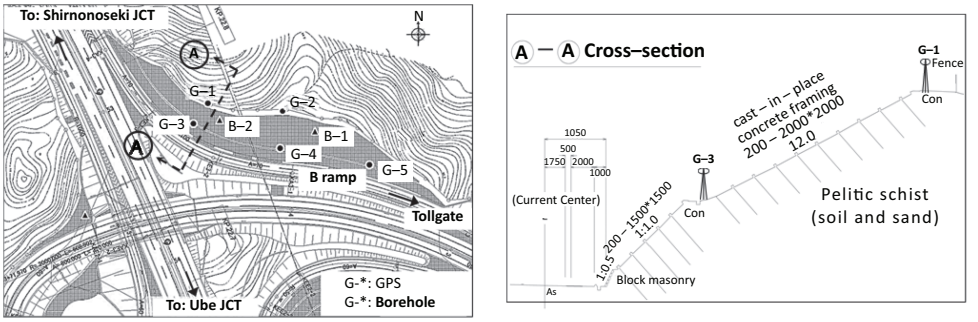
Figure 24 shows the monitoring results at G-4 by GPS. It is found that the landslide movement became slow after March 20 and almost converged until March 23. Although the total amount of the movement of the toe of the slope reached about 250m and the landslide crushed several houses, there were no injuries to the residents themselves due to the evacuation advisory issued by referring to the monitoring results.

4.4 Cut slope beside an expressway

Continuously monitoring slopes has become more important for the safety management of expressways, since slope disasters caused by heavy rain have increased. The GPS displacement monitoring system was installed on a cut slope prone to instability beside an expressway. Detecting a large displacement due to heavy rain, that exceeded the criterion, the expressway was temporally closed for traffic safety. Monitoring contributed to the prevention of any accidents (Shitano *et al.*, 2014).

4.4.1 Monitoring site

The monitoring site was located at a cut slope at the ramp of an expressway. Figure 25 shows the plan view and a vertical section of the slope. The slope is composed of mainly strong weathering pelitic schist. After construction of the expressway was completed in 2001, a slope maintenance inspection was periodically conducted and it indicated that the slope was prone to instability. GPS sensors were set on the slope denoted by G-1, G-2, G-3, and G-4, and monitoring started from June 2008.



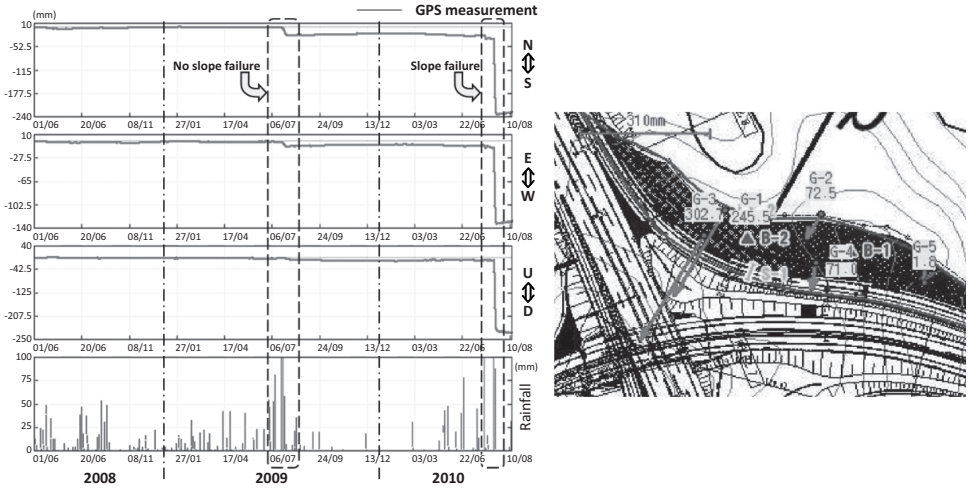
(a) Plan view (b) Cross section

Figure 25 Cut slope at ramp of expressway (Shitano *et al.*, 2014).

4.4.2 Monitoring results

Figure 26(a) shows the monitoring results at G-1 on the top of the slope. From June 2008 until July 2010, the displacement increased only a few millimeters per year, except for a short period in July 2009. The displacement increased up to about 30 mm in a few days due to heavy rainfall during the rainy season in July 2009.

From July 12, 2010, the displacement increased rapidly due to continuously heavy rain with more than 100 mm per day. The criteria for safety were given as 2 mm per 5 days as primary caution, 5 mm per 5 days as the secondary caution, and 10 mm per day as the warning. The displacement monitored by GPS increased and exceeded the criteria as the



(a) Displacements for two years (b) Displacement vectors in plan view

Figure 26 Displacement monitoring results (Shitano *et al.*, 2014).

primary caution at 19:00, July 12, the secondary caution at 23:00, and the warning at 2:00, July 13. Since the movement increased even further, the expressway was closed for traffic safety at 12:00, July 13. A counterweight fill was constructed to prevent slope failure, and then the velocity of the displacement decreased until it converged at the end of July. Figure 26(b) shows the displacement vectors of the slope in the plan view.

Although the total amount of the displacement at G-1reached about 300 mm and open cracks were propagated on the top of the slope, it was possible to avoid a collapse over the whole slope due to the early application of the countermeasures based on the monitoring results.

4.5 Slope movements due to tunnel excavations

When a tunnel is constructed in a landslide area, the excavations may induce the instability of nearby slopes. The stability of the slope around the tunnel entrance is one part that requires great care during the tunnel construction. In order to monitor the stability of a slope above tunnels, due to tunnel excavations, the GPS monitoring system was applied (Hirano *et al.*, 2011).

4.5.1 Monitoring site

The slope is composed of metamorphic diabase, schalstein, serpentinite, etc., and covered with colluvial deposits. Since landslide movement had been continuing for a long time, countermeasure works had been completed to reduce the slope displacement and to make the slope stable before the tunnel construction. Two tunnels, "line 1" and "line 2", were constructed just beneath the landslide slope (Figure 27). Five measurement points for GPS displacement monitoring, G-1 to G-4 and G-13, were

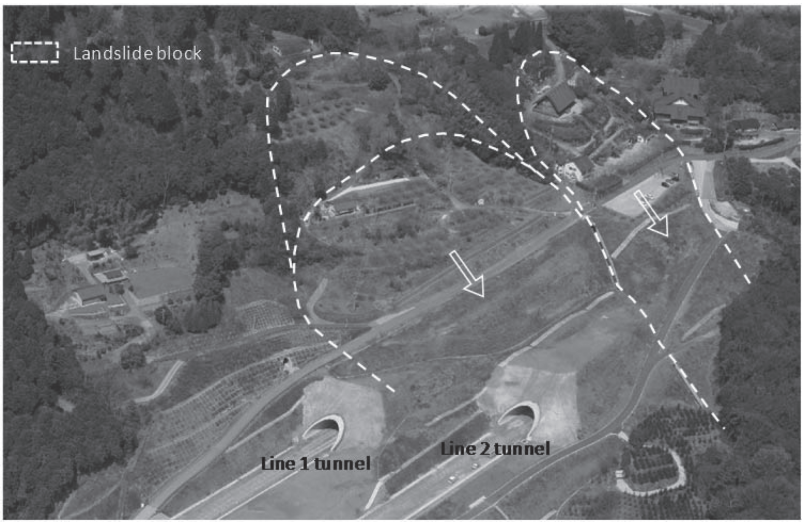


Figure 27 Tunnels constructed beneath landslide slope after completion (courtesy of Shimizu Corp.)

set on the main block of the landside. The reference point was located on a stable ground about 400 m away from the slope. The epoch interval and the session length were 30 seconds and 1 hour, respectively.

4.5.2 Monitoring results

The three-dimensional displacements were automatically and continuously monitored for about four years including the tunnel excavation period for the main landslide block (Nov., 2004 to May, 2005), as shown in Figures 28 and 29. The displacements of all the measurement points, except G-1 located out of the landslide block, increased as the "line 1" tunnel was approaching. The "line 2"

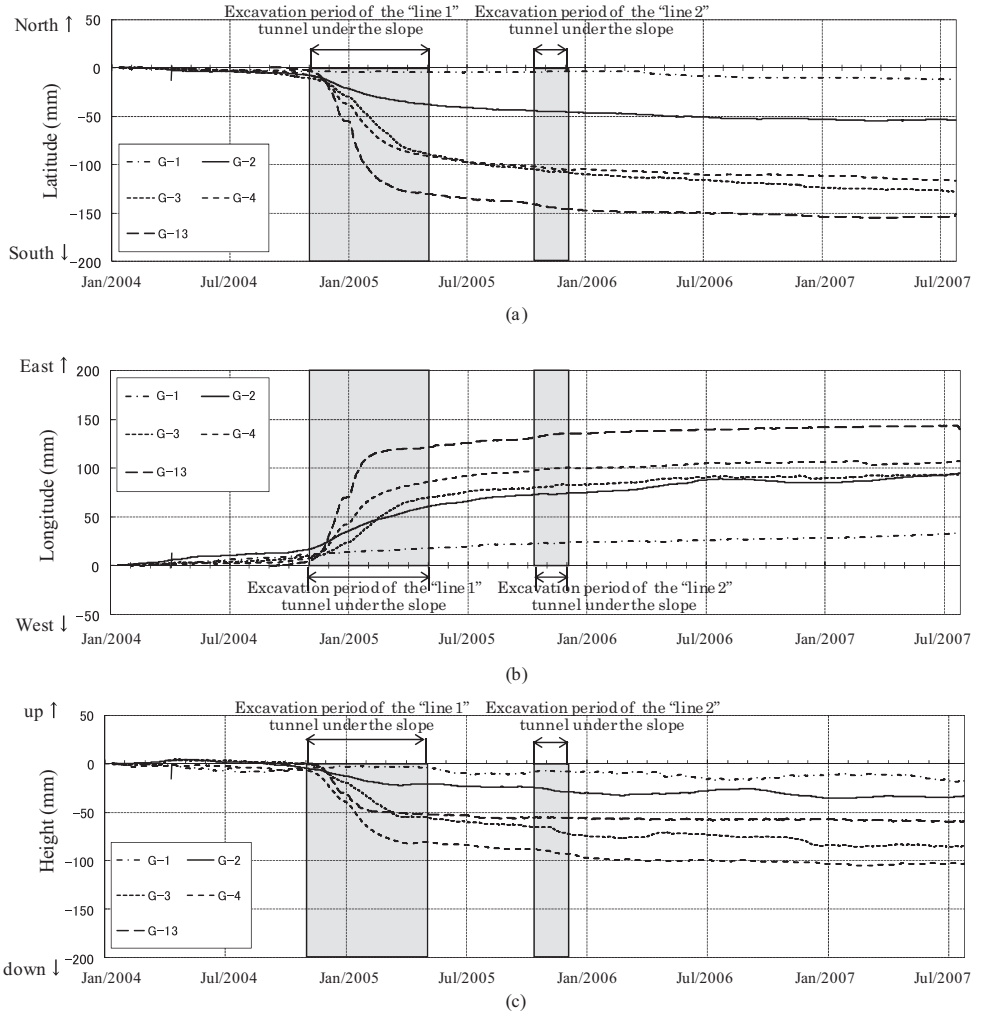
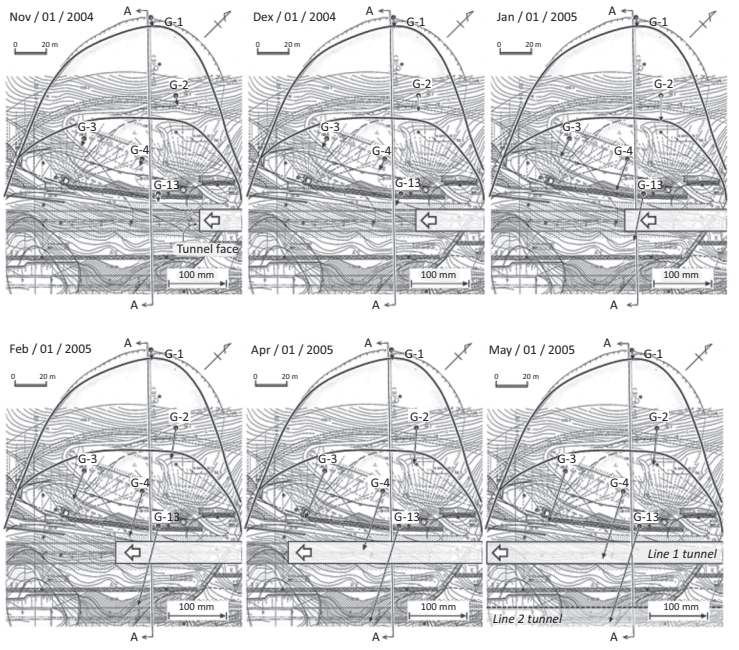
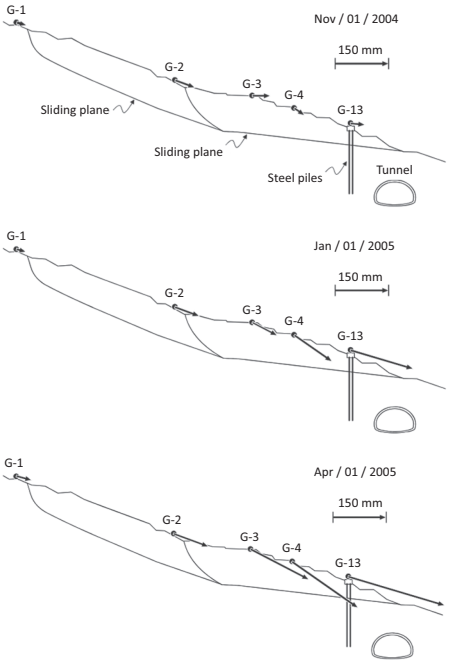


Figure 28 Measurement results of displacements on a landslide slope due to tunnel excavations (Hirano *et al.*, 2011).



(a) Plan view



(b) Vertical section

Figure 29 Displacement vectors on a landslide slope due to tunnel excavations (Hirano *et al.*, 2011).

tunnel did not affect the displacement behavior of the slope much in comparison to the "line 1" tunnel. Figure 29 shows the transition in the displacement vectors in the plane view and in the vertical section. The three-dimensional displacements over the extensive area of the slope could be continuously and clearly monitored in relation to the tunnel excavations. Therefore, it is easy to recognize how tunnel excavations influence landslide behavior and how slopes become stable after tunnels are constructed to pass through such areas.

The tunnel was successfully constructed by the observational procedure. The length and the spaces for the rock bolts installed from the tunnel face and the timing of the invert-closure were determined based on the measurement results, including the slope surface displacements monitored by GPS.

4.6 Limestone quarry

GPS has been applied to several quarries in Japan to continuously monitor the stability of the slope and for the safety management of the production. This example is the first practical experience of long-term monitoring over 10 years from 1997 to 2007 using GPS in Japan (Shimizu, 1999; Hirabayashi *et al.*, 2008).

4.6.1 Monitoring site

The area of the quarry is approximately 2,000 m in length by 600 m in width. The quarry contains 4 billion tons of limestone reserves. The height of the slope was

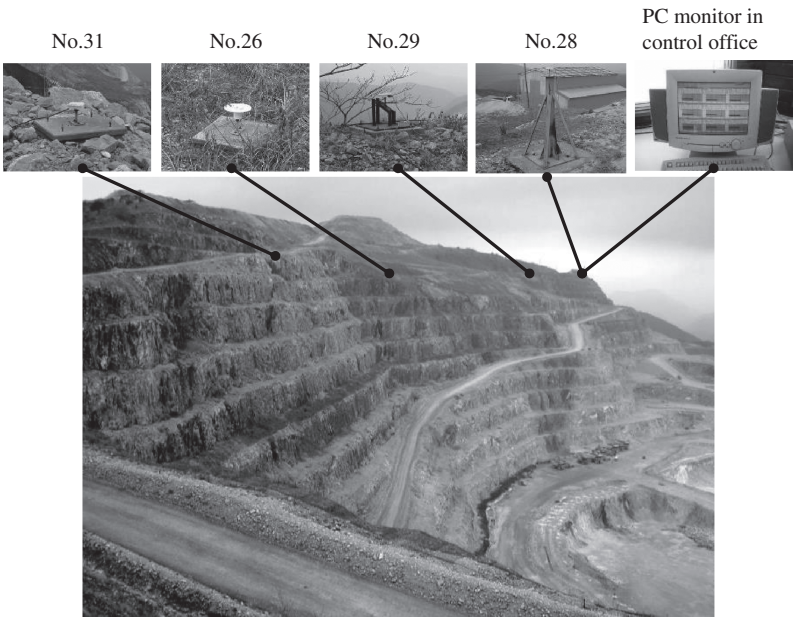


Figure 30 Slope of limestone quarry and monitoring points (Hirabayashi *et al.*, 2008).

above 150 m in 2007 and the final height will be 300 m. The height of each bench is 15 m and the average angle of the slope is 60 degrees. One bench was excavated every year and a half.

The automatic monitoring system using the kinematic method of the relative positioning (Shimizu *et al.*, 1996; Shimizu, 1999) was used here, while other examples in this article employ the system using the static method.

Sensors were set on measurement point Nos. 26, 29, and 31 located around the crest of the slope (see Figure 30). Another sensor, No. 28, was set as the reference point. Monitoring was continuously conducted over 10 years.

4.6.2 Monitoring results

Figure 31 shows the measured displacement vectors together with the numerical solutions obtained by a three-dimensional elastic analysis in plan-view and section A-C, respectively. Elastic displacements tend to be directed upward and backward to the slope. The direction of the measured displacement at No. 31 almost coincides with the direction obtained from the elastic analysis. This means that the behavior of the slope around No. 31 is elastic and then it is stable.

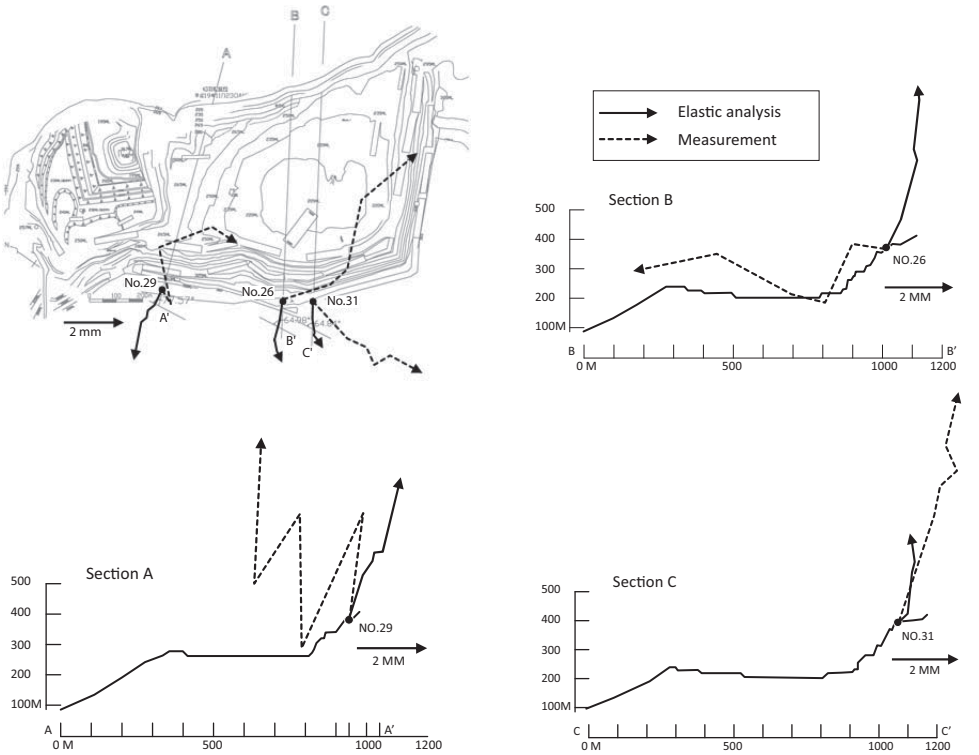


Figure 31 Comparison of measured and elastic displacements (Hirabayashi *et al.*, 2008).

On the other hand, the direction of the measured displacement at No. 26 differs from the direction obtained by the elastic analysis. The real displacement goes downward, although the elastic one goes upward. This means that the behavior around No. 26 is inelastic. The measured displacement at No. 29 repeats the elastic and inelastic behavior.

Since the total amount of those displacements was small, the slope was stable. Careful monitoring should be conducted, however, to confirm whether such behavior will cause the instability of the slope, especially around Nos. 26 and 29.

Continuous three-dimensional monitoring by GPS provides an opportunity to discuss the detailed interpretation of the behavior of a slope, as illustrated above.

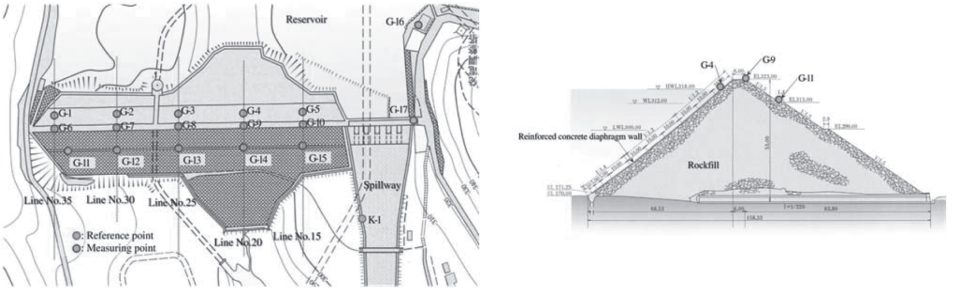
4.7 Rock-fill dam in the Great East Japan Earthquake

Exterior deformation is one of the most important items to measure when managing the safety of rock-fill dams. Exterior deformation is usually measured by a conventional surveying method using targets installed on the crest and the slopes of the dams. It is difficult, however, to measure the deformation by such a method immediately after an earthquake or other emergency. The GPS displacement monitoring system was applied to continuously monitor the deformation of dams (Nakashima *et al.*, 2011), and detected displacements due to the Great East Japan Earthquake (Kobori *et al.*, 2014).

4.7.1 Monitoring site

The GPS monitoring system was applied to Ishibuchi Dam, which is an old concrete-face rock-fill dam completed in 1953 with a height of 53 m. It is located 216 km away from the epicenter of the Great East Japan Earthquake. Figure 32 shows a plan view and a vertical section of the dam with the monitoring points. The sensors were installed at 17 monitoring points denoted by G-1 to G-17and 1 point as a reference point denoted by K-1 (see Figure 32). The sensors on the dam were fixed to the surface of the concrete facing with anchor bolts.

The measurements were started on June 26, 2008, which was 12 days after the Iwate-Miyagi Nairiku Earthquake and three years before the Great East Japan Earthquake.



(a) Plan view

(b) Cross section (Line No. 20)

Figure 32 Dam embankment and layout of GPS sensors (Kobori *et al.*, 2014).

4.7.2 Monitoring results

The monitoring results at G-4, G-9, and G-14 on section line No. 20, which is the maximum section of the dam (Figure 32), are shown with the water level of the reservoir in Figure 33. The three-dimensional displacements in the up-downstream, the dam axis, and the vertical direction were continuously measured every hour.

Upon the occurrence of the Great East Japan Earthquake on March 11, 2011 (denoted by "the main shock" in this paper), a seismograph on a right bank terrace recorded a maximum acceleration value of 184 gal. When the largest aftershock occurred on April 7, the acceleration value of 140 gal was recorded by a seismograph in the same place. The broken and dashed-dotted lines in Figure 33 represent the time of the main shock (2:46 p.m. on March 11, 2011) and the time of the largest aftershock (11:32 p.m. on April 7, 2011), respectively. It is found that the main shock caused displacements of

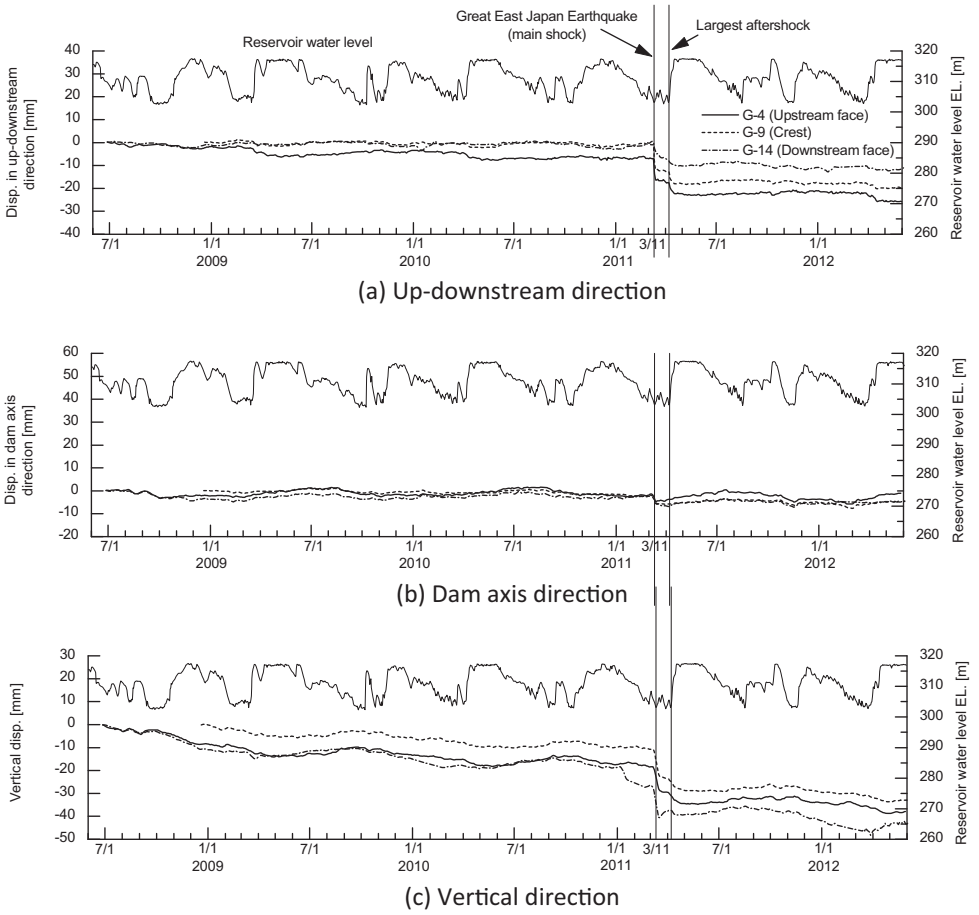


Figure 33 Displacement monitoring results of GPS at G-4, G-9, and G-14 located on line No. 20 and water level of reservoir (Kobori *et al.*, 2014).

about 10 mm in the downstream direction, about 3 mm in the right bank direction, and about 10 mm in the settlement direction at G-9. The largest after shock caused displacements of about 2 mm in the downstream direction and about 2 mm in the settlement direction.

Figure 34 focuses on the monitoring results at G-9 during the period before and after the main shock. The displacements in all directions were almost zero until 14:00 on March 11 before the earthquake. The earthquake occurred at 14:46. After 15:00 on the same day, the GPS monitoring system clearly detected displacements due to the earthquake (bullets in Figure 34), *i.e.*, both a displacement in the direction of the downstream side and a settlement were about 10 mm, and a displacement in the direction of the right bank side was about 3mm.

For the other GPS monitoring points, the main shock and the largest aftershock caused similar displacements to those shown in Figures 33 and 34. No remarkable displacement occurred after the largest aftershock, and the displacements gradually decreased and became stable.

It is found that continuous monitoring using GPS is quite effective for detecting displacements due to an earthquake immediately after it occurs.

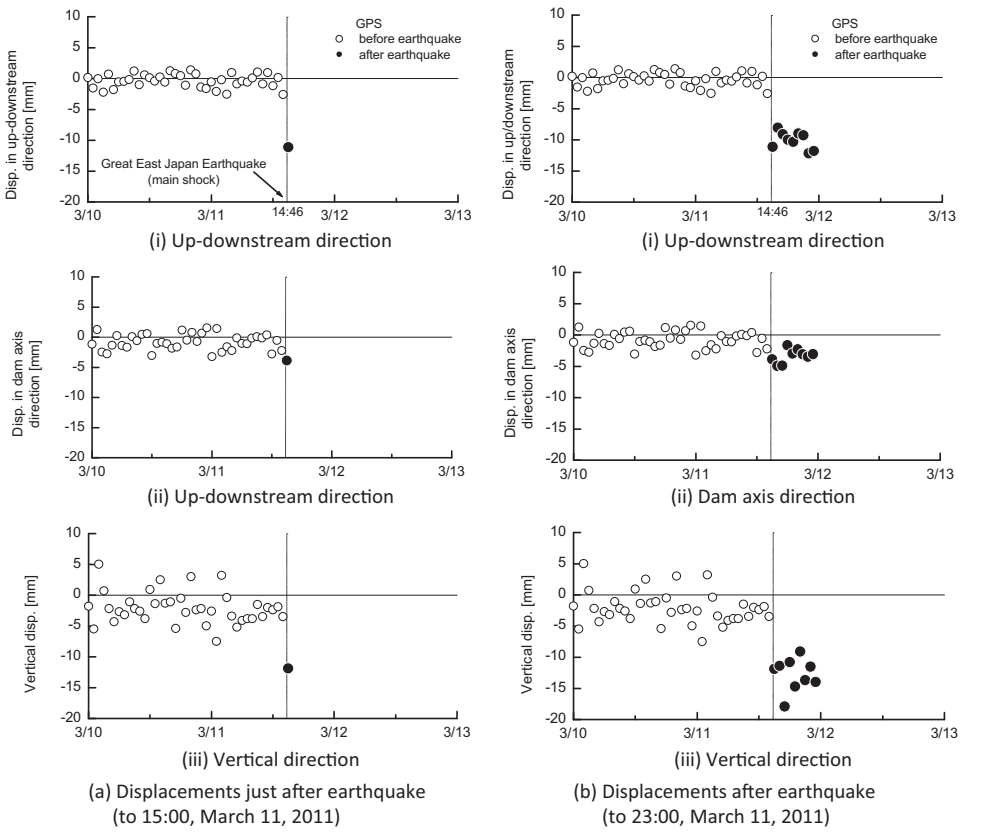


Figure 34 Detection of three-dimensional displacement by GPS at G-9 due to Great East Japan Earthquake in 2011 (Kobori *et al.*, 2014).

5 CONCLUSIONS

The fundamental technology of displacement monitoring using GPS has been established over the last 25 years. It can monitor the three-dimensional displacements of the surface of rocks and structures automatically and continuously over extensive areas.

The accuracy is affected by the baseline length, tropospheric delays (the difference in height and the meteorological conditions), and obstructions above the antennas. When error correction methods recommended in the ISRM Suggested Method are applied, monitoring with mm-level accuracy can be realized.

This article has described examples of practical applications of GPS displacement measurements for monitoring the stability of an unstable steep slope, a natural dam, a landslide, a cut slope, slope movement, a quarry, and a rock-fill dam.

Moreover, it has been applied to monitoring displacements of ground surfaces, gravity and arch dams, bridges, viaducts, towers, pipelines, retaining walls, breakwaters, railway trucks, runways, etc., for safety construction and maintenance. GPS has been successfully performed in many projects, and it has become common technology for monitoring in Rock Engineering and other related fields of engineering.

ACKNOWLEDGMENTS

This research has been partially supported by JSPS KAKENHI (Grant-in-Aid for Scientific Research, Japan Society for the Promotion of Science) Grant Numbers 17560445, and 25350506. The authors wish to express their appreciation to their students and associates for their contributions to the field work and the analysis of the data. They also extend their thanks to Ms. H. Griswold for proofreading this paper.

REFERENCES

Bond, J. (2004) *An investigation on the use of GPS for deformation monitoring in open pit mines*, Technical Report Report No. 222, Department of Geodesy and Geomatics Engineering, University of New Brunswick, Canada.

Burkholder, E. F. (ed.) (1988) Special Issue: GPS88. *Journal of Surveying Engineering*, 114(4), ASCE.

Burkholder, E. F. (ed.) (1989) Special Issue: GPS88. *Journal of Surveying Engineering*, 115(1), ASCE.

Chrzanowski, A. & Wells, W. (eds.) (1988) *Proceedings of the 5th FIG International Symposium on Deformation Measurements and 5th Canadian Symposium on Mining Surveying and Rock Deformation Measurements*, Fredericton, Canada.

Furuyama, Y., Nakashima, S. & Shimizu, N. (2014) Displacement monitoring using GPS for assessing stability of unstable steep slope by means of ISRM suggested method, *Proceedings of the 2014 ISRM International Symposium – 8th Asian Rock Mechanics Symposium (ARMS8)*, 1897–1904.

Gili, JA., Corominas, J. & Rius, J. (2000) Using Global Positioning System techniques in landslide monitoring, *Engineering Geology*, 55, 167–192.

Hirabayashi, K., Nakaya, K., Shimizu, N., Matsubara, S. & Matsumoto, T. (2008) Continuous three-dimensional displacements monitoring for assessment of the slope stability: A case

study of limestone quarry, *Proceedings of Korean Rock Mechanics Symposium 2008*, 199–206.

Hirano, H., Usuda, Y., Kanzawa, K., Miyata, K. & Shimizu, N. (2011) Application of the GPS monitoring system to measuring the three-dimensional displacements of a landslide slope during tunnel construction and its interpretation. *Journal of the Japan Landslide Society*, 48(2), 7–18 (in Japanese).

Hoffman-Wellenhof, B., Lichtengger, H. & Collins, J. (2001) *GPS – Theory and Practice*. 5th revised edition, Springer.

Hudnut, KW. & Behr, JA. (1998) Continuous GPS monitoring of Structural Deformation at Pacoima Dam, California. *Seismological Research Letters,* 69(4), 299–308.

Iwasaki, T., Takechi, K., Takeishi, A., Masunari, T., Takechi, Y. & Shimizu, N. (2003) Web-based displacement monitoring system using GPS for the maintenance of roadside slopes. *Proceedings of the 6th International Symposium on Field Measurements in Geomechanics*, FMGM03, Oslo, 137–143.

Kim, D., Langley, RB., Bond, J. & Chrzanowski, A. (2003) Local deformation monitoring using GPS in an open pit mine: initial study. *GPS Solutions,* 7, 176–185.

Kitagawa, G. & Gersch, W. (1984) A smoothness priors-state space modeling of time series with trend and seasonality. *Journal of the American Statistical Association,* 79(386), 378–389.

Kobori, T., Yamaguchi, Y., Nakashima, S. & Shimizu, N. (2014) Displacement Monitoring of a Rockfill Dam Before, During and After The Great East Japan Earthquake Using GPS. *Proceedings of the 2014 ISRM International Symposium – 8th Asian Rock Mechanics Symposium (ARMS8)*, 930–938.

Malet, JP., Maquaire, O. & Calais, E. (2002) The use of Global Positioning System techniques for the continuous monitoring of landslides: application to the Super-Sauze earthflow (Alpes-de-Haute-Provence, France). *Geomorphology* 43, 33–54.

Manetti, L. & Glisic, B. (2003) Monitoring a harbor structure during reinforcement using GPS-based monitoring system. *Proceedings of International Symposium on Field Measurements in Geomechanics*, FMGM03, Oslo, 531–536.

Masunari, T., Tanaka, K., Okubo, N, Oikawa, H., Takechi, K., Iwasaki, T. & Shimizu, N. (2003) GPS-based continuous displacement monitoring system. *Proceedings of International Symposium on Field Measurements in Geomechanics*, FMGM03, Oslo, 537–543.

Matsuda, H., Tsutsui, T., Ikeda, K., Shimizu, N. (2012) Application of GPS displacement measurements for monitoring slope displacements at a tunnel entrance. *Journal of Japan Society of Civil Engineers*, Ser. F1 (Tunnel Engineering), 68(2), 21–28 (in Japanese).

Misra, P. & Enge, P. (2006) *Global Positioning System –Signals, Measurements, and Performance*. 2nd Edn, Ganga-Jamuna Press.

Nakashima, S., Kawasaki, H., Kubota, S., Nakano, T. & Shimizu, N. (2011) Measurement of Exterior Deformation of an Earth-filled Dam Using GPS Displacement Monitoring System. *Proceedings of the 12th ISRM International Congress on Rock Mechanics*, 1069–1172.

Nakashima, S., Shimizu, N., Hirabayashi, K., Masunari, T., Iwasaki, T. & Ono, M. (2012) Effects of correction of atmospheric delay on GPS displacement measurements in large slopes. *Journal of Mining and Materials Processing Institute of Japan,* 128(6), 255–264 (in Japanese).

Satoh, W., Iwasaki, T., Sakurai, W., Fujii, A. & Shimizu, N. (2014) Monitoring the Stability of a Large-scale Colluvium Deposited by Slope Failures due to Heavy Rainfall Using a GPS Automatic Monitoring System, *Proceedings of the 2014 ISRM International Symposium – 8th Asian Rock Mechanics Symposium (ARMS8)*, 1778–1783.

Shimizu, N. (1999) Displacement monitoring by using Global Positioning System for assessment of slopes. *Proceedings of the 9th International Congress on Rock Mechanics*, Paris, 1435–1438.

Shimizu, N., Kondo, H., Ono, H. & Mizuta, Y. (1996) A new GPS real-time monitoring system for deformation measurements and its application. *Proceedings of the 8th FIG International Symposium on Deformation Measurements*, Hong Kong, 47–54.

Shimizu, N., Masunari, T. & Iwasaki, T. (2011) GPS displacement monitoring system for the precise measuring of rock movements. *Proceedings of 11th International Congress on Rock Mechanics*, Beijing, 1117–1120.

Shimizu, N. & Matsuda, H. (2002) Practical applications of the Global Positioning System for the assessment of slope stability based on the Displacement Monitoring Approach. *Proceedings of the 3rd Korea-Japan Joint Symposium on Rock Engineering*, ISRM Regional Symposium, Seoul, 57–70.

Shimizu, N. & Matsuda, H. (2003) Displacement monitoring using GPS and its interpretation method for the assessment of slope stability. *Proceedings of the 6th International Symposium on Field Measurements in Geomechanics*, FMGM03, Oslo, 657–664.

Shimizu, N., Nakashima, S. & Masunari, T. (2014) ISRM Suggested Method for Monitoring Rock Displacements Using the Global Positioning System, *Rock Mech. Rock Eng.*, 47, 313–328. Available from: doi:10.1007/s00603-013-0521-5 (In *The ISRM Suggested Methods for Rock Characterization, Testing and Monitoring*: 2007–2017, ed. R. Ulusay, Springer, 205–220, 2014).

Shitano, M., Murakami, T. & Shimizu, N. (2014) Application of the GPS Displacement Monitoring System for the Preventive Maintenance of a Cut Slope along a National Expressway - a Case Study. *Proceedings of the 2014 ISRM International Symposium – 8th Asian Rock Mechanics Symposium (ARMS8)*, 1877–1886.

Tasci, L. (2008) Dam deformation measurements with GPS. *Geodesy and Cartography*, 34(4), 116–121.

Tosa, S., Yamasaki, T., Ito, K, Suganuma, T., Oikawa, N., Takeishi, A. & Shimizu, N. (2014) Case Studies on Landslide Monitoring Using the GPS Displacement Monitoring System, *Proceedings of the 2014 ISRM International Symposium – 8th Asian Rock Mechanics Symposium (ARMS8)*, 1887–1896.

US Army Corps of Engineering (2002) Monitoring structural deformations using the Global Positioning System. In: Chapter 8, *Structural Deformation Surveying*, Engineering Manual EM 1110-2-1009, 8-1–8-42.

Vermeer, M. (2002) *Review of the GPS Deformation Monitoring Studies*. STUK-YTO-TR 286 STUK, Finland.

Integrated Engineering Monitoring and Analysis



Taylor & Francis
Taylor & Francis Group
http://taylorandfrancis.com

Chapter 20

Multidisciplinary monitoring of progressive failure processes in brittle rock slopes

Simon Loew[1], *Valentin Gischig*[1], *Franziska Glueer*[1], *Reto Seifert*[1] & *Jeffrey Moore*[1,2]

[1]*Chair of Engineering Geology, Department of Earth Sciences, ETH Zurich, Switzerland*
[2]*now at: Department of Geology and Geophysics, University of Utah, USA*

Abstract: In this chapter we describe key scientific issues and give technical recommendations for the design, installation and operation of in-situ monitoring systems related to the study of progressive failure processes in rock slopes composed of fractured crystalline rocks. The monitoring systems are explained and discussed with landslide examples from the Swiss Alps: the actively creeping Moosfluh toppling instability with a volume of 100–200 million m^3, the slowly moving complex instability at Randa (5–6 million m^3), and the compound sliding instability at Preonzo (300,000–400,000 m^3), which partially failed in 2012.

1 INTRODUCTION

Hazard analysis of unstable rock slopes that may fail catastrophically requires thorough understanding of the mechanisms driving slope movements. The immediate cause of a slope failure – or trigger – must be separated from the long-term mechanisms that weaken rock mass strength and promote failure – so-called preparatory or driving factors (Gunzburger *et al.*, 2005). Typical examples of triggers are strong earthquakes (Mw > 6) or rain storms, while examples of preparatory factors include deep weathering or pore pressure cycling. There are many cases of catastrophic failure where a trigger could not be identified, such as the Randa rock slope collapse of 1991 (Schindler *et al.*, 1993b).

In simplified mechanical terms, preparatory factors are long-term (typically 10^2 to 10^4 years) physical processes leading to stress and strength changes within the rock mass, while triggers are shorter-term (typically 10^{-6} to 10^{-1} years) disturbing forces exceeding mechanical resistance (Gunzburger *et al.*, 2005). Long-term strength degradation of brittle rock masses is typically related to progressive failure, *i.e.* the propagation of new fractures through intact rock bridges and shearing along pre-existing discontinuities (Terzaghi, 1962). A fundamental difficulty lies in experimental observation of progressive failure under in-situ conditions, *i.e.* the monitoring or measurement of strength degradation of real heterogeneous, fractured rock masses in brittle rock slopes, and the assessment of how close a given slope is from failure. This difficulty has major practical consequences, as the factor of safety of a slope at a certain point in time defines the magnitude of a short-term disturbance (trigger) required to bring the slope to failure (Figure 1). For this reason, many unstable

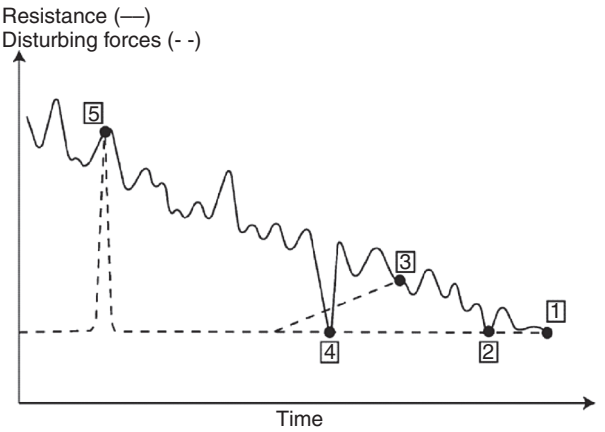


Figure 1 Conceptual model of landslide evolution, based on Gunzburger *et al.* (2005). Point 1 & 2: Failure caused by long-term driving factors without obvious trigger, Point 3: Failure caused by long-term increase in slope stresses (*e.g.* from river erosion and slope steepening), Point 4: Failure caused by heavy rainfall significantly lowering rock mass strength (resistance), Point 5: Failure caused by strong earthquake increasing short-term stress levels (loading).

slopes have failed unexpectedly in the past, and early warning systems have led to false alarms.

The goals of monitoring programs for progressive failure are related to process understanding, stability and hazard analysis of potentially catastrophic rock slope failures. The development of such monitoring programs should primarily be based on time-series analysis, *i.e.* include continuous monitoring of deformations and external forcing factors, because only time series have the potential to unravel clear causal relationships. If such a monitoring program is related to hazard analysis, risk mitigation and early warning, it should be complemented by a comprehensive understanding of the local structural conditions, displacement kinematics, potentially released volumes and post-failure transport characteristics (Loew *et al.*, 2012a, b). These important aspects are not covered in this contribution.

Monitoring progressive failure under in-situ conditions of a large (>100,000 m^3) rock slope instability is a challenging task because the key processes take place below ground surface, *i.e.* they are not directly observable and require drilling and indirect geophysical measurements. The authors of this chapter have successfully conducted such investigations at several sites in the Swiss Alps and this contribution illustrates progressive failure monitoring principles with examples from three study sites at Randa, Preonzo and Moosfluh (Figure 2). At all three sites, the dominant lithologies are quartz-feldspar rich gneisses with subordinate layers of mica-schists and amphibolites, typical lithologies for catastrophic rock slope failures. The gneisses and schists are folded by multiple stages of Alpine ductile deformations and overprinted by ductile-brittle faulting. Systematic steeply dipping joint sets are locally overprinted by younger exfoliation joints. Detailed descriptions of the study sites can be found in Willenberg *et al.* (2008a, b, 2009), Gischig *et al.* (2009a, 2011a), Loew *et al.* (2012b, 2016), Moore *et al.* (2010) and Strozzi *et al.* (2011). The examples shown include

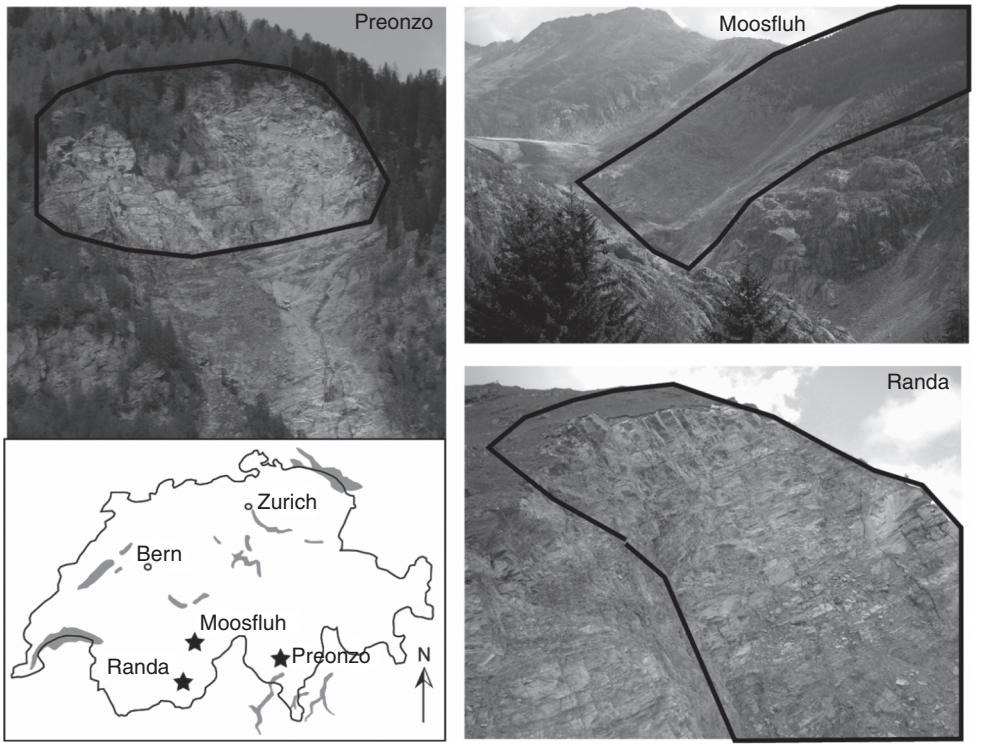


Figure 2 Examples of rock slope instabilities discussed in this paper. Marked are approximate boundaries of recent slope movements. Volumes range from 200'000–400'000 m^3 (Preonzo) to 5–6 million m^3 (Randa) to 100–200 million m^3 (Moosfluh).

retrogressive slope failures of various kinematic modes (stepped planar sliding, compound sliding and toppling). The most recent failures took place in 1991 (10 and 20 million m^3 at Randa) and 2012 (220,000 m^3 at Preonzo).

The goal of this chapter is to discuss selected key methods for studying progressive failure processes in unstable rock slopes. We focus on a selection of modern methods well suited for continuous monitoring of small displacements and deformations at our study sites: Total Station Measurements (Section 2), Fiber Optic Strain Monitoring (Section 3), and Seismic Monitoring (Section 4). We do not discuss in detail but compare with other important technologies for deformation monitoring, which were applied at these sites, such as radar interferometry, electric strain meters, tilt meters, borehole inclinometers and extensometers.

Besides capturing the localization and type of local and absolute deformation, this chapter also discusses how to monitor two key environmental variables that drive progressive failure: surface temperatures (Section 5) and subsurface fluid pressures (Section 6). Again, these are not the only driving factors, seismic waves or chemical weathering may also contribute to progressive failure.

Multidisciplinary monitoring of progressive failure mechanisms requires subsurface data collection, which is mainly based on instrumented boreholes. Such boreholes in

alpine settings and unstable slopes are expensive due to difficult access conditions (mainly by helicopter) and borehole stability. In 2015 typical costs for a 250 m deep cored research borehole with basic instrumentation amount to about 450,000 SFr. (or Euros) excluding transportation costs. Costs for destructive boreholes are about 20-50% lower. For these reasons we tried to combine multiple sensor types in single boreholes which is not a trivial operation. This chapter also illustrates optimal technologies for such borehole completions and how to integrate them with stand-alone power supply and data communication systems in remote areas.

2 TOTAL STATION MONITORING

2.1 Monitoring principles

A standard landslide monitoring technology, used since the beginning of the 20th century is based on optical or electronic tachymeters. A modern tachymeter is an electro-optical theodolite measuring horizontal and vertical angles, integrated with an infrared distance meter. This electronic distance meter sends a microwave or infrared beam to a reflector and measures travel time of the reflected wave, which then can be translated into a distance. From repeat measurements, displacement vectors of prisms (reflectors) mounted on the rock surface can be computed in local or global coordinate systems. Automatic tachymeters with target recognition are called Total Stations or Terrestrial Positioning System (TPS). These systems make it possible to automatically monitor 3D coordinates of moving target points and have become standard equipment for geodetic monitoring of landslides, providing continuous and accurate surface displacement measurements over distances of more than 2 kilometers (Van Cranenbroeck & Brown, 2004). Remotely controlled Total Stations with local power supply and data transmissions are called Robotic Total Stations.

Usually attention is paid to select very stable sites for the Total Stations' location, to ensure that the coordinates computed from the station will remain in a consistent reference frame and to enable the analysis of movements of the monitoring points in this reference frame. If the instrument cannot be located on a stable point, a free-station calculation using measurements to multiple control points can be used to account for movements of the total station (Brown *et al.*, 2008). If in case neither TPS nor control points are stable a combination of Global Navigation Satellite System (GNSS) and TPS measurements is inevitable or only relative movements between points can be determined.

Total station measurements are affected by changes in air temperature, pressure and relative humidity, but these atmospheric effects can be corrected with empirical equations. Shock and stress, beam interruptions and severe heat shimmer (*e.g.* above the glacial surfaces) can also result in deviations of the specified accuracy by the manufacture (Table 1). It is therefore important to check and adjust the instrument before measurement.

Nowadays instrument accuracies of tachymeters (*e.g.* Leica TCP 1201, Leica Nova TM50) are better than 1 mm + 1.5 ppm in distance and less than 1 arc second (0.3 mgon) for angles (Table 1), but over longer distances the main effect on accuracy is caused by atmospheric refraction. Angular measurements are strongly influenced by temperature gradients, distance measurements are affected by temperature and flickering (image

Table 1 Accuracy and range of Leica TCP 1201 and Leica Nova TM50 (with angle measurement accuracy 0.5") Total Stations of the Aletsch Project (Switzerland) in comparison with other Total Stations.

Manufacturer	*type*	*distance measurement accuracy*	*angle measurement accuracy*	*Range/Range with ATR mode*
Leica	TCP 1201	1mm + 1.5ppm	1"	3000m/1000m
Leica	Nova TM50	0.6mm + 1ppm	0.5" or 1"	3500m/3000m
Trimble	S8	1mm+1ppm	0.5" or 1"	5000m/3000m
Trimble	S9	0.8mm+1ppm	0.5" or 1"	5000m/3000m
Topcon	PS	1.5mm+2ppm	1" or 3" or 5"	6000m
Sokkia	Net AXII	0.8mm+1ppm	0.5" or 1"	3500m/1000m

analysis for automatic target recognition). A constant gradient of temperature across the line of sight of only 0.1°C/m could produce a positioning error of 10 mm over 500 m distance (Kharghani, 1987). Chrzanowski and Wilkins (2006) showed for observations in large open pit mines diurnal cyclic variations due to refraction systematic biases of displacements of up to 120 mm over 1 km distances. Positioning the Total Station as high above ground as possible, with no line of sights closely above surfaces, helps minimize the refraction effect. Whitaker *et al.* (2000) concluded for surveys conducted in the early hours (between 3 am and 5 am) the effects of refraction on the determination of displacements could become negligibly small.

Two face, or forward and reverse instrument position measurements, are a pair of observations to the same fixed point made in the two possible instrument positions. With two face measurements some errors associated with the instrument errors can be reduced. The collimation axis error (horizontal axes line of sight error), which is caused when the line of sight is not perpendicular to the tilting axis, can be corrected by taking average of two face measurements in two rounds. Also the vertical axis error (tilting axis error), which occurs when the tilting axis of the total station is not perpendicular to the vertical axis, can be eliminated by tow face measurements. Lastly, the vertical collimation (vertical index) error, which occurs if the 0° to 180° line in the vertical circles does not coincide with the vertical axis, can be compensated by taking two face measurements. Only the compensator index error, caused by not leveling the total station carefully, cannot be eliminated by taking two face measurements. The Total Stations used in the Aletsch project are fitted with a compensator and residual tilts of the instrument are measured and corrections of the horizontal and vertical angles are applied.

Usually the design of a monitoring network composed of Total Stations and reflectors on monitoring targets considers the following basic principles. Monitoring points are placed within the moving area and fixed points are placed in the surrounding stable zone. Extrapolation should be avoided, which means connection points on stable ground surround the monitoring points within the instability. With this technique the influence of atmospheric effects can be minimized. The accuracy of the orientation measurement of a Total Station can be increased with increasing distance from the Total Station of connection points. By raising redundancy at least 3 fixed points in a free stationing should be measured. This increases accuracy as well as reliability. Connection points can be checked for stability if redundancy is high enough.

2.2 Application examples from Moosfluh

The Moosfluh landslide is part of a larger research and monitoring program called the Aletsch project. In this project we have employed two Robotic Total Stations, four permanent GNSS stations, two meteo-stations and more than 60 reflectors. Two observation towers consist each of a Total Station and a GNSS antenna mounted on a structural arm directly above the center of the TPS instrument. A STS (Sensor Technik Simach) meteo-sensor measuring temperature and air pressure covered by a multi-plate radiation shield complements the two towers. The power supply is provided by solar panels (total 2 m^2) and power is stored in car batteries which can approximately run without solar input for more than 72 hours. A local high-speed 4G und WLAN Router with integrated GNSS receiver from AnyRower ™ connects the sensors with our monitoring software installed on a server at ETH Zurich.

The observation pillar carries the Total Station and the GNSS antenna. Since the Total Stations are located in a high alpine environment with no road connection, the pillars had to be lightweight light enough to be transported by helicopter but stable for precise measurements. To account for thermal deformation, unilateral temperature changes from solar radiation or vibrations due to high wind speeds, the system consists of two independently anchored aluminum pillars (Figure 3). The inner pillar carries the measurement equipment like total station and GNSS antenna, the outer pillar protects the inner one from *e.g.* direct sun or violent winds and carries the mechanical protection roof. With a height of 1.45 m the pillar is high enough to protect the instrumentation from being snow covered in winter. The inner pillar has a diameter of 0.21 m, the outer pillar a diameter of 0.30 m and both have a wall thickness of 5 mm. The pillars are connected to the ground by glued threaded bars. Studies by the institute for Geodesy and

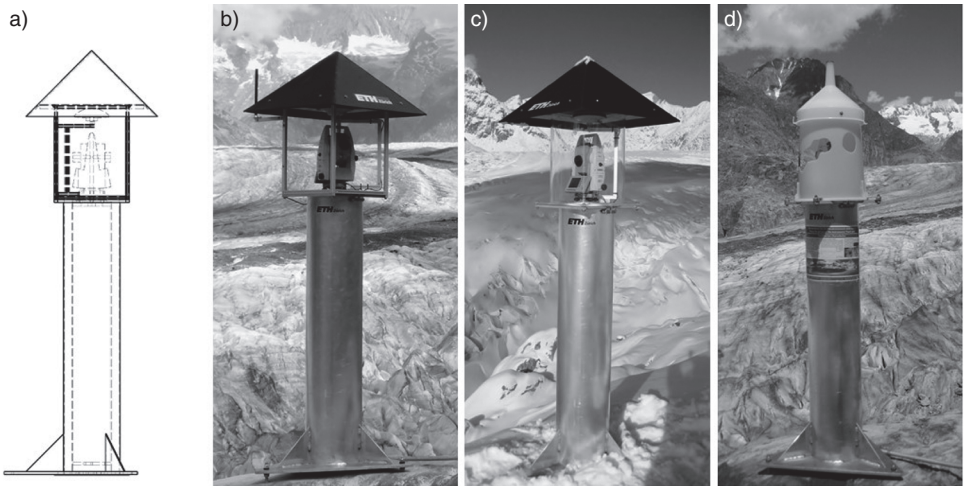


Figure 3 Development of the shelter of TPS1 at Aletsch. a) Drawing showing the outer and inner pillar, which are individually grounded, the protection roof, the construction of the GNSS-antenna and aluminum profiles for inserting the Plexiglas-windows. b) Setup of TPS1 with Plexiglas windows and Polyamid roof. c) Plexiglas cylinder for orthogonal measurements which interfered with ATR. d) Final solution with PE-protection with holes for measuring without any obstruction.

Photogrammetry (Stahlhut & Bonassi, 2014) show that height changes of the inner pillar go up to 0.3 mm, whereas horizontal displacement due to thermo-elastic effects can be negligible (< 0.04 mm).

The Total Stations are housed in a protection shelter. In the beginning, four 6 mm thick Plexiglas windows surrounded the tachymeter at Chatzulecher (TPS1), covered by a protection roof with ventilation openings and made of GNSS-antenna friendly Polyamide (Figure 3a, b). After the removal of the windows for revision purposes, erratic changes in angular measurements of up to 20 mgon (for 600 m distance) appeared and it was obvious that the shelter has an unusually high refraction effect. To avoid this problem a Plexiglas-cylinder was installed giving the opportunity to always measure orthogonal through the curved window no matter which location the appropriate reflectors are mounted (Figure 3c). After some testing it became obvious that the ATR (automatic target recognition) could not operate with the distortion of the picture caused by the curved glass, and measurements were rarely conducted automatically anymore. The Chair of Geosensors and Engineering Geodesy at ETH Zurich built a lab test facility to analyze the influence of several protection systems, showing that the deviation of angles and distances vary immense within a Plexiglas window. Additionally the four roof-holding poles of the first setup cause partial shadowing effects of more than 5 mgon until no more measurements are possible because of the aluminum profile. The distance and zenith measurements are affected by the Plexiglas as expected from the refractive index, whereas angular measurements have a strong influence depending on the thickness variations within the window. Finally, the best solution for the Total Stations was a Polyamid-cylinder with holes at the reflectors' location for completely undisturbed measurements (Figure 3d).

The surveying system of the Aletsch project includes 65 high precision round prisms (Leica GPR) with directional reflection for each total station. The round prisms consist of a triple-prism glass assembly coated with copper reflecting the pulsed infrared beam send from the total station. The prisms require being aligned with the line of sight of the instrument within a deviation of ±10°. To protect the prism itself from environmental influences like snow, dust or rock fall a protection roof is recommendable and was specially designed for this project in high alpine environment and installed above the reflectors (Figure 4). In this project, two Total Stations on opposite sides of the valley



Figure 4 Protection roofs for installed prisms. a) Protection of prisms from birds for installation in cities (photo: Goecke GmbH & Co. KG). b) Monitoring prism from Leica Geosystems with rain shelter for permanent installation (Leica Geosystems). c) Protection of prism for alpine environment at Aletsch with high snowloads and heavy rainfall designed by R. Seifert (ETH Zurich). d) Proof of function of the protection roof during harsh winter conditions e) another roof design with fewer stability properties being bent down by rockfall and/or snowload.

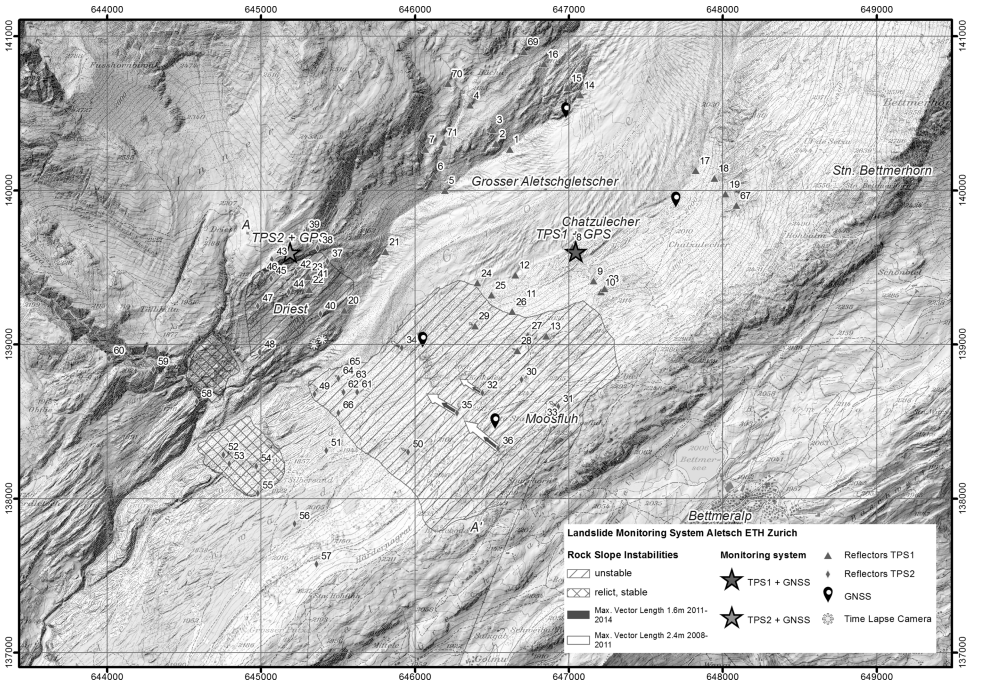


Figure 5 Monitoring network installed at the glacier tongue of the Great Aletsch Glacier (Valais, Switzerland) with two Total Stations, automated GNSS stations, reflectors along 4 profiles, and reflectors within the perimeter of the instabilities Driest and Moosfluh. Swiss coordinate system with kilometer grid.

glacier are surrounded by reflectors with a maximum distance of 2018 m and a minimum distance of 43 m. The network monitors mainly four profiles crossing orthogonally the valley axis, which comprise up to eight reflectors per profile to monitor reversible rock slope deformation within glaciated (Profile 1-3 in Figure 5) and non-glaciated areas (Profile 4 in Figure 5). Further reflectors are installed within two large rock slope instabilities at Driest (compound slide) and Moosfluh (topple, see Figure 5) which show movement rates between centimeters per year (Driest) up to meters per day (Moosfluh).

The monitoring system is managed from a server running Leica GeoMoS. GeoMoS is a system able to analyze data from different types of sensors (Total Station, meteo sensors, GNSS, inclinometer), send messages ("alarms") if user defined limits are exceeded and generate a variety of graphical and numerical representations of measurements and results. GeoMoS Monitor is responsible for sensor maintenance, measurements, storing data, computing results, measurement and result checks and message generation, GeoMos Analyzer is responsible for analyzing the measurements and results (Leica Geosystems, 2010). In this work, GeoMoS Monitor is mainly used to detect whether the sensors are working properly and to manage the measurements. However, in this project almost no results from GeoMoS are directly used: all raw measurements are exported and analyzed with a Visual Basic xls-macro to create specified results for particular questions.

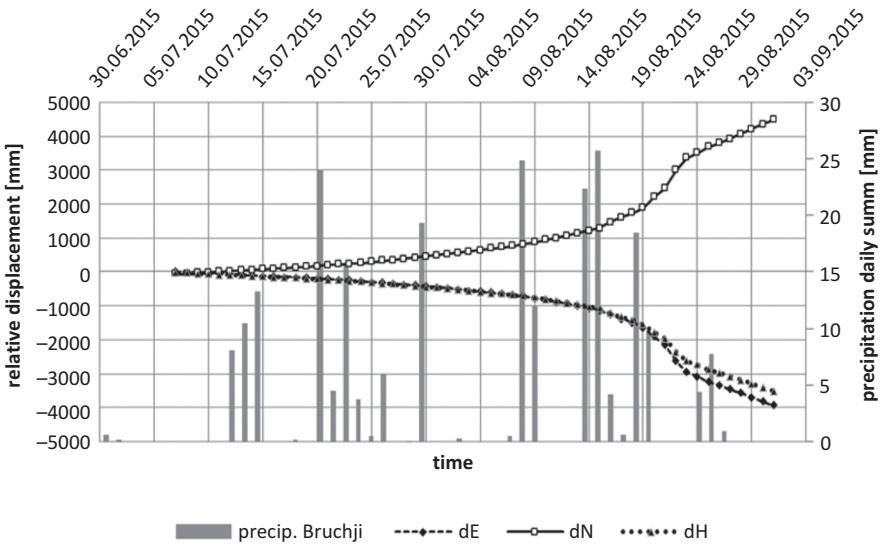


Figure 6 Time series of reflector point 65 within the Moosfluh instability showing displacements downwards (negative dH) and to the northwest for a time period of two months, as derived from nightly mean values of hourly measurements between 10 pm and 5 am.

Example daily mean displacement vector components resulting from the fastest reflector within the Mossfluh instability, as well as precipitation for the same period of time, are presented in Figure 6. This reflector belongs to a very fast moving compartment of 100,000 to 300,000 m^3 volume at the landslide toe, called Silbersand, where currently the glacier tongue is retreating (Figure 7). The Silbersand compartment is moving so rapidly that features of progressive rock slope failure can be directly observed on the ground surface. These features include progressive opening and propagation of a tension crack in the head scarp area and progressive rotation of toppling blocks. This is an unusual situation for brittle rocks, which typically move much slower, even during the stage of accelerating creep. As discussed in the next section, the investigation of progressive failure in such rockslides requires downhole monitoring systems with even higher strain resolution.

3 FIBER OPTIC STRAIN MONITORING

3.1 Monitoring principles

A relatively new class of in-situ strain monitoring sensors, based on fiber optic (FO) technology, offers a dramatic increase in strain resolution and is a promising new technology for advancing the state of the art in landslide monitoring (Moore *et al.*, 2010). General performance advantages over traditional in-situ strain sensors (*e.g.* vibrating wire type) include high resolution, rapid sampling rate, multiplexing potential, and insensitivity to electrical disturbances (such as lightning). To date, however, there are only a few cases where FO strain sensors have been used for monitoring slope deformations in landslide investigations (*e.g.* Brunner *et al.* 2007; Woschitz & Brunner, 2008). Several

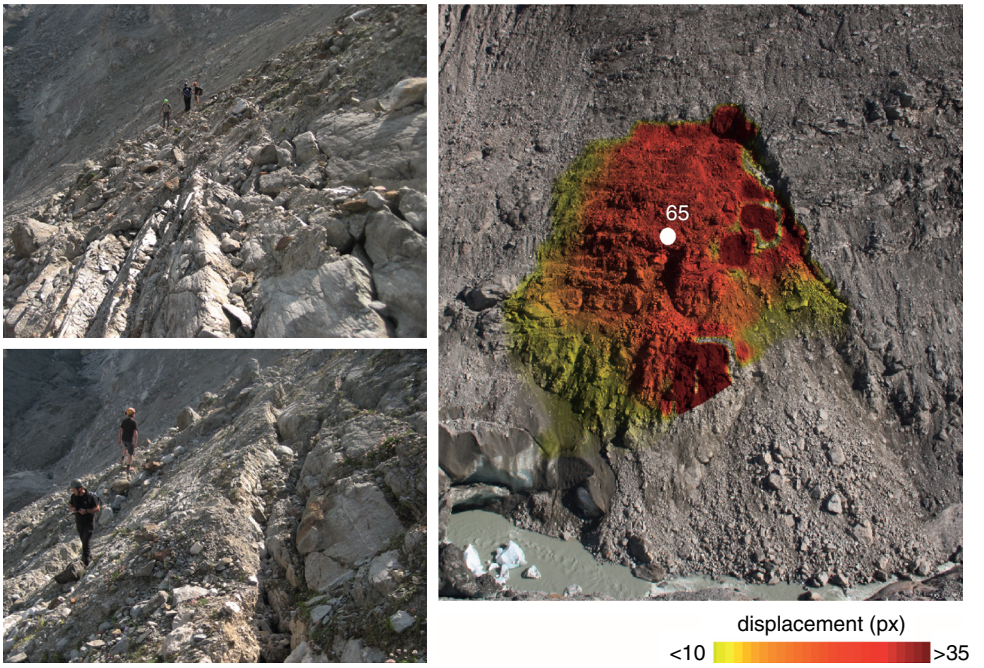


Figure 7 Silbersand compartment of Moosfluh landslide, with active tension cracks at the head scarp and toppling blocks (left) and clearly visible instability boundaries as derived from optical image processing of a standard remote webcam at Driest (right). The color coding represents displacements measured as pixel offsets between August 26th and September 7th, 2015, which can be compared to the measured displacements of reflector No 65 (Fig. 6). Optical image processing provided by Dr. A. Manconi (ETH).

types of FO sensors are available with varying resolution and cost (Schmidt-Hattenberger *et al*., 2003; Inaudi & Casanova, 2000; Inaudi *et al*., 2013). Fiber Bragg grating (FBG) sensors offer optimal balance between performance and costs, and are among the most commonly used in geotechnical and civil monitoring (*e.g*. Moyo *et al*. 2005; Pei *et al*. 2011).

Fiber Bragg gratings are short sections of an optical fiber with inscribed variation in the index of refraction. When illuminated by broadband light, each FBG reflects a particular wavelength while transmitting all others (Ferraro & De Natale, 2002). As the grating strains, the reflected wavelength changes, and is measured by an optical interrogator. Multiple sensors may be placed in series on the same optical fiber, tuned at non-intersecting wavelength bands. Typical strain resolution of FBG systems is <1 με, with sampling rates up to 1 kHz. This offers new possibility to detect small increments of progressive failure or dynamic strains associated with passing seismic waves.

A typical FBG strain monitoring system consists of several elements: (1) optical interrogator, (2) control unit and data logger (sensing processor), (3) sensors and mechanical anchorage, (4) connecting cable, (5) power supply (Figure 8). Installation in remote areas without dedicated power resources makes the latter especially challenging, as most FBG systems capable of fast sampling rates are relatively power hungry.

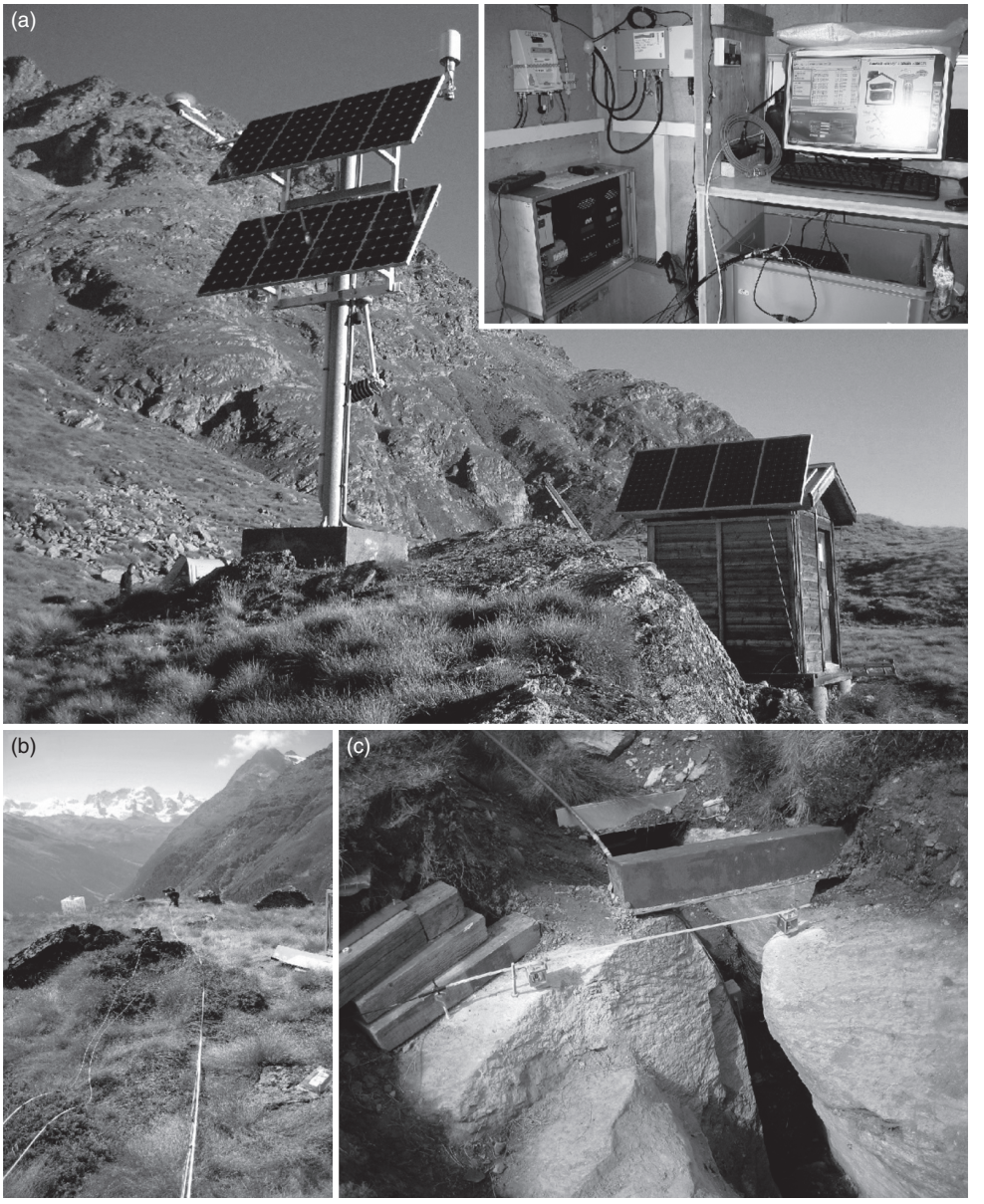


Figure 8 Components of an FBG geotechnical monitoring system installed at the Randa in-situ laboratory, Switzerland: a) solar power array, inset showing optical interrogator and processor, b) laying out borehole FBG strain sensors for installation, c) installed FBG crackmeter next to traditional vibrating wire sensors (under covers).

3.2 Application examples from Randa

Our system installed at the Randa in-situ laboratory was designed for a continuous power draw of 50 W, which required a 1.2 kW solar array and 1350 A-h of battery storage to achieve ~90% continuous operation (up-time). The system only failed during a few prolonged (>5 day) winter storms. Lightning protection and proper grounding were also critical.

At Randa, one key measurement goal was to capture dynamic strains associated with regional earthquakes that are relatively common in the Valais area of the southern Swiss Alps. At the same time, we were interested in continuous measurements at low sampling rates to provide data on steady deformation comparable with other installed borehole and surface sensing systems. Therefore, we selected a dynamic optical interrogator operating at a 100 Hz scan rate, but which could also log continuous data. Our system utilized a Micron Optics SM130 interrogator and a Micron Optics SP130 processing module (computer). The system was packaged with software from Smartec SA that allowed for customizable data logging to record both continuous and triggered-dynamic measurements. We recorded one data point every 5 minutes (the average of all 100 Hz data over this time), while also monitoring a set trigger threshold (defined as a strain amplitude over a set time interval). In the event of a trigger, the system recorded 5 s of pre-trigger and 25 s post-trigger data at 100 Hz (all fully selectable intervals). A radio clock was used to set absolute time of the processing computer, in order to allow comparison with off-site regional seismic data.

Long-baselength FBG sensors are configured with an active zone containing the Bragg grating situated between two anchors. The length of the active zone may vary from several cm to several meters, and controls both the absolute resolution of the sensor and the measurement range over which the sensors behave linearly. Active zones may be joined in series by passive zones, which have lengths from ~1 m to 100 m, as *e.g.* in a borehole sensor string. At Randa, we installed two types of sensors: surface crackmeters and borehole extensometers (Figure 8). Table 2 indicates sensor base-length and corresponding resolution and accuracy parameters, along with the measurement range. Data averaging can greatly improve the measurement resolution, if the noise is assumed to be random. For example, averaging N = 30,000 data points (100 Hz over 5 minutes) can improve the measurement resolution by a factor of $N^{0.5} = 173$. FBG sensors may also record temperature (via an unstressed FBG), which can be used for calculating temperature-compensated strains. However, care must be taken to ensure the region of the sensor containing the temperature sensor does not undergo strain, which would produce false temperature readings.

Mechanically anchoring long-baselength FBG sensors to bedrock at the surface and in a borehole is challenging, since the ultra-precision sensors demand greater levels of

Table 2 Resolution parameters for FO borehole and crack sensors; "+" indicates elongation while "−" designates shortening.

Sensor	*Base length*	*Resolution*	*Accuracy*	*Measurement range*
Borehole	1.5 m	0.7 μm	3 μm	+11 mm / −7.5 mm
Surface	0.8 m	0.4 μm	1.6 μm	+6 mm / −4 mm

anchor stability. At the surface, anchor systems are relatively straightforward, but the short measurement range of some FBG sensors means the baselength may need reset at frequent intervals. We reset the baselength, *i.e.* de-tensioned, FBG crackmeters at Randa approximately once per year, which while not challenging proved laborious and introduced error in long-term continuous measurements. In a borehole, sensor anchoring was more challenging. Long-baselength FBG sensors must be pre-stressed and then anchored. We explored mechanical anchoring options to hold the sensors inside common inclinometer casing, but in the end selected full grouting as the preferred anchoring option. We pre-stressed each of three in-line FBG sensor along three parallel and redundant borehole strings by tensioning each and securing it to a section of thin cable with cable-ties (Figure 8). The method was effective since shortening strain was anticipated. Then each string was inserted into the borehole, and the borehole filled with an expanding grout. The sensors had been previously tested to be submersible in up to 150 m of water.

While grout initially cures quickly, the curing process continues over weeks and months as the concrete slowly loses water to the drier surroundings (Nawy, 2008). The result is long-term volumetric shrinkage termed drying shrinkage. Our borehole sensors at Randa sensed this shrinkage as an accelerated phase of shortening immediately following sensor installation (Figure 9). After installation, our borehole sensors experienced an extended (2–3 month) phase of accelerated shortening that we attribute

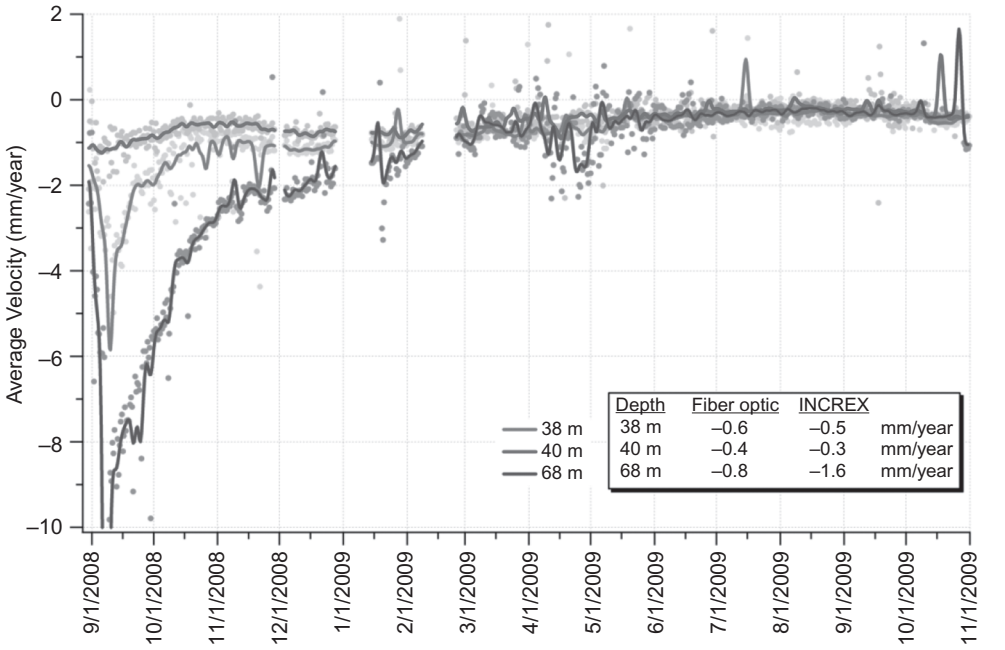


Figure 9 Velocity time series for three borehole FBG strain sensors at Randa. Dots indicate half-day average velocities, solid lines are smoothed. Inset shows comparison of the long-term average velocities with those determined from previous INCREX extensometer surveys. Accelerated shortening is visible in the first 2–3 months. Dates are m/d/y. Figure from Moore *et al.* (2010).

to long-term drying shrinkage. This issue must be accounted for in future similar installations, and is a drawback of full grouting. To resolve the problem, an accelerating agent could be added to the grout mixture, though high temperatures generated during curing may be damaging.

Connecting cable running between the optical sensing unit and various sensors is robust. Each of the two active borehole sensor chains at Randa, plus each of the two crackmeters had a dedicated cable running along the ground surface to the central measurement point about 150 m distant. These armored cables consisted of an optical fiber protected with stainless steel tubing, stainless steel reinforcing fibers, and a polyamide sheath. They have high mechanical and chemical resistance and are well suited for the harsh environments of landslide monitoring.

Following the curing phase, our borehole sensors experienced axial shortening accompanying normal mode offset along steeply-dipping active fractures as anticipated. Measured rates of shortening are consistent with previous extensometer survey data, and show clear annual trends also observed in other borehole monitoring (Gischig *et al.*, 2011a) (Figure 10). A number of transient signals indicate periods of rapid extension that contrast against the otherwise steady shortening. These may result from complex kinematic behavior of the blocks; *i.e.*, intermittent mobilization of nearby discontinuities (see Willenberg *et al.*, 2008a,b). An alternative explanation, however, is such transient deformation events (or 'steps') may result from fracturing of the intact grout surrounding the sensors, and thus represent only local perturbations rather than large-scale rockslide deformation mechanisms.

With resolution two orders of magnitude better than the traditional VW instruments, the new FO crackmeters allowed us to observe previously unidentified signals in the crack aperture data. Crack opening showed a complex long-term trend that is the combination of both near-surface thermal effects and rockslide deformation (Figure 10). A brief period of accelerated crack opening in the spring was investigated in detail and found to consist of a daily pattern where movements are greatest at night and slower during the day (Figure 11). We explain this displacement pattern through the effect of snowmelt seeping into the soil that fills the crack space, which then freezes during the night and generates localized expansive pressure on the crack walls. The trend only occurs during times of rapid snow-melt, which is confirmed by borehole piezometer data. The observed crack displacements are irreversible, in that the ice-induced opening is not recovered during successive melting periods.

In May 2010, an earthquake of M_W 3.2 occurred about 5 km north of Randa at a focal depth of ~5 km (Moore *et al.*, 2011a). Data from the two surface crackmeters (Cracks Z9 and Z10; about 20 m apart) are shown in Figure 12. Peak amplitude of induced fracture displacements reached ~50 μm, while no significant permanent offset was recorded. Transient displacements are clearly resolved by the FBG measurement system. Spectra from these crack measurements show distinct peaks at ~3 and 5 Hz (Figure 12). Narrow band-pass filtering of displacement signals revealed that the 3 Hz components for both tension fractures are in-phase, while 5 Hz signals are out-of-phase. We interpret the latter as representing resonance of a block vibrating between the two sensors, while the former spectral peak at 3 Hz likely represents resonance of the larger unstable rock mass (Burjanek *et al.*, 2012; Fah *et al.*, 2012). Borehole sensors did not detect observable transient displacements during the earthquake.

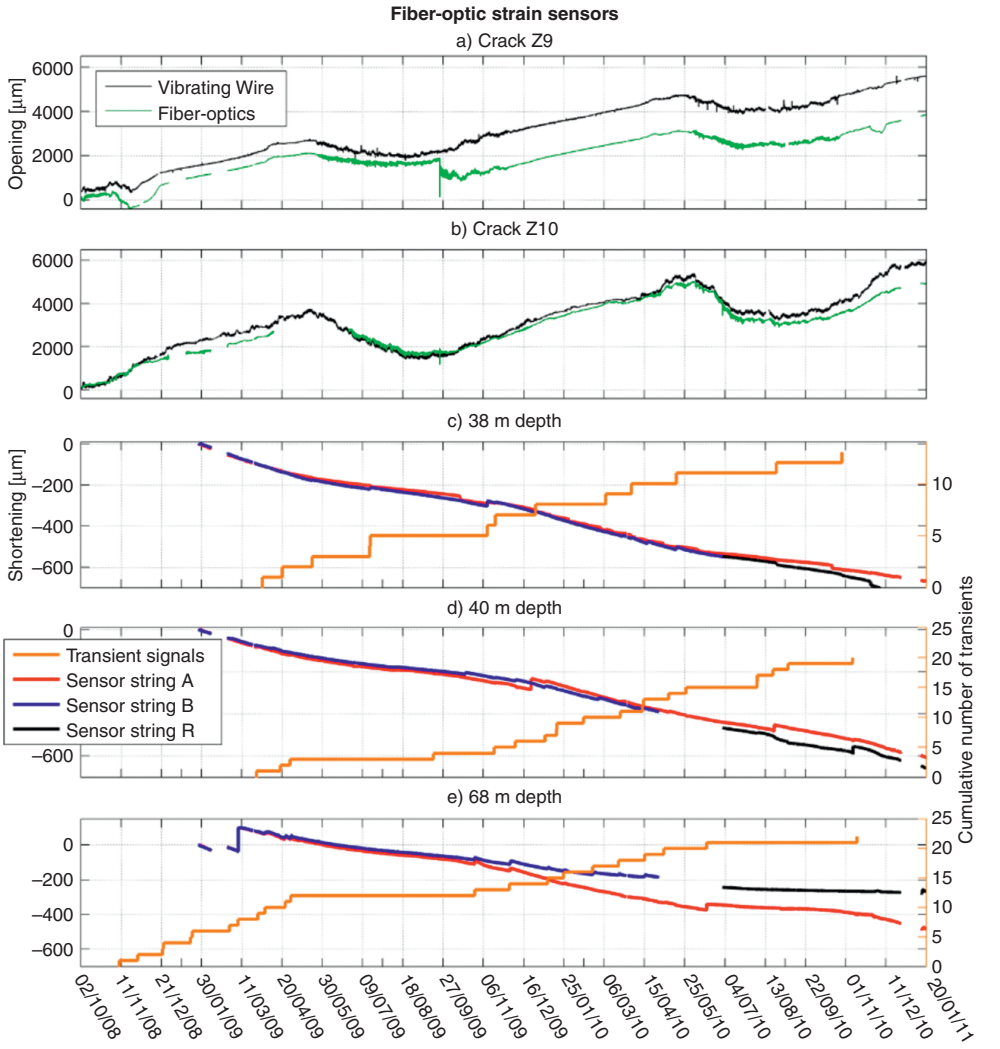


Figure 10 Fiber optic strain data from surface cracks and three different borehole depths. a) Crack Z9, also showing data from the vibrating-wire sensor for comparison. b) Same for crack Z10. c) Borehole data from 38 m depth showing vertical shortening across discontinuities. Also included are cumulative counts of transient events, which are typically characterized by short-term elongation, followed by increased rates of shortening. d) Same as above for 40 m, and e) 68 m depth. Figure from Gischig (2011).

We also performed dynamic tests on our FBG crackmeters at Randa to explore the sensor response (Moore *et al.*, 2010). These tests compared the dynamic crack aperture response to an independent measured of ground motion (using geophones) as generated from a ground-coupled shotgun blast. Results revealed that low-frequency signals are represented well by the FO sensor, but that the fiber optic record suffers from aliasing of higher frequency energy (greater than 50 Hz). This outcome is not expected

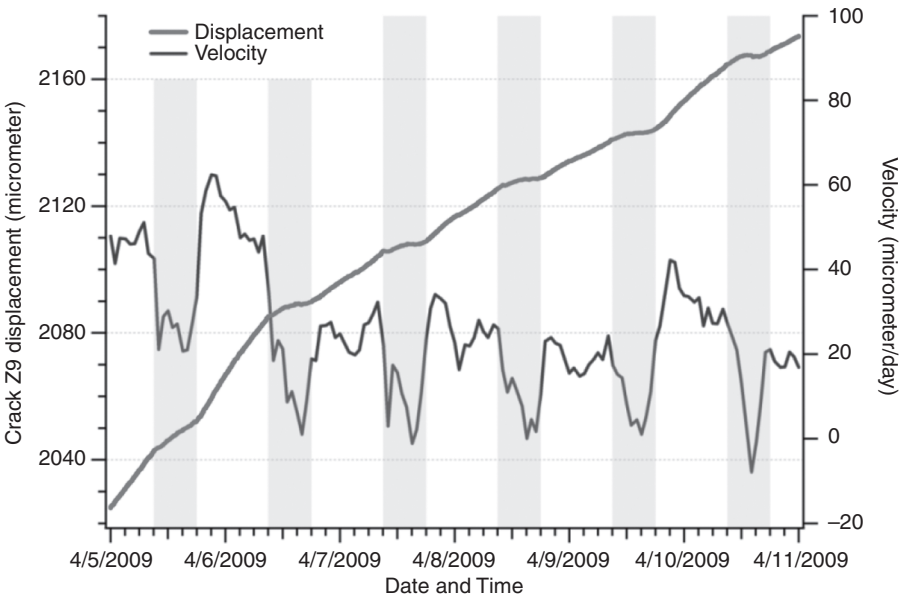


Figure 11 Detail of accelerated crack opening during April, 2009. Daytime hours from 09:00 to 18:00 are shaded. Deformation data show a step pattern with a daily period, marked by accelerated opening at night and a slower rate of opening during the day, which likely reflects freezing and thawing of soil pore water. Dates are m/d/y. Figure from Moore *et al.* (2010).

to adversely affect measurements of co-seismic deformation, as typical earthquake ground motions are not rich in energy at high frequencies.

3.3 Advantages and disadvantages

The main performance advantage of FBG strain monitoring systems is the improvement in resolution and accuracy. Our system at Randa had resolution about two orders of magnitude better than that of the high-quality traditional sensors (Table 1), which improved further with data averaging. We easily detect sub-micrometer deformations in the long-term record, which allows us, for example, to resolve daily strain patterns or small transients associated with different deformation processes. The possibility of triggered 100 Hz sampling offered the advantage of being able to capture dynamic deformations associated with passing seismic waves, which enabled us to investigate the seismic performance of the unstable rock mass. Fiber optic systems have the general advantage of being insensitive to electrical disturbances such as lightning, which can be a significant source of difficulties for field applications. Furthermore, the optical cabling is robust and suitable for use in harsh landslide environments. Finally, the FBG system offers the possibility to place many sensors on only a few cables, which makes for easier and more secure installations.

The main disadvantage of FBG systems is cost. These systems are typically several times more expensive than their traditional in-situ monitoring counterparts. Another

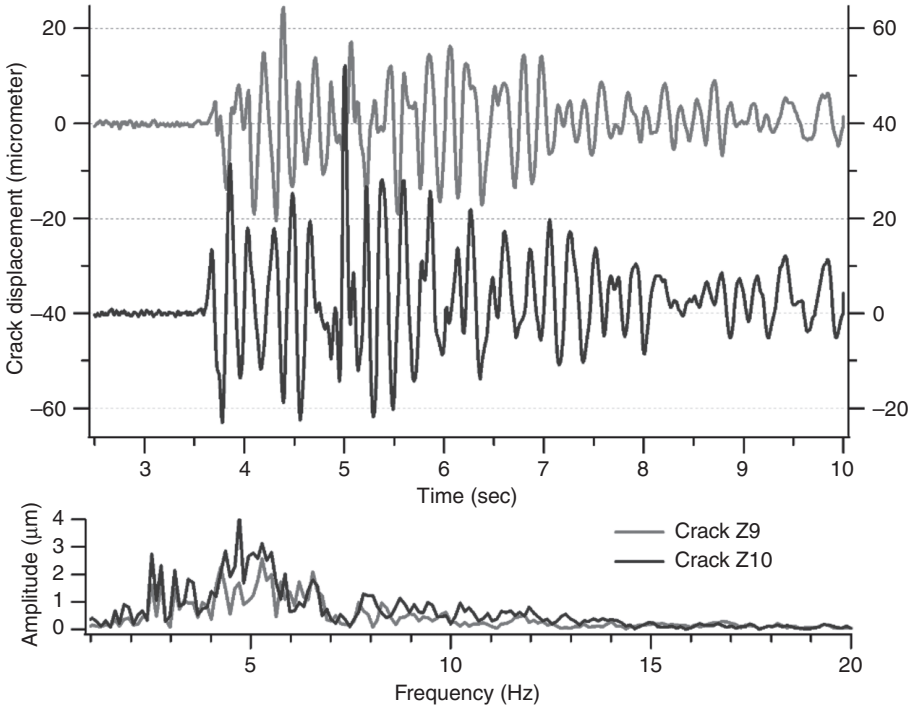


Figure 12 Triggered measurement of crack displacements at Randa resulting from a nearby M_w = 3.2 earthquake in May 2010 (top), with corresponding spectra (bottom). Figure from Fah *et al.* (2012).

draw-back is the relatively large power consumption, which in our case required construction of a large solar array. Installation of the FO sensors also raised new challenges. At Randa, because we installed the borehole sensors into an existing inclinometer casing, we wanted to use an expanding grout to ensure secure contact at this interface. However, this prompted concerns that high swelling pressures could damage the sensors, and led us to carefully consider the choice and quantity of expanding agent. Finally, it is important to note that the FO sensors have a limited range (Table 1), and after straining beyond this point they become inaccurate, inoperable, and can even break. This is a problem primarily for long-term monitoring applications, and can be alleviated by installing the sensors so that the base length can be readjusted, or by choosing a longer sensor base length.

4 SEISMIC MONITORING

Fracture growth accompanying progressive failure of unstable slopes is likely to radiate seismic energy. Local seismic sensor networks may be able to observe fracturing by detecting micro-seismic events. Sensors, digitizers, storage and data communication have developed toward smaller size, higher speed and improved stability in the last

decades. Thus, monitoring of the seismic wave fields in unstable rock masses in rugged and harsh environments has become feasible, as the many case studies that recently have appeared in literature demonstrate (Spillmann *et al.*, 2007a; Levy *et al.*, 2010; Levy *et al.*, 2011; Helmstetter & Garambois, 2010; Lacroix & Helmstetter, 2011; Gomberg *et al.*, 2011; Burjanek *et al.*, 2010; Burjanek *et al.*, 2012). There is a vast range of methods to analyze such seismic records, most of which can be assigned to one of the following three applications: event counting, locating micro-seismic events, and ambient noise analysis.

4.1 Event counting

Counting and classifying seismic signals are the simplest methods in terms of number of required instruments and complexity of the analysis. Event counts can be obtained by counting the number of times a defined threshold value is exceeded. This can be based either on the instrument output (voltage or ground motion in m/s or m/s^2 depending on sensor type), or a derived quantity such as the short term average to long term average ratio (STA/LTA) that is more selective in terms of signal length and frequency content. Due to its simplicity the method has been applied already decades ago. For instance, after the first of two large catastrophic failures above the village Randa within three weeks in 1991 (total volume of 30 Mm^3), a monitoring system counting seismic events was able to warn remediation workers of an intermediate size failure (about 100,000 m^3; Schindler *et al.*, 1993a). However, not only counting local seismic activity as a proxy for increased rock mass deformation can be used for monitoring and early warning purposes. Seismic monitoring has also been used to detect rock fall activity to assess and reduce the rock fall hazard below slopes where infrastructure or people may be at risk (Zimmer & Sitar, 2015). Similarly, seismic instruments are also used to detect debris flow activity as part of early warning systems (*e.g.* Coviello *et al.*, 2015).

A major challenge of this kind of monitoring is distinguishing between different kinds of seismic events. Events triggering the predefined threshold may not only be related to fracturing processes. They can have various sources such local noise (*e.g.* people or animals walking by; environmental impact on the sensors such as rain drops), nearby traffic (cars, helicopters), regional or teleseismic events, rock fall, avalanches, glacier serac falls, or electronic noise impacting the system electronics. It is recommendable to deploy several stations at different locations to compare signals and to help distinguishing coincidences from events that are only local to an instrument. Further information on the possible source of seismic events can be obtained from spectrograms that show the frequency spectrum as a function of time across the signal (*e.g.* Levy *et al.*, 2011; Helmstetter & Garambois, 2010). In particular, traffic noise can be clearly identified from rock fall events. Also local seismic events can be distinguished from a distant earthquake by their much higher frequency content. Nevertheless, automatic detection of local seismic events associated with fracturing is challenging to date, as good quality event counts still rely on involved post-processing.

An example of event counting using two seismometers at the current Preonzo instability is shown in Figure 13. Events were detected using a STA/LTA triggering routine and the constraint that they had to be coincident on both instruments. Detected events were then carefully re-examined visually to distinguish potential micro-seismic events from other noise sources. Note that periods with high micro-seismic activity coincide with

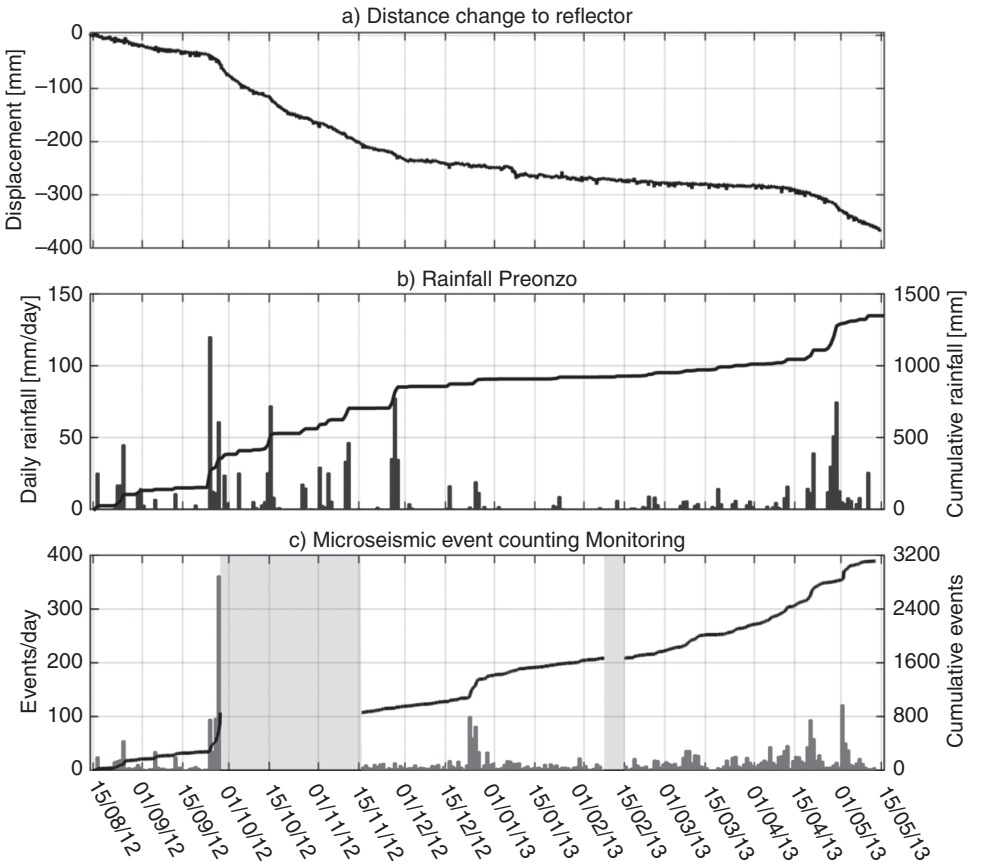


Figure 13 Daily and cumulative reflector displacement, rainfall and seismic event counts at Preonzo after the failure of May 2012.

strong rainfall events and increased rock mass deformation detected from total station measurements. The case also illustrates that it is challenging to keep seismic monitoring stations operational over extended time periods. In the case of Preonzo, lighting strikes caused major data gaps, as well as high material and maintenance costs.

4.2 Micro-earthquake location and source characterization

Micro-earthquake location and source characterization requires a seismic network with a minimum number of seismic stations and sufficient spatial coverage. Although theoretically five stations are enough to determine a location, 10–20 stations are typically installed close to the presumed source volume to ensure optimal location accuracy. One of the earliest attempt of such an application was done at the Randa instability (*i.e.* on the rock mass that remained unstable after the 1991 catastrophic failures) by Spillmann *et al.* (2007a). Nine three-component geophones (8 Hz) were installed in boreholes at depths of 0.3–4.6 m, and three three-component geophones (28 Hz) at the

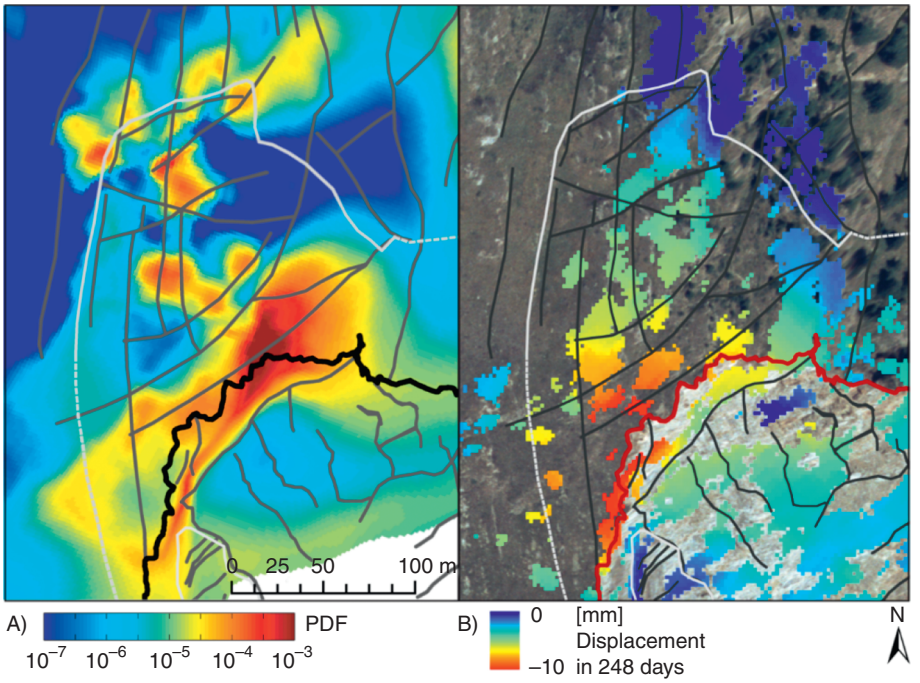


Figure 14 (A) Micro-seismic activity map. The locations of 223 microseismic events recorded between 2002 and 2004 are represented as cumulative probabilistic density functions (PDF). High PDF values correspond to high micro-seismic activity. The values are representative for a surface at 15m vertically below the topographic surface. (B) Unwrapped GB-DInSAR images as in Figure 2.8. Both images include the boundary of the instability as derived from GB-DInSAR as well as the discontinuity map from Willenberg *et al.* (2008b), data from Spillmann *et al.*, (2007b) and Gischig *et al.* (2009).

bottom of two 50 m boreholes and one 120 m deep borehole. The lateral aperture of the network was about ~250 m. Over the course of 31 months about 223 seismic events that could be identified as local micro-seismic events were located. Spillmann *et al.* (2007b) used a probabilistic location algorithm that considers uncertainties in determining signal onset time. The result is a 3D distribution of a probability density function (pdf) describing the probability that a micro-seismic event has occurred at a given location (Figure 14). A comparison with a displacement map derived from radar measurements (GB-InSAR; Gischig *et al.*, 2009) revealed that the rock mass just behind the scarp of the 1991 failures moved fastest and also hosts the most micro-seismic activity. Patches of increased seismic activity behind this zone may be associated with slip along deep pre-existing faults. A temporal relationship between the occurrence of the increased micro-seismic activity and rainfall or snowmelt was not found. A major challenge in locating seismicity in unstable rock masses is – similar to simple event counting – distinguishing between local micro-seismic events and signals from other origins. For the Randa case, it was also suggested that strong attenuation in the fractured rock mass probably concealed many seismic events and made location of detected ones difficult.

Despite these challenges, location and event characterization has been successfully been performed in many cases. Lacroix & Helmstetter (2011) used the beam-forming method relying on cross-correlation of signals from different stations to estimate event locations produced by rock fall and micro-seismic activity on the Sechilienne rock-slides. They were able to assign magnitudes between –1.1 and 0.1 to the recorded micro-seismic events, and concluded that most of the rock mass deformation is aseismic and only a small fraction is accompanied by seismic activity. A similar approach was taken by Gomberg *et al.* (2011). Micro-seismic monitoring on the Slumgullion land-slide – a large soil slide – revealed that slip along the sliding surface is aseismic, while little seismic activity occurs at the side boundaries of the moving mass.

4.3 Ambient noise monitoring

Ambient noise monitoring differs from the aforementioned methods that rely on seismic signal detection, because it focuses on the noise characteristics between signals. For this application, the wave field ideally is not recorded in a triggered but in continuous mode. It relies on the assumption that seismic noise mostly contains wave field components generated at large distances from the site, *e.g.* by oceanic wave-shore interaction, meteorological forcing, anthropogenic noise. These waves travel as plane waves vertically toward the ground surface if originating from large distances, and should produce similar noise characteristics at neighboring seismic stations unless the local rock mass conditions are the same. Hence, differences in these ambient noise characteristics may indicate local disturbances to the rock mass.

Burjanek *et al.* (2010) deployed an array of seismic stations on the Randa instability for a short time period of about an hour. Analysis of ambient noise recordings showed that within the instability waves at distinct frequencies of 3 and 5 Hz were amplified by up to a factor 10. Additionally, the waves at these frequencies were polarized into the direction perpendicular to nearby open tension fractures. Similar observations were made at the Walkerschmatt instability (Burjanek *et al.*, 2012) few kilometres north of Randa; here amplification of up to 7 was found at frequencies of 1.6 Hz. It was suggested that such spatially heterogeneous wave amplification and polarization results from eigenmode vibration of blocks separated by deep tension fractures. Moore *et al.* (2011a) were able to confirm this interpretation by numerical modeling. Gischig *et al.* (2015) and Moore *et al.* (2011a) further suggested that amplification characteristics may be a qualitative indicator for the degree of damage within the unstable rock mass. Time-dependent analysis of ambient noise characteristics was done by Levy *et al.* (2010). They found that resonance frequencies derived from noise recordings dropped if temperature decreases, and – more importantly – shortly before failure of an unstable rock column. Mainsant *et al.* (2012) applied cross-correlation analysis of noise to derive seismic velocity changes and found that decreasing seismic velocity of the instability correlates with increasing groundwater table in the unstable material.

Currently, seismic monitoring of unstable slopes is still an emerging field and applications as well as data analysis are not standard for landslides problems. Harsh conditions and often limited accessibility is typical for many monitoring sites. Hence, power supply, lightning protection and real-time communication of vast data streams can be challenging, which explains abundant data gaps. Nevertheless, results presented in literature show that seismic monitoring along with the diversity of analysis methods

is promising to advance process understanding of progressive slope failures and will strongly contribute to future early warning systems.

5 TEMPERATURE MONITORING

5.1 Monitoring principles

Along with other environmental parameters (rainfall, snow height, pressure, wind speed, relative humidity, etc.), temperature is an important observable to help uncover possible forcing mechanisms driving progressive failure. However, air temperature alone only contains minimal information on in-situ temperature conditions (*e.g.* mean annual temperature, seasonal temperature fluctuation, periods of freezing conditions). For understanding the connection between meteorological conditions and landslide deformation, complementary temperature observations on ground surface and within rock or soil are essential. A combined analysis of various temperature records and other observables allows analyzing – directly or indirectly - a multitude of processes including: thermo-elastic effects (Gischig *et al.*, 2011c; Hasler *et al.*, 2012), freeze-thaw effects (Hasler *et al.*, 2012, Matsuoka, 2001), abundance of permafrost and permafrost melting (Phillips *et al.*, 2009), air ventilation effects (Delaloye & Lambiel, 2005; Moore *et al.*, 2011b), onset of snowmelt period (Matsuoka, 2001).

5.2 Application examples from Randa

Generally, many monitoring instruments that are not dedicated to measure temperature (such as vibrating wire extensometers, inclinometers, piezosensors, or fiber-optic strain gauges) feature a temperature sensor for correction of temperature effects on the sensing device. At the Randa instability, these temperature sensors provided relevant information to understand temporal deformation patterns before 2008. It was found that deformation rates correlate with temperature rather than with heavy rainfall or snowmelt as is the case for most instabilities (Willenberg *et al.*, 2008a; Gischig *et al.*, 2011b,c). Hence, temperature monitoring was intensified after 2008, and temperature sensors measuring air, ground, soil or rock temperature were installed.

The main purpose of temperature monitoring at the Randa instability was correlating the seasonal changes in deformation rates observed across fractures at the surface and at depths to possible external forcing. As shown in Figure 17, times of increased deformation rates correlate with time of low temperature. Deformation rates decrease in spring after the onset of snowmelt, although water pressure within the rock mass is expected to be highest during this time. Based on these observations, it was demonstrated by means of numerical models that thermo-elastic effects control deformation at Randa (Figure 15; Gischig *et al.*, 2011b,c).

Temperature monitoring at Randa, however, yielded information beyond correlation between temperature and deformation rates, as illustrated in the following examples.

In-situ estimates of thermal properties could be derived from time series analysis of temperature profiles recorded in rock and in soil. Assuming temperature conduction as the only heat transfer mechanism, 1D temperature profiles can be described using the 1D-heat transfer equation:

$$\frac{\partial T}{\partial t} = \alpha \frac{\partial^2 T}{\partial z^2} \tag{1}$$

with z being depth and α [m^2/s] the thermal diffusivity (Gueguen & Palciauskas, 1994). The spatial and temporal response to a harmonic temperature disturbance at depth z_0 can be analytically solved using Equation 1:

$$T(z,t) = T_o(z_o) \cdot e^{-k(z-z_o)} \cdot \sin\left(\frac{2\pi}{\tau} - k(z-z_o)\right) \tag{2}$$

Where T_o is the amplitude of the temperature wave at z_0, and τ the period of the harmonic wave. The constant k is a function of the period τ and the thermal diffusivity α:

$$k = \sqrt{\frac{\pi}{\alpha\tau}} \tag{3}$$

To obtain a simple thermal diffusivity estimate from temperature profiles, we can fit a sinusoidal temperature history with a one year period to the measured time series as a first-order approach. In particular we can derive the mean annual temperature, the amplitude of the annual signal, as well as the phase lag at different depth with respect to the surface temperature evolution. Such an analysis was performed for the temperature profiles in rock and soil shown in Figure 16 (Gischig, 2011). Equation 4 predicts that the amplitude $T_o(z)$ at depth z is predicted from the temperature amplitude $T_o(z_0)$ at the surface as:

$$T_o(z) = T_o \cdot e^{-kz} \tag{4}$$

Fitting such a curve to the amplitudes estimated at different depths (Figure 17), an average thermal diffusivity along the profiles in rock and soil can be obtained; thermal diffusivity for rock is 2.16 E^{-6} m^2/s, for soil, one order of magnitude smaller, *i.e.* 2.8E^{-7} m^2/s.

Onset and end of snowmelt period: For the interpretation of monitoring data, but also for early warning purposes, it is important to observe when snowmelt starts and ends. In case that automatic snow height sensors, webcams or time-lapse photography are unavailable, ground and air temperature can give useful information. An example is shown in Figure 18a, which shows one year of temperature data recorded at two crack extensometers (labelled Z10 and Z9) on the Randa instability. In winter, temperature at crack Z9 stays close to about 0°C. Temperatures of about 0°C below a snowpack is characteristic for snow heights of several decameters in a non-permafrost region; this time window of near-constant 0°C is generally referred to as the zero-curtain (*e.g.* Matsuoka, 2001). Temperatures at crack Z10 drop lower and show more variability implying that snow thickness is smaller than for Z10. At the site, it was observed that the sensor was usually covered with 0.1–0.2 m of snow in the year (Figure 18), and less in other years. Once temperature variations start again in spring and begin following air temperature, it can be assumed that the sensors have become snow free. Hence, in absence of any other observations of the onset and end of the snowmelt period, temperature monitoring can be used as a proxy. The tension cracks become snow free with a time difference of more than a month. Crack Z9 lies in a depression, where

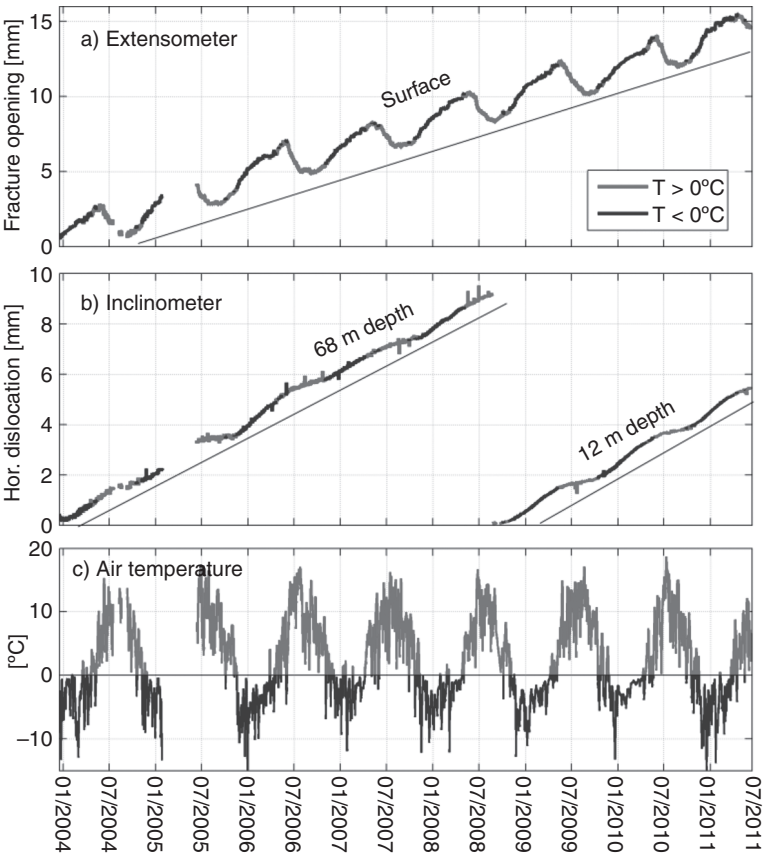


Figure 15 Fracture dislocations at ground surface a) and at 12 m and 68 m depth b) in borehole SB120 at Randa, and a function of surface temperature c). Dark gray are periods when surface temperatures drop below 0 degrees, light gray are periods when surface temperatures are above 0 degrees.

snow usually persists the longest, and thus can be used to determine the end of the snowmelt period.

Convective heat transport in the rock mass was detected and characterized at the Randa instability using temperature sensors that were hung into a wide open and deep-reaching tension crack (Figure 18b). It was observed that holes in the snowpack appeared above some of the open tension cracks in winter (Moore *et al.*, 2011b). Warm air (about 4°C) relative to the air temperature rises up from the cracks and is able melt though the more than a meter thick snowpack. As shown from the temperature records in Figure 18b, air ventilation starts as soon as air temperature drops below ~4°C, crack temperature at all depths become nearly constant indicating that air from depths is carried to the ground surface. When air temperature is higher than ~4°C, crack temperature mimics air temperature cycles, however, with an amplitude more strongly damped at greater depths. These observations show that there is a transition from conductive to convective heat transport through the crack as temperature drops below the average rock mass

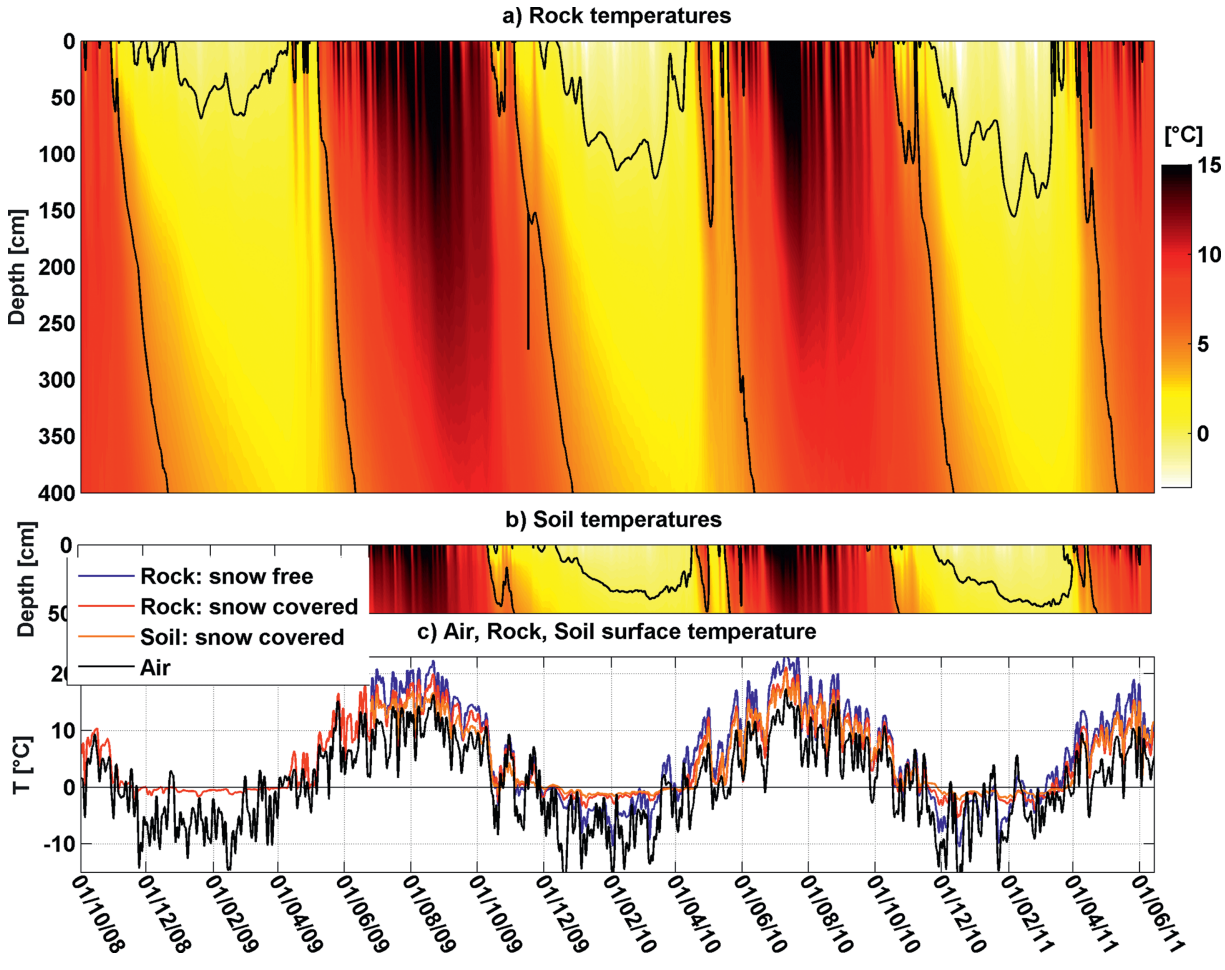


Figure 16 a) Rock and b) and soil temperature profiles as a function of depth and time; data are filtered witha 3-days low-pass filter. c) Temperatures of air, soil surface, rock surface and the steep rock face, also filtered with a 3-day low-pass filter. These data are used to derive thermal transport properties (Gischig, 2011).

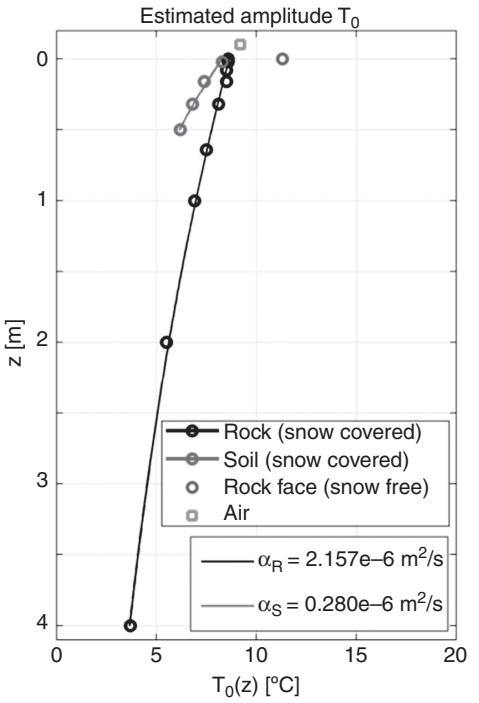


Figure 17 Amplitude $T_0(z)$ by fitting sinusoidal temperature wave into the temperature time series at different depths z (Gischig, 2011).

temperature. Such convective heat transport explains deviations from purely conductive temperature profiles identified in a borehole at the Randa instability (Moore *et al.*, 2011b).

6 FLUID PRESSURE MONITORING AND BOREHOLE COMPLETION

6.1 Monitoring principles

Precipitation or snow melt can accelerate rockslide displacements or trigger slope failure through groundwater pressure and hydro-mechanical coupling. In contrast to slopes in soils and weak rocks, only few investigations exist that focus on detailed analysis of pore pressure measurements in brittle rock slopes. Based on the catastrophic experience at Vajont in 1963, most of these borehole-based investigations have been carried out in rockslides adjacent to hydropower lakes such as the Downie Slide (Imrie *et al.*, 1991), Dutchman's Ridge Slide (Moore & Imrie, 1995), and Little Chief Slide (Watson *et al.*, 2007) located near hydropower reservoirs of the Columbia River in Canada. In addition, detailed hydrogeological investigations have been carried out in hazardous rock slopes along populated fjords (Aknes Slide in western Norway; *e.g.* Groneng *et al.*, 2011), in large creeping rockslides damaging villages (Bonzanigo *et al.*, 2007) or along hydropower drifts and penstocks (Rosone Slide in Orco Valley, Italy; *e.g.* Pisani *et al.*, 2010).

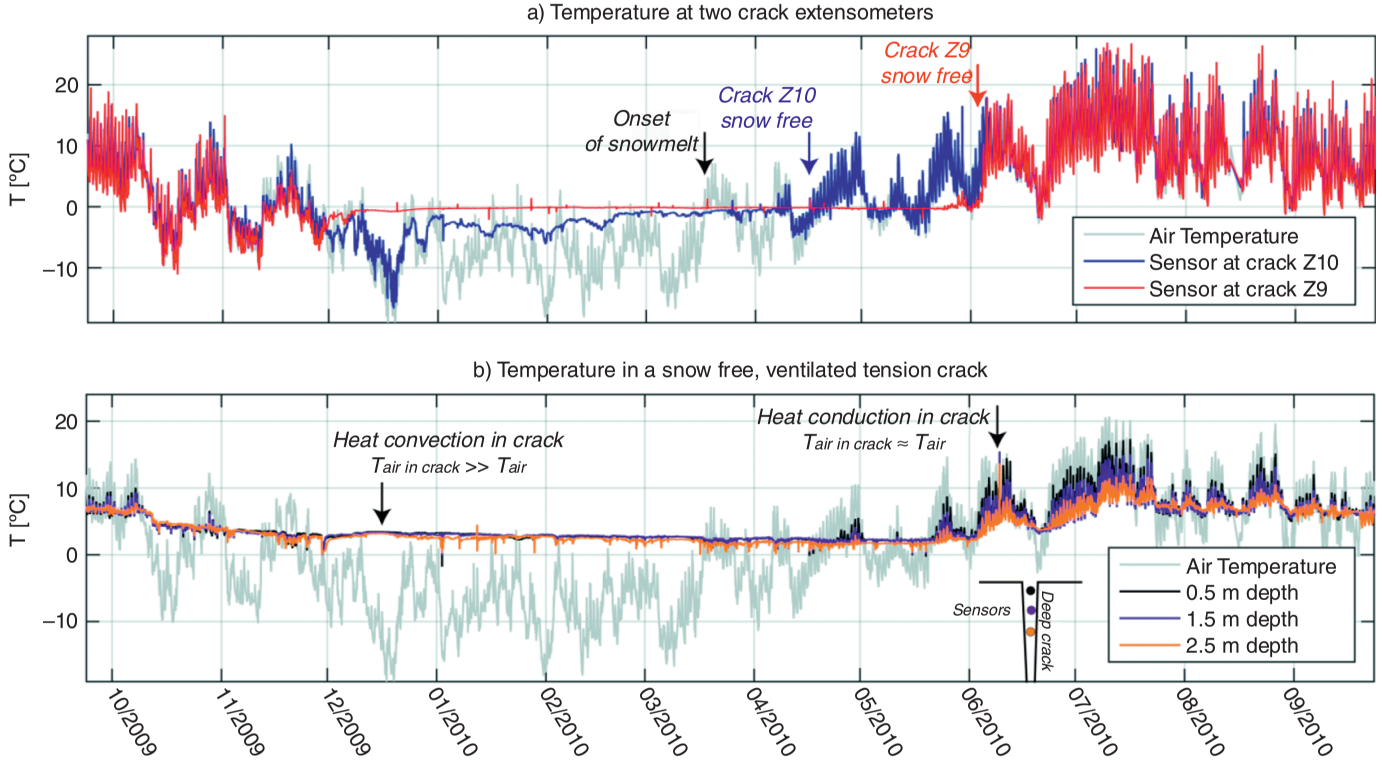


Figure 18 Onset of snow cover and snow melt, and air ventilation in open cracks, as derived from one year of temperature data recorded at two crack extensometers (labeled Z10 and Z9) at the Randa instability (Gischig, 2011).

Accurate and meaningful pore or fluid pressure monitoring in such slopes requires hydraulic isolation of monitoring intervals of limited length (1–10 m), because most rock slopes show fluid pressure compartmentalization, multiple piezometric levels, and strong vertical gradients in hydraulic head (*e.g.* Bonzanigo *et al.*, 2007; Watson *et al.*, 2006; Moore & Imrie, 1995). These gradients lead to strong ambient flow in open boreholes (Thöny *et al.*, 2008), and piezometric levels measured in long open boreholes rarely reflect true spatial variations in pore pressure and hydraulic head. Hydraulic isolation of monitoring intervals is traditionally achieved with retrievable and inflatable multi-packer systems (*e.g.* Westbay, RST Instruments, Solexperts AG), fully grouted vibrating wire pore pressure transducers or multiple piezometer pipes with permanently grouted sections or bentonite-seals. The location of monitoring intervals should be based on the identification of conductive fractures or brittle shear zones with flow logging, core analysis or optical televiewer images. Many active sliding planes correspond to fluid pressure boundaries, often separating a confined aquifer from perched groundwater above the sliding plane: monitoring intervals should not create shortcuts through such pressure boundaries.

Continuous monitoring of pressure fluctuations is typically based on piezoresistive or capacitive pressure transducers with vibrating wires or strain gauges. Time lag for these systems is negligible and sensitivity is excellent –traditional vibrating wire piezometers commonly have accuracies of up to 0.1 % of the sensor pressure range (Geokon Incorporated, 2007; Keller AG). High end instruments based on a precision quartz crystal resonator, whose frequency of oscillation varies with pressure-induced stress, are mainly used in research and have accuracies as high as 0.01 % of the selected pressure range (Paroscientific Inc.). Pore pressure transmitters are either installed down hole in submersible waterproof housings or - in case of artesian pressure conditions - at ground surface connected to standpipes or pressure lines. Corrections for atmospheric pressure variations with a second pressure transducer, or differential pressure measurements are essential.

In most landslide projects and especially for the analysis of progressive failure, both downhole fluid pressure and deformation data are required. Some projects have tried to collect such data sets by combining dedicated fluid pressure monitoring boreholes with deformation monitoring boreholes (*e.g.* Imrie *et al.*, 1991). However, this concept can only lead to reliable results, if the deformation monitoring boreholes are fully grouted to prevent ambient borehole flow and fluid pressure disturbances, or located far away from the fluid pressure monitoring boreholes. An alternative and cheaper solution consists of combining fluid pressure and deformation monitoring systems within the same borehole. This poses technical challenges when considering the required hydraulic isolation, but feasible solutions have been established. One type of technical solution is based on grouted Vibrating Wire pore pressure sensors attached to an inclinometer tube or tremie pipe, or flow lines with filter caps between grouted sections of an inclinometer tube using geotextiles (Figure 19).

6.2 Application examples from Randa

The final borehole completions of the three research boreholes drilled at Randa are shown on Figure 20. In these boreholes Vibrating Wire pore pressure transducers have been placed in the lower most part of the inclinometer casing, which was perforated

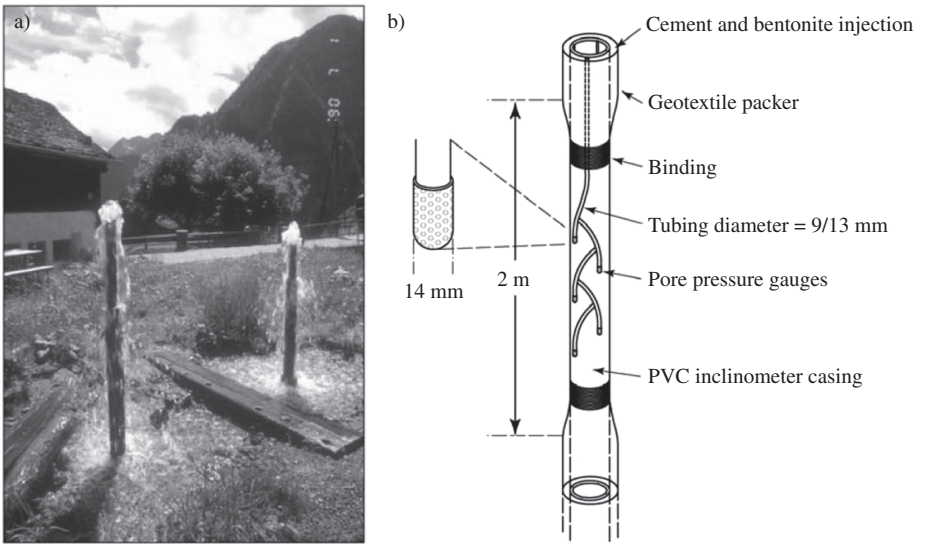


Figure 19 Integration of isolated fluid pressure and deformation monitoring in single artesian boreholes. From Bonzanigo *et al*., 2007.

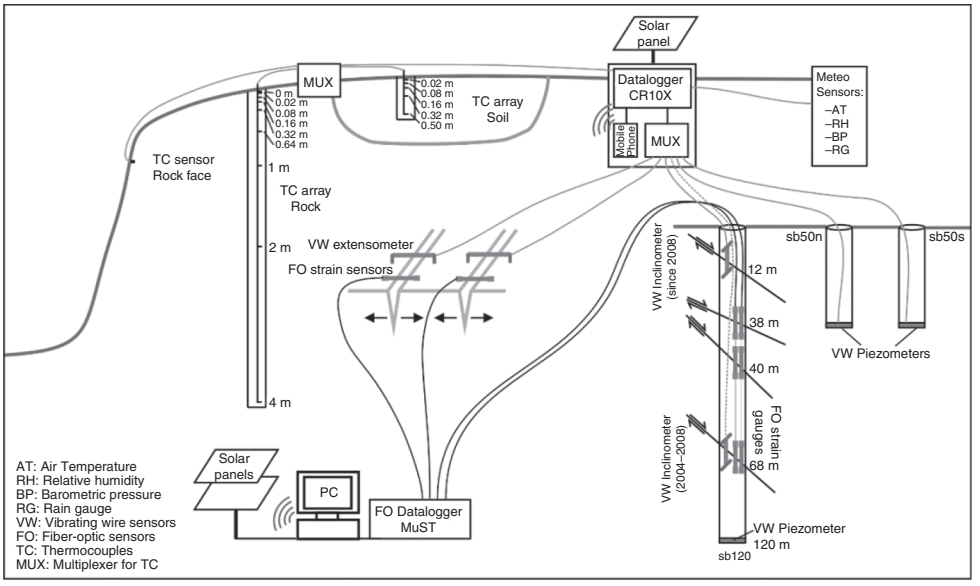


Figure 20 Final borehole completion and surface monitoring system at Randa (Gischig, 2011).

and not grouted on the outside. The upper part of the 120 m deep borehole was grouted in two sections using a geotextile. In between the two geotextile sections the casing was again perforated, such that the inclinometer casing could initially also be used as a standpipe piezometer monitoring a short interval between 100 and 105 m depth.

The inclinometer tube of borehole SB 120 could be used for repeat inclinometer and Inkrex-extensometer measurements for about 7 years (2001–2008), until localized shearing stopped these logging operations. Before full closure of this borehole, multiple fiber-optic strain sensors where installed and the borehole was fully borehole to a depth of 19 m bgs (as discussed in section 3).

As the current instability at Randa forms a downslope trending ridge of an intensively fractured and high permeability rock mass, the regional groundwater table lies below the main body of the instability and only locally perched water bodies (water-filled fractures) were recorded with the installed pressure transducers (Loew *et al.*, 2012). This is the main reason, why progressive failure at Randa is primarily driven by surface temperature variations (section 5). This stands in contrast to the planar or convergent slope morphologies at Moosfluh or Preonzo where fluid pressure coupling is clearly visible and most probably driven by a phreatic groundwater table surface moving within the landslide mass.

7 SUMMARY

Monitoring progressive failure under in-situ conditions in unstable rock slopes is far from trivial and requires substantial investments into the design, installation, operation and analysis of monitoring systems characterized by high sampling frequency, accuracy and spatial resolution. Due to their accuracy, robustness and reliability Robotic Total Stations recording the displacements of large numbers of reflectors form the backbone of many landslide monitoring systems. With Total Stations surface expressions of progressive failure, such as crack propagations, crack dislocations and block movements can be directly recorded at the ground surface and compared with changes in environmental factors driving progressive failure, such as rainfall, snowmelt and surface air temperature.

As progressive failure processes mainly occur in the subsurface, either along a basal sliding surface and/or within the sliding body above a compound rupture plane, direct observations of fracture dislocations, local strains and the corresponding driving forces require borehole based monitoring installations. In this chapter, we focus on fiber optic strain sensors, temperature and fluid pressure sensors. The combined installation of strain and fluid pressure sensors in deep boreholes requires careful planning, as many rock slope instabilities are characterized by significant vertical gradients of hydraulic head. These borehole installations can be complemented by non-destructive monitoring systems such as seismic event counting, micro-earthquake localization or ambient noise investigations. The integration of these monitoring systems can lead to detailed insights into progressive failure processes, as demonstrated by the long term investigations at the current Randa instability.

REFERENCES

Bonzanigo, L., Eberhardt, E. and Loew, S., 2007. Long-term investigation of a deep-seated creeping landslide in crystal-line rock. Part I. Geological and hydromechanical factors controlling the Campo Vallemaggia landslide. *Canadian Geotechnical Journal*, 44(10): 1157–1180.

Brown, N., Kaloustlan, S. and Roeckle, M., 2008. Monitoring of Open Pit Mines using Combined GNSS Satellite Receivers and Robotic Total Stations. *Leica Geosystems Switzerland*: 13.

Brunner, F.K., Woschitz, H. and Macheiner, K., 2007. Monitoring of deep-seated mass movements. *Proceedings 3rd International Conference on Structural Health Monitoring of Intelligent Infrastructure*.

Burjanek, J., Gassner-Stamm, G., Poggi, V., Moore, J.R. and Faeh, D., 2010. Ambient vibration analysis of an unstable mountain slope. *Geophysical Journal International*, 180(2): 820–828.

Burjanek, J., Moore, J.R., Molina, F.X.Y. and Faeh, D., 2012. Instrumental evidence of normal mode rock slope vibration. *Geophysical Journal International*, 188(2): 559–569.

Chrzanowski, A. and Wilkins, R., 2006. Accuracy Evaluation of Geodetic Monitoring of Deformations in large Open Pit Mines. *12th FIG Symposium on Deformation Measurements*, Baden, May 2006: 11.

Coviello, V., Chiarle, M., Arattano, M., Pogliotti, P. and di Cella, U.M., 2015. Monitoring Rock Wall Temperatures and Microseismic Activity for Slope Stability Investigation at JA Carrel Hut, Matterhorn. *Engineering Geology for Society and Territory*, Vol 1: Climate Change and Engineering Geology, Springer International Publishing, Switzerland, pp. 305–309.

Delaloye, R. and Lambiel, C., 2005. Evidences of winter ascending air circulation throughout talus slopes and rock glaciers situated in the lower belt of alpine discontinuous permafrost. *Norwegian Journal of Geography*, 59: 194–203.

Fah, D., Moore, J.R., Burjanek, J., Iosifescu, I., Dalguer, L., Dupray, F., Michel, C., Woessner, J., Villiger, A., Laue, J., Marschall, I., Gischig, V., Loew, S., Marin, A., Gassner, G., Alvarez, S., Balderer, W., Kastli, P., Giardini, D., Iosifescu, C., Hurni, L., Lestuzzi, P., Karbassi, A., Baumann, C., Geiger, A., Ferrari, A., Laloui, L., Clinton, J. and Deichmann, N., 2012. Coupled seismogenic geohazards in Alpine regions. *Bollettino Di Geofisica Teorica Ed Applicata*, *53*(4): 485–508.

Ferraro, P. and De Natale, G., 2002. On the possible use of optical fiber Bragg gratings as strain sensors for geodynamical monitoring. *Optics and Lasers in Engineering*, 37(2–3): 115–130.

Gischig, V.S. 2011. Kinematics and Failure Mechanisms of the Randa Rock Slope Instability (Switzerland). Ph.D. thesis, ETH Zurich, Zurich, Switzerland.

Gischig, V., Amann, F., Moore, J.R., Loew, S., Eisenbeiss, H. and Stempfhuber, W., 2011a. Composite rock slope kinematics at the current Randa instability, Switzerland, based on remote sensing and numerical modeling. *Engineering Geology*, 118(1–2): 37–53.

Gischig, V., Loew, S., Kos, A., Moore, J.R., Raetzo, H. and Lemy, F., 2009. Identification of active release planes using ground-based differential InSAR at the Randa rock slope instability, Switzerland. *Natural Hazards and Earth System Sciences*, 9(6): 2027–2038.

Gischig, V.S., Eberhardt, E., Moore, J.R. and Hungr, O., 2015. On the seismic response of deep-seated rock slope instabilities – Insights from numerical modeling. *Engineering Geology*, 193: 1–18.

Gischig, V.S., Moore, J.R., Evans, K.F., Amann, F. and Loew, S., 2011b. Thermomechanical forcing of deep rock slope deformation: 1. Conceptual study of a simplified slope. *Journal of Geophysical Research-Earth Surface*, 116.

Gischig, V.S., Moore, J.R., Evans, K.F., Amann, F. and Loew, S., 2011c. Thermomechanical forcing of deep rock slope deformation: 2. The Randa rock slope instability. *Journal of Geophysical Research-Earth Surface*, 116.

Gomberg, J., Schulz, W., Bodin, P. and Kean, J., 2011. Seismic and geodetic signatures of fault slip at the Slumgullion Landslide Natural Laboratory. *Journal of Geophysical Research-Solid Earth*, 116.

Groneng, G., Christiansen, H.H., Nilsen, B. and Blikra, L.H. 2011a. Meteorological effects on seasonal displacements of the Aknes rockslide, Western Norway. *Landslides*, 8: 1–5.

Gueguen, Y. and Palciauskas, V., 1994. Introduction to the physics of rocks. Princeton, NJ, Princeton University Press.

Gunzburger, Y., Merrien-Soukatchoff, V. and Guglielmi, Y., 2005. Influence of daily surface temperature fluctuations on rock slope stability: case study of the Rochers de Valabres slope (France). *International Journal of Rock Mechanics and Mining Sciences*, 42(3): 331–349.

Hasler, A., Gruber, S. and Beutel, J., 2012. Kinematics of steep bedrock permafrost. *Journal of Geophysical Research-Earth Surface*, 117.

Helmstetter, A. and Garambois, S., 2010. Seismic monitoring of Sechilienne rockslide (French Alps): Analysis of seismic signals and their correlation with rainfalls. *Journal of Geophysical Research-Earth Surface*, 115.

Imrie A.S., Moore, D.P. and Enegren, E.G. 1991. Performance and maintenance of the drainage sytem at Downie Slide. In: Bell (Editor), *International Symposium on Landslides*. ISL IV. Balkema, Christchurch, pp. 751–757.

Inaudi, D. and Casanova, N., 2000. Geo-structural monitoring with long-gage interferometric sensors. In: E.M. Aktan and S.R. Gosselin (Editors), *Nondestructive Evaluation of Highways, Utilities, and Pipelines Iv. Proceedings of the Society of Photo-Optical Instrumentation Engineers (Spie)*. Spie-Int Soc Optical Engineering, Bellingham, pp. 164–174.

Inaudi, D., Cottone, I. and Figini, A., 2013. Monitoring Dams and Levees with distributed Fiber Optic Sensing. SHMII-6: 6th International Conference on Structural Health Monitoring of Intelligent Infrastructure, Hong Kong.

Kharghani, G., 1987. Propagation of refraction errors in trigonometric height traversing and geodetic levelling. *Geodesy and Geomatics Engineering Technical Report*, 132: 173.

Lacroix, P. and Helmstetter, A., 2011. Location of Seismic Signals Associated with Microearthquakes and Rockfalls on the Sechilienne Landslide, French Alps. *Bulletin of the Seismological Society of America*, 101(1): 341–353.

Levy, C., Baillet, L., Jongmans, D., Mourot, P. and Hantz, D., 2010. Dynamic response of the Chamousset rock column (Western Alps, France). *Journal of Geophysical Research-Earth Surface*, 115.

Levy, C., Jongmans, D. and Baillet, L., 2011. Analysis of seismic signals recorded on a prone-to-fall rock column (Vercors massif, French Alps). *Geophysical Journal International*, 186(1): 296–310.

Loew, S., Gischig, V. and Moore, J.R., 2012a. Monitoring of potentially catastrophic rockslides. *Landslides and Engineered Slopes: Protecting Society through Improved Understanding*: 16.

Loew, S., Gischig, V., Willenberg, H., Alpiger, A. and Moore, J., 2012b. Randa: Kinematics and driving mechanisms of a large complex rockslide as determined from comprehensive field and laboratory investigations. In: J. Clague and D. Stead (Editors), Landslides: Types, Mechanisms and Modelling. Cambridge University Press, 297–309.

Loew, S., Gschwind, S., Gischig, V., Keller-Signer, A. and Valenti, G., 2016. Monitoring and early warning of the 2012 Preonzo catastrophic rockslope failure. *Landslides online first*, April 2016, pp. 14.

Mainsant, G., Larose, E., Broennimann, C., Jongmans, D., Michoud, C. and Jaboyedoff, M., 2012. Ambient seismic noise monitoring of a clay landslide: Toward failure prediction. *Journal of Geophysical Research-Earth Surface*, 117.

Matsuoka, N., 2001. Direct observation of frost wedging in alpine bedrock. *Earth Surface Processes and Landforms*, 26(6): 601–614.

Moore D.P., 1992. Panelist Contribution: Stabilization of Downie Slide and Dutchman´s Ridge, International Conference on Soil Mechanics and Foundation Engineering. *ICSMFE Conference XII*. Balkema, Rio de Janeiro, pp. 3063–3065.

Moore D.P. & Imrie A.S. 1995. Stabilization of Dutchman´s Ridge. In: Bell (Editor), *International Symposium on Landslides*. ISL VI. Balkema, Christchurch, pp. 1783–1788.

Moore, J.R., Gischig, V., Burjanek, J., Loew, S. and Faeh, D., 2011a. Site Effects in Unstable Rock Slopes: Dynamic Behavior of the Randa Instability (Switzerland). *Bulletin of the Seismological Society of America*, 101(6): 3110–3116.

Moore, J.R., Gischig, V. Katterbach, M. & Loew, S., 2011b. Air Circulation in Deep Fractures and the Temperature Field of an Alpine Rock Slope, Earth Surface Processes and Landforms, 36(15): 1985–1996.

Moore, J.R., Gischig, V., Button, E. and Loew, S., 2010. Rockslide deformation monitoring with fiber optic strain sensors. *Natural Hazards and Earth System Sciences*, 10(2): 191–201.

Moyo, P., Brownjohn, J.M.W., Suresh, R. and Tjin, S.C., 2005. Development of Fiber Bragg grating sensors for monitoring civil infrastructure. *Engineering Structures*, 27(12): 1828–1834.

Pei, H., Cui, P., Yin, J., Zhu, H., Chen, X., Pei, L. and Xu, D., 2011. Monitoring and warning of landslides and debris flows using an optical fiber sensor technology. *Journal of Mountain Science*, 8(5): 728–738.

Phillips, M., Mutter, E.Z., Kern-Luetschg, M. and Lehning, M., 2009. Rapid Degradation of Ground Ice in a Ventilated Talus Slope: Fluela Pass, Swiss Alps. *Permafrost and Periglacial Processes*, 20(1): 1–14.

Pisani, G., Castelli, M. and Scavia, C. 2010. Hydrogeological model and hydraulic behaviour of a large landslide in the Italian Western Alps. *Natural Hazards and Earth System Science*, 10: 2391–2406.

Schindler, C., Cuenod, Y. and Eisenlohr, T., 1993a. Die Ereignisse vom 18. April und 9. Mai 1991 bei Randa (VS): Ein atypischer Bergsturz in Raten. *Eclogae Geologicae Helvetiae*, 86(3): 24.

Schindler, C., Cuenod, Y., Eisenlohr, T. and Joris, C.L., 1993b. The events of Randa, April 18th and May 9th, 1991 –An uncommon type of rockfall. *Eclogae Geologicae Helvetiae*, 86(3): 643–665.

Schmidt-Hattenberger, C., Naumann, M. and Borm, G., 2003. Fiber Bragg grating strain measurements in comparison with additional techniques for rock mechanical testing. *IEEE Sensors Journal*, 3(1): 50–55.

Spillmann, T., Maurer, H., Green, A.G., Heincke, B., Willenberg, H. and Husen, S., 2007a. Microseismic investigation of an unstable mountain slope in the Swiss Alps. *Journal of Geophysical Research-Solid Earth*, 112(B7).

Spillmann, T., Maurer, H., Green, A.G., Heincke, B., Willenberg, H. and Husen, S., 2007b. Microseismic investigation of an unstable mountain slope in the Swiss Alps. *Journal of Geophysical Research*, 112(B07301).

Stahlhut, F. and Bonassi, N., 2014. Detecting and mitigating short term variations of systematic effects on a TPS-based monitoring system at Aletsch Glacier. *Interdisciplinary Master Project Geomatics*: 81.

Terzaghi, K., 1962. Stability of steep slopes on hard unweathered rock. *Geotechnique*, 12: 20.

Thoeny, R. 2008. Dynamic fluid electrical conductivity logging for identification and characterization of preferential groundwater flow in the Aknes rockslide (Norway). *MSc Thesis*, ETH Zurich, Zürich, p. 105

Van Cranenbroeck, J. and Brown, N., 2004. Networking Motorized Total Stations and GPS Receivers for Deformation Measurements. *TS16 Deformation Measurements and Analysis I*: 15.

Watson, A.D., Moore, D.P. and Stewart, T.W., 2004. Temperature influence on rock slope movements at Checkerboard Creek. *Landslides: Evaluation and Stabilization, Proceedings of the Ninth International Symposium on Landslides*. Taylor and Francis Group, London. pp. 1293–1298.

Watson, A.D., Moore, D.P., Stewart, T.W. and Psutka, J.F., 2007. Investigations and monitoring of rock slopes at Checkerboard Creek and Little Chief Slide. *Rock Mechanics: Meeting Society's Challenges and Demands*. Taylor and Francis Group, London. pp. 1015–1022.

Watson, A.D., Martin, C.D., Moore, D.P., Stewart, T.W. and Lorig L.J., 2006. Integration of Geology, Monitoring and Modelling to Assess Rockslide Risk. *Felsbau* 24/3: 50–58.

Whitaker, C., Duffy, M. and Chrzanowski, A., 2000. Design of an automated dam deformation Monitoring System: A case study. *Journal of Geospatial Engineering*, 2(1): 12.

Willenberg, H., Evans, K.F., Eberhardt, E., Spillmann, T. and Loew, S., 2008a. Internal structure and deformation of an unstable crystalline rock mass above Randa (Switzerland): Part II – Three-dimensional deformation patterns. *Engineering Geology*, 101(1–2): 15–32.

Willenberg, H., Loew, S., Eberhardt, E., Evans, K.F., Spillmann, T., Heincke, B., Maurer, H. and Green, A.G., 2008b. Internal structure and deformation of an unstable crystalline rock mass above Randa (Switzerland): Part I - Internal structure from integrated geological and geophysical investigations. *Engineering Geology*, 101(1–2): 1–14.

Woschitz, H. and Brunner, F.K., 2008. Monitoring a deep-seated mass movement using a large strain rosette. *Proceeding 13th FIG Symposium on Deformation Measurements and Analysis*.

Zimmer, V.L. and Sitar, N., 2015. Detection and location of rock falls using seismic and infrasound sensors. *Engineering Geology*, 193: 49–60.

Chapter 21

Particle velocities for rockbursts recorded at seismic stations distributed throughout the Karviná coal mining district

K. Holub[1], *J. Rušajová*[1] & *J. Holečko*[2]
[1]*Institute of Geonics of the Academy of Sciences of the Czech Republic, Ostrava-Poruba, Czech Republic*
[2]*Green Gas DPB a.s., Rudé armády, Paskov, Czech Republic*

Abstract: As a consequence of geomechanical and geotechnical conditions, as well as anthropogenic activities, in the mines of the Ostrava-Karviná coal basin (Czech Republic), rockbursts have been recognized to be a serious seismic risk. Therefore, local as well as regional monitoring arrays were deployed there in order to investigate the actual seismic activity on a continuous basis. The particle velocity of P- and S-waves was one of the essential parameters that was investigated on the seismograms recorded at the seismic stations placed *in situ*. This paper summarises the results of underground seismic measurements conducted between 1993 and 2013, and seeks to identify some empirical dependencies by determining the decay of particle velocity according to the scaled distance from the foci of the rockbursts. The scaling distance r* is defined for rockbursts by the formula $r^* = d/\sqrt{E}$ ($m.J^{-1/2}$), while for explosions the formula $r^* = d/\sqrt[3]{Q}$ ($m.kg^{-1/3}$) is usually used. The seismic energy, local magnitude and focus coordinates of the rockbursts, as well as positions where damage to workings occurred, were employed as additional inputs. Furthermore, the degree of this damage was tested, based on the particle velocity value generated by rockbursts occurring during exploitation of the longwalls. We tried to estimate the manifestations of individual rockbursts by the length of the damaged workings, specifically the roads, affected by the respective, and anomalous, geomechanical event. At the same time, a complex elaboration of the state of the workings following each rockburst has been carried out after the inspection conducted by the professionals of the Regional Mining Authority who determine the further progress of mining activities in the affected locality.

1 HISTORICAL PREFACE

Archaeological discoveries at Landek Hill in the environs of Ostrava document that this area had already been settled during the Stone Age by mammoth hunters living in camps. Coincidentally, their settlements of 25,000 years ago were concentrated at localities where outcrops of hard (black) coal seams appeared. Assuming that these mammoth hunters discovered the combustible properties of coal, they are probably among the first people to have routinely used hard coal to maintain a fire. In fact, this notion was proved by the fragments of hard coal and coked remains of coal from the nearby seams that were found in the fireplaces of these hunters. Moreover, some

exposed parts of the hard coal layers coming close to the surface at this site were changed from coal to coke during the oxidative alteration processes acting in the environs (Klika, 1999). During the later systematic archaeological survey at this location, undertaken by the Institute of Archaeology of the Czechoslovak Academy of Sciences, one member of the research team in 1953 found the famous 'Venus of Landek' (Klíma, 1955). This artifact takes the form of a 45 mm high torso of a woman carved from haematite. Further systematic archaeological surveys at this site found evidence of continuous occupation throughout the Neolithic and Bronze Ages.

Following this brief historical exposition relating to a vanished past, we will progress from the Stone Age through the Neolithic and Bronze Ages to the eighteenth century, namely to the years 1763 and 1781, when the first mention of the start of mining activities referred to the valley of Burna close to Silesian Ostrava (OstravaFOTO, 2015) and the well-known locality in the vicinity of Landek Hill, respectively, with the first mine named Anselm. At that time, the first coal seam outcrops were mined either in shallow pits of around 30 m depth or via galleries of up to 200 m in length (Hrady, 2015; Landek Park, 2015).

2 INTRODUCTION

This chapter considers the fundamental role of seismic monitoring in the eastern part of the Ostrava-Karviná coal basin (OKCB), where rockbursts have occurred for more than 100 years, although mining started in this region more than 200 years ago. The first geodynamic event denoted as 'mining shock' was felt on 26 July 1912 on the surface of the Hohenegger Mine (at present in the mine field of the Darkov Mine), and after an underground inspection only a small coal burst was found. There followed a period until 1930 without any seismic event. A series of weak induced seismic events started in the 1930s, which culminated in the occurrence of a relatively strong 'mining shock' on 9 January 1936. This was felt at the surface of the Trojice Mine in Silesian Ostrava, on territory adjacent to the Czechoslovakia–Poland border, with an estimated macroseismic intensity of 3° to 5° MCS. After an inspection in the mine it was stated that this dynamic phenomenon had not caused any extensive damage within the mine but it claimed two lives. This event was reported in the Catalogue of Earthquakes by Kárník *et al.* (1958) as a weak local earthquake and/or rockburst. Further investigations of these 'mining shocks' and other geodynamic phenomena were estimated according to their macroseismic manifestations at the surface and within mines.

The first instrumental detection of the phenomena started in the 1980s in the OKCB (Trávníček & Holečko, 1980; Knotek & Holub, 1980). The origin of these mining-induced events is closely related to coal extraction processes and is also affected by other factors, for example, by specific mining and geological conditions, the physical and mechanical properties of the rock mass, the mining techniques used in the past and present, the stability of all types of pillars, and changes in the stress-strain state of the rock mass (Holub, 1997a). In the layers underlying a coal deposit, induced seismic events occur frequently and, moreover, some of them have the character of damaging rockbursts. In areas affected by these dangerous seismic events, therefore, both passive (*e.g.* mine design, choice of mining equipment, selection of suitable mounting, etc.) and

active preventive measures (*e.g.* destressing, drilling and blasting, water infusion of coal seams, large-scale non-productive blasting operations in the roof, etc.) have been applied in order to mitigate their devastation of underground workings (Holub, 1997b; Holub *et al.*, 1988; Dvorský & Koníček, 2005).

Within the scope of the geomechanical service of the Ostrava-Karviná mines, a rockburst is generally characterized as a sudden failure of a coal seam and accompanying rocks into the surrounding workings and roadways. Elastic energy accumulated in the coal seam and/or surrounding rocks is released at the same time. The consequence is that workings are permanently destroyed, regardless of the amount of energy involved, as they can no longer fulfill their operational function. For the purpose of our study, a series of 105 rockbursts in the period from 1993 to 2013 was selected, each of which was recorded, simultaneously, at three underground seismic stations where tri-axial sensors had been deployed. Between 40,000 and 50,000 induced seismic events, representing a broad span of energies (up to 10^8 J), were observed at the seismic stations every year in the coal mine district as a whole. Within the long-term history of mining in this area it was concluded that the strongest rockburst occurred on 27 April 1983 in the Czechoslovak Army (ČSA) Mine, and this was accompanied by catastrophic consequences underground, that is, devastation of workings, roadways, and face and roadway supports, as well as 50 deaths and injuries to many miners. The rockburst was classified as having an energy $E \approx 10^{10}$ J and/or by magnitude scale M = 3.75 ± 0.5, according to the Euro-Mediterranean Seismological Centre (EMSC) in France. Moreover, this event was recorded to an epicentral distance of about 2,000 km (Trávníček *et al.*, 1987).

The particle velocity of P- and S-waves were chosen as the basic parameter for observation, while the focus location, released seismic energy and local magnitude were calculated subsequently, using the first-arrival times of these seismic waves. The subject of our interest was determination of the coefficient of decay of the maximum P- and S-wave particle velocities in dependence on scaled distance in the rock mass and prevailing frequency of vibrations.

3 SOME CHARACTERISTIC FEATURES OF THE COAL DEPOSIT

The OKCB represents roughly a third of the Upper Silesian Basin area, which is mostly situated within the territory of Poland. Figure 1 shows the basic structural units of the Bohemian Massif, including the position of the Upper Silesian Coal Basin.

It is obvious that the OKCB mining district is situated between two large tectonic units, that is, the older Bohemian Massif and the younger Carpathian system, which had a major influence on the evolution of structure formation in the sedimentary basin. The sedimentation of this basin started in the latest Upper Carboniferous stage, and the coal-bearing strata belong to the Namurian A, B and C, and Westphalian A stages. The whole mining district of the OKCB is divided into three partial coal basins referred to as the Ostrava, Petřvald and Karviná basins, the central Petřvald basin being separated from other two by the Michálkovice and Orlovská structures of anticlinal character. These three basins, the general position of the OKCB within the Czech Republic, and also the distribution of the seismic stations A, C, D, K and M are shown in Figure 2.

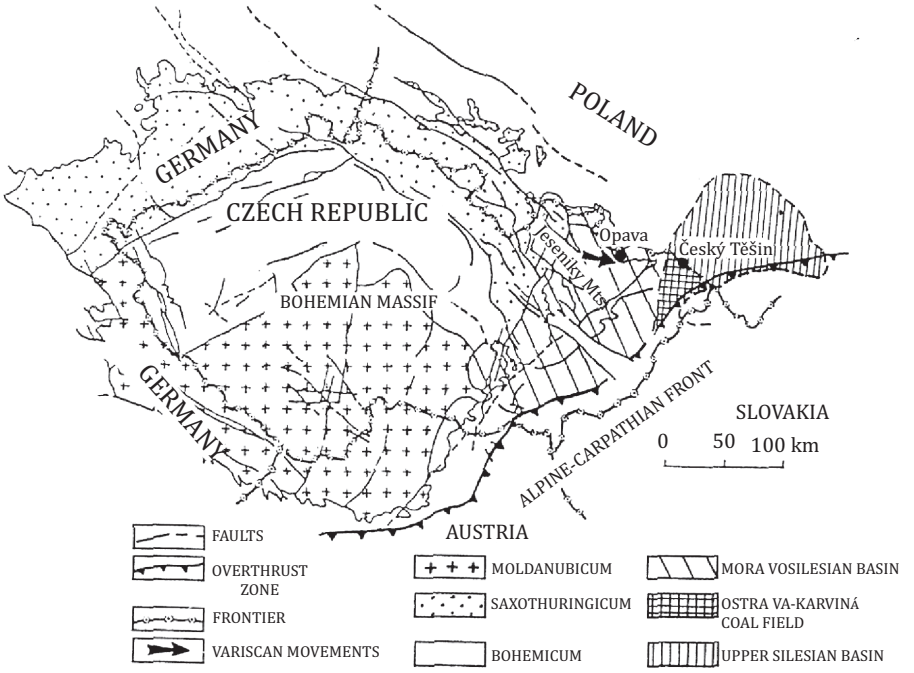


Figure 1 Schematic structural map of the Bohemian Massif with the Upper Silesian Coal Basin shown upper right (Adapted from Dopita & Kumpera, 1993).

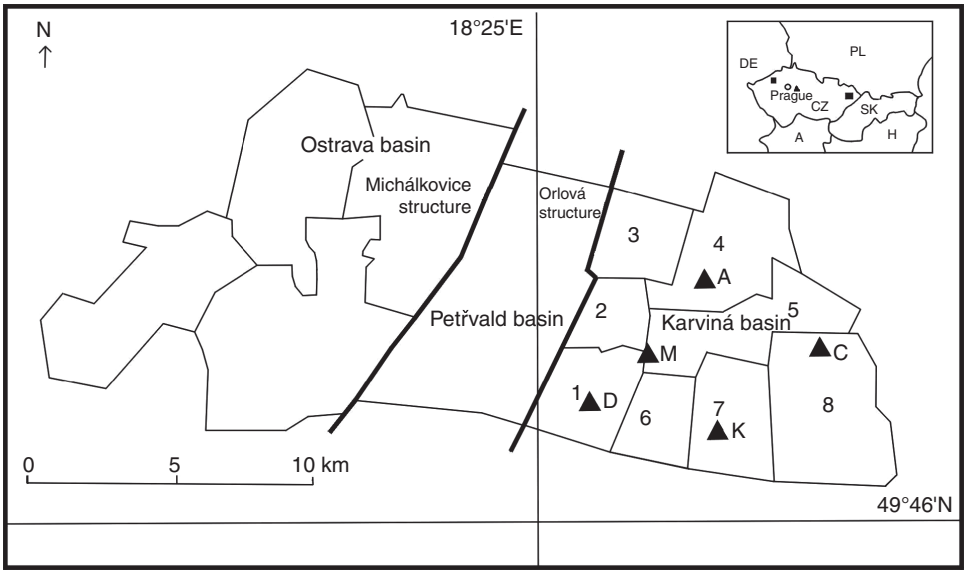


Figure 2 Map of boundaries of coal basins (—) and demarcations of mines (–) in the OKCB: 1 – Dukla (closed); 2 – Lazy; 3 – Doubrava; 4 – ČSA; 5 – Darkov; 6 – František (closed); 7 – Květen; 8 – ČSM (according to Dopita, 1997); ▲ A, C, D, K and M represent positions of underground seismic stations; Miniature map at upper right corner documents: ■ area of the OKCB, ▪ locality of the Šverma Mine, ○ locality of the Filip Mine.

Considering that mining started in this region more than two hundred years ago, it is unsurprising that the mines in the Ostrava and Petřvald basins have now been closed. Since the 1980s, mining has been concentrated in the eastern part of the OKCB, that is, in the Karviná basin. At present, mines Dukla (#1), František (#6) and Barbora (originally merged into the May 1st Mine, which then evolved into the Darkov Mine) are closed.

The important structural changes in this area were in progress during the Cadomian, Variscan and Alpine foldings, when the Variscan stage, in particular, caused disruption of all the layers in the coal deposit oriented roughly east–west and north–south. The tectonic faults now form demarcations between the individual mining and/or tectonic blocks. The inner structure of the coal seams consists of two basic formations: the Ostrava Formation (Lower Namurian) in the basement of the basin, and the Karviná Formation (Middle and Upper Namurian, and Westphalian), which represents the higher horizons.

The most important and dangerous disruption was the space between coal seams 33 and 37, which belong to the so-called Saddle Members that form the lower part of the Karviná Formation and which are considered identical to the bottom of coal seam 40 (named Prokop), while the upper part of the Saddle Members was accepted as underlying the bed of coal seam 33. The Saddle Members are formed of hard rocks (*e.g.* solid siltstone, sandstone and conglomerate) with a compression strength of 70–100 MPa, while samples of coal exhibit much lower values, approximately 20–25 MPa. Due to this strength of rock, the space mentioned above – the thickness of which is roughly 120–175 m – was considered a dangerous zone where, during coal extraction in coal seams 37 to 40, stress concentrations occurred. Once the ultimate strength limit of the rocks in the roof is exceeded, the strain energy in the rock mass is released in the form of individual seismic-induced events, sometimes also generated in the form of rockbursts. A schematic vertical cross section of the Saddle Members of the coal deposit along the profile X – Y in the southern part of the ČSA Mine is displayed in Figure 3. The upper

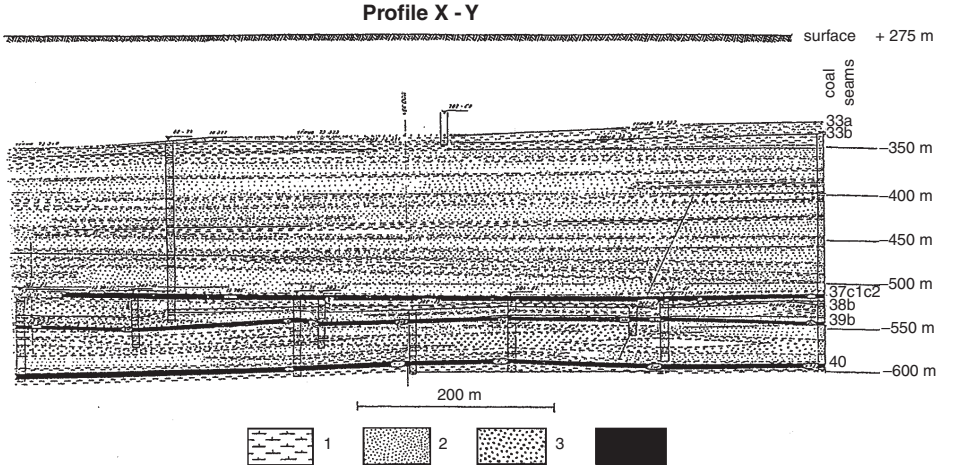


Figure 3 Vertical geological cross section in E – W direction in the southern part of the ČSA Mine; 1-siltstone, 2-sandstone, 3-conglomerate, 4-coal seams.

part of the geological profile (above coal seam 33), as far as the surface, consists of similar rocks and its uppermost part, where thinner coal seams also occur (*e.g.* coal seam 29), is built almost entirely of superficial deposits of Miocene age. The geological structure of the region under discussion has been described in detail by Dopita *et al.* (1997). In terms of mining methods, a retreating mining system with controlled caving and/or pneumatic filling is predominantly applied in the OKCB.

4 MONITORING OF SEISMIC ACTIVITY IN THE OKCB

The mining-induced seismicity in the eastern part of the OKCB has been continuously monitored by two different seismological systems. The first of these is a local network consisting of about 30 underground seismic stations distributed among individual mines. These stations are equipped only with short-period vertical seismometers, as described by Holub *et al.* (2012). In addition, a regional network also exists, created from ten stations equipped with tri-axial sensors which encompass the whole mining field. Three of these ten stations are deployed underground and can be moved short distances (roughly ± 500 m) as local mining approaches the respective station. Then the minimum shift of the seismic station is applied in order to avoid sources of local disturbance, such as coal combines, belt conveyors, drilling machines and ventilators. Six fixed stations are situated at the surface in shallow boreholes ($h \approx 30$ m) and the tenth station is situated in a short experimental gallery near the Ostrava-Krásné Pole seismic station (OKC), located approximately 25 km west of the coalfield's center, which is currently part of the Czech National Seismological Network. The individual stations are equipped with WDS 202 tri-axial short-period seismographs (Lennartz Electronic, Tübingen, Germany) ($f_0 = 2$Hz), and the complex set of applied instrumentation provides automatic data recording, preprocessing and transmission to a central laboratory via radio through a relay station situated at the top of the Beskydy Hills. The substantial advantage of this type of processing is that it guarantees to obtain all the data needed to inform a geomechanical service in real time, mainly assessing the results of preventive measures applied in individual endangered longwall panels. Five positions of underground seismic stations, denoted as A, C, D, K and M and pertaining to the regional network, are shown in Figure 2. Three trios of station combination have always been used to monitor the induced seismic events, including rockbursts, during the period 1993–2013. The individual rotating schedules of seismic station operation are A+K+M, A+D+K and A+C+K. An overview of the series of 105 rockbursts that occurred during this period is displayed in Figure 4, while a plot of their foci is shown in Figure 5.

It is worth mentioning here that, throughout this study, the original names of mines and/or plants have been retained, although during the last twenty years some structural changes in mines have taken place which have also caused corresponding changes to their names.

5 DATA PROCESSING

Regardless of the monitoring system operation's fundamental purpose of the detection of seismic events, other information – such as calculation of foci location, delimitation

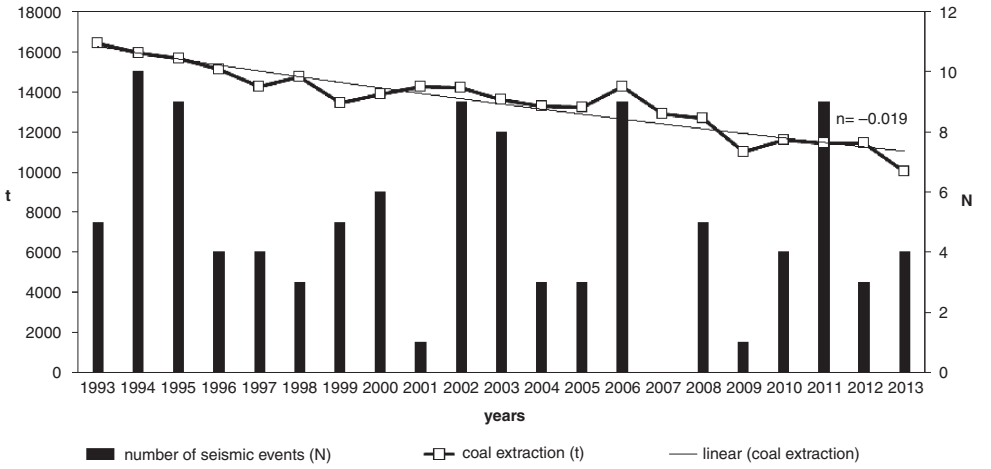


Figure 4 A series of 105 rockbursts observed between 1993 and 2013, together with a graph showing annual output decline defined by the formula $y = 1.656 \times 10^4 \times e^{-0.019x}$.

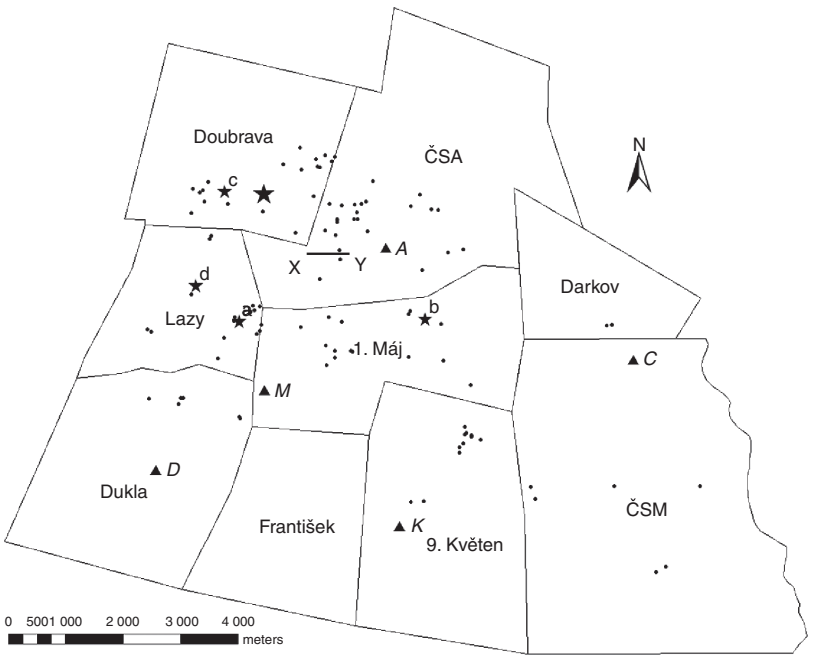


Figure 5 Distribution of localized rockbursts in the OKCB: • rockburst foci; ▲ A, C, D, K and M represent positions of underground seismic stations; X—Y is the course of the geological cross section shown in Figure 3.

of rockburst endangered areas due to foci concentration, and Benioff and energy-frequency graphs – is being constructed on a daily basis in the operation center described by Holub *et al.* (2012). Subsequently, local magnitude was also determined. For this study, only the values of the observed particle velocities stored in the database were used. However, after the final assessment of the rockbursts, the spatial coordinates of the foci, the amount of seismic energy released, and the calculated local magnitude were also provided.

5.1 Particle velocity in deep mines

Given that this research was concentrated on identifying some dependencies, in which several parameters had a crucial significance in the process of deriving the relationships, one problem had to be solved first, that is, to pick a suitable value of the so-called scaled distance. At present, a large number of papers deal with the application of scaled distance r* using various values of exponent n, although $n = ½$ or $n = ⅓$ are the most widely used. For instance, Siskind *et al.* (1980), Egan *et al.* (2001) and Sambuelli (2009) applied $n = ½$, while Isaac (1991), Isaac & Bubb (1981), Hedley (1991), Dowding (1992), Hendron (1997), Chen *et al.* (2000), Jiao *et al.* (2003) and many others preferred cube-root scaling in blasting operations, that is, they applied $n = ⅓$. On the other hand, Holečko & Koníček (2007) and Holub *et al.* (2012), for example, tested in regression analysis using both values, $n = ½$ and $n = ⅓$. Given that the energetic source in our case was seismic energy released during the rockbursts, then the amount of explosives Q (kg) in the form $d^* = d/\sqrt{Q}$ was substituted by the energy quantity of E (J). After this substitution, the scaled distance takes the form $r^* = d/\sqrt{E}$, with dimensions (m/$\sqrt{\text{J}}$), and this was used throughout this paper. The philosophy that we applied in our approach to the calculations was based on the assumption that because of the mechanism of rockbursts, a cylindrical waveform is generated. Previous experience indicates that the best results for establishing various relationships between the individual parameters related to the particle velocities of P- and S-waves could be reached by using the vectorial sum described by the following relation: $\sum u_{\max} = [(u_i^{Z})^2 + (u_i^{NS})^2 + (u_i^{EW})^2]^{1/2}$. Equations 1 and 2 were derived to determine the dependence of the particle velocity on the scaled distance for the vectorial sum of P- and S-wave data.

$$P_{max}\text{-waves} \quad u_{max}(\text{m/s}) = 1.060 \times 10^{-4} \times r*^{-0.899} R^2 = 0.6995 \tag{1}$$

$$S_{max}\text{-waves} \quad u_{max}(\text{m/s}) = 5.190 \times 10^{-4} \times r*^{-1.153} R^2 = 0.8637 \tag{2}$$

In previous papers, we have presented only the final phase of the solution, that is, the calculation of the vectorial sum of the individual components of the particle velocities. In this paper, we wanted to acknowledge this and show the intermediate steps by which the individual components gradually contribute to the final waveform. For this reason, all equations of the respective R^2 correlation coefficients for the components of motion in directions North–South (A), East–West (B) and Z-axis (C), and their vectorial sum-(D) are displayed separately, as shown, for example, on the bilogarithmic scales for S-waves in Figure 6.

It was proved that the maximum scatter of particle velocity u_i of P- and S-waves was evident in both horizontal components, which corresponded to the minimum values of

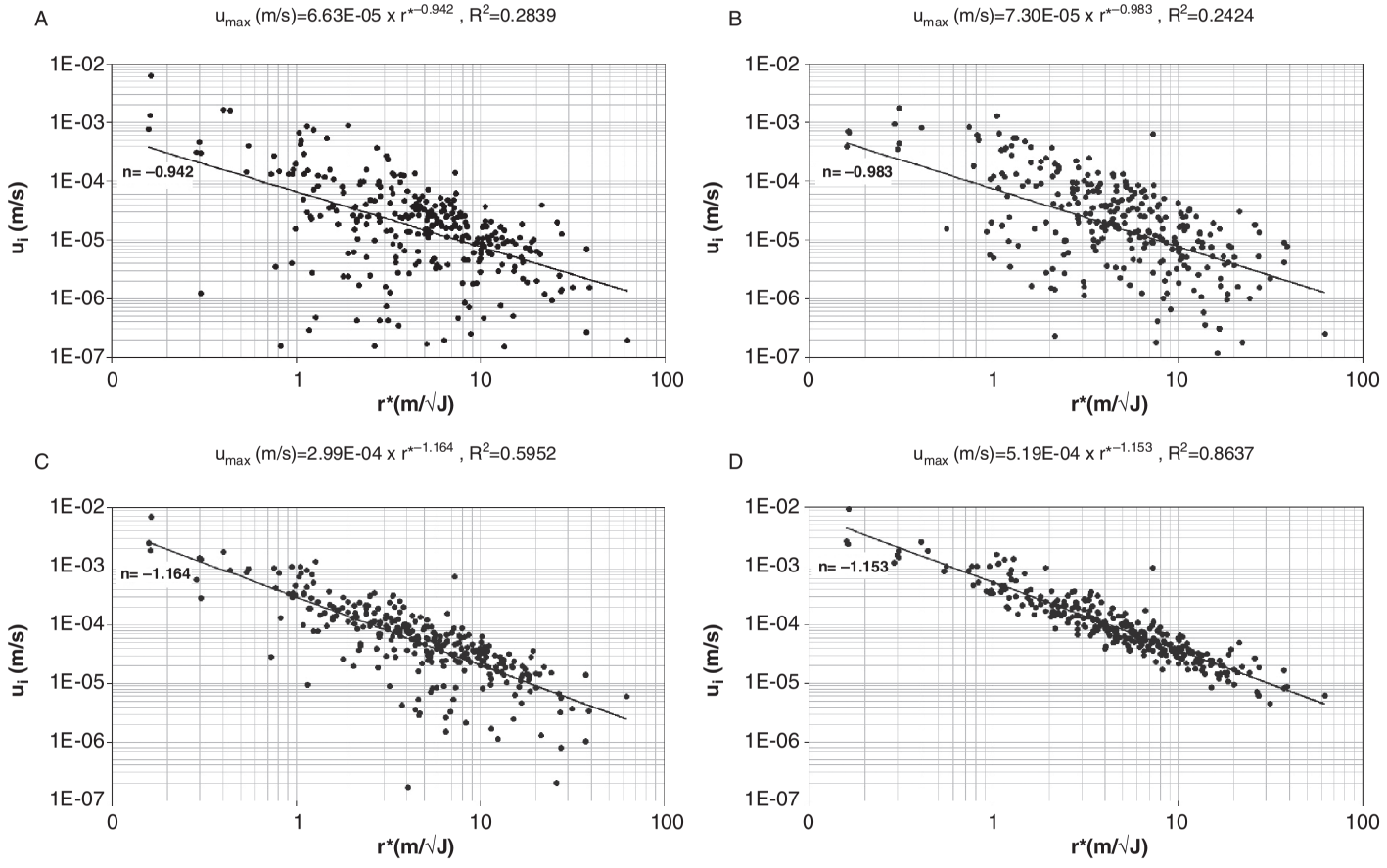


Figure 6 Dependencies of particle velocity of S-waves (log u_i) vs log-scaled distance (r^*) and resulting straight line approximations displayed on a bilogarithmic scale; (a) North–South; (b) East-West; (c) Z-axis; (d) vectorial sum.

the R^2 correlation coefficients. Slightly higher correlation coefficients were indicated for the vertical components and the best solution, that is, minimum scatter of u_i and maximal R^2, was guaranteed when the vectorial sum of the individual components of the particle velocities was applied. The explanation for the higher scatter values of particle velocities recorded by fixed, horizontally oriented sensors is quite simple: it is because seismic rays are approaching the seismic stations from the rockburst foci from different back azimuths.

5.2 Particle velocity in open-pit mines

Different mining and geological situations pertain in the hard-coal mines in the OKCB and in the open-pit mines of brown coal – the Šverma Mine in north-west Bohemia – and of shale – the Filip Mine in Central Bohemia (see Figure 2 – miniature map in upper right). Different instrumentation for experiments has to be applied, because shot-hole explosions were used to generate seismic waves in all locations (Holub & Tobyáš, 1987, 1989; Holub & Rušajová, 2011).

The setup for measurements in the open-pit mines consisted of special massive sensors (VPB-3, Russian origin) and a six-channel recorder. This instrumentation was applicable for seismological measurements in zones nearest to large explosions. The field experiments were aimed at investigation of the open-pit face stability, and for this purpose only the radial component of ground motion was recorded. The blast holes in Šverma Open-pit Mine were drilled from the surface of the stripping bank; the maximum depths amounted to 18 m and charges (Q) in the range 9–120 kg were put into hollows and then were tamped with sand. By contrast, in Filip Open-pit Mine the shots were fired in holes roughly 10 m in depth with charges in the range 5–50 kg.

For experimental measurements in Šverma Open-pit Mine, where surface mining of brown coal has recently been terminated, two sites were chosen. The sites differ in the lithology of their sediments and in the degree and character of disruption, because they were situated at different stripping levels. The first site (A) was at the level where the massif was represented by overlying compact gray clays and the height of the wall was 9–10 m, while the second site (B) was situated at another stripping level, roughly 20 m above the first site. The structure of the geological sheet was rather complicated, because the upper part (3–4 m) of the profile was built of horizontally deposited layers of gray clays, whereas the middle and lower parts of the profile were prevailingly represented by diagenetically little-consolidated sandstones (8–9 m), and, finally, the lowest part of the profile was hidden by a talus fan of sandy material.

Filip Open-pit Shale Mine is in Central Bohemia near Nové Strašecí, approximately 50 km north-west of Prague. The mine is located at the southern margin of the Kladno-Rakovník Basin, where Upper Cretaceous rocks, lying subhorizontally, cover the Upper Carboniferous sediments transgressively. The sedimentary profile is represented by coarse-grained kaolinited sandstones, shales, conglomerates and, in the upper horizons, some layers of celadon green were also found.

The results of the interpreted data from these two open-pit mines in north-western and Central Bohemia are described in Equations 3, 4 and 5, and an example of a visual demonstration, in this case for Equation 4, is provided in Figure 7.

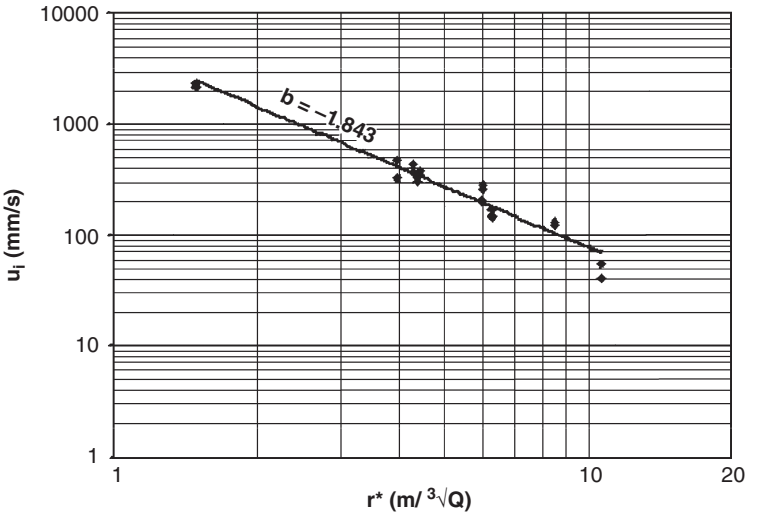


Figure 7 The bilogarithmic graph of dependence of log u_i vs log r* for test site B in Šverma Open-pit Mine.

- Šverma Open-pit Mine (test site A):

$$u_i(\mathrm{m/s}) = 4.120 \times r^{*-1.894} \quad R^2 = 0.8612 \tag{3}$$

- Šverma Open-pit Mine (test site B):

$$u_i(\mathrm{m/s}) = 5.186 \times r^{*-1.843} \quad R^2 = 0.9519 \tag{4}$$

- Filip Open-pit Mine:

$$u_i(\mathrm{m/s}) = 6.009 \times r^{*-2.256} \quad R^2 = 0.8935 \tag{5}$$

If the individual exponents of the scaled distance r* in Equations 3, 4 and 5 are compared with one another, one can see that they vary around a value of 2, that is, that the decay of the respective particle velocities fulfills the conditions for their spreading from the seismic source according to common law $1/d^2$, *i.e.* they propagate in a spherical waveform.

5.3 The predominant frequencies of body waves

The investigation of the predominant frequencies created during earthquakes, as well as during instances of rockbursts having different intensities, is part of the scope when investigating the properties of foci and seeking to understand the processes progressing inside them. It is, therefore, important to understand the dependencies of frequency on the seismic energy released and on the dimensions of the focus. It makes sense that increased energy corresponds to a larger zone of irreversible deformation. Our experience also proved that the larger the zone of irreversible deformations is, then the lower

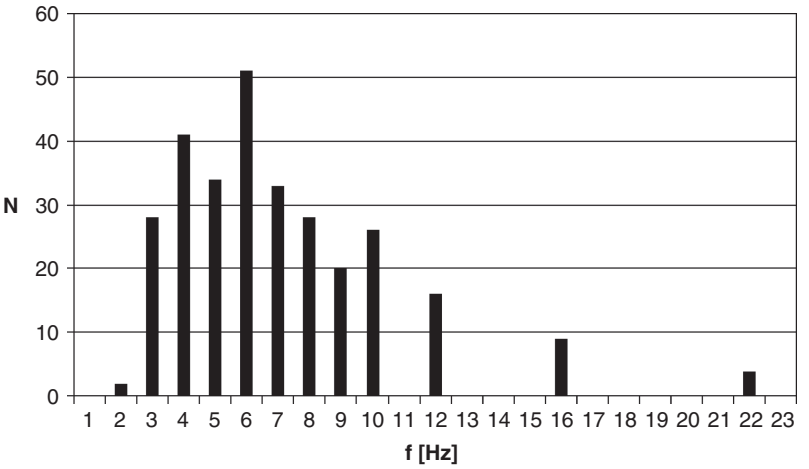


Figure 8 Histogram of prevailing frequencies of P-waves.

the predominant frequencies of vibrations radiated from the focus. The way in which rockbursts transfer their released energy from focus to the surrounding rock mass, and which different factors affect the propagation of the induced stress waves, are both difficult problems to solve. Apart from the obvious separation of individual types of seismic waves, which propagate with different velocities, the properties of these waves also influence both the amplitude and frequency of vibrations. The considerable disruptions of layers inside the coal basin provide essential barriers against propagation of the seismic waves and, at the same time, they partly influence the amplitude and frequency content of the wave train due to the dissipation of energy on these tectonic disruptions.

We constructed two datasets based on recorded and archived frequency data determined from readings on seismograms: (a) a histogram of practical frequency values, as shown in Figures 8 and 9; (b) a graph of the dependence of average frequency on the seismic energy released. In order to assess the predominant vibration frequencies of complex amplitudes of particle velocities, both P- and S-waves were used.

In comparing both graphs, it is evident that the range of frequencies for individual sets differ from each other. The range of P-waves at the level of 0.7 N_{max} of maximum, predominantly involves a frequency span of 4–6 Hz, while S-waves show frequencies approximately within the interval 3–4 Hz. In the second approach, frequencies were taken into account together with the relevant maximum of rockburst energies, for both wave groups. Notice the considerable scatter of individual values displayed, for example, in Figure 10, which presents a visual illustration of the dependency of frequency vs log E for P-waves, calculated as the weighted average given by the formula $f(\mathrm{Hz}) = \sum \mathrm{E.f} / \sum \mathrm{E}$. For the calculation of the prevailing frequency value, rockbursts estimated by energies within the span E = 6.2E + 03 J to E = 1.7E + 07 J were used. The resulting values for the vertical components of P- and S-waves were defined by values of f = 7.07 Hz and f = 3.93 Hz, respectively.

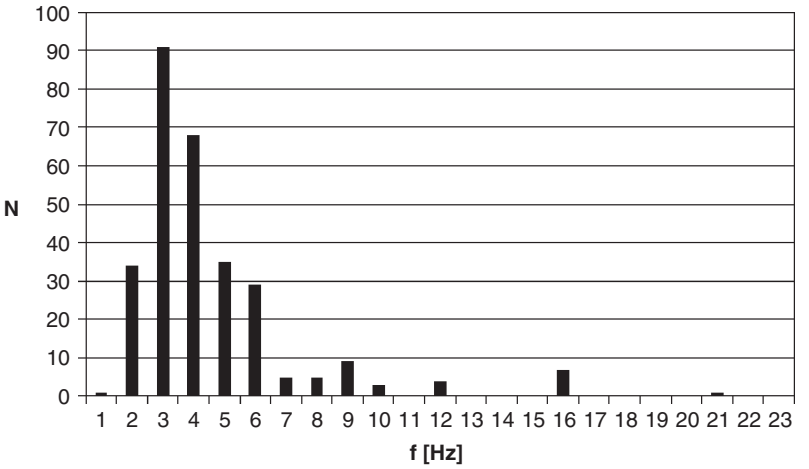


Figure 9 Histogram of prevailing frequencies of S-waves.

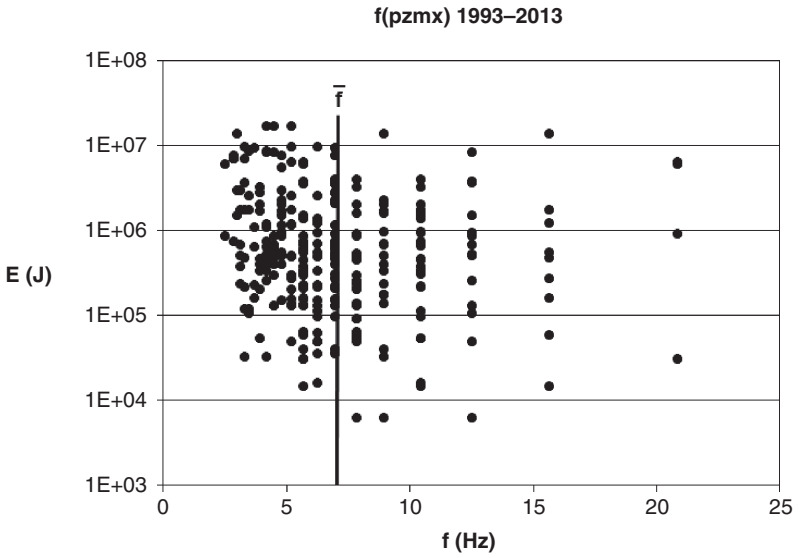


Figure 10 Dependence of frequency vs weighted average of energy for P-waves (vertical component).

5.4 Seismic energy

The estimation of the energy of mining-induced seismic events, recorded automatically at the seismic stations of the regional network within the OKCB, is determined by Equation 6 (for underground seismic stations, values related to S-waves are applied):

$$E_S = k.u_i^2.d^2.t.e^{2\alpha(d-1)} \quad (6)$$

where:

E_S – released seismic energy (J)
k – 8.748×10^{12} ($kg.m^{-2}.s^{-1}$)
u_i – complex value of particle velocity ($m.s^{-1}$)
d – hypocentral distance of focus (km)
t – length of the relevant wave duration (s)
α – attenuation coefficient (for S-waves $\alpha \approx 0.04$ km^{-1}).

5.5 Local magnitude M_L

The magnitude calculation is based on applying Equation 7 for the coal deposit, derived for the conditions of the OKCB which satisfy the equation:

$$M_L = 5.202 \log u_{max} + \log d + \alpha \log e^{(d-1)} \quad (7)$$

where:

u_{max} – vectorial sum of the particle velocity (m/s) observed at the respective seismic station
d – hypocentral distance between the rockburst focus and the seismic station (km)
α – attenuation coefficient (for P-waves $\alpha \approx 0.006$ km^{-1}).

In the process of finding the mutual relationship between the released seismic energy E and the value of the local magnitude M_L, the following empirical formula (Equation 8) was derived, which is also displayed in Figure 11:

$$E(J) = 341.1 \times e^{3.927 M_L} \; R^2 = 0.9135 \quad (8)$$

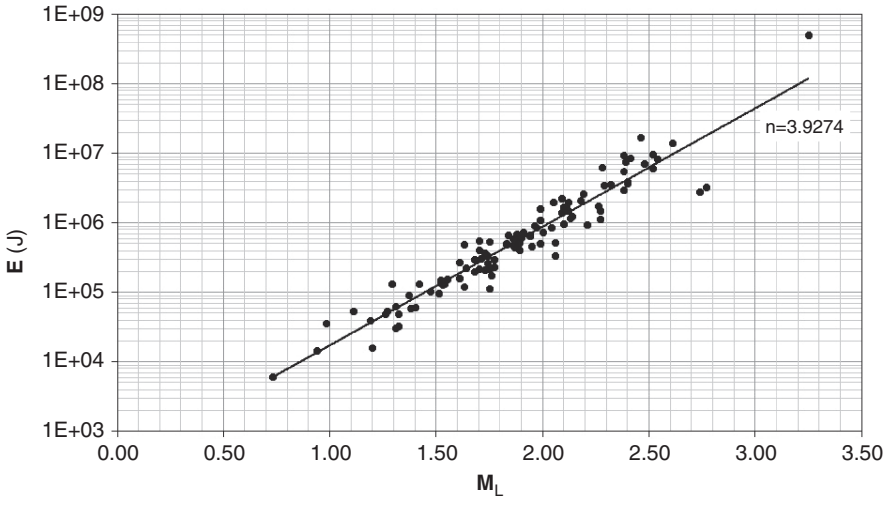


Figure 11 Depiction of linearity of log E vs M_L.

It can be observed that the data fit the linearity of both parameters very well, as is also evidenced by the relatively high value of correlation coefficient R^2: only three values for magnitude $M_L > 2.7$ disturb the minimal scatter of the strip of values.

5.6 Hypocentral distance calculation

In principle, two types of hypocentral distance calculation were performed, namely, the distance from the focus of the rockburst to the underground seismic station, and the distance from the rockburst focus to the center of the damage caused. Separate versions of Equation 9, using $_S$ or $_D$ as appropriate, were used for the calculation:

$$d_{FS,D}(m) = [(x_F - x_{S,D})^2 + (y_F - y_{S,D})^2 + (z_F - z_{S,D})^2]^{\frac{1}{2}} \quad (9)$$

where:

x_F, y_F, z_F; x_S, y_S, z_S and x_D, y_D, z_D are the coordinates of focus (F), seismic station (S) and center of damage (D), respectively.

5.7 Rockburst and explosion mechanisms

Based on detailed analysis of the waveforms, it was concluded that the essential feature that most of the rockbursts in the Ostrava-Karviná coal mine district have in the initial phase at their nuclei is a prevailing implosive component of motion, which is caused by the crushing of remnant pillars in the seams or a rock fall of gob situated in the roof. The rock failure follows on in combination with more or less proportionate shear failure along the planes associated with tectonic faults in the near field of the focus. This is distinct from rockbursts in the initial phase of blasting operations in which the predominant characteristic of the ground motion is represented by an explosive component, when particles of mass are propagating from the source into surrounding space. However, if a rockburst originates from blasting then the initial phase is, as a rule, short-lived with subdued amplitude by comparison with the implosion and/or shear failure described above.

6 STRESS WAVE AND WORKING DAMAGE

The stress during the propagation of the seismic wave can be calculated using the formula (Equation 10) derived, for example, by Brepta & Prokopec (1972):

$$\sigma_s = \rho_h \cdot v_i \cdot u_{max} \quad (10)$$

where:

σ_s – stress (Pa)
ρ_h – density (kg/m^3)
v_i – propagation velocity of seismic wave (m/s)
u_{max} – maximal particle velocity (m/s).

The average density of the adjacent Carboniferous rocks is about 2,600 kg/m^3 and the anticipated velocity of body wave propagation is approximately $v_P \approx 3{,}700$ m/s

and $v_S \approx 2{,}142$ m/s. The dependency of the particle velocities of body waves u_{max} versus the scaled distance r* is described in Section 5.1, and the values of particle velocities are defined by Equations 1 and 2. Using Equation 9 the hypocentral distance from the focus was used to calculate distances for determining the stress values which cause devastation of workings as a result of the propagation of seismic waves. The length of heavy falls in entries and roadways were taken as the criteria for the extent of such damage.

7 CASE STUDIES

7.1 Rockburst on 26 August 2008

The rockburst on 26 August 26 2008, at 18:10:56.88 UTC, occurred during extraction of coalface No. 139704-1 in coal seam 39, situated in the Lazy Mine at a depth of about 650–700 m. This coalface is part of the group of Saddle Members (Karviná Formation), the thickness of which was roughly estimated at between 4 m and 6 m, and the length of its face at approximately 180 m. The thickness of the main roof up to the nearest coal seam above, seam 38, varies between 10 m and 35 m and consists of fine- to medium-grained sandstone and siltstone. Toward the bottom, the interlayer thickness between coal seam 39 and seam 40 below amounts to about 50 m and has almost the same composition as the roof of coal seam 39. This particular rockburst released seismic energy amounting to a value $E = 6.02 \times 10^5$ J and, according to the local magnitude M_L scale, its interpreted magnitude was 1.9.

The focal region was localized to the upper roof, approximately 80 – 100 m above coal seam 39, and the rockburst was accompanied by a mining shock felt at the surface. The face layout showing the places where devastation occurred in the workings is illustrated in Figure 12. The main road, No. 39 705-1, was found to be free of any manifestations, whereas in the region of coalface No. 139 704-1, coal discharging from the pillar was found roughly 90 m along the face, some sections of the mounting were distorted, the power loader was damaged, the drag conveyor was displaced toward the caving, and both floor lift and mechanical damage to roadway pillar springers were evident.

The hanging wall throughout the whole length of the coalface was not damaged. Along ventilation gate No. 39 703-1, a floor lift of less than 1 m occurred, confined within a distance of roughly 40 m, and was accompanied by a moderate reduction of the cross section. Besides this, some timber posts were knocked out and the water barrier was damaged. All of the basic physical parameters were tabulated and heavy falls in the roadway are indicated in Figure 12 by bold crosses.

7.2 Rockburst on 2 October 2011

The rockburst on 2 October 2011 at 17:19:03.436 UTC in the Darkov Mine was triggered by a blast of high explosive charge, the total mass of which was 3,700 kg, being placed in the roof of coal seam 40 during mining of coalface No. 340 206. Destressing blasting and camouflet shotfiring of a large amount of explosive are the principal preventive measures employed to reduce rockburst hazard. Their efficiency can be verified by the use of seismic methods (Holub, 1999). In this case, the efficiency

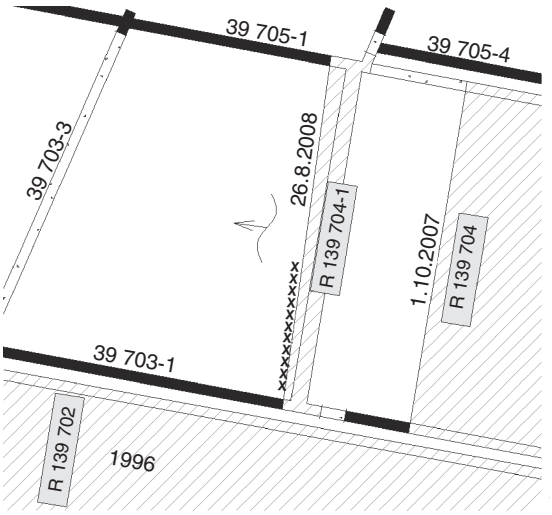


Figure 12 Underground situation after rockburst on 26 August 2008.

reached the value $\eta \approx 1{,}010$ or, in other words, the time to perform these blasting operations was overdue, because the state of stress in the massif was critical.

It is worth mentioning that another rockburst at this locality has already occurred on 23 May 2011 during the installation of technical equipment for this panel. The operation of the coalface under discussion started on 13 July 2011. In the zone immediately in front of the face were irregular unmined pillars, situated in goaf which were partly at the limits of stress state. Moreover, the southern part of the coalface was affected by additional stress from the edges of the irregular, unmined overlying seams 39 and 37. According to the results of the seismic evaluation, the focus was located in the immediate roof strata, approximately 20 m above seam 40 and approximately 70 m into the forefield of the coalface. Eventually, it was identified that this area corresponded with the positions of fired charges. In terms of manifestations in the workings some concluding remarks were withdrawn, for example, due to the rockburst a section of the main gate No. 340 226 was afflicted in length of 131 m. In this location, the lifting of the floor was such that the entire profile of the gate was gradually filled with mixed material (rocks and coal). Not only were deformations of the supports found, but by that time most of the supports had lost their shape. The situation underground in the area of the rockburst focal zone is illustrated in Figure 13.

7.3 Rockburst on 1 January 2012

The origin of this rockburst, in the ČSA Mine in Karviná on 1 January 2012 at 02:17:15.011 UTC, was localized to panel No. 22 3752, which was mined in seam 37. The released energy was calculated as 9.5×10^6 J. The panel was situated in the southern part of tectonic block 22, which represents the liquidated safety pillar of the main central shafts of the former Doubrava Mine. A very high predisposition to

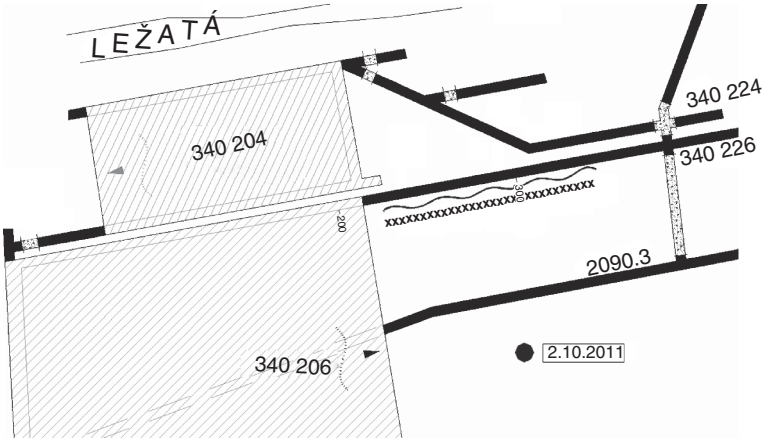


Figure 13 Underground situation after the rockburst on 2 October 2011.

rockbursts had already been documented during coal extraction in all of the surrounding coal seams mined at that time, not just in the course of mining coal seam 37 but also in other layers belonging to this series of Saddle Members, for example, seams 39 and 40. A deterioration in contemporary stress conditions caused the existence of pillars abandoned for protection of cross-cuts in overburden. In this way, a system of unmined seam edges was created, which with their additional stress influenced the stress state of the region, especially at the penetration area of both cross-cuts. Mining coal reserves in the safety pillar started at the level of coal seam 34, that is, at a depth of approximately 700 m below the surface.

The bedding of coal seam 37 was at a depth of roughly 800–850 m, the thickness of which was around 5 m. The roof of this seam, with a thickness of about 110 m, is built mainly from heavy layers of sandstones and conglomerates. After detailed analysis of this rockburst, it was documented that the focal region was situated in the upper roof, approximately 80 m above seam 37. After inspection of long face No. 22 3752, it was proved that some manifestations occurred exclusively along the opening gate, to a length of roughly 68 m, with a simultaneous floor lift of about 1 m, as illustrated in Figure 14. Moreover, because of the rockburst impact, some partial deformations of arched iron supports and damage to mechanical and electrical installations were documented.

7.4 Rockburst on 30 January 2013

The focal region of this rockburst was localized to the Lazy Mine, in the Karviná locality. It originated on 30 January 2013 at 00:31:01 UTC and released seismic energy $E = 1.4 \times 10^6$ J. The focus region was immediately adjacent to the floor of coal seam 38. Manifestations of this rockburst were concentrated along roads, Nos. 38 907-1, 38 917-3 and 38 809, all in the 8th tectonic block and in coal seam 38. In this area,

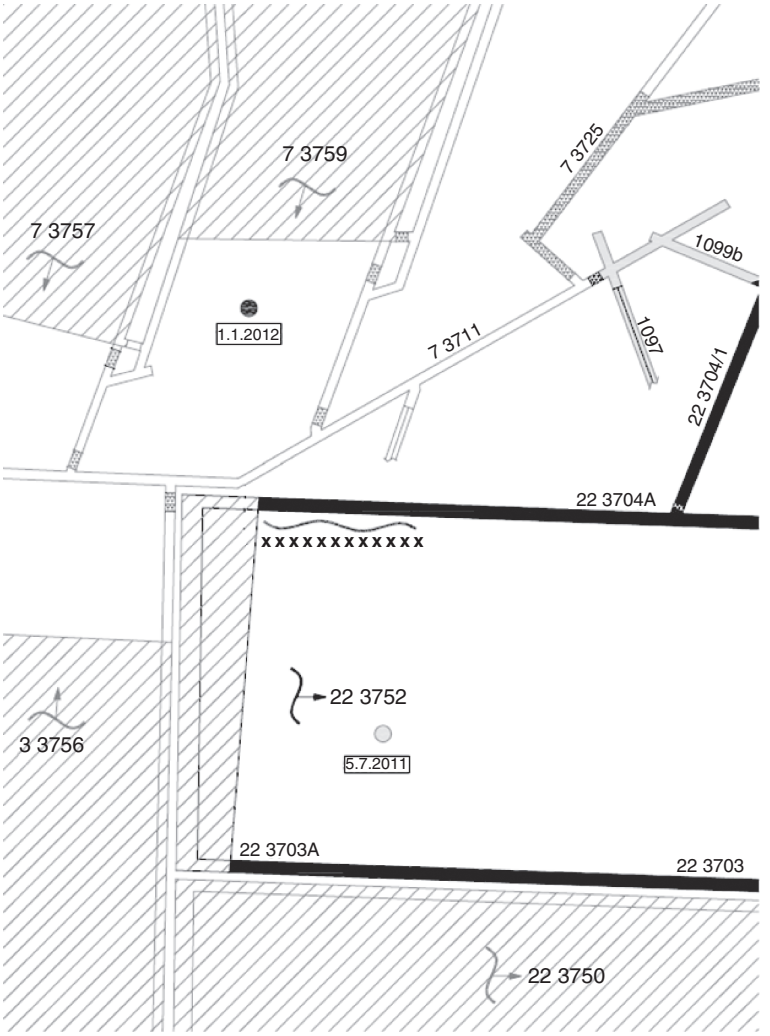


Figure 14 Underground situation after rockburst 1 January 2012.

the final coalface was under preparation. Coal seam 38 is situated in the western part of tectonic block 8 and is seated at a depth of 700–750 m under the surface with a typical thickness of 3.5–5 m. From a geomechanical viewpoint, the 8th tectonic block represents a very complicated structure because a lot of old workings, gates, residual pillars and some washouts are in existence. Coal seam 38 is flat-lying subhorizontally with a moderate slope to the north-west. The roof of this seam consists of sandstones, conglomerates and siltstones. At the time of the rockburst, which originated in the area of planned coalface No. 138 806, only preparatory mining activities had been conducted. The complicated situation, from a general operational viewpoint, around the focal region is presented in Figure 15.

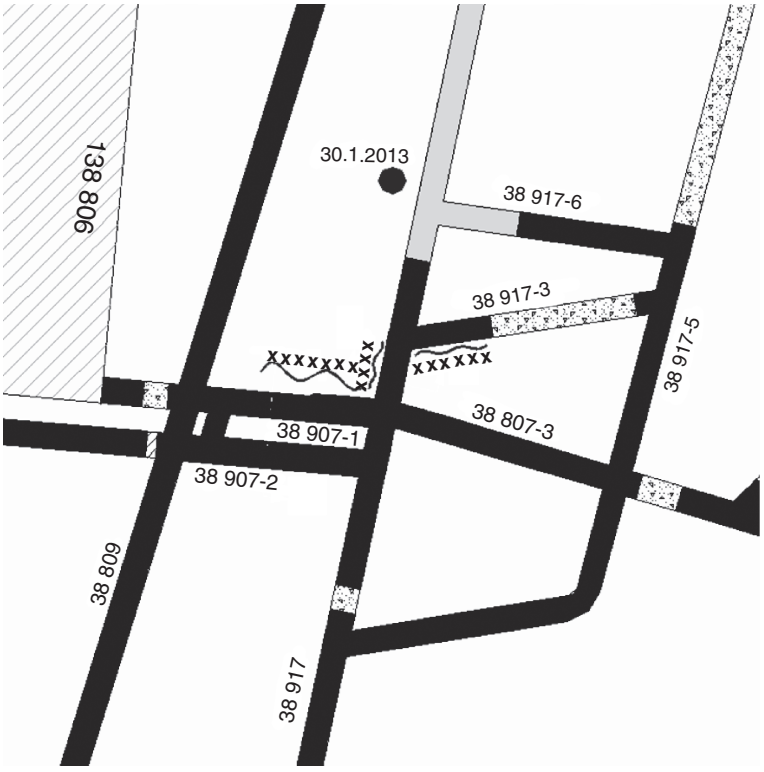


Figure 15 Underground situation after rockburst 30 January 2013.

7.5 Rockburst on 14 November 2014

This rockburst was detected in the ČSA Mine by seismic stations of the local, as well as regional, networks on 14 November 2014 at 10:44:18.191 UTC in the cross entry No. 22 3756 and its enlargement in the scope of development work for a new coalface No. 22 3756 in coal seam 37, as shown in Figure 16. Its released seismic energy was estimated as $E = 8.6 \times 10^6$ J and, according to the local magnitude M_L scale, this value corresponds to $M_L \approx 2.7$. Based on the seismological assessment of the situation, the focal region was localized in the roof approximately 80 m above coal seam 37, roughly 390 m eastwards from the position of its manifestations within the workings. It was stated that at that time no disturbances were observed that could cause interference with the equilibrium of the rock massif.

After inspection of the area afflicted, it was found that some explosion-proof barriers had been destroyed, a block of coal had been thrown into the gate and, moreover, a floor uplift was detected, the length of which was about 75 m having an average height of roughly 0.75 m. Another floor uplift was found in the enlarged part of the cross entry up to the roof; locally, this shift was represented by a height of up to 2 m, and elsewhere in a part of a gate that was not enlarged to start with, over time the uplift reached a height of 1.5 m. Several instances of damage to technical installations were also found.

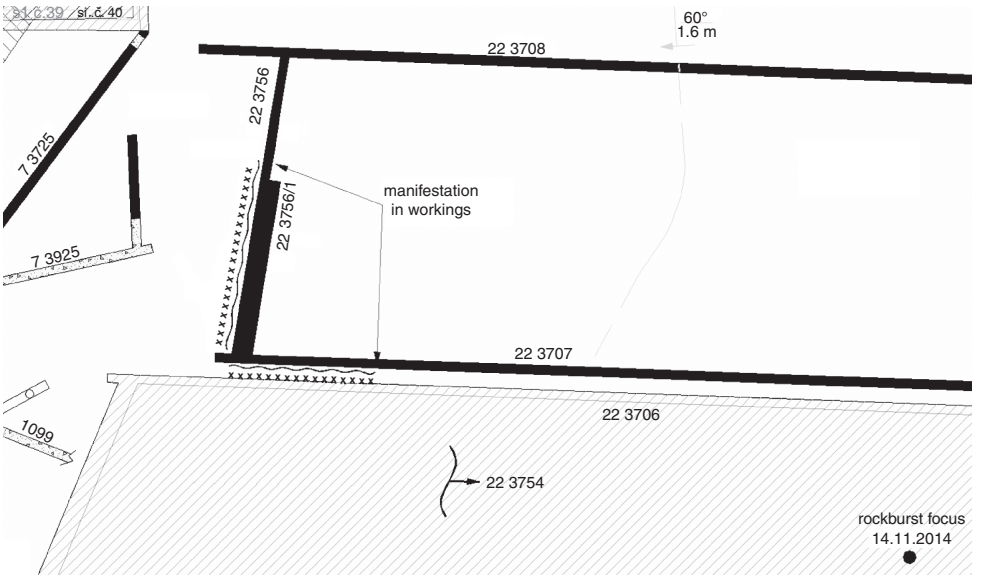


Figure 16 Underground situation after rockburst November 14, 2014.

8 SUMMARY

Our long-term underground seismic observations in the eastern part of the OKCB, which are being carried out on a continuous basis, have documented the existence of mining-induced seismicity. The origin of this phenomenon is closely linked to the existence of strata series with a relatively high strength, specifically in the form of thick and rigid overlying rocks, which are prone to rockburst occurrence and which overlay the coal seams. The rock failure process may then be triggered either by the long-lasting effects of mining-induced stresses that eventually exceed the strength of the rocks, or by the passage of seismic waves from a distant source. Taking into consideration the varying amounts of seismic energy released, only the events that caused evident and permanent deformation in working and roadway supports are classified as rockbursts, insofar as these supports are not designed to withstand the higher loadings generated by a rockburst. In short, many seismic field experiments have documented that the damage to both underground workings and surface structures caused by blasting could be determined by means of one parameter, namely, particle velocity, which, in fact, seems to be the best criterion for damage estimation. Since particle velocity during blastings proved to be a reliable criterion, the same parameter was accepted as a basis for evaluation of the underground damage induced by rockbursts. The investigations presented here focused on the measurements of particle velocity at underground seismic stations, which could be useful in research dealing with the study of physical and mechanical properties of rocks under dynamic loading, which in turn simulates the influence of rockbursts on workings. Consequently, a particle velocity parameter corresponding to the devastation in workings at various

hypocentral distances from rockburst foci can be determined. The present analysis of these dynamic phenomena derives from *in situ* seismic measurements, together with some additional and calculated data. Basically, we first of all investigated empirical dependencies of particle velocities with respect to scaled distance to calculate the decay factor for P- and S-waves. Given that we wanted to identify the contribution of individual components, especially of horizontal ones, to the vectorial sum, a detailed analysis was performed (displayed in Figure 6). It is obvious that the maximum scatter of values is exhibited in the graphs for both horizontal components, where regression coefficient R^2 subsequently has the minimal values. Therefore, the essential Equations 1 and 2 for decay of particle velocity were derived for complex amplitudes, and the slopes of regression straight lines were simultaneously computed. As demonstrated in Section 5.1, many authors can be cited as having arrived at similar values for the straight lines of slopes obtained from linear regression, which were mostly around the value of n = 1.0 ± 0.5. In principle, this parameter corresponds to the geometrical spreading of a planar wavefront according to the law 1/d. On the other hand, our experiments in open-pit mines proved that short charges put in shallow boreholes generated quite different waveforms, namely spherical ones. This type of waveform, spreading from a source in a spherical shape, can generally be approximated by the law $1/d^2$, as derived in Equations 3, 4 and 5, where the slope n of regression straight lines varies between 1.85 and 2.26. The circumstances of our experiments did not facilitate a continuous investigation of the distance at which the change of spherical waveform to cylindrical one becomes effective. Nevertheless, this change was to be expected, although some of the deliberations associated with an unambiguous explanation of this phenomenon are based only on speculation. Besides the investigation of particle velocity decay, the five case studies selected supplement the presentation of our effort to investigate some criteria for defining the extent of rock mass damage due to loading caused by the propagation of stress waves. When these stress waves are propagating through fractures and/or fractured zones, increased or reduced attenuation is observed. A lot of theories and models exist that attempt to establish laws for the propagation of stress waves, but it is not easy to find a universal approach that gives reliable results and is also applicable to geomechanical practice. Based on the frequency data gathered, two views were prepared: (a) histograms of practical frequencies for P- and S-waves; (b) graphs for both wave groups of the dependency between the weighted average of frequency and the released energy of rockbursts. It was found that the P-waves arriving first have the wider frequency range (4–6 Hz), while S-waves have the narrower range (3–4 Hz) with a distinct maximum at 3 Hz. The application of seismic observations aims to detect seismically active regions, investigate the development of seismic activity to assess rockburst hazard, and check the efficiency of measures applied in rockburst prevention. Seismic methods are used, for example, to check the efficiency of large-scale, non-productive blasting operations in the roof, which is based on the empirical formula, $\eta \approx$ seismic energy (J) / 2.6 × Q (kg) (Holub, 1999). This efficiency generally has low values, for example, $\eta \approx 1$–3, and we seldom find efficiency at the level of 10, 100 or more. Coincidentally, however, our selection of case studies does show one such highly efficient event. This special case, dated 2 October 2011, was the blasting operation with a total charge of 3,700 kg, whose efficiency had an extraordinary value equivalent to 1,010, which needs no further comment!

ACKNOWLEDGMENTS

The authors are grateful to the Institute of Geonics, which funded this work in terms of financial support to the research institutions. The authors thank Green Gas DPB (Paskov) for providing selected data for the period 2010–2015 from the material 'Analytical analysis of rockburst'. We are also indebted to Ing. V. Kajzar, PhD, for his assistance in preparation of the graphical supplements.

REFERENCES

Brepta, R. & Prokopec, M. (1972). *Propagation of stress waves and shocks in bodies*. Prague, Academia.

Chen, S.G., Cai, J.G., Zhao, J. & Zhou, Y.X. (2000). 3DEC modeling of a small-scale field explosion test. In: Girard, J., Liebman, M., Breeds, C. & Doe, T. (eds.) *Proceedings of the Fourth North American Rock Mechanics Symposium, Seattle, USA, 'Pacific Rock 2000'*. Rotterdam, Balkema. pp. 571–576.

Dopita, M. & Kumpera, O. (1993). Geology of the Ostrava-Karvina coalfield, Upper Silesian Basin, Czech Republic, and its influence on mining. *International Journal of Coal Geology*, 23, 291–321.

Dopita, M., Aust, J., Brieda, J., Černý, I., Dvořák, P., Fialová, V., *et al*. (1997). *Geology of the Czech Part of the Upper Silesian Basin*. Prague, Ministry of the Environment of the Czech Republic. pp. 278.

Dowding, C. H. (1992). Suggested method for blast vibration monitoring. *International Journal of Rock Mechanics and Mining Science & Geomechanics Abstracts*, 29(2), 145–156.

Dvorský, P. & Koníček, P. (2005). Systems of Rock Blasting as a Rockburst Measure in the Czech Part of Upper Silesian Coal Basin. In: Potvin, Y., Hudyma, M. & Potvin, Y. (eds.) *Controlling Seismic Risk*. Perth, Australia, Australian Centre for Geomechanics. pp. 493–496.

Egan, J., Kermode, J., Skyrman, M. & Turner, L.L. (2001). *Ground vibration monitoring for construction blasting in urban areas*. Sacramento, CA, State of California Department of Transportation.

Hedley, D.G.F. (1991). Peak particle velocity for rockbursts in some Ontario mines. In: Fairhurst, C. (ed.) *Rockbursts and Seismicity in Mines*. Rotterdam, Balkema. pp. 345–348.

Hendron, Jr. H.J. (1997). Engineering of rock blasting on civil projects. In: Hall, W.J. (ed.) *Structural and Geotechnical Mechanics*. Englewood Cliffs, NJ, Prentice Hall. pp. 242–277.

Holečko, J. & Koníček, P. (2007). Selected geological factors impacting effects of induced seismicity on surface in conditions of Ostrava-Karvina coalfield in the Czech Republic. In: Ribero e Sousa, L., Olalla, C. & Grossmann, N. (eds.) *11th Congress of the International for Society Rock Mechanics, Lisbon, Portugal*. London, Taylor & Francis. pp. 1177–1184.

Holub, K. (1997a). Predisposition to Induced Seismicity in Some Czech Coal Mines. *Pure Appl Geophys*, 150, 435–450.

Holub, K. (1997b). Seismic Monitoring for Rockburst Prevention in the Ostrava-Karviná coalfield, Czech Republic. In: Gayer, R. & Pesek, J. (eds.) *European Coal Geology and Technology*, Geolog Soc Special Publication No. 125. London, The Geological Society. pp. 321–328.

Holub, K. (1999). A Survey of Blasting Efficiency. *Publications of the Institute of Geophysics Polish Academy of Sciences*, M-22(310), 231–236.

Holub, K. & Tobyáš, V. (1987). Velocity of Ground Motion near Blasts in an Open-pit Mine. *Travaux Géophysiques XXXII (1984)*, No. 594. Prague, Institute of Geophysics of Czech Academy of Sciences. pp. 261–280.

Holub, K. & Tobyáš, V. (1989). Particle Velocities near Blast in Shale Open-pit Mine. *Travaux Géophysiques XXXIV (1987)*, No. 621. Prague, Institute of Geophysics of Czech Academy of Sciences. pp. 43–53.

Holub, K. & Rušajová, J. (2011). Peak particle velocity generated by rockbursts in underground coal mines and for shot-hole explosions in open-pit mines. *Acta Geodaetica et Geophysica Hungarica*, 46, 104–114.

Holub, K., Knotek, S. & Vajter, Z. (1988). Microseismology and Its Application in the Prevention of Rockbursts. *Publications of the Institute of Geophysics Polish Academy of Sciences*, M-10(213), 203–215.

Holub, K., Holečko, J., Rušajová, J. & Dombková, A. (2012). Long-term development of the seismic monitoring networks in the Ostrava-Karviná coal mine district. *Acta Geodynamica et Geomaterialia*, 9(2), 115–132.

Hrady. (2015). http://www.hrady.cz/index.php.?OID=3991, accessed 21 Mar. 2015.

Isaac, I.D. & Bubb, C. (1981). A study of blast vibrations – Part 1. *Tunnels and Tunneling*, July, 35–41.

Isaac, I.D. (1991). Effects of constructional vibrations upon an urban environment. In: *Earthquake, Blast and Impact – Measurement and Effects of Vibration*. London, Elsevier Applied Science. pp. 442–462.

Jiao, Y.Y., Zhao, J. & Cai, J.G. (2003). Consideration for 2-D and 3-D modelling of shock wave propagation in jointed rock masses. In: *ISRM 2003 – Technology roadmap for rock mechanics*. Johannesburg, Southern African Institute of Mining and Metallurgy. pp. 583–586.

Kárník, V., Michal, E. & Molnár, A. (1958). Erdbebenkatalog der Tschechoslowakei bis zum Jahre 1956. *Travaux de l'Institut Géophysique de l'Academie Tchécoslovaque des Sciences*, No. 69. pp. 411–598.

Klika, Z. (1999). Oxidative altered coal from Upper Silesian Coal Basin. *Journal Czech Geological Society*, 44(3–4), 335–342.

Klíma, B. (1955). Výsledky archeologického výzkumu na tábořišti lovců mamutů v Petřkovicích, okr. Ostrava v roce 1952 a 1953 [The results of archeological research at the camping-site of the mammoth hunters in Petřkovice, district Ostrava in the years 1952 and 1953]. *Časopis Slezského Musea*, IV series B – Historia, 1–35.

Knotek, S. & Holub, K. (1980). Application of seismoacoustics in the Ostrava-Karviná coalfield. In: Proceedings of the 7th National Conference of Geophysicists, Gottwaldov, Czechoslovakia. pp. 79–83.

Landek Park. (2015). http://www.landekpark.cz/landek-park, accessed 21 Mar. 2015.

OstravaFOTO. (2015). Historie těžby v Ostravě, http://www.ostravafoto.cz/historie-tezby-v-ostrave, accessed 21 Mar. 2015.

Petroš, V. & Holub, K. (2003). Investigation of ground velocities during the rockbursts. *Acta Montana,* Series A, 22(129), 15–20.

Sambuelli, L. (2009). Theoretical derivation of a peak particle velocity-distance for the prediction of vibrations from blasting. *Rock Mechanics Rock Engineering*, 42, 547–556.

Siskind, D.E., Stagg, M.S., Kopp, J.W. & Dowding, C.H. (1980). *Structure Response and Damage Produced by Ground Vibration from Surface Blasting, RI-8507*. Minneapolis, MN, US Department of the Interior, Bureau of Mines.

Trávníček, L. & Holečko, J. (1980). First results of the seismic recording of rock bursts in the Ostrava-Karviná Coal District. *Publications of the Institute of Geophysics Polish Academy of Sciences*, M-3(134), 73–83.

Trávníček, L., Holečko, J., Klíma, K., Ruprechtová, L. & Špičák, A. (1987). Seismological development of progressive failure of the rock mass in an area prone to anomalous rock bursts. *Acta Montana, Series A*, 75, 175–191.

Chapter 22

Rockburst induced ground motion

Z. Zembaty
Faculty of Civil Engineering, Opole University of Technology, Opole, Poland

Abstract: The local magnitudes m_L of strong rockbursts from 4 to 5, with respective depths of their focuses from 1 to 3km may lead to substantially strong ground motion, comparable to the surface effects of nuclear underground explosions and respective damages in buildings and civil infrastructure. In this chapter characteristic features of the ground motion records acquired during mine tremors are analyzed in detail. Based on this data a proposal for design response spectra and an adaptation of Eurocode 8 to mitigate the rockburst surface ground motion effects on structures is presented.

1 INTRODUCTION

In a paper from the early nineties of the 20th century, Jonstone (1992) provided a simple classification of rockbursts by describing six distinct mechanisms of their origin (Jonstone, 1992). She also divided rockbursts into two general categories:

– Type I – directly related with mining activities and with low to medium magnitude.
– Type II – only loosely correlated with mining activities and with focuses in a wider area around the mine, but with potentially higher magnitude.

It was demonstrated later, in a paper by Zembaty (2004), that this classification also holds for the epicentral (or close to epicentral) surface records of the respective mine tremors.

Type I rockbursts occur with a return period of 1–3 months and their acceleration records resemble distant records of surface quarry blasts (Dowding, 1996). Type II rockbursts occur rarely in a 3–4 years return period and their records are similar to the epicentral records of weak, shallow earthquakes. Indeed, type II rockbursts are attributed to earthquakes triggered by the mining activities on pre-existing faults, which without the mining activities would stay inactive.

The aim of this chapter is to present more information on the surface ground motion produced by rockbursts and better asses the intensities of mine seismic events on the ground surface. A brief information on modeling rockbursts as civil engineering loads in structural design will also be reported.

2 GROUND MOTION PARAMETERS

For the purpose of this study the ground motion parameters can be divided into five categories:

– descriptive intensity parameters (local Mercalli intensities),
– energy measures of ground motion records like the Arias (1970) intensity,
– measures of peak ground motion (acceleration – PGA, velocity – PGV and displacements – PGD),
– spectral parameters (Fourier and response spectra),
– measures of strong motion duration.

The local Mercalli intensities applied here are Modified Mercalli (MM), Medvedev, Sponhauer Karnik (MSK-64) and Mercalli, Cancani, Sieberg (MCS). The first two of them (MM and MSK-64) can be treated as almost identical for civil engineering purposes (Trifunac & Brady, 1975a). The third (MCS) differs more, though not very substantially (Trifunac & Zivcic, 1991).

The Arias intensity (1970) in a modified form, as applied in this study, is a measure of energy transmitted through the ground surface:

$$I_A = \int_0^{t_k} a^2(\tau)d\tau \tag{1}$$

where *a(t)* stands for the acceleration record with total duration t_k. Using the cumulative Arias intensity, *i.e.* so called Husid plot:

$$H(t) = \frac{\int_0^{t} a^2(\tau)d\tau}{\int_0^{t_k} a^2(\tau)d\tau} \tag{2}$$

Trifunac & Brady (1975b), proposed their definition of strong motion duration, t_d as the time for the Husid plot to stay between 5 and 95 per cent.

Except for the descriptive Mercalli intensities, all the other ground motion parameters are separately defined for each of the three Cartesian axes *x, y z*. To apply these parameters independently of the instrument orientation they should be formulated separately for horizontal and vertical direction. The latter one remains unchanged as there is only one vertical axis, whereas from two horizontal records along *x* and *y* axes, one measure should be derived. From a civil engineering point of view the roles of horizontal and vertical excitations are totally different because buildings differ with respect to their horizontal and vertical properties. In particular vertical building stiffness is usually much more substantial than the horizontal one.

The peak ground motion parameters (*PGA, PGV* and *PGD*) are formulated as vertical and horizontal, with the horizontal ones being just 2D surface maxima:

$$\max \sqrt{x^2(t) + y^2(t)} \tag{3}$$

and denoted as PGA_{hor}, PGV_{hor} and PGD_{hor} respectively.

The horizontal and vertical Arias intensities can be formulated as follows:

$$I_A^{hor} = \frac{1}{2}\int_0^{t_k}[a_x^2(\tau) + a_y^2(\tau)]d\tau,$$
$$I_A^{ver} = \int_0^{t_k} a_z^2(\tau)d\tau. \tag{4}$$

The horizontal and vertical strong motion durations are formulated using analogously modified Husid plots of Equation 2:

$$H^{hor}(t) = \frac{\int_0^{t}[a_x^2(\tau) + a_y^2(\tau)]d\tau}{\int_0^{t_k}[a_x^2(\tau) + a_y^2(\tau)]d\tau},$$
$$H^{ver}(t) = \frac{\int_0^{t} a_z^2(\tau)d\tau}{\int_0^{t_k} a_z^2(\tau)d\tau}. \tag{5}$$

The horizontal Arias intensity can be interpreted as averaged values of these quantities derived from their respective measures along x and y axes. This way respective horizontal strong motion durations can easily be formulated.

3 SURFACE RECORDS OF ROCKBURSTS AND THEIR INTENSITY

3.1 Selected records of rockbursts and their analysis

Consider a surface record of a rockburst measured on March 15th, 2000 in a Copper Basin "LGOM" of south-western Poland (Fig. 1).

It can be seen that the duration of this record is very short. Taking into account the Trifunac-Brady (1975b) criterion of the time needed to build 5–95% of the Husid plot (Equation 5), its horizontal duration equals t_d = 1.43s, while the vertical duration is even shorter and equals 1.18s. Another interesting observation is its spectral content, seen in the plots of the power spectral densities (Fourier spectra) of the three acceleration components. The dominating energy content is well above 10Hz. What is more the contribution of the energy below 5Hz is only marginal. And it is the frequency band from 0 to 5Hz, which decides about exciting the typical buildings into vibrations. For these reasons, in spite of rather high Peak Ground Accelerations (PGA) respective peak velocities (PGV) are relatively small, at about 2cm/s. The ratio of PGA/PGV for the 'y' component equals about 35. For typical earthquakes

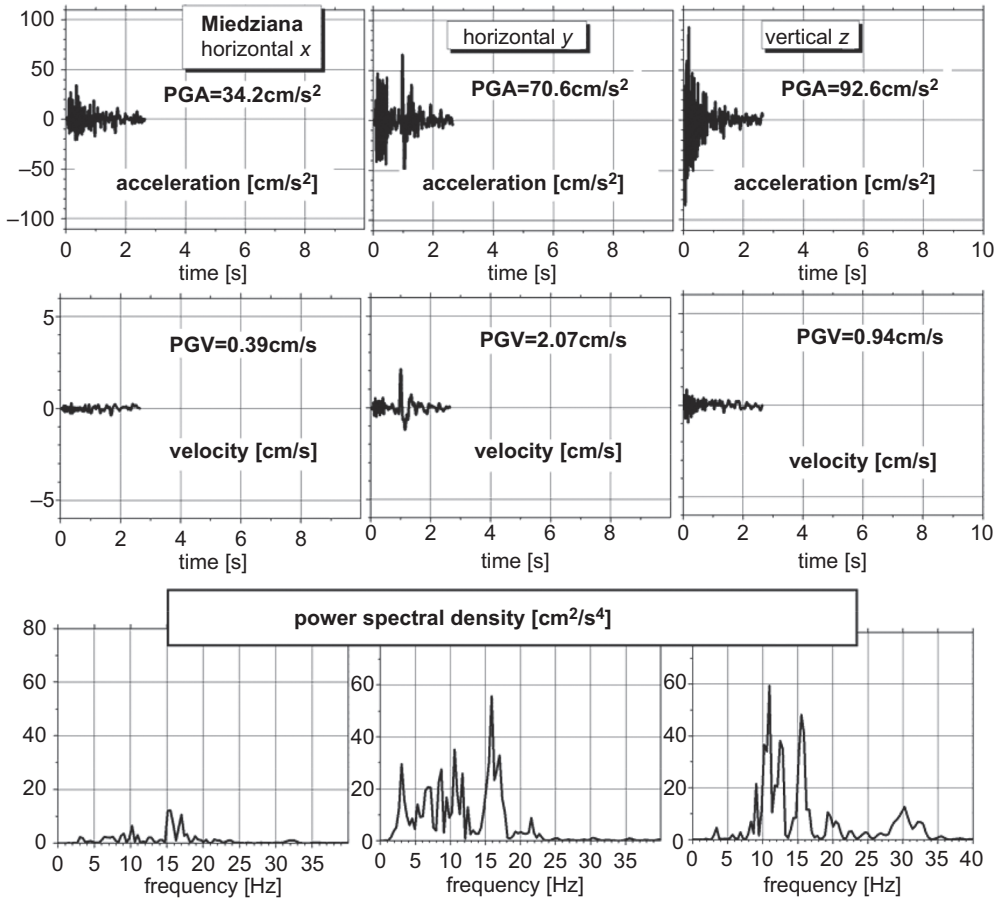


Figure 1 Surface accelerations and velocities of a rockburst measured at station "Miedziana" street on March 15th, 2000 in the city of Polkowice (Copper Basin LGOM in Poland) together with Fourier spectra of the acceleration records in two horizontal directions (*x*, *y*), as well as in the vertical one (*z*).

shaping engineering design codes (like the well known El Centro record) it equals about 10. Such the record with many respects resembles close distant ground records of quarry blasts. The only similarity to seismic record is the fact that the vertical component is the most shifted to higher frequencies, which is characteristic for very close epicentral distances of natural earthquakes. The PGA/PGV ratio reached in this case almost 100.

Consider now another rockburst record from the *LGOM* City of Polkowice, shown in Fig. 2. It is the most intensive record from very strong rockburst of May 21st 2006 (magnitude $m_L = 4.3$).

The strong motion duration equals in this case 4.93s for the horizontal components and 1.27s for the vertical one. Examining the respective spectral content of this rockburst record, reveals that almost total energy of the '*y*' acceleration record stays within

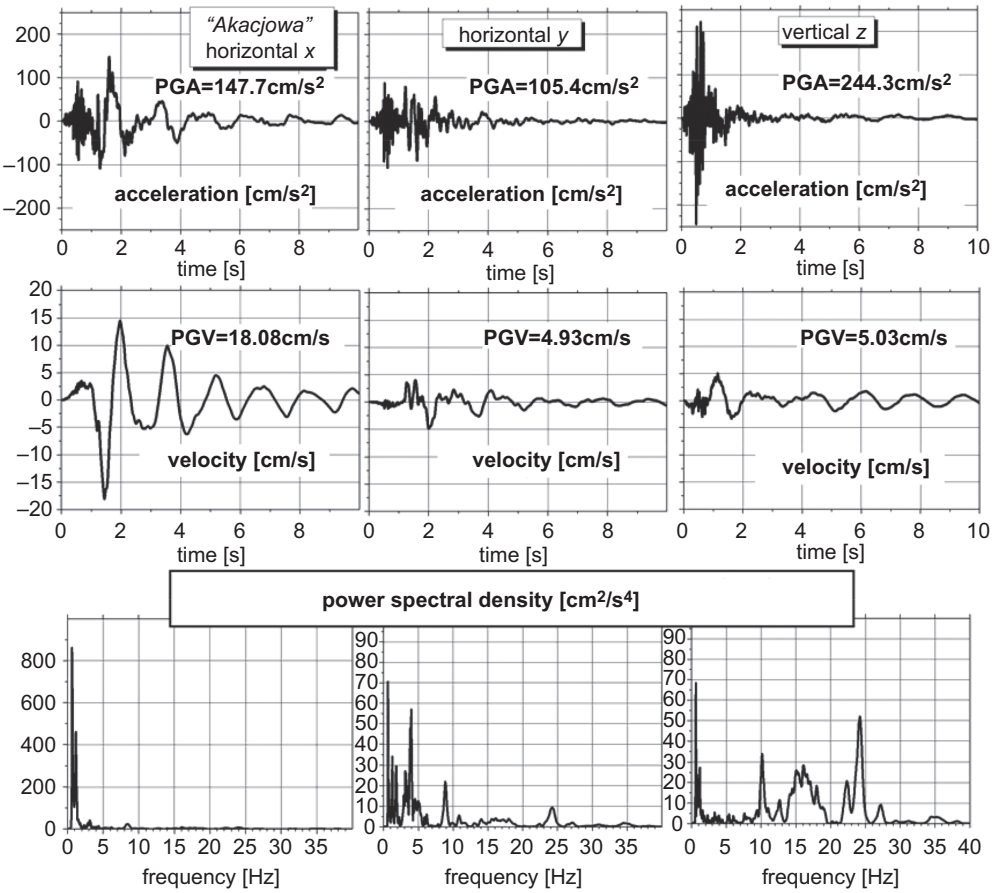


Figure 2 Surface accelerations and velocities of a rockburst measured at station "Akacjowa" street on May 21st, 2000 in the city of Polkowice (Copper Basin LGOM in Poland) together with Fourier spectra of the acceleration records in two horizontal directions (*x, y*), as well as in the vertical one (z). Note different vertical scale of the 'psd' of the 'x' component.

the 0–5Hz frequency band. The '*y*' record displays a velocity pulse typical for very short epicentral records of natural earthquakes (see *e.g.* Makris & Black, 2004).

Consider now yet another record of a strong rockburst, this time the most intensive record of the rockburst of magnitude m_L = 4.2, which took place in Katowice (Upper Silesian Coal Basin of southern Poland).

Respective strong motion duration of the horizontal component equals 1.52s in this case and 1.64s for the vertical component. In spite of this rather short duration the spectral content of this record, particularly for one of its horizontal components (*y*) dominates in the frequency range of 0–5Hz.

A broader set of rockburst records and earthquakes was studied in detail, in an earlier paper by Zembaty (2004). The main conclusion of these studies confirm the Jonstone (1992) classification of rockbursts onto the type I and type II. When it comes to surface acceleration records the type I and type II rockbursts differ with respect to

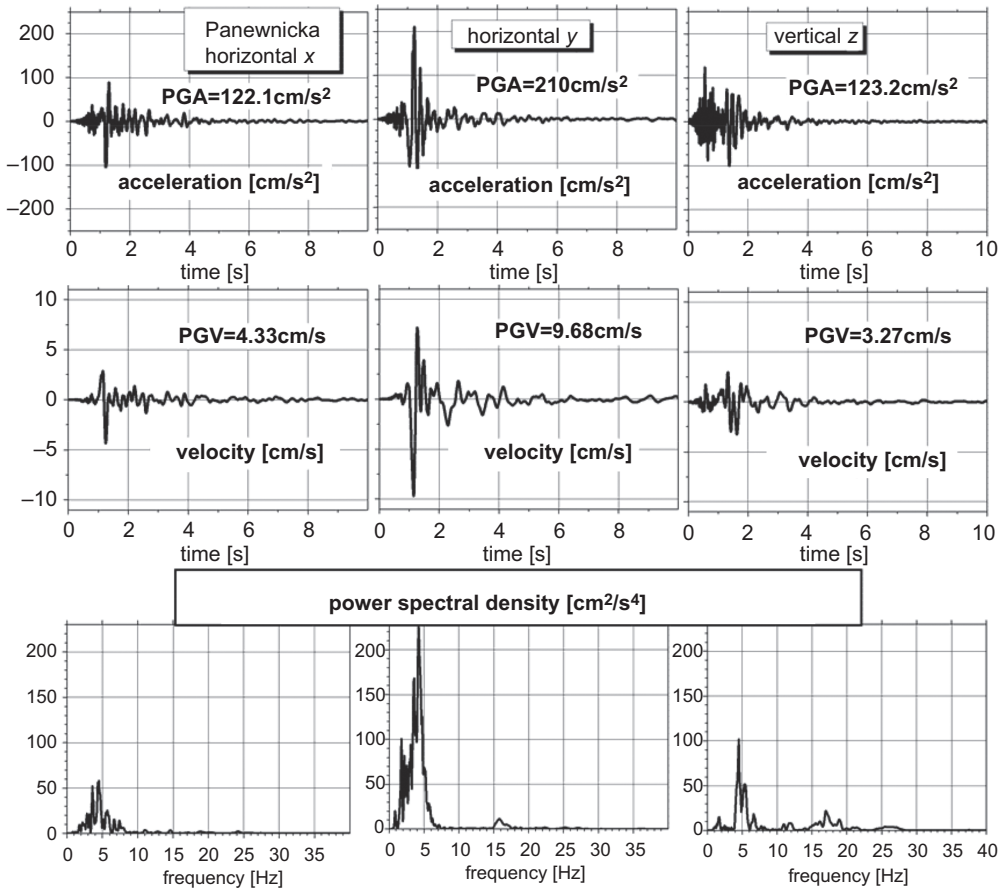


Figure 3 Surface accelerations and velocities of a rockburst measured at station "Panewnicka" street on April 18th, 2015 in the Katowice (Upper Silesian Coal Basin in Poland) together with Fourier spectra of the acceleration records in two horizontal directions (*x*, *y*), as well as in the vertical one (*z*).

their spectral content and PGA/PGV ratio. This is illustrated in Fig. 4 in which both types of record are shown.

It can be seen from this figure that in spite of rather high peak acceleration (PGA = 101cm/s^2), respective peak velocities of type I records are rather low (PGA/PGV = 40). The type II record showing PGA = 70cm/s^2 and PGV = 5.2cm/s (PGA/PGV = 13.5) displayed also longer duration of 5s compare to about 1s of the type I accelerogram. The power spectral density of both records compared with Fourier spectra of typical earthquakes reveals that type I records simply lack the spectral band from 0–5s critical for structural excitations. Indeed the record of type I and PGA = 101cm/s^2 did not cause even minor structural damages, while the type II record of PGA 70cm/s^2 strongly shaken nearby buildings leading to various non-structural damages. That is why not only for natural earthquakes their peak velocity is a much better measure of intensity. The role of peak velocity is particularly important

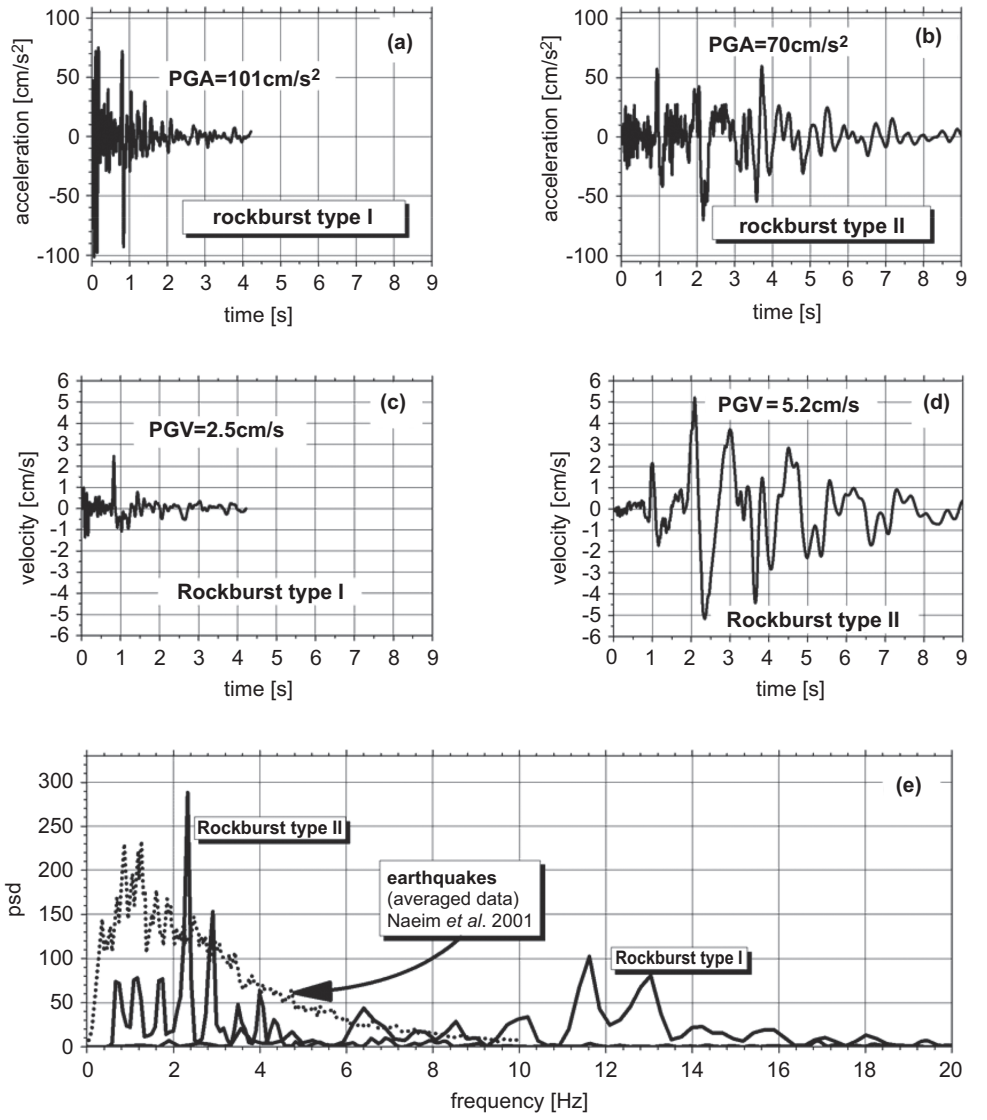


Figure 4 Comparison of typical type I (a, c) and type II (b, d) rockburst records with natural earthquakes (Naeim, 2001) in frequency domain (e).

to measure rockburst intensity, just like it is reported for the industrial blasts (Dowding, 1996).

3.2 Intensity of surface rockburst records

Taking into account energy released, strong type II rockbursts with their magnitudes m_L exceeding 4.0 in Europe and even reaching 5.3 in South Africa (McGarr *et al.*, 1989;

Durrheim, 2010) should be classified close to nuclear underground explosions, but after typical quarry blasts which were extensively studied during the 20th century (see *e.g.* book by Dowding, 1996). Local magnitudes of 4 to 5, with the focal depths of 1 to 3km may lead to epicentral intensities of *MM* VI to VIII, and indeed structural damages even exceeding *MM* = VIII are reported from the strongest rockbursts (see *e.g.* Durrheim, 2010). Since the vicinity around mines is often a place of building and construction activities, the problem of assessing rockburst intensity, in order to properly manage seismic risk, is of great importance (see *e.g.* Van Eck *et al.*, 2006).

Proper assessment o the surface intensity is the first step in mitigating these effects on civil engineering structures, however it is not a straightforward task. When using instrumental measures, well known from seismic engineering, like the peak ground accelerations (PGA) the intensities may be substantially overestimated because in many cases, due to the reported frequency shifts, the peak accelerations could resemble natural earthquakes of much stronger surface intensity. That is why the old descriptive scales (*MM, MSK-64* or *EMS*) still should be used to asses rockburst intensity. On the other hand, usually the mining areas are well instrumented with ground vibration sensors, which may tempt to build relations based on the actual measurements. In the papers by Zembaty (1998, 2004, 2007) these problems are analyzed in detail taking into account specific diversities of the rockburst records with respect to their spectral content and duration. In Fig. 5 two important instrumental measures of low intensity earthquakes and rockbursts PGA and PGV are shown together.

It is interesting to note the substantial difference between records of the natural earthquakes and rockbursts with respect to their peak values. The type II rockbursts are, on the other hand, much more similar to the earthquake records. It should however be noted that the durations of the records of rockburst type II is still much shorter than durations of typical earthquakes. Although some, selected earthquake records (*e.g.* the strong record of the Friuli Italian earthquake) can be as short as 5s, the majority of them, particularly those, which help calibrate the Mercalli intensity scales, are much longer, usually at about 15–30s. For the purpose of computer simulations seismic code Eurocode 8 (2005) is using a 15s lasting definition of seismic time history record. In the case of the two rockbursts of May 21st 2006 (Fig. 2) and April 18th 2015 (Fig. 3) with their horizontal durations of 4.93s and 1.52s respectively, the actual intensities, as obtained from structural damages observed at the recording sites, could be assessed at about MM = VI for the first one and MM = IV for the second one.

4 MODELING ROCKBURST LOADS FOR THE DESIGN OF CIVIL INFRASTRUCTURE

4.1 Methodology

Problems with proper assessment of the surface rockburst intensities are not the only ones met when one wants to mitigate rockburst effects on buildings and civil engineering structures. The key problem is the proper adaptation of the civil engineering seismic codes of practice, *e.g.* Eurocode 8 (2005) or the International Building Code (2009) applied in USA.

These codes are prepared for the natural earthquakes, typically with the return period of about 500 years, which correspond to peak ground acceleration level to be exceeded

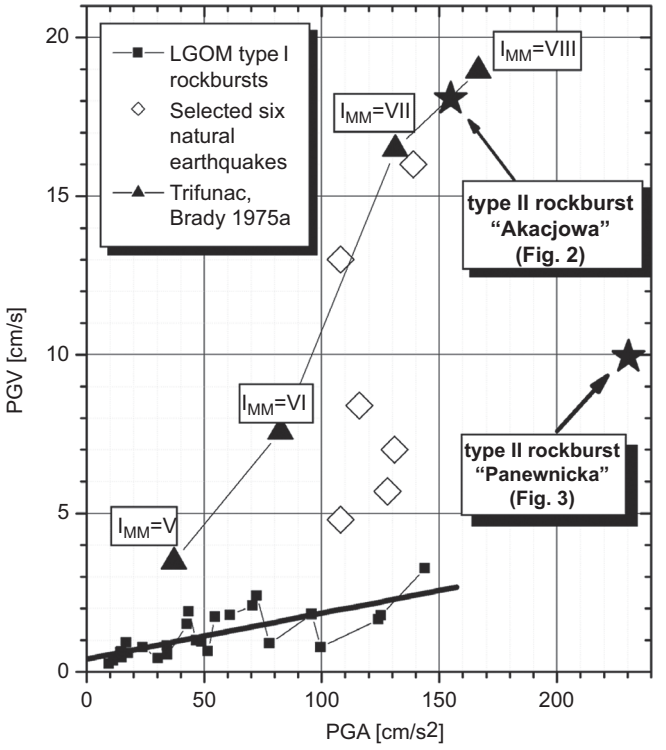


Figure 5 Peak Ground Acceleration vs. Peak Ground Velocity of type I and type II rockbursts and selected low intensity earthquakes listed in the paper by Zembaty (2004) as well as intensity estimations of Trifunac & Brady (1975a).

with 10% probability in 50 years as defined for the 475 years in Eurocode 8 (2005). For such the rare events, buildings are allowed to substantially deform, accumulating seismic energy by specially designed zones of plastic deformations. The typical expected, strong rockburst return period equals 2–4 years clearly not fitting to the natural seismic risk definition. On the other hand, if one assumes "no damage" policy in the seismic design applying linear structural response approach, the resulting design forces could be overwhelming and leading to a unnecessary very conservative design.

These problems where analyzed in detail within the framework of a 3 year research program (Zembaty *et al.*, 2012) and resulted in an adaptation of Eurocode 8 (2005) for the purpose of the design of structures under rockburst seismic loads.

Consider a simple representation of an oscillator, standing for a single-degree-of-freedom (*sdof*) model of a structure with mass m and horizontal stiffness k, under seismic excitations $u(t)$ (Fig. 6).

The typical approach of seismic civil engineering codes is to generate an averaged acceleration response spectrum as a function of natural period and structural damping and to apply it in modeling of so called *base shear force* representing horizontal structural load for either *sdof* or *mdof* (multi-degree-of-freedom) structures. The shape of the

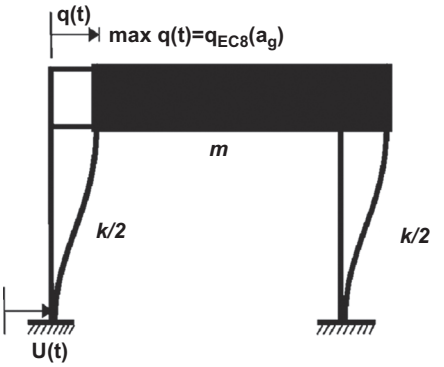


Figure 6 Single-degree-of-freedom structure under seismic, rockburst excitations u(t) with displacement response q(t) corresponding with equivalent Eurocode 8, maximum displacements.

design response spectrum is based on spectral properties of the expected excitations. The key problem to address is to properly decide about the level of assumed excitations which is modeled by the design acceleration a_g. In the seismic codes this is a probabilistic value applied based on long term seismic risk studies and decide by national authorities. In Eurocode 8 it is the value expected with 475 years return period or not to be exceeded with the 90% probability in 50 years. The level of expected mine tremors depends on the mine activity and is forecasted by special geophysical services of the mines. Because the ground velocity seems so far the best rockburst intensity measure (Zembaty, 2004), it was decided to relate the design acceleration with the velocity forecasted by the mines, with an appropriate level of confidence. The only remaining problem is to link the expected peak ground velocity with the design acceleration. It was done by calculating the displacement response spectrum $S_d(T)$ based on the acceleration response spectrum $S_a(T)$ using the familiar formula of seismic engineering (*e.g.* Clough & Penzien, 1976).

$$S_d(T) = (T/2\pi)^2 S_a(T) \tag{6}$$

and fitting the design displacement response spectra to the rockbursts displacement response spectra of particular intensities measured by peak velocities v_g (Zembaty, 2011). This way the same effective level of structural response is confirmed for the rockburst record of particular ground velocity v_g and for the acceleration design response spectrum of particular design acceleration a_g. The procedure is repeated for all the available records of strong, type II rockbursts and the results are statistically processed with an assumed, appropriate level of confidence, which leads to special coefficient 'r' linking forecasted ground velocity with the appropriate value of design acceleration. In the recommendations for the LGOM Copper Basin of Poland (Zembaty *et al.*, 2012) the value of $r = 7.74$ obtained from the numerical analyses was decided to be changed to $r = 10$, taking into account some conservatism expected in structural design, when accounting for the well known uncertainty of the rockburst phenomenon.

More detailed description of the methodology is given in the paper by Zembaty *et al.* (2015). In what follows a brief description of the key findings are given.

4.2 Site-dependent, design response spectra

When the number of credible strong, type II records of rockburst ground motion with PGV > 2.5cm/s, reached about 18 or more samples, it became possible to follow typical seismic engineering procedures of building the averaged, design response spectra depending on the Eurocode 8 (2005) site classification. An algorithm leading to the design response spectrum for three specific sub-soil types *A*, *B* and *C*, of Eurocode 8 was prepared (Zembaty *et al.*, 2012, 2015) and the resulting response spectra are given in Equations 7 and 8 for the linear response

$$S_a = a_g\beta(T) = a_g S\begin{cases}\left[1+\dfrac{T}{T_B}(2.5\eta-1)\right] & 0<T<T_B\\ 2.5\eta & T_B\le T\le T_C\\ 2.5\eta\dfrac{T_C}{T} & T_C<T\le T_D\\ 2.5\eta\dfrac{T_C T_D^2}{T^3} & T>T_D\end{cases} \tag{7}$$

and for soil *C*

$$S_a = a_g\beta(T) = a_g S\begin{cases}\left[1+\dfrac{T}{T_B}(2.5\eta-1)\right] & 0<T<T_B\\ 2.5\eta & T_B\le T\le T_C\\ 2.5\eta\dfrac{T_C^{1.5}}{T^{1.5}} & T_C<T\le T_D\\ 2.5\eta\dfrac{T_C^{1.5}T_D^{1.5}}{T^3} & T>T_D\end{cases} \tag{8}$$

where β represents a dynamic factor, while coefficient η stands for damping other than 5%

$$\eta = \sqrt{\frac{10}{5+100}} \ge 0.55 \tag{9}$$

with the parameters S, T_B, T_C and T_D given in Tab. 1

In Equations 10 and 11 respective response spectra accounting for partial inelastic response are given for soil type *A* and *B*:

Table 1 Parameters describing site depended response spectra (Equations 7–11) for soil types *A, B & C*.

Soil type	*S*	T_B	T_C	T_D
A (v_{S30} > 800m/s)	0.8	0.1	0.85	1.3
B (800m/s > v_{S30} > 360m/s)	1.0	0.1	0.95	1.3
C (360m/s > v_{S30} > 180m/s)	1.5	0.3	0.80	1.3

Note: v_{S30} – averaged shear wave velocity in the top 30m sub-soil of the site, a primary parameter defining local site conditions (Eurocode 8, 2005)

$$S_a = a_g \beta(T) = a_g S \begin{cases} \left[\frac{2}{3} + \frac{T}{T_B}\left(\frac{2.5}{q} - \frac{2}{3}\right)\right] & 0 < T < T_B \\ \frac{2.5}{q} & T_B \le T \le T_C \\ \frac{2.5}{q}\frac{T_C}{T} & T_C < T \le T_D \\ \frac{2.5}{q}\frac{T_C T_D^2}{T^3} & T > T_D \end{cases} \tag{10}$$

and for soil C:

$$S_a = a_g \beta(T) = a_g S \begin{cases} \left[\frac{2}{3} + \frac{T}{T_B}\left(\frac{2.5}{q} - \frac{2}{3}\right)\right] & 0 < T < T_B \\ \frac{2.5}{q} & T_B \le T \le T_C \\ \frac{2.5}{q}\frac{T_C^{1.5}}{T^{1.5}} & T_C < T \le T_D \\ \frac{2.5}{q}\frac{T_C^{1.5} T_D^{1.5}}{T^3} & T > T_D \end{cases} \tag{11}$$

In Fig. 7 plots of the response spectra given by Equations 7 and 8 are shown.

It should be noted that the inelastic spectra of Equations 10 and 11 can be applied with the EC-8 behavior factor equal to 1.5 for most of the structures except for the free standing walls or chimneys or so called inverted pendulum structures of high elevated mass (see the respective definitions in Eurocode 8), in which case linear approach of Equations 7–8 is recommended.

5 SUMMARY AND CONCLUSIONS

An analysis of the intensive, surface records of rockbursts is presented in detail. Based on their spectral content the surface rockburst records are classified as two main types:

- Type I – with low intensity and typical return period of a few months, characterized by high accelerations, low particle velocities and very short durations (about 1s) and Fourier spectra shifted to higher frequencies, often above 20Hz,
- Type II – with much stronger intensity and return period of a few years, characteristic, higher particle velocity, longer duration and spectral content dominating in the lower frequency part of the spectrum, similar to the records of low intensity, natural earthquakes.

Based on the extended analyses of many rockburst records it was concluded (Zembaty, 2004) that the best parameter measuring surface intensity of the rockburst excitations is its peak horizontal velocity (*PGV*). When comparing rockbursts with natural earthquakes, substantially shorter strong motion durations should also be taken into account.

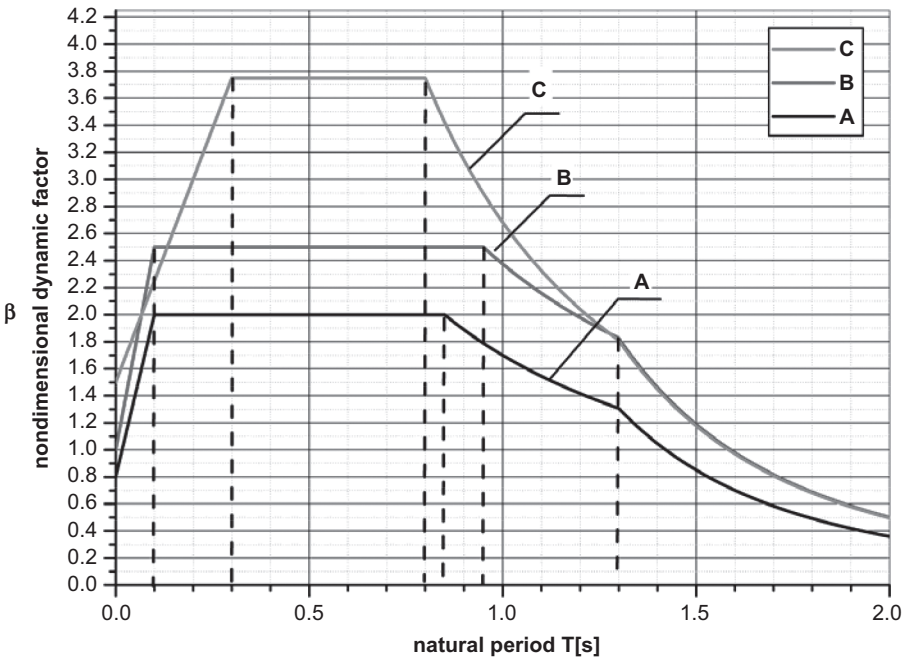


Figure 7 Plots of design response spectra (formulas 7 and 8) for the damping ratio $\xi = 0.05$ and three Eurocode 8 soil profiles A, B, C (design acceleration $a_g = 1 m/s^2$).

Based on this research results, a detailed algorithm is formulated to mitigate these effects in structural design. Respective procedure consists of following steps:

- Preparation of maps with maximum surface peak, horizontal velocity as forecasted by the mine services for the whole period of the mine exploitation.
- A design response spectrum accounting for the local site conditions is prepared (based on a viable set of strong, type II records and using respective soil amplification information available)
- The design response spectrum is scaled using so called 'displacement approach' approach of seismic engineering to obtain equivalent design acceleration corresponding to forecasted peak ground velocity. This calibration corresponds with the same maximum displacement response of the oscillator of Fig. 6 due to rockburst of particular peak velocity and under the design accelerations.
- Respective design response spectrum together with the design accelerations corresponding to respective zones of forecasted max ground velocities are used in the design of structures which may also partly account for inelastic structural response.

REFERENCES

Arias, A. (1970): A measure of earthquake intensity, in: Seismic Design for Nuclear Power Plants, edited by: Hansen, R. J., MIT Press, Cambridge, Massachusetts, 438–483.

Clough, R.W., Penzien, J. (1993) *Dynamics of Structures*, McGraw Hill, Inc., New York.
Dowding, C.H. (1996) *Construction Vibrations*, Prentice-Hall, New Jersey.
Durrheim, R.J. (2010) Mitigating the risk of rockbursts in the deep hard rock mines of South African: 100 years of research. In: J. Brune (Editor), *Extracting the Science: A Century of Mining Research, Society for Mining*, Metallurgy, and Exploration, Inc., pp. 156–171.
EN 1998-1. Eurocode 8 (2005) *Design of Structures for Earthquake Resistance*. CEN, Brussels.
IBC (2009), International Building Code, International Code Council 2009, Inc., www.iccsafe.org/Pages/default.aspx
Johnston, J.C. (1992) Rockbursts from a global perspective. In: P. Knoll (Editor), *Induced Seismicity*. Balkema, Rotterdam, Brookfield, pp. 63–78.
Makris, N., Black C.J. (2004) Evaluation of peak ground velocity as a "good" intensity measure for near-source ground motions. *Journal of Engineering Mechanics, ASCE*, vol. 130, no. 9, pp. 1032–1044.
McGarr, A., Bicknell, J., Sembera, E., Green, R.W.E. (1989) Analysis of exceptionally large tremors in two gold mining districts of South Africa. *Pure and Applied Geophysics*, vol. 129, pp. 295–307.
Naeim, F. (2001) *The Seismic Design Handbook*, 2nd edition, Kluwer, Dordrecht.
Trifunac, M.D., Brady A.G. (1975a) On the correlation of seismic intensity scales with the peaks of recorded strong ground motion, *Bulletin of the Seismological Society of America*, vol. 65, 139–162.
Trifunac, M.D., Brady A.G. (1975b) A study on the duration of strong earthquake ground motion, *Bulletin of the Seismological Society of America*, vol. 65, pp. 581–626.
Trifunac, M.D., Zivicic, M. (1991) A note on instrumental comparison of the Modified Mercalli Intensity (MMI) in the western United States and the Mercall-Cancani-Sieberg (MCS) intensity in Yougoslavia, *European Earthquake Engineering*, vol. 5, pp. 22–26.
Van Eck, T., Goutbeek, F., Haak, H., Dost, B. (2006) Seismic hazard due to small-magnitude, shallow-source, induced earthquakes in The Netherlands, *Engineering Geology*, vol. 87, pp. 105–121.
Zembaty, Z. (2004) Rockburst induced ground motion – a comparative study, *Soil Dynamics and Earthquake Engineering*, vol. 24, pp. 11–23.
Zembaty, Z. (2007) Non-stationary random vibrations of a shear beam under high frequency seismic effects, *Soil Dynamics and Earthquake Engineering*, vol. 27, no. 11, pp. 1000–1011.
Zembaty, Z. (2011) How to model rockburst seismic loads for civil engineering purposes?, *Bulletin of Earthquake Engineering*, vol. 9, no. 5, pp. 1403–1416.
Zembaty, Z., Lai, C., Kokot, S., Scandella, L., Bozzoni, F., Nowak, H., Kuś, J, Bobra, P., Jaśkiewicz, K., Król, P. (2012) *Code of Practice for Approval and Reviewing of Design Solutions Related to Mitigate Mine Tremors Effects in LGOM Region*. Report of Opole University of Technology for KGHM Consortium, vol. 1 & vol. 2, pp. 1–177.

Chapter 23

Settlements induced by TBM excavation

S. Aversa[1], *E. Bilotta*[2], *A.M. Ferrero*[3] & *M. Migliazza*[4]
[1]*Department of Engineering, University of Napoli Parthenope, Naples, Italy*
[2]*Department of Civil, Architectural and Environmental Engineering, University of Napoli Federico II, Naples, Italy*
[3]*Department of Earth Sciences, University of Torino, Turin, Italy*
[4]*Department of Earth Sciences, University of Milano, Milan, Italy*

Abstract: The need for a correct evaluation of settlements induced by TBM excavation in weak rocks is particularly high in urban areas, where shallow tunneling is carried out underneath or in the proximity of existing buildings or lifelines. It is worth noting that the deformation process occurring during tunneling is rather difficult to reproduce completely in modeling, hence simplifications are needed. This chapter describes existing methodologies to predict the displacement generated by excavation with TBM.

1 INTRODUCTION

The construction of a shallow tunnel not only affects the underground stress field but, overall, it induces a displacement field that eventually involves the structures located in the tunnel proximity. Similarly, the presence of structures modifies the ground response and, consequently, it changes the induced field of displacements. Buildings and other structures close to the tunneling area are hence affected by differential displacement, rotation and strain that can be a source of functional or structural damage. Although the topic is dealt with in most cases with reference to shallow tunneling in soft ground conditions, the importance of such an issue has been increasingly highlighted in weak rocks, with special reference to weathered rocks. Several degrees of weathering, from intact rock to residual soil, are often found along the same stretch of a shallow tunnel. In such cases, TBM excavation may be helpful, particularly in urban areas, to minimize the impact of excavation underneath existing sensitive buildings.

If based on the induced displacements field, the design process of tunnels follows the subsequent steps:

- definition of acceptable values of settlement (absolute, differential, rotation or angular and horizontal strains); these depend on the site characteristics and the structural features of the buildings or other existing structures possibly affected by the excavation;
- analysis of the excavation process that generates the surface and subsurface displacements; often the transient condition of underpassing TBM is more critical than the stationary conditions at the end of the excavation phases.
- technical and economical design optimization through the detailed definition of all the construction phases and the choice of possible mitigation works.

Due to the linear extension of the urban tunnels, several typological and structural differences may exist among the buildings and structures affected by the excavation. It is generally not economically convenient to carry out rigorous and detailed analysis along the whole tunnel path and for all the structures nearby. For this reason, a preliminary evaluation of the induced settlement is generally carried out, aimed at defining the potential building damage. Hence, a simplified approach is often followed, as for instance that suggested by Burland (1995), Mair *et al.* (1996), Potts & Addenbrooke (1997) and Franzius (2003). More rigorous and detailed analyses (*i.e.* 3D FEM analyses) are carried out only in those situations where the simplified approach indicates a moderate or severe level of damage and a further refined assessment is required.

This chapter presents some of the existing methodologies for assessing ground movements induced by TBM excavation. Empirical, analytical and numerical approaches are discussed. They have been widely adopted for prediction of tunneling induced movements in soft ground, nevertheless they can be useful for weathered rock and mixed ground conditions where tunneling in presence of ubiquitous discontinuities or complex formations can also induce large settlements. However, only a few case histories of settlement induced by TBM excavations in rock masses are reported in the literature (Chiriotti *et al.*, 2004; Grasso *et al.*, 2003, 2007).

For this reason a collection of empirical and analytical methods specifically developed for soil are suggested in the following. Their application to discontinuous media like fractured rock masses needs the mechanical characterization of an equivalent medium taking into account the presence of discontinuities. Furthermore, the use of empirical methods in such ground conditions needs an initial calibration phase by means of the comparison between theoretical prediction and in situ measurements and observation.

When the rock mass cannot be considered as an equivalent continuum or if the empirical–analytical methods do not give reliable results, a numerical model is needed. In section 6 some possible numerical approaches and the main relevant issues are described.

2 EXCAVATION TECHNOLOGIES – TUNNEL BORING MACHINES

The need for a faster tunnel construction led to adopting excavation techniques, which allow the installation of the long-term lining soon after the excavation. Shields are used for this purpose, also in open face excavations, but in the last decades much progress has been made in constructing and using closed-face shields. Tunnel Boring Machines (TBMs) are able to pressurize the front and to sustain with their shields the lateral boundary of the cavity up to their tail. The provisional lining can therefore be avoided, provided that the permanent one is installed just after the TBM, inside the shield. The permanent lining is usually made of pre-cast concrete segments.

The term TBM is adopted worldwide for all the excavation machines having a full-face cutterhead for excavating a tunnel.

Several classifications of full-face tunneling machines have been proposed (Guglielmetti *et al.*, 2008) by different national associations: the Japan Tunnelling Association subdivided TBMs on the basis of the excavation mode that can be either full- or partial-face. They group them on the basis of the contrast system used to apply the thrust (grippers or

longitudinal jacks); the German tunnelling association (*Deutscher Ausschuss fur unterirdisches Bauen* – DAUB) in 1996 proposed to classify TBM depending on the presence of the shield; the French tunnel society (*Association Française des Travaux En Souterrain* – AFTES) suggested its classification based on the type of support during excavation.

The classification developed by the International Tunnelling Association (ITA), and accepted by the Italian Tunnel Society (Società Italiana Gallerie – SIG) subdivided TBMs according to both the support that the machine is able to supply and the type of ground they can excavate. In particular open, single and double shielded, TBMs for rocks and compressed air closed shields, slurry shields Earth Pressure Balance (EPB) shields for soft ground TBMs.

The choice among different typologies of machine is driven by geotechnical conditions, and it heavily influences the advance rate, especially in hard rock.

The progress in shields technology and the increased experience of workmanship nowadays allow lower tunnel-induced ground movements than in the past, but both aspects still influence significantly the potential of predicting accurately such induced movements.

Depending on the kind of adopted technology, several sources of ground loss may be identified (see next sections). These components have differing importance on the total amount of ground loss around the excavation.

It can be observed clearly that the deformation process occurring during tunneling is a very complex three-dimensional problem that is rather difficult to reproduce completely in modeling. The problem becomes even more complex when the excavation interacts with existing tunnels or structures in the vicinity. Therefore, simplifications are necessary and inevitable.

3 SETTLEMENT INDUCED BY TUNNELING: 3D GEOMETRY AND MAIN CAUSES

The amount of ground movements that develops during tunneling is of course related to the chosen technologies and to the geotechnical characteristics of the excavated medium and of its overburden. A typical settlement through induced by shallow tunneling is shown in Figure 1.

A sketch of the main components of ground movement caused by tunneling with a shield is shown in Figure 2.

The displacement field induced by tunnel excavation with a Tunnel Boring Machine is the result of various phenomena:

1. face deformation due to stress release: this is a negligible quantity if Tunnel Boring Machines are used with an appropriate pressure control;
2. movements induced by shield advancing: these are due to the extra cutting (which is necessary to reduce friction between the shield and the ground) and to the shield pitching and yawing. These latter contributions are more evident for large shields and when the workmanship is not trained to the peculiar ground conditions;
3. closing of the gap between the lining and the shield tail: it can be reduced by means of properly designed grout injections;
4. lining deflection due to the earth pressure: this is often a negligible quantity;
5. long term volume change due to the consolidation process induced in clayey soils or induced by delayed deformation in weak rocks.

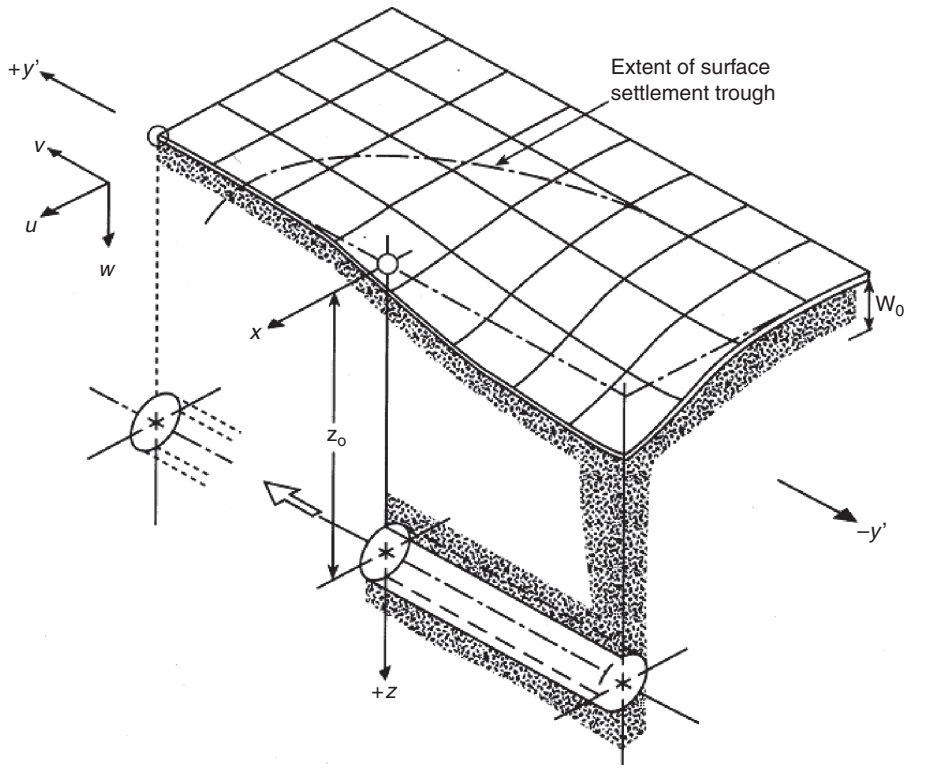


Figure 1 Ground movements induced by tunnel excavation (after Attewell *et al.*, 1986).

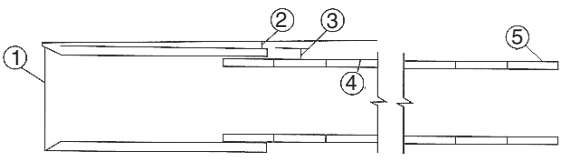


Figure 2 Components of ground movements induced by shield excavation (after Cording, 1991).

In Figure 3 the main components of displacements and strain are shown:

- Settlements $w_o(x)$ and subsurface vertical displacements $w(x,z)$ in a transverse vertical section;
- Surface $u_o(x)$ and subsurface $u(x,z)$ horizontal displacements in a transverse vertical section;
- Horizontal surface strain $\varepsilon_x(x)$ (positive if compressive, negative if tensile)
- Longitudinal surface displacement profile along a vertical longitudinal plane.

Ground movements induced by tunneling can be predicted by different methods: empirical methods, analytical approaches and numerical models, as discussed in the following sections.

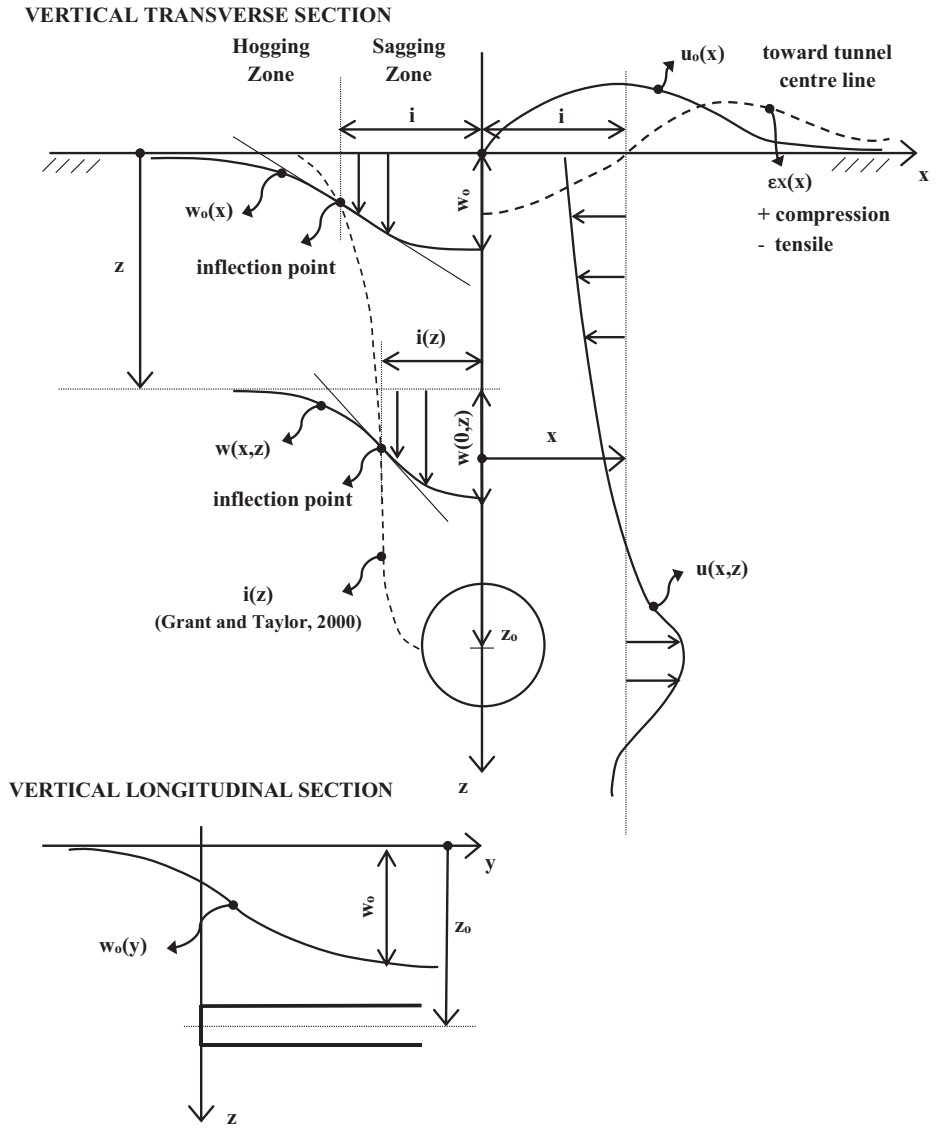


Figure 3 Surface and subsurface displacement and strain distributions in transverse section and longitudinal direction.

4 EMPIRICAL AND SEMI-EMPIRICAL APPROACHES

Peck (1969) showed that the transverse settlement trough induced by a single tunnel excavation, in 'greenfield' conditions (*i.e.* without structures above), is closely described by a normal Gaussian distribution (Figure 3):

$$w_o(x) = w_o \exp\left(\frac{-x^2}{2i^2}\right) \tag{1}$$

where

$$w_o = \frac{0.31 V' D^2}{i} \tag{2}$$

V′ is the volume loss defined as the ratio between the volume of settlement trough V_S and the nominal volume excavated ($V_T = \pi D^2/4$) per unit length.

The value of V_S can be computed by the integral of the Gaussian function reported in (1):

$$V_S = \int_{-\infty}^{\infty} w_o(x) = \sqrt{2\pi} i \, w_o \tag{3}$$

A large number of site measurements justifies the use of an empirical method based on the Gaussian distribution. One of the first cases in which the induced ground movements were widely measured is reported by Attewell & Farmer (1974). The large number of available data permitted to the Authors to draw interesting remarks on the various amounts of volume loss coming from the different abovementioned sources.

It is commonly assumed that the surface trough volume equals the extra-volume excavated around the cavity. This assumption is valid in clay at short term, *i.e.* in undrained conditions, while consolidation occurs in clay at long term. In dense granular soil, the trough volume reduces because dilatancy occurs. The amount of V′ depends on the type of ground and on the excavation method. Mair & Taylor (1997) revised a wide series of case histories and concluded that:

- in open face excavations in stiff clay, V′ ranges between 1% and 2%;
- if a sprayed concrete lining is adopted, its values reduce between 0.5% and 1.5%;
- in excavation with Tunnel Boring Machines, V′ can be lower than 0.5% in sand while it is between 1% and 2% in soft clay.

The parameter *i* represents the half-width of the sagging part of the settlement trough. O'Reilly and New (1982) showed that this parameter is approximately linear with the depth z_o of the tunnel axis, and proposed:

$$i = 0.43 z_o + 1.1 \quad \text{for fine grained soils} \tag{4}$$

$$i = 0.28 z_o - 0.1 \quad \text{for granular soils} \tag{5}$$

However, they suggest to assume:

$$i = K z_o \tag{6}$$

which is now common practice. The choice of *K* depends largely on the type of ground: Mair & Taylor (1997) analyzed a large number of case histories confirming the conclusions by O'Reilly & New (1982) on the values assumed by *K*. It generally varies between 0.4 and 0.6 for fine grained soils. Values above 0.5 often occur in soft clay and can be justified by the major difficulty in isolating the consolidation settlements. For

granular soils, Mair & Taylor (1997) observed that K ranges between 0.25 and 0.35, with a larger scatter than for clays, but without a clear distinction between soils above and below the groundwater, in spite of what suggested by Peck (1969).

For complex geological conditions, Chiriotti *et al.* (2001) proposed to adopt the values shown in Table 1. It takes into account both the condition at the front and the overburden ground.

As far as the subsurface vertical displacements at a given depth z are concerned they can be evaluated by empirical method adopting again a Gaussian distribution with a distance of inflection point from the tunnel centerline (Figure 3), estimated as:

$$i(z) = K_z(z_o - z) \tag{7}$$

On the basis of both field measurements and centrifuge tests, Mair *et al.* (1993) showed that K_z is not constant but increases non-linearly with depth:

$$K_z = \frac{0.175 + 0.325(1 - z/z_o)}{(1 - z/z_o)} \tag{8}$$

For granular soils, Moh *et al.* (1996) proposed a general formula to evaluate the trough width parameter, *i(z)*, at a depth of z:

$$i(z) = bD\left(\frac{z_0 - z}{D}\right)^m \tag{9}$$

where D is the tunnel diameter, (z_0-z) the elevation from the tunnel axis depth, z_0, and b and m two parameters.

Combining a Gaussian distribution of vertical subsurface displacement, characterized by a distance of inflection point defined by the combination of Equations 2, 7 and 8 it is possible to define the maximum settlement of subsurface trough as:

$$w(0,z) = \frac{0.31 \cdot V'}{0.175 + 0.325\left(1 - \frac{z}{z_o}\right)} \frac{D^2}{z_o} \tag{10}$$

Assuming that the resultant displacement vectors point toward the center of the tunnel, the horizontal surface displacement can be derived as (O'Reilly & New, 1982):

$$u_o(x) = -\frac{x \cdot w_o(x)}{z_o} \tag{11}$$

They are directed toward the tunnel center line and their distribution reaches the maximum value in correspondence of the inflection point i.

By differentiating the horizontal displacement with respect to x it is possible obtain the surface horizontal strain distribution, necessary to estimate the damage degree induced to the structure

$$\varepsilon_x(x) = \frac{w_o(x)}{z_o}\left(\frac{x^2}{i^2} - 1\right) \tag{12}$$

The empirical method can be adopted also to predict the ground movements in the three-dimensional problem of an advancing tunnel. In this case, the longitudinal profile

Table 1 V′ and K in mixed condition (after Chiriotti *et al.*, 2001 in Guglielmetti *et al.*, 2008).

		Ground conditions at the tunnel face			
		Soil like material	*Mixed conditions (soil &rock mass)*	*Faults or weathered bands*	*Discontinuous rock mass and weak rock*
Overburden conditions	*Soil like material*	c = 0 → V′ = 1%; K = 0.3 c > 0 → V′ = 0.8%; K = 0.5	c = 0 → V′ = 1.2%; K = 0.3 c > 0 → V′ = 1%; K = 0.5	c = 0 → V′ = 1%; K = 0.3 c > 0 → V′ = 0.8%; K = 0.5	c = 0 → V′ = 0.8%; K = 0.3 c > 0 → V′ = 0.5%; K = 0.5
	Mixed conditions (soil & rock mass)	V′ = 0.5–0.7%; c = 0 → K = 0.3 c > 0 → K = 0.5	V′ = 0.6–0.8%; c = 0 → K = 0.3 c > 0 → K = 0.5	V′ = 0.5–0.8%; K = 0.5–0.7	V′ < 0.5%; K = 0.5–0.7
	Faults or weathered bands	V′ = 0.4–0.8%; c = 0 → K = 0.3 c > 0 → K = 0.5	V′ = 0.5–0.9%; c = 0 → K = 0.3 c > 0 → K = 0.5	V′ = 0.6–1.2%; c = 0 → K = 0.3 c > 0 → K = 0.5	V′ = 0.4–0.9%; K = 0.5–0.7
	Discontinuous rock mass and weak rock	V′ = 0.3–0.5%; K = 0.5–0.7	V′ = 0.4–0.6%; K = 0.5–0.7	V′ < 0.4% K > 0.7	V′ < 0.2%; K > 0.7

of settlement can be fitted by a complementary error function (erfc) as suggested by Attewell & Woodman (1982).

The generic settlement can be expressed as:

$$\frac{w}{w_o} = \frac{1}{2} erfc\left(\frac{-\mathrm{y}}{\sqrt{2} \cdot \mathrm{i}}\right) \tag{13}$$

where w_o is the settlement in plane strain that can be calculated following Equation 2.

The Authors also reported six case histories showing that the measured value of settlement at the front may differ from 0.5 w_o as follows form Equation 13, depending on the kind of face support. In fact in open shield excavation in clay, without face support, the volume loss mainly occurs at the front, and the measured surface settlement in that section is closer to 0.5 w_o. On the contrary, in closed shield excavations in sand the volume loss occurs prevalently over the shield and at the shield tail, as also reported by Cording & Hansmire (1975), hence the surface settlement at the front is lower than 0.5 w_o.

The method proposed by Attewell & Farmer (1974) to assess greenfield ground movements induced by tunneling is usually applied to single tunnels in homogeneous (non-layered) ground, or even multiple tunnels if they do not interact each other.

Hansmire & Cording (1985) report the results of a wide monitoring along a stretch of the twin tunnels of Washington Underground. They are able to observe a clear asymmetry in the displacement field above the twin tunnels and to justify it with the low distance between the two tunnels (about 1.5 diameters between the two axes).

Mair & Taylor (1997) report other case histories available in literature and conclude that when the tunnels are very closely spaced, non-negligible shear strains are caused by the construction of the first tunnel. Hence, the resulting reduced stiffness justifies the increase of volume loss when excavating the second tunnel.

It is worth noticing that in fine grained soils the methods allow only for short term 'undrained' settlement evaluation. Calculating long term settlements requires the knowledge of the lining permeability in order to make realistic hypotheses on the induced excess pore-pressures around the excavation (Samarasekera & Eisenstein, 1992; Wongsaroj *et al.*, 2007). The larger increase of settlement with time is generally observed the higher the ratio between the lining permeability and the ground permeability, *i.e.* the more the lining tends to act like a drain.

Some Authors (De la Fuente & Oteo, 1996; Romo & Diaz, 1981) proposed empirical equations for defining the longitudinal surface settlements profile. On the basis of Finite Element analysis results and in situ monitoring and observations, De la Fuente & Oteo (1996) proposed a semi-empirical approach to define the vertical settlement along both cross and longitudinal vertical sections. The settlement along the cross section can be estimated as:

$$w(x) = \Psi \frac{\gamma D^2}{E} (0,85 - \upsilon) \exp\left(-\frac{x^2}{2i^2}\right) \tag{14}$$

where i is the position of the inflection point, Ψ is an empirical parameter to be obtained from monitoring data analysis (0.3–0.7 for clayey soil, Melis *et al.*, 2002), E and ν the ground axial stiffness modulus and Poisson ratio, respectively, D the tunnel diameter and γ the ground unit weight. Moreover, the Authors propose an estimation of the

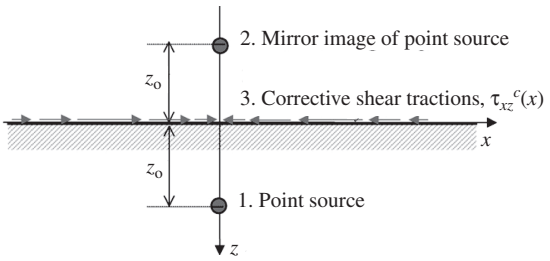


Figure 4 Framework of the analysis by Sagaseta (1987) (adapted after Pinto & Whittle, 2014).

longitudinal settlement profile along the tunnel, where the excavation process affects the progressive ground deformation.

5 ANALYTICAL APPROACHES

A solution for a homogeneous isotropic linear elastic incompressible half-space has been proposed by Sagaseta (1987). The presence of the top free surface is considered by means of a mirror source, symmetric about the boundary with the source of movement, and some results for the elastic half-space (Boussinesq's and Cerruti's solutions). In Figure 4 the framework of the analysis is shown: three solutions are superimposed in order to get the solution of the actual problem, only the third one involves the elastic behavior of the medium.

In plane strain conditions the horizontal (x direction) and vertical (z-direction) displacements at surface are:

$$u_o(x) = -V' \frac{D^2}{4} \frac{x}{x^2 + z_o^2} \tag{15a}$$

$$w_o(x) = V' \frac{D^2}{4} \frac{z_o}{x^2 + z_o^2} \tag{15b}$$

where D is the tunnel diameter, z_o the tunnel axis depth and V′ the volume loss per unit length of excavation.

Uriel & Sagaseta (1989) compared this solution with measurements obtained by Cording & Hansmire (1975) at the Washington Metro. They are similar, but the observed trough appears narrower than the prediction. In the same paper, the Authors extended the solution to include stiffness and stress anisotropy: it seems that the former is much less influent on the displacement field than the latter. In practice, they stated that the solution for the isotropic case can be used with confidence for the analysis of ground movements in anisotropic soils.

Verruijt & Booker (1996) extended the Sagaseta (1987) solution to a compressible ground and accounted for the ovalization of the cavity in the long term. It is worth noticing that the elastic behavior has to be considered in every step of their analysis, contrarily to Sagaseta procedure, in order to account for ground compressibility. Two parameters need to be defined: the first is a uniform radial strain ε, which determines the

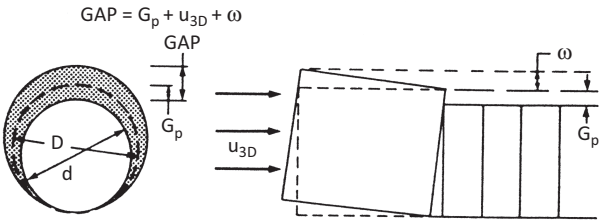


Figure 5 Definition of GAP parameter (Rowe *et al.*, 1983).

ground loss, the second is a dimensionless parameter δ ruling the long-term purely distortional deformation (ovalization) of the tunnel boundary.

Since a uniform contraction of the cavity is assumed, the radial strain ε can be well approximated by half the volume loss per unit length V′.

Loganathan & Poulos (1998) modified the Verruijt & Booker (1996) solution, considering the parameter GAP proposed by Rowe *et al.* (1983) (Figure 5):

$$GAP = G_P + u_{3D} + \omega \tag{16}$$

where G_P is the physical clearance between the ground and the lining, u_{3D} is a term which accounts for the intrusion of soil from the excavation face, ω is an allowance for workmanship, mainly related to the ability of steering the shield. In fact, the gap parameter represents an equivalent crown displacement in a plane strain model, as shown in Figure 5.

The main difficulty of this 'gap' approach is to assess a likely value for the GAP parameter. For cohesive soils Lee *et al.* (1992) show a procedure for evaluating this parameter. The term G_P descends from the shield and lining sizes and it is determined once the machine-support system has been chosen. The term u_{3D} is evaluated by using the results of a parametric three-dimensional numerical analysis. In fact, this analysis has been performed for a circular tunnel in an elasto-plastic half space, excavated in undrained conditions, for given ranges of parameters (E_u/c_u between 200 and 800, z_0/D between 1.5 and 4.5, K_o between 0.6 and 1.4 and a given unit volume weight $\gamma = 20$ kN/m^3). The Authors propose to express the term u_{3D} as a half the maximum axial intrusion at the tunnel face. Finally, they propose to relate the term ω to the elasto-plastic plane strain radial displacement at the crown u if the ground deformation at crown is not restrained by the lining; alternatively they relate ω to the physical gap G_P, if the lining restrains the ground deformation at crown. Hence, they assume:

$$\omega = min\left(\frac{1}{3}u,\ 0.6G_p\right) \tag{17}$$

In order to improve the Verruijt & Booker (1996) solution, Loganathan & Poulos (1998) assumed that the circular cavity contracts in a non-uniform way and the radial displacement varies from zero at the invert to g at the crown, where $g \equiv GAP$.

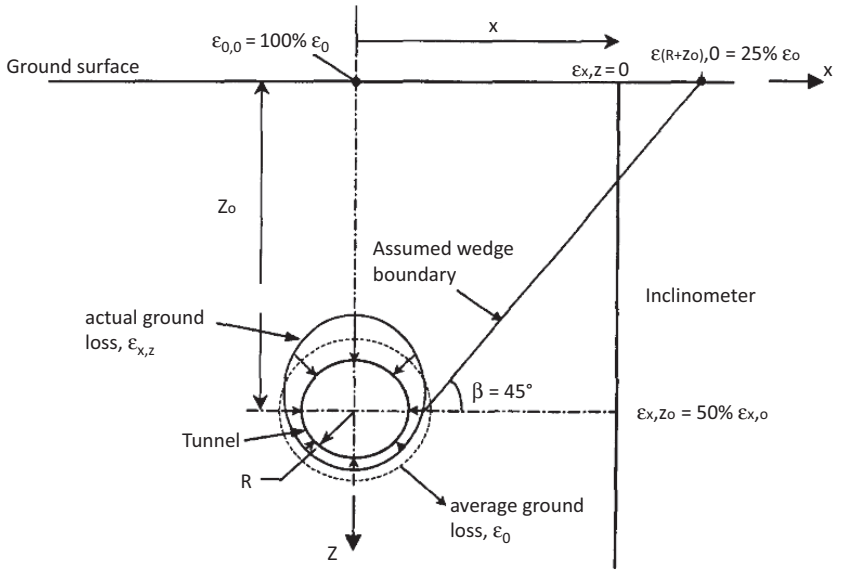


Figure 6 Sketch of the boundary value problem after Loganathan & Poulos (1998).

This assumption leads to modify the expression for ε, that is not constant in the half-plane:

$$\varepsilon_{x,z} = \varepsilon_o \cdot B \exp[-Ax^2] \cdot C \exp[-Dz^2] \tag{18}$$

The parameter ε_o is equivalent to V′ and it is defined through geometrical considerations on the shape of the radial deformation of the cavity boundary as:

$$\varepsilon_o = \frac{2gD + g^2}{D^2} \cong \frac{2g}{D} \tag{19}$$

The parameters A and B are determined by imposing that the surface settlement above the tunnel axis u(0,0) results from the whole volume loss $\varepsilon(0,0) = \varepsilon_o$ whereas the surface settlement at a horizontal distance z_o+R (or z_o+D/2) from the tunnel axis results from 25% of the whole volume loss: $\varepsilon(z_o + R, 0) = 0.25\varepsilon_o$. The parameters C and D are determined by imposing $\varepsilon(x, z_o) = 0.5\varepsilon(x, 0)$: this assumption follows from the shape of the non-uniform distribution of displacement at the tunnel boundary. A sketch of the boundary value problem is shown in Figure 6.

To model an undrained excavation in clay ($\nu = 0.5$), Loganathan & Poulos (1998) assume that no long-term ovalization occurs, hence $\delta = 0$. At surface (z = 0), the displacement components are expressed as:

$$u = -\frac{4gR + g^2}{4R^2} \cdot \exp\left(-\frac{1.38x^2}{(z_0 + R)^2}\right) \cdot \frac{D^2}{4} \cdot \frac{x}{x^2 + z_0^2} \cdot \left[1 + \frac{y}{\sqrt{x^2 + y^2 + z_0^2}}\right] \tag{20a}$$

$$v = \frac{4gR + g^2}{4R^2} \cdot \exp\left(-\frac{1.38x^2}{(z_0 + R)^2}\right) \cdot \frac{D^2}{4} \cdot \frac{1}{\sqrt{x^2 + y^2 + z_0{}^2}} \tag{20b}$$

$$w = \frac{4gR + g^2}{4R^2} \cdot \exp\left(-\frac{1.38x^2}{(z_0 + R)^2}\right) \cdot \frac{D^2}{4} \cdot \frac{z_0}{x^2 + z_0{}^2} \cdot \left[1 + \frac{y}{\sqrt{x^2 + y^2 + z_0{}^2}}\right] \tag{20c}$$

The assessment of the gap parameter is a crucial issue: this parameter permits to take empirically into account the excavation techniques, the three-dimensional effects and the non-linearity of the soil in a linear elastic closed form solution, provided that a sound engineering judgment is adopted.

More recently, Pinto & Whittle (2014) presented a simplified closed-form analytical solutions to predict settlements due to a shallow tunnel in a linear – elastic ground, based on superposition of fundamental singularity solutions (after Sagaseta, 1987) and considering two basic modes of deformation corresponding to uniform convergence and ovalization at the wall of a circular tunnel cavity (after Verruijt & Booker, 1996). The Authors propose a method to account for soil plasticity in the analysis and illustrate closed-form solutions for a three-dimensional tunnel heading obtained by the derivation of 3D ground movements for a spherical cavity point contraction embedded at depth z_0 in an elastic half-space based on the method of singularity superposition (after Sagaseta, 1987; Sen, 1950; Mindlin & Cheng, 1950).

Bobet (2001) developed a solution for the estimation of ground deformation due to shallow tunnels in saturated ground able to take into account both the drainage conditions (short and long terms) and the construction method (face pressure). This solution derives by that developed for deep tunnels considering the relative stiffness method (Einstein & Schwarz, 1979; Bobet, 2001) for a circular cross section tunnel having a depth to radius ratio larger than 1.5 (for neglecting the effect of ground surface). The approach can be applied to the tunnel cross section in homogeneous and isotropic ground under plane strain conditions, considering small deformation and linear elastic behavior for both the ground and lining (assumption more appropriate for stiff clay and rock and shield excavation method). The excavation procedure can be taken into account by defining some parameters as: the geometry and stiffness of the liner (made of steel or prefabricated concrete), the tunnel and the ground; the gap between the tail of the shield and the lining, considered uniform along the tunnel wall; and the internal pressure acting on the tunnel wall and equal to water pressure at the tunnel invert.

In Figure 7 the influence of ground and tunnel geometry, groundwater condition and construction methods on surface settlements are presented.

6 NUMERICAL MODELING

The benefits of the numerical methods over analytical or closed form solutions stem from the possibility of: simulating the construction sequence; dealing with complex ground conditions; modeling realistic ground behavior; handling complex hydraulic conditions; dealing with ground treatment; accounting for adjacent services and structures; simulating intermediate and long-term conditions; dealing with multiple tunnels.

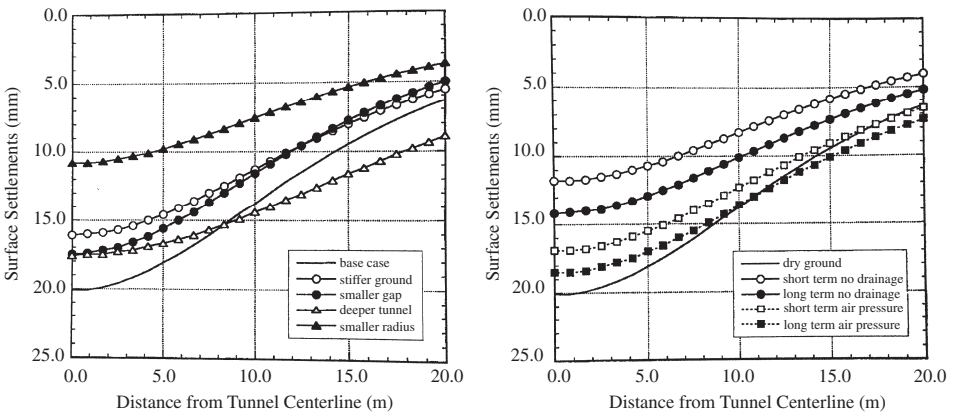


Figure 7 Influence of ground and tunnel geometry (left) and groundwater condition and construction methods (right) on the surface settlements (Bobet, 2001).

Normally, they are conducted in greenfield conditions and they allow to perform a first-second level damage analyses without considering the presence of structure but analyzing more complex ground conditions.

Although the excavation process should be analyzed in three dimensions and a large progress in solving techniques and computational tools has occurred nowadays, bi-dimensional analyses have been the most common in practice even in recent years. For this reason a lot of efforts have been done to establish procedures to take into account three-dimensional effects in plane strain analyses.

Potts & Zdravkovic (2001) listed the following methods widely adopted in the practice to model tunnel excavation in equivalent 2D analyses.

1) 'gap' method (Rowe *et al.*, 1983): a predefined void is introduced in the FE mesh, to represent the total expected volume loss;
2) 'convergence-confinement' method (Panet & Guenot, 1982): the stress release occurring before the installation of the lining is prescribed through a parameter λ;
3) 'progressive softening' method (Swoboda, 1979): this involves the reduction of ground stiffness in the tunnel heading before lining installation (and is therefore more suitable for NATM excavation rather than TBM);
4) 'volume loss control method': the expected volume loss is prescribed, by reducing the stresses at the tunnel boundary until reaching the targeted volume loss, then the lining is installed.

As far as the settlement induced in rock mass by shallow tunnels are concerned, it is necessary to observe that normally they are evident if the tunnel is dug out in very fractured or weathered rock mass. So, for tunnel-induced ground movements analyses in soil as well as in rock mass, 3D continuous models are used in such a way to allow:

1. the modeling of complex ground conditions;
2. the simulation of progressive excavation phases and activation of support elements;
3. the execution of structure-ground coupled analysis that considers their real stiffness and 3D geometry.

An important assumption to be made is the kind of schematization to represent the excavated ground. The definition of the rock mass model has to be set up to analyze the static behavior during excavation. Three basic approaches are usually available which depend on the rock mass structure and rock matrix features: continuum, discontinuum and equivalent continuum. Continuum model can be applied to soil and weak rock where the lithotype mechanical features rule the rock mass behavior. When the rock mass shows higher strength, the other two approaches are adopted, depending on the rock discontinuity patterns. Basically, the discontinuum approach is indicated when the whole rock mass behavior is ruled by the discontinuities, while the equivalent continuous is better at reproducing a material whose stress-strain behavior is due to the characteristics of the rock discontinuity-rock matrix system. Discontinuous approach is typically deemed necessary when the discontinuity sets identify blocks with volumes that are not much smaller than the excavation volumes. Several analytical and numerical methods are available to develop the different described approaches.

Numerical methods available for rock mechanics and rock engineering are widely described by Jing & Hudson (2002) and Jing (2003), who illustrated the peculiarities of the different approaches. Continuum approaches are mostly based on Finite Element Methods (FEM), Finite Difference Method (FDM), or on Boundary Element Methods (BEM). Discontinuum approaches are mostly based on discrete block models like such as Distinct Element Method (DEM), introduced by Cundall (1971) and Discontinuous Deformation Analysis (DDA), introduced by Shi & Goodman (1985).

A synthetic description of the relation between the rock mass structure and the most convenient modeling approach can be based on a rock mass classification system like the Q-system and which is illustrated in Figure 8 (Barton, 1995).

The evaluation of the geotechnical parameters to be used for the calculation of structures in the rock mass is an important aspect of the design of underground excavations. The "input data", to be used for the computation of the stability condition of a tunnel, concern the geological-geotechnical characterization of the rock mass which, in general, includes an evaluation of (Bieniawski, 1984; Barla, 1986):

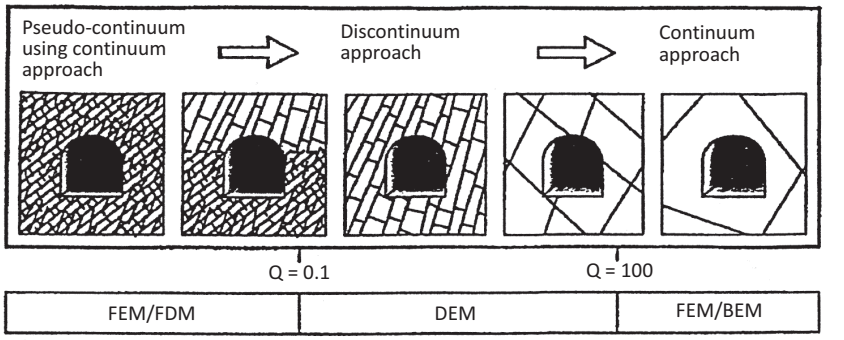


Figure 8 schematic correlation between rock mass condition and modeling approaches based on Q-system (Barton, 1995).

- deformability at short and long terms;
- strength characteristics;
- permeability characteristics;
- natural state of stress, hydraulic conditions another natural loads.

The required design parameters and the criteria adopted for their determination are closely related to the model used in the design stage.

The parameters that are used to represent the behavior of the rock mass are different depending on whether it should be considered a discontinuous medium or may be idealized as an equivalent continuum.

When the rock mass must be represented by a discontinuous model, the parameters of deformability and strength concern both the intact rock and the discontinuities. Classic laboratory tests on discontinuities and matrix can be performed to this purpose. DEM modeling requires a deep knowledge of the geometry of discontinuities. Advanced surveying techniques (Ferrero *et al.*, 2009) and models for the reconstruction of the set of blocks (Dershowitz & Einstein, 1988) are a useful support to the development of discontinuous models.

When the rock mass can be represented by an equivalent continuum, it is necessary to distribute the effect of the discontinuities over the entire volume of rock, thus considering a "homogenized" medium. The law that describe the mechanical behavior of such equivalent continuum is characterized by global deformability and strength parameters.

The equivalent continuum medium is generally considered isotropic, homogeneous and having a linear elastic behavior (described by the generalized law of Hooke).

In reality, the presence of discontinuities can make the behavior of the rock mass strongly anisotropic, especially in the case of weakly fractured rock masses or where discontinuities have a strong orientation recurrence. In this case, Min & Jing (2004) have shown that both the axial stiffness modulus E_{RM} and the Poisson's ratio of the rock mass can be strongly influenced by the orientation of the discontinuities. Figure 9 shows the strong variability of elastic modulus and Poisson's ratio (calculated as the ratio of strain in the y-axis to the x-axis when stress is applied in the x-axis direction) in relation to the rotation of the plans of discontinuity. In this case a transversely isotropic medium characterized by an axis of symmetry with isotropy plane orthogonal to it may be adopted. The authors also show how another factor that can greatly influence the elastic behavior of a rock mass as, for example, the state of stress. Figure 10 shows the variability of the elastic properties of the rock mass obtained through numerical simulations on a highly fractured rock mass; one can see that by increasing the stress state the rock mass becomes gradually more and more rigid and less deformable laterally.

The deformability and strength parameters of the equivalent continuum must be representative of a global behavior of the rock mass; for this reason in situ tests should be performed on rock mass which must have significant volume. These tests are not only economically burdensome, but also difficult to perform. For these reasons, in engineering practice, empirical relations, developed in recent decades by various authors, are used. These relations allow the parameters characteristic of the mechanical behavior to be correlated with the indexes of quality of the rock mass.

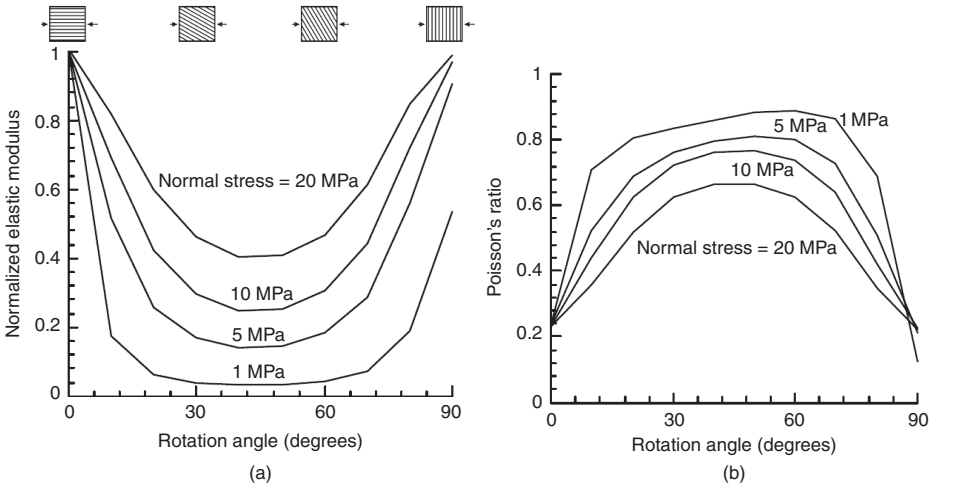


Figure 9 Variability of the elastic properties with the rotation of discontinuity orientation and for different values of the stress conditions. (a) Elastic Modulus, (b) Poisson's ratio. (Min & Jing, 2004).

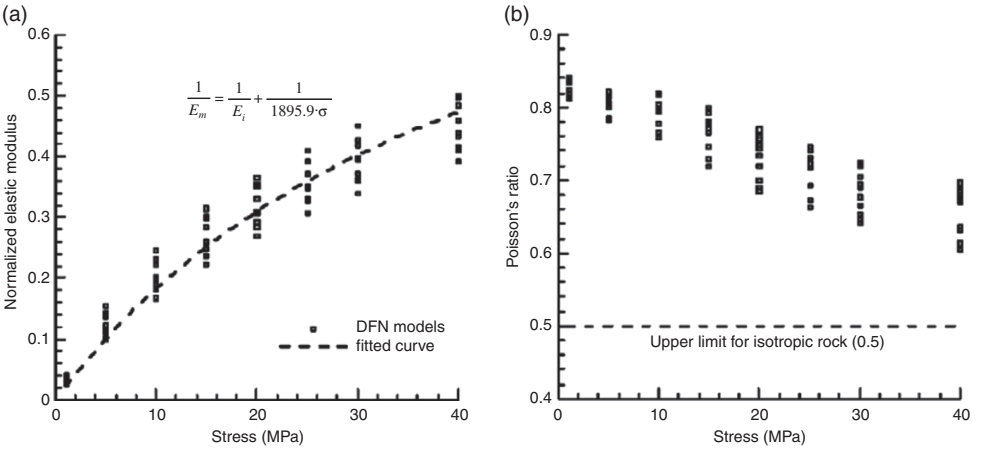


Figure 10 Variability of the elastic properties with stress conditions. (a) Elastic Modulus, (b) Poisson's ratio. (Min & Jing, 2004).

The modulus of deformability of the rock is the geomechanical parameter that best represents the mechanical behavior of the rock mass in the elastic range.

The empirical equations available in the technical literature relate the deformability module E_{RM} with the quality indexes of the rock mass. Those proposed by Bieniawski (1978), Serafim & Pereira (1983), Nicholson & Bieniawski (1990), Mitri *et al.* (1994) and Verman (1997) consider the RMR index sometimes together with other mechanical quantities of the rock, such as the modulus of elasticity the intact rock E_i or

geometric characteristics of the work in the project. Those indicated by Barton (1980, 1995) concerning the index Q, either in its formulation classical or in the correct one, Qc, take in to account the uniaxial compressive rock strength. Palmstrøm (1996) and Palmstrøm & Singh (2001) proposed to link the deformability modulus of fractured rock mass, E_{RM}, to the value of Rock Mass index (RMi). More recently, Hoek & Diederichs (2006) proposed a relation (reported below) useful for the estimation of the deformability modulus of fractured rock mass E_{RM}

$$E_{RM} = E_i \left(0.02 + \frac{1 - D/2}{1 + \exp^{\frac{60+15D-GSI}{11}}} \right) \tag{21}$$

where E_i is the deformability modulus of intact rock, GSI is the value of Geological Strength Index (Hoek *et al.*, 1998) and D is the disturbance factor, taking into account the excavation methods.

GSI and RMR indexes allow to obtain the parameters of shear strength with reference to several failure criteria. A nonlinear criterion best describes the dependency of the strength of the rock mass on the state of stress to which it is subject. For this reason, generally, the Hoek & Brown (1997) and Hoek *et al.* (2002) strength criterion is used.

As aforementioned, the ground deformation process induced by shallow tunnel is strongly affected not only by the ground mechanical features but also by the tunneling technologies and procedures. The latter are taken into account in the empirical approaches through single empirical coefficients whose value considers the whole excavation process. Analytical solutions are able to explicitly consider only some technological parameters (*e.g.* pressure applied at the tunnel face, liner, etc.). On the other hand, numerical models, and particularly the fully 3D models, are able to simulate all the excavation phases and the activation of support elements.

The 3D greenfield analysis can be also useful to study the influence of parameters representing ground conditions, geometry of the tunnel (diameter, depth) and further technological issues such as:

- shield length and unsupported tunnel length;
- different conditions of the pressure applied on tunnel face (uniform or incremental distribution, equal or larger than the initial stress),
- presence of tunnel shield that allows an initial limited free convergence of tunnel wall,
- activation of pre-cast lining and grout-filling of the clearance between tunnel wall and lining.

These analyses can improve the predictive capabilities of the displacement field as implemented by empirical and analytical formulations.

In Figure 11 an example of fully 3D FEM model (Migliazza *et al.*, 2008) carried out in greenfield condition with two soil layers and a free water surface, simulating the excavation process with a step by step approach, is reported as well as the comparison between the numerical results and monitoring data in term of vertical settlement. Once calibrated against monitoring data along greenfield stretches of the tunnel, the same numerical model can be adapted to perform an analysis of soil-structure interaction for the assessment of the response to tunneling of buildings that are located along the tunnel path.

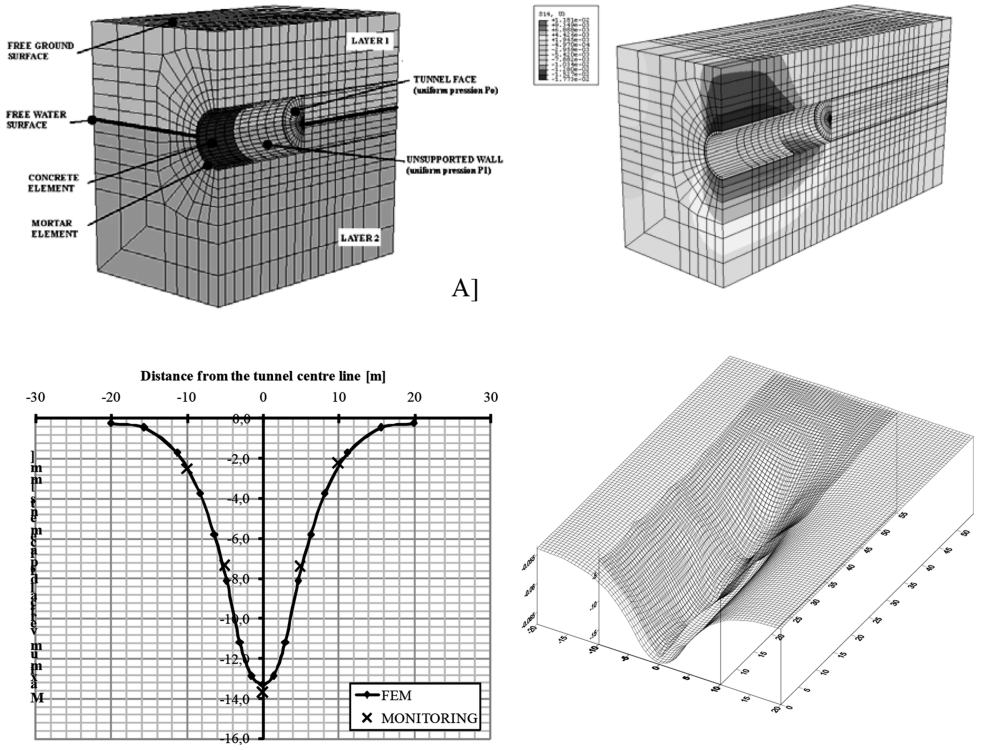


Figure 11 Example of fully 3D FEM model of a shallow tunnel with the comparison of vertical displacements field obtained from FEM and in situ topographical survey (Migliazza *et al.*, 2008).

SYMBOL LIST

0,x,y,z	Reference system used for ground displacement definition: x is the horizontal axis parallel to the tunnel cross vertical section; y is the horizontal axis parallel to the tunnel axis; z is the vertical downward axis crossing the tunnel center; the origin 0 is at the ground surface
z_o	Center tunnel depth
D, R	Tunnel diameter and radius
u, v, w	Components of displacement along the x, y and z directions respectively
w_o, w(0,z)	Maximum settlement and maximum sub-surface vertical displacement in correspondence of the tunnel centerline
$w_o(x)$, w(x,z)	Settlement and vertical sub-surface displacement in cross vertical section
$w_o(y)$	Settlement profile along the axial vertical section
$u_o(x)$, u(x,z)	Horizontal surface and subsurface displacement profile in the cross section

ε_o, $\varepsilon_x(x)$	Maximum horizontal strain component and surface horizontal strain profile
V′, Vs, V_T	Volume loss, Volume of settlement trough and Volume excavated, respectively
i, i(z)	Distance from the tunnel centerline of the inflection point of the vertical displacement profile in correspondence of the ground surface and sub-surface, respectively
K, K_z	Empirical parameter for defining the inflection point position i in surface and sub-surface, respectively.
b,m	Empirical parameter for defining the inflection point position i(z) (Moh *et al.*, 1996)
Ψ	Empirical parameter of the De la Fuente & Oteo method (1996)
E,ν	Axial stiffness modulus and Poisson ratio, respectively
E_i, E_{RM}	Deformability modulus of intact rock and rock masses, respectively
c_u	Undrained shear strength
Ko	Coefficient of earth pressure at rest
γ	Ground total unit weight
GAP, g	Tunnel cavity contraction (Rowe *et al.*, 1996)
Gp	Physical clearance between the ground and the lining
U_{3d}	Term accounting for the intrusion of soil from the excavation face
ω	Term accounting for workmanship

REFERENCES

Attewell, P.B. and Farmer, I.W. (1974) Ground deformations resulting from shield tunnelling in London Clay. *Canadian Geotechnical Journal*, 11(3), 380–395.

Attewell, P.B. and Woodman, J.P. (1982) Predicting the dynamics of ground settlement and its derivatives caused by tunnelling in soil. *Ground Engineering*, 15(7), 13–22.

Attewell, P.B., Yeates, J. and Selby, A.R. (1986) *Soil movements induced by tunnelling and their effects on pipelines and structure*. Blackie, Glasgow.

Barla, G. (1986) Introduzione. Proceedings of the 1° Ciclo di conferenze di meccanica e ingegneria delle rocce MIR, SGE Editoriali.

Barton, N., Løset, F., Lien, R. and Lunde, J. (1980) Application of the Q-system in design decision concerning dimensions and appropriate support for underground installations. *International Conference on Subsurface Space*, Rockstore, Stockholm, Vol. 2, 553–561.

Barton, N. (1995) The influence of joint properties in modelling jointed rock mass, Keynote Lecture. *8th Congress ISRM*, Tokyo, Vol. 3.

Bieniawski, Z.T. (1978) Determining rock mass deformability, Experience from case histories. *International Journal of Rock Mechanics and Mining Sciences & Geomechanics Abstracts*, 15, 237–247.

Bobet, A. (2001) Analytical solutions for shallow tunnels in saturated ground. *Journal of Engineering Mechanics*, 127(12), 1258–1266.

Burland, J.B. (1995) Assessment of risk of damage to buildings due to tunnelling and excavations. Invited special lecture. *Proc. 1st International Conference on Earthquake Geotechnical Engineering*, ISTokyo'95, 1189–1201.

Chiriotti, E., Marchionni, V. and Grasso, P. (2001) Porto Light Metro System, Lines C, S and J. Interpretation of the Results of the Building Condition Survey and Preliminary Assessment of

Risk. Methodology for Assessing the Tunnelling Induced Risks on Buildings along the Tunnel Alignment. Normetro – Transmetro, Internal technical report (in Italian and Portuguese).
Chiriotti, E., Grasso, P., Gaj, F. and Giacomini, G. (2004) Risk control for mechanized tunnelling in urban areas. *Proc. IX National Geotechnical Congress*, Aveiro, Portugal.
Cording, E.J. and Hansmire, W.H. (1975) Displacements around soft ground tunnels. *General Report 5th Pan American Conference on Soil Mechanics and Foundation Engineering*, Buenos Aires, Session IV, 571–632.
Cording, E.J. (1991) Control of ground movements around tunnels in soil. General report. *Proc. 9th Pan American Conference on Soil Mechanics and Foundation Engineering*, Chile.
Cundall, P. (1971) A computer model for simulating progressive large scale movements in blocky rock systems. Rock Fracture. *Proc. International Symposium on Rock Fracture*.
De la Fuente, P. and Oteo, C. (1996) Theoretical research on the subsidence originated by the underground construction in urban areas. *Proc. Danube International Symposium*, Rumania.
Dershowitz, W.S. and Einstein, H.H. (1988) Characterizing Rock Joint Geometry with Joint System Models. *Rock Mechanics and Rock Engineering*, 1(1), 21–51.
Ferrero, A.M., Forlani, G., Roncella, R. and Voyat, H.I. (2008) Advanced geo structural survey methods applied to rock mass characterization. *Rock mechanics and Rock Engineering*. Springer Wien New York. August 2009, Vol. 42, Issue 4, 631–665. DOI 10.1007/s00603-008-0010-4.
Franzius, J.N. (2003) *Behaviour of buildings due to tunnel induced subsidence*. PhD Thesis, Imperial College London, 1–358.
Grant, R.J. and Taylor, R.N. (2000) Stability of tunnels in clay with overlying layers of coarse grained soil. *GeoEng2000: An International Conference on Geotechnical & Geological Engineering*, Melbourne, Australia.
Grasso, P., Xu, S., Del Fedele, M., Russo, G. and Chiriotti, E. (2003) Particular failure mechanism of weathered granite observed during construction of metro tunnels by TBM. In *(Re) Claiming the Underground Space, Proceedings of the ITA World Tunnelling Congress 2003, Amsterdam, Balkema, The Netherlands*, 497–503.
Grasso, P., Chiriotti, E., Xu, S. and Kazilis, N. (2007) Use of risk management plan for urban mechanized tunnelling projects: From the establishment of the method to the successful practice. *Proceedings of the 33rd ITA-AITES World Tunnel Congress – Underground Space – The 4th Dimension of Metropolises*, Vol. 2, 1535–1540.
Guglielmetti, V., Grasso, P., Mahtab, A. and Xu, S. (2008) Mechanized Tunnelling in Urban Areas: Design Methodology and Construction Control. Taylor & Francis/ Balkema, Leiden, The Netherlands, 1–507.
Hansmire, W.H. and Cording, E.J. (1985) Soil tunnel test section: Case history summary. *Journal of Geotechnical Engineering (ASCE)*, 111(11), 1301–1320.
Hoek, E. and Brown, E.T. (1997) Practical estimates of rock mass strength. *International Journal of Rock Mechanics and Mining Sciences*, 8(34), 1165–1186.
Hoek, E., Marinos, P. and Benissi, M. (1998) Applicability of the Geological Strength Index (GSI) classification for very weak and sheared rock masses. The case of the Athens Schist Formation. *Bulletin Engineering Geology and the Environment*, 57(2), 151–160.
Hoek, E., Carranza-Torres, C.T. and Corkum, B. (2002) Hoek-Brown failure criterion – 2002 edition. *Proc. North American Rock Mechanics Society*, Toronto, July.
Hoek, E. and Diederichs, M.S. (2006) Empirical estimation of rock mass modulus. *International Journal of Rock Mechanics and Mining Sciences*, 43, 203–215.
Jing, L. and Hudson, J.A. (2002) Numerical methods in rock mechanics. *International Journal of Rock Mechanics and Mining Sciences*, 39(4), 409–427.
Jing, L. (2003) Review of techniques, advances and outstanding issues in numerical modelling for rock mechanics and rock engineering. *International Journal of Rock Mechanics and Mining Sciences*, 40(3), 283–353

Lee, K.M., Kerry Rowe, R. and Lo, K.Y. (1992a) Subsidence owing to tunnelling. I. Estimating the gap parameter. *Canadian Geotechnical Journal*, 29, 929–940.

Lee, K.M., Kerry Rowe, R. and Lo, K.Y. (1992b) Subsidence owing to tunnelling. II. Evaluation of a prediction technique. *Canadian Geotechnical Journal*, 29, 941–954.

Loganathan, N. and Poulos, H.G. (1998) Analytical prediction for tunneling-induced ground movements in clays. *Journal of Geotechnical and Geoenvironmental Engineering*, 124(9), 846–856.

Mair, R., Taylor, R. and Bracegirdle, A. (1993) Subsurface settlement profiles above tunnels in clays. *Géotechnique*, 43(2), 315–320.

Mair, R.J., Taylor, R.N. and Burland, J.B. (1996) Prediction of ground movements and assessment of risk of building damage due to bored tunneling. *Proc. International Symposium on Geotechnical Aspects of Underground Construction in Soft Ground*, Blakema, 713–718.

Mair, R.J. and Taylor, R.N. (1997) Bored tunnelling in the urban environment. *Theme Lecture, 14th ECSMGE – Hamburg*, 2353–2385

Melis, M., Medina, L. and Rodriguez, J.M. (2002) Prediction and analysis of subsidence induced by shield tunnelling in the Madrid Metro extension. *Canadian Geotechnical Journal*, 39, 1273–1287.

Migliazza, M., Chiorboli, M. and Giani, G.P. (2008) Comparison of analytical method, 3D finite element model with experimental subsidence measurements resulting from the extension of the Milan underground. *Computers and Geotechnics*, 36, 113–124.

Min, K.B. and L. Jing (2004) Stress dependent mechanical properties and bounds of Poisson's ratio for fractured rock masses investigated by a DFN-DEM technique. *Proc. SINOROCK2004 Symposium, International Journal of Rock Mechanics and Mining Sciences*, 41, No. 3, CD_ROM.

Mindlin, R.D. and Cheng, D.H. (1950) Thermoelastic stress in the semi-infinite solid. *Journal of Applied Physics*, 21, 931–935.

Mitri, H.S., Edrissi, R. and Henning, J. (1994) Finite element modelling of cable-bolted stopes in hard rock ground mines. *SME Annual Meeting*, Albuquerque, 94–116.

Moh, Z.C., Hwang, R.N. and Ju, D.H. (1996) Ground movements around tunnels in soft ground. *Geotechnical Aspects of Underground Construction in Soft Ground* – Mair & Taylor (eds), Balkema, Rotterdam, 725–730.

Nicholson, G.A. and Bieniawski, Z.T. (1990) A nonlinear deformation modulus based on rock mass classification. *International Journal of Mining and Geo-Engineering*, 8, 181–202.

O'Reilly, M.P. and New, B.M. (1982) Settlements above tunnels in the United Kingdom – their magnitude and prediction. *Proc. Tunnelling '82 Symposium, Institution of Mining and Metallurgy*, London, 55–64.

Palmstrøm, A. (1996a) Characterization of rock masses by the RMi for use in practical rock engineering (part 1). *Tunnelling and Underground Space Technology*, 11(2), 175–186.

Palmstrøm, A. (1996b) Characterization of rock masses by the RMi for use in practical rock engineering (part 2). *Tunnelling and Underground Space Technology*, 11(3), 287–303.

Palmstrøm, A. and Singh, R. (2001) The deformation modulus of rock masses – comparison between in situ tests and indirect estimates. *Tunnelling and Underground Space Technology*, 16(2), 115–131.

Panet, M., and Guenot, A. (1982) Analysis of convergence behind the face of a tunnel. *Proc. International Conference on Tunnelling*, The Institution of Mining and Metallurgy, Brighton, 197–204

Peck, R.B. (1969) Deep excavations and tunneling in soft ground. *Proc. 7th Pan American Conference on Soil Mechanics and Foundation Engineering*, State of the art volume, Sociedad Mexican de Mecanica de Suelos, 225–290.

Pinto F., Whittle A. (2014). Ground movement due to shallow tunnels in soft ground. I: Analytical solution. *J. Geotech. Geoenviron. Engng*, 2014, 140, No. 4: 04013040.

Potts, D.M and Addenbrooke, T.I. (1997) A structure's influence on tunneling-induced ground movements. *Proc. Institution of Civil Engineers-civil Engineering*, 125, 109–125.

Potts, D.M. and Zdravković, L. (2001) *Finite Element Analysis in Geotechnical Engineering. Applications*. Thomas Telford, London, UK.

Romo, M P. and Diaz, M. (1981) Face stability and ground settlement in shield tunneling. *Proc. 10th International Conference on Soil Mechanics and Foundation Engineering*, Stockholm, 357–360.

Rowe, R.K., Lo, K.Y. and Kack, G.J. (1983) A method of estimating surface settlement above tunnels constructed in soft ground. *Canadian Geotechnical Journal*, 20, 11–22.

Sagaseta, C. (1987) Analysis of undrained soil deformation due to ground loss. *Géotechnique*, 37 (3), 301–320.

Samarasekera, L. and Eisenstein, Z. (1992) Pore pressure around tunnels in clay. *Canadian Geotechnical Journal*, 29, 819–831.

Sen, B. (1950) Note on the stresses produced by nuclei of thermo-elastic strain in a semi-infinite elastic solid. *Quarterly Applied Mathematics*, 8, 365–369.

Serafim JL, Pereira JP Considerations on the geomechanical classification of Bieniawski (1983). In: International Symposium on Engineering Geology and Underground Openings, Portugal, Lisbon, SPG, 1133–1144.

Shi, G. and Goodman, R.E. (1985) Two dimensional discontinuous deformation analysis. *International Journal for Numerical and Analytical Methods Geomechanics*, 9, 541–556.

Swoboda, G. (1979) Finite element analysis of the New Austrian Tunnelling Method (NATM). In: *Proc. 3rd International Conference on Numerical Methods in Geomechanics*, Vol. 2, Aachen, 581–586.

Uriel, A.O. and Sagaseta, C. (1989) Selection of design parameters for underground construction. *Proc. 12th ICSMFE*, Rio de Janeiro, 4, 2521–2551.

Verman, M., Singh, B., Viladkar, M.N. and Jethua, J.L. (1997) Effect of tunnel depth on modulus of deformation of rock mass. *Rock mechanics and Rock Engineering*, 30(3), 121–127.

Verruijt, A. and Booker, J.R. (1996) Surface settlements due to deformation of a tunnel in a elastic half plane. *Géotechnique*, 46(4), 753–756.

Wongsaroj, J., Soga, K. and Mair, R.J. (2007) Modelling of long-term ground response to tunnelling under St James's Park, London. *Géotechnique*, 57(1), 75–90.



Taylor & Francis
Taylor & Francis Group
http://taylorandfrancis.com

The five-volume set *Rock Mechanics and Engineering* consists of the following volumes

Volume 1: Principles
ISBN: 978-1-138-02759-6 (Hardback)
ISBN: 978-1-315-36426-1 (eBook)

Volume 2: Laboratory and Field Testing
ISBN: 978-1-138-02760-2 (Hardback)
ISBN: 978-1-315-36425-4 (eBook)

Volume 3: Analysis, Modeling and Design
ISBN: 978-1-138-02761-9 (Hardback)
ISBN: 978-1-315-36424-7 (eBook)

Volume 4: Excavation, Support and Monitoring
ISBN: 978-1-138-02762-6 (Hardback)
ISBN: 978-1-315-36423-0 (eBook)

Volume 5: Surface and Underground Projects
ISBN: 978-1-138-02763-3 (Hardback)
ISBN: 978-1-315-36422-3 (eBook)